

# RECENT ADVANCES IN THERMALLY ACTIVATED DELAYED FLUORESCENCE MATERIALS

EDITED BY: Eli Zysman-Colman, Sebastian Reineke, Guohua Xie and  
Chihaya Adachi  
PUBLISHED IN: Frontiers in Chemistry





# frontiers

## Frontiers eBook Copyright Statement

The copyright in the text of individual articles in this eBook is the property of their respective authors or their respective institutions or funders. The copyright in graphics and images within each article may be subject to copyright of other parties. In both cases this is subject to a license granted to Frontiers.

The compilation of articles constituting this eBook is the property of Frontiers.

Each article within this eBook, and the eBook itself, are published under the most recent version of the Creative Commons CC-BY licence.

The version current at the date of publication of this eBook is CC-BY 4.0. If the CC-BY licence is updated, the licence granted by Frontiers is automatically updated to the new version.

When exercising any right under the CC-BY licence, Frontiers must be attributed as the original publisher of the article or eBook, as applicable.

Authors have the responsibility of ensuring that any graphics or other materials which are the property of others may be included in the CC-BY licence, but this should be checked before relying on the CC-BY licence to reproduce those materials. Any copyright notices relating to those materials must be complied with.

Copyright and source acknowledgement notices may not be removed and must be displayed in any copy, derivative work or partial copy which includes the elements in question.

All copyright, and all rights therein, are protected by national and international copyright laws. The above represents a summary only. For further information please read Frontiers' Conditions for Website Use and Copyright Statement, and the applicable CC-BY licence.

ISSN 1664-8714

ISBN 978-2-88966-393-4

DOI 10.3389/978-2-88966-393-4

## About Frontiers

Frontiers is more than just an open-access publisher of scholarly articles: it is a pioneering approach to the world of academia, radically improving the way scholarly research is managed. The grand vision of Frontiers is a world where all people have an equal opportunity to seek, share and generate knowledge. Frontiers provides immediate and permanent online open access to all its publications, but this alone is not enough to realize our grand goals.

## Frontiers Journal Series

The Frontiers Journal Series is a multi-tier and interdisciplinary set of open-access, online journals, promising a paradigm shift from the current review, selection and dissemination processes in academic publishing. All Frontiers journals are driven by researchers for researchers; therefore, they constitute a service to the scholarly community. At the same time, the Frontiers Journal Series operates on a revolutionary invention, the tiered publishing system, initially addressing specific communities of scholars, and gradually climbing up to broader public understanding, thus serving the interests of the lay society, too.

## Dedication to Quality

Each Frontiers article is a landmark of the highest quality, thanks to genuinely collaborative interactions between authors and review editors, who include some of the world's best academicians. Research must be certified by peers before entering a stream of knowledge that may eventually reach the public - and shape society; therefore, Frontiers only applies the most rigorous and unbiased reviews.

Frontiers revolutionizes research publishing by freely delivering the most outstanding research, evaluated with no bias from both the academic and social point of view. By applying the most advanced information technologies, Frontiers is catapulting scholarly publishing into a new generation.

## What are Frontiers Research Topics?

Frontiers Research Topics are very popular trademarks of the Frontiers Journals Series: they are collections of at least ten articles, all centered on a particular subject. With their unique mix of varied contributions from Original Research to Review Articles, Frontiers Research Topics unify the most influential researchers, the latest key findings and historical advances in a hot research area! Find out more on how to host your own Frontiers Research Topic or contribute to one as an author by contacting the Frontiers Editorial Office: [frontiersin.org/about/contact](http://frontiersin.org/about/contact)



# RECENT ADVANCES IN THERMALLY ACTIVATED DELAYED FLUORESCENCE MATERIALS

Topic Editors:

**Eli Zysman-Colman**, University of St Andrews, United Kingdom

**Sebastian Reineke**, Technische Universität Dresden, Germany

**Guohua Xie**, Wuhan University, China

**Chihaya Adachi**, Kyushu University, Japan

**Citation:** Zysman-Colman, E., Reineke, S., Xie, G., Adachi, C., eds. (2021). Recent Advances in Thermally Activated Delayed Fluorescence Materials. Lausanne: Frontiers Media SA. doi: 10.3389/978-2-88966-393-4

# Table of Contents

- 06 Editorial: Recent Advances in Thermally Activated Delayed Fluorescence Materials**  
Chihaya Adachi, Guohua Xie, Sebastian Reineke and Eli Zysman-Colman
- 08 Organic Light-Emitting Diodes Based on Conjugation-Induced Thermally Activated Delayed Fluorescence Polymers: Interplay Between Intra- and Intermolecular Charge Transfer States**  
Yungui Li, Qiang Wei, Liang Cao, Felix Fries, Matteo Cucchi, Zhongbin Wu, Reinhard Scholz, Simone Lenk, Brigitte Voit, Ziyi Ge and Sebastian Reineke
- 20 Synthesis and Electroluminescent Properties of Through-Space Charge Transfer Polymers Containing Acridan Donor and Triarylboron Acceptors**  
Fan Chen, Jun Hu, Xingdong Wang, Shiyang Shao, Lixiang Wang, Xiabin Jing and Fosong Wang
- 30 5H-Benzo[d]Benzo[4,5]Imidazo[2,1-b][1,3]Thiazine as a Novel Electron-Acceptor Cored High Triplet Energy Bipolar Host Material for Efficient Solution-Processable Thermally Activated Delayed Fluorescence Organic Light-Emitting Diodes**  
Mallesham Godumala, Jiwon Yoon, Seo Yeon Park, Chiho Lee, Youngseo Kim, Ji-Eun Jeong, Sungnam Park, Han Young Woo, Min Ju Cho and Dong Hoon Choi
- 39 Sensitizing TADF Absorption Using Variable Length Oligo(phenylene ethynylene) Antennae**  
Olga Franco, Marius Jakoby, Rebekka V. Schneider, Fabian Hundemer, Daniel Hahn, Bryce S. Richards, Stefan Bräse, Michael A. R. Meier, Uli Lemmer and Ian A. Howard
- 48 Asymmetric Thermally Activated Delayed Fluorescence Materials With Aggregation-Induced Emission for High-Efficiency Organic Light-Emitting Diodes**  
Huanhuan Li, Yibin Zhi, Yizhong Dai, Yunbo Jiang, Qingqing Yang, Mingguang Li, Ping Li, Ye Tao, Hui Li, Wei Huang and Runfeng Chen
- 55 Efficient Aggregation-Induced Delayed Fluorescence Luminogens for Solution-Processed OLEDs With Small Efficiency Roll-Off**  
Zheyi Cai, Hao Chen, Jingjing Guo, Zujin Zhao and Ben Zhong Tang
- 64 Stimuli-Responsive Thermally Activated Delayed Fluorescence in Polymer Nanoparticles and Thin Films: Applications in Chemical Sensing and Imaging**  
Nathan R. Paisley, Christopher M. Tonge and Zachary M. Hudson
- 78 Trap-Controlled White Electroluminescence From a Single Red-Emitting Thermally Activated Delayed Fluorescence Polymer**  
Yun Yang, Liuqing Yang, Xuefei Li, Lei Zhao, Shumeng Wang, Junqiao Ding and Lixiang Wang
- 88 Saturated Red Electroluminescence From Thermally Activated Delayed Fluorescence Conjugated Polymers**  
Hongmei Zhan, Yanjie Wang, Kuofei Li, Yuannan Chen, Xiaohu Yi, Keyan Bai, Guohua Xie and Yanxiang Cheng

- 97 ***Molecular Design Based on Donor-Weak Donor Scaffold for Blue Thermally-Activated Delayed Fluorescence Designed by Combinatorial DFT Calculations***  
Youichi Tsuchiya, Keita Tsuji, Ko Inada, Fatima Bencheikh, Yan Geng, H. Shaun Kwak, Thomas J. L. Mustard, Mathew D. Halls, Hajime Nakanotani and Chihaya Adachi
- 107 ***TADF Dye-Loaded Nanoparticles for Fluorescence Live-Cell Imaging***  
Carina I. C. Crucho, João Avó, Ana M. Diniz, Sandra N. Pinto, José Barbosa, Poppy O. Smith, Mário Nuno Berberan-Santos, Lars-Olof Pålsson and Fernando B. Dias
- 121 ***Highly Efficient Deep Blue Luminescence of 2-Coordinate Coinage Metal Complexes Bearing Bulky NHC Benzimidazolyl Carbene***  
Rasha Hamze, Muazzam Idris, Daniel Sylvinson Muthiah Ravinson, Moon Chul Jung, Ralf Haiges, Peter I. Djurovich and Mark E. Thompson
- 130 ***High-Efficiency Diphenylpyrimidine Derivatives Blue Thermally Activated Delayed Fluorescence Organic Light-Emitting Diodes***  
Sunyoung Sohn, Min Woo Ha, Jiyong Park, Yoo-Heon Kim, Hyungju Ahn, Sungjune Jung, Soon-Ki Kwon and Yun-Hi Kim
- 139 ***Recent Advancement in Boron-Based Efficient and Pure Blue Thermally Activated Delayed Fluorescence Materials for Organic Light-Emitting Diodes***  
Hyuna Lee, Durai Karthik, Raju Lampane, Jae Hong Ryu and Jang Hyuk Kwon
- 155 ***Molecular Orientations of Delayed Fluorescent Emitters in a Series of Carbazole-Based Host Materials***  
Hisahiro Sasabe, Yuki Chikayasu, Satoru Ohisa, Hiroki Arai, Tatsuya Ohsawa, Ryutaro Komatsu, Yuichiro Watanabe, Daisuke Yokoyama and Junji Kido
- 164 ***Impact of Boron Acceptors on the TADF Properties of Ortho-Donor-Appended Triarylboron Emitters***  
Hanif Mubarak, Woochan Lee, Taehwan Lee, Jaehoon Jung, Seunghyup Yoo and Min Hyung Lee
- 174 ***Recent Developments on Multi-Functional Metal-Free Mechanochromic Luminescence and Thermally Activated Delayed Fluorescence Organic Materials***  
Debasish Barman, Rajdikshit Gogoi, Kavita Narang and Parameswar Krishnan Iyer
- 195 ***High Triplet Energy Host Materials for Blue TADF OLEDs—A Tool Box Approach***  
Francesco Rodella, Sergey Bagnich, Eimantas Duda, Tobias Meier, Julian Kahle, Stavros Athanasopoulos, Anna Köhler and Peter Strohhriegl
- 211 ***Recent Advances in Metal-TADF Emitters and Their Application in Organic Light-Emitting Diodes***  
Wai-Pong To, Gang Cheng, Glenna So Ming Tong, Dongling Zhou and Chi-Ming Che
- 218 ***Recent Advances in Thermally Activated Delayed Fluorescent Polymer—Molecular Designing Strategies***  
Xia Yin, Ying He, Xu Wang, Zexin Wu, Erbao Pang, Jing Xu and Jun-an Wang

- 241 Conformation Control of Iminodibenzyl-Based Thermally Activated Delayed Fluorescence Material by Tilted Face-to-Face Alignment With Optimal Distance (tFFO) Design**  
Yu Kusakabe, Yoshimasa Wada, Hiromichi Nakagawa, Katsuyuki Shizu and Hironori Kaji
- 250 What Controls the Orientation of TADF Emitters?**  
Bilal A. Naqvi, Markus Schmid, Ettore Crovini, Prakhar Sahay, Tassilo Naujoks, Francesco Rodella, Zhen Zhang, Peter Strohriegl, Stefan Bräse, Eli Zysman-Colman and Wolfgang Brütting
- 261 Corrigendum: What Controls the Orientation of TADF Emitters?**  
Bilal A. Naqvi, Markus Schmid, Ettore Crovini, Prakhar Sahay, Tassilo Naujoks, Francesco Rodella, Zhen Zhang, Peter Strohriegl, Stefan Bräse, Eli Zysman-Colman and Wolfgang Brütting
- 263 Thermally Activated Delayed Fluorescence: Beyond the Single Molecule**  
Marc K. Etherington
- 271 OBO-Fused Benzo[fg]tetracene as Acceptor With Potential for Thermally Activated Delayed Fluorescence Emitters**  
Zhen Zhang, Shiv Kumar, Sergey Bagnich, Eduard Spuling, Fabian Hundemer, Martin Nieger, Zahid Hassan, Anna Köhler, Eli Zysman-Colman and Stefan Bräse
- 284 Design, Synthesis, and Temperature-Driven Molecular Conformation-Dependent Delayed Fluorescence Characteristics of Dianthrylboron-Based Donor–Acceptor Systems**  
Umesh Pratap Pandey, Rajendra Prasad Nandi and Pakkirisamy Thilagar
- 297 Fast Delayed Emission in New Pyridazine-Based Compounds**  
Simonas Krotkus, Tomas Matulaitis, Stefan Diesing, Graeme Copley, Emily Archer, Changmin Keum, David B. Cordes, Alexandra M. Z. Slawin, Malte C. Gather, Eli Zysman-Colman and Ifor D. W. Samuel



# Editorial: Recent Advances in Thermally Activated Delayed Fluorescence Materials

Chihaya Adachi<sup>1</sup>, Guohua Xie<sup>2</sup>, Sebastian Reineke<sup>3</sup> and Eli Zysman-Colman<sup>4\*</sup>

<sup>1</sup> Center for Organic Photonics and Electronics Research (OPERA), Kyushu University, Fukuoka, Japan, <sup>2</sup> Hubei Key Laboratory on Organic and Polymeric Optoelectronic Materials, Department of Chemistry, Sauvage Center for Molecular Sciences, Wuhan University, Wuhan, China, <sup>3</sup> Dresden Integrated Center for Applied Physics and Photonic Materials (IAPP), School of Science, Technische Universität Dresden, Dresden, Germany, <sup>4</sup> Organic Semiconductor Centre, EaStCHEM School of Chemistry, University of St Andrews, St. Andrews, United Kingdom

**Keywords:** thermally activated delay fluorescence (TADF), OLED - organic light emitting devices/display, organic semiconductor (OSC), metal complexes, polymers

## Editorial on the Research Topic

### Recent Advances in Thermally Activated Delayed Fluorescence Materials

Thermally activated delayed fluorescence (TADF) materials design has rapidly evolved over the past 8 years since Adachi and co-workers demonstrated that organic donor-acceptor compounds could recruit both singlet and triplet excitons in electroluminescent devices, reaching nearly 100% internal quantum efficiency (Uoyama et al., 2012). Accompanying new and improved TADF materials has been the enhanced performance of the organic light-emitting diodes (OLEDs), underpinned by a refined understanding of the TADF mechanism and the design rules that govern materials design.

This themed issue of Frontiers in Chemistry documents recent advances in TADF materials. Paisley et al. reviewed stimuli-responsive TADF in polymer nanoparticles and how these are relevant to sensing and imaging. Yin et al. provided an overview of TADF polymer materials. Etherington summarized the solid-state solvation effects and aggregate effects in organic TADF emitters. Barman et al. reviewed mechanochromic organic TADF materials. Lee et al. focused on boron containing TADF materials. To et al. contributed a perspective on metal complexes that showed TADF and their use as emitters in OLEDs. Hamze et al. demonstrated highly efficient deep blue luminescence of 2-coordinate coinage metal complexes. Crucho et al. reported on TADF dye-loaded nanoparticles for fluorescence live-cell imaging. Li Y. et al. showed how through-space charge transfer states can be recruited within polymers to produce high-performance solution-processed OLEDs, while Chen et al. showed how similar excited states can be exploited in small molecule TADF emitters. Mubarak et al. likewise exploited through-space CT states in triarylborane-containing TADF emitters. Kusakabe et al. revealed the importance of the relative orientation of donor and acceptor groups in through space TADF small molecule emitters. TADF polymer design was featured in the work of Yang et al. who reported white OLEDs while red OLEDs were reported by Zhan et al.. Franco et al. demonstrated how TADF absorption can be sensitized by using variable length oligo(phenylene ethynylene) antennae. Cai et al. revealed how aggregation-induced delayed fluorescence materials can be recruited for high-performance solution-processed OLEDs. Li H. et al. provided examples of small molecule emitters that showed aggregation-induced delayed fluorescence. Distinct high triplet energy ambipolar TADF host materials were independently reported by Rodella et al. for vacuum-deposited OLEDs and Godumala et al. for solution-processed OLEDs. High-performance OLEDs also require horizontally oriented emitters.

## OPEN ACCESS

### Edited and reviewed by:

Iwao Ojima,  
Stony Brook University, United States

### \*Correspondence:

Eli Zysman-Colman  
eli.zysman-colman@st-andrews.ac.uk

### Specialty section:

This article was submitted to  
Organic Chemistry,  
a section of the journal  
Frontiers in Chemistry

**Received:** 04 November 2020

**Accepted:** 06 November 2020

**Published:** 30 November 2020

### Citation:

Adachi C, Xie G, Reineke S and  
Zysman-Colman E (2020) Editorial:  
Recent Advances in Thermally  
Activated Delayed Fluorescence  
Materials. *Front. Chem.* 8:625910.  
doi: 10.3389/fchem.2020.625910

Naqvi et al. revealed molecular design rules for small molecular TADF emitters to exhibit more preferentially horizontal orientation. Sasabe et al. demonstrated how molecular orientation could be controlled in carbazole-containing host materials. Improved performances of blue TADF OLEDs have been of particular focus within the OLED community. Zhang et al. reported on a family of blue emitters containing an OBO-Fused Benzo[fg]tetracene acceptor. Sohn et al. demonstrated high-performance blue OLEDs using a pyrimidine-containing TADF emitter. Tsuchiya et al. showed how computational modeling can effectively guide blue emitter design. The greater exploration of chemical space has led to unorthodox emitter design. For instance, delayed fluorescence was reported by Pandey et al. in compounds containing dianthrylboron-based donor-acceptor systems, while Krotkus et al. showed fast delayed fluorescence in pyridazine-based emitters.

## REFERENCES

Uoyama, H., Goushi, K., Shizu, K., Nomura, H., and Adachi, C. (2012). Highly efficient organic light-emitting diodes from delayed fluorescence. *Nature* 492, 234–238. doi: 10.1038/nature11687

**Conflict of Interest:** The authors declare that the research was conducted in the absence of any commercial or financial relationships that could be construed as a potential conflict of interest.

The articles in this themed issue provide insight into how TADF materials design has evolved and how the use of TADF materials has expanded beyond OLEDs to sensing and imaging. Despite the intense focus over the past 8 year, this collection clearly demonstrates that there is still much to learn and much from which to be inspired.

## AUTHOR CONTRIBUTIONS

All authors listed have made a substantial, direct and intellectual contribution to the work, and approved it for publication.

## FUNDING

EZ-C thanks EPSRC (EP/P010482/1) for financial support.

Copyright © 2020 Adachi, Xie, Reineke and Zysman-Colman. This is an open-access article distributed under the terms of the Creative Commons Attribution License (CC BY). The use, distribution or reproduction in other forums is permitted, provided the original author(s) and the copyright owner(s) are credited and that the original publication in this journal is cited, in accordance with accepted academic practice. No use, distribution or reproduction is permitted which does not comply with these terms.



# Organic Light-Emitting Diodes Based on Conjugation-Induced Thermally Activated Delayed Fluorescence Polymers: Interplay Between Intra- and Intermolecular Charge Transfer States

## OPEN ACCESS

### Edited by:

Jonathan G. Rudick,  
Stony Brook University, United States

### Reviewed by:

Lixiang Wang,  
Changchun Institute of Applied  
Chemistry (CAS), China  
Ying Wang,  
Technical Institute of Physics and  
Chemistry (CAS), China

### \*Correspondence:

Yungui Li  
yungui.li@iapp.de  
Qiang Wei  
weiqiang@nimte.ac.cn  
Ziyi Ge  
geziyi@nimte.ac.cn  
Sebastian Reineke  
sebastian.reineke@tu-dresden.de

### Specialty section:

This article was submitted to  
Organic Chemistry,  
a section of the journal  
Frontiers in Chemistry

**Received:** 20 August 2019

**Accepted:** 04 October 2019

**Published:** 23 October 2019

### Citation:

Li Y, Wei Q, Cao L, Fries F, Cucchi M,  
Wu Z, Scholz R, Lenk S, Voit B, Ge Z  
and Reineke S (2019) Organic  
Light-Emitting Diodes Based on  
Conjugation-Induced Thermally  
Activated Delayed Fluorescence  
Polymers: Interplay Between Intra-  
and Intermolecular Charge Transfer  
States. *Front. Chem.* 7:688.  
doi: 10.3389/fchem.2019.00688

Yungui Li<sup>1\*</sup>, Qiang Wei<sup>2\*</sup>, Liang Cao<sup>2,3</sup>, Felix Fries<sup>1</sup>, Matteo Cucchi<sup>1</sup>, Zhongbin Wu<sup>1</sup>,  
Reinhard Scholz<sup>1</sup>, Simone Lenk<sup>1</sup>, Brigitte Voit<sup>4,5</sup>, Ziyi Ge<sup>2\*</sup> and Sebastian Reineke<sup>1\*</sup>

<sup>1</sup> Dresden Integrated Center for Applied Physics and Photonic Materials (IAPP), Institute for Applied Physics, Technische Universität Dresden, Dresden, Germany, <sup>2</sup> Ningbo Institute of Materials Technology & Engineering, Chinese Academy Sciences, Ningbo, China, <sup>3</sup> Key Laboratory of Advanced Textile Materials and Manufacturing Technology, Ministry of Education, Zhejiang Sci-Tech University, Hangzhou, China, <sup>4</sup> Leibniz-Institut für Polymerforschung Dresden e.V., Dresden, Germany, <sup>5</sup> Organic Chemistry of Polymers, Technische Universität Dresden, Dresden, Germany

In this work, interactions between different host materials and a blue TADF polymer named P1 are systematically investigated. In photoluminescence, the host can have substantial impact on the photoluminescence quantum yield (PLQY) and the intensity of delayed fluorescence ( $\Phi_{DF}$ ), where more than three orders of magnitude difference of  $\Phi_{DF}$  in various hosts is observed, resulting from a polarity effect of the host material and energy transfer. Additionally, an intermolecular charge-transfer (CT) emission with pronounced TADF characteristics is observed between P1 and 2,4,6-tris[3-(diphenylphosphinyl)phenyl]-1,3,5-triazine (PO-T2T), with a singlet-triplet splitting of 7 meV. It is noted that the contribution of harvested triplets in monochrome organic light-emitting diodes (OLEDs) correlates with  $\Phi_{DF}$ . For devices based on intermolecular CT-emission, the harvested triplets contribute ~90% to the internal quantum efficiency. The results demonstrate the vital importance of host materials on improving the PLQY and sensitizing  $\Phi_{DF}$  of TADF polymers for efficient devices. Solution-processed polychrome OLEDs with a color close to a white emission are presented, with the emission of intramolecular (P1) and intermolecular TADF (PO-T2T:P1).

**Keywords:** thermally activated delayed fluorescence, electroluminescent polymer, exciplex, charge-transfer state, organic light-emitting diodes

## INTRODUCTION

Since the first report of organic light-emitting diodes (OLEDs) by Tang and Vanslyke (1987), great efforts have been dedicated to achieve efficient and cost-effective OLED architectures for display and lighting applications. In the early stage of research, the device efficiency was limited by non-radiative triplets with a share of ~75% of all excitons, generated directly under electrical excitation in conventional fluorescent emitters (Segal et al., 2003). As though



triplet-triplet-annihilation can generate one emissive singlet from two triplets, the theoretical limit of the internal quantum efficiency (IQE) utilizing this bimolecular pathway is limited to 62.5% (Zhang and Forrest, 2012). The development of phosphorescent emitters, generally organometallic compounds with heavy metal atoms such as iridium, palladium and gold, allows harvesting triplet excitons through phosphorescence emission, making unity IQE values possible (Thompson, 2007). Highly efficient monochrome and white OLEDs have been demonstrated with phosphorescent emitters by using optimized multilayer architectures via thermal deposition under high vacuum condition (Reineke et al., 2009, 2013; Li et al., 2017, 2018). Still, phosphorescent emitters have several drawbacks in their use in OLEDs. The use of metal ingredients, leading to concerns of environmental hazards and high costs, drives the research community to find more environmentally friendly and cost effective alternatives. Furthermore, vacuum deposition has a high energy footprint compared to solution processes such as spin-coating or printing. The development of solution processable, purely organic materials is still active both in scientific and industry fields (Zheng et al., 2013; JOLED, 2018; Wei et al., 2018a).

An alternative way to utilize triplets is converting them to singlets by finely matching the triplet and singlet state energy with a small singlet-triplet splitting  $\Delta E_{ST}$ , where reverse intersystem crossing (RISC) occurs by harvesting the environmental thermal energy, known as thermally activated delayed fluorescence (TADF). In 2011, the first purely organic, reliable TADF emitter PIC-TRZ was reported by Endo et al., with a moderate photoluminescence quantum yield (PLQY) of 39% and merely 32% triplet harvesting efficiency when doped in 1,3-bis(N-carbazolyl)benzene (mCP) in the device (Endo et al., 2011). Later in 2012, the same group has reported purely organic TADF emitters with almost 100% triplet harvesting efficiency (Uoyama et al., 2012). After this breakthrough, numerous efforts have been devoted to the purely organic TADF small molecules, which can be purified by sublimation and processed by physical vapor deposition to obtain multilayer devices (Uoyama et al., 2012; Dias et al., 2013; Jankus et al., 2014; Zhang et al., 2016; Wong and Zysman-Colman, 2017).

On the other hand, TADF devices based on dendrimers and/or polymers have also gained huge attention, because of the possibility of easy fabrication by solution processes and high efficiency at the same time. As a proof-of-concept, solution-processed high efficiency OLEDs based on modified TADF small molecules with a better solubility have been reported (Cho et al., 2014). Meanwhile, to achieve macromolecules showing TADF, there are in general two approaches: (i) incorporating TADF monomers into polymer side chains with a non-conjugated backbone, and (ii) polymerizing donor and acceptor parts to form the main chain where the charge transfer state emission has TADF character, and each TADF unit is separated without conjugation (Li et al., 2016; Huang et al., 2018; Lin et al., 2018b; Wei et al., 2018b). For the first design principle, it is quite straightforward to achieve TADF macromolecules by binding the TADF monomeric units to a non-conjugated polymer side chain or linking with dendrimer

groups without breaking  $\pi$ -conjugation among the TADF moieties (Luo et al., 2016; Xie et al., 2017; Yang et al., 2018). For the second approach, the conjugation between different TADF units are supposed to be disturbed by  $\sigma$  bonds. The first TADF polymer was denoted as “intermonomer TADF” based on the second strategy, and a high external quantum efficiency (EQE) of 10% was obtained (Nikolaenko et al., 2015). It should be noted that besides these two general design principles, there are other possibilities to achieve TADF polymers. Wang et al. reported solution-processed OLEDs with a maximum EQE (EQE<sub>max</sub>) of 12.1% based on a TADF polymer via the so-called through-space charge transfer effect (Shao et al., 2017). Previously, we reported a method to generate an efficient blue TADF polymer, denoted P1 (Figure 1), by polymerizing a non-TADF monomer (4-(3,6-dibromo-carbazol-9-yl)phenyl)(4-(dodecyloxy)phenyl)methanone to conjugated polymer macrocycles. The appearance of TADF is resulting from the conjugation-induced reduction of the effective energy splitting  $\Delta E_{ST}$ , while keeping a sufficient fast radiative decay rate (Wei et al., 2017). The previous report on P1 focused on the synthesis and the origin of the TADF characteristics, without further investigation of its device integration and, in particular, on the influence of host materials in a device surrounding.

For small molecule TADF emitters in host-guest systems, the host materials can have a significant impact on the device efficiency and lifetime (Nakanotani et al., 2013; Cui et al., 2017). Recently, Han et al. reported that the host-guest dipole interaction can influence the PLQY of a group of blue TADF small molecules. Reducing the excited-state dipole moments of host materials can slightly reduce the rate of RISC, while the non-radiative rate is significantly suppressed, leading to a large improvement of the device performance (Han et al., 2018). However, there is still a lack of understanding of the interaction between host materials and TADF polymer emitters. Furthermore, even though tremendous efforts have been put on intermolecular charge transfer state (CT-state) TADF (in the OLED community typically referred to as “exciplex”) between small molecules (Goushi et al., 2012; Liu et al., 2015; Wu et al., 2017; Lin et al., 2018a; Ullbrich et al., 2019), the first report of intermolecular CT-emission with TADF characteristics based on a non-TADF polymer (poly(9-vinylcarbazole), PVK) and small molecule (2,4,6-tris[3-(diphenylphosphinyl)phenyl]-1,3,5-triazine, PO-T2T) was recently reported by Pander et al. (2018). In their system, the concentration of small molecule component has only minor influence on the transient PL decay profile of the CT-emission.

Here, we report our detailed investigation of the interactions between different host materials and the guest TADF polymer P1. We note that the host material can induce important effects on the PLQY and TADF characteristics (time dynamics and efficiency) of the polymer emitter. In the non-doped system (neat polymer film), weak delayed fluorescence is observed with a fraction of 2.95% of the total photoluminescence (PL). In the wide-gap and high triplet level 9-(4-tert-butylphenyl)-3,6-bis(triphenylsilyl)-9H-carbazole (CzSi) host, the PLQY is reduced, and the delayed fluorescence is almost completely quenched (0.014% of the entire emission). Both the PLQY



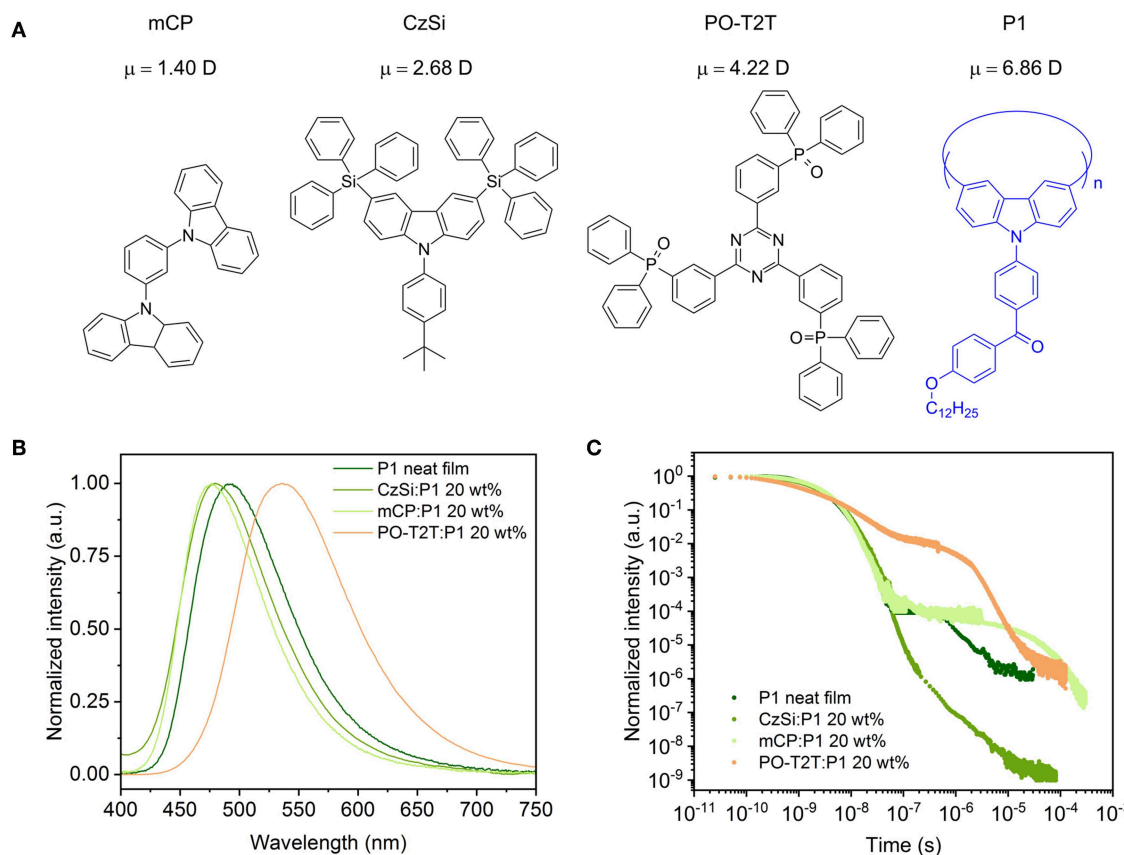


**FIGURE 1 | (A)** Chemical structure of host materials and the blue TADF polymer P1, with the calculated electrical dipole moment  $\mu$  for different host materials. The trimer of P1 ( $n = 3$ ) is set as the host for the P1 neat film in dipole moment calculations. **(B)** PL spectra of different spin-coated films with P1. **(C)** Transient PL decay measured at room temperature (ca. 297 K), detected at the peak wavelength of the respective steady state PL spectrum, excited with a pulse laser at a wavelength of 373 nm.

and the delayed fluorescence are significantly increased when using mCP as host material. The PLQY is increased to 49.8% for mCP:P1 (20 wt%), which is about 2.5 times higher than that for CzSi:P1 (20 wt%). Moreover, the fraction of delayed fluorescence reaches about 66% of the entire fluorescence in the mCP host. This indicates that the absolute quantum yield of delayed fluorescence ( $\Phi_{DF}$ ) is enhanced by a factor of about 5,900 with mCP as host compared to CzSi. Further investigations show that P1 and PO-T2T can form an intermolecular CT-emission with substantial TADF characteristics. The emission spectrum is hardly dependent on the P1 concentration in the range of 20–60 wt%. The singlet-triplet splitting  $\Delta E_{ST}$  for the intermolecular CT-emission is as small as 7 meV, leading to a very pronounced TADF emission, with a ratio of 2.13 between  $\Phi_{DF}$  and the quantum yield of prompt fluorescence ( $\Phi_{PF}$ ). It is estimated that in OLEDs utilizing the delayed emission, P1:PO-T2T intermolecular CT-emission contributes to about 90% to the IQE. Combining blue emission from P1 and yellow emission from the PO-T2T:P1 CT-emission, we demonstrate broadband, polychromatic OLEDs with a single emission layer, which holds promise for solution-processed white OLEDs based on the collective effect of two distinct CT-states, both giving rise to TADF.

## RESULTS AND DISCUSSION

### Host Environment-Enhanced TADF of P1

The PLQY and the delayed fluorescence for the TADF polymer P1 are sensitive to the surrounding environment. The P1 neat film shows a moderate PLQY of 30.7%, with a PL spectrum peaking at  $\sim 490$  nm. When embedded in a host material (structures shown in **Figure 1A**) with a wide energy gap and high triplet energy (**Figure 3A**), the PLQY for the mixed film changes. As summarized in **Table 1**, when P1 doped with a concentration of 20 wt% in CzSi, a widely used host material for blue emitters with a wide bandgap (Cho et al., 2014), a lowering of the PLQY (23.9%) is observed. The PLQY in CzSi is slightly increased up to  $\sim 30\%$ , with different P1 concentration from 10 to 25 wt%, as shown in **Figure S1**. For mCP:P1 films, the PLQY reaches 57.7% at 10 wt% of P1. It decreases to 49.4% for an increased doping concentration of P1 of 25 wt%. The PLQY values of P1 in this study do not reach the values as initially reported previously (Wei et al., 2017), which was obtained for a different host material (polystyrene). The change of the doping concentration within the range of 10–25 wt% has only a minor influence on the PL spectrum, as shown in **Figure S1**. The PL

**TABLE 1** | Photophysical properties of thin films with P1.

Film	$\Phi_{\text{PLQY}}$ (%)	$\lambda_{\text{max}}$ (nm)	$\Phi_{\text{PF}}$ (%)	$\Phi_{\text{DF}}$ (%)	$\Phi_{\text{DF}}/\Phi_{\text{PF}}$	$\tau_{\text{PF}}$ (ns)	$\tau_{\text{DF}}$ ( $\mu\text{s}$ )	$k_r$ ( $\times 10^7 \text{ s}^{-1}$ )
P1 neat film	30.7	490	29.8	0.90	0.03	3.60	1.81	8.27
CzSi: P1 20 wt%	23.9	477	23.9	$2.86 \times 10^{-3}$	$1.20 \times 10^{-4}$	3.85	0.72	6.21
mCP: P1 20 wt%	49.8	476	32.9	16.9	0.52	3.44	44.32	9.50
PO-T2T: P1 20 wt%	8.1	532	2.6	5.5	2.13	13.00	1.21	0.20

spectrum of mCP:P1 (20 wt%) film peaks at 477 nm, which is slightly blue-shifted compared to the P1 neat film, beneficial for achieving blue OLEDs. CzSi is a widely used host material with photoluminescence in the UV/deep blue spectral range (Tsai et al., 2006). Furthermore, with HOMO and LUMO values of 6.0 and 2.5 eV, respectively (Baranoff and Curchod, 2015), CzSi forms a type-I hetero-interface, not allowing for a charge-transfer state to form. Thus, the blue emission of CzSi:P1 mixture can be attributed to the intrinsic P1 emission. The change of the emission spectrum of mCP, CzSi and non-doped film can be attributed to the different interaction of P1 with the various hosts having different permanent dipole moments (Reineke et al., 2010). As shown in **Figure 1A**, the dipole moment of the mCP ground state is as small as 1.40 D, while it is 6.86 D for P1. Here, a trimer section of P1 ( $n = 3$ ) is assumed as the embedding material for the P1 neat film in the density functional theory (DFT) calculation in an attempt to properly model the surrounding environment. In case of the PO-T2T:P1 mixture (20 wt%), a substantial red-shift of the PL emission peak to 532 nm is observed, suggesting a different origin of this emission. Here, an intermolecular CT-emission between P1 and PO-T2T gives rise to this distinct PL. Before systematically investigating the photophysical property of the PO-T2T and P1 mixture, the detailed influence of host materials mCP and CzSi on the TADF characteristics is analyzed.

Time-correlated single-photon-counting (TCSPC) measurements performed at the peak wavelength of the PL spectra show that the host molecule has a substantial influence on the decay profile of the prompt and delayed fluorescence. As summarized in **Supplementary Note 1**, the average lifetime of prompt ( $\tau_{\text{PF}}$ ) and delayed fluorescence ( $\tau_{\text{DF}}$ ) can be obtained by fitting the decay curves with multiple exponential functions, while the quantum yield of the prompt and delayed fluorescence  $\Phi_{\text{PF}}$  and  $\Phi_{\text{DF}}$  can be calculated with the weighting ratio of the integrated area of these decay curves (Lakowicz, 2006). The detailed fitting process is shown in **Figure S3** and the fitting parameters are summarized in **Tables S1, S2**. The photophysical properties of P1 in different hosts are summarized in **Table 1**. The  $\tau_{\text{PF}}$  is 3.60 ns for P1 neat film. It is slightly different for CzSi (3.85 ns) and mCP (3.44 ns). The  $\tau_{\text{DF}}$  varies significantly for the neat and doped films. The  $\tau_{\text{DF}}$  is 1.81  $\mu\text{s}$  for P1 neat film, while it is 0.72  $\mu\text{s}$  in CzSi and 44.3  $\mu\text{s}$  in mCP. Moreover, big variations of the  $\Phi_{\text{PF}}$ ,  $\Phi_{\text{DF}}$ , and further the ratio of  $\Phi_{\text{PF}}/\Phi_{\text{DF}}$  are observed. In the neat film, only a very small amount of delayed fluorescence ( $\Phi_{\text{DF}} = 0.90\%$ ) is observed, with a ratio of  $\Phi_{\text{DF}}/\Phi_{\text{PF}} = 0.03$ . When embedding P1 in the CzSi host, the delayed fluorescence is negligible, with  $\Phi_{\text{DF}}$  of only 0.0029%,

and extremely low  $\Phi_{\text{DF}}/\Phi_{\text{PF}}$  (0.00014). The delayed fluorescence is much more pronounced when using mCP as host material, for which  $\Phi_{\text{DF}} = 16.9\%$  and  $\Phi_{\text{DF}}/\Phi_{\text{PF}} = 0.52$  are obtained. Compared to the CzSi host material, the  $\Phi_{\text{DF}}$  in mCP host is more than 5,900 times higher.

It is interesting to note that, even though the singlet state is decreasing by increasing the dipole moment of host materials (**Figure 1A**), the ratio  $\Phi_{\text{DF}}/\Phi_{\text{PF}}$  is not fully following the trend. As we can see, the PL emission is red-shifted for the non-doped film compared to the mCP:P1 system, while the ratio  $\Phi_{\text{DF}}/\Phi_{\text{PF}}$  is still much lower compared to the later. Thus, a deeper blue emission together with a higher fraction of delayed fluorescence are obtained at the same time in mCP, which is beneficial for fabricating blue OLEDs. According to the photophysical investigation and DFT analysis, factors including host-guest energy transfer, dipole moment of host materials, and CT-state generation can contribute to different  $\Phi_{\text{DF}}/\Phi_{\text{PF}}$  ratios for the TADF polymer in different hosts.

A low value of  $\Phi_{\text{DF}}/\Phi_{\text{PF}}$  can jeopardize the triplet harvesting in electroluminescence, since triplets are generated directly with a large fraction (75%) (Segal et al., 2003), while they are generated from singlets via intersystem crossing (ISC) under optical excitation. The extremely low value of  $\Phi_{\text{DF}}/\Phi_{\text{PF}}$  in the CzSi host gives a hint that most of the generated triplets in the device cannot efficiently transfer to singlets, rendering this specific material combination unsuitable for device applications.

## Photophysical Properties of the PO-T2T:P1 Mixture

As mentioned above, the large shift of the PL spectrum of the PO-T2T:P1 mixed film indicates a possible intermolecular CT-emission. As shown in **Figure 2A**, compared to the pure emission of PO-T2T and P1, the spectrum of the mixed film is red-shifted by  $\sim 170$  and 60 nm, respectively. According to previous reports, the LUMO level of PO-T2T is about 3.5 eV and the HOMO level of P1 is 5.7–5.8 eV (Wu et al., 2017). The PO-T2T as the donor and P1 as the acceptor can form a CT-state with an energy gap of about 2.2–2.3 eV, which is close to the emission energy of the PO-T2T:P1 mixture, supporting the concept that the yellow light emission in the PO-T2T:P1 blend is resulting from charge transfer between PO-T2T and P1. As shown in **Figure 2B**, there is no significant change of the PL spectra measured under ambient condition, with the PL peak at  $\sim 540$  nm, when varying the P1 concentration in the PO-T2T and P1 mixture films from 20 to 60 wt%. Increasing the concentration of P1 to 80 wt% can slightly shift the PL maximum to 548 nm.

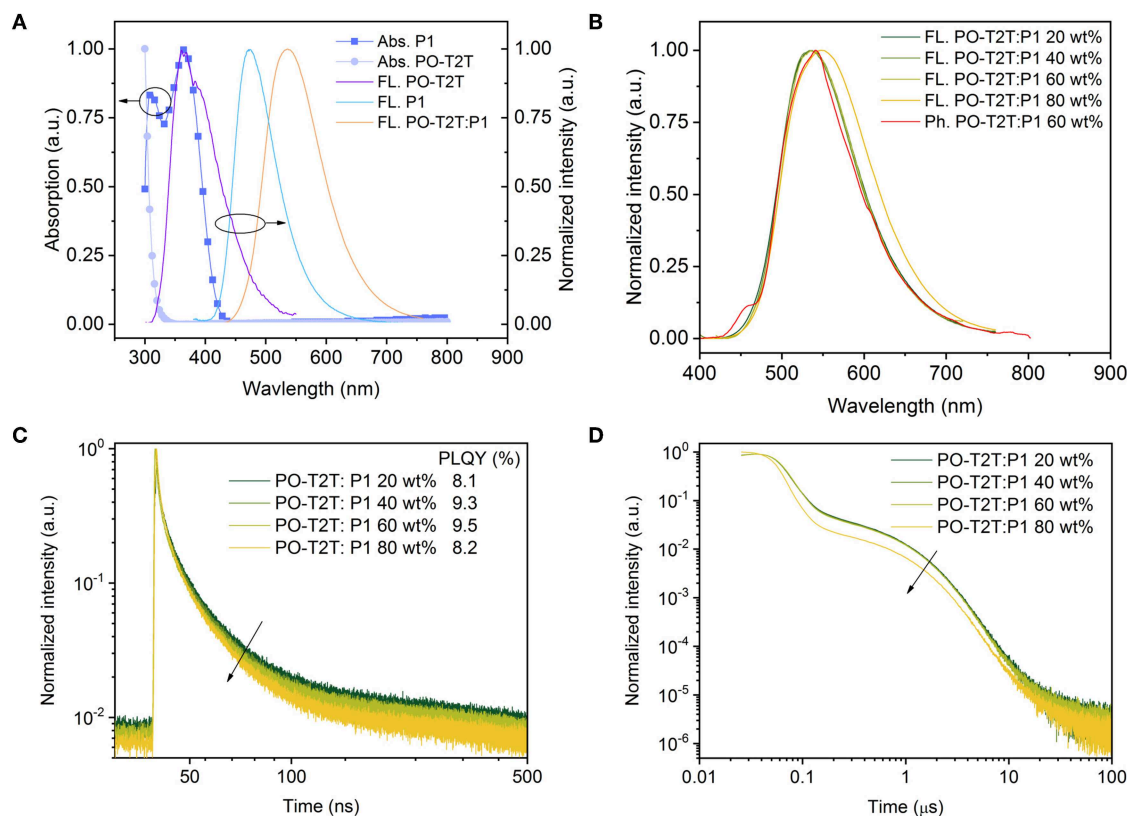


**FIGURE 2 |** The CT-emission between PO-T2T and P1 showing thermally activated delayed fluorescence. **(A)** Normalized absorption, fluorescence spectrum of P1 and PO-T2T, and the CT-emission of the PO-T2T:P1 mixture. **(B)** Room temperature steady state fluorescence spectra of PO-T2T:P1 with different mixing ratios, compared to a representative phosphorescence spectrum of the PO-T2T:P1 60 wt% film obtained in liquid nitrogen. **(C)** Prompt fluorescence decay of the PO-T2T:P1 CT-emission. The PLQY for the various mixtures is given in the legend. **(D)** Overview of the PL decay for the different PO-T2T:P1 compositions showing prompt and delayed fluorescence (TADF). At very long times, a third channel ( $>10 \mu$ s) is visible, suggesting weak phosphorescence.

In the following, the emission dynamics of this PO-T2T:P1 mixture are discussed. The phosphorescence spectra measured at 77 K show only a small red-shift compared to the steady PL spectra, as shown in **Figure 2B** and **Figure S2**. The similarity of PL spectra at room temperature and the phosphorescence spectra (77 K) indicates a small  $\Delta E_{ST}$ . According to **Supplementary Note 2**, as shown in **Figure S4** and **Table S3**, by fitting the fluorescence and phosphorescence spectra, the singlet energy level is 2.162 eV, while the triplet energy level is 2.155 eV, giving a splitting  $\Delta E_{ST}$  as small as 7 meV.

Similar PL transients have been obtained for the PO-T2T:P1 mixture with varied P1 concentration from 20 to 80 wt%, as shown in **Figures 2C,D**. The decay time of prompt fluorescence  $\tau_{PF}$  is 13.0 ns for 20 wt% P1, while it only slightly decreases to 11.1, 11.2, and 8.6 ns, for 40, 60, and 80 wt% P1 films, respectively. The decay time of delayed fluorescence  $\tau_{DF}$  is around 1.2  $\mu$ s, with a minor variation with different P1 concentrations from 20 to 60 wt%. A more pronounced change for the PO-T2T:P1 (80 wt%) film goes hand in hand with the observed red-shift of steady state PL emission, as shown in **Figure 2B**. Our results show that the ratio between donor and acceptor has minor influence on the transient decay of the CT-emission, which is

similar compared to the first reported CT-emission with TADF characteristics between small molecules and polymers (Pander et al., 2018).

The PLQY of the PO-T2T:P1 system is about 8–10% (**Figure 2C**), demonstrating that non-radiative decay dominates the relaxation process. Nevertheless, a significant delayed fluorescence is observed from the CT-emission, with a ratio of  $\Phi_{DF}/\Phi_{PF}$  larger than 2, indicating that there are cycling processes from triplets and singlets (Wei et al., 2017). The detailed photophysical properties of PO-T2T:P1 (20 wt%) are also summarized in **Table 1**.

## Monochrome OLEDs Based on P1

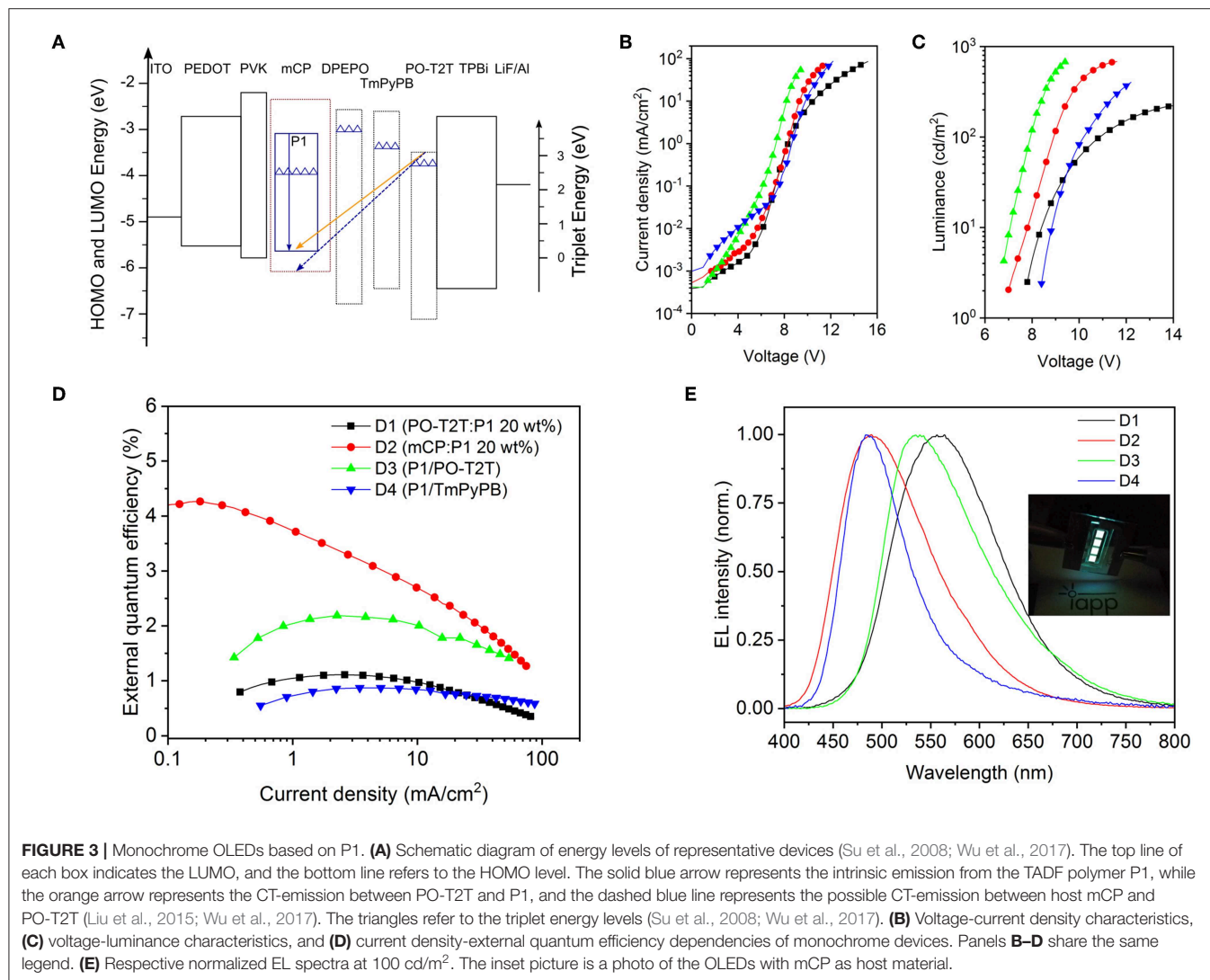
Based on the photophysical investigations, we further explore monochrome OLEDs based on P1 with different device structures. The device structures and characteristics are summarized in **Table 2**. The energy diagram is shown in **Figure 3A** (Su et al., 2008; Wu et al., 2017). As depicted in **Figure 3B**, for the monochrome devices D1 (PO-T2T:P1 [20 wt%]) and D2 (mCP:P1 [20 wt%]), the slight difference of the voltage-current density characteristics stems from the different transport properties of host materials. However, a large difference

**TABLE 2** | Summary of the device characteristics.

Device	Device structure <sup>a</sup> (EBL/EML/HBL/ETL/EIL)	EQE <sub>max</sub> (%)	CE <sub>max</sub> (cd/A)	LE <sub>max</sub> (lm/W)	CIE (x, y) <sup>b</sup>
D1	PVK (15 nm)/PO-T2T:P1 20 wt% (50 nm)/DPEPO (10 nm)/TPBi (50 nm)/LiF (1 nm)	1.1	0.9	0.9	(0.42, 0.52)
D2	PVK (15 nm)/mCP:P1 20 wt% (50 nm)/DPEPO (10 nm)/TPBi (50 nm)/LiF (1 nm)	4.3	3.0	2.5	(0.24, 0.37)
D3	P1 (30 nm)/PO-T2T (10 nm)/Bphen:Cs (50 nm)	2.2	1.9	1.9	(0.39, 0.54)
D4	P1 (30 nm)/TmPyPB (10 nm)/Bphen:Cs (50 nm)	0.9	0.7	0.4	(0.20, 0.35)
D5	PVK (15 nm)/PO-T2T:P1 99 wt% (50 nm)/DPEPO (10 nm)/TPBi (50 nm)/LiF (1 nm)	1.7	1.8	1.8	(0.28, 0.40)
D6	PVK (15 nm)/PO-T2T:P1 99.5 wt% (50 nm)/DPEPO (10 nm)/TPBi (50 nm)/LiF (1 nm)	1.2	1.3	1.6	(0.31, 0.44)

<sup>a</sup>The complete device is composed of ITO/PEDOT:PSS (70 nm)/EBL/EML/HBL/EIL/Al (100 nm). For D3 and D4, no EBL, and EIL are used.

<sup>b</sup>D1–D4 are obtained at a driving current of 0.5 mA, while D5–D6 are obtained at 100 cd/m<sup>2</sup>.



of voltage-current density behavior is noted for D3 (P1/PO-T2T) and D4 (P1/1,3,5-tri(m-pyridin-3-ylphenyl)benzene, TmPyPB), as shown in **Figure 3B**. The reason can be ascribed to the difference between the LUMO levels for PO-T2T and TmPyPB (**Figure 3A**). As shown in **Figure 3C**, a voltage larger than 6 V is needed to turn D1–D4 on. Many reasons may

contribute to the high turn-on voltage of D1 and D2, including limited transport mobility of the PVK and PEDOT:PSS layer (Pander et al., 2018).

For D4 with P1 neat film as emitting layer, as shown in **Figure 3D** and **Table 2**, a quite low EQE<sub>max</sub> of 0.87% is obtained. The reason could be an imbalanced charge carrier injection, an



intrinsically lower PLQY and/or an inefficient RISC process. A further device optimization may enhance the charge balance and triplet diffusion to the hole transport layer. A medium EQE<sub>max</sub> of 4.26% can be obtained for D2 with 20 wt% P1 doped in mCP, as shown in **Figure 3D** and **Table 2**. The EQE<sub>max</sub> is 1.11% for D1 and 2.19% for D3, both showing the CT-emission between PO-T2T and P1.

As shown in **Figure 3E** and **Table 2**, the emission color for D2 and D4 is cyan blue, with the Commission Internationale de l'Eclairage (CIE) coordinates (0.24, 0.37) for D2 and (0.20, 0.35) for D4. However, a substantially different emission color is noted for D1 (PO-T2T:20 wt% P1) and D3 (P1/PO-T2T). The EL spectra with a peak wavelength located at about 530 nm for D3 is very close to the PL spectrum of the CT-emission between PO-T2T and P1 (**Figure 2B**). The device cavity and the emission from intrinsic P1 may contribute to a slight deviation of electroluminescence for D1 from the PL spectrum of the PO-T2T:P1 CT-state.

### Triplet Harvesting in Monochrome OLEDs

Under electroluminescence in OLEDs, 75% of the excitons are generated as triplets in the first place (Segal et al., 2003). Hence, if there is a lack of efficient RISC within the TADF system, the triplets cannot fully transfer to emissive singlets. Without the consideration of bimolecular annihilation processes, the EQE is determined by the following equation (Li et al., 2018):

$$\text{EQE} = \gamma \eta_{\text{int}} \eta_{\text{out}} \quad (1)$$

where  $\gamma$  is the electrical efficiency,  $\eta_{\text{int}}$  is the IQE and  $\eta_{\text{out}}$  is the outcoupling efficiency. For OLEDs based on TADF emitter,  $\eta_{\text{int}}$  can be calculated as (Endo et al., 2011; Goushi et al., 2012):

$$\eta_{\text{int}} = 0.25\phi_{\text{PF}} + \sum_{i=1}^{\infty} 0.25\phi_{\text{PF}} (\phi_{\text{ISC}}\phi_{\text{RISC}})^i + \sum_{i=0}^{\infty} 0.75\phi_{\text{PF}}\phi_{\text{RISC}} (\phi_{\text{ISC}}\phi_{\text{RISC}})^i \quad (2)$$

where  $\phi_{\text{ISC}}$  indicates the quantum yield of ISC, while  $\phi_{\text{RISC}}$  is the quantum yield of RISC. The term of  $\phi_{\text{ISC}}\phi_{\text{RISC}}$  indicates the cycling process  $i$  from singlets to triplets. The contribution of the prompt fluorescence  $\eta_{\text{int\_PF}}$  can be calculated as (Goushi et al., 2012; Lee et al., 2013):

$$\eta_{\text{int\_PF}} = 0.25\phi_{\text{PF}} \quad (3)$$

The final mathematical form of Equation (2) can be written as:

$$\eta_{\text{int}} = \phi_{\text{PF}} \left( \frac{0.25}{1 - \phi_{\text{ISC}}\phi_{\text{RISC}}} + \frac{0.75}{1 - \phi_{\text{ISC}}\phi_{\text{RISC}}} \phi_{\text{RISC}} \right) \quad (4)$$

Kinetically, for an efficient TADF emitter with a predominant delayed emission, the non-radiative rate of the singlet is of similar magnitude as the radiative rate of the singlet, in the range of  $10^8 \text{ s}^{-1}$ . For the triplets, the non-radiative rate should be comparable to the rate of reverse intersystem crossing, which is normally lower than  $10^6 \text{ s}^{-1}$  (Dias et al., 2016, 2017). Since the non-radiative rate of singlets is orders higher than the non-radiative rate of triplets, we assume that the non-radiative relaxation comes

merely from the singlets state. Under this assumption,  $\phi_{\text{RISC}} = 1$ , while  $\phi_{\text{ISC}}$  can be calculated as (Dias et al., 2017):

$$\phi_{\text{ISC}} = \frac{\phi_{\text{DF}}}{\phi_{\text{DF}} + \phi_{\text{PF}}} \quad (5)$$

With Equation (5),  $\eta_{\text{int}}$  in form of Equation (4) can be calculated with  $\phi_{\text{DF}}$  and  $\phi_{\text{PF}}$ :

$$\eta_{\text{int}} = \phi_{\text{DF}} + \phi_{\text{PF}} \quad (6)$$

The contribution of delayed fluorescence  $\eta_{\text{int\_DF}}$  or the quantum efficiency from harvesting triplets, can be then calculated from:

$$\eta_{\text{int\_DF}} = \eta_{\text{int}} - 0.25\phi_{\text{PF}} = \phi_{\text{DF}} + 0.75\phi_{\text{PF}} \quad (7)$$

Based on Equations (6) and (7),  $\eta_{\text{int}}$  and  $\eta_{\text{int\_DF}}$  for devices D1–D4 can be calculated, as summarized in **Table 3**. The dependency of the  $\eta_{\text{int}}$  and  $\eta_{\text{int\_DF}}$  on  $\phi_{\text{DF}}$  for D1–D4 is shown in **Figure 4**. Since  $\eta_{\text{int}}$  depends on the PLQY of the emitting layer, the  $\eta_{\text{int}}$  of D2 with mCP:P1 as the emissive layer is 49.8%, which is about 6 times higher compared to D1 and D3 based on the PO-T2T:P1 mixture and 1.6 times higher than the D4 with P1 neat film. For devices based on a P1 neat film, the  $\eta_{\text{int}}$  remains 30.7%, but the delayed fluorescence contributes only 76% to the IQE. For the PO-T2T:P1 emission system, even though  $\eta_{\text{int}}$  for D1 and D3 is only 8.1%, the  $\eta_{\text{int\_DF}}$  contributes 92% to  $\eta_{\text{int}}$ , which can be assigned to the predominant delayed fluorescence with  $\phi_{\text{DF}}/\phi_{\text{PF}}$  as high as 2.13. Since  $\phi_{\text{DF}}/\phi_{\text{PF}}$  for mCP:P1 is slightly lower compared to PO-T2T:P1 mixture, the delayed emission contributes ~83% among  $\eta_{\text{int}}$  in D2.

The outcoupling efficiency  $\eta_{\text{out}}$  can be simulated by transfer matrix method (details in the experimental section), and the results are summarized in **Table 3**. The electrical efficiency corresponds to the charge balance and recombination. For state-of-the-art thermal deposited OLEDs, the electrical efficiency  $\gamma$  is around 0.8–1.0 (Furno et al., 2012). The electrical efficiency for each device can be calculated according to Equation (1) based on  $\eta_{\text{out}}$  and  $\eta_{\text{int}}$  with the EQE<sub>max</sub>. As shown in **Table 3**, the electrical efficiency  $\gamma$  for D1 and D2 is 0.88 and 0.69, while it is 1.22 for D3, which is physically not meaningful. One possible reason could be the improper assumption of an isotropic emitter and the emission from intrinsic P1. Nevertheless, the electrical

**TABLE 3 |** Summary of device performance of monochrome OLEDs.

Device	EML structure	$\eta_{\text{int}}$ (%) <sup>a</sup>	$\eta_{\text{int\_DF}}$ (%) <sup>b</sup>	$\eta_{\text{int\_DF}}/\eta_{\text{int}}$	$\eta_{\text{out}}$ (%) <sup>c</sup>	$\gamma$ <sup>d</sup>
D1	PO-T2T:P1 20 wt%	8.1	7.4	0.92	15.3	0.88
D2	mCP:P1 20 wt%	49.8	41.6	0.83	12.3	0.69
D3	PO-T2T/P1	8.1	7.4	0.92	22.2	1.22
D4	P1 neat film	30.7	23.2	0.76	21.1	0.13

<sup>a</sup>Calculated from Equation (6).

<sup>b</sup>Calculated from Equation (7).

<sup>c</sup>Simulation results. Details in experimental sections.

<sup>d</sup>Electrical efficiency, calculated from Equation (1).

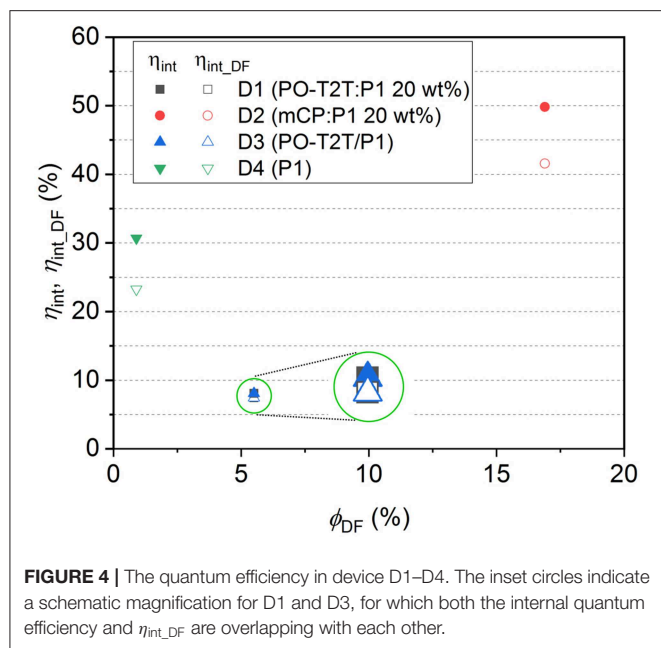


**FIGURE 4 |** The quantum efficiency in device D1–D4. The inset circles indicate a schematic magnification for D1 and D3, for which both the internal quantum efficiency and  $\eta_{int\_DF}$  are overlapping with each other.

efficiency for D4 is only 0.13, indicating that the electrical loss also contributes to the low device efficiency. Further optimization of D4 may give a slightly higher efficiency. The HOMO and LUMO level of the host materials can influence the charge carrier injection barriers from the adjacent layers with direct influence on the electrical efficiency through altered charge injection and/or charge recombination. Various host materials with different HOMO and LUMO levels in D1–D4, as shown in **Figure 3A**, can be one of the possible reasons for the difference of the estimated electrical efficiency.

It should be noted that the triplets can also give non-radiative relaxation for the TADF emitters, leading an over-estimation of the contribution of harvested triplets to the IQE. Even though the real  $\eta_{int\_DF}$  and  $\eta_{int}$  for D1–D4 may be varied slightly, it is clear that higher IQE can be obtained for OLEDs based on emissive layer with a high  $\phi_{DF}$  and  $\phi_{PF}$ . Therefore, the suppression of non-radiative relaxation for TADF systems from either singlets or triplets is of vital importance to achieve efficient OLEDs. On the other hand, the ratio  $\phi_{DF}/\phi_{PF}$  can largely affect the contribution of the delayed emission among the total quantum efficiency in a device.

## Polychrome OLEDs With Dual Emission From P1 and CT-State

Polychrome OLEDs where the emission in general originates from more than one luminescent species are constructed here with a single emitting layer combining the blue emission from P1 and the yellow CT-emission between PO-T2T and P1. As shown in **Figure 5A**, in such a mixed film, there are two TADF processes: (i) TADF governing the luminescence of P1 itself and (ii) the CT-emission between PO-T2T and P1, which also shows TADF characteristics, as discussed above. Excitons

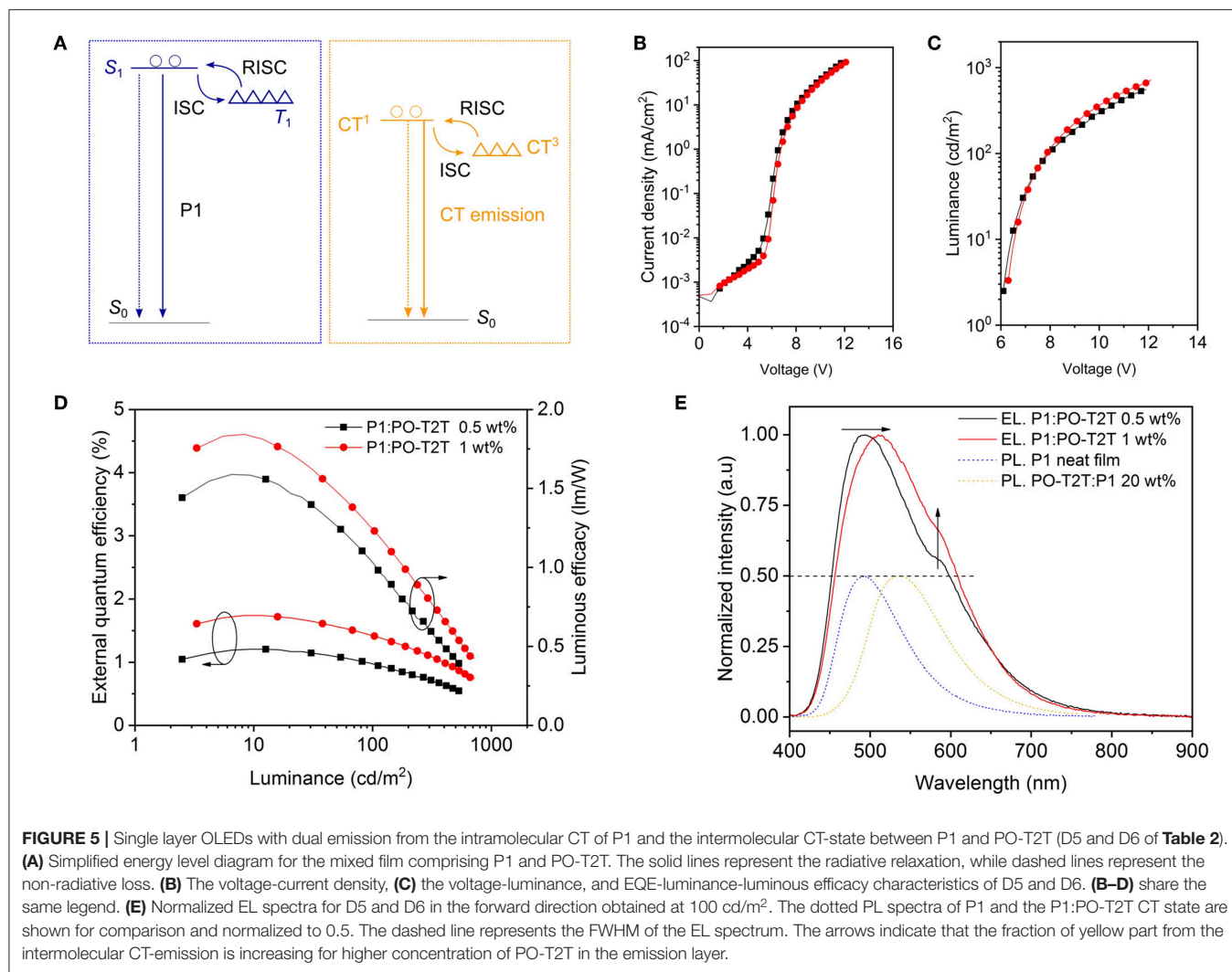
generated in P1 can transfer to the CT-state by several processes: Förster resonance or Dexter energy transfer determined by the exciplex concentration (Higuchi et al., 2015). Here, the acceptor state is the PO-T2T:P1 CT-state characterized with—compared to local transitions—weak oscillator strength that ultimately defines the strength of these energy transfer pathways (Ullbrich et al., 2019). Additionally, the CT-state can be populated by charge separation from local donor (P1) to CT excitons as occurring in solar cells as the initial step of charge separation (Ullbrich et al., 2019). Of course, direct CT exciton formation at the interface between P1 and PO-T2T is possible. Since the increase of PO-T2T concentration in the mixed film can tune the emission to yellow (e.g., D1), the major part of the film should be P1 to achieve a double-color emission. Based on these prerequisites, we tested the P1 polymer film embedded with 0.5 wt% (D6) and 1 wt% PO-T2T (D5) to demonstrate double-color emission close to white spectrum in a single emission layer architecture.

As shown in **Figure 5B** and **Table 2**, the slight change of the PO-T2T concentration has little influence on the electrical performance of D5 and D6. The luminance for D5 is slightly higher than D6, as shown in the **Figure 5C**. Maximum EQEs of 1.74 and 1.20% are achieved for D5 and D6 at around 10  $\text{cd}/\text{m}^2$ , respectively, as shown in **Figure 5D**. The EQE slightly rolls off to 1.41% at 100  $\text{cd}/\text{m}^2$  for D5 and 0.97% at 100  $\text{cd}/\text{m}^2$  for D6. These devices show maximum luminous efficacy values of 1.84  $\text{lm}/\text{W}$  for D5 and 1.59  $\text{lm}/\text{W}$  for D6.

The EL spectra are shown in **Figure 5E**. The device D6 with 0.5 wt% PO-T2T shows two separate peaks, located at  $\sim 490$  and 570 nm, giving a CIE of (0.31, 0.43) with a full width at half maximum (FWHM) of 146 nm. Slightly increasing the concentration of PO-T2T to 1 wt% can shift the first peak to about 510 nm, while the intensity of the shoulder peak is enhanced. In the end, D5 gives a final CIE of (0.28, 0.40) with a FWHM of 153 nm. In this architecture, constructed from a combination of a TADF polymer and a small molecule host, two different TADF mechanisms are brought together to collectively achieve broadband emission ( $\sim 150$  nm FWHM). These results indicate its potential to reach both high IQE and white light emission.

## CONCLUSION

In this work, we report the substantial influence of host materials on the photophysical properties of a TADF polymer P1 and further, the triplet harvesting ability in OLEDs comprising this emitter. Almost no delayed fluorescence is observed in the neat film or in the host CzSi. The delayed fluorescence can be enhanced by more than three orders of magnitude when replacing the host material CzSi by mCP. Furthermore, we observe a CT-emission between the PO-T2T and P1, which shows substantial TADF in line with a  $\Delta E_{ST}$  as small as 7 meV and a ratio of 2.13 between delayed fluorescence to prompt fluorescence. When using the TADF polymer P1 to build monochrome OLEDs, cyan blue devices can be achieved



for a P1 neat film, or for P1 embedded in mCP. A maximum EQE of 4.26% is achieved for devices with mCP as the host material, while it is only 0.87% for the device based on the P1 neat film. This demonstrates that in the device with mCP, an IQE of ~50% can be obtained with the delayed emission contributing ~76%. For devices based on a PO-T2T:P1 mixture, the delayed emission contributes ~90% to the IQE. The results clearly demonstrate the vital importance of host materials on sensitizing the delayed fluorescence in TADF polymers for efficient OLEDs.

Together with the yellow CT-emission from PO-T2T:P1 and the intrinsic blue emission from P1, OLEDs with polychromatic emission can be realized for a low doping concentration of PO-T2T. A maximum EQE of 1.74% and a luminous efficacy of 1.84 lm/W are achieved. This concept for polychrome OLEDs based on two distinct TADF routes, where one is a CT-emission between a TADF polymer and a small molecule host, can be a starting point to develop high efficiency white OLEDs based on solution processes with purely organic TADF polymers.

## Experimental Materials

The PEDOT:PSS (AI4083, Heraeus Clevios™) is filtered before spin-coating. The other organic materials, 1,3-bis(N-carbazolyl)benzene (mCP, Lumtec), 9-(4-tert-butylphenyl)-3,6-bis(triphenylsilyl)-9H-carbazole (CzSi, Lumtec), 2,4,6-tris[3-(diphenylphosphinyl)phenyl]-1,3,5-triazine (PO-T2T, Lumtec), bis[2-(diphenylphosphino)phenyl] ether oxide (DPEPO, Lumtec), 4,7-diphenyl-1,10-phenanthroline (BPhen, Lumtec), 2,2',2''-(1,3,5-benzenetriyl)-tris[1-phenyl-1H-benzimidazole] (TPBi, Lumtec) and 1,3,5-tri(m-pyridin-3-ylphenyl)benzene (TmPyPB, Lumtec) are sublimated before deposition. poly(9-vinylcarbazole) (PVK, Mw ~1,100,000, Sigma-Aldrich), lithium fluoride and aluminum are used as they are purchased.

## Photophysical Properties

Quartz substrates are cleaned with isopropanol, acetone and DI water. After heating at 110°C in an oven, the substrates are then treated with oxygen plasma for 10 min. The host-guest films are

prepared by spin-coating. The film with CzSi as host is annealed at 100°C for 20 min while the mCP film is annealed at 40°C for 20 min, because of the low glass transition temperature of mCP. For transient measurements of PL emission, the TCSPC technique is used. After exciting the sample with a laser at 373 nm with pulse width of 44 ps, the emitted photons are collected by a photomultiplier tube (PicoQuant PMA Hybrid) and the data acquisition is done by a TCSPC module (PicoQuant TimeHarp 260). The PLQY of these films is confirmed by using a calibrated integrating sphere in nitrogen atmosphere, with a CAS 140 CT spectrometer and a UV-LED (Thorlabs, 340 nm). The steady-state PL spectra for P1 neat film, doped film within mCP and CzSi are collected during the PLQY measurement and used for the evaluation (Mello et al., 1997). The detailed steady-state PL spectra for the CT-emission are obtained with a Spex FluoroMax spectrofluorometer. The UV-absorption measurement is done in toluene solution, with Shimadzu MPC 3100.

### Dipole Moment Calculation

The calculation is based on density functional theory applied to molecules in the ground state, using the functional B3LYP and a 6–31 g(d) basis set. The dipole moment for P1 is calculated on the trimer.

### Thickness Calibration

The thickness of spin-coated films is confirmed by a profilometer (Veeco Dektak 150) and cross-checked by an imaging ellipsometer (EP4, Accurion GmbH).

### Device Fabrication

The PEDOT:PSS solutions are filtered, spin-coated with a speed of 1,000 rpm, and then annealed at 120°C for 30 min in ambient atmosphere. The following spin-coating processes are done inside a glovebox with oxygen and water concentration lower than 1 ppm. The PVK in 1,2-dichlorobenzene with a concentration of 10 mg/ml is coated with a speed of 2,000 rpm on top of PEDOT:PSS. Before casting the emissive layer, the film is annealed at 150°C for 10 min and cooled down to room temperature. The P1 neat film has a thickness of about 30 nm by spin-coating at 1,000 rpm with a concentration of 5 mg/ml in toluene. For host-guest doped system, films with a thickness of about 50 nm can be obtained by spin-coating at a speed of 1,000 rpm with a solution concentration of 7.5 mg/ml in toluene. The emissive materials are dissolved in toluene and spin-coated on the PVK layer, with a post-annealing at 40°C for 20 min. The following organic layers are fabricated in facilities from Kurt J. Lesker Co., under the vacuum of about  $10^{-7}$  to  $10^{-8}$  mbar. The deposition rates for the organic materials are about 1 Å/s, detected during material evaporation through calibrated quartz crystals. The devices are then encapsulated in a glovebox before the device characterization. A finely structured mask is used for doped layers to reduce the leakage current.

### Device Characterization

The current-voltage characteristics are measured by a Source Measure Unit (Keithley 2400), and luminance is measured simultaneously through a calibrated photodiode. The spectral radiant intensity is recorded via a calibrated spectrometer (CAS140, Instrument Systems GmbH).

EQE and luminous efficacy are further measured by a calibrated integrating sphere. The active area size is 6.49 mm<sup>2</sup>.

### Outcoupling Efficiency Simulation

The simulation is based on a transfer matrix algorithm, where the theory is summarized in reference (Furno et al., 2012). The anisotropy factor of the emitters for these devices is set to 0.33, corresponding to an isotropic distribution. Regarding the spectra in the optical simulation, the PL spectrum of CT-emission is used for D1 and D3, while the PL spectrum of mCP:P1 20 wt% is used for D2 and the PL spectrum of P1 neat film is used for D4. The refractive index and extinction coefficient of TPBi and PEDOT:PSS are set as measured results, shown in **Figure S5**. For other organic materials, the refractive index is set to 1.7, while the extinction coefficient is vanishing. The emission location is set at the interface between the emission layer and the hole blocking layer.

### DATA AVAILABILITY STATEMENT

All datasets generated for this study are included in the article/**Supplementary Files**.

### AUTHOR CONTRIBUTIONS

YL did the photophysical measurements and device investigations. The polymer synthesis is done by QW, LC, BV, and ZG. The dipole moment simulation is done by MC. FF contributed to the PLQY setup building and the data analysis code. YL and RS did the line shape analysis. YL, SL, and SR analyzed the device data. All the authors commented the manuscript. SL and SR organized the entire project.

### FUNDING

YL acknowledges the financial support of China Scholarship Council (No. 201506160049). The results are previously published online as part of the PhD thesis of YL at TU Dresden (Li, 2019). ZW appreciates the funding from the Alexander von Humboldt-Foundation. Beneficial discussions with P. Imbrasas and J. Yu are also acknowledged. This work was financially supported by the National Key R&D Program of China (2017YFE0106000, 2016YFB0401000), National Natural Science Foundation of China (21805296, 51773212, 21574144, and 21674123), China Postdoctoral Science Foundation (2017M621987), Ningbo Natural Science Foundation (2018A610134), Zhejiang Provincial Natural Science Foundation of China (LR16B040002), Ningbo Municipal Science and Technology Innovative Research Team (2015B11002 and 2016B10005), CAS Interdisciplinary Innovation Team, CAS Key Project of Frontier Science Research (QYZDB-SSW-SYS030), and CAS Key Project of International Cooperation (174433KYSB20160065). This project has received funding from the European Research Council (ERC) under the European Union's Horizon 2020 research and innovation program (grant agreement No. 679213 BILUM).



## SUPPLEMENTARY MATERIAL

The Supplementary Material for this article can be found online at: <https://www.frontiersin.org/articles/10.3389/fchem.2019.00688/full#supplementary-material>

## REFERENCES

- Baranoff, E., and Curchod, B. F. E. (2015). FIrpic: archetypal blue phosphorescent emitter for electroluminescence. *Dalt. Trans.* 44, 8318–8329. doi: 10.1039/C4DT02991G
- Cho, Y. J., Yook, K. S., and Lee, J. Y. (2014). High efficiency in a solution-processed thermally activated delayed-fluorescence device using a delayed-fluorescence emitting material with improved solubility. *Adv. Mater.* 26, 6642–6646. doi: 10.1002/adma.201402188
- Cui, L.-S., Ruan, S.-B., Bencheikh, F., Nagata, R., Zhang, L., Inada, K., et al. (2017). Long-lived efficient delayed fluorescence organic light-emitting diodes using n-type hosts. *Nat. Commun.* 8:2250. doi: 10.1038/s41467-017-02419-x
- Dias, F. B., Bourdakos, K. N., Jankus, V., Moss, K. C., Kamtekar, K. T., Bhalla, V., et al. (2013). Triplet harvesting with 100% efficiency by way of thermally activated delayed fluorescence in charge transfer OLED emitters. *Adv. Mater.* 25, 3707–3714. doi: 10.1002/adma.201300753
- Dias, F. B., Penfold, T. J., and Monkman, A. P. (2017). Photophysics of thermally activated delayed fluorescence molecules. *Methods Appl. Fluoresc.* 5:012001. doi: 10.1088/2050-6120/aa537e
- Dias, F. B., Santos, J., Graves, D. R., Data, P., Nobuyasu, R. S., Fox, M. A., et al. (2016). The role of local triplet excited states and D-A relative orientation in thermally activated delayed fluorescence: photophysics and devices. *Adv. Sci.* 3, 1–10. doi: 10.1002/advs.201600080
- Endo, A., Sato, K., Yoshimura, K., Kai, T., Kawada, A., Miyazaki, H., et al. (2011). Efficient up-conversion of triplet excitons into a singlet state and its application for organic light emitting diodes. *Appl. Phys. Lett.* 98, 2009–2012. doi: 10.1063/1.3558906
- Furno, M., Meerheim, R., Hofmann, S., Lüssem, B., and Leo, K. (2012). Efficiency and rate of spontaneous emission in organic electroluminescent devices. *Phys. Rev. B* 85, 1–21. doi: 10.1103/PhysRevB.85.115205
- Goushi, K., Yoshida, K., Sato, K., and Adachi, C. (2012). Organic light-emitting diodes employing efficient reverse intersystem crossing for triplet-to-singlet state conversion. *Nat. Photonics* 6, 253–258. doi: 10.1038/nphoton.2012.31
- Han, C., Zhang, Z., Ding, D., and Xu, H. (2018). Dipole-dipole interaction management for efficient blue thermally activated delayed fluorescence diodes. *Chem* 4, 2154–2167. doi: 10.1016/j.chempr.2018.06.005
- Higuchi, T., Nakanotani, H., and Adachi, C. (2015). High-efficiency white organic light-emitting diodes based on a blue thermally activated delayed fluorescent emitter combined with green and red fluorescent emitters. *Adv. Mater.* 27, 2019–2023. doi: 10.1002/adma.201404967
- Huang, T., Jiang, W., and Duan, L. (2018). Recent progress in solution processable TADF materials for organic light-emitting diodes. *J. Mater. Chem. C* 6, 5577–5596. doi: 10.1039/C8TC01139G
- Jankus, V., Data, P., Graves, D., McGuinness, C., Santos, J., Bryce, M. R., et al. (2014). Highly efficient TADF OLEDs: how the emitter-host interaction controls both the excited state species and electrical properties of the devices to achieve near 100% triplet harvesting and high efficiency. *Adv. Funct. Mater.* 24, 6178–6186. doi: 10.1002/adfm.201400948
- JOLED (2018). *JOLED to Start Providing OLED Display Panel Samples to ASUS*. JOLED Inc. Available online at: <https://www.j-oled.com/news-eng/2018-1-5/> (accessed August 9, 2018).
- Lakowicz, J. R. (2006). *Principles of Fluorescence Spectroscopy*, 3rd Edn. New York, NY: Springer.
- Lee, J., Shizu, K., Tanaka, H., Nomura, H., Yasuda, T., and Adachi, C. (2013). Oxadiazole- and triazole-based highly-efficient thermally activated delayed fluorescence emitters for organic light-emitting diodes. *J. Mater. Chem. C* 1:4599. doi: 10.1039/c3tc30699b
- Li, Y. (2019). *Photon Generation and Dissipation in Organic Light-Emitting Diodes* (Ph.D. thesis). Technische Universität Dresden, Dresden, Germany.
- Li, Y., Gao, X., Wang, L., and Tu, G. (2017). Deep-red organic light-emitting diodes with stable electroluminescent spectra based on zinc complex host material. *RSC Adv.* 7, 40533–40538. doi: 10.1039/C7RA06105F
- Li, Y., Tang, Z., Hänisch, C., Will, P.-A., Kovačič, M., Hou, J.-L., et al. (2018). Ultrathin MoO<sub>3</sub> layers in composite metal electrodes: improved optics allow highly efficient organic light-emitting diodes. *Adv. Opt. Mater.* 7:1801262. doi: 10.1002/adom.201801262
- Li, Y., Xie, G., Gong, S., Wu, K., and Yang, C. (2016). Dendronized delayed fluorescence emitters for non-doped, solution-processed organic light-emitting diodes with high efficiency and low efficiency roll-off simultaneously: two parallel emissive channels. *Chem. Sci.* 7, 5441–5447. doi: 10.1039/C6SC00943C
- Lin, T.-C., Sarma, M., Chen, Y.-T., Liu, S.-H., Lin, K.-T., Chiang, P.-Y., et al. (2018a). Probe exciplex structure of highly efficient thermally activated delayed fluorescence organic light emitting diodes. *Nat. Commun.* 9:3111. doi: 10.1038/s41467-018-05527-4
- Lin, X., Zhu, Y., Zhang, B., Zhao, X., Yao, B., Cheng, Y., et al. (2018b). Highly efficient TADF polymer electroluminescence with reduced efficiency roll-off via interfacial exciplex host strategy. *ACS Appl. Mater. Interfaces* 10, 47–52. doi: 10.1021/acsami.7b16887
- Liu, X. K., Chen, Z., Qing, J., Zhang, W. J., Wu, B., Tam, H. L., et al. (2015). Remanagement of singlet and triplet excitons in single-emissive-layer hybrid white organic light-emitting devices using thermally activated delayed fluorescent blue exciplex. *Adv. Mater.* 27, 7079–7085. doi: 10.1002/adma.201502897
- Luo, J., Xie, G., Gong, S., Chen, T., and Yang, C. (2016). Creating a thermally activated delayed fluorescence channel in a single polymer system to enhance exciton utilization efficiency for bluish-green electroluminescence. *Chem. Commun.* 52, 2292–2295. doi: 10.1039/C5CC09797E
- Mello, J. C., de, Wittmann, H. F., and Friend, R. H. (1997). An improved experimental determination of external photoluminescence quantum efficiency. *Adv. Mater.* 9, 230–232. doi: 10.1002/adma.1997009308
- Nakanotani, H., Masui, K., Nishide, J., Shibata, T., and Adachi, C. (2013). Promising operational stability of high-efficiency organic light-emitting diodes based on thermally activated delayed fluorescence. *Sci. Rep.* 3:2127. doi: 10.1038/srep02127
- Nikolaenko, A. E., Cass, M., Bourcet, F., Mohamad, D., and Roberts, M. (2015). Thermally activated delayed fluorescence in polymers: a new route toward highly efficient solution processable OLEDs. *Adv. Mater.* 27, 7236–7240. doi: 10.1002/adma.201501090
- Pander, P. H., Gogoc, S., Colella, M., Data, P., and Dias, F. B. (2018). Thermally-activated delayed fluorescence in polymer-small molecule exciplex blends for solution-processed organic light-emitting diodes. *ACS Appl. Mater. Interfaces* 10, 28796–28802. doi: 10.1021/acsami.8b07554
- Reineke, S., Lindner, F., Schwartz, G., Seidler, N., Walzer, K., Lüssem, B., et al. (2009). White organic light-emitting diodes with fluorescent tube efficiency. *Nature* 459, 234–238. doi: 10.1038/nature08003
- Reineke, S., Rosenow, T. C., Lüssem, B., and Leo, K. (2010). Improved high-brightness efficiency of phosphorescent organic LEDs comprising emitter molecules with small permanent dipole moments. *Adv. Mater.* 22, 3189–3193. doi: 10.1002/adma.201000529
- Reineke, S., Thomschke, M., Lüssem, B., and Leo, K. (2013). White organic light-emitting diodes: status and perspective. *Rev. Mod. Phys.* 85, 1245–1293. doi: 10.1103/RevModPhys.85.1245
- Segal, M., Baldo, M., Holmes, R., Forrest, S., and Soos, Z. (2003). Excitonic singlet-triplet ratios in molecular and polymeric organic materials. *Phys. Rev. B* 68:075211. doi: 10.1103/PhysRevB.68.075211
- Shao, S., Hu, J., Wang, X., Wang, L., Jing, X., and Wang, F. (2017). Blue thermally activated delayed fluorescence polymers with nonconjugated backbone and

- through-space charge transfer effect. *J. Am. Chem. Soc.* 139, 17739–17742. doi: 10.1021/jacs.7b10257
- Su, S.-J., Chiba, T., Takeda, T., and Kido, J. (2008). Pyridine-containing triphenylbenzene derivatives with high electron mobility for highly efficient phosphorescent OLEDs. *Adv. Mater.* 20, 2125–2130. doi: 10.1002/adma.200701730
- Tang, C. W., and Vanslyke, S. A. (1987). Organic electroluminescent diodes. *Appl. Phys. Lett.* 51, 913–915. doi: 10.1063/1.98799
- Thompson, M. (2007). The evolution of organometallic complexes in organic light-emitting devices. *MRS Bull.* 32, 694–701. doi: 10.1557/mrs2007.144
- Tsai, M. H., Lin, H. W., Su, H. C., Ke, T. H., Wu, C. C., Fang, F. C., et al. (2006). Highly efficient organic blue electrophosphorescent devices based on 3,6-Bis(triphenylsilyl)carbazole as the host material. *Adv. Mater.* 18, 1216–1220. doi: 10.1002/adma.200502283
- Ullbrich, S., Benduhn, J., Jia, X., Nikolis, V. C., Tvingstedt, K., Piersimoni, F., et al. (2019). Emissive and charge-generating donor–acceptor interfaces for organic optoelectronics with low voltage losses. *Nat. Mater.* 18, 459–464. doi: 10.1038/s41563-019-0324-5
- Uoyama, H., Goushi, K., Shizu, K., Nomura, H., and Adachi, C. (2012). Highly efficient organic light-emitting diodes from delayed fluorescence. *Nature* 492, 234–238. doi: 10.1038/nature11687
- Wei, Q., Fei, N., Islam, A., Lei, T., Hong, L., Peng, R., et al. (2018a). Small-molecule emitters with high quantum efficiency: mechanisms, structures, and applications in OLED devices. *Adv. Opt. Mater.* 6:1800512. doi: 10.1002/adom.201800512
- Wei, Q., Ge, Z., and Voit, B. (2018b). Thermally activated delayed fluorescent polymers: structures, properties, and applications in OLED devices. *Macromol. Rapid Commun.* 40:1800570. doi: 10.1002/marc.201800570
- Wei, Q., Kleine, P., Karpov, Y., Qiu, X., Komber, H., Sahre, K., et al. (2017). Conjugation-induced thermally activated delayed fluorescence (TADF): from conventional non-TADF units to TADF-active polymers. *Adv. Funct. Mater.* 27, 1–11. doi: 10.1002/adfm.201605051
- Wong, M. Y., and Zysman-Colman, E. (2017). Purely organic thermally activated delayed fluorescence materials for organic light-emitting diodes. *Adv. Mater.* 29:1605444. doi: 10.1002/adma.201605444
- Wu, Z., Yu, L., Zhao, F., Qiao, X., Chen, J., Ni, F., et al. (2017). Precise exciton allocation for highly efficient white organic light-emitting diodes with low efficiency roll-off based on blue thermally activated delayed fluorescent exciplex emission. *Adv. Opt. Mater.* 5:1700415. doi: 10.1002/adom.201700415
- Xie, G., Luo, J., Huang, M., Chen, T., Wu, K., Gong, S., et al. (2017). Inheriting the characteristics of TADF small molecule by side-chain engineering strategy to enable bluish-green polymers with high PLQYs up to 74% and external quantum efficiency over 16% in light-emitting diodes. *Adv. Mater.* 29:1604223. doi: 10.1002/adma.201604223
- Yang, Y., Wang, S., Zhu, Y., Wang, Y., Zhan, H., and Cheng, Y. (2018). Thermally activated delayed fluorescence conjugated polymers with backbone-donor/pendant-acceptor architecture for nondoped OLEDs with high external quantum efficiency and low roll-off. *Adv. Funct. Mater.* 28:1706916. doi: 10.1002/adfm.201706916
- Zhang, D., Cai, M., Zhang, Y., Zhang, D., and Duan, L. (2016). Sterically shielded blue thermally activated delayed fluorescence emitters with improved efficiency and stability. *Mater. Horiz.* 3, 145–151. doi: 10.1039/C5MH00258C
- Zhang, Y., and Forrest, S. R. (2012). Triplets contribute to both an increase and loss in fluorescent yield in organic light emitting diodes. *Phys. Rev. Lett.* 108:267404. doi: 10.1103/PhysRevLett.108.267404
- Zheng, H., Zheng, Y., Liu, N., Ai, N., Wang, Q., Wu, S., et al. (2013). All-solution processed polymer light-emitting diode displays. *Nat. Commun.* 4:1971. doi: 10.1038/ncomms2971

**Conflict of Interest:** The authors declare that the research was conducted in the absence of any commercial or financial relationships that could be construed as a potential conflict of interest.

Copyright © 2019 Li, Wei, Cao, Fries, Cucchi, Wu, Scholz, Lenk, Voit, Ge and Reineke. This is an open-access article distributed under the terms of the Creative Commons Attribution License (CC BY). The use, distribution or reproduction in other forums is permitted, provided the original author(s) and the copyright owner(s) are credited and that the original publication in this journal is cited, in accordance with accepted academic practice. No use, distribution or reproduction is permitted which does not comply with these terms.



# Synthesis and Electroluminescent Properties of Through-Space Charge Transfer Polymers Containing Acridan Donor and Triarylboron Acceptors

Fan Chen<sup>1,2</sup>, Jun Hu<sup>1,2</sup>, Xingdong Wang<sup>1</sup>, Shiyang Shao<sup>1\*</sup>, Lixiang Wang<sup>1\*</sup>, Xiabin Jing<sup>1</sup> and Fosong Wang<sup>1</sup>

<sup>1</sup> State Key Laboratory of Polymer Physics and Chemistry, Changchun Institute of Applied Chemistry, Chinese Academy of Sciences, Changchun, China, <sup>2</sup> School of Applied Chemistry and Engineering, University of Science and Technology of China, Hefei, China

## OPEN ACCESS

### Edited by:

Eli Zysman-Colman,  
University of St Andrews,  
United Kingdom

### Reviewed by:

Takeshi Fujita,  
University of Tsukuba, Japan  
Basem Moosa,  
KAUST Catalysis Center (KCC),  
Saudi Arabia

### \*Correspondence:

Shiyang Shao  
ssyang@ciac.ac.cn  
Lixiang Wang  
lixiang@ciac.ac.cn

### Specialty section:

This article was submitted to  
Organic Chemistry,  
a section of the journal  
Frontiers in Chemistry

Received: 01 October 2019

Accepted: 25 November 2019

Published: 10 December 2019

### Citation:

Chen F, Hu J, Wang X, Shao S,  
Wang L, Jing X and Wang F (2019)  
Synthesis and Electroluminescent  
Properties of Through-Space Charge  
Transfer Polymers Containing Acridan  
Donor and Triarylboron Acceptors.  
Front. Chem. 7:854.  
doi: 10.3389/fchem.2019.00854

We report the design, synthesis and electroluminescent properties of three kinds of through-space charge transfer (TSCT) polymers consisting of non-conjugated polystyrene backbone, acridan donor and triarylboron acceptors having different substituents such as hydrogen (H), fluorine (F), and trifluoromethyl (CF<sub>3</sub>). Owing to the weak electron interaction between acridan donor and triarylboron acceptor through non-conjugated connection, blue emission with peaks in range of 429–483 nm can be achieved for the polymers in solid-state film, accompanied with photoluminescence quantum yields of 26–53%. The resulting TSCT polymers exhibit small  $\Delta E_{ST}$  values below 0.1 eV owing to the separated HOMO and LUMO distributions, showing thermally activated delayed fluorescence with lifetimes in range of 0.19–0.98  $\mu$ s. Meanwhile, the polymers show aggregation-induced emission (AIE) effect with the emission intensity increased by up to  $\sim 33$  folds from solution to aggregation state. Solution-processed organic light-emitting diodes based on the polymers containing trifluoromethyl substituent exhibit promising electroluminescent performance with maximum luminous efficiency of 20.1 cd A<sup>-1</sup> and maximum external quantum efficiency of 7.0%, indicating that they are good candidates for development of luminescent polymers.

**Keywords:** thermally activated delayed fluorescence, through-space charge transfer, triarylboron, electroluminescent polymer, organic light-emitting diodes

## INTRODUCTION

Charge transfer (CT) is a crucial process in determining the emission behaviors of luminescent materials (Muller et al., 2003; Wu et al., 2004; Yuan et al., 2012; Liu et al., 2018; Sarma and Wong, 2018; Li J. et al., 2019). Luminescent polymers with CT emission have enabled important applications in solution-processed optoelectronic devices owing to their tunable emission color and promising luminescent efficiency (Yu et al., 2013; Bai et al., 2017). For example, thermally activated delayed fluorescence (TADF) polymers with finely manipulated CT process between electron donors and acceptors have emerged as attractive materials for organic light-emitting

diodes (OLEDs) in recent years (Uoyama et al., 2012; Albrecht et al., 2015; Nikolaenko et al., 2015; Lee et al., 2016; Li et al., 2016, 2017; Luo et al., 2016; Zhu et al., 2016; Freeman et al., 2017; Wei et al., 2017; Wong and Zysman-Colman, 2017; Xie et al., 2017; Hu et al., 2018; Kim D. H. et al., 2018; Li C. S. et al., 2019). By separating the highest occupied molecular orbital (HOMO) and the lowest unoccupied molecular orbital (LUMO) orbitals to realize small singlet-triplet energy splitting ( $\Delta E_{ST}$ ), the CT polymers with TADF characteristics can utilize the spin-forbidden triplet excitons through reverse intersystem crossing (RISC) process, shedding light on the potential of achieving solution-processed OLEDs with 100% internal quantum efficiency (IQE) based on pure organic polymers (Zhang et al., 2012; Hirata et al., 2015; Suzuki et al., 2015; Wang et al., 2015; Huang et al., 2018; Kim H. J. et al., 2018; Spuling et al., 2018; Wu et al., 2018; Ahn et al., 2019; Ban et al., 2019; Zhao et al., 2019).

So far, most luminescent polymers with CT emission are based on conjugated backbone, with feature of through-bond charge transfer (TBCT) emission from covalently bonded donors and acceptors. Owing to the strong electron coupling between donors and acceptors, the polymers are able to show large oscillator strength and high photoluminescence quantum efficiency (PLQY). However, the strong electron coupling mediated by covalent bonds tends to induce considerable red-shift of emission for the resulting polymers, undesirable for blue/deep blue emission. Meanwhile,  $\Delta E_{ST}$  of the polymer can also be increased by the strong electron interaction between donor and acceptor, which could be unfavorable for realizing TADF effect (Li et al., 2016; Nobuyasu et al., 2016; Hu et al., 2018).

Different from conjugated donor-acceptor polymers with TBCT emission, non-conjugated polymers with through-space charge transfer (TSCT) emission between spatially separated acridan donors and triazine acceptors have been reported to realize blue emission with TADF effect (Shao et al., 2017; Hu et al., 2019). Due to the physical separation of donor and acceptor, through-space charge transfer, rather than through-bond charge transfer occurs in this motif. This molecular design has the following merits. First, the non-conjugated polymer backbone avoids the strong electron coupling between donor and acceptor, favorable for blue emission of the resulting

polymers. Second, the spatially separated donors and acceptors result in small overlap of HOMO and LUMO distributions, leading to small  $\Delta E_{ST}$  and TADF effect. By modulating the CT strength through introducing substituents with different electron-accepting capability, TSCT polymers with emission color ranging from deep-blue to red can be realized with external quantum efficiency (EQE) up to 16.2%, suggesting their potential in development of novel luminescent materials for solution-processed OLEDs.

Recently triarylborons have been attractive building blocks for luminescent materials with CT character because of their promising electron-accepting properties endowed by the vacant p-orbitals of central boron atoms that can participate in  $\pi$ -conjugation with aryl groups (Hirai et al., 2015; Numata et al., 2015; Suzuki et al., 2015; Hatakeyama et al., 2016; Wu et al., 2018; Ahn et al., 2019; Kondo et al., 2019; Møllerup and Wang, 2019). The CT character of triarylboron-based donor-acceptor compounds strongly influences their photophysical properties and makes them useful for design of luminescent materials. For example, Adachi et al. first reported efficient blue TADF materials having a boron-containing acceptor combined with various donors, producing deep blue emission (450 nm) with maximum EQE of 20% (Numata et al., 2015). Recently, Hatakeyama et al. demonstrated triarylboron polycyclic aromatic compounds with multiple resonance effect of boron and nitrogen atoms, showing ultrapure blue emission with full-width at half-maximum of 18 nm and maximum EQE of 34.4%, indicating the great potential of triarylboron in developing efficient luminescent materials (Kondo et al., 2019).

Here we report the design, synthesis and properties of three kinds of through-space charge transfer polymers containing non-conjugated polystyrene backbone, acridan donor and triarylboron acceptors having different substituents such as hydrogen (H), fluorine (F), and trifluoromethyl ( $CF_3$ ). The triarylboron units are used as acceptors because of their weak electron-accepting capability which is favorable for realizing blue emission. By decorating the triarylboron acceptors with H, F, and  $CF_3$  groups to tune the charge transfer strength between donor and acceptor, the emission color can be tuned from deep blue (429 nm) to sky blue (483 nm) region in solid-state film, accompanied with improved photoluminescence quantum yield

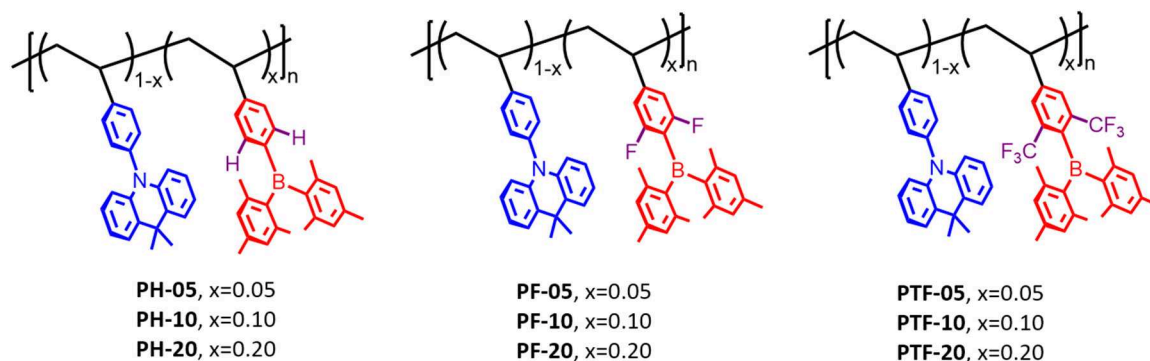


**FIGURE 1 |** Molecular design and chemical structures of the through-space charge-transfer polymers containing triarylboron units.



(PLQY) from 26 to 53%. The polymers exhibit small  $\Delta E_{ST}$  values ( $<0.1$  eV) because of the separated HOMO and LUMO distributions, allowing them to show TADF effect. Meanwhile, the polymers show aggregation-induced emission effect with the emission intensity increased by up to  $\sim 33$  folds from solution to aggregation state (Luo et al., 2001; Hong et al., 2011; Mei et al., 2015). Solution-processed organic light-emitting diodes (OLEDs) based on the triarylboron-containing polymers show maximum EQEs up to 7.0%, indicating that they are promising candidates for development of luminescent polymers.

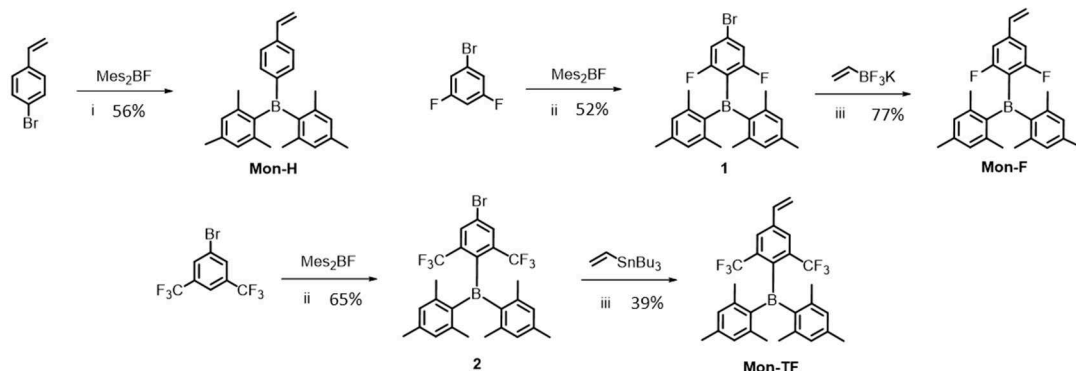
## RESULTS AND DISCUSSION

### Molecular Design and Synthesis

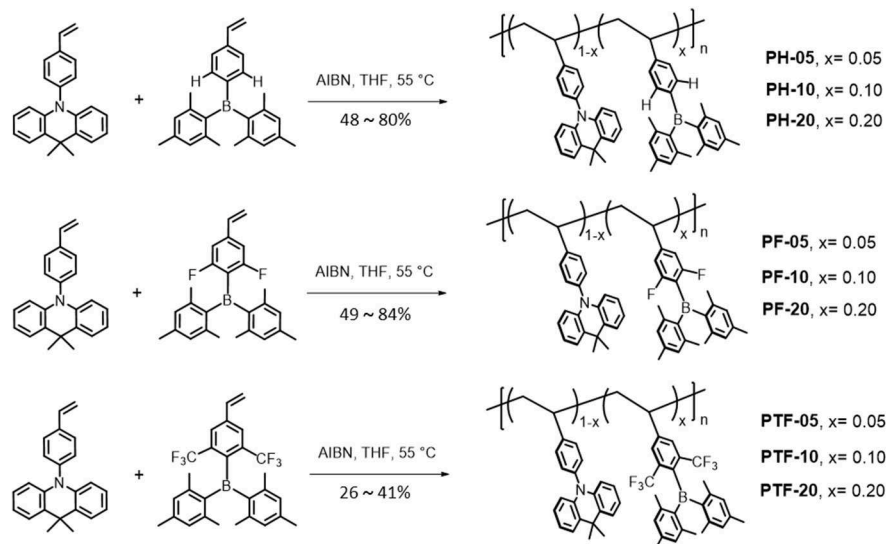
To design luminescent polymers with through-space charge transfer, selection of polymer backbone, donor and acceptor plays the key role in determining the photophysical and

electroluminescent properties of the resulting polymers. In this work polystyrene is selected as backbone because it provides the non-conjugated connection between donor and acceptor, while acridan is chosen as donor because of its good electron-donating ability as well as the rigid bridged structure. Moreover, triarylboron units are used as acceptors because they exhibit weak electron-accepting capability owing to the empty  $p_z$  orbital of boron that is capable to participate in  $\pi$ -conjugation with aryl groups. To tune the emissive color, three kinds of substituents hydrogen (H), fluorine (F), and trifluoromethyl ( $CF_3$ ) are introduced to the polymers, denoted as PH-05–PH-20, PF-05–PF-20, and PTF-05–PTF-20, respectively (**Figure 1**). The three substituents are selected because their electron affinity are gradually increased in order of H, F, and  $CF_3$ , which can enhance the CT strength between the acridan donor and the triarylboron acceptor, allowing the modulation of TSCT emission of the resulting polymers. In addition, the content of acceptors

#### A Triarylboron monomers



#### B Triarylboron-based TSCT polymers



**SCHEME 1** | Synthetic routes for the triarylboron monomers (**A**) and TSCT polymers (**B**). Reagents and conditions: (i)  $n$ -BuLi, THF,  $-78^\circ\text{C}$ ; (ii) LDA, THF,  $-78^\circ\text{C}$ ; (iii)  $\text{Pd}(\text{PPh}_3)_2\text{Cl}_2$ ,  $\text{Cs}_2\text{CO}_3$ , THF/ $\text{H}_2\text{O}$ ,  $80^\circ\text{C}$ , 24 h; (iv)  $\text{Pd}(\text{PPh}_3)_4$ , toluene,  $105^\circ\text{C}$ , 20 h.

are tuned at 5, 10, and 20 mol% to explore the influence of relative ratio between donor and acceptor on photophysical properties of the polymers.

Synthetic routes of the polymers are outlined in **Scheme 1**. The monomer Mon-H was prepared by a two-step procedure where the commercially available 4-bromovinylbenzene was first lithiated with *n*-BuLi, and then reacted with dimesitylfluoroborane ( $\text{Mes}_2\text{BF}$ ) to afford the product in yield

of 56%. For Mon-F and Mon-TE, 1-bromo-3,5-difluorobenzene (**1**) and 1-bromo-3,5-bis(trifluoromethyl)benzene (**3**) were first lithiated by lithium diisopropylamide (LDA) and then treated with  $\text{Mes}_2\text{BF}$  to afford the bromide intermediates **2** and **4**. Consequently **2** and **4** were cross-coupled with vinyltrifluoroborate or tributylvinylstannane under palladium-catalyzed conditions to afford the desired monomers. With the monomers in hand, TSCT polymers were synthesized by free

**TABLE 1** | Physical properties of the TSCT polymers.

Polymer	$M_n^a$ (KDa)	PDI <sup>a</sup>	$T_g$ (°C)	$T_d$ (°C)	$\lambda_{PL}^b$ (nm)	$\lambda_{PL}^c$ (nm)	PLQY <sup>f</sup> (%)	$\tau_p/\tau_d^d$ (μs)	$\Delta E_{ST}^e$ (eV)
PH-05	21.8	1.68	176	356	438	429	26	0.007/0.19	0.076
PH-10	29.5	1.44	196	335	440	429	27	0.009/0.22	0.083
PH-20	43.2	1.55	193	303	439	435	27	0.008/0.21	0.096
PF-05	24.6	1.61	195	360	465	443	27	0.021/0.49	0.070
PF-10	31.6	1.51	197	343	467	453	30	0.036/0.44	0.073
PF-20	38.2	1.54	170	336	470	459	38	0.029/0.46	0.090
PTF-05	20.4	1.56	201	341	494	481	34	0.018/0.86	0.068
PTF-10	14.6	1.63	204	338	496	472	44	0.019/0.95	0.087
PTF-20	9.0	1.73	207	317	501	483	53	0.024/0.98	0.084

<sup>a</sup>Determined by gel permeation chromatography with polystyrene standards.

<sup>b</sup>Measured in toluene at room temperature with a concentration of  $1 \times 10^{-4}$  M.

<sup>c</sup>Measured in neat films at room temperature.

<sup>d</sup>Lifetimes of prompt emission ( $\tau_p$ ) and delayed emission ( $\tau_d$ ) in toluene at 298 K in  $N_2$ .

<sup>e</sup>Calculated from the onset wavelength of fluorescent and phosphorescent emission in film state.

<sup>f</sup>Absolute PL quantum yield in neat films determined in nitrogen.

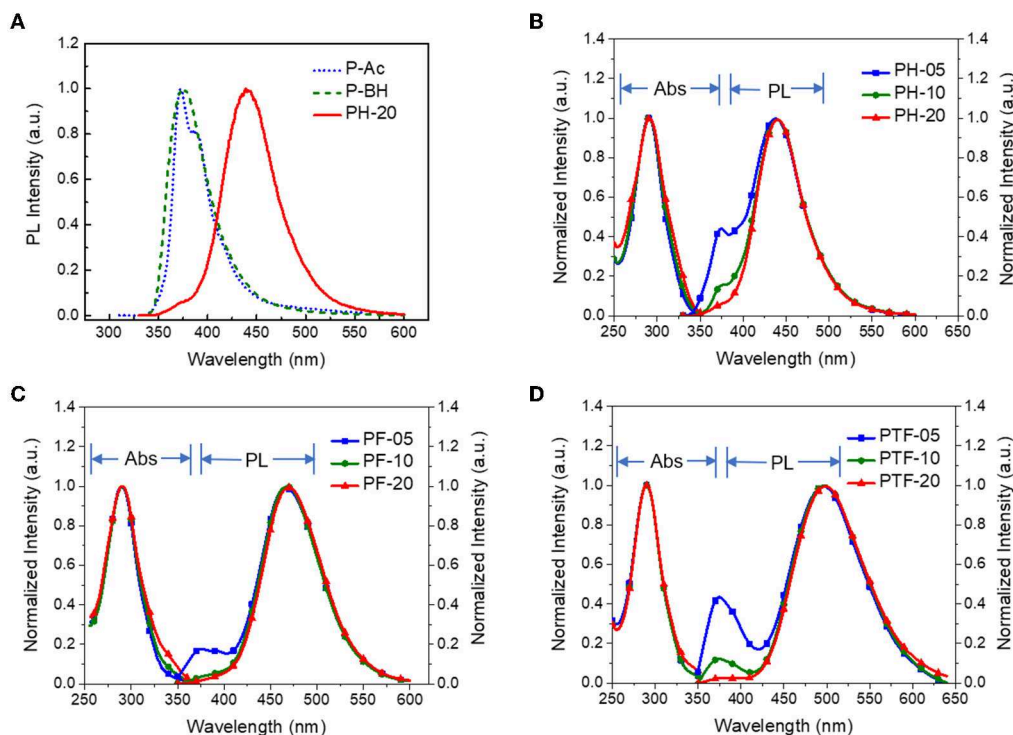


**FIGURE 2** | PL spectra of PH-20, P-Ac containing only acridan donor and P-BH containing only triarylboron acceptor (**A**); as well as absorption and PL spectra of PH-05–PH-20 (**B**), PF-05–PF-20 (**C**), and PTF-05–PTF-20 (**D**) in toluene at 298 K with concentration of  $1 \times 10^{-4}$  M ( $\lambda_{ex} = 310$  nm).

radical polymerization of the corresponding vinyl-functionalized acridan and triarylboron monomers using 2-azoisobutyronitrile as initiator and tetrahydrofuran (THF) as solvent. The content of triarylboron acceptors of the polymers are controlled through feed ratio (5–20 mol% for PX-5–PX-20). For comparison, three triarylboron model compounds bearing no vinyl groups and two control polymers with only acridan donors and triarylboron acceptors are also synthesized (**Scheme S1**). Number-average molecular weights ( $M_n$ s) of the polymers measured by gel permeation chromatography using polystyrene as standard exhibit typical values of 9–45 KDa with polydispersity index (PDI) of 1.44–1.73 (**Table 1**). The decomposition temperatures ( $T_d$ ) of the polymers with 5% weight loss under nitrogen are higher than 300°C, while glass transition temperatures ( $T_g$ ) for the polymers are observed at 170–210°C (**Figure S1**). There are no exothermic peaks produced by crystallization within the scanning range, indicating the amorphous nature of the polymers. The TSCT polymers are readily soluble in common organic solvents, such as toluene, chloroform, tetrahydrofuran and chlorobenzene, ensuring the formation of high-quality films through solution process.

## Photophysical Properties

The UV-vis absorption and fluorescence spectra of the polymers in toluene at 298K are shown in **Figure 2**, with the data

summarized in **Table 1**. The polymers show similar absorption peaks at 290 nm which are mainly attributed to  $\pi$ - $\pi^*$  transition of acridan and triarylboron units under diluted solutions. PL spectra of the polymers exhibit weak emission bands at 374 nm coming from the acridan unit, together with a strong, broad, and featureless emission bands at longer wavelength. These featureless bands are red-shifted compared with those of acridan and triarylboron units as well as the acridan- and triarylboron-containing homopolymers (**Figure 2A** and **Figure S2**). Moreover, these emissions show strong positive solvation effect as the polarity of the solvent increases. For instance, the emission maxima ( $\lambda_{em,max}$ ) of PH-20 shifts from 417 nm in cyclohexane to 476 nm in THF (**Figure S3**), confirming that the emissions are originating from CT transition between the donors and acceptors. By increasing electron-accepting ability of the triarylboron acceptors, the CT emission can be red-shifted from 438 nm (PH-05) to 465 nm (PF-05) and 494 nm (PTF-05). The content of the acceptor also have influence on the emission wavelength of the polymers. As the content of the acceptor increases from 5 to 20 mol%, the emission wavelength is red-shifted by 2–7 nm, consistent with the observations for triazine-based TSCT polymers (Shao et al., 2017). Different from those in solution, PL spectra of the polymers in film state show only CT emission from 429 to 483 nm (**Figure 3**), indicating that excited state energy of acridan donor has been

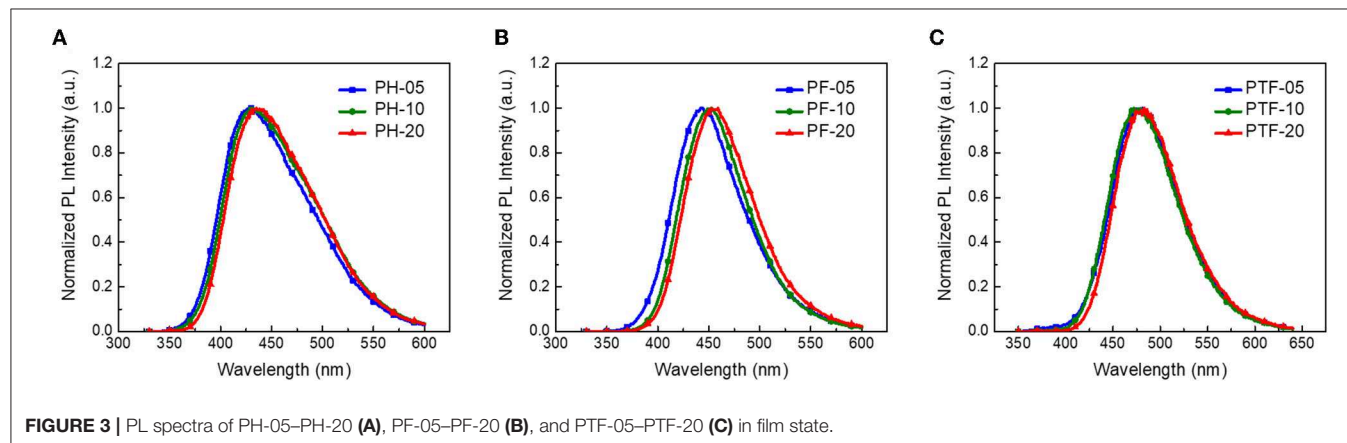


**FIGURE 3** | PL spectra of PH-05–PH-20 (A), PF-05–PF-20 (B), and PTF-05–PTF-20 (C) in film state.

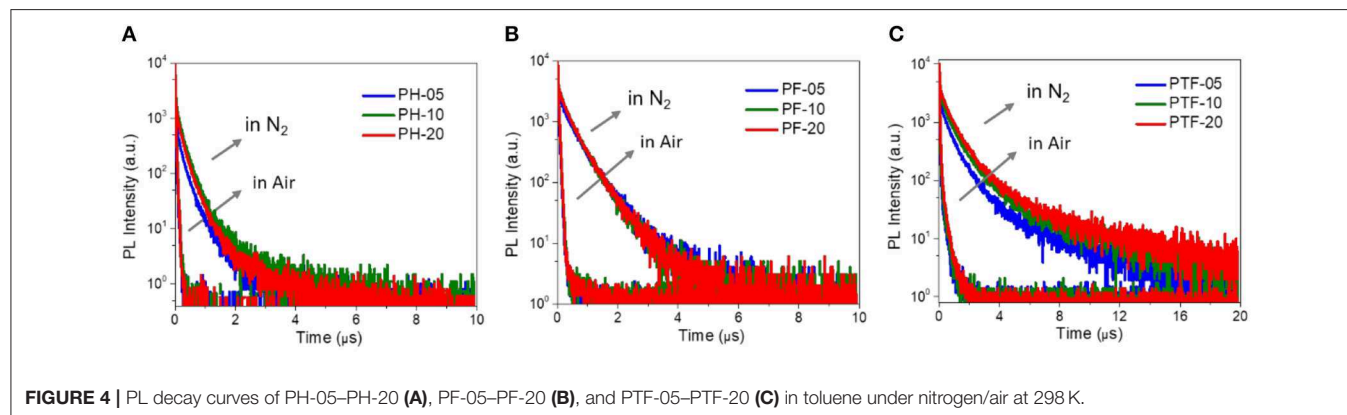


**FIGURE 4** | PL decay curves of PH-05–PH-20 (A), PF-05–PF-20 (B), and PTF-05–PTF-20 (C) in toluene under nitrogen/air at 298 K.

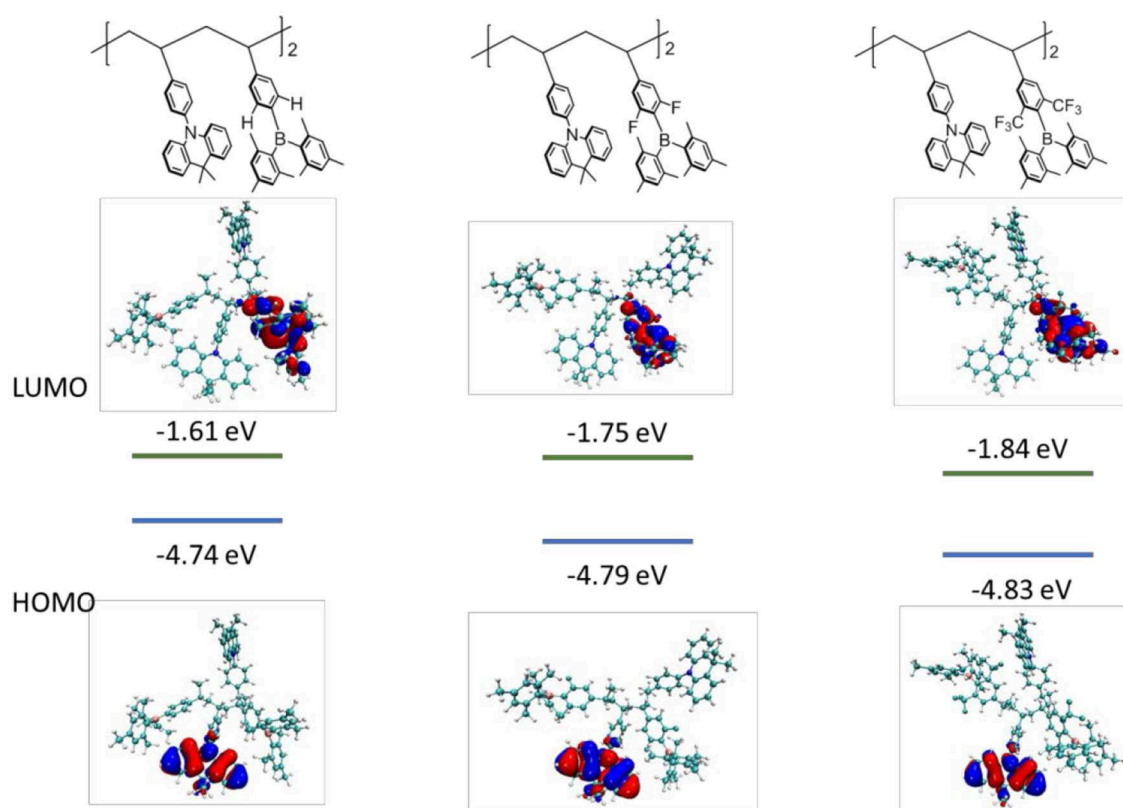


**FIGURE 5** | HOMO/LUMO distributions and energy levels for the polymer models consisting of two repeating units using density functional theory (DFT) method at B3LYP/6-31G(d) level.

completely transferred to the CT emissive species. The PLQYs of the polymers determined by integrating sphere is 26–27% for PH-05–PH-20, 27–38% for PF-05–PF-20 and 34–53% for PTF-05–PTF-20 (**Table 1**). As the content of acceptor increases, PLQYs of the polymers do not decrease, implying the weak concentration quenching effect of the TSCT emissive species.

To investigate the TADF properties of the polymers, PL decay characteristics are measured in nitrogen and air. As shown in **Figure 4** and **Table 1**, under nitrogen, all polymers in toluene displays distinctive delayed emissions with lifetimes ( $\tau_d$ ) in microsecond scale, together with prompt emissions with lifetimes ( $\tau_p$ ) in nanosecond scale. For example, PH-5, PF-5, and PTF-5 show  $\tau_{ds}$  of 0.19, 0.49, and 0.86  $\mu$ s, respectively. The content of triarylboron units has slightly influence on  $\tau_d$ , with values of 0.21, 0.46, and 0.98  $\mu$ s detected for PH-20, PF-20, and PTF-20, respectively. Under air, the delayed components are not detectable for all the polymers, indicating that the delayed emission is arising from triplets which can be quenched by oxygen, consistent with typical TADF behaviors. To further explore the TADF character,  $\Delta E_{ST}$ s of the polymers were determined from the onset of fluorescence spectra at room temperature and phosphorescence spectra at 77 K (**Figure S4**), which are smaller than 0.1 eV (**Table 1**). Such small  $\Delta E_{ST}$ s are consistent with the TADF effect since the rapid RISC process

can be favored by small  $\Delta E_{ST}$  to convert non-forbidden triplet excitons to radiative singlet excitons.

To get insight into the electronic structures of the triarylboron-based TSCT polymers, frontier orbital distributions were investigated by density functional theory (DFT) calculations. It is found that for all the polymers with different substitution patterns, the HOMOs are predominantly located on the acridan units, whereas the LUMOs are distributed over the triarylboron acceptors, suggesting the CT character of the polymers (**Figure 5**). Moreover, the LUMO level of the polymers decreases from  $-1.61$  to  $-1.75$  eV and  $-1.84$  eV as the substituent changes from H to F and CF<sub>3</sub>, indicating that the electron-accepting ability becomes stronger. Since the HOMO and LUMO are well-separated, the polymers show close singlet state ( $S_1$ ) and triplet state ( $T_1$ ) energy levels with the  $\Delta E_{ST}$  values estimated to be  $\sim$ zero according to time-dependent density functional theory (TD-DFT) calculations, which are consistent with the experimental  $\Delta E_{ST}$  values.

It is noteworthy that the triarylboron-based TSCT polymers exhibit aggregation-induced emission (AIE) effect through measuring their PL spectra in THF/water mixed solvents (Luo et al., 2001; Hong et al., 2011; Mei et al., 2015). As shown in **Figure 6**, PTF-20 in pure THF solution shows a weak emission band at  $\sim 520$  nm. As water is added, a slight increase in PL



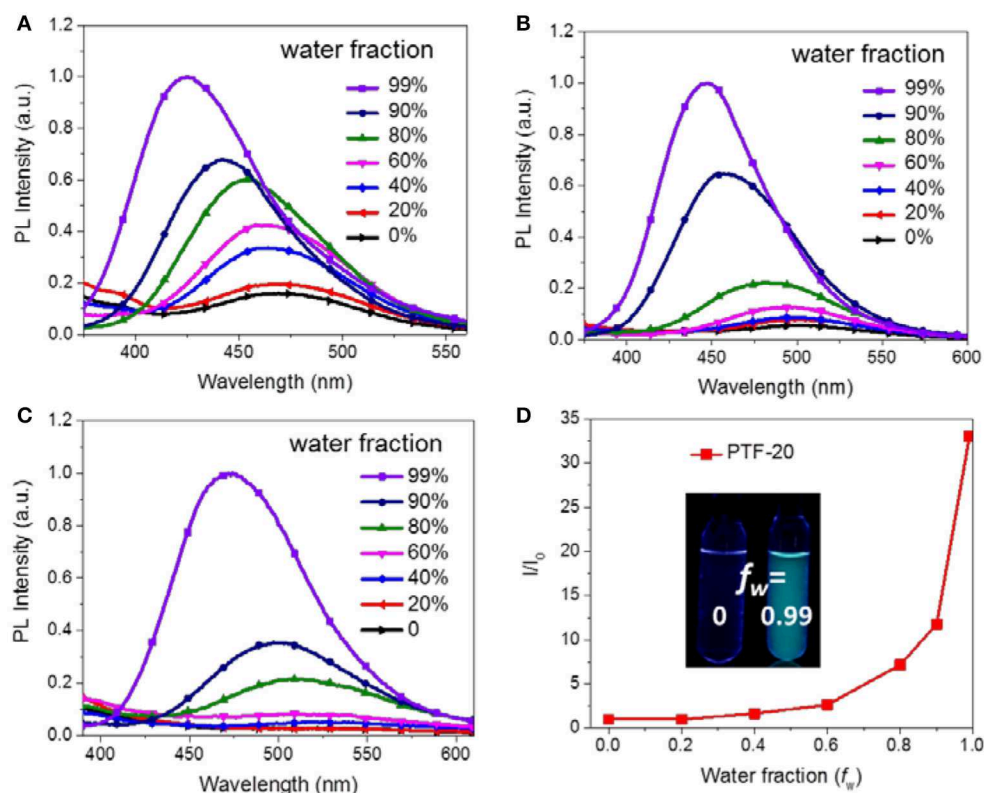


**FIGURE 6 |** PL spectra of PH-20 (A), PF-20 (B), and PTF-20 (C) in THF/water mixture with different water fractions (concentration of polymers was  $1 \times 10^{-5}$  M,  $\lambda_{\text{ex}} = 310$  nm), and relative emission intensity of PTF-20 in THF/water mixture (D). Inset, PL images of polymers with different water fractions under 254 nm UV light.

intensity was observed, which is accompanied with blue-shift of emission band. When the weight water ( $f_w$ ) is higher than 60%, the PL intensity increases drastically. Especially, at  $f_w$  of 99%, the polymer shows a dramatic increased intensity that is  $\sim 33$  times higher than the initial THF solution ( $f_w = 0$ ). Similar AIE effect is also observed for PH-20 and PF-20 with emission enhanced by  $\sim 6$  and  $\sim 18$  folds, respectively, as  $f_w$  increases from 0 to 0.99, which can be attributed to aggregation-induced dipole-dipole interaction between donors and acceptors.

## Electroluminescent Properties

To investigate the electroluminescent properties of the triarylboron TSCT polymers, solution-processed OLEDs were fabricated with device configuration of ITO/PEDOT:PSS (40 nm)/polymer (40 nm)/TSPO1 (8 nm)/TmPyPB(42 nm)/LiF (1 nm)/Al (100 nm) (Figure 7). Here PEDOT:PSS stands for poly(3,4-ethylenedioxythiophene):poly(styrene sulfonate) which serves as the hole-injection layer. TSPO1 (diphenyl(4-(triphenylsilyl)phenyl)phosphine oxide) (Mamada et al., 2011) and TmPyPB (1,3,5-tri(m-pyrid-3-yl-phenyl) benzene) (Su et al., 2008) act as the exciton blocking layer and the electron-transporting layer, respectively. As shown in Figures 7D–F, the polymers containing H substituents (PH-05, PH-10, and PH-20) show multiple emission bands at  $\sim 420$  and  $\sim 480$  nm. The former emission bands are similar to those observed in

film-state PL spectra and therefore can be assigned to the CT emission. However, the origin of the latter emission bands is not clear yet. Similar behavior is also observed for PF-05–PF-20, showing CT emission at  $\sim 460$  nm and unattributable emission bands at  $\sim 570$  nm. Despite of this, the polymer bearing  $\text{CF}_3$  groups (PTF-05–PTF-20) show mainly CT emission regardless of the triarylboron content, with CIE coordinates in range of (0.25, 0.39)–(0.29, 0.47).

EQE–luminance and current density–voltage–luminance characteristics of the devices are shown in Figures 7G–I and Figure S5. The device performance is summarized in Table 2. All the devices show low driving voltages at 3.0–3.4 V, implying the good carrier injection and transport from the electrodes. The device efficiency of the TSCT polymers is dependant on both the substituent and the content of triarylboron units. For example, from PH-05 to PF-05 and PTF-05, the maximum LE increases from 5.5 to 16.3  $\text{cd A}^{-1}$ , and the maximum EQE increases from 2.9 to 5.7%. This observation is consistent with the enhanced PLQYs of the polymer films. Meanwhile, from PTF-05 to PTF-20 with increasing triarylboron content, the maximum LE increases slightly from 16.3 to 20.1  $\text{cd A}^{-1}$ , implying the negligible concentration quenching effect in the polymers. We note that the maximum EQEs of PTF-05–PTF-20 with values of 5.7–7.0% are much higher than the upper limit of conventional fluorescent materials (EQE = 5%), confirming the

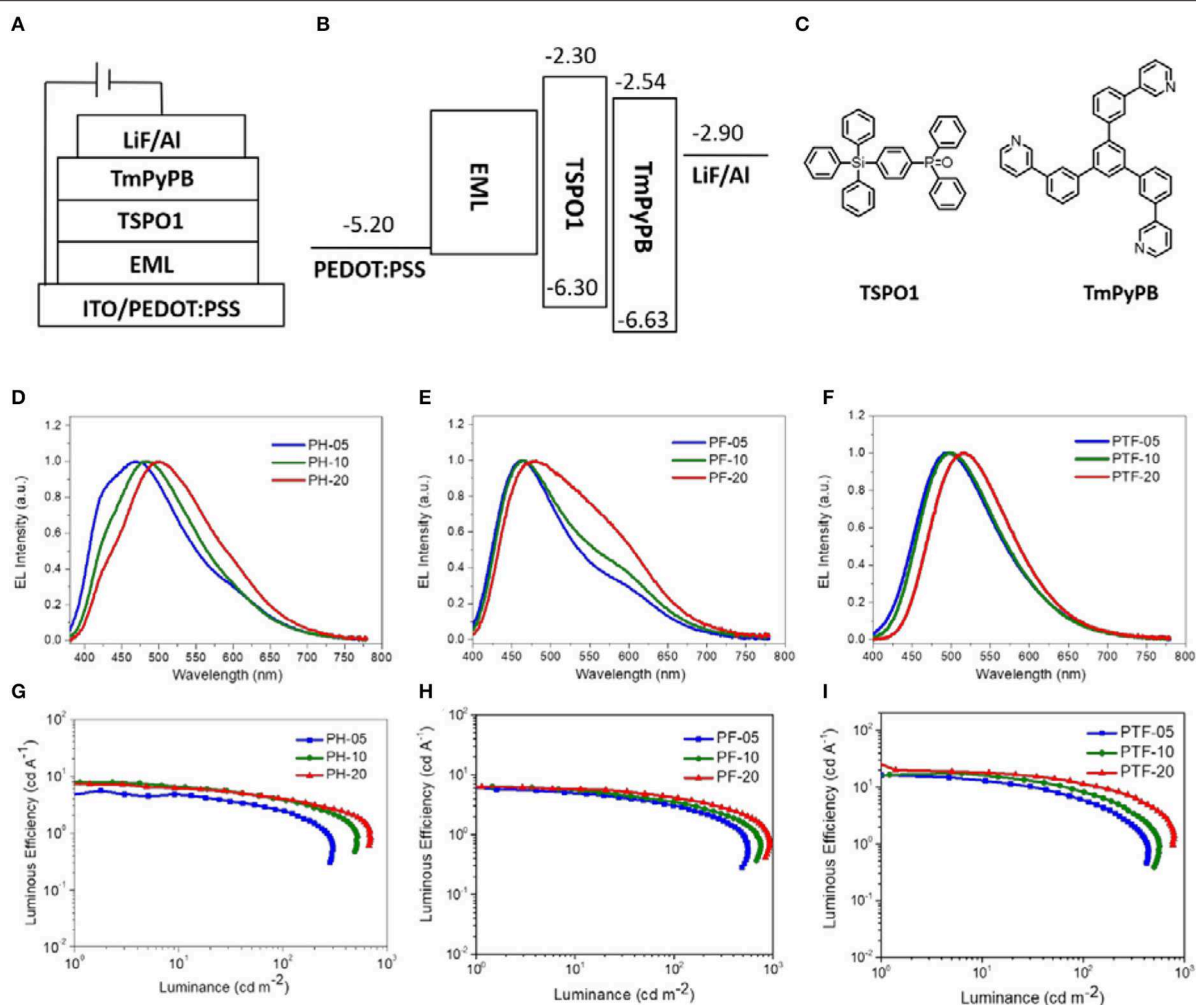


**FIGURE 7 |** Device configuration (A–C), EL spectra (D–F), and current efficiency-luminance curves (G–I) of the solution-processed OLEDs.

**TABLE 2 |** Summary of the device performance of the TSCT polymers.

Polymer	$V_{on}^a$ (V)	$LE^b$ (cd/A)	$EQE^c$ (%)	CIE (x, y) <sup>d</sup>
Maximum value/at 100 cd m <sup>-2</sup>				
PH-05	3.4	5.5/2.4	2.9/1.4	0.23, 0.27
PH-10	3.4	7.7/3.7	3.6/1.8	0.23, 0.31
PH-20	3.4	7.7/4.1	3.0/1.8	0.27, 0.36
PF-05	3.2	5.7/2.9	2.9/1.6	0.23, 0.26
PF-10	3.2	6.4/3.5	3.1/1.9	0.25, 0.29
PF-20	3.2	6.3/4.1	2.8/1.9	0.28, 0.34
PTF-05	3.0	16.3/6.2	5.7/2.6	0.25, 0.39
PTF-10	3.0	17.4/8.2	6.7/3.3	0.25, 0.41
PTF-20	3.0	20.1/11.4	7.0/4.2	0.29, 0.47

<sup>a</sup> Turn-on voltage at the luminance of 1 cd m<sup>-2</sup>.

<sup>b</sup> Luminous efficiency.

<sup>c</sup> External quantum efficiency.

<sup>d</sup> CIE coordinates at 4 V.

contributions of the triplets for EL emission, and indicating the promising potential of triarylboron TSCT polymers to serve as luminescent materials.

## CONCLUSION

In summary, three kinds of through-space charge transfer polymers with triarylboron acceptors bearing substituents of hydrogen (H), fluorine (F), and trifluoromethyl (CF<sub>3</sub>) are designed and synthesized for solution-processed OLEDs. The substitution effect on their photophysical and electroluminescent properties are investigated. It is found that as the substituent changes from H to F and CF<sub>3</sub>, the polymers show deep blue (429 nm) to sky-blue emission (483 nm) in solid-state film due to the increase of electron-accepting ability of the triarylboron units. Owing to the small  $\Delta E_{ST}$  of <0.1 eV, the TSCT polymers exhibit typical delayed fluorescence with  $\tau_d$  of 0.19–0.98  $\mu$ s in the absence of oxygen, with promising PLQY up to 53% in

solid-state film. Aggregation-induced emission effect is observed for the polymers with the emission intensity increased by up to ~33 folds from solution to aggregation state. The TSCT polymer bearing trifluoromethyl substituent with 20 mol% acceptor content exhibits promising electroluminescent performance with maximum external quantum efficiency of 7.0%, suggesting that they are prospective candidates for the development of luminescent polymers in the future. Further investigation on enhancing the color purity and emission efficiency of the triarylboron-based TSCT polymers is currently underway.

## DATA AVAILABILITY STATEMENT

The datasets generated for this study are available on request to the corresponding author.

## AUTHOR CONTRIBUTIONS

FC did the polymer synthesis, photophysical measurements, and device investigations. JH and XW did the synthesis of monomers. FC and SS analyzed the photophysical and device data. SS and LW wrote the manuscript. LW, XJ, and FW organized the project.

## REFERENCES

- Ahn, D. H., Kim, S. W., Lee, H., Ko, I. J., Karthik, D., Lee, J. Y., et al. (2019). Highly efficient blue thermally activated delayed fluorescence emitters based on symmetrical and rigid oxygen-bridged boron acceptors. *Nat. Photonics* 13:540. doi: 10.1038/s41566-019-0415-5
- Albrecht, K., Matsuoka, K., Fujita, K., and Yamamoto, K. (2015). Carbazole dendrimers as solution-processable thermally activated delayed-fluorescence materials. *Angew. Chem. Int. Ed.* 54, 5677–5682. doi: 10.1002/anie.201500203
- Bai, K. Y., Wang, S. M., Zhao, L., Ding, J. Q., and Wang, L. X. (2017). Efficient blue, green, and red electroluminescence from carbazole-functionalized poly(spirobifluorene)s. *Macromolecules* 50, 6945–6953. doi: 10.1021/acs.macromol.7b01393
- Ban, X. X., Chen, F., Liu, Y., Pan, J., Zhu, A. Y., Jiang, W., et al. (2019). Design of efficient thermally activated delayed fluorescence blue host for high performance solution-processed hybrid white organic light emitting diodes. *Chem. Sci.* 10, 3054–3064. doi: 10.1039/C8SC05456H
- Freeman, D. M. E., Musser, A. J., Fros, J. M., Stern, H. L., Forster, A. K., Fallon, K. J., et al. (2017). Synthesis and exciton dynamics of donor-orthogonal acceptor conjugated polymers: reducing the singlet-triplet energy gap. *J. Am. Chem. Soc.* 139, 11073–11080. doi: 10.1021/jacs.7b03327
- Hatakeyama, T., Shiren, K., Nakajima, K., Nomura, S., Nakatsuka, S., Kinoshita, K., et al. (2016). Ultrapure blue thermally activated delayed fluorescence molecules: efficient HOMO-LUMO separation by the multiple resonance effect. *Adv. Mater.* 28, 2777–2781. doi: 10.1002/adma.201505491
- Hirai, H., Nakajima, K., Nakatsuka, S., Shiren, K., Ni, J., Nomura, S., et al. (2015). One-step borylation of 1,3-diaryloxybenzenes towards efficient materials for organic light-emitting diodes. *Angew. Chem. Int. Ed.* 54, 13581–13585. doi: 10.1002/anie.201506335
- Hirata, S., Sakai, Y., Masui, K., Tanaka, H., Lee, S. Y., Nomura, H., et al. (2015). Highly efficient blue electroluminescence based on thermally activated delayed fluorescence. *Nat. Mater.* 14, 330–336. doi: 10.1038/nmat4154
- Hong, Y. N., Lam, J. W. Y., and Tang, B. Z. (2011). Aggregation-induced emission. *Chem. Soc. Rev.* 40, 5361–5388. doi: 10.1039/c1cs15113d
- Hu, J., Li, Q., Wang, X. D., Shao, S. Y., Wang, L. X., Jing, X. B., et al. (2019). Developing through-space charge transfer polymers as a general approach to realize full-color and white emission with thermally

## FUNDING

We acknowledge financial support from the National Key Research and Development Program of China (No. 2017YFB0404402), the National Natural Science Foundation of China (Nos. 51833009, 51573182, and 21975247), the 973 Project (No. 2015CB655000), and the Youth Innovation Promotion Association of Chinese Academy of Sciences (No. 2015180).

## SUPPLEMENTARY MATERIAL

The Supplementary Material for this article can be found online at: <https://www.frontiersin.org/articles/10.3389/fchem.2019.00854/full#supplementary-material>

The Supporting Information includes the synthetic routes for model compounds and control polymers; TGA and DSC curves of the polymers; PL spectra of PH-20, PF-20, and PTF-20 in solutions with different polarities; Phosphorescence spectra of the TSCT polymers; Current density (J)–voltage (V)–luminance, and EQE–L characteristics of the solution-processed OLEDs based on TSCT polymers.

- activated delayed fluorescence. *Angew. Chem. Int. Ed.* 58, 8405–8409. doi: 10.1002/anie.201902264
- Hu, Y. Y., Cai, W. Q., Ying, L., Chen, D. J., Yang, X. Y., Jiang, X. F., et al. (2018). Novel efficient blue and bluish-green light-emitting polymers with delayed fluorescence. *J. Mater. Chem. C* 6, 2690–2695. doi: 10.1039/C7TC04064D
- Huang, T. Y., Jiang, W., and Duan, L. (2018). Recent progress in solution processable TADF materials for organic light-emitting diodes. *J. Mater. Chem. C* 6, 5577–5596. doi: 10.1039/C8TC01139G
- Kim, D. H., D'Aleo, A., Chen, X. K., Sandanayaka, A. D. S., Yao, D. D., Zhao, L., et al. (2018). High-efficiency electroluminescence and amplified spontaneous emission from a thermally activated delayed fluorescent near-infrared emitter. *Nat. Photonics* 12:98. doi: 10.1038/s41566-017-0087-y
- Kim, H. J., Lee, C., Godumala, M., Choi, S., Park, S. Y., Cho, M. J., et al. (2018). Solution-processed thermally activated delayed fluorescence organic light-emitting diodes using a new polymeric emitter containing non-conjugated cyclohexane units. *Pol. Chem.* 9, 1318–1326. doi: 10.1039/C7PY02113E
- Kondo, Y., Yoshiura, K., Kitera, S., Nishi, H., Oda, S., Gotoh, H., et al. (2019). Narrowband deep-blue organic light-emitting diode featuring an organoboron-based emitter. *Nat. Photonics* 13, 678–682. doi: 10.1038/s41566-019-0476-5
- Lee, S. Y., Yasuda, T., Komiyama, H., Lee, J., and Adachi, C. (2016). Thermally activated delayed fluorescence polymers for efficient solution-processed organic light-emitting diodes. *Adv. Mater.* 28, 4019–4024. doi: 10.1002/adma.201505026
- Li, C. S., Nobuyasu, R. S., Wang, Y. K., Dias, F. B., Ren, Z. J., Bryce, M. R., et al. (2017). Solution-processable thermally activated delayed fluorescence white OLEDs based on dual-emission polymers with tunable emission colors and aggregation-enhanced emission properties. *Adv. Opt. Mater.* 5:1700435. doi: 10.1002/adom.201700435
- Li, C. S., Ren, Z. J., Sun, X. L., Li, H. H., and Yan, S. K. (2019). Deep-blue thermally activated delayed fluorescence polymers for nondoped solution-processed organic light-emitting diodes. *Macromolecules* 52, 2296–2303. doi: 10.1021/acs.macromol.9b00083
- Li, J., Shen, P., Zhao, Z., and Tang, B. Z. (2019). Through-space conjugation: a thriving alternative for optoelectronic materials. *CCS Chem.* 1, 181–196. doi: 10.31635/ccschem.019.20180020
- Li, Y. F., Xie, G. H., Gong, S. L., Wu, K. L., and Yang, C. L. (2016). Dendronized delayed fluorescence emitters for non-doped, solution-processed

- organic light-emitting diodes with high efficiency and low efficiency roll-off simultaneously: two parallel emissive channels. *Chem. Sci.* 7, 5441–5447. doi: 10.1039/C6SC00943C
- Liu, Y. C., Li, C. S., Ren, Z. J., Yan, S. K., and Bryce, M. R. (2018). All-organic thermally activated delayed fluorescence materials for organic light-emitting diodes. *Nat. Rev. Mater.* 3:18020. doi: 10.1038/natrevmater.2018.20
- Luo, J. D., Xie, Z. L., Lam, J. W. Y., Cheng, L., Chen, H. Y., Qiu, C. F., et al. (2001). Aggregation-induced emission of 1-methyl-1,2,3,4,5-pentaphenylsilole. *Chem. Commun.* 1740–1741. doi: 10.1039/b105159h
- Luo, J. J., Xie, G. H., Gong, S. L., Chen, T. H., and Yang, C. L. (2016). Creating a thermally activated delayed fluorescence channel in a single polymer system to enhance exciton utilization efficiency for bluish-green electroluminescence. *Chem. Commun.* 52, 2292–2295. doi: 10.1039/C5CC09797E
- Mamada, M., Ergun, S., Perez-Bolivar, C., and Anzenbacher, P. (2011). Charge transport, carrier balance, and blue electrophosphorescence in diphenyl 4-(triphenylsilyl)phenyl phosphine oxide devices. *Appl. Phys. Lett.* 98:073305. doi: 10.1063/1.3555335
- Mei, J., Leung, N. L. C., Kwok, R. T. K., Lam, J. W. Y., and Tang, B. Z. (2015). Aggregation-induced emission: together we shine, united we soar! *Chem. Rev.* 115, 11718–11940. doi: 10.1021/acs.chemrev.5b00263
- Møllerup, S. K., and Wang, S. (2019). Boron-doped molecules for optoelectronics. *Trends Chem.* 1, 77–89. doi: 10.1016/j.trechm.2019.01.003
- Muller, C. D., Falcou, A., Reckefuss, N., Rohahn, M., Wiederhorn, V., Rudati, P., et al. (2003). Multi-colour organic light-emitting displays by solution processing. *Nature* 421, 829–833. doi: 10.1038/nature01390
- Nikolaenko, A. E., Cass, M., Bourcet, F., Mohamad, D., and Roberts, M. (2015). Thermally activated delayed fluorescence in polymers: a new route toward highly efficient solution processable OLEDs. *Adv. Mater.* 27:7236. doi: 10.1002/adma.201501090
- Nobuyasu, R. S., Ren, Z. J., Griffiths, G. C., Batsanov, A. S., Data, P., Yan, S. K., et al. (2016). Rational design of TADF polymers using a donor-acceptor monomer with enhanced TADF efficiency induced by the energy alignment of charge transfer and local triplet excited states. *Adv. Opt. Mater.* 4, 597–607. doi: 10.1002/adom.201500689
- Numata, M., Yasuda, T., and Adachi, C. (2015). High efficiency pure blue thermally activated delayed fluorescence molecules having 10H-phenoxaborin and acridan units. *Chem. Commun.* 51, 9443–9446. doi: 10.1039/C5CC00307E
- Sarma, M., and Wong, K. T. (2018). Exciplex: an intermolecular charge-transfer approach for TADF. *ACS Appl. Mater. Interfaces* 10, 19279–19304. doi: 10.1021/acsami.7b18318
- Shao, S. Y., Hu, J., Wang, X. D., Wang, L. X., Jing, X. B., and Wang, F. S. (2017). Blue thermally activated delayed fluorescence polymers with nonconjugated backbone and through-space charge transfer effect. *J. Am. Chem. Soc.* 139, 17739–17742. doi: 10.1021/jacs.7b10257
- Spuling, E., Sharma, N., Samuel, I. D. W., Zysman-Colman, E., and Brase, S. (2018). (Deep) blue through-space conjugated TADF emitters based on 2,2-paracyclophanes. *Chem. Commun.* 54, 9278–9281. doi: 10.1039/C8CC04594A
- Su, S. J., Chiba, T., Takeda, T., and Kido, J. (2008). Pyridine-containing triphenylbenzene derivatives with high electron mobility for highly efficient phosphorescent OLEDs. *Adv. Mater.* 20:2125. doi: 10.1002/adma.200701730
- Suzuki, K., Kubo, S., Shizu, K., Fukushima, T., Wakamiya, A., Murata, Y., et al. (2015). Triarylboron-based fluorescent organic light-emitting diodes with external quantum efficiencies exceeding 20 %. *Angew. Chem. Int. Ed.* 54, 15231–15235. doi: 10.1002/anie.201508270
- Uoyama, H., Goushi, K., Shizu, K., Nomura, H., and Adachi, C. (2012). Highly efficient organic light-emitting diodes from delayed fluorescence. *Nature* 492:234. doi: 10.1038/nature11687
- Wang, S. P., Yan, X. J., Cheng, Z., Zhang, H. Y., Liu, Y., and Wang, Y. (2015). Highly efficient near-infrared delayed fluorescence organic light emitting diodes using a phenanthrene-based charge-transfer compound. *Angew. Chem. Int. Ed.* 54, 13068–13072. doi: 10.1002/anie.201506687
- Wei, Q., Kleine, P., Karpov, Y., Qiu, X. P., Komber, H., Sahre, K., et al. (2017). Conjugation-induced thermally activated delayed fluorescence (TADF): from conventional non-TADF units to TADF-active polymers. *Adv. Funct. Mater.* 27:1605051. doi: 10.1002/adfm.201605051
- Wong, M. Y., and Zysman-Colman, E. (2017). Purely organic thermally activated delayed fluorescence materials for organic light-emitting diodes. *Adv. Mater.* 29:1605444. doi: 10.1002/adma.201605444
- Wu, T. L., Huang, M. J., Lin, C. C., Huang, P. Y., Chou, T. Y., Chen-Cheng, R. W., et al. (2018). Diboron compound-based organic light-emitting diodes with high efficiency and reduced efficiency roll-off. *Nat. Photonics* 12:235. doi: 10.1038/s41566-018-0112-9
- Wu, W. S., Inbasekaran, M., Hudack, M., Welsh, D., Yu, W. L., Cheng, Y., et al. (2004). Recent development of polyfluorene-based RGB materials for light emitting diodes. *Microelectron. J.* 35, 343–348. doi: 10.1016/j.mejo.2003.07.001
- Xie, G. H., Luo, J. J., Huang, M. L., Chen, T. H., Wu, K. L., Gong, S. L., et al. (2017). Inheriting the characteristics of TADF small molecule by side-chain engineering strategy to enable bluish-green polymers with high PLQYs up to 74% and external quantum efficiency over 16% in light-emitting diodes. *Adv. Mater.* 29:1604223. doi: 10.1002/adma.201604223
- Yu, L., Liu, J., Hu, S. J., He, R. F., Yang, W., Wu, H. B., et al. (2013). Red, green, and blue light-emitting polyfluorenes containing a dibenzothiophene-S,S-dioxide unit and efficient high-color-rendering-index white-light-emitting diodes made therefrom. *Adv. Funct. Mater.* 23, 4366–4376. doi: 10.1002/adfm.201203675
- Yuan, W. Z., Gong, Y. Y., Chen, S. M., Shen, X. Y., Lam, J. W. Y., Lu, P., et al. (2012). Efficient solid emitters with aggregation-induced emission and intramolecular charge transfer characteristics: molecular design, synthesis, photophysical behaviors, and OLED application. *Chem. Mater.* 24, 1518–1528. doi: 10.1021/cm300416y
- Zhang, Q. S., Li, J., Shizu, K., Huang, S. P., Hirata, S., Miyazaki, H., et al. (2012). Design of efficient thermally activated delayed fluorescence materials for pure blue organic light emitting diodes. *J. Am. Chem. Soc.* 134, 14706–14709. doi: 10.1021/ja306538w
- Zhao, J., Zheng, C., Zhou, Y., Li, C., Ye, J., Du, X., et al. (2019). Novel small-molecule energy donor for solution-processed ternary exciplex with 24% external quantum efficiency in organic light-emitting diode. *Mater. Horiz.* 6, 1425–1432. doi: 10.1039/C9MH00373H
- Zhu, Y. H., Zhang, Y. W., Yao, B., Wang, Y. J., Zhang, Z. L., Zhan, H. M., et al. (2016). Synthesis and electroluminescence of a conjugated polymer with thermally activated delayed fluorescence. *Macromolecules* 49, 4373–4377. doi: 10.1021/acs.macromol.6b00430

**Conflict of Interest:** The authors declare that the research was conducted in the absence of any commercial or financial relationships that could be construed as a potential conflict of interest.

Copyright © 2019 Chen, Hu, Wang, Shao, Wang, Jing and Wang. This is an open-access article distributed under the terms of the Creative Commons Attribution License (CC BY). The use, distribution or reproduction in other forums is permitted, provided the original author(s) and the copyright owner(s) are credited and that the original publication in this journal is cited, in accordance with accepted academic practice. No use, distribution or reproduction is permitted which does not comply with these terms.





# 5H-Benzo[d]Benzo[4,5]Imidazo[2,1-b][1,3]Thiazine as a Novel Electron-Acceptor Cored High Triplet Energy Bipolar Host Material for Efficient Solution-Processable Thermally Activated Delayed Fluorescence Organic Light-Emitting Diodes

## OPEN ACCESS

### Edited by:

Guohua Xie,  
Wuhan University, China

### Reviewed by:

Wei Jiang,  
Southeast University, China  
Shumeng Wang,  
Changchun Institute of Applied  
Chemistry (CAS), China

### \*Correspondence:

Dong Hoon Choi  
dhchoi8803@korea.ac.kr

### Specialty section:

This article was submitted to  
Organic Chemistry,  
a section of the journal  
Frontiers in Chemistry

**Received:** 09 December 2019

**Accepted:** 20 January 2020

**Published:** 07 February 2020

### Citation:

Godumala M, Yoon J, Park SY, Lee C,  
Kim Y, Jeong J-E, Park S, Woo HY,  
Cho MJ and Choi DH (2020)  
5H-Benzo[d]Benzo[4,5]Imidazo[2,1-  
b][1,3]Thiazine as a Novel  
Electron-Acceptor Cored High Triplet  
Energy Bipolar Host Material for  
Efficient Solution-Processable  
Thermally Activated Delayed  
Fluorescence Organic Light-Emitting  
Diodes. *Front. Chem.* 8:61.  
doi: 10.3389/fchem.2020.00061

*Mallesham Godumala, Jiwon Yoon, Seo Yeon Park, Chiho Lee, Youngseo Kim,  
Ji-Eun Jeong, Sungham Park, Han Young Woo, Min Ju Cho and Dong Hoon Choi\**

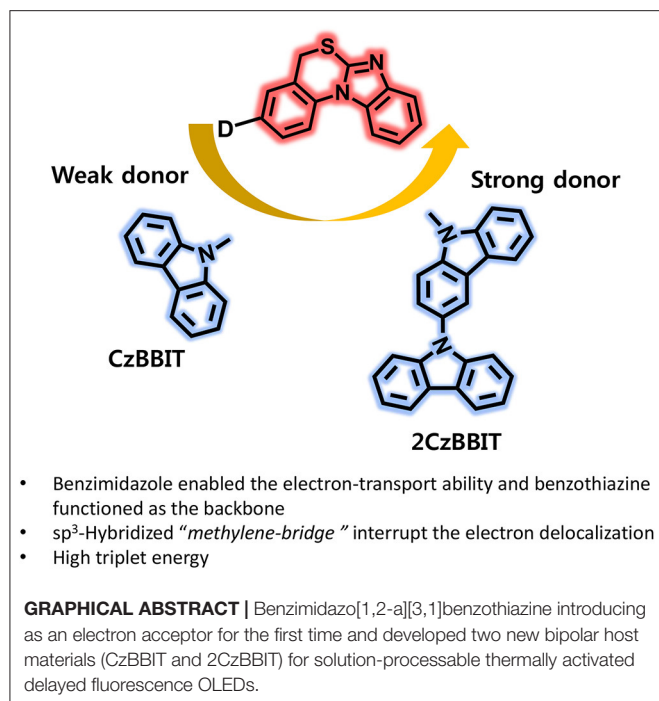
*Department of Chemistry, Research Institute for Natural Sciences, Korea University, Seoul, South Korea*

Organic entities that can transport electrons are seldom available to develop adequate bipolar host materials applicable for solution-processable thermally activated delayed fluorescence (TADF)-organic light-emitting diodes (OLEDs). Therefore, the introduction of new electron-affine entities that plausibly demonstrate high triplet energy ( $E_T$ ) is of urgent need. In this contribution, we introduced benzimidazo[1,2-a][3,1]benzothiazine (BBIT) as a novel electron-affine entity and developed two new bipolar host materials, CzBBIT and 2CzBBIT. Both host materials exhibit high  $E_T$  of 3.0 eV, superior thermal robustness with the thermal decomposition temperature of up to 392°C, a glass transition temperature of up to 161°C, and high solubility in common organic solvents. Consequently, the solution-processable OLEDs fabricated using a recognized IAcTr-out as the green TADF emitter doped into CzBBIT as the host, realized a maximum external quantum efficiency (EQE) of 23.3%, while the 2CzBBIT:IAcTr-out blend film-based device displayed an EQE of 18.7%. These outcomes corroborated that this work could shed light on the scientific community on the design of new electron-affine entities to establish the effective use of bipolar host materials toward proficient solution-processable TADF-OLEDs.

**Keywords:** new electron-acceptor core, bipolar hosts, thermally activated delayed fluorescence, solution process, organic light emitting diodes

## INTRODUCTION

Metal-free organic molecules that exhibit thermally activated delayed fluorescence (TADF) properties have attracted a great deal of attention with their breakthrough performances in organic light-emitting diodes (OLEDs) (Uoyama et al., 2012; Godumala et al., 2016; Ahn et al., 2019; Kondo et al., 2019). The TADF materials render the potential to utilize both singlet and



triplet excitons through reverse intersystem crossing (RISC) by virtue of the minimal energy gap between the singlet and triplet excited states ( $\Delta E_{ST}$ ), resulting in a theoretical internal quantum efficiency approaching 100% (Uoyama et al., 2012). In contrast, phosphorescent OLEDs (PhOLEDs) exhibit excellent device performance, but there are still improvements to be made such as the use of rare earth metal complexes, their toxicity, and high manufacturing costs. Consequently, TADF materials are the best alternatives to PhOLEDs in terms of efficiency and cost. Similar to phosphorescent emitters, TADF emitters also suffer from concentration quenching through triplet-triplet annihilations and triplet-polaron annihilations owing to the long lifetime of triplet excitons ( $\tau_d$ ), which could be suppressed by uniformly dispersing into a suitable host matrix (Godumala et al., 2018, 2019; Chatterjee and Wong, 2019). Therefore, both hosts and emitters contribute equally toward the high performance of OLEDs. However, the host materials have not been explored much compared to the emitters.

In recent years, various TADF materials processed through vacuum deposition have been developed, and the majority of them have already been employed to achieve high external quantum efficiency (EQE) of over 25.0% (up to 38.0%) (Uoyama et al., 2012; Ahn et al., 2019; Kondo et al., 2019). In spite of the high performances of vacuum processed devices, the OLEDs fabricated through the solution process have many unique advantages, including an easy fabrication process, mass production of large-scale products, easy control of dopant concentration and low-cost manufacturing (Shao et al., 2017; Huang et al., 2018; Zou et al., 2018; Tsai et al., 2019).

Several host materials reported in the literature perform a monopolar-type (predominant hole-transport) behavior (for instance, CBP, mCP, mCBP, and SiCz) due to the lack of

sufficient electron-transport entities. The monopolar behavior of hosts can move the charge recombination zone close to the adjacent transport layers, which can be detrimental to the device performance as well as color purity. Therefore, monopolar behavior and poor thermal stability of these host materials restrict their widespread applications in OLEDs (Godumala et al., 2018). In contrast, host materials constructed of the donor-acceptor structure can enable balanced charge-carrier transport, which can broaden the exciton recombination zone in the emissive layer, thereby boosting the overall device performance (Cui et al., 2016; Kim et al., 2017; Jung et al., 2019; Konidena et al., 2019). Thus, far, numerous host materials reported in TADF-OLEDs have been designed by molecular engineering or by changing the ratio or position of the known donor and acceptor entities (Fan et al., 2015; Zhang et al., 2016a,b; Jeon et al., 2018). Very few new electron-acceptor cores are reported to develop bipolar host materials in OLEDs. For instance, Adachi et al. demonstrated a new rigid electron-deficient benzimidazobenzothiazole (BID-BT) and developed two new bipolar host materials, 29Cz-BID-BT and 39Cz-BID-BT (Cui et al., 2016). By employing them as hosts and a familiar DPAC-TRZ as a blue TADF emitter, the devices achieved an EQE of approximately 21.0%. Later, our group introduced chromenopyrazole (CP) as the new electron-acceptor entity and developed two new bipolar hosts by appending carbazole or bicarbazole as donors (CzCP and 2CzCP). The devices employing CzCP as the host, and the well-known TCzTrz as the blue TADF emitter realized a maximum EQE of 27.9% [CIE coordinates of (0.15, 0.21)] (Godumala et al., 2018). However, the aforementioned host materials were deposited through vacuum thermal evaporation owing to their poor solubility. Therefore, the exploration of new electron-acceptor cores for application as suitable bipolar host materials that demonstrate high solubility is imperative in promoting solution-processable OLEDs.

In this study, we introduced another new electron-deficient heterocyclic entity, benzimidazo[1,2-a][3,1]benzothiazine (BBIT), for the first time and developed two new solution-processable bipolar host materials, namely 3-(9H-carbazol-9-yl)-5H-benzo[d]benzo[4,5]imidazo[2,1-b][1,3]thiazine (CzBBIT) and 3-(9H-[3,9'-bicarbazol]-9-yl)-5H-benzo[d]benzo[4,5]imidazo[2,1-b][1,3]thiazine (2CzBBIT), which were integrated with electron-rich carbazole or bicarbazole entities. The electron-deficient benzimidazole enabled the electron-transport property, while benzothiazine functioned as the backbone to BBIT. The existence of a  $sp^3$ -hybridized methylene bridge could interrupt the electron delocalization between the electron donor and acceptor cores to some extent, and was, therefore, advantageous to retain high triplet energy ( $E_T$ ) and partially enables solubility. The synthesis of BBIT is moderately facile and rather economical, because expensive catalysts, such as palladium and gold, are not employed. As already envisaged from the design principles, both these compounds manifested a high  $E_T$  ( $\sim 3.0$  eV), adequate highest occupied molecular orbital (HOMO) and lowest unoccupied molecular orbital (LUMO) energies, high solubility, and an excellent thermal stability and homogeneous film formation, which enabled their application as host materials for OLEDs. Consequently, the solution-processable OLEDs were fabricated

by implementing these new materials as hosts and IAcTr-out as the green TADF emitter (Park et al., 2018). The CzBBIT and 2CzBBIT accomplished a remarkably high device performance with EQE values as high as 23.3 and 18.7%, respectively. This first report demonstrating a breakthrough performance corroborates that BBIT is an outstanding electron-acceptor core to develop versatile host materials for solution-processable OLEDs in the near future.

## EXPERIMENTAL

### Synthesis

#### Synthesis of 3-(9H-Carbazol-9-yl)-5H-Benzo[d]Benzo[4,5]imidazo[2,1-b][1,3]Thiazine (CzBBIT)

1H-benzo[d]imidazole-2-thiol (0.5 g, 3.3 mmol), CuI (63 mg, 0.33 mmol), and Cs<sub>2</sub>CO<sub>3</sub> (2.17 g, 6.7 mmol) were mixed in dimethylformamide (DMF, 20 mL) and stirred for 20 min under nitrogen atmosphere. Compound 4a (1.68 g, 3.3 mmol) in DMF (20 mL) and L-proline (77 mg, 0.67 mmol) were subsequently added and stirred at 110°C for 8 h. The mixture was poured into deionized water after cooled down to room temperature (RT), and extracted with ethyl acetate. The organic extracts were dried over Na<sub>2</sub>SO<sub>4</sub> and concentrated *in vacuo*, and the residue was chromatographed by eluting with methylene chloride (MC) to afford CzBBIT as a white solid. The compound was further purified by precipitating in MC: hexane (1:3) (1.2 g, 89% yield). <sup>1</sup>H NMR (500 MHz, CDCl<sub>3</sub>): δ (ppm) 8.18–8.14 (m, 2H), 8.07 (d, *J* = 8.5 Hz, 1H), 7.91–7.86 (m, 1H), 7.82–7.77 (m, 1H), 7.68 (dd, *J* = 8.5, 2.1 Hz, 1H), 7.61 (d, *J* = 2.1 Hz, 1H), 7.47–7.41 (m, 4H), 7.39–7.35 (m, 2H), 7.34–7.29 (m, 2H), 4.10 (s, 2H). <sup>13</sup>C NMR (125 MHz, CDCl<sub>3</sub>): δ (ppm) 150.40, 144.02, 140.73, 135.18, 134.39, 132.61, 127.52, 127.48, 126.61, 126.17, 123.76, 123.52, 123.33, 120.49, 120.38, 119.77, 119.45, 111.36, 109.55, 30.32. MS (MALDI-TOF) [*m/z*]: Calcd for C<sub>26</sub>H<sub>17</sub>N<sub>3</sub>S, 403.114; Found, 403.115 [M<sup>+</sup>]. Elemental analysis (%) calcd for C<sub>26</sub>H<sub>17</sub>N<sub>3</sub>S: C 77.39, H 4.25, N 10.41, S 6.60. Found: C 77.26, H 4.38, N 10.30, S 6.73.

#### Synthesis of 3-(9H-[3,9'-bicarbazol]-9-yl)-5H-benzo[d]benzo[4,5]imidazo[2,1-b][1,3]thiazine (2CzBBIT)

The synthetic procedure described for CzBBIT was adopted to afford 2CzBBIT by combining 1H-benzo[d]imidazole-2-thiol (0.5 g, 3.3 mmol), CuI (63 mg, 0.33 mmol), Cs<sub>2</sub>CO<sub>3</sub> (2.17 g, 6.7 mmol), compound 4b (2.23 g, 3.3 mmol), and L-proline (77 mg, 0.67 mmol) in DMF (50 mL). 2CzBBIT was obtained as a white solid (1.6 g, 85% yield). <sup>1</sup>H NMR (500 MHz, CDCl<sub>3</sub>): δ (ppm) 8.30 (d, *J* = 1.8 Hz, 1H), 8.20–8.16 (m, 2H), 8.15–8.10 (m, 2H), 7.93–7.88 (m, 1H), 7.83–7.78 (m, 1H), 7.76 (dd, *J* = 8.5, 2.4 Hz, 1H), 7.69 (d, *J* = 2.1 Hz, 1H), 7.62 (d, *J* = 8.5 Hz, 1H), 7.57 (dd, *J* = 8.7, 2.0 Hz, 1H), 7.53–7.47 (m, 2H), 7.43–7.37 (m, 6H), 7.36–7.33 (m, 1H), 7.32–7.26 (m, 2H), 4.14 (s, 2H). <sup>13</sup>C NMR (125 MHz, CDCl<sub>3</sub>): δ (ppm) 150.36, 144.02, 141.77, 141.44, 139.83, 134.81, 134.73, 132.58, 130.29, 127.67, 127.60, 126.89, 126.68, 125.87, 125.69, 124.55, 123.82, 123.38, 123.12, 123.07, 120.80, 120.75, 120.30, 119.80, 119.67, 119.62, 119.58, 111.35,

110.67, 109.92, 109.69, 30.31. MS (MALDI-TOF) [*m/z*]: Calcd for C<sub>38</sub>H<sub>24</sub>N<sub>4</sub>S, 568.172; Found, 568.152 [M<sup>+</sup>]. Elemental analysis (%) calcd for C<sub>38</sub>H<sub>24</sub>N<sub>4</sub>S: C 80.26, H 4.25, N 9.85, S 5.64. Found: C 80.17, H 4.36, N 9.92, S 5.57.

### Characterization

All reagents and solvents were purchased from Aldrich, Alfa Aesar, and TCI Chemicals, and used as received unless otherwise mentioned. <sup>1</sup>H and <sup>13</sup>C nuclear magnetic resonance spectra were recorded using Varian Mercury 500 MHz spectrometers in CDCl<sub>3</sub> solvent (Cambridge Isotope Laboratories, Inc.) using tetramethylsilane as the internal standard. The elemental analysis was conducted using the EA1112 elemental analyzer (Thermo Electron Corporation) at the Center for Organic Reactions. The Bruker Daltonics LRF-20 MALDI-TOF spectrometer was utilized to record the mass spectrometry. The glass transition temperature (*T<sub>g</sub>*) was estimated by acquiring differential scanning calorimetry (DSC) thermograms measured using a Mettler 821 instrument under the nitrogen atmosphere at a heating rate of 10°C min<sup>−1</sup>. The decomposition temperature (*T<sub>d</sub>*) was obtained by conducting thermogravimetric analysis (TGA) using Mettler STAR<sup>c</sup> at a heating rate of 10°C min<sup>−1</sup> under the nitrogen atmosphere. The absorption spectra were attained using the Agilent 8453 UV–Vis (ultraviolet–visible) spectrophotometer. A Hitachi F-7000 fluorescence spectrophotometer was utilized to measure the photoluminescence (PL) spectra at RT. The HITACHI F-7000 fluorescence spectrometer was used to measure the phosphorescence spectra at a temperature of 77 K in the 2-methyltetrahydrofuran solvent. The JASCO FP-8500 fluorescence spectrometer equipped with an integrated sphere was utilized to measure the PL quantum yield (PLQY) for the blend films. CzBBIT: IAcTr-out (45 wt%) and 2CzBBIT: IAcTr-out (35 wt%) blend films were prepared with a thickness of 40 nm on a quartz substrate using the toluene solution to measure the PLQY. The same substrates were utilized to study the transient PL (TRPL) at RT. The PL decays were obtained between 0 and 50 μs. The TRPL and exciton lifetimes were restricted with a train of 1064 nm pulses at a 5 ns interval, produced at 10 Hz using an Nd:YAG laser (Powerlite Precision II 8000, Continuum). A wavelength was attained at 355 nm pulse by the generation of the third harmonic and used to directly excite the film sample prepared on quartz. The emission from the film sample was focused using a lens (focal length: 10 cm), passed through a monochromator, and distinguished by a photomultiplier tube connected to a 100 MHz digital oscilloscope (DSO-X 3014A, Keysight). The prompt and delayed components were recognized by single- and triple-exponential decaying functions. Cyclic voltammetry measurements were performed to evaluate the oxidation potential of host materials in their film state by employing a potentiostat (EA161, eDAQ) at a scan rate of 100 mV s<sup>−1</sup>. CzBBIT and 2CzBBIT dissolved in MC were drop-casted on a platinum (working) electrode and freshly prepared 0.1 M NBu<sub>4</sub>PF<sub>6</sub> in dry acetonitrile was used as the electrolytic solution. Ag/AgCl was used as the reference electrode, and a platinum wire with a diameter of 0.5 mm was used as the counter electrode.

## Single-Carrier Devices

Single-carrier devices, such as hole-only devices (HODs) and electron-only devices (EODs), were fabricated using a neat glass substrate coated with indium tin oxide (ITO; thickness of 150 nm) with an active pattern size of  $2 \times 2$  mm<sup>2</sup> and a sheet resistance of  $10 \Omega \text{ cm}^{-2}$ , for use as the anode. The HODs were fabricated with the structure ITO (150 nm)/PEDOT:PSS (40 nm)/PVK (10 nm)/Host (30 nm)/Al (100 nm), and the EODs were fabricated with the structure ITO (150 nm)/Host (30 nm)/TPBi (40 nm)/LiF (0.8 nm)/Al (100 nm). PEDOT:PSS as a hole injection layer was deposited as received (annealed at 155°C for 15 min), PVK was dissolved in chlorobenzene (annealed at 130°C for 20 min), and the toluene solution of the host materials was spin-coated as required. Finally, the other essential layers, such as TPBi, LiF, and Al, were deposited using a vacuum thermal evaporator in a glove box.

## OLED Device Fabrication

The ITO-coated (150 nm) glass substrate with a sheet resistance of  $10 \Omega \text{ cm}^{-2}$  and active pattern size of  $2 \times 2$  mm<sup>2</sup> acting as the anode was used to fabricate OLEDs. The IAcTr-out, which was reported by our group, was adopted as the green TADF emitter. The device structure was as follows: ITO (150 nm)/PEDOT:PSS (40 nm)/PVK (10 nm)/CzBBIT or 2CzBBIT: IAcTr-out (40 nm, x wt%)/TPBi (40 nm)/LiF (0.8 nm)/Al (100 nm), where x is the dopant concentration of 45.0 wt% for CzBBIT and 35.0 wt% for 2CzBBIT. The hole-injecting PEDOT:PSS was directly spin-coated on ITO and thermally annealed at 155°C for 15 min, whereas the hole-transporting PVK dissolved in chlorobenzene was spin-coated on PEDOT:PSS before annealing at 130°C for 20 min. The emissive layer was spin-coated on the PVK layer from the toluene solution. The aforementioned steps were conducted at ambient conditions, and the substrates were moved into a vacuum chamber for depositing TPBi, LiF, and Al sequentially using a thermal evaporator. The current density–voltage–luminance (*J–V–L*) data were measured using the Keithley SMU 236 instrument and SpectraScan PR-655 colorimeter. All the measurements were performed at atmospheric conditions without protecting the devices from any encapsulations.

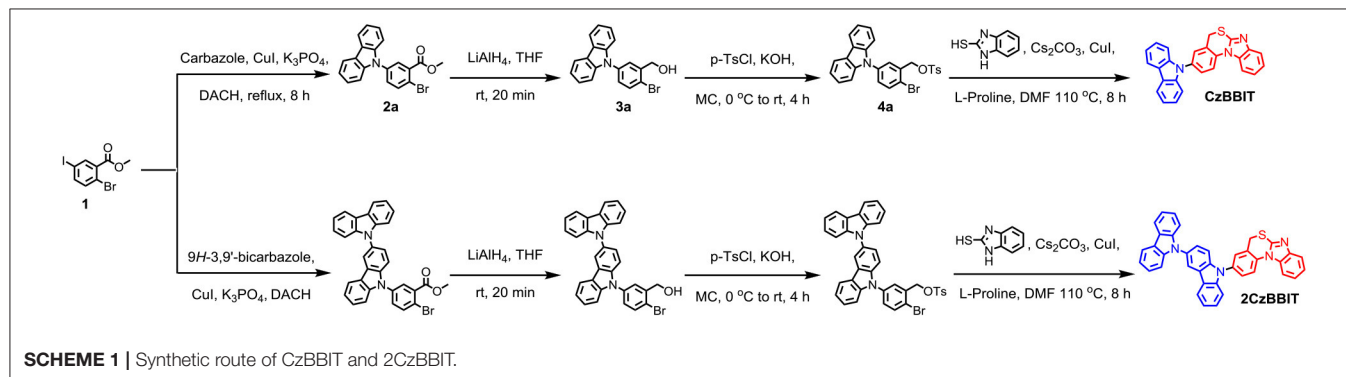
## RESULTS AND DISCUSSION

### Synthesis

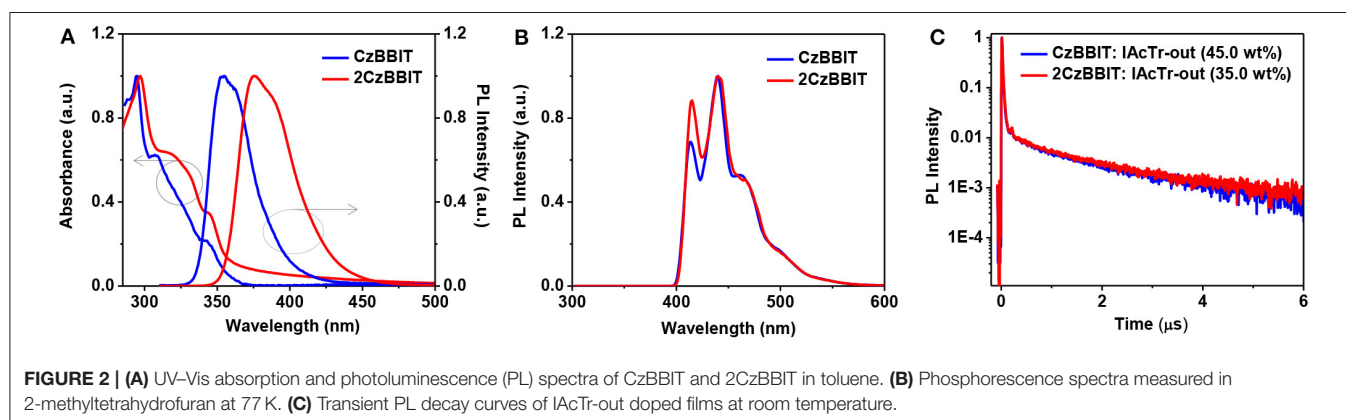
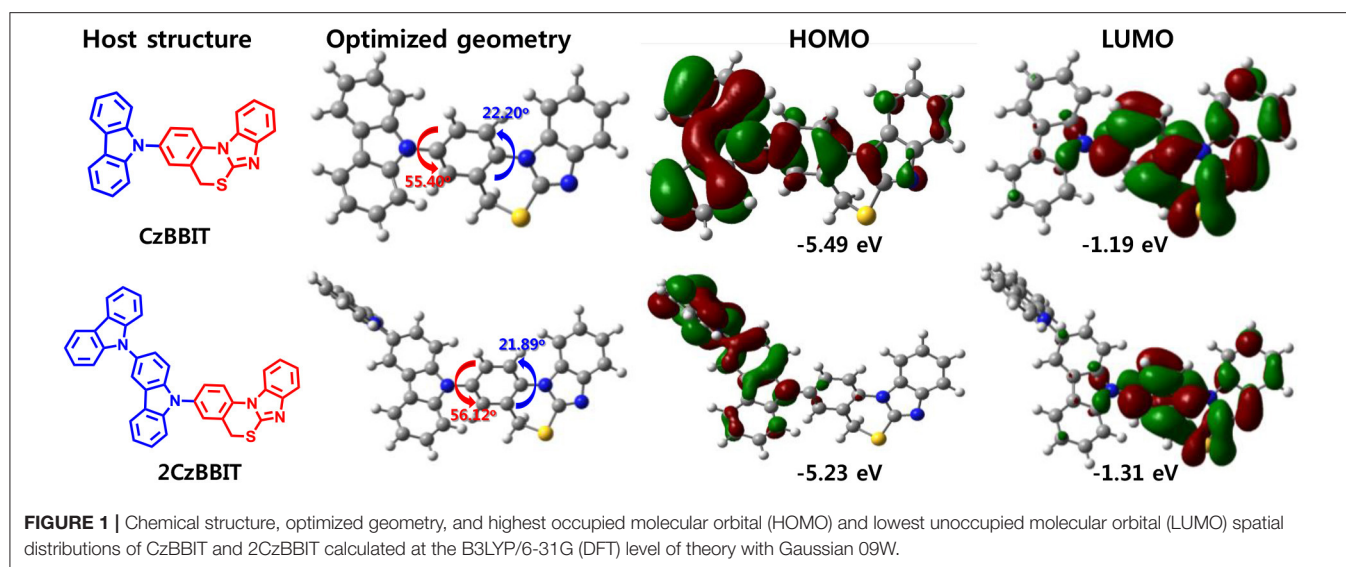
The synthetic details of both the targeted BBIT derivatives are shown in **Scheme 1**. Compound **1** was synthesized by adopting the reported synthetic procedure (Dressler et al., 2015). It was treated with 9*H*-carbazole or 9*H*-3,9'-bicarbazole, probing Cu(I)-catalyzed Ullmann reaction conditions using K<sub>3</sub>PO<sub>4</sub> as the base and (±)-*trans*-1,2-diaminocyclohexane as the ligand to obtain **2a** and **2b** with moderate yields. Then, their ester groups were converted to the corresponding alcohols using LiAlH<sub>4</sub> as the reducing agent with a reaction time of no longer than 20 min (Aline et al., 2008). Subsequently, the hydroxyl group was tosylated using *p*-toluenesulfonyl chloride and KOH as the base. Next, compounds **4a** and **4b** were treated with 2-mercaptobenzimidazole to provide CzBBIT and 2CzBBIT, respectively in high yields (refer to the experimental section for detailed information).

### Theoretical Calculations

To obtain a deeper understanding of the molecular energy levels and energy distribution of CzBBIT and 2CzBBIT, density functional theory (DFT) and time-dependent DFT (TD-DFT) calculations using the B3LYP/6-31G(d) method were probed. The molecular structure, optimized geometry, and HOMO and LUMO spatial distributions of CzBBIT and 2CzBBIT calculated at the B3LYP/6-31G (DFT) level of theory with Gaussian 09W are presented in **Figure 1**. The dihedral angle perceived between the donor and BBIT entities of both hosts is approximately 56.0°, implying twisted geometry. BBIT itself possesses a dihedral angle of 22.0°, denoting that it does not demonstrate a planar structure. The electron cloud distributions of the HOMO are primarily localized on the electron-rich carbazole entities, which contribute to form a hole-transport channel. The LUMO is predominantly distributed over the electron-deficient BBIT core that provides the electron-transport channel. The well-separated HOMO and LUMO distributions could support the bipolar nature of the host materials. The HOMO/LUMO energy levels for CzBBIT and 2CzBBIT are calculated to be -5.49/-1.19 eV and -5.23/-1.31 eV, respectively. Besides, the *E*<sub>T</sub> of CzBBIT is 3.17 eV, and that of 2CzBBIT is 3.14 eV. Therefore, it is established that the high *E*<sub>T</sub> values and well-separated HOMO and LUMO distributions guaranteed these materials to function as bipolar hosts in OLEDs.







## Optical and Photophysical Properties

The UV-Vis absorption and PL spectra were recorded in a toluene solution for CzBBIT and 2CzBBIT to evaluate their optical properties (Figure 2A and Table 1). Both compounds display similar absorption profiles with strong  $\pi$ - $\pi^*$  transition bands under 300 nm, and the weak absorbance at about 330–350 nm mainly corresponds to the  $n$ - $\pi^*$  transition of 9-phenyl carbazole units (Ma et al., 2019). The absorption profiles are not significantly influenced by the solution to film state (Figure S1 and Table 1), thereby revealing that there are negligible intermolecular interactions in the ground state. The optical bandgap ( $E_g$ ) values of CzBBIT and 2CzBBIT were derived from the absorption threshold in the film state as 3.44 and 3.32 eV, respectively.

As shown in Figure 2A, the PL spectrum of CzBBIT in toluene shows partially unstructured emissions with the 0-0 band at 355 nm and 0-1 band at 362 nm, respectively, while those two bands are observed at 376 nm and 388 nm for 2CzBBIT. The emission behavior at room temperature is due to charge-transfer excited states (Ma et al., 2019). The somewhat red-shifted emission for 2CzBBIT is attributed to the stronger

electron-donating property for the bicarbazole donor than single carbazole.

Further, the absorption and emission spectra were not remarkably influenced by solvent polarity, indicating that the intramolecular charge-transfer nature is considerably weak in the ground and excited states (Figure S2 and Table S1). The phosphorescence spectrum was recorded at 77 K in 2-methyltetrahydrofuran for both compounds to obtain their  $E_T$ , and the results are shown in Figure 2B. The spectra of CzBBIT and 2CzBBIT exhibit structured emission behavior with three vibronic peaks, which is mainly due to locally-excited (LE) states. The  $E_T$  values of both compounds are calculated from the highest energy vibronic sub-bands to be  $\sim 3.0$  eV (Figure S3), which is sufficiently high for them to function as hosts for IAcTr-out, a TADF emitter ( $E_T$  of 2.62 eV) (Park et al., 2018). It should be noted that the high  $E_T$  observed for both host compounds could be expected from the interruption of  $\pi$ -conjugation by the non-conjugated methylene bridge.

## TRPL and Kinetic Parameters

TRPL studies were conducted to distinguish the TADF behavior of IAcTr-out doped into CzBBIT and 2CzBBIT in the film

**TABLE 1** | Photophysical and electrochemical data of hosts.

Host	$T_g/T_d$ (°C)	Absorption (nm)		PL (nm)		$E_g$ (eV) <sup>c</sup>	$E_T$ (eV) <sup>d</sup>	Energy levels (eV)	
		Sol. <sup>a</sup>	Film <sup>b</sup>	Sol. <sup>a</sup>	Film <sup>b</sup>			HOMO <sup>e</sup>	LUMO <sup>f</sup>
CzBBIT	106/333	294, 311, 341	297, 316, 344	355, 362	359, 367	3.44	3.0	−5.67	−2.23
2CzBBIT	161/392	295, 307, 343	297, 311, 345	376, 389	382, 394	3.32	3.0	−5.57	−2.25

<sup>a</sup> Measured in toluene.<sup>b</sup> Thin film.<sup>c</sup> From the absorption threshold (film state).<sup>d</sup> Calculated from the phosphorescence spectra recorded in the 2-methyltetrahydrofuran.<sup>e</sup> Calculated using oxidation onset in the film state.<sup>f</sup> Calculated using HOMO +  $E_g$ .

state under the nitrogen atmosphere (**Figure 2C**). It was also confirmed that both non-doped host films display only prompt ( $\tau_p$ ) fluorescence lifetime, demonstrating typical fluorescence behavior. The  $\tau_p$  values of CzBBIT and 2CzBBIT were obtained as 0.5 ns (**Figure S4**). On the other hand, both blend films display  $\tau_p$  and delayed ( $\tau_d$ ) fluorescence lifetimes to corroborate the presence of TADF behavior of IAcTr-out in both host environments. The  $\tau_p$  and  $\tau_d$  values were evaluated by fitting a double-exponential decay mode  $I(t) = A_1 \exp(-t/\tau_p) + A_2 \exp(-t/\tau_d)$ , where  $A_1$  and  $A_2$  are fitting parameters (Xie et al., 2016). The  $\tau_p/\tau_d$  values of CzBBIT and 2CzBBIT were obtained as 19.4 ns/1.94  $\mu$ s and 20.9 ns/2.10  $\mu$ s, respectively (**Table S2**). In addition, the absolute PLQY ( $\Phi_{PL}$ ) values of the compounds were evaluated for the doped films using the integrating sphere. These values for CzBBIT and 2CzBBIT were observed to be 70.96 and 62.29%, respectively. However, the total  $\Phi_{PL}$  of a TADF emitter comprises the prompt ( $\Phi_p$ ) and delayed fluorescence ( $\Phi_d$ ) components. The  $\Phi_p/\Phi_d$  values of CzBBIT and 2CzBBIT were calculated to be 42.77%/28.19% and 37.84%/24.45%, respectively.

Besides, to obtain a deeper understanding of the TADF mechanism, we calculated the essential kinetic parameters, such as the singlet excited state radiative decay rate constant ( $k_r^S$ ), intersystem crossing (ISC) rate constant from the singlet excited state to the triplet excited state ( $k_{ISC}$ ), RISC rate constant from the lowest triplet excited state to the lowest singlet excited state ( $k_{RISC}$ ), and non-radiative (nr) decay rate constant for the singlet excited state ( $k_{nr}^S$ ), for the blended films (**Table S2**). Here,  $k_{nr}^S$  at RT was intended to be zero (Tao et al., 2014). The  $k_{RISC}$  values of CzBBIT:IAcTr-out and 2CzBBIT:IAcTr-out were calculated to be  $8.6 \times 10^5 \text{ s}^{-1}$  and  $7.9 \times 10^5 \text{ s}^{-1}$ , respectively. A faster  $k_{RISC}$  value resulted from the stabilized  $S_1$  state of the emitter in the host. The rate constants, such as prompt ( $k_p = 1/\tau_p$ ) and delayed ( $k_d = 1/\tau_d$ ) fluorescence decays, were deliberated using their corresponding prompt and delayed lifetimes.

## Electrochemical Properties

Cyclic voltammetry measurements were performed using a three-electrode electrochemical cell to evaluate the electrochemical properties of CzBBIT and 2CzBBIT in the film state (**Figure S5** and **Table 1**). During the anodic sweep, both compounds exhibited a quasi-reversible oxidation peak instigated from the electron-rich carbazole/bicarbazole entities. The onset oxidation potentials ( $E_{ox}^{onset}$ ) vs. Ag/Ag<sup>+</sup> were

determined as +1.23 and +1.13 V for CzBBIT and 2CzBBIT, respectively. The HOMO energy levels were estimated using the following equation:  $\text{HOMO} = -e(4.8 + E_{ox}^{onset} - E_{Fc/Fc^+})$  eV (Pommerehne et al., 1995), where the Fc/Fc<sup>+</sup> potential was equal to +0.36 V. Accordingly, the HOMO levels were calculated as −5.67 and −5.57 eV, respectively, which are in line with DFT studies. The relatively shallower HOMO level attained for 2CzBBIT originated from the relatively stronger electron-donating ability of bicarbazole compared to the single carbazole derivative. The LUMO energy levels of CzBBIT and 2CzBBIT were determined to be −2.23 and −2.25 eV, respectively, by adding the  $E_g$  values to HOMO levels. The difference between the LUMO levels of both hosts was insignificant because of the identical electron-acceptor core.

## Thermal and Morphological Properties

The thermal stability of both new materials was examined using TGA and DSC measurements performed at a heating rate of 10°C min<sup>−1</sup> under nitrogen (**Figure S6** and **Table 1**). The TGA results corroborate that CzBBIT and 2CzBBIT have high decomposition temperatures ( $T_d$ , corresponding to 5% weight loss) of 333°C and 392°C, respectively. The glass transition temperatures ( $T_g$ ) of CzBBIT and 2CzBBIT observed from the DSC thermograms are 106 and 161°C, respectively. The remarkable thermal stability of these two materials implies that both are potentially applicable in multilayered OLEDs fabricated through vacuum thermal deposition or solution processes. In particular, the enhanced thermal stability of 2CzBBIT compared to CzBBIT is due to the increased molecular weight. The thermal robustness of these materials is beneficial in producing smooth amorphous and homogeneous films during device fabrication, which is among the essential parameters to achieve a highly stable device performance.

The surface morphology of the blend films of CzBBIT:IAcTr-out and 2CzBBIT:IAcTr-out was examined by atomic force microscopy (**Figure S7**). Both the blend films are homogeneous, with very low root-mean-square roughness values of 0.30 nm for CzBBIT and 0.40 nm for 2CzBBIT. These results confirm that both hosts exhibit superior thermal and morphological stability, which is beneficial in enhancing device stability and electroluminescence (EL) performance during device operations.

## Single-Carrier Devices

The carrier-only devices, such as HODs and EODs, were fabricated, and their characteristics were examined to obtain a deeper insight into the carrier transport abilities of CzBBIT and 2CzBBIT. The device configuration of ITO (150 nm)/PEDOT:PSS (40 nm)/PVK (10 nm)/Host (30 nm)/Al (100 nm) was used for the HOD, and that of ITO (150 nm)/Host (30 nm)/TPBi (40 nm)/LiF (0.8 nm)/Al (100 nm) was employed for the EOD. The current density vs. voltage ( $J$ - $V$ ) curves of the corresponding devices are presented in **Figure S8**. Both hosts exhibit significant hole and electron current densities, which confirm their bipolar nature. However, both hosts exhibited that the electron current densities are much larger than the

hole current densities at a given driving-voltage, demonstrating unbalanced charge transport. It can be assumed that the intrinsic electron character of BBIT is relatively high.

## Electroluminescence Properties

The excellent solubility, thermal robustness, tolerable electrochemical and optical properties, and bipolar nature of CzBBIT and 2CzBBIT propelled us to investigate them as host materials in solution-processable TADF-OLEDs. IAcTr-out was designated as the green TADF emitter because the triplet energy values of both hosts ( $\sim 3.0$  eV) are sufficiently higher than that of IAcTr-out (2.62 eV) (Park et al., 2018) to prevent back energy transfer from the dopant to host, in addition to other

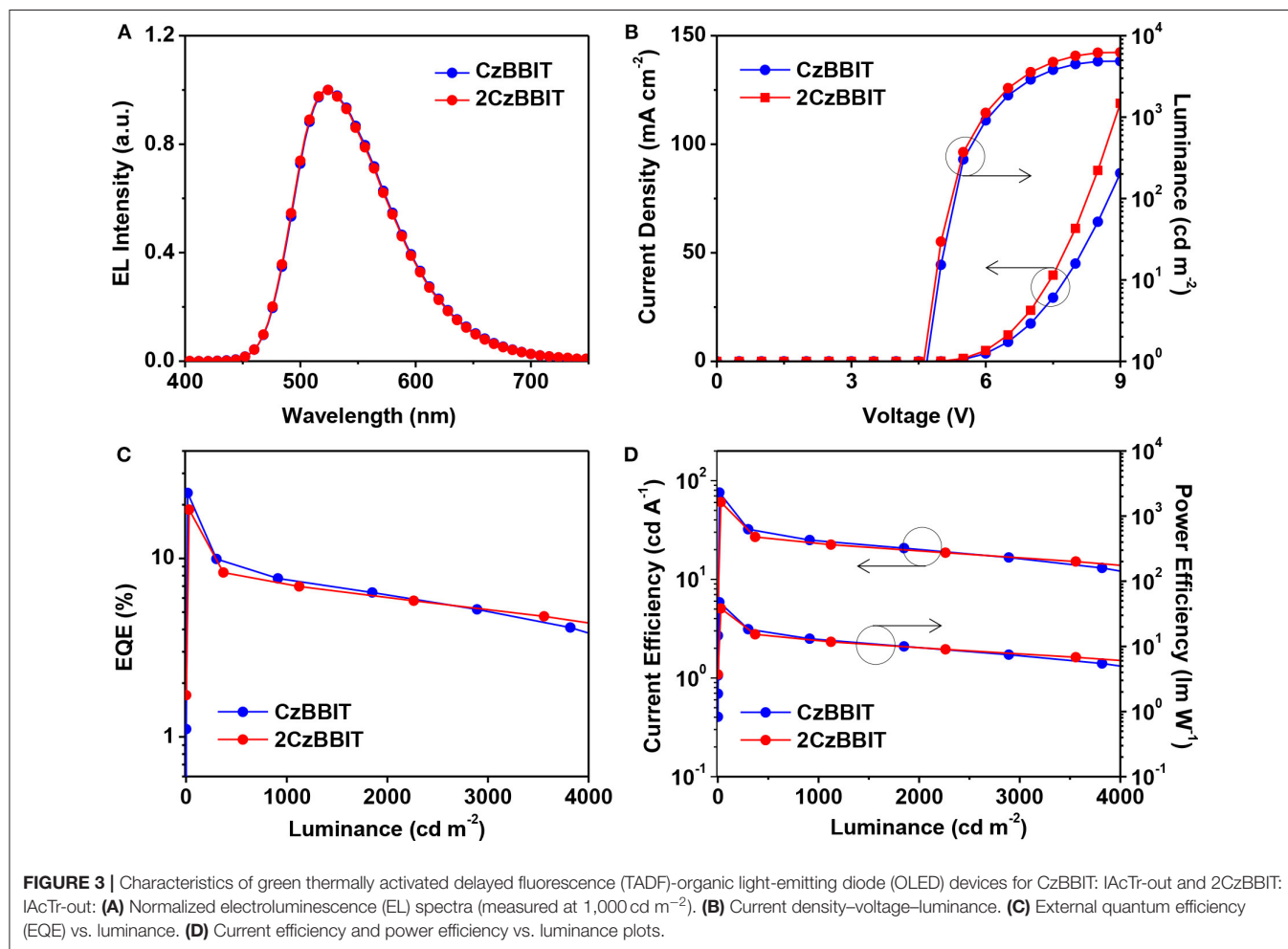


**TABLE 2 |** CzBBIT and 2CzBBIT based TADF-OLED performance data.

Host	$V_{on}$ (V) <sup>a</sup>	Quantum efficiency (%)			Current efficiency (cd A <sup>-1</sup> )			Power efficiency (lm W <sup>-1</sup> )			CIE color Coordinates (x, y) <sup>b</sup>
		Max.	100 cd/m <sup>2</sup>	500 cd/m <sup>2</sup>	Max.	100 cd/m <sup>2</sup>	500 cd/m <sup>2</sup>	Max.	100 cd/m <sup>2</sup>	500 cd/m <sup>2</sup>	
CzBBIT	4.7	23.3	19.3	9.2	75.7	62.8	29.9	47.6	38.8	16.8	(0.33, 0.57)
2CzBBIT	4.6	18.7	16.7	8.1	60.6	53.7	14.8	38.1	40.4	14.8	(0.33, 0.57)

<sup>a</sup> Turn-on voltage at a luminance of 1.0 cd m<sup>-2</sup>.

<sup>b</sup> At a luminance of 1,000 cd m<sup>-2</sup>.

commensurate physical and electrochemical properties. Further, the absorption spectrum of IAcTr-out is well-overlapped with the emission spectrum of both hosts (**Figure S9**), which enable the efficient energy transfer from the host to the dopant. In particular, the PL spectrum of CzBBIT is more overlapped compared to that of 2CzBBIT and thus, a higher performance can be anticipated.

The configuration of OLED was used as follows: ITO (150 nm)/PEDOT:PSS (40 nm)/PVK (10 nm)/CzBBIT or 2CzBBIT: IAcTr-out (40 nm, x wt%)/TPBi (40 nm)/LiF (0.8 nm)/Al (100 nm). PEDOT:PSS functioned as the hole-injection layer, PVK served as the hole-transporting layer, TPBi and LiF functioned as the electron-transport and electron-injection layers, respectively, and Al was the cathode. IAcTr-out doped into CzBBIT or 2CzBBIT was employed as the emissive layer with an optimized dopant concentration of 45.0 wt% for CzBBIT and 35.0 wt% for 2CzBBIT. The EL spectra,  $J$ - $V$ - $L$  spectra, EQE against luminance, and the current efficiency and power efficiency against the luminance curves are displayed in **Figure 3**. The pertinent data for the EL performance are summarized in **Table 2**. The schematic energy level diagram and chemical structures of the materials used in this study are shown in **Figure S10**.

As shown in **Figure 3A**, the maximum EL wavelength of IAcTr-out in both host environments has appeared at a similar wavelength of 524 nm, with CIE color coordinates of (0.33, 0.57). The EL spectra obtained for both devices are similar to the PL spectra of the emitter in the film state (**Figure S11**). The absence of host emissions substantiates that complete energy transfer occurs from the host to the emitter, and all the electro-generated excitons are decayed through the emitter during radiative decay without any detrimental endothermic energy transfer. The similarity between the EL spectra in both host circumstances is attributed to the insignificant polarity variations, as evidenced by the solvatochromic PL studies.

Remarkable performances were achieved in the case of both the devices with an EQE/current efficiency/power efficiency of 23.3%/75.7 cd A<sup>-1</sup>/47.6 lm W<sup>-1</sup> for CzBBIT and 18.7%/60.6 cd A<sup>-1</sup>/38.1 lm W<sup>-1</sup> for 2CzBBIT, respectively. The EQE was retained at 19.3 and 16.7% for CzBBIT and 2CzBBIT, respectively at a luminance of 100 cd m<sup>-2</sup>. However, the EQE in the devices of CzBBIT and 2CzBBIT decreased sharply to 9.2 and 8.1%, respectively, at a brightness of 500 cd m<sup>-2</sup>, indicating significant efficiency roll-off. This can be assumed to be due to unbalanced charge transport in the EML of both devices.

The EQEs of both the devices are much superior to the theoretical EQE limitation for conventional fluorescent emitters (~5%). This is practical evidence for IAcTr-out that utilizes triplet excitons generated after electric excitation through an efficient RISC process during the EL emission. The results verified that BBIT is an outstanding electron-acceptor core that can include a variety of bipolar host materials to achieve high performances in TADF-OLEDs.

## CONCLUSION

In conclusion, benzo[4,5]imidazo[2,1-b][1,3]thiazine (BBIT) as an electron-acceptor core was introduced for the first time

and two new bipolar host materials (CzBBIT and 2CzBBIT) were developed by tethering electron-rich carbazole/bicarbazole entities as donors. The benzimidazole moiety provided an electron-deficient nature to enable an electron-transport nature and benzothiazine functioned as the backbone to BBIT. Besides, the non-conjugated sp<sup>3</sup> hybridized methylene bridge was beneficial to retain the high  $E_T$  by interrupting electron delocalization and partially enabling the solubility. The systematic investigations proved that both hosts not only exhibited a high  $E_T$  value (3.0 eV) and a bipolar nature but also revealed thermal robustness and appropriate optical and electrochemical properties. As a result, the TADF-OLEDs fabricated through the solution process by employing CzBBIT and 2CzBBIT as hosts in the emissive layer demonstrated excellent performances with the maximum EQE values of 23.3 and 18.7%, respectively. The superior electron current density and state-of-the-art device performances substantiate that BBIT is an emerging electron-acceptor core to include versatile host materials suitable for OLEDs. As this is the first report about the BBIT core in OLED applications, there is much room to promote in the future.

## DATA AVAILABILITY STATEMENT

The raw data supporting the conclusions of this article will be made available by the authors, without undue reservation, to any qualified researcher.

## AUTHOR CONTRIBUTIONS

MG designed and synthesized the two new host materials, conducted the photophysical, electrochemical, device characterization, and drafted the entire manuscript. JY, J-EJ, and HW evaluated the thermal and PLQY measurements. SYP provided support during OLED fabrication. CL, YK, and SP conducted the TRPL measurements. MC advised on the synthesis. DC supervised the work and provided many suggestions in all aspects.

## FUNDING

The authors declare that this study received funding from LG Display Co. Limited (2019). The funder was not involved in the study design, collection, analysis, interpretation of data, the writing of this article or the decision to submit it for publication.

## ACKNOWLEDGMENTS

The authors acknowledge the financial support from the National Research Foundation of Korea (NRF2019R1A2C2002647, NRF2019R1A6A1A11044070) and also thanks to the Korea Basic Science Institute in Seoul for allowing us to use MALDI-TOF MS instrument.



## SUPPLEMENTARY MATERIAL

The Supplementary Material for this article can be found online at: <https://www.frontiersin.org/articles/10.3389/fchem.2020.00061/full#supplementary-material>

The supplementary material includes the synthesis of key intermediates; UV-Vis absorption and PL spectra of CzBBIT and 2CzBBIT in film states and in different polar solvents; Fluorescence and phosphorescence spectra of CzBBIT

and 2CzBBIT measured in 2-methyltetrahydrofuran; Cyclic voltammograms, thermogravimetric analysis and differential scanning calorimetry thermograms of CzBBIT and 2CzBBIT; Atomic force microscopy topographic images of blend films; Hole-only devices (HOD) and electron-only devices (EOD) for CzBBIT and 2CzBBIT; UV-Vis absorption spectra of the dopant IAcTr-out and PL spectra of CzBBIT and 2CzBBIT in the film state; Energy-level diagram and chemical structures of the materials used in this study.

## REFERENCES

- Ahn, D. H., Kim, S. W., Lee, H., Ko, I. J., Karthik, D., Lee, J. Y., et al. (2019). Highly efficient blue thermally activated delayed fluorescence emitters based on symmetrical and rigid oxygen-bridged boron acceptors. *Nat. Photonics* 13, 540–546. doi: 10.1038/s41566-019-0415-5
- Aline, G., Holler, M., Teresa, M., Duarte, F., and Nierengarten, J.-F. (2008). Synthesis of oligophenylenevinylene heptamers substituted with fullerene moieties. *Eur. J. Org. Chem.* 3627–3634. doi: 10.1002/ejoc.200800312
- Chatterjee, T., and Wong, K.-T. (2019). Perspective on host materials for thermally activated delayed fluorescence organic light emitting diodes. *Adv. Optical Mater.* 7, 1800565–1800598. doi: 10.1002/adom.201800565
- Cui, L. S., Kim, J. U., Nomura, H., Nakanotani, H., and Adachi, C. (2016). Benzimidazobenzothiazole-based bipolar hosts to harvest nearly all of the excitons from blue delayed fluorescence and phosphorescent organic light-emitting diodes. *Angew. Chem. Int. Ed.* 55, 6864–6868. doi: 10.1002/anie.201601136
- Dressler, J. J., Miller, S. A., Meeuwse, B. T., Riel, A. M. S., and Dahl, B. J. (2015). Synthesis of dilactone bridged terphenyls with crankshaft architectures. *Tetrahedron* 7, 283–292. doi: 10.1016/j.tet.2014.11.055
- Fan, C., Duan, C., Wei, Y., Ding, D., Xu, H., and Huang, W. (2015). Dibenzothiophene-based phosphine oxide host and electron-transporting materials for efficient blue thermally activated delayed fluorescence diodes through compatibility optimization. *Chem. Mater.* 27:5131. doi: 10.1021/acs.chemmater.5b02012
- Godumala, M., Choi, S., Cho, M. J., and Choi, D. H. (2016). Thermally activated delayed fluorescence blue dopants and hosts: from the design strategy to organic light-emitting diode applications. *J. Mater. Chem. C* 4, 11355–11381. doi: 10.1039/C6TC04377A
- Godumala, M., Choi, S., Park, S. Y., Cho, M. J., Kim, H. J., Ahn, D. H., et al. (2018). Chromenopyrazole-based bipolar blue host materials for highly efficient thermally activated delayed fluorescence organic light-emitting diodes. *Chem. Mater.* 30:5005. doi: 10.1021/acs.chemmater.8b01207
- Godumala, M., Yoon, J., Jeong, C. H., Lee, C., Jeong, J.-E., Park, S., et al. (2019). Excellent bipolar host material exhibiting EQE of 24.0% with small efficiency roll-off in solution-processable thermally activated delayed fluorescence OLEDs. *J. Mater. Chem. C* 7, 13930–13938. doi: 10.1039/C9TC04812J
- Huang, T., Jiang, W., and Duan, L. (2018). Recent progress in solution processable TADF materials for organic light-emitting diodes. *J. Mater. Chem. C* 6, 5577–5596. doi: 10.1039/C8TC01139G
- Jeon, S. K., Park, H.-J., and Lee, J. Y. (2018). Highly efficient soluble blue delayed fluorescent and hyperfluorescent organic light-emitting diodes by host engineering. *ACS Appl. Mater. Interfaces* 10, 5700–5705. doi: 10.1021/acsami.7b17260
- Jung, M., Lee, K. H., and Lee, J. Y., and Kim, T. (2019). A bipolar host based high triplet energy electroplex for an over 10 000 h lifetime in pure blue phosphorescent organic light-emitting diodes. *Mater. Horiz.* doi: 10.1039/C9MH01268K
- Kim, S. M., Yun, J. H., Han, S. H., and Lee, J. Y. (2017). A design strategy of bipolar host materials for more than 30 times extended lifetime in phosphorescent organic light-emitting diodes using benzocarbazole and quinoxaline. *J. Mater. Chem. C* 5, 9072–9079. doi: 10.1039/C7TC02973J
- Kondo, Y., Yoshiura, K., Kitera, S., Nishi, H., Oda, S., Gotoh, H., et al. (2019). Narrowband deep-blue organic light-emitting diode featuring an organoboron-based emitter. *Nat. Photonics* 13, 678–682. doi: 10.1038/s41566-019-0476-5
- Konidena, R. K., Lee, K. H., and Lee, J. Y. (2019). Molecular design and synthetic approach to C2,C3,C4-modified carbazoles: high triplet energy bipolar host materials for efficient blue phosphorescent organic light emitting diodes. *Chem. Commun.* 55, 8178–8181. doi: 10.1039/C9CC03843D
- Ma, Z., Dong, W., Hou, J., Duan, Q., Shao, S., and Wang, L. (2019). Dendritic host materials with non-conjugated adamantane cores for efficient solution-processed blue thermally activated delayed fluorescence OLEDs. *J. Mater. Chem. C* 7, 11845–11850. doi: 10.1039/C9TC04143E
- Park, S. Y., Choi, S., Park, G. E., Kim, H. J., Lee, C., Moon, J. S., et al. (2018). Unconventional three-armed luminogens exhibiting both aggregation-induced emission and thermally activated delayed fluorescence resulting in high-performing solution-processed organic light-emitting diodes. *ACS Appl. Mater. Interfaces* 10:14966. doi: 10.1021/acsami.7b19681
- Pommerehne, J., Vestweber, H., Guss, W., Mahrt, R. F., Bassler, H., Porsch, M., et al. (1995). Efficient two layer leds on a polymer blend basis. *Adv. Mater.* 7, 551–554. doi: 10.1002/adma.19950070608
- Shao, S., Hu, J., Wang, X., Wang, L., Jing, X., and Wang, F. (2017). Blue thermally activated delayed fluorescence polymers with nonconjugated backbone and through-space charge transfer effect. *J. Am. Chem. Soc.* 139, 17739–17742. doi: 10.1021/jacs.7b10257
- Tao, Y., Yuan, K., Chen, T., Xu, P., Li, H., Chen, R., et al. (2014). Thermally activated delayed fluorescence materials towards the breakthrough of organoelectronics. *Adv. Mater.* 26, 7931–7958. doi: 10.1002/adma.201402532
- Tsai, K.-W., Hung, M.-K., Mao, Y.-H., and Chen, S.-A. (2019). Solution-processed thermally activated delayed fluorescent OLED with high EQE as 31% using high triplet energy crosslinkable hole transport materials. *Adv. Funct. Mater.* 29:1901025. doi: 10.1002/adfm.201901025
- Uoyama, H., Goushi, K., Shizu, K., Nomura, H., and Adachi, C. (2012). Highly efficient organic light-emitting diodes from delayed fluorescence. *Nature* 492, 234–238. doi: 10.1038/nature11687
- Xie, G., Chen, D., Li, X., Cai, X., Li, Y., Chen, D., et al. (2016). Polarity-tunable host materials and their applications in thermally activated delayed fluorescence organic light-emitting diodes. *ACS Appl. Mater. Interfaces*, 2016, 8, 27920–27930. doi: 10.1021/acsami.6b08738
- Zhang, J., Ding, D., Wei, Y., Han, F., Xu, H., and Huang, W. (2016a). Multiphosphine-oxide hosts for ultralow-voltage-driven true-blue thermally activated delayed fluorescence diodes with external quantum efficiency beyond 20%. *Adv. Mater.* 28, 479–485. doi: 10.1002/adma.201502772
- Zhang, J., Ding, D., Wei, Y., and Xu, H. (2016b). Extremely condensing triplet states of DPEPO-type hosts through constitutional isomerization for high-efficiency deep-blue thermally activated delayed fluorescence diodes. *Chem. Sci.* 7, 2870–2882. doi: 10.1039/C5SC04848F
- Zou, Y., Gong, S., Xie, G., and Yang, C. (2018). Design strategy for solution-processable thermally activated delayed fluorescence emitters and their applications in organic light-emitting diodes. *Adv. Optical Mater.* 6:1800568. doi: 10.1002/adom.201800568

**Conflict of Interest:** The authors declare that the research was conducted in the absence of any commercial or financial relationships that could be construed as a potential conflict of interest.

Copyright © 2020 Godumala, Yoon, Park, Lee, Kim, Jeong, Park, Woo, Cho and Choi. This is an open-access article distributed under the terms of the Creative Commons Attribution License (CC BY). The use, distribution or reproduction in other forums is permitted, provided the original author(s) and the copyright owner(s) are credited and that the original publication in this journal is cited, in accordance with accepted academic practice. No use, distribution or reproduction is permitted which does not comply with these terms.



# Sensitizing TADF Absorption Using Variable Length Oligo(phenylene ethynylene) Antennae

Olga Franco<sup>1\*</sup>, Marius Jakoby<sup>2</sup>, Rebekka V. Schneider<sup>3</sup>, Fabian Hundemer<sup>4</sup>, Daniel Hahn<sup>3</sup>, Bryce S. Richards<sup>1,2</sup>, Stefan Bräse<sup>4,5</sup>, Michael A. R. Meier<sup>3,5</sup>, Uli Lemmer<sup>1,2</sup> and Ian A. Howard<sup>1,2\*</sup>

<sup>1</sup> Department of Electrical Engineering and Information Technology, Light Technology Institute, Karlsruhe Institute of Technology, Karlsruhe, Germany, <sup>2</sup> Department of Electrical Engineering and Information Technology, Institute of Microstructure Technology, Karlsruhe Institute of Technology, Eggenstein-Leopoldshafen, Germany, <sup>3</sup> Laboratory of Applied Chemistry, Institute of Organic Chemistry, Karlsruhe Institute of Technology, Karlsruhe, Germany, <sup>4</sup> Institute of Organic Chemistry, Karlsruhe Institute of Technology, Karlsruhe, Germany, <sup>5</sup> Institute of Biological and Chemical Systems - Functional Molecular Systems, Karlsruhe Institute of Technology, Eggenstein-Leopoldshafen, Germany

## OPEN ACCESS

### Edited by:

Chihaya Adachi,  
Kyushu University, Japan

### Reviewed by:

Sebastiano Di Pietro,  
University of Pisa, Italy  
Basem Moosa,  
KAUST Catalysis Center (KCC),  
Saudi Arabia

### \*Correspondence:

Olga Franco  
olga.franco@kit.edu  
Ian A. Howard  
ian.howard@kit.edu

### Specialty section:

This article was submitted to  
Organic Chemistry,  
a section of the journal  
Frontiers in Chemistry

**Received:** 10 December 2019

**Accepted:** 12 February 2020

**Published:** 26 February 2020

### Citation:

Franco O, Jakoby M, Schneider RV, Hundemer F, Hahn D, Richards BS, Bräse S, Meier MAR, Lemmer U and Howard IA (2020) Sensitizing TADF Absorption Using Variable Length Oligo(phenylene ethynylene) Antennae. *Front. Chem.* 8:126. doi: 10.3389/fchem.2020.00126

Beyond their applications in organic light-emitting diodes (OLEDs), thermally activated delayed fluorescence (TADF) materials can also make good photonic markers. Time-gated measurement of their delayed emission enables “background-free” imaging in, for example, biological systems, because no naturally-occurring compounds exhibit such long-lived emission. Attaching a strongly-absorbing antenna, such as a phenylene ethynylene oligomer, to the TADF core would be of interest to increase their brightness as photonic markers. With this motivation, we study a sequence of TADF-oligomer conjugates with oligomers of varying length and show that, even when the absorption of the oligomer is almost resonant with the charge-transfer absorption of the TADF core, the antenna transfers energy to the TADF core. We study this series of compounds with time resolved emission and transient absorption spectroscopy and find that the delayed fluorescence is essentially turned-off for the longer antennae. Interestingly, we find that the turn-off of the delayed fluorescence is not caused by quenching of the TADF charge-transfer triplet state due to triplet energy transfer of the lower-lying triplet state to the antenna, but must be associated with a decrease in the reverse intersystem crossing rate. These results are of relevance for the further development of TADF “dyes” and also, in the broader context, for understanding the dynamics of TADF molecules in the vicinity of energy donors/acceptors (i.e., in fluorescent OLEDs wherein TADF molecules are used as an assistant dopant).

**Keywords:** thermally activated delayed fluorescence (TADF), time-resolved photoluminescence spectroscopy, transient absorption spectroscopy (TAS), sequence-defined oligomer, charge-transfer state (CT-state)

## 1. INTRODUCTION

Since the initial reports on compounds that displayed thermally activated delayed fluorescence (TADF) (Parker and Hatchard, 1961; Maciejewski et al., 1986; Uoyama et al., 2012), their use as photonic probes and markers has also been considered. In a few examples, TADF molecules can be utilized as temperature and oxygen sensors (Méhes et al., 2012, 2014; Kochmann et al., 2013; DeRosa et al., 2015; Steinegger et al., 2017; Tonge et al., 2020); they have been used as special dyes

(optionally incorporated into nanoparticles to negate the effect of environmental quenchers such as oxygen) that enable time-gated background free imaging due to delayed fluorescence (Xiong et al., 2014; Li et al., 2017, 2019; Zhu et al., 2018; Ni et al., 2019; Zhang et al., 2019b) and they have enable photodynamic therapy (Zhang et al., 2016, 2019a). In order to increase the brightness of the delayed emission for sensor or marking applications (or rate of singlet oxygen generation for photodynamic therapy), a strong absorption of incoming photons is desired. The charge-transfer (CT) nature of the absorption of the TADF core means that the photon absorption of the TADF core is rather weak.

In this contribution, we consider TADF cores attached to a sequence of strongly-absorbing antennae based on phenylene ethynylene oligomers (OPEs) of varying length (see **Figure 1** for the chemical structures of the investigated molecules). By tuning the antenna length, we can achieve strong absorption in resonance with the energy of the TADF CT band. The photons absorbed by the antenna are transferred into the TADF core with good efficiency. However, the delayed fluorescence is also turned off for the compounds with the longer antennae. Examining the kinetics of these systems with time-resolved photoluminescence (PL) and transient absorption, we can exclude quenching of the TADF triplet CT state due to Dexter energy transfer to the lower-lying triplet state on the antenna. Rather, it appears that the reverse intersystem crossing (RISC) rate is diminished in the presence of the antenna. These findings are encouraging for the development of TADF based dyes (and fluorescent OLEDs using TADF assistant dopants) showing that Dexter transfer to a nearby and energetically accessible triplet state is not necessarily kinetically favored and thus might be avoided by chemical design.

## 2. RESULTS AND DISCUSSION

### 2.1. Materials

We attached rod-like monodisperse oligo(phenylene ethynylene)s (OPEs) to a modified 2,4,5,6-tetra(9H-carbazol-9-yl)isophthalonitrile (4CzIPN) core, a compound known for its TADF function (Uoyama et al., 2012). We synthesized a TADF molecule inspired by 4CzIPN, but in which one cyano acceptor group has been replaced by an oxadiazole-phenylene group onto which the OPE can be conjugated, **T** (for synthesis details please refer to Hundemer et al., 2020). Compared to the cyano group, the oxadiazole is a weaker acceptor (Wong et al., 2018). Monodisperse OPEs of varying length were previously synthesized through the use of sequence-defined routes Schneider et al. (2018). Herein the OPE monomer, trimer, and pentamer were coupled to **T** (forming the T-oligomers **T1**, **T3**, and **T5**, respectively). The chromatography results confirmed the monodispersity of the compounds (cf. **Figure 2**) The antennae on **Tn** are formed of a chain of  $n+2$  phenylene units conjugated by  $n+1$  ethynylene bonds (see **Figure 1** for the chemical structures of all the investigated molecules). A detailed report of the synthesis of these compounds can be found in the **Supplementary Material**.

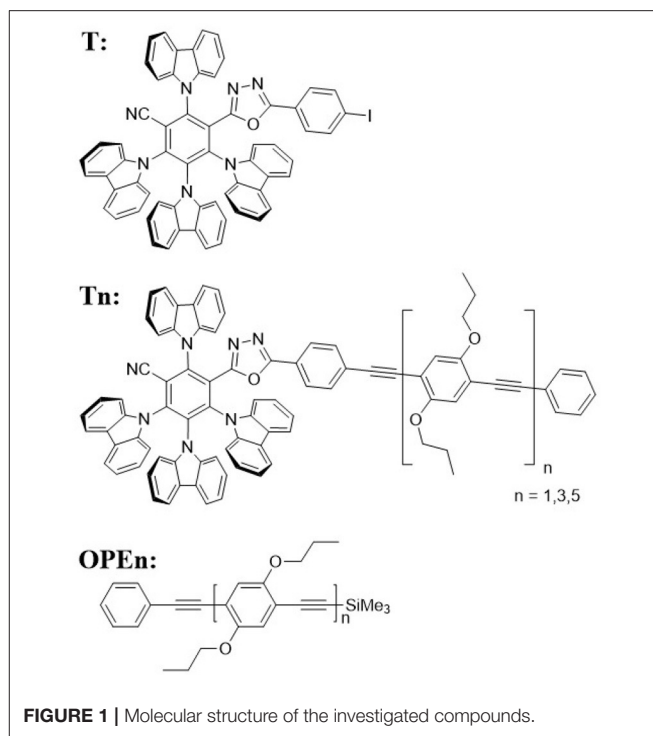


**FIGURE 1** | Molecular structure of the investigated compounds.

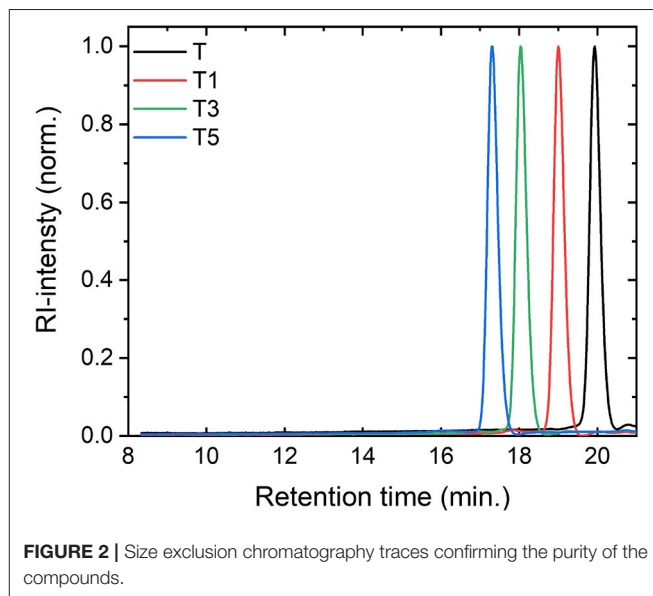


**FIGURE 2** | Size exclusion chromatography traces confirming the purity of the compounds.

### 2.2. UV-Vis Absorption and Photoluminescence Spectroscopy

**Figure 3** shows the steady-state absorption and emission spectra of **T**, **T1**, **T3**, and **T5**. Alongside, the absorption and emission spectra of the reference OPEs are also shown. The reference OPEs were chosen to have the closest number of conjugated phenyl rings as the antennae on the TADF-conjugates. For **T1** and **T3**, OPEs with the precisely same number of phenylene units are available, whereas for **T5** the OPE has one fewer phenylene ring.



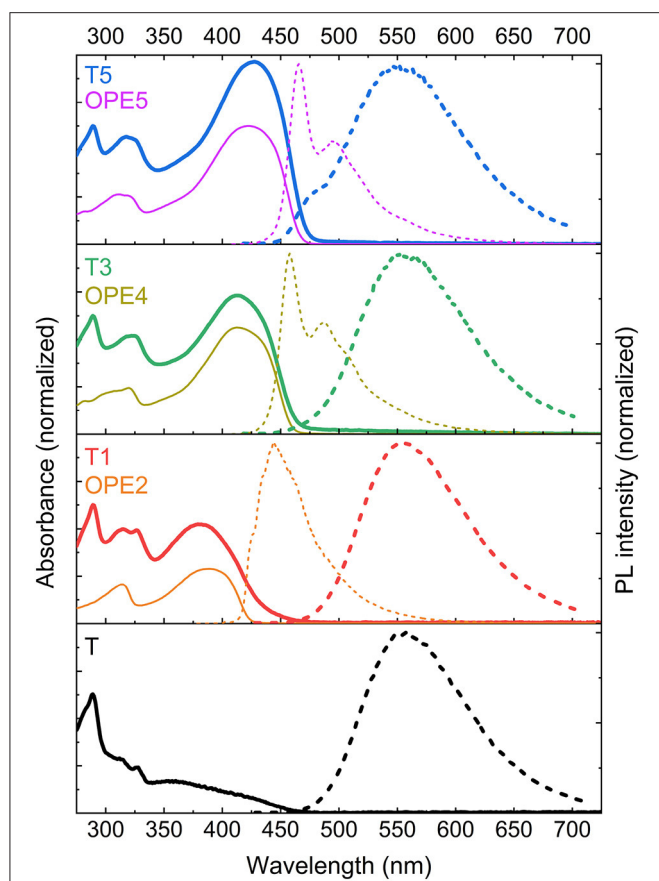


**FIGURE 3** | UV-Vis spectra of the investigated compounds (absorption in thick solid lines and emission in thick dashed lines) and their corresponding OPEs (absorption in fine solid lines and emission in fine dashed lines) in chloroform (concentration  $\leq 5 \cdot 10^{-4}$  mol/l). The absorption spectra of **T**, **T1**, **T3** and **T5** were normalized to the peak around 290 nm that corresponds to a Cz absorption. The absorption spectra of the OPEs were normalized to the maximum value for **OPE5**. The OPE data were adapted from Schneider et al. (2018), which is an article licensed under a Creative Commons Attribution 4.0 International License (<https://creativecommons.org>). Specifically, we have calculated the absorbance from the original optical attenuation data. The PL intensity data were used as in the original article.

In all cases, the agreement between the **T<sub>n</sub>** and reference **OPE<sub>n</sub>** absorption spectra is pronounced, allowing accurate conclusions to be drawn. Upon the addition of an antenna the absorbance spectrum of **T** is modified with an intense low energy band whose peak position and intensity corresponds to that of the reference oligomer (cf. **Figure 3**). The strong band associated to the antenna greatly influences the absorbance of the TADF-antenna conjugates. Increasing oligomer length increases the oscillator strength of the absorbance and shifts it to lower energies, as expected from  $\pi-\pi^*$  transitions with enhanced conjugation. The increase in the cross-section of the absorption due to the antenna can be easily observed by considering the ratio of the absorbance for the 290 nm peak resulting from the Cz units on the TADF core with the absorbance for the maximum of the bands associated with the antennae. Whereas the CT absorption band for **T** (in the region 340–480 nm) is far weaker

than the Cz absorption at 290 nm, the absorption of the longer **T**-oligomers **T3** and **T5** is stronger at 400 nm (which lies within the CT band) than it is at 290 nm. This is clearly an effect of the antenna. Indeed, strong absorption bands are obtained, with the absorption in the region of the CT band now exceeding the UV carbazole absorption for both **T3** and **T5**. From these data we conclude that the addition of an OPE antenna is an effective way to introduce a strong absorption band, and that for **T5** the oligomer has reached sufficient length that this strong absorption is in resonance with the CT absorption of the original core. Thus, should energy transfer occur from the antenna to the core for **T3** or **T5** they may represent good candidates for TADF-based photonic markers.

In order to investigate whether energy transfer from the antenna to the TADF core is possible, data for the time-integrated PL after excitation at 355 nm were collected, and compared with the PL spectra for the reference OPE compounds. These data are also shown in **Figure 3**. Although the emission spectrum of the isolated OPE oligomers shifts steadily to the red with increasing length they remain higher in energy than the emission of the unsubstituted molecule **T**. The emission spectra of the TADF-antenna conjugates **T1**, **T3**, and **T5** remain essentially constant and identical to the spectra of **T** with their peak around 560 nm (a comparison of these spectra on a single plot and their time evolution is also shown in **Supplementary Figure 8**; from these data molecular aggregation can be ruled out). The observation that the emissions for **T** and **T1**, **T3**, come from the same state despite stronger absorption from the antenna at the excitation wavelength indicates that there is energy transfer from the antenna to the core. Even for **T5**, the majority of the emitted photons come from the TADF core, although a small high energy shoulder in the emission indicate a minority of singlet states on the antenna can emit before they are transferred in this case. Given this shoulder accounts for only a minor contribution to the overall emission, and also in light of the transient absorption results discussed below, the PL data indicate that for all conjugates energy transfer from the antenna to the TADF core is efficient.

The good transfer to the TADF core from the antennae is achieved because the Stokes shift for **T** is significantly larger than for the individual OPEs. This means that even as the absorption of the antenna becomes similar in energy to the lowest energy CT absorption of the core, the emission of the core is still at a significantly lower energy than that of the antenna. In all cases there is sufficient overlap between the emission of the OPE antenna and the CT absorption of the core to support Förster transfer enabling efficient singlet energy transfer from antenna to core.

For the interested reader, three minor notes regarding the steady-state absorption and emission spectra are made. Firstly, we note that the absorption and emission data for the OPE compounds were previously published Schneider et al. (2018), but reproduced here due to their relevance to the discussion of the new observations. Secondly, we point out that our measurements are made using chloroform as a solvent rather than toluene (commonly used for 4CzIPN) because the TADF was more intense for our molecules in chloroform. This result

is consistent with literature findings for 4CzIPN and various carbazole benzonitrile derivatives where the reverse intersystem crossing rate is increased in solvents more polar than toluene (Ishimatsu et al., 2013; Nobuyasu et al., 2016; Hosokai et al., 2018). The decrease in the TADF emission for 4CzIPN in more polar solvents than toluene is attributed to increased non-radiative rates (Ishimatsu et al., 2013). Thirdly, we point out that the Stokes shift for **T** is significantly larger than the Stokes shift observed for 4CzIPN in toluene (Uoyama et al., 2012). There are two effects at play here. On the one hand, the more polar nature of the solvent leads to a greater stabilization of the CT state and a larger Stokes shift. For example the emission peak of 4CzIPN shifts from 507 nm in toluene to 536 nm in dichloromethane (a solvent more polar than chloroform). On the other hand, an increased structural relaxation in the excited state might be introduced by the substitution of the cyano group with the oxadiazole-phenylene group. The emission peak for **T** in toluene is already at 540 nm, significantly red-shifted compared to 4CzIPN. Therefore, the substitution of the cyano group with the weaker accepting oxadiazole group enables a relaxation in the excited state that reduces the energy of the emitted photons and increases the Stokes shift (perhaps supported by the reduced symmetry of the substituted molecule).

### 2.3. Time-Resolved Photoluminescence Spectroscopy

We examined the time-resolved emission to establish how the addition of the antenna oligomers affects the prompt and delayed fluorescence emitted from the TADF-antenna conjugates. The temporal evolution of the PL is depicted in **Figure 4**. Lifetimes obtained from biexponential fits to the data are shown in **Table 1**. It is immediately apparent that the delayed PL is drastically reduced from **T** to **T1** and suppressed to such a great extent for **T3** and **T5** that no delayed emission can be detected with our sensitive ICCD setup. These results are clearly negative in terms of applying these materials for photonic markers that show strong absorption and delayed emission. Although the absorption is strong on the antenna and energy from the singlet state of the antenna can transfer to the TADF core, once the triplet state is created on the TADF core it is very unlikely to reverse intersystem cross and yield delayed emission. Although this lack of delayed emission precludes the intended application of the molecules, the process by which the delayed fluorescence is turned off is studied in more detail. The results of this investigation are interesting both in terms of understanding how to design molecules for the intended application, and also in terms of their implications regarding the quenching of triplets by fluorescence acceptors in hyperfluorescent systems.

The most obvious hypothesis to explain the lack of delayed emission is the introduction of a new loss channel from the TADF triplet CT state upon the introduction of the antenna: namely the transfer of the CT triplet state on the TADF core to a lower-lying triplet state on the OPE antenna. As the singlet-triplet gap on the OPE antenna is around 0.7 eV (Köhler et al., 2002; Köhler and Beljonne, 2004), and the singlet energies of the CT state on the TADF core and the OPE antenna are similar, the

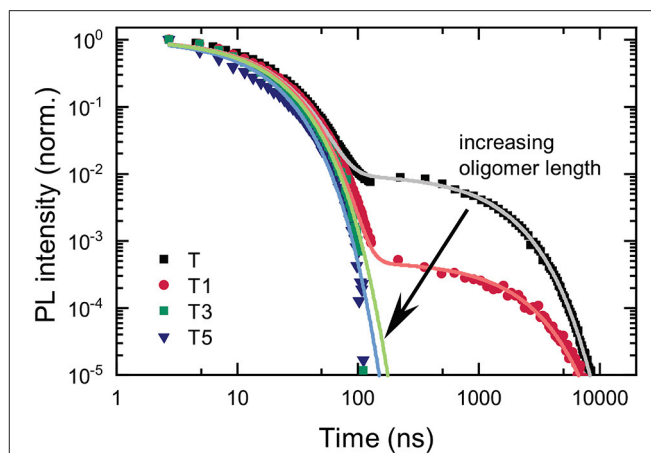


**FIGURE 4** | Temporal decay of the PL of the investigated compounds in deoxygenated chloroform ( $c = 5 \cdot 10^{-4}$  mol/l). Lifetimes and amplitudes of the biexponential fits are stated in **Table 1**.

**TABLE 1** | Prompt and delayed lifetimes ( $\tau_p$  and  $\tau_d$ ), and prompt and delayed amplitudes ( $A_p$  and  $A_d$ ) from biexponential fits of the PL kinetics. Prompt to delayed emission ratio (p/d) calculated using  $\tau_p A_p / (\tau_d A_d)$ .

	<b>T</b>	<b>T1</b>	<b>T3</b>	<b>T5</b>
$\tau_p$ /ns	16	16	15	14
$\tau_d$ /ns	1,200	1,700	NA	NA
$A_p$	1	1	1	1
$A_d$	$1 \times 10^{-2}$	$5 \times 10^{-4}$	0	0
p/d	1.5	21	NA	NA

triplet energy of the OPE antenna must lay significantly below the energy of the CT triplet state on the TADF core. Therefore, the transfer of the CT triplet to the triplet state on the antenna is energetically possible.

However, none of the data we collected are consistent with this hypothesis. This is examined in greater detail in the section below presenting the transient absorption. Already the data shown in **Figure 4** are inconsistent with the hypothesis of transfer of the CT triplet to a triplet state localized on the OPE. The prompt and delayed lifetimes along with the ratio of the prompt to delayed emission obtained from biexponential fits of the data shown in **Figure 4** are presented in **Table 1**. In TADF molecules, the lifetime of the delayed fluorescence reveals the decay of the charge-transfer triplet state population. If a new loss channel was introduced to the charge-transfer triplet population, the initial intensity of the delayed PL would be similar to that without the loss channel (i.e., the intensity of the delayed PL at 100 ns would be similar) but the lifetime of the delayed PL would be substantially shorter. However, these are not the observations made in the data. Rather the opposite, between **T** and **T1** the intensity of the delayed PL in the first instance (at 100 ns) is substantially decreased, and the lifetime of the delayed PL is not shortened (in fact it slightly increases in **T1**). The observations in the data rather suggest that the RISC rate is decreased, decreasing

the intensity of the delayed PL from a similar concentration CT triplet states.

In order to visualize this argument, simulated PL transient showing the prompt and delayed emission are obtained for three solutions to the rate equations for the singlet and triplet CT populations on the TADF core. The first solution is the reference case, with typical values from the literature used for the kinetic parameters. In the second case, an extra decay channel for the CT triplet state is added to express a transfer of the CT triplet state to a triplet state on the antenna. In the third case, the rate of RISC is reduced by a factor of 20. The rate equations are shown in Equation (1), where  $c_s$  and  $c_t$  are the concentrations of CT states in the singlet and triplet manifold respectively,  $k_{ISC}$  is the intersystem crossing rate,  $k_{rad}$  is the radiative decay rate from the CT singlet state (note non-radiative decay from the singlet state to the ground state is neglected, as common in the literature),  $k_{RISC}$  is the reverse intersystem crossing rate, and  $k_{nr+trans}$  is the total rate of states exiting the CT triplet population due to non-radiative decay to the ground state or transfer to the triplet state on the antenna.

$$\frac{\partial}{\partial t} c_s = -(k_{ISC} + k_{rad})c_s + k_{RISC} \cdot c_t, \quad (1a)$$

$$\frac{\partial}{\partial t} c_t = -(k_{RISC} + k_{nr+q})c_t + k_{ISC} \cdot c_s, \quad (1b)$$

The parameters used for the reference simulation are: loss of CT triplet population due to triplet transfer to antenna and decreased RISC rate. They are shown in **Table 2**. The parameters are chosen to be consistent with the literature values for 4CzIPN (Uoyama et al., 2012; Yurash et al., 2019), with slight adjustment (slight increases in  $k_{rad}$ ,  $k_{ISC}$ , and  $k_{nr+q}$ ) so that the reference simulation mimics the kinetics observed for **T**. The results of the simulations are compared with the data for **T** and **T1** in **Figure 5**. The parameters used for the reference simulation reproduce well the observed PL transient for **T**. However, the addition of a significant extra channel for loss of the CT triplet state, for example caused by transfer of the CT triplet to the oligomer triplet, is not able to explain the observed data for **T1**. In the simulation labeled “triplet transfer,”  $k_{nr+q}$  is doubled, to represent significant population of the CT triplet transferring to the antenna. As described above, although the total delayed PL is significantly reduced in the triplet transfer model, the initial delayed emission (around 100 ns) is hardly affected. The simulation labeled “reduced RISC,” on the other hand, fits the observed data for **T1** very well. The reduced RISC simulation differs only from the reference case in that  $k_{RISC}$  is reduced by a factor of 20.

## 2.4. Transient Absorption Spectroscopy

The results of the transient PL experiments confirm that it is a change in the  $k_{RISC}$  that limits the delayed emission from **T1** through **T5**. In order to substantiate this hypothesis (and gain insights into the intermediate states involved), we investigated the excited-state dynamics of the molecules **T**, **T1**, and **T5** using transient absorption spectroscopy (TAS). We measured the

**TABLE 2** | Parameters used for simulation of PL transients.

	Reference	Triplet transfer	Decreased RISC
$k_{rad}/s^{-1}$	$1.3 \cdot 10^7$	$1.3 \cdot 10^7$	$1.3 \cdot 10^7$
$k_{ISC}/s^{-1}$	$3.9 \cdot 10^7$	$3.9 \cdot 10^7$	$3.9 \cdot 10^7$
$k_{RISC}/s^{-1}$	$6 \cdot 10^5$	$6 \cdot 10^5$	$3 \cdot 10^4$
$k_{nr+q}/s^{-1}$	$6 \cdot 10^5$	$1.2 \cdot 10^6$	$6 \cdot 10^5$

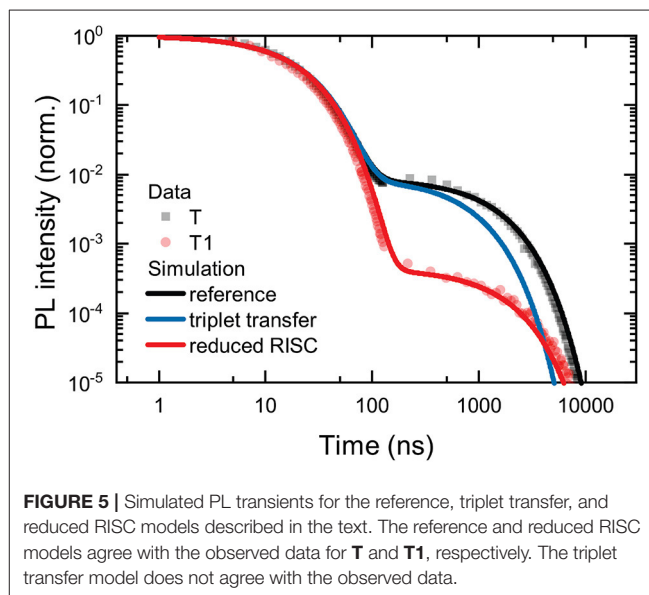
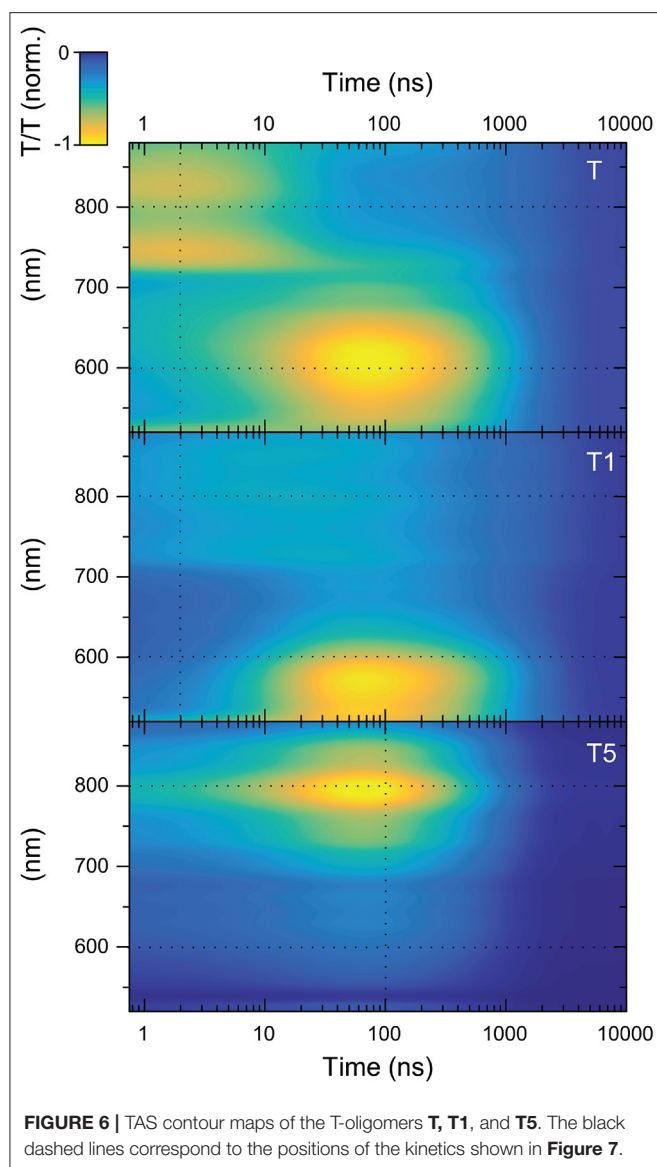


**FIGURE 5** | Simulated PL transients for the reference, triplet transfer, and reduced RISC models described in the text. The reference and reduced RISC models agree with the observed data for **T** and **T1**, respectively. The triplet transfer model does not agree with the observed data.

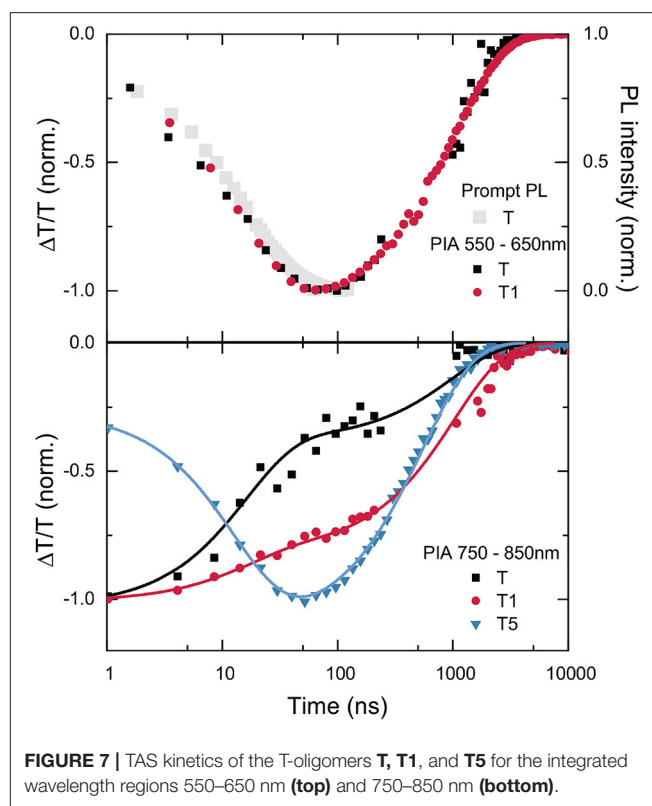
change in transmission ( $\Delta T/T$ ) of the samples in the wavelength range of 520–880 nm induced by a previous excitation pulse with a wavelength of 355 nm. Details of the transient absorption setup are given in the experimental section. We note that the time resolution is sub-nanosecond and the excitation fluence was kept under  $20 \text{ nJcm}^{-2}$ . To ascertain that all kinetics presented are caused by linear processes, and that the sample was not degraded during the investigation, measurements at a sequence of excitation fluences were taken.

**Figure 6** shows the TAS contour maps of the three samples under study for delay times between the pump and probe beams of 0.8 ns to 10  $\mu s$ . Immediately, a difference between **T5** and the other two samples is apparent. For **T** and **T1**, two distinct photo-induced absorption (PIA) bands are visible whose maxima occur at significantly different points in time: (i) a band centered around 800 nm present at early times ( $< 5 \text{ ns}$ ) and (ii) a PIA band centered around 600 nm which rises within the first 100 ns after excitation. For **T** and **T1** the data matrix is rank 2. However, this is not the case for **T5**. There is only one feature visible for the case of **T5** (for **T5** the data matrix is rank 1).

Already at this level of analysis, these data again provide evidence against the hypothesis that the reduction in delayed emission in **T1**, **T3**, and **T5** stems from triplet transfer from the triplet CT state of the TADF core to a localized triplet on the OPE antenna. If the CT triplet excitations were transferred to the OPE oligomer, this should happen most favorably in **T5**. In **T5**



a new spectral feature should emerge after ISC that corresponds to the excited-state absorption of an OPE triplet while the initial excited-state absorption due to the TADF-core CT state should disappear. This is inconsistent with the observed data matrix for **T5**. The observations show that the data matrix for **T5** is rank 1 (meaning that it can be expressed by the outer product of only one spectral vector with a single time-evolution vector). This means that only a single-excited state species is responsible for the entire TA surface for **T5**. This species cannot be an OPE triplet for two reasons. Firstly, the signal is there immediately after excitation. Although the signal grows stronger with time in the first 100 ns, the signal height is roughly 25% of its maximum immediately (cf. lower panel of **Figure 7**). There is no possibility that such a significant population of triplet states on OPE could be created immediately upon excitation. The second argument against this feature being related to a triplet state on the OPE is its lifetime. The triplet lifetime of poly(p-phenylene ethynylene) was



able to be easily determined as it was one of the first materials to show delayed emission due to triplet-triplet annihilation (Partee et al., 1999). This delayed emission allowed a triplet lifetime of 200  $\mu$ s to be estimated for powder samples (Partee et al., 1999). Later pulse radiolysis measurements agreed well with this, finding a triplet lifetime of 300  $\mu$ s in deoxygenated toluene solution. We also note that the triplet induced absorption for poly(p-phenylene ethynylene) shows a strong feature at 780 nm. For this reason, we can be confident that we would see signals from the triplet exciton species on the OPE in the spectral range that we observe in case OPE triplet excitons were created.

We now examine the transient absorption data in more detail. A comparison with the detailed TAS study of Hosokai et al. (2017) on 4CzIPN supports the assignment of the band at 600 nm that grows in within the first 100 ns to be associated with a local triplet state on the phthalonitrile core of the molecule ( $^3$ LE). Such bands are only observed for **T** and **T1**. We note that this band is shifted between the two samples. For **T**, the band is centered at 600 nm, but for **T1**, it is blue shifted to 550 nm. This shift in the induced absorption band suggests a shift in the energy levels of the  $^3$ LE between **T** and **T1**. For **T5**, this band is either entirely absent, or significantly shifted in energy. The development of the intensity of this PIA as a function of time is shown in **Figure 7**, where it is also compared to the decay of the prompt PL. The growth of the PIA and the decay of the prompt PL exactly coincide, reinforcing the conclusion that the species responsible for the PIA is a direct product of ISC from the CT singlet state.



The energetic resonance of the CT states with  $^3\text{LE}$  is proposed to be crucial for enabling RISC (Etherington et al., 2016; Evans et al., 2018). The  $^3\text{LE}$  can couple to the CT singlet state, allowing the CT triplet to return to the CT singlet with the help of this local triplet intermediate. Therefore, the observation of a local triplet absorption band growing in with  $1/(k_{\text{ISC}} + k_{\text{rad}})$  has been observed to be critical for efficient RISC (Hosokai et al., 2017). The presence of this band suggests that the triplet CT efficiently mixes with the local triplet state. The upper panel of **Figure 7** shows how this induced absorption grows in for **T** suggesting that mixing dominates the TA spectra after 100 ns. In **T1** it is slightly less dominant with respect to the 800 nm feature (and also shifted). For **T5** this feature is absent and the 800 nm feature dominates the spectrum at later times. Thus, we conclude that there is a correlation between the growth of a strong PIA, likely stemming from a  $^3\text{LE}$  state close to resonance with the CT triplet state, and a reasonable RISC rate. The observations are consistent with our conclusions that it is a reduced RISC rate that is responsible for the reduction of delayed PL. The similar lifetime of this PIA signal from **T** and **T1** again speaks against the hypothesis of quenching of the CT triplet state by transfer to a lower lying triplet on the antenna.

There is a second clear feature in all of the TA surfaces. The PIA around 800 nm can be assigned to an absence of electron density on the Cz units as a consequence of a CT state formation as it closely resembles the induced absorption for Cz cations (Yamamoto et al., 1989; Tsujii et al., 1990). This induced absorption associated with a reduction of electron density on the Cz units is present for all times in all samples; however, the intensity of this induced absorption does change upon ISC in all samples. The lower panel of **Figure 7** depicts the evolution of this PIA due to the Cz reduced electron density in the range 750–850 nm. For **T**, the PIA in this region decreases by more than 50% with the same lifetime as the prompt decay. This indicates that for **T**, the transition from the singlet to the triplet CT state is accompanied by a reduction in the PIA caused by a decreased electron density on the carbazole units. This could be explained by a sufficiently small difference in energy between the CT triplet state and a  $^3\text{LE}$  state, that allows the excited state to spend time in the  $^3\text{LE}$  once intersystem crossing has occurred (and thus reducing the amount of time spent in the CT state which causes the 800 nm PIA). Such an explanation is consistent with the work of Etherington et al., who found a changing ratio of the induced absorption of the CT triplet to the  $^3\text{LE}$  state as the energetic gap between these two states was varied (Etherington et al., 2016). Returning to our data, for **T1** the PIA in this region is also reduced on the same time scale as the prompt PL decay. However, in this case the reduction is less than half as large as it was for **T**. This could indicate that again, once the CT state in **T1** has undergone intersystem crossing, it can spend time in a  $^3\text{LE}$  state. However, it spends much less time in the  $^3\text{LE}$ , and consequently more time in the CT triplet state. For this reason, the PIA that stems from a reduction in electron density on the carbazoles (in the CT state) is better preserved in this case. For **T5**, the kinetics are notably different. The PIA in the 800 nm region actually increases with the same rate as the prompt PL lifetime. Although the physical mechanism causing this increase in the strength of

the PIA associated with the CT state is not able to be determined with certainty, this observation of a strong CT-associated PIA for **T5** is certainly consistent with lack of population of a  $^3\text{LE}$  in this case (and its negligible rate of RISC).

## 2.5. Low-Temperature Photoluminescence

Finally, we investigated the emission spectra of the compounds at cryogenic temperatures. A comparison of the emission spectrum at room temperature and at 77 K is often used to estimate the singlet-triplet splitting in the CT state of TADF molecules. Also, if the CT triplet could transfer its energy to lower-energy triplet states on the antenna, the phosphorescence from these lower energy triplet states should become observable at low temperature. Comparisons of the room temperature and cryogenic photoluminescence spectra are shown in **Supplementary Figures 9–11**. Consistent with our observations above, in no case is a low-energy phosphorescence (from a triplet on an antenna) observable. The phosphorescence spectra is not significantly altered between the compounds. In conjugation with their similar fluorescence spectra, this indicates that the energetic levels of the CT state on the TADF core are not drastically altered. From the onsets of the fluorescence and phosphorescence spectra at 77 K, we estimate similar values for the singlet-triplet splittings of **T**, **T1**, and **T3**, [ $\Delta E_{\text{ST}}(\text{T}) = 0.02$  eV,  $\Delta E_{\text{ST}}(\text{T1}) = 0.01$  eV, and  $\Delta E_{\text{ST}}(\text{T3}) = 0.02$  eV]. Despite these similar values for  $\Delta E_{\text{ST}}$  across the compounds, the previous sections demonstrate that the rate of RISC differs significantly amongst the series.

## 3. CONCLUSIONS

We have investigated a sequence of molecules composed of a TADF core conjugated to an OPE antenna whose length varies across the sequence. We find that an OPE antenna of appropriate length can bestow strong photon absorption on the molecule in the spectral region wherein previously only the weak CT absorption was present. This increase of the molar extinction coefficient in the visible by a factor of 5 would assist the application of TADF molecules as photonic markers offering background-free delayed emission. However, although we find that energy transfer from the singlet state of the antenna to the CT singlet of the TADF core can be quantitative, we also find that the delayed emission becomes greatly weakened by the attachment of a short OPE antenna, and completely suppressed for longer antennae.

At first thought, the most probable hypothesis for this turn-off of the delayed emission would be Dexter transfer from the CT triplet state of the TADF core to the lower-lying triplet state present on the OPE antenna. Such a quenching mechanism is also thought to play a role in the TADF-assisted fluorescent OLEDs when the fluorescent dopant is present at too high concentrations. Surprisingly, we find that this simple hypothesis is not consistent with the observed data (neither the time-resolved PL nor the TA data). Rather, the data show that a reduction of the rate of RISC occurs upon the addition of the OPE tails, and suggest that this reduction in RISC rate may be due to a change in the position of a  $^3\text{LE}$ . Certainly, the TA of these



blends presents interesting insights into the changing nature of the intermediate species present for a sequence of molecules over which the delayed emission is turned off.

This work suggests that further work to obtain strong delayed emission from TADF core-antenna combinations is not futile but that further work is needed to understand how RISC rates can be maintained upon addition of the antenna. In this regard, a study of more symmetric TADF core dual antenna conjugates may be a fruitful avenue to explore. In general, these results also highlight that careful observation and understanding of Dexter transfer from a TADF molecule to nearby acceptors is an area of continued interest for designing application-optimized TADF materials.

## 4. EXPERIMENTAL

### 4.1. Methods

#### 4.1.1. UV-Vis Absorption

We used a commercial UV-Vis spectrometer (Lambda1050, Perkin Elmer Inc.) to collect the absorption spectra.

#### 4.1.2. Photoluminescence

For the PL measurements (both steady state and time resolved) we used a gated camera setup. As excitation source we used a diode-pumped solid state (DPSS) pulsed laser (Piccolo-10, Innolas GmbH) with 0.8 ns pulses at 355 nm and a repetition rate of 5 kHz. The emission was detected with a spectrograph (Acton SpectraPro-2300, Princeton Instruments Inc.) coupled to an intensified CCD camera (PiMax4, Princeton Instruments Inc.).

#### 4.1.3. Transient Absorption

TA spectra were recorded by using a pump-probe setup. The setup has two modes of operation: a short-delay mode, for delays between pump and probe pulses in the range from 100 fs to 2 ns, and another one to work in long-delay mode, for delays longer than 2 ns. A commercial Ti:Sa amplifier with 100 fs width pulses at 800 nm and operating at a repetition rate of 1 kHz (Spitfire Pro XP, Spectra Physics, Newport Corp.) is split into two beams. The probe beam is directed to a 2 mm thick sapphire crystal to generate white light pulses (450–1,000 nm) and then to the sample. The pump beam passes first through a light chopper that reduces its repetition rate to the half and then through a barium borate (BBO) crystal that generates second harmonics resulting in a 400 nm pulse with a repetition rate of 500 Hz. The pump beam passes then through a delay stage that consists of a stage with a mirror combination that can be precisely driven over 600 mm to increase or decrease the light path of the pump pulse. The so-delayed pump pulse is then directed to the sample. The light transmitted through the sample is then

detected with a spectrograph (Acton SpectraPro-300i, Princeton Instruments Inc.) coupled to an intensified CCD camera (PiMax 512, Princeton Instruments Inc.). Adjacent spectra correspond to the transmission of the sample with and without pump pulse and are used to calculate  $\frac{\Delta I}{I}$ . To work in long-delay mode, the pump pulses are provided by a pulsed DPSS laser (Piccolo-AOT MOPA, Innolas GmbH) with 0.8 ns pulses at 355 nm and a repetition rate of 500 Hz. The delay between pump and white light pulses is controlled by an electronic delay generator (DG535, Stanford Research Systems Inc.).

## DATA AVAILABILITY STATEMENT

All data are provided in the experimental section of the article/**Supplementary Material**. Original data are available upon request from the authors.

## AUTHOR CONTRIBUTIONS

OF performed the steady-state absorption and PL experiments and the time-resolved PL experiments. MJ performed the simulation of the PL transients and the transient absorption experiments. RS synthesized the T-oligomers (T1, T3, and T5) and prepared the samples. FH synthesized the TADF molecule T. DH synthesized the T-oligomers (T1, T3, and T5) and prepared the samples. IH performed the time-resolved PL, the transient absorption experiments, and the simulation of the PL transients. All authors contributed to the discussion and writing of the manuscript.

## FUNDING

OF, RS, FH, DH, SB, MM, UL, and IH would like to acknowledge funding by the German Research Council (DFG) in the context of the SFB 1176 (project A4). SB and UL acknowledge the support by the Cluster of Excellence 3DMM2O (EXC-2082/1-390761711) funded by the German Research Council (DFG).

## ACKNOWLEDGMENTS

OF thanks Andreas Arndt for providing the optical attenuation spectra of the OPEs.

## SUPPLEMENTARY MATERIAL

The Supplementary Material for this article can be found online at: <https://www.frontiersin.org/articles/10.3389/fchem.2020.00126/full#supplementary-material>

## REFERENCES

- DeRosa, C. A., Samonina-Kosicka, J., Fan, Z., Hendargo, H. C., Weitzel, D. H., Palmer, G. M., et al. (2015). Oxygen sensing difluoroboron dinaphthoylethane poly(lactide). *Macromolecules* 48, 2967–2977. doi: 10.1021/acs.macromol.5b00394
- Etherington, M. K., Gibson, J., Higginbotham, H. F., Penfold, T. J., and Monkman, A. P. (2016). Revealing the spin-vibronic coupling mechanism of thermally activated delayed fluorescence. *Nat. Commun.* 7:13680. doi: 10.1038/ncomms13680
- Evans, E. W., Olivier, Y., Puttisong, Y., Myers, W. K., Hele, T. J., Menke, S. M., et al. (2018). Vibrationally assisted intersystem crossing in benchmark thermally

- activated delayed fluorescence molecules. *J. Phys. Chem. Lett.* 9, 4053–4058. doi: 10.1021/acs.jpclett.8b01556
- Hosokai, T., Matsuzaki, H., Nakanotani, H., Tokumaru, K., Tsutsui, T., Furube, A., et al. (2017). Evidence and mechanism of efficient thermally activated delayed fluorescence promoted by delocalized excited states. *Sci. Adv.* 3:e1603282. doi: 10.1126/sciadv.1603282
- Hosokai, T., Noda, H., Nakanotani, H., Nawata, T., Nakayama, Y., Matsuzaki, H., et al. (2018). Solvent-dependent investigation of carbazole benzonitrile derivatives: does the  $^3\text{le}^{-1}\text{ct}$  energy gap facilitate thermally activated delayed fluorescence? *J. Photon. Energy* 8:032102. doi: 10.1117/1.JPE.8.032102
- Hundemer, F., Graf von Reventlow, L., Leonhardt, C., Polamo, M., Nieger, M., Seifermann, S. M., et al. (2020). Acceptor derivatization of the 4czipn tadf system: color tuning and introduction of functional groups. *ChemistryOpen* 8, 1413–1420. doi: 10.1002/open.201900141
- Ishimatsu, R., Matsunami, S., Shizu, K., Adachi, C., Nakano, K., and Imato, T. (2013). Solvent effect on thermally activated delayed fluorescence by 1, 2, 3, 5-tetrakis (carbazol-9-yl)-4, 6-dicyanobenzene. *J. Phys. Chem. A* 117, 5607–5612. doi: 10.1021/jp404120s
- Kochmann, S., Baleizaõ, C., Berberan-Santos, M. N., and Wolfbeis, O. S. (2013). Sensing and imaging of oxygen with parts per billion limits of detection and based on the quenching of the delayed fluorescence of  $^{13}\text{C}_{70}$  fullerene in polymer hosts. *Analyt. Chem.* 85, 1300–1304. doi: 10.1021/ac303486f
- Köhler, A., and Beljonne, D. (2004). The singlet–triplet exchange energy in conjugated polymers. *Adv. Funct. Mater.* 14, 11–18. doi: 10.1002/adfm.200305032
- Köhler, A., Wilson, J. S., Friend, R. H., Al-Suti, M. K., Khan, M. S., Gerhard, A., et al. (2002). The singlet–triplet energy gap in organic and PT-containing phenylene ethynylene polymers and monomers. *J. Chem. Phys.* 116, 9457–9463. doi: 10.1063/1.1473194
- Li, T., Yang, D., Zhai, L., Wang, S., Zhao, B., Fu, N., et al. (2017). Thermally activated delayed fluorescence organic dots (TADF odots) for time-resolved and confocal fluorescence imaging in living cells and *in vivo*. *Adv. Sci.* 4:1600166. doi: 10.1002/advs.201600166
- Li, X., Baryshnikov, G., Deng, C., Bao, X., Wu, B., Zhou, Y., et al. (2019). A three-dimensional ratiometric sensing strategy on unimolecular fluorescence–thermally activated delayed fluorescence dual emission. *Nat. Commun.* 10, 1–9. doi: 10.1038/s41467-019-08684-2
- Maciejewski, A., Szymanski, M., and Steer, R. P. (1986). Thermally activated delayed s1 fluorescence of aromatic thiones. *J. Phys. Chem.* 90, 6314–6318. doi: 10.1021/j100281a051
- Méhes, G., Goushi, K., Potscavage, W. J. Jr., and Adachi, C. (2014). Influence of host matrix on thermally-activated delayed fluorescence: effects on emission lifetime, photoluminescence quantum yield, and device performance. *Organ. Electron.* 15, 2027–2037. doi: 10.1016/j.orgel.2014.05.027
- Méhes, G., Nomura, H., Zhang, Q., Nakagawa, T., and Adachi, C. (2012). Enhanced electroluminescence efficiency in a spiro-acridine derivative through thermally activated delayed fluorescence. *Angew. Chem. Int. Edn.* 51, 11311–11315. doi: 10.1002/anie.201206289
- Ni, F., Zhu, Z., Tong, X., Zeng, W., An, K., Wei, D., et al. (2019). Hydrophilic, red-emitting, and thermally activated delayed fluorescence emitter for time-resolved luminescence imaging by mitochondrion-induced aggregation in living cells. *Adv. Sci.* 6:1801729. doi: 10.1002/advs.201801729
- Nobuyasu, R. S., Ren, Z., Griffiths, G. C., Batsanov, A. S., Data, P., Yan, S., et al. (2016). Rational design of tadf polymers using a donor–acceptor monomer with enhanced TADF efficiency induced by the energy alignment of charge transfer and local triplet excited states. *Adv. Opt. Mater.* 4, 597–607. doi: 10.1002/adom.201500689
- Parker, C., and Hatchard, C. (1961). Triplet-singlet emission in fluid solutions. Phosphorescence of eosin. *Trans. Faraday Soc.* 57, 1894–1904. doi: 10.1039/TF9615701894
- Partee, J., Frankevich, E. L., Uhlhorn, B., Shinar, J., Ding, Y., and Barton, T. J. (1999). Delayed fluorescence and triplet-triplet annihilation in  $\pi$ -conjugated polymers. *Phys. Rev. Lett.* 82, 3673–3676. doi: 10.1103/PhysRevLett.82.3673
- Schneider, R. V., Waibel, K. A., Arndt, A. P., Lang, M., Seim, R., Busko, D., et al. (2018). Sequence-definition in stiff conjugated oligomers. *Sci. Rep.* 8:17483. doi: 10.1038/s41598-018-35933-z
- Steinberger, A., Klimant, I., and Borisov, S. M. (2017). Purely organic dyes with thermally activated delayed fluorescence—a versatile class of indicators for optical temperature sensing. *Adv. Opt. Mater.* 5:1700372. doi: 10.1002/adom.201700372
- Tonge, C. M., Paisley, N. R., Polgar, A. M., Lix, K., Algar, W. R., and Hudson, Z. M. (2020). Color-tunable thermally activated delayed fluorescence in oxadiazole-based acrylic copolymers: photophysical properties and applications in ratiometric oxygen sensing. *ACS Appl. Mater. Interfaces* 12, 6525–6535. doi: 10.1021/acsami.9b22464
- Tsujii, Y., Tsuchida, A., Onogi, Y., and Yamamoto, M. (1990). Stabilization of carbazole radical cation formed in poly(n-vinylcarbazole) by charge delocalization. *Macromolecules* 23, 4019–4023. doi: 10.1021/ma00219a023
- Uoyama, H., Goushi, K., Shizu, K., Nomura, H., and Adachi, C. (2012). Highly efficient organic light-emitting diodes from delayed fluorescence. *Nature* 492, 234–238. doi: 10.1038/nature11687
- Wong, M. Y., Krotkus, S., Copley, G., Li, W., Murawski, C., Hall, D., et al. (2018). Deep-blue oxadiazole-containing thermally activated delayed fluorescence emitters for organic light-emitting diodes. *ACS Appl. Mater. Interfaces* 10, 33360–33372. doi: 10.1021/acsami.8b11136
- Xiong, X., Song, F., Wang, J., Zhang, Y., Xue, Y., Sun, L., et al. (2014). Thermally activated delayed fluorescence of fluorescein derivative for time-resolved and confocal fluorescence imaging. *J. Am. Chem. Soc.* 136, 9590–9597. doi: 10.1021/ja502292p
- Yamamoto, M., Tsujii, Y., and Tsuchida, A. (1989). Near-infrared charge resonance band of intramolecular carbazole dimer radical cations studied by nanosecond laser photolysis. *Chem. Phys. Lett.* 154, 559–562. doi: 10.1016/0009-2614(89)87152-0
- Yurash, B., Nakanotani, H., Olivier, Y., Beljonne, D., Adachi, C., and Nguyen, T.-Q. (2019). Photoluminescence quenching probes spin conversion and exciton dynamics in thermally activated delayed fluorescence materials. *Adv. Mater.* 31:1804490. doi: 10.1002/adma.201804490
- Zhang, J., Chen, W., Chen, R., Liu, X.-K., Xiong, Y., Kershaw, S. V., et al. (2016). Organic nanostructures of thermally activated delayed fluorescent emitters with enhanced intersystem crossing as novel metal-free photosensitizers. *Chem. Commun.* 52, 11744–11747. doi: 10.1039/C6CC05130H
- Zhang, J., Fang, F., Liu, B., Tan, J.-H., Chen, W.-C., Zhu, Z., et al. (2019a). Intrinsically cancer-mitochondria-targeted thermally activated delayed fluorescence nanoparticles for two-photon activated fluorescence imaging and photodynamic therapy. *ACS Appl. Mater. Interfaces* 11, 41051–41061. doi: 10.1021/acsami.9b14552
- Zhang, Q., Xu, S., Li, M., Wang, Y., Zhang, N., Guan, Y., et al. (2019b). Rationally designed organelle-specific thermally activated delayed fluorescence small molecule organic probes for time-resolved biological applications. *Chem. Commun.* 55, 5639–5642. doi: 10.1039/C9CC00898E
- Zhu, Z., Tian, D., Gao, P., Wang, K., Li, Y., Shu, X., et al. (2018). Cell-penetrating peptides transport noncovalently linked thermally activated delayed fluorescence nanoparticles for time-resolved luminescence imaging. *J. Am. Chem. Soc.* 140, 17484–17491. doi: 10.1021/jacs.8b08438

**Conflict of Interest:** The authors declare that the research was conducted in the absence of any commercial or financial relationships that could be construed as a potential conflict of interest.

Copyright © 2020 Franco, Jakoby, Schneider, Hundemer, Hahn, Richards, Bräse, Meier, Lemmer and Howard. This is an open-access article distributed under the terms of the Creative Commons Attribution License (CC BY). The use, distribution or reproduction in other forums is permitted, provided the original author(s) and the copyright owner(s) are credited and that the original publication in this journal is cited, in accordance with accepted academic practice. No use, distribution or reproduction is permitted which does not comply with these terms.



# Asymmetric Thermally Activated Delayed Fluorescence Materials With Aggregation-Induced Emission for High-Efficiency Organic Light-Emitting Diodes

Huanhuan Li<sup>1†</sup>, Yibin Zhi<sup>1†</sup>, Yizhong Dai<sup>1</sup>, Yunbo Jiang<sup>1</sup>, Qingqing Yang<sup>1</sup>, Mingguang Li<sup>1</sup>, Ping Li<sup>1</sup>, Ye Tao<sup>1\*</sup>, Hui Li<sup>1</sup>, Wei Huang<sup>1,2</sup> and Runfeng Chen<sup>1\*</sup>

<sup>1</sup> Key Laboratory for Organic Electronics and Information Displays & Jiangsu Key Laboratory for Biosensors, Jiangsu National Synergetic Innovation Center for Advanced Materials (SICAM), Institute of Advanced Materials (IAM), Nanjing University of Posts and Telecommunications, Nanjing, China, <sup>2</sup> Institute of Flexible Electronics, Northwestern Polytechnical University, Xi'an, China

## OPEN ACCESS

### Edited by:

Guohua Xie,  
Wuhan University, China

### Reviewed by:

Kai Wang,  
Soochow University, China  
Shiyang Shao,  
Changchun Institute of Applied  
Chemistry (CAS), China

### \*Correspondence:

Ye Tao  
iamytao@njupt.edu.cn  
Runfeng Chen  
iamrfchen@njupt.edu.cn

<sup>†</sup>These authors have contributed  
equally to this work

### Specialty section:

This article was submitted to  
Organic Chemistry,  
a section of the journal  
Frontiers in Chemistry

Received: 13 December 2019

Accepted: 15 January 2020

Published: 26 February 2020

### Citation:

Li H, Zhi Y, Dai Y, Jiang Y, Yang Q,  
Li M, Li P, Tao Y, Li H, Huang W and  
Chen R (2020) Asymmetric Thermally  
Activated Delayed Fluorescence  
Materials With Aggregation-Induced  
Emission for High-Efficiency Organic  
Light-Emitting Diodes.  
Front. Chem. 8:49.  
doi: 10.3389/fchem.2020.00049

The exploitation of thermally activated delayed fluorescence (TADF) emitters with aggregation-induced emission is highly prerequisite for the construction of highly efficient electroluminescent devices in materials science. Herein, two asymmetric TADF emitters of **SFCOCz** and **SFCODPAC** with charming aggregation-induced emission are expediently designed and prepared based on highly twisted strong electron-withdrawing acceptor (A) of sulfurafluorene (**SF**)-modified ketone (**CO**) and arylamine donor (D) in D<sub>1</sub>–A–D<sub>2</sub> architecture by simple synthetic procedure in high yields. High photoluminescence quantum yields up to 73% and small singlet–triplet splitting of 0.03 eV; short exciton lifetimes are obtained in the resultant molecules. Strikingly, efficient non-doped and doped TADF organic light-emitting diodes (OLEDs) facilitated by these emitters show high luminance of 5,598 and 11,595 cd m<sup>−2</sup>, current efficiencies (CEs) of 16.8 and 35.6 cd/A, power efficiencies (PEs) of 9.1 and 29.8 lm/W, and external quantum efficiencies (EQEs) of 7.5 and 15.9%, respectively. This work furnishes a concrete instance in exploring efficient TADF emitter, which is highly conducive and encouraging in stimulating the development of TADF OLEDs with high brightness and excellent efficiencies simultaneously.

**Keywords:** thermally activated delayed fluorescence, asymmetric structure, aggregation-induced emission, charge-transfer, electroluminescence

## INTRODUCTION

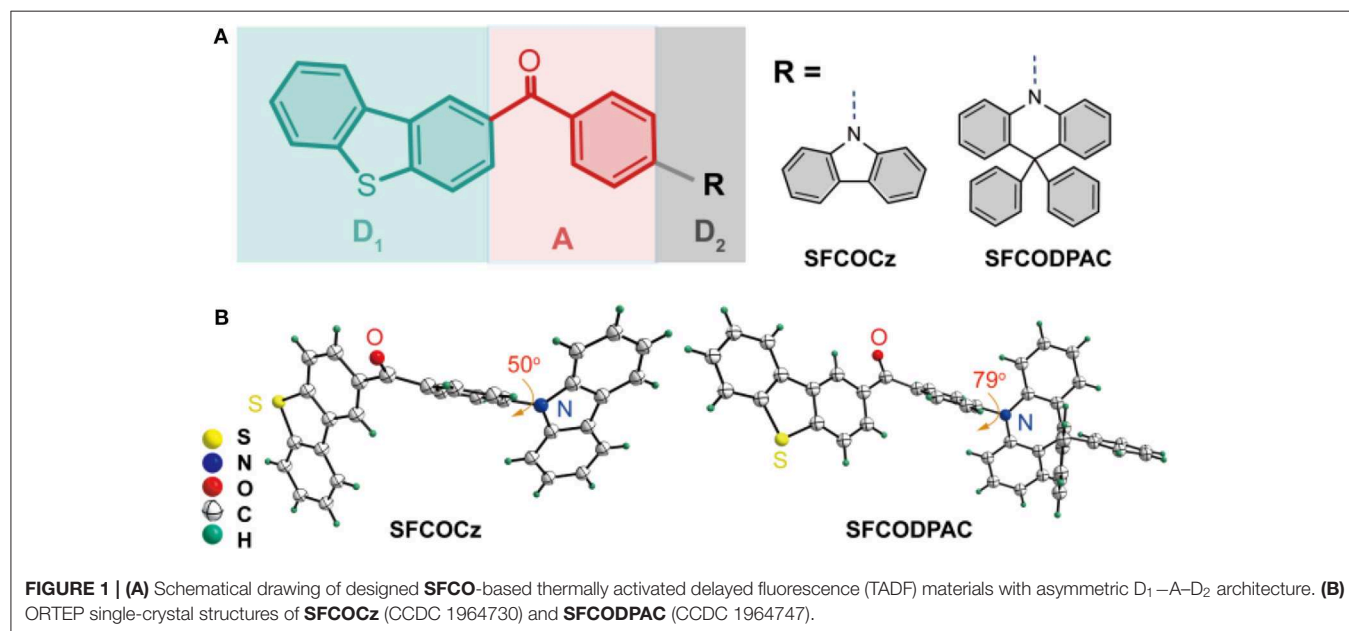
Luminescent materials that are capable of thermally activated delayed fluorescent (TADF) have been widely investigated not only because of their great potential in utilizing theoretically 100% internal quantum efficiency (IQE) through the back transfer of non-radiative triplet exactions (75%) into radiative singlet excitons conferred by small single–triplet energy splitting ( $\Delta E_{ST}$ ) for efficient reverse intersystem crossing (RISC), but also due to their fundamental significance both in scientific investigations and technological applications of organic electronics

(Uoyama et al., 2012; Tao et al., 2014; Etherington et al., 2016; Guo et al., 2018; Han et al., 2018; Kotadiya et al., 2019; Pershin et al., 2019; Zhang Y. L. et al., 2019). With flourish developments over the past few years, considerable attention has been devoted to designing and exploiting excellent TADF materials with the consideration of the following rational metrics (Park et al., 2016; Chen et al., 2017; Im et al., 2017; Wong and Zysman-Colman, 2017; Yang Z. et al., 2017; Zhang Y. et al., 2019): (i) the separated highest occupied molecular orbital (HOMO) and lowest unoccupied molecular orbital (LUMO) distributions for enabling small  $\Delta E_{ST}$ ; (ii) slight overlap of frontier molecular orbital (FMO) for maintaining high photoluminescence quantum yield (PLQY); (iii) short exciton lifetimes to eliminate the concentration-induced quenching effect; (iv) reduced intermolecular interactions to alleviate aggregation quenching processes; and (v) acceptable thermal stability for long-term device operation and ease synthesis procedure for mass productions. Nonetheless, most of the reported TADF materials suffer from serious aggregation caused quenching (ACQ) phenomenon that obviously hinders their practical applications (Einzinger et al., 2017; Wei et al., 2017, 2019; Wong and Zysman-Colman, 2017; Gan et al., 2019). Therefore, it remains forbidden issues to construct prominent TADF materials because of the great challenge in obtaining such aforementioned features in a molecule simultaneously, especially for alleviating the serious ACQ (Aydemir et al., 2017).

Aggregation-induced emission (AIE) is a fascinating optical phenomenon with greatly enhanced luminescent efficiency in solid state, which has been increasingly emerging as a promising candidate in organic electronics, bio-electronics, and photonics (Huang et al., 2017; Mao et al., 2017; Tsujimoto et al., 2017; Yang J. et al., 2017; Chen et al., 2019). The implantation of AIE properties into TADF materials has demonstrated a possibility to suppress the ACQ of solid films (Lee et al., 2017; Zheng et al., 2019).

Generally, the linkage of donor and acceptor units through the spiro- and/or twist structure to lessen the overlap of FMO and to inhibit the molecular aggregation has been proven to be a perspective strategy for achieving AIE-TADF materials. Following this guideline, an extensive collection of AIE-TADF materials has been designed and explored in fabricating efficient TADF organic light-emitting diodes (OLEDs). Recently, diphenyl ketone, which can not only serve as an electron-deficient core to construct charge transfer (CT) molecule with spatially separated HOMO and LUMO distributions through the incorporation of varieties of donor units for achieving a small  $\Delta E_{ST}$  but can also be used as the twist and rotation center to reduce the interactions for alleviating the self-quenching effect of multiple molecules and to incorporate AIE for boosting emission of the resultant materials in solid state, has been regarded as one of the most key building blocks in constructing TADF materials with the AIE character (Guo et al., 2017; Huang et al., 2017). These impressive advantages have stimulated us to explore new diphenyl ketone-based TADF derivatives for fabricating high-performance OLEDs.

Herein, to achieve the AIE-TADF materials, we designed and synthesized two emitters of **SFCOCz** and **SFCODPAC** with asymmetric  $D_1$ –A– $D_2$  architecture (**Figure 1A**) through the direct linkage of sulfurafluorene (SF)-modified ketone (CO) and arylamine of carbazole (Cz) or 9,9-diphenyl-9,10-dihydroacridine (DPAC). In this moiety, the  $D_1$ –A– $D_2$  can effectively render separated HOMO and LUMO distributions to guarantee a small  $\Delta E_{ST}$  for the promotion of RISC process under thermal activation; moreover, the twisted and asymmetric molecular configuration can endow AIE and restrain intermolecular interaction of  $\pi$ – $\pi$  stacking and/or aggregation to reduce ACQ in solid state (Aydemir et al., 2017; Wang et al., 2017; Zeng et al., 2018; Liu et al., 2019). These newly constructed AIE-TADF materials in  $D_1$ –A– $D_2$  skeleton can be easily prepared





with high yields up to 68%. Strikingly, **SFCOCz** and **SFCODPAC** exhibited excellent TADF with small  $\Delta E_{ST}$  of  $\sim 0.03$  eV, high PLQY ( $\Phi_{PL}$ ) of  $\sim 73\%$ , and efficient RISC rate and relatively short delayed fluorescence lifetime. High-performance non-doped and doped TADF OLEDs endowed by these emitters were fabricated, showing high luminance of 5,598 and 11,595  $\text{cd m}^{-2}$  and external quantum efficiencies (EQEs) of 7.5 and 15.9%, respectively. The ease of synthetic route, excellent optoelectronics, and high device performance make the **SFCO**-based asymmetric TADF emitters promising candidates in practical applications, conferring a new paradigm for next-generation organoelectronics.

## RESULTS AND DISCUSSION

### Design, Synthesis, and Characterization

To prepare the asymmetric TADF materials exhibiting AIE trait, two molecules, namely (4-(9*H*-carbazol-9-yl)phenyl)(dibenzo[*b,d*]thiophen-2-yl)methanone (**SFCOCz**) and dibenzo[*b,d*]thiophen-2-yl(4-(9,9-diphenylacridin-10(9*H*)-yl)phenyl)methanone (**SFCODPAC**), were designed and synthesized in  $D_1$ -A- $D_2$  architecture through the direct connection of sulfurafluorene-tailored diphenyl ketone and donor of Cz (**SFCOCz**) or DPAC (**SFCODPAC**) by a conventional two-step procedure composed of Friedel-Crafts acylation and C-N coupling reaction (Figure 1A and Scheme S1, Figures S1–S4). As revealed by single-crystal X-ray diffraction (XRD) analysis, the dihedral angle between arylamine and **SFCO** in these two molecules is up to  $79^\circ$  (Figure 1B and Table S1). Such a highly twisted molecular conformation would not only

be beneficial to reduce electron communications, ensuring an optimized HOMO and LUMO separation for acquiring a small  $\Delta E_{ST}$ , but can also effectively suppress the molecular aggregations in solid state for eliminating ACQ (Wang et al., 2017). **SFCOCz** and **SFCODPAC** display high thermal stabilities (Figure S5), exposing the decomposition temperatures ( $T_d$ ) of 386 and  $429^\circ\text{C}$  as revealed by the thermogravimetric (TGA) measurements and melting temperature ( $T_m$ ) of 197 and  $251^\circ\text{C}$  as measured by differential scanning calorimetry (DSC) analyses. The slightly higher  $T_d$  and  $T_m$  of **SFCODPAC** than those of **SFCOCz** could be well-explained by its high molecular weight and rigid structure. In addition, the vacuum-evaporated thin films on glass substrates are amorphous and uniform with quite small root-mean-square roughness (RMS) of 0.307 and 0.173 nm for (Figure S6) **SFCOCz** and **SFCODPAC**. The excellent thermal and morphology stabilities of resultant AIE-TADF materials would be favored for vacuum-deposited device fabrication and long-term operation stability.

### Photophysical Properties

The photophysical profiles of asymmetric TADF molecules **SFCOCz** and **SFCODPAC** in dilute dichloromethane solution ( $\text{CH}_2\text{Cl}_2$ ,  $1 \times 10^{-5}$  mol  $\text{L}^{-1}$ ) and neat and doped films (Figure 2 and Figures S7–S11) were detailedly investigated by UV-visible absorption and photoluminescence (PL) spectra. **SFCOCz** and **SFCODPAC** imply that the  $n-\pi^*$  transition dominated absorption band peaked  $\sim 300$  nm, and the CT band at  $\sim 350$  nm originated from intramolecular CT (ICT) from arylamine to CO (Table 1 and Table S2) (Lee et al., 2017). The PL

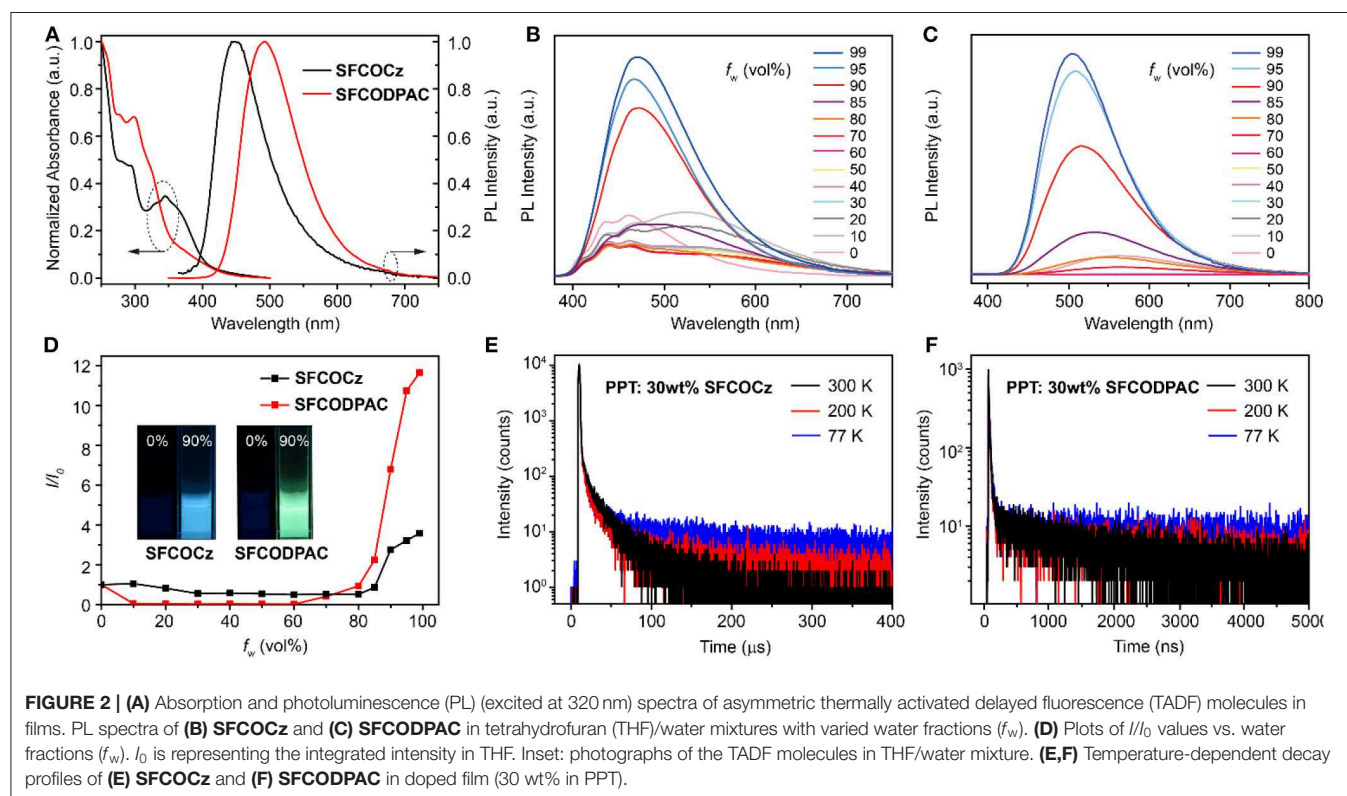


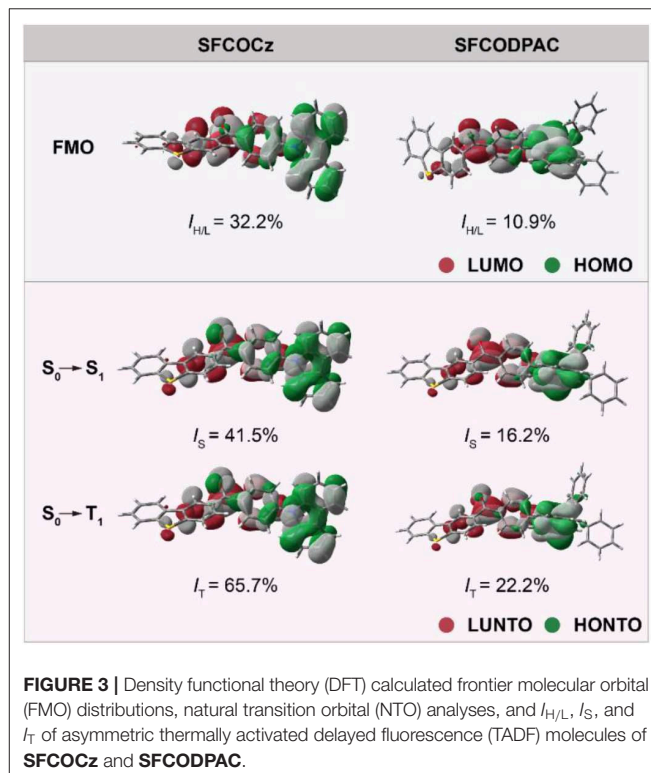


**TABLE 1** | Optical, thermal, and electrical properties of **SFCOCz** and **SFCODPAC**.

Compound	$T_m/T_d$ (°C)	$\lambda_{\text{abs}}$ (nm)		opt $E_g$ (eV)	$\lambda_{\text{em}}$ (nm)		CV (eV)
		CH <sub>2</sub> Cl <sub>2</sub>	Film		CH <sub>2</sub> Cl <sub>2</sub>	Film	
SFCOCz	197/386	273, 293, 328, 342	283, 295, 331, 346	3.04	484	449	−5.70/−2.66
SFCODPAC	251/429	273, 295, 315, 360	276, 297, 322, 359	2.88	558	492	−5.52/−2.64

spectra of **SFCOCz** and **SFCODPAC** exhibit typical structureless ICT fluorescence bands located at 484 and 558 nm in CH<sub>2</sub>Cl<sub>2</sub>, respectively. The ICT characters were also demonstrated by the red-shifted emission bands with the increasing in solvent polarities (**Figure S8**). In film states, these two molecules reveal nearly the same absorption profiles to those of the solution, showing absorption peaks at 295 and 346 nm for **SFCOCz** and 297 and 359 nm for **SFCODPAC**. These findings verify the effective suppressing of molecule aggregation in the films. The optical bandgaps ( $^{\text{opt}}E_g$ s), calculated by the onset edge of the absorption spectra, were 3.04 and 2.88 eV for **SFCOCz** and **SFCODPAC**, respectively. For the PL spectra, **SFCOCz** and **SFCODPAC** also show structureless ICT bands at ~450 and 492 nm with corresponding  $\Phi_{\text{PL}}$  of ~22 and 73%, respectively. Notably, the  $\Phi_{\text{PL}}$ s of **SFCOCz** and **SFCODPAC** in the solid state are up to ~3.7-fold that in the solution, indicating the obvious AIE characteristics. To further demonstrate the AIE properties of these two TADF molecules, the PL spectra in tetrahydrofuran (THF) with varied water fractions ( $f_w$ ) were performed. **SFCOCz** and **SFCODPAC** exhibit intense emissions as the formation of nanoaggregates upon injecting a large amount of poor solvent of H<sub>2</sub>O (fraction >80%) into THF solutions (**Figures 2B–D**), suggesting again the AIE features. This significantly enhanced photoluminescence in nanoaggregates should be due to the suppressed molecule rotation and motion that are highly active in the solution, thus blocking the non-radiative decay of excitons. In addition, we also explore the PL properties of **SFCOCz** (30 wt%) and **SFCODPAC** (30 wt%) doped films using 2,8-bis(diphenylphosphoryl)-dibenzo[b,d]thiophene (PPT) as the host material (**Figure S9**). Because of the strong polarity of PPT, the doped films showcase the red-shifted emission peaks with lower  $\Phi_{\text{PL}}$  compared to their corresponding neat films (Méhes et al., 2014).

To demonstrate their TADF properties, a set of experiments was carried out. We attempted to estimate the  $\Delta E_{\text{ST}}$  of **SFCOCz** and **SFCODPAC** on the basis of the fluorescence spectra and phosphorescence spectra at 77 K. As shown in **Figure S10**, the  $\Delta E_{\text{ST}}$ s of **SFCOCz** and **SFCODPAC** in neat and (30 wt%) doped films were 0.17 and 0.03 eV in the neat films, and 0.21 and 0.02 eV in the doped films, respectively, potentially enabling the process of RISC by thermal activation. The transient photoluminescence profiles were also performed to understand the photophysical process of **SFCOCz** and **SFCODPAC** (**Figures 2D,E** and **Figure S11**). The double exponential lifetime decay curve was observed in both of **SFCOCz** and **SFCODPAC** in neat and doped films, showing a short nanosecond lifetime of prompt fluorescence ( $\tau_{\text{PF}}$ ) and a microsecond lifetime ( $\tau_{\text{DF}}$ ) of delayed emission (**Table S2**). Contributed by the small  $\Delta E_{\text{ST}}$ ,  $\tau_{\text{DF}}$  of **SFCODPAC** were 0.22 and 0.84  $\mu\text{s}$  in the neat and doped films, respectively, which is 1,513- and 24-fold smaller than those of



**SFCOCz**. The temperature-dependent lifetime measurements of the doped films further present efficient proof of the TADF characteristics of these two materials. The delayed component afforded by the RISC was increased gradually, with the temperature increasing from 77 to 300 K (**Figures 2E,F**), obviously indicating the TADF trait. By means of the PLQY and lifetime, the calculated rate of RISC (**Supplementary Material**) are  $0.1 \times 10^5$  and  $6.16 \times 10^6 \text{ s}^{-1}$  in neat films, and  $1.3 \times 10^5$  and  $2.16 \times 10^6 \text{ s}^{-1}$  in doped films for **SFCOCz** and **SFCODPAC**, respectively. The greatly improved RISC of **SFCODPAC** could be attributed to its smaller  $\Delta E_{\text{ST}}$ .

## Theoretical and Electrochemical Investigations

As shown in **Figure 3**, the spatial distributions of HOMOs and LUMOs of **SFCOCz** and **SFCODPAC** were clearly observed (Leitl et al., 2014). The HOMOs are largely located on the electron-donating (D<sub>2</sub>) unit of **Cz** for **SFCOCz** and **DPAC** for **SFCODPAC**, while the LUMOs are mainly concentrated on **CO** and slightly located on the **SF** unit, showing an overlap extent ( $I_{\text{H/L}}$ ) of 32.2 and 10.9%, respectively (Chen et al., 2015). The discrete HOMOs and LUMOs distribution in the asymmetric

$D_1-A-D_2$  materials would be favorable for realizing small  $\Delta E_{ST}$ . The simulated  $\Delta E_{ST}$ s were 0.38 and 0.01 eV for **SFCOCz** and **SFCODPAC** in the monomeric state. The decreased  $\Delta E_{ST}$  of **SFCODPAC** may be originated from the combined effect of the strong electron-donating ability of **DPAC** and large dihedral angle between **CO** and **DPAC** for more separated FMO distributions. The FMO energy levels of these two molecules were analyzed by the cyclic voltammetric (CV) curves. According to the oxidation onset at 0.94 and 0.76 V, the HOMOs were evaluated to be  $-5.70$  and  $-5.52$  eV for **SFCOCz** and **SFCODPAC**, respectively. By means of optical bandgaps and HOMOs, the LUMOs were speculated to be  $-2.66$  and  $-2.64$  eV. To reveal the electron transition components of excited states in **SFCOCz** and **SFCODPAC**, the natural transition orbital (NTO) analyses were also carried out (Li et al., 2018). The highest occupied NTO (HONTO) and the lowest unoccupied NTO (LUNTO) distributions of **SFCOCz** and **SFCODPAC** at excited states are almost identical to their corresponding ground-state FMOs. The HONTOs of these two molecules were primarily dominated by the donor moiety; the LUNTO were largely assigned on the **CO** core with slight extension on the **SF** unit. The overlap extent of HONTO and LUNTO is 41.5 and 16.2% on singlet state ( $I_s$ ), and 65.7 and 22.2% on triplet state ( $I_T$ ) for **SFCOCz** and **SFCODPAC**, respectively. The overlap at the

excited state should play an important role in guaranteeing high PLQY.

## Electroluminescent Performance of OLEDs

To further elucidate the feasibility of asymmetric  $D_1-A-D_2$  molecules in constructing high-performance thermal-evaporated devices, the non-doped (TA-TB) and doped (TC-TD) TADF OLED of **SFCOCz** (TA, TC) and **SFCODPAC** (TB, TD) were successfully fabricated using the following configurations (**Figure 4A**): ITO/MoO<sub>3</sub> (30 nm)/4,4'-bis[*N*-(1-naphthyl)-*N*-phenylamino]-1,1'-biphenyl (NPB) (50 nm)/1,3-bis(carbazol-9-yl)benzene (*m*CP) (5 nm)/EML (20 nm)/PPT (5 nm)/bathophenanthroline (BPhen) (5 nm)/LiF (1 nm)/Al (100 nm). In these devices, NPB and BPhen were hole- and electron-transporting layers, and *m*CP and PPT were exciton-blocking layers. TA-TD exhibited pure electroluminescence (EL) spectra inherited from their neat and doped films at different driving voltages, showing maximum emission peaks at 451, 482, 468, and 485 nm with corresponding Commission International de l'Eclairage (CIE) coordinates of (0.16, 0.11), (0.20, 0.37), (0.15, 0.18), and (0.19, 0.37), respectively (**Table S3**). Compared to **SFCOCz**-based TA and TC, **SFCODPAC**-endowed TADF OLEDs of TB and TD revealed slightly decreased driving voltages ( $V_{on}$ s) of 4.4 and 3.8 V, respectively. In addition to the decreased  $V_{on}$ , TB and TD also

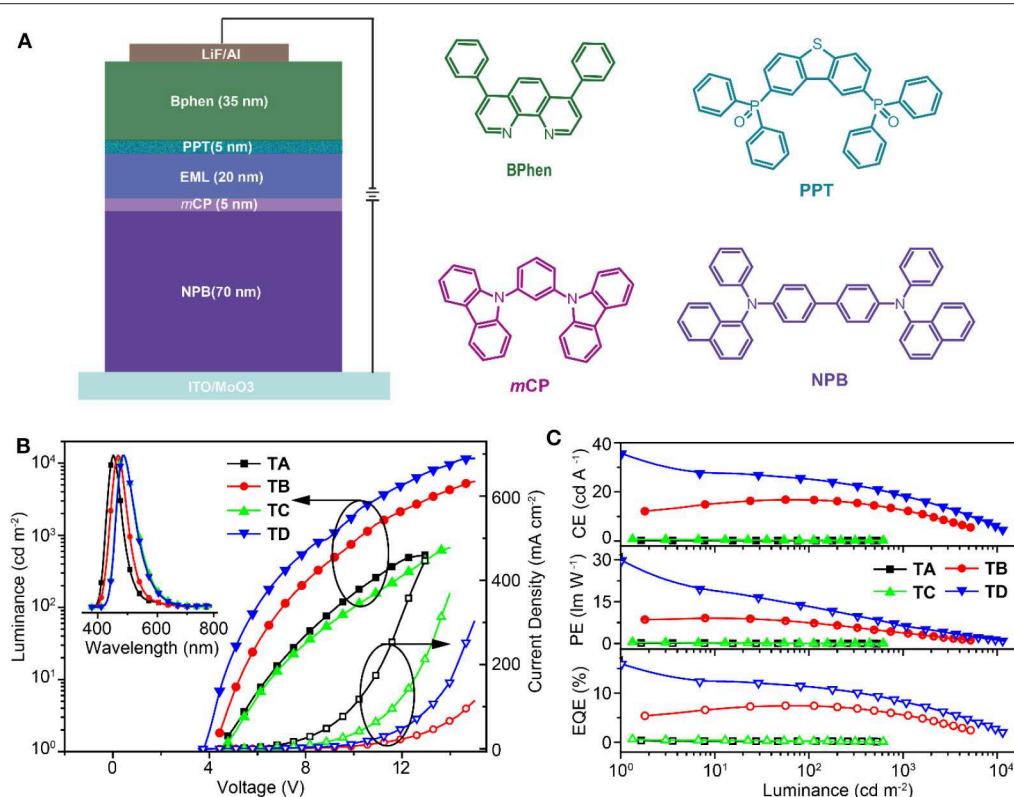


**FIGURE 4 | (A)** Device configuration and chemical structures of the adopted materials, **(B)** luminance (solid symbols)–current density (open symbols)–voltage inset: electroluminescence (EL) spectra of thermally activated delayed fluorescence organic light-emitting diodes (TADF OLEDs) at 6.0 V, and **(C)** efficiencies–luminance curves of the non-doped and doped TADF OLEDs.

demonstrated improved luminance up to 5,598 and 11,595  $\text{cd m}^{-2}$  than those of TA and TC. The low  $V_{\text{ons}}$  and high luminance of TB and TD should be attributed to its high HOMO and PLQYs of **SFCODPAC** for the promotion of hole injection from the adjacent layer and the generation of excitons. Not surprisingly, TADF OLEDs based on **SFCODPAC** show much better device efficiencies with current efficiencies (CEs) of 16.8 and 35.6  $\text{cd/A}$ , power efficiencies (PEs) of 9.1 and 29.8  $\text{lm/W}$ , and EQEs of 7.5 and 15.9% for TB and TD, respectively (Figures 4B,C and Table S3). These values are comparable to the best results of non-doped and doped TADF OLEDs based on AIE-type TADF emitters (Table S4). In addition, TD displays acceptable device performance with 29.1 and 21.0  $\text{cd A}^{-1}$  for CE, 11.8 and 5.6  $\text{lm W}^{-1}$  for PE, and 13.1 and 9.4% for EQE at 100 and 1,000  $\text{cd m}^{-2}$ , respectively. Although the non-doped films suggest enhanced PLQYs, the poor charge transport properties in neat films induced by highly twisted asymmetric molecular skeleton should be responsible for the decreased device performance of non-doped TADF OLEDs.

## CONCLUSIONS

In summary, we have succeeded in designing and developing two asymmetric TADF molecules of **SFCOCz** and **SFCODPAC** in the  $D_1-A-D_2$  skeleton through a simple and effective procedure in high yields. The resultant TADF molecules exhibit small  $\Delta E_{\text{ST}}$ , short delayed lifetimes, and robust AIE characteristics with high PLQY up to 73%. More impressively, benefiting from the excellent optoelectronic properties, the non-doped and doped TADF OLEDs conferred by **SFCODPAC** display high efficiencies with peak EQEs of 7.5 and 15.9%, accompanied with the CIE coordinates of (0.20, 0.37) and (0.19, 0.37), respectively. Our work here provides a delicate molecular design strategy for the construction of asymmetric AIE-type TADF emitters, and clearly

manifests the significant advance of the combined TADF and AIE features in exploiting high-performance organic emitters.

## DATA AVAILABILITY STATEMENT

The datasets generated for this study can be found in the Cambridge Structural Database under the following identifiers: CCDC/1964730, CCDC/1964747.

## AUTHOR CONTRIBUTIONS

HuaL, YZ, YT, WH, and RC conceived the experiment. HuaL, YZ, YJ, and HuiL performed the characterizations of optoelectronic properties. YD, YT, and ML designed and fabricated the devices. QY and PL contributed the theoretical simulations. HuaL, YZ, YJ, and YT wrote the manuscript. All authors contributed to the scientific discussion.

## FUNDING

This work was financially supported in part by the National Natural Science Foundation of China (21604039, 21704042, 61875090, 91833306, and 51873159), the Six Talent Plan of Jiangsu Province (XCL-049), 1311 Talents Program of Nanjing University of Posts and Telecommunications (Dingshan), China Postdoctoral Science Foundation project (2018M642284), and Nanjing University of Posts and Telecommunications Start-up Fund (NUPTSF) (NY219007 and NY217140).

## SUPPLEMENTARY MATERIAL

The Supplementary Material for this article can be found online at: <https://www.frontiersin.org/articles/10.3389/fchem.2020.00049/full#supplementary-material>

## REFERENCES

- Aydemir, M., Xu, S., Chen, C., Bryce, M. R., Chi, Z., and Monkman, A. P. (2017). Photophysics of an asymmetric donor-acceptor-donor TADF molecule and reinterpretation of aggregation-induced TADF emission in these materials. *J. Phys. Chem. C* 121, 17764–17772. doi: 10.1021/acs.jpcc.7b06299
- Chen, F., Hu, J., Wang, X., Shao, S., Wang, L., and Jing, X. (2019). Synthesis and electroluminescent properties of through-space charge transfer polymers containing acridan donor and triarylboron acceptors. *Front. Chem.* 7:854. doi: 10.3389/fchem.2019.00854
- Chen, T., Zheng, L., Yuan, J., An, Z., Chen, R., and Tao, Y. (2015). Understanding the control of singlet-triplet splitting for organic exciton manipulating: a combined theoretical and experimental approach. *Sci. Rep.* 5:10923. doi: 10.1038/srep10923
- Chen, X. K., Tsuchiya, Y., Ishikawa, Y., Zhong, C., Adachi, C., and Brédas, J. L. (2017). A new design strategy for efficient thermally activated delayed fluorescence organic emitters: from twisted to planar structures. *Adv. Mater.* 29:1702767. doi: 10.1002/adma.201702767
- Einzinger, M., Zhu, T., de Silva, P., Belger, C., Swager, T. M., Van Voorhis, T., et al. (2017). Shorter exciton lifetimes via an external heavy-atom effect: alleviating the effects of bimolecular processes in organic light-emitting diodes. *Adv. Mater.* 29:1701987. doi: 10.1002/adma.201701987
- Etherington, M. K., Gibson, J., Higginbotham, H. F., Penfold, T. J., and Monkman, A. P. (2016). Revealing the spin-vibronic coupling mechanism of thermally activated delayed fluorescence. *Nat. Commun.* 7:13680. doi: 10.1038/ncomms13680
- Gan, L., Xu, Z., Wang, Z., Li, B., Li, W., Cai, X., et al. (2019). Utilizing a spiro TADF moiety as a functional electron donor in TADF molecular design toward efficient “multichannel” reverse intersystem crossing. *Adv. Funct. Mater.* 29:1808088. doi: 10.1002/adfm.201808088
- Guo, J., Li, X., Nie, H., Luo, W., Gan, S., Hu, S., et al. (2017). Achieving high-performance nondoped OLEDs with extremely small efficiency roll-off by combining aggregation-induced emission and thermally activated delayed fluorescence. *Adv. Funct. Mater.* 27:1606458. doi: 10.1002/adfm.201606458
- Guo, J., Zhao, Z., and Tang, B. Z. (2018). Purely organic materials with aggregation-induced delayed fluorescence for efficient nondoped OLEDs. *Adv. Opt. Mater.* 6:1800264. doi: 10.1002/adom.201800264
- Han, C., Zhang, Z., Ding, D., and Xu, H. (2018). Dipole-dipole interaction management for efficient blue thermally activated delayed fluorescence diodes. *Chem* 4, 2154–2167. doi: 10.1016/j.chempr.2018.06.005
- Huang, J., Nie, H., Zeng, J., Zhuang, Z., Gan, S., Cai, Y., et al. (2017). Highly efficient nondoped OLEDs with negligible efficiency roll-off fabricated from aggregation-induced delayed fluorescence luminogens. *Angew. Chem. Int. Ed.* 56, 12971–12976. doi: 10.1002/anie.201706752
- Im, Y., Kim, M., Cho, Y. J., Seo, J., Yook, K. S., and Lee, J. Y. (2017). Molecular design strategy of organic thermally activated delayed fluorescence emitters. *Chem. Mater.* 29, 1946–1963. doi: 10.1021/acs.chemmater.6b05324

- Kotadiya, N. B., Blom, P. W. M., and Wetzelaer, G. A. H. (2019). Efficient and stable single-layer organic light-emitting diodes based on thermally activated delayed fluorescence. *Nat. Photon.* 13, 765–769. doi: 10.1038/s41566-019-0488-1
- Lee, J., Aizawa, N., Numata, M., Adachi, C., and Yasuda, T. (2017). Versatile molecular functionalization for inhibiting concentration quenching of thermally activated delayed fluorescence. *Adv. Mater.* 29:1604856. doi: 10.1002/adma.201604856
- Leitl, M. J., Krylova, V. A., Djurovich, P. I., Thompson, M. E., and Yersin, H. (2014). Phosphorescence versus thermally activated delayed fluorescence controlling singlet–triplet splitting in brightly emitting and sublimable Cu(I) compounds. *J. Am. Chem. Soc.* 136, 16032–16038. doi: 10.1021/ja508155x
- Li, C., Duan, C., Han, C., and Xu, H. (2018). Secondary acceptor optimization for full-exciton radiation: toward sky-blue thermally activated delayed fluorescence diodes with external quantum efficiency of ~30%. *Adv. Mater.* 30:1804228. doi: 10.1002/adma.201804228
- Liu, J., Zhou, K., Wang, D., Deng, C., Duan, K., Ai, Q., et al. (2019). Pyrazine-based blue thermally activated delayed fluorescence materials: combine small singlet–triplet splitting with large fluorescence rate. *Front. Chem.* 7:312. doi: 10.3389/fchem.2019.00312
- Mao, D., Wu, W., Ji, S., Chen, C., Hu, F., Kong, D., et al. (2017). Chemiluminescence-guided cancer therapy using a chemiexcited photosensitizer. *Chem* 3, 991–1007. doi: 10.1016/j.chempr.2017.10.002
- Méhes, G., Goushi, K., Potscavage, W. J., and Adachi, C. (2014). Influence of host matrix on thermally-activated delayed fluorescence: effects on emission lifetime, photoluminescence quantum yield, and device performance. *Org. Electron.* 15, 2027–2037. doi: 10.1016/j.orgel.2014.05.027
- Park, I. S., Lee, S. Y., Adachi, C., and Yasuda, T. (2016). Full-color delayed fluorescence materials based on wedge-shaped phthalonitriles and dicyanopyrazines: systematic design, tunable photophysical properties, and OLED performance. *Adv. Funct. Mater.* 26, 1813–1821. doi: 10.1002/adfm.201505106
- Pershin, A., Hall, D., Lemaire, V., Sancho-Garcia, J., Muccioli, L., Zysman-Colman, E., et al. (2019). Highly emissive excitons with reduced exchange energy in thermally activated delayed fluorescent molecules. *Nat. Commun.* 10:597. doi: 10.1038/s41467-019-08495-5
- Tao, Y., Yuan, K., Chen, T., Xu, P., Li, H., Chen, R., et al. (2014). Thermally activated delayed fluorescence materials towards the breakthrough of organoelectronics. *Adv. Mater.* 26, 7931–7958. doi: 10.1002/adma.201402532
- Tsujiimoto, H., Ha, D., Markopoulos, G., Chae, H. S., Baldo, M. A., and Swager, T. M. (2017). Thermally activated delayed fluorescence and aggregation induced emission with through-space charge transfer. *J. Am. Chem. Soc.* 139, 4894–4900. doi: 10.1021/jacs.7b00873
- Uoyama, H., Goushi, K., Shizu, K., Nomura, H., and Adachi, C. (2012). Highly efficient organic light-emitting diodes from delayed fluorescence. *Nature* 492, 234–238. doi: 10.1038/nature11687
- Wang, K., Zheng, C., Liu, W., Liang, K., Shi, Y., Tao, S., et al. (2017). Avoiding energy loss on TADF emitters: controlling the dual conformations of D-A structure molecules based on the pseudoplanar segments. *Adv. Mater.* 29:1701476. doi: 10.1002/adma.201701476
- Wei, X., Chen, Y., Duan, R., Liu, J., Wang, R., Liu, Y., et al. (2017). Triplet decay-induced negative temperature dependence of the transient photoluminescence decay of thermally activated delayed fluorescence emitter. *J. Mater. Chem. C* 5, 12077–12084. doi: 10.1039/C7TC04025C
- Wei, X., Liu, Y., Hu, T., Li, Z., Liu, J., Wang, R., et al. (2019). Design of efficient exciplex emitters by decreasing the energy gap between the local excited triplet (3LE) state of the acceptor and the charge transfer (CT) states of the exciplex. *Front. Chem.* 7:188. doi: 10.3389/fchem.2019.00188
- Wong, M. Y., and Zysman-Colman, E. (2017). Purely organic thermally activated delayed fluorescence materials for organic light-emitting diodes. *Adv. Mater.* 29:1605444. doi: 10.1002/adma.201605444
- Yang, J., Ren, Z., Xie, Z., Liu, Y., Wang, C., Xie, Y., et al. (2017). AIEgen with fluorescence-phosphorescence dual mechanoluminescence at room temperature. *Angew. Chem. Int. Ed.* 56, 880–884. doi: 10.1002/anie.201610453
- Yang, Z., Mao, Z., Xie, Z., Zhang, Y., Liu, S., and Zhao, J. (2017). Recent advances in organic thermally activated delayed fluorescence materials. *Chem. Soc. Rev.* 46, 915–1016. doi: 10.1039/c6cs00368k
- Zeng, W., Lai, H., Lee, W., Jiao, M., Shiu, Y., Zhong, C., et al. (2018). Achieving nearly 30% external quantum efficiency for orange-red organic light emitting diodes by employing thermally activated delayed fluorescence emitters composed of 1,8-naphthalimide-acridine hybrids. *Adv. Mater.* 30:1704961. doi: 10.1002/adma.201704961
- Zhang, Y., Li, Z., Li, C., and Wang, Y. (2019). Suppressing efficiency roll-off of TADF based OLEDs by constructing emitting layer with dual delayed fluorescence. *Front. Chem.* 7:302. doi: 10.3389/fchem.2019.00302
- Zhang, Y. L., Ran, Q., Wang, Q., Liu, Y., Hänisch, C., Reineke, S., et al. (2019). High-efficiency red organic light-emitting diodes with external quantum efficiency close to 30% based on a novel thermally activated delayed fluorescence emitter. *Adv. Mater.* 31:1902368. doi: 10.1002/adma.201902368
- Zheng, K., Ni, F., Chen, Z., Zhong, C., and Yang, C. (2019). Polymorph-dependent thermally activated delayed fluorescence emitters: understanding TADF from a perspective of aggregation state. *Angew. Chem. Int. Ed.* doi: 10.1002/anie.201913210. [Epub ahead of print].

**Conflict of Interest:** The authors declare that the research was conducted in the absence of any commercial or financial relationships that could be construed as a potential conflict of interest.

Copyright © 2020 Li, Zhi, Dai, Jiang, Yang, Li, Li, Tao, Li, Huang and Chen. This is an open-access article distributed under the terms of the Creative Commons Attribution License (CC BY). The use, distribution or reproduction in other forums is permitted, provided the original author(s) and the copyright owner(s) are credited and that the original publication in this journal is cited, in accordance with accepted academic practice. No use, distribution or reproduction is permitted which does not comply with these terms.





# Efficient Aggregation-Induced Delayed Fluorescence Luminogens for Solution-Processed OLEDs With Small Efficiency Roll-Off

Zheyi Cai<sup>1</sup>, Hao Chen<sup>1</sup>, Jingjing Guo<sup>1</sup>, Zujin Zhao<sup>1\*</sup> and Ben Zhong Tang<sup>1,2\*</sup>

<sup>1</sup> State Key Laboratory of Luminescent Materials and Devices, Guangdong Provincial Key Laboratory of Luminescence From Molecular Aggregates, Guangzhou, China, <sup>2</sup> Department of Chemistry, Hong Kong Branch of Chinese National Engineering Research Center for Tissue Restoration and Reconstruction, The Hong Kong University of Science and Technology, Kowloon, China

## OPEN ACCESS

### Edited by:

Guohua Xie,  
Wuhan University, China

### Reviewed by:

Yanqin Miao,  
Taiyuan University of  
Technology, China  
Dongxia Zhu,  
Northeast Normal University, China

### \*Correspondence:

Zujin Zhao  
mszjzhao@scut.edu.cn  
Ben Zhong Tang  
tangbenz@ust.hk

### Specialty section:

This article was submitted to  
Organic Chemistry,  
a section of the journal  
Frontiers in Chemistry

Received: 24 January 2020

Accepted: 02 March 2020

Published: 07 April 2020

### Citation:

Cai Z, Chen H, Guo J, Zhao Z and  
Tang BZ (2020) Efficient  
Aggregation-Induced Delayed  
Fluorescence Luminogens for  
Solution-Processed OLEDs With  
Small Efficiency Roll-Off.  
Front. Chem. 8:193.  
doi: 10.3389/fchem.2020.00193

Purely organic small molecules with thermally-activated delayed fluorescence have a high potential for application in organic light-emitting diodes (OLEDs), but overcoming severe efficiency roll-off at high voltages still remains challenging. In this work, we design and synthesize two new emitters consisting of electron-withdrawing benzoyl and electron-donating phenoxazine and 9,9-dihexylfluorene. Their electronic structures, thermal stability, electrochemical behaviors, photoluminescence property, and electroluminescence performance are thoroughly investigated. These new emitters show weak fluorescence in dilute solution, but they can emit strongly with prominent delayed fluorescence in the aggregated state, indicating the aggregation-induced delayed fluorescence (AIDF) character. The solution-processed OLEDs based on the two emitters show high external quantum efficiency of 14.69%, and the vacuum-deposited OLEDs can also provide comparable external quantum efficiency of 14.86%. Significantly, roll-offs of the external quantum efficiencies are very small (down to 0.2% at 1,000 cd m<sup>-2</sup>) for these devices, demonstrating the evidently advanced efficiency stability. These results prove that the purely organic emitters with AIDF properties can be promising to fabricate high-performance solution-processed OLEDs.

**Keywords:** aggregation-induced delayed fluorescence, thermally activated delayed fluorescence, electroluminescence, organic light-emitting diodes, efficiency roll-off

## INTRODUCTION

Organic light-emitting diodes (OLEDs) are attracting considerable attention across academia and industry because of their advantages of flexibility, fast response, high stability, light weight, and so forth. Generally, for conventional fluorescent organic materials, the ratio of electrically generated singlet and triplet excitons is 1:3, leading to a low internal quantum efficiency (IQE) limited to only 25%. One way to enhance the IQE is making full use of triplet excitons. As for phosphorescent materials, the theoretical maximum value of the IQE can reach 100%, resulting from utilizing both triplet and singlet excitons, but most of these materials have to incorporate precious heavy metals to promote intersystem crossing (ISC). The OLEDs based on such materials have high costs in noble metals, and often encounter aggregation or concentration caused emission quenching. Another way to enhance the IQE of purely organic materials is transforming triplet excitons to singlet excitons.



According to the reports in recent years, there are several strategies to make use of the non-radiative triplet excitons, and thermally activated delayed fluorescence (TADF) is the method with most potential, in which triplet excitons can be converted to singlet excitons via reverse intersystem crossing (RISC) due to small singlet-triplet energy gap ( $\Delta E_{ST}$ ) (Gong et al., 2011; Uoyama et al., 2012; Hirata et al., 2015; Kang et al., 2018). TADF materials are able to harvest both singlet and triplet excitons and thus can reach high exciton utilization without noble metal, but suffer from severe efficiency roll-off (Rajamalli et al., 2016, 2017; Xie et al., 2017). Recently, by taking the advantages of aggregation-induced emission (AIE) and TADF, a new molecular design strategy of aggregation-induced delayed fluorescence (AIDF) was proposed and a series of novel luminogens based on AIDF were developed. These AIDF materials could not only harness both singlet and triplet excitons, but also showed the merit of very small efficiency roll-off at high luminance (Huang et al., 2017; Guo et al., 2018, 2019).

On the other hand, compared to vacuum deposition, solution-processed film preparation techniques, including spin-coating, inkjet printing, roll to roll processing, etc., are fitter to manufacture large-area OLED devices with lower cost and less material waste (Gather et al., 2011; Gong et al., 2013; Cho et al., 2014; Albrecht et al., 2015; Zeng et al., 2019). Currently, luminescent polymers are the major choice to fabricate solution-processed devices due to their excellent film-forming ability (Lee et al., 2016; Shao et al., 2017; Kim et al., 2018; Zou et al., 2018). However, it is generally hard to remove the metal catalyst residue completely from the products, and as a result they are in low purity and have defects in many cases, which undermine their EL performance. Meanwhile, the reproducibility is another problem for the polymers. In opposition, small molecules have the advantages of clearly defined structures, easy purification, and better photoluminescence (PL) performance. So, in addition to conventional fluorescent and phosphorescent small molecules (Zhao et al., 2007, 2009; Yang et al., 2018), developing solution-processable small molecules with delayed fluorescence is of high significance. However, the currently reported solution-processable TADF molecules also suffer from severe efficiency roll-off at high voltages (Wu et al., 2009; Suzuki et al., 2015; Zhong et al., 2020). To solve this problem, in this work, we designed and synthesized two small molecules with AIDF property. Long alkyl chains are introduced into the molecules to enhance the film-forming ability for solution-processed OLED devices. They emit strong yellow to orange-yellow light with evident delayed fluorescence in solid film. The solution-processed OLEDs using them as emitting layers exhibit high EL efficiencies and very small efficiency roll-off.

## EXPERIMENTAL

### Synthesis

#### 9,9-Dihexyl-9H-fluorene (1)

Potassium *tert*-butoxide (16.83 g, 150 mmol) was added to a mixture of fluorene (8.30 g, 50 mmol) and 1-bromohexane (17.45 mL, 125 mmol) in dehydrated tetrahydrofuran (100 mL) and stirred for 12 h under 65°C. The reaction mixture was poured

into water and extracted with dichloromethane several times. The combined organic layers were washed with water twice, and then dried over anhydrous NaSO<sub>4</sub>. After filtration, the crude product was concentrated and purified by column chromatography on silica gel (petroleum ether) to afford **1** as colorless liquid in 97% yield (16.21 g). <sup>1</sup>H NMR (500 MHz, CDCl<sub>3</sub>)  $\delta$  (TMS, ppm): 7.70–7.65 (m, 2H), 7.33–7.23 (m, 6H), 1.99–1.92 (m, 4H), 1.13–0.98 (m, 12H), 0.74 (t, *J* = 7.2 Hz, 6H), 0.67–0.54 (m, 4H). <sup>13</sup>C NMR (125 MHz, CDCl<sub>3</sub>)  $\delta$  (TMS, ppm): 150.65, 141.12, 126.97, 126.76, 122.79, 119.62, 55.12, 39.69, 32.17, 29.75, 23.57, 22.49, 13.99.

#### (9,9-Dihexyl-9H-fluorene-2-yl)(4-fluorophenyl) Methanone (2a) and (9,9-dihexyl-9H-fluorene-2,7-diyl) bis(4-fluorophenyl)Methanone (2b)

Aluminum trichloride (12.00 g, 90 mmol) was added into a stirred solution of **1** (9.70 g, 29 mmol) and 4-fluorobenzoyl chloride (14.22 g, 90 mmol) in dehydrated dichloromethane (50 mL) in 45°C and stirred for 6 h. The reaction was quenched with ice water and hydrochloric acid (50 mL, 2:1 v/v), and extracted with dichloromethane several times. The combined organic layers were washed with water twice, and then dried over anhydrous NaSO<sub>4</sub>. After filtration and solvent evaporation under reduced pressure, the residue was purified by column chromatography on silica gel (dichloromethane: petroleum ether, 2:3 v/v) to afford **2a** as yellow solid in 50% yield (6.61 g) and **2b** as yellow solid in 18% yield (3.02 g). For **2a**, <sup>1</sup>H NMR (500 MHz, CD<sub>2</sub>Cl<sub>2</sub>)  $\delta$  (TMS, ppm): 7.83–7.75 (m, 4H), 7.71–7.64 (m, 4H), 7.44–7.32 (m, 3H), 2.05–1.97 (m, 4H), 1.16–0.98 (m, 12H), 0.76 (t, *J* = 7.2 Hz, 6H), 0.66–0.56 (m, 4H). <sup>13</sup>C NMR (125 MHz, CD<sub>2</sub>Cl<sub>2</sub>)  $\delta$  (TMS, ppm): 196.66, 153.28, 152.12, 147.08, 141.11, 138.51, 136.91, 132.80, 132.77, 130.91, 129.74, 128.35, 128.19, 125.84, 124.46, 121.96, 120.65, 56.63, 41.38, 32.81, 30.90, 25.10, 23.84, 15.05, 0.90. For **2b**, <sup>1</sup>H NMR (500 MHz, CDCl<sub>3</sub>)  $\delta$  (TMS, ppm): 7.91–7.84 (m, 6H), 7.83–7.79 (m, 4H), 7.23–7.16 (m, 4H), 2.06–1.99 (m, 4H), 1.17–1.01 (m, 12H), 0.78 (t, *J* = 7.2 Hz, 6H), 0.70–0.60 (m, 4H). <sup>13</sup>C NMR (125 MHz, CDCl<sub>3</sub>)  $\delta$  (TMS, ppm): 198.49, 168.36, 164.38, 151.96, 144.94, 137.63, 134.25, 132.74, 129.80, 125.55, 119.88, 114.74, 113.69, 57.91, 39.34, 32.03, 29.55, 23.93, 22.55, 15.40.

#### ((4-(10H-Phenoxazin-10-yl)phenyl)(9,9-dihexyl-9H-fluorene-2-yl)methanone) (FC6-BP-PXZ)

A mixture of **2a** (0.46 g, 1.0 mmol), phenoxazine (0.24 g, 1.3 mmol) and potassium *tert*-butoxide (0.23 g, 2.0 mmol) in deaerated *N,N*-dimethylformamide (20 mL) was heated up to 130°C and stirred for 12 h under nitrogen. After cooling down to room temperature, the reaction was quenched with water (20 mL), and extracted with dichloromethane several times. The combined organic layers were washed with water twice, and then dried over anhydrous NaSO<sub>4</sub>. After filtration and solvent evaporation under reduced pressure, the residue was purified by column chromatography on silica gel (dichloromethane: petroleum ether, 1:1 v/v) to afford orange solid of FC6-BP-PXZ in 37% yield (0.23 g). <sup>1</sup>H NMR (500 MHz, CD<sub>2</sub>Cl<sub>2</sub>)  $\delta$  (TMS, ppm): 8.05–8.02 (m, 2H), 7.90 (s, 1H), 7.86–7.79 (m, 3H), 7.54–7.49 (m, 2H), 7.45–7.35 (m, 3H), 6.94–6.42 (m, 6H), 6.06 (s, 2H), 2.14–1.97 (m, 4H), 1.18–0.97 (m, 12H), 0.75 (t, *J* = 7.1 Hz, 6H),

0.70–0.57 (m, 4H).  $^{13}\text{C}$  NMR (125 MHz,  $\text{CD}_2\text{Cl}_2$ )  $\delta$  (TMS, ppm): 195.86, 153.14, 151.38, 146.89, 140.24, 139.06, 136.09, 133.05, 130.32, 127.48, 124.87, 123.61, 120.45, 119.25, 113.41, 56.84, 40.52, 31.93, 29.54, 24.25, 22.48, 15.73. HRMS ( $\text{C}_{44}\text{H}_{45}\text{NO}_2$ ):  $m/z$  619.1476 [ $\text{M}^+$ , calcd 619.3450].

**((9,9-Dihexyl-9H-fluorene-2,7-diyl)bis((4-(10H-phenoxazin-10-yl)phenyl)methanone)) (FC6-2BP-PXZ)**

A mixture of **3b** (0.8674 g, 1.5 mmol), phenoxazine (0.8238 g, 4.5 mmol) and potassium *tert*-butoxide (0.5049 g, 4.5 mmol) in deaerated *N,N*-dimethylformamide (20 mL) was heated up to 130°C and stirred for 12 h under nitrogen. After cooling down to room temperature, the reaction was quenched with water (20 mL), and extracted with dichloromethane several times. The combined organic layers were washed with water twice, and then dried over anhydrous  $\text{NaSO}_4$ . After filtration and solvent evaporation under reduced pressure, the residue was purified by column chromatography on silica gel (dichloromethane: petroleum ether, 1:1 v/v) to afford orange solid of FC6-2BP-PXZ in 66% yield (0.90 g).  $^1\text{H}$  NMR (500 MHz,  $\text{CD}_2\text{Cl}_2$ )  $\delta$  (TMS, ppm): 8.09–8.03 (m, 4H), 7.99–7.94 (m, 4H), 7.93–7.88 (m, 2H), 7.56–7.42 (m, 4H), 6.84–6.56 (m, 12H), 6.07 (s, 4H), 2.16–2.08 (m, 4H), 1.18–0.98 (m, 12H), 0.74 (t,  $J = 7.0$  Hz, 6H), 0.72–0.65 (m, 4H).  $^{13}\text{C}$  NMR (125 MHz,  $\text{CDCl}_3$ )  $\delta$  (TMS, ppm): 195.56, 137.77, 136.80, 133.74, 130.82, 130.12, 123.29, 120.45, 115.75, 31.49, 23.98, 22.54, 13.97. HRMS ( $\text{C}_{63}\text{H}_{56}\text{N}_2\text{O}_2$ ):  $m/z$  904.1583 [ $\text{M}^+$ , calcd 904.4240].

## OLED Fabrication and Characterization

The solution-processed devices were fabricated on clean glass substrates pre-coated with a 180 nm-thin layer of indium tin oxide (ITO) with a sheet resistance of 10  $\Omega$  per square. The ITO surface was treated with an ultrasonic detergent bath for 90 min, followed by soaking in ultrasonic de-ionized water for 20 min, then dried at 120°C for 1 h, and UV/Ozone cleaning for 15 min before spin-coating. A 50 nm-thin poly(3,4-ethylenedioxythiophene):poly(styrenesulfonate) (PEDOT:PSS) layer was spin-coated onto ITO surface at 3,000 rpm, then baked at 150 °C for 50 min to remove the residual water. Then, the substrates were moved into a glovebox under a nitrogen atmosphere, and a poly(9-vinylcarbazole) (PVK) layer was spin-coated onto the PEDOT:PSS layer at 2,500 rpm (the thickness achieved 30 nm) from a filtered 10 mg  $\text{mL}^{-1}$  chlorobenzene solution, followed by drying at 120°C for 20 min. Then, the emitting layer was spin-coated according to the configuration requirement. Solutions of FC6-BP-PXZ (30 wt%) or FC6-2BP-PXZ (10 wt%) doped in 4,4'-bis(carbazol-9-yl)biphenyl (CBP) with an overall concentration of 20 mg  $\text{mL}^{-1}$  in toluene were spin-coated at 2,500 rpm for 45 s to get films with a thickness of 50 nm. Finally, an electron-transport layer of 1,3,5-tri(*m*-pyrid-3-yl-phenyl)benzene (TmPyPB), a LiF layer, and an Al layer were deposited consecutively onto the spin-coated film in a vacuum chamber under  $10^{-4}$  Pa. Vacuum-evaporation OLEDs were fabricated on clean glass substrates pre-coated with a 180-nm-thin layer of ITO with a sheet resistance of 10  $\Omega$  per square. Organic layers were deposited by high-vacuum ( $5 \times$

$10^{-4}$  Pa) thermal evaporation onto a glass substrate pre-coated with an ITO layer. All organic layers were deposited sequentially. Thermal deposition rates for the organic materials, LiF and Al were 0.5, 0.5, and 1  $\text{\AA s}^{-1}$ , respectively. The thicknesses of the vacuum deposited layers were monitored by quartz crystal microbalance and were calibrated by Dektak XT profilometer. The emission area of the devices is  $3 \times 3 \text{ mm}^2$  as shaped by the overlapping area of the anode and cathode. All the device characterization steps were carried out at room temperature under ambient laboratory conditions without encapsulation. EL spectra were taken by an optical analyzer, FLAME-S-VIS-NIR. Current density and luminance vs. driving voltage characteristics were measured by Keithley 2400 and Konica Minolta chromameter CS-200. External quantum efficiencies were calculated by assuming that the devices were Lambertian light sources.

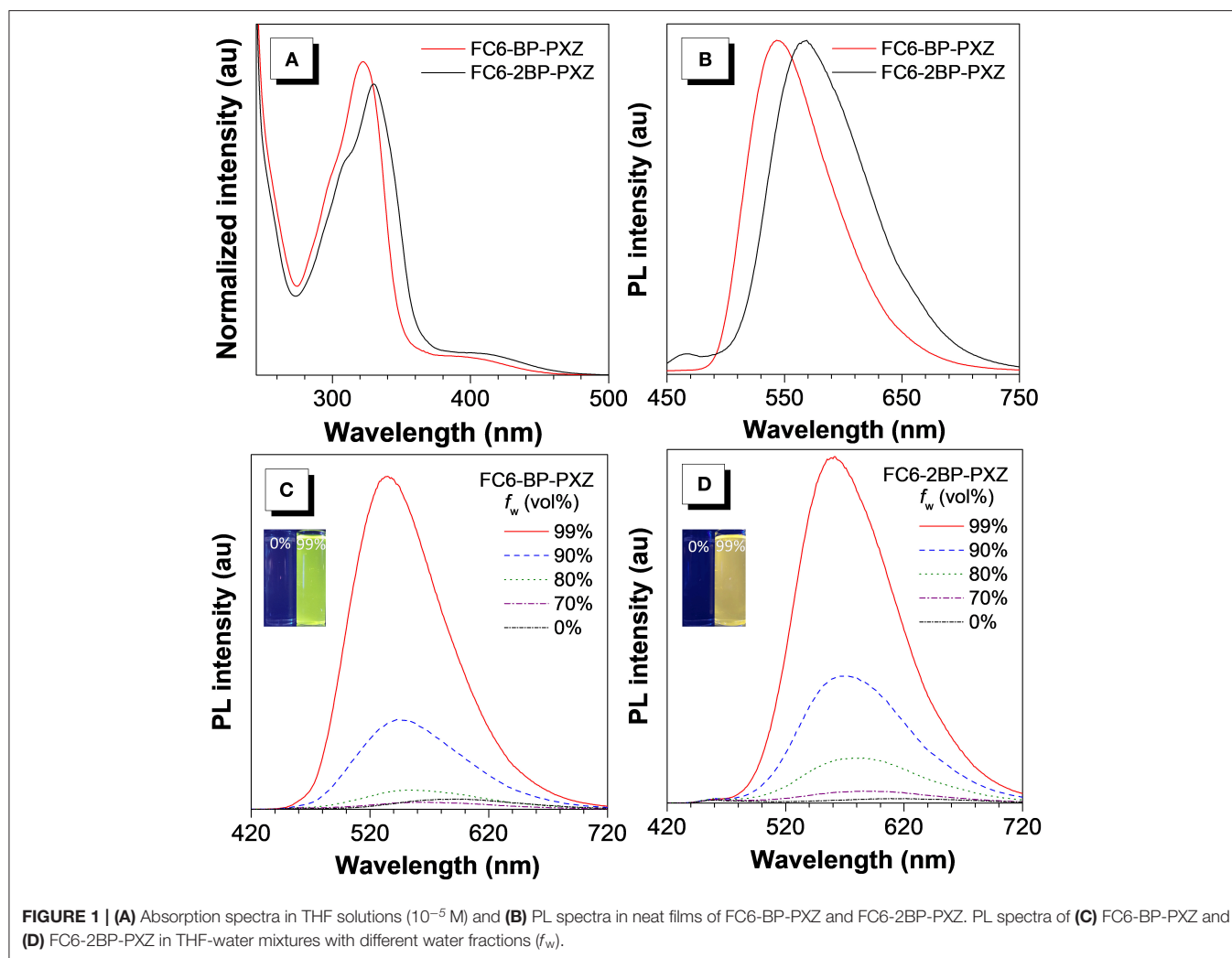
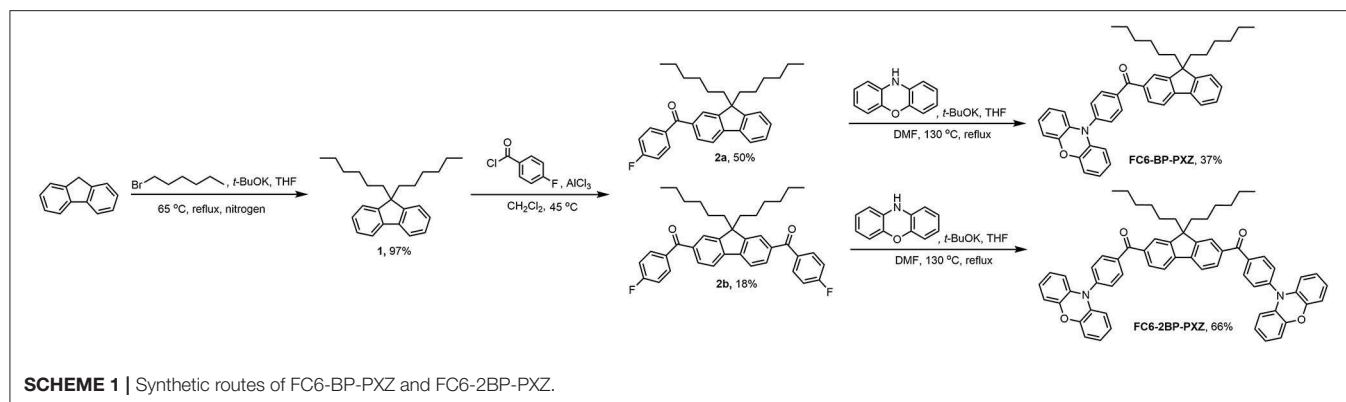
## RESULTS AND DISCUSSION

### Synthesis and Thermal Stability

The target compounds FC6-BP-PXZ and FC6-2BP-PXZ were simply and efficiently synthesized. As shown in **Scheme 1**, 9,9-dihexyl-9H-fluorene (**1**) that was prepared by the method in reported literature underwent Friedel-Crafts acylation reaction with compound **2** to yield intermediate **3a** and **3b**. The treatments of **3a** and **3b** with phenoxazine (PXZ) furnished the final compounds FC6-BP-PXZ and FC6-2BP-PXZ, respectively, in high yields. The molecular structures had been well-characterized by NMR and high-resolution mass spectra. Owing to the presence of hexyl groups, both compounds have good solubility in common organic solvents, such as chlorobenzene, toluene, chloroform, dichloromethane, tetrahydrofuran (THF), and so on, but do not dissolve easily in water because of the hydrophobic structures. The thermal stability of both compounds is characterized thoroughly by thermogravimetric analysis (TGA) and differential scanning calorimetry (DSC) under nitrogen. FC6-BP-PXZ and FC6-2BP-PXZ show high decomposition temperatures of 340.1 and 424.5°C, and high glass-transition temperatures of 85.7 and 84.0°C, respectively (**Figure S1**). The good thermal and morphological stabilities of both compounds enable them to function in OLEDs, and benefit device performances.

### Photophysical Behavior

FC6-BP-PXZ and FC6-2BP-PXZ show strong absorption bands at around 317 and 330 nm in THF solution, associated with  $\pi$ - $\pi^*$  transition of the molecules. There are also weak absorption bands at around 400 nm resulting from twisted intramolecular charge transfer (TICT) from the electronic donating-accepting (D-A) structure (**Figure 1A**) (Kashihara et al., 2017; Thorat et al., 2017; Higginbotham et al., 2018). In THF solution, FC6-BP-PXZ and FC6-2BP-PXZ emit weakly at 543 and 550 nm, with low fluorescence quantum yields ( $\Phi_{\text{FS}}$ ) of 3.5 and 2.0%, (**Figure 2A**) respectively. However, they can emit strongly at 544 and 567 nm with higher  $\Phi_{\text{FS}}$  of 32.0 and 17.0% in neat films at 300 K, respectively, indicating they have AIE property (**Figures 1B, 2B**



and Table S2). To further confirm this, the PL behaviors are measured in their water-THF mixtures (Figures 1C,D). The emission intensity is much stronger and the emission peak is blue-shifted when water fraction in the mixture gets high. Since these compounds are insoluble in water, they are prone to form aggregates when the water fraction becomes high, indicating

the enhanced emission is caused by the aggregate formation. In the aggregated state, the intramolecular motions that are active in solution state are restricted by the spatial constraint. In consequence, the non-radiative decay channel is blocked, and the excited state energy can be released as photons, leading to greatly enhanced emissions (Mei et al., 2015; Zhao et al., 2015;

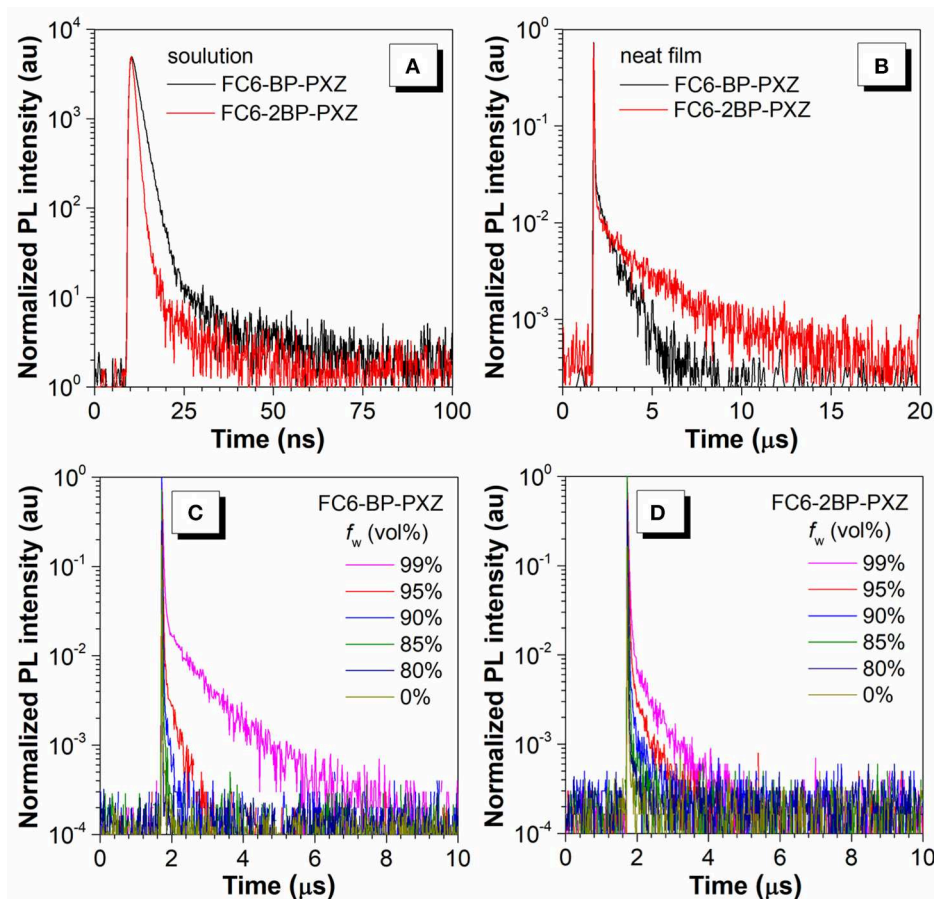


**FIGURE 2 |** Transient PL decay spectra of FC6-BP-PXZ and FC6-2BP-PXZ **(A)** in THF solutions ( $10^{-5}$  M) and **(B)** in neat films, measured at 300 K under nitrogen. The water fraction dependent transient PL decay spectra of **(C)** FC6-BP-PXZ and **(D)** FC6-2BP-PXZ in THF-water solutions.

Shen et al., 2018). These results confirm that both compounds indeed have AIE properties. And from the fluorescence and phosphorescence spectra of FC6-BP-PXZ and FC6-2BP-PXZ at 77 K (**Figure S2**), the  $\Delta E_{ST}$  values are estimated to be 0.017 and 0.068 eV, respectively, which are small enough for promoting RISC process.

The transient PL decay spectra show that both FC6-BP-PXZ and FC6-2BP-PXZ have short average lifetimes within 2.0 ns and the delayed fluorescence is hardly observed in solution. However, FC6-BP-PXZ and FC6-2BP-PXZ in neat films show much longer mean lifetimes of 0.22 and 0.62  $\mu$ s, with prompt components of 20.7 ns and 29.0 ns and evident delayed components of 0.66 and 2.12  $\mu$ s (**Figures 2C,D**), respectively. Moreover, the transient PL decay spectra in water-THF mixtures are further measured. It can be seen that when the water fraction increases, the mean lifetimes become longer. And the ratios of delayed components and the rate constant of RISCs are enhanced greatly (**Table 1, Table S1**). These findings demonstrate that the delayed fluorescence of both compounds is induced by the aggregation formation, indicative of their AIDF nature apparently. In solution state, the excited state is readily deactivated by fast

internal conversion (IC) of vigorous intramolecular motions, and thus the ISC and RISC processes cannot readily occur. In the aggregated state, however, the intramolecular motions are greatly suppressed by spatial hindrance, and the IC channel is blocked. Therefore, given their small  $\Delta E_{ST}$  values, the ISC and RISC are able to occur, leading to noticeable delayed fluorescence (Guo et al., 2018, 2019).

## Theoretical Calculation

The DFT/TDDFT calculation is applied to investigate the molecular orbital amplitude plots and energy levels of the highest occupied molecular orbitals (HOMOs) and lowest unoccupied molecular orbitals (LUMOs) of both compounds. As shown in **Figure 3**, the HOMOs of both compounds are distributed on fluorene and benzoyl moieties, and the LUMOs are concentrated on PXZ. The apparently separated distribution of HOMOs and LUMOs is necessary to achieve small  $\Delta E_{ST}$  values and thus to promote RISC process and delayed fluorescence. The theoretical  $\Delta E_{ST}$  values of FC6-BP-PXZ and FC6-2BP-PXZ are calculated to as small as 0.0442 and 0.0422 eV, respectively.



**TABLE 1** | Photophysical properties of FC6-BP-PXZ and FC6-2BP-PXZ.

	Solution <sup>a</sup>			Neat film <sup>b</sup>				
	$\lambda_{\text{abs}}$ (nm)	$\lambda_{\text{em}}$ (nm)	$\Phi_F^c$ (%)	$\lambda_{\text{em}}$ (nm)	$\Phi_F^c$ (%)	$\tau_{\text{prompt}}^d$ (ns)	$\tau_{\text{delayed}}^d$ ( $\mu\text{s}$ )	$\Delta E_{\text{ST}}^e$ (eV)
FC6-BP-PXZ	317	543	3.5	544	32.0	20.7	0.7	0.017
FC6-2BP-PXZ	330	550	2.0	567	17.0	29.0	2.1	0.068

<sup>a</sup>In THF solution ( $10^{-5}$  M) at room temperature. <sup>b</sup>Spin-coated on a quartz substrate. <sup>c</sup>Absolute fluorescence quantum yield determined by a calibrated integrating sphere under nitrogen at room temperature. <sup>d</sup>PL lifetimes of prompt ( $\tau_{\text{prompt}}$ ) and delayed ( $\tau_{\text{delayed}}$ ) decay components evaluated at 300 K under vacuum. <sup>e</sup>Estimated from the high-energy onsets of fluorescence and phosphorescence spectra at 77 K.

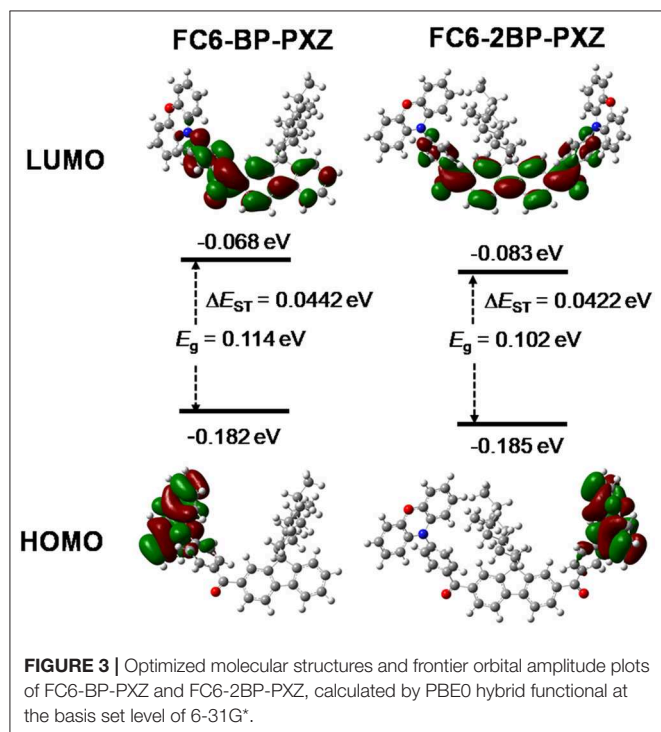


**FIGURE 3** | Optimized molecular structures and frontier orbital amplitude plots of FC6-BP-PXZ and FC6-2BP-PXZ, calculated by PBE0 hybrid functional at the basis set level of 6-31G\*.

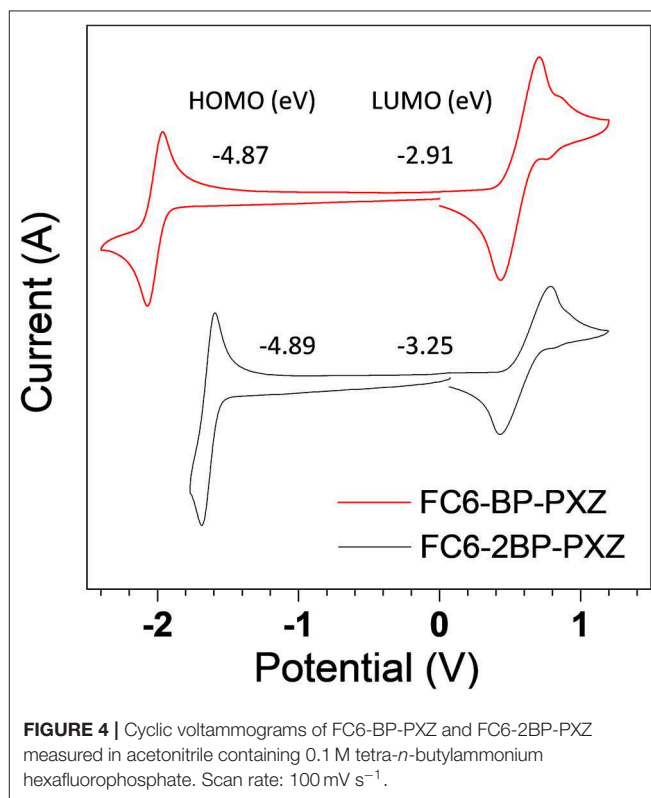


**FIGURE 4** | Cyclic voltammograms of FC6-BP-PXZ and FC6-2BP-PXZ measured in acetonitrile containing 0.1 M tetra-*n*-butylammonium hexafluorophosphate. Scan rate: 100 mV s<sup>-1</sup>.

## Electrochemical Property

Cyclic voltammetry (CV) is conducted to investigate the electrochemical behaviors of FC6-BP-PXZ and FC6-2BP-PXZ in a solution of acetonitrile with tetra-*n*-butylammonium hexafluorophosphate (Bu<sub>4</sub>NPF<sub>6</sub>, 0.1 M). Three-electrode system (Ag/Ag<sup>+</sup>, platinum wire and glassy carbon electrodes as reference, counter and work electrodes, respectively) is used and the scan rate is 100 mV s<sup>-1</sup> in the measurement. As illustrated in **Figure 4**, both compounds undergo reversible oxidation and reduction processes, indicating good electrochemical stability. The oxidation peaks of FC6-BP-PXZ and FC6-2BP-PXZ are both located at 0.435 V and the reduction peaks at -1.96 and -1.60 V, respectively. The HOMO energy levels of FC6-BP-PXZ and FC6-2BP-PXZ are calculated to be -4.87 to -4.89 eV, from the onset oxidation potentials, and the LUMO energy levels are -2.91 to -3.25 eV, from the onset reduction potentials (HOMO = -[E<sub>ox</sub> + 4.8] eV, and LUMO = -[E<sub>re</sub> + 4.8] eV, in which E<sub>ox</sub> and E<sub>re</sub> represent the onset oxidation and reduction potentials relative to Fc/Fc<sup>+</sup>, respectively).

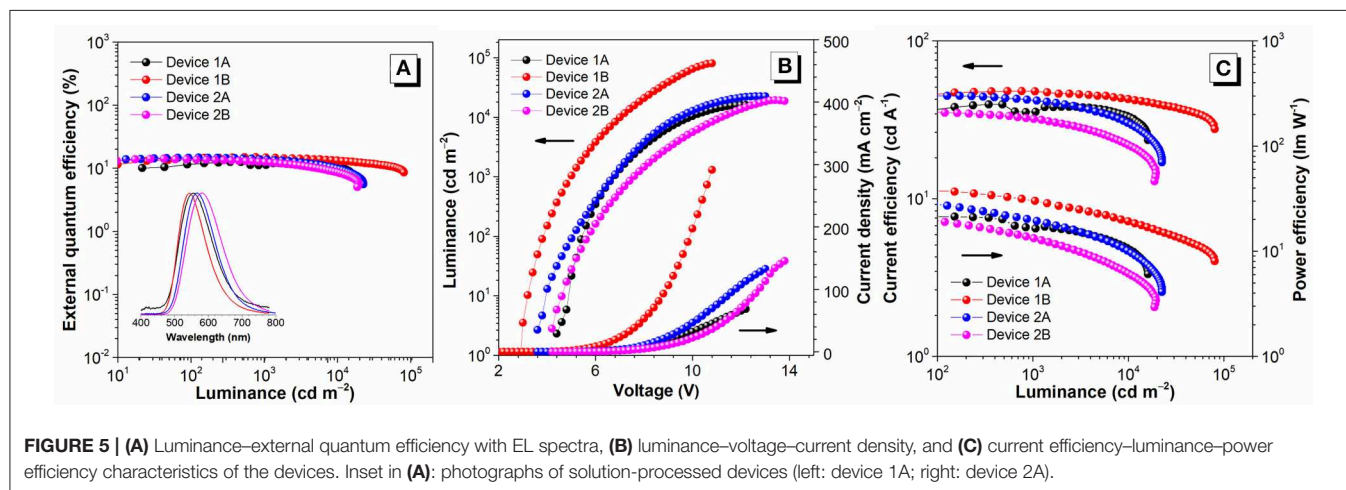
## Electroluminescence

Based on the excellent PL properties of FC6-BP-PXZ and FC6-2BP-PXZ, their EL performances in solution-processed OLEDs and vacuum-deposited OLEDs were further investigated. The key data of these OLEDs are summarized in **Table 2**, and the relative characteristic curves are plotted in **Figure 5**. The solution-processed OLEDs with a configuration of ITO/PEDOT:PSS (50 nm)/PVK (30 nm)/emitter/TmPyPB (40 nm)/LiF (1 nm)/Al [Device 1A: emitter = CBP:30 wt% FC6-BP-PXZ (50 nm); Device 2A: emitter = CBP:10 wt% FC6-2BP-PXZ (50 nm)] were fabricated, in which PEDOT:PSS and LiF were used as hole- and electron-injecting layers, respectively; PVK and TmPyPB were selected as hole- and electron-transporting layers, respectively; CBP functioned as a host. As shown in **Figure 5**, the turn-on voltage at 10 cd m<sup>-2</sup> of Devices 1A and 2A are 5.0 and 3.9 V, radiating orange-yellow light at ~555 nm (CIE<sub>x,y</sub> = 0.402, 0.549) and ~568 nm (CIE<sub>x,y</sub> = 0.432, 0.543), respectively. The

**TABLE 2** | EL performances of OLEDs based on FC6-BP-PXZ and FC6-2BP-PXZ<sup>a</sup>.

		$V_{on}$ (V)	Maximum values				Values at 1,000 $\text{cd m}^{-2}$					
			$\eta_c$ ( $\text{cd A}^{-1}$ )	$\eta_p$ ( $\text{lm W}^{-1}$ )	$\eta_{ext}$ (%)	L ( $\text{cd m}^{-2}$ )	$\eta_c$ ( $\text{cd A}^{-1}$ )	$\eta_p$ ( $\text{lm W}^{-1}$ )	$\eta_{ext}$ (%)	RO (%)	$\lambda_{EL}$ (nm)	CIE (x, y)
FC6-BP-PXZ	1A	5.0	39.61	21.29	12.49	16100	35.49	16.39	11.20	10.30	555	(0.402, 0.549)
	1B	3.2	48.02	38.91	14.86	80507	47.84	30.06	14.83	0.20	544	(0.392, 0.569)
FC6-2BP-PXZ	2A	3.9	44.83	32.03	14.69	22530	41.76	19.28	13.80	6.06	568	(0.432, 0.543)
	2B	4.6	36.12	25.52	14.12	19455	34.10	31.98	13.22	6.33	582	(0.446, 0.523)

<sup>a</sup> $V_{on}$  = turn-on voltage at 10  $\text{cd m}^{-2}$ ;  $\eta_c$  = current efficiency;  $\eta_p$  = power efficiency;  $\eta_{ext}$  = external quantum efficiency; RO = current efficiency roll-off from maximum value to that at 1,000  $\text{cd m}^{-2}$ ;  $\lambda_{EL}$  = electroluminescence maximum; CIE = Commission Internationale de l'Eclairage coordinates at condition of maximum  $\eta_{ext}$ .



maximum luminance ( $L_{max}$ ), current efficiency ( $\eta_{C,max}$ ), power efficiency ( $\eta_{P,max}$ ) and external quantum efficiency ( $\eta_{ext,max}$ ) of Device 2A are 22530  $\text{cd m}^{-2}$ , 44.83  $\text{cd A}^{-1}$ , 32.03  $\text{lm W}^{-1}$ , and 14.69%, respectively. It is significant that the external quantum efficiency at luminance of 1,000  $\text{cd m}^{-2}$  is 13.80%, showing a very low efficiency roll-off of 6.06%. The EL properties of Device 1A is somewhat inferior than those of Device 2A.

To further investigate the EL properties of both compounds, vacuum-deposited OLEDs with a configuration of ITO/TAPC (25 nm)/emitter/TmPyPB (55 nm)/LiF (1 nm)/Al [Device 1B: emitter = CBP:30 wt% FC6-BP-PXZ (35 nm); Device 2B: emitter = CBP: 10 wt% FC6-2BP-PXZ (35 nm)] were fabricated, in which 4,4'-cyclohexylidenebis[N, N-bis(p-tolyl)aniline] (TAPC) and TmPyPB were selected as hole- and electron-transporting layers, respectively. As shown in **Figure 5**, the turn-on voltage at 10  $\text{cd m}^{-2}$  of Devices 1B and 2B are 3.2 V and 4.6 V, emitting orange-yellow light at  $\sim 544$  nm ( $\text{CIE}_{x,y} = 0.392, 0.569$ ) and  $\sim 582$  nm ( $\text{CIE}_{x,y} = 0.446, 0.523$ ), respectively. The  $L_{max}$ ,  $\eta_{C,max}$ ,  $\eta_{P,max}$ , and  $\eta_{ext,max}$  of Devices 1B and 2B are 80,507  $\text{cd m}^{-2}$ , 48.02  $\text{cd A}^{-1}$ , 38.91  $\text{lm W}^{-1}$  and 14.86%, and 19,455  $\text{cd m}^{-2}$ , 36.12  $\text{cd A}^{-1}$ , 25.52  $\text{lm W}^{-1}$  and 14.12%, respectively, in which the efficiency roll-off is extremely small especially for Device 1B (0.20% at luminance of 1,000  $\text{cd m}^{-2}$ ). These new emitters with AIDF property provide good EL performance, and according to the photophysical parameters, the exciton utilization of these OLEDs has approached nearly 100%. More importantly,

extremely small efficiency roll-offs are successfully achieved, which should be an apparent advance to conventional TADF emitters for solution-processed OLEDs and vacuum-deposited OLEDs. And the AIDF character of the materials should be important for achieving high performance, which combines the superior features of efficient solid-state emission, high exciton utilization and low exciton quenching.

## CONCLUSIONS

In summary, two new emitters built with electron-withdrawing group benzoyl and electron-donating phenoxazine and 9,9-dihexylfluorene are designed and synthesized. They have high thermal and morphological stabilities and good electrochemical stability. Whereas, in dilute solution state they emit weakly with faint delayed fluorescence, they can emit strongly with prominent delayed fluorescence in the aggregated state, demonstrating the AIDF property. In addition, they fluoresce intensely in spin-coated films with notable delayed fluorescence, owing to the small  $\Delta E_{ST}$ , and thus fast RISC process. As a consequence, they can perform excellently as light-emitting layers in solution-processed OLEDs, providing high  $\eta_{ext,max}$  of up to 14.69% and very small efficiency roll-off at the luminance of 1,000  $\text{cd m}^{-2}$ , demonstrating the outstanding efficiency stability. On the other hand, their vacuum-deposited OLEDs also have good  $\eta_{ext,max}$  of up to 14.86% and negligible efficiency roll-off at 1,000  $\text{cd m}^{-2}$ . These results indicate the

great potential of small molecules with AIDF property for the fabrication of high-performance solution-processed and vacuum-deposited OLEDs.

## DATA AVAILABILITY STATEMENT

The datasets generated for this study are available on request to the corresponding author.

## AUTHOR CONTRIBUTIONS

All authors listed have made a substantial, direct and intellectual contribution to the work, and approved it for publication.

## REFERENCES

- Albrecht, K., Matsuoka, K., Fujita, K., and Yamamoto, K. (2015). Carbazole dendrimers as solution-processable thermally activated delayed-fluorescence materials. *Angew. Chem. Int. Ed.* 54, 5677–5682. doi: 10.1002/anie.201500203
- Cho, Y. J., Yook, K. S., and Lee, J. Y. (2014). High efficiency in a solution-processed thermally activated delayed-fluorescence device using a delayed-fluorescence emitting material with improved solubility. *Adv. Mater.* 26, 6642–6646. doi: 10.1002/adma.201402188
- Gather, M. C., Köhnen, A., and Meerholz, K. (2011). White organic light-emitting diodes. *Adv. Mater.* 23, 233–248. doi: 10.1002/adma.201002636
- Gong, S., Fu, Q., Wang, Q., Yang, C., Zhong, C., Qin, J., et al. (2011). Highly efficient deep-blue electrophosphorescence enabled by solution-processed bipolar tetraarylsilane host with both a high triplet energy and a high-lying HOMO level. *Adv. Mater.* 23, 4956–4959. doi: 10.1002/adma.201102758
- Gong, S., Zhong, C., Fu, Q., Ma, D., Qin, J., and Yang, C. (2013). Extension of molecular structure toward solution-processable hosts for efficient blue phosphorescent organic light-emitting diodes. *J. Phys. Chem. C* 117, 549–555. doi: 10.1021/jp309100e
- Guo, J., Fan, J., Lin, L., Zeng, J., Liu, H., Wang, C. K., et al. (2019). Mechanical insights into aggregation-induced delayed fluorescence materials with anti-kasha behavior. *Adv. Sci.* 6:1801629. doi: 10.1002/advs.201801629
- Guo, J., Zhao, Z., and Tang, B. Z. (2018). Purely organic materials with aggregation-induced delayed fluorescence for efficient nondoped OLEDs. *Adv. Opt. Mater.* 6:1800264. doi: 10.1002/adom.201800264
- Higginbotham, H. F., Yi, C. L., Monkman, A. P., and Wong, K. T. (2018). Effects of ortho-phenyl substitution on the rISC rate of D-A type TADF molecules. *J. Phys. Chem. C* 122, 7627–7634. doi: 10.1021/acs.jpcc.8b01579
- Hirata, S., Sakai, Y., Masui, K., Tanaka, H., Lee, S. Y., Nomura, H., et al. (2015). Highly efficient blue electroluminescence based on thermally activated delayed fluorescence. *Nat. Mater.* 14, 330–336. doi: 10.1038/nmat4154
- Huang, J., Nie, H., Zeng, J., Zhuang, Z., Gan, S., Cai, Y., et al. (2017). Highly efficient nondoped OLEDs with negligible efficiency roll-off fabricated from aggregation-induced delayed fluorescence luminogens. *Angew. Chem. Int. Ed.* 56, 12971–12976. doi: 10.1002/anie.201706752
- Kang, Y., Zhao, L., and Leng, J. (2018). Delocalization of frontier orbitals induced red emission for heptazine based thermally activated delayed fluorescence molecule: first-principles study. *Chem. Phys. Lett.* 698, 187–194. doi: 10.1016/j.cplett.2018.03.017
- Kashihara, R., Morimoto, M., Ito, S., Miyasaka, H., and Irie, M. (2017). Fluorescence photoswitching of a diarylethene by irradiation with single-wavelength visible light. *J. Am. Chem. Soc.* 139, 16498–16501. doi: 10.1021/jacs.7b10697
- Kim, H. J., Lee, C., Godumala, M., Choi, S., Park, S. Y., Cho, M. J., et al. (2018). Solution-processed thermally activated delayed fluorescence organic light-emitting diodes using a new polymeric emitter containing non-conjugated cyclohexane units. *Polym. Chem.* 9, 1318–1326. doi: 10.1039/C7PY02113E
- Lee, S. Y., Yasuda, T., Komiyama, H., Lee, J., and Adachi, C. (2016). Thermally activated delayed fluorescence polymers for efficient solution-processed organic light-emitting diodes. *Adv. Mater.* 28, 4019–4024. doi: 10.1002/adma.201505026
- Mei, J., Leung, N. L., Kwok, R. T., Lam, J. W., and Tang, B. Z. (2015). Aggregation-induced emission: together we shine, united we soar! *Chem. Rev.* 115, 11718–11940. doi: 10.1021/acs.chemrev.5b00263
- Rajamalli, P., Senthilkumar, N., Gandeepan, P., Huang, P. Y., Huang, M. J., Ren-Wu, C. Z., et al. (2016). A new molecular design based on thermally activated delayed fluorescence for highly efficient organic light emitting diodes. *J. Am. Chem. Soc.* 138, 628–634. doi: 10.1021/jacs.5b10950
- Rajamalli, P., Senthilkumar, N., Huang, P. Y., Ren-Wu, C. C., Lin, H. W., and Cheng, C. H. (2017). New molecular design concurrently providing superior pure blue, thermally activated delayed fluorescence and optical out-coupling efficiencies. *J. Am. Chem. Soc.* 139, 10948–10951. doi: 10.1021/jacs.7b03848
- Shao, S., Hu, J., Wang, X., Wang, L., Jing, X., and Wang, F. (2017). Blue thermally activated delayed fluorescence polymers with nonconjugated backbone and through-space charge transfer effect. *J. Am. Chem. Soc.* 139, 17739–17742. doi: 10.1021/jacs.7b10257
- Shen, P., Zhuang, Z., Zhao, Z., and Tang, B. Z. (2018). AIEgens based on main group heterocycles. *J. Mater. Chem. C* 6, 11835–11852. doi: 10.1039/C8TC02956C
- Suzuki, Y., Zhang, Q., and Adachi, C. (2015). A solution-processable host material of 1, 3-bis [3-(9-carbazolyl) phenyl]-9-carbazolyl benzene and its application in organic light-emitting diodes employing thermally activated delayed fluorescence. *J. Mater. Chem. C* 3, 1700–1706. doi: 10.1039/C4TC02211D
- Thorat, K. G., Ray, A. K., and Sekar, N. (2017). Modulating TICT to ICT characteristics of acid switchable red emitting boradiazaindacene chromophores: perspectives from synthesis, photophysical, hyperpolarizability and TD-DFT studies. *Dyes. Pigm.* 136, 321–334. doi: 10.1016/j.dyepig.2016.08.049
- Uoyama, H., Goushi, K., Shizu, K., Nomura, H., and Adachi, C. (2012). Highly efficient organic light-emitting diodes from delayed fluorescence. *Nature* 492, 234–238. doi: 10.1038/nature11687
- Wu, H., Ying, L., Yang, W., and Cao, Y. (2009). Progress and perspective of polymer white light-emitting devices and materials. *Chem. Soc. Rev.* 38, 3391–3400. doi: 10.1039/b816352a
- Xie, G., Luo, J., Huang, M., Chen, T., Wu, K., Gong, S., et al. (2017). Inheriting the characteristics of TADF small molecule by side-chain engineering strategy to enable bluish-green polymers with high PLQYs up to 74% and external quantum efficiency over 16% in light-emitting diodes. *Adv. Mater.* 29:1604223. doi: 10.1002/adma.201604223
- Yang, X., Guo, H., Liu, B., Zhao, J., Zhou, G., Wu, Z., et al. (2018). Diarylboron-based asymmetric red-emitting Ir (III) complex for solution-processed phosphorescent organic light-emitting diode with external quantum efficiency above 28%. *Adv. Sci.* 5:1701067. doi: 10.1002/advs.201701067
- Zeng, W., Zhou, T., Ning, W., Zhong, C., He, J., Gong, S., et al. (2019). Realizing 22.5% external quantum efficiency for solution-processed thermally activated delayed-fluorescence OLEDs with red emission at 622 nm via a synergistic strategy of molecular engineering and host selection. *Adv. Mater.* 31:1901404. doi: 10.1002/adma.201901404

## FUNDING

This work was financially supported by the National Natural Science Foundation of China (21788102 and 21673082), the Natural Science Foundation of Guangdong Province (2019B030301003), the Science and Technology Program of Guangzhou (201804020027).

## SUPPLEMENTARY MATERIAL

The Supplementary Material for this article can be found online at: <https://www.frontiersin.org/articles/10.3389/fchem.2020.00193/full#supplementary-material>

- Zhao, Z., He, B., and Tang, B. Z. (2015). Aggregation-induced emission of siloles. *Chem. Sci.* 6, 5347–5365. doi: 10.1039/C5SC01946J
- Zhao, Z., Li, J. H., Chen, X., Wang, X., Lu, P., and Yang, Y. (2009). Solution-processable stiff dendrimers: synthesis, photophysics, film morphology, and electroluminescence. *J. Org. Chem.* 74, 383–395. doi: 10.1021/jo802237c
- Zhao, Z., Li, J. H., Lu, P., and Yang, Y. (2007). Fluorescent, carrier-trapping dopants for highly efficient single-layer polyfluorene LEDs. *Adv. Fun. Mater.* 17, 2203–2210. doi: 10.1002/adfm.200700195
- Zhong, P. L., Zheng, C. J., Zhang, M., Zhao, J. W., Yang, H. Y., He, Z. Y., et al. (2020). Highly efficient ternary polymer-based solution-processable exciplex with over 20% external quantum efficiency in organic light-emitting diode. *Org. Electron.* 76:105449. doi: 10.1016/j.orgel.2019.105449
- Zou, Y., Gong, S., Xie, G., and Yang, C. (2018). Design strategy for solution-processable thermally activated delayed fluorescence emitters and their applications in organic light-emitting diodes. *Adv. Opt. Mater.* 6:1800568. doi: 10.1002/adom.201800568
- Conflict of Interest:** The authors declare that the research was conducted in the absence of any commercial or financial relationships that could be construed as a potential conflict of interest.

Copyright © 2020 Cai, Chen, Guo, Zhao and Tang. This is an open-access article distributed under the terms of the Creative Commons Attribution License (CC BY). The use, distribution or reproduction in other forums is permitted, provided the original author(s) and the copyright owner(s) are credited and that the original publication in this journal is cited, in accordance with accepted academic practice. No use, distribution or reproduction is permitted which does not comply with these terms.





# Stimuli-Responsive Thermally Activated Delayed Fluorescence in Polymer Nanoparticles and Thin Films: Applications in Chemical Sensing and Imaging

Nathan R. Paisley, Christopher M. Tonge and Zachary M. Hudson\*

Department of Chemistry, The University of British Columbia, Vancouver, BC, Canada

## OPEN ACCESS

### Edited by:

Eli Zysman-Colman,  
University of St Andrews,  
United Kingdom

### Reviewed by:

Juozas Vidas Grazulevicius,  
Kaunas University of  
Technology, Lithuania  
Marc Kenneth Etherington,  
Northumbria University,  
United Kingdom

### \*Correspondence:

Zachary M. Hudson  
zhudson@chem.ubc.ca

### Specialty section:

This article was submitted to  
Polymer Chemistry,  
a section of the journal  
Frontiers in Chemistry

**Received:** 30 January 2020

**Accepted:** 10 March 2020

**Published:** 09 April 2020

### Citation:

Paisley NR, Tonge CM and  
Hudson ZM (2020)  
Stimuli-Responsive Thermally  
Activated Delayed Fluorescence in  
Polymer Nanoparticles and Thin Films:  
Applications in Chemical Sensing and  
Imaging. *Front. Chem.* 8:229.  
doi: 10.3389/fchem.2020.00229

Though molecules exhibiting thermally activated delayed fluorescence (TADF) have seen extensive development in organic light-emitting diodes, their incorporation into polymer nanomaterials and thin films has led to a range of applications in sensing and imaging probes. Triplet quenching can be used to probe oxygen concentration, and the reverse intersystem crossing mechanism which gives rise to TADF can also be used to measure temperature. Moreover, the long emission lifetimes of TADF materials allows for noise reduction in time-gated microscopy, making these compounds ideal for time-resolved fluorescence imaging (TRFI). A polymer matrix enables control over energy transfer between molecules, and can be used to modulate TADF behavior, solubility, biocompatibility, or desirable mechanical properties. Additionally, a polymer's oxygen permeability can be tuned to suit imaging applications in a range of media. Here we review the applications of polymer nanoparticles and films exhibiting TADF in sensing and imaging, demonstrating that this class of materials has great potential beyond electroluminescent devices still waiting to be explored.

**Keywords:** TADF, imaging, oxygen sensing, polymer films, polymer nanostructure, temperature sensing

## INTRODUCTION

Since the demonstration of their utility in organic light-emitting diodes (OLEDs) in 2011 (Endo et al., 2011), molecules exhibiting thermally activated delayed fluorescence (TADF) have generated tremendous research interest (Wu et al., 2009; Goushi et al., 2012; Zhang et al., 2012; Cho et al., 2015; Li et al., 2017; Steinegger et al., 2017; Wong and Zysman-Colman, 2017; Yang et al., 2017; Chen et al., 2018). When used as emitters in OLEDs, internal quantum efficiencies up to 100% can be achieved due to their ability to harvest both singlet and triplet excitons (Jankus et al., 2014; Wu et al., 2016). Concurrently, the incorporation of TADF materials into polymer nanostructures led to a range of emerging applications as sensors and imaging probes (Kochmann et al., 2013; Xiong et al., 2014; Gan et al., 2017; Li et al., 2017; Steinegger et al., 2017; Zhu et al., 2018; Tsuchiya et al., 2019; Tonge et al., 2020). TADF emitters can be incorporated into polymer nanostructures either as small molecules dispersed in a polymeric matrix or covalently incorporated into the polymer itself. By incorporating TADF materials into polymers, the solubility, biocompatibility, and oxygen permeability of the material can be readily tuned, and rates of energy transfer within the material

can be controlled as well. In this way, the desirable properties of TADF materials can be applied to a wider range of media and combined with other chemical functionality for cellular uptake, targeting, or drug delivery.

In TADF materials, forward and reverse intersystem crossing processes (ISC/RISC) interconvert excitons between singlet and triplet excited states. While transitions between states of unlike spin are generally forbidden, a suitably small singlet-triplet energy gap ( $\Delta E_{ST}$ ) allows for state mixing such that these transitions become observable. To design molecules with a small  $\Delta E_{ST}$ , donor (D) and acceptor (A) moieties are arranged so as to limit the overlap between the HOMO and LUMO, minimizing the exchange energy which causes the singlet-triplet energy gap (Endo et al., 2011). TADF is realized when  $\Delta E_{ST}$  is small enough such that thermal energy alone is sufficient to promote RISC from a triplet state to a higher-energy singlet (Penfold et al., 2018). In applications where a high triplet concentration is detrimental to the material's function, a short emission lifetime and, therefore, high RISC rate ( $k_{RISC}$ ) is desirable. El-Sayed's rule for intersystem crossing (ISC) states that transitions between a pure triplet charge transfer state ( $^3CT$ ) and pure singlet charge transfer state ( $^1CT$ ) are prohibited, and thus even with a small  $\Delta E_{ST}$ , the  $^3CT \rightarrow ^1CT$  RISC process is generally slow (Lim et al., 1981). Recent research, however, has found that  $k_{RISC}$  can be increased by the presence of energetically proximate locally excited triplet ( $^3LE$ ) states, such that a small  $^3LE$ - $^3CT$  energy gap ( $|\Delta E_{3LE-3CT}|$ ) can facilitate conversion between  $^3CT$  and  $^1CT$  (Chen et al., 2015; Dias et al., 2016; Gibson et al., 2016; Marian, 2016; Gibson and Penfold, 2017; Hosokai et al., 2017). The converse of this observation is that molecules can also be intentionally designed to have low  $k_{RISC}$  values, and thus long emissive lifetimes, increasing sensitivity in numerous imaging applications.

The fluorescent mechanism of TADF dyes has significant potential for applications beyond electroluminescent devices, including in sensing and fluorescence imaging. TADF emission lifetimes are typically biexponential, with a short component (<10 ns) due to fluorescence directly from the first excited singlet state ( $S_1$ ) as well as a second, delayed component ( $\mu s$  to ms) arising from the RISC process (Dias, 2015; Palmeira and Berberan-Santos, 2018). The involvement of triplet excited states in TADF makes these emitters particularly susceptible to fluorescence quenching from triplet oxygen. This response can be exploited to develop emitters that are sensitive to the  $O_2$  concentration in a given medium by measuring the change in emission intensity and lifetime of delayed fluorescence (Baleizão et al., 2008; DeRosa et al., 2015). Similarly,  $k_{RISC}$  depends directly on the temperature of the environment in which the emitter is located, meaning the temperature of a sample can be determined directly from a fluorescence lifetime (Palmeira and Berberan-Santos, 2018). In applications such as these, longer emission lifetimes result in probes with higher sensitivity.

The presence of delayed emission lifetimes without the costly or potentially toxic metallic elements typically found in phosphorescent dyes also makes TADF materials well-suited to time-resolved fluorescence imaging (TRFI) (Zhang et al., 2019). In typical biological systems, autofluorescence from background processes and structures within the cell can significantly reduce

the resolution of fluorescent cell imaging (He et al., 2018). These background processes, however, are generally complete in <100 ns, while TADF emission may be detected over a significantly longer timescale. This makes photostable TADF dyes with high brightness highly desirable for TRFI, as background fluorescence can be filtered out by resolving the integrated signal over time or gating the detected luminescence.

In sensing or imaging applications, seclusion of the TADF emitter to control aggregation, limit the influence of environmental factors, and introduce solubility in aqueous systems is the primary goal in host material selection and can be efficiently achieved through incorporation in a polymer host. Characteristics such as charge mobility have minimal effect on sensors unlike small molecule hosts typically used in TADF OLEDs (Chatterjee and Wong, 2019). Such polymer encapsulation can be performed by covalent or non-covalent interactions, with minimal effect on the absorption spectrum of the TADF material. The emission spectrum, however, can be tuned depending on the ability of the polymer matrix to stabilize the emitter's CT excited state. Quantum yield ( $\Phi_F$ ) values will also vary depending on the polarity of the host polymer and the impact of aggregation on the dye (Gan et al., 2017; Li et al., 2017; Marghad et al., 2019). Indeed, encapsulation within a polymer host results in a reduction of rotational and vibrational degrees of freedom, often resulting in enhanced  $\Phi_F$  and elongated fluorescence lifetimes.

Herein, we discuss recent examples of TADF in polymer nanostructures and thin films. The application of these systems in oxygen and thermal sensing is discussed, as well as methods by which polymer structure can be used to modulate TADF behavior. Progress and current areas of research focus are highlighted, alongside potential avenues for further advancement.

## TADF IN SENSORS

### TADF Sensors for Oxygen

Luminescent sensors for oxygen can make use of polymeric hosts to control the interaction of  $O_2$  with a fluorophore, helping to define the sensitivity and dynamic range of the sensor (Kochmann et al., 2013; Steinegger et al., 2017). TADF was first exploited in oxygen sensing by Wolfbeis and coworkers in 2013, by doping  $^{13}C_{70}$  into a series of polymer hosts (Kochmann et al., 2013).  $^{13}C_{70}$  has a  $\Phi_F$  of 9%, the highest of any fullerene known, due to increased TADF efficiency from the increased nuclear mass of  $^{13}C$ , as well as a nuclear magnetic effect that increases RISC rates (Baleizão and Berberan-Santos, 2011). Moreover,  $^{13}C_{70}$  exhibits a high triplet quantum yield of 0.994 and a 170-fold enhancement in  $\Phi_F$  under inert atmosphere (Baleizão and Berberan-Santos, 2011). In this study,  $^{13}C_{70}$  was doped into a series of hosts, specifically polystyrene (PS), ethyl cellulose (EC), and organically modified silica (Ormocsil), to investigate a range of oxygen permeabilities ( $P_{O_2}$ ) from moderate to high. A thermostated flow cell (298 or 333 K) was used to prevent interference from temperature variations, and decay lifetimes in the wavelength range 670–700 nm were monitored as  $O_2$  concentrations were varied (Figure 1A). In these experiments,

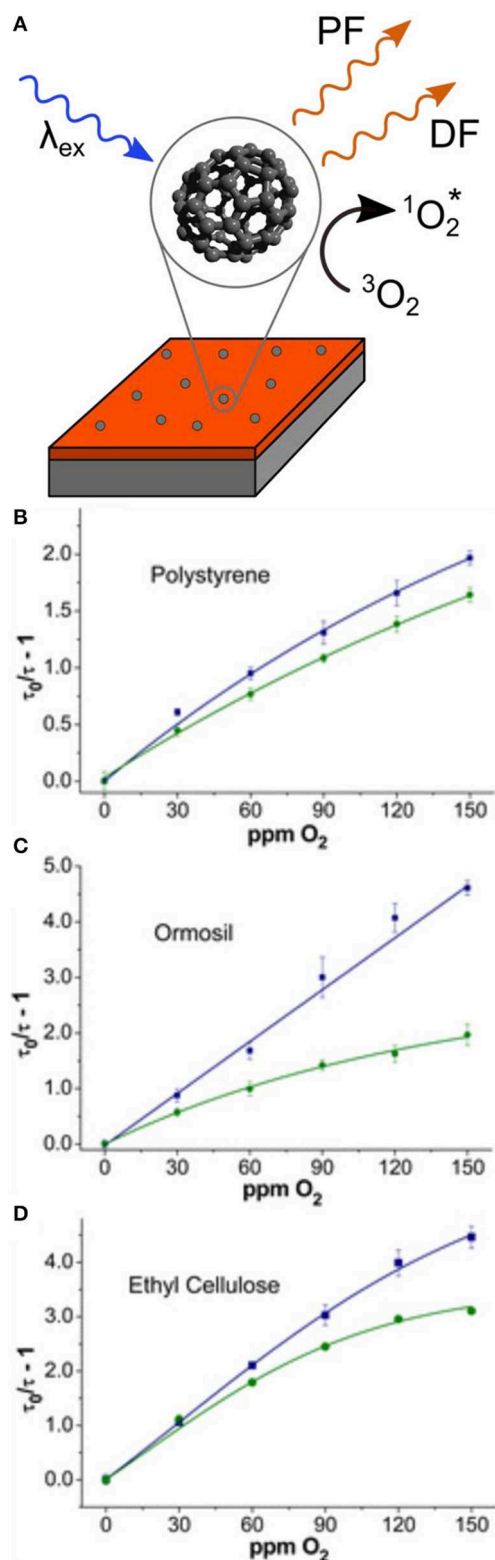


**FIGURE 1 | (A)** Schematic representation of  $^{13}\text{C}_{70}$  films with excited state quenching by triplet oxygen; **(B–D)** lifetime-based Stern-Volmer plots at 298 K (blue squares) and 333 K (green circles) for  $^{13}\text{C}_{70}$  in **(B)** PS, **(C)** Ormosil, and **(D)** EC. Adapted from reference (Kochmann et al., 2013) with permission from the American Chemical Society.

Stern-Volmer plots of  $\frac{\tau_0}{\tau} - 1$  vs.  $\text{O}_2$  concentration could be fit using a two-site model which accounted for two distinct probe environments (**Figures 1B–D**). The linearity of the fit was found to decrease in all films with increasing temperature, due to increased efficiency of RISC and an increased oxygen quenching rate. The lowest limit of detection (LOD) for all films was measured at 0.25 ppm by volume (ppmv) in EC, with upper detection limits of 4,900 ppmv giving the sensors a four order of magnitude dynamic range. These limits of detection were competitive with state-of-the-art sensors using phosphorescent palladium(II) porphyrin complexes in fluorinated polymer hosts, without the use of transition metals.

Despite the success of the  $^{13}\text{C}_{70}$ -based films, their low  $\Phi_F$  presents a barrier to more widespread use. An improved sensor design was demonstrated by Borisov and coworkers, who used TADF compounds based on dicyanobenzene (DCB) and anthraquinone (AQ) electron acceptors with arylamine-based electron donors (**Figure 2**) doped into PS films (Steinegger et al., 2017). The combination of these donors and acceptors affords compounds with absorption in the visible region, high  $\Phi_F$ , and good photostability (Zhang et al., 2015). Compounds **1–14** dispersed in PS films have  $\pi$ - $\pi^*$  absorption maxima ranging from 329 to 375 nm and charge transfer bands ranging from 440 to 490 nm. Compared to toluene solution the PS host results in blue shifted emission, with DCB dyes **11–14** showing emission maxima from 493 to 531 nm and AQ dyes **1–10** ranging from 577 to 614 nm in PS films. A significant enhancement in  $\Phi_F$  and excited state lifetimes of **1–10** is also observed upon polymer encapsulation due to a restriction in rotational degrees of freedom, decreasing the rate of non-radiative decay. Multicomponent fluorescence lifetimes for films containing **1–14** were observed, including a delayed fluorescence component in the  $\mu\text{s}$ -ms range. Photodegradation studies revealed that DCB dyes **11–14** are highly resistant to photobleaching, while AQ dyes **1–10** degrade 2–5 times faster.

To investigate **1–14** as potential oxygen sensors, the PS films were tested using a flow cell thermostated at 298 K to eliminate cross-sensitivity to temperature. **11–14** have relatively short delayed lifetimes (9–40  $\mu\text{s}$ ) and formed devices with low oxygen sensitivity, while **1–5** (2,830–5,560  $\mu\text{s}$  lifetimes) gave sensors with sensitivities up to 1.15  $\text{hPa}^{-1}$ . Similarly to  $^{13}\text{C}_{70}$ -based sensors, a two-site model was used to fit the Stern-Volmer quenching behavior of **1–14** in thin films. The Stern-Volmer constant ( $K_{\text{SV}}$ ) ranged from 0.00169 to 1.15  $\text{hPa}^{-1}$  and results in devices with similar sensitivities to common metal-based phosphorescent oxygen sensors in PS such as platinum(II) pentafluorophenylphosphyrin ( $K_{\text{SV}} = 1.81 \text{ Pa}^{-1}$ ) (Borisov and Klimant, 2007), platinum(II) tetraphenyltetraabenzoporphyrins ( $K_{\text{SV}} = 1.65\text{--}2.18 \text{ Pa}^{-1}$ ) (Borisov et al., 2008), and ruthenium(II) tris(4,7-diphenyl)-1,10-phenanthroline ( $K_{\text{SV}} = 0.215 \text{ Pa}^{-1}$ ) (Borisov and Klimant, 2007), however, sensitivities were significantly lower than palladium(II) tetraphenyltetraabenzoporphyrins ( $K_{\text{SV}} = 9.1\text{--}10.4 \text{ Pa}^{-1}$ ) (Borisov et al., 2008). Temperature was found to have significant cross-sensitivity with oxygen in these materials however, hindering their application in situations where temperature is uncontrolled.

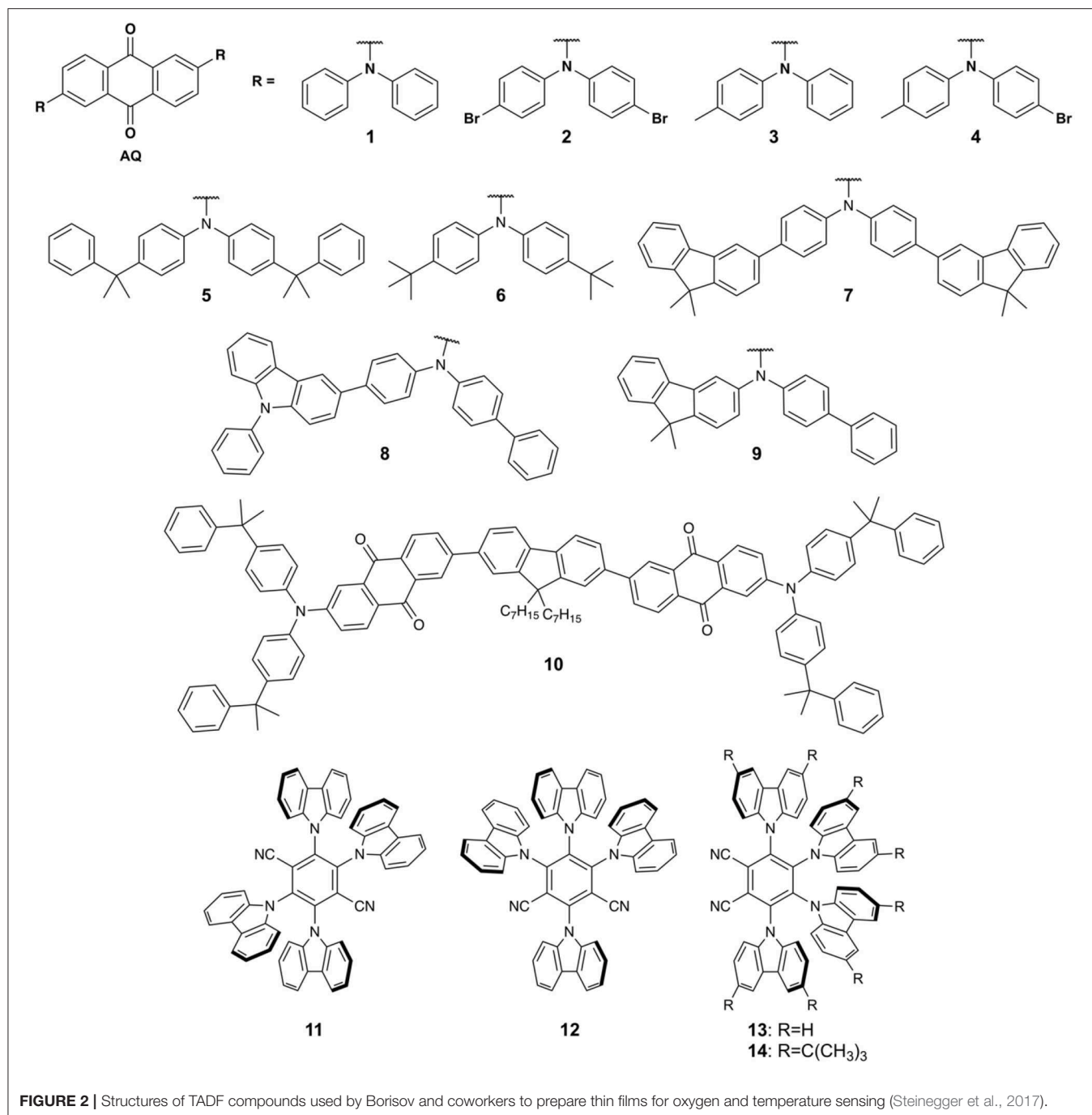


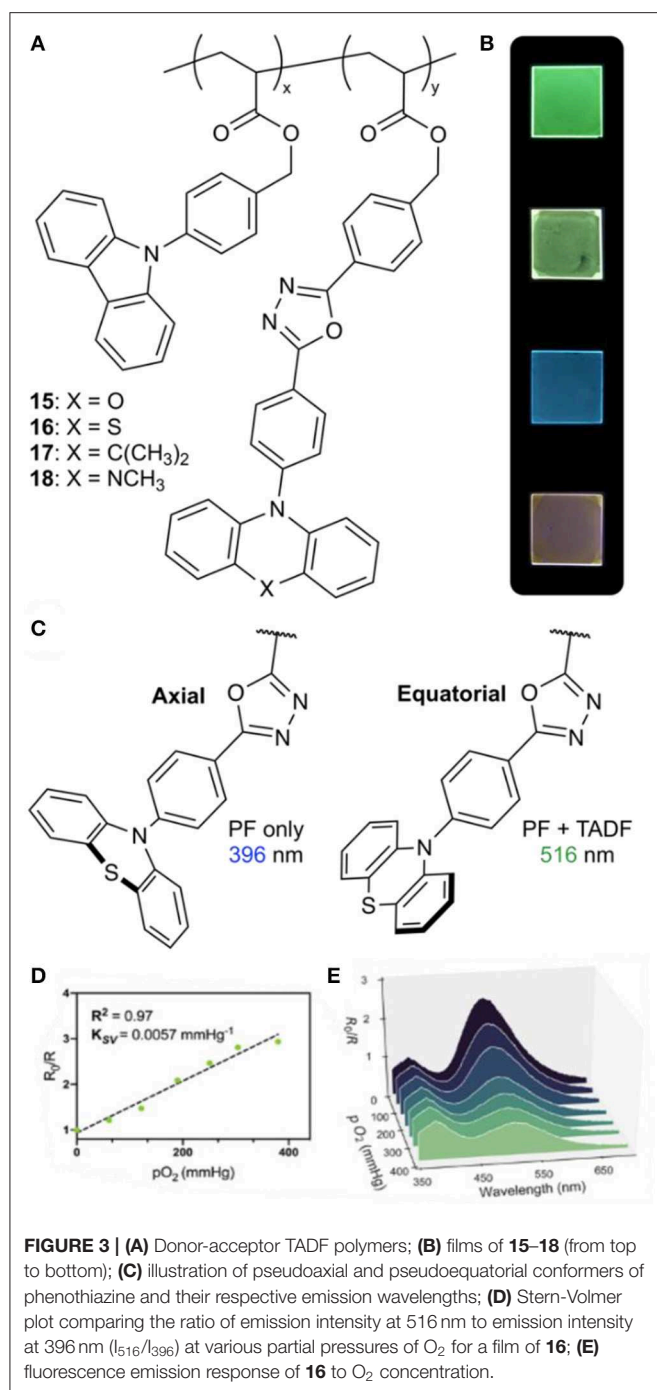
**FIGURE 2 |** Structures of TADF compounds used by Borisov and coworkers to prepare thin films for oxygen and temperature sensing (Steinegger et al., 2017).

Polymers exhibiting TADF were recently developed in our laboratory that act as ratiometric sensors for oxygen, based on the dual-emissive nature of a TADF chromophore. A series of TADF dopants were prepared using an oxadiazole acceptor paired with either phenoxazine (POZ, **15**), phenothiazine (PTZ, **16**), dimethylacridan (DMAC, **17**), or *N*-methylphenazine (MPAZ, **18**) donors to achieve emission ranging from blue to orange (Figures 3A,B) (Tonge et al., 2020). These materials were doped into a carbazole-based host using copper(0)

reversible deactivation radical polymerization (Cu(0)-RDRP), giving molecular weights of  $\sim 20$  kDa with dispersities from 1.10 to 1.45 (Anastasakis et al., 2016; Sauv et al., 2018; Tonge et al., 2019). Using this method, polymers were synthesized containing 5–15 wt.% TADF emitter, with  $\Phi_F$  values as high as 96%.

The PTZ-containing polymer **16** was found to exhibit dual emission in both solution and the solid state, with emission maxima at 396 and 516 nm. The higher-energy violet emission was found to remain constant regardless of





oxygen concentration, while the green emission exhibited oxygen sensitivity characteristic of TADF. There have been several literature reports of PTZ-based donor-acceptor emitters exhibiting dual emission (Daub et al., 2001; Stockmann et al., 2002; Acar et al., 2003; Tanaka et al., 2014; Okazaki et al., 2017; Marghad et al., 2019), arising from two stable conformers of the phenothiazine moiety (Malrieu and Pullman, 1964; Bodea and Silberg, 1968). The pseudoaxial conformer gives a locally excited state with higher-energy emission, while the pseudoequatorial conformer participates in charge transfer,

leading to lower-energy emission and TADF (**Figure 3C**). By taking advantage of the stable emission of the pseudoaxial conformer, oxygen concentration can be determined using the relative intensity of the locally excited and charge transfer emission bands. Stern-Volmer behavior ( $K_{SV} = 0.0057 \text{ mmHg}^{-1}$ ) was observed using neat thin films of **16** with a linear relationship observed between the emission intensity ratio and  $O_2$  concentration up to 50% oxygen by volume at 1 atm (**Figures 3D,E**).

While oxygen-sensitive thin films have potential applications as standalone oxygen sensors, oxygen sensing in aqueous solution would enable applications in biological imaging as well. To demonstrate  $O_2$ -responsiveness in aqueous environments, polymer nanoparticles were prepared by coprecipitating **16** with an amphiphilic polymer, polystyrene-*co*-poly(maleic anhydride) (PS-*co*-PMA). This gave water-soluble “polymer dots” (Pdots) with diameters of  $82 \pm 38 \text{ nm}$ , whose fluorescent properties were similar to those of **16** in thin films. The dual emission of the Pdots showed a responsive color change through the full range of  $O_2$  solubility in water (up to 44 ppm at  $25^\circ\text{C}$ ). In contrast to the thin films, this response was non-linear due the distribution of TADF chromophores in the interior of the Pdots and at the surface, giving environments with variable accessibility to  $O_2$ .

### TADF Temperature Probes

In order to employ TADF materials as temperature-sensing probes, the access of oxygen to the dyes must be limited. Borisov and coworkers developed TADF-based temperature probes by encapsulating compounds **1–14** in the low-oxygen permeability polymer poly(vinylidene chloride-*co*-acrylonitrile) (P(VDC-*co*-AN)) (Steinegger et al., 2017). The use of P(VDC-*co*-AN) gives similar absorption maxima compared with PS films, however, a slight red shift in emission is observed due to the higher polarity of the P(VDC-*co*-AN) host.  $\Phi_F$  and lifetimes are reduced compared to PS with the decrease most pronounced in **6–9** having  $\Phi_F$  values dropping to  $\sim 0.05$ . Lifetimes as a function of temperature could be fit by an Arrhenius model (Equation 1):

$$\tau = \left( k_0 + k_1 e^{-\frac{\Delta E_{ST}}{k_B T}} \right)^{-1} \quad (1)$$

where  $k_0$  is the temperature-independent decay rate,  $k_1$  is a pre-exponential factor,  $k_B$  is the Boltzman constant, and  $T$  the temperature in kelvin. The relative sensitivity (% change in  $\tau$  per K) of the sensors was found to be  $-1.4$  to  $-4.2 \text{ \% K}^{-1}$ , exceeding the sensitivity of similar europium(III) (Khalil et al., 2004), ruthenium(II) (Liebsch et al., 1999), or chromium(III)-doped (Borisov et al., 2010) yttrium aluminum borate-based thermal sensors ( $-0.6$  to  $-2.3 \text{ \% K}^{-1}$ ). **12** and **14** were then incorporated into cationic Eudragit RL100 (ERL) nanoparticles, which are cell-penetrating and provide a route to intracellular fluorescence measurements. ERL is moderately oxygen permeable, and dyes **12** and **14** were chosen to minimize oxygen cross-sensitivity. **12** and **14** ERL dots retained a high sensitivity to temperature, with sensitivities of  $-2.2$  and  $-2.8 \text{ \% K}^{-1}$  at  $298 \text{ K}$ , respectively

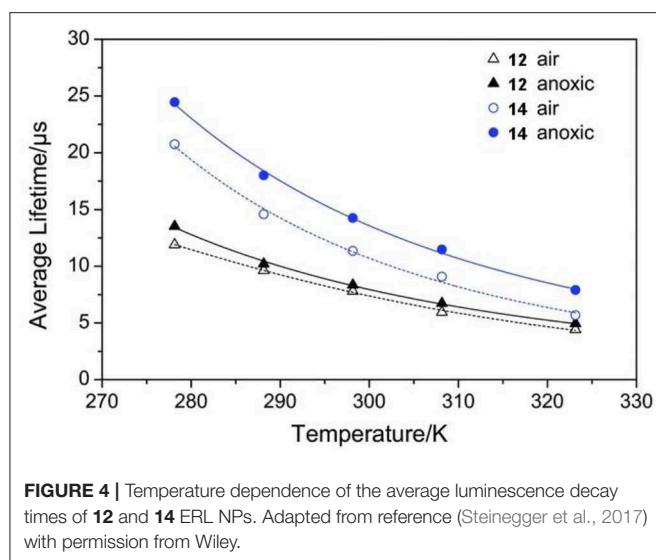


(Figure 4). A small oxygen cross-sensitivity error of  $\pm 4$  K was found for **12** with **14** having a reduced error of  $\pm 1.5$  K.

## FLUORESCENCE LIFETIME-BASED IMAGING AGENTS

Delayed emission from compounds free from phosphorescent heavy-metal dopants are of significant interest in biological imaging. The absence of metals decreases the toxicity and reduces the cost of emitters used as imaging probes. In typical biological systems, autofluorescence and other background fluorescence processes cause significant noise that is detrimental to high resolution imaging. These fluorescent processes have lifetimes in the ns range, however, allowing the use of time gating to remove background fluorescence and allowing only emission from species with long excited-state lifetimes to be detected.

In 2014, Peng and coworkers reported the use of a purely organic fluorophore for TRFI, using fluorescein derivative **19** (Figure 5A) (Xiong et al., 2014). **19** has two absorption features at 485 and 550 nm which density functional theory (DFT) calculations suggest result from transitions between the xanthene and pyran moieties ( $S_0 \rightarrow S_1$ ) and within the xanthene moiety itself ( $S_0 \rightarrow S_4$ ). Steady-state emission in aerated acetonitrile gives emission peaks at 525 and 649 nm and a  $\Phi_F$  of 0.28 is observed in ethanol (Xiong et al., 2013). In deoxygenated solution the peak at 649 nm enhances in intensity 24-fold, and with the application of a 100  $\mu$ s gating time, the 525 nm peak disappears entirely. A multicomponent decay curve is observed with a two-component portion in the  $\mu$ s time scale, with an average lifetime of 22.11  $\mu$ s. Unsurprisingly **19** shows no DF in aerated 10 mM phosphate-buffered saline (PBS), however, upon the addition of BSA DF is observed. **19** has a suitable size and polarity to enter the hydrophobic cavity of BSA, which secludes the fluorophore from molecular oxygen. Additionally, it has been found that BSA has cell-penetrating qualities that enhance cellular uptake (Xiong et al., 2014). TRFI

experiments with nanoparticles (NPs) of **19** encapsulated in BSA using MCF-7 cancer cells demonstrated a large reduction of background fluorescence (Figures 5B–E). Moreover, confocal fluorescence imaging showed extensive permeation of the cell membrane by the TADF NPs, with fluorescence signals localized in the lysosomes. Colocalization experiments using a commercial lysosome tracking dye (LysoSensor Green DND-189) also showed good signal overlap from the two emitters. Finally, biological toxicity of free **19** using the MCF-7 cell line showed minimal cell death observed after 10 h, making this compound promising for applications in TADF-based TRFI.

While the use of BSA as a biopolymer encapsulation matrix enables imaging in aqueous environments, a low  $\Phi_F$  is often observed from the resulting NPs. Tang and coworkers argued that aggregation-caused quenching (ACQ) resulting from high concentrations of fluorophore inside the BSA NPs was responsible, and proposed that this problem could be resolved using TADF molecules that exhibit aggregation-induced emission (AIE) (Gan et al., 2017). Compounds with a benzophenone acceptor and POZ or PTZ donors were investigated, giving materials **20–23** with highly twisted conformations which inhibit  $\pi$  stacking (Figures 6A,B). Solid-state emission maxima for these compounds ranged from 544 to 558 nm, with  $\Phi_F$  values from 0.14 to 0.24 and delayed lifetimes between 0.66 and 1.36  $\mu$ s. Encapsulation in BSA gave TADF NPs in water with diameters ranging from 109 to 150 nm. Confocal laser scanning microscopy (CLSM) showed that the TADF NPs effectively stain HeLa cells and show green to yellow emission within the cytoplasm (Figures 6C–H). Moreover, differences in intracellular viscosities result in the measurement of two distinctive lifetime regions ( $\sim 1,000$  and  $\sim 2,000$  ps, respectively) by TRFI.

While the use of AIE materials facilitates imaging at high brightness within BSA nanoparticles, the cross-sensitivity with intracellular viscosity suggests that the TADF dyes are not well-isolated from the cytoplasm. Alternatively, the use of Pdots formed from amphiphilic polymers offers the ability to encapsulate organic molecules within a hydrophobic core, surrounded by a hydrophilic, biocompatible corona (Kuo et al., 2015; Massey et al., 2015; Yu et al., 2017). The amphiphilic polymer acts as a barrier against oxygen and polar molecules, allowing for time-gated imaging under biological conditions. Moreover, the exclusion of TADF dyes from the cytoplasm prevents cell damage from singlet oxygen produced through triplet quenching or innate toxicity from the fluorophores themselves.

Huang and coworkers investigated the use of TADF Pdots for biological imaging by employing the amphiphilic polymer 1,2-distearoyl-*sn*-glycero-3-phosphoethanolamine-*N*-[methoxy(polyethylene glycol)-2000] (DSPE-PEG, Figure 7) and the TADF material 2,3,5,6-tetracarbazole-4-cyano-pyridine (**24**) (Li et al., 2017). **24** has been shown to have increased emission in the solid state ( $\Phi_F = 54.9\%$ ) compared with chloroform solution ( $\Phi_F = 24.7\%$ ) and, therefore, would not be negatively affected by aggregation within the Pdot. **24** displays green emission, absorbs in the visible range, and exhibits a DF lifetime of 8.3  $\mu$ s in deoxygenated toluene. DSPE-PEG and **24** were precipitated to

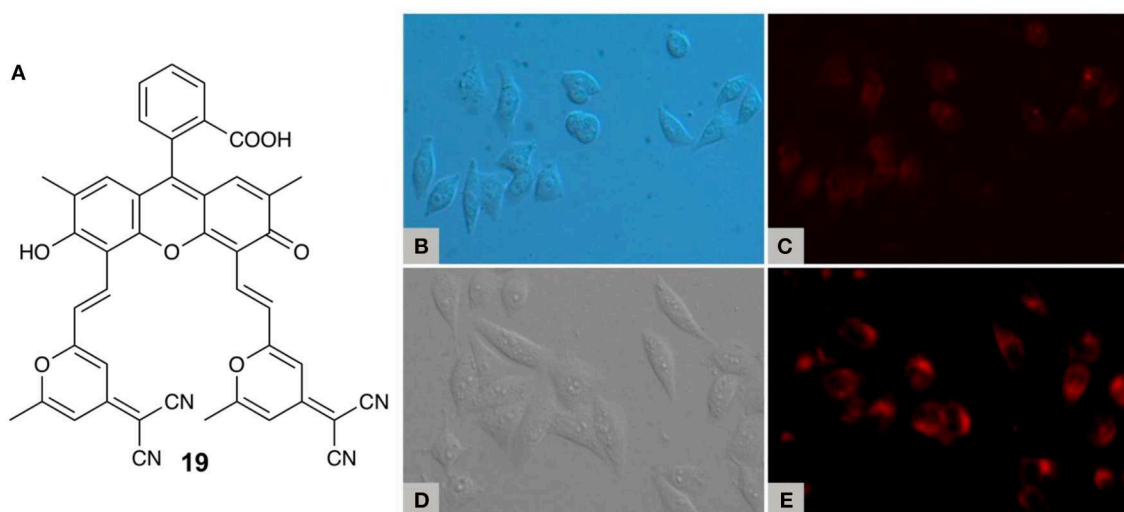


**FIGURE 5 | (A)** Fluorescein derivative **19**; **(B)** bright-field image and **(C)** steady-state luminescence (510–560 nm excitation) of MCF-7 cells immunostained with **19** (20  $\mu$ M) and BSA (40  $\mu$ L, 10 mM) at 37°C; **(D)** bright-field image and **(E)** time-resolved luminescence (510–560 nm excitation) of MCF-7 cells stained with **19** (20  $\mu$ M) and BSA (40  $\mu$ L, 10 mM) at 37°C. Adapted from reference (Xiong et al., 2014) with permission from the American Chemical Society.

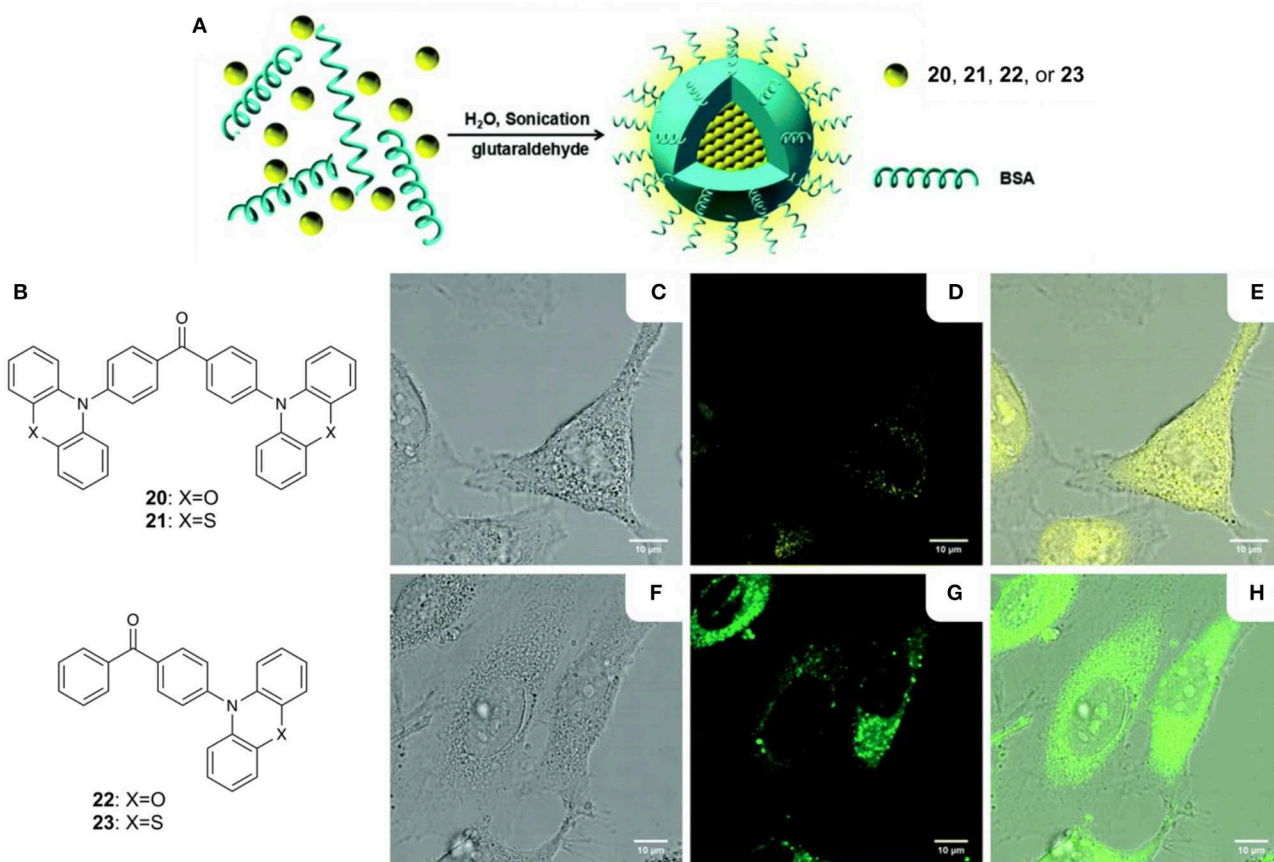


**FIGURE 6 | (A)** Fabrication of BSA NPs; **(B)** AIE TADF compounds **20–23**; confocal fluorescence images of HeLa cells after incubation with **(C–E)** BSA NPs of **21** (10  $\mu$ M of **21**) and **(F–H)** BSA NPs of **22** (10  $\mu$ M of **22**) at 37°C for 0.5 h; **(C,F)** bright-field images; **(D,G)** fluorescence images; **(E,H)** merged bright field and fluorescence images; scale bar = 10  $\mu$ m. Adapted from reference (Gan et al., 2017) with permission from The Royal Society of Chemistry.



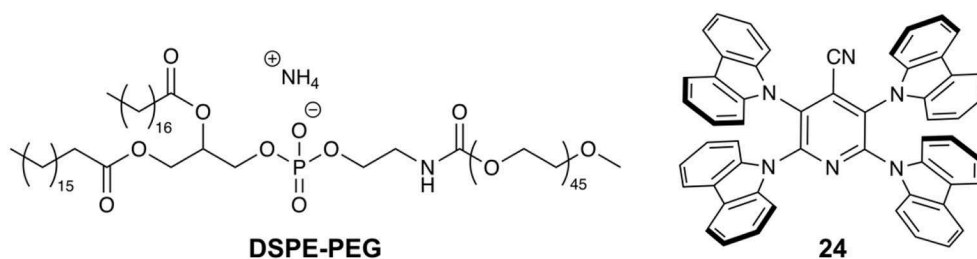


**FIGURE 7** | The amphiphilic polymer DSPE-PEG and TADF **24** used by Huang and coworkers (Li et al., 2017).

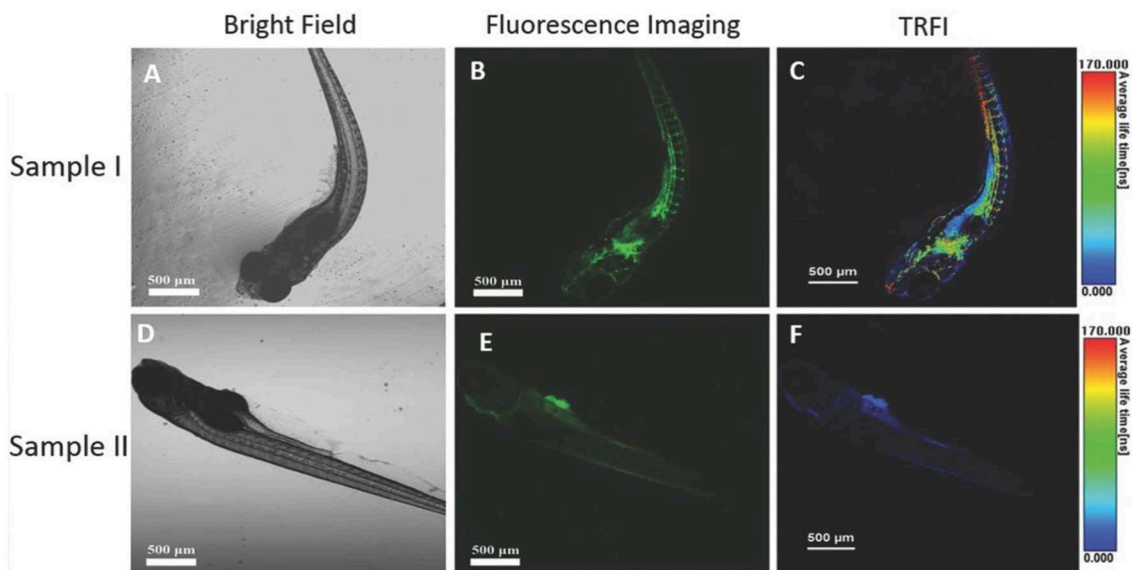


**FIGURE 8** | Confocal fluorescence images of zebrafish: (A–C) zebrafish injected with **24** Pdts; (D–F) zebrafish without any Pdts injected; (A,D) bright field images; (B,E) confocal fluorescence images recorded with 480–580 nm bandpass filters for **24** Pdts upon excitation at 405 nm; (C,F) fluorescence lifetime images. Reproduced from reference (Li et al., 2017) under the Creative Commons CC-BY license.

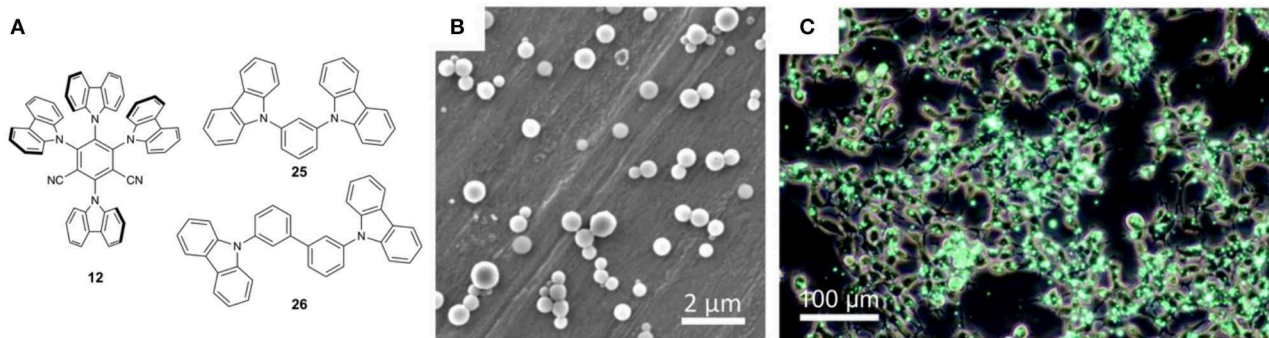


**FIGURE 9** | (A) TADF emitter and host materials; (B) SEM image of 6 wt.% glassy Pdts (2 μm scale bar); (C) combined phase contrast image of glassy Pdts in HEK293 cells after 12 h of incubation (100 μm scale bar). Adapted from reference (Tsuchiya et al., 2019) with permission from The Royal Society of Chemistry.

form Pdts which had a spherical morphology with an average diameter of 17 nm by TEM and  $23 \pm 5$  by DLS. Pdts of **24** show a CT absorption band at  $\sim 450$  nm in water which is red-shifted

compared to free **24** in THF, and emission at 535 nm with  $\Phi_F = 0.38$ . In aerated water a biexponential decay is observed with a long lifetime component of 9.4 μs. Photobleaching studies



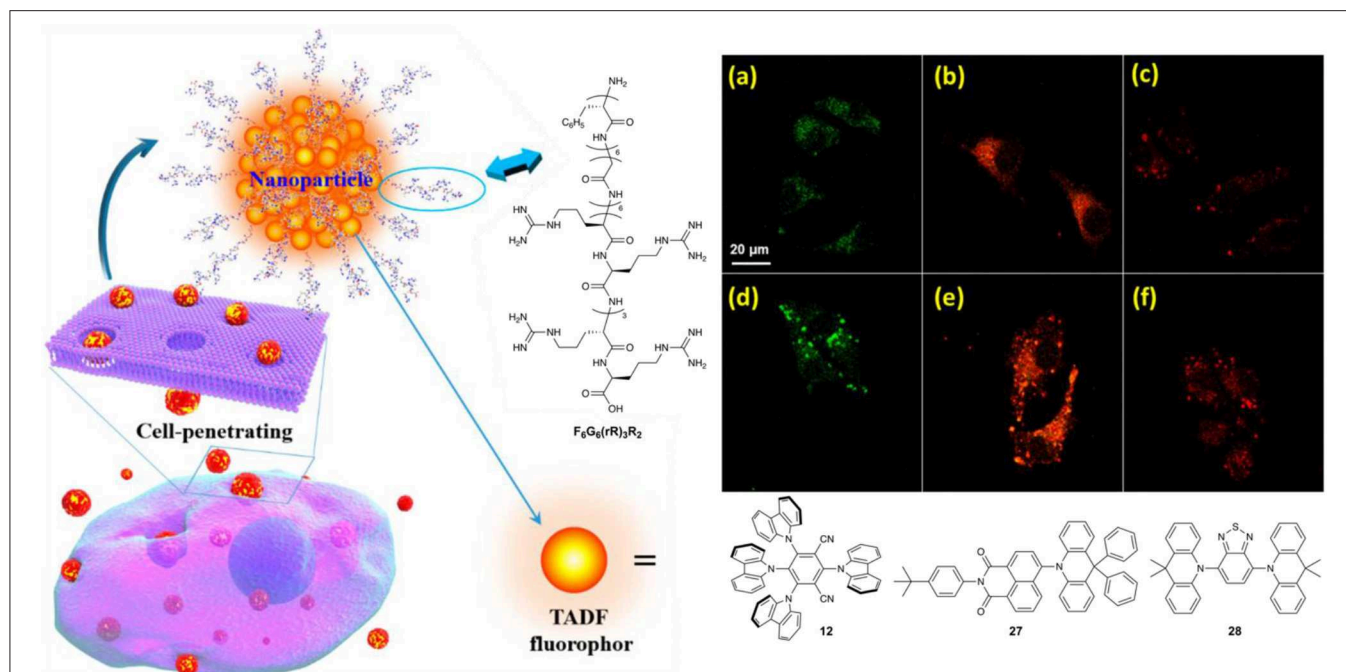


**FIGURE 10 |** Schematic of CPP Pdts fabricated from  $F_6G_6(rR)_3R_2$  and TADF emitters **12**, **27**, and **28**. CLSM images of HeLa cells after incubation with CPP encapsulated (a,d) **12**, (b,e) **27**, (c,f), and **28** Pdts for (a–c) 5 min and (d–f) 15 min. [**12**] = [**27**] = [**28**] =  $2 \mu\text{g mL}^{-1}$ . Adapted from reference (Zhu et al., 2018) with permission from the American Chemical Society.

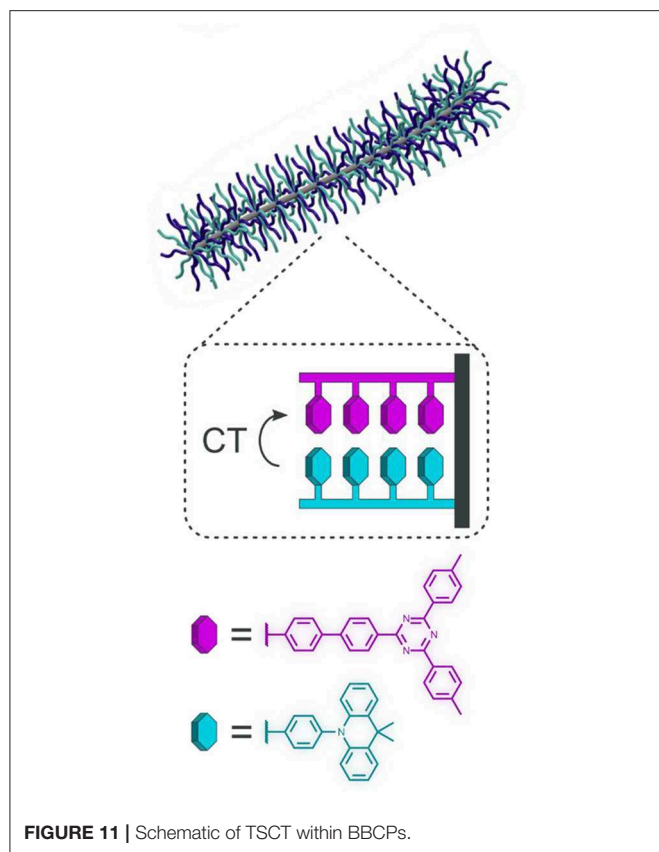
revealed Pdts of **24** retained 90% of their original fluorescence intensity after 45 min of laser irradiation ( $55.6 \text{ mW cm}^{-2}$  at 405 nm).

Pdts of **24** show good  $\Phi_F$ , long lifetimes, and resistance to photobleaching, however, their stability and biocompatibility had to be investigated. To test the chemical stability of the Pdts fluorescence measurements were made in Milli-Q water, PBS, and tris-acetate buffer. Dulbecco's modified Eagle medium (DMEM) was also used to simulate physiological conditions. Compared to the Milli-Q water solution, the fluorescence intensity was minimally affected by PBS and tris-acetate buffer and only decreased by 20% in DMEM. Moreover, in all cases the fluorescence intensity remained stable after 48 h in solution at  $37^\circ\text{C}$ . Toxicity studies were also conducted by incubating HeLa cells with variable concentrations of Pdts for 24 h. A maximum concentration of  $9 \mu\text{M}$  could be used while retaining  $>80\%$  cell viability and concentrations of  $4.5 \mu\text{M}$  or lower resulted in minimal cell death.

The effectiveness of **24** as an imaging probe for *in vitro* studies was determined using HeLa cells as an example system. The cells were incubated with Pdts of **24** ( $0.5 \mu\text{M}$ ) in PBS for 2 h. Short-lived background fluorescence is observed from the cytoplasm while emission from **24** is detected from the cell membrane with an average lifetime of 165 ns. Co-staining with **24** Pdts and a cell membrane marker, 1,1'-diiodoctadecyl-3,3,3',3'-tetramethylindocarbocyanine perchlorate (DiIC18), gives overlapping emission confirming the localization of the

Pdts. It was also proposed that the lipophilicity of DSPE-PEG causes Pdts near the cell to interact with the cell membrane. During this process, dye **24** can transfer from the Pdot into the cell membrane, where it is retained. This mechanism is consistent with the observation that excited state lifetimes shortened significantly during imaging compared to free Pdts of **24** measured in water. Finally, the membrane-labeling property of Pdts of **24** was explored by confocal imaging and TRFI of a living zebrafish, giving a clear picture of the vascular network of the animal with minimal background fluorescence (**Figure 8**).

While polymer encapsulation often reduces  $\Phi_F$  values and red-shifts the emission of TADF dyes, Adachi and coworkers recently applied concepts from OLED design to address these issues and improve the performance of TADF Pdts (Tsuchiya et al., 2019). Organic semiconductor host materials are commonly used in OLEDs to isolate emitters and prevent aggregation quenching effects, and it was hypothesized that these same ideas could be used to increase  $\Phi_F$ , reduce aggregation, and enhancing the stability of the TADF dyes in Pdts. By incorporating TADF dyes into the glassy semiconductor host **25** within DSPE-PEG, TADF dye **12** (**Figure 9A**) could be effectively protected from the surrounding medium and aggregation could be prevented. The combination of **12**+**25** had previously been shown to be an effective dye/matrix combination in the emissive layer of OLEDs (Uoyama et al., 2012; Nakanotani et al., 2013), suggesting that energy transfer from **25** to **12** should be highly favorable. Aqueous mixtures of **12**, **25**, and DSPE-PEG were heated to  $180^\circ\text{C}$  under pressure and then rapidly cooled to



melt and subsequently solidify **12** and **25** within the Pdot. This produced spherical particles (**Figure 9B**) with an average diameter of 371 nm by DLS. The use of host **26** in place of **25** was also attempted, but it was found that the high melting point of **26** (268.7°C) and lower crystallization temperature (131.3°C) resulted in microcrystal formation during processing. Aqueous glassy Pdots of **12+25** gave slightly red-shifted emission and higher  $\Phi_F$  ( $\lambda_{em} = 516$  nm and  $\Phi_F = 0.94$ ) compared with **12** alone in toluene solution ( $\lambda_{em} = 498$  nm and  $\Phi_F = 0.83$ ), suggesting that the strategy was promising. Importantly, the fabrication of glassy Pdots in argon-saturated water was found to be essential as the use of aerated water during fabrication resulted in a drastic decrease in  $\Phi_F$  of 32%. A delayed lifetime of 3.1  $\mu$ s was observed from the glassy Pdots which was nearly insensitive to the presence of oxygen. High photo-stability was observed with intensity dropping by only 25% after 115 min of irradiation. Minimal cytotoxicity was observed with HEK293 cells, consistent with the work of Huang and coworkers (Li et al., 2017) and the known biocompatibility of DSPE-PEG. The Pdots showed strong fluorescence in HEK293 cells (**Figure 9C**) with cells retaining their emission after 7 days of culturing. Long-term traceability experiments were also conducted with HEK293 cells to utilize the high stability and low cytotoxicity of the glassy Pdots. The glassy Pdots were observable for 21 days with cell viability matching that of the control cells. Interestingly, cell membrane labeling was not observed in this study, despite the use of the same amphiphilic

polymer employed in the earlier study by Huang and coworkers (Li et al., 2017).

Despite the utility of non-glassy and glassy Pdots in TRFI imaging, both require several hours of incubation time to effectively stain cells due to their low membrane permeability. Zhao and coworkers used a cell-penetrating peptide (CPP) as an alternative encapsulating amphiphile to address this issue (Zhu et al., 2018). The CPP ( $F_6G_6(rR)_3R_2$ ) consisted of a hydrophilic octamer  $[(rR)_3R_2]$  formed from L-arginine (R) and D-arginine (r), a hexamer of glycine (G), and a hydrophobic hexamer of phenylalanine (F) (**Figure 10**) (Zhu et al., 2018).  $(rR)_3R_2$  was used as the hydrophilic moiety of the CPP amphiphile due to previous research showing the high biocompatibility of the fragment (Ma et al., 2012). The TADF dyes **12**, **27**, and **28** were used as they have been successfully incorporated into high performance OLEDs and give a range of emission wavelengths. Aqueous CPP Pdot solutions were formed using a reprecipitation method giving particles 92 to 177 nm in diameter by DLS. **12**, **27**, and **28** Pdots showed emission at 555, 607, and 657 nm with  $\Phi_F$  values of 0.12, 0.025, and 0.008, respectively. Emission is red-shifted and  $\Phi_F$  values were drastically reduced compared to their values in toluene solution due to the effects of aggregation and the polar amide backbone of  $F_6G_6(rR)_3R_2$ . All fluorescence decays were multi-exponential with delayed lifetimes ranging from 1.8 to 93.7  $\mu$ s. No significant change in lifetime was observed between aerated and deoxygenated solution.

HeLa and 3T3 cells were used to test the cell-penetrating TADF PDots as imaging agents. As expected, low cytotoxicity was observed from all three TADF Pdots using both cell lines with 24 h of incubation at 37°C. Cell viabilities remained above 80% with up to 10  $\mu$ g/mL of TADF dye. After only 5 min of incubation with these Pdots (2  $\mu$ g/mL of TADF dye) HeLa cells showed fluorescence by CLSM, with a 44% or higher fluorescence-positive rate by flow cytometry (**Figures 10A–C**). With an incubation time of 15 min the fluorescence-positive-rate rose to a minimum of 54%, cellular accumulation of the TADF Pdots increased dramatically (**Figures 10D–F**). Cellular uptake was also conducted with 3T3 cells with similar results. In this study, TRFI could be used with a delay time of only 50 ns to remove background fluorescence, yet delays as long as 500 ns could also be used with observable emission.

## Controlling TADF With Polymer Morphology

Given the applications of TADF materials in polymers for imaging and sensing, our group has recently explored methods for modulating TADF behavior in polymers by controlling polymer morphology (Tonge and Hudson, 2019). With typical TADF emitters it can be challenging to achieve turn-on/off delayed fluorescence emission using a small molecule emitter in which the donor and acceptor are bound covalently. In 2017, Wang and coworkers reported that TADF behavior could be observed in non-conjugated copolymers of discrete donor and acceptor monomers using a through-space charge transfer (TSCT) mechanism (Shao et al., 2017). Wang and coworkers hypothesized that minimization of donor-acceptor overlap and

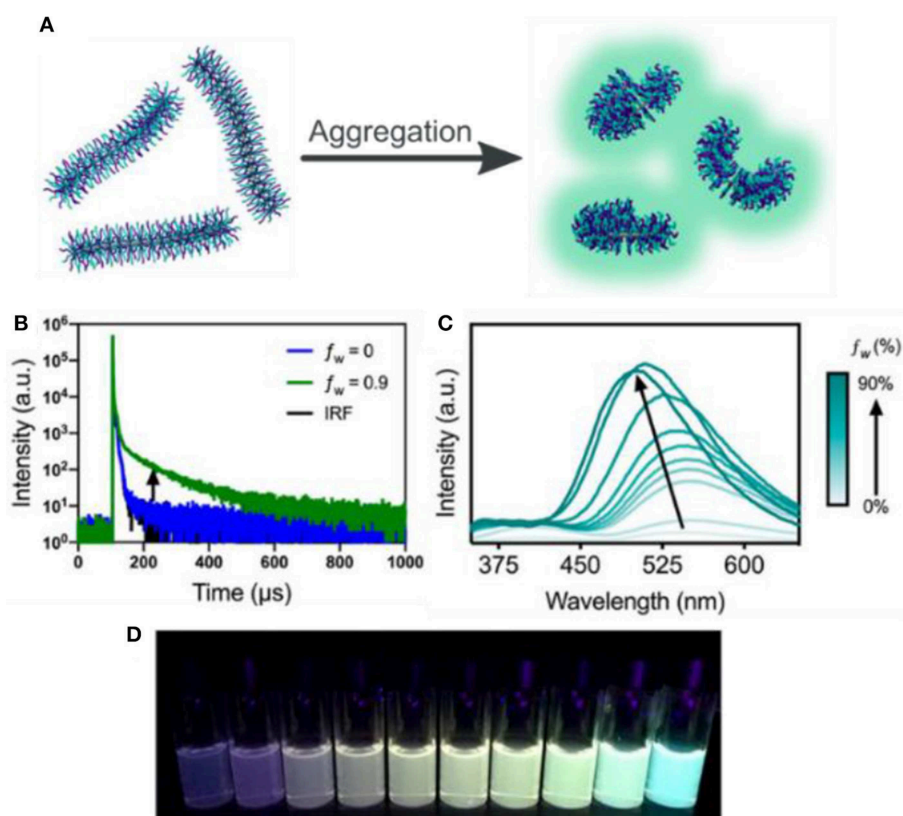


**FIGURE 12 | (A)** Schematic of conformational changes in the aggregated state; **(B)** lifetime increase from increasing water fraction ( $f_w = 0$  to 90%) at a concentration of 0.02 mg mL<sup>-1</sup>; **(C)** aggregation induced emission of miktoarm bottlebrush copolymer (0.02 mg mL<sup>-1</sup>), normalized such that the maximum intensity at  $f_w = 0\%$  is set to 1 and all other spectra are scaled accordingly; **(D)** image of the fluorescent emission of the corresponding aggregated samples from  $f_w = 0$ –90%.  $\lambda_{\text{ex}} = 313$  nm.

a small  $\Delta E_{\text{ST}}$  could be achieved simply by copolymerizing electron-rich and electron-poor organic semiconductors, using a polymer backbone to achieve close D-A contact. This strategy was used successfully to fabricate high-efficiency blue OLEDs, as well as achieving color-tunable emission by modifying the acceptor electronic properties (Hu et al., 2019). Excited by this new paradigm in TADF polymer research, we sought to determine if alternative polymer morphologies could be used to control TSCT emission, using bottlebrush copolymers (BBCPs). Consisting of polymeric side chains attached to a linear backbone, the steric interactions of the densely packed side chains induce an extended backbone conformation, allowing for discrete nanoscale domains to be prepared along the length of the polymer.

Using this approach, we designed a series of BBCPs composed of acridine-based donors and triazine-based acceptors, varying the degree of donor-acceptor blending along the BBCP to control TSCT (**Figure 11**) (Tonge and Hudson, 2019). Grafting density along the bottlebrush backbone was maximized by employing a grafting-through polymerization strategy, in which short linear polymers functionalized with reactive norbornene end groups (termed “macromonomers”) are prepared first, then polymerized using ring-opening metathesis polymerization to give the BBCPs. Three bottlebrush copolymers containing

50% acridine-based donor and 50% triazine-based acceptor were prepared: one bottlebrush in which the macromonomers themselves were random D-A copolymers, another mixed arm (or “miktoarm”) bottlebrush consisting of a random copolymer of D or A macromonomers, and a third in which the D and A macromonomers were polymerized to give a diblock BBCP.

These blended BBCPs were found to exhibit unique photophysical properties as a direct result of their morphology. The diblock copolymer displayed only prompt fluorescence in both the solution and solid state, while the miktoarm and random copolymers showed some degree of TSCT emission. The fully blended BBCP exhibited only TSCT emission in both the solid state and in solution, as near-complete mixing was ensured by the microstructure of the bottlebrush. Interestingly, by segregating the donor and acceptor functionalities in the diblock polymer, minimal interpenetration of these blocks was observed in the solid state or in solution, resulting in emission from only the monomers themselves. This result is noteworthy as a simple spin-cast film of a blend of linear donor and acceptor polymers gives both monomer and TSCT emission. This implies that using a bottlebrush backbone, the degree of interaction between these monomers can be controlled simply by modulating polymer morphology.



The TSCT in these bottlebrushes was also found to exhibit a substantial AIE effect, particularly in the case of the miktoarm copolymer (**Figure 12A**). When dissolved in THF, the miktoarm polymer demonstrates an approximately equal mix of prompt emission and TSCT emission, as adjacent chains are spread out due to favorable interactions with the solvent. Upon aggregation in the presence of water, however, the solvent is excluded, leading to a significant increase in TSCT emission and a corresponding decrease in prompt fluorescence (**Figures 12B–D**). This results in a 15.8-fold increase in brightness for the delayed fluorescence peak, which is not observed in the case of the diblock bottlebrush where TSCT is prevented by the polymer morphology. The fluorescence lifetime was also found to increase substantially upon aggregation of the random and miktoarm BBCPs, a feature that can potentially be taken advantage of for fluorescence lifetime imaging and other sensing applications.

## CONCLUSIONS AND OUTLOOK

Alongside their applications in OLEDs, TADF materials are becoming increasingly attractive as emitters for sensors and imaging probes. Embedding TADF materials in polymer films or nanostructures has unlocked many such applications, allowing these materials to be compatible for applications such as biological imaging, and presenting new avenues for controlling the photophysics of the TADF dopant. Taking advantage of triplet quenching processes, polymer thin films have been demonstrated as effective sensors for molecular oxygen with tunable sensitivity depending on the polymer host chosen. Using a TADF material with dual emission, it has been demonstrated that oxygen sensing is also possible without internal calibrants, enabling color-contrast imaging with water-soluble nanoparticles. Using polymers with low oxygen permeability, effective temperature sensors with high sensitivity have also been developed with dynamic ranges tunable simply by the TADF dopant used. The effect of TADF dopant concentration on oxygen permeability and TADF is understudied and would bring benefit to the community.

Using BSA to encapsulate TADF emitters, water-soluble, biocompatible nanoparticles can be formed which permit the use of TADF compounds in TRFI. By using TADF compounds exhibiting AIE behavior or by incorporating glassy semiconductor hosts into the nanoparticle, the detrimental

effects of aggregation can be alleviated and imaging using TADF nanoparticles can be improved. TADF Pdots can be formed from amphiphilic polymers to retain the high brightness of the dyes in aqueous media, and cell-penetrating peptides can be used as effective encapsulating agents to increase cellular uptake. Finally, polymer morphology alone has recently been found to be an effective method for controlling TSCT TADF, either by aggregation of TADF-based bottlebrush fibers, or by controlling the extent of D-A mixing along a bottlebrush backbone to give the level of TADF desired.

Stimuli-responsive polymers exploiting TADF have now opened up a wide range of future avenues for research in sensors and biological imaging. Time-gated detection is now possible in aqueous environments at high brightness without the use of phosphorescent metal complexes, and in some cases without the need for colocalization dyes for calibration. This is sure to create opportunities for TADF materials in the growing field of theranostics, wherein chemistries for cell targeting, imaging, and therapy are combined onto a single nanoparticle carrier. In imaging applications, the potential for TADF dopant leakage has yet to be addressed, with current implementations relying on the poor solubility of TADF dyes in water to prevent emitter loss from the polymer particle. Covalent incorporation of TADF dyes into the polymer structure would prevent this entirely, and presents a promising strategy deserving of further research. Moreover, imaging probes with high stability to photobleaching, high  $\Phi_F$ , and enhanced cellular uptake have yet to be achieved and are sure to be actively sought by the community. Overall, we believe that stimuli-responsive polymers exhibiting TADF have only begun to be explored, and are sure to have a bright future in biological, analytical, and photophysical research.

## AUTHOR CONTRIBUTIONS

This review was written by NP, CT, and ZH.

## ACKNOWLEDGMENTS

The authors thank the Natural Sciences and Engineering Council of Canada (NSERC) for financial support. NP thanks NSERC for a postgraduate scholarship, and ZH is grateful for support from the Canada Research Chairs Program.

## REFERENCES

- Acar, N., Kurzawa, J., Fritz, N., Stockmann, A., Roman, C., Schneider, S., et al. (2003). Phenothiazine—pyrene dyads: photoinduced charge separation and structural relaxation in the CT state. *J. Phys. Chem. A* 107, 9530–9541. doi: 10.1021/jp036250u
- Anastasakis, A., Nikolaou, V., Nurumbetov, G., Wilson, P., Kempe, K., Quinn, J. F., et al. (2016). Cu(0)-mediated living radical polymerization: a versatile tool for materials synthesis. *Chem. Rev.* 116, 835–877. doi: 10.1021/acs.chemrev.5b00191
- Baleizão, C., and Berberan-Santos, M. N. (2011). The brightest fullerene: a new isotope effect in molecular fluorescence and phosphorescence. *ChemPhysChem* 12, 1247–1250. doi: 10.1002/cphc.201100156
- Baleizão, C., Nagl, S., Schäferling, M., Berberan-Santos, M. N., and Wolfbeis, O. S. (2008). Dual fluorescence sensor for trace oxygen and temperature with unmatched range and sensitivity. *Anal. Chem.* 80, 6449–6457. doi: 10.1021/ac801034p
- Bodea, C., and Silberg, I. (1968). Recent advances in the chemistry of phenothiazines. *Adv. Heterocycl. Chem.* 9, 321–460. doi: 10.1016/S0065-2725(08)60375-X
- Borisov, S. M., Gatterer, K., Bitschnau, B., and Klimant, I. (2010). Preparation and characterization of chromium(III)-activated yttrium aluminum borate: a new thermographic phosphor for optical sensing and imaging at ambient temperatures. *J. Phys. Chem. C* 114, 9118–9124. doi: 10.1021/jp1016467
- Borisov, S. M., and Klimant, I. (2007). Ultrabright oxygen optodes based on cyclometalated iridium(III) coumarin complexes. *Anal. Chem.* 79, 7501–7509. doi: 10.1021/ac0710836



- Borisov, S. M., Nuss, G., and Klimant, I. (2008). Red light-excitable oxygen sensing materials based on platinum(II) and palladium(II) benzoporphyrins. *Anal. Chem.* 80, 9435–9442. doi: 10.1021/ac801521v
- Chatterjee, T., and Wong, K. T. (2019). Perspective on host materials for thermally activated delayed fluorescence organic light emitting diodes. *Adv. Opt. Mater.* 4:1800565. doi: 10.1002/adom.201800565
- Chen, X.-K., Kim, D., and Brédas, J.-L. (2018). Thermally Activated Delayed Fluorescence (TADF) path toward efficient electroluminescence in purely organic materials: molecular level insight. *Acc. Chem. Res.* 51, 2215–2224. doi: 10.1021/acs.accounts.8b00174
- Chen, X. K., Zhang, S. F., Fan, J. X., and Ren, A. M. (2015). Nature of highly efficient thermally activated delayed fluorescence in organic light-emitting diode emitters: nonadiabatic effect between excited states. *J. Phys. Chem. C* 119, 9728–9733. doi: 10.1021/acs.jpcc.5b00276
- Cho, Y. J., Jeon, S. K., Chin, B. D., Yu, E., and Lee, J. Y. (2015). The design of dual emitting cores for green thermally activated delayed fluorescent materials. *Angew. Chem. Int. Ed.* 54, 5201–5204. doi: 10.1002/anie.201412107
- Daub, J., Engl, R., Kurzawa, J., Miller, S. E., Schneider, S., Stockmann, A., et al. (2001). Competition between conformational relaxation and intramolecular electron transfer within phenothiazine-pyrene dyads. *J. Phys. Chem. A* 105, 5655–5665. doi: 10.1021/jp0037293
- DeRosa, C. A., Samonina-Kosicka, J., Fan, Z., Hendargo, H. C., Weitzel, D. H., Palmer, G. M., et al. (2015). Oxygen sensing difluoroboron dinaphthoylethane poly(lactide). *Macromolecules* 48, 2967–2977. doi: 10.1021/acs.macromol.5b00394
- Dias, F. B. (2015). Kinetics of thermal-assisted delayed fluorescence in blue organic emitters with large singlet-triplet energy gap. *Philos. Trans. R. Soc. A Math. Phys. Eng. Sci.* 373:20140447. doi: 10.1098/rsta.2014.0447
- Dias, F. B., Santos, J., Graves, D. R., Data, P., Nobuyasu, R. S., Fox, M. A., et al. (2016). The role of local triplet excited states and D-A relative orientation in thermally activated delayed fluorescence: photophysics and devices. *Adv. Sci.* 3:1600080. doi: 10.1002/advs.201600080
- Endo, A., Sato, K., Yoshimura, K., Kai, T., Kawada, A., Miyazaki, H., et al. (2011). Efficient up-conversion of triplet excitons into a singlet state and its application for organic light emitting diodes. *Appl. Phys. Lett.* 98:083302. doi: 10.1063/1.3558906
- Gan, S., Zhou, J., Smith, T. A., Su, H., Luo, W., Hong, Y., et al. (2017). New AIEgens with delayed fluorescence for fluorescence imaging and fluorescence lifetime imaging of living cells. *Mater. Chem. Front.* 1, 2554–2558. doi: 10.1039/C7QM00286F
- Gibson, J., Monkman, A. P., and Penfold, T. J. (2016). The importance of vibronic coupling for efficient reverse intersystem crossing in thermally activated delayed fluorescence molecules. *ChemPhysChem* 17, 2956–2961. doi: 10.1002/cphc.201600662
- Gibson, J., and Penfold, T. J. (2017). Nonadiabatic coupling reduces the activation energy in thermally activated delayed fluorescence. *Phys. Chem. Chem. Phys.* 19, 8428–8434. doi: 10.1039/C7CP00719A
- Goushi, K., Yoshida, K., Sato, K., and Adachi, C. (2012). Organic light-emitting diodes employing efficient reverse intersystem crossing for triplet-to-singlet state conversion. *Nat. Photonics* 6, 253–258. doi: 10.1038/nphoton.2012.31
- He, T., Ren, C., Li, Z., Xiao, S., Li, J., Lin, X., et al. (2018). Thermally activated delayed fluorescence organic dots for two-photon fluorescence lifetime imaging. *Appl. Phys. Lett.* 112:211102. doi: 10.1063/1.5034375
- Hosokai, T., Matsuzaki, H., Nakanotani, H., Tokumaru, K., Tsutsui, T., Furube, A., et al. (2017). Evidence and mechanism of efficient thermally activated delayed fluorescence promoted by delocalized excited states. *Sci. Adv.* 3:e1603282. doi: 10.1126/sciadv.1603282
- Hu, J., Li, Q., Wang, X., Shao, S., Wang, L., Jing, X., et al. (2019). Developing through-space charge transfer polymers as a general approach to realize full-color and white emission with thermally activated delayed fluorescence. *Angew. Chem. Int. Ed.* 58, 8405–8409. doi: 10.1002/anie.201902264
- Jankus, V., Data, P., Graves, D., McGuinness, C., Santos, J., Bryce, M. R., et al. (2014). Highly efficient TADF OLEDs: how the emitter-host interaction controls both the excited state species and electrical properties of the devices to achieve near 100% triplet harvesting and high efficiency. *Adv. Funct. Mater.* 24, 6178–6186. doi: 10.1002/adfm.201400948
- Khalil, G. E., Lau, K., Phelan, G. D., Carlson, B., Gouterman, M., Callis, J. B., et al. (2004). Europium beta-diketonate temperature sensors: effects of ligands, matrix, and concentration. *Rev. Sci. Instrum.* 75, 192–206. doi: 10.1063/1.1632997
- Kochmann, S., Baleizão, C., Berberan-Santos, M. N., and Wolfbeis, O. S. (2013). Sensing and imaging of oxygen with parts per billion limits of detection and based on the quenching of the delayed fluorescence of  $^{13}\text{C}_{70}$  fullerene in polymer hosts. *Anal. Chem.* 85, 1300–1304. doi: 10.1021/ac303486f
- Kuo, S.-Y., Li, H.-H., Wu, P.-J., Chen, C.-P., Huang, Y.-C., and Chan, Y.-H. (2015). Dual colorimetric and fluorescent sensor based on semiconducting polymer dots for ratiometric detection of lead ions in living cells. *Anal. Chem.* 87, 4765–4771. doi: 10.1021/ac504845t
- Li, T., Yang, D., Zhai, L., Wang, S., Zhao, B., Fu, N., et al. (2017). Thermally activated delayed fluorescence organic dots (TADF Odots) for time-resolved and confocal fluorescence imaging in living cells and *in vivo*. *Adv. Sci.* 4:1600166. doi: 10.1002/advs.201600166
- Liebsch, G., Klimant, I., and Wolfbeis, O. S. (1999). Luminescence lifetime temperature sensing based on sol-gels and poly(acrylonitrile)s dyed with ruthenium metal-ligand complexes. *Adv. Mater.* 11, 1296–1299. doi: 10.1002/(SICI)1521-4095(199910)11:15<1296::AID-ADMA1296>3.0.CO;2-B
- Lim, B. T., Okajima, S., Chandra, A. K., and Lim, E. C. (1981). Radiationless transitions in electron donor-acceptor complexes: selection rules for  $S1 \rightarrow T$  intersystem crossing and efficiency of  $S1 \rightarrow S0$  internal conversion. *Chem. Phys. Lett.* 79, 22–27. doi: 10.1016/0009-2614(81)85280-3
- Ma, Y., Gong, C., Ma, Y., Fan, F., Luo, M., Yang, F., et al. (2012). Direct cytosolic delivery of cargoes *in vivo* by a chimera consisting of D- and L-arginine residues. *J. Control. Release* 162, 286–294. doi: 10.1016/j.jconrel.2012.07.022
- Malrieu, J. P., and Pullman, B. (1964). Sur les propriétés électroniques de la phénothiazine et de son radical. *Theor. Chim. Acta* 2, 293–301. doi: 10.1007/BF00527056
- Marghad, I., Bencheikh, F., Wang, C., Manolikakes, S., Rérat, A., Gosmini, C., et al. (2019). Control of the dual emission from a thermally activated delayed fluorescence emitter containing phenothiazine units in organic light-emitting diodes. *RSC Adv.* 9, 4336–4343. doi: 10.1039/C8RA10393C
- Marian, C. M. (2016). Mechanism of the triplet-to-singlet upconversion in the assistant dopant ACRXTN. *J. Phys. Chem. C* 120, 3715–3721. doi: 10.1021/acs.jpcc.6b00060
- Massey, M., Wu, M., Conroy, E. M., and Algar, W. R. (2015). Mind your P's and Q's: the coming of age of semiconducting polymer dots and semiconductor quantum dots in biological applications. *Curr. Opin. Biotechnol.* 34, 30–40. doi: 10.1016/j.copbio.2014.11.006
- Nakanotani, H., Masui, K., Nishide, J., Shibata, T., and Adachi, C. (2013). Promising operational stability of high-efficiency organic light-emitting diodes based on thermally activated delayed fluorescence. *Sci. Rep.* 3:2127. doi: 10.1038/srep02127
- Okazaki, M., Takeda, Y., Data, P., Pander, P., Higginbotham, H., Monkman, A. P., et al. (2017). Thermally activated delayed fluorescent phenothiazine-dibenzo[a,j]phenazine-phenothiazine triads exhibiting tricolor-changing mechanochromic luminescence. *Chem. Sci.* 8, 2677–2686. doi: 10.1039/C6SC04863C
- Palmeira, T., and Berberan-Santos, M. N. (2018). “TADF kinetics and data analysis in photoluminescence and in electroluminescence,” in *Highly Efficient OLEDs* (Weinheim: Wiley-VCH Verlag GmbH & Co. KGaA), 229–255. doi: 10.1002/9783527691722.ch7
- Penfold, T. J., Dias, F. B., and Monkman, A. P. (2018). The theory of thermally activated delayed fluorescence for organic light emitting diodes. *Chem. Commun.* 54, 3926–3935. doi: 10.1039/C7CC09612G
- Sauvé, E. R., Tonge, C. M., Paisley, N. R., Cheng, S., and Hudson, Z. M. (2018). Cu(0)-RDRP of acrylates based on p-type organic semiconductors. *Polym. Chem.* 9, 1397–1403. doi: 10.1039/C8PY00295A
- Shao, S., Hu, J., Wang, X., Wang, L., Jing, X., and Wang, F. (2017). Blue thermally activated delayed fluorescence polymers with nonconjugated backbone and through-space charge transfer effect. *J. Am. Chem. Soc.* 139, 17739–17742. doi: 10.1021/jacs.7b10257
- Steingegger, A., Klimant, I., and Borisov, S. M. (2017). Purely organic dyes with thermally activated delayed fluorescence—a versatile class of

- indicators for optical temperature sensing. *Adv. Opt. Mater.* 5:1700372. doi: 10.1002/adom.201700372
- Stockmann, A., Kurzawa, J., Fritz, N., Acar, N., Schneider, S., Daub, J., et al. (2002). Conformational control of photoinduced charge separation within phenothiazine-pyrene dyads. *J. Phys. Chem. A* 106, 7958–7970. doi: 10.1021/jp0142987
- Tanaka, H., Shizu, K., Nakanotani, H., and Adachi, C. (2014). Dual intramolecular charge-transfer fluorescence derived from a phenothiazine-triphenyltriazine derivative. *J. Phys. Chem. C* 118, 15985–15994. doi: 10.1021/jp501017f
- Tonge, C. M., and Hudson, Z. M. (2019). Interface-dependent aggregation-induced delayed fluorescence in bottlebrush polymer nanofibers. *J. Am. Chem. Soc.* 141, 13970–13976. doi: 10.1021/jacs.9b07156
- Tonge, C. M., Paisley, N. R., Polgar, A. M., Lix, K., Algar, W. R., and Hudson, Z. M. (2020). Color-tunable thermally activated delayed fluorescence in oxadiazole-based acrylic copolymers: photophysical properties and applications in ratiometric oxygen sensing. *ACS Appl. Mater. Interfaces* 12, 6525–6535. doi: 10.1021/acsami.9b22464
- Tonge, C. M., Yuan, F., Lu, Z.-H., and Hudson, Z. M. (2019). Cu(0)-RDRP as an efficient and low-cost synthetic route to blue-emissive polymers for OLEDs. *Polym. Chem.* 10, 3288–3297. doi: 10.1039/C9PY00294D
- Tsuchiya, Y., Ikesue, K., Nakanotani, H., and Adachi, C. (2019). Photostable and highly emissive glassy organic dots exhibiting thermally activated delayed fluorescence. *Chem. Commun.* 55, 5215–5218. doi: 10.1039/C9CC01420A
- Uoyama, H., Goushi, K., Shizu, K., Nomura, H., and Adachi, C. (2012). Highly efficient organic light-emitting diodes from delayed fluorescence. *Nature* 492, 234–238. doi: 10.1038/nature11687
- Wong, M. Y., and Zysman-Colman, E. (2017). Purely organic thermally activated delayed fluorescence materials for organic light-emitting diodes. *Adv. Mater.* 29:1605444. doi: 10.1002/adma.201605444
- Wu, H., Ying, L., Yang, W., and Cao, Y. (2009). Progress and perspective of polymer white light-emitting devices and materials. *Chem. Soc. Rev.* 38, 3391–3400. doi: 10.1039/b816352a
- Wu, Z., Yu, L., Zhou, X., Guo, Q., Luo, J., Qiao, X., et al. (2016). Management of singlet and triplet excitons: a universal approach to high-efficiency all fluorescent WOLEDs with reduced efficiency roll-off using a conventional fluorescent emitter. *Adv. Opt. Mater.* 4, 1067–1074. doi: 10.1002/adom.201600117
- Xiong, X., Song, F., Sun, S., Fan, J., and Peng, X. (2013). Red-emissive fluorescein derivatives and detection of bovine serum albumin. *Asian J. Org. Chem.* 2, 145–149. doi: 10.1002/ajoc.201200109
- Xiong, X., Song, F., Wang, J., Zhang, Y., Xue, Y., Sun, L., et al. (2014). Thermally activated delayed fluorescence of fluorescein derivative for time-resolved and confocal fluorescence imaging. *J. Am. Chem. Soc.* 136, 9590–9597. doi: 10.1021/ja502292p
- Yang, Z., Mao, Z., Xie, Z., Zhang, Y., Liu, S., Zhao, J., et al. (2017). Recent advances in organic thermally activated delayed fluorescence materials. *Chem. Soc. Rev.* 46, 915–1016. doi: 10.1039/C6CS00368K
- Yu, J., Rong, Y., Kuo, C.-T., Zhou, X.-H., and Chiu, D. T. (2017). Recent advances in the development of highly luminescent semiconducting polymer dots and nanoparticles for biological imaging and medicine. *Anal. Chem.* 89, 42–56. doi: 10.1021/acs.analchem.6b04672
- Zhang, J., Chen, R., Zhu, Z., Adachi, C., Zhang, X., and Lee, C.-S. (2015). Highly stable near-infrared fluorescent organic nanoparticles with a large Stokes shift for noninvasive long-term cellular imaging. *ACS Appl. Mater. Interfaces* 7, 26266–26274. doi: 10.1021/acsami.5b08539
- Zhang, Q., Li, J., Shizu, K., Huang, S., Hirata, S., Miyazaki, H., et al. (2012). Design of efficient thermally activated delayed fluorescence materials for pure blue organic light emitting diodes. *J. Am. Chem. Soc.* 134, 14706–14709. doi: 10.1021/ja306538w
- Zhang, Q., Xu, S., Li, M., Wang, Y., Zhang, N., Guan, Y., et al. (2019). Rationally designed organelle-specific thermally activated delayed fluorescence small molecule organic probes for time-resolved biological applications. *Chem. Commun.* 55, 5639–5642. doi: 10.1039/C9CC00898E
- Zhu, Z., Tian, D., Gao, P., Wang, K., Li, Y., Shu, X., et al. (2018). Cell-penetrating peptides transport noncovalently linked thermally activated delayed fluorescence nanoparticles for time-resolved luminescence imaging. *J. Am. Chem. Soc.* 140, 17484–17491. doi: 10.1021/jacs.8b08438

**Conflict of Interest:** The authors declare that the research was conducted in the absence of any commercial or financial relationships that could be construed as a potential conflict of interest.

Copyright © 2020 Paisley, Tonge and Hudson. This is an open-access article distributed under the terms of the Creative Commons Attribution License (CC BY). The use, distribution or reproduction in other forums is permitted, provided the original author(s) and the copyright owner(s) are credited and that the original publication in this journal is cited, in accordance with accepted academic practice. No use, distribution or reproduction is permitted which does not comply with these terms.



# Trap-Controlled White Electroluminescence From a Single Red-Emitting Thermally Activated Delayed Fluorescence Polymer

Yun Yang<sup>1,2†</sup>, Liuqing Yang<sup>1,2†</sup>, Xuefei Li<sup>1,2</sup>, Lei Zhao<sup>1</sup>, Shumeng Wang<sup>1\*</sup>, Junqiao Ding<sup>1,2\*</sup> and Lixiang Wang<sup>1,2</sup>

<sup>1</sup> State Key Laboratory of Polymer Physics and Chemistry, Changchun Institute of Applied Chemistry, Chinese Academy of Sciences, Changchun, China, <sup>2</sup> School of Applied Chemistry and Engineering, University of Science and Technology of China, Hefei, China

## OPEN ACCESS

### Edited by:

Chihaya Adachi,  
Kyushu University, Japan

### Reviewed by:

Chin-Yu Chan,  
Kyushu University, Japan  
Hao-Wu Lin,  
National Tsing Hua University, Taiwan

### \*Correspondence:

Shumeng Wang  
wangshumeng@ciac.ac.cn  
Junqiao Ding  
junqiaod@ciac.ac.cn

<sup>†</sup>These authors have contributed  
equally to this work

### Specialty section:

This article was submitted to  
Polymer Chemistry,  
a section of the journal  
Frontiers in Chemistry

**Received:** 17 December 2019

**Accepted:** 23 March 2020

**Published:** 21 April 2020

### Citation:

Yang Y, Yang L, Li X, Zhao L, Wang S,  
Ding J and Wang L (2020)  
Trap-Controlled White  
Electroluminescence From a Single  
Red-Emitting Thermally Activated  
Delayed Fluorescence Polymer.  
Front. Chem. 8:287.  
doi: 10.3389/fchem.2020.00287

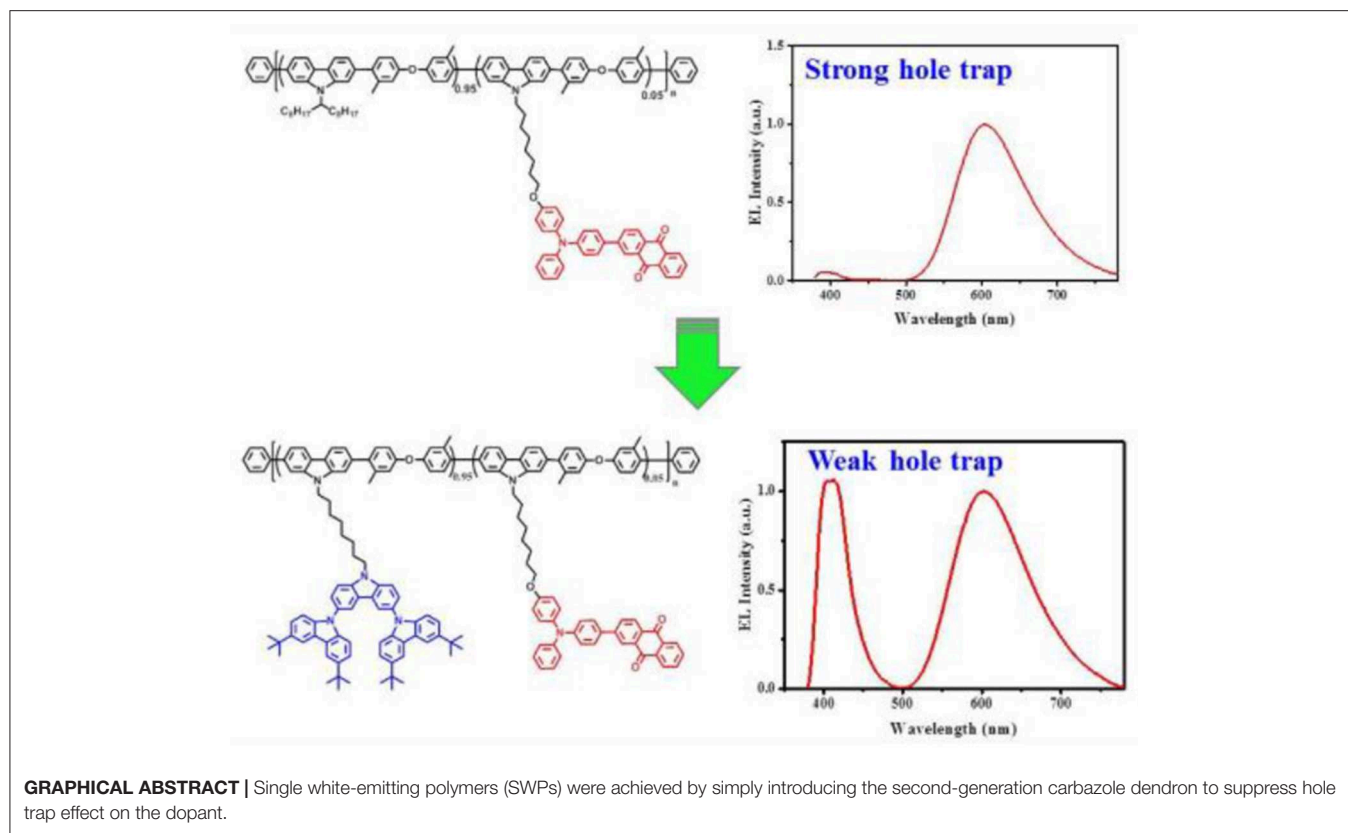
Single white-emitting polymers have been reported by incorporating the second-generation carbazole dendron into the side chain of a red-emitting thermally activated delayed fluorescence (TADF) polymer. Due to the prevented hole trap effect, in this case, excitons can be generated simultaneously on the polymeric host and the red TADF dopant to give a dual emission. Consequently, a bright white electroluminescence is achieved even at a dopant loading as high as 5 mol.%, revealing a maximum luminous efficiency of 16.1 cd/A (12.0 lm/W, 8.2%) and Commission Internationale de l'Eclairage (CIE) coordinates of (0.42, 0.32). The results clearly indicate that the delicate tuning of charge trap is a promising strategy to develop efficient single white-emitting polymers, whose low-band-gap chromophore content can be up to a centesimal level.

**Keywords:** single white-emitting polymers, carbazole dendron, thermally activated delayed fluorescence (TADF), charge trap, dual emission

## INTRODUCTION

Single white-emitting polymers (SWPs) have attracted much attention owing to their potential applications in flat-panel displays and solid-state lightings (Reineke et al., 2013). In this case, several fluorescence, phosphorescence, and/or thermally activated delayed fluorescence (TADF) chromophores with either two complementary colors (blue and yellow) or three primary colors (blue, green, and red) are covalently incorporated into a single polymeric host at the same time so as to generate white electroluminescence (EL) (Liu et al., 2007a,b; Shao et al., 2012; Li et al., 2017; Wang et al., 2017). Compared with the physical blend systems, the undesirable phase segregation can be avoided effectively, leading to improved device performance as well as good spectral stability (Tu et al., 2004). However, the molar ratio of the long-wavelength chromophores in SWPs is often required to be in the range of one ten thousandth to one thousandth (Liu et al., 2007a; Shao et al., 2012; Wang et al., 2017). The extremely low doping concentration is difficult to be controlled during polymerization, which may bring about batch-to-batch variation for the synthesis of SWPs, and thus poor device reliability and reproducibility.

We note that there are few studies on how to address such an issue, although a great progress has been made on the power efficiency of SWPs recently (Shao et al., 2018). Here, we report TADF-based SWPs, whose low-band-gap chromophore content can be raised up to a centesimal level. This is achieved by simply introducing the second-generation carbazole dendron into the side chain of a previously-reported red-emitting TADF polymer PCzDMPE-R5.0 (**Figure 1**)



(Yang et al., 2019). Because of the suppressed hole trap effect on the dopant, an interesting dual emission originating from both host and dopant is observed under the electrical excitation for all the resultant SWPs (D2-PCzDMPE-R2.5 ~ D2-PCzDMPE-R10). Among them, D2-PCzDMPE-R5.0 gives a more balanced white EL, revealing a maximum luminous efficiency of 16.1 cd/A (12.0 lm/W, 8.2%) and Commission Internationale de l'Eclairage (CIE) coordinates of (0.42, 0.32). The results clearly indicate that the delicate tuning of charge trap is a promising strategy to develop efficient SWPs with a high loading of long-wavelength chromophores.

## RESULTS AND DISCUSSION

### Synthesis and Characterization

The synthetic route of the TADF-based SWPs is depicted in **Scheme 1**. Starting from the second-generation oligocarbazole D2, two successive N-alkylated reactions were carried out to afford the key monomer M1. Combined with other two comonomers M2 and M3, then a Suzuki polymerization was adopted to produce the target polymers D2-PCzDMPE-R2.5, D2-PCzDMPE-R5.0, D2-PCzDMPE-R7.5, and D2-PCzDMPE-R10. Their number-average molecular weights and polydispersity indexes were determined to be 63–101 kDa and 1.58–1.66, respectively (**Table 1**). And the actual content of the red TADF dopant incorporated into polymer can be calculated using their  $^1\text{H}$  NMR spectra. As one can see in **Figure S1**, the characteristic signals of  $\delta$ 8.46 and  $\delta$ 8.28 are subjected to the anthraquinone

segment in the red TADF emitter, while the peak at about  $\delta$ 2.31 is from the methyl group in the 3,3'-dimethyldiphenyl ether building block. By comparing their relative integrals, the red dopant loading is estimated to be in the range of 2.4–10.0%, very close to the feed ratio (**Table 1**). This implies that the red TADF emitter has been successfully bonded into the SWPs during polymerization.

In addition, they all exhibit a decomposition temperature ( $T_d$ : corresponding to a 5% weight loss) of 455–470°C and a glass transition temperature ( $T_g$ ) of 259–266°C (**Figure S2**), much higher than those of PCzDMPE-R5.0 ( $T_d = 417^\circ\text{C}$ ,  $T_g = 94^\circ\text{C}$ ) (Yang et al., 2019). The introduced oligocarbazole functionalized with tert-butyl groups may be responsible for the improved thermal stability of D2-PCzDMPE-R2.5 ~ D2-PCzDMPE-R10 (Zhao et al., 2015, 2018). Also, it contributes to their good solubility in common organic solvents (toluene, chlorobenzene, and chloroform etc.), which ensures the generation of high quality films via spin coating.

### Photophysical Properties

The UV-Vis absorption and photoluminescent (PL) spectra of D2-PCzDMPE-R2.5 ~ D2-PCzDMPE-R10 were firstly measured in neat films to investigate their photophysical properties. As can be clearly seen in **Figure 2A**, these SWPs show not only the absorptions peaked at 241 and 300 nm from the tethered oligocarbazole dendron, but also the elongated absorption bands of 270 and 319 nm from the backbone poly(2,7-carbazole-co-3,3'-dimethyldiphenyl ether) (Zhao et al.,



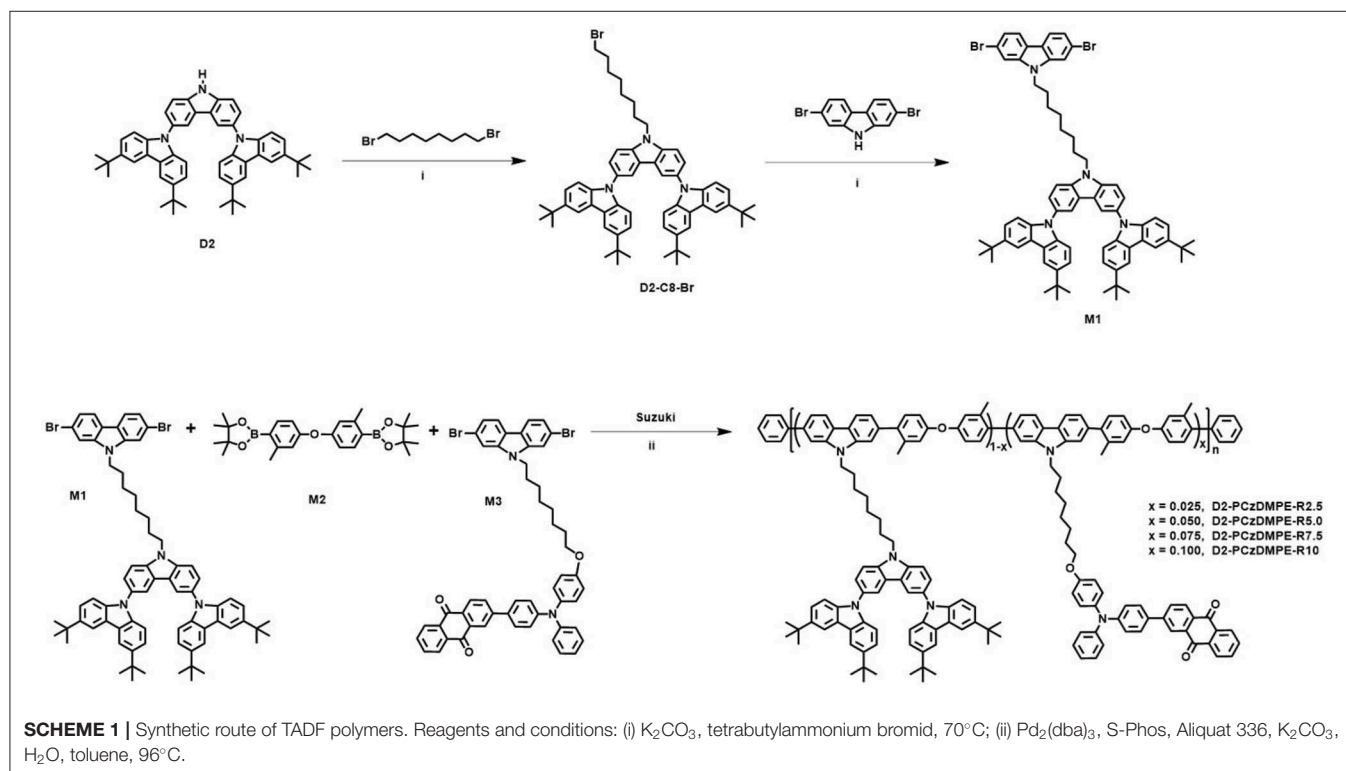
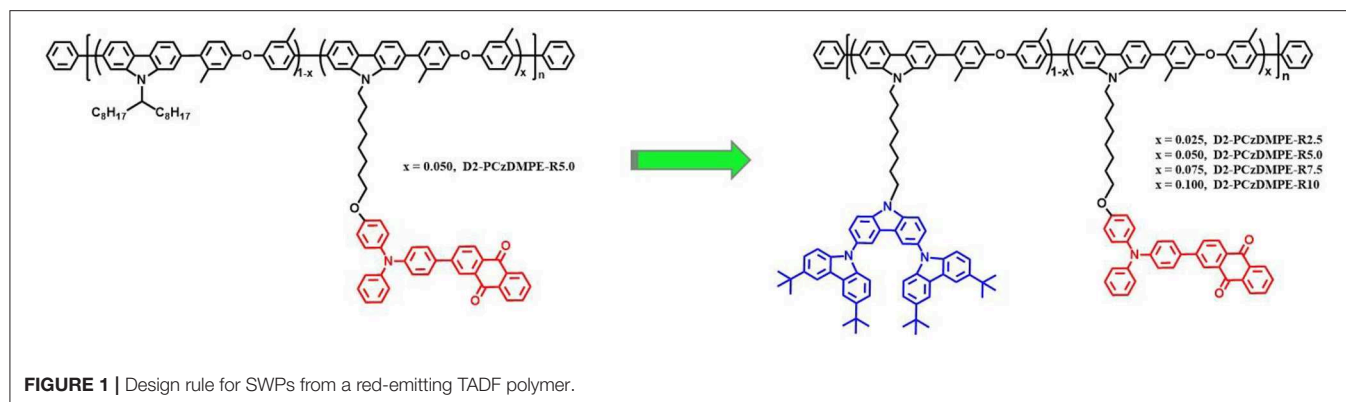


**TABLE 1** | Physical properties of the polymers D2-PCzDMPE-R2.5 ~ D2-PCzDMPE-R10.

Polymers	Red emitter content in the polymers (mol%)		$M_n^b$ (kDa)	PDI <sup>b</sup>	$T_g^c$ ( $^\circ C$ )	$T_d^d$ ( $^\circ C$ )
	Feed ratio	Actual content <sup>a</sup>				
D2-PCzDMPE-R2.5	2.5	2.4	64	1.61	266	455
D2-PCzDMPE-R5.0	5.0	5.0	63	1.58	262	470
D2-PCzDMPE-R7.5	7.5	7.4	101	1.62	264	460
D2-PCzDMPE-R10	10.0	10.0	100	1.66	259	457

<sup>a</sup> Calculated from the  $^1H$  NMR spectra.

<sup>b</sup> Determined by GPC in THF using polystyrene as the standard.

<sup>c</sup> Glass transition temperatures determined by TGA in  $N_2$ .

<sup>d</sup> Decomposition temperatures corresponding to a 5% weight loss.

2015). And the charge transfer (CT) absorption related to the red TADF dopant seems to be weak but distinguishable, lying in the range of 400–550 nm. Due to the incomplete energy transfer, moreover, a dual emission is detected for all the polymers. One is from the blue polymeric host, the other is from the red TADF dopant, whose intensity is found to be gradually increased with the increasing doping concentration.

To demonstrate their TADF nature, the film transient PL spectra were also recorded under nitrogen at 298 K for D2-PCzDMPE-R2.5 ~ D2-PCzDMPE-R10 (Figure 2B and Figure S3). Obviously, they display both the prompt fluorescence with an excited lifetime of 7.0–10.8 ns, and the delayed fluorescence with an excited lifetime of 97–157  $\mu s$ . When the feed

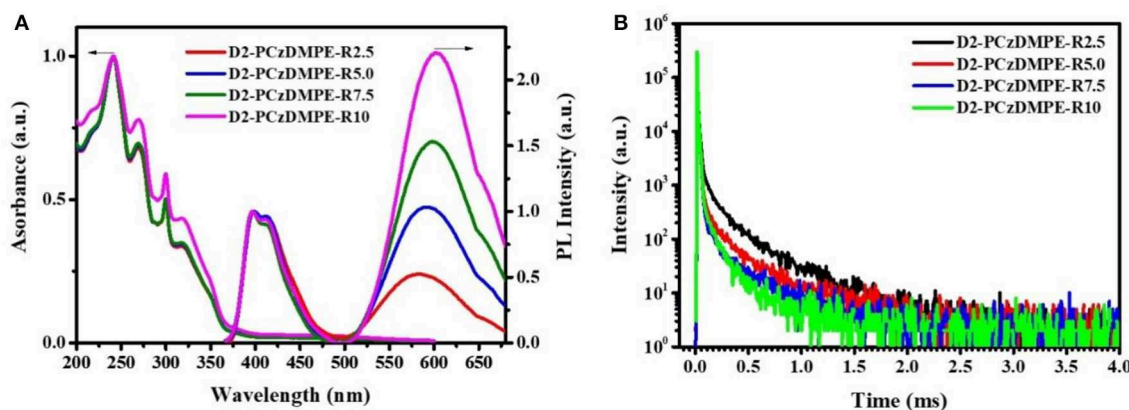


**FIGURE 2** | Photophysical properties of D2-PCzDMPE-R2.5 ~ D2-PCzDMPE-R10: **(A)** UV-vis absorption and PL spectra in films; **(B)** transient PL spectra in films under N<sub>2</sub> at 298 K.

**TABLE 2** | Photophysical properties of the polymers D2-PCzDMPE-R2.5 ~ D2-PCzDMPE-R10.

Polymers	$\lambda_{\text{abs}}^a$ [nm]	$\lambda_{\text{em}}^a$ [nm]	$\Phi_P^b$	$\tau_P^c$ [ns]	$\tau_d^c$ [us]
D2-PCzDMPE-R2.5	241/270/300/319/475	398/415/584	0.38	10.8	157
D2-PCzDMPE-R5.0	241/270/300/319/476	399/413/592	0.32	8.4	136
D2-PCzDMPE-R7.5	241/270/300/319/478	397/412/598	0.29	8.3	126
D2-PCzDMPE-R10	241/270/300/319/478	397/413/603	0.24	7.0	97
PCzDMPE-R5.0 (Yang et al., 2019)	317/492	393/579	0.37	5.9	165

<sup>a</sup>Measured in film at 298 K. <sup>b</sup>Measured by integrating-sphere in film under N<sub>2</sub> atmosphere for TADF polymers; <sup>c</sup>Measured in film N<sub>2</sub> atmosphere for TADF polymers, and the prompt and delayed lifetimes ( $\tau_P$  and  $\tau_d$ ) were calculated using  $\tau_{\text{av}} = \sum A_i \tau_i^2 / \sum A_i \tau_i$ .

ratio of the red TADF dopant rises, it is found that the delayed lifetime is down from 157 us of D2-PCzDMPE-R2.5 to 136 us of D2-PCzDMPE-R5.0, 126 us of D2-PCzDMPE-R7.5, and 97 us of D2-PCzDMPE-R10, respectively (Table 2). The trend may be ascribed to the triplet-triplet annihilation (TTA) induced by aggregation. This is further verified by their film PL quantum yields (PLQYs) (Tao et al., 2014). For example, the PLQY of D2-PCzDMPE-R10 ( $\Phi_P = 0.24$ ) is reduced by about 37% compared with D2-PCzDMPE-R2.5 ( $\Phi_P = 0.38$ ).

## Electroluminescent Properties

To evaluate the electroluminescent (EL) properties of D2-PCzDMPE-R2.5 ~ D2-PCzDMPE-R10, at first, the non-doped devices were fabricated with a configuration of ITO/PEDOT:PSS (50 nm)/EML (40 nm)/TmPyPB (50 nm)/LiQ (1 nm)/Al (Figure S4). Herein PEDOT:PSS [poly(3,4-ethylenedioxythiophene): poly(styrenesulfonate)] and TmPyPB [1,3,5-tris(3-pyridyl-3-phenyl)benzene] serve as the hole-injection layer and electron-transporting layer, respectively. And the emitting layer (EML) is composed of the polymer D2-PCzDMPE-R2.5, D2-PCzDMPE-R5.0, D2-PCzDMPE-R7.5, or D2-PCzDMPE-R10 independently.

Figure 3 plots the EL spectra, the current density-voltage-luminance characteristics together with the current efficiency, power efficiency and external quantum efficiency (EQE) as a function of current density, and the corresponding data are

tabulated in Table 3. Similar to the PL counterparts, both red and blue emissions are observed in the EL spectra (Figure 3A and Figure S5). Ongoing from D2-PCzDMPE-R2.5 to D2-PCzDMPE-R5.0, D2-PCzDMPE-R7.5, and D2-PCzDMPE-R10, the red-to-blue ratio is enhanced, and the corresponding CIE coordinates are red-shifted from (0.36, 0.27) to (0.45, 0.33), (0.48, 0.36) and (0.49, 0.36), respectively. Following such a tendency, the current density at the same driving voltage is also found to be reduced (Figure 3B), indicative of the existed charge trap to some degree (Tong et al., 2007; Tsung and So, 2008; Li et al., 2012). Despite this, the turn-on voltages defined at 1 cd/m<sup>2</sup> are in the range of 3.4–3.6 V for D2-PCzDMPE-R2.5 ~ D2-PCzDMPE-R10, lower than that of PCzDMPE-R5.0 (6.2 V) (Yang et al., 2019). The reduced driving voltage may originate from the introduction of oligocarbazole as the side chain, which can facilitate the hole injection and transporting (Promarak et al., 2007, 2008; Hasan et al., 2017; Wang et al., 2018). As a result, D2-PCzDMPE-R5.0 achieves the best white device performance among these polymers, revealing a maximum luminance of 1,971 cd/m<sup>2</sup>, a peak current efficiency of 5.4 cd/A, a peak power efficiency of 4.3 lm/W and a peak EQE of 3.1% (Figures 3C,D).

Unlike the red-emitting PCzDMPE-R5.0, we note, D2-PCzDMPE-R5.0 obtains a dual emission from both the polymeric host and small-molecular TADF dopant (Figure 4). Given the same feed ratio, the additional second-generation carbazole dendron plays an important role on the observed difference. As

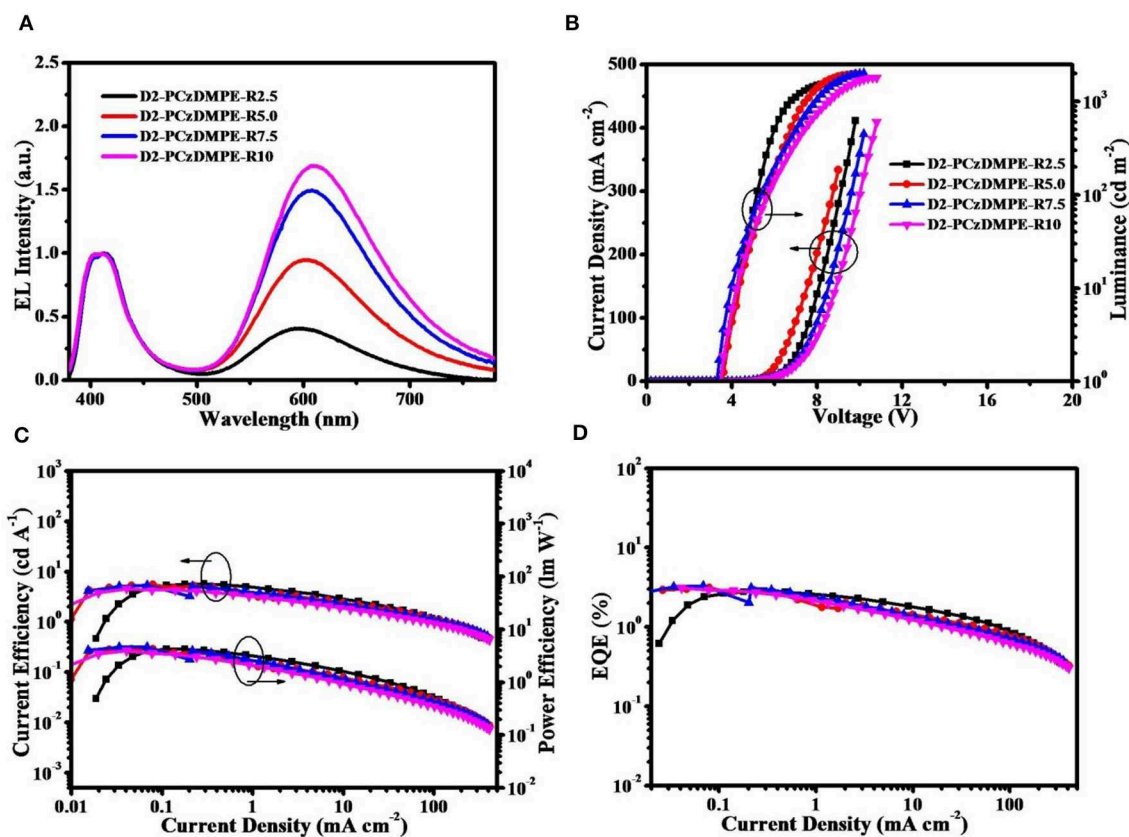


**FIGURE 3** | Non-doped device performance of D2-PCzDMPE-R2.5 ~ D2-PCzDMPE-R10: **(A)** EL spectra at 1,000 cd m<sup>-2</sup>; **(B)** current density–voltage–luminance characteristics; **(C)** current efficiency and power efficiency as a function of current density; **(D)** EQE as a function of current density.

**TABLE 3** | Non-doped and doped device performance for the polymers D2-PCzDMPE-R2.5 ~ D2-PCzDMPE-R10.

Devices	$V_{on}$ (V)	Max performance				CIE (x, y)
		$L$ (cd/m <sup>2</sup> )	CE (cd/A)	PE (lm/W)	EQE (%)	
D2-PCzDMPE-R2.5	3.6	1,622	5.7	4.2	2.9	(0.36, 0.27)
D2-PCzDMPE-R5.0	3.6	1,971	5.4	4.3	3.1	(0.45, 0.33)
D2-PCzDMPE-R7.5	3.4	2,008	5.3	4.7	3.3	(0.48, 0.36)
D2-PCzDMPE-R10	3.6	1,809	4.6	4.0	3.1	(0.49, 0.36)
D2-PCzDMPE-R5.0 +mCP	4.2	1,837	16.1	12.0	8.2	(0.42, 0.32)
PCzDMPE-R5.0 (Yang et al., 2019)	6.2	1,386	3.24	1.46	1.74	(0.57, 0.42)

$V_{on}$ , turn-on voltage at 1 cd/m<sup>2</sup>;  $L$ , luminance; CE, current efficiency; PE, power efficiency; EQE, external quantum efficiency; CIE (x, y), CIE@1000 cd/m<sup>2</sup>.

for PCzDMPE-R5.0, there exists a strong hole trap effect owing to the much deeper highest occupied molecular orbital (HOMO) level of the polymeric host relative to the red TADF dopant ( $-5.92$  eV vs.  $-5.20$  eV). In this case, the injected holes cannot be stored on host but trapped by dopant completely, while electrons are injected into dopant via an electrostatic attraction (Adachi et al., 2000; Tessler et al., 2000; Lane et al., 2001; Gong et al., 2003). Then excitons are generated directly on dopant, and only red emission appears in the EL spectrum of PCzDMPE-R5.0 (Figure 4A). By contrast, the incorporated oligocarbazole has led

to a distinct HOMO upshift from  $-5.92$  to  $-5.47$  eV for the polymeric host in D2-PCzDMPE-R5.0 (Figure S6). Benefitting from the suppressed hole trap, holes can be accumulated either on host or on dopant. After recombination with the injected electrons via an electrostatic attraction, two classes of excitons are able to be formed on both host and dopant, resulting in a dual emission and thus white EL (Figure 4B) (Liu et al., 2005; Farmer et al., 2011; Li et al., 2014).

To avoid the above-mentioned aggregation induced TTA in neat films, doped devices were further assembled with

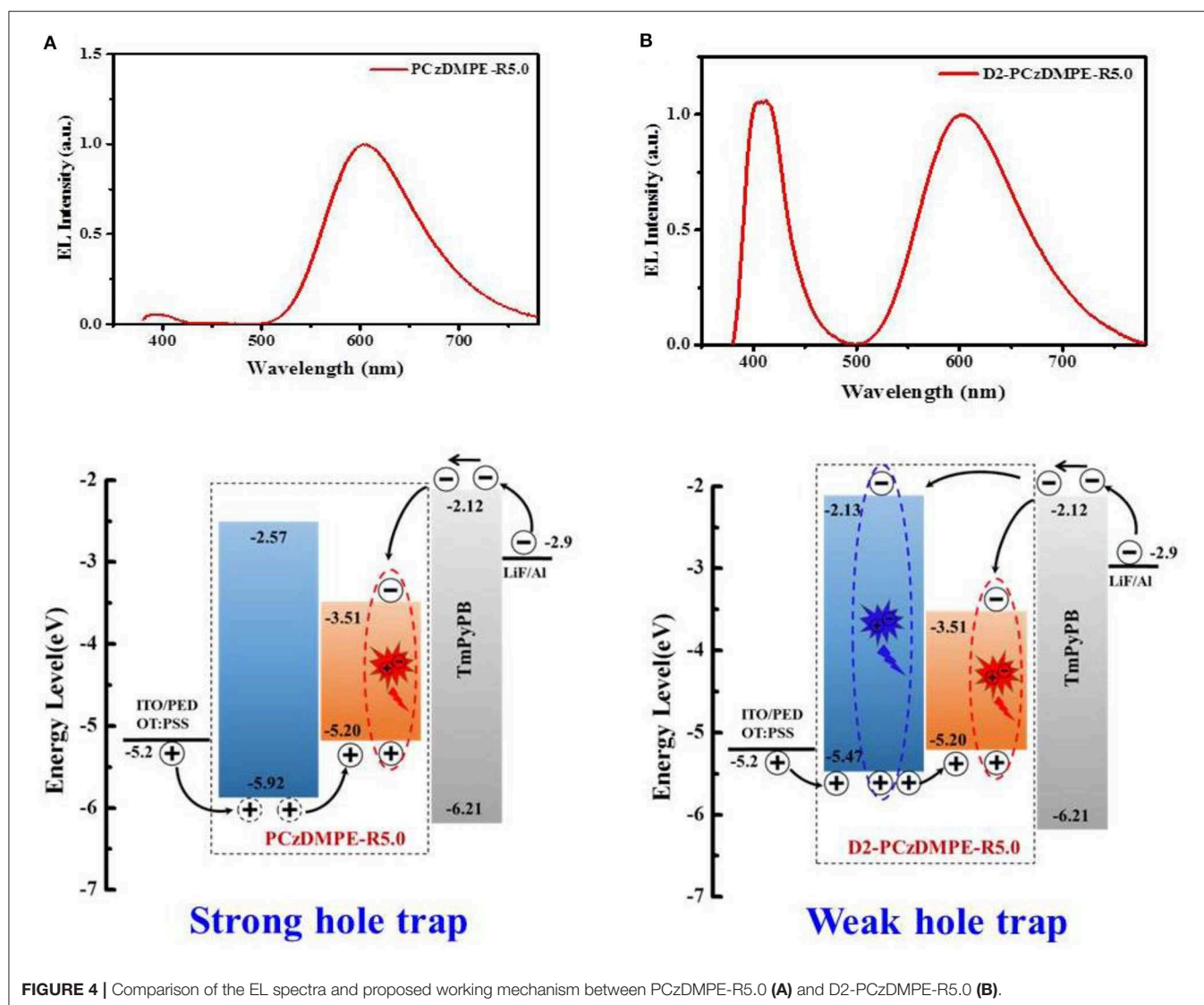


**FIGURE 4** | Comparison of the EL spectra and proposed working mechanism between PCzDMPE-R5.0 (A) and D2-PCzDMPE-R5.0 (B).

D2-PCzDMPE-R5.0 as an example. When it is doped into 1,3-bis(9H-carbazol-9-yl)benzene (mCP) at a 30 wt.% concentration, the current efficiency, power efficiency and EQE are optimized to be 16.1 cd/A, 12.0 lm/W and 8.2%, respectively (Figure 5 and Figure S7). Meanwhile, the EL spectrum remains nearly unchanged, accompanied by similar CIE coordinates of (0.42, 0.32) to the non-doped device. Although the obtained performance is moderate, the loading of long-wavelength dopant here is as high as 5 mol.%, one or two order magnitude higher than those of previously-reported SWPs (Chuang et al., 2007; Liu et al., 2007a; Luo et al., 2007; Shao et al., 2012; Wang et al., 2017). This is very instructive when trying to solve the batch-to-batch variation in material synthesis.

## CONCLUSIONS

In summary, a red to white conversion has been demonstrated by incorporating the second-generation carbazole dendron into

the side chain of a red-emitting TADF polymer. Benefitting from the elevated HOMO level of the polymeric host, the hole trap effect between host and dopant is reasonably weakened. As a consequence, a dual emission from both host and dopant is observed simultaneously, leading to a bright white EL even at a 5 mol.% dopant content. This work provides an effective strategy to improve the loading of long-wavelength chromophores up to a centesimal level, which will shed light on the development of SWPs showing not only high power efficiency but also good reproducibility.

## EXPERIMENTAL SECTION

### Measurements and Characterization

$^1\text{H}$  NMR and  $^{13}\text{C}$  NMR spectra were recorded with a Bruker Avance 400 spectrometer or Bruker Avance 500 spectrometer. MALDI/TOF (matrix-assisted laser desorption ionization/time-of flight) mass spectra were performed on an AXIMA CFR



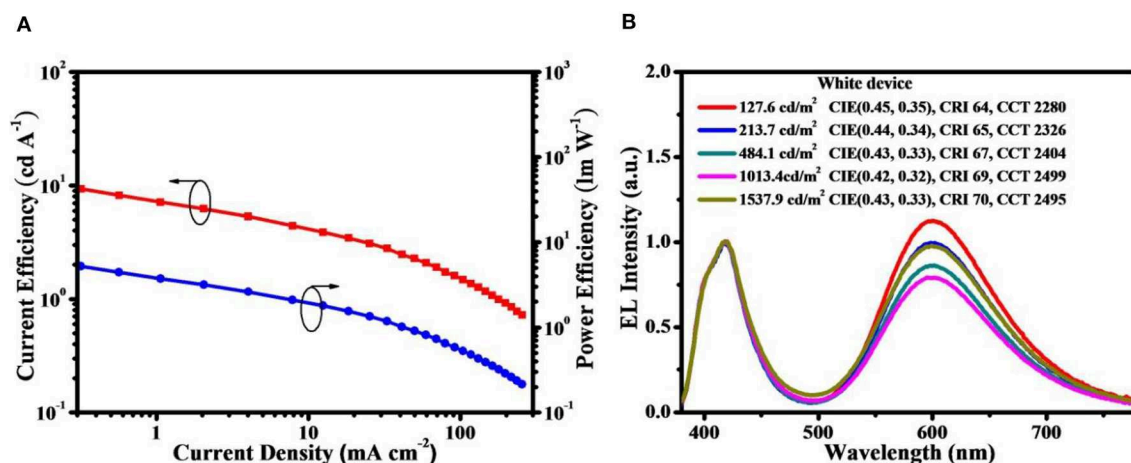


**FIGURE 5 |** Performance for the doped device of D2-PCzDMPE-R5.0: **(A)** Current efficiency and power efficiency as a function of current density; **(B)** EL spectra at different luminance.

MS apparatus (COMPACT). Molecular weights of the polymers were determined by Gel permeation chromatography (GPC) in tetrahydrofuran (THF) using polystyrene as the standard. Thermal gravimetric analysis (TGA) and differential scanning calorimetry (DSC) were performed under a flow of nitrogen with PerkinElmer-TGA 7 and PerkinElmer-DSC7 systems, respectively. UV-vis absorption and PL spectra were measured with a PerkinElmer Lambda 35 UV-vis spectrometer and a PerkinElmer LS 50B spectrofluorometer, respectively. By dropping 0.5 ml solution of polymers dissolved in toluene to an optical colorimetric dish and then drying under vacuum, the films used for PLQY measurement are formed on the walls of the colorimetric dish. The film PLQYs were measured using a quantum yield measurement system (C10027, Hamamatsu Photonics) excited at 350 nm under argon protection. PLQYs are calculated from the area integral ratio of emission to absorption. And the transient PL spectra were carried out with Edinburgh fluorescence spectrometer (FLS980). The HOMO and lowest unoccupied molecular orbital (LUMO) levels were estimated from the cyclic voltammetry (CV), which was performed on a CHI660a electrochemical analyzer with Bu<sub>4</sub>NClO<sub>4</sub> (0.1 mol/L) as the electrolyte at a scan rate of 100 mV/s. A glass carbon electrode, a saturated calomel electrode, and a Pt wire were used as the working electrode, the reference electrode, and the counter electrode, respectively. All the potentials were calibrated by ferrocene/ferrocenium (Fc/Fc<sup>+</sup>). HOMO = -e (E<sub>ox onset</sub> + 4.8 V), LUMO = HOMO + E<sub>g</sub>, where E<sub>ox onset</sub> is the onset value of the first oxidation wave and the E<sub>g</sub> is the optical bandgap estimated from the absorption onset.

## Device Fabrication and Testing

The indium tin oxide (ITO) (20 Ω per square) substrates were cleaned with acetone, detergent, distilled water and then in an ultrasonic solvent bath. After baking in a heating chamber at

130°C for 2 h, the ITO-glass substrates were treated with UV-ozone for 25 min. Firstly, PEDOT:PSS (Batron-P4083, Bayer AG) was spin-coated on top of the ITO at a speed of 5,000 rpm for 60 s, and baked at 120°C for 45 min. After transferred into a nitrogen-filled glove-box, subsequently, solutions of polymers in toluene were spin-coated on PEDOT:PSS as the EML at a speed of 1,500 rpm for 60 s, and annealed at 80°C for 0.5 h. Finally, the other layers including TmPyPB (50 nm), LiF (1 nm) and Al (100 nm) were deposited in a vacuum chamber at a base pressure of  $>4 \times 10^{-4}$  Pa. The EL spectra and CIE coordinates were measured using a CS2000A spectra colorimeter. The current-voltage and brightness-voltage curves of devices were measured using a Keithley 2,400/2,000 source meter and a calibrated silicon photodiode. All the measurements were carried out at room temperature under ambient conditions.

## Synthesis

All chemicals were purchased from the Energy Chemical, Aldrich, or Alfa and used without further purification unless otherwise stated. Toluene was freshly distilled before usage. Compound D2, monomer M2 and M3 were prepared according to the previous reports (Yang et al., 2018, 2019).

### 9-(8-bromooctyl)-3,6-bis(3,6-di-tert-butyl-carbazol-9yl)-carbazole (D2-C8-Br)

A mixture of D2 (5.00 g, 6.90 mmol), 1,8-dibromooctane (9.40 g, 34.70 mmol), K<sub>2</sub>CO<sub>3</sub> (4.80 g, 34.70 mmol), and tetrabutylammonium bromide (0.11 g, 0.35 mmol) was dissolved in 100 mL THF. The mixture was heated to reflux and stirred for 12 h under argon. After cooling to room temperature, the mixture was extracted with dichloromethane, washed with deionized water, dried by anhydrous sodium sulfate, and concentrated under vacuum. The crude product was purified by column chromatography on silica gel using petroleum

ether/dichloromethane ( $v/v = 8/1$ ) as eluent to give D2-C8-Br as a white powder (5.30 g, 86.5%).  $^1\text{H}$  NMR (400 MHz,  $\text{CDCl}_3$ )  $\delta$  8.16 (t,  $J = 6.2$  Hz, 6H), 7.66–7.59 (m, 4H), 7.44 (dd,  $J = 8.6, 1.9$  Hz, 4H), 7.31 (d,  $J = 8.6$  Hz, 4H), 4.47 (s, 2H), 3.44–3.38 (m, 2H), 2.11–1.99 (m, 2H), 1.92–1.81 (m, 2H), 1.46 (s, 44H).

### [[3,6-bis(3,6-di-tert-butylcarbazol-9-yl)-carbazole]-9yl]octyl-2,7-dibromo-9H-carbazole (M1)

A mixture of D2-C8-Br (5.20 g, 5.69 mmol), 2,7-dibromo-9H-carbazole (1.68 g, 5.17 mmol),  $\text{K}_2\text{CO}_3$  (3.57 g, 0.26 mmol) and tetrabutylammonium bromide (0.08 g, 0.35 mmol) was dissolved in 100 mL THF. The mixture was heated to reflux and stirred for 20 h under argon. After cooling to room temperature, the mixture was extracted with dichloromethane, washed with deionized water, dried by anhydrous sodium sulfate, and concentrated under vacuum. The crude product was purified by column chromatography on silica gel using petroleum ether/ethyl acetate ( $v/v = 20/1$ ) as eluent. Finally, the product was recrystallized with ethyl acetate/dichloromethane to give M1 as a white solid (4.78 g, 80%), (Figure S8).  $^1\text{H}$  NMR (400 MHz,  $\text{CDCl}_3$ )  $\delta$  8.16 (t,  $J = 4.9$  Hz, 6H), 7.86 (d,  $J = 8.3$  Hz, 2H), 7.65–7.57 (m, 4H), 7.53 (d,  $J = 1.5$  Hz, 2H), 7.44 (dd,  $J = 8.6, 1.7$  Hz, 4H), 7.35–7.27 (m, 6H), 4.44 (s, 2H), 4.21 (t,  $J = 7.2$  Hz, 2H), 2.04–1.94 (m, 2H), 1.92–1.83 (m, 2H), 1.50–1.38 (m, 44H). MALDI-TOF MS ( $m/z$ ): Calcd for  $\text{C}_{72}\text{H}_{76}\text{Br}_2\text{N}_4$ , Exact Mass: 1154.44, Found: 1154.4 ( $\text{M}^+$ ).

General synthesis of white-emitting TADF polymers with D2-PCzDMPE-R2.5 as an example (Figure S10). M1 (0.3385 g, 0.2925 mmol), M2 (0.1351 g, 0.3000 mmol), M3 (0.0068 g, 0.0075 mmol),  $\text{Pd}_2(\text{dba})_3$  (1.1000 mg, 0.0010 mmol), 2-dicyclohexylphosphino-2,6'-dimethoxybiphenyl (S-Phos) (3.7000 mg, 0.0075 mmol) and Aliquat 336 (0.1 mL) were added to a mixture of toluene (9 mL) and aqueous  $\text{K}_2\text{CO}_3$  (3.0 mL, 2 M) under argon. The mixture was heated to  $95^\circ\text{C}$  and stirred for 2.50 h. Subsequently, benzenboronic acid (36 mg) in toluene of 4.5 mL was added, and the mixture was refluxed for 5 h. Then bromobenzene of 0.5 mL was added, and the mixture was kept refluxed for another 5 h. Finally, sodium diethyldithiocarbamate trihydrate (1.0 g) dissolved in deionized water (15 mL) was added into the mixture. The solution was kept at  $80^\circ\text{C}$  with vigorous stirring under argon for 24 h. After cooling to room temperature, the mixture was extracted by dichloromethane, which was washed for five times with deionized water and dried by anhydrous sodium sulfate. The polymer was purified by column chromatography on silica gel using dichloromethane as eluent. After removal of the solvent, the polymers were obtained by precipitation in methanol. The final purification was performed by Soxhlet extraction with acetone for about 24 h and then precipitated in methanol to give the desired polymer D2-PCzDMPE-R2.5 (251 mg, 70%).  $^1\text{H}$  NMR (500 MHz,  $\text{CDCl}_3$ )  $\delta$  8.46 (s, 0.019H), 8.28 (d,  $J = 7.9$  Hz, 0.082H), 8.23–7.94 (m, 7.481H), 7.90 (d,  $J = 8.1$  Hz, 0.040H), 7.78–7.71 (m, 0.072H), 7.59 (dd,  $J = 8.6, 1.8$  Hz, 2H), 7.54 (d,  $J = 8.6$  Hz, 2H), 7.39 (m, 4H), 7.37–7.30 (m, 4H), 7.30 (s, 3H), 7.25 (s, 1H), 7.19 (t,  $J = 9.6$  Hz, 2H), 7.06 (m, 2H), 6.98 (d,  $J = 8.3$  Hz, 2H), 6.81 (d,  $J = 8.3$  Hz, 0.077H), 4.34

(m, 4H), 3.87 (t,  $J = 6.3$  Hz, 0.051H), 2.31 (s, 6H), 1.92 (m, 4H), 1.75–1.67 (m, 0.104H), 1.47–1.33 (m, 43.258H).  $^{13}\text{C}$  NMR (126 MHz,  $\text{CDCl}_3$ )  $\delta$  156.56, 142.65, 141.00, 140.44, 140.09, 139.22, 138.24, 137.66, 131.57, 130.03, 125.89, 123.72, 123.56, 123.25, 121.63, 120.98, 120.72, 120.06, 119.63, 43.81, 43.31, 34.91, 32.25, 29.56, 29.36, 29.28, 27.63, 27.54, 21.11. Anal. calcd for  $[(\text{C}_{86}\text{H}_{88}\text{N}_4\text{O})_{97.5}(\text{C}_{66}\text{H}_{54}\text{N}_2\text{O}_4)_{2.5}]_n$ : C, 86.41; H, 7.34; N, 4.66; found: C, 86.23; H, 7.45; N, 4.45.

### D2-PCzDMPE-R5.0 (239 mg, 67%)

M1 (0.3298 g, 0.2850 mmol), M2 (0.1351 g, 0.3000 mmol), and M3 (0.0135 g, 0.0150 mmol) were used (Figure S11).  $^1\text{H}$  NMR (500 MHz,  $\text{CDCl}_3$ )  $\delta$  8.46 (s, 0.038H), 8.28 (d,  $J = 7.8$  Hz, 0.163H), 8.24–7.96 (m, 7.253H), 7.90 (d,  $J = 7.9$  Hz, 0.084H), 7.79–7.69 (m, 0.149H), 7.59 (m, 2H), 7.54 (m, 2H), 7.40 (m, 4H), 7.33 (d,  $J = 7.7$  Hz, 4H), 7.28 (d,  $J = 5.5$  Hz, 3H), 7.25 (s, 1H), 7.18 (d,  $J = 7.9$  Hz, 2H), 7.02 (d,  $J = 14.6$  Hz, 2H), 7.01 (s, 2H), 6.81 (d,  $J = 8.8$  Hz, 0.147H), 4.34 (m, 4H), 3.87 (t,  $J = 6.3$  Hz, 0.106H), 2.31 (s, 6H), 2.05–1.77 (m, 4H), 1.71 (s, 0.219H), 1.54–1.23 (m, 42.080H).  $^{13}\text{C}$  NMR (126 MHz,  $\text{CDCl}_3$ )  $\delta$  156.56, 142.65, 141.00, 140.44, 140.09, 139.22, 138.24, 137.66, 134.28, 134.08, 133.93, 131.57, 130.03, 129.51, 128.31, 128.09, 127.97, 127.39, 127.34, 125.89, 124.30, 123.72, 123.56, 123.25, 121.63, 120.99, 120.72, 120.06, 119.63, 116.36, 115.67, 110.07, 109.68, 109.32, 43.81, 43.31, 34.91, 32.25, 29.56, 29.36, 29.28, 27.63, 27.54, 21.11, 0.22. Anal. calcd for  $[(\text{C}_{86}\text{H}_{88}\text{N}_4\text{O})_{95}(\text{C}_{66}\text{H}_{54}\text{N}_2\text{O}_4)_5]_n$ : C, 86.37; H, 7.31; N, 4.47; found: C, 86.30; H, 7.39; N, 4.47.

### D2-PCzDMPE-R7.5 (212 mg, 65%)

M1 (0.3211 g, 0.2775 mmol), M2 (0.1351 g, 0.3000 mmol) and M3 (0.0203 g, 0.0225 mmol) were used (Figure S12).  $^1\text{H}$  NMR (500 MHz,  $\text{CDCl}_3$ )  $\delta$  8.46 (s, 0.067H), 8.28 (d,  $J = 8.0$  Hz, 0.230H), 8.21–7.96 (m, 7.228H), 7.90 (dd,  $J = 8.2, 1.8$  Hz, 0.098H), 7.78–7.70 (m, 0.176H), 7.58 (dt,  $J = 8.1, 4.1$  Hz, 2H), 7.56–7.50 (m, 2H), 7.40 (dd,  $J = 8.7, 1.6$  Hz, 4H), 7.33 (d,  $J = 7.7$  Hz, 4H), 7.27 (d,  $J = 8.3$  Hz, 3H), 7.25 (s, 1H), 7.19 (t,  $J = 9.9$  Hz, 2H), 7.10–7.02 (m, 2H), 6.98 (d,  $J = 8.4$  Hz, 2H), 6.81 (d,  $J = 8.9$  Hz, 0.168H), 4.34 (m, 4H), 3.87 (t,  $J = 6.3$  Hz, 0.159H), 2.31 (s, 6H), 1.99–1.83 (m, 4H), 1.76–1.65 (m, 0.200H), 1.39 (m, 41.726H).  $^{13}\text{C}$  NMR (126 MHz,  $\text{CDCl}_3$ )  $\delta$  156.56, 142.65, 141.00, 140.44, 140.09, 139.22, 138.24, 137.66, 134.28, 134.09, 133.82, 131.57, 130.03, 129.51, 128.26, 128.09, 127.97, 127.39, 127.34, 125.89, 124.30, 123.72, 123.57, 123.25, 121.63, 120.99, 120.72, 120.06, 119.63, 116.36, 115.67, 110.07, 109.68, 109.32, 43.81, 43.30, 34.91, 32.25, 29.56, 29.36, 29.28, 27.63, 27.54, 21.11, 0.22. Anal. calcd for  $[(\text{C}_{86}\text{H}_{88}\text{N}_4\text{O})_{92.5}(\text{C}_{66}\text{H}_{54}\text{N}_2\text{O}_4)_{7.5}]_n$ : C, 86.33; H, 7.27; N, 4.59; found: C, 86.00; H, 7.41; N, 4.37.

### D2-PCzDMPE-R10 (253 mg, 72%)

M1 (0.3125 g, 0.2700 mmol), M2 (0.1351 g, 0.3000 mmol) and M3 (0.0271 g, 0.0300 mmol) were used (Figure S13).  $^1\text{H}$  NMR (500 MHz,  $\text{CDCl}_3$ )  $\delta$  8.46 (s, 0.090H), 8.28 (d,  $J = 7.8$  Hz, 0.309H), 8.22–7.95 (m, 7.166H), 7.90 (d,  $J = 8.1$  Hz, 0.123H), 7.79–7.69 (m, 0.232H), 7.59 (dd,  $J = 8.6, 1.7$  Hz, 2H), 7.54 (dd,  $J = 8.4, 3.8$  Hz, 2H), 7.40 (dd,  $J = 8.7, 1.6$  Hz, 4H), 7.33 (d,  $J = 7.7$  Hz, 4H), 7.27 (d,  $J = 6.2$  Hz, 3H), 7.25 (s, 1H), 7.18 (d,  $J = 7.9$  Hz, 2H), 7.06 (m, 2H), 6.98 (d,  $J = 8.4$  Hz, 2H), 6.81 (d,  $J =$

= 8.8 Hz, 0.198H), 4.34 (m, 4H), 3.87 (d,  $J$  = 5.9 Hz, 0.206H), 2.31(s, 6H), 1.98 – 1.84 (m, 4H), 1.69 (m, 0.280H), 1.39 (m, 40.815H).  $^{13}\text{C}$  NMR (126 MHz,  $\text{CDCl}_3$ )  $\delta$  156.56, 142.65, 141.00, 140.44, 140.09, 139.22, 138.24, 137.66, 134.29, 134.08, 133.93, 131.58, 130.03, 129.50, 128.24, 128.09, 127.97, 127.39, 127.34, 125.89, 124.31, 123.72, 123.56, 123.25, 121.63, 120.99, 120.72, 120.06, 119.63, 116.36, 115.67, 110.07, 109.68, 109.32, 43.81, 43.31, 34.91, 32.25, 29.56, 29.36, 29.28, 27.63, 27.54, 21.11, 0.22. Anal. calcd for  $[(\text{C}_{86}\text{H}_{88}\text{N}_4\text{O})_{90}(\text{C}_{66}\text{H}_{54}\text{N}_2\text{O}_4)_{10}]_n$ : C, 86.28; H, 7.24; N, 4.55; found: C, 86.15; H, 7.42; N, 4.38.

### D2-PCzDMPE (196 mg, 70%)

M1 (0.2893 g, 0.25 mmol) and M2 (0.1125 g, 0.25 mmol) were used (Figure S9).  $^1\text{H}$  NMR (500 MHz,  $\text{CDCl}_3$ )  $\delta$  8.12 (m, 8H), 7.59 (dd,  $J$  = 8.6, 1.9 Hz, 2H), 7.54 (d,  $J$  = 8.7 Hz, 2H), 7.40 (dd,  $J$  = 8.7, 1.8 Hz, 4H), 7.35 (m, 4H), 7.29–7.24 (m, 4H), 7.18 (d,  $J$  = 8.1 Hz, 2H), 7.03 (d,  $J$  = 1.6 Hz, 2H), 6.98 (d,  $J$  = 9.6 Hz, 2H), 4.34 (m, 4H), 2.31(s, 6H), 1.92 (m, 4H), 1.49–1.35 (m, 44H).  $^{13}\text{C}$  NMR (126 MHz,  $\text{CDCl}_3$ )  $\delta$  156.56, 142.65, 141.00, 140.44, 140.09, 139.22, 138.24, 137.66, 131.57, 130.03, 125.89, 123.72, 123.56, 123.25, 121.63, 120.99, 120.72, 120.06, 119.63, 116.36, 110.07, 109.68, 109.32, 43.80, 43.31, 34.91, 32.25, 29.56, 29.36, 29.28, 27.62, 27.54, 21.11. Anal. calcd for  $[\text{C}_{86}\text{H}_{88}\text{N}_4\text{O}]_n$ : C, 86.45; H, 7.37; N, 4.69; found: C, 86.45; H, 7.44; N, 4.55.

## DATA AVAILABILITY STATEMENT

All datasets generated for this study are included in the article/Supplementary Material.

## REFERENCES

- Adachi, C., Baldo, M. A., and Forrest, S. R. (2000). Electroluminescence mechanisms in organic light emitting devices employing a europium chelate doped in a wide energy gap bipolar conducting host. *J. Appl. Phys.* 87, 8049–8055. doi: 10.1063/1.373496
- Chuang, C.-Y., Shih, P.-I., Chien, C.-H., Wu, F. I., and Shu, C. F. (2007). Bright-white light-emitting devices based on a single polymer exhibiting simultaneous blue, green, and red emissions. *Macromolecules* 40, 247–252. doi: 10.1021/ma062192
- Farmer, D. B., Perebeinos, V., Lin, Y.-M., Dimitrakopoulos, C., and Avouris, P. (2011). Charge trapping and scattering in epitaxial graphene. *Phys. Rev. B* 84, 1–5. doi: 10.1103/PhysRevB.84.205417
- Gong, X., Ostrowski, J. C., Bazan, G. C., Moses, D., and Heeger, A. J. (2003). Electrophosphorescence from a conjugated copolymer doped with an iridium complex: high brightness and improved operational stability. *Adv. Mater.* 15, 45–49. doi: 10.1002/adma.200390007
- Hasan, Z. A., Woon, K. L., Wong, W. S., Ariffin, A., and Chen, S.-A. (2017). Solution processed multilayer red, green and blue phosphorescent organic light emitting diodes using carbazole dendrimer as a host. *J. Lumines.* 183, 150–158. doi: 10.1016/j.jlumin.2016.11.054
- Lane, P. A., Palilis, L. C., O'Brien, D. F., Giebler, C., Cadby, A. J., Lidzey, D. G., et al. (2001). Origin of electrophosphorescence from a doped polymer light emitting diode. *Phys. Rev. B* 63, 1–8. doi: 10.1103/PhysRevB.63.235206
- Li, C., Duan, L., Sun, Y., Li, H., and Qiu, Y. (2012). Charge transport in mixed organic disorder semiconductors: trapping, scattering, and effective energetic disorder. *J. Mater. Chem. C* 116, 19748–19754. doi: 10.1021/jp307951h

## AUTHOR CONTRIBUTIONS

YY and LZ synthesized and characterized the polymers. LY and XL prepared non-doped and doped devices. SW, JD, and LW contributed conception and design of the study. YY wrote the first draft of the manuscript. JD revised manuscript. All authors contributed to manuscript revision, read, and approved the submitted version.

## ACKNOWLEDGMENTS

The authors acknowledge the financial support from the National Key Research and Development Program (2016YFB0401301), and the National Natural Science Foundation of China (Nos. 51873205 and 51573183).

## SUPPLEMENTARY MATERIAL

The Supplementary Material for this article can be found online at: <https://www.frontiersin.org/articles/10.3389/fchem.2020.00287/full#supplementary-material>

The **Supporting Information** includes the  $^1\text{H}$  NMR and MALDI-TOF MS of M1, the  $^1\text{H}$  NMR and  $^{13}\text{C}$  NMR spectra, TGA curves, DSC curves, transient decay spectra of polymers, the structure of the OLED devices and molecular structures of the related materials, the molecular structures, cyclic voltammograms and energy level alignment of PCzDMPE and D2-PCzDMPE as hosts and ROC8 as guest, the current–voltage–luminance and current efficiency–luminance–power efficiency curves of white device performance.

- Li, C., Nobuyasu, R. S., Wang, Y., Dias, F. B., Ren, Z., Bryce, M. R., et al. (2017). Solution-processable thermally activated delayed fluorescence white OLEDs based on dual-emission polymers with tunable emission colors and aggregation-enhanced emission properties. *Adv. Opt. Mater.* 5, 1–9. doi: 10.1002/adom.201700435
- Li, H., Li, C., Duan, L., and Qiu, Y. (2014). Charge transport in amorphous organic semiconductors: effects of disorder, carrier density, traps, and scatters. *Isr. J. Chem.* 54, 918–926. doi: 10.1002/ijch.201400057
- Liu, J., Shao, S. Y., Chen, L., Xie, Z. Y., Cheng, Y. X., Geng, Y. H., et al. (2007a). White electroluminescence from a single polymer system: improved performance by means of enhanced efficiency and red-shifted luminescence of the blue-light-emitting species. *Adv. Mater.* 19, 1859–1863. doi: 10.1002/adma.200602942
- Liu, J., Xie, Z. Y., Cheng, Y. X., Geng, Y. H., Wang, L. X., Jing, X. B., et al. (2007b). Molecular design on highly efficient white electroluminescence from a single-polymer system with simultaneous blue, green, and red emission. *Adv. Mater.* 19, 531–535. doi: 10.1002/adma.200601580
- Liu, J., Zhou, Q. G., Cheng, Y. X., Geng, Y. H., Wang, L. X., Ma, D. G., et al. (2005). The first single polymer with simultaneous blue, green, and red emission for white electroluminescence. *Adv. Mater.* 17, 2974–2978. doi: 10.1002/adma.200501850
- Luo, J., Li, X., Hou, Q., Peng, J. B., Yang, W., and Cao, Y. (2007). High-efficiency white-light emission from a single copolymer: fluorescent blue, green, and red chromophores on a conjugated polymer backbone. *Adv. Mater.* 19, 1113–1117. doi: 10.1002/adma.200601241
- Promarak, V., Ichikawa, M., Sudyoasuk, T., Saengsuwan, S., Jungsuttiwong, S., and Keawin, T. (2007). Synthesis of electrochemically and thermally stable

- amorphous hole-transporting carbazole dendronized fluorene. *Synth. Met.* 157, 17–22. doi: 10.1016/j.synthmet.2006.11.013
- Promarak, V., Ichikawa, M., Sudyoadsuk, T., Saengsuwan, S., Jungsuttiwong, S., and Keawin, T. (2008). Thermally and electrochemically stable amorphous hole-transporting materials based on carbazole dendrimers for electroluminescent devices. *Thin Solid Films* 516, 2881–2888. doi: 10.1016/j.tsf.2007.05.062
- Reineke, S., Thomschke, M., Lüssem, B., and Leo, K. (2013). White organic light-emitting diodes: status and perspective. *Rev. Modern Phys.* 85, 1245–1293. doi: 10.1103/RevModPhys.85.1245
- Shao, S., Ding, J., Wang, L., Jing, X., and Wang, F. (2012). White electroluminescence from all-phosphorescent single polymers on a fluorinated poly(arylene ether phosphine oxide) backbone simultaneously grafted with blue and yellow phosphors. *J. Am. Chem. Soc.* 134, 20290–20293. doi: 10.1021/ja310158j
- Shao, S., Wang, S., Xu, X., Yang, Y., Lv, J., Ding, J., et al. (2018). Realization of high-power-efficiency white electroluminescence from a single polymer by energy-level engineering. *Chem. Sci.* 9, 8656–8664. doi: 10.1039/c8sc03753a
- Tao, Y., Yuan, K., Chen, T., Xu, P., Li, H., Chen, R., et al. (2014). Thermally activated delayed fluorescence materials towards the breakthrough of organoelectronics. *Adv. Mater.* 26, 7931–7958. doi: 10.1002/adma.201402532
- Tessler, N., Ho, P. K. H., Cleave, V., Pinner, D. J., Friend, R. H., Yahioglu, G., et al. (2000). Material and device related properties in the context of the possible making of electrically pumped polymer laser. *Thin Solid Films* 363, 64–67. doi: 10.1016/S0040-6090(99)00986-4
- Tong, K. L., Tsang, S. W., Tsung, K. K., Tse, S. C., and So, S. K. (2007). Hole transport in molecularly doped naphthyl diamine. *J. Appl. Phys.* 102, 1–5. doi: 10.1063/1.2804109
- Tsung, K. K., and So, S. K. (2008). Carrier trapping and scattering in amorphous organic hole transporter. *Appl. Phys. Lett.* 92:103315. doi: 10.1063/1.2894013
- Tu, G., Zhou, Q., Cheng, Y., Wang, L., Ma, D., Jing, X., et al. (2004). White electroluminescence from polyfluorene chemically doped with 1,8-naphthalimide moieties. *Appl. Phys. Lett.* 85, 2172–2174. doi: 10.1063/1.1793356
- Wang, S., Zhao, L., Zhang, B., Ding, J., Xie, Z., Wang, L., et al. (2018). High-energy-level blue phosphor for solution-processed white organic light-emitting diodes with efficiency comparable to fluorescent tubes. *iScience* 6, 128–137. doi: 10.1016/j.isci.2018.07.016
- Wang, Y., Zhu, Y., Xie, G., Zhan, H., Yang, C., and Cheng, Y. (2017). Bright white electroluminescence from a single polymer containing a thermally activated delayed fluorescence unit and a solution-processed orange OLED approaching 20% external quantum efficiency. *J. Mater. Chem. C* 5, 10715–10720. doi: 10.1039/c7tc03769d
- Yang, Y., Zhao, L., Wang, S., Ding, J., and Wang, L. (2018). Red-emitting thermally activated delayed fluorescence polymers with poly(fluorene-co-3,3'-dimethyl diphenyl ether) as the backbone. *Macromolecules* 51, 9933–9942. doi: 10.1021/acs.macromol.8b02050
- Yang, Y., Zhao, L., Wang, S., Ding, J., and Wang, L. (2019). Synthesis and characterization of red-emitting thermally activated delayed fluorescent polymers based on poly(2,7-carbazole-co-3,3'-dimethyldiphenyl ether) as the main chain. *Acta Polym. Sin.* 50, 685–694. doi: 10.11777/j.issn1000-3304.2018.18266
- Zhao, L., Wang, S., Ding, J., and Wang, L. (2018). Solution processible distyrylarylene-based fluorescent dendrimers: tuning of carbazole-dendron generation leads to nondoped deep-blue electroluminescence. *Org. Electron.* 53, 43–49. doi: 10.1016/j.orgel.2017.11.003
- Zhao, L., Wang, S., Shao, S., Ding, J., Wang, L., Li, Z., et al. (2015). Stable and efficient deep-blue terfluorenes functionalized with carbazole dendrons for solution-processed organic light-emitting diodes. *J. Mater. Chem. C* 3, 8895–8903. doi: 10.1039/c5tc01711d

**Conflict of Interest:** The authors declare that the research was conducted in the absence of any commercial or financial relationships that could be construed as a potential conflict of interest.

Copyright © 2020 Yang, Yang, Li, Zhao, Wang, Ding and Wang. This is an open-access article distributed under the terms of the Creative Commons Attribution License (CC BY). The use, distribution or reproduction in other forums is permitted, provided the original author(s) and the copyright owner(s) are credited and that the original publication in this journal is cited, in accordance with accepted academic practice. No use, distribution or reproduction is permitted which does not comply with these terms.





# Saturated Red Electroluminescence From Thermally Activated Delayed Fluorescence Conjugated Polymers

Hongmei Zhan<sup>1</sup>, Yanjie Wang<sup>1</sup>, Kuofei Li<sup>1</sup>, Yuannan Chen<sup>1</sup>, Xiaohu Yi<sup>1\*</sup>, Keyan Bai<sup>1</sup>, Guohua Xie<sup>2,3\*</sup> and Yanxiang Cheng<sup>1\*</sup>

<sup>1</sup> State Key Laboratory of Polymer Physics and Chemistry, Changchun Institute of Applied Chemistry, Chinese Academy of Sciences, Changchun, China, <sup>2</sup> Sauvage Center for Molecular Sciences, Hubei Key Lab on Organic and Polymeric Optoelectronic Materials, Department of Chemistry, Wuhan University, Wuhan, China, <sup>3</sup> Guangdong Provincial Key Laboratory of Luminescence From Molecular Aggregates (South China University of Technology), Guangzhou, China

## OPEN ACCESS

### Edited by:

Nikhil Kumar Singha,  
Indian Institute of Technology  
Kharagpur, India

### Reviewed by:

Lei Yang,  
Arkema, United States  
Wei Jiang,  
Southeast University, China

### \*Correspondence:

Xiaohu Yi  
xhyi@ciac.ac.cn  
Guohua Xie  
guohua.xie@whu.edu.cn  
Yanxiang Cheng  
yanxiang@ciac.ac.cn

### Specialty section:

This article was submitted to  
Polymer Chemistry,  
a section of the journal  
Frontiers in Chemistry

**Received:** 16 December 2019

**Accepted:** 31 March 2020

**Published:** 24 April 2020

### Citation:

Zhan H, Wang Y, Li K, Chen Y, Yi X,  
Bai K, Xie G and Cheng Y (2020)  
Saturated Red Electroluminescence  
From Thermally Activated Delayed  
Fluorescence Conjugated Polymers.  
Front. Chem. 8:332.  
doi: 10.3389/fchem.2020.00332

Two sets of conjugated polymers with anthraquinone groups as pendant acceptors were designed and synthesized. The acceptor is tethered to an diphenylamine group via a phenylene bridge, constructing a thermally activated delayed fluorescence (TADF) unit, which is embedded into the polymer backbone through its donor fragment, while the backbone is composed of dibenzothiophene-S, S-dioxide and 2, 7-fluorene or 2, 7-carbazole groups. The polymers show distinct TADF characteristics, confirmed by transient photoluminescence spectra and theoretical calculations. The carbazole-based polymers exhibit shorter delay lifetimes and lower energy emission relative to the fluorene-based polymers. The non-doped organic light-emitting diodes fabricated via solution processing approach produce efficient red emissions with the wavelengths of 625–646 nm. The carbazole containing polymer with 2% molar content of the TADF unit exhibits the best maximum external quantum efficiency of 13.6% and saturated red electroluminescence with the Commission Internationale de l'Eclairage coordinates of (0.62, 0.37).

**Keywords:** thermally activated delayed fluorescence, red emission, conjugated polymers, anthraquinone, electroluminescence

## INTRODUCTION

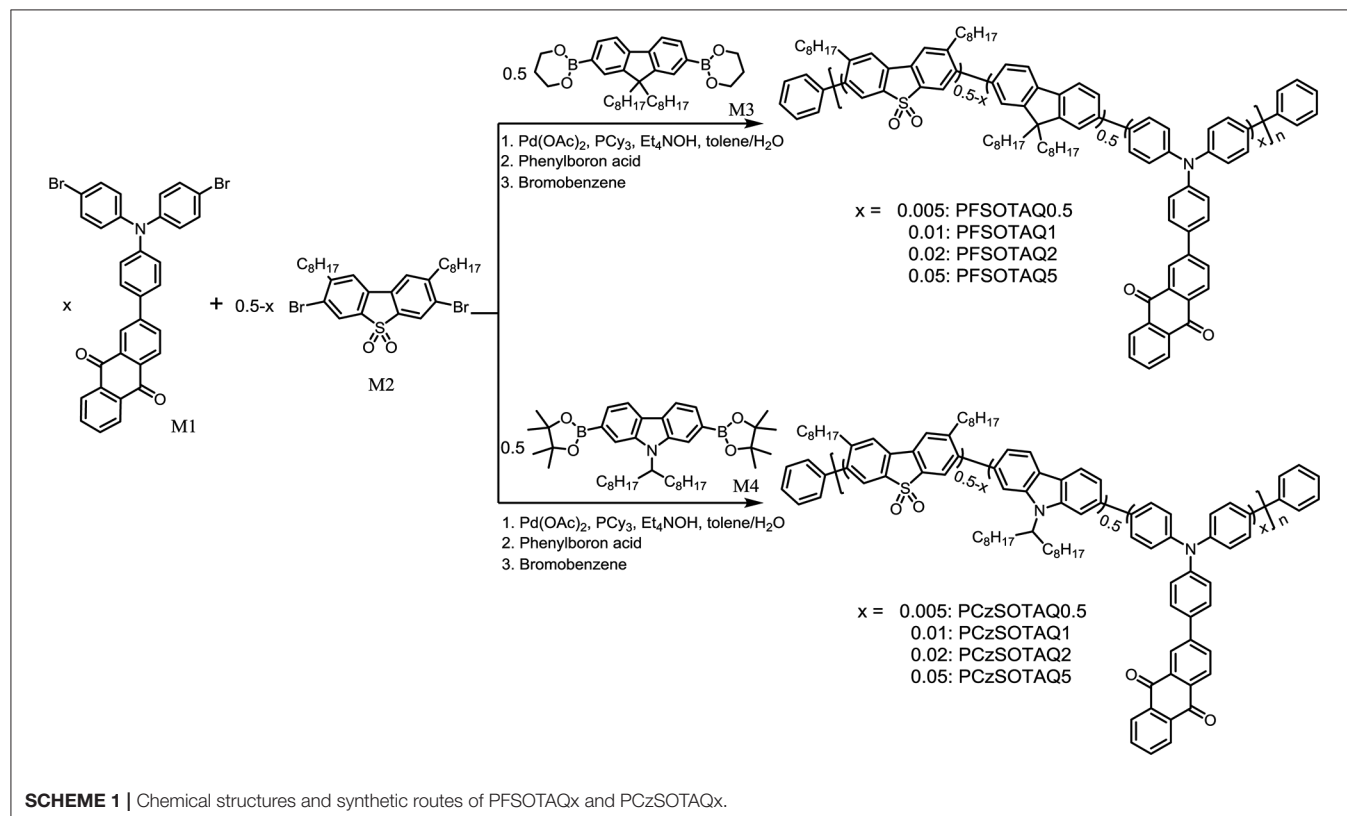
As the new-generation luminescent materials, metal-free thermally activated delayed fluorescence (TADF) emitters have drawn great attentions in the field of organic light-emitting diodes (OLEDs) because they could theoretically achieve 100% internal quantum efficiency through reverse intersystem crossing (RISC) process of non-radiative triplet excitons (Tao et al., 2014; Im et al., 2017; Yang et al., 2017; Huang et al., 2018; Liu et al., 2018; Zou et al., 2018; Godumala et al., 2019). Since Uoyama et al. accomplished a great breakthrough in TADF OLEDs in 2012, realizing the maximum external quantum efficiency (EQE) close to 20% (Uoyama et al., 2012), significant progresses in the development of novel materials and device engineering have been committed, especially in blue and green TADF OLEDs with the EQEs even over 30% (Lin et al., 2016; Wu et al., 2018). However, as one of the three primary colors, the electroluminescent (EL) performances of red TADF emitters still lag far behind due to high non-radiative transition rates and serious concentration quenching effect (Kim et al., 2018a,b; Chen et al., 2019; Wang et al., 2019; Zeng et al., 2019). In addition, the currently reported red TADF materials are mainly based on organic

small molecules with the twisted donor/acceptor structures (Furue et al., 2018; Zhang et al., 2019). In contrast, red TADF polymer has rarely been reported so far, partially due to the challenging material design and synthesis (Wang et al., 2018; Yang et al., 2018a). In view of the good solubility and film-forming property, polymers are more suitable for solution process, which is advantageous for the preparation of low-cost, large area, and non-doped devices (Xie and Li, 2017; Zhang and Cheng, 2019). Therefore, it is urgent to develop efficient red TADF polymers with some new molecular structures.

Conjugated polymer can form a large conjugated system due to the  $\pi$ -electron delocalization in backbone. Theoretically, it is easier to obtain a small energy gap and thus realize red emission. However, the traditional conjugated polymers with conjugation along backbone generally lead to fluorescence rather than TADF due to the lack of the sufficiently twisted donor/acceptor structure. Therefore, a few novel polymeric structures have been presented to produce TADF effect. For example, a red TADF unit is attached on the poly(aryl ether) backbone through an alkyl chain and the resultant polymers exhibit red emission peaked at 606 nm with an EQE of up to 5.6% (Yang et al., 2018a). In our previous work, based on the backbone-donor/pendant-acceptor (BDPA) strategy (Zhu et al., 2016, 2018; Yang et al., 2018b, 2019), a series of long-wavelength emissive TADF conjugated polymers containing the narrow bandgap TADF unit 2-(4-(diphenylamino)-phenyl)-9H-thioxanthen-9-one-10,10-dioxide were also prepared (Wang Y. et al., 2017). The polymers not only inherited the inherent

TADF characteristics of the small molecules as monomers, but also exhibited the red-shifted emission compared with the monomers. Among these polymers, PFSOTT2 showed bright orange emission and a considerably high maximum EQE close to 20%. These results motivate us to further develop efficient red TADF polymers by improving the polymer architecture design.

Herein, two series of TADF conjugated polymers PFSOTAQx and PCzSOTAQx ( $x = 0.5, 1, 2$  and 5, respectively) were designed and synthesized based on the BDPA strategy (**Scheme 1**). A rigid anthraquinone group with the stronger electron-withdrawing ability, compared with 9H-thioxanthen-9-one-10,10-dioxide, is attached to the diphenylamine fragment of polymer backbone via a phenylene bridge to form a narrow bandgap TADF unit (TAQ, seemingly consisting of a triphenylamine donor and an anthraquinone acceptor). The apparent difference between two sets of the polymers originates from the polymer backbones, consisting of dibenzothiophene-S, S-dioxide (SO) and 2, 7-fluorene (F) or SO and 2, 7-carbazole (Cz) groups, respectively, in which the introduction of SO group can weaken the conjugation of the polymer backbone and thus raise the triplet energy level of the polymers (Wang Y. et al., 2017). In comparison with fluorene group, Cz ring has a stronger electron donating ability and acts a better hole transporting role. As expected, the carbazole-based polymers PCzSOTAQx display better device performances. Especially, PCzSOTAQ2 achieves the saturated red emission with the Commission Internationale de l'Eclairage (CIE) coordinates of (0.62, 0.37) and a maximum EQE of 13.6%.



## RESULTS AND DISCUSSION

### Synthesis and Characterization

As shown in **Scheme 1**, polymers PFSOTAQx and PCzSOTAQx were synthesized via Suzuki polycondensation of the corresponding monomers, 2-(4-(bis(4-bromophenyl)amino)phenyl)-anthraquinone (M1), 3,7-dibromo-2,8-dioctyldibenzothiophene-S,S-dioxide (M2) and alkyl substituted fluorene or carbazole diboronic ester (M3 or M4), using Pd(OAc)<sub>2</sub>/PCy<sub>3</sub> as catalyst and tetraethylammonium hydroxide (Et<sub>4</sub>NOH) as an emulsifying base, followed by end-capping with phenyl boronic acid and bromobenzene (Liu et al., 2008a). Higher molecular weight can be obtained under the reaction condition instead of Pd(P(*o*-tol)<sub>3</sub>)<sub>2</sub>Cl<sub>2</sub>/K<sub>3</sub>PO<sub>4</sub>/THF catalytic system generally used in the previous works (Zhu et al., 2016, 2018; Yang et al., 2018b, 2019). The molar feed ratio (x) of M1 was varied from 0.5 to 5%, and the corresponding polymers were named as PFSOTAQx and PCzSOTAQx, respectively. TAQ molecule was prepared by Suzuki coupling reaction of 2-bromoanthraquinone and 4-(diphenylamino)-phenylboronic acid, followed by bromination with *N*-bromosuccinimide (NBS) in the dark to afford the monomer M1 (**Scheme S1**). Monomers M2-M4 with alkyl substituents were synthesized according to the literatures (Xin et al., 2005; Blouin et al., 2007; Kamtekar et al., 2010). The introduction of alkyl groups allows the polymers to have excellent solubility in common organic solvents, such as THF, chloroform and toluene, etc., which is favorable for solution processing of light-emitting device. The number average molecular weights (*M<sub>n</sub>*) of PFSOTAQx range from 54.2 to 65.8 kDa with polydispersity indexes (PDIs) of 2.0–2.3, while PCzSOTAQx have the relatively low *M<sub>n</sub>*s of 25.4–39.1 kDa and similar PDI values (**Table S1**), as determined by gel permeation chromatography (GPC) with 1,2,4-trichlorobenzene as eluent and calibrated against polystyrene standards. All polymers show excellent thermal stability with a high decomposition temperature of over 426°C (*T<sub>d</sub>*, corresponding to 5% weight loss, **Figure S1**). The *T<sub>d</sub>* values of PCzSOTAQx are higher than those of PFSOTAQx because carbazole is fully aromatic in contrast to fluorene group, providing a better chemical and environmental stability (Blouin et al., 2007). The film forming abilities of

PFSOTAQ2 and PCzSOTAQ2 were also studied by atomic force microscopy (AFM) technology (**Supporting Information**). The root mean square (RMS) roughness of thin films is 0.193 nm for PFSOTAQ2 and 0.179 nm for PCzSOTAQ2, indicating that both film surfaces are quite smooth. The superior film morphologies further confirm that these polymers are suitable for preparing OLED devices via solution processing method.

### Photophysical Properties

The polymers PFSOTAQx and PCzSOTAQx exhibit similar UV-vis absorption and photoluminescence (PL) profiles either in dilute solution or neat films (**Figures 1, 2**). Taking PFSOTAQx as examples, the strong absorption bands at around 336 nm are ascribed to the  $\pi$ - $\pi^*$  transition of the conjugated backbone, and the weak absorption band between 400 and 550 nm observed in PFSOTAQ2 and PFSOTAQ5 with the higher contents of the TAQ unit can be assigned to the intramolecular charge-transfer (ICT) transition. In dilute solution, PFSOTAQ1-PFSOTAQ5 display dual emissions with a dominant blue emission which peaks at around 405 nm and originates from the polymer backbone. Moreover, a weak red emission peaked at around 611 nm results from the TADF unit. In contrast, PFSOTAQ0.5 with a low content of the TAQ unit only exhibits a blue emission. Unlike their absorption spectra, the clearly intensified red emission, especially in PFSOTAQ5, indicates the occurrence of the intramolecular Förster energy transfer from the polymer backbone to the TADF unit. This is supported by the sufficient overlap between the PL emission of the backbone and the ICT absorption of the TADF unit (**Figure S2**). In neat film, the polymers exhibit a dominant red emission and a weak blue emission, indicating that the more efficient energy transfer from the backbone to the TADF unit occurs due to the synergistic effect of intramolecular and intermolecular interactions in the solid state. Concurrently, the red emission of PFSOTAQx gradually shifts from 587 to 627 nm as the content of the TADF unit increases owing to the enhanced aggregation of the TADF unit. In comparison with PFSOTAQx, the maximum emission peaks of PCzSOTAQx show some red shifts of 1–19 nm due to the stronger electron-donating ability of carbazole

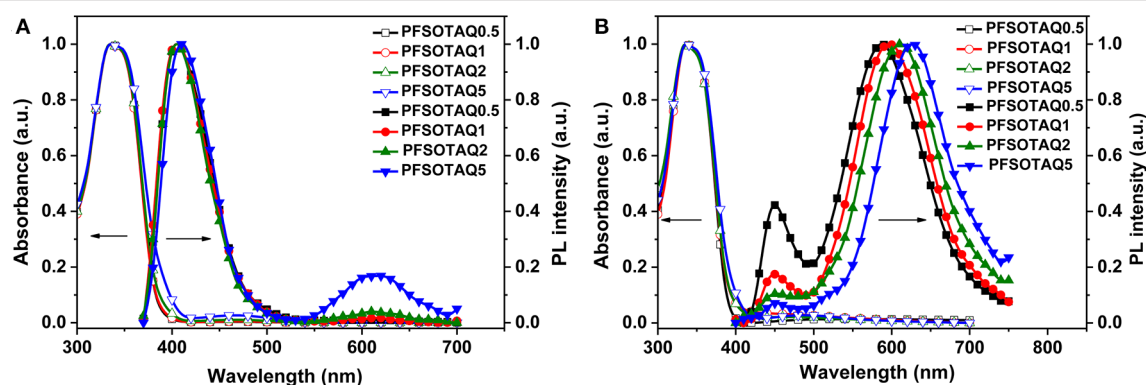


**FIGURE 1** | Normalized UV-vis absorption and PL spectra of PFSOTAQx in oxygen-free toluene **(A)** and neat film **(B)** at 298 K.

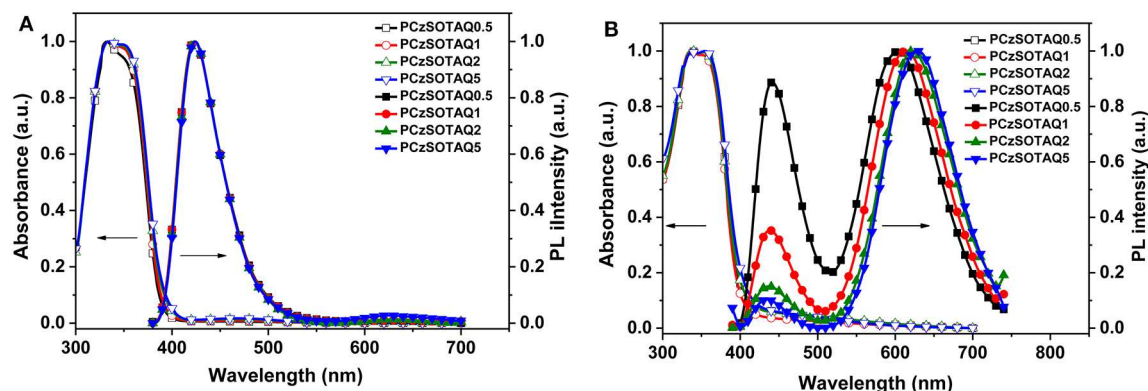


**FIGURE 2** | Normalized UV-vis absorption and PL spectra of PCzSOTAQx in oxygen-free toluene (A) and neat film (B) at 298 K.

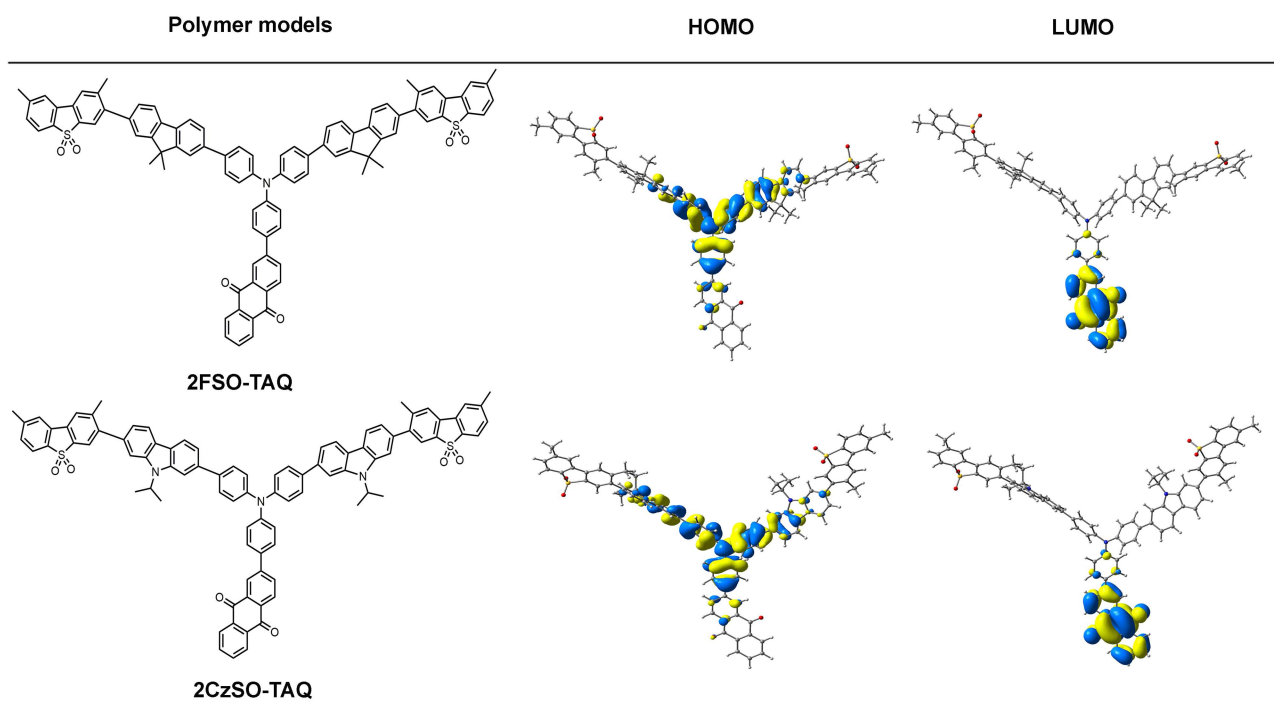


**FIGURE 3** | The molecular structures and HOMO/LUMO distributions of the polymer models in the  $S_0$  state. They were optimized at the DFT/BMK/6-31G(d) level.

compared with the fluorene group. These results demonstrate that the red emission of conjugated polymer could be achieved simply by enhancing the strength of pendant acceptor and/or backbone donor.

In order to understand the relationship between the geometric structures and intrinsic electronic characteristics of the polymers, time-dependent density functional theory (TD-DFT) calculations were performed. 2FSO-TAQ and 2CzSO-TAQ containing one TADF unit, two fluorene or carbazole and two dibenzothiophene-S,S-dioxide rings were chosen as the polymer models. Their ground-state ( $S_0$ ) geometries were optimized at

the BMK/6-31G(d) level in toluene. In the  $S_0$  geometries, the dihedral angles between the donor and phenylene bridge are  $36.5^\circ$  for 2FSO-TAQ and  $38.0^\circ$  for 2CzSO-TAQ (Figure S7), which are similar to those of TADF small molecules based on the diphenylamine donor (Zhang et al., 2014; Bin et al., 2017; Wang S. et al., 2017; Furue et al., 2018), indicating that the change of the backbone building segment has no significant effect on the twisted angle between the acceptor and donor of the TADF unit, and that the polymers could inherit the TADF characteristics of the TADF unit. As shown in Figure 3, the lowest unoccupied molecular orbitals (LUMOs) of 2FSO-TAQ and 2CzSO-TAQ are



predominantly located on the anthraquinone acceptor, whereas the highest occupied molecular orbitals (HOMOs) are mainly distributed on the diphenylamine donor, the adjacent fluorene or carbazole rings and phenylene bridge. There is a certain degree of overlap on the phenylene bridge. The calculated singlet-triplet energy gaps ( $\Delta E_{ST}$ s) are 0.20 eV for 2FSO-TAQ and 0.16 eV for 2CzSO-TAQ, which are in good agreement with the experimental values of PFSOTAQ2 and PCzSOTAQ2 in film (Figure S3 and Tables S2, S3). The small  $\Delta E_{ST}$  values are in favor of the up-conversion from  $T_1$  to  $S_1$  states. In comparison with PFSOTAQx, the polymers PCzSOTAQx show the smaller  $\Delta E_{ST}$ , attributed to the stronger electron-donating ability of carbazole group. Additionally, 2CzSO-TAQ shows a slightly large oscillator strength ( $f$ ) relative to 2FSO-TAQ, which is beneficial to increase the fluorescence radiative rate (Zhang et al., 2014; Furue et al., 2018). This is also reflected that in the neat film the  $\Phi_{PL}$ s are up to 0.71 for PFSOTAQx and 0.75 for PCzSOTAQx, respectively.

To verify the TADF features of the polymers, the transient PL decay spectra were measured in neat film under nitrogen.

As depicted in Figure 4 and Table 1, both PFSOTAQx and PCzSOTAQx show distinct nanosecond-scale prompt decay and microsecond-scale delayed decay. The lifetimes of the delayed fluorescence components ( $\tau_{DF}$ ) of PCzSOTAQx significantly decrease, compared with those of PFSOTAQx, probably benefited from their smaller  $\Delta E_{ST}$ s. Meanwhile, PCzSOTAQx exhibits an increased prompt fluorescence rate constant ( $k_F$ ) and a higher delayed fluorescence rate ( $k_{TADF}$ ) relative to PFSOTAQx under the same molar content of the TAQ unit (Table S5, Supporting Information), which are in favor of effective utilization of triplet excitons and good device performance.

## Electroluminescent Properties

To evaluate their EL, the non-doped OLEDs were fabricated with a structure of ITO/PEDOT:PSS (40 nm)/PFSOTAQx or PCzSOTAQx (40 nm)/SPPO13 (70 nm)/LiQ (1 nm)/Al (100 nm), where PEDOT:PSS [poly(3,4-ethylenedioxythiophene):poly(styrene sulfonate)],

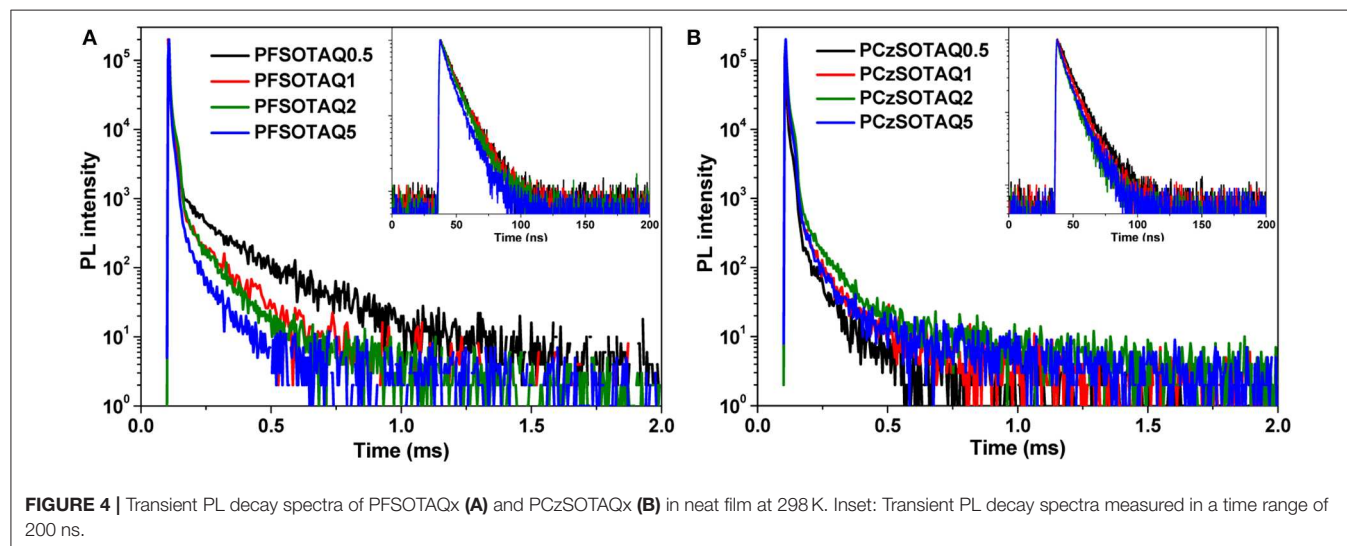


**TABLE 1** | Photophysical data for polymers PFSOTAQx and PCzSOTAQx.

Polymers	$\lambda_{abs}$	$\lambda_{PL}$	$\Phi_{PL}$	$\tau_{PF}$ (ratio)	$\tau_{DF}$ (ratio)	HOMO	LUMO
	[nm]sol <sup>a</sup> /film <sup>b</sup>	[nm]sol <sup>a</sup> /film <sup>b</sup>		[ns (%)] <sup>d</sup>	[ $\mu$ s (%)] <sup>d</sup>		
PFSOTAQ0.5	335/337	405/451, 587	70	10.8 (82)	226 (18)	−6.19	—
PFSOTAQ1	336/336	405,611/450,597	71	10.9 (84)	125 (16)	−6.17	—
PFSOTAQ2	336/336	405,611/443,612	58	10.2 (85)	93 (15)	−6.16	−4.12
PFSOTAQ5	337/337	410,615/451,627	39	8.9 (92)	83 (8)	−6.13	−4.09
PCzSOTAQ0.5	332/336	423/442,606	75	10.8 (94)	57 (6)	−5.92	—
PCzSOTAQ1	335/336	424,632/439,615	62	9.8 (89)	85 (11)	−5.91	—
PCzSOTAQ2	335/337	424,627/437,623	53	8.9 (86)	89 (14)	−5.90	−3.86
PCzSOTAQ5	335/355	424,625/434,628	48	8.8 (90)	60 (10)	−5.89	−3.85

<sup>a</sup>Measured in toluene at room temperature.

<sup>b</sup>Measured in neat film at room temperature.

<sup>c</sup>Measured in the neat film free of oxygen.

<sup>d</sup>The lifetimes and fractional contributions of the prompt ( $\tau_{PF}$ ) and delayed ( $\tau_{DF}$ ) decay components in neat film measured at 298 K.

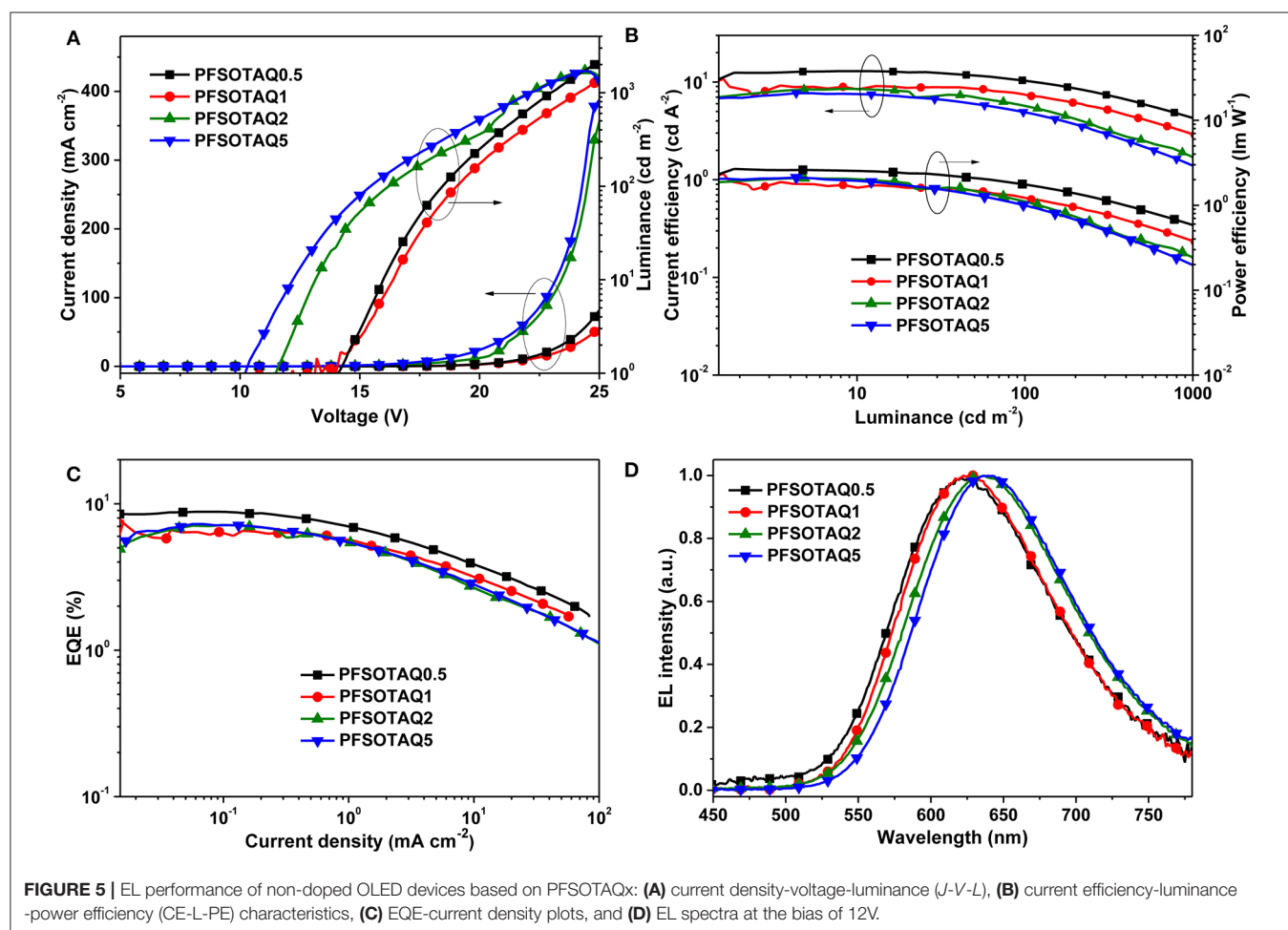
<sup>e</sup>Determined by cyclic voltammetry in neat films.

<sup>f</sup>Deduced from the HOMO and the optical energy gap ( $E_g$ ) values.

Liq (8-hydroxyquinolinolato-lithium), and SPPO13 (2,7-bis(diphenylphosphoryl)-9,9'-spirobifluorene) were used as the hole-injection layer, the electron-injection layer and the electron-transporting layer, respectively. **Figures 5, 6** show the characteristic EL curves, and the key devices parameters are summarized in **Table 2**. All devices exhibit predominant red EL emission with the single peak at 625–638 nm for PFSOTAQx and 630–646 nm for PCzSOTAQx, in which the emissive peaks gradually red-shift with the increasing content of the TAQ unit, which is consistent with dominant emissive peaks of these polymers in PL spectra of neat film. There is no residual blue EL emission from the polymer backbones, even at 0.5 mol% TAQ content, which totally differs from the corresponding PL spectra. Such dramatic difference between the EL and PL spectra may be partially attributed to the direct charge trapping of the TADF unit in terms of the fact that the HOMO and LUMO energy levels of the model compound TAQ lie between those of PFSO or PCzSO (**Figure S6**; Gong et al., 2003), in addition to more effective energy transfer from the backbone to TAQ unit in the solid state. For PCzSOTAQx, the significant changes in blue emission peaks from the PL to EL spectra indicate that direct charge trapping on the TADF unit serves as the dominant EL mechanism rather than Förster energy transfer (Liu et al., 2008b; Ma et al., 2010). It can

be further confirmed by the current density-voltage-luminance curves of the polymers. Moreover, in the same set of polymers, the variation trends of EL efficiencies basically correspond to the proportions of delayed fluorescence component, demonstrating that the EL process in the polymers comes from the TADF mechanism.

By replacing fluorene in the polymer backbone with a 2,7-carbazole group, the polymers PCzSOTAQx exhibit superior EL performances compared with PFSOTAQx, complemented by the excellent hole transporting ability of carbazole group. The turn-on voltages of the devices are significantly reduced from 10.2–14.1 V to 7.1–8.5 V because the shallow HOMO energy levels of PCzSOTAQx reduce the injection barrier of holes from PEDOT:PSS. The maximum EQEs of all devices are over 7% while the CIE coordinates for PCzSOTAQ1–5 are (0.61, 0.39), (0.62, 0.37), and (0.63, 0.37), respectively. Among these polymers, PCzSOTAQ2 achieves the highest maximum EQE of 13.6%. To the best of our knowledge, it is the best one of the solution-processed OLEDs based on red TADF polymers reported so far (Wang et al., 2018; Yang et al., 2018a; Hu et al., 2019). It is worth noting that our designed conjugated polymers show much better EL performances than the previously reported polymers PFDMP-E-R01-10 with the



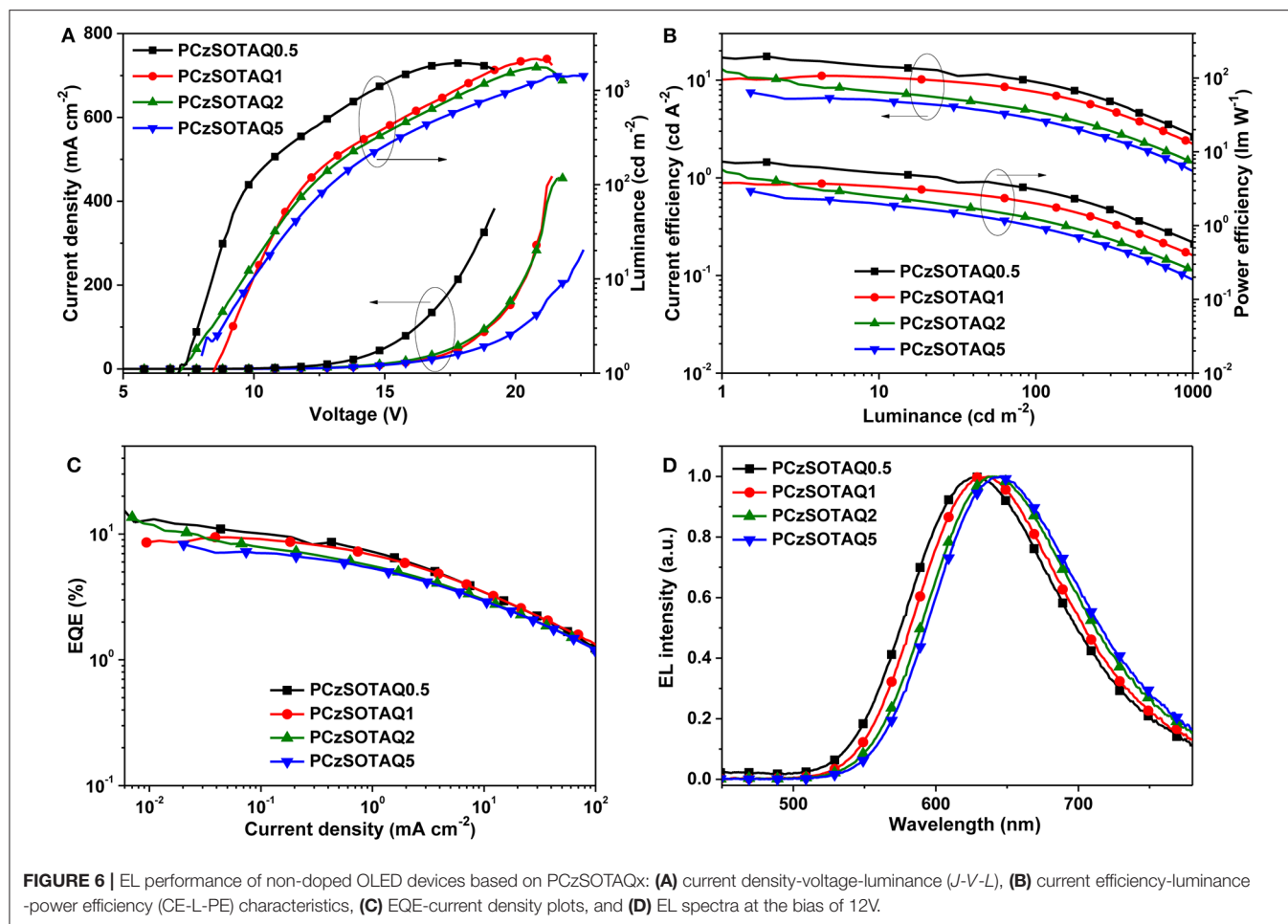


**FIGURE 6 |** EL performance of non-doped OLED devices based on PCzSOTAQx: **(A)** current density-voltage-luminance (*J-V-L*), **(B)** current efficiency-luminance-power efficiency (*CE-L-PE*) characteristics, **(C)** EQE-current density plots, and **(D)** EL spectra at the bias of 12V.

**TABLE 2 |** EL data of the non-doped devices based on PFSOTAQx and PCzSOTAQx.

Devices	V <sub>on</sub> <sup>a</sup> (V)	L <sub>max</sub> <sup>b</sup> (cd m <sup>-2</sup> )	CE <sub>max</sub> <sup>c</sup> (cd A <sup>-1</sup> )	EQE <sub>max</sub> <sup>d</sup> (%)	PE <sub>max</sub> <sup>e</sup> (lm W <sup>-1</sup> )	EL <sup>f</sup> (nm)	CIE (x, y)
PFSOTAQ0.5	14.1	2,107	12.9	8.8	2.7	625	(0.57, 0.41)
PFSOTAQ1	13.8	1,365	10.8	7.8	2.4	627	(0.59, 0.40)
PFSOTAQ2	11.5	1,716	8.5	7.2	2.1	637	(0.60, 0.39)
PFSOTAQ5	10.2	1,708	7.7	7.3	2.1	638	(0.62, 0.38)
PCzSOTAQ0.5	7.1	1,947	17.5	13.1	7.2	630	(0.59, 0.39)
PCzSOTAQ1	8.4	2,158	11.2	9.5	3.7	637	(0.61, 0.39)
PCzSOTAQ2	7.1	1,753	12.2	13.6	5.3	642	(0.62, 0.37)
PCzSOTAQ5	7.7	1,434	7.5	8.3	2.9	646	(0.63, 0.37)

<sup>a</sup>The turn-on voltage (V<sub>on</sub>).

<sup>b</sup>The maximum luminance brightness (L<sub>max</sub>).

<sup>c</sup>The maximum current efficiency (CE<sub>max</sub>).

<sup>d</sup>The maximum external quantum efficiency (EQE<sub>max</sub>).

<sup>e</sup>The maximum power efficiency (PE<sub>max</sub>).

<sup>f</sup>The peak wavelength of EL spectra.

TAQ unit [EQE: 5.6% and CIE: (0.57, 0.42)] (Yang et al., 2018a). To confirm the effect of carbazole group on the EL behavior, the hole and electron transporting abilities of PFSOTAQ2 and PCzSOTAQ2 were also investigated by the preparation of single

carrier devices, as shown in **Figure S7**. Clearly, the carbazole-based PCzSOTAQ2 exhibits better hole transport capability, ascribed to the shallower HOMO energy level of PCzSOTAQ2, relative to the fluorene-based polymer PFSOTAQ2, while they

show similar electron transport behaviors due to the same acceptor group and the similar conjugation. This may be one of the reasons for better comprehensive device performance of PCzSOTAQ2 than PFSOTAQ2. These results indicate that the backbone structure has a crucial influence on the EL behaviors of the polymers, and thus confirm that the conjugated structure is more favorable for obtaining more efficient red TADF polymer.

## CONCLUSIONS

In summary, the strong electron-withdrawing group anthraquinone was employed as pendant acceptor to successfully prepare red TADF conjugated polymers. Although the polymers all exhibited obvious the delayed fluorescence with microsecond-scale lifetimes, the introduction of carbazole group, instead of fluorene of the polymer backbone, created a positive effect on the PL and EL behaviors. The highest PL quantum yield in neat film is up to 0.75 and the maximum EQEs in the non-doped solution-processed devices all exceed the upper limit of 5% of the traditional fluorescent OLEDs. Especially, the device using the carbazole-based polymer PCzSOTAQ2 displays the saturated red EL emission with the CIE coordinates of (0.62, 0.37) and a very promising EQE of 13.6%. These results demonstrated that conjugated polymers have great potential as red TADF materials in the field of OLEDs and their PL and EL properties can be effectively improved through simple modification of the polymer structure.

## DATA AVAILABILITY STATEMENT

All datasets generated for this study are included in the article/**Supplementary Material**.

## REFERENCES

- Bin, H., Ji, Y., Li, Z., Zhou, N., Jiang, W., Feng, Y., et al. (2017). Simple aggregation-induced delayed fluorescence materials based on anthraquinone derivatives for highly efficient solution-processed red OLEDs. *J. Lumin.* 187, 414–420. doi: 10.1016/j.jlumin.2017.03.038
- Blouin, N., Michaud, A., and Leclerc, M. (2007). A low-bandgap poly(2,7-Carbazole) derivative for use in high-performance solar cells. *Adv. Mater.* 19, 2295–2300. doi: 10.1002/adma.200602496
- Chen, J. X., Tao, W. W., Chen, W. C., Xiao, Y. F., Wang, K., Cao, C., et al. (2019). Red/near-infrared thermally activated delayed fluorescence OLEDs with near 100 % internal quantum efficiency. *Angew. Chem. Int. Ed.* 58, 14660–14665. doi: 10.1002/anie.201906575
- Furue, R., Matsuo, K., Ashikari, Y., Ooka, H., Amanokura, N., and Yasuda, T. (2018). Highly efficient red-orange delayed fluorescence emitters based on strong  $\pi$ -accepting dibenzophenazine and dibenzoquinoxaline cores: toward a rational pure-red OLED design. *Adv. Opt. Mater.* 6:1701147. doi: 10.1002/adom.201701147
- Godumala, M., Choi, S., Cho, M. J., and Choi, D. H. (2019). Recent breakthroughs in thermally activated delayed fluorescence organic light emitting diodes containing non-doped emitting layers. *J. Mater. Chem. C* 7, 2172–2198. doi: 10.1039/c8tc06293e
- Gong, X., Ostrowski, J. C., Moses, D., Bazan, G. C., and Heeger, A. J. (2003). Electrophosphorescence from a polymer guest-host system

## AUTHOR CONTRIBUTIONS

HZ, YW, and KL performed the synthesis and characterization of materials, and photophysical properties measurements. YuC performed the theoretical calculation. KB carried out the EL experiments. HZ prepared the manuscript. HZ, XY, GX, and YaC conducted the discussion and analysis of the experimental results as well as the improvement of the manuscript.

## FUNDING

This work was financially supported by the National Key R&D Program of China (No. 2016YFB0401000), the National Natural Science Foundation of China (Nos. 21674110, 51973210, and 21805271), and the Science and Technology Development Project of Jilin Province (China, No. 20190201071JC). GX was supported by the Open Fund of Guangdong Provincial Key Laboratory of Luminescence from Molecular Aggregates, Guangzhou, China (South China University of Technology) (No. 2019B030301003).

## ACKNOWLEDGMENTS

We thank the Network and Computing Center, Changchun Institute of Applied Chemistry, Chinese Academy of Sciences for the essential support.

## SUPPLEMENTARY MATERIAL

The Supplementary Material for this article can be found online at: <https://www.frontiersin.org/articles/10.3389/fchem.2020.00332/full#supplementary-material>

- with an iridium complex as guest: Förster energy transfer and charge trapping. *Adv. Funct. Mater.* 13, 439–444. doi: 10.1002/adfm.200304334
- Hu, J., Li, Q., Wang, X., Shao, S., Wang, L., Jing, X., et al. (2019). Developing through-space charge transfer polymers as a general approach to realize full-color and white emission with thermally activated delayed fluorescence. *Angew. Chem. Int. Ed.* 58, 8405–8409. doi: 10.1002/anie.201902264
- Huang, T., Jiang, W., and Duan, L. (2018). Recent progress in solution processable TADF materials for organic light-emitting diodes. *J. Mater. Chem. C* 6, 5577–5596. doi: 10.1039/c8tc01139g
- Im, Y., Kim, M., Cho, Y. J., Seo, J.-A., Yook, K. S., and Lee, J. Y. (2017). Molecular design strategy of organic thermally activated delayed fluorescence emitters. *Chem. Mater.* 29, 1946–1963. doi: 10.1021/acs.chemmater.6b05324
- Kamtekar, K. T., Vaughan, H. L., Lyons, B. P., Monkman, A. P., Pandya, S. U., and Bryce, M. R. (2010). Synthesis and spectroscopy of poly(9,9-dioctylfluorene-2,7-diyl-co-2,8-dihexyldibenzothiophene-S,S-dioxide-3,7-diyl)s: solution-processable, deep-blue emitters with a high triplet energy. *Macromolecules* 43, 4481–4488. doi: 10.1021/ma100566p
- Kim, J. H., Lee, D. R., Han, S. H., and Lee, J. Y. (2018b). Over 20% external quantum efficiency in red thermally activated delayed fluorescence organic light-emitting diodes using a reverse intersystem crossing activating host. *J. Mater. Chem. C* 6, 5363–5368. doi: 10.1039/c7tc05811j



- Kim, J. H., Yun, J. H., and Lee, J. Y. (2018a). Recent progress of highly efficient red and near-infrared thermally activated delayed fluorescent emitters. *Adv. Opt. Mater.* 6:1800255. doi: 10.1002/adom.201800255
- Lin, T. A., Chatterjee, T., Tsai, W. L., Lee, W. K., Wu, M. J., Jiao, M., et al. (2016). Sky-blue organic light emitting diode with 37% external quantum efficiency using thermally activated delayed fluorescence from spiroacridine-triazine hybrid. *Adv. Mater.* 28, 6976–6983. doi: 10.1002/adma.201601675
- Liu, J., Chen, L., Shao, S., Xie, Z., Cheng, Y., Geng, Y., et al. (2008a). Highly efficient red electroluminescent polymers with dopant/host system and molecular dispersion feature: polyfluorene as the host and 2,1,3-benzothiadiazole derivatives as the red dopant. *J. Mater. Chem.* 18, 319–327. doi: 10.1039/b712562c
- Liu, J., Zou, J., Yang, W., Wu, H., Li, C., Zhang, B., et al. (2008b). Highly efficient and spectrally stable blue-light-emitting polyfluorenes containing a dibenzothiophene-S,S-dioxide unit. *Chem. Mater.* 20, 4499–4506. doi: 10.1021/cm800129h
- Liu, Y., Li, C., Ren, Z., Yan, S., and Bryce, M. R. (2018). All-organic thermally activated delayed fluorescence materials for organic light-emitting diodes. *Nat. Rev. Mater.* 3:18020. doi: 10.1038/natrevmats.2018.20
- Ma, Z., Ding, J., Zhang, B., Mei, C., Cheng, Y., Xie, Z., et al. (2010). Red-emitting polyfluorenes grafted with quinoline-based iridium complex: “simple polymeric chain, unexpected high efficiency”. *Adv. Funct. Mater.* 20, 138–146. doi: 10.1002/adfm.200901595
- Tao, Y., Yuan, K., Chen, T., Xu, P., Li, H., Chen, R., et al. (2014). Thermally activated delayed fluorescence materials towards the breakthrough of organoelectronics. *Adv. Mater.* 26, 7931–7958. doi: 10.1002/adma.201402532
- Uoyama, H., Goushi, K., Shizu, K., Nomura, H., and Adachi, C. (2012). Highly efficient organic light-emitting diodes from delayed fluorescence. *Nature* 492, 234–238. doi: 10.1038/nature11687
- Wang, B., Yang, H., Zhang, Y., Xie, G., Ran, H., Wang, T., et al. (2019). Highly efficient electroluminescence from evaporation- and solution-processable orange-red thermally activated delayed fluorescence emitters. *J. Mater. Chem. C* 7, 12321–12327. doi: 10.1039/c9tc04418c
- Wang, S., Cheng, Z., Song, X., Yan, X., Ye, K., Liu, Y., et al. (2017). Highly efficient long-wavelength thermally activated delayed fluorescence OLEDs based on dicyanopyrazino phenanthrene derivatives. *ACS Appl. Mater. Interfaces* 9, 9892–9901. doi: 10.1021/acsami.6b14796
- Wang, Y., Zhu, Y., Xie, G., Xue, Q., Tao, C., Le, Y., et al. (2018). Red thermally activated delayed fluorescence polymers containing 9H-thioxanthen-9-one-10,10-dioxide acceptor group as pendant or incorporated in backbone. *Org. Electron.* 59, 406–413. doi: 10.1016/j.orgel.2018.05.058
- Wang, Y., Zhu, Y., Xie, G., Zhan, H., Yang, C., and Cheng, Y. (2017). Bright white electroluminescence from a single polymer containing a thermally activated delayed fluorescence unit and a solution-processed orange OLED approaching 20% external quantum efficiency. *J. Mater. Chem. C* 5, 10715–10720. doi: 10.1039/c7tc03769d
- Wu, T.-L., Huang, M.-J., Lin, C.-C., Huang, P.-Y., Chou, T.-Y., Chen-Cheng, R.-W., et al. (2018). Diboron compound-based organic light-emitting diodes with high efficiency and reduced efficiency roll-off. *Nat. Photon.* 12, 235–240. doi: 10.1038/s41566-018-0112-9
- Xie, Y., and Li, Z. (2017). Thermally activated delayed fluorescent polymers. *J. Polym. Sci. Part A Polym. Chem.* 55, 575–584. doi: 10.1002/pola.28448
- Xin, Y., Wen, G.-A., Zeng, W.-J., Zhao, L., Zhu, X.-R., Fan, Q.-L., et al. (2005). Hyperbranched oxadiazole-containing polyfluorenes: toward stable blue light PLEDs. *Macromolecules* 38, 6755–6758. doi: 10.1021/ma050833f
- Yang, Y., Li, K., Wang, C., Zhan, H., and Cheng, Y. (2019). Effect of a pendant acceptor on thermally activated delayed fluorescence properties of conjugated polymers with backbone-donor/pendant-acceptor architecture. *Chem. Asian. J.* 14, 574–581. doi: 10.1002/asia.201801813
- Yang, Y., Wang, S., Zhu, Y., Wang, Y., Zhan, H., and Cheng, Y. (2018b). Thermally activated delayed fluorescence conjugated polymers with backbone-donor/pendant-acceptor architecture for nondoped OLEDs with high external quantum efficiency and low roll-off. *Adv. Funct. Mater.* 28:1706916. doi: 10.1002/adfm.201706916
- Yang, Y., Zhao, L., Wang, S., Ding, J., and Wang, L. (2018a). Red-emitting thermally activated delayed fluorescence polymers with poly(fluorene-co-3,3'-dimethyl diphenyl ether) as the backbone. *Macromolecules* 51, 9933–9942. doi: 10.1021/acs.macromol.8b02050
- Yang, Z., Mao, Z., Xie, Z., Zhang, Y., Liu, S., Zhao, J., et al. (2017). Recent advances in organic thermally activated delayed fluorescence materials. *Chem. Soc. Rev.* 46, 915–1016. doi: 10.1039/c6cs00368k
- Zeng, W., Zhou, T., Ning, W., Zhong, C., He, J., Gong, S., et al. (2019). Realizing 22.5% external quantum efficiency for solution-processed thermally activated delayed-fluorescence OLEDs with red emission at 622 nm via a synergistic strategy of molecular engineering and host selection. *Adv. Mater.* 31:1901404. doi: 10.1002/adma.201901404
- Zhang, B., and Cheng, Y. (2019). Recent advances in conjugated TADF polymer featuring in backbone-donor/pendant-acceptor structure: material and device perspectives. *Chem. Rec.* 19, 1624–1643. doi: 10.1002/tcr.201800152
- Zhang, Q., Kuwabara, H., Potscavage, W. J. Jr., Huang, S., Hatae, Y., Shibata, T., et al. (2014). Anthraquinone-based intramolecular charge-transfer compounds: computational molecular design, thermally activated delayed fluorescence, and highly efficient red electroluminescence. *J. Am. Chem. Soc.* 136, 18070–18081. doi: 10.1021/ja510144h
- Zhang, Y. L., Ran, Q., Wang, Q., Liu, Y., Hanisch, C., Reineke, S., et al. (2019). High-efficiency red organic light-emitting diodes with external quantum efficiency close to 30% based on a novel thermally activated delayed fluorescence emitter. *Adv. Mater.* 31:1902368. doi: 10.1002/adma.201902368
- Zhu, Y., Yang, Y., Wang, Y., Yao, B., Lin, X., Zhang, B., et al. (2018). Improving luminescent performances of thermally activated delayed fluorescence conjugated polymer by inhibiting the intra- and interchain quenching. *Adv. Opt. Mater.* 6:1701320. doi: 10.1002/adom.201701320
- Zhu, Y., Zhang, Y., Yao, B., Wang, Y., Zhang, Z., Zhan, H., et al. (2016). Synthesis and electroluminescence of a conjugated polymer with thermally activated delayed fluorescence. *Macromolecules* 49, 4373–4377. doi: 10.1021/acs.macromol.6b00430
- Zou, Y., Gong, S., Xie, G., and Yang, C. (2018). Design strategy for solution-processable thermally activated delayed fluorescence emitters and their applications in organic light-emitting diodes. *Adv. Opt. Mater.* 6:1800568. doi: 10.1002/adom.201800568

**Conflict of Interest:** The authors declare that the research was conducted in the absence of any commercial or financial relationships that could be construed as a potential conflict of interest.

Copyright © 2020 Zhan, Wang, Li, Chen, Yi, Bai, Xie and Cheng. This is an open-access article distributed under the terms of the Creative Commons Attribution License (CC BY). The use, distribution or reproduction in other forums is permitted, provided the original author(s) and the copyright owner(s) are credited and that the original publication in this journal is cited, in accordance with accepted academic practice. No use, distribution or reproduction is permitted which does not comply with these terms.



# Molecular Design Based on Donor-Weak Donor Scaffold for Blue Thermally-Activated Delayed Fluorescence Designed by Combinatorial DFT Calculations

Youchi Tsuchiya<sup>1,2\*</sup>, Keita Tsuji<sup>1,3</sup>, Ko Inada<sup>1,2</sup>, Fatima Bencheikh<sup>1,2</sup>, Yan Geng<sup>1</sup>, H. Shaun Kwak<sup>4</sup>, Thomas J. L. Mustard<sup>4</sup>, Mathew D. Halls<sup>4</sup>, Hajime Nakanotani<sup>1,2,3</sup> and Chihaya Adachi<sup>1,2,3,5\*</sup>

<sup>1</sup> Center for Organic Photonics and Electronics Research (OPERA), Kyushu University, Fukuoka, Japan, <sup>2</sup> Japan Science and Technology Agency (JST), ERATO, Adachi Molecular Exciton Engineering Project, Fukuoka, Japan, <sup>3</sup> Department of Chemistry and Biochemistry, Kyushu University, Fukuoka, Japan, <sup>4</sup> Schrödinger Inc, San Diego, CA, United States, <sup>5</sup> International Institute for Carbon Neutral Energy Research (WPI-I2CNER), Kyushu University, Fukuoka, Japan

## OPEN ACCESS

### Edited by:

Seiji Mori,  
Ibaraki University, Japan

### Reviewed by:

Siriporn Jungsuttiwong,  
Ubon Ratchathani University, Thailand  
Shi-Jian Su,  
South China University of  
Technology, China

### \*Correspondence:

Youchi Tsuchiya  
tsuchiya@opera.kyushu-u.ac.jp  
Chihaya Adachi  
adachi@cstf.kyushu-u.ac.jp

### Specialty section:

This article was submitted to  
Organic Chemistry,  
a section of the journal  
Frontiers in Chemistry

Received: 30 January 2020

Accepted: 16 April 2020

Published: 06 May 2020

### Citation:

Tsuchiya Y, Tsuji K, Inada K,  
Bencheikh F, Geng Y, Kwak HS,  
Mustard TJL, Halls MD, Nakanotani H  
and Adachi C (2020) Molecular Design  
Based on Donor-Weak Donor Scaffold  
for Blue Thermally-Activated Delayed  
Fluorescence Designed by  
Combinatorial DFT Calculations.  
Front. Chem. 8:403.  
doi: 10.3389/fchem.2020.00403

Quantum chemical calculations are necessary to develop advanced emitter materials showing thermally-activated delayed fluorescence (TADF) for organic light-emitting diodes (OLEDs). However, calculation costs become problematic when more accurate functionals were used, therefore it is judicious to use a multimethod approach for efficiency. Here we employed combinatorial chemistry *in silico* to develop the deep blue TADF materials with a new concept of homo-junction design. The homo-junction materials containing TADF candidates designed by calculation were synthesized and analyzed. We found that these materials showed the emission from charge transfer (CT) state, and the clear delayed emission was provided in solid state. Because the homo-junction TADF materials showed three exponential decayed emission in solid state, we employed novel four-state kinetic analysis.

**Keywords:** TADF, homo-junction design, combinatorial DFT calculation, photo-physics, four-state rate equations

## INTRODUCTION

TADF materials have received significant attention for application in high efficiency OLEDs. This is because TADF materials can realize nearly 100% internal quantum efficiency of electroluminescence by harvesting all electrically generated singlet and triplet excitons as prompt and delayed emission. The effective upconversion of excitons from a triplet excited-state ( $T_1$ ) to a singlet excited-state ( $S_1$ ) is possible because of the small energy splitting between the  $S_1$  and  $T_1$  states ( $\Delta E_{ST}$ ), resulting in nearly 100% reverse intersystem crossing (RISC) efficiency (Uoyama et al., 2012). While the TADF phenomenon has been known as E-type delayed fluorescence since the 1940s (Lewice et al., 1941), no comprehensive molecular design aiming to realize high efficiency TADF has been reported. In 2012, our group reported high efficiency TADF materials by molecular design with electron donor (D) and acceptor (A) units separated by a distance controlled by a linkage/spacer unit (Uoyama et al., 2012). Because  $\Delta E_{ST}$  is theoretically proportional to the exchange integral  $J$  (Yersin, 2018), then

$$\Delta E_{ST} = E_S - E_T = 2J \quad (1)$$

$J$  depends on the electron density overlap between the highest occupied molecular orbital (HOMO) and lowest unoccupied molecular orbital (LUMO), i.e.,

$$J = \iint \phi_H(\mathbf{r}_1)\phi_L(\mathbf{r}_2) \frac{1}{|\mathbf{r}_2 - \mathbf{r}_1|} \phi_H(\mathbf{r}_2)\phi_L(\mathbf{r}_1) d\mathbf{r}_1 d\mathbf{r}_2 \quad (2)$$

where  $\phi_H$  and  $\phi_L$  are the spatial distributions of the HOMO and LUMO, respectively, and  $\mathbf{r}_1$  and  $\mathbf{r}_2$  are position vectors. Thus, it follows that reducing the overlap integral between the HOMO and LUMO decreases the  $J$  and  $\Delta E_{ST}$ . The oscillator strength  $f$ , which is an index for the light emission intensity, is proportional to the square of the transition dipole moment  $Q$ .

$$f \propto |Q|^2 \quad (3)$$

Here, the magnitude of  $Q$  also depends on the orbital overlap between the HOMO and LUMO, i.e.,

$$Q = \iint \phi_H(\mathbf{r}_1)\phi_L(\mathbf{r}_2) |\mathbf{r}_2 - \mathbf{r}_1| \phi_H(\mathbf{r}_2)\phi_L(\mathbf{r}_1) d\mathbf{r}_1 d\mathbf{r}_2 \quad (4)$$

These equations indicate that a well-tuned partial orbital overlap between the HOMO and LUMO is a requisite condition for obtaining both a small  $\Delta E_{ST}$  and high emissivity. The molecular design of a D-A pair combined with  $\pi$ -linkers providing a large dihedral angle or insulating  $\sigma$ -spacers can separate the HOMO and LUMO with a small orbital overlap (Tanaka et al., 2012; Geng et al., 2017). Based on this concept, a wide variety of D-A “hetero-junction” type TADF materials were developed by combining D units that are easily oxidized and A units that are easily reduced, resulting in highly efficient TADF materials (Wong and Zysman-Colman, 2017; Yang et al., 2017; Bui et al., 2018; Liu et al., 2018). However, this D-A architecture largely limits the composite selection to triphenylamines and carbazoles derivatives as donors, and triazines, cyanobenzenes, oxadiazoles, sulphonyls, and carbonyls derivatives as acceptors. Such limitation makes it difficult to expand the TADF scaffold. In particular, there is strong demand for blue TADF emitters based on new molecular structures. General consensus has been that the D-A architecture is mandatory to obtain TADF characteristics. Basically, D and A moieties are categorized by the major properties of each unit with considering its substituents (Hansch et al., 1991). However, we recognized that separation of the HOMO and LUMO, that is, a small  $\Delta E_{ST}$ , can theoretically be obtained even by strong donor-weak donor ( $sD$ - $wD$ ) and strong acceptor-weak acceptor ( $sA$ - $wA$ ) combinations. Because the electron donating and accepting ability is relative between two moieties. Thus, even the homo combination of  $sD$ - $wD$  and  $sA$ - $wA$  should theoretically provide TADF characteristics when the HOMO and LUMO are separated and the material have a small  $\Delta E_{ST}$ . The homo-junction molecular design approach will alleviate the limitation of unit selection for novel blue TADF materials. In this study, we examined the design of TADF materials based on a homo-junction of  $sD$ - $wD$ , particularly aimed for blue TADF emitters.

## RESULTS AND DISCUSSIONS

### Molecular Design Through Combinatorial DFT Calculations

In this work, density functional theory (DFT) analysis was used to identify synthetic motifs for promising blue TADF candidates. First, we estimated  $\Delta E_{ST}$  values for four molecules with a homo-junction design by DFT calculations with a B3LYP/6-31+g\* level of theory. The synthesized compounds showed very large  $\Delta E_{ST}$  values compared with the calculated  $\Delta E_{ST}$  values (Table S1). These large differences were based on the underestimation of exciton energy by the standard functional, B3LYP (Dreuw and Head-Gordon, 2004).  $\Delta E_{ST}$  values estimated using the LC- $\omega$ PBE functional with long-range correction using a tuned  $\omega$  value showed good agreement with the experimental values (Sun et al., 2015). Most of compounds calculated in homo-junction design showed a large  $\Delta E_{ST}$  value in LC- $\omega$ PBE level while the value is small in B3LYP level. Ideally, we would have employed the tuned  $\omega$  LC- $\omega$ PBE functional to evaluate the homo-junction molecules. However, DFT calculations with the tuned  $\omega$  LC- $\omega$ PBE functional is excessively time-consuming. Therefore, we used the combinatorial DFT calculation to discover/locate blue TADF candidates with the homo-junction design using the MacroModel, Jaguar and Gaussian16 software packages. The 87 donor units used to construct TADF molecules were analyzed, and the HOMO, LUMO,  $S_1$  and  $T_1$  energy levels were estimated by DFT calculation with the B3LYP/6-31+g\* level of theory. Figure S1 shows the correlation between the HOMO and LUMO for these composite units. For example, dibenzofuran (DBF, HOMO =  $-0.23$  eV), carbazole (HOMO =  $-0.21$  eV) and 9,9-dimethylacridane (DMAc, HOMO =  $-0.19$  eV) were located in the weak, middle and strong electron donating groups, respectively. Generated  $sD$ - $wD$  combinations using these donor units were screened by the DFT calculation with different functional levels of theory (B3LYP, M06-2X, and LC- $\omega$ PBE). All donor fragments with one, two or more modifiable locations were then modified with all donors with only one modifiable location. This generated a library of 2618 candidate  $sD$ - $wD$  TADF molecules. Candidates were then verified by further DFT calculations with the LC- $\omega$ PBE/6-31+g\* level of theory. From the obtained TADF candidates, we chose the DMac-DBF combinations listed in Figure 1 and Table S2 as the final blue TADF candidates for the homo-junction design.

### Photophysical Properties of Homo-Junction Materials

We therefore synthesized seven  $sD$ - $wD$  materials shown in Figure 1, which included the molecules suggested by the results of the calculation. All compounds with the homo-junction design showed good HOMO-LUMO separation similar to that for the conventional D-A design (Table S3). The natural transition orbitals (NTO) for the lowest singlet excitation of 1–7 showed good agreement with their HOMO and LUMO distributions. The Figure 2 shows ultraviolet (UV) absorption, fluorescence and phosphorescence spectra of 1–7 in toluene solution ( $1.0 \times 10^{-5}$  mol L $^{-1}$ ). By Gauss curve fitting of the absorption spectra (Figure S2), the molar absorption coefficients of the

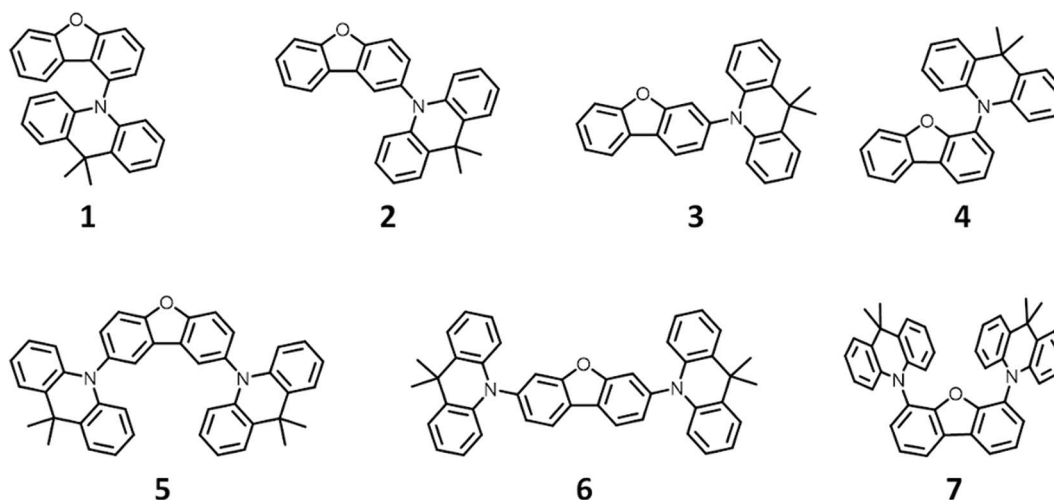


**FIGURE 1** | Chemical structures of TADF candidates with homo-junction design.

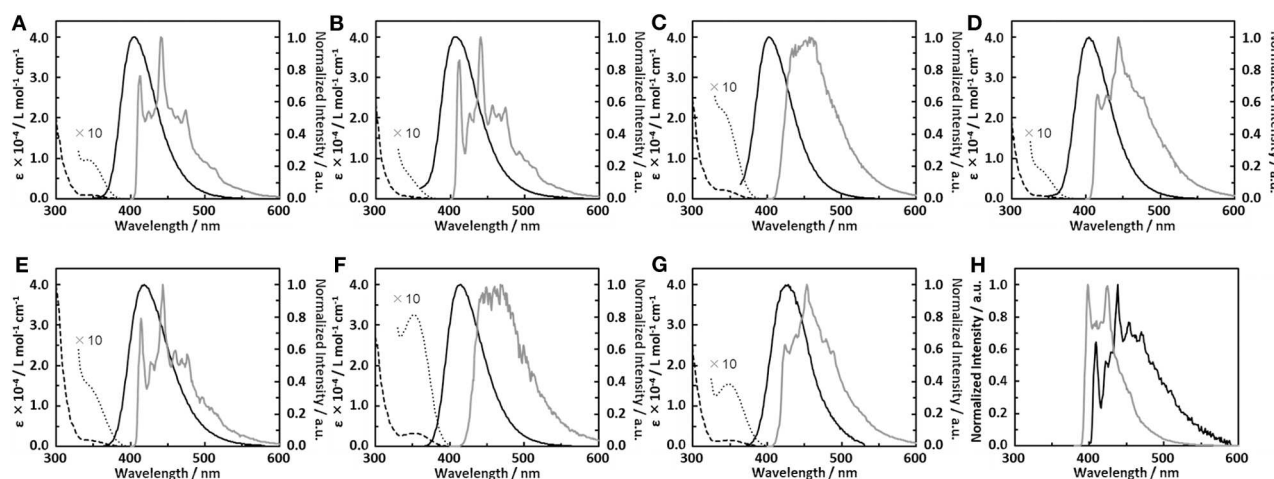


**FIGURE 2** | (A–G) UV absorption (dashed line), fluorescence (solid black line) and phosphorescence (gray line) spectra of dimethylacridine-dibenzofurane combinations; (A) **1**, (B) **2**, (C) **3**, (D) **4**, (E) **5**, (F) **6**, (G) **7**; 10 times enlarged absorption spectrum around 350 nm (dotted line). (H) Phosphorescence spectra of dibenzofurane (black line) and 9,9-dimethyl-10-phenylacridine (**Ph-DMAc**, gray line).

CT absorptions (around 350 nm) for **1**, **2**, **3**, **4**, **5**, **6**, and **7** were estimated to be 1019, 501, 1793, 680, 1477, 3168, and 1522 L mol<sup>-1</sup> cm<sup>-1</sup>, respectively (Table 1). While this clearly indicated the presence of CT transitions in the sD-WD molecules, the experimentally estimated oscillator strength  $f$  of the CT absorption was quite small at  $< 0.03$  (Hirata et al., 2015). All compounds showed emission in the deep blue region (FL<sub>max</sub> values were shown at 400–430 nm) with large full width at half maximum (FWHM) values of around 70 nm and non-vibronic structure, indicating that the fluorescence originated from the CT excited state. The PLQYs of all compounds were low, reflecting the weak oscillator strength in toluene solution. The trend in radiative decay rate constant ( $k_r^S$ ) estimated from the absorption and fluorescence spectra showed good agreement

with the rate constants from emission decay measurements. Larger  $f$  and  $Q$  values of **3** and **6**, rather than other mono-substituted series, means the modification on 3 and 7 positions of DBF have larger orbital overlap between HOMO on DMAc and LUMO on DBF than others. On the other hand, **2** and **4** have similar  $f$ ,  $Q$  values, and other photophysical properties. Therefore, the photophysical properties would not be affected by the donor modification of 2 (8) and 4 (6) positions on DBF. Furthermore, the photochemical properties of compounds **2**, **4**, **5**, and **7** can be directly compared. The modification of two strong donors showed red-shifted emission, meaning reduction of the S<sub>1</sub> energy level which is also observed in conventional D-A type TADF molecules in generally (Wong and Zysman-Colman, 2017; Yang et al., 2017; Bui et al., 2018; Liu et al.,



**TABLE 1** | Photophysical values of compounds **1–7** in toluene.

	<b>1</b>	<b>2</b>	<b>3</b>	<b>4</b>	<b>5</b>	<b>6</b>	<b>7</b>
$\lambda_{\text{abs}}^{\text{CT}}$ (nm) <sup>a</sup>	345	341	345	340	342	356	349
$\epsilon^{\text{CT}}$ (L mol <sup>-1</sup> cm <sup>-1</sup> ) <sup>a</sup>	1019	501	1793	680	1477	3168	1522
$f$ [b]	0.010	0.004	0.014	0.005	0.016	0.026	0.015
$Q$ [b]	0.932	0.612	1.122	0.686	1.197	1.526	1.170
$k_{\text{r}}^{\text{S}}$ (10 <sup>7</sup> s <sup>-1</sup> ) <sup>b</sup>	1.17	0.54	1.82	0.74	1.73	2.92	1.56
PLQY <sup>c</sup>	0.047	0.057	0.182	0.040	0.053	0.175	0.063
$\text{FL}_{\text{max}}$	406	405	402	404	418	415	428
$S_1$ (eV) <sup>d</sup>	3.32	3.33	3.35	3.34	3.24	3.25	3.20
$T_1$ (eV)	3.01 <sup>e</sup>	3.02 <sup>e</sup>	2.98 <sup>d</sup>	3.00 <sup>d</sup>	3.01 <sup>e</sup>	2.92 <sup>d</sup>	3.01 <sup>d</sup>
$\Delta E_{\text{ST}}$ (eV)	0.31	0.31	0.38	0.34	0.23	0.33	0.19
$\tau_{\text{PL}}$ (ns) <sup>c</sup>	3.37	6.34	2.32	3.89	8.26	4.46	7.04
$\tau_{\text{DE}}$ ( $\mu\text{s}$ ) <sup>c</sup>	0.45	0.27	–	0.25	0.26	–	0.30
$k_{\text{r}}^{\text{S}}$ (10 <sup>7</sup> s <sup>-1</sup> ) <sup>c</sup>	1.34	0.85	7.72	1.02	0.63	3.88	0.84
$k_{\text{ISC}}$ (10 <sup>8</sup> s <sup>-1</sup> ) <sup>c</sup>	2.84	1.42	3.54	2.47	1.14	1.85	1.33
$k_{\text{RISC}}$ (10 <sup>4</sup> s <sup>-1</sup> ) <sup>c</sup>	9.21	3.62	–	4.98	4.29	–	4.37
$k_{\text{nr}}^{\text{T}}$ (10 <sup>6</sup> s <sup>-1</sup> ) <sup>c</sup>	2.20	3.71	–	4.08	3.86	–	3.29

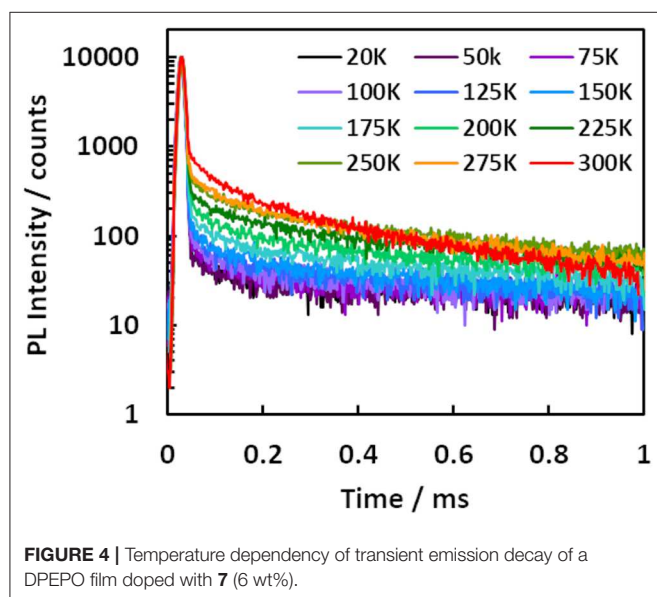
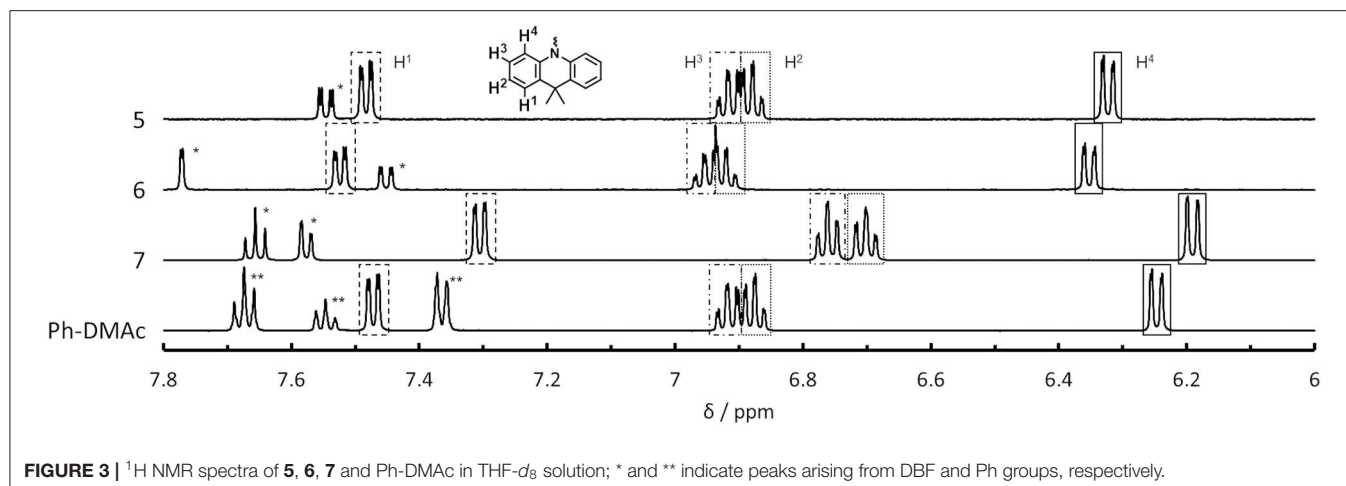
<sup>a</sup>Results from Gauss curve fitting (see **Figure S2**).<sup>b</sup>Estimated using equations reported in literature (see **Supporting Information**).<sup>c</sup>Inert gas saturated conditions.<sup>d</sup>Estimated from the onset value of the spectrum.<sup>e</sup>Estimated from the shortest wavelength peak maximum in the phosphorescence spectrum.

2018). The  $S_1$  energy of **7** showed a larger red-shift than **5** (0.09 and 0.14 eV for **5** and **7** from **2** and **4**, respectively), however, the  $T_1$  energy shift scarcely had any different because of the local excited (LE) state as described hereinbelow. The red-shifted CT emission between the same interacting groups meaning an enhancement of interaction strength between D-A. As a result, 4,6-modification of DBF provided smaller  $\Delta E_{\text{ST}}$  values than 2,8-modification of DBF (**Figure S3**). The smaller  $\Delta E_{\text{ST}}$  should mean the material has small orbital overlap as shown by Equations 1 and 2, however, we could not find the large difference in  $f$  values.

All materials showed very strong phosphorescence in frozen toluene at 77 K. The PLQYs at 77 K reached nearly 100%, confirming that non-radiative decay from the  $T_1$  state in **1–7** was the main deactivation process at room temperature. The phosphorescence spectral profiles of **1–7** showed significant differences with substitution position on the DBF. The vibronic structures based on the DBF were clearly observed by DMac modification at the 1-, 2- and 4-position of DBF (**1**, **2** and **4**), while **3** showed broad CT emission. The phosphorescence spectra of the di-functionalized compounds were consistent with the respective mono-modified compounds. Overall, the  $T_1$  states of **1**, **2**, **4**, **5**, and **7** originated from the LE states of the DBFs, and those of **3** and **6** were based on the CT states between the DMac and DBF units. Four and seven from the emission lifetime measurements in toluene solution, **1**, **2**, **4**, **5**, and **7** showed a very weak long lifetime component under  $N_2$  saturated conditions (**Figure S4**). These long lifetime decay components were suppressed under air saturated conditions, so the delayed component was ascribed to TADF.

## Relative Electron Density on Homo-Junction Materials

We found an interesting relationship between the  $\Delta E_{\text{ST}}$  values of **5–7** and their proton nuclear magnetic resonance ( $^1\text{H}$  NMR) spectra. The chemical shift in the NMR spectra indicates the shielding strength of the magnetic field to the atomic nucleus by the electron orbitals. Thus, the NMR spectra allow the relative electron density on each composite unit to be determined (Schaefer and Schneider, 1963). **Figure 3** shows  $^1\text{H}$  NMR spectra for the aromatic protons on the DMac unit for **5–7** and for *N*-phenyl-9,9-dimethylacridane (Ph-DMac) ( $^1\text{H}$  NMR data for **1–7** including the DBF unit region are shown in **Figure S5**, and chemical shifts are summarized in **Tables S4, S5**). The peaks of **5** and **6** showed similar chemical shifts or slightly downfield shifts compared with those of Ph-DMac. Compound **7** showed upfield shifts for all aromatic protons on the DMac unit. The methyl group on the DMac unit of **7** showed a strong upfield shift ( $\Delta\delta = 0.26$  ppm) without peak splitting. This upfield shift for **7** compared with that of Ph-DMac indicates that the DBF unit is an electron donor in the ground state. This may have reflected the resonating effect of the lone electron pair on the DBF oxygen atom. Thus, **7** achieved efficient HOMO-LUMO separation while retaining the conjugation by the electron back donation from DMac to DBF units at the excited state. Smaller  $\Delta E_{\text{ST}}$  values of 0.33, 0.23 and 0.19 eV were obtained for **6**, **5** and **7**, respectively, and this trend well-corresponded to the opposite magnitude of the relative electron density on DMac; that was **6** < **5** < **7**. The electron donation from DBF ( $w_D$ ) to DMac ( $s_D$ ) at the ground state could also be observed from the shift of the HOMO level. Compound **7** showed a shallower



### Solid State Photophysical Properties With Four State Analysis

All compounds **1–7** showed delayed emission in a bis[2-(diphenylphosphino)phenyl]ether oxide (DPEPO) host (6 wt%), and the delayed components for **1–7** were suppressed by decreasing the temperature (Figure 4, Figures S6, S7). Therefore, all delayed emissions for **1–7** at room temperature were ascribed to TADF. However, the TADF activity was very small in **3** and **6**, reflecting their solution properties. Because **7** showed clear temperature dependence of the emission decay profile in the DPEPO host (6 wt%), a detailed kinetic analysis was performed. In Figure 4, the long lifetime component clearly increased with increasing temperature, indicating that the delayed emission observed at higher temperatures was based on TADF. Two decay components of  $\tau_{DE1} = 0.17$  ms and  $\tau_{DE2} = 2.20$  ms were observed at 300 K in the delayed emission. The spectrum of the longer delayed emission (1–10 ms) gradually blue-shifted with increasing temperature (Figure S8). This indicated that the secondary delayed component was not pure phosphorescence but rather the mixed emission of TADF and phosphorescence, and their ratio gradually changed with increasing temperature. While the reported three-state ( $S_0$ ,  $S_1$ , and  $T_1$ ) model could not well-explain these three order decays (Masui et al., 2013), the expanded four-state ( $S_0$ ,  $S_1$ ,  $T_1$ , and  $T_n$ ) model could well explain it (Figure 5). Recent reports revealed that the  $T_n$  state plays an important role for efficient RISC (Etherington et al., 2016; Kobayashi et al., 2017; Noda et al., 2019). These reports revealed the  $T_n$  state acts as an intermediate state of intersystem crossing (ISC) and RISC processes. Our results could be explained by a similar TADF system with multi-exponential decays. Therefore, we applied the four-state kinetic analysis. In this case, these two delayed components are explained by the decay rates of  $T_n$  ( $k_1^T = \frac{1}{\tau_{DE1}}$ ) and  $T_1$  ( $k_2^T = \frac{1}{\tau_{DE2}}$ ). When we assumed that there are very small contribution of direct non-radiative decay from both the  $S_1$  and  $T_n$  states to  $S_0$  ( $\Phi_{nr}^S, \Phi_{nr}^{Tn} \approx 0$ ), and very small contribution of direct ISC and RISC between the  $S_1$  and  $T_1$  states, we can obtain the rate equations. Thus,  $k_r^S$  and ISC rate ( $k_{ISC}$ ) of the  $S_1$  state are written by

HOMO level ( $-5.73$  eV) than those of **5** and **6** ( $-5.85$  and  $-5.84$  eV, respectively), indicating that the electron-rich DMAc group played an important role in achieving the small  $\Delta E_{ST}$  for TADF. The peaks of **4** showed no upfield shift compared to Ph-DMAc and were similar to those for other mono-substituted compounds except for **1**. This indicated that the upfield shift of **7** did not originate from the ring current effect by the DBF unit. A clear ring current effect was observed in the NMR spectrum of **1** with the peak splitting of methyl groups on the DMAc units. The mono-substituted **4** showed a larger high magnetic field shift of 6-position proton on the unmodified phenyl ring of DBF instead on DMAc than **2**, **3** and DBF (Figure S5 and Table S5). In addition, a low magnetic field shift for **7** compared with **4** were observed for the comparable proton peak on DBF. The strong electronic interaction found in **7** between DMAc and DBF might induce the energy shift of  $S_1$  and resulting the smaller  $\Delta E_{ST}$  values.

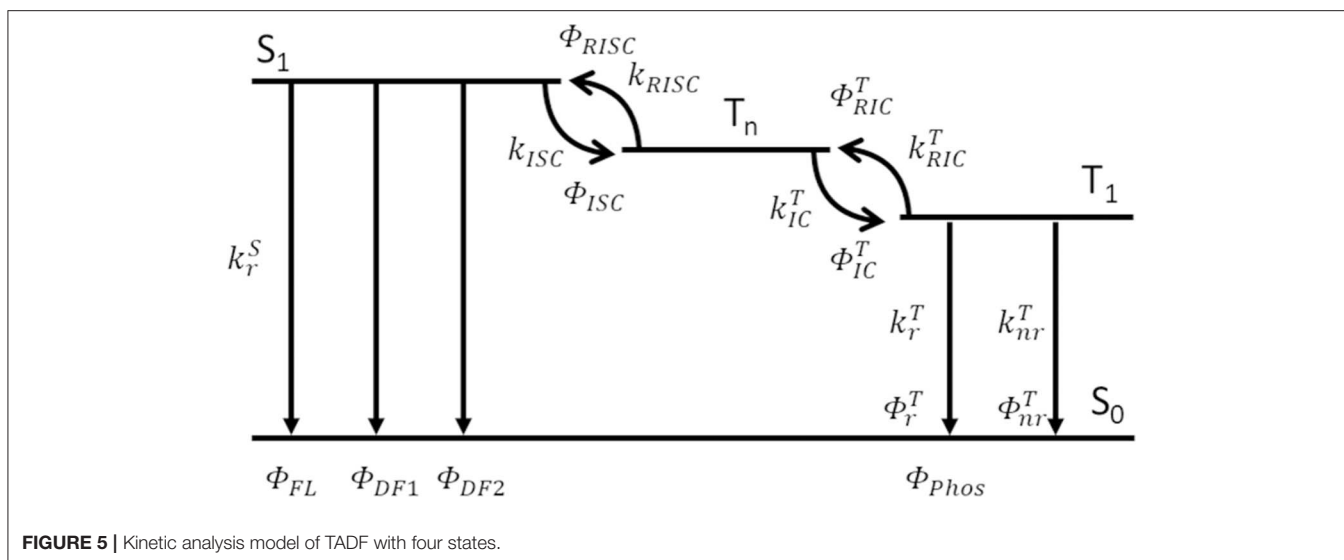


**TABLE 2** | Observed photophysical values and rate constants of 6 wt% 7: DPEPO film at **(A)** 300 K and **(B)** 100 K.

<b>(A)</b>						
$\Phi_{PLQY}$	$\tau_{FL}$ (ns)	$\tau_{DE1}$ ( $\mu$ s)	$\tau_{DE2}$ (ms)	$\Phi_{PL}$	$\Phi_{DE1}$	$\Phi_{DE2}$
0.15	3.4	172.0	2.2	0.036	0.043	0.072
$k_r^S$ ( $s^{-1}$ )	$k_{ISC}$ ( $s^{-1}$ )	$k_{RISC}$ ( $s^{-1}$ )	$k_{IC}^T$ ( $s^{-1}$ )	$k_{RIC}^T$ ( $s^{-1}$ )	$k_r^T$ ( $s^{-1}$ )	$k_{nr}^T$ ( $s^{-1}$ )
$1.05 \times 10^7$	$2.84 \times 10^8$	$7.15 \times 10^3$	$5.56 \times 10^3$	$7.19 \times 10^2$	3.58	$4.18 \times 10^2$
<b>(B)</b>						
$\Phi_{PLQY}$	$\tau_{FL}$ (ns)	$\tau_{DE1}$ ( $\mu$ s)	$\tau_{DE2}$ (ms)	$\Phi_{PL}$	$\Phi_{DE1}$	$\Phi_{DE2}$
0.98	4.9	264.4	339.4	0.028	0.005	0.944
$k_r^S$ ( $s^{-1}$ )	$k_{ISC}$ ( $s^{-1}$ )	$k_{RISC}$ ( $s^{-1}$ )	$k_{IC}^T$ ( $s^{-1}$ )	$k_{RIC}^T$ ( $s^{-1}$ )	$k_r^T$ ( $s^{-1}$ )	$k_{nr}^T$ ( $s^{-1}$ )
$1.05 \times 10^7$	$1.98 \times 10^8$	$6.45 \times 10^2$	$3.76 \times 10^3$	34.8	2.71	0.072

$$k_r^S = k^S \Phi_{FL} \quad (5)$$

$$k_{ISC} = k^S \Phi_{ISC} \quad (6)$$

where  $k^S$  is the decay rate of the  $S_1$  exciton ( $k^S = \frac{1}{\tau_{FL}}$ ,  $\tau_{FL}$  is the lifetime of the fluorescence component),  $\Phi_{FL}$  is the PL efficiency of the fluorescence component and  $\Phi_{ISC}$  is the ISC efficiency ( $1 - \Phi_{FL}$ ). Because the  $T_n$  exciton had only two decay paths, the rate constants for RISC ( $k_{RISC}$ ) to  $S_1$  and for exothermic internal conversion ( $k_{IC}^T$ ) to  $T_1$  are written by

$$k_{RISC} = \frac{\Phi_{DE1}}{\Phi_{FL}} \cdot \frac{k^S k_1^T}{k_{ISC}} \quad (7)$$

$$k_{IC}^T = k_1^T - \Phi_{FL} k_{RISC} \quad (8)$$

where  $\Phi_{DE1}$  is the PL efficiency of the first delayed component ( $\Phi_{DF1}$  in **Figure 5**). Because the PL efficiency of the second delayed component ( $\Phi_{DE2}$ ) was the total of the emission from the  $T_1$  state via endothermic reverse internal conversion ( $\Phi_{RIC}^T$ ) and radiative decay ( $\Phi_r^T$ ), i.e.,  $\Phi_{DF2} + \Phi_{Phos}$  in **Figure 5**, their rate

constants ( $k_{RIC}^T$  and  $k_r^T$ ) are written by

$$\Phi_{RIC}^T + \Phi_r^T = \frac{\Phi_{DE2}}{\Phi_{ISC} \Phi_{IC}^T} \quad (9)$$

$$k_{RIC}^T = k_2^T \cdot \frac{\Phi_{RIC}^T}{\Phi_{RISC}} \quad (10)$$

$$k_r^T = k_2^T \Phi_r^T \quad (11)$$

where  $\Phi_{IC}^T$  and  $\Phi_{RISC}$  are the efficiencies of exothermic internal conversion (IC) and RISC, respectively ( $\Phi_{IC}^T = 1 - \Phi_{RISC}$ ). The efficiency of non-radiative decay from  $T_1$  ( $\Phi_{nr}^T$ ) could be estimated from the total PL efficiency ( $\Phi_{PLQY}$ ), and its rate constant is written by

$$k_{nr}^T = k_2^T \cdot \frac{1 - \Phi_{PLQY}}{\Phi_{ISC} \Phi_{IC}^T} \quad (12)$$

The phosphorescence ( $\Phi_{phos}$ ) ratio in the third decay component ( $\Phi_{DE2}$ ) could be estimated from the time dependent spectra. In this case, all rate constants were provided experimentally from Equation 9. There was no difference of the  $\Phi_{PL}$  values (**Table 2**)

at 100 and 300 K, so we can use an assumption of  $\Phi_{nr}^S$  as 0. **Table 2** shows the rate constants for **7** in a DPEPO film (6 wt%). The values of  $k_r^S$  and  $k_{ISC}$  at 300 K showed good agreement with the result in toluene solution. The  $k_{RISC}$  showed an acceptable difference compared to that in the solution state (**Table 1**, values using an assumption of  $\Phi_r^T$  as 0 for **1–7** are provided in **Table S6**). The four-magnitude-smaller value of  $k_{nr}^T$  compared with the solution state suggested suppressed molecular vibration in the solid state at 300 K. Because of the strong molecular vibration in solution, most of the  $T_1$  excitons would have decayed non-radiatively without reverse internal conversion (RIC). Therefore, only a small delayed emission was observed in solution. The IC speed would have been considerably decreased in the solid state when a large configuration difference was necessary between the  $T_n$  and  $T_1$  states. That explained why some TADF materials showed an additional long exponential decay in their delayed emission. The rate constants of the endothermic processes ( $k_{RISC}$  and  $k_{RIC}^T$ ) were suppressed at low temperature, but the rate constants of the exothermic processes ( $k_r^S$ ,  $k_{ISC}$  and  $k_{IC}^T$ ) were largely unchanged except for  $k_{nr}^T$ . These results clearly indicated that the slow endothermic IC with the large conformation change was detrimental to TADF activity. It is necessary to continue discussion about what is happening in the actual photophysical process. None-the-less, the expanded kinetic analysis should reveal details of the photophysical behavior of TADF in the solid state.

## OLED Derivatives Using Homo-Junction Materials as an Emitter

Finally, we fabricated an OLED with **7** as an emitter (**Figure S8**) with the device structure of indium tin oxide (ITO)/N, N'-di-1-naphthyl-N, N'-diphenylbenzidine ( $\alpha$ -NPD, 20 nm)/4,4',4''-tris(carbazol-9-yl)-triphenylamine (TCTA, 20 nm)/3-bis(9-carbazolyl) benzene (mCP, 10 nm)/DPEPO doped with 6 wt% of **7** (20 nm)/DPEPO (10 nm)/2,2',2''-(1,3,5-benzinetriyl)-tris(1-phenyl-1-H-benzimidazole) (TPBi, 30 nm)/LiF (0.8 nm)/Al (100 nm) (Cui et al., 2017). The electroluminescence spectrum showed good agreement with the PL spectrum of **7** in a DPEPO host. The CIE coordinates were (0.16, 0.08). The maximum external quantum efficiency (EQE<sub>max</sub>) was 2.0%. Considering the low PLQY of **7** (15%), the EQE<sub>max</sub> value would have been 0.75% if **7** had acted as a conventional fluorescence emitter. The obtained EQE<sub>max</sub> clearly indicated that **7** acted as a TADF emitter in this OLED. Therefore, the homo-junction design has potential in the development of deep blue TADF materials.

## CONCLUSIONS

In summary, we prepared conceptual TADF materials based on a homo-junction design analyzed via a combinatorial computational method. The obtained TADF material with the homo-junction design showed deep blue emission when incorporated into an OLED. The results of NMR experiments identified a mechanism for reducing the  $\Delta E_{ST}$  in the homo-junction design, that is, electron back donation in an excited

state. The electron donation from a weak donor (LUMO-distributed DBF) to a strong donor (HOMO-distributed DMac) at the ground state provided a small  $\Delta E_{ST}$  without changing its oscillator strength. We demonstrated an expanded kinetics analysis based on four states. The conventional three-state kinetic analysis could not be applied to several TADF materials exhibiting three exponential decays in the solid-state emission. In contrast, rate constants provided by the four-state analysis could explain the results very well. Further discussion on the meaning of a " $T_n$  state" in actual photophysical processes is necessary. For example, the  $T_n$  state maybe an actual high energy triplet state but maybe electronically non-relaxed state of  $T_1$  by surrounding molecules. However, the results clearly suggested that the highly emissive TADF materials required large rate constants for radiative decay, spin flip and endothermic IC in the solid state. This indicated that the formation of a finely tuned HOMO-LUMO overlap, large spin-orbit coupling and small conformational changes were mandatory in the excited state. The TADF materials obtained in this study had limited PLQYs at 300 K. To obtain highly emissive TADF materials with the homo-junction design, a large oscillator strength material with a small  $\Delta E_{ST}$  will likely be necessary. On-going screening by combinatorial DFT calculation should lead to promising blue TADF materials.

## MATERIALS AND METHODS

### Chemicals and Instruments

All reactants and solvents were used as purchased from Tokyo Chemical Industry (Tokyo, Japan) or Fuji Film-Wako Chemicals (Tokyo, Japan). All reactions were carried out under N<sub>2</sub> atmosphere. In general, the evaporation and concentration of solvents were carried out under reduced pressure below 50°C, unless otherwise noted. Proton nuclear magnetic resonance (<sup>1</sup>H NMR) spectra were obtained using a Biospin Avance III 500 spectrometer (Bruker, MA, USA) with THF-*d*<sub>8</sub> as the solvent. Peak multiplicities are given as: s, singlet; d, doublet; dd, double doublet; ddd, double double doublet; t, triplet; dt, double triplet. Mass spectra were measured in positive-ion atmospheric pressure solid analysis probe (ASAP) mode using a Waters 3100 mass detector (Waters, MA, USA). Absorption spectra of the samples were measured using an ultraviolet-visible-near infrared spectrometer (Lambda 950-PKA, Perkin-Elmer, MA, USA). The photoluminescence quantum yield (PLQY) was measured using a PLQY measurement system (Quantaaurus-QY, Hamamatsu Photonics, Hamamatsu, Japan). The transient photoluminescence (PL) decay characteristics of samples were measured using an emission lifetime measurement system (Quantaaurus-Tau, Hamamatsu Photonics, Hamamatsu, Japan). The transient PL emission and PL decay of **1–5** in mCBP films was recorded under vacuum conditions by a streak camera (C4334, Hamamatsu Photonics, Hamamatsu, Japan) with a nitrogen laser (337 nm, 20 Hz, Ken-X, Usho Optical System, Japan) as an excitation source. The nitrogen laser was employed to measure prompt emission lifetimes.



## Combinatorial DFT Calculations

The 87 donor units used to construct TADF molecules were analyzed by DFT calculation with the B3LYP/6-31+g\* (Lee et al., 1988; Becke, 1993) level of theory on Jaguar 9.0 software package (Bochevarov et al., 2013; Jaguar 9.0, 2016; Schrödinger LLC 2015). Because our target was blue TADF emitters, units estimated to have  $S_1$  and  $T_1$  energy levels  $<2.5$  eV were excluded from the donor list. sD-wD combinations and their initial structures for DFT calculation were generated by using these donor units with the MM2 level on MacroModel 11.0 software package (MacroModel 11.0, 2015; Schrödinger LLC 2015). Generated sD-wD combinations were screened by the DFT calculation with the B3LYP/6-31+g\* level of theory using Jaguar. By checking with the HOMO-LUMO distribution, the sD-wD combinations were selected as a first screening for TADF candidates. Then, candidates having  $\Delta E_{ST} < 0.3$  eV were also screened using the M06-2X/6-31+g\* level of theory (Zhao and Truhlar, 2008), and these candidates were then verified both in vertical and adiabatic excited state energies by DFT calculation with the LC- $\omega$ PBE/6-31+g\* (Vydrov and Scuseria, 2006) level of theory using Gaussian16 (Frisch et al., 2016; Gaussian Inc 2016). The NTO analysis of sD-wD combinations also performed with the B3LYP/6-31+g\* level of theory using Jaguar.

## Photophysical Measurement

Synthesized DMAc-DBF compounds 1–7 were measured in inert gas saturated toluene solution ( $1.0 \times 10^{-5}$  mol L $^{-1}$ ) or thermally evaporated film (6 wt% in DPEPO) under vacuum condition.

## Synthesis of DMAc-DBF Compounds

Compounds 1–7 were synthesized by the Buchwald-Hartwig amination with 9,9-dimethyl acridine and the corresponding brominated dibenzofuran. The synthesis 1 is given below as a representative procedure.

## General Synthesis

A mixture of 9,9-dimethyl acridine (0.42 g, 2 mmol), 1-bromodibenzofuran (0.24 g, 1 mmol), tri-*tert*-butylphosphonium tetrafluoroborate (35 mg, 0.12 mmol), sodium *tert*-butoxide (0.23 g, 2.4 mmol), and tris(dibenzylideneacetone)dipalladium (0) (35 mg, 0.06 mmol) was dissolved in anhydrous toluene (40 mL) under an inert atmosphere. After refluxing overnight, the reaction mixture was washed with water and the organic phase was separated, dried with sodium sulfate, filtered to remove sodium sulfate, and then reduced by rotary evaporation. The residue was purified by silica-gel column chromatography (Wako gel 60, eluent was chloroform: hexane = 1: 6). The target compound 1 was obtained as a white powder. The obtained material was purified by sublimation twice. Compounds 2–7 were synthesized similarly using the corresponding brominated dibenzofuran.

**10-(dibenzofuran-1-yl)-9,9-dimethylacridine (1):** Yield, 60%;  $^1\text{H}$  NMR (500 MHz, THF- $d_8$ ):  $\delta$  7.84 (d, 1H,  $J$  = 8.0 Hz,  $H^4$  on dibenzofuran (DBF)), 7.76 (t, 1H,  $J$  = 8.0 Hz,  $H^3$  on DBF), 7.61 (d, 1H,  $J$  = 8.0 Hz,  $H^6$  on DBF), 7.58 (dd, 2H,  $J$  = 1.0, 7.5 Hz,  $H^4$  on dimethylacridane (DMAc)), 7.39 (ddd,

1H,  $J$  = 1.0, 7.5, 8.0 Hz,  $H^7$  on DBF), 7.35 (d, 1H,  $J$  = 8.0 Hz,  $H^2$  on DBF), 7.22 (dd, 1H,  $J$  = 1.0, 7.5 Hz,  $H^9$  on DBF), 7.02 (d, 1H,  $J$  = 7.5 Hz,  $H^8$  on DBF), 6.88 (dt, 2H,  $J$  = 1.0, 8.0 Hz,  $H^3$  on DMAc), 6.80 (dt, 2H,  $J$  = 1.0, 7.5 Hz,  $H^2$  on DMAc), 6.15 (dd, 2H,  $J$  = 1.0, 8.0 Hz,  $H^4$  on DMAc), 1.97 (s, 3H, Me on DMAc), 1.68 (s, 3H, Me on DMAc) ppm; MS (ASAP)  $m/z$  376.15  $[\text{M}+\text{H}]^+$ .

**10-(dibenzofuran-2-yl)-9,9-dimethylacridine (2):** Yield, 90%;  $^1\text{H}$  NMR (500 MHz, THF- $d_8$ ):  $\delta$  8.06 (d, 1H,  $J$  = 2.0 Hz,  $H^1$  on DBF), 8.03 (dd, 1H,  $J$  = 1.0, 7.5 Hz,  $H^9$  on DBF), 7.87 (d, 1H,  $J$  = 8.5 Hz,  $H^4$  on DBF), 7.66 (d, 1H,  $J$  = 8.0 Hz,  $H^6$  on DBF), 7.52 (ddd, 1H,  $J$  = 1.0, 7.5, 8.0 Hz,  $H^7$  on DBF), 7.46 (dd, 2H,  $J$  = 2.0, 7.0 Hz,  $H^1$  on DMAc), 7.43 (dd, 1H,  $J$  = 2.0, 8.5 Hz,  $H^3$  on DBF), 7.36 (t, 1H,  $J$  = 7.5 Hz,  $H^8$  on DBF), 6.87 (dt, 2H,  $J$  = 2.0, 7.5 Hz,  $H^3$  on DMAc), 6.85 (dt, 2H,  $J$  = 1.5, 7.5 Hz,  $H^2$  on DMAc), 6.26 (dd, 2H,  $J$  = 1.5, 7.5 Hz,  $H^4$  on DMAc), 1.69 (s, 6H, Me on DMAc) ppm; MS (ASAP)  $m/z$  376.32  $[\text{M}+\text{H}]^+$ .

**10-(dibenzofuran-3-yl)-9,9-dimethylacridine (3):** Yield, 63%;  $^1\text{H}$  NMR (500 MHz, THF- $d_8$ ):  $\delta$  8.34 (d, 1H,  $J$  = 8.0 Hz,  $H^1$  on DBF), 8.16 (dd, 1H,  $J$  = 1.0, 7.5 Hz,  $H^9$  on DBF), 7.69 (d, 1H,  $J$  = 8.0 Hz,  $H^6$  on DBF), 7.68 (d, 1H,  $J$  = 1.5 Hz,  $H^4$  on DBF), 7.56 (ddd, 1H,  $J$  = 1.0, 7.5, 8.0 Hz,  $H^7$  on DBF), 7.50 (dd, 2H,  $J$  = 1.5, 7.5 Hz,  $H^1$  on DMAc), 7.45 (t, 1H,  $J$  = 7.5 Hz,  $H^8$  on DBF), 7.36 (dd, 1H,  $J$  = 1.5, 8.0 Hz,  $H^2$  on DBF), 6.92 (dt, 2H,  $J$  = 1.5, 7.5 Hz,  $H^3$  on DMAc), 6.90 (dt, 2H,  $J$  = 1.5, 7.5 Hz,  $H^2$  on DMAc), 6.31 (dd, 2H,  $J$  = 1.5, 7.5 Hz,  $H^4$  on DMAc), 1.72 (s, 6H, Me on DMAc) ppm; MS (ASAP)  $m/z$  376.11  $[\text{M}+\text{H}]^+$ .

**10-(dibenzofuran-4-yl)-9,9-dimethylacridine (4):** Yield, 75%;  $^1\text{H}$  NMR (500 MHz, THF- $d_8$ ):  $\delta$  8.25 (dd, 1H,  $J$  = 1.0, 8.0 Hz,  $H^1$  on DBF), 8.14 (dd, 1H,  $J$  = 1.5, 7.5 Hz,  $H^9$  on DBF), 7.64 (t, 1H,  $J$  = 8.0 Hz,  $H^2$  on DBF), 7.54 (dd, 1H,  $J$  = 1.0, 8.0 Hz,  $H^3$  on DBF), 7.53 (dd, 2H,  $J$  = 2.0, 7.0 Hz,  $H^1$  on DMAc), 7.50 (dd, 1H,  $J$  = 1.5, 8.0 Hz,  $H^6$  on DBF), 7.47 (dt, 1H,  $J$  = 1.5, 8.0 Hz,  $H^7$  on DBF), 7.40 (ddd, 1H,  $J$  = 1.5, 7.5, 8.0 Hz,  $H^8$  on DBF), 6.91 (dt, 2H,  $J$  = 2.0, 7.0 Hz,  $H^3$  on DMAc), 6.88 (dt, 2H,  $J$  = 1.5, 7.0 Hz,  $H^2$  on DMAc), 6.26 (dd, 2H,  $J$  = 1.5, 7.0 Hz,  $H^1$  on DMAc), 1.72 (s, 6H, Me on DMAc) ppm; MS (ASAP)  $m/z$  376.10  $[\text{M}+\text{H}]^+$ .

**2,8-bis(9,9-dimethylacridin-10-yl)dibenzofuran (5):** Yield, 86%;  $^1\text{H}$  NMR (500 MHz, THF- $d_8$ ):  $\delta$  8.13 (d, 1H,  $J$  = 2.0 Hz,  $H^1$  on DBF), 8.00 (d, 1H,  $J$  = 8.5 Hz,  $H^4$  on DBF), 7.55 (t, 1H,  $J$  = 2.0, 8.5 Hz,  $H^3$  on DBF), 7.48 (dd, 2H,  $J$  = 1.5, 7.5 Hz,  $H^1$  on DMAc), 6.92 (dt, 2H,  $J$  = 1.5, 7.5 Hz,  $H^3$  on DMAc), 6.88 (dt, 2H,  $J$  = 1.5, 7.5 Hz,  $H^2$  on DMAc), 6.32 (dd, 2H,  $J$  = 1.5, 7.5 Hz,  $H^4$  on DMAc), 1.70 (s, 6H, Me on DMAc) ppm; MS (ASAP)  $m/z$  583.54  $[\text{M}+\text{H}]^+$ .

**3,7-bis(9,9-dimethylacridin-10-yl)dibenzofuran (6):** Yield, 55%;  $^1\text{H}$  NMR (500 MHz, THF- $d_8$ ):  $\delta$  8.46 (d, 1H,  $J$  = 8.5 Hz,  $H^1$  on DBF), 7.77 (d, 1H,  $J$  = 1.5 Hz,  $H^4$  on DBF), 7.52 (dd, 2H,  $J$  = 1.5, 7.5 Hz,  $H^1$  on DMAc), 7.45 (t, 1H,  $J$  = 1.5, 8.5 Hz,  $H^2$  on DBF), 6.95 (ddd, 2H,  $J$  = 1.5, 7.5, 8.0 Hz,  $H^3$  on DMAc), 6.92 (dt, 2H,  $J$  = 1.5, 7.5 Hz,  $H^2$  on DMAc), 6.35 (dd, 2H,  $J$  = 1.5, 8.0 Hz,  $H^4$  on DMAc), 1.74 (s, 6H, Me on DMAc) ppm; MS (ASAP)  $m/z$  583.39  $[\text{M}+\text{H}]^+$ .

**4,6-bis(9,9-dimethylacridin-10-yl)dibenzofuran (7):** Yield, 88%;  $^1\text{H}$  NMR (500 MHz, THF- $d_8$ ):  $\delta$  8.31 (dd, 1H,  $J$  = 1.0, 7.5 Hz,  $H^1$  on DBF), 7.66 (d, 1H,  $J$  = 7.5 Hz,  $H^2$  on DBF), 7.58

(t, 1H,  $J = 1.0$ , 7.5 Hz,  $H^3$  on DBF), 7.31 (dd, 2H,  $J = 1.5$ , 7.5 Hz,  $H^1$  on DMAc), 6.76 (dt, 2H,  $J = 1.5$ , 8.0 Hz,  $H^3$  on DMAc), 6.70 (ddd, 2H,  $J = 1.0$ , 7.5, 8.0 Hz,  $H^2$  on DMAc), 6.19 (dd, 2H,  $J = 1.0$ , 8.0 Hz,  $H^4$  on DMAc), 1.42 (s, 6H, Me on DMAc) ppm; MS (ASAP)  $m/z$  583.26  $[M+H]^+$ .

## DATA AVAILABILITY STATEMENT

All datasets generated for this study are included in the article/**Supplementary Material**.

## AUTHOR CONTRIBUTIONS

YT performed some experiments, most analysis, construction of rate equations, and co-wrote the paper. KT performed most organic synthesis, most experiment, and some analysis.

## REFERENCES

- Becke, A. D. (1993). Density-functional thermochemistry. III. The role of exact exchange. *J. Chem. Phys.* 98, 5648–5652. doi: 10.1063/1.464913
- Bochevarov, A. D., Harder, E., Hughes, T. F., Greenwood, J. R., Braden, D. A., Philipp, D. M., et al. (2013). Jaguar: A high-performance quantum chemistry software program with strengths in life and materials sciences. *Int. J. Quantum. Chem.* (2013) 113, 2110–2142. doi: 10.1002/qua.24481
- Bui, T.-T., Goubard, F., Ibrahim-Ouali, M., Gimes, D., and Dumur, F. (2018). Recent advances on organic blue thermally activated delayed fluorescence (TADF) emitters for organic light-emitting diodes (OLEDs). *Beilstein J. Org. Chem.* 14, 282–308. doi: 10.3762/bjoc.14.18
- Cui, L.-S., Nomura, H., Geng, Y., Kim, J.-U., Nakanotani, H., and Adachi, C. (2017). Controlling singlet–triplet energy splitting for deep-blue thermally activated delayed fluorescence emitters. *Angew. Chem. Int. Ed.* 56, 1571–1575. doi: 10.1002/anie.201609459
- Dreuw, A., and Head-Gordon, M. (2004). Failure of time-dependent density functional theory for long-range charge-transfer excited states: the zincbacteriochlorin–bacteriochlorin and bacteriochlorophyll–spheroidene complexes. *Am. Chem. Soc.* 126, 4007–4016. doi: 10.1021/ja039556n
- Etherington, M. K., Gibson, J., Higginbotham, H. F., Penfold, T. J., and Monkman, A. P. (2016). Revealing the spin-vibronic coupling mechanism of thermally activated delayed fluorescence. *Nat. Commun.* 7:13680. doi: 10.1038/ncomms13680
- Frisch, M. J., Trucks, G. W., Schlegel, H. B., Scuseria, G. E., Robb, M. A., Cheeseman, J. R., et al. (2016). *Gaussian 16, Revision A.03* Gaussian Inc., Wallingford: CT.
- Geng, Y., D'Aleo, A., Inada, K., Cui, L.-S., Kim, J.-U., Nakanotani, H., et al. (2017). Donor– $\sigma$ -acceptor motifs: thermally activated delayed fluorescence emitters with dual upconversion. *Angew. Chem. Int. Ed.* 56, 16536–16540. doi: 10.1002/anie.201708876
- Hansch, C., Leo, A., and Taft, R. W. (1991). A survey of hammett substituent constants and resonance and field parameters. *Chem. Rev.* 91, 165–195. doi: 10.1021/cr00002a004
- Hirata, S., Sakai, Y., Masui, K., Tanaka, H., Lee, S.-Y., Nomura, H., et al. (2015). Highly efficient blue electroluminescence based on thermally activated delayed fluorescence. *Nat. Mater.* 14, 330–336. doi: 10.1038/nmat4154
- Jaguar 9.0 (2016). *Schrödinger Release 2016-4*. New York, NY: Schrödinger, LLC.
- Kobayashi, T., Niwa, A., Takaki, K., Haseyama, S., Nagase, T., Goushi, K., et al. (2017). Contributions of a higher triplet excited state to the emission properties of a thermally activated delayed-fluorescence
- KI, TM, HK, and MH performed molecular modeling and combinatorial DFT calculation. FB helped construction of rate equations. YG performed some organic synthesis, and some experiment. HN and CA interpreted the results, and co-wrote the paper.
- Lee, C., Yang, W., and Parr, R. G. (1988). Development of the Colle-Salvetti correlation-energy formula into a functional of the electron density. *Phys. Rev. B* 37, 785–789. doi: 10.1103/PhysRevB.37.785
- Lewice, G. W., Lipkin, D., and Magel, T. T. (1941). Reversible photochemical processes in rigid media. A study of the phosphorescent state. *J. Am. Chem. Soc.* 63, 3005–3018. doi: 10.1021/ja01856a043
- Liu, Y., Li, C., Ren, Z., Yan, S., and Bryce, M. R. (2018). All-organic thermally activated delayed fluorescence materials for organic light-emitting diodes. *Nat. Rev. Mater.* 3:18020. doi: 10.1038/natrevmats.2018.20
- MacroModel 11.0 (2015). *Schrödinger Release 2015-4*. New York, NY: Schrödinger, LLC.
- Masui, K., Nakanotani, H., and Adachi, C. (2013). Analysis of exciton annihilation in high-efficiency sky-blue organic light-emitting diodes with thermally activated delayed fluorescence. *Org. Electronics* 14, 2721–2726. doi: 10.1016/j.orgel.2013.07.010
- Noda, H., Chen, X.-K., Nakanotani, H., Hosokai, T., Miyajima, M., Notsuka, N., et al. (2019). Critical role of intermediate electronic states for spin-flip processes in charge-transfer-type organic molecules with multiple donors and acceptors. *Nat. Mater.* 18, 1084–1090. doi: 10.1038/s41563-019-0465-6
- Schaefer, T., and Schneider, W. G. (1963). Proton magnetic resonance shifts and the electron density distribution in aromatic systems. *Can. J. Chem.* 41, 966–982. doi: 10.1139/v63-136
- Sun, H., Zhong, C., and Brédas, J.-L. (2015). Reliable prediction with tuned range-separated functionals of the singlet–triplet gap in organic emitters for thermally activated delayed fluorescence. *J. Chem. Theory Comput.* 11, 3851–3858. doi: 10.1021/acs.jctc.5b00431
- Tanaka, H., Shizu, K., Miyazaki, H., and Adachi, C. (2012). Efficient green thermally activated delayed fluorescence (TADF) from a phenoxazine–triphenyltriazine (PXZ–TRZ) derivative. *Chem. Commun.* 48, 11392–11394. doi: 10.1039/c2cc36237f
- Uoyama, H., Goushi, K., Shizu, K., Nomura, H., and Adachi, C. (2012). Highly efficient organic light-emitting diodes from delayed fluorescence. *Nature* 492, 234–238. doi: 10.1038/nature11687
- Vydrov, O. A., and Scuseria, G. E. (2006). Assessment of a long-range corrected hybrid functional. *J. Chem. Phys.* 125:234109. doi: 10.1063/1.2409292
- Wong, M. Y., and Zysman-Colman, E. (2017). Purely organic thermally activated delayed fluorescence (TADF) materials for organic light-emitting

- diodes (OLEDs). *Adv. Mater.* 29:1605444. doi: 10.1002/adma.201605444
- Yang, Z., Mao, Z., Xie, Z., Zhang, Y., Liu, S., Zhao, J., et al. (2017). Recent advances in organic thermally activated delayed fluorescence materials. *Chem. Soc. Rev.* 46, 915–1016. doi: 10.1039/C6CS00368K
- Yersin, H. (2018). *Highly Efficient OLEDs: Materials Based on Thermally Activated Delayed Fluorescence*. Weinheim: Wiley-VCH. doi: 10.1002/9783527691722
- Zhao, Y., and Truhlar, D. G. (2008). The M06 suite of density functionals for main group thermochemistry, thermochemical kinetics, noncovalent interactions, excited states, and transition elements: two new functionals and systematic testing of four M06-class functionals and 12 other functionals. *Theor. Chem. Acc.* 120, 215–241. doi: 10.1007/s00214-007-0310-x

**Conflict of Interest:** TM, HK, and MH are employed by the company Schrödinger Inc.

The remaining authors declare that the research was conducted in the absence of any commercial or financial relationships that could be construed as a potential conflict of interest.

Copyright © 2020 Tsuchiya, Tsuji, Inada, Bencheikh, Geng, Kwak, Mustard, Halls, Nakanotani and Adachi. This is an open-access article distributed under the terms of the Creative Commons Attribution License (CC BY). The use, distribution or reproduction in other forums is permitted, provided the original author(s) and the copyright owner(s) are credited and that the original publication in this journal is cited, in accordance with accepted academic practice. No use, distribution or reproduction is permitted which does not comply with these terms.



# TADF Dye-Loaded Nanoparticles for Fluorescence Live-Cell Imaging

Carina I. C. Crucho<sup>1</sup>, João Avó<sup>1\*</sup>, Ana M. Diniz<sup>1</sup>, Sandra N. Pinto<sup>1</sup>, José Barbosa<sup>1</sup>, Poppy O. Smith<sup>2</sup>, Mário Nuno Berberan-Santos<sup>1</sup>, Lars-Olof Pålsson<sup>2</sup> and Fernando B. Dias<sup>3\*</sup>

<sup>1</sup> IBB-Institute for Bioengineering and Biosciences, Instituto Superior Técnico, Universidade de Lisboa, Lisbon, Portugal,

<sup>2</sup> Department of Chemistry, Durham University, Durham, United Kingdom, <sup>3</sup> Department of Physics, Durham University, Durham, United Kingdom

## OPEN ACCESS

### Edited by:

Sebastian Reineke,  
Dresden University of  
Technology, Germany

### Reviewed by:

Lei Yang,  
Arkema, United States  
Jiefei Wang,  
Henan University, China

### \*Correspondence:

João Avó  
joao.avo@tecnico.ulisboa.pt  
Fernando B. Dias  
f.m.b.dias@durham.ac.uk

### Specialty section:

This article was submitted to  
Polymer Chemistry,  
a section of the journal  
Frontiers in Chemistry

**Received:** 25 February 2020

**Accepted:** 17 April 2020

**Published:** 08 May 2020

### Citation:

Crucho CIC, Avó J, Diniz AM,  
Pinto SN, Barbosa J, Smith PO,  
Berberan-Santos MN, Pålsson L-O  
and Dias FB (2020) TADF Dye-Loaded  
Nanoparticles for Fluorescence  
Live-Cell Imaging.  
Front. Chem. 8:404.  
doi: 10.3389/fchem.2020.00404

Thermally activated delayed fluorescence (TADF) molecules offer nowadays a powerful tool in the development of novel organic light emitting diodes due to their capability of harvesting energy from non-emissive triplet states without using heavy-metal complexes. TADF emitters have very small energy difference between the singlet and triplet excited states, which makes thermally activated reverse intersystem crossing from the triplet states back to the singlet manifold viable. This mechanism generates a long-lived delayed fluorescence component which can be explored in the sensing of oxygen concentration, local temperature, or used in time-gated optical cell-imaging, to suppress interference from autofluorescence and scattering. Despite this strong potential, until recently the application of TADF outside lighting devices has been hindered due to the low biocompatibility, low aqueous solubility and poor performance in polar media shown by the vast majority of TADF emitters. To achieve TADF luminescence in biological media, careful selection or design of emitters is required. Unfortunately, most TADF molecules are not emissive in polar media, thus complexation with biomolecules or the formation of emissive aggregate states is required, in order to retain the delayed fluorescence that is characteristic of these compounds. Herein, we demonstrate a facile method with great generalization potential that maintains the photophysical properties of solvated dyes by combining luminescent molecules with polymeric nanoparticles. Using an established swelling procedure, two known TADF emitters are loaded onto polystyrene nanoparticles to prepare TADF emitting nanomaterials able to be used in live-cell imaging. The obtained particles were characterized by optical spectroscopy and exhibited the desired TADF emission in aqueous media, due to the polymeric matrix shielding the dye from solvent polarity effects. The prepared nanoparticles were incubated with live human cancer cells and showed very low cytotoxicity and good cellular uptake, thus making fluorescence microscopy imaging possible at low dye concentrations.

**Keywords:** TADF, dye-loaded nanoparticles, luminescent probes, optical imaging, fluorescence imaging, fluorescence microscopy



## INTRODUCTION

Thermally Activated Delayed Fluorescence (TADF) emitters attracted great attention from both academia and industry due to their potential for efficient triplet harvesting in organic light emitting diodes (OLEDs) (Yang et al., 2017). In OLEDs charge recombination results in the formation of singlets and triplet states in a ratio 1:3. As the triplet state is often non-emissive, the internal efficiency of OLEDs is limited to 25%. The need to improve device efficiency triggered the application of heavy-metal complexes in the OLEDs field (Baldo et al., 1998). However, metal-based phosphors may create potential problems in industries with high production rates. Moreover, these complexes show tendency to chemically degrade during the vacuum deposition process used in device fabrication, often show short working lifetimes in devices, and more important, there are no stable complexes with emission in the deep-blue region, which is essential for both high quality displays and lighting. TADF molecules promised to solve these problems in an elegant way (Uoyama et al., 2012).

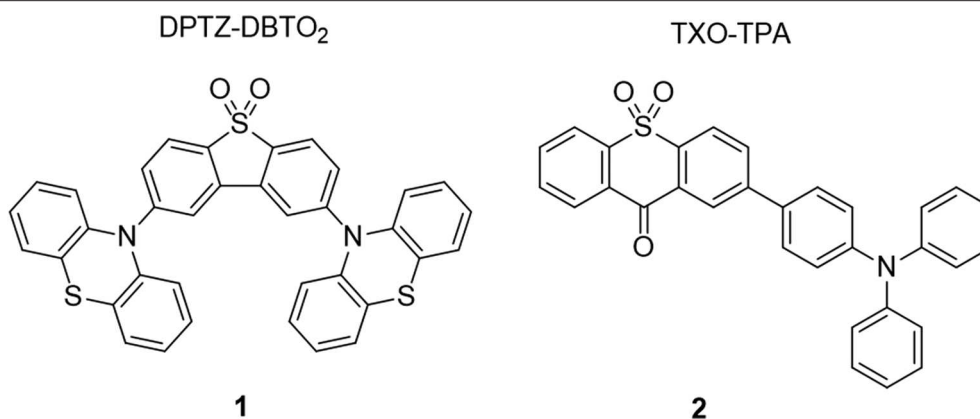
TADF molecules create excited states with strong charge transfer character (CT) which can have vanishingly small electron exchange energies, resulting in nearly equivalent singlet and triplet energies. Using thermal energy to promote the up-conversion of non-emissive triplet states back to the singlet manifold is thus efficient through reverse intersystem crossing (RISC), thereby giving a method of “harvesting” up to 100% of triplet states formed by charge recombination in OLEDs (Dias et al., 2013). TADF emitters can thus combine the most desirable properties of metal-carrying phosphorescent emitters, namely 100% triplet harvesting, with the added benefit of the long-term stability of a fluorescent emitter. This is what both display and lighting manufacturers seek, but as yet not been materialized fully in the blue spectral region (Bui et al., 2018).

Due to the involvement of long-lived triplet states, the luminescent from TADF molecules shows two clear time regimes. A first component, appearing due to the decay of singlet states created immediately after excitation, shows lifetimes in the order of few nanoseconds. This component is often referred as the prompt fluorescence (PF) and shows small variation with temperature or the presence of oxygen. A second luminescent component, appearing due to the up conversion of triplet states to the emissive singlet manifold, usually shows lifetimes that range from a few microseconds to milliseconds and is identified as delayed fluorescence (DF). The DF intensity can show strong variation with temperature and the presence of oxygen (Baleizão et al., 2008; Dias et al., 2017). Besides lifetime, PF and DF also contrast their variation with temperature. While the PF tends to decrease in intensity with increasing temperature (due to the emergence of non-radiative pathways), the DF intensity does exactly the opposite. Essentially, this happens because the DF component appears from a process involving the reverse intersystem crossing between the triplet and singlet states, which are separated by a small energy difference. TADF is thus a thermally activated mechanism, which is strongly affected by intra-molecular phenomena that can influence the triplet state, e.g., internal conversion, singlet-triplet energy splitting,

intersystem crossing, triplet quenching mechanisms, medium properties etc. The DF is, therefore, extremely sensitive to the presence of oxygen, temperature, the dielectric medium, and may even vary due to the presence of analytes. As an example, if the TADF molecule selectively interacts with an analyte, most probably this will have a significant effect on the properties of the triplet excited state of the TADF emitter. These changes will be inevitably reflected in the TADF efficiency and lifetime (Chen and Song, 2019).

The DF component can be used as a long-lived luminescence to enable time-gated acquisition methods that ignore nonspecific and non-negligible resolution-limiting signals from autofluorescence and light-scattering (Zhao et al., 2011). For these reasons, TADF emitters have attracted significant scientific interest as an alternative to heavy metal-based complexes in optical imaging (Chen and Song, 2019). Despite these very interesting properties the application of TADF molecules in the optical imaging and sensing remains largely unexplored. Since most TADF dyes are weakly soluble in water and show very weak luminescence in polar solvents due to their charge transfer properties, their direct use in biological media has been critically hindered. To overcome these drawbacks, TADF emitters have been encapsulated in macromolecules (Xiong et al., 2014), precipitated onto nanoaggregates (Ni et al., 2018, 2019; Zhu et al., 2018) or assembled in amphiphilic polymer micelles with other small-molecular-weight dopants (Li et al., 2017; Luo et al., 2019; Tsuchiya et al., 2019). In addition, we previously reported the preparation of TADF emitting silica nanoparticles using a simple doping procedure with a silane-bearing TADF derivative (Crucho et al., 2020). These approaches were successful in achieving TADF emission in aqueous media, and even in mitigating oxygen quenching, providing an interesting platform to develop TADF-based optical probes for time-resolved optical imaging. However, most reported strategies rely on particular structural features of TADF emitters to allow complexation with macromolecules, aggregated induced or enhanced emission or synthetically challenging dye derivatization. On the other hand, polymer micelle doping procedures can be applied to a wider range of TADF molecules but require demanding and small-scale preparation steps.

Herein we explore the viability of conventional TADF dyes encapsulated in a polymeric nanocarrier as luminescent probes for optical fluorescence microscopy studies in cells. Luminescent nanomaterials are increasingly gaining relevance for biological and biomedical applications, offering many advantages over conventional molecular probes (Wolfbeis, 2015; Yu et al., 2017; Peng et al., 2018). Amongst them, dye-doped fluorescent nanoparticles exhibit improved biocompatibility, photostability, and optical brightness when compared to free dyes, and find application in biological optical imaging, theragnostic, and chemical sensing (Montalti et al., 2014; Li et al., 2019). In this work, we describe the preparation of TADF emitting polymeric nanoparticles using a simple straightforward swelling procedure, which is advantageous for the encapsulation of dyes with strong potential for generalization. Two well-studied TADF emitters (Wang et al., 2014; Dias et al., 2016) were selected and encapsulated in polystyrene (PS) nanoparticles. PS is a versatile



**SCHEME 1** | Chemical structures of TADF emitters used for the preparation of luminescent nanoparticles.

and attractive matrix for dye encapsulation, being commercially available as nanoparticles in a broad size range and has been extensively used in the encapsulation of organic and inorganic fluorophores for imaging and sensing applications (Mader and Wolfbeis, 2010; Lee et al., 2013). However, to the best of our knowledge, PS nanoparticles have never been used for the encapsulation of TADF emitters. In this respect, we studied the influence of dye encapsulation and aqueous dispersion on the optical properties of these TADF emitters and evaluated the applicability of their dye-loaded PS nanoparticles in live-cell fluorescence microscopy imaging.

## RESULTS AND DISCUSSION

### Synthesis and Preparation of TADF Dye-Loaded Nanoparticles

For the preparation of TADF emitting nanoparticles and to evaluate the effects of dye-encapsulation in the particle matrix, we selected two known TADF emitters (**Scheme 1**). Both compounds were previously studied toward their TADF properties and were successfully applied in the preparation of OLEDs with good to excellent external quantum efficiencies (Wang et al., 2014; Dias et al., 2016). 2,8-Di(phenothiazine-10-yl)dibenzothiophene-S,S-dioxide (DPTZ-DBTO<sub>2</sub>, dye **1**) is a well-known TADF emitter that displays highly efficient triplet harvesting in nonpolar media through the electronic coupling between the local triplet (<sup>3</sup>LE) and singlet and triplet charge transfer states (<sup>1</sup>CT and <sup>3</sup>CT respectively). However, in polar solvents, the energy level of the charge transfer states are reduced, drastically affecting the TADF efficiency. This makes dye **1** a good candidate to probe the polarity of polymeric nanoparticles and the dye-encapsulation effect on the TADF properties. Synthesis of DPTZ-DBTO<sub>2</sub>, dye **1**, was prepared following published procedures (Dias et al., 2016). The dye was characterized by NMR (<sup>1</sup>H, <sup>13</sup>C) and compound purity was established by elemental analysis. Commercially available 2-(4-(triphenylamino)-thioxanthene

(TXO-TPA, dye **2**), was also selected in order to evaluate the generalization potential of the preparation method of TADF emitting nanoparticles. Similarly, to dye **1**, this dye displays a small singlet-triplet energy gap ( $\Delta E_{ST}$ ) in nonpolar media and exhibits strong polarity dependence of its optical properties (Nobuyasu et al., 2019).

Aiming at a straightforward procedure for the preparation of TADF-emitting particles using non-functionalized fluorophores, we selected a well-established swelling procedure based on the adsorption of hydrophobic dyes onto the matrix of polymeric nanoparticles (Behnke et al., 2011). This method allows the preparation of dye-loaded nanomaterials using pre-formed polymeric nanoparticles, resulting in optical probes with enhanced stability, biocompatibility and applicability in biological media (Lee et al., 2011; Wang et al., 2013). For this purpose, polystyrene (PS) nanoparticles were chosen not only because nanosized and spherical particles are easy to synthesize, but also due to their commercial availability in a wide range of sizes and distinct surface characteristics. In addition, PS is permeable to oxygen, allowing the direct evaluation of the TADF properties of the luminescent nanomaterials in aqueous suspension. In this work, we used non-functionalized PS nanoparticles freshly prepared from emulsion polymerization procedures (PSP) and commercially available PS nanoparticles modified with positively charged amino-groups (PSNH<sub>2</sub>). This allowed us also to analyze the effect of nanoparticle surface functionalization on cell function and on dye loading and photophysics. While PSP can be easily obtained in large quantities using straightforward procedures, the lack of surface charge may hinder their application as optical probes in biological media.

Non-functionalized PSPs were synthesized by emulsion polymerization. Following synthesis, the obtained suspensions were centrifuged. Due to the high hydrophobic character of these particles, stable aqueous suspensions are usually difficult to obtain from aggregated PSPs. For this reason and because aggregation could reduce cellular uptake, the centrifuged pellets

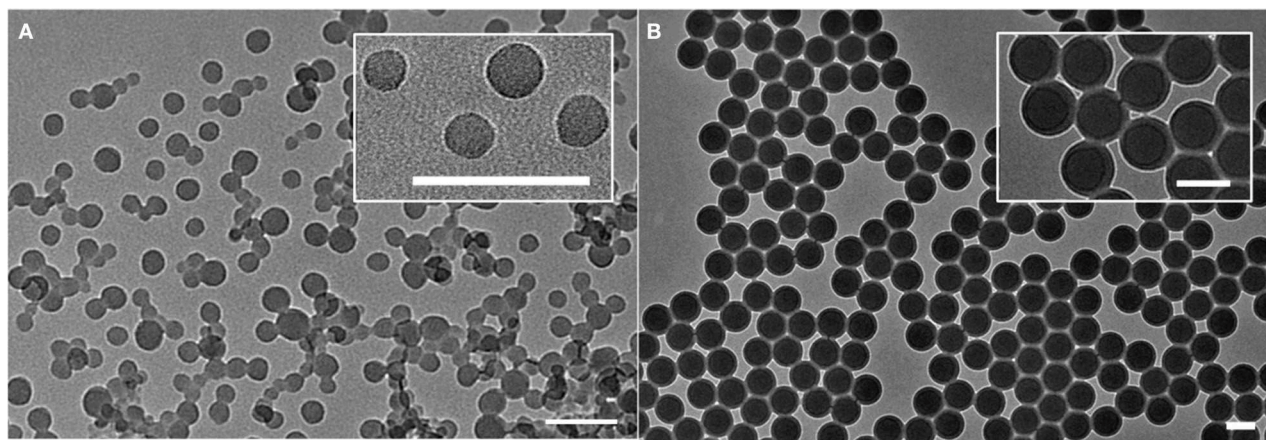


**FIGURE 1 |** TEM images of the unloaded nanomaterials PSP (A) and PSNH<sub>2</sub> (B). Scale bar = 100 nm.

**TABLE 1 |** Morphological properties of prepared and dye-loaded PS nanoparticles.

	PSP	PSNH <sub>2</sub>	Dye 1@PSP (PS1)	Dye 1@PSNH <sub>2</sub> (PS2)	Dye 2@PSP (PS3)	Dye 2@PSNH <sub>2</sub> (PS4)
Diameter <sup>a</sup> (nm)	31.7	103.0	35.6	106.4	37.1	107.2
PDI	0.02	<0.01	0.02	0.01	0.02	0.01
Dye concentration (w/w %)	no dye	no dye	0.97	0.31	0.59	0.34

<sup>a</sup>determined by TEM.

were discarded and the supernatants were extensively dialyzed against water to remove surfactant molecules and traces of unreacted styrene monomer, which are the main source of PSPs cytotoxicity. The washed suspensions were characterized by TEM and exhibited nanoparticles of spherical morphology with diameters of  $32 \pm 4$  nm, as shown in **Figure 1A**. The amino-modified particles (PSNH<sub>2</sub>) were also imaged by TEM, showing spherical morphologies with diameters of ca. 100 nm (**Figure 1B**).

Both dyes, **1** and **2**, were loaded into PSP and PSNH<sub>2</sub> materials through swelling methods using tetrahydrofuran (THF) as organic solvent, and the effects of dye-loading on the physicochemical properties of obtained nanomaterials were studied. From TEM images and dynamic light scattering spectroscopy measurements, it is evidenced that the addition of dye does not significantly affect particle morphology and suspension stability (**Figures S2–S4**). The effects of the swelling step on size distribution and on the surface charge were also analyzed and compared to the amount of incorporated dye (**Table 1**). For dye **1**, it is shown that the incorporation in pristine polystyrene particles is more efficient when compared to the amine-modified polymer, with neutral particles (PS1) bearing over 3-fold more amount of dye than their charged counterparts (PS2) after isolation. Since the dye loading procedure is based on the hydrophobic interactions between dye and matrix, this difference can be attributed to the positively charged surface of PSNH<sub>2</sub> nanoparticles that may affect dye adsorption. This effect was also noticed in the incorporation of dye **2**, with the

loading into pristine polystyrene particles (PS3) being more effective than into the amino-modified material (PS4, **Table 1**). The different degree of dye-loading is also reflected on the increase in size of the nanomaterials after the swelling procedure. While the neutral PS nanoparticles undergo an increase of ca. 15%, this effect is less evident in the amino-modified counterparts (ca. 4%).

## Photophysical Characterization of TADF-Dyes Encapsulated in PSP Nanoparticles

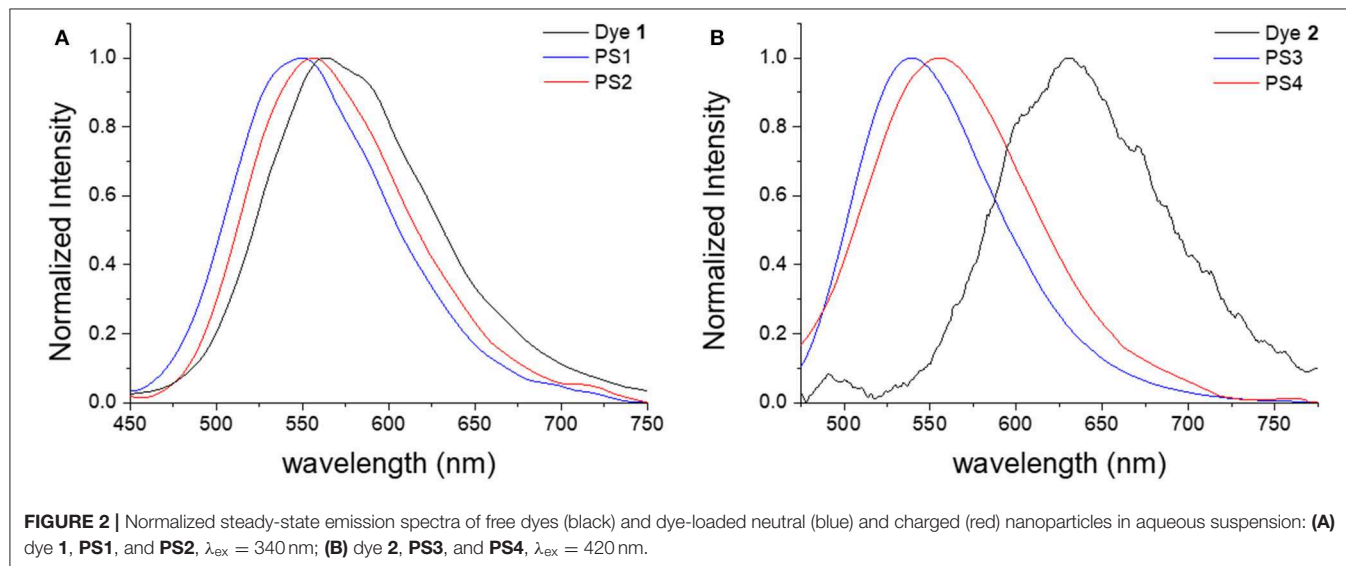
Following the preparation of the luminescent TADF nanomaterials, their optical properties were characterized and compared to those of free dyes. The aim is to evaluate the effects of encapsulation on the dyes photophysics, with a particular focus on their TADF properties. **Table 2** summarizes the determined photophysical parameters regarding the emission wavelength ( $\lambda_{em}$ ), prompt fluorescence quantum yield ( $\Phi_{PF}$ ) and lifetime ( $\tau_{PF}$ ) and delayed fluorescence quantum yield ( $\Phi_{DF}$ ) and lifetime ( $\tau_{DF}$ ).

Comparing the emission spectra of the prepared materials with those of free dyes in aqueous media, it is evidenced that the encapsulation of the dye leads to a blue-shift in the emission (**Figure 2**). While for dye **1** this effect is not significantly pronounced (e.g.,  $\lambda_{em}^1 = 563$  nm and  $\lambda_{em}^{PS1} = 550$  nm, **Figure 2A**), for dye **2** the emission is markedly shifted when the dye is incorporated in the nanomaterial (e.g.,  $\lambda_{em}^2 = 629$  nm and

**TABLE 2** | Prompt fluorescence and total quantum yield ( $\Phi_{PF}$ ,  $\Phi_{PL}$ ), prompt and delayed emission lifetime ( $\tau_{PF}$ ,  $\tau_{DF}$ ) and wavelength ( $\lambda_{em}$ ) of dyes **1** and **2**, and luminescent nanomaterials **PS1–4**, measured in aqueous media.

	$\lambda_{em}$ (nm)	$\Phi_{PF}^a$	$\tau_{PF}$ (ns)	$\Phi_{PL}^b$	DF/PF ratio	$\tau_{DF}$ ( $\mu$ s)
Dye <b>1</b>	563	0.02	6.59	0.02	n.d. <sup>c</sup>	n.d. <sup>c</sup>
<b>PS1</b>	550	0.05	4.58	0.18	2.6	5.11
<b>PS2</b>	556	0.03	4.60	0.11	2.7	2.89
Dye <b>2</b>	629	<0.01	6.3	<0.01	n.d. <sup>c</sup>	n.d. <sup>c</sup>
<b>PS3</b>	539	0.18	16.5	0.24	0.3	11.78
<b>PS4</b>	555	0.07	7.5	0.09	0.3	9.56

<sup>a</sup>measured in aerated conditions; <sup>b</sup>measured in degassed conditions; <sup>c</sup>not detected.



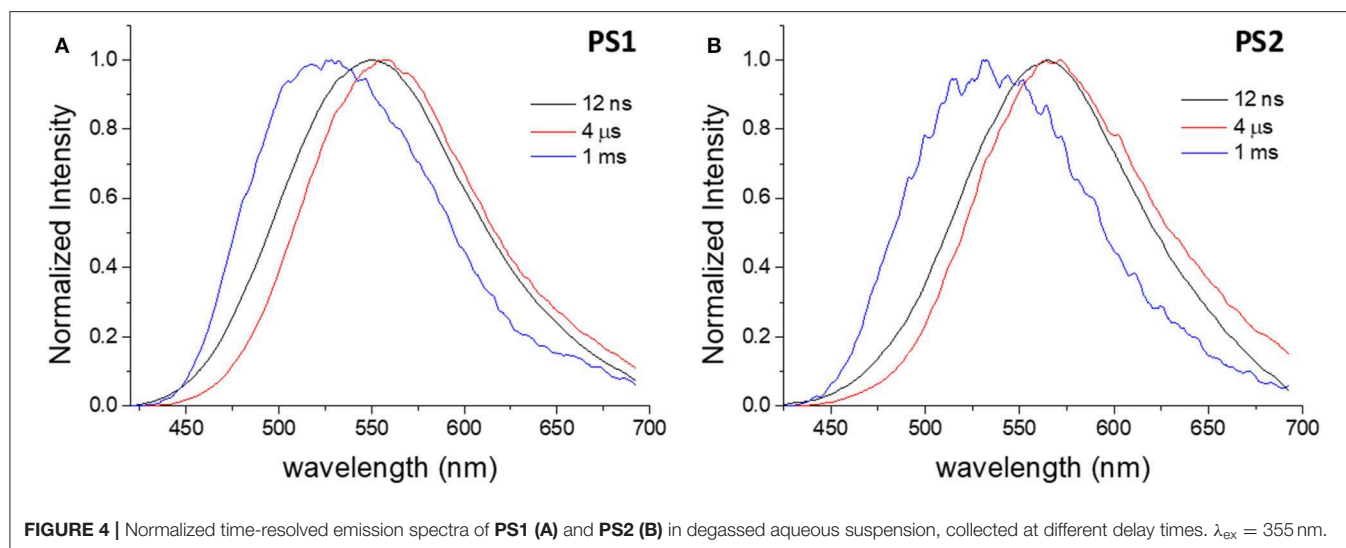
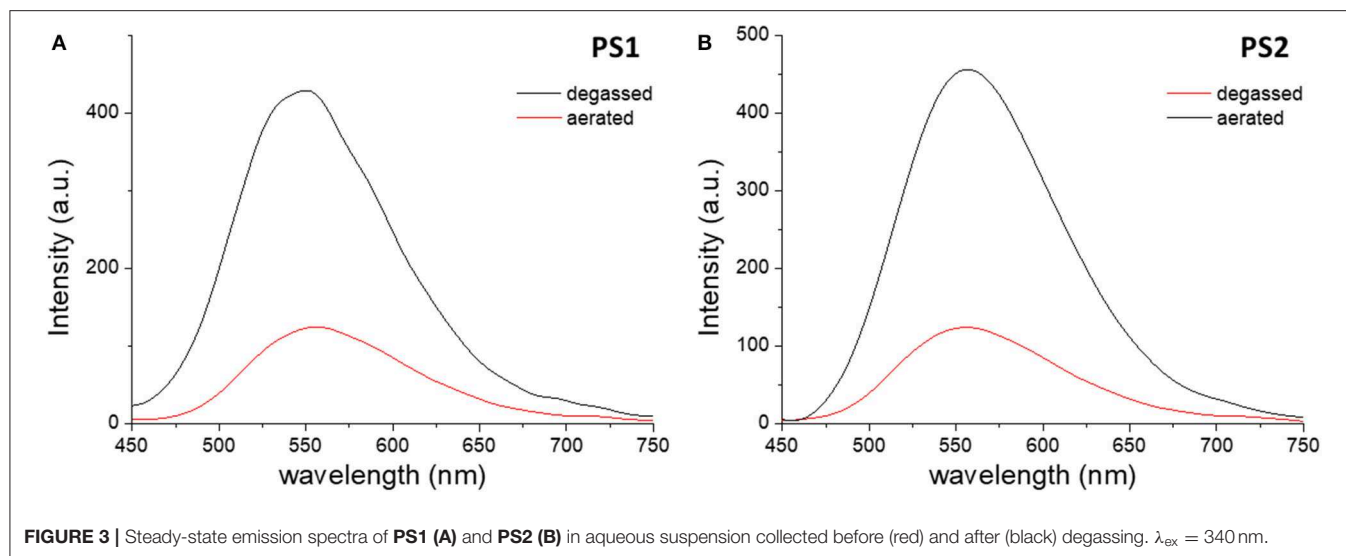
$\lambda_{em}^{PS3} = 539$  nm, **Figure 2B**). The emission spectra of the dye-loaded nanomaterials is also significantly blue-shifted when compared to the emission of the dyes in most organic solvents (**Figure S5**). These results demonstrate the relatively low polarity of polystyrene matrix and the absence of water in the local environment of the dye, pointing to complete encapsulation. The difference in polymer polarity due to the modification with amine moieties can also be detected in the emission spectra of the nanomaterials. As observed in **Figure 2**, the emission of the neutral nanoparticles (**PS1** and **PS3**) is blue-shifted compared to that of their positively charged counterparts (**PS2** and **PS4**). These differences are more pronounced for the materials loaded with dye **2** ( $\lambda_{em}^{PS3} = 539$  nm vs.  $\lambda_{em}^{PS4} = 555$  nm) than those with dye **1** ( $\lambda_{em}^{PS1} = 550$  nm vs.  $\lambda_{em}^{PS2} = 556$  nm), due to the different polarity sensitivity of both dyes, in terms of optical properties.

The effects of encapsulation on the luminescence quantum yields are also evident. Comparing the prompt fluorescence quantum yields of dye **1** in solution with those of materials **PS1** and **PS2** in aqueous suspension, it is evidenced the encapsulation into polystyrene nanoparticles enhances the prompt emission quantum yield ( $\Phi_{PF}$ ) in fluid media, taking it to values closer to those of **1** in solid film (**Table S1**). Regarding the desired

long-lived fluorescence, while degassed aqueous suspensions of dye **1** do not show any emission, **PS1** and **PS2**, suspended in water, exhibit an increase in the emission spectra intensity upon degassing (**Figure 3**).

Through time-resolved spectroscopy it is possible to verify that both materials show TADF and phosphorescence under degassed conditions (**Figure 4**). As previously described, in non-polar organic solvents and in solid film, dye **1** exhibits TADF ( $\lambda_{em}^{TADF} = 560$  nm) in the microsecond time-range, arising from reverse intersystem crossing that involves the local triplet excited state ( $^3LE$ ), the triplet ( $^3CT$ ) and the singlet ( $^1CT$ ) states of charge transfer character. As in previous studies of dye **1**, the phosphorescence is observed at long time delays (1 ms), and appears blue-shifted, when compared with the PF and DF spectra, peaking at  $\lambda_{em}^{phos} = 525$  nm. Phosphorescence is dominated by the direct decay of the  $^3LE$  state to the ground state, which for dye **1**, in moderately polar solvents is slight above the CT manifold. Thus, it is demonstrated that the encapsulation of dye **1** in PS particles effectively preserves and transfers the optical properties of the free dye into the luminescent nanomaterials and enables TADF in aqueous media. Regarding the quantum efficiency of the long-lived emission and the DF/PF ratio, the determined values are substantially lower in PS particles (**Table 2**) than the reported



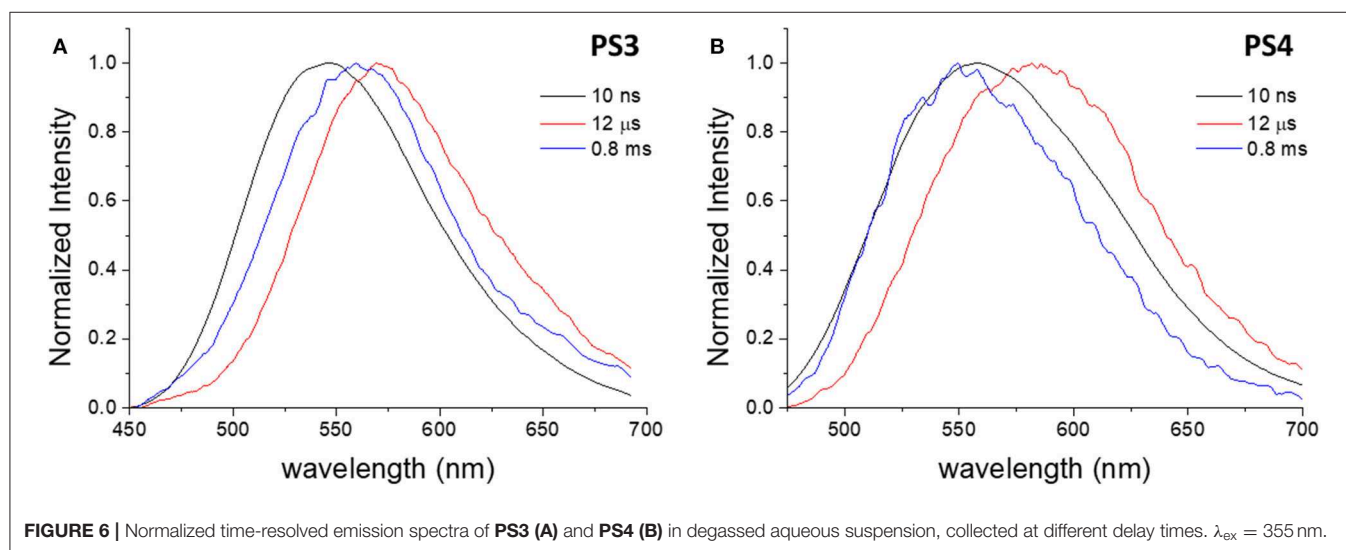
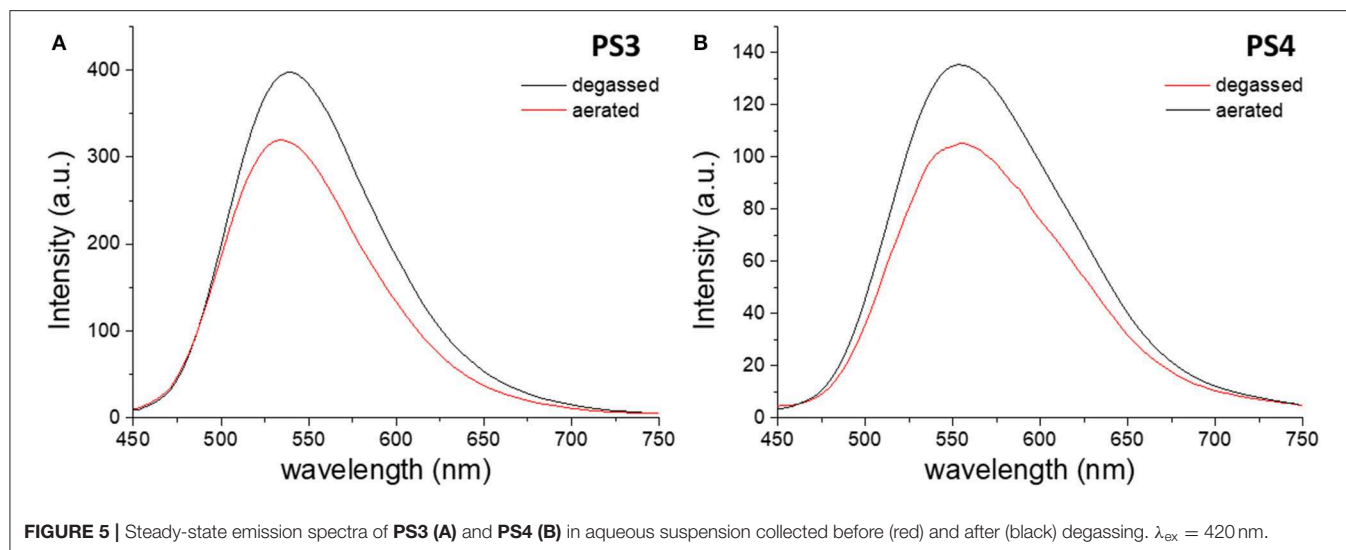


values for nonpolar (zeonex) films (Dias et al., 2016; Nobuyasu et al., 2019). However, these results are consistent with the values obtained in more polar media, such as PS film and toluene (Table S1). Accordingly, the photoluminescence quantum yield (PLQY) is significantly higher for **PS1** than for **PS2**, and can be explained by polarity effects.

In the case of dye **2**, the differences between free dye and dye-loaded materials are more evident. Comparing the emission in aqueous media, the nanomaterials show remarkably higher efficiency than the free dye, whose luminescence in water is almost negligible, and show an increase in emission intensity upon removal of oxygen (Figure 5). However, the increase in intensity due to oxygen removal is less than that observed for dye **1**. Figure 6 depicts the time-resolved emission spectra of **PS3** and **PS4**, suspended in water, where it is evidenced that a delayed fluorescence component is observed in the microsecond time range ( $\lambda_{\text{em}}^{\text{TADF}} = 571$  nm for **PS3** and  $\lambda_{\text{em}}^{\text{TADF}} = 581$  nm for

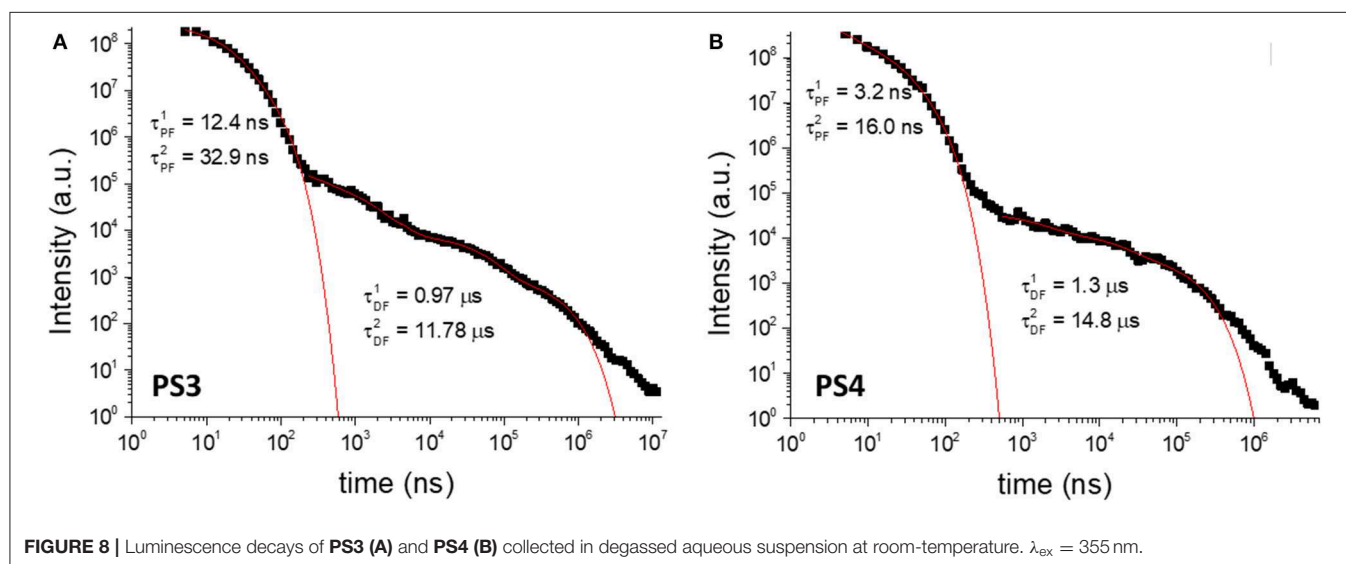
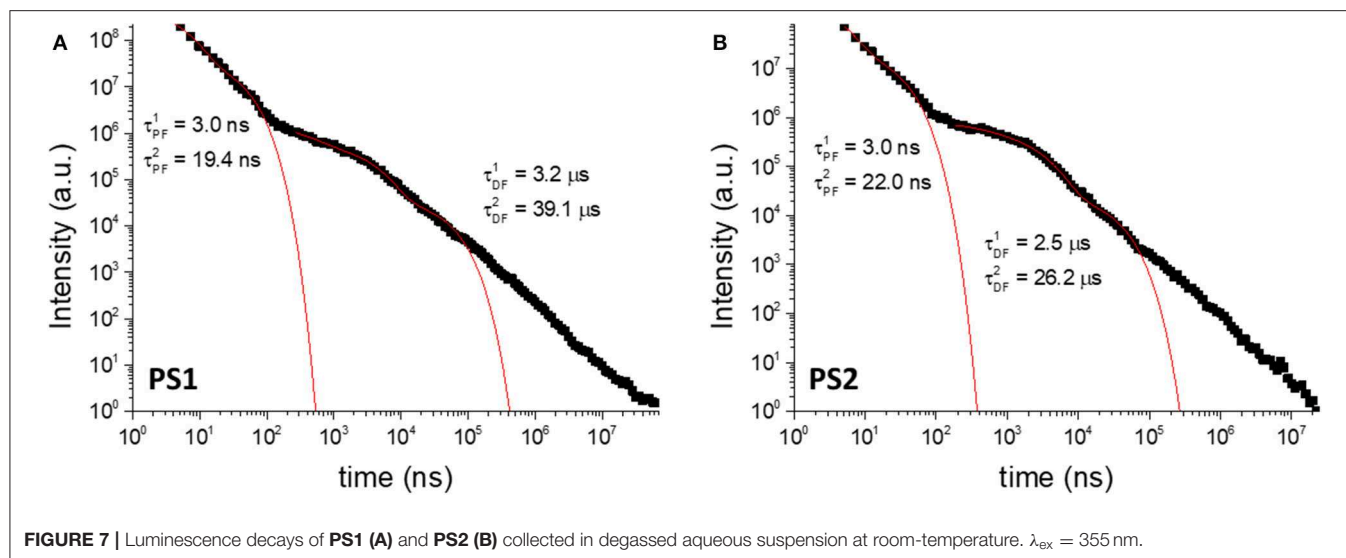
**PS4**). Similarly to what is observed for materials loaded with dye **1**, both materials also exhibit a blue-shifted phosphorescence in the millisecond time-scale ( $\lambda_{\text{em}}^{\text{Phos}} = 559$  nm for **PS3** and  $\lambda_{\text{em}}^{\text{Phos}} = 553$  nm for **PS4**). Probably due to polarity effects, the PLQY value is ca. 3 times higher for **PS3** than for **PS4**, affecting both  $\Phi_{\text{PF}}$  and  $\Phi_{\text{DF}}$  values. Nevertheless, the DF/PF ratio is the same for both materials, suggesting that the reverse intersystem crossing step is not significantly affected. These results demonstrate that similarly to what occurred with dye **1**, the encapsulation of dye **2** in PS nanoparticles enables TADF detection in aqueous media.

To further elucidate on the mechanism behind the long-lived emission, the full luminescence decay was measured for **PS1/PS2** (Figure 7) and **PS3/PS4** (Figure 8) at RT, and for **PS3** as a function of temperature (Figure S7A). Clear distinct luminescence decay regions are observed for dye **1** and dye **2** encapsulated in their respective nanoparticles. For dye **1** the PF decay is similar comparing **PS1** and **PS2**, but the



DF decay becomes slightly faster in **PS2**. Interestingly, for dye **2** the DF decay is practically not affected from **PS3** to **PS4**, however the PF decay is significantly faster in **PS4**. These variations are probably mostly due to the effects of the medium on the compound ISC and RISC rates. For example, it is clear from the decays in **Figures 7, 8** that the RISC rate is faster in **PS1/PS2** than in **PS3/PS4**. Comparing the intensity amplitudes at initial times for the PF and DF decays, **PS1/PS2** give DF/PF amplitude ratios  $\sim 10^{-2}$ , whereas **PS3/PS4** give amplitude ratios around  $\sim 10^{-3}$  and  $\sim 10^{-4}$ , respectively. Thus, the DF regime starts later in **PS3/PS4** than in **PS1/PS2**. This could be due to a slower RISC rate, but as the DF lifetime and the singlet-triplet energy gap are both similar to those of dye **1**, we have no evidence for this. Instead the stronger PLQY of the PF component indicates that the ISC rate is slower in **PS3/PS4**. Thus, fewer

triplets are formed in these systems, compared to **PS1/PS2**, and thus weaker DF is observed. Nonetheless, the decays obtained as a function of temperature demonstrate that the long-lived component decaying in the  $\mu\text{s}$  range is associated with TADF, showing increasing intensity with temperature, as expected from a thermally activated process. Furthermore, the luminescence intensity measured as a function of excitation power shows a strictly linear variation, strongly suggesting that it is due to a unimolecular process (**Figure S7B**), compatible with TADF. The longer-lived emission decaying in the ms range, shows also a behavior that is compatible with phosphorescence emission. In contrast with the TADF decay, the emission associated with a decay time in the ms range increases at lower temperature. This indicates that the longer-lived emission is stronger as temperature decreases, which is consistent with phosphorescence.



In summary, these results clearly show that the encapsulation of hydrophobic TADF dyes in polymeric nanoparticles can be efficiently achieved using swelling methodologies and that this strategy results in an enhancement of their luminescent properties due to the shielding of solvent effects, allowing the application of these dyes in aqueous media.

### Live-Cell Imaging Tests With TADF Dye-Loaded Nanoparticles

To assess the applicability of the prepared nanomaterials in biological imaging, uptake, cytotoxicity, retention, and cell internalization of TADF functionalized materials were evaluated for immortalized human breast cancer (MCF-7) cells. Due to the fact that dye **1** does not absorb above 400 nm, it was not yet possible to test materials **PS1** and **PS2** in imaging scenarios, since the available excitation source for our confocal microscopy

apparatus cannot excite in the UV range. For this reason, only materials **PS3** and **PS4** were tested.

**Figure 9** depicts the cytotoxicity evaluation for these nanomaterials, assessed by measuring the cell metabolic activity with a colorimetric assay (results for dye **2** in **Supplementary Material, Figure S8**). It is evidenced that both pristine and modified PS particle display low dark cytotoxicity, with **PS3** virtually not affecting cell viability in the studied concentration range. The amino-modified **PS4** exhibits higher cytotoxicity, which can be attributed both to a positively charged surface and a larger size of these nanoparticles. This difference in cytotoxicity between neutral and positively charged particles is in agreement with previous reports (Saei et al., 2017).

After this assessment, nanomaterials **PS3** and **PS4** were added to the incubation medium of MCF-7 cells for 24 h

at different concentrations. Following this period, the cell membranes were stained with a selective dye and the resulting confocal microscopy images are depicted in **Figures 10, 11**. It is evident that both nanomaterials are internalized with a 24 h incubation period and that both materials are located primarily in the cytosol. However, comparing the images obtained for **PS3** with those for **PS4** (**Figures 10, 11** and **Figures S9–S11**), two main differences become apparent. Firstly, the positively charged nanoparticles are more uniformly dispersed, with most of the cytosol exhibiting fluorescence from the nanomaterial at all tested concentrations. Conversely, **PS3** appears predominantly in the form of aggregates, which can be attributed to their neutral and hydrophobic surface. Secondly, the internalization and retention of **PS4** is significantly more efficient than for

the neutral nanomaterial. Although the fluorescence quantum yield and dye concentration are lower in **PS4** than in **PS3**, the measured intracellular luminescence intensity is considerably higher for cells incubated with the positively charged particles (**Figure 12** and **Figure S12**).

## CONCLUSIONS

The results shown in this work demonstrate that PS nanoparticles are efficient carriers for hydrophobic TADF emitters, enabling straightforward loading methodologies without requiring previous functionalization of luminescent dyes. Through an established swelling procedure, we prepared four luminescent nanomaterials, starting from two TADF emitters and two types of PS nanoparticles. The dye loading proved more efficient in pristine polystyrene nanomaterial than in the amino-modified analog. The encapsulation in polystyrene nanoparticles enhanced the optical properties of the TADF emitters in fluid media and even enabled the detection of delayed fluorescence and room-temperature phosphorescence in water. Due to the CT character of the excited states involved in the TADF process, the increase in polarity due to the presence of amine moieties led to an overall decrease in the PLQY of the positively charged nanoparticles. When added to the incubation medium of breast cancer cells, the dye-loaded nanoparticles exhibited very low dark cytotoxicity. Confocal microscopy revealed that both neutral and positive nanoparticles were internalized, locating primarily in the cytosol. The amino-modified particles were internalized more efficiently and were more uniformly dispersed inside the cells than the pristine polystyrene particles. We expect that this strategy can be generalized to a large variety of TADF dyes and extend their application beyond lighting devices. In order to achieve optimal DF/PF ratios for fluorescence imaging, care should be taken in the selection of TADF emitters, mainly regarding the polarity effects on the TADF process.

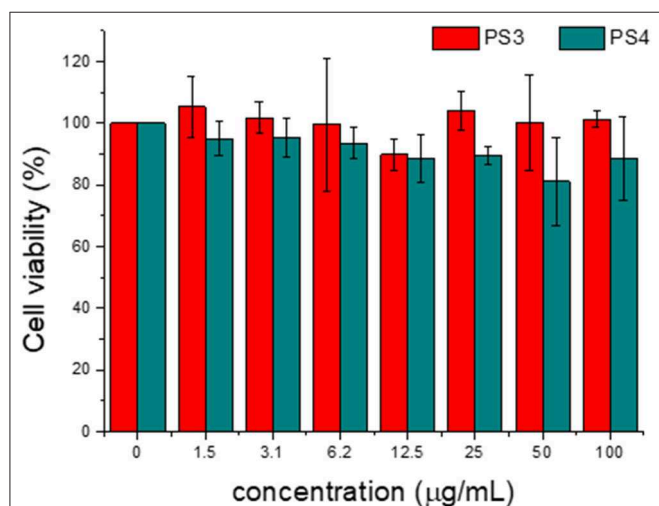


**FIGURE 9** | Effect of PS3 and PS4 on MCF-7 cell viability as a function of concentration in incubation medium for 24 h. The percentages refer to cell viability represented as a percentage of control.

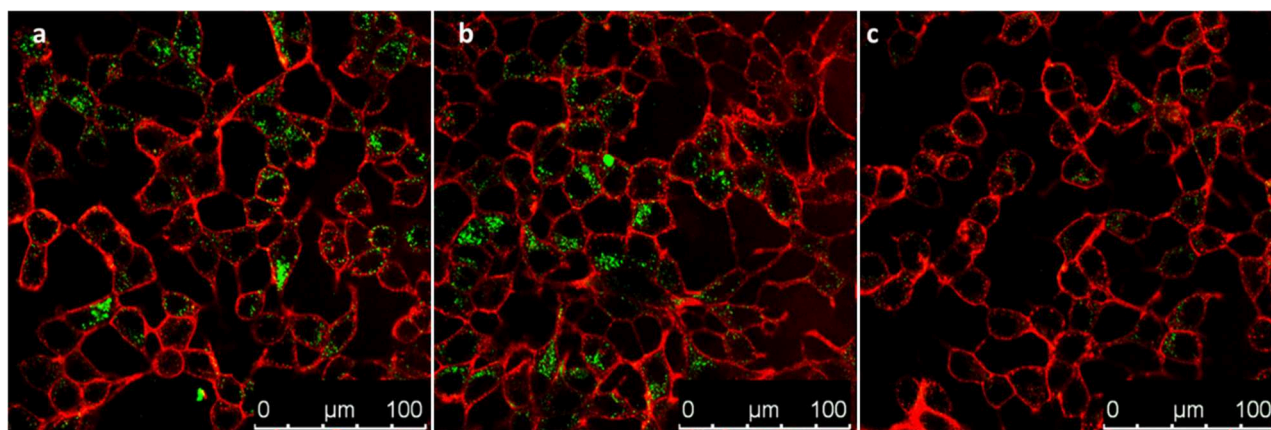


**FIGURE 10** | Confocal microscopy images of MCF-7 cells incubated for 24 h in the presence of **PS3** at different concentrations in incubation medium: (a) 100 µg/mL; (b) 50 µg/mL; (c) 25 µg/mL. Images show **PS3** emission in green and plasma membrane labeled with WGA-Alexa Fluor 633 in red.



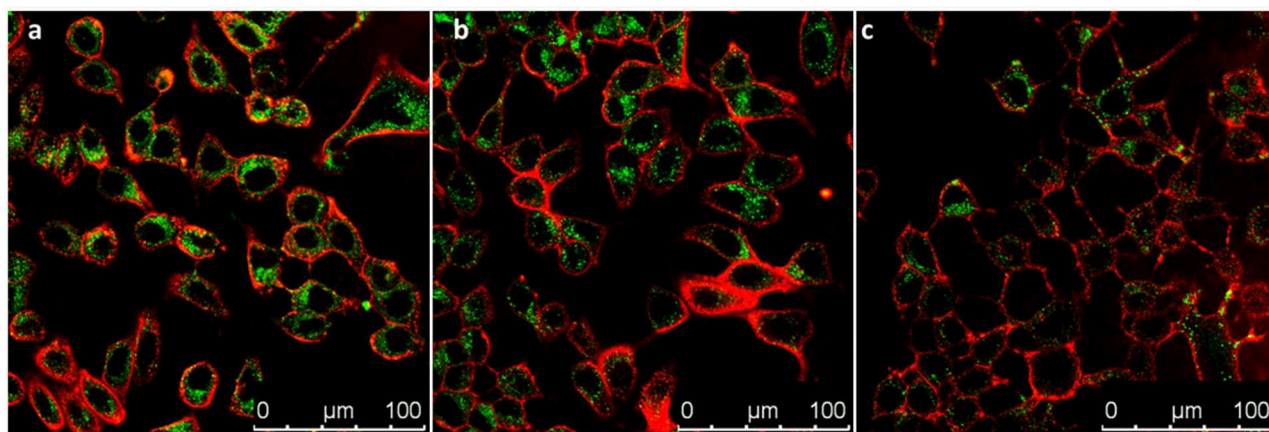


**FIGURE 11** | Confocal microscopy images of MCF-7 cells incubated for 24 h in the presence of **PS4** at different concentrations in incubation medium: **(a)** 100 µg/mL; **(b)** 50 µg/mL; **(c)** 25 µg/mL. Images show **PS4** emission in green and plasma membrane labeled with WGA-Alexa Fluor 633 in red.

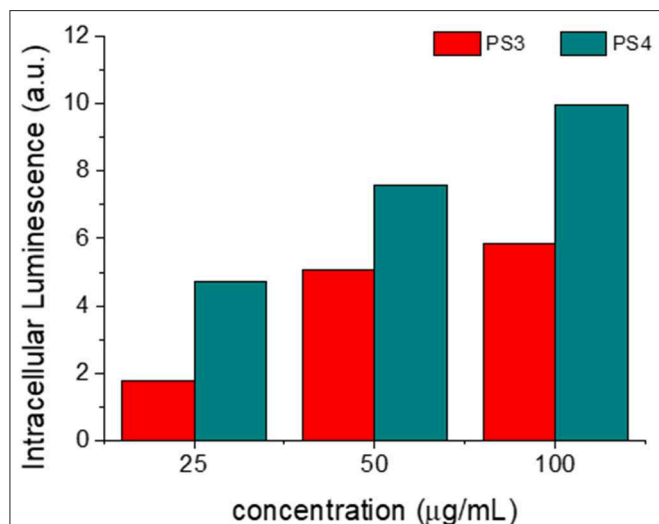


**FIGURE 12** | Integrated intracellular nanoparticle fluorescence, measured as a function of concentration of **PS3** (red) and **PS4** (blue) in the incubation medium. Analyzed area = 240 × 240 µm.

## EXPERIMENTAL

### Materials and Reagents

All chemical reagents were purchased from commercial suppliers without further purification unless otherwise noted. Styrene (St), Potassium persulfate (KPS), Divinylbenzene (DVB), Sodium dodecyl sulfate (SDS) were supplied by Sigma-Aldrich. KPS was purified via re-crystallization in deionized water. St and DVB were purified by passing through a basic alumina column. Amino-modified polystyrene nanoparticles (PSNH<sub>2</sub>) from Polybead® (type amino 100 nm spheres, 2.6 % suspension of solid particles in water) were purchased from Poly-sciences, Inc. (www.polysciences.com). Dialysis membranes with a molecular weight cutoff between 100–500 Da and a volume per length

ratio of 1.8 mL cm<sup>-1</sup> were obtained from Spectra/Por® Dialysis Membrane Biotech CE Tubing. Prior to usage, the membranes were soaked in distilled H<sub>2</sub>O for ~15 min and rinsed thoroughly with distilled H<sub>2</sub>O. All chemicals employed for synthesis were of reagent grade from TCI and used as received. For optical measurements, solvents were of spectroscopic grade and used without prior purification. Toluene was PA grade and was dried using metallic sodium and benzophenone and distilled before use. Tetrahydrofuran (THF) was of UV-spectroscopic grade and purchased from Sigma-Aldrich. Deionized water purified using a Millipore Milli-Q system to a resistivity of 18.2 MΩ was used throughout the experiments unless otherwise stated. Argon (Ar) gas (Alphagaz 1, 99,999%) was purchased from Air Liquid. Reagents and solvents used in synthesis were all analytical grade.

### Dye and Particle Synthesis/Preparation

#### Synthesis of DPTZ-DBTO<sub>2</sub> (1)

The synthesis of **1** was carried out according to a previously reported strategy (Dias et al., 2016).

2,8-Dibromodibenzothiophene-S,S-dioxide (150 mg, 0.401 mmol, 1 eq.), phenothiazine (159 mg, 0.802 mmol, 2 eq.), were dried under vacuum for 0.5 h in a two-neck 25 mL round-bottomed flask fitted with a reflux condenser. The flask was back-filled with argon and dry toluene (9 mL) was added. The reaction mixture was bubbled with argon for 0.5 h, then Pd<sub>2</sub>(dba)<sub>3</sub> (18.4 mg, 0.020 mmol, 5 mol%) and HP<sup>t</sup>Bu<sub>3</sub>BF<sub>4</sub> (11.6 mg, 40.1 µmol, 10 mol%) were added and the reaction mixture was bubbled with argon for a further 0.5 h. NaO<sup>t</sup>Bu (11.6 mg, 0.12 mmol, 3 eq.) was added under a high flow of argon and the reaction was then stirred at 115°C for 21 h. Upon cooling, the solvent was removed at low pressure. The resulting residue was chromatographed (silica gel, eluent hexane/DCM 1:2 v/v) to give DPTZ-DBTO<sub>2</sub> as a yellow solid (92.7 mg, 37.8%). Recrystallization of the residue from boiling dichloromethane followed by hot filtration and cooling at room temperature gave pale yellow crystals. <sup>1</sup>H-NMR (400 MHz, DMSO-d<sub>6</sub>; **Figure S1**):

$\delta = 7.99$  (d, 2H,  $H_8$ ,  $^3J_{H8-H7} = 11.3$  Hz),  $7.69$  (s, 2H,  $H_6$ ),  $7.40$  (d, 4H,  $H_4$ ,  $^3J_{H4-H3} = 9.9$  Hz),  $7.33$  (d, 2H,  $H_7$ ,  $^3J_{H7-H8} = 11.1$  Hz),  $7.25$  (t, 4H,  $H_2$ ,  $^3J_{H2-H3, H2-H1} = 10.1$  Hz),  $7.17$  (t, 4H,  $H_3$ ,  $^3J_{H3-H4} = 9.9$  Hz,  $^3J_{H3-H2} = 9.6$  Hz),  $7.01$  (d, 4H,  $H_1$ ,  $^3J_{H1-H2} = 10.4$  Hz).  $^{13}\text{C-NMR}$  (100 MHz, DMSO- $d_6$ ):  $\delta = 148.9$ ,  $141.8$ ,  $133.4$ ,  $133.1$ ,  $128.5$  ( $C_4$ ),  $128.3$  ( $C_2$ ),  $127.8$ ,  $125.8$  ( $C_3$ ),  $124.5$  ( $C_8$ ),  $123.0$  ( $C_1$ ),  $118.2$ ,  $115.4$  ( $C_6$ ). EA. Calc. for  $\text{C}_{36}\text{H}_{22}\text{N}_2\text{S}_3 \cdot 0.6 \text{CH}_2\text{Cl}_2$ , C 66.43; H 3.53; N 4.23. Found: C 66.35; H 3.45; N 4.11.

### Synthesis of Polystyrene Nanoparticles (PSP)

PS nanoparticles were synthesized by an emulsion polymerization process (Zhang et al., 2015). A mixture composed of 0.25 g of SDS and 15 mL of water was first placed into a two-neck round-bottom flask equipped with a magnetic stirrer, a reflux condenser and an argon inlet. Purified styrene (1.68 mL) and DVB (0.25 mL) were added and the mixture was stirred under constant agitation (700 rpm) and purged with argon for 0.5 h. The temperature of the system was then raised to  $70^\circ\text{C}$ . 0.01 g of KPS was added with argon purging. After that, the reaction was allowed to occur for 5 h and argon was fluxed during the entire polymerization procedure. The mixture was cooled down to room temperature and sonicated for 15 min. The obtained PS nanoparticles were first centrifuged (30,000 rpm,  $22^\circ\text{C}$ , 3 h). The supernatants were purified by repeated dialyses against distilled water (cellulose membrane, molecular weight cut-off 100–500 Da), obtaining a 1.0 % (w/v) suspension of solid particles in water. This stock suspension was stored at  $4^\circ\text{C}$ .

### Dye-Loading Swelling Procedure

The swelling method has been described previously (Behnke et al., 2011). In a typical swelling procedure, dye (**1** or **2**) was dissolved in THF to give a stock solution. Dye loading of the PSP was performed by addition of the dye solution to an aqueous suspension of the PSP. This was then stirred at room temperature for 0.5 h. The solvent was allowed to evaporate overnight in a fume cupboard. The nanoparticle concentration in the remaining aqueous suspension was determined by drying and weighing a known volume.

#### Swelling procedure PS1

Dye **1** was dissolved in THF to give a stock solution ( $1.6 \times 10^{-3}$  mol  $\text{L}^{-1}$ ). Dye loading of the PSP was performed by addition of 1.7 mL of the dye solution to 10 mL of an aqueous suspension of the PSP (1.0% w/v). After evaporation of the THF the suspension was centrifuged (2,000 g) and only the supernatant was used for the measurements.

#### Swelling procedure PS2

Dye **1** was dissolved in THF to give a stock solution ( $2.2 \times 10^{-3}$  mol  $\text{L}^{-1}$ ). Dye loading of the PS-NH<sub>2</sub> was performed by addition of 200  $\mu\text{L}$  of the dye solution to 5 mL of an aqueous suspension of the PS-NH<sub>2</sub> (0.5 % w/v).

#### Swelling procedure PS3

Dye **2** was dissolved in THF to give a stock solution ( $2.1 \times 10^{-3}$  mol  $\text{L}^{-1}$ ). Dye loading of the PSP was performed by addition of 1.7 mL of the dye solution to 10 mL of an aqueous suspension of

the PSP (1.0 % w/v). After evaporation of the THF the suspension was centrifuged (2,000 g) and only the supernatant was used for the measurements.

#### Swelling procedure PS4

Dye **2** was dissolved in THF to give a stock solution ( $2.7 \times 10^{-3}$  mol  $\text{L}^{-1}$ ). Dye loading of the PS-NH<sub>2</sub> was performed by addition of 200  $\mu\text{L}$  of the dye solution to 5 mL of an aqueous suspension of the PS-NH<sub>2</sub> (0.5 % w/v).

To determine the amount of dye incorporated into the PS nanoparticles, 300  $\mu\text{L}$  of particle suspension were dissolved in 3 mL of THF followed by subsequent measurement of the absorption spectra of the transparent THF solutions. The average amount of dye incorporated into the nanomaterial was calculated from the absorbance measured at the dye's longest wavelength absorption maximum, using the Lambert-Beer law and the previously determined molar absorption coefficient of the dye in THF.

### NMR Spectroscopy

$^1\text{H}$  and  $^{13}\text{C}$  NMR spectra were recorded at 400 MHz and 100 MHz respectively using a Bruker Avance III 400 spectrometer (Bruker BioSpin GmbH, Rheinstetten, Germany) in DMSO- $d_6$ , referenced to the solvent for both proton and carbon spectra.

### Electron Microscopy

Transmission Electron Microscopy (TEM) images were obtained with a Hitachi 8100 electron microscope operating at 200 kV and 20  $\mu\text{A}$ . Samples were dispersed in water and then a drop was placed on Formvar<sup>®</sup>/Carbon Coated Grid (200 mesh) and dried before examination. The dry nanoparticle size was estimated by measuring the average diameter of 100 nanoparticles by using ImageJ software.

### Optical Spectroscopy

Photophysical data were collected using optical spectroscopy apparatus previously described (Menezes et al., 2013; Crucho et al., 2020). Absorption and reflectance spectra were collected using a Shimadzu UV-3600 double beam spectrophotometer. Reflectance spectra were obtained for silica nanoparticles dispersed in BaSO<sub>4</sub>. Emission spectra were collected in a Jobin Yvon Fluorolog fluorescence spectrometer, respectively. Emission is independent of excitation wavelength. The luminescence temperature dependence measurements were acquired using a model liquid nitrogen cryostat (Janis Research). Fluorescence decays of dyes were measured by the single-photon timing method using nanoLED (IBH) excitation at 373 nm, with 500 ps pulse width. The electronic start pulses are shaped in a constant fraction discriminator (Canberra 2126) and directed to a time to amplitude converter (TAC, Canberra 2145). Emission wavelength (450 nm) is selected by a monochromator (Oriel 77,250) imaged in a fast photomultiplier (9814B Electron Tubes Inc.), the PM signal is shaped as before and delayed before entering the TAC as stop pulses. The analog TAC signals are digitized (ADC, ND582) and stored in a PC. For luminescent nanoparticles, fluorescence

decays were measured by the single-photon timing method with laser excitation (365 nm) and emission at 550–620 nm. The setup consisted of a diode-pumped solid state (DPSS) continuous wave green Nd:YVO<sub>4</sub> laser (Millennia Xs, Spectra Physics) that pumped a mode locked Ti:sapphire laser (Tsunami, Spectra Physics, with tuning range 700–1,000 nm, output pulses of 100 fs, and 80 MHz repetition rate that can be reduced down to 4 MHz by a pulse picker) or mode locked DPSS Nd:YVO<sub>4</sub> green laser (Vanguard 2000-HM532, Spectra Physics) synchronously pumping two cavity dumped dye lasers (701, Coherent, delivering 3–4 ps pulses of about 40 nJ/pulse at 3.4 MHz) working with rhodamine 6G and DCM. Intensity decay measurements were made by an alternating collection of impulses and decays with the emission polarizer set at the magic angle position. Impulses were recorded slightly away from the excitation wavelength with a scattering suspension, thus defining the instrument response function (IRF). Particle samples were prepared either as suspensions in solvent (0.1–0.5% w/v) or immobilized in quartz plates using zeonex (20% in toluene) as binder. Temperature dependent time-resolved emission spectra were focused onto a spectrograph and detected on a sensitive gated iCCD camera (Stanford Computer Optics) with sub-nanosecond resolution. Solutions were prepared with concentrations in the 10<sup>-5</sup>–10<sup>-4</sup> M range in different solvents, and samples were degassed using five freeze-pump-thaw cycles or bubbling Argon for 1 h. Films for optical characterization were prepared in zeonex or poly(vinylalcohol) matrix by drop-casting onto a quartz substrate with an emitter concentration of 1% (w/w). Prompt fluorescence quantum yields ( $\Phi_{PF}$ ) were determined using the standard method for free dyes (vs. quinine sulfate in H<sub>2</sub>SO<sub>4</sub> 0.01 M), and with the absolute method using an integrating sphere for luminescent nanomaterials. Delayed fluorescence quantum yields ( $\Phi_{DF}$ ) using  $\Phi_{PF}$  as internal reference and the ratio of the integrated areas of full luminescence decays acquired in degassed conditions, as given by Equation (1)

$$\Phi_{DF} = \Phi_{PF} \left( \frac{I_{DF}}{I_{PF}} \right) \quad (1)$$

Phosphorescence, prompt fluorescence, and delayed emission (DF) spectra and decays were recorded using nanosecond gated luminescence and lifetime measurements (from 400 ps to 1 s) using either a high energy pulsed Nd:YAG laser emitting at 355 nm (EKSPLA) or a N<sub>2</sub> laser emitting at 337 nm. Emission was focused onto a spectrograph and detected on a sensitive gated iCCD camera (Stanford Computer Optics) having subnanosecond resolution. PF/DF time resolved measurements were performed by exponentially increasing gate and delay times; details can be found elsewhere (Rothe and Monkman, 2003).

Dynamic Light Spectroscopy (DLS) was carried out on a Horiba nanoPartica SZ-100 V2 Nanoparticle Analyzer. Nanomaterials were suspended in water (1 mg/mL) and the analyzed samples were prepared by diluting the stock suspensions (1:100). Measurements were carried out at 90°

scattering angle on quartz cuvettes at 25°C. All tests were run six times for 30 s and the average values were presented and particle size was calculated by fitting the correlation curves using solver mathematical software from the Stokes-Einstein equation.

## Live-Cell Imaging

MCF-7 cell line (European Collection of Authenticated Cell Cultures, ECACC) were cultured in DMEM (ThermoFisher Scientific) supplemented with 10% fetal bovine serum (FCS) (GIBCO) and 1% of penicillin-streptomycin (Sigma Chemical Co., St. Louis, MO) at the incubator with controlled temperature (37°C), humidity and CO<sub>2</sub> levels (5%). For confocal and two-photon excitation microscopic studies, the cells were grown on Ibidi  $\mu$ -Slide 8 well glass bottom with an initial density of 1  $\times$  10<sup>4</sup> cells per well. After cell confluency reached  $\sim$ 70%, 25–100  $\mu$ g/mL of **PS3** and **PS4** or 1.5–200  $\mu$ M of **2** were added separately in two different sets of experiments and maintained/cultured for a period of 24 h. After the desired incubation time, cells were carefully washed with DPBS (Thermo Fisher Scientific) and labeled with WGA-Alexa Fluor 633 according with instructions of the supplier (Thermo Fisher Scientific, Plasma Membrane and Nuclear Labeling dyes). A final washing step with DPBS was also included. The cells were imaged using a laser scanning confocal microscope (Leica TCS-SP5) equipped with a continuous Ar-ion, HeNe and a Ti:sapphire laser. WGA – Alexa Fluor 633 emission was collected from 640 to 700 nm and nanoparticle emission was collected from 500 to 600 nm. A 63 $\times$  (1.2 N.A.) water immersion objective was used in the experiments. Quantification analysis was carried out using the ImageJ software (version 1.48, <http://imagej.nih.gov/ij/>). For each image, individual cells are selected using membrane staining with WGA-Alexa 633, and a mask is attributed to each cell. The total fluorescence signal in the nanoparticle channel (500–600 nm) was integrated for cells incubated with and without (autofluorescence) nanoparticles, in order to determine the concentration dependent intracellular nanoparticle fluorescence signal and the fraction of cells that exhibit nanoparticle internalization. Number of cells analyzed per condition > 40.

## Cytotoxicity Assay

The effect of the prepared nanomaterials on cell metabolic activity was determined by MTT [3-(4,5-dimethylthiazol-2-yl)-2,5-tetrazolium bromide] assay previously described (Raj and Das, 2017). Briefly, MCF-7 cells were plated at a density of 2  $\times$  10<sup>4</sup> cells per well into the 96-well plate and cultured for 24 h at 37°C in 5% CO<sub>2</sub> atmosphere. Then, **PS3** and **PS4** at different concentrations (0–100  $\mu$ g/mL) were added in duplicate and incubated for additional 24 h. After the incubation period, media was carefully replaced with 100  $\mu$ L of fresh complete media without disturbing cell contents followed by addition of 20  $\mu$ L of MTT solution (5 mg/mL) and incubated for 3–4 h. Finally, the formazan crystals formed in the wells were dissolved using 150  $\mu$ L of MTT solvent and the absorbance



was read at 590 nm using a microplate reader (bmj labtech 96 Spectrostar Nano).

## DATA AVAILABILITY STATEMENT

All datasets generated for this study are included in the article/**Supplementary Material**.

## AUTHOR CONTRIBUTIONS

Experimental: CC did the nanoparticle synthesis and characterization. JA did the photophysical measurements. AD did the organic dye synthesis. SP did the microscopy imaging and cytotoxicity studies. JB did cytotoxicity studies. PS performed cell culture preparation. Writing: The data was analyzed and validated by JA, FD, MB-S, and L-OP. The manuscript was written by JA and FD with contributions from all authors.

## REFERENCES

- Baldo, M., O'Brien, D., You, Y., Shoustikov, A., Sibley, S., Thompson, M., et al. (1998). Highly efficient phosphorescent emission from organic electroluminescent devices. *Nature* 395, 151–154. doi: 10.1038/25954
- Baleizão, C., Nagl, S., Schaferling, M., Berberan-Santos, M., and Wolfbeis, O. (2008). Dual fluorescence sensor for trace oxygen and temperature with unmatched range and sensitivity. *Anal. Chem.* 80, 6449–6457. doi: 10.1021/ac801034p
- Behnke, T., Würth, C., Hoffmann, K., Hübner, M., Panne, U., Resch-Genger, U. et al. (2011). Encapsulation of hydrophobic dyes in polystyrene micro and nanoparticles via swelling procedures. *J. Fluoresc.* 21, 937–944. doi: 10.1007/s10895-010-0632-2
- Bui, T., Goubard, F., Ibrahim-Ouali, M., Gimes, D., and Dumur, F. (2018). Recent advances on organic blue thermally activated delayed fluorescence (TADF) emitters for organic light-emitting diodes (OLEDs). *Beilstein J. Org. Chem.* 14, 282–308. doi: 10.3762/bjoc.14.18
- Chen, W., and Song, F. (2019). Thermally activated delayed fluorescence molecules and their new applications aside from OLEDs. *Chin. Chem. Lett.* 30, 1717–1730. doi: 10.1016/j.ccl.2019.08.032
- Crucho, C., Avó, J., Nobuyasu, R., Pinto, S., Fernandes, F., Lima, J., et al. (2020). Silica nanoparticles with thermally activated delayed fluorescence for live cell imaging. *Mater. Sci. Eng. C* 109:110528. doi: 10.1016/j.msec.2019.110528
- Dias, F., Penfold, T., and Monkman, A. (2017). Photophysics of thermally activated delayed fluorescence molecules. *Methods Appl. Fluoresc.* 5:012001. doi: 10.1088/2050-6120/aa537e
- Dias, F., Santos, J., Graves, D., Data, P., Nobuyasu, R., Fox, M., et al. (2016). The role of local triplet excited states and D-A relative orientation in thermally activated delayed fluorescence: photophysics and devices. *Adv. Sci.* 3:1600080. doi: 10.1002/advs.201600080
- Dias, F. B., Bourdakos, K. N., Jankus, V., Moss, K. C., Kamtekar, K. T., Bhalla, V., et al. (2013). Triplet harvesting with 100% efficiency by way of thermally activated delayed fluorescence in charge transfer OLED emitters. *Adv. Mater.* 25, 3707–3714. doi: 10.1002/adma.201300753
- Lee, J., Gomez, I., Sitterle, V., and Meredith, J. (2011). Dye-labeled polystyrene latex microspheres prepared via a combined swelling-diffusion technique. *J. Coll. Interf. Sci.* 363, 137–144. doi: 10.1016/j.jcis.2011.07.047
- Lee, J., White, A., Rice, D., and Smith, D. (2013). *In vivo* imaging using polymeric nanoparticles stained with near-infrared chemiluminescent and fluorescent squaraine catenane endoperoxide. *Chem. Commun.* 49, 3016–3018. doi: 10.1039/c3cc40630j
- Li, L., Wang, W., Tang, J., Wang, Y., Liu, J., Huang, L., et al. (2019). Classification, synthesis, and application of luminescent silica nanoparticles: a review. *Nanoscale Res. Lett.* 14:190. doi: 10.1186/s11671-019-3006-y
- Li, T., Yang, D., Zhai, L., Wang, S., Zhao, B., Fu, N., et al. (2017). Thermally activated delayed fluorescence organic dots (TADF Odots) for time-resolved and confocal fluorescence imaging in living cells and *in vivo*. *Adv. Sci.* 4:1600166. doi: 10.1002/advs.201600166
- Luo, X., Meng, J., Li, B., Peng, A., and Tian, Z. (2019). Development of fluorescent nanoparticles with aggregation-induced delayed fluorescence features, improved brightness and photostability for living cells imaging. *New J. Chem.* 43, 10735–10743. doi: 10.1039/C9NJ01945F
- Mader, H., and Wolfbeis, O. (2010). Optical ammonia sensor based on upconverting luminescent nanoparticles. *Anal. Chem.* 82, 5002–5004. doi: 10.1021/ac1007283
- Menezes, F., Fedorov, A., Baleizão, C., Valeur, B., and Berberan-Santos, M. (2013). Methods for the analysis of complex fluorescence decays: sum of Becquerel functions versus sum of exponentials. *Methods Appl. Fluoresc.* 1:015002. doi: 10.1088/2050-6120/1/1/015002
- Montalti, M., Prodi, L., Rampazzo, E., and Zaccaroni, N. (2014). Dye-doped silica nanoparticles as luminescent organized systems for nanomedicine. *Chem. Soc. Rev.* 43, 4243–4268. doi: 10.1039/C3CS60433K
- Ni, F., Zhu, Z., Tong, X., Xie, M., Zhao, Q., Zhong, C., et al. (2018). Organic emitter integrating aggregation-induced delayed fluorescence and room-temperature phosphorescence characteristics, and its application in time-resolved luminescence imaging. *Chem. Sci.* 9, 6150–6155. doi: 10.1039/C8SC01485J
- Ni, F., Zhu, Z., Tong, X., Zeng, W., An, K., Wei, D., et al. (2019). Hydrophilic, red-emitting, and thermally activated delayed fluorescence emitter for time-resolved luminescence imaging by mitochondrion-induced aggregation in living cells. *Adv. Sci.* 6:1801729. doi: 10.1002/advs.201801729
- Nobuyasu, R., Ward, J., Gibson, J., Laidlaw, B., Ren, Z., Data, P., et al. (2019). The influence of molecular geometry on the efficiency of thermally activated delayed fluorescence. *J. Mater. Chem. C* 7, 6672–6684. doi: 10.1039/c9tc00720b
- Peng, J., Li, J., Xu, W., Wang, L., Su, D., Teoh, C., et al. (2018). Silica nanoparticle-enhanced fluorescent sensor array for heavy metal ions detection in colloid solution. *Anal. Chem.* 90, 1628–1634. doi: 10.1021/acs.analchem.7b02883
- Raj, R., and Das, S. (2017). Development and application of anticancer fluorescent CdS nanoparticles enriched *Lactobacillus* bacteria as therapeutic microbots for human breast carcinoma. *Appl. Microbiol. Biotechnol.* 101, 5439–5451. doi: 10.1007/s00253-017-8298-1
- Rothe, C., and Monkman, A. (2003). Triplet exciton migration in a conjugated polyfluorene. *Phys. Rev. B* 68:075208. doi: 10.1103/PhysRevB.68.075208

## ACKNOWLEDGMENTS

Aleksander Fedorov was acknowledged for the acquisition of prompt emission decays of dyes in solution. Fundação para a Ciência e a Tecnologia (FCT, I.P.) was acknowledged for funding under grant SFRH/BPD/120599/2016 and projects PTDC/QUI-QFI/32007/2017, UID/04565/2020, and SAICT/0019/2015. Liga Portuguesa Contra o Cancro for funding under Terry/Fox Research Grant. Portuguese Platform for Bioimaging was also acknowledged (PPBI-POCI-01-0145-FEDER-022122).

## SUPPLEMENTARY MATERIAL

The Supplementary Material for this article can be found online at: <https://www.frontiersin.org/articles/10.3389/fchem.2020.00404/full#supplementary-material>



- Saei, A., Yazdani, M., Lohse, S., Bakhtiary, Z., Serpooshan, V., Ghavami, M., et al. (2017). Nanoparticle surface functionality dictates cellular and systemic toxicity. *Chem. Mater.* 29, 6578–6595. doi: 10.1021/acs.chemmater.7b01979
- Tsuchiya, Y., Ikesue, K., Nakanotani, H., and Adachi, C. (2019). Photostable and highly emissive glassy organic dots exhibiting thermally activated delayed fluorescence. *Chem. Commun.* 55, 5215–5218. doi: 10.1039/C9CC01420A
- Uoyama, H., Goushi, K., Shizu, K., Nomura, H., and Adachi, C. (2012). Highly efficient organic light-emitting diodes from delayed fluorescence. *Nature* 492, 234–238. doi: 10.1038/nature11687
- Wang, H., Xie, L., Peng, Q., Meng, L., Wang, Y., Yi, Y., et al. (2014). Novel thermally activated delayed fluorescence materials–thioxanthone derivatives and their applications for highly efficient OLEDs. *Adv. Mater.* 26, 5198–5204. doi: 10.1002/adma.201401393
- Wang, X., Achatz, D., Hupf, C., Sperber, M., Wegener, J., Bange, S., et al. (2013). Imaging of cellular oxygen via two-photon excitation of fluorescent sensor nanoparticles. *Sensor. Actuat. B Chem.* 188, 257–262. doi: 10.1016/j.snb.2013.06.087
- Wolfbeis, O. (2015). An overview of nanoparticles commonly used in fluorescent bioimaging. *Chem. Soc. Rev.* 44, 4743–4768. doi: 10.1039/c4cs00392f
- Xiong, X., Song, F., Wang, J., Zhang, Y., Xue, Y., Sun, N., et al. (2014). Thermally activated delayed fluorescence of fluorescein derivative for time-resolved and confocal fluorescence imaging. *J. Am. Chem. Soc.* 136, 9590–9597. doi: 10.1021/ja502292p
- Yang, Z., Mao, Z., Xie, Z., Zhang, Y., Liu, S., Zhao, J., et al. (2017). Recent advances in organic thermally activated delayed fluorescence materials. *Chem. Soc. Rev.* 46, 915–1016. doi: 10.1039/c6cs00368k
- Yu, J., Rong, Y., Kuo, C., Zhou, X., and Chiu, D. (2017). Recent advances in the development of highly luminescent semiconducting polymer dots and nanoparticles for biological imaging and medicine. *Anal. Chem.* 89, 42–56. doi: 10.1021/acs.analchem.6b04672
- Zhang, Y., Zhuang, X., Gu, X., and Zhao, J. (2015). Synthesis of polyacrylonitrile nanoparticles at high monomer concentrations by AIBN-initiated semi-continuous emulsion polymerization method. *Eur. Polym. J.* 67, 57–65. doi: 10.1016/j.eurpolymj.2015.03.057
- Zhao, Q., Huang, C., and Li, F. (2011). Phosphorescent heavy-metal complexes for bioimaging. *Chem. Soc. Rev.* 40, 2508–2524. doi: 10.1039/C0CS00114G
- Zhu, Z., Tian, D., Gao, P., Wang, K., Li, Y., Shu, Z., et al. (2018). Cell-penetrating peptides transport noncovalently linked thermally activated delayed fluorescence nanoparticles for time-resolved luminescence imaging. *J. Am. Chem. Soc.* 140, 17484–17491. doi: 10.1021/jacs.8b08438

**Conflict of Interest:** The authors declare that the research was conducted in the absence of any commercial or financial relationships that could be construed as a potential conflict of interest.

Copyright © 2020 Crucho, Avó, Diniz, Pinto, Barbosa, Smith, Berberan-Santos, Pålsson and Dias. This is an open-access article distributed under the terms of the Creative Commons Attribution License (CC BY). The use, distribution or reproduction in other forums is permitted, provided the original author(s) and the copyright owner(s) are credited and that the original publication in this journal is cited, in accordance with accepted academic practice. No use, distribution or reproduction is permitted which does not comply with these terms.



# Highly Efficient Deep Blue Luminescence of 2-Coordinate Coinage Metal Complexes Bearing Bulky NHC Benzimidazolyl Carbene

Rasha Hamze<sup>††</sup>, Muazzam Idris<sup>†</sup>, Daniel Sylvinson Muthiah Ravinson, Moon Chul Jung, Ralf Haiges, Peter I. Djurovich and Mark E. Thompson<sup>\*</sup>

Department of Chemistry, University of Southern California, Los Angeles, CA, United States

## OPEN ACCESS

### Edited by:

Chihaya Adachi,  
Kyushu University, Japan

### Reviewed by:

Yun CHI,  
City University of Hong Kong,  
Hong Kong  
Shin-ya Takizawa,  
The University of Tokyo, Japan  
Feng Li,  
Jilin University, China

### \*Correspondence:

Mark E. Thompson  
met@usc.edu

<sup>†</sup>These authors have contributed  
equally to this work

### \*Present address:

Rasha Hamze,  
Universal Display Corporation, Ewing,  
NJ, United States

### Specialty section:

This article was submitted to  
Inorganic Chemistry,  
a section of the journal  
Frontiers in Chemistry

Received: 27 February 2020

Accepted: 16 April 2020

Published: 08 May 2020

### Citation:

Hamze R, Idris M, Muthiah  
Ravinson DS, Jung MC, Haiges R,  
Djurovich PI and Thompson ME  
(2020) Highly Efficient Deep Blue  
Luminescence of 2-Coordinate  
Coinage Metal Complexes Bearing  
Bulky NHC Benzimidazolyl Carbene.  
Front. Chem. 8:401.  
doi: 10.3389/fchem.2020.00401

The structural, photophysical and electrochemical properties of three luminescent 2-coordinate coinage metal (i.e., M = Cu, Ag, Au) complexes bearing a sterically bulky benzimidazolyl carbene, 1,3-bis(2,6-diisopropylphenyl)-1-H-benzo[d]imidazol-2-ylidene (**BZI**), and carbazolidine (Cz) as the anionic ligand were investigated. All the complexes emit in the deep blue region (~430 nm) with relatively narrow spectra (full width at half maximum = 44 nm, 2,300 cm<sup>-1</sup>) characterized by vibronic fine structure in nonpolar media (methylcyclohexane at room temperature), and with high photoluminescence quantum yields ( $\Phi_{PL} > 80\%$ ) and radiative rate constants ( $k_r \sim 7.8 \times 10^5 \text{ s}^{-1}$ ). The luminescence is solvatochromic, undergoing a red-shift in a polar solvent (CH<sub>2</sub>Cl<sub>2</sub>) at room temperature that are accompanied by a decrease in quantum yields ( $\Phi_{PL} < 23\%$ ) and radiative rate constants ( $k_r < 4.0 \times 10^4 \text{ s}^{-1}$ ), whereas the non-radiative rate constants remain nearly constant ( $k_{nr} \sim 1.0 \times 10^5 \text{ s}^{-1}$ ). The radiative rate is controlled via thermally assisted delayed fluorescence (TADF) and temperature-dependent luminescence studies of the gold complex (**Au<sup>BZI</sup>**) in methylcyclohexane solution reveal an energy difference between the lowest singlet and triplet excited states of 920 cm<sup>-1</sup>. An organic light-emitting diode (OLED) fabricated using **Au<sup>BZI</sup>** as a luminescent dopant has an external quantum efficiency of 12% and narrow, deep-blue emission (CIE = 0.16, 0.06).

**Keywords:** OLED, TADF, high efficiency, deep blue, copper, silver, gold, short lifetime

## INTRODUCTION

Highly luminescent, neutral two-coordinate, linear d<sup>10</sup> metal complexes of coinage metals i.e., Cu(I), Ag(I), Au(I) have recently been reported (Di et al., 2017; Romanov et al., 2018, 2019; Hamze et al., 2019a,b; Shi et al., 2019). These complexes have redox active carbene (acceptor) and amide (donor) ligands connected by a metal in a linear fashion i.e., (carbene)M<sup>(I)</sup>(amide). Their photoluminescence efficiencies are close to 100% in solution and in thin films, with phosphorescent lifetimes in the range of 1–3  $\mu\text{s}$ . These (carbene)M<sup>(I)</sup>(amide) complexes emit from an amide-N (donor) to carbene-C (acceptor) intramolecular charge transfer (ICT) state, a transition also referred to as ligand-to-ligand charge transfer (LLCT). Because of their excellent photophysical properties, these complexes are potential candidates for application in photocatalysis (Kalyanasundaram, 1982), chemo- and biosensing (Keefe et al., 2000; Lo et al., 2010), dye-sensitized solar cells (Grätzel, 2005) and organic electronics (Lamansky et al., 2001). In particular, their fast

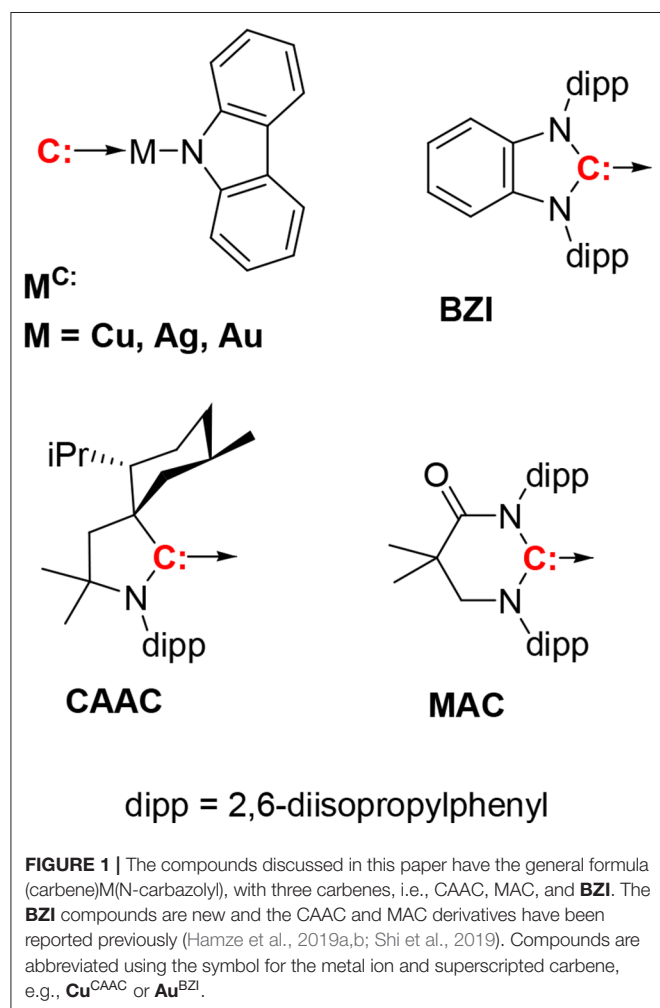
radiative lifetimes make them promising candidates as dopants in organic light emitting diodes (OLEDs) (Di et al., 2017; Romanov et al., 2018, 2019; Hamze et al., 2019a,b; Shi et al., 2019). Unlike phosphors like iridium and platinum complexes, which rely on strong spin-orbit coupling (SOC) to induce what is principally triplet metal ligand charge transfer ( $^3\text{MLCT}$ ) emission (Yersin et al., 2011), the two-coordinate coinage metal complexes emit via E-type fluorescence or thermally activated delayed fluorescence (TADF). Their fast radiative lifetimes are due to two factors; the small energy separation between their lowest singlet and triplet excited states ( $\Delta E_{\text{ST}}$ ) and spin orbit coupling via the metal ion. Together these two parameters lead to rapid endothermic intersystem crossing from the long-lived triplet to the faster radiating singlet state. Recent work has shown that  $\Delta E_{\text{ST}}$  in these complexes is dependent on the identity of the metal atom. The copper and gold complexes have similar values for  $\Delta E_{\text{ST}}$ , whereas the  $\Delta E_{\text{ST}}$  for the silver complexes is smaller (Romanov et al., 2018; Hamze et al., 2019b). The small  $\Delta E_{\text{ST}}$  in the silver analogs leads to extremely fast radiative rate constants ( $k_r > 10^6 \text{ s}^{-1}$ ), faster than the Ir and Pt phosphorescent emitters. The emission energy of complexes,

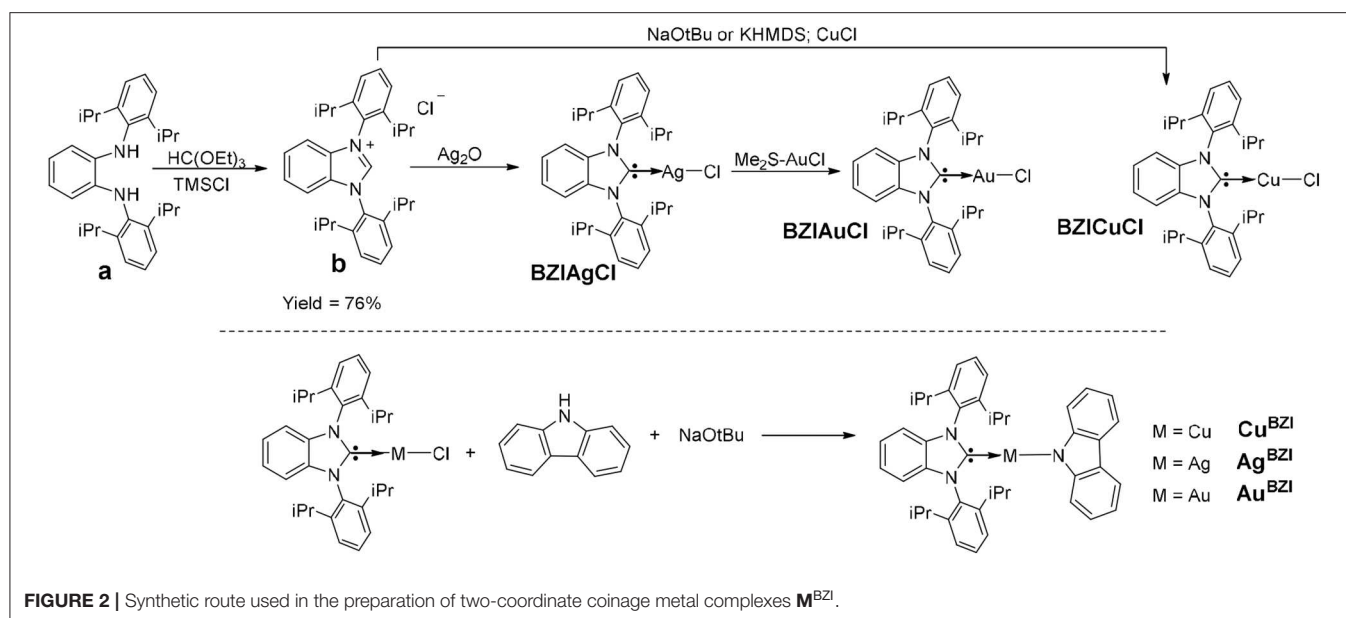
although nearly independent of the metal, can be altered using different carbenes with varying electrophilicity or amides with different nucleophilicity, allowing the luminescence color to be varied from deep blue to deep red (Hamze et al., 2019a; Shi et al., 2019). Developing alternative blue dopants is crucial in tackling the long-standing problem of stability in blue OLEDs. Complexes based on the CAAC ligand ( $\text{M}^{\text{CAAC}}$ , **Figure 1**) are reported to have efficient blue photoluminescence and give good efficiencies as dopants in OLEDs (Hamze et al., 2019a). Unfortunately, the emission spectra of these complexes are broad, which is not ideal for display applications. Additionally, the ability to vary the physical and electronic properties of CAAC ligands is limited and therefore inconvenient for modifying the characteristics needed for OLEDs. Complexes based on the MAC ligand ( $\text{M}^{\text{MAC}}$ ) can be used to fabricate high efficiency OLEDs; however, emission in these derivatives is bathochromically shifted to green owing to the electrophilic MAC ligand (Hamze et al., 2019b). Substitution of the carbazole ligand with cyano groups was therefore used to stabilize the HOMO and blue-shift the emission (Shi et al., 2019). Alternatively, carbenes based on benzimidazoles (BZI), originally used in luminescent two-coordinate Au complexes (Wang et al., 1999), lead to metal complexes with LUMO energies similar to CAAC (Krylova et al., 2014; Hamze et al., 2017, 2020), suggesting that replacing CAAC with benzimidazolyl-carbene ligands should give similar photophysical and electrochemical properties as  $\text{M}^{\text{CAAC}}$ . Herein, we examine monovalent, linear, 2-coordinate coinage metal (i.e.,  $\text{M} = \text{Cu, Ag, Au}$ ) complexes ( $\text{M}^{\text{BZI}}$ ) bearing a sterically bulky benzimidazolyl carbene, 1,3-bis(2,6-diisopropylphenyl)-1-H-benzo[d]imidazol-2-ylidene (**BZI**), and carbazolidine (Cz) as the anionic ligand. We have investigated the structural and photophysical properties of the  $\text{M}^{\text{BZI}}$  derivatives to elucidate the role of the carbene and the metal ion in the excited-state properties. The  $\text{M}^{\text{BZI}}$  complexes have structures, redox potentials and photoluminescent efficiencies ( $\Phi_{\text{PL}} = 0.8\text{--}1.0$ ) similar to the  $\text{M}^{\text{CAAC}}$  analogs, but different excited-state dynamics. Analysis of the luminescence at low temperature reveals that the triplet carbazole ( $^3\text{Cz}$ ) state and the singlet/triplet intramolecular charge transfer ( $^1/^3\text{ICT}$ ) manifold of the  $\text{M}^{\text{BZI}}$  complexes are near degenerate, resulting in photophysical properties that are distinct from the  $\text{M}^{\text{CAAC}}$  complexes. The  $\text{Au}^{\text{BZI}}$  complex has also been successfully employed a dopant to fabricate efficient blue OLEDs.

## RESULTS AND DISCUSSION

### Synthesis

The synthesis of  $\text{M}^{\text{BZI}}$  complexes is depicted in **Figure 2**. Cyclization of the dianiline derivative (**a**) to the benzimidazolium salt is reported to be extremely challenging, due to steric bulk imposed by the isopropyl groups, with a reaction yield of only 16% (Grieco et al., 2015). We modified the literature procedure, using excess triethyl orthoformate  $[\text{HC}(\text{OEt})_3]$  and distilling the excess off during the reaction, which increases the yield of the reaction to 76%. Similar to  $\text{M}^{\text{CAAC}}$  and  $\text{M}^{\text{MAC}}$  complexes, the synthesis of  $\text{M}^{\text{BZI}}$  complexes starts with addition of  $\text{Ag}_2\text{O}$  to the benzimidazolium salt or  $\text{CuCl}$  to BZI carbene generated *in situ* with base to form





the respective benzoimidazole silver(I) or copper(I) chloride complexes. The isolated BZIAgCl is transmetalated with  $(Me_2S)AuCl$  to form the BZIAuCl complex. Reaction of the chloride complexes with carbazole in the presence of NaOtBu forms the  $M^{BZI}$  complexes in good yields (70–85%).

### X-Ray Analysis

The structures were determined for  $Cu^{BZI}$ ,  $Ag^{BZI}$ , and  $Au^{BZI}$  by single crystal X-ray diffraction (details can be found in the **Supporting Information** and the datasets generated for this study can be found in the Cambridge Crystallographic Data Center, <https://www.ccdc.cam.ac.uk/structures/>, under the identifiers  $Cu^{BZI}$ : 1984269,  $Ag^{BZI}$ : 1984268 and  $Au^{BZI}$ : 1984267).  $Cu^{BZI}$  and  $Au^{BZI}$  show only a single conformer, with bond distances and interligand torsion angles similar to our previously reported linear coinage metal complexes (summarized in the Supporting Information) (Di et al., 2017; Romanov et al., 2018, 2019; Hamze et al., 2019a,b; Shi et al., 2019). In contrast, the unit cell for the  $Ag^{BZI}$  complex contains two conformers (**Figure 3**). The first, like its copper and gold analogs, has a coplanar conformation of its carbene and amide ligands (dihedral angle =  $0^\circ$ ), whereas the second displays an orthogonal conformation (dihedral angle =  $95^\circ$ ). The  $C_{carbene} \cdots N_{Cz}$  distances of  $M^{BZI}$  fall in the order Cu ( $\sim 3.73$  Å) < Au ( $\sim 4.00$  Å) < Ag ( $\sim 4.11$  Å). The C–M–N bond angles are all close to  $180^\circ$  (range =  $174$ – $180^\circ$ ).

### Electrochemistry

The electrochemical properties of the complexes were determined using cyclic voltammetry (CV) and differential pulse voltammetry (DPV). The copper and the silver complexes show irreversible reduction, whereas the gold analog shows a quasi-reversible reduction (see section Supporting Information). The reduction potentials for the  $M^{BZI}$  series are identical ( $E_{red} = -2.84 \pm 0.02$  V) and greater (more negative) than those of  $M^{CAAC}$  ( $E_{red} = -2.78 \pm 0.06$  V) and  $M^{MAC}$  ( $E_{red} =$

$-2.45 \pm 0.06$  V) complexes. The reduction potentials of  $M^{BZI}$  relative to their  $M^{CAAC}$  and  $M^{MAC}$  analogs indicates that the electrophilicity of the coordinated BZI carbene is lower than the CAAC and MAC ligands in similar complexes. All the complexes undergo irreversible oxidation (**Table 1**) and, unlike the  $M^{CAAC}$  and  $M^{MAC}$  complexes where the oxidation potential is the same across the series, the potential of the  $M^{BZI}$  complexes increases from Cu ( $E_{ox} = 0.11 \pm 0.06$  V) to Au ( $E_{ox} = 0.32 \pm 0.06$  V), suggesting participation of the metal in the oxidation process. Thus, values for the redox gap ( $\Delta E_{redox}$ ) are greater for the silver and gold complexes than the copper analog.

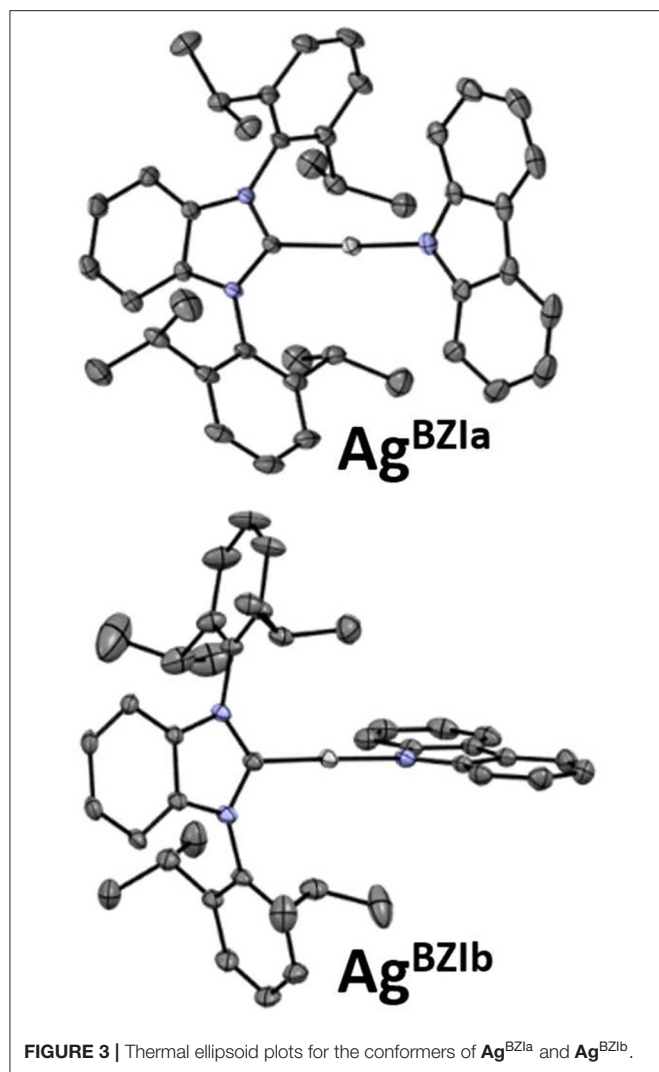
### Computational Analysis

The structure calculated using density function theory (DFT) for the ground state of  $Au^{BZI}$  is shown in **Figure 4**. The HOMO density is localized largely on the carbazolidine (Cz) ligand, whereas the LUMO is primarily confined to the carbene ligand, with smaller contributions from the metal d-orbitals to both MOs. Time dependent DFT (TD-DFT) calculations find that  ${}^3Cz$  is the lowest-energy state and lies  $<0.09$  eV below the manifold of the  ${}^{1/3}ICT$  states (**Table S8**). Additionally, the oscillator strength calculated for the silver complex is weaker than that of its Cu and Au analogs (**Table S8**), consistent with the lower molar absorptivity observed for the ICT transition in the absorption spectra of the silver complex (see below). Large molecular dipole moments calculated for the ground state are directed along the metal-ligand bond axis toward the carbazolidine ligand ( $\mu_{calc} \approx -12.5$  debye), whereas the moments for the excited  ${}^1ICT$  state is comparable in magnitude but directed toward the BZI ligand ( $\mu_{calc} \approx 13.5$  debye).

### Photophysical Characterization

Absorption spectra of the  $M^{BZI}$  complexes in polar (2-methyltetrahydrofuran, 2-MeTHF) and nonpolar (methylcyclohexane, MeCy) solvents are shown in **Figure 5**.





Absorption bands between 300 and 375 nm of **M<sup>BZI</sup>** are assigned to  $\pi$ - $\pi^*$  transitions localized on the carbazolyl ligand (Hamze et al., 2019a,b; Shi et al., 2019). The band at lower energy (>375 nm) is assigned to an intramolecular ligand-to-ligand charge transfer (ICT/LLCT) transition from Cz to **BZI**. The energy of the ICT band of **M<sup>BZI</sup>** is higher than in the **M<sup>CAAC</sup>** and **M<sup>MAC</sup>** complexes, consistent with the order of reduction potentials in these complexes. The ICT band extends to 410 nm in MeCy and has two features separated by 1100  $\text{cm}^{-1}$  indicative of vibronic coupling. Similar to **M<sup>CAAC</sup>** and **M<sup>MAC</sup>** complexes, the ICT band of the **M<sup>BZI</sup>** complexes displays negative solvatochromism and merges into the higher lying ligand  $\pi$ - $\pi^*$  transitions in polar solvents. These shifts with solvent polarity are due to the large change in the molecular dipole moments between the ground and excited ICT states. The molar absorptivities of the **M<sup>BZI</sup>** complexes decrease in the order  $\text{Au} > \text{Cu} > \text{Ag}$  in all media. The same trend was observed in the **M<sup>CAAC</sup>** and **M<sup>MAC</sup>** analogs and attributed to a decrease in the overlap integrals between orbitals on the donor Cz and acceptor ligands mediated by the metal center (Hamze et al., 2019b).

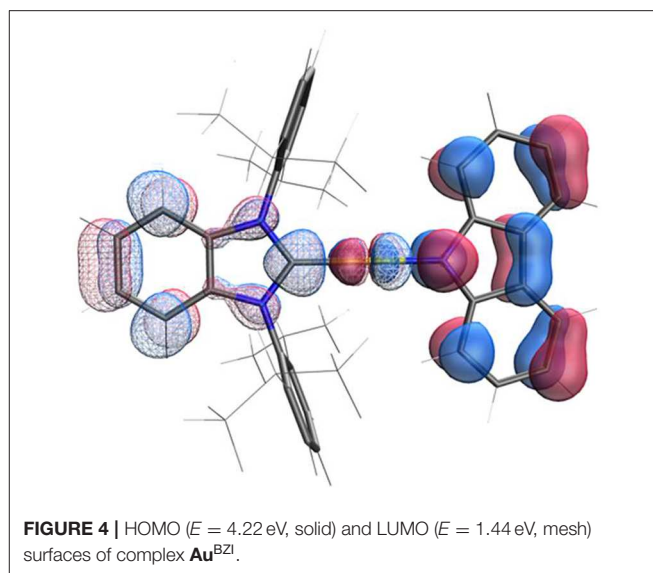


**TABLE 1** | Redox potentials of complexes **M<sup>BZI</sup>** and the associated experimental frontier orbital energies.

Complex	$E_{\text{ox}}$ (V)	$E_{\text{red}}$ (V)	$\Delta E_{\text{redox}}$ (V)	$E_{\text{HOMO}}$ (eV)	$E_{\text{LUMO}}$ (eV)
<b>Cu<sup>BZI</sup></b>	0.113	-2.85	2.96	-4.92	-1.47
<b>Ag<sup>BZI</sup></b>	0.284	-2.84	3.12	-5.12	-1.48
<b>Au<sup>BZI</sup></b>	0.318	-2.82	3.14	-5.16	-1.51

Electrochemical studies performed in acetonitrile with tetrabutylammonium hexafluorophosphate (TBAF) as the electrolyte and referenced to  $\text{Fc}^+/\text{Fc}$ . The redox values were obtained using DPV and converted to HOMO/LUMO energies using the equations in Sworakowski et al. (2016).

Emission spectra of the **M<sup>BZI</sup>** compounds in MeCy, 2-MeTHF solution and polystyrene (PS) films at room temperature and 77 K are shown in **Figure 5** and tabulated in **Table 2**. The spectra from the **M<sup>BZI</sup>** complexes are blue-shifted relative to their **M<sup>CAAC</sup>** and **M<sup>MAC</sup>** counterparts, yet display similar solvatochromic behavior, undergoing red shifts in polar solvents. Spectra recorded in MeCy are relatively narrow ( $\text{FWHM} = 44$  nm,  $2,300$   $\text{cm}^{-1}$ ) and show underlying vibronic features. The photoluminescence quantum yields ( $\Phi_{\text{PL}}$ ) of **M<sup>BZI</sup>** complexes are close to unity in MeCy and PS films but decrease with increasing solvent polarity (**Table 2**). Furthermore, increasing solvent polarity is correlated with increased spectral width and loss of the vibronic features, suggesting structural distortion in the excited states. To explain the blue-shift in absorption spectra and red-shift in emission spectra observed in these complexes with increasing solvent polarity, a diagram representing the potential energy surfaces for the ground state ( $S_0$ ) and excited states ( $^3\text{Cz}$  and  $^1,^3\text{ICT}$ ) as a function of nuclear coordinates in MeCy and  $\text{CH}_2\text{Cl}_2$  is proposed (**Figure 6**). The vibronically structured absorption and emission spectra in nonpolar solvents (MeCy) indicate that the potential energy surfaces are well-nested, such that ICT transitions are induced with small reorganization energies. In

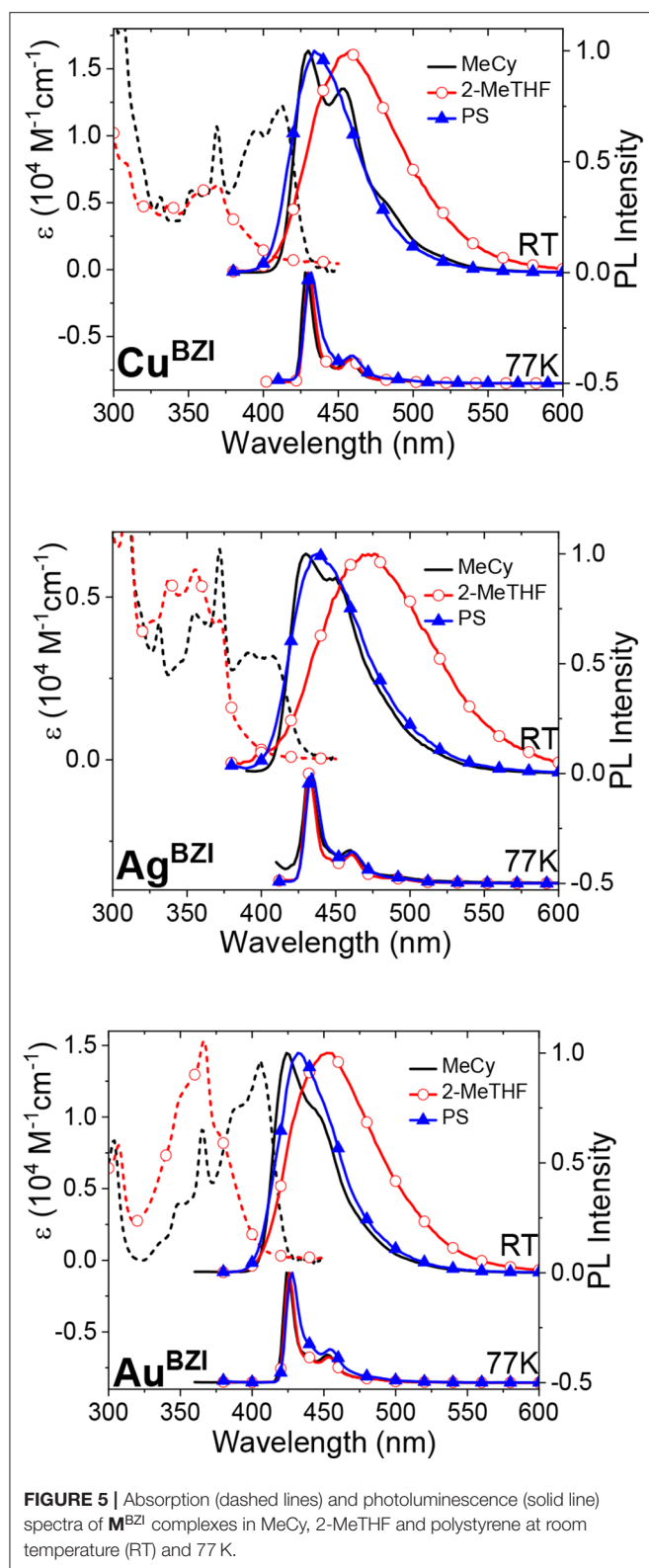


**FIGURE 5 |** Absorption (dashed lines) and photoluminescence (solid line) spectra of  $M^{BZI}$  complexes in MeCy, 2-MeTHF and polystyrene at room temperature (RT) and 77 K.

contrast, the blue-shifted absorption and broad, featureless red-shifted emission observed in polar solvents ( $CH_2Cl_2$ ) indicate that significant reorganization occurs within the metal complex

**TABLE 2 |** Luminescence properties of complexes  $M^{BZI}$  in various media.

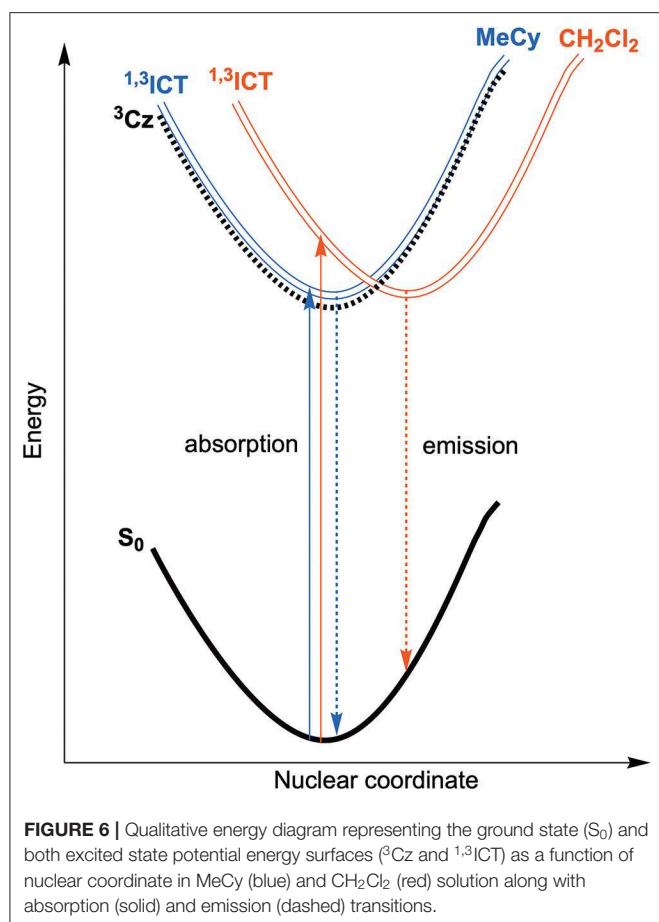
Complex	$\lambda_{max}$ (nm)	$\Phi_{PL}$	$\tau$ ( $\mu s$ )	$k_r$ ( $10^5 s^{-1}$ )	$k_{nr}$ ( $10^5 s^{-1}$ )	$\lambda_{max, 77K}$ (nm)	$\tau_{77K}$ ( $\mu s$ )
<b>Cu<sup>BZI</sup></b>	MeCy	0.80	1.23	6.50	1.63	428	6300
	Toluene	0.75	1.50	5.0	1.7	—	—
	2-MeTHF	0.35	2.06	1.7	3.2	430	11000
	$CH_2Cl_2$	0.03	1.24	0.24	7.8	—	—
	PS film	0.86	0.97 (36%); 4.8 (64%)	2.5 <sup>a</sup>	0.41 <sup>a</sup>	432	3000
<b>Ag<sup>BZI</sup></b>	MeCy	0.58	1.04	5.6	4.4	432	18000
	Toluene	0.50	3.27	1.5	1.5	—	—
	2-MeTHF	0.19	5.66	0.34	1.4	432	20000
	$CH_2Cl_2$	0.03	1.64	0.18	5.9	—	—
	PS film	0.85	0.69 (26%); 5.1 (74%)	2.2 <sup>a</sup>	0.38 <sup>a</sup>	434	6600
<b>Au<sup>BZI</sup></b>	MeCy	0.89	1.15	7.8	0.9	424	340
	Toluene	0.94	1.11	8.5	5.4	—	—
	2-MeTHF	0.79	2.63	3.0	0.8	426	640
	$CH_2Cl_2$	0.23	5.79	0.40	1.3	—	—
	PS film	1.0	0.74 (46%); 3.6 (54%)	4.4 <sup>a</sup>	< 0.04 <sup>a</sup>	428	190

<sup>a</sup>Calculated from the weighted averages of both contributions.

and its surrounding media (to a larger extent) as a result of the large change in dipole moment upon excitation ( $\Delta\mu_{calc} > 24$  debye). Unlike  $M^{CAAC}$  and  $M^{MAC}$  complexes, where the radiative rate constant ( $k_r$ ) is fastest for the silver analog (Romanov et al., 2018; Hamze et al., 2019b),  $Au^{BZI}$  has the fastest  $k_r$  in accord with gold having the largest SOC constant.

The biexponential character of the emission decay in PS thin films could be due to the presence of  $M^{BZI}$  complexes in different conformations, one where the carbene and carbazole are in a coplanar orientation and another where the two ligands are twisted relative to each other. In our previous studies of (CAAC)Cu(carbazole) complexes we found that while the two forms display similar emission spectra the twisted form has a markedly longer excited state lifetime and lower oscillator strength than the coplanar form (Hamze et al., 2019a). In solution the excited  $M^{BZI}$  can effectively rotate to the coplanar form prior to relaxing to the ground state. However, the rigid PS matrix will prevent the conformers from equilibrating in the excited state and thus they are expected to emit independently with different individual emission lifetimes.

The emission spectra display a pronounced rigidochromic shift upon cooling to 77 K and become extremely narrow and vibronically structured, with luminescence lifetimes in the millisecond regime. Thus, emission at low temperatures is consistent with a triplet transition localized on the carbazolid



ligand ( $^3Cz$ ). This change in emission properties with temperature is attributed to the close energy separation between the  $^3Cz$  and  $^{1,3}ICT$  manifolds, making the ICT manifold thermally accessible at room temperature, but inaccessible in frozen MeCy and 2-MeTHF at 77 K. The fact that the  $M^{BZI}$  complexes display  $^3Cz$  emission in PS (as well as MeCy and 2-MeTHF) at 77 K is different from the behavior observed in  $M^{CAAC}$  and  $M^{MAC}$  complexes. Emission from the latter complexes remains broad and featureless in a polystyrene matrix at all temperatures, even down to 4 K (Hamze et al., 2019b). Thus, in the case of the  $M^{CAAC}$  and  $M^{MAC}$  complexes, the  $^3ICT$  state lies below the energy of the  $^3Cz$  state in PS at all temperatures (Hamze et al., 2019b). However, for the  $M^{BZI}$  complexes in PS films, it is evident that the lowest excited triplet state is indeed  $^3Cz$  at all temperatures. This difference suggests that the  $^3Cz$  and  $^3ICT$  states in the  $M^{BZI}$  complexes are near degenerate in energy, and TADF emission occurs via thermal activation from the  $^3Cz$  to  $^1ICT$  states, not just within the ICT manifold as in the case of the  $M^{CAAC}$  and  $M^{MAC}$  complexes.

Another difference in the properties of the  $M^{BZI}$  complexes compared to the  $M^{CAAC}$  and  $M^{MAC}$  analogs is the pronounced decrease in luminescence efficiency with increasing solvent polarity. For example, the quantum yield of  $Cu^{BZI}$  is severely diminished in  $CH_2Cl_2$  relative to that recorded in MeCy ( $\Phi_{PL}$  =

0.03 in the former and 0.80 in the latter), whereas this decrease in efficiency is less pronounced for  $Cu^{CAAC}$  ( $\Phi_{PL}$  = 0.4 in  $CH_2Cl_2$  and 0.92 in MeCy) and  $Cu^{MAC}$  ( $\Phi_{PL}$  = 0.5 in  $CH_2Cl_2$  and 0.90 in MeCy). To better understand the origin of this decrease in  $\Phi_{PL}$  with solvent polarity, photophysical properties of  $Au^{BZI}$  were characterized in mixtures of MeCy and  $CH_2Cl_2$  at various ratios. The ICT band in the absorption spectra gradually blue shifts with increasing  $CH_2Cl_2$  concentration and the vibronic fine structure observed in MeCy disappears in mixtures with  $\geq 5$  vol%  $CH_2Cl_2$  (Figure 7A and Figure S6). Figure 7B shows that the radiative rate constant of  $Au^{BZI}$  decreases with increasing solvent polarity, whereas the non-radiative rate constant ( $k_{nr}$ ) remains near constant, consequently decreasing the  $\Phi_{PL}$ . The fact that the non-radiative rate constant of  $Au^{BZI}$  is largely independent of  $CH_2Cl_2$  concentration, despite the similar reduction potentials for the  $Au^{BZI}$  excited state ( $E^{0/+*}$  = -2.67 V) and  $CH_2Cl_2$  ( $E^{0/-}$  = -2.73 V), indicates that there is no oxidative quenching of excited  $Au^{BZI}$  by  $CH_2Cl_2$ . Therefore, the lower  $\Phi_{PL}$  of  $Au^{BZI}$  in  $CH_2Cl_2$  comes about from a decrease in the radiative rate constant. This change is likely due to a decrease in the Franck-Condon factors for the ICT transition caused by the shift of the excited state surface in the polar solvent, as illustrated in Figure 6.

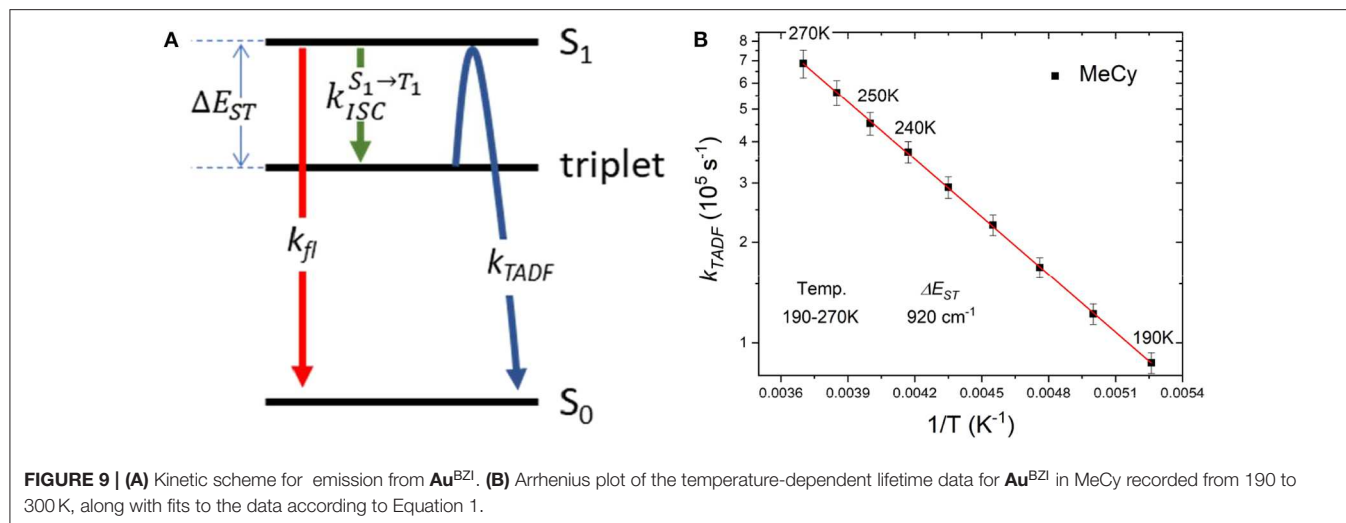
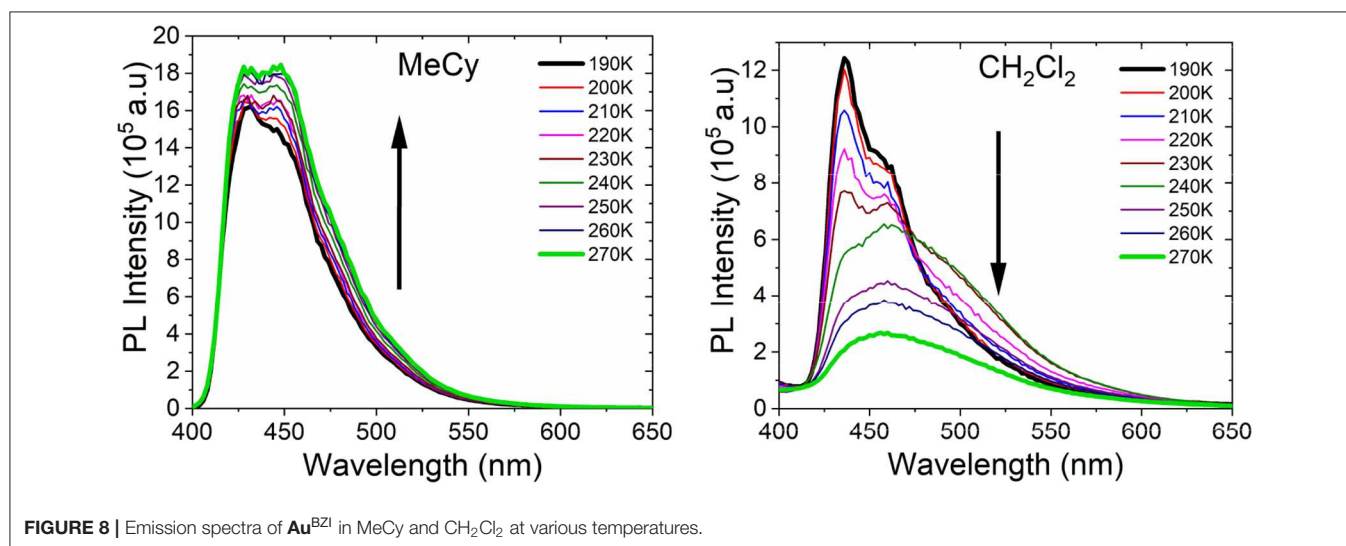
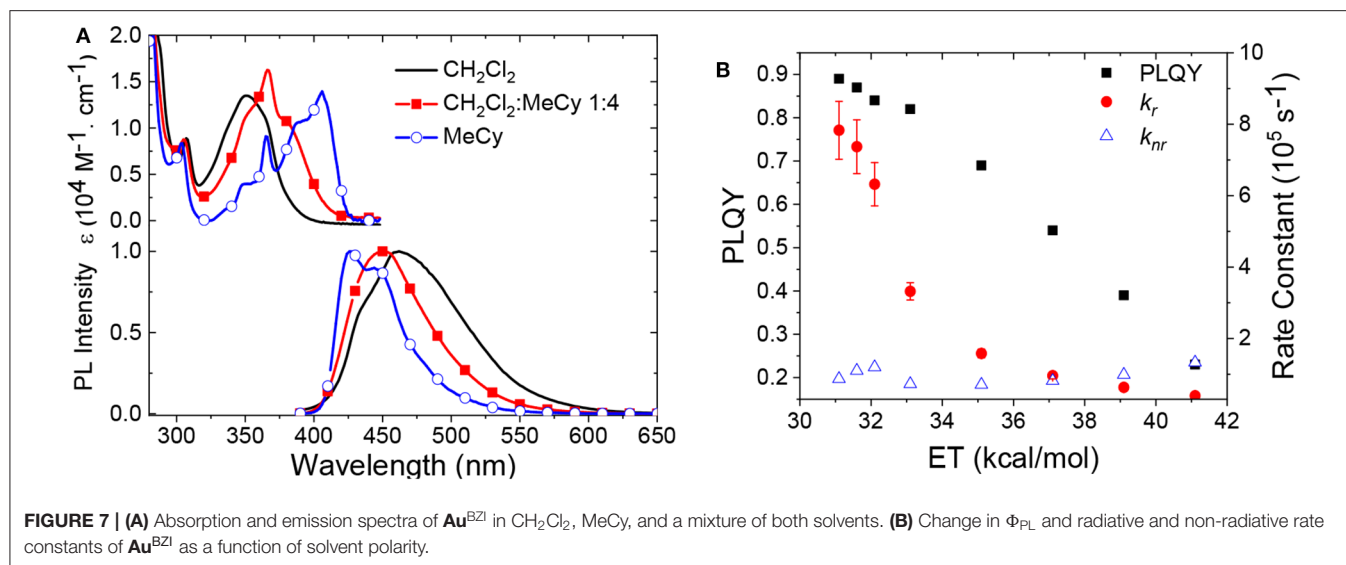
Emission studies of  $Au^{BZI}$  at variable temperature were conducted in MeCy and  $CH_2Cl_2$  to investigate the parameters controlling TADF (Figure 8). Emission in MeCy slightly increases in intensity and displays limited changes in line shape with increasing temperature. In contrast, spectra recorded in  $CH_2Cl_2$  reveal a drop in intensity with increasing temperature. Vibronic features resolved at low temperatures (190–230 K) are found to broaden abruptly at 240 K. The  $k_f$ -values calculated from the quantum yields measured at various temperatures (see Supplementary Information) were fit to a two level model using Equation 1 (Figure 9A) (Hamze et al., 2019b).

$$\ln(k_{TADF}) = \ln\left(\frac{k_{ISC}^{S_1 \rightarrow T_1}}{3} \left(1 - \frac{k_{ISC}^{S_1 \rightarrow T_1}}{k_{fl} + k_{ISC}^{S_1 \rightarrow T_1}}\right)\right) - \frac{\Delta E_{ST}}{k_B T} \quad (1)$$

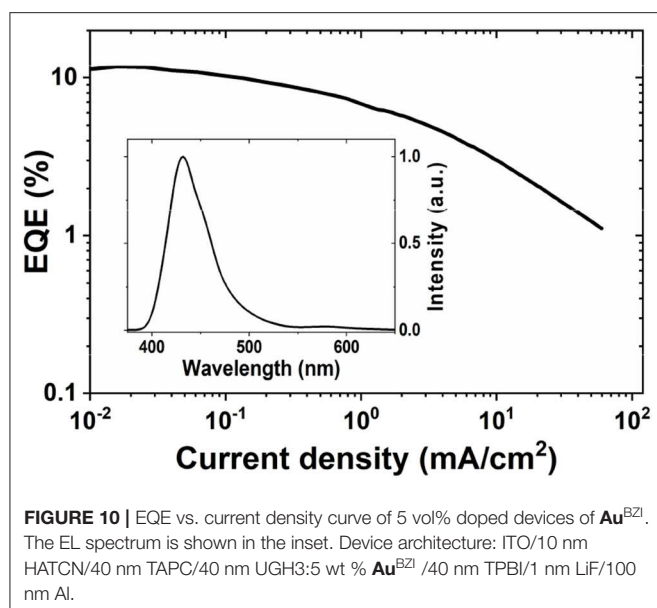
Where,  $k_B$  is the Boltzmann constant,  $k_{TADF}$  and  $k_{fl}$  are the radiative rate constants of the TADF and fluorescence, respectively and  $k_{ISC}^{S_1 \rightarrow T_1}$  is the intersystem crossing rate (see Figure 9A). The best fit to the MeCy data (Figure 9B) give an energy difference between the triplet and emitting singlet state of  $Au^{BZI}$  of  $920 \text{ cm}^{-1}$ . However, the Arrhenius plot of the radiative rate constant of  $Au^{BZI}$  recorded in  $CH_2Cl_2$  at variable temperature is decidedly non-linear (Figure S10). Variable temperature NMR spectra indicate that an aquo species is formed with residual water below 240 K (Figure S11). The formation of this aquo complex likely leads to the anomalous behavior observed in  $CH_2Cl_2$  at lower temperatures, making the analysis using the simple two-level model problematic.

## OLED Characterization

The  $Au^{BZI}$  complex is stable to sublimation and was thus used as dopant to fabricate OLEDs by thermal evaporation. Device optimization and details are shown in







the **Supplementary Information**. Considering the high triplet energy of  $\text{Au}^{\text{BZI}}$  ( $E_{\text{T}} = 3.1$  eV), 1,3-bis(triphenylsilyl)benzene (UGH3,  $E_{\text{T}} = 3.5$  eV) was employed as the host matrix. Devices were fabricated using different doping levels (5, 10 and 15 wt%) and the best performance was obtained with 5 wt%  $\text{Au}^{\text{BZI}}$  (see **Supplementary Information**). Optimized devices achieved reasonably high efficiencies (maximum EQE = 12%, **Figure 10**) and electroluminescence (EL) spectra ( $\lambda_{\text{max}} = 430$  nm, FWHM = 45 nm) identical to the PL spectrum in PS, demonstrating efficient exciton confinement on the complex. The color coordinates of the EL spectrum (CIE = 0.16, 0.06) make  $\text{Au}^{\text{BZI}}$  an efficient *deep blue* dopant for phosphorescent OLEDs.

## CONCLUSION

A series of 2-coordinate coinage metal (i.e., M = Cu, Ag, Au) complexes bearing a sterically bulky benzimidazolyl-carbene, 1,3-bis(2,6-diisopropylphenyl)-1-H-benzo[d]imidazol-2-ylidene (BZI), and carbazolide (Cz) as the anionic ligand were investigated. X-ray analysis reveals a linear geometry at the metal center with the ligands in a coplanar conformation, as well as orthogonal for  $\text{Ag}^{\text{BZI}}$ . The redox gap of all the complexes is large ( $\Delta E_{\text{redox}} > 3$  V), in agreement with the high-energy absorption band ( $> 400$  nm in  $\text{CH}_2\text{Cl}_2$ ) corresponding to the carbazolide-to-carbene ICT transition. The complexes have high luminescence efficiencies ( $\Phi_{\text{PL}} > 80\%$ ) and display deep blue narrow emission in MeCy and PS films. Their absorption spectra display negative solvatochromism, whereas their emission spectra undergo bathochromic shifts in polar solvents that is accompanied by decrease in quantum yields ( $\Phi_{\text{PL}} < 23\%$ ) and radiative rate constants ( $k_{\text{r}} < 4.0 \times 10^4 \text{ s}^{-1}$ ). The non-radiative rate constants, however, are unaffected by the medium, remaining nearly the same in polar and

nonpolar media ( $k_{\text{nr}} \sim 1 \times 10^5 \text{ s}^{-1}$ ). Temperature-dependent studies reveal that the energy difference between the singlet and triplet excited states in methylcyclohexane is  $920 \text{ cm}^{-1}$ . Vapor-deposited OLEDs fabricated using  $\text{Au}^{\text{BZI}}$  as an emissive dopant have high efficiency (EQE = 12%) and a narrow and deep blue emission (CIE = 0.16, 0.06). These two-coordinate complexes present new opportunities for use as dopants in blue OLEDs. Lifetime studies on devices will need to be carried out to determine if these coinage metal-based emitters could serve as alternatives to state-of-the-art Ir(III) complexes commonly used in OLEDs.

## SUPPORTING INFORMATION

Synthesis of precursors and complexes, differential pulse voltammetry, cyclic voltammetry curves, photophysical data of the final complexes in various solvents, computational data and x-ray crystallographic data of the final complexes, OLED device fabrication procedure and device characteristics,  $^1\text{H}$  and  $^{13}\text{C}$  NMR of precursors and final complexes.

## DATA AVAILABILITY STATEMENT

The datasets generated for this study can be found in the Cambridge Crystallographic Data Center (<https://www.ccdc.cam.ac.uk/structures/>) under the identifiers CuBZI: 1984269, AgBZI: 1984268, and AuBZI: 1984267.

## AUTHOR CONTRIBUTIONS

RHam synthesized and measured the photophysical properties of the copper, silver, and gold compounds. MI measured and analyzed the temperature dependent photophysical properties of the gold complex. DM carried out the theoretical modeling. MJ prepared and characterized the OLEDs. RHai determined all of the crystal structures. RHam, PD, and MT conceived of the project. MI, PD, and MT wrote the manuscript.

## FUNDING

This work was supported solely by the Universal Display Corporation. No funds have been received from Universal Displays, our institution or any other source to cover publication fees or open access fees.

## ACKNOWLEDGMENTS

The authors wish to thank the Universal Display Corporation for their support of this work.

## SUPPLEMENTARY MATERIAL

The Supplementary Material for this article can be found online at: <https://www.frontiersin.org/articles/10.3389/fchem.2020.00401/full#supplementary-material>

## REFERENCES

- Di, D., Romanov, A. S., Yang, L., Richter, J. M., Rivett, J. P. H., Jones, S., et al. (2017). High-performance light-emitting diodes based on carbene-metal-amides. *Science* 356:159. doi: 10.1126/science.aah4345
- Grätzel, M. (2005). Solar energy conversion by dye-sensitized photovoltaic cells. *Inorganic Chem.* 44, 6841–6851. doi: 10.1021/ic0508371
- Grieco, G., Blacque, O., and Berke, H. (2015). A facile synthetic route to benzimidazolium salts bearing bulky aromatic N-substituents. *Beilstein J. Organ. Chem.* 11, 1656–1666. doi: 10.3762/bjoc.11.182
- Hamze, R., Kapper, S. C., Ravinson, D. S. M., Haiges, R., Djurovich, P. I., Thompson, M. E. (2020). Molecular dynamics of four-coordinate carbene-Cu(I) complexes employing tris(pyrazolyl)borate ligands. *Polyhedron*. 180:114381. doi: 10.1016/j.poly.2020.114381
- Hamze, R., Jazsar, R., Soleilhavoup, M., Djurovich, P. I., Bertrand, G., and Thompson, M. E. (2017). Phosphorescent 2-, 3- and 4-Coordinate Cyclic (Alkyl)(Amino)Carbene (Caac) Cu(I) Complexes. *Chem. Commun.* 53, 9008–9011. doi: 10.1039/C7CC02638B
- Hamze, R., Peltier, J. L., Sylvinson, D., Jung, M., Cardenas, J., Haiges, R., et al. (2019a). Eliminating Nonradiative Decay in Cu(I) Emitters: >99% quantum efficiency and microsecond lifetime. *Science* 363:601. doi: 10.1126/science.aav2865
- Hamze, R., Shi, S., Kapper, S. C., Muthiah Ravinson, D. S., Estergreen, L., Jung, M.-C., et al. (2019b). “Quick-Silver” from a systematic study of highly luminescent, two-coordinate, D10 coinage metal complexes. *J. Am. Chem. Soc.* 141, 8616–8626. doi: 10.1021/jacs.9b03657
- Kalyanasundaram, K. (1982). Photophysics, photochemistry and solar energy conversion with Tris(Bipyridyl)Ruthenium(II) and its analogues. *Coord. Chem. Rev.* 46, 159–244. doi: 10.1016/0010-8545(82)85003-0
- Keefe, M. H., Benkstein, K. D., and Hupp, J. T. (2000). Luminescent sensor molecules based on coordinated metals: a review of recent developments. *Coord. Chem. Rev.* 205, 201–228. doi: 10.1016/S0010-8545(00)00240-X
- Krylova, V. A., Djurovich, P. I., Conley, B. L., Haiges, R., Whited, M. T., Williams, T. J., et al. (2014). Control of emission colour with N-heterocyclic carbene (Nhc) ligands in phosphorescent three-coordinate Cu(I) Complexes. *Chem. Commun.* 50, 7176–7179. doi: 10.1039/C4CC02037E
- Lamansky, S., Djurovich, P., Murphy, D., Abdel-Razzaq, F., Lee, H.-E., Adachi, C., et al. (2001). Highly phosphorescent bis-cyclometalated iridium complexes: synthesis, photophysical characterization, and use in organic light emitting diodes. *J. Am. Chem. Soc.* 123, 4304–4312. doi: 10.1021/ja003693s
- Lo, K. K.-W., Louie, M.-W., and Zhang, K. Y. (2010). Design of Luminescent Iridium(III) and Rhenium(I) polypyridine complexes as *in vitro* and *in vivo* ion, molecular and biological probes. *Coord. Chem. Rev.* 254, 2603–2622. doi: 10.1016/j.ccr.2010.01.014
- Romanov, A. S., Jones, S. T. E., Yang, L., Conaghan, P. J., Di, D., Linnolahti, M., et al. (2018). Mononuclear silver complexes for efficient solution and vacuum-processed oleds. *Adv. Opt. Mater.* 6:1801347. doi: 10.1002/adom.201801347
- Romanov, A. S., Yang, L., Jones, S. T. E., Di, D., Morley, O. J., Drummond, B. H., et al. (2019). Dendritic carbene metal carbazole complexes as photoemitters for fully solution-processed oleds. *Chem. Mater.* 31, 3613–3623. doi: 10.1021/acs.chemmater.8b05112
- Shi, S., Jung, M. C., Coburn, C., Tadde, A., Sylvinson, M. R., D., Djurovich, P. I., et al. (2019). Highly efficient photo- and electroluminescence from two-coordinate Cu(I) complexes featuring nonconventional N-Heterocyclic carbenes. *J. Am. Chem. Soc.* 141, 3576–3588. doi: 10.1021/jacs.8b12397
- Sworakowski, J., Lipinski, J., and Janus, K. (2016). On the reliability of determination of energies of homo and lumo levels in organic semiconductors from electrochemical measurements. A simple picture based on the electrostatic model. *Organ. Electron.* 33, 300–310. doi: 10.1016/j.orgel.2016.03.031
- Wang, H. M. J., Chen, C. Y. L., and Lin, I. J. B. (1999). Synthesis, structure, and spectroscopic properties of Gold(I)–carbene complexes. *Organometallics* 18, 1216–1223. doi: 10.1021/om980718b
- Yersin, H., Rausch, A. F., Czerwieniec, R., Hofbeck, T., and Fischer, T. (2011). The triplet state of organo-transition metal compounds. Triplet harvesting and singlet harvesting for efficient oleds. *Coord. Chem. Rev.* 255, 2622–2652. doi: 10.1016/j.ccr.2011.01.042

**Conflict of Interest:** MT has a financial interest in the Universal Display Corporation. RHam is currently an employee of the Universal Display Corporation, however, all of her work in this paper was carried out when she was a graduate student at the University of Southern California.

The remaining authors declare that the research was conducted in the absence of any commercial or financial relationships that could be construed as a potential conflict of interest.

Copyright © 2020 Hamze, Idris, Muthiah Ravinson, Jung, Haiges, Djurovich and Thompson. This is an open-access article distributed under the terms of the Creative Commons Attribution License (CC BY). The use, distribution or reproduction in other forums is permitted, provided the original author(s) and the copyright owner(s) are credited and that the original publication in this journal is cited, in accordance with accepted academic practice. No use, distribution or reproduction is permitted which does not comply with these terms.



## OPEN ACCESS

## Edited by:

Chihaya Adachi,  
Kyushu University, Japan

## Reviewed by:

Linsong Cui,  
University of Cambridge,  
United Kingdom  
Hisahiro Sasabe,  
Yamagata University, Japan

## \*Correspondence:

Sungjune Jung  
sjjung@postech.ac.kr  
Soon-Ki Kwon  
skwon@gnu.ac.kr  
Yun-Hi Kim  
ykim@gnu.ac.kr

<sup>†</sup>These authors have contributed  
equally to this work

## Specialty section:

This article was submitted to  
Organic Chemistry,  
a section of the journal  
Frontiers in Chemistry

Received: 31 January 2020

Accepted: 07 April 2020

Published: 14 May 2020

## Citation:

Sohn S, Ha MW, Park J, Kim Y-H,  
Ahn H, Jung S, Kwon S-K and  
Kim Y-H (2020) High-Efficiency  
Diphenylpyrimidine Derivatives Blue  
Thermally Activated Delayed  
Fluorescence Organic Light-Emitting  
Diodes. *Front. Chem.* 8:356.  
doi: 10.3389/fchem.2020.00356

# High-Efficiency Diphenylpyrimidine Derivatives Blue Thermally Activated Delayed Fluorescence Organic Light-Emitting Diodes

Sunyoung Sohn<sup>1†</sup>, Min Woo Ha<sup>2†</sup>, Jiyong Park<sup>3,4</sup>, Yoo-Heon Kim<sup>2</sup>, Hyungju Ahn<sup>5</sup>,  
Sungjune Jung<sup>1\*</sup>, Soon-Ki Kwon<sup>6\*</sup> and Yun-Hi Kim<sup>2\*</sup>

<sup>1</sup> Department of Creative IT Engineering, Pohang University of Science and Technology, Pohang-si, South Korea,

<sup>2</sup> Department of Chemistry and Research Institute for Green Energy Convergence Technology, Gyeongsang National University, Jinju-si, South Korea, <sup>3</sup> Center for Catalytic Hydrocarbon Functionalizations, Institute for Basic Science (IBS), Daejeon, South Korea, <sup>4</sup> Department of Chemistry, Korea Advanced Institute of Science and Technology (KAIST), Daejeon, South Korea, <sup>5</sup> Pohang Accelerator Laboratory, Pohang-si, South Korea, <sup>6</sup> Department of Materials Engineering and Convergence Technology and ERI, Gyeongsang National University, Jinju-si, South Korea

Organic light-emitting diodes with thermally activated delayed fluorescence emitter have been developed with highly twisted donor–acceptor configurations and color-pure blue emitters. Synthesized 4-(4-(4,6-diphenylpyrimidin-2-yl)phenyl)-10H-spiro[acridine-9,9'-fluorene] (4,6-PhPMAF) doped device with spiroacridine as a donor unit and diphenylpyrimidine as acceptor exhibits the device characteristics such as the luminescence, external quantum efficiencies, current efficiencies, and power efficiencies corresponding to 213 cd/m<sup>2</sup>, 2.95%, 3.27 cd/A, and 2.94 lm/W with Commission International de l'Eclairage (CIE) coordinates of (0.15, 0.11) in 4,6-PhPMAF-doped DPEPO emitter. The reported 10-(4-(2,6-diphenylpyrimidin-4-yl)phenyl)-10H-spiro[acridine-9,9'-fluorene] (2,6-PhPMAF) doped device exhibit high device performance with 1,445 cd/m<sup>2</sup>, 12.38%, 19.6 cd/A, and 15.4 lm/W, which might be originated from increased internal quantum efficiency by up-converted triplet excitons to the singlet state with relatively smaller  $\Delta E_{ST}$  of 0.17 eV and higher reverse intersystem crossing rate ( $k_{RISC}$ ) of  $1.0 \times 10^8$ /s in 2,6-PhPMAF than 0.27 eV and  $3.9 \times 10^7$ /s in 4,6-PhPMAF. Despite low performance of 4,6-PhPMAF doped device, synthesized 4,6-PhPMAF has better color purity as a deep-blue emission with y axis (0.11) than reported 2,6-PhPMAF with y axis (0.19) in CIE coordinate. The synthesized 4,6-PhPMAF has higher thermal stability of any transition up to 300°C and decomposition

temperature with only 5% weight loss in 400°C than reported 2,6-PhPMAF. The maximum photoluminescence emission of 4,6-PhPMAF in various solvents appeared at 438 nm, which has blue shift about 20 nm than that of 2,6-PhPMAF, which contributes deep-blue emission in synthesized 4,6-PhPMAF.

**Keywords:** organic light-emitting diode, thermally activated delayed fluorescence, blue emitter, diphenylpyrimidine, singlet-triplet energy gap

## INTRODUCTION

The organic light-emitting diodes (OLEDs) using thermally activated delayed fluorescence (TADF) material have been widely investigated for high-efficiency device performance or low triplet and singlet energy levels for reduced driving voltage by narrow host bandgap, since the Adachi group reported the intersystem crossing (ISC) and reverse intersystem crossing (RISC) for triplet-to-singlet state conversion (Goushi et al., 2012; Nakanotani et al., 2014; Kim et al., 2015). It can harvest both single and triplet excitons because TADF involves small singlet-triplet state energy splitting by thermally activation (Tao et al., 2014; Sun et al., 2016; Cui et al., 2017). Improvement in device efficiency has been reported for device based on TADF molecules that the azasilene donor unit-based intermolecular charge-transfer exhibited deep blue TADF dye of high efficiency of 22.3% in mixed co-host (Kwon et al., 2015), and the methoxy substituents to replace tert-butyl substituents on the carbazole donors have been found to decrease the singlet-triplet state energy splitting ( $\Delta E_{ST}$ ), as well as long lifetime and reducing the device efficiency roll-off (Wu et al., 2014; Shizu et al., 2015). Triplet energy levels and reduction potentials of various acceptor cyano-substituted pyrazines were reported with combined small singlet-triplet splitting and large fluorescence rate (Liu et al., 2019). This molecular design can be accomplished with acridine, carbazole, and phenoxazine as electron donor units and/or sulfone, phosphine oxide, dimesitylboryl, and polycyclic borazine as electron acceptor units (Ganesan et al., 2018). Furthermore, as way of improving efficiency by device engineering, introducing the dual delayed fluorescence in the host material exhibited the slow-efficiency roll-offs (Zhang et al., 2019). Another device engineering technique involves measuring transition dipole moment, where the emitter with planar molecular structure becomes horizontally orientated, resulting in improved light-outcoupling efficiency of more than 30% (Mayr et al., 2014; Komino et al., 2017). In other groups, highly ordered morphology and horizontal transition dipole moment ratio of Pt(II)-based  $[Pt(fppz)_2]$  and spiro[acridine-9,9'-fluorene] donor with varied pyridyl orientation have been reported. High horizontal transition dipole moment ratio in para-linked donor between the donor-acceptor orientation has been measured using angle-dependent photoluminescence (PL) measurement (Ganesan et al., 2018). In our previous TADF work, we found that an *m*-phenyl linker between the electron-donating and the electron-accepting units showed higher device efficiencies; analysis of scattered X-ray intensities revealed a weak overlap in the phenyl linker, as well as well-aligned structure in the horizontal direction compared to those of the

*p*-phenyl linker (Sohn et al., 2017). Based on the reported linker material and molecular orientation, we analyzed the properties of synthesized emitters with spiroacridine-based electron donor (D) and diphenylpyrimidine group of electron acceptor (A) with different substance nitrogenous position.

## RESULTS AND DISCUSSION

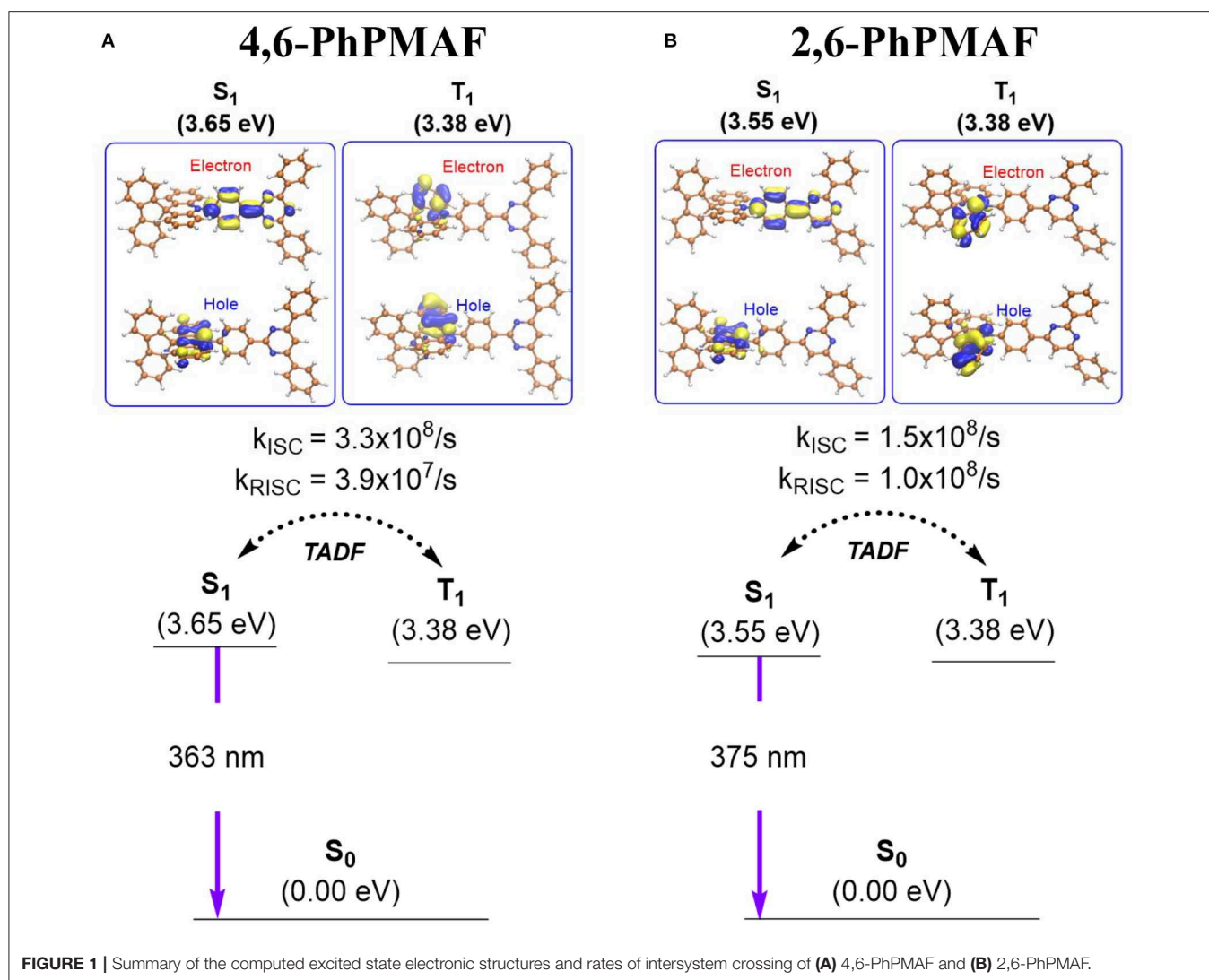
### Synthesis and Characterization

The synthetic routes of 4,6-PhPMAF instead of 2,6-PhPMAF are shown in **Scheme S1**. The intermediate 10-(4-bromophenyl)-10*H*-spiro[acridine-9,9'-fluorene] and 2-chloro-4,6-diphenylpyrimidine were synthesized by Buchwald-Hartwig amination and Suzuki coupling reaction, respectively. The 4,6-PhPMAF was obtained by Suzuki coupling. The chemical structure of the synthesized intermediates and 4,6-PhPMAF were characterized by nuclear magnetic resonance ( $^1H$ -NMR,  $^{13}C$ -NMR) spectroscopy and mass spectroscopy. Detailed synthesis and characterization procedures are described in the Supporting Information (**Supplementary Figures 1, 2**).

### Computational Analysis

The ground state ( $S_0$ ) and the excited state electronic structures of 4,6-PhPMAF and 2,6-PhPMAF were compared by means of density functional theory (DFT). We located the  $S_0$  geometries using CAM-B3LYP/def2-SVP level of the theory (**Supplementary Figure 3**). The renditions of frontier molecular orbitals confirmed that the highest occupied molecular orientation (HOMO) levels of the two compounds are localized at the spiroacridinyl group, and the lowest unoccupied molecular orientation (LUMO) levels are present at the diphenyl pyrimidinyl group (**Supplementary Figure 4**). The computed HOMO and LUMO energy gaps of the two molecules were comparable: 5.61 eV for 4,6-PhPMAF and 5.70 eV for 2,6-PhPMAF. **Figure 1** summarizes the computed excited state electronic structures of the first singlet excited state ( $S_1$ ) and the triplet excited state geometries ( $T_1$ ). The excited state geometries of the synthesized chromophores were optimized using a time-dependent DFT, namely, TD-CAM-B3LYP/def2-SVP level of the theory. The adiabatic electronic energies of the  $S_1$  states are 3.65 and 3.55 eV for 4,6-PhPMAF and 2,6-PhPMAF, respectively, relative to those of the optimized  $S_0$  geometries. The calculated vertical excitation energies of the  $S_1$  were 3.40 eV (363 nm) and 3.30 eV (375 nm) for 4,6-PhPMAF and 2,6-PhPMAF, respectively, which is in line with the observation that there is a blue shift in the photoluminescent spectrum of 4,6-PhPMAF with respect to that of 2,6-PhPMAF. The renditions of natural transition orbitals (NTOs) of the





S<sub>1</sub> states suggested the excited states bear charge transfer (CT) characters (**Supplementary Figure 5**): the hole (e<sup>+</sup>) is localized at the donor, and the electron (e<sup>-</sup>) is situated at the acceptor. The CT characters explained the solvatochromism observed experimentally (*vide infra*). The computed oscillator strength (*f*) for analyzing the radiative transition from S<sub>1</sub> and to S<sub>0</sub> exhibits same scale at the order of 10<sup>-3</sup> in 4,6-PhPMAF (*f* = 0.002640) or 2,6-PhPMAF (*f* = 0.004138). The dipole moment was measured to analyze the molecular orientation, as summarized in **Supplementary Table 1**. We also identified the triplet excited state geometries that are responsible for the observed TADF. The computed  $\Delta E_{ST}$  were 0.27 and 0.17 eV for 4,6-PhPMAF and 2,6-PhPMAF, respectively. The visualizations of NTOs suggested the triplet excited states exhibit the characteristic of  $\pi$ - $\pi^*$  transitions localized at the donor group (spiroacridine). We also computed the vibrational spin-orbit coupling (*V*<sub>SOC</sub>) strengths and the rates of ISC and RISC of the two molecules, as detailed in the supporting information. The *V*<sub>SOC</sub> of two molecules IS obtained as 1.511 and 1.460

cm<sup>-1</sup>, as listed in **Supplementary Table 2**. The computed rates of ISCs explained the observed TADF behaviors (**Figure 1** and **Supplementary Table 2**). For 4,6-PhPMAF, the computed rate of ISC (*k*<sub>ISC</sub>) was  $3.3 \times 10^8/s$ , whereas that of the reverse ISC (*k*<sub>RISC</sub>) was  $3.9 \times 10^7/s$ . For 2,6-PhPMAF, the computed rate of ISC (*k*<sub>ISC</sub>) was  $1.5 \times 10^8/s$ , whereas that of the reverse ISC (*k*<sub>RISC</sub>) was  $1.0 \times 10^8/s$ . Of note, the computed rates of RISC are significantly faster than the rates of phosphorescence quenching, which progresses in a time scale of microsecond or equivalently in a rate of 10<sup>6</sup>/s. Accordingly, the singlet and the triplet excited states are in equilibrium, and the fluorescence quenching from the S<sub>1</sub> is the dominant channel of PL decaying. The PL quantum yield (PLQY) values of two molecules under excitation at 300 nm are determined to be 16.9% and 29.5%, as shown in **Supplementary Table 2**. It is measured by the absolute method using a Hamamatsu Quantaurus-QY. The luminescence quantum efficiencies are calculated by Quantaurus-QY Absolute PL quantum yield spectrometer (C11347-11). The maximum PL spectra of DPEPO:4,6-PhPMAF or DPEPO:2,6-PhPMAF in

dilute oxygen-free chlorobenzene solution at low temperature are observed at 467.26 and 493.48 nm (**Supplementary Figure 6**).

## Thermal Properties

The thermal stability of 4,6-PhPMAF was studied by thermogravimetric analysis and differential scanning calorimetry. 4,6-PhPMAF did not show any transition up to 300°C, and the decomposition temperature ( $T_d$ ), corresponding to 5% weight loss, was 400°C, whereas the reported 2,6-PhPMAF was observed in the glass transition at 158°C and  $T_d$  at 400°C. The results indicate that the 4,6-PhPMAF shows better thermal stability (**Supplementary Figure 7** and **Supplementary Table 3**).

## Optical Properties

The photophysical properties of 4,6-PhPMAF in various media are shown in **Figure 2** and **Supplementary Figure 8** and are summarized in **Supplementary Table 2**. The PL spectroscopy of various solution of 4,6-PhPMAF was measured in cyclohexane ( $\epsilon = 2.02$ ), toluene ( $\epsilon = 2.38$ ), chloroform ( $\epsilon = 4.8$ ), acetone ( $\epsilon = 20.7$ ), and DMF ( $\epsilon = 36.7$ ) (**Supplementary Figure 8**). 4,6-PhPMAF displayed strong solvatochromism with a red shift of its PL peak from 400 nm in cyclohexane to 530 nm in DMF, which indicates the charge transfer-type emission. On the contrary, the 2,6-PhPMAF shows stronger solvatochromism with a red shift of its PL peak from 410 nm in cyclohexane to 560 nm, which is more than that of 4,6-PhPMAF. The absorbance and fluorescence spectra of  $10^{-5}$  M 4,6-PhPMAF in toluene are depicted. The intense absorption in the range of 300–350 nm may be assigned to the absorption of *N*-phenyl-spiroacridine, whereas the relatively weak and broad absorption from 350 to 410 nm may be assigned to the intramolecular charge transfer excitation (Woo et al., 2019). The absorption behavior of 2,6-PhPMAF was similar to that of 4,6-PhPMAF. The UV-visible (UV-vis) onset of 4,6-PhPMAF and 2,6-PhPMAF was 3.03 and 2.95 eV, respectively. The maximum PL emission of 4,6-PhPMAF appeared at 438 nm, which was 20 nm blue shifted than that of 2,6-PhPMAF. From the results, it is expected that the color purity of newly synthesized 4,6-PhPMAF will be better than that of reported 2,6-PhPMAF.

## Electrochemical Properties

The HOMO level of 4,6-PhPMAF was determined as  $-5.30$  eV from the cyclic voltametric measurement, and LUMO level was determined as  $-2.27$  eV by adding the optical bandgap (3.03 eV), whereas the HOMO and LUMO levels of 2,6-PhPMAF were determined as  $-5.26$  and  $-2.31$  eV by adding the optical bandgap (2.95 eV) (**Supplementary Figure 9**).

## Structural Properties

The synthesized dopant 4,6-PhPMAF and 2,6-PhPMAF will be denoted as 1 and 2 from these results. The topographical three- and two-dimensional (2D) images of 22 wt.% 1 and 2 doped DPEPO emitters with thicknesses of 50 nm are measured using atomic force microscopy (AFM) analysis with  $2 \times 2$ - $\mu\text{m}$  scan size, as shown in **Figure 3**. The root-mean-square (RMS) surface roughness ( $R_q$ ), average surface roughness ( $R_a$ ), and RMS roughness values of DPEPO:4,6-PhPMAF film in **Figure 3A** show uniform surface morphology of 0.2, 0.16, and 0.18 nm,

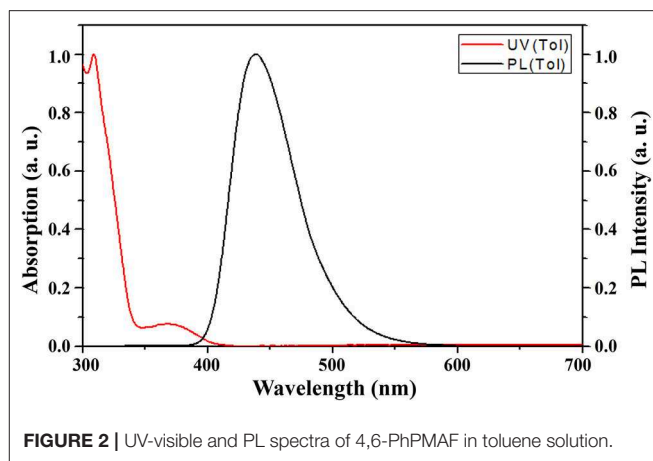


**FIGURE 2** | UV-visible and PL spectra of 4,6-PhPMAF in toluene solution.

respectively, and the DPEPO:2,6-PhPMAF film in **Figure 3B** shows 0.193, 0.153, and 0.15 nm, respectively. All films exhibit very uniform surfaces with a roughness value  $<0.2$  nm due to strong  $\pi$ - $\pi$  stacking with closely packed structures that yield good electrical device properties (Sohn et al., 2017). In order to precisely analyze the structural property of the emitters, we measured the two-dimensional grazing-incident wide-angle X-ray diffraction (2D GI-WAXD) to characterize the molecular orientation, as well as the packing properties of the emitters (**Figure 4**). In the patterns,  $q_{xy}$  and  $q_z$  represent the in-plane and out-of-plane components of the scattering vector  $q$ , which are normal to the plane of incidence and the film surface plane. The azimuthal intensity curve is measured to analyze the plots of orientation distribution. All films present similar distributions with a strong and broad diffraction peak, which might be attributed to the planar packing of randomly oriented emitters along the out-of-plane direction at  $q_z = 0.75 \text{ \AA}^{-1}$  in **Figures 4A,B**. To compare the diffraction peak position and crystallographic property, the in-plane (**Figure 4C**) and out-of-plane (**Figure 4D**) intensity profiles for DPEPO:4,6-PhPMAF and DPEPO:2,6-PhPMAF films are extracted from the 2D GI-WAXD pattern. The azimuthal angle scan X-rays of (100) reflection are measured to elucidate the molecular orientation of emitter in **Figure 4E**. Calculated full width at half maximum values for azimuthal intensity distributions in DPEPO:4,6-PhPMAF and DPEPO:2,6-PhPMAF emitters are estimated as  $27.2^\circ$  and  $25.3^\circ$  by Gaussian model fitting. The FWHM of DPEPO:2,6-PhPMAF film is relatively narrow compared to those of DPEPO:4,6-PhPMAF film, which can improve the outcoupling efficiency in the devices as implying horizontal plane-on orientation (Kim et al., 2016; Sohn et al., 2018).

## Transient PL Spectra Properties

Transient PL decay curve of the 4,6-PhPMAF and 2,6-PhPMAF doped DPEPO films (22%, 40 nm) are obtained to identify prompt and delayed fluorescent as shown in **Figure 5**. The prompt PL emission (**Figure 5A**) exhibited similar spectral distribution, which implied similar fluorescence emissive states,

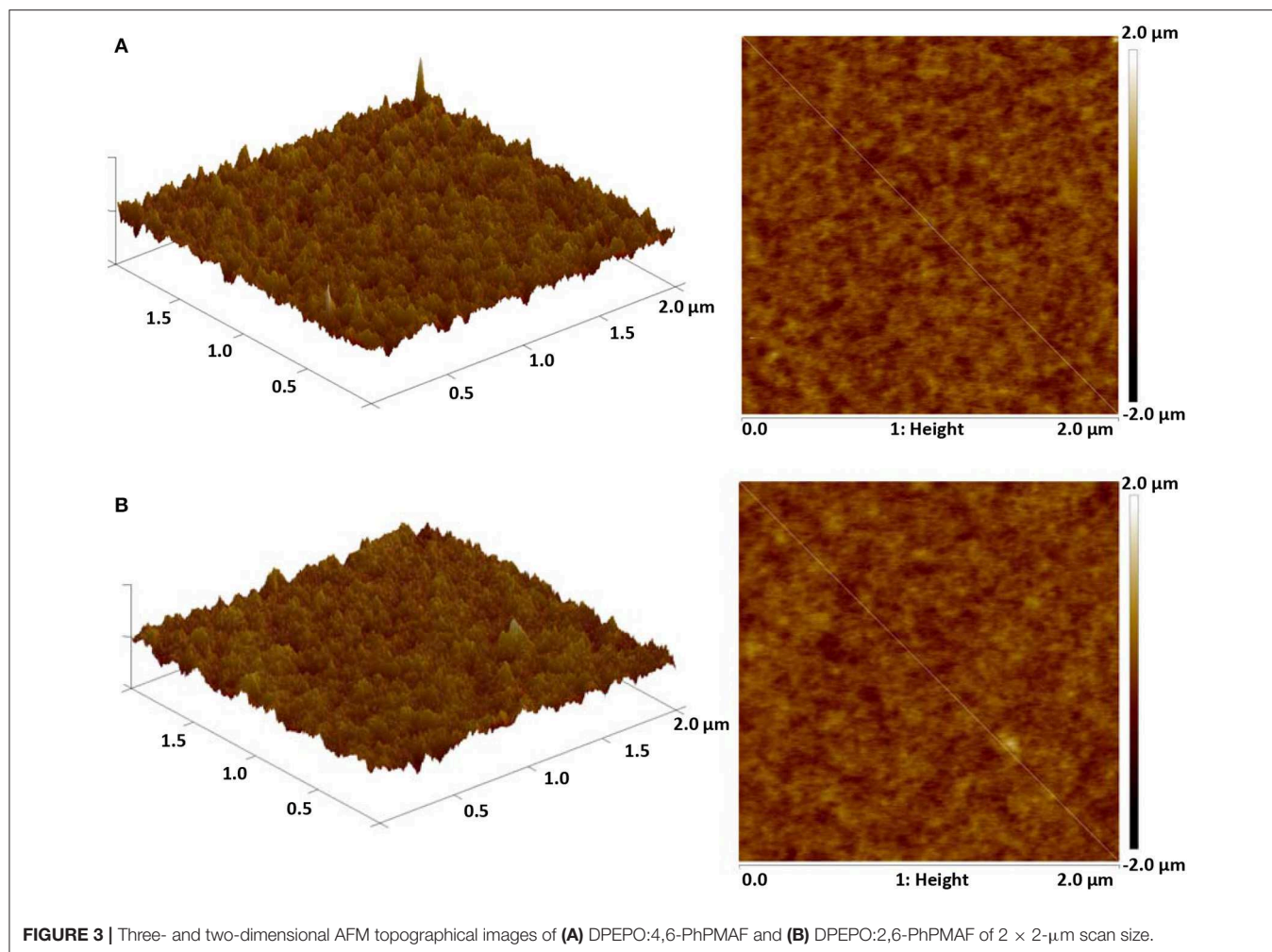


**FIGURE 3 |** Three- and two-dimensional AFM topographical images of **(A)** DPEPO:4,6-PhPMAF and **(B)** DPEPO:2,6-PhPMAF of  $2 \times 2\text{-}\mu\text{m}$  scan size.

whereas the lifetimes of the delayed components of 4,6-PhPMAF and 2,6-PhPMAF doped films were 301.15 and 130.15  $\mu\text{s}$ . In **Figure 5B**, the delayed emission of DPEPO:4,6-PhPMAF exhibited relatively weak spectra compared to those of DPEPO:2,6-PhPMAF, which implied reduced triplet exciton action, as well as suppressed Dexter energy transfer in TADF emission (Fukagawa et al., 2017; Han et al., 2019). A  $\Delta E_{\text{ST}}$  of 4,6-PhPMAF and 2,6-PhPMAF dopants had been calculated to 0.27 and 0.17 eV, respectively. The small  $\Delta E_{\text{ST}}$  can contribute to improved internal quantum efficiency by up-converted triplet excitons (Liu et al., 2019). However, the small  $\Delta E_{\text{ST}}$  value of faster RISC from triplet to singlet can result in short or similar TADF lifetime (Zhang et al., 2019).

## Device Characteristics

The energy-band diagram of the device structure is shown, and the chemical structure of synthesized 4,6-PhPMAF and 2,6-PhPMAF dopants into DPEPO host material is attached in **Figure 6A**. For effective hole and electron balancing, we have chosen hole or electron transport layers (ETLs) carefully by considering their HOMO and LUMO energy levels and charge mobility. The HOMO and LUMO values of 4,6-PhPMAF and

2,6-PhPMAF are determined using DFT calculation and cyclic voltammetry (CV) measurement for blue emitter. The HOMO-LUMO levels of molybdenum trioxide ( $\text{MoO}_3$ ), TAPC, TCTA, DPEPO, and TmPyPB materials are obtained from Ossila Co. The normalized electroluminescent (EL) spectra are obtained for 4,6-PhPMAF and 2,6-PhPMAF doped devices (**Figure 6B**). The EL spectra of all the devices show solely emission peaks with any shoulder peaks, which could be contributed to good color gamut OLEDs. However, the EL spectra 4,6-PhPMAF doped device is red-shifted compared to the PL spectra, as discussed in reported 2,6-PhPMAF material (Ganesan et al., 2018). In the spectra, the EL maximum peak of the device with 4,6-PhPMAF dopant exhibit 458-nm emission, which is blue shifted compared to those of 2,6-PhPMAF dopant of 471 nm. It is caused by the different substance nitrogenous position in diphenylpyrimidine group of electron acceptor with spiroacridine-based electron donor. The current-density, luminance, external quantum efficiency, current efficiency, and power efficiency vs. applied voltage of devices are shown in **Figure 7**. The Commission International de l'Eclairage (CIE) coordinates of devices are displayed. The devices with DPEPO:4,6-PhPMAF emitter exhibit maximum luminescence of  $213\text{ cd/m}^2$  at 8 V, external quantum efficiencies of 2.95%, current efficiency of  $3.27\text{ cd/A}$ , and power efficiencies of  $2.94\text{ lm/W}$ .



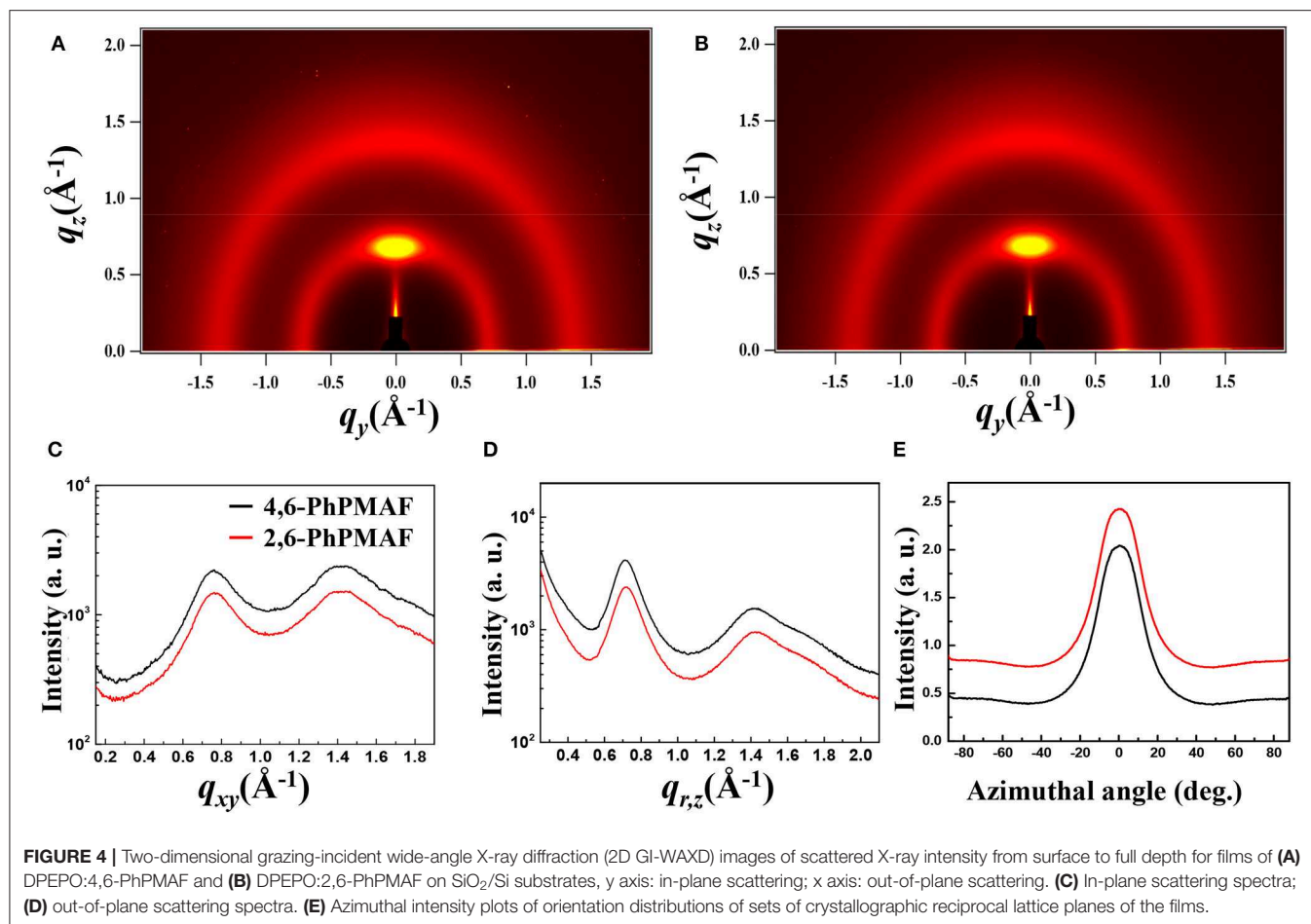


**FIGURE 4** | Two-dimensional grazing-incident wide-angle X-ray diffraction (2D GI-WAXD) images of scattered X-ray intensity from surface to full depth for films of (A) DPEPO:4,6-PhPMAF and (B) DPEPO:2,6-PhPMAF on  $\text{SiO}_2/\text{Si}$  substrates, y axis: in-plane scattering; x axis: out-of-plane scattering. (C) In-plane scattering spectra; (D) out-of-plane scattering spectra. (E) Azimuthal intensity plots of orientation distributions of sets of crystallographic reciprocal lattice planes of the films.

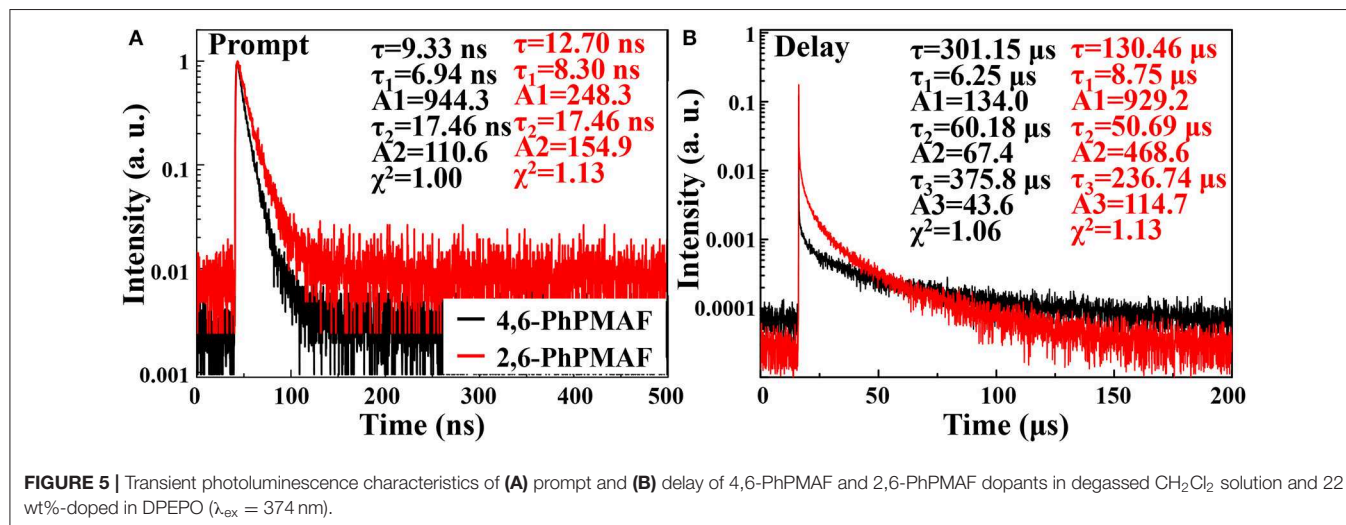
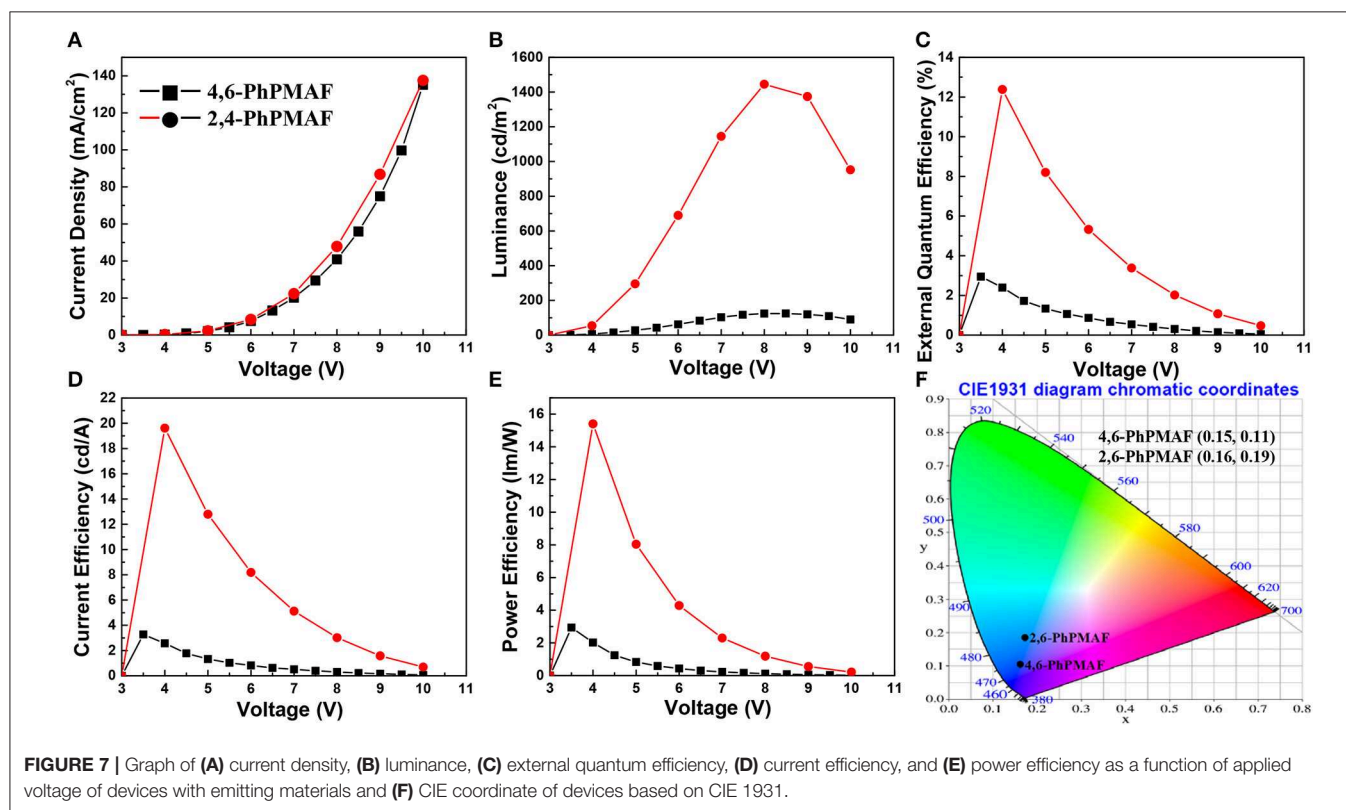
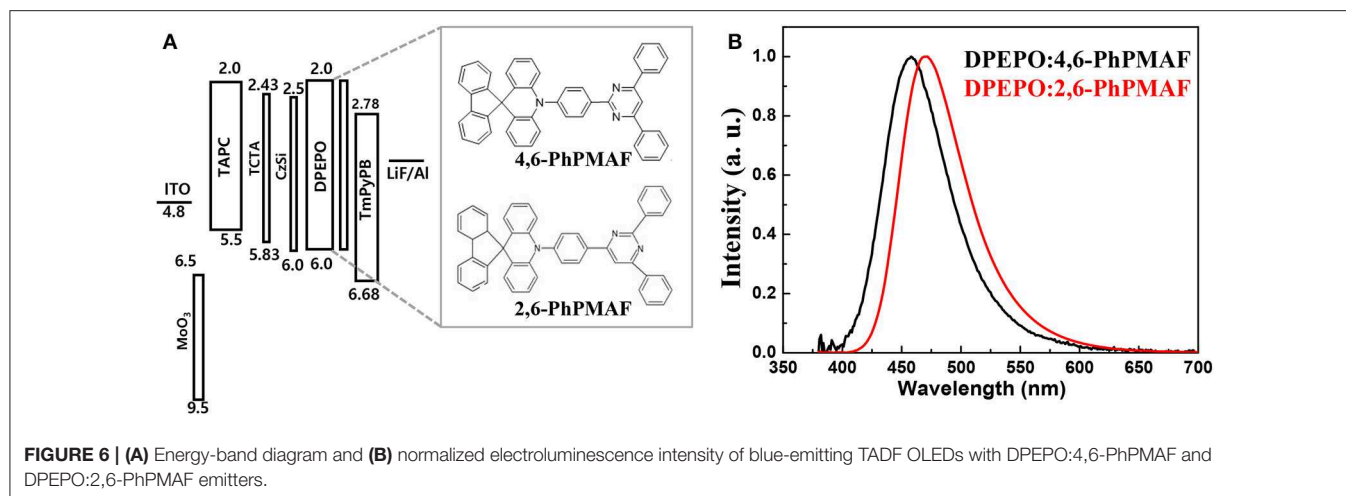


**FIGURE 5** | Transient photoluminescence characteristics of (A) prompt and (B) delay of 4,6-PhPMAF and 2,6-PhPMAF dopants in degassed  $\text{CH}_2\text{Cl}_2$  solution and 22 wt%-doped in DPEPO ( $\lambda_{\text{ex}} = 374 \text{ nm}$ ).

The CIE coordinates of 4,6-PhPMAF doped device have (0.15, 0.11) at  $x$  and  $y$  axes, which is close to the deep-blue TADF OLEDs. These deep-blue emitters with CIE  $y$  coordinate  $< 0.15$  can be attributed the low-power consumption, as well as the color gamut when it will be applied in full-color OLEDs. The devices with DPEPO:2,6-PhPMAF emitter and TADF emitter

exhibit bright luminescence with  $1,445 \text{ cd/m}^2$  at 8 V, maximum external quantum efficiencies of 12.38%, current efficiency of  $19.6 \text{ cd/A}$ , power efficiencies of  $15.4 \text{ lm/W}$ , and cobalt blue emitting with CIE coordinates of (0.16, 0.19). The reason that the efficiency of the device is approximately four times different is due to three reasons as follows: First, the improved device





efficiencies in 2,6-PhPMAF doped device is caused by fast up-converted triplet excitons to the singlet state with relatively smaller  $\Delta E_{ST}$  of 0.17 eV compared to 0.27 eV in 4,6-PhPMAF dopant. Second is that it is believed to be due to improved internal quantum efficiency by the relatively higher PLQY value of the 2,6-PhPMAF (29.5%) emitter than 4,6-PhPMAF (16.9%) because the device efficiency is depends on the solid-state PLQY of the emitter, as discussed in literatures (de Sá Pereira et al., 2017; Maasoumi et al., 2018). As mentioned in the azimuthal intensity distributions, finally, it can be explained because the relatively narrow FWHM of DPEPO:2,6-PhPMAF film compared with the DPEPO:4,6-PhPMAF film has relatively horizontal plane-on orientation to the substrate, resulting in improved outcoupling

efficiency in the emitting layer. The synthesized acridine (D) and diphenylpyrimidine (A) based emitters can be used as high-performance deep-blue emitters in a TADF-OLEDs.

## CONCLUSION

The blue-emitting TADF materials with spiroacridine-based electron donor and diphenylpyrimidine group of electron acceptor with different substance nitrogenous position are successfully synthesized. The performance of reported 2,6-PhPMAF doped TADF device is over four times higher than synthesized 4,6-PhPMAF doped device. It is due to improved fast up-converted triplet excitons to the singlet state and smaller

$\Delta E_{ST}$  as well as higher PL quantum yield in 2,6-PhPMAF than the 4,6-PhPMAF. Minor reason could be due to outcoupling efficiency in the emitting layer of the 2,6-PhPMAF-doped TADF device with relatively horizontal plane-on orientation. Despite the relatively low device efficiency with 4,6-PhPMAF, the  $y$  axis in CIE coordinate exhibits 0.11, which is close to the deep-blue OLEDs. This deep-blue 4,6-PhPMAF emitter could be contributed to the low power consumption, as well as good color gamut when it will be fabricated in full-color OLEDs.

## EXPERIMENTAL SECTION

### Materials

Detailed descriptions are given in the **Supporting Information**.

### Instruments

$^1\text{H}$  NMR spectra were recorded using a Bruker Avance 300 MHz FT-NMR spectrometer,  $^{13}\text{C}$  NMR were recorded using a Bruker Avance 300 MHz FT-NMR spectrometer. Chemical shifts (ppm) were reported with tetramethylsilane as an internal standard. Thermogravimetric analysis (TGA) under  $\text{N}_2$  gas was performed using a TA instrument 2050 thermogravimetric analyzer. Differential scanning calorimetry (DSC) under  $\text{N}_2$  gas was conducted using a TA instrument DSC Q10. Samples for TGA and DSC were heated at  $10^\circ\text{C}/\text{min}$ . UV-visible spectra were measured using a Shimadzu UV-1065PC UV-vis spectrophotometer. Photoluminescence spectra were measured using a Perkin-Elmer LS50B fluorescence spectrophotometer. The electrochemical properties of the materials were measured by CV using an Epsilon C3 in a 0.1 M solution of tetrabutyl ammonium perchlorate in acetonitrile. The topographies of 22 wt.-%-doped 1 and 2 films in DPEPO had been analyzed using AFM (VEECO Dimension 3100+Nanoscope V) in non-contact mode. Grazing-incident wide-angle X-ray diffraction measurements were performed at the 9A U-SAXS beamline of the Pohang Light Source in South Korea. Grazing-incident wide-angle X-ray diffraction samples were prepared by the same processing condition with active layer casting on the  $\langle 100 \rangle$  silicon wafer. The wavelength of X-rays was  $1.12148 \text{ \AA}$  ( $E = 11.055 \text{ keV}$ ); the incidence angle was  $0.12^\circ$ , and the sample exposure time was 30 s. The GI-WAXD images were recorded with a 2D CCD (Rayonix MX170-HS). The diffraction angles were calibrated by a precalibrated sucrose solution (Monoclinic, P21,  $a = 10.8631 \text{ \AA}$ ,  $b = 8.7044 \text{ \AA}$ ,  $c = 7.7624 \text{ \AA}$ , and  $\beta = 102.938^\circ$ ). The sample-to-detector distance was 221 mm. The prompt and delayed fluorescence lifetimes are measured by a fluorescence lifetime spectrometer, a Quantaaurus-Tau C11367-31 instrument of Hamamatsu, as measured in literature (Han et al., 2019).

### Device Fabrication and Measurements

For comparing dopant property as well as electron and hole balancing, the devices of ITO/MoO<sub>3</sub> (20%): TAPC (20 nm)/TAPC (45 nm)/TCTA (5 nm)/CzSi (2 nm)/DPEPO: 4,6-PhPMAF or DPEPO: 2,6-PhPMAF 22% (20 nm)/DPEPO (3 nm)/TmPyPB (50 nm)/lithium fluoride (LiF) (1 nm)/aluminum (Al) (120 nm) had been fabricated on

ITO-coated glass substrates in a class-1000 cleanroom. An ITO-coated glass was sequentially cleaned using deionized water, acetone, and isopropyl alcohol for 15 min in an ultrasonic bath and then dried in an oven at  $70^\circ\text{C}$  during 1 day to remove residual organic solvents and moisture on the ITO substrate. An MoO<sub>3</sub> doped 4,4'-cyclohexylidenebis[N,N-bis(4-methylphenyl)benzenamine] (TAPC) mixed layer was used for improve hole injection. Tris(4-carbazoyl-9-ylphenyl)amine (TCTA) was used as a hole-transport layer, as well as exciton or electron-blocking layer due to its high-lying LUMO level in the devices. 9-(4-*tert*-Butylphenyl)-3,6-bis(triphenylsilyl)-9H-carbazole (CzSi) with high triplet energy (3.02 eV) and wide bandgap (3.5 eV) was used for enhancing morphological and electrochemical stability. To achieve efficient TADF OLEDs, bis[2-(diphenylphosphino)phenyl]ether oxide (DPEPO) host material was used because it has thermal and morphological stability as well as the ETL and a hole-blocking layer with high HOMO level ( $\sim 6.1 \text{ eV}$ ). As an ETL material, 1,3,5-tri(m-pyrid-3-yl-phenyl)benzene (TmPyPB) was used because of its triplet energy level with deep HOMO level (6.75 eV). The TmPyPB can be used as a co-host material with the hole transporting TCTA due to its high electron mobility. Lithium fluoride and Al were, respectively, evaporated as an interlayer and a cathode. The devices were encapsulated with glass, and then their current density, luminance, and efficiencies vs. driving voltages of the devices were measured using a Keithley 236 and a CS-1000 (Konica Minolta Co.) system.

## DATA AVAILABILITY STATEMENT

All datasets generated for this study are included in the article/**Supplementary Material**.

## AUTHOR CONTRIBUTIONS

SS has written a manuscript and contributed the optoelectrical analysis and the fabrication of the OLEDs. MH have written a synthetic part of manuscript and characterize the synthesized materials. Y-HK synthesized the emitting materials. JP contributed to the computational analysis. HA analyzed the 2D GI-WAXD images using scattered X-ray beam. SJ and S-KK have made a substantial and intellectual contribution to the work. Y-HK proposed the idea of this manuscript and analyzed the experiment results.

## FUNDING

This research was supported by the National Research Foundation (NRF-2019R1I1A1A01064203 and NRF-2018R1A2A1A05078734) of Korea grant funded by the Korea government and was supported by the Institute for Basic Science (Grant No. IBS-R10-A1).

## SUPPLEMENTARY MATERIAL

The Supplementary Material for this article can be found online at: <https://www.frontiersin.org/articles/10.3389/fchem.2020.00356/full#supplementary-material>

## REFERENCES

- Cui, L. S., Nomura, H., Geng, Y., Kim, J. U. K., Nakanotani, H., Adachi, C., et al. (2017). Controlling singlet-triplet energy splitting for deep-blue thermally activated delayed fluorescence emitters. *Angew. Chem.* 56, 1571–1575. doi: 10.1002/anie.201609459
- de Sá Pereira, D., Data, P., and Monkman, A. P. (2017). Methods of analysis of organic light emitting diodes. *Display Imaging* 2, 323–337. Available online at: <http://www.oldcitypublishing.com/wp-content/uploads/2017/04/DAIv2n3-4p323-337Pereira.pdf>
- Fukagawa, H., Shimizu, T., Iwasaki, Y., and Yamamoto, T. (2017). Operational lifetimes of organic light-emitting diodes dominated by Förster resonance energy transfer. *Sci. Rep.* 7:1735. doi: 10.1038/s41598-017-02033-3
- Ganesan, P., Chen, D. G., Liao, J. L., Li, W. C., Lai, Y. N., Luo, D. I., et al. (2018). Isomeric spiro-[acridine-9,9'-fluorene]-2,6-dipyridylpyrimidine based TADF emitters: insights into photophysical behaviors and OLED performances. *J. Mater. Chem. C* 6, 10088–10100. doi: 10.1039/c8tc03645d
- Goushi, K., Yoshida, K., Sato, K., and Adachi, C. (2012). Organic light-emitting diodes employing efficient reverse intersystem crossing for triplet-to-singlet state conversion. *Nat. Photonics* 6, 253–258. doi: 10.1038/nphoton.2012.31
- Han, S. H., Jeong, J. H., Yoo, J. W., and Lee, J. Y. (2019). Ideal blue thermally activated delayed fluorescence emission assisted by a thermally activated delayed fluorescence assistant dopant through a fast reverse intersystem crossing mediated cascade energy transfer process<sup>†</sup>. *J. Mater. Chem. C* 7, 3082–3089. doi: 10.1039/C8TC06575F
- Kim, K. H., Liao, J. L., Lee, S. W., Sim, B., Moon, C. K., Lee, G. H., et al. (2016). Crystal organic light-emitting diodes with perfectly oriented non-doped pt-based emitting layer. *Adv. Mater.* 28, 2526–2532. doi: 10.1002/adma.201504451
- Kim, Y., Wolf, C., Cho, H., Jeong, S., and Lee, T. (2015). Highly efficient, simplified, solution-processed thermally activated delayed-fluorescence organic light-emitting diodes. *Adv. Mater.* 28, 734–741. doi: 10.1002/adma.201504490
- Komino, T., Oki, Y., and Adachi, C. (2017). Dipole orientation analysis without optical simulation: Application to thermally activated delayed fluorescence emitters doped in host matrix. *Sci. Rep.* 7:8405. doi: 10.1038/s41598-017-08708-1
- Kwon, S., Kim, Y., and Kim, J. (2015). Thermally activated delayed fluorescence from azasilene based intramolecular charge-transfer emitter (DTPDDA) and a highly efficient blue light emitting diode. *Cham. Mater.* 27:150914132924008. doi: 10.1021/acs.chemmater.5b02515
- Liu, J., Zhou, K., Wang, D., Deng, C., Duan, K., Ai, Q., et al. (2019). Pyrazine-based blue thermally activated delayed fluorescence materials: combine small singlet – triplet splitting with large fluorescence rate. *Front. Chem.* 7:312. doi: 10.3389/fchem.2019.00312
- Maasoumi, F., Vuuren, R. D. J., Shaw, P. E., Puttock, E. V., Nagiri, R. C. R., McEwan, J. A., et al. (2018). An external quantum efficiency of >20% from solution-processed poly(dendrimer) organic light-emitting diodes. *NPJ Flex. Electron.* 2:27. doi: 10.1038/s41528-018-0038-9
- Mayr, C., Lee, S. Y., Schmidt, T. D., Yasuda, T., Adachi, C., and Brütting, W. (2014). Efficiency enhancement of organic light-emitting diodes incorporating a highly oriented thermally activated delayed fluorescence emitter. *Adv. Func. Mater.* 24, 5232–5239. doi: 10.1002/adfm.201400495
- Nakanotani, H., Higuchi, T., Furukawa, T., Masui, K., Morimoto, K., Numata, M., et al. (2014). High-efficiency organic light-emitting diodes with fluorescent emitters. *Nat. Commun.* 5:4016. doi: 10.1038/ncomms5016
- Shizu, K., Sakai, Y., Tanaka, H., Hirata, S., Adachi, C., and Kaji, H. (2015). Meta-linking strategy for thermally activated delayed fluorescence emitters with a small singlet-triplet energy gap. *ITE Trans. Media Technol. App.* 3, 108–113. doi: 10.3169/mta.3.108
- Sohn, S., Hyun Koh, B., Baek, J. Y., Chan Byun, H., Lee, J. H., Shin, D. S., et al. (2017). Synthesis and characterization of diphenylamine derivative containing malononitrile for thermally activated delayed fluorescent emitter. *Dyes Pigm.* 140, 14–21. doi: 10.1016/j.dyepig.2017.01.010
- Sohn, S., Park, K. H., Kwon, S., Lee, H., Ahn, H., Jung, S., et al. (2018). Preferential orientation of tetrahedral silicon-based hosts in phosphorescent organic light-emitting diodes. *ACS Omega* 3, 9989–9996. doi: 10.1021/acsomega.8b01358
- Sun, J. W., Kim, K. H., Moon, C. K., Lee, J. H., and Kim, J. J. (2016). Highly efficient sky-blue fluorescent organic light emitting diode based on mixed cohost system for thermally activated delayed fluorescence emitter (2CzPN). *ACS Appl. Mater. Interfaces* 8, 9806–9810. doi: 10.1021/acsami.6b00286
- Tao, Y., Yuan, K., Chen, T., Xu, P., Li, H., Chen, R., et al. (2014). Thermally activated delayed fluorescence materials towards the breakthrough of organoelectronics. *Adv. Mater.* 26, 7931–7958. doi: 10.1002/adma.201402532
- Woo, S. J., Kim, Y., Kim, Y. H., Kwon, S. K., and Kim, J. J. (2019). A spiro-silafluorene-phenazasilene donor-based efficient blue thermally activated delayed fluorescence emitter and its host-dependent device characteristics. *J. Mater. Chem. C* 7, 4191–4198. doi: 10.1039/c9tc00193j
- Wu, S., Aonuma, M., Zhang, Q., Huang, S., Nakagawa, T., Kuwabara, K., et al. (2014). High-efficiency deep-blue organic light-emitting diodes based on a thermally activated delayed fluorescence emitter. *J. Mater. Chem. C* 2, 421–424. doi: 10.1039/c3tc31936a
- Zhang, Y., Li, Z., Li, C., Wang, Y., and Wang, Y. (2019). Suppressing efficiency roll-off of TADF based OLEDs by constructing emitting layer with dual delayed fluorescence. *Front. Chem.* 7:302. doi: 10.3389/fchem.2019.00302

**Conflict of Interest:** The authors declare that the research was conducted in the absence of any commercial or financial relationships that could be construed as a potential conflict of interest.

Copyright © 2020 Sohn, Ha, Park, Kim, Ahn, Jung, Kwon and Kim. This is an open-access article distributed under the terms of the Creative Commons Attribution License (CC BY). The use, distribution or reproduction in other forums is permitted, provided the original author(s) and the copyright owner(s) are credited and that the original publication in this journal is cited, in accordance with accepted academic practice. No use, distribution or reproduction is permitted which does not comply with these terms.



# Recent Advancement in Boron-Based Efficient and Pure Blue Thermally Activated Delayed Fluorescence Materials for Organic Light-Emitting Diodes

Hyuna Lee<sup>†</sup>, Durai Karthik<sup>†</sup>, Raju Lampande<sup>†</sup>, Jae Hong Ryu and Jang Hyuk Kwon\*

Organic Optoelectronic Device Laboratory, Information Display Department, Kyung Hee University, Seoul, South Korea

## OPEN ACCESS

### Edited by:

Chihaya Adachi,  
Kyushu University, Japan

### Reviewed by:

Takuji Hatakeyama,  
Kwansei Gakuin University, Japan  
Jian Fan,  
Soochow University, China

### \*Correspondence:

Jang Hyuk Kwon  
jhkwon@khu.ac.kr

<sup>†</sup>These authors have contributed  
equally to this work

### Specialty section:

This article was submitted to  
Organic Chemistry,  
a section of the journal  
Frontiers in Chemistry

**Received:** 14 February 2020

**Accepted:** 09 April 2020

**Published:** 19 May 2020

### Citation:

Lee H, Karthik D, Lampande R,  
Ryu JH and Kwon JH (2020) Recent  
Advancement in Boron-Based  
Efficient and Pure Blue Thermally  
Activated Delayed Fluorescence  
Materials for Organic Light-Emitting  
Diodes. *Front. Chem.* 8:373.  
doi: 10.3389/fchem.2020.00373

In the last few years, electron-deficient materials have been actively researched for application in organic light-emitting diode (OLED) as dopant and electron-transporting materials. The boron-containing materials are interesting as they give good emissive properties in solid state with an electron-accepting character. Recently, many boron-containing materials are used as emissive materials for thermally activated delayed fluorescence (TADF) OLED applications. In this review, boron acceptor-based push-pull small molecules used for application in blue TADF OLEDs are reviewed, covering their different types of acceptor, molecular design, structure-property relation, material properties, and device properties. Also, the importance of boron acceptors to address the key issue of blue TADF OLEDs is discussed.

**Keywords:** boron acceptor, thermally activated delayed fluorescence (TADF), multiple resonance, electroluminescence, blue organic light-emitting diode (OLED)

## INTRODUCTION

Organic light-emitting diodes (OLEDs) have been actively investigated in the last three decades since the first discovery by Tang and Vanslyke (1987) because of their incomparable advantages as they offer low power consumption, high brightness, color purity, light weight, large viewing angle, and flexible nature compared to other lighting sources. The first-generation fluorescent OLEDs exhibited lower efficiency due to usage of only 25% of singlet excitons formed during the exciton recombination process. Later, second-generation OLEDs were developed to utilize both singlet and triplet excitons to increase the internal quantum efficiency (IQE) up to 100% using heavy metal atoms, which are also called phosphorescent OLEDs (Baldo et al., 1998). Though the efficiency, color purity, and device lifetime of phosphorescent green and red OLEDs are satisfactory to commercialize, blue phosphorescent OLEDs suffer from low efficiency, poor color purity, and short device lifetime due to high triplet energy of blue emitters (Scholz et al., 2015; Im et al., 2017). Later, third-generation OLEDs were demonstrated with 100% IQE by using the concept of thermally activated delayed fluorescence (TADF) process in pure organic materials (Uoyama et al., 2012). These TADF materials are promising to achieve high efficiency and color purity in the blue OLEDs. Thus, recently, many reports were published on blue TADF emitters based on different types of donor and acceptor design concepts (Liang et al., 2019).



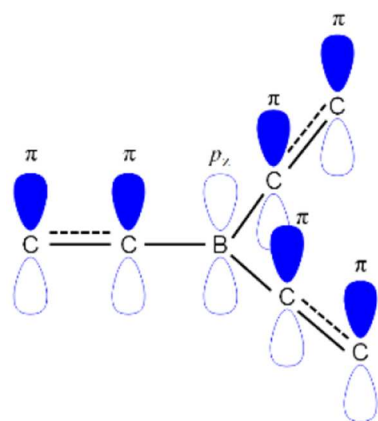


**FIGURE 1** | General configuration of  $p_z$ - $\pi$  conjugation of B-C atoms in the organic conjugated systems.

The boron-based materials have received tremendous interest in the last few years as they are widely used as potential candidates in the optoelectronic devices (Entwistle and Marder, 2004; Turkoglu et al., 2017; Mellerup and Wang, 2019). Boron atom has a vacant  $p_z$ -orbital which gives an electron-deficient nature or Lewis acidic nature (Brown and Dodson, 1957). This electron-deficient boron can make a  $\pi$ -conjugation with organic conjugated system through empty  $p_z$  orbital of boron and  $\pi$ -orbital of carbon as shown in **Figure 1**. Recently, boron-based materials have drawn immense attraction in designing as new TADF acceptor moieties because they offer excellent photophysical and electrochemical properties. Especially, boron materials show high photoluminescence quantum yield (PLQY) because of their  $sp^2$  hybridized trigonal planar geometry which gives rigid/planar molecular structure resulting in less non-radiative decay (Yamaguchi and Wakamiya, 2006; Elbing and Bazan, 2008; Von Grotthuss et al., 2018). Generally, boron-containing materials exhibit largely blue emission due to their weak acceptor nature, which yields a large band gap. Though the boron atom has a weak acceptor nature, boron acceptor materials have exhibited different color emissions varying from blue to red depending on the acceptor design strategy (D'aleo et al., 2017; Yang et al., 2018; Zhang et al., 2019). Not only the tri-coordinate boron shows excellent emission properties, but the tetra-coordinate boron also shows very good emissive properties as evident from BODIPY (boron-dipyrromethene) materials (Bonardi et al., 2008; Schellhammer et al., 2017; Stachelek et al., 2017; Zampetti et al., 2017). Unlike tri-coordinate boron, one important thing in tetra-coordinate boron is to keep the charge neutral of overall material by forming a covalent bond with mono-anionic chelate ligand to dissipate boron's negative charge. Therefore, the rigidity of the molecule is enhanced by virtue of chelation effect resulting in good emissive properties (Frath et al., 2014).

Recently, many TADF materials with boron acceptors have been reported with good performances. There are several boron TADF materials available in the literature for different color OLEDs. However, blue TADF OLEDs are interesting as they are promising alternatives to commercial fluorescent blue emitters.

As boron-based blue TADF materials are promising to realize high efficiency with a long lifetime, the detailed knowledge on the structure-property relation and design tactics of boron-based blue TADF emitters is highly desirable. Thus, in this review, we focus on the boron acceptor-based materials used for blue TADF OLEDs. Also, we discuss the requirements of blue emitters and different types of boron acceptors (tri- and tert-coordinate boron) used for blue TADF materials. In addition, we also discuss multiple resonance TADF materials and their underlying mechanism which is particularly for boron blue TADF OLEDs. Finally, the future outlook summarizes to achieve high efficiency and long lifetime for boron-based blue TADF OLEDs.

## BASIC REQUIREMENT OF BLUE MATERIALS

Over the last few years, huge progress has been made on the synthesis of new blue TADF emitters for OLED applications. To use blue TADF material for OLED applications that should be capable of making high external quantum efficiency (EQE), low-efficiency roll-off, good color purity of  $x < 0.15$ ,  $y < 0.10$ , and a long lifetime. To make OLED containing these properties, blue TADF material should have a high PLQY, wide energy gap ( $\Delta E_{ST}$ ) between highest occupied molecular orbital (HOMO) and lowest unoccupied molecular orbital (LUMO), small  $\Delta E_{ST}$  between the lowest singlet and triplet states, fast reverse intersystem crossing (RISC) from triplet to singlet, narrow full width at half maximum (FWHM), and high horizontal dipole orientation in the film.

Normally, small  $\Delta E_{ST}$  can be achieved by reducing an exchange integral between HOMO and LUMO and a large twist angle between the donor and the acceptor. The use of a rigid and symmetric structure supports to enhance PLQY and to achieve a narrow FWHM. The high bandgap ( $S_1$ ) energy can be reached by applying short  $\pi$ -conjugation length and the donor-acceptor interaction. The high horizontal orientation of the emitter molecule in the film is important to achieve high light out-coupling efficiency. Generally, blue TADF OLED shows the poor lifetime because of the long-delayed exciton lifetime of the emitter. Therefore, short-delayed exciton lifetime is highly required for achieving a long lifetime and high-efficiency OLEDs.

## SEVERAL BORON CHEMICAL STRUCTURES VS. THEIR PERFORMANCES

### Unbridged Boron-Type Acceptor for Blue Thermally Activated Delayed Fluorescence Emitters

Triarylboron compounds have been used as optoelectronic materials due to their electron-withdrawing abilities. In 2015, Suzuki et al. (2015) firstly reported a series of triarylboron-based TADF emitters, **2DAC-Mes<sub>3</sub>B** and **DAC-Mes<sub>3</sub>B**, by introducing amine-based electron donors. Methyl groups at the *ortho* position of C-B bonds protect the centered boron atom from hydrolysis by oxygen and water. They attached bis(diphenylamino)carbazole (2DAC) and diphenylaminocarbazole (DAC) moieties for electron-donating groups. The **2DAC-Mes<sub>3</sub>B** and **DAC-Mes<sub>3</sub>B**

showed sky-blue and blue emission peaks at 487 and 477 nm in 16 wt% doped (Bis[2-(diphenylphosphino)phenyl] ether oxide) (DPEPO) film, respectively. These emitters also showed high PLQY of 1.00 and 0.87 and small  $\Delta E_{ST}$  of 0.058 and 0.062 eV in the doped film state, respectively. The OLED devices showed maximum EQE and the Commission Internationale de l'Éclairage (CIE) color coordinates of 21.6% and (0.18, 0.43) for **2DAC-Mes3B** and 14.0% as well as (0.17, 0.30) for **DAC-Mes3B**. Additionally, Kitamoto et al. (2016) reported another dimesitylarylborane-based blue TADF emitters. They attached carbazole and 9,9-dimethylacridane moieties as electron-donating units (Kitamoto et al., 2016). Both emitters showed blue emission in the toluene solution; however, carbazole-based emitter exhibited a large  $\Delta E_{ST}$  of 0.456 eV and no TADF characteristics. The  $\Delta E_{ST}$  and PLQY of **9,9-dimethyl-10-(4-(dimesitylboryl)phenyl)-9,10-dihydroacridine (DMBP-Ac)** were shown to be 0.041 eV and 0.83 in 6 wt% doped 1,3-Bis(N-carbazolyl)benzene (mCP) film. The OLED device exhibited a maximum EQE of 16.0% and the CIE color coordinates of (0.14, 0.24). They successfully demonstrated the promising potential of organoboron compounds as highly efficient blue TADF emitters. In 2017, Lee et al. (2017) reported triarylboron TADF emitters coupled with the donor in *ortho* and *para* positions. *Ortho*-positioned donor-acceptor skeleton possessed small enough  $\Delta E_{ST}$  to have a good TADF performance, but *para*-positioned emitters had relatively large  $\Delta E_{ST}$ , which was around 0.40 eV. Among *ortho*-positioned emitters, **CzoB** showed a blue emission peak at 466 nm, high PLQY of 0.84, and a small  $\Delta E_{ST}$  of 0.124 eV in 20 wt% of doped DPEPO film. The OLED device showed a maximum EQE of 22.6% (or 24.1%) and CIE color coordinates of (0.139, 0.150) or (0.139, 0.198) depending on the thickness of indium tin oxide (ITO). They showed that spatially hindered *ortho* donor-acceptor skeleton is effective for achieving small  $\Delta E_{ST}$  and efficient TADF emitter. Later, the same group enhanced the TADF device performance and emission color by manipulating the electronic structure (Lee et al., 2018). They synthesized a series of donor-acceptor-type emitters based on **CzoB (BuCzoB, BuCzMeoB, CzMeoB, and CzOMeB)** by introducing substituents into the donor and/or acceptor. They inserted tert-Bu, Me, and OMe into carbazole donor and/or to the phenyl ring of the acceptor. These four emitters showed maximum blue emission peak at 485, 478, 456, and 445 nm in 10–20 wt% doped DPEPO film, respectively. The corresponding PLQYs were 0.91, 0.93, 0.83, and 0.63 and small  $\Delta E_{ST}$  values from 0.084 to 0.14 eV, respectively. The fabricated TADF devices exhibited electroluminescence peak from deep blue to sky blue and high EQE. **BuCzoB** showed a maximum EQE of 26.1% and CIE of (0.142, 0.344). Also, the **BuCzMeoB** device showed the highest EQE of 32.8% and CIE of (0.135, 0.266). On the other hand, **CzMeoB**- and **CzOMeB**-based devices showed a maximum EQE of 18.4 and 17.3% and deep blue color coordinates of (0.138, 0.140) and (0.150, 0.086), respectively. This study showed that the *ortho*-carbazole triarylboron compounds can satisfy the high efficiency of blue TADF emitters. Also, by using substituents to donor and/or acceptor position of CzoB backbone molecule, color and efficiency can be adjusted

successfully. Triarylboron-based blue TADF emitters are listed in **Figure 2** and **Table 1**.

## Partially Bridged Boron-Type Acceptor for Blue Thermally Activated Delayed Fluorescence Emitters

In 2015, Kitamoto et al. (2015) designed boron-incorporated aromatic moiety into the  $\pi$ -conjugated system. Unlike prior triarylboron compounds, they inserted the boron atom into the closed ring system and connected the phenyl linker and donor in the *para* position. They reported 10H-phenoxaborin acceptor-based blue TADF emitters containing carbazole and 9,9-dimethylacridine donors (Kitamoto et al., 2015). They connected 10H-phenoxaborin acceptor and these donors through a phenyl linker at the 1,4 positions. Therefore, quasi anthracene and fluorine units would have a large dihedral angle between hydrogen atoms of phenyl linker, donor, and boron acceptor, resulting in a small overlap of HOMO and LUMO and small  $\Delta E_{ST}$  value. Both molecules showed blue emission in the toluene solution. Even though carbazole-based emitter exhibited deep blue emission, due to the large  $\Delta E_{ST}$  of 0.35 eV, it had no delayed fluorescence component. However, **9,9-dimethyl-10-(4-(10H-phenoxaboryl)phenyl)-9,10-dihydroacridine (DBOP-Ac)** had a small  $\Delta E_{ST}$  of 0.013 eV and high PLQY of 0.98 in 6 wt% doped DPEPO film. The device showed maximum EQE of 15.1% and EL spectrum peak at 466 nm, indicating that the boron-based acceptor can be promising candidates for developing blue TADF emitter. Meanwhile, Numata et al. (2015) reported four types of blue TADF emitters based on 10H-phenoxaborin acceptor and acridan donor units. Using the electron-withdrawing property of boron atom, bulky 2,4,6-triisopropylphenyl (TIPP) unit was directly substituted to boron atom so that it can protect the boron atom against the nucleophilic species such as oxygen and water. In addition, acridan donors and 1,3,6,8-tetramethyl-carbazole were selected as the donor moieties due to their good electron-donating property and expectation of large dihedral angle between acceptor arising from the hydrogen atom. Therefore, they synthesized **9,9-dimethyl-10-(10-(2,4,6-triisopropylphenyl)-10H-dibenzo[b,e][1,4]oxaborinin-3-yl)-9,10-dihydroacridine (PXB-Ac)**, **10-(10-(2,4,6-triisopropylphenyl)-10H-dibenzo[b,e][1,4]oxaborinin-3-yl)-10Hspiro[acridine-9,9'-fluorene] (PXB-SAc)**, **10-(10-(2,4,6-triisopropylphenyl)-10H-dibenzo[b,e][1,4]oxaborinin-3-yl)-10Hspiro[acridine-9,9'-xanthene] (PXB-SAcO)**, and **1,3,6,8-tetramethyl-9-(10-(2,4,6-triisopropylphenyl)-10Hdibenzo[b,e][1,4]oxaborinin-3-yl)-9H-carbazole (PXB-TMCz)**. As expected, all emitters exhibited a small  $\Delta E_{ST}$  of around 0.06–0.12 eV, confirming TADF characteristics. All emitters showed blue emission in toluene solution and maximum PL peaks at 475, 456, 451, and 443 nm and high PLQY of 1.00, 0.76, 0.56, and 0.86 for emitters 1–4, respectively, in 20 wt% doped 2,8-bis(diphenylphosphineoxide)dibenzofuran (PPF) film. The OLED devices based on the TADF emitters (**PXB-Ac**, **PXB-SAc**, **PXB-SAcO**, and **PXB-TMCz**) exhibited high EQE of 21.7, 19.0, 20.1, and 13.3%, respectively, and blue emission. Especially, CIE color coordinates of **PXB-SAcO** and

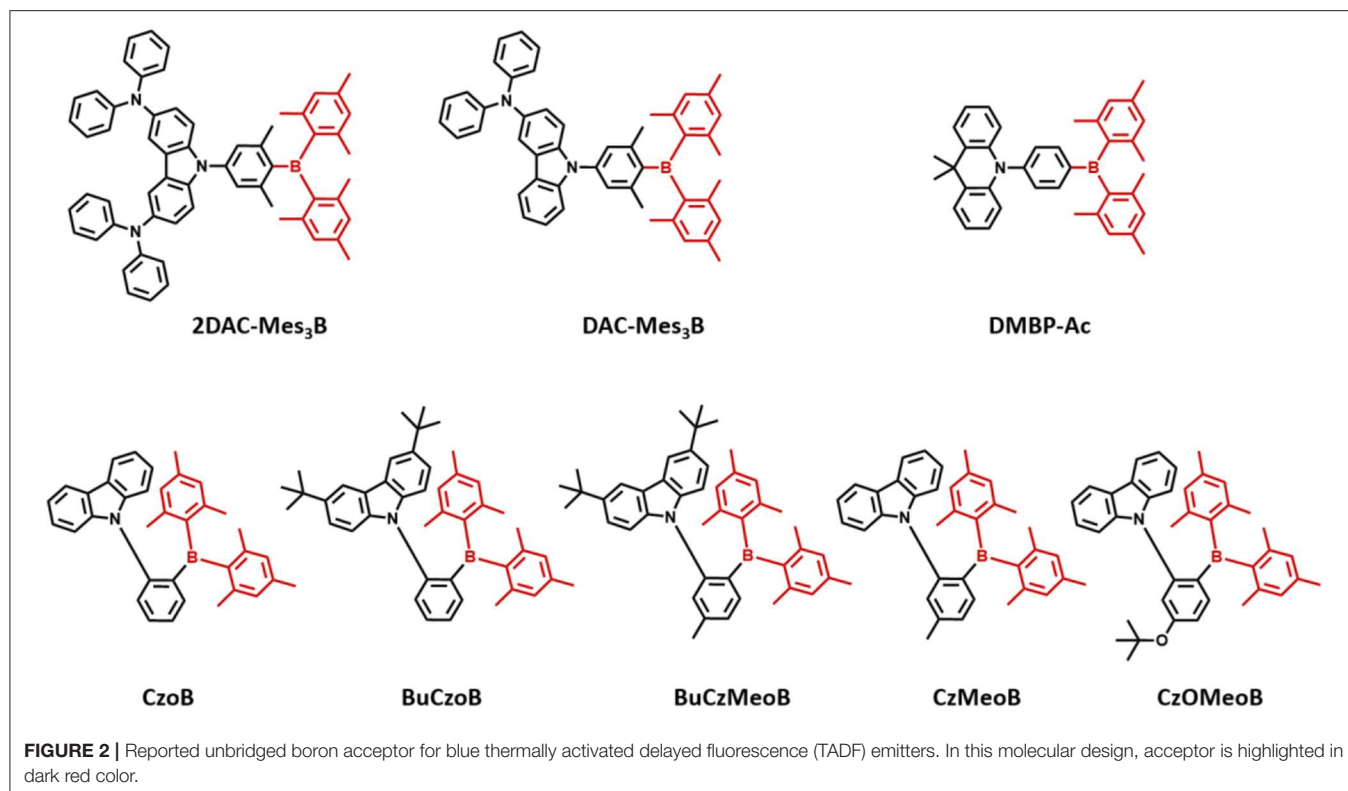


**TABLE 1** | Summary of photophysical properties and device performance of the unbridged boron-type acceptor for blue thermally activated delayed fluorescence (TADF) emitters.

Emitter	$\lambda_{\max}$ [nm]	PLQY	$\Delta E_{\text{ST}}^{\text{d}}$ [eV]	$\tau_{\text{d}}$ $\mu\text{s}$	Host	$\text{EQE}_{\max}$ [%]	$\text{CE}_{\max}$ [ $\text{cdA}^{-1}$ ]	CIE 1931 (x, y)	References
2DAC-Mes <sub>3</sub> B	495 <sup>a</sup>	1.00	0.058	–	DPEPO (16 wt%)	21.6	–	(0.18, 0.43)	Suzuki et al., 2015
DAC-Mes <sub>3</sub> B	477 <sup>a</sup>	0.87	0.062	–	DPEPO (16 wt%)	14.0	–	(0.17, 0.30)	Suzuki et al., 2015
DMBP-Ac	–	0.83	0.041	6.71 <sup>a</sup>	mCP (6 wt%)	16.0	–	(0.14, 0.24)	Kitamoto et al., 2016
CzoB	466 <sup>c</sup>	0.84	0.124	56.3	DPEPO (20 wt%)	22.6	28.5	(0.139, 0.150)	Lee et al., 2017
BuCzoB	485 <sup>b</sup>	0.91	0.084	23.0	DPEPO (10 wt%)	26.1	56.9	(0.142, 0.344)	Lee et al., 2018
BuCzMeoB	478 <sup>c</sup>	0.93	0.092	26.6	DPEPO (20 wt%)	32.8	56.8	(0.135, 0.266)	Lee et al., 2018
CzMeoB	456 <sup>c</sup>	0.83	0.13	76.3	DPEPO (20 wt%)	18.4	20.4	(0.138, 0.140)	Lee et al., 2018
CzOMeOB	445 <sup>c</sup>	0.63	0.14	87.3	DPEPO (20 wt%)	17.3	13.1	(0.150, 0.086)	Lee et al., 2018

<sup>a</sup> Measured in oxygen-free toluene solution ( $10^{-5}$  M).

<sup>b</sup> Measured in 10 wt% doped film in DPEPO host.

<sup>c</sup> Measured in 20 wt% doped film in DPEPO host.

<sup>d</sup>  $\Delta E_{\text{ST}} = S_1 - T_1$ .

PXB-TMCz were (0.14, 0.16). Later, the same group reported phenazineboron-based blue TADF emitter by using spiro-acridan donor, **MFAC-AzB** (Park et al., 2016). For blue emission wavelength, they inserted a phenyl-substituted amino unit in phenazaborin acceptor to weaken the electron-withdrawing

ability of the boron atom. Therefore, their synthesized **MFAC-AzB** material showed a blue emission peak at 467 nm in 20 wt% doped PPF film. Moreover, **MFAC-AzB** exhibited a small  $\Delta E_{\text{ST}}$  value of 0.24 eV and PLQY value of 0.99 in 20 wt% doped PPF film and even 0.53 in the neat film state. The **MFAC-AzB**



device showed a maximum EQE of 18.2% and CIE coordinates of (0.15, 0.23). Both studies demonstrated the suitability of 10H-phenoxaborin or phenazineborin compounds for highly efficient blue emission TADF materials. Later, Park et al. (2018) studied a series of dibenzoheteraborin-based blue TADF emitters. They designed a boron center and adjustable bridging heteroatoms, such as sulfur, oxygen, or nitrogen and connected to the dimethyl-diphenylacridan (MPAc) donor. Among them, oxygen-containing **MPAc-Bo** and nitrogen-containing **MPAc-BN** emitters showed blue emission in devices. They exhibited emission peak at 483 and 465 nm and a small  $\Delta E_{ST}$  of 0.024 and 0.05 eV in 50 wt% doped PPF film for MPAc-Bo and MPAc-BN. Moreover, these emitters showed high PLQY values of 0.99 and 0.75 in the same film condition. In the device, **MPAc-Bo** and **MPAc-BN** exhibited sky-blue emission and corresponding CIE color coordinates of (0.16, 0.38) and (0.14, 0.23). The **MPAc-Bo** and **MPAc-BN**-based devices exhibited maximum EQE of 24.9 and 16.0%, respectively. They developed highly efficient blue TADF emitters utilizing dibenzoheteraborin acceptors such as phenoxaborin and phenazaborin and donor diphenylacridan (MPAc). In 2019, Ahn et al. (2019b) reported two highly efficient blue TADF emitters by using the 10H-phenoxaborin acceptor and two types of indolocarbazole derivative donors, **PXB-mIC** and **PXB-DI**. Due to the weak electron-donating ability of simple carbazole, they introduced carbazole derivative donors such as indolocarbazole and diindolocarbazole (DI). The large electron planes of donors delivered large spatial HOMO volume, leading to high oscillator strength and high PLQY. Also, *meta*-positioned indole moiety caused high steric hindrance between the acceptor and donor, which results in small  $\Delta E_{ST}$  and good TADF performance. The **PXB-DI** and **PXB-mIC** showed blue emission in the toluene solution (emission peak at 458 and 438 nm) and a small  $\Delta E_{ST}$  of 0.09 and 0.19 eV, respectively. Moreover, **PXB-DI** showed a high PLQY of about 0.971 in 20% doped bis(diphenylphosphine oxide)dibenzofuran (DBFPO) film. On the other hand, **PXB-mIC** showed PLQY of 0.631 in the same conditions. Interestingly, **PXB-DI** device exhibited a maximum EQE of 37.4% and CIE color coordinates of (0.16, 0.34). Also, **PXB-mIC** device exhibited a maximum EQE of 18.8% and CIE color coordinates of (0.14, 0.18). Especially, **PXB-mIC** exhibited national television system committee (NTSC) blue characteristic of (0.14, 0.08) and 12.5% of maximum EQE in 5-(5-(2,4,6-triisopropylphenyl)pyridin-2-yl)-5H-benzo[d]benzo[4,5]imidazo[1,2-a]imidazole (PPBI) host (Figure 3).

Later, Agou et al. (2020) reported the pentacyclic ladder-heteraborin blue TADF emitters. Many researchers have investigated the boron-containing  $\pi$ -electron system because of its fascinating properties in terms of TADF emitter. Agou et al. (2006, 2007a,b) reported  $\pi$ -extended ladder-type heteraborins, and they showed novel  $\pi$ -extended ladder-type blue TADF emitters, **MCz-BOBO** and **MCz-BSBS**, by using oxaborin and thiaborin acceptor and MCz donor units, respectively. The **MCz-BOBO** showed a PL emission peak at 476 nm in 20 wt% doped PPF film and a small  $\Delta E_{ST}$  of 0.01 eV. However, **MCz-BSBS** showed a slightly red-shifted emission peak at 483 nm and  $\Delta E_{ST}$  of 0.17 eV. Both emitters exhibited high PLQY values of

1.0 and 0.93, respectively. The **MCz-BOBO** device exhibited maximum EQE of 20.1% and CIE color coordinates of (0.13, 0.20). Also, **MCz-BSBS** showed a maximum EQE of 25.9% and CIE color coordinates of (0.14, 0.33). Both  $\pi$ -extended heteraborins and multi heteroatoms-based materials successively demonstrated excellent blue TADF performance and suggested the development of highly efficient blue TADF emitters.

In 2019, Matsuo and Yasuda (2019) reported boronate- and borinate-based blue TADF emitters. To accomplish a wider energy gap for blue emission wavelength, they examined boronated and borinated esters. They expected that nearby oxygen atoms can donate electrons and diminish the electron-withdrawing ability of boron acceptors. The superiority of borinate- and boronate-containing TADF emitters has not been elucidated yet. Therefore, they synthesized two types of boronate TADF emitter, **10-(8,9-dioxa-8a-borabenzofluorene-2-yl)-2,7-dimethyl-10H-spiro[acridine-9,9'-fluorene]** (**DOB-MSAc**) and **10-(8,9-dithia-8a-borabenzofluorene-2-yl)-2,7-dimethyl-10H-spiro[acridine-9,9'-fluorene]** (**DSB-MSAc**), and one borinate-based TADF emitter, **2,7-dimethyl-10-(6-(2,4,6-triisopropylphenyl)-6H-dibenzo[c,e][1,2]oxaborinin-9-yl)-10H-spiro[acridine-9,9'-fluorene]** (**OB-MSAc**), using spiro[2,7-dimethylacridan-9,9'-fluorene] as a donor moiety. Boronate-based TADF emitters **DOB-MSAc** and **OB-MSAc** showed PL peaks at 462 and 448 nm in toluene solution, which was significantly blue-shifted compared to that of phenoxaborin-based TADF emitter **MPAc-BO** (477 nm). However, boronate-thioester-based emitter (**DSB-MSAc**) showed a PL peak at 483 nm, and this was slightly blue-shifted compared to the **MPAc-BS** (493 nm). These results are attributed to the decreased electron-accepting ability by replacing of the B-C bond with B-O or B-S bond. Their PLQY and PL peak values in 20 wt% doped PPF films were 0.28, 0.81, and 0.53, and 470, 491, and 458 nm, respectively. They also had a small  $\Delta E_{ST}$  of 0.30, 0.12, and 0.06 eV for **DOB-MSAc**, **DSB-MSAc**, and **OB-MSAc**, respectively. In devices, **DOB-MSAc** and **OB-MSAc** exhibited the maximum EQE (CIE color coordinates) of 5.2% (0.16, 0.22) and 12.8% (0.15, 0.15), respectively. Especially, **DSB-MSAc** showed the highest maximum EQE of 20.9% and CIE color coordinates of (0.17, 0.39) due to its high PLQY. They demonstrated a new molecular design for blue TADF by changing heteroatoms directly connected to the boron atom. The abovementioned partially bridged boron blue TADF emitters are listed in Figure 4 and Table 2.

Later, Li P. et al. (2019) reported a new class of four-coordinate fluoroboron acceptor TADF emitters for the first time. They supposed that susceptible cleavage of B-C bond and vacant p-orbital on central boron atom can be the critical reason for short device lifetime. Therefore, they designed four-coordinate boron-centered tridentate 2,2'-(pyridine-2,6-diyl) diphenolate (dppy) ligand, which is O $\wedge$ N $\wedge$ O type of chelate anticipating better chemical and thermal stabilities. They employed 3,6-di-tert-butylcarbazole (DTC) as an electron donor moiety. **DTC-Ph(dppy)BF** showed the blue emission peak at 468 nm and a small  $\Delta E_{ST}$  of 0.27 eV in the toluene solution. Also, the PLQY value was 0.71 in 5 wt% doped of mCP film. Due to the relatively



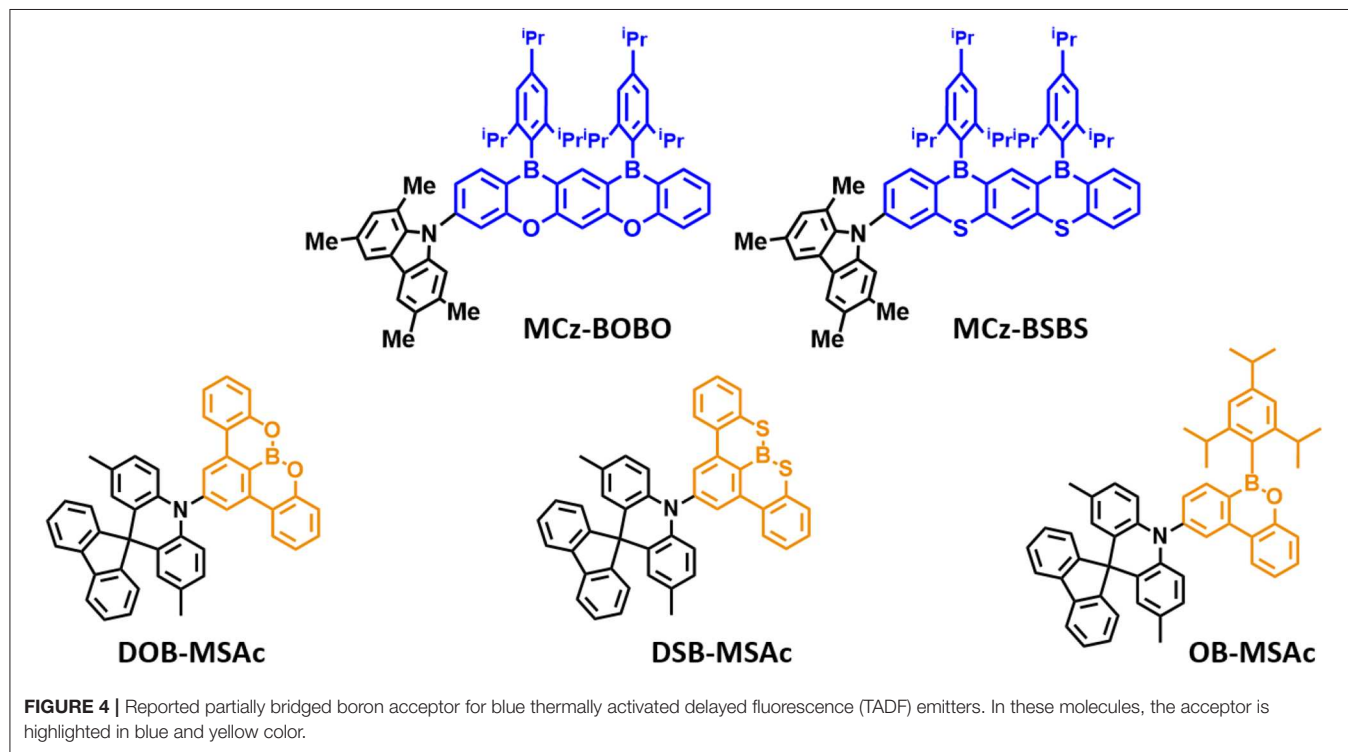
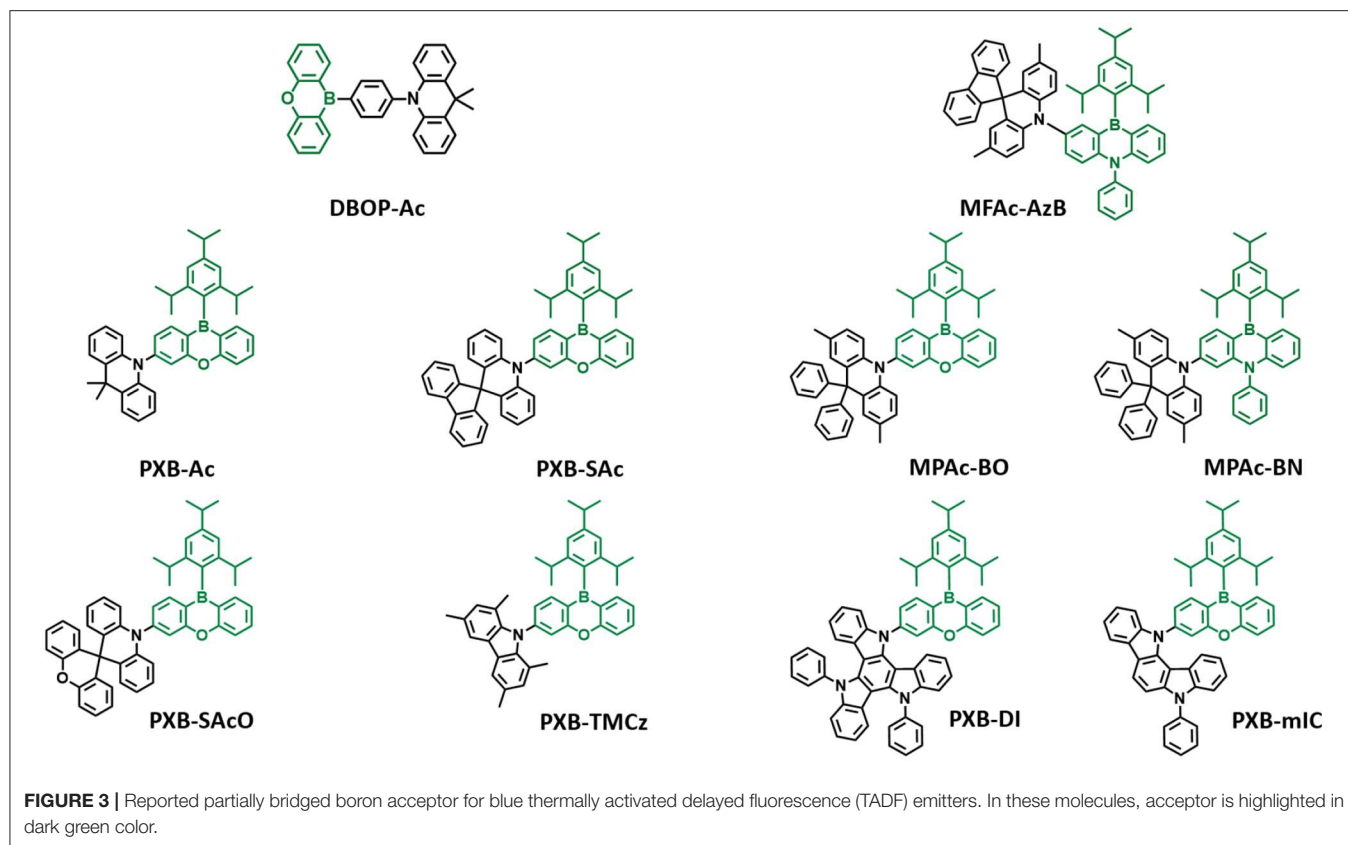


**TABLE 2 |** Summary of photophysical properties and device performance of the partially bridged boron-based type blue thermally activated delayed fluorescence (TADF) emitters.

Emitter	$\lambda_{\max}$ [nm]	PLQY	$\Delta E_{ST}^d$ [eV]	$\tau_d$ $\mu s$	Host	$EQE_{\max}$ [%]	$CE_{\max}$ [cdA <sup>-1</sup> ]	CIE 1931 (x, y)	References
DBOP-Ac	—	0.98	0.013	—	DPEPO (6 wt%)	15.1	—	—	Kitamoto et al., 2015
PXB-Ac	475 <sup>a</sup>	1.00	0.10	1.60 <sup>a</sup>	PPF (50 wt%)	21.7	—	—	Numata et al., 2015
PXB-Sac	456 <sup>a</sup>	0.76	0.12	4.02 <sup>a</sup>	PPF (20 wt%)	19.0	—	—	Numata et al., 2015
PXB-SAcO	451 <sup>a</sup>	0.56	0.06	2.06 <sup>a</sup>	PPF (20 wt%)	20.1	—	(0.14, 0.16)	Numata et al., 2015
PXB-TMCz	443 <sup>a</sup>	0.86	0.12	3.49 <sup>a</sup>	PPF (20 wt%)	13.3	—	(0.14, 0.16)	Numata et al., 2015
MFAC-AzB	467 <sup>c</sup>	0.99	0.24	91 PPF (20 wt%)	PPF (20 wt%)	18.2	32.6	(0.15, 0.23)	Park et al., 2016
MPAc-BO	483 <sup>b</sup>	0.99	0.024	1.8 PPF(50 wt%)	PPF (50 wt%)	24.9	57.0	(0.16, 0.38)	Park et al., 2018
MPAc-BN	465 <sup>b</sup>	0.75	0.05	18 PPF (50 wt%)	PPF (50 wt%)	16.0	23.7	(0.14, 0.23)	Park et al., 2018
PXB-mIC	438 <sup>a</sup>	0.631	0.19	3.89/4.04 DBFPO/PPBI (20 wt%)	DBFPO/PPBI (20 wt%)	18.8/12.5	22.1/8.6	(0.14, 0.18)/ (0.14, 0.08)	Ahn et al., 2019b
PXB-DI	458 <sup>a</sup>	0.971	0.09	2.57/3.33 DBFPO/PPBI (20 wt%)	DBFPO/PPBI (20 wt%)	37.4/28.4	66.2/37.8	(0.16, 0.34)/ (0.14, 0.20)	Ahn et al., 2019b
MCz-BOBO	476 <sup>c</sup>	1.00	0.01	0.78 PPF (20 wt%)	PPF (20 wt%)	20.1	31.5	(0.13, 0.20)	Agou et al., 2020
MCz-BSBS	483 <sup>c</sup>	0.93	0.17	2.7 PPF (20 wt%)	PPF (20 wt%)	25.9	52.9	(0.14, 0.33)	Agou et al., 2020
DOB-MSAc	470 <sup>c</sup>	0.28	0.30	140 PPF (20 wt%)	PPF (20 wt%)	5.2	—	(0.16, 0.22)	Matsuo and Yasuda, 2019
DSB-MSAc	491 <sup>c</sup>	0.81	0.12	22 PPF (20 wt%)	PPF (20 wt%)	20.9	—	(0.17, 0.39)	Matsuo and Yasuda, 2019
OB-MSAc	458 <sup>c</sup>	0.53	0.06	12 PPF (20 wt%)	PPF (20 wt%)	12.8	—	(0.15, 0.15)	Matsuo and Yasuda, 2019

<sup>a</sup> Measured in oxygen-free toluene solution (10<sup>-5</sup> M).<sup>b</sup> Measured in 50 wt% doped film in PPF host.<sup>c</sup> Measured in 20 wt% doped film in PPF host.<sup>d</sup>  $\Delta E_{ST} = S_1 - T_1$ .

large  $\Delta E_{ST}$  value, RISC efficiency was limited, and maximum EQE was up to 8.8% and CIE color coordinates of (0.16, 0.31). However, the half-lifetime at a constant driving current density of 10 mA/cm<sup>2</sup> reached to 2,354 h. They demonstrated the first trial of design and synthesis of four-coordinate boron and tridentate dppy ligand-based blue TADF emitters. Later, Li G. et al. (2019) reported a new series of tetracoordinated blue TADF emitters using donor–acceptor BF<sub>2</sub>-type skeleton. Tetracoordinated difluoroboron molecules are air-stable, and they can enhance the molecular rigidity to have a high PLQY. They synthesized a series of BF<sub>2</sub>-type acceptor using different donors, especially **NOBF<sub>2</sub>-Cz**, **NOBF<sub>2</sub>-DTCz**, **NOBF<sub>2</sub>-DPCz**, and **NOBF<sub>2</sub>-DMAC**. Except for **NOBF<sub>2</sub>-DMAC**, the other three emitters showed blue emission in the toluene solution from 449 to 473 nm and a small  $\Delta E_{ST}$  of around 0.20 eV. The PLQY values of **NOBF<sub>2</sub>-Cz**, **NOBF<sub>2</sub>-DTCz**, and **NOBF<sub>2</sub>-DPCz** in 10 wt% doped DPEPO film were 0.99, 0.74, 0.70, respectively. In device, they showed the maximum EQE and CIE color coordinates of 11.0% and (0.14, 0.16) for **NOBF<sub>2</sub>-Cz**, 12.7% and (0.14, 0.21) for **NOBF<sub>2</sub>-DTCz**, and 15.8% and (0.14, 0.28) for **NOBF<sub>2</sub>-DPCz**. They demonstrated that tetracoordinated difluoroboron-based

materials can act as stable and efficient TADF emitters (**Figure 5** and **Table 3**).

Three-coordinate organoborane compounds successfully act as electron acceptors in the blue TADF, and in most cases, reactive boron center is surrounded by sterically bulky 2,4,6-trimethylphenyl (Mes) groups. Although these bulky aryl groups protect the center boron from hydrolysis and unstable conditions, highly steric moieties disturb intermolecular interaction and cause detrimental results in solid-state performance. And the sole boron atom itself was not enough to satisfy the deep blue emission. Therefore, researchers searched the alternative strategy not only stabilizes the boron but also tunes deeper blue emission, so that they inserted the boron atom in  $\pi$ -conjugated system with heteroatoms. This strategy enables us to have a structurally constraint skeleton, good molecular rigidity, and intermolecular interaction in solid state. Secondly, by introducing the heteroatom, better TADF properties and pure blue color were achieved, demonstrating partially bridged boron-based TADF more sufficiently satisfied the requirement of blue material.

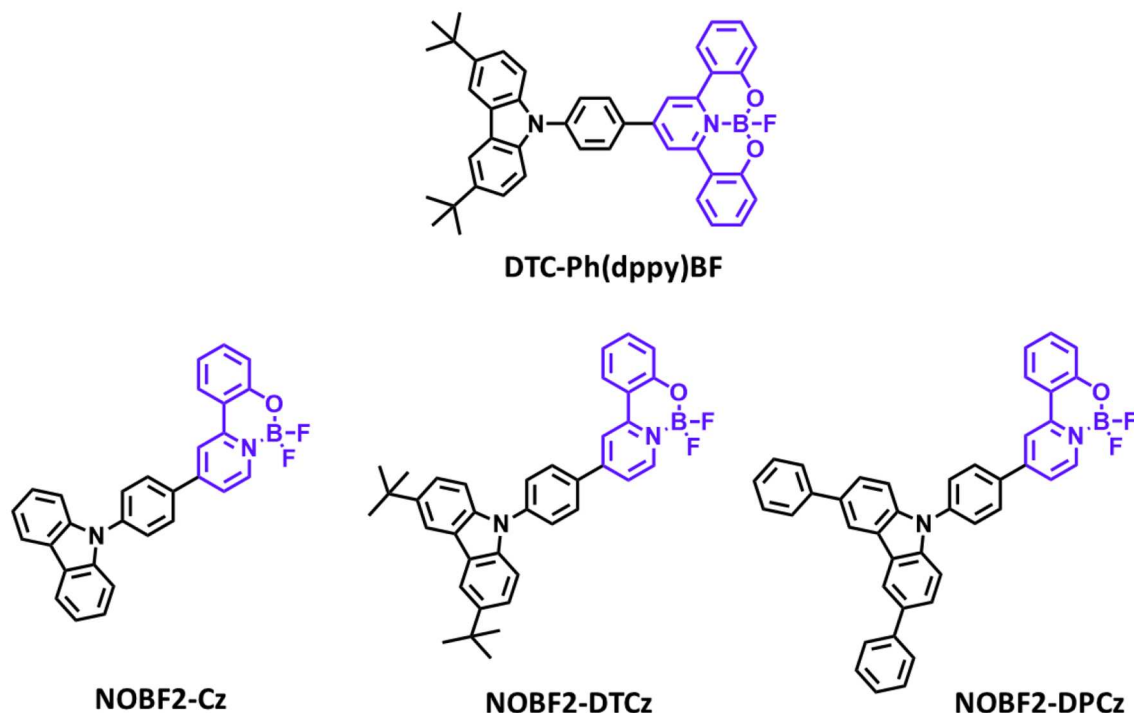


**FIGURE 5** | Reported partially bridged boron acceptors for blue thermally activated delayed fluorescence (TADF) emitters. In these molecules, acceptor is highlighted in purple color.

**TABLE 3** | Summary of photophysical properties and device performance of the tetracoordinated difluoroboron-based blue thermally activated fluorescence (TADF) emitters.

Emitter	$\lambda_{\max}$ [nm]	PLQY	$\Delta E_{ST}^b$ [eV]	$\tau_d$ $\mu s$	Host	$EQE_{\max}$ [%]	$CE_{\max}$ [cdA <sup>-1</sup> ]	CIE 1931 (x, y)	References
DTC-Ph(dppy)BF	468 <sup>a</sup>	0.71	0.27	—	mCBP (14 wt%)	8.8	17.9	(0.16, 0.31)	Li P. et al., 2019
NOBF2-Cz	449 <sup>a</sup>	0.99	0.20	132	mCBP (10 wt%) DPEPO (10 wt%)	11.0	12.6	(0.14, 0.16)	Li G. et al., 2019
NOBF2-DTCz	473 <sup>a</sup>	0.74	0.20	126	mCBP (10 wt%) DPEPO (10 wt%)	12.7	40.6	(0.14, 0.21)	Li G. et al., 2019
NOBF2-DPCz	471 <sup>a</sup>	0.70	0.22	110	mCBP (10 wt%) DPEPO (10 wt%)	15.8	25.3	(0.14, 0.28)	Li G. et al., 2019

<sup>a</sup> Measured in oxygen-free toluene solution ( $10^{-5}$  M).

<sup>b</sup>  $\Delta E_{ST} = S_1 - T_1$ .

## Oxygen-Based Fully Bridged Boron-Type Acceptor for Blue Thermally Activated Delayed Fluorescence Emitters

Recently, triarylboron-based acceptors consisting bridged cyclized unit in donor-acceptor structure have reported good blue TADF performance. Normally, both nitrogen- or oxygen-based fully bridged boron-type acceptor-based materials showed deep-blue emission, narrow FWHM, and good TADF performance. Therefore, such acceptor structure can be used for the design of efficient and stable TADF emitters.

Recently, very few oxygen-based fully bridged boron type TADF emitters have reported by attaching a donor unit to

the central phenyl ring of the oxygen-based fully bridged boron unit on the para-position of the boron atom. The initial sky-blue TADF emitter containing oxygen-based fully bridged boron acceptor and phenoxazine donor (**10-(5,9-dioxo-13b-boranaphtho[3,2,1-de]anthracene-7-yl)-10H-phenoxazine** (DOBNA-PX) was reported by Hirai et al. (2015) in 2015. Their emitter showed a sky-blue emission (492 nm), absolute PLQY of 0.92 in 1 wt% doped poly(methyl methacrylate) (PMMA) film, and a small  $\Delta E_{ST}$  of 0.06 eV due to the localization of the single occupied molecular orbitals (SOMOs). They showed an EQE of about 13.9% for the DOBNA-PX-based OLED. Though the performances of DOBNA-PX emitters are lower than the

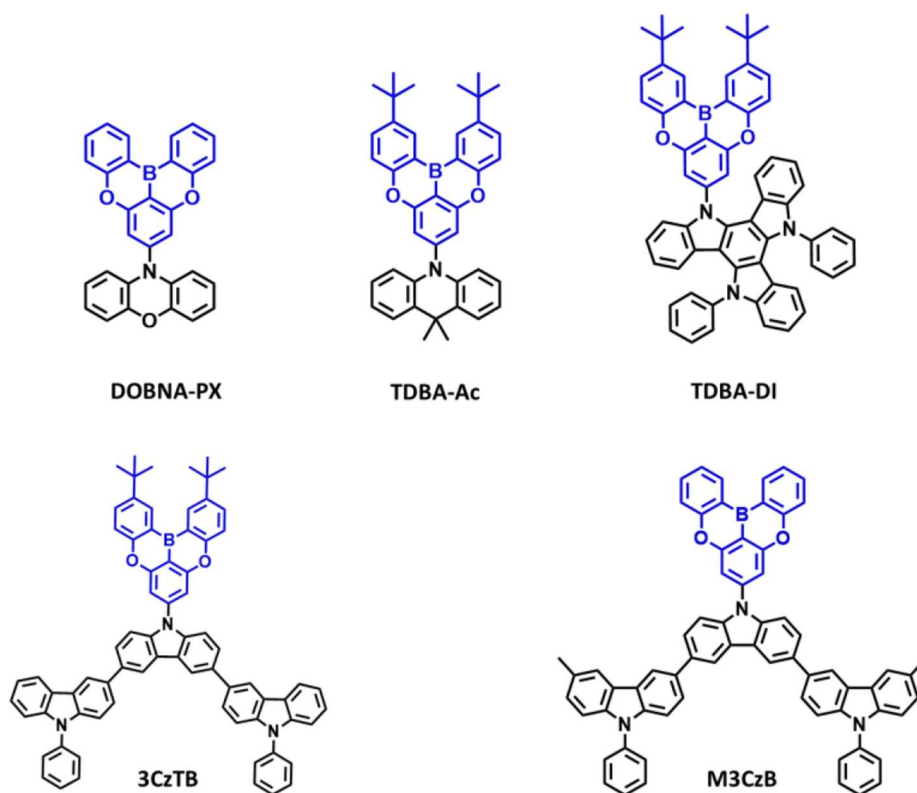


**FIGURE 6** | Reported structures of blue thermally activated delayed fluorescence (TADF) emitters using oxygen-based fully bridged boron acceptor and different donors.

expectation, this study showed the suitable properties of blue TADF emitters. This acceptor moiety can also act as a strong electron acceptor, and it can be suitable to achieve horizontal molecular orientation because of its rigid and symmetrical configuration (Kim and Kim, 2018).

Secondly, in 2019, Ahn et al. (2019a) reported two new highly efficient blue TADF emitters, **TDBA-Ac** and **TDBA-DI** (Figure 6). To satisfy the requirements of the blue TADF materials, they used oxygen-based fully bridged triarylboron with tert-butyl group on the periphery of terminal phenyl ring as an acceptor and DI or acridine (Ac) as donor in the emitter structure. They found that rigid ring-based DI can be used to achieve a large twist angle with an acceptor (Kim et al., 2018). Both emitters, **TDBA-Ac** and **TDBA-DI**, showed a deep-blue emission and maximum PL peak at 458 and 456 nm, respectively, in solution state. These emitters also exhibited a narrow FWHM of about 50 (**TDBA-Ac**) and 55 nm (**TDBA-DI**). The calculated singlet and triplet energies from the onset of the RTPL and LTPL spectra of **TDBA-Ac** and **TDBA-DI** were 3.11/3.05 and 3.06/2.95 eV, respectively. Both of these emitters exhibited small  $\Delta E_{ST}$  values of 0.06 (in solution state) and 0.05 eV (20 wt% doped **TDBA-DI** in DBFPO film) for **TDBA-Ac** and **TDBA-DI**, respectively. They found a delayed exciton lifetime of 1.82 and 1.79  $\mu$ s for **TDBA-Ac** and **TDBA-DI**, respectively, which was shorter than the reported blue TADF

emitters. **TDBA-Ac** (20 wt%) and **TDBA-DI** (20 wt%) in the DBFPO host showed a PLQY of 0.93 and 0.99, respectively. Also, the HOMO dispersing molecular design of emitters and low non-radiative decay rates were responsible for achieving high PLQY. The **TDBA-Ac**- and **TDBA-DI**-based OLEDs (DBFPO host) exhibited maximum EQE of 25.71 and 38.15%, respectively. The **TDBA-DI** device showed a maximum luminance of 47,680  $\text{cd/m}^2$  and a horizontal dipole orientation ratio of 0.89. Such high efficiency, high luminance, and good color coordinates were attributed to the highly conjugated and rigid donor and acceptor combination for high PLQY and narrow emission, the large dihedral angle between the donor and acceptor for small  $\Delta E_{ST}$ , fast RISC, and horizontal molecular orientation. Also, the **TDBA-DI** emitter and mCBP-CN host system device showed an operational lifetime ( $T_{50}$ ) of 55.2 h at the initial luminance of 1,000  $\text{cd/m}^2$ . They also reported **DBA-DI** emitter by removing tert-butyl from the **TDBA-DI** to achieve high efficiency and long lifetime (Ahn et al., 2020). The **DBA-DI** showed slight variations in the photophysical properties compared to the **TDBA-DI** as shown in Table 4. However, the **DBA-DI** device exhibited high EQE of 26.4%, CIE color coordinates of (0.17, 0.40), and lifetime of 540 h at the initial luminance of 1,000  $\text{cd/m}^2$ .

Later, they reported a series of blue TADF emitters consisting of oxygen-based fully bridged triarylboron acceptor and tercarbazole donor. These two emitters, **3CzTB** and **M3CzB**,



**TABLE 4 |** Summary of photophysical and device characteristics of the oxygen-based fully bridged boron type blue thermally activated delayed fluorescence (TADF) emitters.

Emitter	$\lambda_{\text{max}}$ [nm]	PLQY	$\Delta E_{\text{ST}}^d$ [eV]	$\tau_d$ $\mu\text{s}$	Host	$\text{EQE}_{\text{max}}$ [%]	$\text{CE}_{\text{max}}$ [ $\text{cdA}^{-1}$ ]	CIE 1931 (x, y)	References
DOBNA-PX	492 <sup>c</sup>	0.92	0.06	31.8 PMMA (1wt%)	CBP (20 wt%)	13.9	40.1	–	Hirai et al., 2015
TDBA-Ac	458 <sup>a</sup>	0.93	0.06	1.82 DBFPO (20 wt%)	DBFPO (20 wt%)	25.71	27.73	(0.14, 0.15)	Ahn et al., 2019a
TDBA-DI	456 <sup>a</sup>	0.99	0.05	1.79 DBFPO (20 wt%)	DBFPO (20 wt%)	38.15	64.38	(0.15, 0.28)	Ahn et al., 2019a
DBA-DI	467 <sup>a</sup>	95.3	0.03	1.25 mCBP-CN (30 wt%)	mCBP-CN: DDBFT (30 wt%)	26.4	–	(0.17, 0.40)	Ahn et al., 2020
3CzTB	433 <sup>a</sup>	0.87	0.23	9.32 DBFPO (20 wt%)	DBFPO (20 wt%)	29.1	36.4	(0.14, 0.19)	Karthik et al., 2020
M3CzB	445 <sup>a</sup>	0.92	0.14	7.84 DBFPO (20 wt%)	DBFPO (20 wt%)	30.7	46.7	(0.14, 0.26)	Karthik et al., 2020
OBA-O	444 <sup>a</sup>	0.84	0.09	4.14 mCP (10 wt%)	mCP (5 wt%)	17.8	33.2	(0.17, 0.17)	Song et al., 2019
OBA-S	456 <sup>a</sup>	0.75	0.09	4.80 mCP (10 wt%)	mCP (5 wt%)	4.4	6.3	(0.20, 0.31)	Song et al., 2019
OBA-BrO	470 <sup>a</sup>	0.92	0.04	3.74 mCP (10 wt%)	mCP (5 wt%)	22.5	49.2	(0.21, 0.38)	Song et al., 2019
OBA-BrS	478 <sup>a</sup>	0.55	0.07	0.81 mCP (10 wt%)	mCP (5 wt%)	9.2	20.3	(0.29, 0.46)	Song et al., 2019
m-AC-DBNA	492 <sup>b</sup>	0.89	0.009	7.6 BCPO (5 wt%)	BCPO (10 wt%)	17.1	42.0	(0.18, 0.42)	Meng et al., 2019
m'-AC-DBNA	498 <sup>b</sup>	0.96	0.031	1.5 BCPO (5 wt%)	BCPO (10 wt%)	14.1	35.3	(0.18, 0.39)	Meng et al., 2019
p-AC-DBNA	496 <sup>b</sup>	0.87	0.009	7.8 BCPO (5 wt%)	BCPO (10 wt%)	20.5	47.4	(0.17, 0.36)	Meng et al., 2019

<sup>a</sup> Measured in toluene solvent.<sup>b</sup> Measured in 10 wt% doped film in BCPO host.<sup>c</sup> Measured in 1 wt% doped film in PMMA host.<sup>d</sup>  $\Delta E_{\text{ST}} = S_1 - T_1$ .

were designed by alkyl modification on the donor and acceptor units, which changes not only their donor–acceptor interaction but also the electronic nature (Karthik et al., 2020). 6,6'-Dimethyl substituted tercarbazole moiety was used as a donor unit and attached to the oxygen-based fully bridged triarylboron acceptor (**M3CzB**) to improve the electrochemical stability of the TADF emitter. The tert-butyl-modified boron acceptor has attached to the methyl group-modified tercarbazole donor (**3CzTB**) to tune the acceptor strength. These emitters, **3CzTB** and **M3CzB**, showed emission wavelength and  $\Delta E_{\text{ST}}$  of 433 nm and 0.23 eV and 445 nm and 0.14 eV, respectively, in the solution state. Also, **3CzTB** and **M3CzB** showed a delayed exciton lifetime of 9.32 and 7.84  $\mu\text{s}$ , respectively, which was measured from the 20 wt% doped DBFPO films. However, **M3CzB** showed a higher RISC rate and lower triplet non-radiative rate compared to the **3CzTB** because of its low  $\Delta E_{\text{ST}}$ . The **3CzTB**- and **M3CzB**-based OLEDs exhibited a high EQE of 29.1 and 30.7%, respectively, which was attributed to the high PLQY, fast RISC, and horizontal dipole orientation of the emitter. These devices also showed a maximum luminance of 18,160  $\text{cd}/\text{m}^2$  for **M3CzB** and 11,690  $\text{cd}/\text{m}^2$  for **3CzTB**.

Recently, several other TADF materials were synthesized by attaching different donor units to the central phenyl ring of the oxygen-based fully bridged boron acceptor (**OBA**) on the meta-position of the boron. Song et al. (2019) reported four new TADF emitters, **OBA-O**, **OBA-S**, **OBA-BrO**, and **OBA-BrS**, by using oxygen-based fully bridged boron acceptors (**OBA** or **DBA**) and phenoxazine or phenothiazine donors (**Figure 7**). Also, they attached Br- group to the **OBA** unit (**OBA-Br**) to improve the TADF properties of the emitter. The phenothiazyl-based emitters showed longer maximum emission wavelengths of 456 (**OBA-S**) and 478 nm (**OBA-BrS**) in the solution state compared to phenoxazyl-based materials (**OBA-O**: 444 nm and **OBA-BrO**: 470 nm) because of stronger donating ability of the phenothiazyl. The blue TADF emitter **OBA-O** and its blue analog **OBA-BrO** showed higher PLQY values of 0.84 and 0.92, respectively, than both **OBA-S** (0.75) and **OBA-BrS** (0.55). All these emitters showed very small  $\Delta E_{\text{ST}}$  values <0.1 eV and good TADF properties due to the large twist angle near to 90° between the donor and acceptor, which makes separation of the natural transition orbitals. They achieved  $\Delta E_{\text{ST}}$  of 0.09 eV for **OBA-O** and **OBA-S**, while 0.04 and 0.07 eV for **OBA-BrO** and

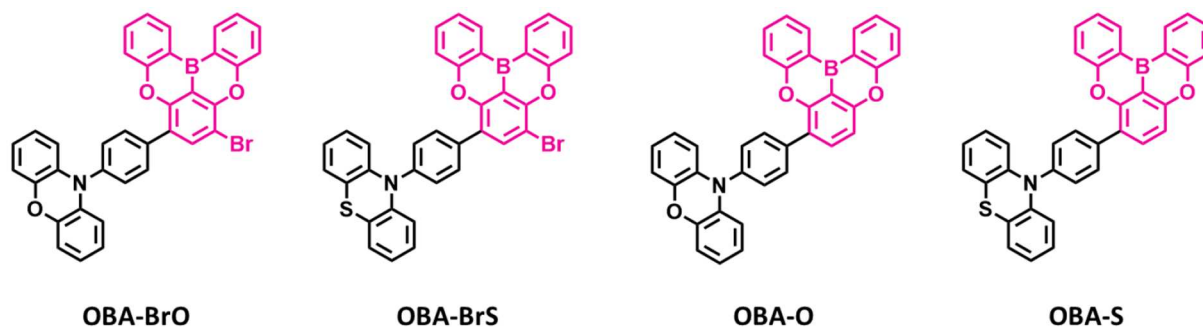


**FIGURE 7** | Reported structures of blue thermally activated delayed fluorescence (TADF) emitters using oxygen-based fully bridged boron acceptor and different donors.

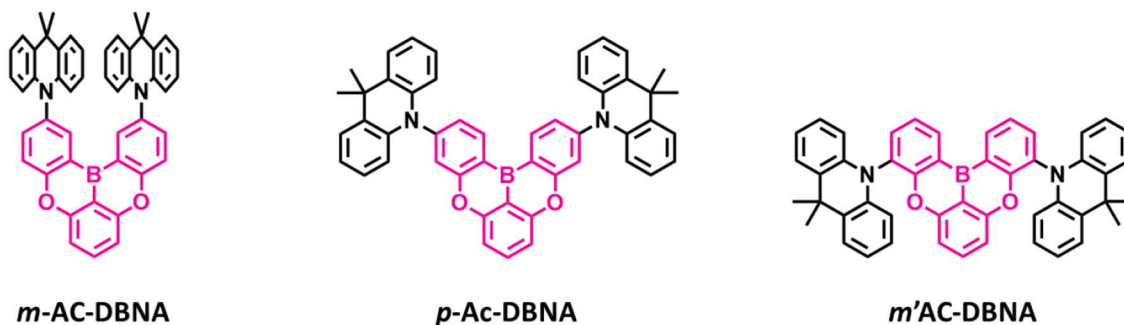


**FIGURE 8** | Reported structures of blue thermally activated delayed fluorescence (TADF) emitters using donor units attached to the different positions of the boron-based acceptor.

**OBA-BrS**, respectively. On the other hand, both -Br-attached TADF emitters showed shorter delayed exciton lifetime (higher  $K_{\text{RISC}}$ ) of  $3.74$  ( $8.97 \times 10^5 \text{ s}^{-1}$ ) and  $0.81 \mu\text{s}$  ( $8.41 \times 10^5 \text{ s}^{-1}$ ) for **OBA-BrO** and **OBA-BrS**, respectively, compared to **OBA-O** ( $4.14 \mu\text{s}$  and  $4.28 \times 10^5 \text{ s}^{-1}$ ) and **OBA-S** ( $4.80 \mu\text{s}$  and  $2.76 \times 10^5 \text{ s}^{-1}$ ) due to their smaller  $\Delta E_{\text{ST}}$  values. Such a high  $K_{\text{RISC}}$  was attributed to the electron-withdrawing ability of -Br group on the OBA acceptor that will improve the TADF process in **OBA-BrO** and **OBA-BrS**. **OBA-O** and **OBA-BrO** devices showed higher EQE of 17.8 and 22.5% than **OBA-S** (4.4%) and **OBA-BrS** (9.2%) devices because of their higher PLQY values. Among these TADF materials, **OBA-O** device showed the bluest CIE color coordinates (0.17, 0.17) and a maximum EL peak of 446 nm. However, other emitter-based devices showed sky-blue CIE color coordinates (**Table 4**).

Also, another series of TADF emitters were reported by using donor unit into the different positions of the oxygen-based fully bridged boron acceptor. Meng et al. (2019) reported the effect of substitutional positions of the donor group on the TADF properties of the oxygen-based fully bridged boron-type acceptor-based emitter. They synthesized three different boron-based TADF emitters, **m-AC-DBNA**, **p-AC-DBNA**, and **m'-AC-DBNA**, by using two dimethyl Ac units at meta-, para-, and meta'-positions of the 5,9-dioxa-13b-boranaphtho[3,2,1-de]anthracene (DBNA) (**Figure 8**). They selected Ac as a donor

unit because of its strong electron-donating property and suitable steric hindrance for the TADF molecule. They checked an effect of such molecular design on intermolecular interactions, thermal and photophysical properties, and EL performance. All three emitters showed an emission peak at 514–518-nm range (film state). However, PL properties of 5 wt% emitter doped **BCPO** films showed sky-blue emission, which were blue-shifted by about 20 nm than the neat films. A para isomer showed higher PLQY of 0.96 than m- (0.89) and m'- (0.87) isomers in the doped film. The  $\Delta E_{\text{ST}}$  values of all three emitters were measured to be 9.0 (**m-AC-DBNA**), 9.1 (**p-AC-DBNA**), and 31 (**m'-AC-DBNA**) meV. Among all the three isomers, **p-AC-DBNA** exhibited the highest  $K_{\text{RISC}}$  value of  $1.17 \times 10^6 \text{ s}^{-1}$  and delayed exciton lifetime of  $1.5 \mu\text{s}$ . The OLEDs (10% doped TADF materials) exhibited maximum EQE of 17.1, 14.1, and 20.5% for m-, m'-, and p-isomers, respectively. On the other hand, neat p-isomer device showed an excellent maximum EQE of 14.1%. This result shows the doping concentration-independent characteristic of these TADF emitters. The TADF devices (m-, m'-, and p-isomers) exhibited maximum EL peak at 492–488 nm and sky-blue CIE color coordinates.

The above-described TADF emitters containing oxygen-based fully bridged boron acceptors and different donor units exhibited good TADF properties and high efficiency. Interestingly, among the above-described oxygen-based fully bridged boron-type

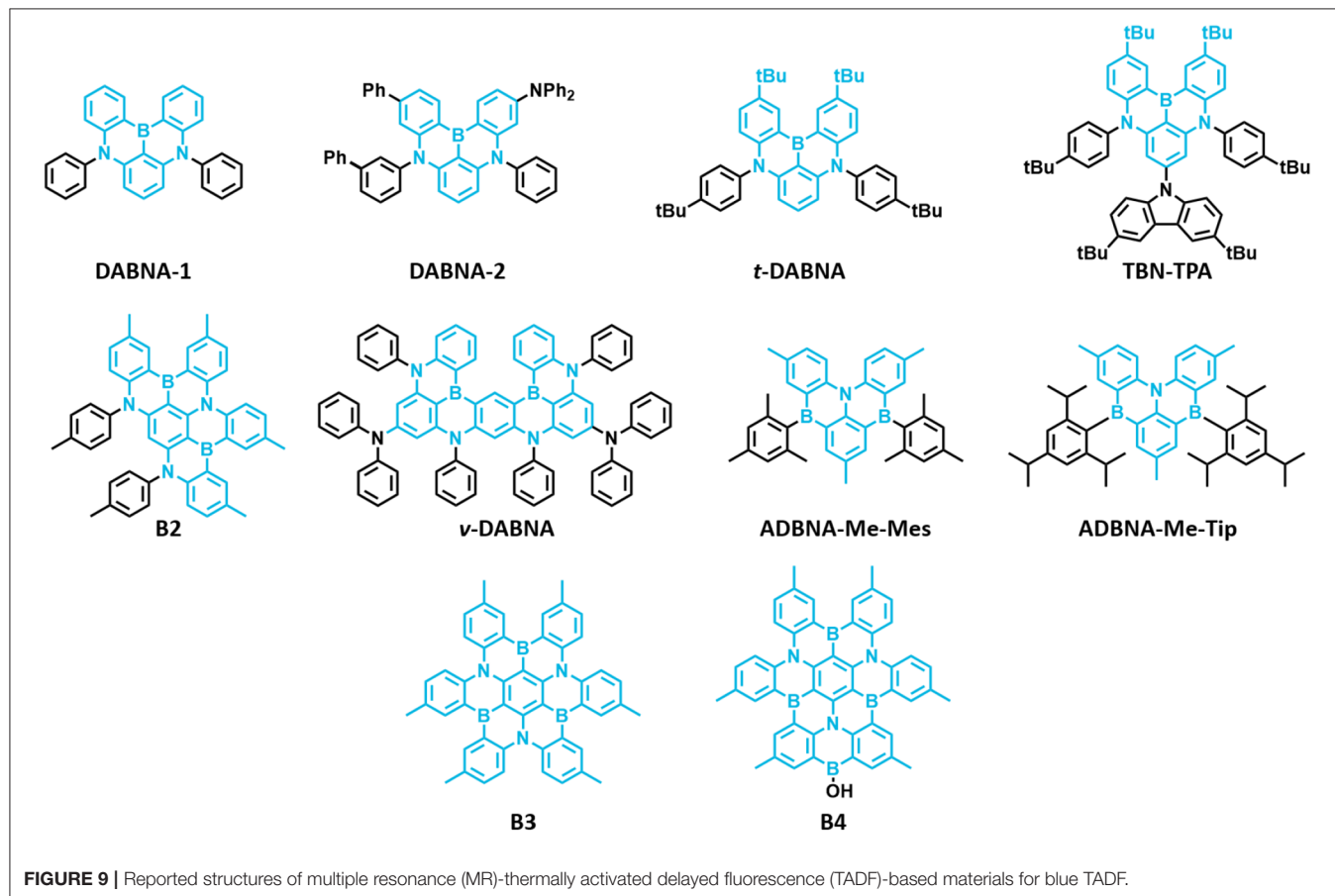
acceptor-based TADF emitters, the design containing donor units attached to the central phenyl ring of the oxygen-based fully bridged boron unit on the para-position of the boron atom exhibited excellent TADF and OLED properties.

## Multiple Resonance-Based Structure for Blue Thermally Activated Delayed Fluorescence Emitters

Recently, multiple resonance-TADF (MR-TADF) materials showed good electroluminescence properties due to their high efficiency and color purity. Generally, these materials show very narrow emission profiles because of their rigid and symmetrical structures. Moreover, MR-TADF materials show majorly deep blue emission with high color purity. Unlike the traditional donor-acceptor-type TADF configuration, this type of MR-TADF materials show HOMO and LUMO orbital separation at *ortho* and *para* positions with respect to nitrogen and boron atoms, respectively, within the same conjugated planar core structure. Moreover, this type of materials shows high oscillator strength along with small  $\Delta E_{ST}$ , which is contradictory to conventional TADF materials. Though MR-TADF materials possess several advantages over conventional TADF emitters, they suffer from very limited chemical modification, complicated synthesis, and high-efficiency roll-off. Additionally, the underlying mechanism

behind the high oscillator strength along with small  $\Delta E_{ST}$  is still not clearly known. However, Pershin et al. (2019) studied the insightful mechanism of multiple resonance-based materials by performing Spin-Component Scaling second-order approximate Coupled-Cluster (SCS-CC2) theoretical calculations. The insightful mechanism was predicted by using the wave functions of two metrics such as the electron-hole charge separation distance ( $\Delta r$ ) and the amount of charge transferred ( $\Delta q$ ) between them at the lowest singlet excited state. From there, it was found that a substantial reshuffling of electron density (large  $\Delta q$ ) occurs over short distances (small  $\Delta r$ ), i.e., the “short-range/local CT” state features both high electron-hole wave function overlaps and small exchange interactions resulting in high oscillator strength and small  $\Delta E_{ST}$ , respectively. Further, these behaviors increase as proportional to the increase in molecular conjugation.

The first MR-TADF materials containing one boron atom and two nitrogen atoms, **DABNA-1** and **DABNA-2**, were reported by Hatakeyama et al. (2016) in 2016. These materials exhibited deep blue emission with PLQY and  $\Delta E_{ST}$  of 0.88 and 0.18 eV and 0.90 and 0.15 eV in 1 wt% doped mCBP film for **DABNA-1** and **DABNA-2**, respectively. Also, they showed high EQE values of 13.5% and 20.2% with deep blue color coordinates of (0.13, 0.09) and (0.12, 0.13) along with very narrow EL spectra of FWHM



28 nm for **DABNA-1** and **DABNA-2**, respectively. The high color purity of these materials is attributed to narrow EL spectra with very small FWHM of 28 nm for both materials. Though these materials showed very high efficiency roll-off, they are promising candidates for developing pure deep blue TADF materials. Later, Han et al. (2019) reported the *tert*-butyl-modified **DABNA-1**, **t-DABNA**, which was used with TADF assistant dopant **DMAC-DPS** to increase the device efficiency and to reduce roll-off. This assistant dopant device exhibited improved maximum efficiency from 25.1 to 31.4% and reduced roll-off compared to without assistant dopant device. In another report, **t-DABNA** structure was modified with the addition of carbazole donor on the *para* position to the boron atom to get **TBN-TBA** (Liang et al., 2018). The addition of donor segment gave high PLQY of up to 0.975 and very small  $\Delta E_{ST}$  of 0.03 eV in toluene solution. Also, the blue TADF OLED fabricated with 4 wt% **TBN-TBA** in **2,6-DCzppy** host showed very high EQE of 32.1% with EL maximum of 447 nm and FWHM of 27 nm. Matsui et al. (2018) reported di- and tri-boron doped nanographenes **B2**, **B3**, and **B4** as multiple resonance TADF materials. All materials showed deep blue emission in the range from 441 to 455 nm with small FWHM of 32–34 nm in 1 wt% doped in PMMA films (Matsui et al., 2018). The PLQY values are in the range of 0.33–0.57 and small  $\Delta E_{ST}$  values in the range of 0.15 eV–0.18 eV in PMMA films. The TADF device with **B2** as 1 wt% emitting dopant in mCBP host exhibited maximum EQE of 18.3% with EL peak maximum of 460 nm and FWHM of 37 nm. Later, Kondo et al.

(2019) reported a dimer of **DABNA-1** core, **v-DABNA** with two boron atoms and two diphenylamine donors attached *para* positions to the boron atoms. The photophysical properties of the **v-DABNA** in 1 wt% doped in **DOBNA-OAr** host showed a deep blue emission peak, PLQY, and  $\Delta E_{ST}$  of 467 nm, 0.9, and 17 meV, respectively. Though the conjugation of **v-DABNA** increased doubly compared to **DABNA-1**, the emission peak is retained in the blue region as in **DABNA-1**. But the increase in PLQY and reduction in  $\Delta E_{ST}$  values are observed for **v-DABNA** compared to **DABNA-1**. The TADF device based on **v-DABNA** showed the highest EQE of 34.4% with deep blue CIE coordinates of (0.12, 0.11) with very narrow FWHM of 18 nm. Also, this device showed very low efficiency roll-off of only 8.6% at 1,000 cd/m<sup>2</sup>. This is the highest efficiency of multiple resonance-based TADF materials reported so far. Recently, Nguyen et al. (2020) evaluated the performances of exciplex host-based TADF devices, and they compared the device performances with and without **v-DABNA** as 1 wt% emitting dopant. The maximum EQE and brightness of 8.9% and 830 cd/m<sup>2</sup> and 19% and 1,260 cd/m<sup>2</sup> for the devices with and without **v-DABNA** were observed. Further, the LT<sub>50</sub> lifetime of both devices showed almost similar values (~350 h) and indicates the promising way of making stable devices (Nguyen et al., 2020). Recently, Oda et al. (2019) reported two multiple resonance-based TADF materials, **ADBNA-Me-Mes** and **ADBNA-Me-Tip**; these materials possess one nitrogen atom in the center of the core and two boron atoms in the outer of the core unit. It is interesting to note that

**TABLE 5 |** Summary of photophysical properties and device performances of the multiple resonance (MR)-thermally activated delayed fluorescence (TADF)-based blue TADF materials.

Emitter	$\lambda_{\max}$ [nm]	PLQY	$\Delta E_{ST}^e$ [eV]	$\tau_d$ $\mu$ s	Host	EQE <sub>max</sub> [%]	CE <sub>max</sub> [cdA <sup>-1</sup> ]	CIE 1931 (x, y)	References
DABNA-1	460 <sup>a</sup>	0.88	0.18	93.7 mCBP (1 wt%)	mCBP (1 wt%)	13.5	10.6	(0.13, 0.09)	Hatakeyama et al., 2016
DABNA-2	469 <sup>a</sup>	0.90	0.14	65.3 mCBP (1 wt%)	mCBP (1 wt%)	20.2	21.1	(0.12, 0.13)	Hatakeyama et al., 2016
B2	455 <sup>b</sup>	0.53	–	30.4 PMMA (1 wt%)	mCBP (1 wt%)	18.3	16.7	(0.13, 0.11)	Matsui et al., 2018
B3	441 <sup>b</sup>	0.33	–	–	–	–	–	–	Matsui et al., 2018
B4	450 <sup>b</sup>	0.57	–	–	–	–	–	–	Matsui et al., 2018
TBN-TPA	470 <sup>c</sup>	0.97	0.14	51.02 DCzppy (4 wt%)	2,6-DCzppy (4 wt%)	32.1	40.2	(0.12, 0.19)	Liang et al., 2018
t-DABNA	–	0.85	0.17	83.3 DPEPO (-wt%)	DPEPO (5 wt%)	25.1	13.0	–	Han et al., 2019
v-DABNA	467 <sup>d</sup>	0.90	0.017	4.1 DOBNA-OAr (1 wt%)	DOBNA-OAr (1 wt%)	34.4	31.0	(0.12, 0.11)	Kondo et al., 2019
ADBNA-Me-Mes	482 <sup>d</sup>	0.89	0.20	165 DOBNA-OAr (1 wt%)	DOBNA-OAr (1 wt%)	16.2	15.4 <sup>f</sup>	(0.10, 0.27)	Oda et al., 2019
ADBNA-Me-Tip	479 <sup>d</sup>	0.88	0.19	147 DOBNA-OAr (1 wt%)	DOBNA-OAr (1 wt%)	21.4	23.5 <sup>f</sup>	(0.11, 0.29)	Oda et al., 2019

<sup>a</sup>Measured in 1 wt% doped film in mCBP host.

<sup>b</sup>Measured in 1 wt% doped film in PMMA host.

<sup>c</sup>Measured in oxygen-free toluene solution ( $5 \times 10^{-5}$  M).

<sup>d</sup>Measured in 1 wt% doped film in DOBNA-OAr host.

<sup>e</sup> $\Delta E_{ST} = S_1 - T_1$ .

<sup>f</sup>Current efficiencies at luminance of maximum, 100 cd/m<sup>2</sup>.



on incorporation of two electron withdrawing boron atoms in the ADBNA core, the emission peak is red-shifted about 20 nm compared to DABNA-1. Though these two materials showed similar PLQY values compared to DABNA-1, they showed little higher  $\Delta E_{ST}$  values than DABNA-1. The TADF OLEDs using ADBNA-Me-Mes and ADBNA-Me-Tip as emitting dopant exhibited sky-blue emission with maximum EQE of 21.4 and 16.2% with little broad emission spectrum (FWHM of 32 and 33 nm), respectively. Apart from blue emission, green multiple resonance-based TADF materials were reported by Zhang et al. (2019) by incorporating weak acceptor groups on the periphery of the DABNA core. These results indicate that incorporation of a donor group at the *para* position to boron atom on the DABNA core retains the deep blue color, whereas the acceptor group incorporation gives a red-shifted emission color (Figure 9 and Table 5).

Further, it is found that the large conjugated DABNA-based material like  $\nu$ -DABNA exhibited the highest blue TADF performances due to its small  $\Delta E_{ST}$  and high PLQY. This result reflects the computational prediction by Pershin et al. (*vide supra*). So, the molecular design for the efficient blue MR-TADF should possess either large conjugated molecular structures or attachment of donor at the *para* position to the boron atom of the DABNA core.

## CONCLUSIONS AND OUTLOOK

We summarized the boron-containing aromatic acceptor moieties connected with several donors of push-pull small molecules for blue TADF OLED applications. The boron-based TADF materials exhibited good TADF performances with maximum EQE value as high as 38.15%, which is the highest value for blue TADF OLEDs reported so far. We found the order of type of boron-based materials to realize pure blue emission color, high PLQY, small  $\Delta E_{ST}$ , short delayed exciton lifetime, and high efficiency for unbridged < partially bridged < fully bridged boron compounds. Exclusively, the fully bridged oxygen-containing boron acceptor shows an additional property of horizontal dipole orientation which is desirable for highly efficient devices. On the other hand, the fully bridged nitrogen-containing boron materials (MR-TADF) show very

narrow emission in deep blue region. It is concluded that the fully bridged boron compounds would be an ideal candidate for designing highly efficient deep blue TADF materials. Also, attachment of donor at the *para* position to the boron atom of MR-TADF materials would give deep blue color, small  $\Delta E_{ST}$ , high PLQY, and high efficiency. These results indicate that the boron materials are promising for the development of blue TADF OLEDs.

Though the boron-containing materials showed high efficiency, the lifetime of the blue TADF device is still a challenging task. As the delayed exciton lifetime of fully bridged boron materials is short, the usage of them as TADF assistant host for MR-TADF dopant materials in hyper-fluorescence devices has advantages of (i) an increase in color purity as emission originates from the MR-TADF dopant, (ii) the dramatically increased device efficiency due to the usage of both host and dopant as TADF materials, and (iii) the increased device lifetime due to the fast Forster resonance energy transfer from the TADF assistant host to the MR-TADF dopant.

## AUTHOR CONTRIBUTIONS

HL, DK, and RL contributed equally to write and revise this manuscript. JR organized all the related tables and figures. JK supervised this work. All authors listed have made a substantial, direct and intellectual contribution to the work, and approved it for publication.

## FUNDING

This work was supported by the National Research Foundation of Korea (Grant No. NRF-2019M3D1A2104019) and the Technology Innovation Program (20006464, Development of TADF sensitized fluorescence RGB emitting layer materials with high color purity and high efficiency for BT 2020) funded by the Ministry of Trade, Industry & Energy (MOTIE, Korea). This work was also supported by Samsung Display Co., Ltd. The funder was not involved in the study design, collection, analysis, interpretation of data, the writing of this article or the decision to submit it for publication.

## REFERENCES

- Agou, T., Kobayashi, J., and Kawashima, T. (2006). Syntheses, structure, and optical properties of ladder-type fused azaborines. *Org. Lett.* 8, 2241–2244. doi: 10.1021/ol060539n
- Agou, T., Kobayashi, J., and Kawashima, T. (2007a). Development of a general route to periphery-functionalized azaborines and ladder-type azaborines by using common intermediates. *Chem. Commun.* 3204–3206. doi: 10.1039/b706418g
- Agou, T., Kobayashi, J., and Kawashima, T. (2007b). Electronic and optical properties of ladder-type heteraborins. *Chem. A Eur. J.* 13, 8051–8060. doi: 10.1002/chem.200700622
- Agou, T., Matsuo, K., Kawano, R., Park, I. S., Hosoya, T., Fukumoto, H., et al. (2020). Pentacyclic ladder-heteraborin emitters exhibiting high-efficiency blue thermally activated delayed fluorescence with an ultrashort emission lifetime. *ACS Mater. Lett.* 2, 28–34. doi: 10.1021/acsmaterialslett.9b00433
- Ahn, D. H., Kim, S. W., Lee, H., Ko, I. J., Karthik, D., Lee, J. Y., et al. (2019a). Highly efficient blue thermally activated delayed fluorescence emitters based on symmetrical and rigid oxygen-bridged boron acceptors. *Nat. Photonics* 13, 540–546. doi: 10.1038/s41566-019-0415-5
- Ahn, D. H., Lee, H., Kim, S. W., Karthik, D., Lee, J., Jeong, H., et al. (2019b). Highly twisted donor-acceptor boron emitter and high triplet host material for highly efficient blue thermally activated delayed fluorescent device. *ACS Appl. Mater. Interfaces* 11, 14909–14916. doi: 10.1021/acsmi.9b00931
- Ahn, D. H., Maeng, J. H., Lee, H., Yoo, Y., Lampande, R., Lee, J. Y., et al. (2020). Rigid oxygen-bridged boron-based blue thermally activated delayed fluorescence emitter for organic light emitting diode: approach towards satisfying high efficiency and long lifetime

- together. *Adv. Optical Mater.* 2000102. doi: 10.1002/adom.202000102
- Baldo, M. A., O'Brien, D. F., You, Y., Shoustikov, A., Sibley, S., Thompson, M. E., et al. (1998). Highly efficient phosphorescent emission from organic electroluminescent devices. *Nature* 395, 151–154. doi: 10.1038/25954
- Bonardi, L., Kanaan, H., Camerel, F., Jolinat, P., Retailleau, P., and Ziesler, R. (2008). Fine-tuning of yellow or red photo- and electroluminescence of functional difluoro-boradiazaindacene films. *Adv. Funct. Mater.* 18, 401–413. doi: 10.1002/adfm.200700697
- Brown, H. C., and Dodson, V. H. (1957). Studies in stereochemistry. XXII. the preparation and reactions of trimesitylborane. evidence for the non-localized nature of the odd electron in triarylborane radical ions and related free radicals. *J. Am. Chem. Soc.* 79, 2302–2306. doi: 10.1021/ja01566a076
- D'aléo, A., Sazzad, M. H., Kim, D. H., Choi, E. Y., Wu, J. W., Canard, G., et al. (2017). Boron difluoride hemicurcuminoid as an efficient far red to near-infrared emitter: toward OLEDs and laser dyes. *Chem. Commun.* 53, 7003–7006. doi: 10.1039/C7CC01786C
- Elbing, M., and Bazan, G. C. (2008). A new design strategy for organic optoelectronic materials by lateral boryl substitution. *Angew. Chem. Int. Ed.* 47, 834–838. doi: 10.1002/anie.200703722
- Entwistle, C. D., and Marder, T. B. (2004). Applications of three-coordinate organoboron compounds and polymers in optoelectronics. *Chem. Mater.* 16, 4574–4585. doi: 10.1021/cm0495717
- Fraht, D., Massue, J., Ulrich, G., and Ziesler, R. (2014). Luminescent materials: locking  $\pi$ -conjugated and heterocyclic ligands with boron(III). *Angew. Chem. Int. Ed.* 53, 2290–2310. doi: 10.1002/anie.201305554
- Han, S. H., Jeong, J. H., Yoo, J. W., and Lee, J. Y. (2019). Ideal blue thermally activated delayed fluorescence emission assisted by a thermally activated delayed fluorescence assistant dopant through a fast reverse intersystem crossing mediated cascade energy transfer process. *J. Mater. Chem. C* 7, 3082–3089. doi: 10.1039/C8TC06575F
- Hatakeyama, T., Shiren, K., Nakajima, K., Nomura, S., Nakatsuka, S., Kinoshita, K., et al. (2016). Ultrapure blue thermally activated delayed fluorescence molecules: efficient HOMO–LUMO separation by the multiple resonance effect. *Adv. Mater.* 28, 2777–2781. doi: 10.1002/adma.201505491
- Hirai, H., Nakajima, K., Nakatsuka, S., Shiren, K., Ni, J., Nomura, S., et al. (2015). One-step borylation of 1,3-diaryloxybenzenes towards efficient materials for organic light-emitting diodes. *Angew. Chem. Int. Ed.* 54, 13581–13585. doi: 10.1002/anie.201506335
- Im, Y., Byun, S. Y., Kim, J. H., Lee, D. R., Oh, C. S., Yook, K. S., et al. (2017). Recent progress in high-efficiency blue-light-emitting materials for organic light-emitting diodes. *Adv. Funct. Mater.* 27:1603007. doi: 10.1002/adfm.201603007
- Karthik, D., Ahn, D. H., Ryu, J. H., Lee, H., Maeng, J. H., Lee, J. Y., et al. (2020). Highly efficient blue thermally activated delayed fluorescence organic light emitting diodes based on tercarbazole donor and boron acceptor dyads. *J. Mater. Chem. C* 8, 2272–2279. doi: 10.1039/C9TC05950D
- Kim, K.-H., and Kim, J. F. (2018). Origin and control of orientation of phosphorescent and TADF dyes for high-efficiency OLEDs. *Adv. Mater.* 30:1705600. doi: 10.1002/adma.201705600
- Kim, K. J., Kim, G. H., Lampande, R., Ahn, D. H., Im, J. B., Moon, J. S., et al. (2018). A new rigid diindolocarbazole donor moiety for high quantum efficiency thermally activated delayed fluorescence emitter. *J. Mater. Chem. C* 6, 1343–1348. doi: 10.1039/C7TC04852A
- Kitamoto, Y., Namikawa, T., Ikemizu, D., Miyata, Y., Suzuki, T., Kita, H., et al. (2015). Light blue and green thermally activated delayed fluorescence from 10H-phenoxaborin-derivatives and their application to organic light-emitting diodes. *J. Mater. Chem. C* 3, 9122–9130. doi: 10.1039/C5TC01380A
- Kitamoto, Y., Namikawa, T., Suzuki, T., Miyata, Y., Kita, H., Sato, T., et al. (2016). Dimesitylarylborane-based luminescent emitters exhibiting highly-efficient thermally activated delayed fluorescence for organic light-emitting diodes. *Org. Electron.* 34, 208–217. doi: 10.1016/j.orgel.2016.04.030
- Kondo, Y., Yoshiura, K., Kitera, S., Nishi, H., Oda, S., Gotoh, H., et al. (2019). Narrowband deep-blue organic light-emitting diode featuring an organoboron-based emitter. *Nat. Photonics* 13, 678–682. doi: 10.1038/s41566-019-0476-5
- Lee, Y. H., Park, S., Oh, J., Shin, J. W., Jung, J., Yoo, S., et al. (2017). Rigidity-induced delayed fluorescence by ortho donor-appended triarylboron compounds: record-high efficiency in pure blue fluorescent organic light-emitting diodes. *ACS Appl. Mater. Interfaces* 9, 24035–24042. doi: 10.1021/acsami.7b05615
- Lee, Y. H., Park, S., Oh, J., Woo, S.-J., Kumar, A., Kim, J.-J., et al. (2018). High-efficiency sky blue to ultradeep blue thermally activated delayed fluorescent diodes based on ortho-carbazole-appended triarylboron emitters: above 32% external quantum efficiency in blue devices. *Adv. Opt. Mater.* 6:1800385. doi: 10.1002/adom.201800385
- Li, G., Lou, W., Wang, D., Deng, C., and Zhang, Q. (2019). Difluoroboron-enabled thermally activated delayed fluorescence. *ACS Appl. Mater. Interfaces* 11, 32209–32217. doi: 10.1021/acsami.9b08107
- Li, P., Chan, H., Lai, S.-L., Ng, M., Chan, M.-Y., and Yam, V. W.-W. (2019). Four-coordinate boron emitters with tridentate chelating ligand for efficient and stable thermally activated delayed fluorescence organic light-emitting devices. *Angew. Chem. Int. Ed.* 58, 9088–9094. doi: 10.1002/anie.201903332
- Liang, X., Tu, Z.-L., and Zheng, Y.-X. (2019). Thermally activated delayed fluorescence materials: towards realization of high efficiency through strategic small molecular design. *Chem. A Eur. J.* 25, 5623–5642. doi: 10.1002/chem.201805952
- Liang, X., Yan, Z.-P., Han, H.-B., Wu, Z.-G., Zheng, Y.-X., Meng, H., et al. (2018). Peripheral amplification of multi-resonance induced thermally activated delayed fluorescence for highly efficient OLEDs. *Angew. Chem. Int. Ed.* 57, 11316–11320. doi: 10.1002/anie.201806323
- Matsui, K., Oda, S., Yoshiura, K., Nakajima, K., Yasuda, N., and Hatakeyama, T. (2018). One-shot multiple borylation toward BN-doped nanographenes. *J. Am. Chem. Soc.* 140, 1195–1198. doi: 10.1021/jacs.7b10578
- Matsuo, K., and Yasuda, T. (2019). Boronate- and borinate-based  $\pi$ -systems for blue thermally activated delayed fluorescence materials. *Chem. Commun.* 55, 2501–2504. doi: 10.1039/C8CC10282A
- Møllerup, S. K., and Wang, S. (2019). Boron-doped molecules for optoelectronics. *Trends Chem.* 1, 77–89. doi: 10.1016/j.trechm.2019.01.003
- Meng, G., Chen, X., Wang, X., Wang, N., Peng, T., and Wang, S. (2019). Isomeric bright sky-blue TADF emitters based on bisacridine decorated DBNA: impact of donor locations on luminescent and electroluminescent properties. *Adv. Opt. Mater.* 7:1900130. doi: 10.1002/adom.201900130
- Nguyen, T. B., Nakanotani, H., Hatakeyama, T., and Adachi, C. (2020). The role of reverse intersystem crossing using a TADF-type acceptor molecule on the device stability of exciplex-based organic light-emitting diodes. *Adv. Mater.* 32:1906614. doi: 10.1002/adma.201906614
- Numata, M., Yasuda, T., and Adachi, C. (2015). High efficiency pure blue thermally activated delayed fluorescence molecules having 10H-phenoxaborin and acridan units. *Chem. Commun.* 51, 9443–9446. doi: 10.1039/C5CC00307E
- Oda, S., Kawakami, B., Kawasumi, R., Okita, R., and Hatakeyama, T. (2019). Multiple resonance effect-induced sky-blue thermally activated delayed fluorescence with a narrow emission band. *Org. Lett.* 21, 9311–9314. doi: 10.1021/acs.orglett.9b03342
- Park, I. S., Matsuo, K., Aizawa, N., and Yasuda, T. (2018). High-performance dibenzoheteraborin-based thermally activated delayed fluorescence emitters: molecular architectonics for concurrently achieving narrowband emission and efficient triplet–singlet spin conversion. *Adv. Funct. Mater.* 28:1802031. doi: 10.1002/adfm.201802031
- Park, I. S., Numata, M., Adachi, C., and Yasuda, T. (2016). A phenazaborin-based high-efficiency blue delayed fluorescence material. *Bull. Chem. Soc. Jpn.* 89, 375–377. doi: 10.1246/bcsj.20150399
- Pershin, A., Hall, D., Lemaire, V., Sancho-Garcia, J.-C., Muccioli, L., Zysman-Colman, E., et al. (2019). Highly emissive excitons with reduced exchange energy in thermally activated delayed fluorescent molecules. *Nat. Commun.* 10:597. doi: 10.1038/s41467-019-08495-5
- Schellhammer, K. S., Li, T.-Y., Zeika, O., Körner, C., Leo, K., Ortmann, F., et al. (2017). Tuning near-infrared absorbing donor materials: a study of electronic, optical, and charge-transport properties of aza-BODIPYs. *Chem. Mater.* 29, 5525–5536. doi: 10.1021/acs.chemmater.7b00653
- Scholz, S., Kondakov, D., Lüssem, B., and Leo, K. (2015). Degradation mechanisms and reactions in organic light-emitting devices. *Chem. Rev.* 115, 8449–8503. doi: 10.1021/cr400704v
- Song, D., Yu, Y., Yue, L., Zhong, D., Zhang, Y., Yang, X., et al. (2019). Asymmetric thermally activated delayed fluorescence (TADF) emitters with 5,9-dioxo-13b-boranaphtho[3,2,1-de]anthracene (OBA) as the acceptor and

- highly efficient blue-emitting OLEDs. *J. Mater. Chem. C* 7, 11953–11963. doi: 10.1039/C9TC04115J
- Stachelek, P., Alsimaree, A. A., Alnoman, R. B., Harriman, A., and Knight, J. G. (2017). Thermally-activated, delayed fluorescence in O,B,O- and N,B,O-strapped boron dipyrromethene derivatives. *J. Phys. Chem. A* 121, 2096–2107. doi: 10.1021/acs.jpca.6b11131
- Suzuki, K., Kubo, S., Shizu, K., Fukushima, T., Wakamiya, A., Murata, Y., et al. (2015). Triarylboron-based fluorescent organic light-emitting diodes with external quantum efficiencies exceeding 20 %. *Angew. Chem. Int. Ed.* 54, 15231–15235. doi: 10.1002/anie.201508270
- Tang, C. W., and Vanslyke, S. A. (1987). Organic electroluminescent diodes. *Appl. Phys. Lett.* 51, 913–915. doi: 10.1063/1.98799
- Turkoglu, G., Cinar, M. E., and Ozturk, T. (2017). Triarylborane-based materials for OLED applications. *Molecules* 22:1522. doi: 10.3390/molecules22091522
- Uoyama, H., Goushi, K., Shizu, K., Nomura, H., and Adachi, C. (2012). Highly efficient organic light-emitting diodes from delayed fluorescence. *Nature* 492, 234–238. doi: 10.1038/nature11687
- Von Grotthuss, E., John, A., Kaese, T., and Wagner, M. (2018). Doping polycyclic aromatics with boron for superior performance in materials science and catalysis. *Asian J. Org. Chem.* 7, 37–53. doi: 10.1002/ajoc.201700495
- Yamaguchi, S., and Wakamiya, A. (2006). Boron as a key component for new  $\pi$ -electron materials. *Pure Appl. Chem.* 78, 1413–1424. doi: 10.1351/pac200678071413
- Yang, X., Guo, H., Liu, B., Zhao, J., Zhou, G., Wu, Z., et al. (2018). Diarylboron-based asymmetric red-emitting Ir(III) complex for solution-processed phosphorescent organic light-emitting diode with external quantum efficiency above 28%. *Adv. Sci.* 5:1701067. doi: 10.1002/advs.201800950
- Zampetti, A., Minotto, A., Squeo, B. M., Gregoriou, V. G., Allard, S., Scherf, U., et al. (2017). Highly efficient solid-state near-infrared organic light-emitting diodes incorporating A-D-A dyes based on  $\alpha,\beta$ -unsubstituted “BODIPY” moieties. *Sci. Rep.* 7:1611. doi: 10.1038/s41598-017-01785-2
- Zhang, Y., Zhang, D., Wei, J., Liu, Z., Lu, Y., and Duan, L. (2019). Multi-resonance induced thermally activated delayed fluorophores for narrowband green OLEDs. *Angew. Chem. Int. Ed.* 58, 16912–16917. doi: 10.1002/anie.201911266

**Conflict of Interest:** The authors declare that the research was conducted in the absence of any commercial or financial relationships that could be construed as a potential conflict of interest.

Copyright © 2020 Lee, Karthik, Lampande, Ryu and Kwon. This is an open-access article distributed under the terms of the Creative Commons Attribution License (CC BY). The use, distribution or reproduction in other forums is permitted, provided the original author(s) and the copyright owner(s) are credited and that the original publication in this journal is cited, in accordance with accepted academic practice. No use, distribution or reproduction is permitted which does not comply with these terms.



# Molecular Orientations of Delayed Fluorescent Emitters in a Series of Carbazole-Based Host Materials

Hisahiro Sasabe<sup>1,2,3\*</sup>, Yuki Chikayasu<sup>3</sup>, Satoru Ohisa<sup>1,2,3</sup>, Hiroki Arai<sup>3</sup>, Tatsuya Ohsawa<sup>3</sup>, Ryutaro Komatsu<sup>3</sup>, Yuichiro Watanabe<sup>3</sup>, Daisuke Yokoyama<sup>1,2,3</sup> and Junji Kido<sup>1,2,3\*</sup>

<sup>1</sup> Research Center for Organic Electronics (ROEL), Yamagata University, Yamagata, Japan, <sup>2</sup> Frontier Center for Organic Materials (FROM), Yamagata University, Yamagata, Japan, <sup>3</sup> Department of Organic Materials Science, Graduate School of Organic Materials Science, Yamagata University, Yamagata, Japan

## OPEN ACCESS

### Edited by:

Chihaya Adachi,  
Kyushu University, Japan

### Reviewed by:

Kai Wang,  
Soochow University, China  
Jang Hyuk Kwon,  
Kyung Hee University, South Korea  
Jean Charles Ribierre,  
Kyushu University, Japan

### \*Correspondence:

Hisahiro Sasabe  
h-sasabe@yz.yamagata-u.ac.jp  
Junji Kido  
kid@yz.yamagata-u.ac.jp

### Specialty section:

This article was submitted to  
Organic Chemistry,  
a section of the journal  
Frontiers in Chemistry

Received: 27 December 2019

Accepted: 23 April 2020

Published: 25 May 2020

### Citation:

Sasabe H, Chikayasu Y, Ohisa S, Arai H, Ohsawa T, Komatsu R, Watanabe Y, Yokoyama D and Kido J (2020) Molecular Orientations of Delayed Fluorescent Emitters in a Series of Carbazole-Based Host Materials. *Front. Chem.* 8:427. doi: 10.3389/fchem.2020.00427

Molecular orientation is one of the most crucial factors to boost the efficiency of organic light-emitting devices. However, active control of molecular orientation of the emitter molecule by the host molecule is rarely realized so far, and the underlying mechanism is under discussion. Here, we systematically investigated the molecular orientations of thermally activated delayed fluorescence (TADF) emitters in a series of carbazole-based host materials. Enhanced horizontal orientation of the TADF emitters was achieved. The degree of enhancement observed was dependent on the host material used. Consequently, our results indicate that  $\pi$ - $\pi$  stacking, CH/ $n$  ( $n = O, N$ ) weak hydrogen bonds, and multiple CH/ $\pi$  contacts greatly induce horizontal orientation of the TADF emitters in addition to the molecular shape anisotropy. Finally, we fabricated TADF-based organic light-emitting devices with an external quantum efficiency ( $\eta_{\text{ext}}$ ) of 26% using an emission layer with horizontal orientation ratio ( $\Theta$ ) of 79%, which is higher than that of an almost randomly oriented emission layer with  $\Theta$  of 62% ( $\eta_{\text{ext}} = 22\%$ ).

**Keywords:** delayed fluorescence, molecular orientation, light out-coupling efficiency, carbazoles, weak hydrogen bonds

## INTRODUCTION

A series of fluorescent emitters exhibiting significant delayed fluorescence, so-called thermally activated delayed fluorescent (TADF) emitters, has attracted much attention due to its potential usefulness in high-performance organic light-emitting devices (OLEDs) that can realize an internal quantum efficiency ( $\eta_{\text{int}}$ ) of 100% (Uoyama et al., 2012; Sasabe and Kido, 2013; Adachi, 2014; Kaji et al., 2015; Lin et al., 2016; Im et al., 2017; Wong and Zysman-Colman, 2017; Yang et al., 2017; Komatsu et al., 2018). In principle, TADF emitters consist of electron-donor (D) and electron-acceptor (A) moieties realizing efficient intramolecular charge transfer (ICT). The connection between D and A moieties is generally accompanied with a small overlap in the frontier molecular orbital (FMO) between the highest occupied molecular orbital (HOMO) and the lowest unoccupied molecular orbital (LUMO), in other words, a small energy difference between singlet and triplet energies ( $\Delta E_{\text{ST}}$ ). Recent rapid development in TADF emitters enables OLEDs to achieve an external quantum efficiency ( $\eta_{\text{ext}}$ ) over 30% (Kaji et al., 2015; Komino et al., 2016; Lin et al., 2016; Liu et al., 2017; Rajamalli et al., 2017; Wu et al., 2018; Ahn et al., 2019; Kondo et al., 2019). To obtain such a high-performance in OLEDs, horizontal orientation of the emission dipole moment (EDM) is absolutely essential. Perfect horizontal orientation of the EDM has been reported to boost OLED



efficiency up to 150% compared to random EDM orientation (Frischeisen et al., 2011; Yokoyama, 2011; Schmidt et al., 2017; Kim and Kim, 2018; Watanabe et al., 2019b). However, the horizontal orientation ratio ( $\Theta$ ) of most TADF emitters used in OLEDs realizing  $\eta_{\text{ext}}$  over 30% is reportedly only around 80%, which is far behind perfect horizontal orientation ( $\Theta = 100\%$ ). In general, a guest TADF emitter is dispersed into a host material to reduce concentration quenching, and to maintain carrier balance in the emission layer (EML). The proportion of guest molecule is commonly much smaller than that of host molecule. Thus, the non-covalent interactions between host and guest molecules should be one of the important factors that controls the molecular orientation.

In an early stage of study on molecular orientation in OLEDs, Yokoyama used variable-angle spectroscopic ellipsometry (VASE) measurements to reveal the anisotropy of the molecular shape, such as in planar and linear structures, is essential to realize horizontal orientation of a series of triphenylamine and carbazole based-fluorescent molecules, even in randomly oriented host molecules (Yokoyama et al., 2009). However, unlike first-generation fluorescent molecules, most TADF molecules do not have a planar structure but instead a winding

chemical structure in needed to realize a small overlap of the frontier molecular orbitals in order to achieve efficient reverse intersystem crossing (RISC). Therefore, in addition to the molecular shape anisotropy, advanced strategies to actively use non-covalent interactions to realize enhanced horizontal orientation are highly desired.

In 2016, Lin and Wong reported three types of sky-blue TADF emitters using triphenyltriazine as an acceptor and substituted acridines as a donor unit (Lin et al., 2016). Among these, **SpiroAc-TRZ** with spirobiphenyl unit showed a photoluminescent quantum yield ( $\eta_{\text{PL}}$ ) of 100%, and a high  $\Theta$  value of 83% in **mCPCN** host. They indicated that this high  $\Theta$  value of **SpiroAc-TRZ** is attributed to the overall planar and balanced/symmetrical structure. The corresponding OLED exhibited an extremely high  $\eta_{\text{ext}}$  of nearly 37%. In the same year, Komino and Adachi reported the complete horizontal orientation of a linear-shaped TADF emitter named **Cis-BOX2** in a randomly oriented host matrix at the temperature of 200 K (Komino et al., 2016). The horizontal orientation ratio of **Cis-BOX2** depended on the deposition temperature and the type of host matrix. A **Cis-BOX2**-based OLED showed a very high  $\eta_{\text{ext}}$  of 33%.

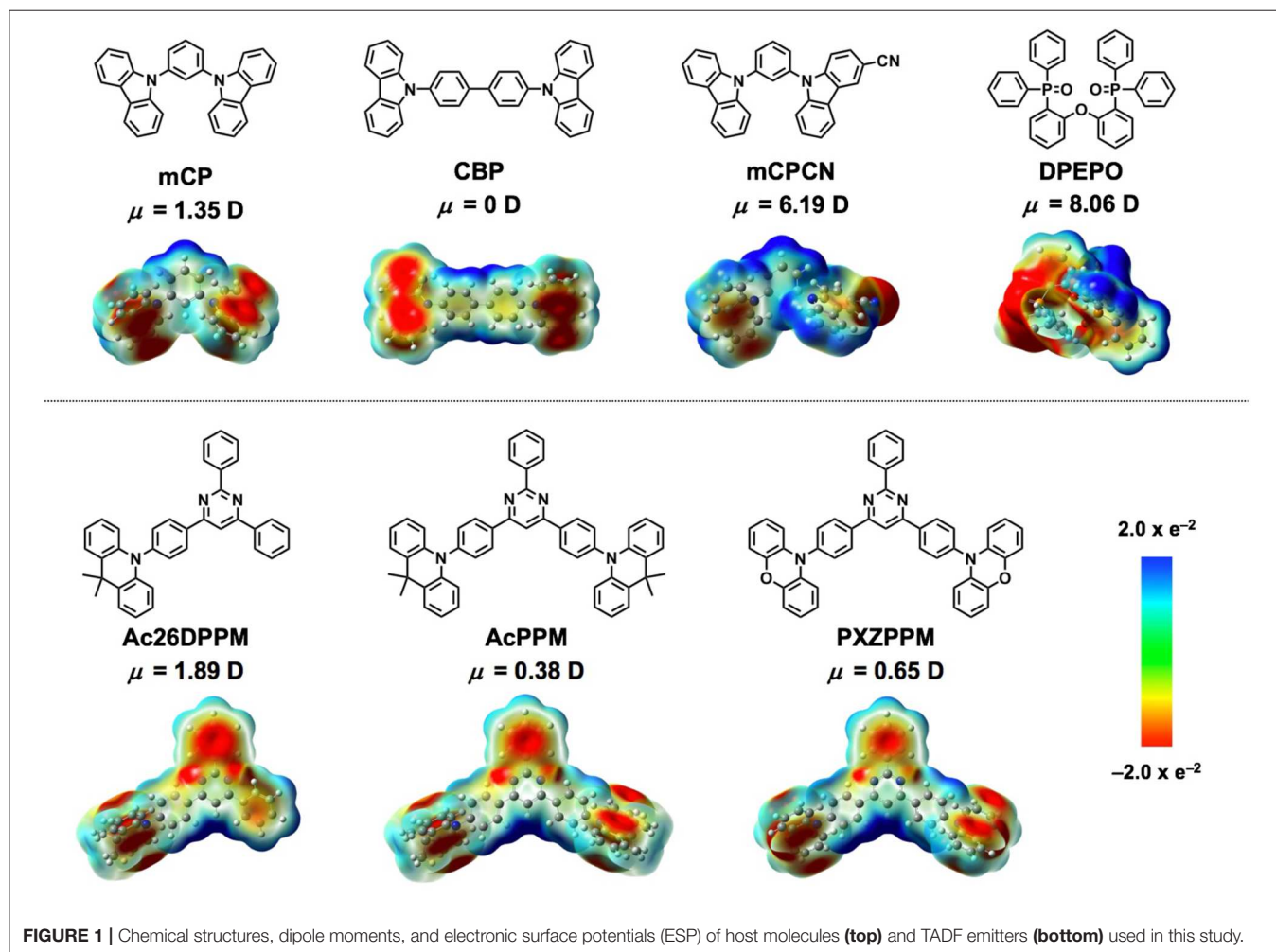


**FIGURE 1** | Chemical structures, dipole moments, and electronic surface potentials (ESP) of host molecules (top) and TADF emitters (bottom) used in this study.

As mentioned above, although a high  $\Theta$  value of up to 100% at 200 K has been reported, the underlying mechanism to realize horizontal orientation is still under discussion at this stage (Yokoyama, 2011; Mayr and Brütting, 2015; Moon et al., 2015; Shibata et al., 2015; Friederich et al., 2017; Schmidt et al., 2017; Gujral et al., 2018; Kim and Kim, 2018; Lee et al., 2018; Pal et al., 2018; Watanabe et al., 2019b). In order to deepen insights into the underlying mechanism, we wish to report a systematic investigation on the molecular orientations of TADF molecules in a series of carbazole-based host materials. To reveal the structure–property relationship for horizontal orientation, a series of TADF emitters, which we can systematically change the parameters one by one, should be necessary. In this context, we have already developed a series of pyrimidine-based TADF emitters with different donor group(s) (Figure 1) (Komatsu et al., 2016a,b; Nakao et al., 2017). By comparing these three molecules, we can obtain insight into the effects of two factors: (i) donor number, which reflects the molecular shape anisotropy in these comparisons, and (ii) donor structure. Consequently, we achieved enhanced  $\Theta$  values of TADF emitters and the degree of enhancement depended on the host material used. Consequently, our results indicate that increased  $\pi$ - $\pi$  stacking, CH/ $n$  ( $n = \text{O}, \text{N}$ ) weak hydrogen bond (H-bond) interaction, and multiple CH/ $\pi$  contacts greatly induce horizontal orientation of TADF emitters in addition to the molecular shape anisotropy. Finally, we fabricated a TADF-based OLED with  $\eta_{\text{ext}}$  of 26% using an emission layer (EML) with a  $\Theta$  value of 79%, which is greater than that of an almost randomly oriented EML with a  $\Theta$  value of 62% ( $\eta_{\text{ext}} = 22\%$ ).

## RESULTS AND DISCUSSION

### Selection of Carbazole-Based Host Molecules and Phosphine-Oxide Host Molecules

Carbazole derivatives are one of the most popular host materials in OLEDs. Therefore, insights into carbazole-based host materials are considered to be highly valuable. To identify the underlying mechanisms of horizontal orientation, we selected four types of host materials to study and sequentially changed their chemical structures (Figure 1 and Table 1). **mCP** was used as the benchmark material. Extending its  $\pi$ -conjugation, results in **CBP**, which can be used to evaluate the effect of  $\pi$ -conjugation or  $\pi$ - $\pi$  stacking when compared to **mCP**. The introduction of CN substituent into **mCP** forms **mCPCN** (Lin et al., 2012). Using this molecule, we can validate the effect of CN substituent, such as the dipole/dipole interaction and CH/N weak H-bonds. A phosphine-oxide host material, **DPEPO** (Han et al., 2011) was used to investigate the effect of the dipole moment and CH/O weak H-bonds of P=O substituents (Figure 2). Note that all the host materials used in this study showed random orientation. DFT calculations were performed at B3LYP 6-31G(d) level to evaluate the dipole moment and visualize the electronic surface potential (ESP), as shown in

**TABLE 1** | Thermal and optical properties of the host molecules.

Compound	Mw (g/mol)	$T_g^a/T_m^a/T_{d5}^b$ (°C)	$I_p^c/E_g^f/E_a^g/E_T^h$ (eV)	$S^i$
mCP	408	60/n.d./280	−6.01/3.49/−2.63/3.00	0.08
CBP	485	62/283/413	−5.91/3.44/−2.67/2.60	−0.07
mCPCN	434	97/222/313	−6.08/3.44/−2.64/3.03	0.08
DPEPO	571	n.d./280/322	−6.70/4.00/−2.70/3.30	0.00

<sup>a</sup> $T_g$  and  $T_m$  were determined using DSC. <sup>b</sup> $T_{d5}$  was determined using TGA. <sup>c</sup> $I_p$  was determined using PYS. <sup>d</sup> $E_g$  was taken as the point where the normalized absorption spectra intersected. <sup>e</sup> $E_a$  was calculated using  $I_p$  and  $E_g$ . <sup>f</sup> $E_T$  was estimated from the onset of the phosphorescent spectra at 5 K. <sup>g</sup>VASE derived order parameter.

**TABLE 2** | Thermal and optical properties of the TADF emitters.

Compound	Mw (g/mol)	$T_g^a/T_m^a/T_{d5}^b$ (°C)	$I_p^c/E_g^f/E_a^g/E_T^h$ (eV)
Ac-26DPPM	516	90/210/383	−5.67/2.90/−2.77/2.80
Ac-PPM	723	n.d./388/442	−5.65/2.80/−2.85/2.65
PXZ-PPM	671	n.d./290/473	−5.65/2.56/−3.09/2.56

<sup>a</sup> $T_g$  and  $T_m$  were determined using DSC. <sup>b</sup> $T_{d5}$  was determined using TGA. <sup>c</sup> $I_p$  was determined using PYS. <sup>d</sup> $E_g$  was taken as the point where the normalized absorption spectra intersected. <sup>e</sup> $E_a$  was calculated using  $I_p$  and  $E_g$ . <sup>f</sup> $E_T$  was estimated from the onset of the phosphorescent spectra at 5 K.

Figure 1 and Figure S1 (in supporting information). Among the host materials, **mCP** and **CBP** had small dipole moment <1.5 D, while **mCPCN** with a cyano group and **DPEPO** with phosphine oxide groups possessed a large dipole moment >6.0 D. ESP exhibited strong negative charge (red color) on the  $\pi$ -plane of the carbazole and on the electron-withdrawing groups of CN and P=O. The hydrogen (H) atoms on the aromatic rings had positive charge (blue color).

### Selection of TADF Emitters

We selected three types of pyrimidine-based TADF emitters named **Ac26DPPM** (Nakao et al., 2017), **AcPPM** (Komatsu et al., 2016a), and **PXZPPM** (Komatsu et al., 2016b) with different donor group(s) such as dimethylacridine (Ac) and phenoxiazine (PXZ) (Figure 1 and Table 2). By comparing these three molecules, we can obtain insight into the effects of two factors: (i) donor number, which reflects the molecular shape anisotropy in these comparisons, and (ii) donor structure. Note that all the emitter molecules showed random orientation in neat film (Figure S2). Similar to the host molecules, DFT calculations were performed to evaluate the dipole moment and visualize the ESP and the results are shown in Figure 1 and Figure S1. All the emitters have a small dipole moment <2.0 D, especially **AcPPM** ( $\mu = 0.38$  D) and **PXZPPM** ( $\mu = 0.65$  D). The ESP indicates strong negative charge on the  $\pi$ -plane of position 2 of pyrimidine and on the electron-donating end-cap unit(s) of Ac and PXZ. Similar to the host molecules, H atoms on the aromatic rings had positive charge.

## Molecular Orientation of TADF Emitters

First, we investigated the molecular orientations of 10 wt% **Ac26DPPM**-doped host films by using angle dependent PL measurements. Here, a  $\Theta$  value of 67% indicates random orientation while a value of 100% indicates perfect horizontal orientation. **Ac26DPPM**-doped **mCP** film showed moderate vertical orientation with  $\Theta = 53\%$ . When **Ac26DPPM** was doped into other host materials (**CBP**, **mCPCN**, and **DPEPO**), all the doped films exhibited almost random orientation with  $\Theta$  of 62–66% (**Figure 3** and **Figure S3**). Although these films showed random orientation due to the small anisotropy of **Ac26DPPM**, the differences of orientation ratio in the different host materials ( $\Delta\Theta$ ) were 9–13%. These differences are not small but meaningfully significant. Similar results were obtained in the case of **AcPPM** (**Figure 4** and **Figure S4**). When host material was changed from **mCP** to one of the other host materials, a significant enhancement of  $\Theta$  values up to 22% was observed. Since **AcPPM** has larger molecular shape anisotropy than that of **Ac26PMM**, **AcPPM** showed increased horizontal orientation with  $\Theta$  of 75–80%. Surprisingly, **PXZPPM** also exhibited similar tendencies as the Ac-end-capped emitters (**Figure 5** and **Figure S5**). When **mCP** was used, the **PXZPPM/mCP** film showed almost random orientation with  $\Theta$  of 62%, while when **PXZPPM** was doped into the other host materials, all the doped films exhibited significant horizontal orientation with  $\Theta$  of 74–81%. Among these emitters, it was determined that bulky methyl groups on Ac end-capping groups do not cause a negative effect toward horizontal orientation as the emitter without methyl groups showed very similar  $\Theta$  values.

## Underlying Mechanism for Horizontal Orientation

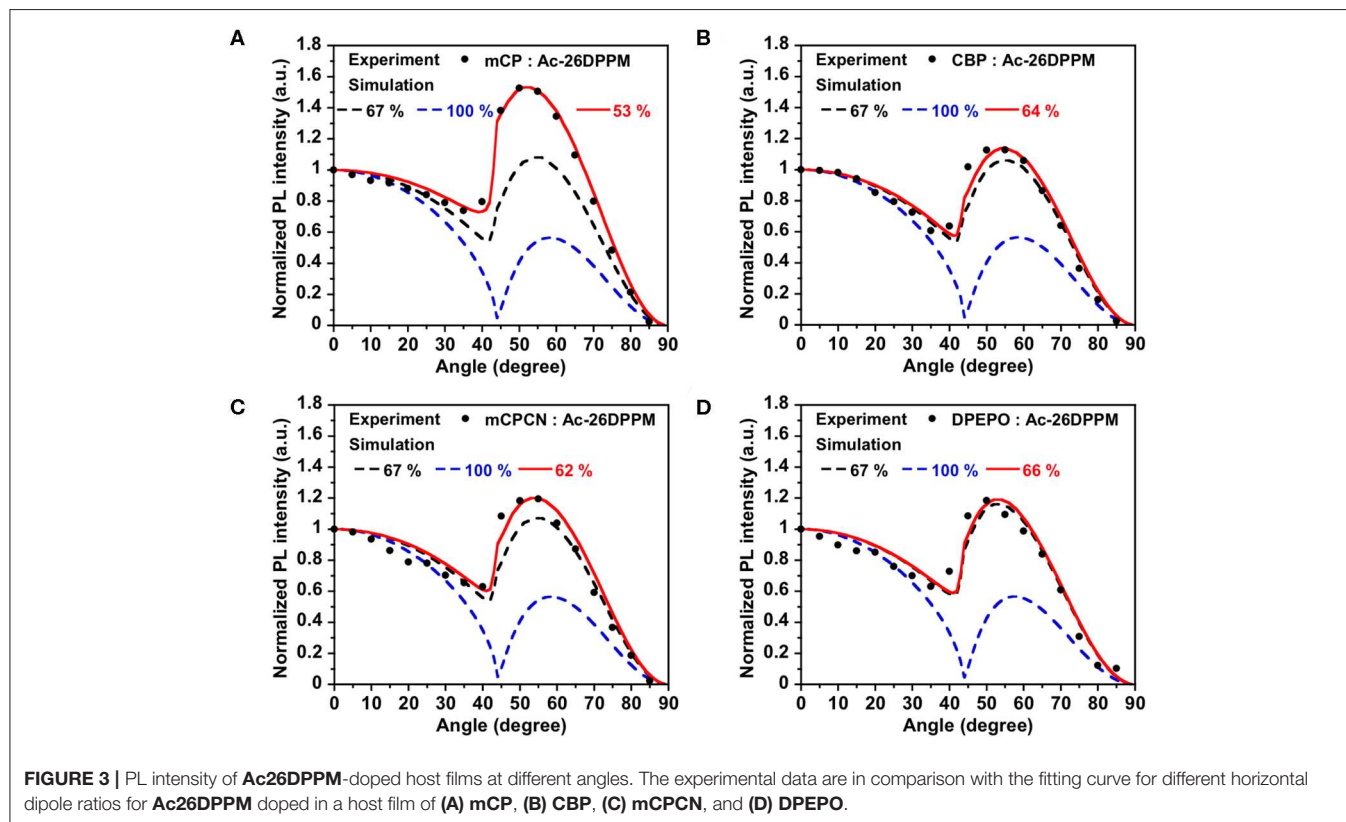
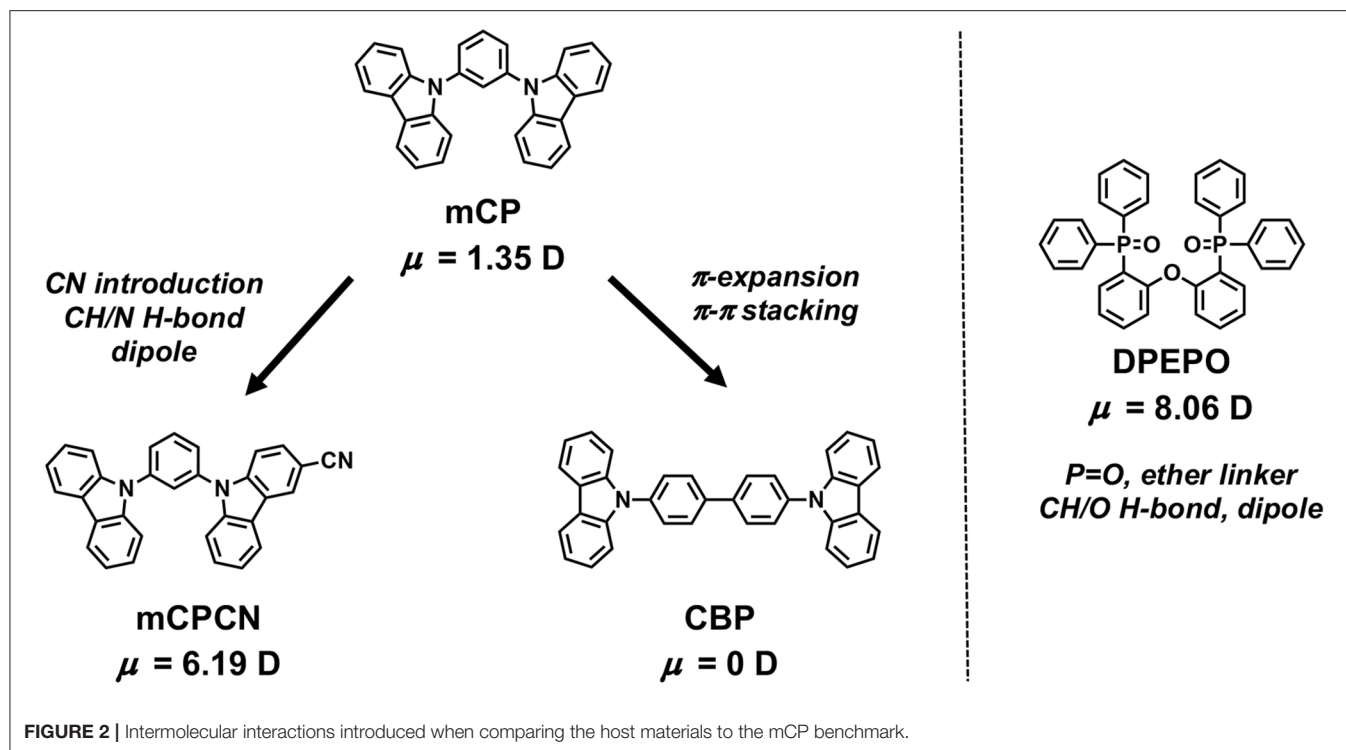
To validate the underlying mechanisms for horizontal orientation, we compared the chemical structures of the host materials. When host was changed from **mCP** to **CBP**,  $\pi$ -conjugation is expanded from phenyl to a biphenyl linker. Therefore, enhanced  $\pi$ - $\pi$  stacking can be considered as an additional interaction. Note that the dipole moment of **CBP** is calculated to be 0 D, while that of **mCP** is 1.35 D. Further, the dipole moments of the emitters are smaller than 2.0 D. Thus, dipole/dipole interaction can be ruled out as a major interaction. In the case of **mCPCN**, the difference of chemical structure is only a CN group on the carbazole plane. Since the CN group is a strong electron-withdrawing group, the resulting **mCPCN** has a large dipole moment of 6.19 D. However, as mentioned in the case of **CBP**, the contributions from dipole/dipole interaction can be considered to be small because the emitters used in this study have very small dipole moment  $<2$  D. In fact, the  $\Delta\Theta$  of **Ac26DPPM** ( $\Delta\Theta = 9\%$ ) with a larger dipole moment ( $\mu = 1.89$  D) was smaller than that of **AcPPM** ( $\Delta\Theta = 17\%$ ) with a smaller dipole moment ( $\mu = 0.38$  D). Therefore, it is only CH/N weak H-bond of CN group plays a key role. The binding energy of CH/N weak H-bond is 10–20 kJ/mol (Desiraju and Steiner, 1999). This interaction has been reported to be a key to controlling horizontal orientation of oligopyridine-containing

electron transporters (Sasabe et al., 2011; Yokoyama et al., 2011; Watanabe et al., 2019a,b). **DPEPO** is a frequently used host material in high efficiency TADF OLEDs, and the films using it as the host showed the largest  $\Theta$  values among the four host materials. **DPEPO** has a large dipole moment of 8.06 D, and therefore the contributions from dipole/dipole interaction are considered to be large. However, similar to the case of **mCPCN**, the contributions from dipole/dipole interaction can be considered to be small because the emitters used in this study have very small dipole moment  $<2$  D. In fact, the  $\Delta\Theta$  of **Ac26DPPM** ( $\Delta\Theta = 13\%$ ) with a larger dipole moment ( $\mu = 1.89$  D) was smaller than that of **AcPPM** ( $\Delta\Theta = 22\%$ ) with a smaller dipole moment ( $\mu = 0.38$  D). Given that **DPEPO** has short conjugation lengths with steric hindrance,  $\pi$ - $\pi$  interaction is relatively small. Thus, it can be considered that CH/O weak H-bond from P=O and ether linker plays a key role in determining the horizontal orientation when **DPEPO** is used as the host material. Recently, Samuel and Zysman-Colman proposed that the significant number of electronegative sites from P=O and ether linker on the surface of **DPEPO** vacuum-deposited film plays an important role for horizontal molecular orientation (Pal et al., 2018). Further, it has also been reported that the strong acceptor property of P=O forms shorter CH...O H-bond, and the bond length of the CH...O H-bond is relatively shorter than that of CH...N H-bond (Desiraju and Steiner, 1999).

Among the three emitters, **PXZPPM** and **AcPPM** showed similar tendencies for horizontal orientation, even though **AcPPM** has four bulky methyl groups on the acridine end-capping units. One possible reason for this is the contributions from multiple CH/ $\pi$  contacts between the methyl groups and the  $\pi$  planes. CH/ $\pi$  contact is a very small interaction, and the binding energy is only 2–3 kJ/mol (Nishio et al., 1998). However, when the molecule has a large number of methyl groups, the contributions would not be negligible in the solid state. In fact, very recently, enhanced horizontal orientation is realized in a series of iridium complexes by introduction of methyl or alkyl groups (Shin et al., 2019). Therefore, we propose that the contributions from multiple CH/ $\pi$  contacts can collaborate with other strong intermolecular interactions to realize significant horizontal orientation.

## OLED Performances

Finally, we fabricated OLEDs using **PXZPPM**/hosts as an emission layer to show the effect of horizontal orientation on the OLED efficiency. Here, we used two types of hosts, **mCP** ( $\Theta = 62\%$ ) and **mCPCN** ( $\Theta = 79\%$ ). Note that we did not use **DPEPO** as a host material because the chemical structure is totally different from **mCP**. The structure of the OLED was [indium tin oxide (ITO) anode (130 nm)/triphenylamine-containing polymer: 4-isopropyl-4'-methyldiphenyliodonium tetrakis(pentafluorophenyl)borate (**PPBI**) (20 nm) (Kido et al., 1997)/di-[4-(N,N-ditolyl-amino)-phenyl]cyclohexane (**TAPC**) (25 nm)/4,4',4''-tris(N-carbazolyl)triphenylamine (**TCTA**) (5 nm)/10 wt% **PXZPPM**-doped **mCP**, or **mCPCN** (10 nm)/3,3'',5,5'-tetra(3-pyridyl)-1,1';3',1''-terphenyl (**B3PyPB**)





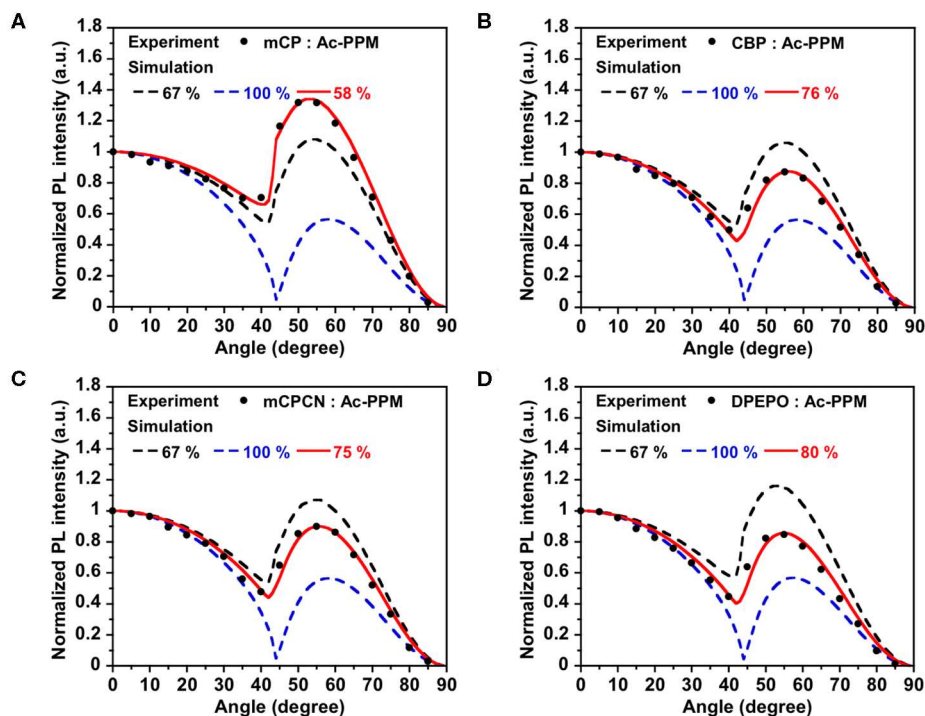


**FIGURE 4 |** PL intensity of AcPPM-doped in (A) mCP, (B) CBP, (C) mCPCN, and (D) DPEPO host films at different angles. The experimental data are in comparison with the fitting curve for different horizontal dipole ratios.

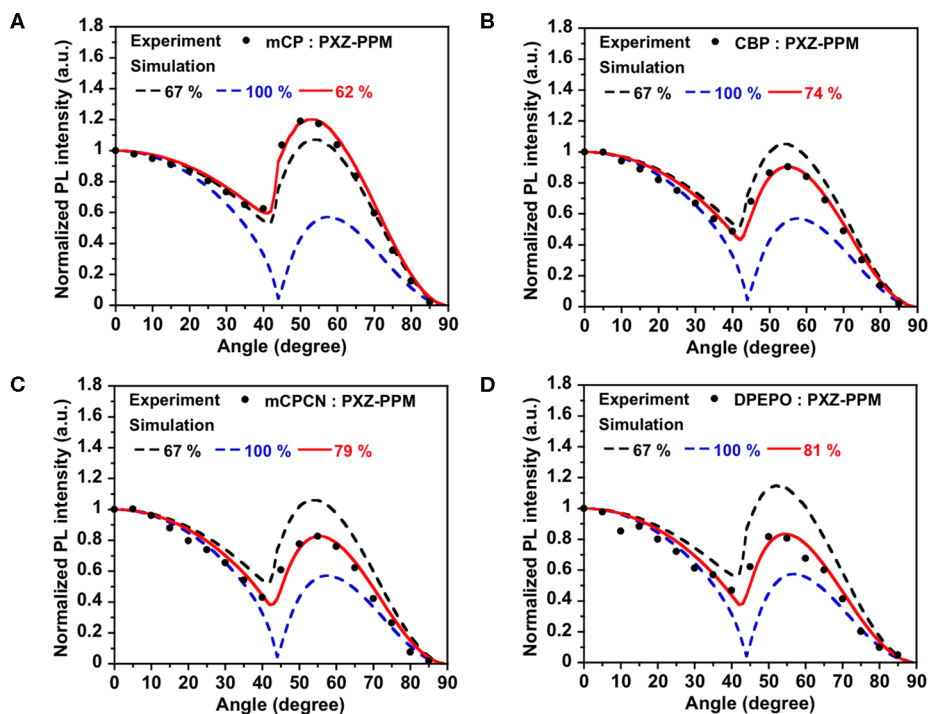


**FIGURE 5 |** PL intensity of PXZPPM-doped in (A) mCP, (B) CBP, (C) mCPCN, and (D) DPEPO host films at different angles. The experimental data are in comparison with the fitting curve for different horizontal dipole ratios.

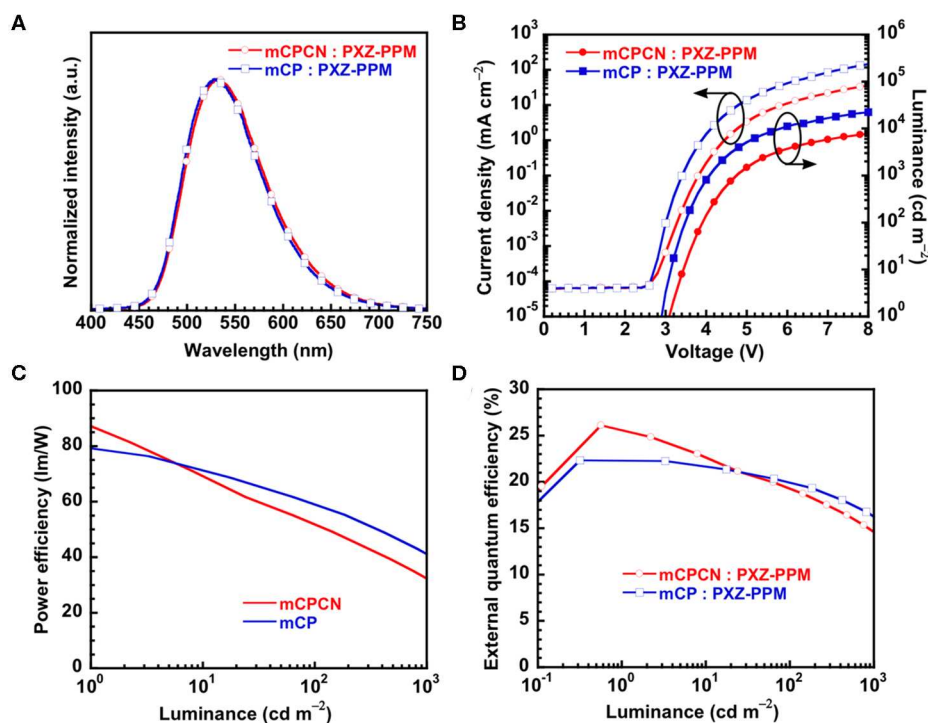


**FIGURE 6** | Device performance of **PXZPPM**-based OLEDs; **(A)** EL spectra; **(B)** current density–voltage–luminance characteristics; **(C)** power efficiency–luminance characteristics; **(D)** external quantum efficiency–luminance characteristics.

**TABLE 3** | Summary of **PXZPPM**-based OLED performance.

Host	$V_{on}^a$ (V)	$V_{100}/\eta_c, 100/\eta_p, 100/\eta_{ext}, 100^b$ (V/cd A <sup>-1</sup> /lm W <sup>-1</sup> /%)	$V_{1000}/\eta_c, 1000/\eta_p, 1000/\eta_{ext}, 1000^c$ (V/cd A <sup>-1</sup> /lm W <sup>-1</sup> /%)	$\eta_{c,max}/\eta_{p,max}/\eta_{ext,max}^d$ (cd A <sup>-1</sup> /lm W <sup>-1</sup> /%)
mCP	2.85	3.46/65.7/59.7/20.0	4.07/53.5/41.4/16.3	73.1/82.1/22.3
mCPCN	3.05	3.89/64.8/52.4/19.4	4.74/48.9/32.5/14.6	87.2/91.4/26.1

<sup>a</sup> Turn-on voltage at 1 cd m<sup>-2</sup>. <sup>b</sup> Voltage (V), current efficiency ( $\eta_c$ ), power efficiency ( $\eta_p$ ), and external quantum efficiency ( $\eta_{ext}$ ) at 100 cd m<sup>-2</sup>. <sup>c</sup>  $V$ ,  $\eta_c$ ,  $\eta_p$ , and  $\eta_{ext}$  at 1,000 cd m<sup>-2</sup>. <sup>d</sup>  $\eta_c$ ,  $\eta_p$ , and  $\eta_{ext}$  at maximum.

(50 nm) (Sasabe et al., 2008)/LiF (0.5 nm)/Al cathode (100 nm)]. **TAPC** and **TCTA** were used as the hole transport layers, **B3PyPB** as the electron transport layer, and LiF as the electron injection layer. The chemical structures of these materials are shown in **Figure S6**. **Figure 6** shows the electroluminescence (EL) spectra, the current density ( $J$ )–voltage ( $V$ )–luminance ( $L$ ), and  $\eta_{ext}$ – $L$  characteristics. The electroluminescent characteristics are summarized in **Table 3**. The EL spectra of both devices showed similar emission with peaks at 529 nm for **mCP** and at 531 nm for **mCPCN** host materials. The maximum  $\eta_{ext}$  values were recorded to be 22.3% for **mCP** and 26.1% for **mCPCN**. Moreover, the light distribution patterns evaluated by Lambertian factor of these devices were similar, and recorded to be 0.99 for **mCP**, and 0.97 for **mCPCN**, as shown in **Figure S6**. The photoluminescent quantum yields ( $\eta_{PL}$ ) of **PXZPPM**/host films were similar for **mCP** (71%) and **mCPCN** (69%) hosts. Given that the carrier balance factor is similar at the peak efficiency, the differences in the maximum  $\eta_{ext}$  values can be attributed to the differences in  $\Theta$  values of the different host

materials. Note that we also fabricated the devices using **CBP** and **DPEPO** as a host material. As a result, higher  $\eta_{PL}$  and  $\Theta$  values gave superior device performances (**Figure S7** and **Table S1**). Enhancing the horizontal orientation of the emitter apparently increases the light coupling efficiency, thus resulting in a higher  $\eta_{ext}$  value.

## CONCLUSION

We performed a systematic investigation on the molecular orientations of TADF emitters in a series of carbazole-based host materials. TADF emitters used in this study have a small dipole moment <2 D. To validate the underlying mechanisms for horizontal orientation, we changed the chemical structure of **mCP** by: (i) extending the  $\pi$ -conjugation to form **CBP**, and (ii) the introduction of a CN substituent to form **mCPCN**. In addition, a phosphine-oxide host material, **DPEPO**, was used. Although all the emitters and the host materials had random orientation as a neat film, the emitters with larger molecular

shape anisotropy, **AcPPM** and **PXZPPM**, showed enhanced horizontal orientation up to  $\Theta \sim 81\%$  in all host films except **mCP**. The third emitter, **Ac26DPPM**, has a smaller molecular shape anisotropy, and subsequently showed vertical orientation in the **mCP** host film ( $\Theta = 53\%$ ). However, when doped into the other host material, **Ac26DPPM** showed random orientation ( $\Theta \sim 66\%$ ). From these results, it can be considered that (i) an increase in the  $\pi$ -conjugation leads to stronger  $\pi$ - $\pi$  stacking, (ii) the introduction of CN group induces CH/N weak H-bonds, and (iii) the introduction of a strong acceptor P=O and ether groups induces CH/O H-bonds, and all these interactions enhance the horizontal orientation of TADF emitters. In addition, we propose that the contributions from multiple CH/ $\pi$  contacts can collaborate with other strong intermolecular interactions such as  $\pi$ - $\pi$  stacking, CH/N and CH/O H-bonds to realize significant horizontal orientation. Finally, we fabricated an **PXZPPM**-based OLED that achieved an  $\eta_{\text{ext}}$  of 26% using an EML with  $\Theta$  of 79%, which is higher than that of an almost randomly oriented EML with  $\Theta$  of 62% ( $\eta_{\text{ext}} = 22\%$ ). We believe that our results will be beneficial in revealing the underlying mechanism for horizontal orientation leading to superior OLED performances.

## DATA AVAILABILITY STATEMENT

All datasets generated for this study are included in the article/**Supplementary Material**.

## REFERENCES

- Adachi, C. (2014). Third-generation organic electroluminescence materials. *Jpn. J. Appl. Phys.* 53:60101. doi: 10.7567/JJAP.53.060101
- Ahn, D. H., Kim, S. W., Lee, H., Ko, I. J., Karthik, D., Lee, J. Y., et al. (2019). Highly efficient blue thermally activated delayed fluorescence emitters based on symmetrical and rigid oxygen-bridged boron acceptors. *Nat. Photonics* 13, 540–546. doi: 10.1038/s41566-019-0415-5
- Desiraju, G. R., and Steiner, T. (1999). *The Weak Hydrogen Bond—In Structural Chemistry and Biology*. New York, NY: Oxford University Press.
- Friedrich, P., Coehoorn, R., and Wenzel, W. (2017). Molecular origin of the anisotropic dye orientation in emissive layers of organic light emitting diodes. *Chem. Mater.* 29:9528. doi: 10.1021/acs.chemmater.7b03742
- Frischeisen, J., Yokoyama, D., Endo, A., Adachi, C., and Brütting, W. (2011). Increased light outcoupling efficiency in dye-doped small molecule organic light-emitting diodes with horizontally oriented emitters. *Org. Electron.* 12, 809–817. doi: 10.1016/j.orgel.2011.02.005
- Gujral, A., Yu, L., and Ediger, M. D. (2018). Anisotropic organic glasses. *Curr. Opin. Solid State Mater. Sci.* 22, 49–57. doi: 10.1016/j.cossms.2017.11.001
- Han, C. M., Zhao, Y. B., Xu, H., Chen, J. S., Deng, Z. P., Ma, D. G., et al. (2011). A simple phosphine-oxide host with a multi-insulating structure: high triplet energy level for efficient blue electrophosphorescence. *Chem. Eur. J.* 17, 5800–5803. doi: 10.1002/chem.201100254
- Im, Y., Kim, M., Cho, Y. J., Seo, J. A., Yook, K. S., and Lee, J. Y. (2017). Molecular design strategy of organic thermally activated delayed fluorescence emitters. *Chem. Mater.* 29, 1946–1963. doi: 10.1021/acs.chemmater.6b05324
- Kaji, H., Suzuki, H., Fukushima, T., Shizu, K., Suzuki, K., Kubo, S., et al. (2015). Purely organic electroluminescent material realizing 100% conversion from electricity to light. *Nat. Commun.* 6:8476. doi: 10.1038/ncomms9476
- Kido, J., Harada, G., Komada, M., Shionoya, H., and Nagai, K. (1997). Aromatic-amine-containing polymers for organic electroluminescent devices. *ACS Symposium Ser.* 672, 381–394. doi: 10.1021/bk-1997-0672.ch025

## AUTHOR CONTRIBUTIONS

HS and SO conceived the project. HS, YC, SO, and DY interpreted the data and prepared the manuscript and supplementary materials. HS, SO, and JK supervised the project. YC, SO, and DY designed experiments. HA, TO, RK, and YW synthesized and characterized materials. YC, YW, and DY prepared samples, performed variable-angle spectroscopic ellipsometry measurements, and related data analysis. YC, SO, and HA prepared samples and performed angle dependent PL measurements. YC and HA fabricated devices. All authors discussed the results and commented on the manuscript.

## ACKNOWLEDGMENTS

We gratefully acknowledge the partial financial support from the Center of Innovation (COI) Program from the Japan Science and Technology Agency, JST. HS acknowledges financial support in part by JSPS KAKENHI (17H03131) from JSPS.

## SUPPLEMENTARY MATERIAL

The Supplementary Material for this article can be found online at: <https://www.frontiersin.org/articles/10.3389/fchem.2020.00427/full#supplementary-material>

- Kim, K. H., and Kim, J. J. (2018). Origin and control of orientation of phosphorescent and TADF dyes for high-efficiency OLEDs. *Adv. Mater.* 30:1705600. doi: 10.1002/adma.201705600
- Komatsu, R., Sasabe, H., Nakao, K., Hayasaka, Y., Ohsawa, T., and Kido, J. (2016a). Unlocking the potential of pyrimidine conjugate emitters to realize high-performance organic light-emitting devices. *Adv. Opt. Mater.* 5. doi: 10.1002/adom.201600675
- Komatsu, R., Sasabe, H., Seino, Y., Nakao, K., and Kido, J. (2016b). Light-blue thermally activated delayed fluorescent emitters realizing a high external quantum efficiency of 25% and unprecedented low drive voltages in OLEDs. *J. Mater. Chem. C* 4:2274. doi: 10.1039/C5TC04057D
- Komatsu, R., Sasabe, H., and Kido, J. (2018). Recent progress of pyrimidine derivatives for high-performance organic light-emitting devices. *J. Photon. Energy* 8:032108. doi: 10.1117/1.JPE.8.032108
- Komino, T., Sagara, Y., Tanaka, H., Oki, Y., Nakamura, N., Fujimoto, H., et al. (2016). Electroluminescence from completely horizontally oriented dye molecules. *Appl. Phys. Lett.* 108:241106. doi: 10.1063/1.4954163
- Kondo, Y., Yoshiura, K., Kitera, S., Nishi, H., Oda, S., Gotoh, H., et al. (2019). Narrowband deep-blue organic light-emitting diode featuring an organoboron-based emitter. *Nat. Photonics* 13, 678–682. doi: 10.1038/s41566-019-0476-5
- Lee, Y. T., Tseng, P. C., Komino, T., Mamada, M., Ortiz, R. J., Leung, M. K., et al. (2018). Simple molecular-engineering approach for enhancing orientation and outcoupling efficiency of thermally activated delayed fluorescent emitters without red-shifting emission. *ACS Appl. Mater. Interfaces* 10, 43842–43849. doi: 10.1021/acsami.8b16199
- Lin, M. S., Yang, S. J., Chang, H. W., Huang, Y. H., Tsai, Y. T., Wu, C. C., et al. (2012). Incorporation of a CN group into mCP: a new bipolar host material for highly efficient blue and white electrophosphorescent devices. *J. Mater. Chem.* 22, 16114–16120. doi: 10.1039/c2jm32717a
- Lin, T. A., Chatterjee, T., Tsai, W. L., Lee, W. K., Wu, M. J., Jiao, M., et al. (2016). Sky-blue organic light emitting diode with 37% external quantum efficiency

- using thermally activated delayed fluorescence from spiroacridine-triazine hybrid. *Adv. Mater.* 28, 6976–6983. doi: 10.1002/adma.201601675
- Liu, M., Komatsu, R., Cai, X., Hotta, K., Sato, S., Liu, K., et al. (2017). Horizontally orientated sticklike emitters: enhancement of intrinsic out-coupling factor and electroluminescence performance. *Chem. Mater.* 29, 8630–8636. doi: 10.1021/acs.chemmater.7b02403
- Mayr, C., and Brütting, W. (2015). Control of molecular dye orientation in organic luminescent films by the glass transition temperature of the host material. *Chem. Mater.* 27, 2759–2762. doi: 10.1021/acs.chemmater.5b00062
- Moon, C.-K., Kim, K.-H., Lee, J. W., and Kim, J.-J. (2015). Influence of host molecules on emitting dipole orientation of phosphorescent iridium complexes. *Chem. Mater.* 27, 2767–2769. doi: 10.1021/acs.chemmater.5b00469
- Nakao, K., Sasabe, H., Komatsu, R., Hayasaka, Y., Ohsawa, T., and Kido, J. (2017). Significant enhancement of blue OLED performances through molecular engineering of pyrimidine-based emitter. *Adv. Opt. Mater.* 5:1600843. doi: 10.1002/adom.201600843
- Nishio, M., Hirota, M., and Umezawa, Y. (1998). *The CH/π Interaction—Evidence, Nature, and Consequences*. New York, NY: Wiley-VCH.
- Pal, A. K., Krotkus, S., Fontani, M., Mackenzie, C. F. R., Cordes, D. B., Slawin, A. M. Z., et al. (2018). High-efficiency deep-blue-emitting organic light-emitting diodes based on iridium(III) carbene complexes. *Adv. Mater.* 30:e1804231. doi: 10.1002/adma.201804231
- Rajamalli, P., Senthilkumar, N., Huang, P. Y., Ren-Wu, C. C., Lin, H. W., and Cheng, C. H. (2017). New molecular design concurrently providing superior pure blue, thermally activated delayed fluorescence and optical out-coupling efficiencies. *J. Am. Chem. Soc.* 139, 10948–10951. doi: 10.1021/jacs.7b03848
- Sasabe, H., Gonmori, E., Chiba, T., Li, Y. J., Tanaka, D., Su, S. J., et al. (2008). Wide-energy-gap electron-transport materials containing 3,5-dipyridylphenyl moieties for an ultra high efficiency blue organic light-emitting device. *Chem. Mater.* 20, 5951–5953. doi: 10.1021/cm801727d
- Sasabe, H., and Kido, J. (2013). Development of high performance OLEDs for general lighting. *J. Mater. Chem. C* 1:1699. doi: 10.1039/c2tc00584k
- Sasabe, H., Tanaka, D., Yokoyama, D., Chiba, T., Pu, Y.-J., Nakayama, K.-I., et al. (2011). Influence of substituted pyridine rings on physical properties and electron mobilities of 2-methylpyrimidine skeleton-based electron transporters. *Adv. Func. Mater.* 21, 336–342. doi: 10.1002/adfm.201001252
- Schmidt, T. D., Lampe, T., Sylvinson, D. M. R., Djurovich, P. I., Thompson, M. E., and Brütting, W. (2017). Emitter orientation as a key parameter in organic light-emitting diodes. *Phys. Rev. Appl.* 8:037001. doi: 10.1103/PhysRevApplied.8.037001
- Shibata, M., Sakai, Y., and Yokoyama, D. (2015). Advantages and disadvantages of vacuum-deposited and spin-coated amorphous organic semiconductor films for organic light-emitting diodes. *J. Mater. Chem. C* 3:11178. doi: 10.1039/C5TC01911G
- Shin, H., Ha, Y. H., Kim, H. G., Kim, R., Kwon, S. K., Kim, Y. H., et al. (2019). Controlling horizontal dipole orientation and emission spectrum of Ir complexes by chemical design of ancillary ligands for efficient deep-blue organic light-emitting diodes. *Adv. Mater.* 31:1808102. doi: 10.1002/adma.201808102
- Uoyama, H., Goushi, K., Shizu, K., Nomura, H., and Adachi, C. (2012). Highly efficient organic light-emitting diodes from delayed fluorescence. *Nature* 492, 234–238. doi: 10.1038/nature11687
- Watanabe, Y., Sasabe, H., and Kido, J. (2019a). Review of molecular engineering for horizontal molecular orientation in organic light-emitting devices. *Bull. Chem. Soc. Jpn.* 92, 716–728. doi: 10.1246/bcsj.20180336
- Watanabe, Y., Yokoyama, D., Koganezawa, T., Katagiri, H., Ito, T., Ohisa, S., et al. (2019b). Control of molecular orientation in organic semiconductor films using weak hydrogen bonds. *Adv. Mater.* 31:1808300. doi: 10.1002/adma.201808300
- Wong, M. Y., and Zysman-Colman, E. (2017). Purely organic thermally activated delayed fluorescence materials for organic light-emitting diodes. *Adv. Mater.* 29:1605444. doi: 10.1002/adma.201605444
- Wu, T.-L., Huang, M.-J., Lin, C.-C., Huang, P.-Y., Chou, T.-Y., Chen-Cheng, R.-W., et al. (2018). Diboron compound-based organic light-emitting diodes with high efficiency and reduced efficiency roll-off. *Nat. Photonics* 12, 235–240. doi: 10.1038/s41566-018-0112-9
- Yang, Z. Y., Mao, Z., Xie, Z. L., Zhang, Y., Liu, S. W., Zhao, J., et al. (2017). Recent advances in organic thermally activated delayed fluorescence materials. *Chem. Soc. Rev.* 46, 915–1016. doi: 10.1039/C6CS00368K
- Yokoyama, D. (2011). Molecular orientation in small-molecule organic light-emitting diodes. *J. Mater. Chem.* 21:19187. doi: 10.1039/c1jm13417e
- Yokoyama, D., Sakaguchi, A., Suzuki, M., and Adachi, C. (2009). Horizontal orientation of linear-shaped organic molecules having bulky substituents in neat and doped vacuum-deposited amorphous films. *Org. Electron.* 10, 127–137. doi: 10.1016/j.orgel.2008.10.010
- Yokoyama, D., Sasabe, H., Furukawa, Y., Adachi, C., and Kido, J. (2011). Molecular stacking induced by intermolecular C-H...N hydrogen bonds leading to high carrier mobility in vacuum-deposited organic films. *Adv. Func. Mater.* 21, 1375–1382. doi: 10.1002/adfm.201001919

**Conflict of Interest:** The authors declare that the research was conducted in the absence of any commercial or financial relationships that could be construed as a potential conflict of interest.

Copyright © 2020 Sasabe, Chikayasu, Ohisa, Arai, Ohsawa, Komatsu, Watanabe, Yokoyama and Kido. This is an open-access article distributed under the terms of the Creative Commons Attribution License (CC BY). The use, distribution or reproduction in other forums is permitted, provided the original author(s) and the copyright owner(s) are credited and that the original publication in this journal is cited, in accordance with accepted academic practice. No use, distribution or reproduction is permitted which does not comply with these terms.





# Impact of Boron Acceptors on the TADF Properties of *Ortho*-Donor-Appended Triarylboron Emitters

Hanif Mubarak<sup>1†</sup>, Woochan Lee<sup>2†</sup>, Taehwan Lee<sup>1</sup>, Jaehoon Jung<sup>1</sup>, Seunghyup Yoo<sup>2\*</sup> and Min Hyung Lee<sup>1\*</sup>

<sup>1</sup> Department of Chemistry, University of Ulsan, Ulsan, South Korea, <sup>2</sup> School of Electrical Engineering, KAIST, Daejeon, South Korea

## OPEN ACCESS

### Edited by:

Sebastian Reineke,  
Technische Universität  
Dresden, Germany

### Reviewed by:

Przemysław Data,  
Silesian University of  
Technology, Poland  
Takuji Hatakeyama,  
Kwansei Gakuin University, Japan

### \*Correspondence:

Seunghyup Yoo  
syoo@ee.kaist.ac.kr  
Min Hyung Lee  
lmh74@ulsan.ac.kr

<sup>†</sup>These authors have contributed  
equally to this work

### Specialty section:

This article was submitted to  
Organic Chemistry,  
a section of the journal  
Frontiers in Chemistry

Received: 21 January 2020

Accepted: 26 May 2020

Published: 24 June 2020

### Citation:

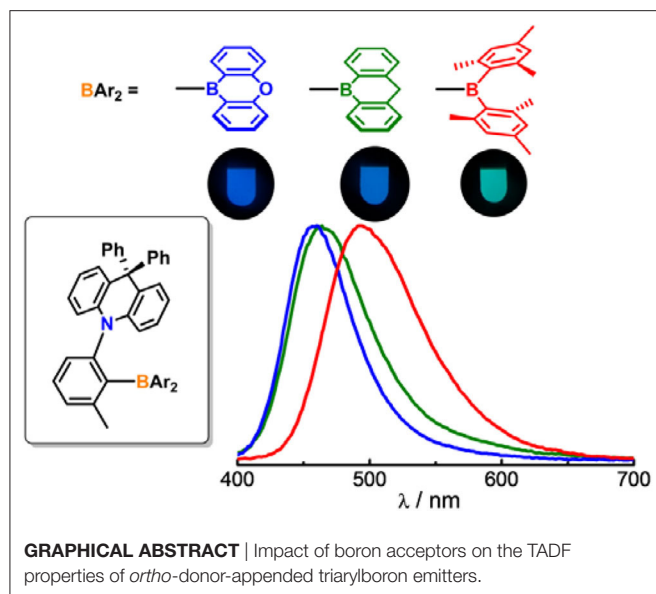
Mubarak H, Lee W, Lee T, Jung J,  
Yoo S and Lee MH (2020) Impact of  
Boron Acceptors on the TADF  
Properties of *Ortho*-Donor-Appended  
Triarylboron Emitters.  
Front. Chem. 8:538.  
doi: 10.3389/fchem.2020.00538

We report the impact of boron acceptors on the thermally activated delayed fluorescence (TADF) properties of *ortho*-donor-appended triarylboron compounds. Different boryl acceptor moieties, such as 9-boraanthryl (**1**), 10*H*-phenoxaboryl (**2**), and dimesitylboryl (BMes<sub>2</sub>, **3**) groups have been introduced into an *ortho* donor (D)–acceptor (A) backbone structure containing a 9,9-diphenylacridine (DPAC) donor. X-ray crystal diffraction and NMR spectroscopy evidence the presence of steric congestion around the boron atom along with a highly twisted D–A structure. A short contact of 2.906 Å between the *N* and *B* atoms, which is indicative of an N→B nonbonding electronic interaction, is observed in the crystal structure of **2**. All compounds are highly emissive (PLQYs = 90–99%) and display strong TADF properties in both solution and solid state. The fluorescence bands of cyclic boryl-containing **1** and **2** are substantially blue-shifted compared to that of BMes<sub>2</sub>-containing **3**. In particular, the PL emission bandwidths of **1** and **2** are narrower than that of **3**. High-efficiency TADF-OLEDs are realized using **1–3** as emitters. Among them, the devices based on the cyclic boryl emitters exhibit pure blue electroluminescence (EL) and narrower EL bands than the device with **3**. Furthermore, the device fabricated with emitter **1** achieves a high external quantum efficiency of 25.8%.

**Keywords:** TADF, *ortho*-donor-acceptor, triarylboron, cyclic boryl acceptor, OLEDs

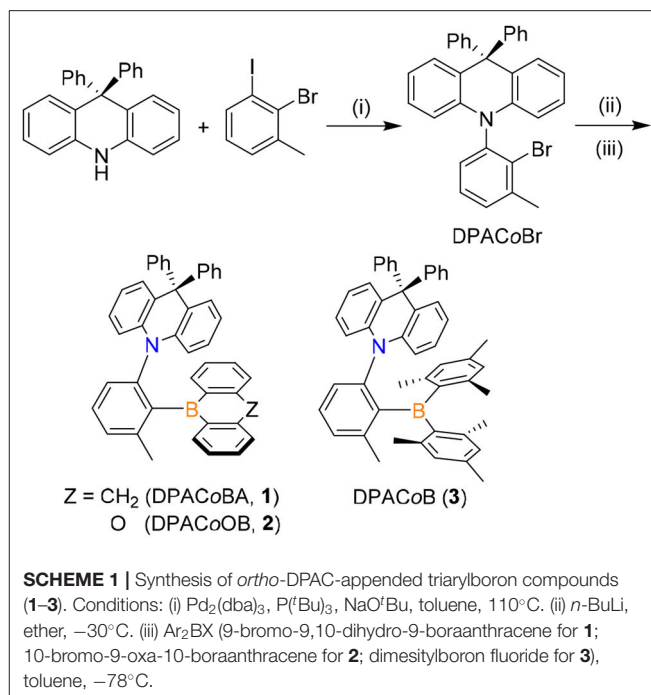
## INTRODUCTION

Thermally activated delayed fluorescence (TADF) compounds have recently received great attention as efficient emitters in organic light-emitting diodes (OLEDs) because TADF-OLEDs can theoretically achieve nearly 100% internal quantum efficiency ( $\eta_{\text{int}}$ ) via the upconversion of triplet excitons into emissive singlet excitons through a thermally activated reverse intersystem crossing (RISC) process (Goushi et al., 2012; Uoyama et al., 2012; Zhang et al., 2012, 2014; Dias et al., 2013; Tao et al., 2014; Hirata et al., 2015; Kaji et al., 2015; Im et al., 2017; Wong and Zysman-Colman, 2017; Yang et al., 2017; Cai and Su, 2018; Kim et al., 2018). To date, various types of TADF emitters have been reported, and those containing boron acceptor moieties are recently attracting special interest because of their excellent TADF properties. Boron acceptors such as triarylborons possess strong electron-accepting properties owing to their sp<sup>2</sup> hybridized, tri-coordinate boron atom, which has a vacant p(B) orbital (Hirai et al., 2015; Hatakeyama et al., 2016; Turkoglu et al., 2017; Matsui et al., 2018). In addition to this electron-deficiency, p(B)– $\pi^*$  conjugation between the boron atom and linked  $\pi$  systems can lead to the stabilization of the LUMO level. Thus, in combination with suitable donors, the boron acceptors may form donor–acceptor (D–A) emitters



exhibiting TADF. In fact, boron-based emitters have been successfully employed in blue and green OLEDs (Kitamoto et al., 2015, 2016; Numata et al., 2015; Suzuki et al., 2015; Liu et al., 2016; Lien et al., 2017; Chen et al., 2018a,b; Liang et al., 2018; Tsai et al., 2018; Meng et al., 2019; Wu et al., 2019). For example, TADF-OLEDs based on diboron and oxaborin emitters show excellent device performance with a very high external quantum efficiency (EQE) of over 38% (Wu et al., 2018; Ahn et al., 2019). Hatakeyama et al. recently demonstrated that boron and nitrogen-doped polycyclic aromatic hydrocarbons exhibit a deep-blue emission with a very narrow band (full width at half maximum, FWHM = 18 nm), and achieve a high EQE of 34% when incorporated in OLEDs (Kondo et al., 2019). Our group also reported that *ortho*-donor-appended triarylboron compounds have strong TADF character because of their highly twisted D–A structure (Lee et al., 2017). We have shown that electronic modification of the donor and/or boryl acceptor moiety in the *ortho* compounds allows facile tuning of the HOMO and LUMO levels, which in turn tunes the emission color over the visible region (Kumar et al., 2019). In particular, TADF-OLEDs having *ortho* compounds as emitters display a high EQE of above 30% in blue OLED devices (Lee et al., 2018). These results demonstrate that boron compounds having an *ortho*-D–A scaffold constitute highly efficient TADF emitters due to their rigid backbone structure.

Considering the growing interest in developing new boron-based emitters for enhancing the efficiency and stability of devices thereof and reducing the emission bandwidth, it is important to systematically examine the effects of boron acceptors on the TADF properties of the emitters. As noted in previous reports, the most widely adopted boron acceptors are dimesitylboryl (BMes<sub>2</sub>) and heteroatom-bridged cyclic boryl moieties (Hirai et al., 2015; Kitamoto et al., 2015; Liang et al., 2018; Park et al., 2018; Meng et al., 2019; Wu et al., 2019). While the former is effective in providing a steric effect due to its bulky

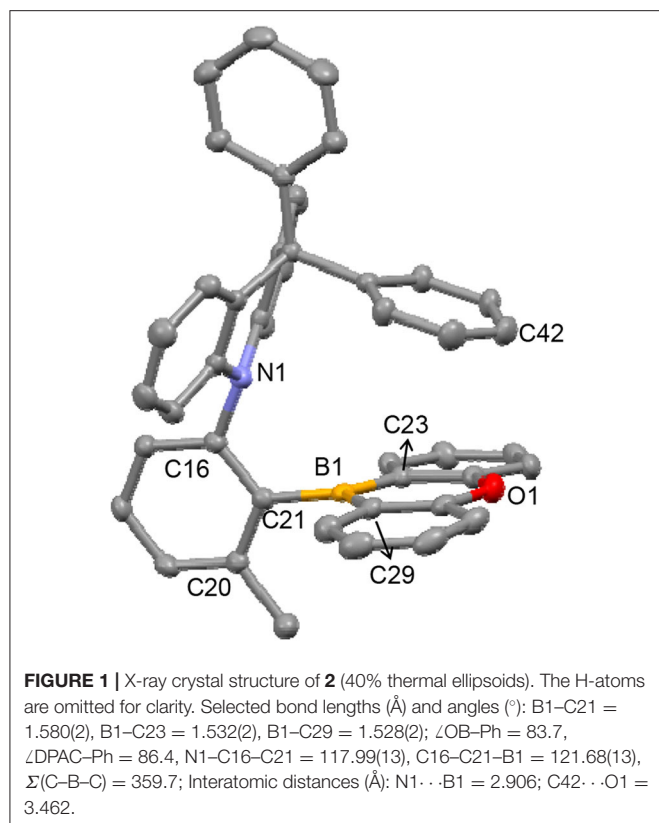


nature, the latter is beneficial for attaining a rigid structure with adjustable electronic effects (Hirai et al., 2019). To elucidate the impact of the boron acceptors on the TADF properties in more detail, we set out to explore a series of *ortho*-donor-appended triarylboron compounds (**1–3**), which contain different boryl acceptor moieties such as BMes<sub>2</sub> and cyclic boryl groups and a fixed donor. The photophysical properties of these boron-based emitters are examined along with theoretical consideration. We demonstrate that the performance of TADF-OLEDs fabricated with these emitters varies with the type of acceptor, and a high EQE of over 25.8% is realized in pure blue devices with the emitter containing a cyclic boryl acceptor.

## RESULTS AND DISCUSSION

### Synthesis and Characterization

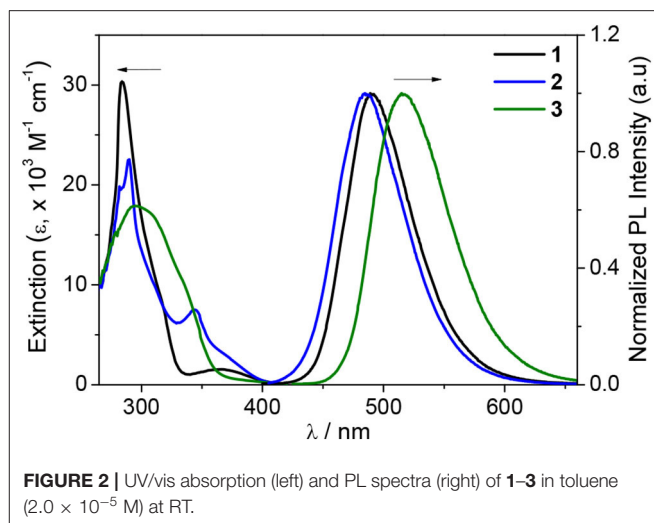
Triarylboron compounds (**1–3**) in which a 9,9-diphenylacridine (DPAC) donor (D) is linked to a boryl acceptor (A) in the *ortho* position of the phenylene ring were prepared (Scheme 1). The cyclic boryl groups [9-boraanthryl (**1**) and 10*H*-phenoxaboryl (**2**)] and a dimesitylboryl group (BMes<sub>2</sub>, **3**) were introduced as acceptors. Buchwald–Hartwig amination reactions between 9,9-diphenyl-10*H*-acridine and 2-bromo-1-iodo-3-methylbenzene produced an *ortho*-DPAC-substituted bromobenzene intermediate, DPACoBr. The lithium salt of DPACoBr was then subjected to reaction with the corresponding boryl-halides to afford the final *ortho*-DPAC-appended triarylboron compounds **1–3**. As expected, compound **3** bearing a bulky BMes<sub>2</sub> group was very stable in air and water. In addition, compounds **1** and **2** having cyclic boryl groups were stable under ambient conditions, presumably due to the steric protection of the boron center by the *ortho*-DPAC and -Me



groups. Consequently, all compounds exhibited high thermal stability, as judged by their high decomposition temperatures ( $T_{d5}$ ) over 320°C.

The compounds were characterized by multinuclear NMR spectroscopy, elemental analysis, and single crystal X-ray crystallography. The  $^1\text{H}$  NMR spectra of **1** and **2** exhibit sharp signals for the cyclic boryl groups, whereas all the methyl and  $\text{C}_{\text{Mes}}\text{-H}$  protons on the two Mes groups in **3** give rise to separate singlets. This feature indicates the highly restricted motion of the bulky  $\text{BMe}_2$  moiety of **3** in solution, which can be attributed to the severe steric hindrance from the *ortho*-DPAC and -Me groups on the phenylene ring (**Supplementary Figures 2–4**) (Lee et al., 2017, 2018). In particular, while the  $^{11}\text{B}$  NMR spectrum of **3** shows a broad signal at  $\delta$  84 ppm, typical of base-free, triarylboron compounds (Wade et al., 2010; Lee et al., 2017), the  $^{11}\text{B}$  signals of **1** and **2** are observed at more upfield regions ( $\delta$  58 ppm for **1** and  $\delta$  65 ppm for **2**). This can be mainly ascribed to the  $\pi$ -donation effect from the ipso-carbon atoms to the empty  $p(\text{B})$  orbital due to the planar structure of the cyclic boryl moieties in **1** and **2** (Zhou et al., 2012).

X-ray diffraction studies conducted on DPACoOB (**2**) confirmed that it exhibits an *ortho* D–A structure, in which both the DPAC and OB rings are almost orthogonal to the phenylene ring ( $\angle$ DPAC–Ph = 86.4° and  $\angle$ OB–Ph = 83.7°), thus facing each other (**Figure 1**). The distance between the N1 and B1 atoms is short (2.906 Å), lying within the sum of the van der Waals radii of the two atoms. This may indicate the presence of an  $\text{N} \rightarrow \text{B}$  nonbonding electronic interaction. Interestingly, the DPAC ring



is puckered at the 9-position, because of the  $\text{sp}^3$  character of the 9-carbon atom, in such a way that one peripheral Ph ring protrudes right above the OB ring. Although the nearest contact between the Ph and OB rings ( $\text{C42} \cdots \text{O1}$ ) is relatively long (3.462 Å), this feature might indicate the occurrence of a  $\pi$ - $\pi$  interaction between the Ph and OB planes. These structural aspects suggest that the boron atom in **2** is sterically and electronically protected, which contributes to its chemical and thermal stability. In the boryl moiety, the boron atom possesses a trigonal planar geometry with a  $\Sigma(\text{C–B–C})$  of 359.7°. It is noteworthy that the two B–C(OB) bond lengths (1.532 and 1.528 Å) are much shorter than that of the B–C(Ph) bond (1.580 Å), the latter being within the range usually found for triarylborons such as  $\text{Ph}_3\text{B}$  (Zettler et al., 1974) and  $\text{Mes}_3\text{B}$  (1.57–1.59 Å) (Blount et al., 1973). As similarly noted in the upfield shifts of the  $^{11}\text{B}$  signals, this finding can be attributed to the presence of  $p(\text{B})$ - $\pi$  interactions in the oxaborin ring, which shorten the B–C(OB) bond lengths.

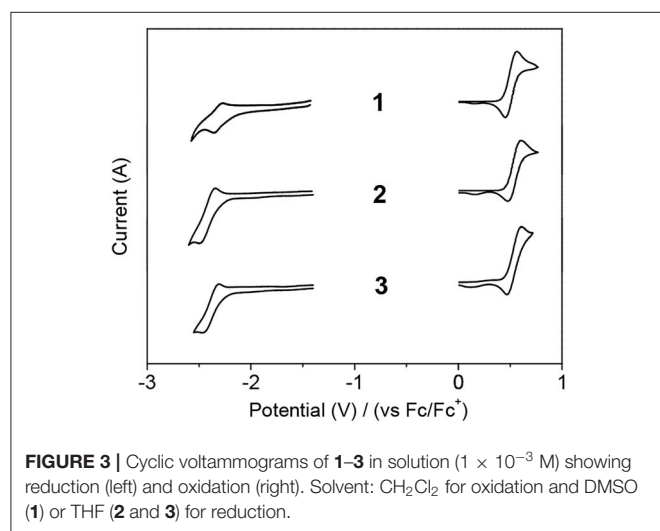
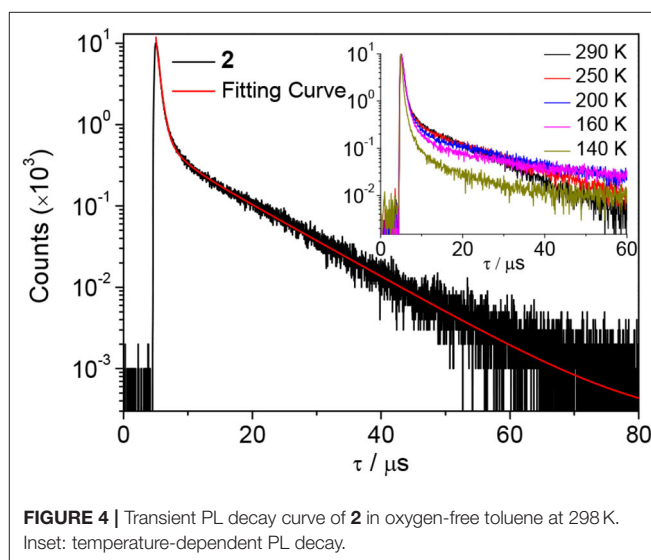
## Photophysical and Electrochemical Properties

The photophysical properties of the compounds were investigated by UV/vis absorption and photoluminescence (PL) measurements in toluene (**Figure 2** and **Table 1**). The intense high-energy absorptions observed at ca. 290 nm can be mainly attributed to the local  $\pi$ - $\pi^*$  transitions centered in the DPAC donor (Park et al., 2018), and the broad bands or shoulders ranging from ca. 300 to 350 nm are assignable to the boryl centered  $\pi$ - $\pi^*$  transitions with  $\pi(\text{Ar})$ - $p(\text{B})$  CT character (see the DFT results below) (Hudson and Wang, 2009; Wade et al., 2010; Zhou et al., 2012). The weak low-energy band for **1** or the tailing found for **2** and **3** above ca. 350 nm can be ascribed to the intramolecular CT (ICT) transitions from the DPAC donor to the boryl acceptor moieties.

To elucidate the ICT transition, the electrochemical properties of the compounds were investigated by cyclic voltammetry (**Figure 3** and **Table 1**, **Supplementary Table 2**). All compounds exhibit DPAC-centered oxidation with similar potential values

**TABLE 1** | Photophysical data of *ortho*-donor-appended triarylboron compounds (**1–3**) in toluene.

Compd	$\lambda_{\text{abs}}^{\text{a}}$ (nm)	$\lambda_{\text{PL}}^{\text{a}}$ (nm)	$\lambda_{\text{FWHM}}^{\text{b}}$ (nm)	$\Phi_{\text{PL}}^{\text{a,c}}$ N <sub>2</sub> /air (%)	$\tau_{\text{p}}^{\text{a,d}}$ ( $\Phi_{\text{PF}}$ ) [ns (%)]	$\tau_{\text{d}}^{\text{a,d}}$ ( $\Phi_{\text{DF}}$ ) [ $\mu\text{s}$ (%)]	HOMO/LUMO <sup>e</sup> (eV)	$E_{\text{g}}^{\text{f}}$ (eV)	$\Delta E_{\text{ST}}^{\text{g}}$ exp/calc (eV)
<b>1</b> (DPACoBA)	284, 318(sh), 367	490	64	91/5.9	62.2 (36)	8.1 (55)	−5.31/−2.61	2.70	0.006/0.039
<b>2</b> (DPACoOB)	290, 344, 368(sh)	485	66	99/6.1	173.4 (52)	8.5 (47)	−5.34/−2.50	2.84	0.020/0.048
<b>3</b> (DPACoB)	295, 335(sh)	516	73	99/4.6	200.7 (13)	8.3 (86)	−5.34/−2.52	2.82	0.013/0.051

<sup>a</sup>In oxygen-free (N<sub>2</sub>) toluene at 298 K ( $5.0 \times 10^{-5}$  M).<sup>b</sup>Full width at half maximum (FWHM).<sup>c</sup>Absolute PLQYs.<sup>d</sup>PL lifetimes of prompt ( $\tau_{\text{p}}$ ) and delayed ( $\tau_{\text{d}}$ ) decay components. The prompt ( $\Phi_{\text{PF}}$ ) and delayed ( $\Phi_{\text{DF}}$ ) portions (%) are given in parentheses.<sup>e</sup>Estimated from the electrochemical oxidation (HOMO) and reduction (LUMO).<sup>f</sup>Electrochemical band gap.<sup>g</sup> $\Delta E_{\text{ST}} = E_{\text{S}} - E_{\text{T}}$ . Singlet ( $E_{\text{S}}$ ) and triplet ( $E_{\text{T}}$ ) energies from the fluorescence and phosphorescence spectra at 77 K. Calculated  $\Delta E_{\text{ST}}$  from TD-DFT at PBE0/6-31G(d,p).**FIGURE 3** | Cyclic voltammograms of **1–3** in solution ( $1 \times 10^{-3}$  M) showing reduction (left) and oxidation (right). Solvent: CH<sub>2</sub>Cl<sub>2</sub> for oxidation and DMSO (**1**) or THF (**2** and **3**) for reduction.**FIGURE 4** | Transient PL decay curve of **2** in oxygen-free toluene at 298 K. Inset: temperature-dependent PL decay.

( $E_{\text{ox}} = 0.51\text{--}0.54$  V) probably because they have the same donor moiety and orthogonal D–A arrangement. However, minor peaks are concomitantly observed at ca. 0.15 V, which might originate from side reactions, such as possible dimerization of radical cations derived from DPAC moieties. As for the reduction, all compounds undergo similar boron-centered reduction with slightly different reduction potentials. Unlike usual triarylboron-based reductions, the reduction process is not completely reversible, but rather to be quasi-reversible. Oxaborin-containing **2** shows the most negative value presumably due to an electron donating effect of oxygen lone pairs through the planar structure, which raises the LUMO level. Although the reduction of boraanthracene-containing **1** occurs at a more positive position, it was measured in DMSO instead of THF because the reduction of **1** was unclear in the latter solvent. It seems that the DMSO solvent stabilizes the boryl moiety, resulting in a more facile reduction. Hence, the band gap ( $E_{\text{g}}$ ) of **1** is smaller than that of **2** despite the similar ICT absorption wavelength of both compounds in toluene (Table 1).

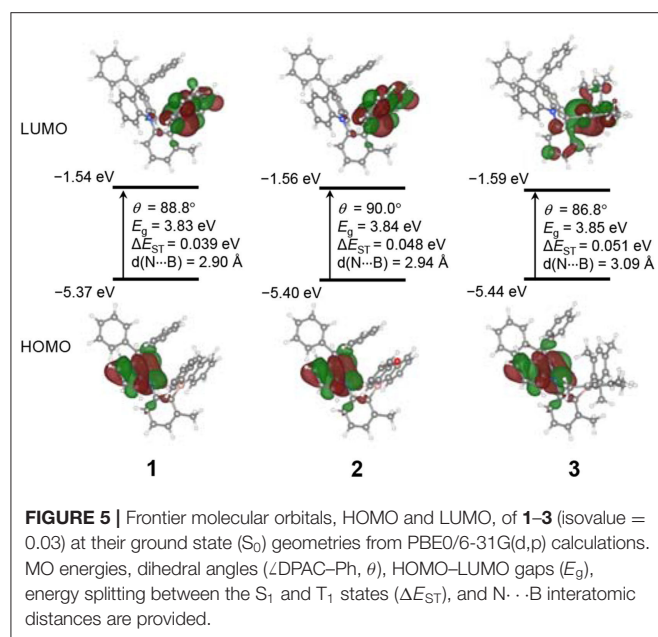
Next, the emission properties of all compounds were examined in toluene (Figure 2). The PL spectra show broad emission bands typical for an ICT transition. Compounds **1** and **2** exhibit sky blue emissions at similar wavelengths ( $\lambda_{\text{PL}}$

= 490 nm for **1** and 485 nm for **2**), whereas **3** displays green emission at 516 nm. In particular, the PL emission bandwidths of **1** and **2** with cyclic boryl moieties ( $\lambda_{\text{FWHM}} = 64\text{--}66$  nm) are narrower than that of **3** with a BMe<sub>2</sub> acceptor ( $\lambda_{\text{FWHM}} = 73$  nm). This indicates a small structural deformation between the ground and excited states of **1** and **2** in solution, presumably due to the rigid cyclic boryl groups. All compounds are highly emissive in oxygen-free toluene with high PL quantum yields (PLQY,  $\Phi_{\text{PL}}$ ) of over 90%; the PLQYs of **2** and **3** are close to 99%, and that of **1** is ca. 91%. In sharp contrast, the PLQYs in air-saturated toluene show drastically decreased values of ca. 5–6% (Table 1 and Supplementary Figure 6). This result suggests that efficient T<sub>1</sub> to S<sub>1</sub> RISC takes place in oxygen-free toluene, thus pointing to the occurrence of strong delayed fluorescence. In fact, the transient PL decay curves exhibit intense delayed components with microsecond lifetimes ( $\tau_{\text{d}}$ ) along with prompt components (Figure 4 and Supplementary Figure 6). The temperature-dependent PL decay also confirms that the delayed component is assignable to TADF (inset in Figure 4) (Uoyama et al., 2012). The  $\Delta E_{\text{ST}}$  values are very small, below 0.02 eV, supporting a fast equilibration between the S<sub>1</sub> and T<sub>1</sub> states. The delayed fluorescence lifetimes ( $\tau_{\text{d}}$ ) of **1–3** are very



**TABLE 2** | Photophysical data of DPEPO films doped with 20 wt% of **1–3**.

Compd	$\lambda_{PL}$ (nm)	$\Delta\lambda_{PL}^a$ (nm)	$\lambda_{FWHM}^b$ (nm)	$\Phi_{PL}$ (%)	$\Phi_{PF}$ (%) <sup>c</sup>	$\Phi_{DF}$ (%) <sup>c</sup>	$\tau_d$ ( $\mu$ s) <sup>d</sup>
<b>1</b>	463	27	71	90	34	56	8.8
<b>2</b>	451	34	62	97	44	53	6.5
<b>3</b>	495	21	74	96	15	81	8.0

<sup>a</sup>Difference in the PL wavelengths obtained in toluene solution and DPEPO film.<sup>b</sup>Full width at half maximum (FWHM).<sup>c</sup>Prompt ( $\Phi_{PF}$ ) and delayed ( $\Phi_{DF}$ ) portions (%) in transient PL decay curves.<sup>d</sup>PL lifetimes of delayed decay components.**FIGURE 5** | Frontier molecular orbitals, HOMO and LUMO, of **1–3** (isovalue = 0.03) at their ground state ( $S_0$ ) geometries from PBE0/6-31G(d,p) calculations. MO energies, dihedral angles ( $\angle$ DPAC–Ph,  $\theta$ ), HOMO–LUMO gaps ( $E_g$ ), energy splitting between the  $S_1$  and  $T_1$  states ( $\Delta E_{ST}$ ), and N...B interatomic distances are provided.

similar to each other (ca. 8  $\mu$ s) and correlate with the  $\Delta E_{ST}$  values. However, the delayed portion ( $\Phi_{DF}$ ) in the transient decay curve is different depending on the boryl acceptors. BMes<sub>2</sub>-containing **3** has the largest portion of delayed fluorescence ( $\Phi_{DF}$  = 86%), whereas the  $\Phi_{DF}$  values for compounds **2** and **3** having cyclic boryl acceptors are in the range of ca. 47–55%.

The photophysical properties of the compounds were further investigated in a doped host film (DPEPO, bis[2-(diphenylphosphino)phenyl]ether oxide) containing 20 wt% of compounds (**Table 2** and **Supplementary Figure 8**). Although the PL wavelengths show the same trend as that found in solution, all compounds display substantial rigidochromic blue-shifts by ca. 21–34 nm. We attribute this result primarily to the high rigidity of **1–3** in film state due to the steric effects of the *ortho*-DPAC and -Me groups. Moreover, the shifts observed for compounds **1** and **2** are greater than those of **3**. This is most likely due to the additional rigidity endowed by the cyclic boryl moieties. As similarly found in solution, the PL emission of **1** and **2** is slightly narrower than that of **3** in the film state ( $\lambda_{FWHM}$  = 62–71 nm for **1** and **2** vs. 74 nm for **3**). In particular, the PLQYs in the host film ( $\Phi_{PL}$  = 90–97%) are very high and comparable to those obtained in solution, also with the value for **1** being

lower than those for **2** and **3**. The delayed fluorescence having long lifetimes (ca. 6.5–8.8  $\mu$ s) and large portions of the delayed components indicate that the strong TADF character of **1–3** is well-retained in film state. It is noteworthy that the portion of the delayed fluorescence follows the order **3** > **1** > **2**, as identically observed in solution state.

## Theoretical Calculations

To gain a deeper understanding of the geometric structures and photophysical properties of compounds **1–3**, computational studies based on density functional theory (DFT) were performed at the PBE0/6-31G(d,p) level. Optimization of the ground state ( $S_0$ ) and excited state ( $S_1$  and  $T_1$ ) geometries was made by DFT and time-dependent DFT (TD-DFT) methods, respectively (**Figure 5** and **Supplementary Table 3**). The short N...B contacts (ca. 2.90–2.94 Å) in **1** and **2** are comparable to that found in the crystal structure of **2** (2.906 Å), whereas that in **3** shows an increased distance of 3.09 Å. All compounds exhibit high dihedral angles close to 90°, which are also comparable to the experimental value for **2** (86.4°), between the DPAC donor and the phenylene ring at the ground state. As a result, the HOMOs and LUMOs are spatially separated and located on the DPAC donor and boryl acceptor moieties, respectively. In particular, the LUMOs of **1** and **2** are almost exclusively contributed by the cyclic boryl moieties, whereas **3** has a substantial LUMO contribution from the phenylene ring (ca. 19%). This finding can be mainly attributed to the strong p(B)– $\pi^*$  electronic conjugation in the cyclic boryl moieties. Moreover, unlike the propeller-like conformation of the PhBMes<sub>2</sub> moiety in **3**, the cyclic boryl rings in **1** and **2** are nearly orthogonal to the phenylene ring. This may weaken the LUMO conjugation between the two rings, which results in the cyclic boryl moieties dominating the LUMOs. The resulting LUMO level is slightly lowered for **3** compared to those of **1** and **2**, as shown in the electrochemical reduction. The computed  $\Delta E_{ST}$  values are in the range of ca. 0.04–0.05 eV for all compounds, similarly to the experimental values. The very small  $\Delta E_{ST}$  values support the observed strong TADF properties. Although the HOMO–LUMO band gaps of all compounds in the ground state are very similar, the  $S_1$  state energy and TD-DFT calculation predict that the lowest-energy absorption and emission energies follow the order **2** > **1** > **3**, which is in agreement with the experimental results and corroborates the blue-shifted emission of cyclic boryl-containing **1** and **2** (**Supplementary Tables 3–5**).

## Electroluminescent Properties

To investigate the electroluminescent (EL) properties of the proposed emitters **1–3**, TADF-OLED devices having the following structure were fabricated (**Figure 6A**): glass/indium-tin-oxide (ITO) (150 nm)/poly(3,4-ethylenedioxy-thiophene):poly(styrenesulfonate) (PEDOT:PSS) (40 nm)/1,1-bis[(di-4-tolylamino)phenyl]cyclohexane (TAPC) (20 nm)/1,3-bis(*N*-carbazolyl)benzene (mCP) (10 nm)/bis[2-(diphenylphosphino)phenyl]ether oxide (DPEPO):emitter (20

wt%, 25 nm)/DPEPO (10 nm)/2,2',2''-(1,3,5-benzinetriyl)-tris(1-phenyl-1-*H*-benzimidazole) (TPBi) (30 nm)/lithium fluoride (LiF) (1 nm)/aluminum (Al) (100 nm) (**D1–D3**). Because of their blue emitting properties, the emitters were doped into a DPEPO host with a high  $T_1$  energy ( $T_1 = 3.3$  eV). Similarly to previous pure blue devices (Lee et al., 2017, 2018), the emitters were codeposited with the host at a dopant concentration of 20 wt%. The preliminary results for the device performance are summarized in **Table 3**. The EL emission of the devices with the

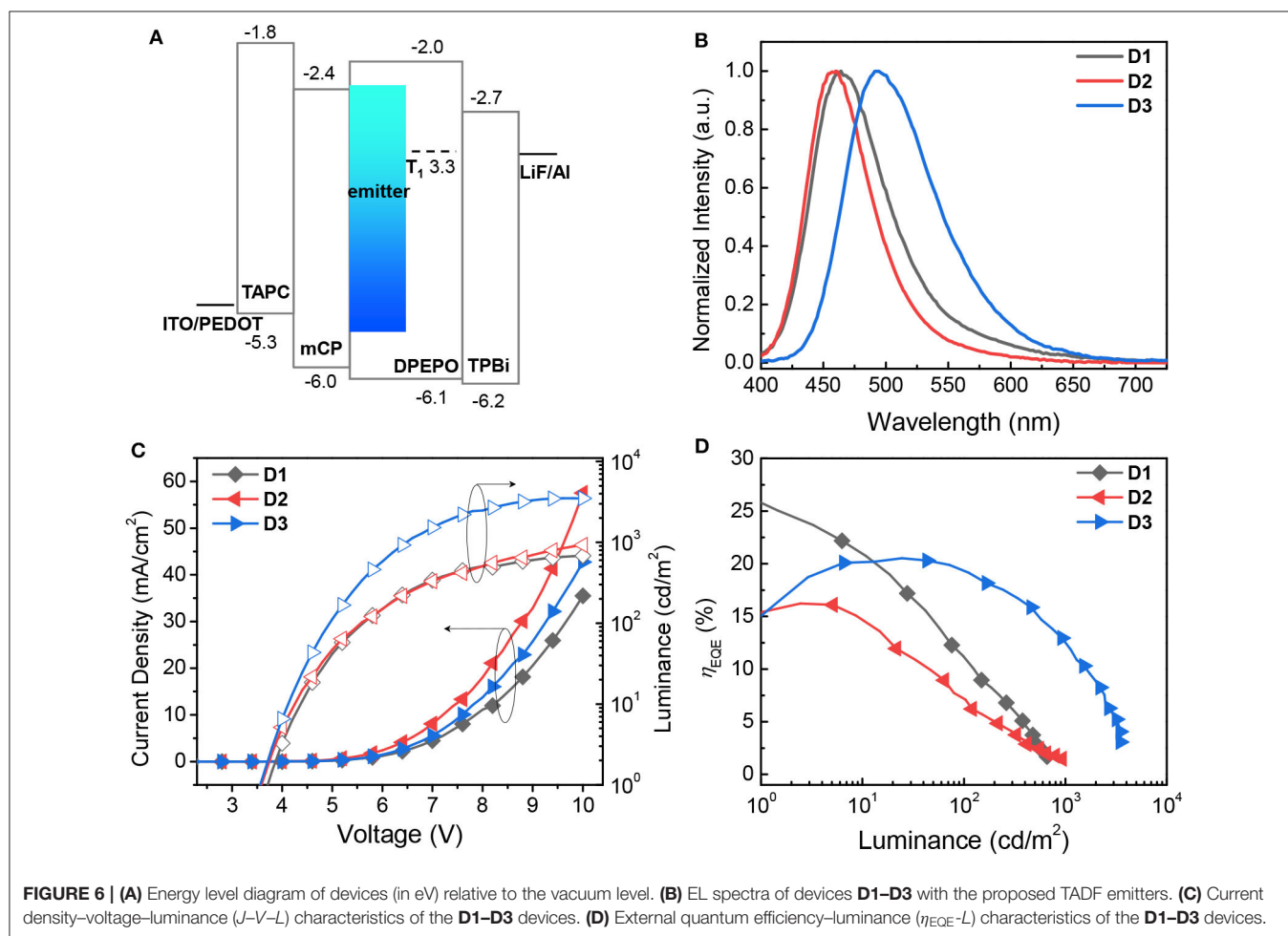


**TABLE 3 |** Device performance of the TADF-OLEDs fabricated with **1–3**.

Device (emitter) <sup>a</sup>	$\lambda_{\text{EL}}$ (nm)	$\lambda_{\text{FWHM}}$ (nm) <sup>b</sup>	CIE (x, y) <sup>c</sup>	$V_{\text{on}}$ (V) <sup>d</sup>	EQE (%) <sup>e</sup>	PE (lm W <sup>−1</sup> ) <sup>f</sup>	CE (cd A <sup>−1</sup> ) <sup>g</sup>
<b>D1 (1)</b>	464	70	(0.167, 0.191)	3.7	25.8	31.1	34.8
<b>D2 (2)</b>	460	59	(0.151, 0.128)	3.6	16.2	15.0	17.7
<b>D3 (3)</b>	492	83	(0.208, 0.421)	3.6	20.5	38.0	54.8

<sup>a</sup>ITO (150 nm)/PEDOT:PSS (40 nm)/TAPC (20 nm)/mCP (10 nm)/DPEPO:emitter (20 wt%, 25 nm)/DPEPO (10 nm)/TPBi (30 nm)/LiF (1 nm)/Al (100 nm).

<sup>b</sup>Full width at half maximum (FWHM).

<sup>c</sup>Color coordinates (CIE 1931) at maximum luminance.

<sup>d</sup> $V_{\text{on}}$ : Applied voltage at a luminance of 1 cd m<sup>−2</sup>.

<sup>e</sup>Maximum external quantum efficiency.

<sup>f</sup>Maximum power efficiency.

<sup>g</sup>Maximum current efficiency.

three different dopants varies from pure blue [CIE ( $x, y$ ) = (0.151, 0.128)] to cyan [CIE ( $x, y$ ) = (0.208, 0.421)], which is similar to the PL spectra of the host films doped with the corresponding emitters (**Figure 6B**). All the devices show negligible spectral variations over the whole angle range, which is indicative of their wide angular stability (**Supplementary Figure 10**). In particular, as consistently observed in the PL spectra of the emitters, the EL emissions of **D1** and **D2** having the emitters based on the cyclic boryl acceptors are narrower than that of **D3** ( $\lambda_{FWHM}$  = 59–70 nm for **D1** and **D2** vs. 83 nm for **D3**). According to the current density–voltage–luminance ( $J$ – $V$ – $L$ ) characteristics and the external quantum efficiency–luminance (EQE– $L$ ) characteristics of the devices shown in **Figures 6C,D**, all the devices exhibit very good performance with high EQE values. In fact, device **D1** achieves a very high maximum EQE of 25.8% without any light-outcoupling enhancement. We attribute these high performances to the efficient TADF properties of the emitters with high PLQY and small  $\Delta E_{ST}$ . However, substantial efficiency roll-off is observed for all devices. This can be mainly attributed to the long delayed fluorescence lifetime of the emitters that may increase the probability of exciton quenching processes such as triplet-triplet annihilation (TTA) and triplet-polaron annihilation (TPA) in the devices. Interestingly, it is noted that the EQE values obtained in this study are somewhat different from the trend found in the PLQYs of the host films. Device **D1**, which is based on the less emissive DPACoBA (**1**), exhibits higher EQEs than devices **D2** and **D3** although the PLQY of **1** is sufficiently high to afford the observed EQEs anyway; further optimization of the device structure would probably result in a more accurate trend in the device efficiency but is beyond the scope of this work. Nevertheless, the results obtained for the devices in this study suggest that the cyclic boryl groups function as good acceptors for TADF emitters, being capable of exhibiting narrow bandwidth emission and high device efficiency.

## CONCLUSION

We have demonstrated the impact of boron acceptors on the TADF properties of *ortho*-donor-appended triarylboron compounds, which consist of an *ortho* D–A backbone structure containing cyclic boryl (**1** and **2**) or BMes<sub>2</sub> (**3**) groups as acceptors and a fixed DPAC donor. The compounds possessed a twisted structure and were sterically congested around the boron atom. All compounds showed strong TADF properties with high PLQYs in both solution and solid state. Blue-shifted fluorescence with narrower bandwidths was observed for the compounds bearing cyclic boryl acceptors (**1** and **2**) compared with that of the BMes<sub>2</sub>-containing **3**. TADF-OLEDs fabricated with **1–3** as emitters exhibited high device performance, and those based on the cyclic boryl emitters showed pure blue emission and narrower EL bands than the device with **3**. A high EQE of 25.8% was also achieved for the device fabricated with emitter **1**. The findings in this study suggest that the cyclic boryl groups may be useful for designing TADF emitters with narrow bandwidth emission and high device efficiency.

## MATERIALS AND METHODS

### General Considerations

All operations were performed under an inert nitrogen atmosphere using standard Schlenk and glovebox techniques. Anhydrous grade solvents were dried by passing them through an activated alumina column and stored over activated molecular sieves (5 Å). Spectrophotometric-grade solvents for photophysical measurements were used as received. Commercial reagents were used without further purification after purchase. 2-Bromo-1-iodo-3-methylbenzene (Ikeuchi et al., 2019), 9-bromo-9,10-dihydro-9-boraanthracene (Zhou et al., 2012), and 10-bromo-9-oxa-10-boraanthracene (Melaïmi et al., 2006) were prepared according to the literature procedures. Deuterated solvents from Cambridge Isotope Laboratories were used. NMR spectra were recorded on a Bruker AM 300 (300.13 MHz for <sup>1</sup>H, 75.48 MHz for <sup>13</sup>C, and 96.29 MHz for <sup>11</sup>B) spectrometer at ambient temperature. Chemical shifts are given in parts per million (ppm), and are referenced against external Me<sub>4</sub>Si (<sup>1</sup>H, <sup>13</sup>C) and BF<sub>3</sub>·OEt<sub>2</sub> (<sup>11</sup>B). Elemental analyses were performed on a Flash 2000 elemental analyzer (Thermo Scientific). Mass spectra were obtained using a JEOL JMS700 high-resolution EI-mass spectrometer (HR EI-MS) at the Korea Basic Science Institute, Daegu, Korea. Melting points (mp) were measured by Melting Point Apparatus SMP30 (Stuart Equipment). Thermogravimetric analysis (TGA) was performed with a TA Instruments Q50 under an N<sub>2</sub> atmosphere at a heating rate of 20°C min<sup>−1</sup>. Cyclic voltammetry experiments were carried out using an Autolab/PGSTAT101 system.

### Synthesis of DPACoBr

The mixture of 9,9-diphenyl-10H-acridine (0.56 g, 1.68 mmol), 2-bromo-1-iodo-3-methylbenzene (1.0 g, 3.37 mmol), tris-(dibenzylideneacetone)dipalladium(0) (Pd<sub>2</sub>(dba)<sub>3</sub>, 0.03 g, 0.02 mmol), tri-*tert*-butylphosphine (0.02 g, 0.06 mmol), and sodium *tert*-butoxide (0.32 g, 3.36 mmol) in dry toluene (20 mL) was refluxed for 48 h. After cooling down to room temperature, the mixture was diluted with CH<sub>2</sub>Cl<sub>2</sub> (20 mL), filtered through a celite pad, and concentrated under reduced pressure. The crude product was purified by silica gel column chromatography using CH<sub>2</sub>Cl<sub>2</sub>/*n*-hexane (1:6, v/v) as an eluent to give 10-(2-bromophenyl)-9,9-diphenyl-10H-acridine (DPACoBr) as a white solid (Yield: 0.68 g, 78%). <sup>1</sup>H NMR (CD<sub>2</sub>Cl<sub>2</sub>):  $\delta$  7.43–7.36 (m, 2H), 7.26 (m, 6H), 7.09–6.99 (m, 7H), 6.94–6.87 (m, 4H), 6.29 (dd,  $J$  = 8.6, 0.6 Hz, 2H), 2.50 (s, 3H). <sup>13</sup>C NMR (CD<sub>2</sub>Cl<sub>2</sub>):  $\delta$  147.2, 147.0, 141.4, 140.5, 139.2, 130.7, 130.6, 130.5, 130.4, 130.3, 128.81, 128.80, 128.4, 127.6, 127.5, 126.9, 126.2, 120.3, 113.4, 56.5, 23.6. HRMS (EI):  $m/z$  Calcd for C<sub>32</sub>H<sub>24</sub>BrN, 501.1092; Found, 501.1088.

### Synthesis of DPACoBA (**1**)

To a solution of DPACoBr (0.22 g, 0.44 mmol) in dry ether (30 mL) was added dropwise *n*-BuLi (0.18 mL, 0.44 mmol) at −30°C. The reaction mixture was allowed to warm to room temperature and stirred for 1 h. The mixture was cooled to −78°C and then 9-bromo-9,10-dihydro-9-boraanthracene (0.17 g, 0.67 mmol) in dry toluene (10 mL) was slowly added.

After stirring at room temperature overnight, the mixture was concentrated under reduced pressure and purified by crystallization from CH<sub>2</sub>Cl<sub>2</sub>/MeOH to give DPACoBA (**1**) as a white crystalline solid (Yield: 0.10 g, 37%). <sup>1</sup>H NMR (CD<sub>2</sub>Cl<sub>2</sub>): δ 7.61 (t, *J* = 7.7 Hz, 1H), 7.47 (d, *J* = 7.5 Hz, 2H), 7.43–7.38 (m, 1H), 7.35 (td, *J* = 7.5, 1.5 Hz, 2H), 7.28 (d, *J* = 8.0 Hz, 1H), 7.22 (d, *J* = 7.8 Hz, 2H), 7.18–7.10 (m, 3H), 7.06–6.91 (m, 5H), 6.77–6.67 (m, 6H), 6.56 (ddd, *J* = 11.0, 8.2, 1.6 Hz, 4H), 6.01 (dd, *J* = 8.5, 1.1 Hz, 2H), 3.98 (d, *J* = 23.8 Hz, 1H), 3.65 (d, *J* = 23.7 Hz, 1H), 1.96 (s, 3H). <sup>13</sup>C NMR (CD<sub>2</sub>Cl<sub>2</sub>): δ 149.1, 147.5, 144.5, 142.4, 142.3, 142.1, 137.7, 132.0, 131.2, 130.4, 129.1, 128.6, 128.5, 128.3, 127.7, 127.5, 127.1, 127.0, 126.01, 125.97, 125.4, 124.3, 119.5, 115.6, 56.0, 38.0, 22.0. <sup>11</sup>B NMR (CD<sub>2</sub>Cl<sub>2</sub>): δ +58.2. Anal. Calcd for C<sub>45</sub>H<sub>34</sub>BN: C, 90.15; H, 5.72; N, 2.34%. Found: C, 90.03; H, 5.66; N, 2.58%. mp = 297°C. *T*<sub>d5</sub> = 324°C.

### Synthesis of DPACoOB (**2**)

This compound was analogously prepared following the procedures for **1** using DPACoBr (0.30 g, 0.59 mmol), *n*-BuLi (0.24 mL, 0.60 mmol), and 10-bromo-9-oxa-10-boranthracene (0.20 g, 0.78 mmol) to give DPACoOB (**2**) as a white crystalline solid (Yield: 0.18 g, 50%). <sup>1</sup>H NMR (CD<sub>2</sub>Cl<sub>2</sub>): δ 7.64 (t, *J* = 7.7 Hz, 1H), 7.56–7.49 (m, 2H), 7.46 (dd, *J* = 7.6, 1.4 Hz, 2H), 7.41 (d, *J* = 7.4 Hz, 1H), 7.36–7.26 (m, 3H), 7.19–7.10 (m, 3H), 7.06 (ddd, *J* = 8.4, 7.3, 1.6 Hz, 2H), 6.94–6.85 (m, 3H), 6.73 (m, 6H), 6.52 (dd, *J* = 8.0, 1.6 Hz, 2H), 6.46–6.38 (m, 2H), 5.80 (dd, *J* = 8.5, 1.2 Hz, 2H), 1.91 (s, 3H). <sup>13</sup>C NMR (CD<sub>2</sub>Cl<sub>2</sub>): δ 158.5, 148.4, 143.8, 143.0, 142.4, 142.3, 136.0, 133.9, 131.2, 130.2, 129.4, 128.63, 128.58, 128.5, 127.2, 127.1, 126.9, 126.1, 125.7, 121.1, 119.5, 117.4, 115.2, 56.0, 22.2. <sup>11</sup>B NMR (CD<sub>2</sub>Cl<sub>2</sub>): δ +64.8. Anal. Calcd for C<sub>44</sub>H<sub>32</sub>BNO: C, 87.85; H, 5.36; N, 2.33%. Found: C, 87.53; H, 5.28; N, 2.50%. mp = 325°C. *T*<sub>d5</sub> = 333°C.

### Synthesis of DPACoB (**3**)

This compound was analogously prepared following the procedures for **1** using DPACoBr (0.30 g, 0.59 mmol), *n*-BuLi (0.24 mL, 0.60 mmol), and dimesitylboron fluoride (Mes<sub>2</sub>BF, 0.19 g, 0.72 mmol). Purification by silica gel column chromatography using CH<sub>2</sub>Cl<sub>2</sub>/*n*-hexane (1:6, v/v) as an eluent followed by recrystallization from CH<sub>2</sub>Cl<sub>2</sub>/MeOH afforded DPACoB (**3**) as a green crystalline solid (Yield: 0.12 g, 31%). <sup>1</sup>H NMR (CD<sub>2</sub>Cl<sub>2</sub>): δ 7.47 (t, *J* = 7.7 Hz, 1H), 7.33–7.22 (m, 4H), 7.15–7.11 (m, 5H), 6.96 (t, *J* = 7.4 Hz, 1H), 6.89 (d, *J* = 7.8 Hz, 1H), 6.80 (t, *J* = 7.2 Hz, 1H), 6.76–6.71 (m, 2H), 6.65 (d, *J* = 9.4 Hz, 6H), 6.31 (d, *J* = 8.2 Hz, 2H), 6.06 (d, *J* = 7.1 Hz, 1H), 5.69 (s, 1H), 2.20 (s, 3H), 2.18 (s, 3H), 2.15 (s, 3H), 2.01 (s, 3H), 1.93 (s, 3H), 1.81 (s, 3H), 0.62 (s, 3H). <sup>13</sup>C NMR (CD<sub>2</sub>Cl<sub>2</sub>): δ 152.8, 148.1, 145.8, 143.3, 142.6, 141.9, 140.0, 138.7, 138.4, 137.2, 132.6, 131.7, 130.8, 129.9, 129.5, 128.0, 127.1, 126.3, 125.7, 125.4, 119.6, 118.8, 117.8, 117.2, 55.8, 26.0, 23.2, 22.6, 21.9, 20.6. <sup>11</sup>B NMR (CD<sub>2</sub>Cl<sub>2</sub>): δ +84.0. Anal. Calcd for C<sub>50</sub>H<sub>46</sub>BN: C, 89.40; H, 6.90; N, 2.09%. Found: C, 89.05; H, 6.81; N, 2.28%. mp = 278°C. *T*<sub>d5</sub> = 326°C.

### Cyclic Voltammetry

The redox behavior of compounds were examined by cyclic voltammetry measurements using a three-electrode cell configuration consisting of platinum working and counter

electrodes and an Ag/AgNO<sub>3</sub> (0.01 M in CH<sub>3</sub>CN) reference electrode. Oxidation curves were recorded in CH<sub>2</sub>Cl<sub>2</sub> solutions ( $1 \times 10^{-3}$  M), while reduction curves were obtained from THF (**2** and **3**) or DMSO (**1**) solutions ( $1 \times 10^{-3}$  M). Tetra-*n*-butylammonium hexafluorophosphate (TBAPF<sub>6</sub>, 0.1 M) was used as the supporting electrolyte. The redox potentials were recorded at a scan rate of 100–200 mV s<sup>−1</sup> and are reported against the Fc/Fc<sup>+</sup> redox couple. The HOMO and LUMO energy levels were estimated from the electrochemical oxidation (*E*<sub>1/2</sub>) and reduction (*E*<sub>onset</sub>) peaks of cyclic voltammograms.

### Photophysical Measurements

UV/vis absorption and photoluminescence (PL) spectra were recorded on a Varian Cary 100 and FS5 spectrophotometer, respectively. Solution PL spectra were obtained from oxygen-free (N<sub>2</sub>-filled) and air-saturated toluene solutions in a sealed cuvette (typically 50 μM). PL spectra and PLQYs of doped host films were obtained on quartz plates. PLQYs of the samples were measured on an absolute PL quantum yield spectrophotometer (Quantaaurus-QY C11347-11, Hamamatsu Photonics) equipped with a 3.3-inch integrating sphere. Transient PL decays were recorded on a FS5 spectrophotometer (Edinburgh Instruments) equipped with an OptistatDN<sup>TM</sup> cryostat (Oxford Instruments).

### Fabrication of Electroluminescent Devices

OLED devices were fabricated on 25 × 25 mm glass substrate with half-patterned ITO layers (AMG). Glass substrates with pre-patterned ITO electrodes were cleaned by a sequential wet-cleaning processes in an ultrasonic bath (Song et al., 2018). After drying in a vacuum oven for a day, the substrates were subject to UV-plasma treatment for 1 min in a plasma cleaner (CUTE-MP, Femto Science). As a hole-injection layer, an aqueous dispersion of PEDOT:PSS (Clevios<sup>TM</sup> P VP AI 4083, Heraeus) was spun (2,500 rpm for 30 s) onto the plasma-treated substrates and annealed on a hot plate (100°C for 10 min). Other organic and metal layers were sequentially deposited in a vacuum chamber (HS-1100, Digital Optics & Vacuum) at less than  $1.5 \times 10^{-6}$  torr. The current density–voltage–luminance (*J*–*V*–*L*) and angle-resolved electroluminescence (EL) intensity characteristics of the fabricated devices were obtained with a source-measure unit (Keithley 2400) using a calibrated photodiode (FDS100, Thorlab) and a fiber optic spectrometer (EPP2000, StellarNet) held on a motorized goniometer. The EQE (*η*<sub>EQE</sub>) and PE (*η*<sub>PE</sub>) of the devices were estimated from the measured full angular characteristics without Lambertian simplification. All device fabrication and measurement, except for the PEDOT:PSS coating, were carried out in a nitrogen (N<sub>2</sub>)-filled glove box, and all characteristics of the devices were measured at room temperature.

### DATA AVAILABILITY STATEMENT

All datasets generated for this study are included in the article/**Supplementary Material**.



## AUTHOR CONTRIBUTIONS

HM performed the synthesis and characterization. WL fabricated the devices. TL carried out DFT computation. JJ discussed the theoretical data. SY discussed the device data. ML designed the experiments and prepared the manuscript. All authors have approved the final version of the manuscript.

## FUNDING

This work was supported by the Basic Science Research Program (NRF-2017R1A2B4002468 and NRF-2019R1A2C1084952 for ML and NRF-2019R1I1A3A01041239 for JJ) through the National Research Foundation of Korea (NRF) funded by the Korean Ministry of Science and ICT (MSIT)

## REFERENCES

- Ahn, D. H., Kim, S. W., Lee, H., Ko, I. J., Karthik, D., Lee, J. Y., et al. (2019). Highly efficient blue thermally activated delayed fluorescence emitters based on symmetrical and rigid oxygen-bridged boron acceptors. *Nat. Photonics* 13, 540–546. doi: 10.1038/s41566-019-0415-5
- Blount, J. F., Finocchiaro, P., Gust, D., and Mislow, K. (1973). Conformational analysis of triarylboranes. *J. Am. Chem. Soc.* 95, 7019–7029. doi: 10.1021/ja00802a024
- Cai, X., and Su, S.-J. (2018). Marching toward highly efficient, pure-blue, and stable thermally activated delayed fluorescent organic light-emitting diodes. *Adv. Funct. Mater.* 28:1802558. doi: 10.1002/adfm.201802558
- Chen, D.-G., Lin, T.-C., Chen, C.-L., Chen, Y.-T., Chen, Y.-A., Lee, G.-H., et al. (2018a). Optically triggered planarization of boryl-substituted phenoxazine: another horizon of TADF molecules and high-performance OLEDs. *ACS Appl. Mater. Interfaces* 10, 12886–12896. doi: 10.1021/acsami.8b00053
- Chen, Y., Li, S., Hu, T., Wei, X., Li, Z., Liu, Y., et al. (2018b). Highly efficient white light-emitting diodes with a bi-component emitting layer based on blue and yellow thermally activated delayed fluorescence emitters. *J. Mater. Chem. C* 6, 2951–2956. doi: 10.1039/C8TC00594J
- Dias, F. B., Bourdakos, K. N., Jankus, V., Moss, K. C., Kamtekar, K. T., Bhalla, V., et al. (2013). Triplet harvesting with 100% efficiency by way of thermally activated delayed fluorescence in charge transfer OLED emitters. *Adv. Mater.* 25, 3707–3714. doi: 10.1002/adma.201300753
- Goushi, K., Yoshida, K., Sato, K., and Adachi, C. (2012). Organic light-emitting diodes employing efficient reverse intersystem crossing for triplet-to-singlet state conversion. *Nat. Photonics* 6, 253–258. doi: 10.1038/nphoton.2012.31
- Hatakeyama, T., Shiren, K., Nakajima, K., Nomura, S., Nakatsuka, S., Kinoshita, K., et al. (2016). Ultrapure blue thermally activated delayed fluorescence molecules: efficient HOMO-LUMO separation by the multiple resonance effect. *Adv. Mater.* 28, 2777–2781. doi: 10.1002/adma.201505491
- Hirai, H., Nakajima, K., Nakatsuka, S., Shiren, K., Ni, J., Nomura, S., et al. (2015). One-Step Borylation of 1,3-diaryloxybenzenes towards efficient materials for organic light-emitting diodes. *Angew. Chem. Int. Ed.* 54, 13581–13585. doi: 10.1002/anie.201506335
- Hirai, M., Tanaka, N., Sakai, M., and Yamaguchi, S. (2019). Structurally constrained boron-, nitrogen-, silicon-, and phosphorus-centered polycyclic  $\pi$ -conjugated systems. *Chem. Rev.* 119, 8291–8331. doi: 10.1021/acs.chemrev.8b00637
- Hirata, S., Sakai, Y., Masui, K., Tanaka, H., Lee, S. Y., Nomura, H., et al. (2015). Highly efficient blue electroluminescence based on thermally activated delayed fluorescence. *Nat. Mater.* 14, 330–336. doi: 10.1038/nmat4154
- Hudson, Z. M., and Wang, S. (2009). Impact of donor-acceptor geometry and metal chelation on photophysical properties and applications of triarylboranes. *Acc. Chem. Res.* 42, 1584–1596. doi: 10.1021/ar900072u
- Ikeuchi, T., Inuki, S., Oishi, S., and Ohno, H. (2019). Gold(I)-catalyzed cascade cyclization reactions of allenynes for the synthesis of fused cyclopropanes and acenaphthenes. *Angew. Chem.* 131, 7874–7878. doi: 10.1002/ange.201903384
- and the Ministry of Education, respectively. SY gives thanks to the Nano-Material Technology Development Program through the NRF funded by the MSIT (NRF-2016M3A7B4910631) and the Engineering Research Center of Excellence (ERC) Program through the NRF funded by the MSIT (NRF-2017R1A5A1014708).

## SUPPLEMENTARY MATERIAL

The Supplementary Material for this article can be found online at: <https://www.frontiersin.org/articles/10.3389/fchem.2020.00538/full#supplementary-material>

These data include NMR spectra of compounds, crystallographic data, photophysical data, computational details, and electroluminescence results.

- Im, Y., Kim, M., Cho, Y. J., Seo, J.-A., Yook, K. S., and Lee, J. Y. (2017). Molecular design strategy of organic thermally activated delayed fluorescence emitters. *Chem. Mater.* 29, 1946–1963. doi: 10.1021/acs.chemmater.6b05324
- Kaji, H., Suzuki, H., Fukushima, T., Shizu, K., Suzuki, K., Kubo, S., et al. (2015). Purely organic electroluminescent material realizing 100% conversion from electricity to light. *Nat. Commun.* 6:8476. doi: 10.1038/ncomms9476
- Kim, J. H., Yun, J. H., and Lee, J. Y. (2018). Recent progress of highly efficient red and near-infrared thermally activated delayed fluorescent emitters. *Adv. Opt. Mater.* 6:1800255. doi: 10.1002/adom.201800255
- Kitamoto, Y., Namikawa, T., Ikemizu, D., Miyata, Y., Suzuki, T., Kita, H., et al. (2015). Light blue and green thermally activated delayed fluorescence from 10H-phenoxaborin-derivatives and their application to organic light-emitting diodes. *J. Mater. Chem. C* 3, 9122–9130. doi: 10.1039/C5TC01380A
- Kitamoto, Y., Namikawa, T., Suzuki, T., Miyata, Y., Kita, H., Sato, T., et al. (2016). Dimesitylarylborane-based luminescent emitters exhibiting highly-efficient thermally activated delayed fluorescence for organic light-emitting diodes. *Org. Electron.* 34, 208–217. doi: 10.1016/j.orgel.2016.04.030
- Kondo, Y., Yoshiura, K., Kitera, S., Nishi, H., Oda, S., Gotoh, H., et al. (2019). Narrowband deep-blue organic light-emitting diode featuring an organoboron-based emitter. *Nat. Photonics* 13, 678–682. doi: 10.1038/s41566-019-0476-5
- Kumar, A., Oh, J., Kim, J., Jung, J., and Lee, M. H. (2019). Facile color tuning of thermally activated delayed fluorescence by substituted ortho-carbazole-appended triarylboron emitters. *Dyes Pigm.* 168, 273–280. doi: 10.1016/j.dyepig.2019.05.002
- Lee, Y. H., Park, S., Oh, J., Shin, J. W., Jung, J., Yoo, S., et al. (2017). Rigidity-induced delayed fluorescence by ortho donor-appended triarylboron compounds: record-high efficiency in pure blue fluorescent organic light-emitting diodes. *ACS Appl. Mater. Interfaces* 9, 24035–24042. doi: 10.1021/acsami.7b05615
- Lee, Y. H., Park, S., Oh, J., Woo, S.-J., Kumar, A., Kim, J.-J., et al. (2018). High-efficiency sky blue to ultradeep blue thermally activated delayed fluorescent diodes based on ortho-carbazole-appended triarylboron emitters: above 32% external quantum efficiency in blue devices. *Adv. Opt. Mater.* 6:1800385. doi: 10.1002/adom.201800385
- Liang, X., Yan, Z.-P., Han, H.-B., Wu, Z.-G., Zheng, Y.-X., Meng, H., et al. (2018). Peripheral amplification of multi-resonance induced thermally activated delayed fluorescence for highly efficient OLEDs. *Angew. Chem. Int. Ed.* 57, 11316–11320. doi: 10.1002/anie.201806323
- Lien, Y.-J., Lin, T.-C., Yang, C.-C., Chiang, Y.-C., Chang, C.-H., Liu, S.-H., et al. (2017). First N-borylated emitters displaying highly efficient thermally activated delayed fluorescence and high-performance OLEDs. *ACS Appl. Mater. Interfaces* 9, 27090–27101. doi: 10.1021/acsami.7b08258
- Liu, Y., Xie, G., Wu, K., Luo, Z., Zhou, T., Zeng, X., et al. (2016). Boosting reverse intersystem crossing by increasing donors in triarylboron/phenoxazine hybrids: TADF emitters for high-performance solution-processed OLEDs. *J. Mater. Chem. C* 4, 4402–4407. doi: 10.1039/C6TC01353H

- Matsui, K., Oda, S., Yoshiura, K., Nakajima, K., Yasuda, N., and Hatakeyama, T. (2018). One-shot multiple borylation toward BN-doped nanographenes. *J. Am. Chem. Soc.* 140, 1195–1198. doi: 10.1021/jacs.7b10578
- Melaïmi, M., Solé, S., Chiu, C.-W., Wang, H., and Gabbai, F. P. (2006). Structural and electrochemical investigations of the high fluoride affinity of sterically hindered 1, 8-Bis(boryl)naphthalenes. *Inorg. Chem.* 45, 8136–8143. doi: 10.1021/ic060709s
- Meng, G., Chen, X., Wang, X., Wang, N., Peng, T., and Wang, S. (2019). Isomeric Bright Sky-Blue TADF emitters based on bisacridine decorated DBNA: impact of donor locations on luminescent and electroluminescent properties. *Adv. Opt. Mater.* 7:1900130. doi: 10.1002/adom.201900130
- Numata, M., Yasuda, T., and Adachi, C. (2015). High efficiency pure blue thermally activated delayed fluorescence molecules having 10H-phenoxaborin and acridan units. *Chem. Commun.* 51, 9443–9446. doi: 10.1039/C5CC00307E
- Park, I. S., Matsuo, K., Aizawa, N., and Yasuda, T. (2018). High-performance dibenzoheteraborin-based thermally activated delayed fluorescence emitters: molecular architectonics for concurrently achieving narrowband emission and efficient triplet-singlet spin conversion. *Adv. Funct. Mater.* 28:1802031. doi: 10.1002/adfm.201802031
- Song, J., Kim, K.-H., Kim, E., Moon, C.-K., Kim, Y.-H., Kim, J.-J., et al. (2018). Lensfree OLEDs with over 50% external quantum efficiency via external scattering and horizontally oriented emitters. *Nat. Commun.* 9:3207. doi: 10.1038/s41467-018-05671-x
- Suzuki, K., Kubo, S., Shizu, K., Fukushima, T., Wakamiya, A., Murata, Y., et al. (2015). Triarylboron-based fluorescent organic light-emitting diodes with external quantum efficiencies exceeding 20. *Angew. Chem. Int. Ed.* 54, 15231–15235. doi: 10.1002/anie.201508270
- Tao, Y., Yuan, K., Chen, T., Xu, P., Li, H., Chen, R., et al. (2014). Thermally activated delayed fluorescence materials towards the breakthrough of organoelectronics. *Adv. Mater.* 26, 7931–7958. doi: 10.1002/adma.201402532
- Tsai, C.-C., Huang, W.-C., Chih, H.-Y., Hsh, Y.-C., Liao, C.-W., Lin, C.-H., et al. (2018). Efficient donor-acceptor-donor borylated compounds with extremely small  $\Delta E_{ST}$  for thermally activated delayed fluorescence OLEDs. *Org. Electron.* 63, 166–174. doi: 10.1016/j.orgel.2018.09.023
- Turkoglu, G., Cinar, M. E., and Ozturk, T. (2017). Triarylborane-based materials for OLED applications. *Molecules* 22:1522. doi: 10.3390/molecules22091522
- Uoyama, H., Goushi, K., Shizu, K., Nomura, H., and Adachi, C. (2012). Highly efficient organic light-emitting diodes from delayed fluorescence. *Nature* 492, 234–238. doi: 10.1038/nature11687
- Wade, C. R., Broomsgrove, A. E. J., Aldridge, S., and Gabbai, F. P. (2010). Fluoride ion complexation and sensing using organoboron compounds. *Chem. Rev.* 110, 3958–3984. doi: 10.1021/cr900401a
- Wong, M. Y., and Zysman-Colman, E. (2017). Purely organic thermally activated delayed fluorescence materials for organic light-emitting diodes. *Adv. Mater.* 29:1605444. doi: 10.1002/adma.201605444
- Wu, T.-L., Huang, M.-J., Lin, C.-C., Huang, P.-Y., Chou, T.-Y., Chen-Cheng, R.-W., et al. (2018). Diboron compound-based organic light-emitting diodes with high efficiency and reduced efficiency roll-off. *Nat. Photonics* 12, 235–240. doi: 10.1038/s41566-018-0112-9
- Wu, T.-L., Lo, S.-H., Chang, Y.-C., Huang, M.-J., and Cheng, C.-H. (2019). Steric switching for thermally activated delayed fluorescence by controlling the dihedral angles between donor and acceptor in organoboron emitters. *ACS Appl. Mater. Interfaces* 11, 10768–10776. doi: 10.1021/acsami.8b21568
- Yang, Z., Mao, Z., Xie, Z., Zhang, Y., Liu, S., Zhao, J., et al. (2017). Recent advances in organic thermally activated delayed fluorescence materials. *Chem. Soc. Rev.* 46, 915–1016. doi: 10.1039/C6CS00368K
- Zettler, F., Hausen, H. D., and Hess, H. (1974). Die kristall- und molekülstruktur des triphenylborans. *J. Organomet. Chem.* 72, 157–162. doi: 10.1016/S0022-328X(00)81488-6
- Zhang, Q., Li, B., Huang, S., Nomura, H., Tanaka, H., and Adachi, C. (2014). Efficient blue organic light-emitting diodes employing thermally activated delayed fluorescence. *Nat. Photonics* 8, 326–332. doi: 10.1038/nphoton.2014.12
- Zhang, Q., Li, J., Shizu, K., Huang, S., Hirata, S., Miyazaki, H., et al. (2012). Design of efficient thermally activated delayed fluorescence materials for pure blue organic light emitting diodes. *J. Am. Chem. Soc.* 134, 14706–14709. doi: 10.1021/ja306538w
- Zhou, Z., Wakamiya, A., Kushida, T., and Yamaguchi, S. (2012). Planarized triarylboranes: stabilization by structural constraint and their plane-to-bowl conversion. *J. Am. Chem. Soc.* 134, 4529–4532. doi: 10.1021/ja211944q

**Conflict of Interest:** The authors declare that the research was conducted in the absence of any commercial or financial relationships that could be construed as a potential conflict of interest.

Copyright © 2020 Mubarak, Lee, Lee, Jung, Yoo and Lee. This is an open-access article distributed under the terms of the Creative Commons Attribution License (CC BY). The use, distribution or reproduction in other forums is permitted, provided the original author(s) and the copyright owner(s) are credited and that the original publication in this journal is cited, in accordance with accepted academic practice. No use, distribution or reproduction is permitted which does not comply with these terms.



# Recent Developments on Multi-Functional Metal-Free Mechanochromic Luminescence and Thermally Activated Delayed Fluorescence Organic Materials

Debasish Barman<sup>1</sup>, Rajdikshit Gogoi<sup>1</sup>, Kavita Narang<sup>1</sup> and Parameswar Krishnan Iyer<sup>1,2\*</sup>

<sup>1</sup> Department of Chemistry, Indian Institute of Technology Guwahati, Guwahati, India, <sup>2</sup> Centre for Nanotechnology, Indian Institute of Technology Guwahati, Guwahati, India

## OPEN ACCESS

### Edited by:

Chihaya Adachi,  
Kyushu University, Japan

### Reviewed by:

Dianming Sun,  
University of St Andrews,  
United Kingdom  
Paloma Lays Dos Santos,  
University of Cambridge,  
United Kingdom  
Rajamalli Pachaiyappan,  
Indian Institute of Science (IISc), India

### \*Correspondence:

Parameswar Krishnan Iyer  
pki@iitg.ac.in

### Specialty section:

This article was submitted to  
Organic Chemistry,  
a section of the journal  
Frontiers in Chemistry

Received: 31 January 2020

Accepted: 11 May 2020

Published: 30 June 2020

### Citation:

Barman D, Gogoi R, Narang K and  
Iyer PK (2020) Recent Developments  
on Multi-Functional Metal-Free  
Mechanochromic Luminescence and  
Thermally Activated Delayed  
Fluorescence Organic Materials.  
Front. Chem. 8:483.  
doi: 10.3389/fchem.2020.00483

Metal-free organic compounds with highly ordered  $\pi$ -conjugated twisted skeletons are capable of generating brilliant multi-colored light. Additionally, the co-existence of numerous other multi-functional properties have endowed them with the potential to be a promising class of materials for several electronic and photonic applications and next-generation advanced luminescent material-based devices. This review highlights the recent developments made in this fascinating class of multi-property encompassing materials, involving a highly twisted donor-acceptor based single molecular platform with synchronized photophysical behavior such as thermally activated delayed fluorescence (TADF), mechanoresponsive (MR), room-temperature phosphorescence (RTP), and aggregation induced emission (AIE) with associated unique and inherently manifested structure-property relationship investigations. Furthermore, a brief summary of the optoelectronic behavior of TADF materials are also presented by correlating their performances in the organic light-emitting diodes (OLEDs) and corresponding EL devices. In addition to mechanochromic luminescence (MCL) with TADF behavior, new types of emitters are also being developed, with tunable color changes such as blue-green, yellow-orange, yellow-red, etc., with some emitters crossing the entire visible span to produce white OLEDs. These developments have enriched the library of fascinating organic materials in addition to providing new directions of multifunctional material design for solutions processed OLED and several other advanced devices.

**Keywords:** delayed fluorescence (DF), phosphorescence, donor - spacer - acceptor structure, organic light emitting diode (OLEDs), mechanochromic fluorescence, aggregation induced emission (AIE), structure property correlation

## INTRODUCTION

Light is an auspicious source of existence in the living world, especially multicolored bioluminescence from natural light emitting pigments, making the universe more beautiful. Inspired by nature, human beings imagined and developed organic, inorganic, and hybrid materials as a source of chemiluminescence to generate light affordably and created many exciting ways in which to use it, for the benefit of living beings. In view of this, organic light emitting diodes (OLEDs) which are widely exploited in the field of lighting technology and emerging luminescent

organic materials, have wielded considerable importance over the past 30 years, to advance the material design and its related functionality, since the first pioneering technology was introduced in 1987 by Tang and VanSlyke (1987). However, in the last 5 years, metal free modern luminescent organic materials with thermally activated delayed fluorescence (TADF) behavior have been gaining prominence as an inevitable class of luminophores, following the invention of first TADF material 4CZIPN by C. Adachi and coworkers in 2012 (Uoyama et al., 2012). Along with notable progress in material synthesis, researchers have devoted persistent efforts to develop underlying fundamental mechanisms and an effective design strategy for multifunctional TADF materials. In particular, TADF materials have a high potential to evolve into versatile applications like flat panel displays and solid-state-lighting (Zhang et al., 2012; Wu et al., 2015; Liu et al., 2018) including photodynamic therapy (Li et al., 2017), sensors (Kinami et al., 2006), security (Yamashita et al., 2005), bioimaging (Hirata and Watanabe, 2006), memory chips (Meher and Iyer, 2018) etc. In the early stages of research, exploration of conventional fluorescence small molecules and polymers had aroused immense research interest. Certain limitations in the device efficiency, however, suffered mainly by non-radiative triplets with a share of  $\sim 75\%$  of all excitons, generated directly under electrical excitation with their poor spin-orbit coupling (SOC), weak intersystem crossing (ISC) and solely singlet excitons contribution, restricted their internal quantum efficiency (IQE) to only 25% and external quantum efficiency (EQE) to 5% (Xu et al., 2015). Further, the involvement of Iridium (Ir), Platinum (Pt) and Ruthenium (Ru) based heavy metal complexes greatly enhanced the SOC, activating the phosphorescence emission from triplet state achieving theoretical 100% IQE (Bolton et al., 2011). However, assimilation of highly expensive and non-environmentally friendly precious heavy metals are not preferred in practical applications. In this regard tremendous effort has been made to explore alternative approaches such as hybridized local charge transfer (HLCT) (Li et al., 2014), triplet-triplet annihilation (TTA) (Chou et al., 2014), including TADF, in order to harvest 100% excitons and to overcome the obstacle faced by conventional fast degradable fluorescence/phosphorescence materials (Scholz et al., 2015). Unlike other discoveries, the most successful breakthrough was achieved in the case of TADF materials, which has been realized as a promising material for lighting applications due to the decent EQE and very high photoluminescence quantum yield (PLQY), as compared to inorganic phosphorescence materials (Zhao et al., 2016). In spite of this exciting phenomenon, of additional extreme importance is the discovery of more closely associated functional features accompanying these TADF materials, that include (but are not limited to) aggregation-induced emission (AIE), white-light emission, and multi-color tunability upon severe external stimuli/mechanical force, which creates a mechanochromism property or so-called TADF-mechanophore, which extends their conceivable application manifold (Tonge and Hudson, 2019). The molecule showed multiple color emissions on application of some external stimuli like grinding, recrystallization, and solvent fuming due to the change in its molecular packing mode and intra and inter molecular interactions. Owing to the unique and easy

to tune chemical and optical properties, wide range of color switching ability, and huge possibilities on structural flexibility in an economical organic molecular platform, these TADF materials are considered to be a promising avenue for the development of next-generation electronic devices (Das et al., 2019). Moreover, an ever-increasing demand to use them as a solution-processed non-doped fabrication technique gives them an extra edge over other existing methods for solid-state lighting. However, the major issues of efficiency improvement affected by emission quenching in non-doped thin-film state is mainly due to singlet-triplet annihilation (STA), long lifetime triplet-polaron, and triplet-triplet annihilation (TTA) (Ban et al., 2017). Yet, quenching the effect of TADF emitters can be fixed by co-existing with an impressive solid state emission property, called aggregation induced emission (AIE), a condensed state emission behavior that can arrest the rotation or vibration in a highly twisted molecular configuration likewise TADF molecular structure. Further, expanding the functionality and accessibility of the multifunctional-TADF molecules enables it to evolve in new processing techniques such as ink-jet printing, spin coating etc. (Müller et al., 2003; Cho et al., 2014), offering enormous advantages over expensive thermal deposition techniques, and which can be effectively integrated in optoelectronic device fabrication platforms (Albrecht et al., 2017).

Impressively, white-light-generating TADF-single emitters have great potential for use in flat-panel displays and have attracted broad interest in future light sources (Sun et al., 2006; Reineke et al., 2009). Most of the reported organic white-light emitters were accomplished by rational blending of red/green/blue or blue/orange emitters, which covers the complete visible-light emission spectrum region (Shao et al., 2012). Notably, single organic white-light solids were often found by harnessing singlet excitons, like monomer/excimer complex, excited-state intramolecular proton transfer (ESIPT) etc. (Tang et al., 2011). However, white radiative decay from both singlet and triplet excitons have recently been found in TADF molecules (Wu et al., 2019). Moreover, development of single molecule white light emitters (SMWLEs) with multi-functional additional exciting key properties are under investigations due to their superior performance, no phase segregation, no color aging with improved stability, good reproducibility, and simple device fabrication protocols (Sun et al., 2019). In addition, by introducing AIE-ML functionality in white TADF emitters, efficient device results have been realized by overcoming the complex material arrangements and by appropriate doping of materials into the host to achieve high electroluminescence (EL) and high external quantum efficiencies (Zheng et al., 2019b). Simple material based high performance organic white-light emitter fabrication therefore remains a challenge.

## FUNDAMENTAL ASPECTS AND WORKING PRINCIPLES OF TADF AND MCL MATERIALS

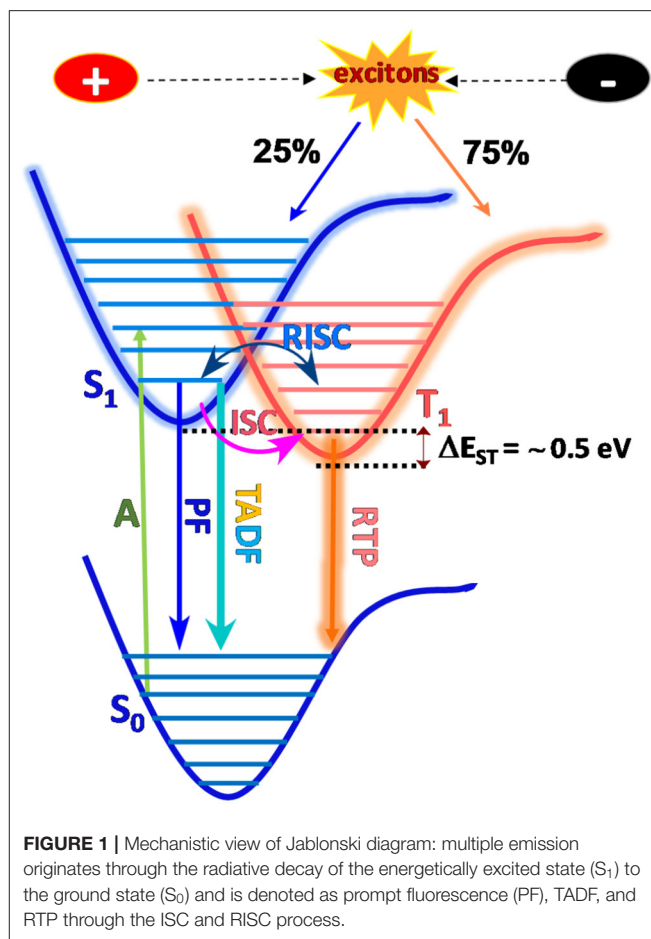
### Approaches to Realize TADF Property

Organic luminogens with electron donor (D) and electron acceptor (A) containing moieties connected either directly or



via spacer units in a hindered orientation, are considered to be promising candidates for multifunctional luminescence behavior in terms of high quantum-efficiency, good charge transporting ability in either an intramolecular or intermolecular fashion, which endows them with tunable electronic properties (Tao et al., 2014). Principally, TADF molecules must exhibit strong spin-orbit coupling which is generally induced by rapid conversion of the singlet and triplet manifolds, without the use of heavy elements and simultaneously without a small energy gap between low lying singlet and triplet states. Consequently to achieve high quantum-efficiency, the molecule should exhibit faster radiative decay via charge transfer states, which minimizes the exchange energy and therefore the singlet-triplet gap (Penfold et al., 2018). In particular, most efficient TADF emitters are based on covalently bonded donors and acceptor conjugated backbones, with features of through-bond charge transfer (TBCT) which is crucial to realize efficient TADF (Ahn et al., 2019), while few of them report to date are through-space and polymers (Tsujimoto et al., 2017). Nonetheless, a strong electron coupling between donors and acceptors mediated by covalent bonds enables the display of large oscillator strength and high PLQY (Nobuyasu et al., 2019). However, due to the lack of universal design methodologies and principles, the development of organic luminogens with multicolor and white-light emissions are predominantly still under investigation. Generally, these types of materials possess numerous versatile photophysical phenomenon brought about by radiative emission, generally mediated through intramolecular charge transfer (ICT), vibrational relaxation, singlet-triplet intersystem crossing (ISC), internal conversion (IC), vibrational relaxation, etc., resulting in either fluorescence and phosphorescence (Itoh, 2012). Emission and relaxation processes are thus carefully investigated by manipulating excited states for donor-acceptor structural configurations (Berberan-Santos and Garcia, 1996), where emission depends on their different excited state's energy levels and probable excitons transition over these states. Therefore, by tuning the excitons of electronically excited states with effective transitions, different and distinct excited energy levels with effective transitions evolved through which photophysical processes can be precisely controlled by means of lifetime and quantum yield (Wu et al., 2018) (summarized in Jablonski diagram **Figure 1**).

According to the El Sayed rule, the photophysical processes under photonic/electronic irradiation of luminogens typically produce 25% of singlet and 75% of triplet excitons, which can travel from excited singlet ( $S_1$ ) to ground state ( $S_0$ ) (i.e., fluorescence), which radiates instantly with the lifetime of a nanosecond (ns), and where the transition from triplet excited state ( $T_1$ ) leads to non-radiative decay due to spin being forbidden (Lower and El-Sayed, 1966). However, TADF is a delayed emission that originates from designing an aromatic compound with bulky steric hindrance and which is expected to resolve the issue of sinking triplet excitons. Surprisingly, triplet excitons can be upconverted into singlet, giving it additional enhanced fluorescence and a lifetime of up to several microseconds. Moreover, the reverse intersystem crossing (RISC) process was efficiently facilitated through a very low  $\Delta E_{ST}$



(energy gap between  $S_1$  and  $T_1$ ) value ( $\sim 0.3$  eV, Sun et al., 2014; Wong and Zysman-Colman, 2017; Wei et al., 2019) which is correlated with the molecular structure of the TADF emitter, as it is proportionate to the exchange integral ( $J$ ) as given in equation 1 & 2 (Shizu et al., 2015). Importantly, exchange integral,  $J$  depends on the electron density overlap between the highest occupied molecular orbital (HOMO) and lowest unoccupied molecular orbital (LUMO), assuming that the  $S_1$  and  $T_1$  states are influenced by HOMO to LUMO transitions and a minimum energy difference is derived/devised from a well-separated HOMO/LUMO in a highly twisted aromatic D-A skeleton (Sun et al., 2014).

$$\Delta E_{ST} = E_S - E_T = 2J \quad (1)$$

$$J = \iint \phi_{\text{HOMO}}(\mathbf{r}_1) \phi_{\text{LUMO}}(\mathbf{r}_2) \frac{1}{|\mathbf{r}_2 - \mathbf{r}_1|} \phi_{\text{HOMO}}(\mathbf{r}_2) \phi_{\text{LUMO}}(\mathbf{r}_1) d\mathbf{r}_1 d\mathbf{r}_2 \quad (2)$$

Where,  $\phi_{\text{HOMO}}$  and  $\phi_{\text{LUMO}}$  are termed as spatial distributions of the HOMO and the LUMO, and  $\mathbf{r}_1$   $\mathbf{r}_2$  are position vectors, respectively (Moral et al., 2015). It obeys the very small overlap between the HOMO and the LUMO, hence, decreases the

exchange integral ( $J$ ) and  $\Delta E_{ST}$  value. Subsequently, if the  $\Delta E_{ST}$  is sufficiently moderate, or is in the presence of a non-metallic heavy atom, carbonyl, thioesters, or when assisted by polymer host matrix, both SOC and faster ISC processes were favored, thereby leading to triplet emission at room temperature, called room temperature phosphorescence (RTP), which has a lifetime span of microseconds to seconds (Chen and Liu, 2019). Therefore, the primary goal is to utilize triplet excitons to achieve 100% internal quantum efficiency (IQE) by utilizing the concept of either TADF or RTP. Moreover, accurate quantum yields of fluorescent ( $\phi_F$ ) and TADF ( $\phi_{TADF}$ ) materials with the rate constants of fluorescent ( $k_F$ ), internal conversion ( $k_{IC}$ ), TADF ( $k_{TADF}$ ), intersystem crossing ( $k_{ISC}$ ), reverse intersystem crossing ( $k_{RISC}$ ), and efficiency of ISC ( $\phi_{ISC}$ ), RISC ( $\phi_{RISC}$ ) can be obtained from formulas 3–8 in the solid state (Lin et al., 2016). By following the aforementioned equation,  $\Delta E_{ST}$  can also be calculated from formula-9, where R and T signify the ideal gas constants, respectively.

$$\phi = \frac{\kappa_F}{(k_F + k_{IC})} \quad (3)$$

$$\phi_{ISC} = \frac{\kappa_F}{(k_F + k_{IC} + k_{ISC})} = \kappa_F \tau_F \quad (4)$$

$$\phi_{ISC} = \frac{\kappa_{ISC}}{(k_F + k_{IC} + k_{ISC})} = \kappa_F \tau_F \quad (5)$$

$$\frac{\phi_{TADF}}{\phi_F} = \frac{(\phi_{ISC} \phi_{RISC})}{(1 - k_{ISC} k_{RISC})} \quad (6)$$

$$k_{TADF} = \frac{\phi_{TADF}}{(\phi_{ISC} \tau_{TADF})} \quad (7)$$

$$k_{RISC} = \frac{k_F k_{TADF} \phi_{TADF}}{(k_{ISC} \phi_F)} \quad (8)$$

$$k_{TADF} = \frac{1}{(3k_F \exp(-\Delta E_{ST}/RT))} \quad (9)$$

## Approaches to Realize MCL Properties

Mechanochromic luminescence (MCL)/electroluminescence (EL) properties are switchable optical processes, which involve many other types of emissions in a viable functional molecule that co-exists with TADF and RTP properties. Furthermore, it remains extremely challenging to design a molecule with different optical properties in a single molecular platform and has aroused a broad potential utility and inherent luminescence mechanism to develop a new class of multi-functional materials. Considering this view, the phenomenon of altering the material properties by external factors such as light, heat, pH, pressure, magnetic, or by electric field of stimuli, is known as “Piezo luminescence” and other terms like mechanofluorochromism, mechanochromic luminescence, and piezochromism are also often used in the literature for the interchangeable properties (Sagara et al., 2007). However, the exact mechanism of MCL is not deliberated precisely, although many strategies that have been investigated, provide certain requirements to design molecules with MCL/MR properties. Yet, the reported MR materials with thermodynamically metastable states which have varying supramolecular assemblies or high order crystallinity, including

the possibilities of conformational change, excimer formation, excitons coupling, and other intermolecular interactions such as hydrogen bonding, ionic interactions,  $\pi$ - $\pi$  stacking, Van der Waals forces, etc., are found to exist (Kasha et al., 1965; Birks, 1975; Schmidbaur and Schier, 2008). Furthermore, aggregation induced emission (AIE) has also been included as a fascinating condensed state property that meets a few requirements such as TADF and MCL/MR, enabling comprehensive and versatile explorations such as security, sensors, data-storage and many other applications (Sagara et al., 2016).

Therefore, TADF materials with multicolor and multi-functional inclusive properties and with a significant AIE-ML field of research, has been in the spotlight recently. Additionally, single molecule white-emissive TADF material with bicolor ML strategies and molecular systems are highly desirable and have rarely been reported so far.

## RECENT PROGRESS ON MULTI-FUNCTIONAL TADF EMITTERS

### Dual-Color Emission Switching TADF-MCL/ECL

Metal free organic compounds which exhibit tunable emission and TADF, are commonly found in donor-acceptor type molecular systems which possess strong charge transfer ability, including well-separated HOMO/LUMO, resulting in a very low  $\Delta E_{ST}$  value ( $\sim 0.3$  eV), thereby facilitating the RISC process effectively and exhibiting the TADF property with high quantum efficiency (Data and Takeda, 2019). D-A materials therefore display reversible and distinct emission in response to external stimuli such as rubbing, grinding, shearing, pressing, temperature, electric field, and vapor and have found multiple applications in organic electronics, sensors, probes, security inks, and many more (Chi et al., 2012). This type of MCL behavior is due to the reversible changes in chemical structures or reformed conformations that do not necessarily, at all times, require breaking chemical bonds, or in physical structures with their different packing modes in the same molecule but thermodynamically stable and metastable states mostly enabling tunable emission. Multi-color changing MCL materials are therefore promising tools toward sensitive sensing of physical environments such as temperature, pressure, and pH and hence they have emerged as a fascinating area of research within the last 5 years.

A TADF emitter (3,5-di(9H-carbazol-9-yl)phenyl)(pyridin-4-yl)methanone (*m*DCBP) comprising two meta carbazolyl units as electron donating moieties and a benzoylpyridine core as an electron accepting moiety was developed by Rajamalli et al. (2016) (Figure 2). The D-A type molecular system was clearly revealed by the DFT study, where, HOMO of the molecule is mostly localized over the donor moiety, whereas the LUMO is localized over the acceptor unit resulting in a very small  $\Delta E_{ST}$  value of 0.06 eV. This small  $\Delta E_{ST}$  value facilitates the RISC process to exhibit TADF property. The molecule exhibited highly enhanced emission in solid state, in addition to a reversible, externally tunable emission (blue emission in the

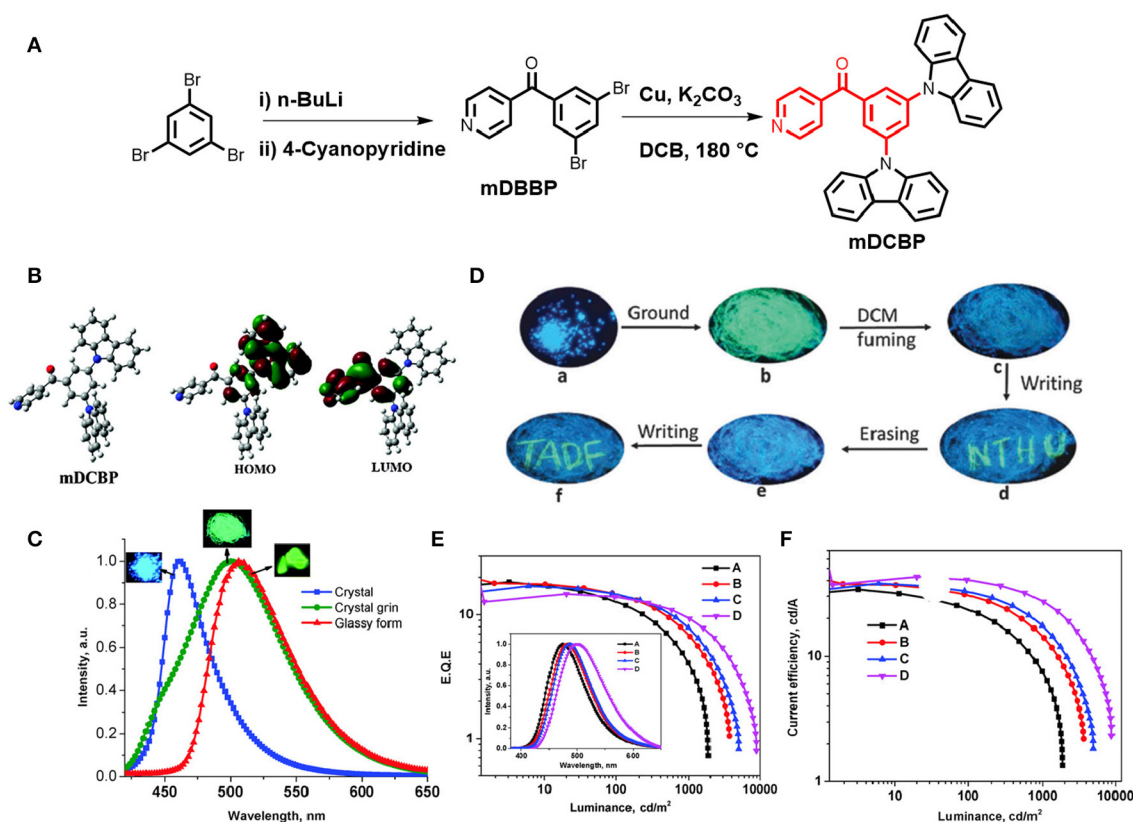


**FIGURE 2 |** (A) Chemical structure of mDCBP and its synthetic scheme. (B) Optimized molecular configuration of mDCBP and calculated HOMO-LUMO with spatial distribution. (C) Emission spectra of mDCBP in its various forms (crystalline, amorphous and glassy); insets are the respective images under UV-irradiation. (D) MCL behavior of mDCBP in response to various external mechanical stimuli. (E) External quantum yields of the fabricated devices (A–D); insets are the EL spectra of the devices. (F) Current efficiency vs. luminescence plot. Reproduced with permission from Rajamalli et al. (2016). Copyright © The Royal Society of Chemistry.

crystalline form and green emission in the amorphous form) response, investigated by alternating applied mechanical stimuli and solvent fuming, (detail theoretical and photophysical results for *m*DCBP-emitters are summarized in **Table 1**). The different colored emission by the same molecule was due to the change in its molecular packing mode under a different mechanical force and external stimuli. For example, the emission maximum was red shifted from 460 to 500 nm after grinding of mDCBP. The red shifting is likely due to the enhancement in the intermolecular interactions triggered by the applied external pressure. The TADF properties were clearly revealed by the transient PL measurements and the lifetime of the delayed component was found to be 0.02  $\mu$ s, and the excited state lifetime was lower than the phosphorescent complexes with iridium. TADF-based blue and green OLEDs have been fabricated using *m*DCBP as the emissive layer, where maximum EQE were found to be 18.4 to 14.7%, respectively (detailed device configuration and performances are summarized in **Table 2**).

In previous work pyridine moiety was found to be an important role to realize both TADF and MCL. Later, pyrimidine moiety was introduced by Ganesan et al. (2017) and a set of four new molecules, T1-T4, were synthesized, where dimethyl

acridine was used as the electron donor and pyrimidine as an electron acceptor (shown in **Figure 3**). Pyrimidine comprises less stabilized unoccupied  $\pi$  orbitals, which facilitates further functionalization. Notably, the subsequent D-A functional molecules exhibited significant TADF characteristics in solution. Theoretical studies reveal that the asymmetric arrangement of nitrogen atoms in pyrimidine for T2 exhibited the smallest  $\Delta E_{ST}$  (0.18 eV), thereby a high possibility of thermal up-conversion ( $T_1$  to  $S_1$ ) and hence the high TADF efficiency. Additionally, the materials exhibited reversible dual emission mechanochromism, which leads to evidence of the existence of two types of molecular packing that give distinct emission colors. The photophysical studies of the materials further confirmed that they undergo both prompt fluorescence and TADF (detailed computational and photophysical properties for T2 is given in **Table 1**). Based on these emitters, OLEDs have been fabricated by employing T2 as an emissive layer, which leads to blue emission with an excellent EQE of 14.2% (**Table 2**).

Notably, a series of D-A type TADF molecules (2CzPN, 4CzPN, 4CzIPN, and 4CzTPN) have been reported by Ishimatsu et al. (2014) where carbazolyl is chosen as the electron donor and dicyanobenzene units are used as the acceptor (shown in

**TABLE 1** | Computational and Photophysical characterizations of TADF-MCL emitters.

Emitter	HOMO (eV)	LUMO (eV)	Osc. Strength(f)	Theo. $\Delta E_{ST}$ (eV)	Exp. $\Delta E_{ST}$ (eV)	$\lambda_{max, abs}$ (nm)	$\lambda_{max, PL}$ (nm)	<sup>a</sup> $\tau_P$ (ns)	<sup>b</sup> $\tau_T$ ( $\mu$ s)	<sup>c</sup> $\phi$ [%]	<sup>d</sup> BS $\lambda_{max, PL}$ (nm)	<sup>e</sup> AS $\lambda_{max, PL}$ (nm)	<sup>f</sup> $T_d/T_g$ (°C)	References
mDCBP	5.72	2.72	-	0.15	0.06	334, 372	467	6.2	0.2	90	460	500	394/105	Rajamalli et al., 2016
T <sub>2</sub>	-4.97	-2.34	-	0.18	-	-	-	4.23	78.5	33.6	433		382/95	Ganesan et al., 2017
2CzPN	-	-	-	-	-	374	533	33.3	20	11				Ishimatsu et al., 2014
1_R	-5.31	-2.85			0.08	416	657	57.8	1.1	7	568 (1_Y), 640 (1_O)	673 (1_R)		Okazaki et al., 2017
5TzPm-PXZ	-5.16	-3	-	0.21	0.10	317, 421	567	-	2.9	64	583	599	471/107	Zeng et al., 2018
MeO2Qx	-5.75	-2.90	-	-	0.14	437	582	-	-	-	534	586	365/110	Pashazadeh et al., 2018b
DMAC-CNQ (Y_crystal)	-5.41	-2.94	-	0.04	-	347, 453	572	28	9.6	34	539	610,576		Zheng et al., 2019a
FDMAC-CNQ (Y_crystal)	-5.49	-3.02	-	0.03	-	343, 442	552	7.3	5.1	13	603	620,561		Zheng et al., 2019a
PTZ-AQ (R-crystal)	-	-	0.0137 (S <sub>1</sub> ), 0.0594 (S <sub>2</sub> )	0.51	0.01	239, 299, 443	606	-	275.6	84	606	~545	-	Huang et al., 2018
TATC-BP	-5.30	-2.83	-	0.08	0.125	324	524	53.5	0.94	22	483	542	>400/>95	Chen et al., 2018
QBP-DMAC	-5.28	-2.83	-	0.40	0.33	342	508	15, 13 (doped)	1.57, 1870(doped)	78	463	525	427/137	Zheng et al., 2019b
DPPZS-DBPHZ	-	-	0.652	0.30	-	397, 420	484	-	-	34	497	534	-	Takeda et al., 2018
OIDBQx	-5.26	-2.75	-	-	0.49	287, 315, 411	534	1.7 $\pm$ 0.2	-	31	494	522	398/146	Pashazadeh et al., 2018a
PTZ-DBPHZ (1_R)	-	-	-	-	-	-	-	38.42	0.98	66	568 (1_Y)	673 (1_R), 640 (1_O)	-	Data et al., 2019
Mono-DMACDPS	-5.30	-2.22	-	0.014	0.09	362	471	-	3.8	39	-	~470	298/69	Zhan et al., 2019
3-DPH-XO (crystal-C)	-	-	-	-	0.02	280, 370	540	8.61	221	44	-	-	-	Zhang et al., 2017

<sup>a</sup>Prompt fluorescence lifetime ( $\tau_P$ ), <sup>b</sup>TADF lifetime ( $\tau_T$ ), <sup>c</sup>photoluminescence quantum yield ( $\phi$ ), <sup>d</sup>before stimuli (BS), <sup>e</sup>after stimuli (AS), <sup>f</sup>thermal decomposition temperature ( $T_d$ )/glass transition ( $T_g$ ) temperature.

**N.B.** All photophysical studies in toluene Rajamalli et al., 2016; Ganesan et al., 2017; all photophysical studied on neat film Chen et al., 2018; Zhan et al., 2019; all photophysical studies in DCM Takeda et al., 2018; all photophysical studies in their respective solid states/crystalline states (Zhang et al., 2017; Huang et al., 2018; Data et al., 2019; Zheng et al., 2019a); only UV/PL in toluene (Okazaki et al., 2017; Pashazadeh et al., 2018b; Zeng et al., 2018; Zheng et al., 2019b); only UV/PL in DCM Ishimatsu et al., 2014; Pashazadeh et al., 2018a; life time study on thin film (CBP host) Zeng et al., 2018; Zheng et al., 2019b; life time study on thin film (zeonex host) (Pashazadeh et al., 2018a,b).

**Figure 4).** Ion-ion annihilation of a radical cation and anion, resulted from an electrochemical reaction that produces an excited state species ( $R^*$ ), which leads to an emission termed electrogenerated chemiluminescence (ECL). Fascinatingly, these molecules exhibited electrogenerated chemiluminescence (ECL) of intense green to red property and an ECL efficiency of up to 50% was achieved, which is comparable with the

corresponding PLQY by applying a square-wave voltage. For common fluorescent molecules there is no contribution of the  $T_1$  state toward ECL due to the non-radiative  $T_1$  to  $S_0$  transition, and, hence, the maximum efficiency of ECL is estimated to be only 25%. Thus, this 50% ECL efficiency indicates that the thermally activated spin up-conversion is very convenient for this particular ECL.



**TABLE 2 |** TADF-OLED device configurations and related EL-device performances.

Emitter	Device structure	Turn on Voltage (V)	CIE values	<sup>a</sup> EQE (%)	Brightness (Cd/m <sup>2</sup> )	<sup>b</sup> CE (Cd/A)	<sup>c</sup> LE (lm/W)	Ref.
mDCBP	ITO/NPB /mCP /DPEPO:mDCBP /PPT/TmPyPb /LiF /Al	3.6	(0.16; 0.25)	18.4	1,870	34.0	26.5	Rajamalli et al., 2016
T2	ITO/TAPC/mCP:T2/DPEPO:T2/ TmPyPB/LiF/Al	3.0	(0.20, 0.39)	14.2	7,385	34.2	29.8	Ishimatsu et al., 2014
1	ITO/NPB/CBP:1/TPBI/LiF/Al	-	-	16.8	≥25,000	19.6	-	Okazaki et al., 2017
5,7TzPmPXZ	ITO/(PEDOT:P-SS)/ CBP:5,7TzPmPXZ / (TmPyPB)/LiF/Al	-	(0.43, 0.53)	14.3	12,210	41.9	-	Zeng et al., 2018
MeO2Qx	ITO/HIL/PVK: PBD-MeO2QX/TPBI/LiF/Al	5.0	(0.41, 0.53)	10.9	16,760	-	-	Pashazadeh et al., 2018b
TATC-BP	ITO/PEDOT:PSS/TATC-BP/TmPyPB/LiF/Al	2.6	(0.41, 0.54)	5.9	-	17.8	20.0	Chen et al., 2018
TATC-BP	ITO/PEDOT:PSS/TATC-BP (30 wt%):H2/TmPyPB/LiF/Al	2.8	(0.37, 0.53)	15.9	-	48.1	47.8	Chen et al., 2018
QBP-DMAC	ITO/ TAPC/ TCTA/CBP: QBP-DMAC/ TmPyPB/LiF/Al	3.6	(0.30, 0.53)	18.8	2,264	56.8	55.8	Zheng et al., 2019b
1	ITO/HIL PEDOT:PSS /CBP:1-DEV <sub>EP</sub> /TPBI/LiF/Al	2.7	-	16	28,642	-	-	Zheng et al., 2019b

<sup>a</sup>External quantum efficiency (EQE), <sup>b</sup>current efficiency (CE), <sup>c</sup>luminous efficiency (LE).

## Multi-Color and Multi-Functional Emission Switching From Crystalline TADF-MCL

In general donor-acceptor systems are very flexible to show dual emission switching under external stimuli. However, it is very challenging to obtain multicolor emission switching from a single molecular system unless it bears a non-planar geometry, either of the donor or acceptor group. Interestingly, most of the materials in this category are very crystalline in nature enabling it to exhibit multi-color emission and multiple forms of crystals, through a simple tuning of the crystal growth environment and non-covalent interactions, to address the structure-property relationship with the TADF phenomenon. In this regard, some of the emitters showed room temperature phosphorescence (RTP), a rare class of photophysical properties of purely organic compounds. Impressively, all the non-radiative excitons can be easily harvested, and device efficiency could be improved by this additional functionality of TADF-MCL emitters.

On the aforementioned view, Okazaki et al. (2017) developed novel donor-acceptor-donor (D-A-D) type U-shaped  $\pi$ -conjugated multifunctional molecules, where the dibenzo[*a,j*]phenazine (DBPHZ) unit was chosen as an acceptor and phenothiazines (PTZ) as donors (shown in **Figure 5**). These molecules showed impressive tricolor-MCL properties, regulated by “two conformation switchable” PTZ units. The D-A-D triad, which is perpendicularly twisted, facilitates efficient intramolecular charge-transfer (ICT) and sufficiently small  $\Delta E_{ST}$  around 20 meV, which triggers the efficient RISC to achieve efficient TADF characteristics. The related photophysical and theoretical results are given in **Table 1** for red emitter1 (R<sub>1</sub>). Time-resolved photophysical measurements of the compounds further confirmed that they underwent TADF emission. Notably, in the D-A-D triad, the bowl-shaped structure of PTZ molecules

would allow it to exist as two individual conformers, one is quasi-axial and another quasi-equatorial. These “two conformation switchable” PTZ units under application of grinding, heating, fuming, and recrystallization, exhibit different packing modes leading to impressive multicolor emission. Additionally, upon recrystallization and depending on different packing modes and interactions, compound **1** exhibited two polymorphic structures 1<sub>Y</sub> (yellow) and 1<sub>O</sub> (orange). However, POZ-DBPHZ (oxygen instead of sulfur in the donor), is devoid of MCL and polymorphism due to the planar oxygen atom containing donor. Moreover, an OLED device was fabricated using these TADF emitters and very impressive external quantum efficiencies (EQEs) up to 16.8% was observed, exceeding that of the theoretical data of orthodox fluorescent emitters.

Later on Zeng et al. (2018) reported three multifunctional organic emitters (5TzPmPXZ, 7TzPmPXZ, and 5,7TzPmPXZ) comprising PXZ-moiety integrated with electron-acceptor [1,2,4]triazolo[1,5-*a*]pyrimidine (TzPm) units, that exhibited TADF with excellent photoluminescence quantum yields (PLQYs) of 49–66%, along with MCL properties caused by transitions between microcrystalline and amorphous phases, in response to external mechanical stimuli. These D-A functional molecules exhibited small  $\Delta E_{ST}$  (0.06–0.10 eV) including good spatial separation between the HOMO and the LUMO, which is greatly encouraged by the large torsion angle between the donor and acceptor moieties (74.68 to 88.17°) resulting from the steric hindrance between the donor units and the neighboring phenyl ring, susceptible to RISC as well as TADF. Interestingly, 7TzPmPXZ exhibits reversible bicolor-tuning MCL, whereas the 5TzPmPXZ and 5,7TzPmPXZ exhibited tricolor-switching behavior in their solid-state (shown in **Figure 6** and detailed TADF-MCL properties for 5TzPmPXZ

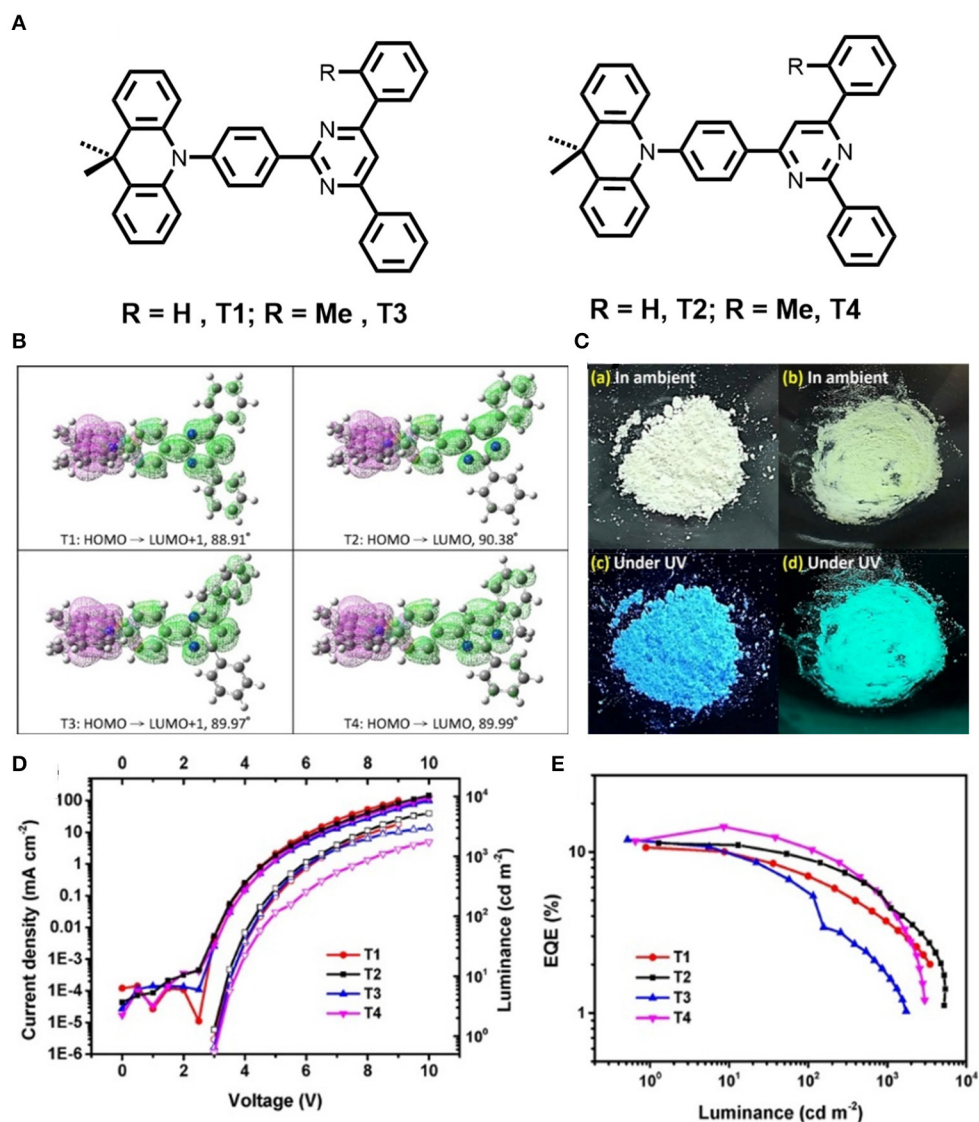
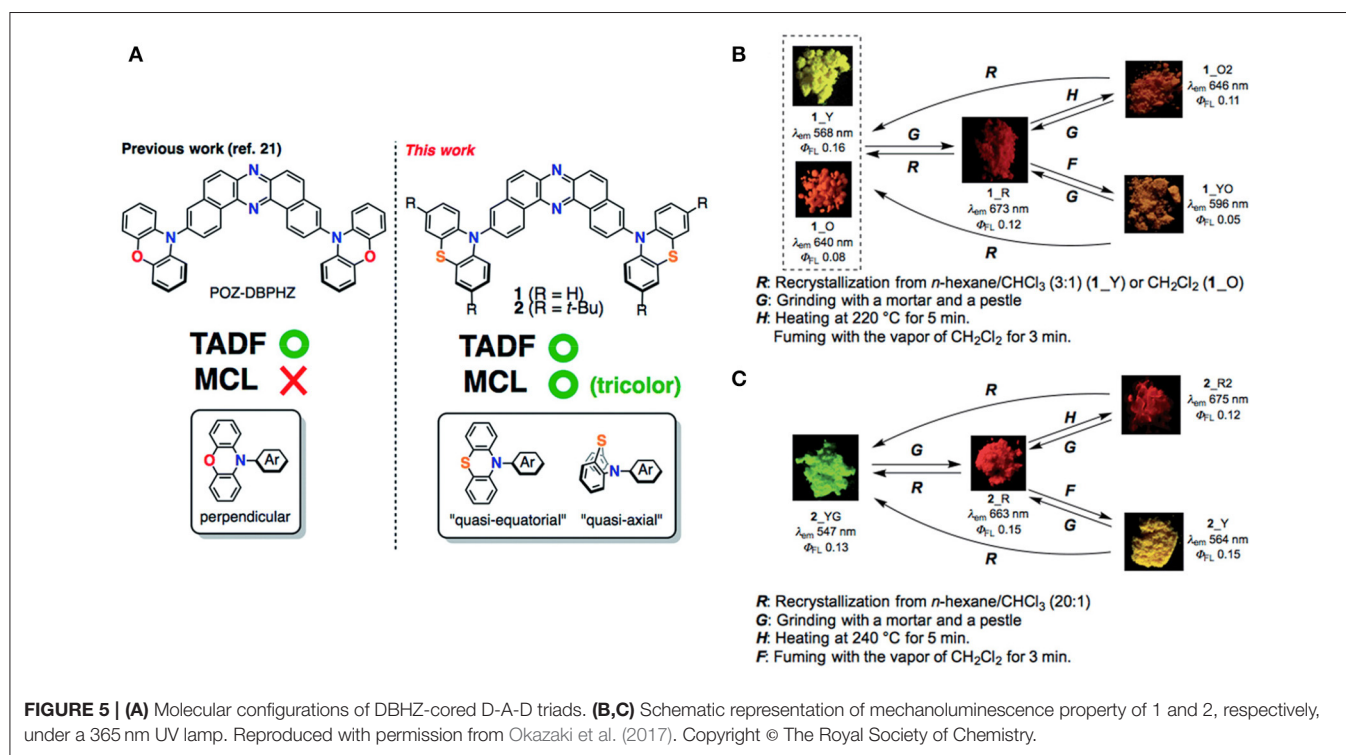
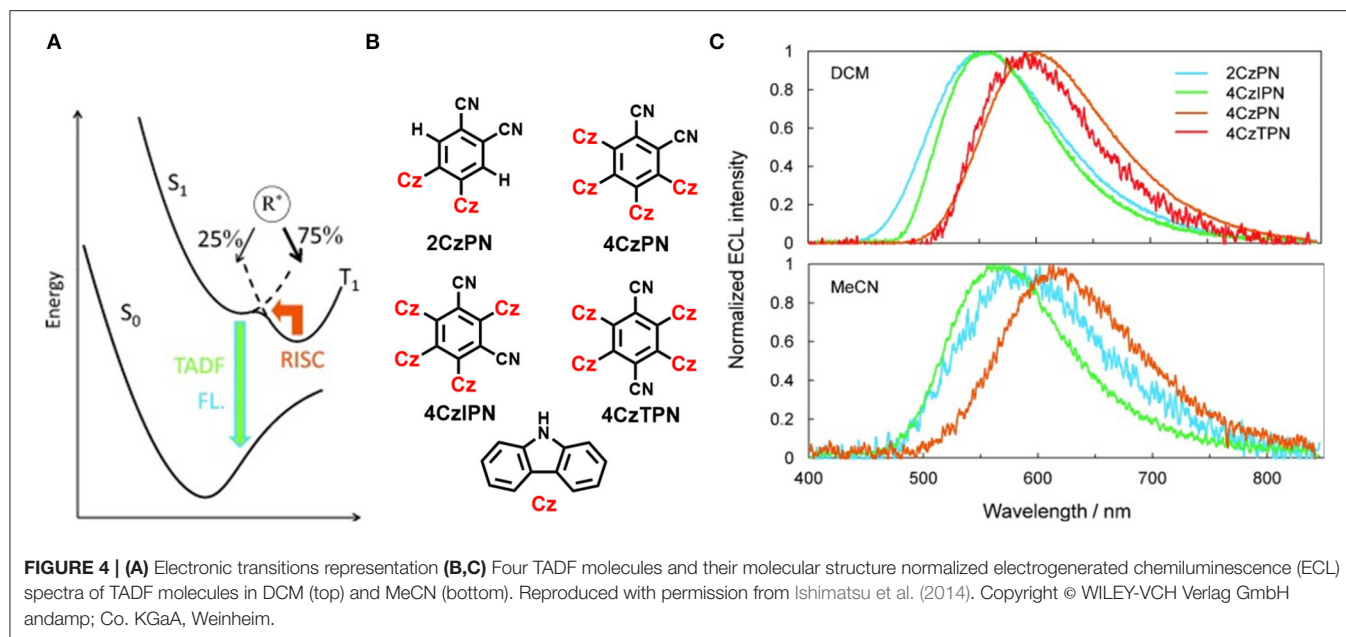


**FIGURE 3 | (A)** Chemical structures of pyrimidine-acceptor core based TADF molecules. **(B)** Frontier molecular orbitals (HOMOs and LUMOs) related to the minimum optical transitions with calculated dihedral angles between the planar dimethyl acridine to the central phenylene substituent are 88.91° and 90.38° for T1-T2, and 89.97° and 89.99° for T3-T4 in DCM, respectively. **(C)** Photographs of the ambient and luminescence materials under UV-lamp; color changes of T2 in response to mechanical grinding. **(D)** Current density (J) -voltage (V)-luminance, and **(E)** EQE-luminance plots of the white OLEDs. Reproduced with permission from Ganesan et al. (2017). Copyright ©WILEY-VCH Verlag GmbH andamp; Co. KGaA, Weinheim.

are discussed in **Table 1**). Reversible phase transitions between amorphous and microcrystalline states during and after the application of external mechanical force are responsible for multi-color changes. Furthermore, solution-processed OLEDs were fabricated by employing the synthesized compounds in the emissive layer to explore their EL properties. A maximum EQE of 14.3% was achieved for a 5,7-TzPmPXZ-based device which is summarized in **Table 2**.

A series of four new D-A-D type TADF-MCL luminogens with reversible turn-on/off TADF properties in the solid state have been reported by the group of J. V. Grazulevicius (Pashazadeh et al., 2018b). In their study, the significance of the synthetic

procedure is that it involves a smaller number of synthetic steps, which are catalyst-free and which have high product yields. Moreover, an electron-rich donor, 3-methoxy-9H carbazole, was used to examine the effect of methoxy group substitution on the carbazole units (**Figure 7A**). Notably, the rate of RISC ( $k_{RISC}$ ) is increased by increasing the donor strength from CzQx to MeO2Qx. The different colors exhibited by the molecule tCzQx were in response to different external stimuli (e.g., grinding, fuming, heating, melting) as shown in **Figure 7B**. Unlike previous reports, MCL materials can be well-aligned, usually by phase transition between crystalline and amorphous state, where delayed emission was not scrutinized precisely;



however, in this work, the TADF property of each crystalline, microcrystalline, and amorphous states of the molecules was monitored properly (Figure 7B). Emission of tCzQx-dh was found to be quenched in the crystalline form where, amorphous and film tCzQx material showed perfect TADF property. Due to TTA and the increase in singlet CT energy, the singlet-triplet energy gap turns to high, thereby, quenching TADF in the crystalline state. A summary of theoretical and

photophysical characterizations for MeO2Qx is provided in Table 1. Furthermore, based on these emitting materials, solution processed OLEDs were fabricated, which gave impressive EQE up to 10.9% (Table 2).

In a very recent report, another exciting finding by Zheng et al. (2019a) demonstrated how molecular packing in condensed states regulated the TADF phenomenon intensely by introducing two multifunctional orange-red AIE-TADF



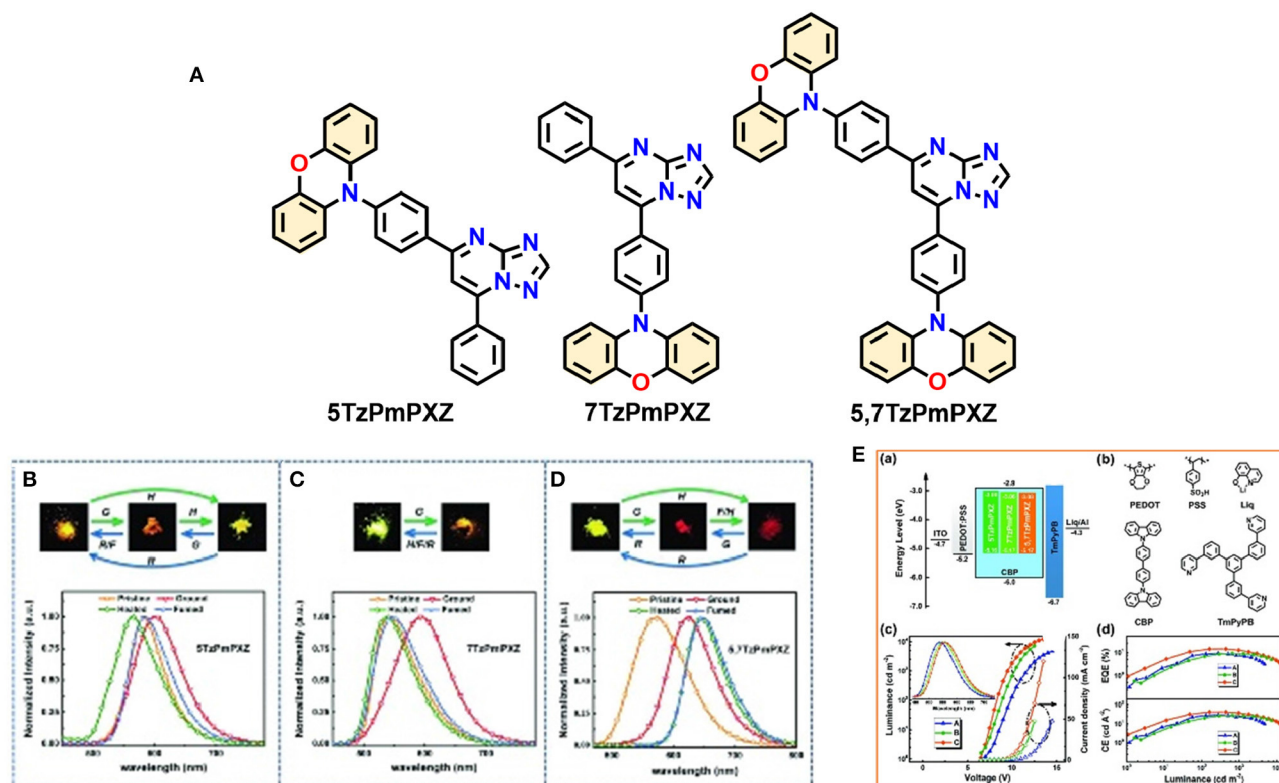


**FIGURE 6 |** (A) Molecular structures of studied compounds. Photos and PL spectra of (B) 5TzPmPXZ, (C) 7TzPmPXZ, and (D) 5,7TzPmPXZ in response to external stimuli. Under 365nm UV irradiation (G: grinding with a mortar and a pestle; H: heating at 150°C for 5TzPmPXZ and 7TzPmPXZ, 200°C for 5,7TzPmPXZ; F: fuming with CH<sub>2</sub>Cl<sub>2</sub> vapor; R: recrystallization from n-hexane/CHCl<sub>3</sub>). (E) OLED performances: (a) the energy level diagrams for the devices A, B, and C, (b) chemical structures of HTL-PEDOT:PSS, CIL-Liq, Host-CBP, and ETL-TmPyPB. (c) J-V-L curves for devices A, B, and C (inset: the normalized EL spectra of devices). (d) EQE and LE vs. luminance curves for devices A, B, and C. Reproduced with permission from Zeng et al. (2018). Copyright © WILEY-VCH Verlag GmbH andamp; Co. KGaA, Weinheim.

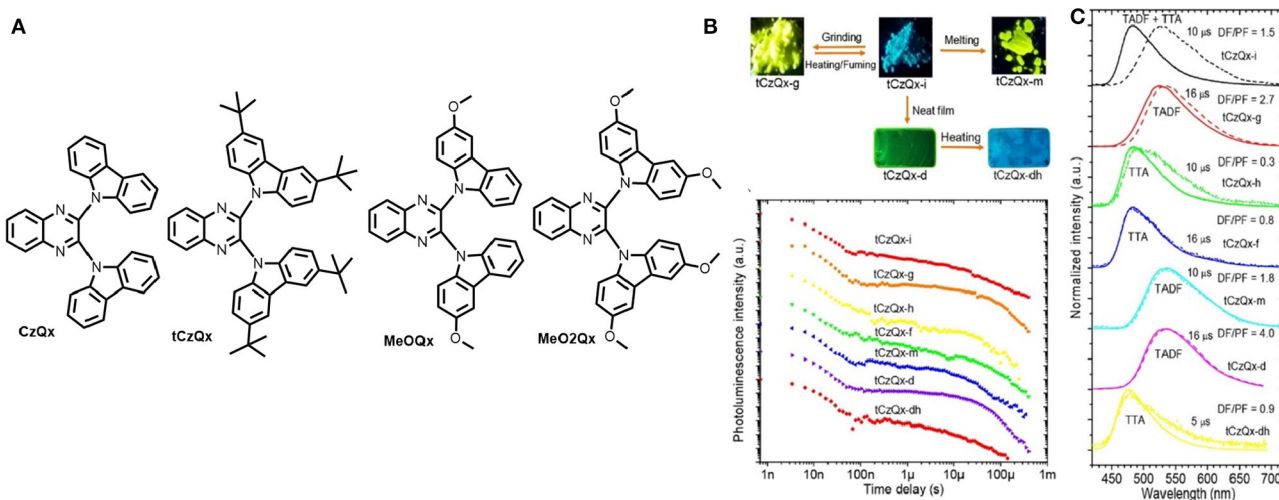


**FIGURE 7 |** (A) TADF chemical structure of D-A-D triads. (B) Images of tCzQx at different forms (top-left); Distinct PL-decay plots of different states of tCzQx (bottom-left). (C) Time-resolved PL spectra of the compound (solid lines: prompt fluorescence, dashed lines: delayed fluorescence). Reproduced with permission from Pashazadeh et al. (2018b). Copyright © American Chemical Society.



emitters, DMAC-CNQ and FDMAC-CNQ, respectively (shown in **Figure 8**). A deep insight established the relationship between multi-conformational aggregation states and TADF features, in terms of emission wavelengths, lifetimes, and PLQYs. In addition, a detailed crystal structure analysis revealed a structure-property relationship with diverse molecular stacking modes obtained from polymorphs, which determined the

impressive TADF characteristic at the aggregated state. Both the emitters exhibited multicolor-MCL, and through grinding, greenish yellow color fluorescence changed red, and after fuming with  $\text{CH}_2\text{Cl}_2$  vapors, the emission turned yellow (photophysical and theoretical results are summarize **Table 1** for the emitters). This emission switching behavior also effects the TADF characteristics in powder form. Overall, this

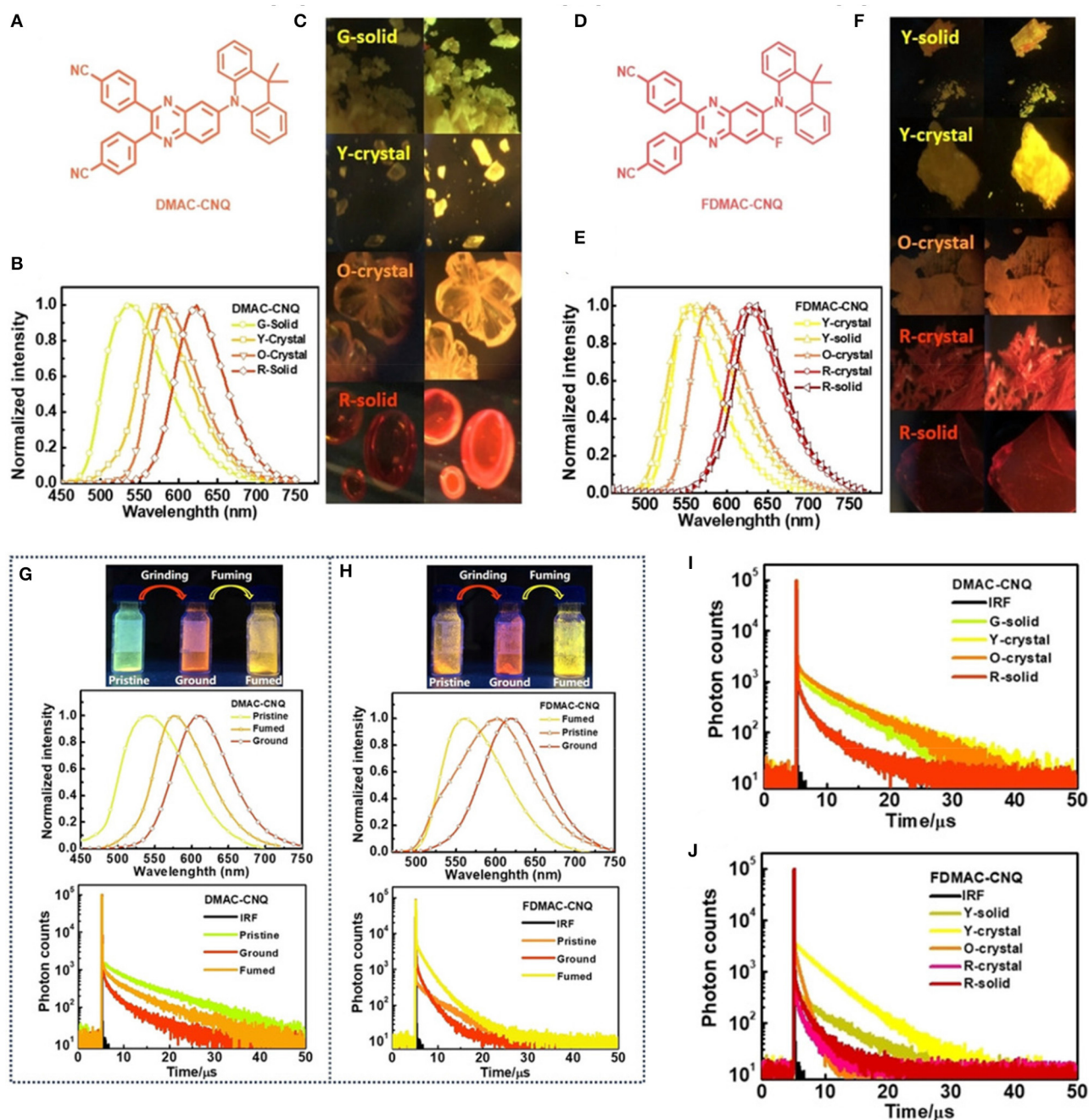


**FIGURE 8 | (A–F)** Chemical structures, Photographs, normalized emission spectra of obtained polymorphic solids of DMAC-CNQ and FDMAC-CNQ, respectively. **(G,H)** Photographs and normalized PL spectra of mechanochromism properties and **(I,J)** transient PL decay spectra of the two TADF-emitters. Reproduced with permission from Zheng et al. (2019a). Copyright © WILEY-VCH Verlag GmbH andamp; Co. KGaA, Weinheim.

work concluded that the “aggregation state affects the TADF emissive feature.”

Huang et al. (2018) reported an exciting multi-assets anthraquinone derivative, 2-(phenothiazine-10-yl)-anthraquinone (PTZ-AQ), which shows polymorphism, multicolor emission, MCL, AIE, and TADF properties in a single molecular platform (shown in **Figure 9**). In particular, the molecule consists of a planar acceptor moiety (AQ) and a non-planar donor moiety (PTZ), caused by a huge twist within the structure, which endows the better separation of the HOMO and LUMO, and further leads to a very small  $\Delta E_{ST}$  value. Additionally, the non-rigid structure of the molecule is very

much susceptible to the modulation of the morphology and molecular interactions, thereby, their respective photophysical properties with different aggregation states (Y-solid, R-solid, Y-crystal, O-crystal, and R-crystal). It is worth noting that the distinct crystal structure and different intermolecular interactions of the polymorphs are responsible for the attributed phenomenon, which cover tunable green to a deep red emission. The aggregation state emission has a substantial impact on the TADF properties of a molecule by regulating the molecular assembling modes. Unlike other polymorphs of PTZ-AQ, R-crystal displays efficient TADF characteristics owing to the very small  $\Delta E_{ST}$  value of 0.01 eV and shows excellent TADF PLQY

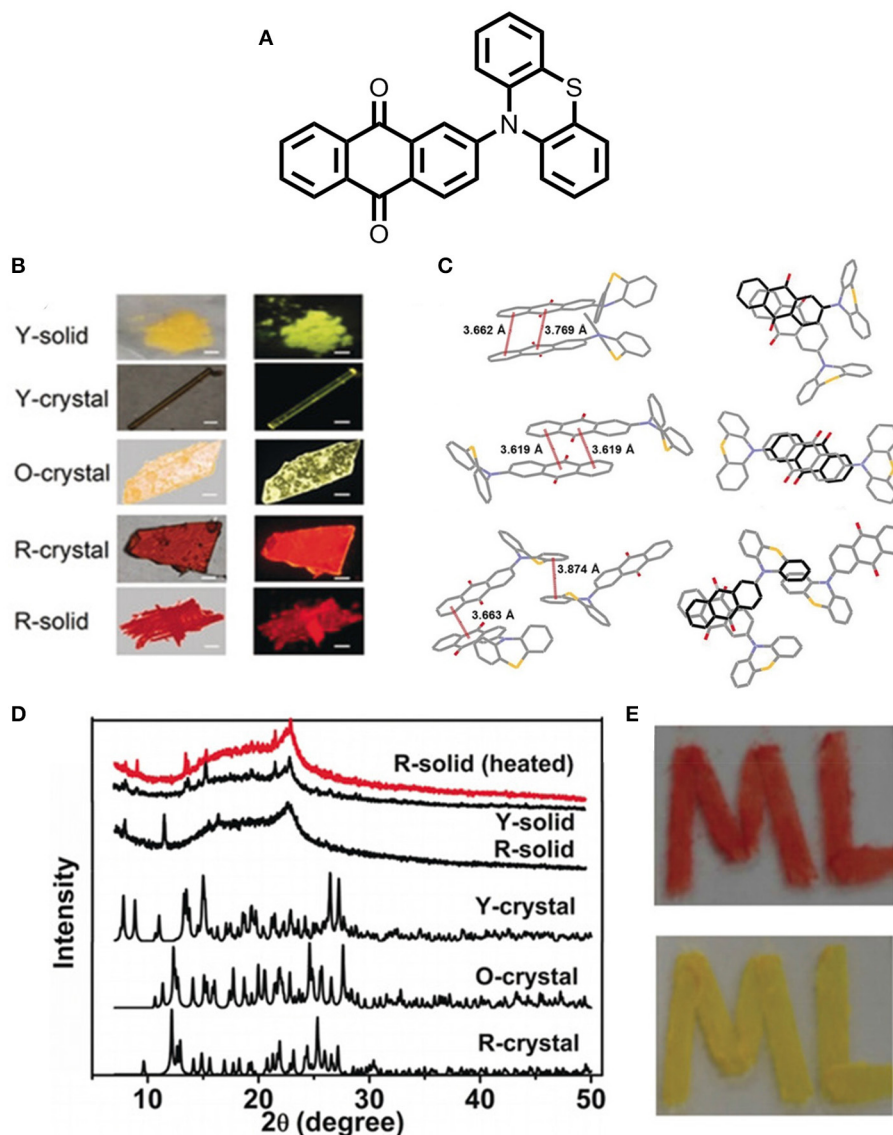


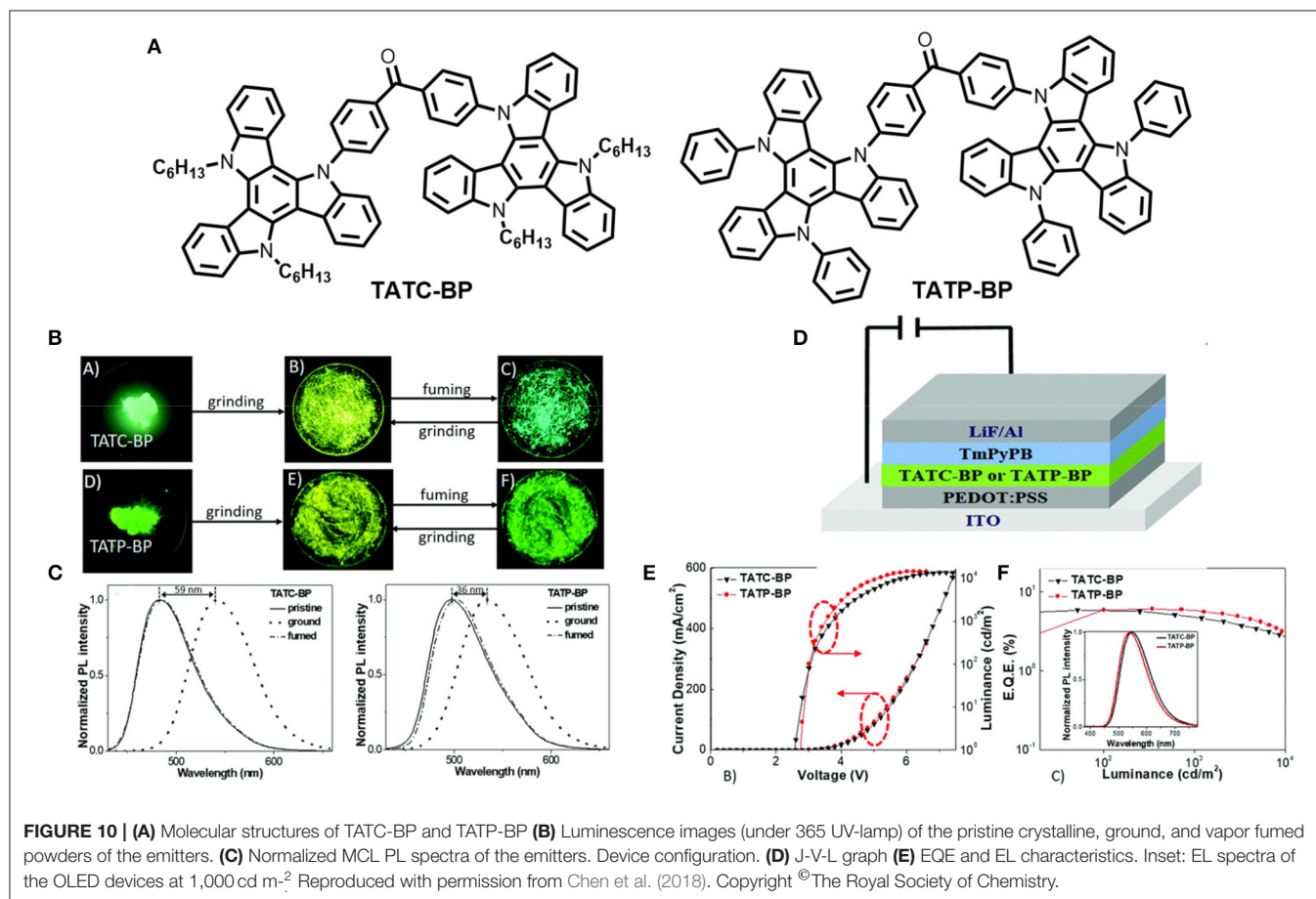
**FIGURE 9 |** (A) Structure of D-A type PTZ-AQ molecule. (B) Photographs taken at different solid states (under ambient light-left; under UV irradiation- right; scale bar: 200  $\mu\text{m}$ ). (C) Intermolecular non-covalent interactions (along the b axis) of Y-crystal, O-crystal and R-crystal, respectively. (D) P-XRD pattern of different solid states of PTZ-AQ. (E) Image of the drawn "ML" shape by the R-solid of PTZ-AQ under daylight (top); the image of shape "ML" (up) under heating condition at 150°C for 30 s in daylight (bottom). Reproduced with permission from Huang et al., 2018. Copyright © WILEY-VCH Verlag GmbH andamp; Co. KGaA, Weinheim.

up to 84.8%. Moreover, this work opens up a new approach for further research on the multifunctional organic emitters (detailed theoretical and photophysical data deliberated in **Table 1**).

Two new solution-processable triazatruxene-based small molecules, Bis(4-(10,15-dihexyl-10,15-dihydro-5H-diindolo[3,2-a:30,20-c]carbazol-5-yl)phenyl) methanone (TATC-BP) and bis(4-(10, 15-diphenyl-10,15-dihydro-5H-diindolo[3,2-a:30,20-c]carbazol-5-yl)phenyl) methanone (TATP-BP), were designed and synthesized by Chen et al. (2018). The molecules consist of two triazatruxene (electron donor) moieties linked through a benzophenone unit (electron acceptor), exhibiting twisted D-A-D conformation and comprising TADF and AIE along with MCL properties (shown in **Figure 10**). TATC-BP contains hexyl substituents on the TAT unit, whereas TATP-BP had phenyl substituents, and the different AIE and MCL behaviors of the molecules were controlled by the different substituents on the TAT unit (detailed computational and photophysical results summarize below **Table 1**). Due to the sterically less hindered and flexible alkyl substituents in TATC-BP compared to bulkier and rigid phenyl substituents in TATP-BP, the former crystal has a more compact packing, stronger intermolecular interaction with a smaller molecular reorganization energy, and emission is more shifted toward the blue region relative to the TATP-BP

crystal. Furthermore, solution processed OLEDs were fabricated using these luminescent materials as an emissive layer and a maximum EQE of 5.9% (non-doped) and 15.9% (with 30 wt % doping) were achieved for the TATC-BP based device, whereas the TATP-BP based device showed a maximum EQE of 6.0% (non-doped) and 15.4% (30 wt% doping). Fascinatingly, the emitters achieved a low efficiency roll-off ratio. TATP-BP showed a much lower efficiency roll-off relative to TATC-BP, which indicates the effect of stiff and bulky phenyl groups.

Zheng et al. (2019b) designed and synthesized two multifunctional D-A-D type emissive molecules (QBP-DMAC and QBP-PXZ) comprising a novel accepting unit (5,6-dihydropyrrolo[2,1-a]isoquinoline-1,3-diyl) bis(phenylmethanone) (QBP). Both emitters exhibit TADF and AIE properties with very low  $\Delta E_{ST}$  values, realized by their highly twisted conformations with dihedral angles (between donor and acceptor) of 87.7 and 79.1° for QBP-PXZ, and 86.1 and 88.1° for QBP-DMAC; including QBP-DMAC which shows MCL characteristics (shown in **Figure 11**). Thermal up conversion of triplet excitons was further confirmed by the temperature dependent (77 K to 300 K) transient PL study. The PL intensity of the delayed component increased gradually with an increase in temperature. The underlying mechanism for this multi-color-MCL behavior has been further





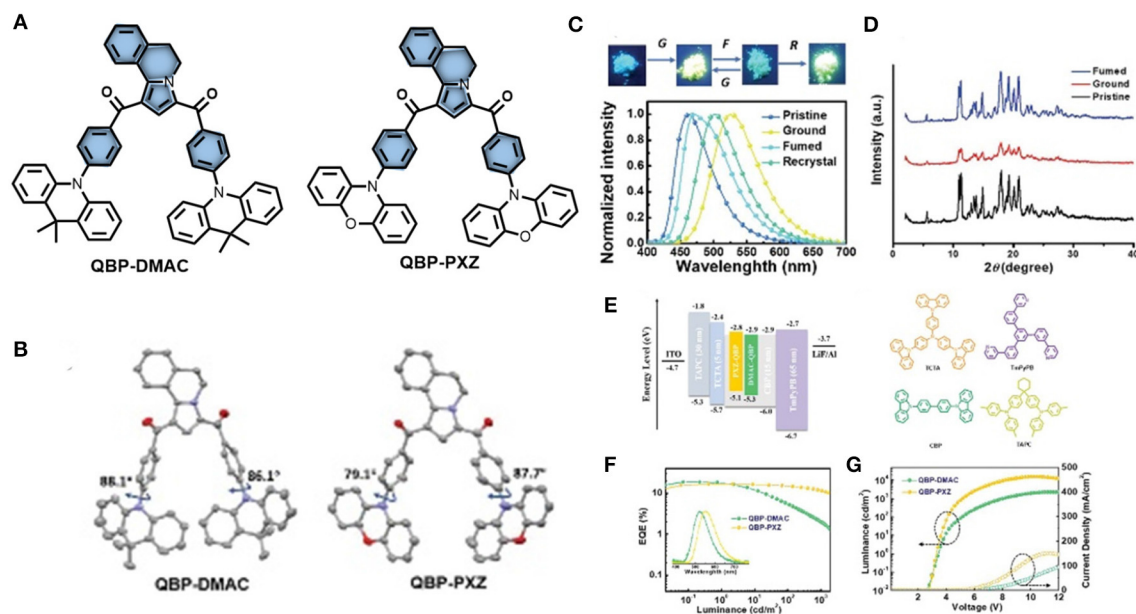


**FIGURE 11 | (A)** Chemical structure of QBP-PXZ and QBP-DMAC **(B)** molecular configurations in single crystal XRD (hydrogen excluded). **(C)** PL spectra and MCL images of QBP-DMAC in (under 365 nm UV light) **(D)** PXRD patterns of QBP-DMAC. **(E)** Energy level diagram, device and material structures **(F)** luminance vs. EQE plots. Inset: Normalized EL spectra. **(G)** Luminance-voltage-current density plots. Reproduced with permission from Zheng et al. (2019b). Copyright © WILEY-VCH Verlag GmbH andamp; Co. KGaA, Weinheim.

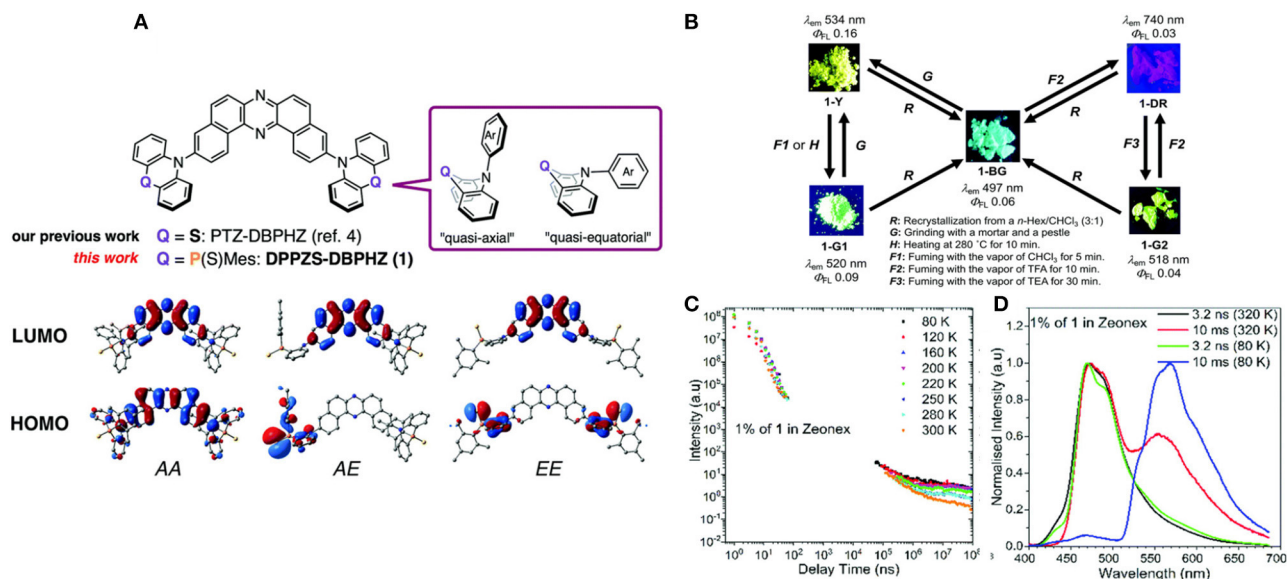


**FIGURE 12 | (A)** Chemical structures of investigated molecules and the frontier orbitals of the conformers of 1. **(B)** Summary of the Mechanoluminescence property of 1 **(C)** Emission intensity at various temperatures of DPPZS-DBPHZ against delay time **(D)** PL spectra (Normalized) of 1 at various temperatures. Reproduced with permission from Takeda et al. (2018). Copyright © The Royal Society of Chemistry.

analyzed by a PL study and powder X-ray diffraction (PXRD) measurements, which revealing that the reversible phase transitions between amorphous and crystalline states, during and after the application of external mechanical force, are responsible for MCL. The careful crystal analysis of QBP-DMAC

reveals that it has a loose molecular packing mode and weak  $\pi$ - $\pi$  interactions between DMAC units, which are responsible for the underlying mechanism for its multicolor tunable MCL property. The photo physical and computational data for QBP-DMAC are given in **Table 1**. Based on these emitting materials, OLEDs



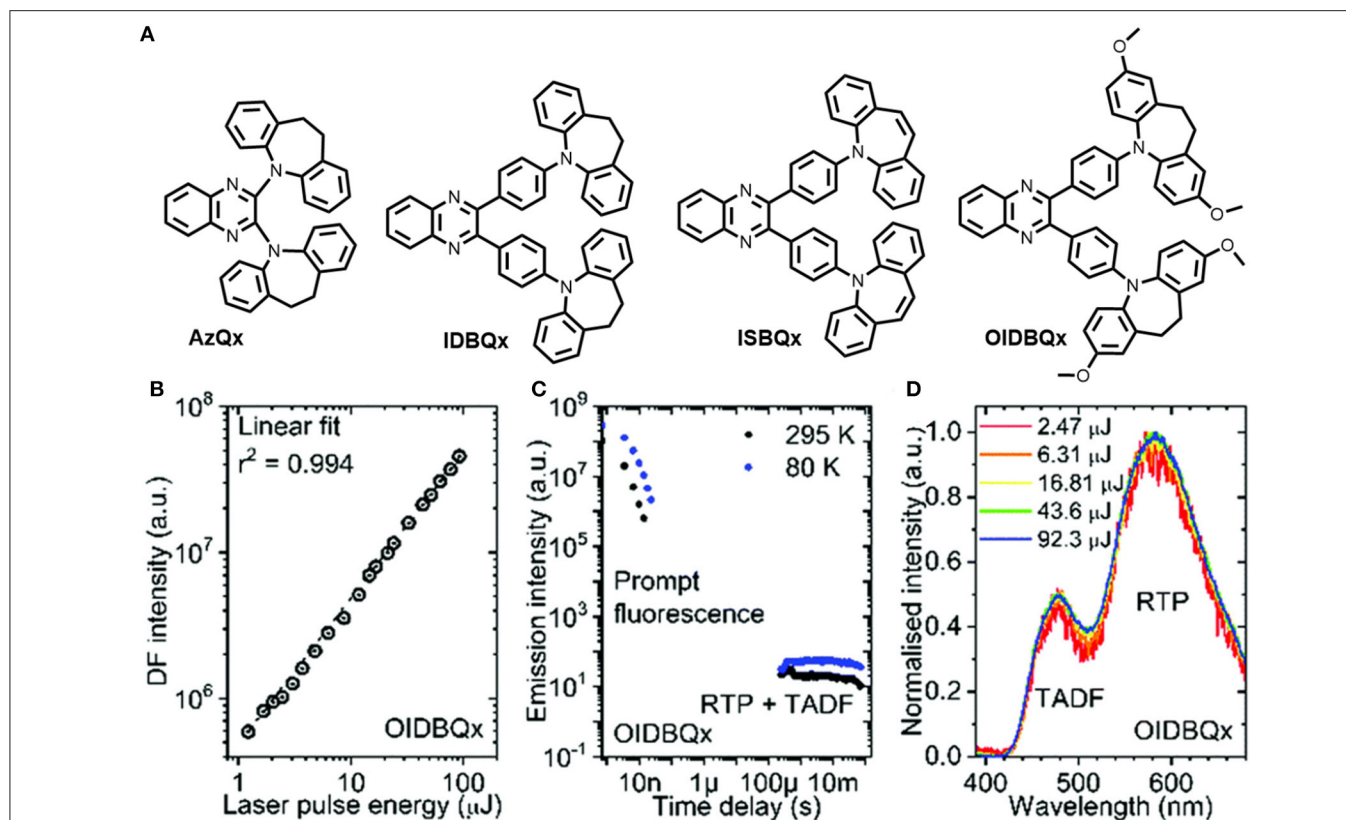


**FIGURE 13 | (A)** Structures of AzQx, IDBQx, ISBQx, OIBDQx. **(B)** DF intensity vs. laser pulse energy plot of OIBDQx (at 295 K); **(C)** PL decay transients of OIBDQx at different temperature; **(D)** DF and RTP spectra (at 295 K) with different excitation pulse energy. Reproduced with permission from Pashazadeh et al. (2018a). Copyright © The Royal Society of Chemistry.

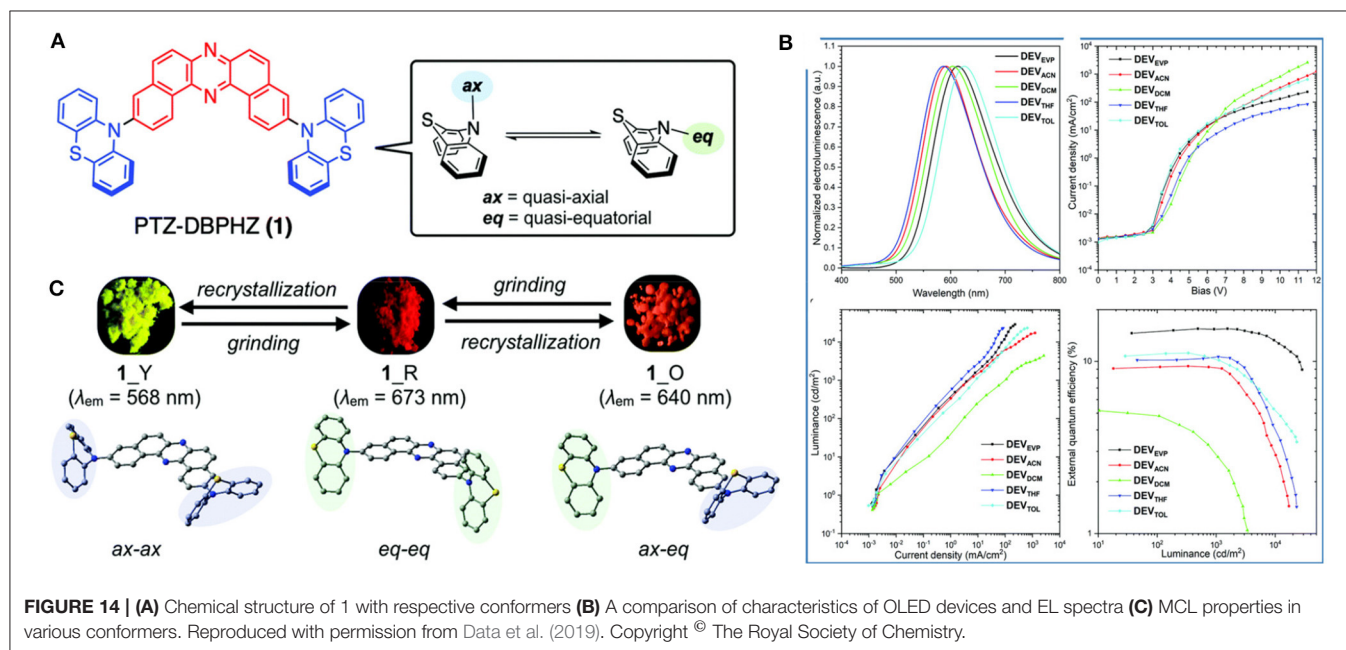


**FIGURE 14 | (A)** Chemical structure of 1 with respective conformers **(B)** A comparison of characteristics of OLED devices and EL spectra **(C)** MCL properties in various conformers. Reproduced with permission from Data et al. (2019). Copyright © The Royal Society of Chemistry.

were fabricated and a maximum EQE of 18.8% was achieved for QBP-DMAC-based OLEDs, which is among the highest efficiencies of TADF-AIE-MCL active organic emitters.

Multi-properties of a novel  $\pi$ -conjugated remarkably twisted D-A-D were investigated in purely organic triad DPPZS-DBPHZ, by Takeda et al. (2018), containing

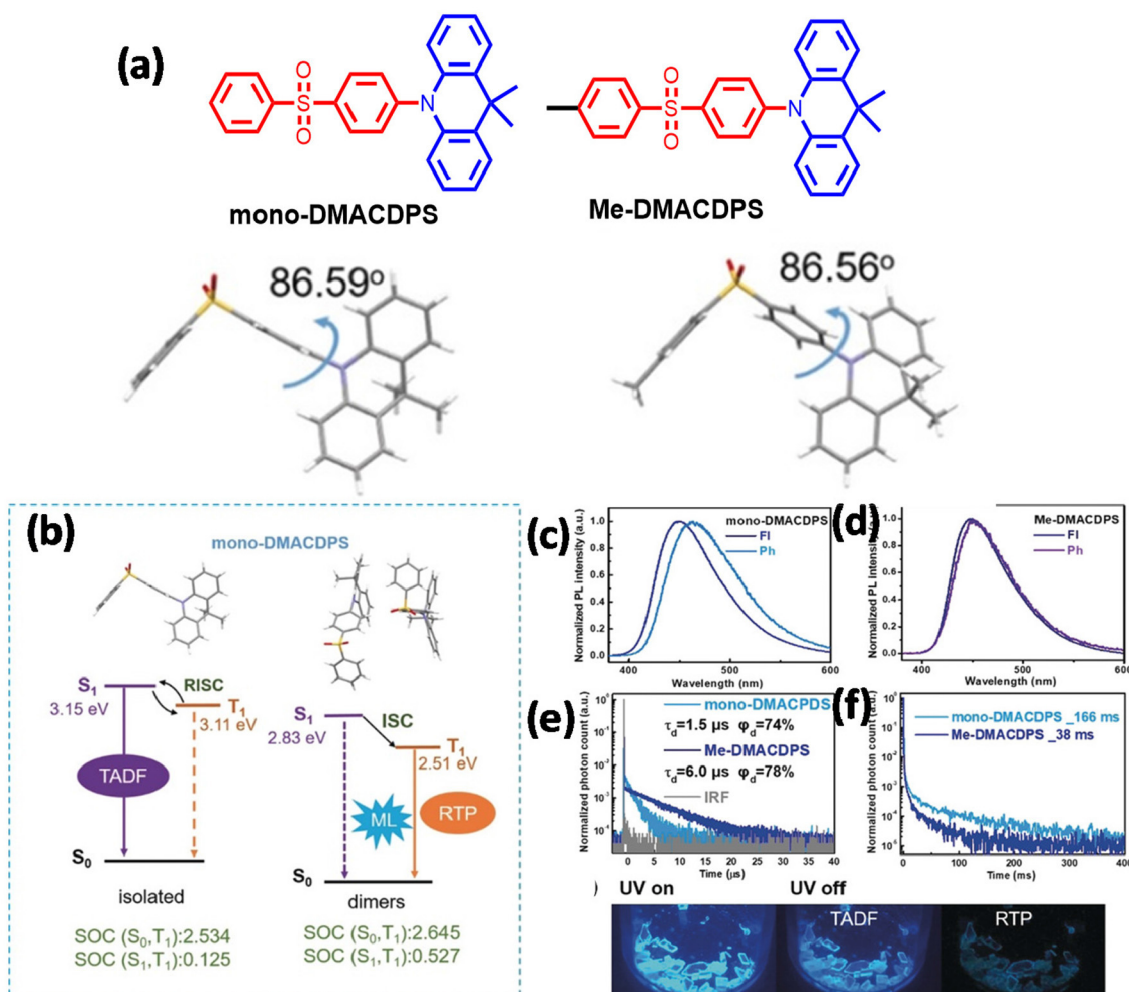


**FIGURE 15 |** (a) Configurations and XRD structures of the molecules. (b) Energy level diagrams (of the monomer and dimer of mono-DMACDPS). (c,d) PL spectra of studied molecules (at 300 K). (e,f) The TRPL spectra of studied molecules. Bottom Crystal images of mono-DMACDPS (UV lamp—on and off). Reproduced with permission from Zhan et al. (2019). Copyright ©WILEY-VCH Verlag GmbH andamp; Co. KGaA, Weinheim.

moderately-electron-donating and conformationally flexible units, where dibenzo[a, j]phenazine (DBPHZ) has been chosen as an acceptor and dihydrophenophosphanizine sulfide (DPPZS) as donors (shown in **Figure 12**). Fascinatingly, the compound exhibited multi-color-changing mechanochromic luminescence (MCL) assisted by conformational interconversion in the molecule, including TADF and unexpected RTP characteristics in presence of the host matrix (ZEONEX®). The delayed emission (DF) time constants decreased gradually, with an increase in the temperature. Furthermore, the molecule undergoes significant acid/base-responsive emission tuning between the visible and NIR region. Their theoretical and photo physical features are included in **Table 1**.

Tashazadeh et al. reported four new derivatives of quinoxaline-containing iminodibenzyl and iminostilbene moieties with TADF, RTP, and MCL properties (shown in **Figure 13**) (Pashazadeh et al., 2018a). To perceive RTP

and TADF simultaneously, a modest singlet–triplet energy splitting is required to tune the RISC rate, to directly harvest all the triplet excitons (phosphorescence). Despite having a large singlet–triplet energy gap, room temperature delayed fluorescence and phosphorescence properties were observed for these luminophores (0.49–0.52). They have developed a quinoxaline-based acceptor of new luminogens. Notably, the emitters IDBQx, ISBQx, and OIBDQx, connected through a phenylene group between the acceptor and the donor units, exhibited orange RTP and blue TADF emission. This is a clear indication of non-aromatic twisted conformation. IDB not only induces strong spin–orbit coupling, but also minimizes the non-radiative decay. Remarkably, TADF or RTP were not observed for ISBQx, and only exhibited prompt fluorescence. Therefore, the non-radiative process was supported by the boat shape structure of ISB (7-membered ring in ISBQx), which triggered the quenching of triplet

excitons. The methoxy group containing iminodibenzyl derivative exhibited MCL behavior due to the increased dipole moment. The introduction of a phenyl spacer between the donor and acceptor units increased the RTP contribution and the non-radiative decay was greatly suppressed by the twisted iminodibenzyl donor and the presence of methoxy groups. **Table 1** includes the photo physical features of OIDBQx.

A multi-color-changing D-A-D type MCL-TADF-RTP material PTZ-DBPHZ was developed by Data et al. (2019) and it has been disclosed that the photophysical properties and multicolor MCL can be tuned using specific conformer-enriched [i.e., 1\_Y: quasi axial-quasi axial (ax-ax), 1\_R: quasi equatorial-quasi equatorial (eq-eq), and 1\_O: quasi axial-quasi equatorial (ax-eq)] solids (shown in **Figure 14**). TADF and RTP characteristics were boosted depending on the dominant conformers of the molecule and were further employed in solution processed OLED devices, which gave excellent performance parameters. The data resulting from the photo physical studies for 1\_R are included in **Table 1**.

Zhan et al. (2019) reported the first example of multifunctional organic material with simultaneous MCL, AIE, RTP, and TADF properties (shown in **Figure 15**). Two blue emitters of mono-DMACDPS and Me-DMACDPS were designed and developed, where diphenyl sulfone acts as an acceptor and 9,9-dimethyl-9,10-dihydroacridine (DMAC) acts as a donor. DMAC is a conventionally used TADF emitter and possibly assists for AIE, whereas diphenyl sulfone is a commonly used acceptor comprising manifold modification sites. The emitters displayed typical TADF and AIE properties in the solution state, while RTP and TADF characteristics were displayed in their crystalline form. A methyl group was introduced to modulate the MCL property *via* regulating intermolecular interactions and packing mode by the steric hindrance of the methyl group, and Me-DMACDPS was found to be MCL inactive, whereas mono-DMACDPS was found to be exhibiting a distinct MCL property. Careful analysis of the crystal structure disclosed that mono-DMACDPS exhibit a large dipole moment and tight packing mode due to multiple intermolecular interactions that endow them with strong MCL (**Table 1**).

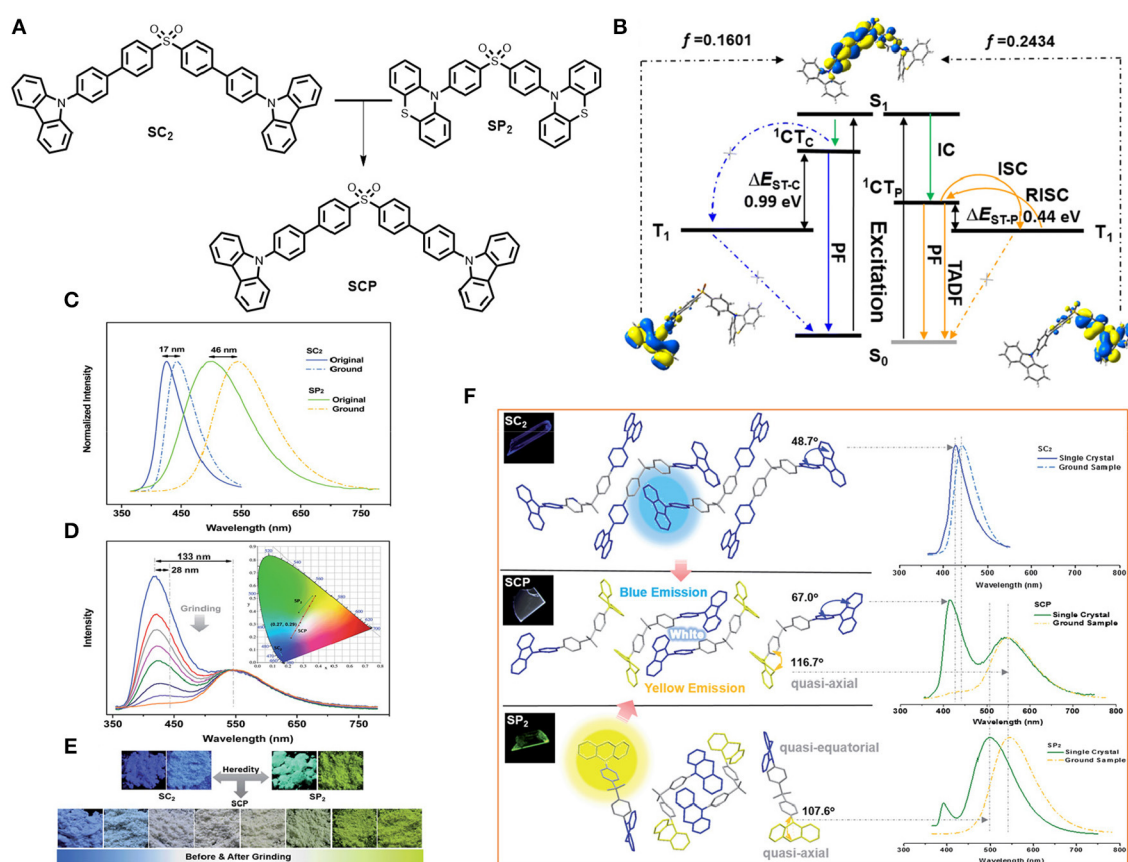


**FIGURE 16 | (A)** Molecular configuration of the compounds. **(B)** Decays associated with corresponding electronic transitions in SCP. **(C)** PL study of the parent molecules in solid-powder form. **(D)** Mechanochromism in SCP molecule. **(E)** Compound images under the UV-irradiation of 365 nm. **(F)** Single crystal analysis and crystalline molecular packing of the compounds along with corresponding photo luminescence spectra of the single crystals and normal compounds. Insets: fluorescence images (365 nm UV-excitation). Reproduced with permission from Xu et al. (2016). Copyright © The Royal Society of Chemistry.

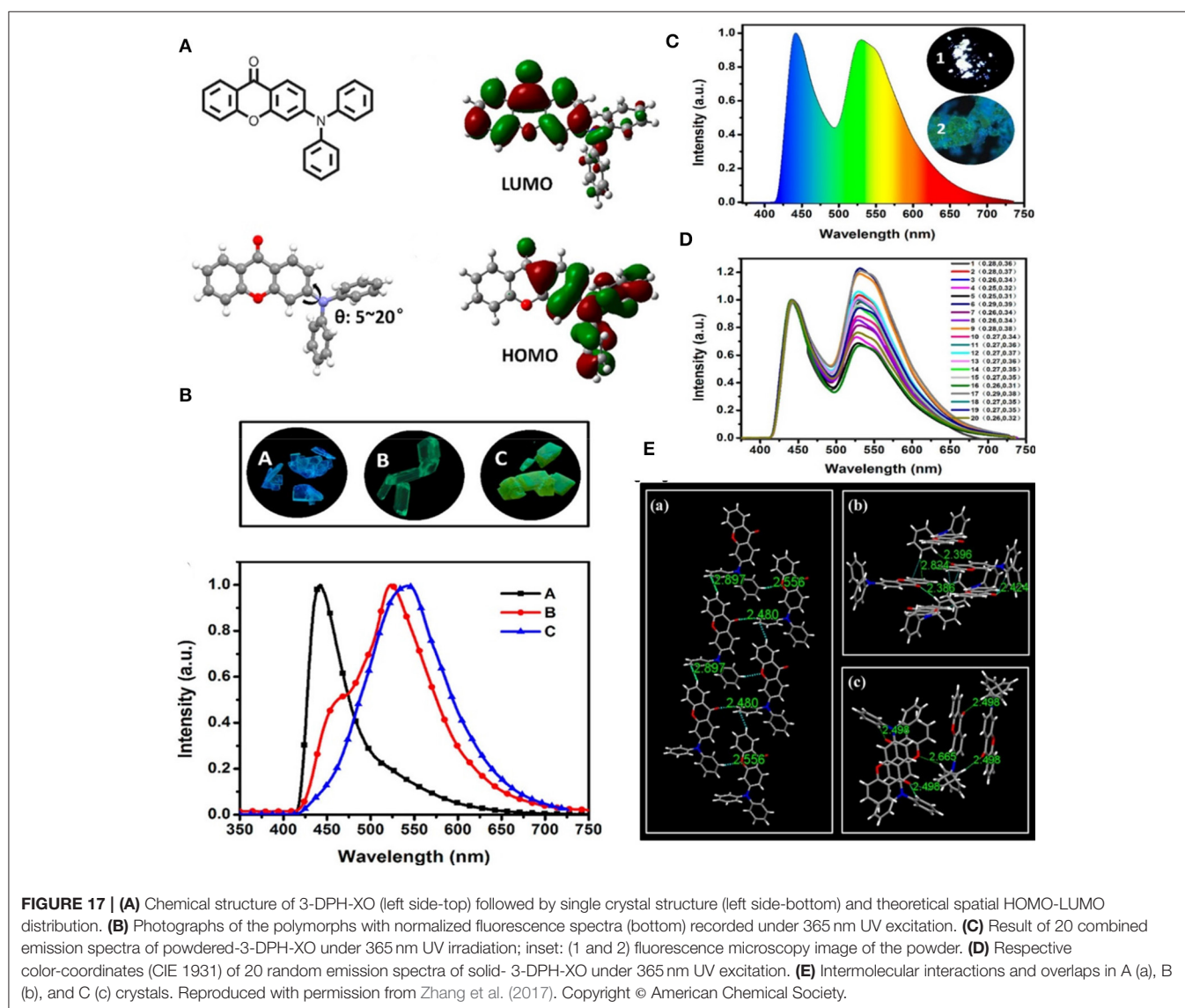


## Single Emitting White-TADF-MCL

Single molecule based white-light emitting TADF emitters have long-standing demand in solid-state lighting, display, and OLED applications due to their high triplet energy and full width at half maximum (FWHM). In addition, very few white-TADF emitters inherently manifest MCL behavior which are strongly governed by weak non-covalent interactions and constructed by a dual color emissive entity in a single molecular platform, enabling the transfer of full energy either to counter the green and red fluorescent emitter or by the complementary yellow emitter. Hence, a smart design and effective non-covalent interactions are prerequisites to realizing TADF-white light in the accompanying tunable emission.

Xu et al. (2016) established the strategy of molecular heredity to achieve high contrast linearly tunable mechanochromism with white light emission [CIE value: (0.27, 0.29)] from a single compound, and established the origin of the compound's

dual emission (shown in Figure 16). The two parent molecules, SC2 and SP2, are symmetrical by means of donor, where SC2 exhibited deep blue emission and SP2 yields impressive greenish-yellow TADF emission. Interestingly, their offspring is an asymmetric molecule, namely SCP, which thus inherited both deep blue and greenish-yellow colors that combine to generate white light emission along with TADF by means of molecular heredity, enabling a potential candidate for multi-responsive and efficient white-light emitting photoelectric devices. The dual-emission behavior of SCP can be dispensed to two independent emissions of the excited charge transfer states of the carbazole and phenothiazine units, respectively. Moreover, the underlying mechanism of MCL for SCP driven by the mechanical strength, associates with the conformational planarization of the phenylcarbazole unit along with the stronger energy transfer from the blue band to the yellow light emission band.





An efficient and simple D-A approach to achieve white light from organic solids with a polymorph dependent TADF property has been developed by Ban et al. (2017). A purely organic molecule of 3-(diphenylamino)-9H-xanthen-9-one (3-DPH-XO) has been reported, which was found to display bright white light emission with the CIE value (0.27, 0.35) in its solid state, facilitated by spontaneous formation of polymorphs with distinguished intermolecular non-covalent interaction features that determined the different emission colors, and which was further demonstrated by single crystal studies of the compound (shown in **Figure 17**). Three unprecedented different 3-DPH-XO-based single crystals were achieved with different supramolecular structures and emission properties and two of the polymorphs with acceptor-acceptor stacking revealed TADF characteristics (**Table 1**). This indicates that appropriate non-covalent interactions like  $\pi$ - $\pi$  stacking, C-H- $\pi$  interaction, and hydrogen bonding could offer a promising TADF feature by influencing the reverse intersystem crossing (RISC) process.

## CONCLUSION AND OUTLOOK

In summary, the rapid development of TADF research has resulted in a new dimension of luminescence features, by building up the substantial information into new material designs, exciting and unique key functional behaviors, and essentially providing a mechanistic understanding of TADF processes. However, this review has attempted to concentrate on the recent progress made in the development of multifunctional metal free organic emitters, focusing on aggregate state emissions, TADF, and other multi-functionalities such as ML, MCL, ECL, and white light emission properties in a single molecular platform. Furthermore, a brief overview was provided on the structure-property relationship between self-assembled solid state and excited state dynamics in order to

explore the opportunities for the rational design of multiple emission functions into single organic molecules and the further implementation into lighting applications, which are still in their infancy. In addition, this review includes the “state of the art” simple OLED device fabrications protocol and emphasized impressive output by exploiting multi-function TADF materials. More importantly, these multifunctional emitters are considered to be promising candidates for solution processed economical device fabrications owing to their tunable condensed state emissions. We believe that the rapid developments taking place in this field is generating enthusiasm, motivating researchers to explore a deeper understanding and finding new advancements in this exciting area of research. We expect this review to provide a clear prospect and to attract researchers with diverse interests to these novel multi-functional materials, to devote themselves to the development of materials, methods, and applications in this interesting interdisciplinary topic.

## AUTHOR CONTRIBUTIONS

DB planned and compiled the review article. RG compiled the text, figures, and references. KN compiled the text and references. PI initiated, planned, and compiled the review. All authors contributed to the article and approved the submitted version.

## ACKNOWLEDGMENTS

The authors thank DST (TSG and CRG), India project numbers CRG/2019/002614, DST/TSG/PT/2009/23, Max-Planck-Gesellschaft project number IGSTC/MPG/PG(PKI)/2011A/48 and DeiTy, India project no. 5(9)/2012-NANO (Vol. II) for financial support. No funding agency has supported for open access publication fees, neither has our host institution supported us.

## REFERENCES

- Ahn, D. H., Kim, S.W., Lee, H., Ko, I. J., Karthik, D., Lee, J. Y., et al. (2019). Highly efficient blue thermally activated delayed fluorescence emitters based on symmetrical and rigid oxygen-bridged boron acceptors. *Nat. Photonics* 13, 540–546. doi: 10.1038/s41566-019-0415-5
- Albrecht, K., Matsuoka, K., Yokoyama, D., Sakai, Y., Nakayama, A., Fujita, K., et al. (2017). Thermally activated delayed fluorescence OLEDs with fully solution processed organic layers exhibiting nearly 10% external quantum efficiency. *Chem. Commun.* 53, 2439–2442. doi: 10.1039/C6CC09275F
- Ban, X., Zhu, A., Zhang, T., Tong, Z., Jiang, W., and Sun, Y. (2017). Design of encapsulated hosts and guests for highly efficient blue and green thermally activated delayed fluorescence OLEDs based on a solution-process. *Chem. Commun.* 53, 11834–11837. doi: 10.1039/C7CC06967G
- Berberan-Santos, M. N., and Garcia, J. M. M. (1996). Unusually strong delayed fluorescence of C70. *J. Am. Chem. Soc.* 118, 9391–9394. doi: 10.1021/ja961782s
- Birks, J. B. (1975). Excimers. *Rep. Prog. Phys.* 38, 903–974. doi: 10.1088/0034-4885/38/8/001
- Bolton, O., Lee, K., Kim, H. J., Lin, K. Y., and Kim, J. (2011). Activating efficient phosphorescence from purely organic materials by crystal design. *Nat. Chem.* 3, 205–210. doi: 10.1038/nchem.984
- Chen, K. C., and Liu, B. (2019). Enhancing the performance of pure organic room-temperature phosphorescent luminophores. *Nat. Commun.* 10:2111. doi: 10.1038/s41467-019-10033-2
- Chen, Y., Wang, S., Wu, X., Xu, Y., Li, H., Liu, Y., et al. (2018). Triazatruxene-based small molecules with thermally activated delayed fluorescence, aggregation-induced emission and mechanochromic luminescence properties for solution-processable nondoped OLEDs. *J. Mat. Chem. C* 6, 12503–12508. doi: 10.1039/C8TC04721A
- Chi, Z., Zhang, X., Xu, B., Zhou, X., Ma, C., Zhang, Y., et al. (2012). Recent advances in organic mechanofluorochromic materials. *Chem. Soc. Rev.* 41, 3878–3896. doi: 10.1039/C2CS35016E
- Cho, Y. J., Yook, K. S., and Lee, J. Y. (2014). High efficiency in a solution-processed thermally activated delayed-fluorescence device using a delayed-fluorescence emitting material with improved solubility. *Adv. Mater.* 26, 6642–6646. doi: 10.1002/adma.201402188
- Chou, P.-Y., Chou, H.-H., Chen, Y.-H., Su, T.-H., Liao, C.-Y., Lin, H.-W., et al. (2014). Efficient delayed fluorescence via triplet-triplet annihilation for deep-blue electroluminescence. *Chem. Commun.* 50, 6869–6871. doi: 10.1039/C4CC01851F
- Das, D., Gopikrishna, P., Barman, D., Yathirajula, R. B., and Iyer, P. K. (2019). White light emitting diode based on purely organic fluorescent to modern thermally activated delayed fluorescence (TADF) and perovskite materials. *Nano Convergence* 6:31. doi: 10.1186/s40580-019-0201-6
- Data, P., Okazaki, M., Minakata, S., and Takeda, Y. (2019). Thermally activated delayed fluorescence vs. room temperature phosphorescence by conformation control of organic single molecules. *J. Mat. Chem. C* 7, 6616–6662. doi: 10.1039/C9TC00909D

- Data, P., and Takeda, Y. (2019). Recent advancements in and the future of organic emitters: TADF- and RTP-active multifunctional organic materials. *Chem. Asian J.* 14, 1613–1636. doi: 10.1002/asia.201801791
- Ganesan, P., Ranganathan, R., Chi, Y., Liu, X.-K., Lee, C.-S., Liu, S.-H., et al. (2017). Functional pyrimidine-based thermally activated delay fluorescence emitters: photophysics, mechanochromism, and fabrication of organic light-emitting diodes. *Chem. Eur. J.* 23, 2858–2866. doi: 10.1002/chem.201604883
- Hirata, S., and Watanabe, T. (2006). Reversible thermoresponsive recording of fluorescent images (TRF). *Adv. Mater.* 18, 2725–2727. doi: 10.1002/adma.200600209
- Huang, B., Chen, W.-C., Li, Z., Zhang, J., Zhao, W., Feng, Y., et al. (2018). Manipulation of molecular aggregation states to realize polymorphism, AIE, MCL, and TADF in a single molecule. *Angew. Chem. Int. Ed.* 57, 12473–12477. doi: 10.1002/anie.201806800
- Ishimatsu, R., Matsunami, S., Kasahara, T., Mizuno, J., Edura, T., Adachi, C., et al. (2014). Electrogenerated chemiluminescence of donor-acceptor molecules with thermally activated delayed fluorescence. *Angew. Chem. Int. Ed.* 53, 6993–6996. doi: 10.1002/anie.201402615
- Itoh, T. (2012). Fluorescence and phosphorescence from higher excited states of organic molecules. *Chem. Rev.* 112, 4541–4568. doi: 10.1021/cr200166m
- Kasha, M., Rawls, H. R., and El-Bayoumi, M. A. (1965). The exciton model in molecular spectroscopy. *Pure Appl. Chem.* 11, 371–392. doi: 10.1351/pac196511030371
- Kinami, M., Crenshaw, R. B., and Weder, C. (2006). Polyesters with built-in threshold temperature and deformation sensors. *Chem. Mater.* 18, 946–955. doi: 10.1021/cm052186c
- Li, T. T., Yang, D. L., Zhai, L. Q., Wang, S. L., Zhao, B. M., Fu, N. N., et al. (2017). Thermally activated delayed fluorescence organic dots (TADF Odots) for time-resolved and confocal fluorescence imaging in living cells and *in vivo*. *Adv. Sci.* 4:1600166. doi: 10.1002/advs.201600166
- Li, W. J., Pan, Y., Yao, L., Liu, H. C., Zhang, S. T., Wang, C., et al. (2014). A hybridized local and charge-transfer excited state for highly efficient fluorescent OLEDs: molecular design, spectral character, and full exciton utilization. *Adv. Opt. Mater.* 2, 892–901. doi: 10.1002/adom.201400154
- Lin, T.-A., Chatterjee, T., Tsai, W.-L., Lee, W.-K., Wu, M.-J., Jiao, M., et al. (2016). Sky-blue organic light emitting diode with 37% external quantum efficiency using thermally activated delayed fluorescence from spiroacridine-triazine hybrid. *Adv. Mater.* 28, 6976–6983. doi: 10.1002/adma.201601675
- Liu, Y., Li, C., Ren, Z., Yan, S., and Bryce, M. R. (2018). All-organic thermally activated delayed fluorescence materials for organic light-emitting diodes. *Nat. Rev. Mater.* 3:18020. doi: 10.1038/natrevmats.2018.20
- Lower, S. K., and El-Sayed, M. A. (1966). The triplet state and molecular electronic processes in organic molecules. *Chem. Rev.* 66, 199–241. doi: 10.1021/cr60240a004
- Meher, N., and Iyer, P. K. (2018). Spontaneously self-assembled naphthalimide nanosheets: aggregation-induced emission and unveiling a-pet for sensitive detection of organic volatile contaminants in water. *Angew. Chem. Int. Ed.* 57, 8488–8492. doi: 10.1002/anie.201802842
- Moral, M., Muccioli, L., Son, W. J., Olivier, Y., and Sancho-García, J. C. (2015). Theoretical rationalization of the singlet-triplet gap in OLEDs materials: impact of charge-transfer character. *J. Chem. Theo. Comp.* 11, 168–177. doi: 10.1021/ct500957s
- Müller, C. D., Falcou, A., Reckefuss, N., Rojahn, M., Wiederhorn, V., Rudati, P., et al. (2003). Multi-colour organic light-emitting displays by solution processing. *Nature* 421, 829–833. doi: 10.1038/nature01390
- Nobuyasu, R.S., Ward, J.S., Gibson, J., Laidlaw, B.A., Ren, Z., Data, P., et al. (2019). The influence of molecular geometry on the efficiency of thermally activated delayed fluorescence. *J. Mater. Chem. C* 7, 6672–6684. doi: 10.1039/C9TC00720B
- Okazaki, M., Takeda, Y., Data, P., Pander, P., Higginbotham, H., Monkman, A. P., et al. (2017). Thermally activated delayed fluorescent phenothiazine-dibenzo[a,j]phenazine-phenothiazine triads exhibiting tricolor-changing mechanochromic luminescence. *Chem. Sci.* 8, 2677–2686. doi: 10.1039/C6SC04863C
- Pashazadeh, R., Pander, P., Bucinskas, A., Skabara, P. J., Dias, F. B., and Grazulevicius, J. V. (2018a). An iminodibenzyl-quinoxaline-iminodibenzyl scaffold as a mechanochromic and dual emitter: donor and bridge effects on optical properties. *Chem. Commun.* 54, 13857–13860. doi: 10.1039/C8CC06981F
- Pashazadeh, R., Pander, P., Lazauskas, A., Dias, F. B., and Grazulevicius, J. V. (2018b). Multicolor luminescence switching and controllable thermally activated delayed fluorescence turn on/turn off in carbazole-quinoxaline-carbazole triads. *J. Phys. Chem. Lett.* 9, 1172–1177. doi: 10.1021/acs.jpclett.8b00136
- Penfold, T. J., Dias, F. B., and Monkman, A. P. (2018). The theory of thermally activated delayed fluorescence for organic light emitting diodes. *Chem. Commun.* 54, 3926–3935. doi: 10.1039/C7CC09612G
- Rajamalli, P., Senthilkumar, N., Gandeepan, P., Ren-Wu, C.-Z., Lin, H.-W., and Cheng, C.-H. (2016). A thermally activated delayed blue fluorescent emitter with reversible externally tunable emission. *J. Mat. Chem. C* 4, 900–904. doi: 10.1039/C5TC03943F
- Reineke, S., Lindner, F., Schwartz, G., Seidler, N., Walzer, K., Lüssem, B., et al. (2009). White organic light-emitting diodes with fluorescent tube efficiency. *Nature* 459, 234–238. doi: 10.1038/nature08003
- Sagara, Y., Mutai, T., Yoshikawa, I., and Araki, K. (2007). Material design for piezochromic luminescence: hydrogen-bond-directed assemblies of a pyrene derivative. *J. Am. Chem. Soc.* 129, 1520–1521. doi: 10.1021/ja0677362
- Sagara, Y., Yamane, S., Mitani, M., Weder, C., and Takashim, K. T. (2016). Mechanoresponsive luminescent molecular assemblies: an emerging class of materials. *Adv. Mater.* 28, 1073–1095. doi: 10.1002/adma.201502589
- Schmidbaur, H., and Schier, A. (2008). A briefing on aurophilicity. *Chem. Soc. Rev.* 37, 1931–1951. doi: 10.1039/B708845K
- Scholz, S., Kondakov, D., Lüssem, B., and Leo, K. (2015). Degradation mechanisms, and reactions in organic light-emitting devices. *Chem. Rev.* 115, 16, 8449–8503. doi: 10.1021/cr400704v
- Shao, S., Ding, J., Wang, L., Jing, X., and Wang, F. (2012). White electroluminescence from all-phosphorescent single polymers on a fluorinated poly (arylene ether phosphine oxide) backbone simultaneously grafted with blue and yellow phosphors. *J. Am. Chem. Soc.* 134, 20290–20293. doi: 10.1021/ja310158j
- Shizu, K., Sakai, Y., Tanaka, H., Hirata, S., Adachi, C., and Kaji, H. (2015). Meta-linking strategy for thermally activated delayed fluorescence emitters with a small singlet-triplet energy gap. *ITE Trans. Media Technol. Appl.* 3, 108–113. doi: 10.3169/mta.3.108
- Sun, J., Zhang, J., Liang, Q., Wei, Y., Duan, C., Han, C., et al. (2019). Charge-transfer exciton manipulation based on hydrogen bond for efficient white thermally activated delayed fluorescence. *Adv. Funct. Mater.* 2019:1908568. doi: 10.1002/adfm.201908568
- Sun, J. W., Lee, J. H., Moon, C. K., Kim, K. H., Shin, H., and Kim, J. J. (2014). A fluorescent organic light-emitting diode with 30% external quantum efficiency. *Adv. Mater.* 26, 5684–5688. doi: 10.1002/adma.201401407
- Sun, Y., Giebink, N.C., Kanno, H., Ma, B., Thompson, M. E., and Forrest, S. R. (2006). Management of singlet and triplet excitons for efficient white organic light-emitting devices. *Nature* 440, 908–912. doi: 10.1038/nature04645
- Takeda, Y., Kaihara, T., Okazaki, M., Higginbotham, H., Data, P., Tohrai, N., et al. (2018). Conformationally-flexible and moderately electron-donating units-installed D-A-D triad enabling multicolor-changing mechanochromic luminescence, TADF and room-temperature phosphorescence. *Chem. Commun.* 54, 6847–6850. doi: 10.1039/C8CC02365D
- Tang, C. W., and VanSlyke, S. A. (1987). Organic electroluminescent diodes. *Appl. Phys. Lett.* 51, 913–915. doi: 10.1063/1.98799@apl.2019.APLCLASS2019.issue-1
- Tang, K. C., Chang, M. J., Lin, T. Y., Pan, H. A., Fang, T. C., Chen, K. Y., et al. (2011). Fine tuning the energetics of excited-state intramolecular proton transfer (ESIPT): white light generation in a single ESIPT system. *J. Am. Chem. Soc.* 133, 17738–17745. doi: 10.1021/ja2062693
- Tao, Y., Yuan, K., Chen, T., Xu, P., Li, H., Chen, R., et al. (2014). Thermally activated delayed fluorescence materials towards the breakthrough of organoelectronics. *Adv. Mater.* 26, 7931–7958. doi: 10.1002/adma.201402532
- Tonge, C. M., and Hudson, Z. M. (2019). Interface-dependent aggregation-induced delayed fluorescence in bottlebrush polymer nanofibers. *J. Am. Chem. Soc.* 141, 13970–13976. doi: 10.1021/jacs.9b07156
- Tsujimoto, H., Ha, D. G., Markopoulos, G., Chae, H. S., Baldo, M. A., and Swager, T. M. (2017). Thermally activated delayed fluorescence and aggregation

- induced emission with through-space charge transfer. *J. Am. Chem. Soc.* 139, 4894–4900. doi: 10.1021/jacs.7b00873
- Uoyama, H., Goushi, K., Shizu, K., Nomura, H., and Adachi, C. (2012). Highly efficient organic light-emitting diodes from delayed fluorescence. *Nature* 492, 234–238. doi: 10.1038/nature11687
- Wei, Q., Ge, Z., and Voit, B. (2019). Thermally activated delayed fluorescent polymers: structures, properties, and applications in OLED devices. *Macromol. Rapid Commun.* 40:1800570. doi: 10.1002/marc.201800570
- Wong, M. Y., and Zysman-Colman, E. (2017). Purely organic thermally activated delayed fluorescence materials for organic light-emitting diodes. *Adv. Mater.* 29:1605444. doi: 10.1002/adma.201605444
- Wu, T. L., Huang, M. J., Lin, C. C., Huang, P. Y., Chou, T. Y., Chen-Cheng, R. W., et al. (2018). Diboron compound-based organic light-emitting diodes with high efficiency and reduced efficiency roll-off. *Nat. Photonics* 12, 235–240. doi: 10.1038/s41566-018-0112-9
- Wu, W., Tang, R., Li, Q., and Li, Z. (2015). Functional hyperbranched polymers with advanced optical, electrical and magnetic properties. *Chem. Soc. Rev.* 44, 3997–4022. doi: 10.1039/C4CS00224E
- Wu, Z., Liu, Y., Yu, L., Zhao, C., Yang, D., Qiao, X., et al. (2019). Strategic-tuning of radiative excitons for efficient and stable fluorescent white organic light-emitting diodes. *Nat. Commun.* 10:2380. doi: 10.1038/s41467-019-10104-4
- Xu, B., Mu, Y., Mao, Z., Xie, Z., Wu, H., Zhang, Y., et al. (2016). Achieving remarkable mechanochromism and white-light emission with thermally activated delayed fluorescence through the molecular heredity principle. *Chem. Sci.* 7, 2201–2206. doi: 10.1039/C5SC04155D
- Xu, S., Liu, T., Mu, Y., Wang, Y., Chi, Z., Lo, C., et al. (2015). An organic molecule with asymmetric structure exhibiting aggregation-induced emission, delayed fluorescence, and mechanoluminescence. *Angew. Chem. Int. Ed.* 54, 874–878. doi: 10.1002/anie.201409767
- Yamashita, T. K., Yamaguchi, K., and Aida, T. (2005). Rewritable phosphorescent paper by the control of competing kinetic and thermodynamic self-assembling events. *Nat. Mater.* 4, 546–549. doi: 10.1038/nmat1401
- Zeng, X., Zhou, T., Liu, J., Wu, K., Li, S., Xiao, X., et al. (2018). Incorporating thermally activated delayed fluorescence into mechanochromic luminescent emitters: high-performance solution-processed yellow organic light emitting diodes. *Adv. Opt. Mat.* 6:1801071. doi: 10.1002/adom.201801071
- Zhan, L., Chen, Z., Gong, S., Xiang, Y., Ni, F., Zeng, X., et al. (2019). A simple organic molecule realizing simultaneous TADF, RTP, AIE, and mechanoluminescence: understanding the mechanism behind the multifunctional emitter. *Angew. Chem. Int. Ed.* 58, 17651–17655. doi: 10.1002/anie.201910719
- Zhang, Q., Li, B., Huang, S., Nomura, H., Tanaka, H., and Adachi, C. (2012). Efficient blue organic light-emitting diodes employing thermally activated delayed fluorescence. *Nat. Photonics* 8, 326–332. doi: 10.1038/nphoton.2014.12
- Zhang, Y., Miao, Y., Song, X., Gao, Y., Zhang, Z., Ye, K., et al. (2017). Single-molecule-based white-light emissive organic solids with molecular-packing-dependent thermally activated delayed fluorescence. *J. Phys. Chem. Lett.* 8, 4808–4813. doi: 10.1021/acs.jpclett.7b02213
- Zhao, W., He, Z., Lam, W.Y., Qian, P., Ma, H., Shuai, Z., et al. (2016). Rational molecular design for achieving persistent and efficient pure organic room-temperature phosphorescence. *Chemistry* 1, 592–602. doi: 10.1016/j.chempr.2016.08.010
- Zheng, K., Hannan, Y., Ni, F., Chen, Z., Gong, S., Lu, Z., et al. (2019b). Multifunctional thermally activated delayed fluorescence emitters and insight into multicolor-mechanochromism promoted by weak intra- and intermolecular interactions. *Adv. Optical Mater.* 2019:1900727. doi: 10.1002/adom.201900727
- Zheng, K., Ni, F., Chen, Z., Zhong, C., and Yang, C. (2019a). Polymorph-dependent thermally activated delayed fluorescence emitters: understanding TADF from a perspective of aggregation state. *Angew. Chem. Int. Ed.* doi: 10.1002/anie.201913210

**Conflict of Interest:** The authors declare that the research was conducted in the absence of any commercial or financial relationships that could be construed as a potential conflict of interest.

Copyright © 2020 Barman, Gogoi, Narang and Iyer. This is an open-access article distributed under the terms of the Creative Commons Attribution License (CC BY). The use, distribution or reproduction in other forums is permitted, provided the original author(s) and the copyright owner(s) are credited and that the original publication in this journal is cited, in accordance with accepted academic practice. No use, distribution or reproduction is permitted which does not comply with these terms.



# High Triplet Energy Host Materials for Blue TADF OLEDs—A Tool Box Approach

Francesco Rodella<sup>1†</sup>, Sergey Bagnich<sup>2†</sup>, Eimantas Duda<sup>2</sup>, Tobias Meier<sup>2</sup>, Julian Kahle<sup>2</sup>, Stavros Athanasopoulos<sup>3</sup>, Anna Köhler<sup>2,4</sup> and Peter Strohriegl<sup>1,4\*</sup>

<sup>1</sup> Macromolecular Chemistry I, University of Bayreuth, Bayreuth, Germany, <sup>2</sup> Soft Matter Optoelectronics, University of Bayreuth, Bayreuth, Germany, <sup>3</sup> Departamento de Física, Universidad Carlos III de Madrid, Madrid, Spain, <sup>4</sup> Bayreuth Institute of Macromolecular Research (BIMF), University of Bayreuth, Bayreuth, Germany

## OPEN ACCESS

### Edited by:

Thierry Brigaud,  
Université de Cergy-Pontoise, France

### Reviewed by:

Juozas Vidas Grazulevicius,  
Kaunas University of  
Technology, Lithuania  
Xiankai Chen,  
University of Arizona, United States

### \*Correspondence:

Peter Strohriegl  
peter.strohriegl@uni-bayreuth.de

<sup>†</sup> These authors have contributed  
equally to this work

### Specialty section:

This article was submitted to  
Organic Chemistry,  
a section of the journal  
Frontiers in Chemistry

**Received:** 22 February 2020

**Accepted:** 23 June 2020

**Published:** 29 July 2020

### Citation:

Rodella F, Bagnich S, Duda E, Meier T,  
Kahle J, Athanasopoulos S, Köhler A  
and Strohriegl P (2020) High Triplet  
Energy Host Materials for Blue TADF  
OLEDs—A Tool Box Approach.  
Front. Chem. 8:657.  
doi: 10.3389/fchem.2020.00657

The synthesis of stable blue TADF emitters and the corresponding matrix materials is one of the biggest challenges in the development of novel OLED materials. We present six bipolar host materials based on triazine as an acceptor and two types of donors, namely, carbazole, and acridine. Using a tool box approach, the chemical structure of the materials is changed in a systematic way. Both the carbazole and acridine donor are connected to the triazine acceptor via a para- or a meta-linked phenyl ring or are linked directly to each other. The photophysics of the materials has been investigated in detail by absorption-, fluorescence-, and phosphorescence spectroscopy in solution. In addition, a number of DFT calculations have been made which result in a deeper understanding of the photophysics. The presence of a phenyl bridge between donor and acceptor cores leads to a considerable decrease of the triplet energy due to extension of the overlap electron and hole orbitals over the triazine-phenyl core of the molecule. This decrease is more pronounced for the para-phenylene than for the meta-phenylene linker. Only direct connection of the donor group to the triazine core provides a high energy of the triplet state of 2.97 eV for the carbazole derivative **CTRZ** and 3.07 eV for the acridine **ATRZ**. This is a major requirement for the use of the materials as a host for blue TADF emitters.

**Keywords:** thermally activated delayed fluorescence, TADF, host, organic light emitting diode, tool box approach, high triplet energy

## INTRODUCTION

Organic light emitting diodes (OLEDs) are overtaking the field of display applications due to several favorable characteristics in comparison with classic liquid crystal devices (LCDs) such as lower energy consumption and simpler technology (Endo et al., 2011; Sasabe and Kido, 2013). For these reasons, in the past years, much effort was dedicated to develop new materials and technologies for OLEDs. The current focus is, in particular, to improve their efficiency and long-time stability. Starting from classic fluorescent emitters (1st generation) with an internal quantum efficiency (IQE) limited to 25%, research moved to phosphorescence emitters (2nd generation) with an increased IQE of 100% and then to thermally activated delayed fluorescence (TADF), which represents the last and very promising generation of OLED materials (Endo et al., 2011; Uoyama et al., 2012). In comparison with phosphorescence emitters that use less available and more expensive noble metals, TADF emitters often rely on pure organic molecules with donor



and acceptor groups. This donor-acceptor structure often leads to a small singlet ( $S_1$ )-triplet ( $T_1$ ) energy gap ( $\Delta E_{ST}$ ) that allows reverse intersystem crossing (RISC) from the triplet into the singlet state, permitting a theoretical 100% IQE by emission of prompt and delayed fluorescence. Lin et al. reported a state of the art TADF OLED with an IQE of 100%, and, more surprisingly, an external quantum efficiency (EQE) of 37%. So far this is one of the highest efficiency ever reported for TADF emitters (Lin et al., 2016). Another promising way to obtain TADF molecules with pure emission is based on multiple resonance effect (Hatakeyama et al., 2016). Most of the work on TADF focuses on new emitters. Pure emitter layers usually show self quenching, thus it is necessary to dilute the emitters in suitable host materials. These hosts have to fulfill several requirements such as having a high triplet energy level, chemical and thermal robustness, and balanced charge carrier mobilities (Wong and Zysman-Colman, 2017). One of the recent challenges is to develop efficient and stable blue OLED host/emitter systems that can replace the less efficient fluorescent ones of the 1st generation, currently used in display applications (Cai and Su, 2018). While designing a host, the triplet energy level is the first key point to look at, especially if the aim is to use it for blue emitters since they require hosts with a triplet energy of about 3 eV. So far, the reported hosts with a triplet energy suitable for blue emitters are mostly monopolar and made with groups such as phosphine oxide, which are known to have limited stability (Hirata et al., 2014; Chen et al., 2015; Kim et al., 2015; Yook and Lee, 2015; Zhang et al., 2015; Chatterjee and Wong, 2018). Among them, DPEPO is one of the most used hosts for TADF blue emitters since it has a high energy triplet level of 3 eV (Han et al., 2011). Several carbazole-based hosts have been developed, with the advantage to have higher stability. Some of them, still monopolar, come from

the 2nd generation such as mCP and mCBP (Wong and Zysman-Colman, 2017). Successively, in order to have a balanced charge carrier transport, bipolar carbazole-based hosts were developed by adding acceptor units such as cyano, triazine, and phosphine oxide groups (An et al., 2011; Ding et al., 2015; Kukhta et al., 2017; Shin et al., 2018) or formation of dimers and trimers (Tomkeviciene et al., 2011). Most of these carbazole-based hosts are limited to the use of blue greenish emitters since their triplet energies are below 3 eV. Hosts with less common functional groups such as cyclophosphazene (Nishimoto et al., 2014), silicon (Ren et al., 2004), and benzimidazobenzothiazole (Cui et al., 2016a) were also developed in order to increase the triplet energy. Furthermore, trying to avoid the problem of suitable hosts, non-doped emitting layers are also under investigation by using sterically demanding molecules such as dendrimers, but they still suffer from lower efficiencies in comparison with doped emitting layers (Wong and Zysman-Colman, 2017; Cai and Su, 2018; Wei et al., 2018). Overall, host materials remain less developed in comparison with emitters, therefore some standard approaches and guidelines could be helpful to progress this field.

In this paper we present a systematic study called “tool box approach” illustrated in **Figure 1** in order to understand how to increase the triplet energy of triazine-based bipolar molecules. Namely, one acceptor (triazine), two linkers (meta and ortho phenyl rings), and two donors (carbazole and acridine) were chosen as building blocks because of their stability and common use, then combined to obtain six molecules (**pCTRZ**, **mCTRZ**, **CTRZ**, **pATRZ**, **mATRZ**, **ATRZ**), of which two are new (**mATRZ** and **ATRZ**). All the target compounds were compared through spectroscopic characterization and theoretical calculations. This allows to understand the contribution of the single building blocks on the triplet energy of the final molecules and so to give

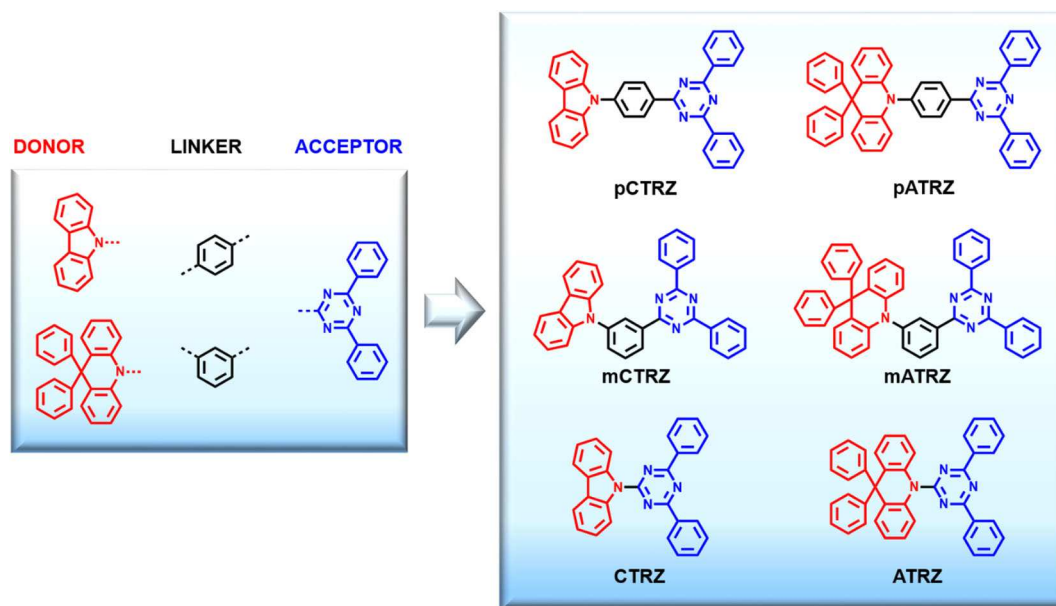


**FIGURE 1 |** Tool box approach. Chemical structures of the molecular constituents used and the resulting target compounds, along with their names.

a structure-property relationship. We note that spectroscopic and computational data on **pCTRZ**, **mCTRZ**, **CTRZ**, **pATRZ** are already available, yet sometimes not complete across the series, and sometimes contradictory. Here we study the entire set of 6 compounds under identical conditions which facilitates comparison. We show that by using a direct linkage between donor and acceptor it is possible to reach triplet  $T_1$  energy values above 3 eV. The strategy here proposed can be helpful to design new bipolar molecules with high triplet energies and stable functional groups, permitting to obtain potential hosts for blue TADF OLEDs.

## METHODS

### Materials

All the starting materials needed for the synthesis were purchased from abcr and Acros Organics. The two reference compounds **pATRZ** and **pCTRZ** were purchased from Lumtec. The reference compounds CBP and spiro-2CBP were purchased from Sigma Aldrich. mCBP was synthesized as described in literature (Schroegel et al., 2011). Their chemical structures can be found in the **Supplementary Information**.

### Purification

The synthesized compounds **mCTRZ**, **mATRZ**, **CTRZ**, and **ATRZ** were purified by train sublimation in a Carbolite split tube furnace HZS 12/450.

### Characterization

$^1\text{H}$  NMR and  $^{13}\text{C}$  NMR spectra were recorded on a Bruker Avance III HD (500 MHz) and the chemical shifts were referred to chloroform- $d_3$  (7.26 ppm). MS spectra were obtained on a Finnigan MAT 8500 using electron impact ionization.

### Photophysical Measurements

For the absorption and emission measurements, we prepared solutions of 0.05 mg/ml of the compounds in toluene. Absorption spectra were recorded at room temperature on a Cary 5000 double beam spectrophotometer. Steady-state and time resolved photoluminescence spectra in solution and films were recorded at 298 and 77 K using a Jasco FP-8600 spectrofluorometer. For **pCTRZ** and **pATRZ**, fluorescence could be taken at 77 K in steady state operation without superimposed phosphorescence signal. For **mCTRZ** and **mATRZ**, the stronger intensity of the phosphorescence required us to use the chopped excitation from the Jasco spectrofluorometer and gated detection (delay time of 50  $\mu\text{s}$ , integration time of 50  $\mu\text{s}$ ) in order to obtain only fluorescence without contribution of the phosphorescence. To exclude the even stronger phosphorescence signal in the fluorescence measurements of **CTRZ** and **ATRZ**, we used a 355 nm pulsed laser excitation with iCCD camera, a delay time of 10 ns and an integration time of 30 ns.

Values for the photoluminescence quantum yield (PL QY) of the molecules in solution were obtained using the Jasco FP-8600 spectrofluorometer equipped with an integrating sphere. The intensity decay of the fluorescence was measured using a Q-switched QS laser MPL15100-DP at  $\lambda = 355$  nm as the excitation

source and an Andor iCCD camera (iStar A-DH334T-18F-03) as the detector. Rate constants for the decay of singlet state were calculated using following relation:  $\Phi = \kappa_r / (\kappa_r + \kappa_{nr})$ ,  $\tau = 1 / (\kappa_r + \kappa_{nr})$ , where  $\Phi$  is fluorescence quantum yield and  $\tau$  is the decay time.  $\kappa_r$  is the rate of radiative decay of the singlet state,  $\kappa_{nr}$  is the rate of the non-radiative deactivation of the singlet state.

## Computational Calculations

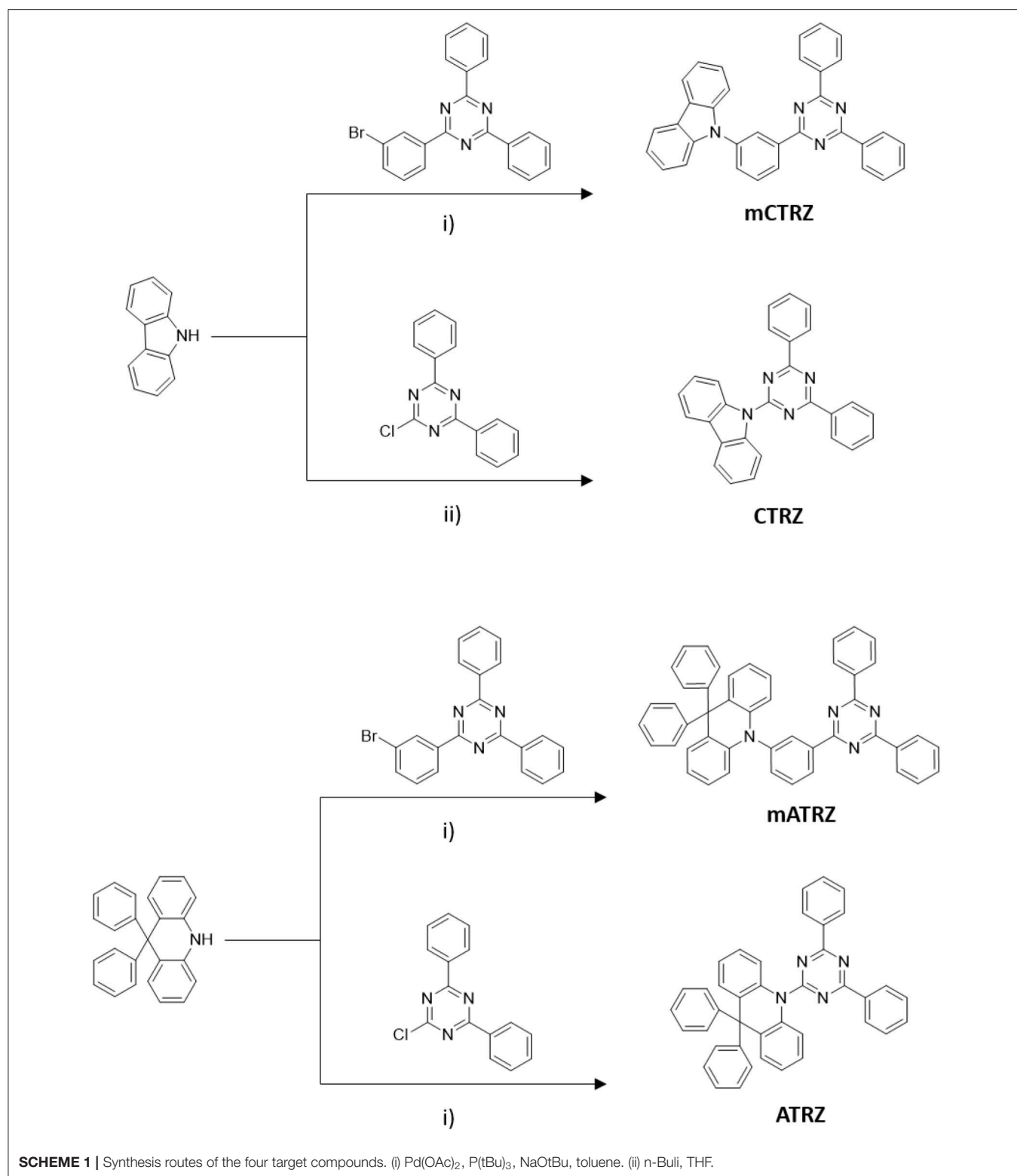
*Density functional theory* (DFT) and linear response time-dependent density functional theory (TD-DFT) calculations have been performed using the Gaussian 16 package (Frisch et al., 2016). For the calculation of ground and excited state configurations the hybrid exchange-correlation functional M06-2X has been used, unless stated otherwise (Zhao and Truhlar, 2008). This functional is considered suitable for predicting singlet-triplet gaps (Uoyama et al., 2012; Sun et al., 2015). It also offers the possibility to calculate excited state geometries. The 6-31+G(d) atomic basis set has been chosen as it provides a good balance between accuracy and computational cost (Sun et al., 2015). Furthermore, the Tamm-Dancoff approximation (TDA) has been used for more accurate triplet energies (Hirata and Head-Gordon, 1999; Peach et al., 2011).

## SYNTHESIS

### The Tool Box Approach

The aim of this work is to obtain new bipolar and high energy triplet host materials suitable for blue TADF emitters and to consolidate a new molecular strategy that allows to increase the triplet energy of bipolar molecules. For this purpose we introduce a systematic study called tool box approach (**Figure 1**). Basically, we choose building blocks (donor, acceptor, and linker) that are known to be stable and to have high triplet energies. Practically, triazine was chosen as acceptor group and carbazole and acridine as donor moieties. These groups were combined both with or without linkers obtaining essentially two classes of donor-acceptor molecules (carbazole-triazine and acridine-triazine). For each class we can distinguish between para-phenyl linker, meta-phenyl linker, and without linker. This approach allows us to understand how varying the linker between donor and acceptor affects the final molecule, and so to understand the structure-property relationship. Furthermore, by studying in parallel two classes of molecules, we can demonstrate that via direct linkage between donor and acceptor it is possible to increase the triplet energy above 3 eV and so to create potential bipolar host materials for TADF blue emitters. The reference molecules **pCTRZ** and **pATRZ** were commercially available. The other four molecules (**mCTRZ**, **mATRZ**, **CTRZ**, and **ATRZ**) were synthesized.

The compounds **mCTRZ**, **mATRZ**, and **ATRZ** were synthesized following a general Buchwald-Hartwig protocol, where the NH group comes from carbazole and acridine derivatives, while the halogenated part is contained in the triazine acceptor (or in the meta-linker-acceptor moiety). The compound **CTRZ** can be obtained via simple nucleophilic aromatic substitution of the carbazole with



the electron poor triazine ring using  $n\text{BuLi}$  (**Scheme 1**). The compounds were obtained with yields from 30 to 57%. **CTRZ** and **mCTRZ** were purified, respectively, via

precipitation and column chromatography in a first step. All the compounds were finally purified through vacuum train sublimation.

### 9-(3-(4,6-diphenyl-1,3,5-triazin-2-yl)phenyl)-9H-carbazole (mCTRZ)

9H-carbazole (259 mg, 1.55 mmol), 2-(3-bromophenyl)-4,6-diphenyl-1,3,5-triazine (500 mg, 1.29 mmol), sodium tert-butoxide (207 mg, 2.15 mmol), palladium acetate (12 mg, 0.05 mmol) and toluene (10 ml) were added to a three necked flask equipped with a stirring bar. The solution was degassed by three freeze-pump-thaw cycles and the flask backfilled with argon. Tri(*tert*-butyl)phosphine in toluene (1 mol/l, 0.1 mmol) was subsequently added to the flask and the mixture refluxed 12 h. After cooling to room temperature, ethyl acetate was added and the solution washed with water. The organic phase was dried over sodium sulfate, filtered and the solvent evaporated under reduced pressure. The pure white product was obtained after purification by column chromatography on silica gel (hexane:dichloromethane = 9:1) and by train sublimation (yield 38%). <sup>1</sup>H NMR (CDCl<sub>3</sub>, 500 MHz): δ [ppm] 8.98 (s, 1H), 8.90 (d, J = 7.0 Hz, 2H), 8.76 (d, J = 7.0 Hz, 4H), 8.21 (d, J = 7.5 Hz, 2H), 7.82 (m, 2H), 7.59 (m, 6H), 7.47 (m, 4H), 7.34 (t, J = 7.0 Hz, 2H). <sup>13</sup>C NMR (CDCl<sub>3</sub>, 500 MHz): δ [ppm] 171.9, 171.0, 141.0, 138.5, 138.3, 136.0, 132.7, 131.2, 130.3, 129.0, 128.7, 128.1, 127.7, 126.2, 123.5, 120.4, 120.1, 109.8. EI-MS *m/z* [M]<sup>+</sup>: 474.

### 10-(3-(4,6-diphenyl-1,3,5-triazin-2-yl)phenyl)-9,9-diphenyl-9,10-dihydroacridine (mATRZ)

The synthesis of **mATRZ** was adapted from Lin et al.<sup>[4]</sup> A reaction set up similar to that of **mCTRZ** is performed by using 9,9-diphenyl-9,10-dihydroacridine (200 mg, 0.6 mmol), 2-(3-bromophenyl)-4,6-diphenyl-1,3,5-triazine (210 mg, 0.54 mmol), sodium tert-butoxide (68 mg, 0.7 mmol), palladium acetate (5 mg, 0.022 mmol), tri(*tert*-butyl)phosphine in toluene (1 mol/l, 0.044 mmol) and toluene (20 ml). After refluxing 12 h, the mixture was filtered through a pad of celite while still hot. Then the filtrate was washed with water and brine, then dried over MgSO<sub>4</sub> and the solvent evaporated under reduced pressure. The brownish yellow crude product was washed with hexane and dichloromethane and finally purified by train sublimation, obtaining a light yellow solid (yield 30%). <sup>1</sup>H NMR (CDCl<sub>3</sub>, 500 MHz): δ [ppm] 8.90 (d, J = 8.0 Hz 1H), 8.73 (d, J = 7.0 Hz, 4H), 8.50 (s, 1H), 7.76 (t, J = 8 Hz, 1H), 7.60 (m, 6H), 7.31 (m, 7H), 7.07 (m, 6H), 6.92 (m, 4H), 6.52 (d, J = 8.0 Hz, 2H). <sup>13</sup>C NMR (CDCl<sub>3</sub>, 500 MHz): δ [ppm] 171.8, 170.8, 146.4, 142.1, 141.1, 139.1, 136.0, 135.7, 132.7, 131.9, 130.9, 130.5, 130.0, 129.8, 129.1, 128.8, 128.7, 127.7, 127.0, 126.3, 120.3, 114.1, 56.9. EI-MS *m/z* [M]<sup>+</sup>: 640.

### 9-(4,6-diphenyl-1,3,5-triazin-2-yl)-9H-carbazole (CTRZ)

**CTRZ** was synthesized according to the procedure reported by An et al. (2011) without using a catalyst. 9H-carbazole (150 mg, 0.9 mmol) and dry tetrahydrofuran (15 ml) were added to a pre-dried three-necked flask under argon atmosphere. The solution was cooled in an ice bath and stirred for 10 min. Then *n*-butyllithium in hexane (2.5 mol/l, 0.9 mmol) was slowly added and the solution was stirred for 30 min at room temperature.

Subsequently, a solution of 2-chloro-4,6-diphenyl-1,3,5-triazine (200 mg, 0.75 mmol) in tetrahydrofuran (5 ml) was added and the mixture was then refluxed for 12 h. The precipitate was filtered and washed with water, acetone and chlorobenzene. The pure white product was obtained after purification by train sublimation (yield 57%). <sup>1</sup>H NMR (CDCl<sub>3</sub>, 500 MHz): δ [ppm] 9.17 (d, J = 8.5 Hz, 2H), 8.78 (d, J = 6.5 Hz, 4H), 8.10 (d, J = 8.0 Hz, 2H), 7.64 (m, 8H), 7.45 (t, J = 7.0 Hz, 2H). <sup>13</sup>C NMR (CDCl<sub>3</sub>, 500 MHz): δ [ppm] 172.49, 165.26, 139.2, 136.3, 132.8, 129.2, 128.9, 127.0, 126.7, 123.3, 119.7, 117.7. EI-MS *m/z* [M]<sup>+</sup>: 398.

### 10-(4,6-diphenyl-1,3,5-triazin-2-yl)-9,9-diphenyl-9,10-dihydroacridine (ATRZ)

The synthesis of **ATRZ** was adapted from Lin et al. (2016) 9,9-diphenyl-9,10-dihydroacridine (273 mg, 0.82 mmol), 2-chloro-4,6-diphenyl-1,3,5-triazine (200 mg, 0.75 mmol), sodium tert-butoxide (93 mg, 0.97 mmol), palladium acetate (7 mg, 0.03 mmol) and toluene (20 ml) were added to a three necked flask equipped with a stirring bar. The solution was degassed by three freeze-pump-thaw cycles and the flask backfilled with argon. Tri(*tert*-butyl)phosphine in hexane (10% wt, 0.018 ml, 0.06 mmol) was subsequently added to the flask and the mixture refluxed 12 h. After cooling to room temperature an extraction with water was performed. The organic phase was dried over sodium sulfate, filtered and the solvent evaporated under reduced pressure. The pure light yellow product was obtained after purification by train sublimation (yield 30%). <sup>1</sup>H NMR (CDCl<sub>3</sub>, 500 MHz): δ [ppm] 8.36 (d, J = 8.0 Hz 4H), 7.98 (d, J = 8.0 Hz, 2H), 7.51 (7, J = 7.0 Hz 2H), 7.45 (t, J = 7.5 Hz, 6H), 7.24 (t, J = 7.5 Hz 2H), 7.03 (m, 8H), 6.88 (m, 4H). <sup>13</sup>C NMR (CDCl<sub>3</sub>, 500 MHz): δ [ppm] 168.5, 162.3, 141.4, 140.8, 137.4, 134.4, 129.6, 129.6, 126.5, 126.1, 126.0, 125.3, 125.2, 124.5, 123.6, 122.8, 56.6. EI-MS *m/z* [M]<sup>+</sup>: 564.

Except for **mATRZ** and **ATRZ**, all compounds have already been investigated in some part, either experimentally, or by calculations, or both (An et al., 2011, 2015; Lin et al., 2016; Duan et al., 2018; Arjona-Esteban et al., 2019; Fan et al., 2019; Liu et al., 2019; Sharma et al., 2019). These previous investigations do not form a complete and consistent data set, and sometimes are even contradictory. We therefore decided to perform a systematic spectroscopic and theoretical study that is conducted for all compounds under identical conditions.

## TD-DFT-ANALYSIS

### Choice of Functional

The calculation of excitation energies for donor-acceptor type molecules with charge-transfer characteristic can be a challenge for density functional theory calculations (Sun et al., 2015). In order to obtain results with good accuracy, we therefore first performed a study on the suitable choice of the functional. For this, we employed six popular exchange-correlation functionals on the molecule **CTRZ** which has been well-characterized experimentally in previous works (An et al., 2011; Duan



**TABLE 1** | Emission energies as well as their difference (in eV) in optimized  $S_1$  and  $T_1$  geometries for the molecule **CTRZ** calculated with different exchange-correlation DFT functionals and a 6-31+G(d) basis set.

	$S_1$	$T_1$	$\Delta(S_1 - T_1)$
Experiment	3.21	2.97	0.24
M06-2X	3.18	3.00	0.18
CAM-B3LYP	3.26	2.77	0.49
M06-HF	3.57	3.28	0.29
PBE0	2.29	2.31	-0.02
PW6B95D3	2.36	2.38	-0.02
$\omega$ B97XD	3.51	2.85	0.66

The experimental value is taken from the spectroscopic analysis in this paper.

et al., 2018) as well as in this work. We used two range-separated hybrid functionals, CAM-B3LYP (Yanai et al., 2004) and  $\omega$ B97XD (Chai and Head-Gordon, 2008), three hybrid meta-GGA functionals, M06-2X (56% exact exchange), M06-HF (100 % exact exchange) (Zhao and Truhlar, 2008) and PW6B95D3 (28% exact exchange) (Zhao and Truhlar, 2005) and a meta-GGA functional, PBE0 (25% exact exchange) (Adamo and Barone, 1999). **Table 1** compares the calculated  $S_1$  and  $T_1$  emission energies, in the relaxed excited state geometry, obtained for **CTRZ** with these 6 functionals with the experimentally measured value (see next section). The best match between experiment and calculation for the  $S_1$  energy is found for the functional CAM-B3LYP, closely followed by M06-2X. However, for the  $T_1$  energy, which is most important to us, M06-2X is closest to the experimental value. We therefore decided to calculate the  $S_1$  and  $T_1$  excitation energies for all 6 molecules with M06-2X, and, for reference, also with the widely employed functional CAM-B3LYP. **Table 2** compares the resulting energies with the experimental values all taken from the subsequent section “spectroscopic analysis.” While all calculated values are in good agreement with the experiment, the excellent match obtained for the triplet energies using M06-2X is noteworthy. Even though this functional is considered suitable for predicting singlet-triplet gaps (Uoyama et al., 2012; Sun et al., 2015), the agreement between calculated values and experimental ones is lessened for the singlet-triplet gap. Results for the functional CAM-B3LYP can be found in the supporting information (**Table S1**).

We next considered how the natural transition orbitals (NTO) obtained with M06-2X for our reference molecule **CTRZ** compare to those obtained by other functionals. The NTOs obtained for the ground state  $S_0$  geometry of **CTRZ** for M06-2X are shown in the supporting information (**Figure S2**). The orbitals are in excellent agreement with the ones from Duan et al. (2018) who used the range-separated functional LC- $\omega$ PBE. Finally, we calculated and compared the NTOs in the excited state  $S_1$  geometry for all 6 functionals (**Figure S3**). Five out of six functionals show a strong charge transfer character for the  $S_1$  state and a localized excitation for the  $T_1$  state, among them M06-2X, suggesting that this is likely to be the prevailing scenario (as will be confirmed on the basis of the spectroscopic data further below).

**TABLE 2** | Emission energies (in eV) in optimized  $S_1$  and  $T_1$  geometries calculated at the M06-2X/6-31+G(d) level.

	$S_1^a$ exp. (eV)	$T_1^b$ exp. (eV)	$\Delta E_{ST}$ , exp. (eV)	$S_1$ (M06- 2X)	$T_1$ (M06- 2X)	$\Delta E_{ST}$ (eV)
<b>pCTRZ</b>	3.22	2.76	0.46	3.48	2.69	0.79
<b>mCTRZ</b>	3.21	2.82	0.39	3.44	2.82	0.62
<b>CTRZ</b>	3.21	2.97	0.24	3.18	3.00	0.18
<b>pATRZ</b>	2.92	2.67	0.25	3.06	2.60	0.46
<b>mATRZ</b>	2.94	2.72	0.22	3.02	2.92	0.10
<b>ATRZ</b>	3.25	3.07	0.18	3.33	3.03	0.30

For comparison, the experimental values are also given for molecules in toluene at 77 K, as derived below.

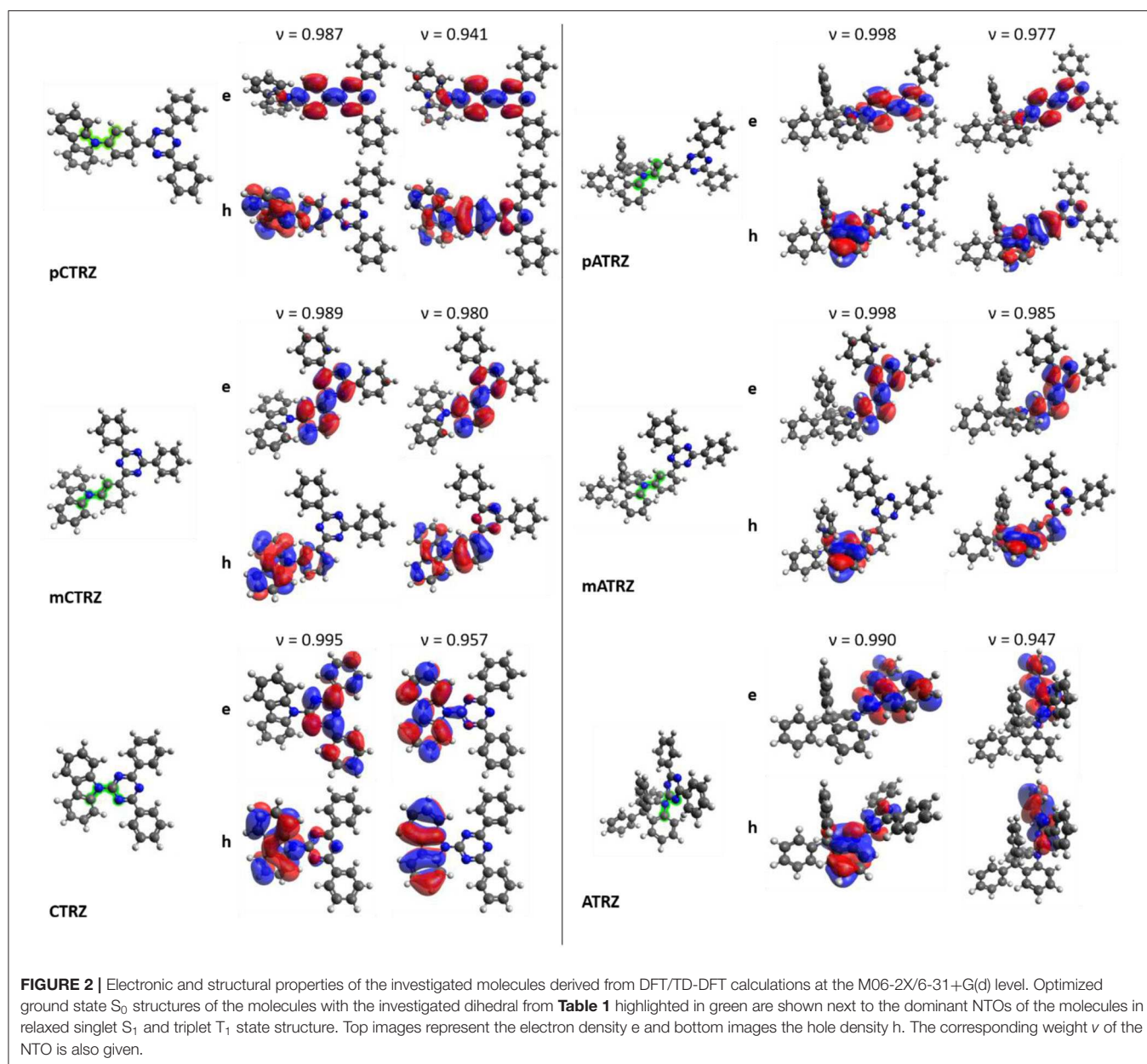
<sup>a</sup>The energy of the singlet state was determined by fitting the spectral lineshape of the CT absorption and fluorescence, **Figure 4** <sup>b</sup>The energy of the triplet state was taken from the 0-0 the position of the phosphorescence at 77 K.

## Ground State Geometries and Excited State NTOs

**Figure 2** shows the molecules in the relaxed  $S_0$  ground state geometry, alongside the dominant NTOs for the  $S_1$  and  $T_1$  in the relaxed excited state geometry. It is well-known that the electronic coupling between the donor and acceptor depends strongly on the dihedral angle between them. This angle is indicated in **Figure 2** in green color and detailed in **Table 3**. We find that **pCTRZ** and **mCTRZ** are strongly twisted with practically the same value of about  $52^\circ$ , while **CTRZ** is more planar. Similarly, for the acridine based molecules **pATRZ** and **mATRZ** we observe an almost orthogonal configuration between donor and acceptor moiety while **ATRZ** shows essentially no twist between donor and acceptor though it has a bended shape of acridine core. When going from the ground to the excited states, we find an overall more planar geometry for the  $T_1$  state, while the  $S_1$  state becomes even slightly more twisted for the carbazole-derivatives. For the **pATRZ** and **mATRZ**, the  $S_1$  geometry remains more or less unaltered, and it planarizes for the **ATRZ**.

The NTOs of the molecules in the optimized lowest singlet  $S_1$  and triplet  $T_1$  excited state geometry deserve some consideration. For all molecules, the calculations predict that the  $S_1 \rightarrow S_0$  transition is accompanied by an electron transfer from the acceptor part of molecule to the donor unit, though there is also some overlap of differing degree on the phenyl bridge or triazine ring. This implies a mixed nature of the transition, with a dominant charge transfer (CT) character, in agreement with conclusions published earlier for some of the compounds (An et al., 2011; Lin et al., 2016; Duan et al., 2018; Fan et al., 2019; Liu et al., 2019). The oscillator strengths for this transition is given in **Table 3**. From the para to the meta-connection, the oscillator strength reduces significantly, while there is no further significant reduction when going from **mCTRZ** to **CTRZ** and even a small increase from **mATRZ** to **ATRZ**.

Regarding the triplet  $T_1$  state, we find a pronounced difference between the molecules with a p-phenyl or m-phenyl bridge and



the molecules without a linker between donor and acceptor. With the phenyl bridge, and in particular for the *p*-phenyl, the electron and hole orbitals of  $T_1$  demonstrate a somewhat stronger overlap than for the  $S_1$  state, even though some charge transfer still takes place. In previous works, the character of the  $T_1$  state was therefore interpreted either as a CT state with strong overlap of electron and hole orbitals at the triazine, phenyl bridge, and the amino part of the carbazole unit, (Fan et al., 2019) or as a localized excitation (LE) spread over the triazine, phenyl bridge, and carbazole unit (Sun et al., 2015). It was also described as a superposition of the CT state with an LE state in the acceptor (Duan et al., 2018). Our calculations confirm the general

mixed CT-LE character of the *p*-phenyl and *m*-phenyl bridge donor-acceptor compounds, with a stronger LE contribution for  $T_1$  than for  $S_1$ .

In contrast to this, we find a strongly LE character for the  $T_1$  state of the molecules without bridge, i.e., **ATRZ** and **CTRZ**, with the excitation fully on the donor for **CTRZ** and fully on the acceptor for **ATRZ**. For **CTRZ**, this differs from the prediction of Duan et al. who predicts a strong contribution from orbitals delocalized over the entire molecule (Duan et al., 2018). We attribute this difference to the fact that Duan et al. based their calculations on the ground state geometry, while we were considering the relaxed  $T_1$  excited state geometry. The calculations predict the triplet from this confined LE state to be at

higher energy than the triplet from the molecules with the phenyl ring bridge.

## SPECTROSCOPIC ANALYSIS

### Absorption and Fluorescence in Toluene Solution at Room Temperature

The absorption spectra of our 6 molecules under investigation in toluene at low concentration are shown in **Figure 3**. The spectra are consistent with those published previously (An et al., 2015;

Lin et al., 2016; Fan et al., 2019; Liu et al., 2019). For reference, the spectra of the constituent units, carbazole, diphenyltriazine, and diphenylacridine, are displayed in the supporting information (**Figure S1**).

The absorption of **pCTRZ** is characterized by presence of strong broad band in the range 3.1–4.1 eV with maximum at 3.41 eV, followed by structured features at 3.63 and 3.80 eV. Comparison with the absorption spectrum of carbazole (**Figure S1**) readily identifies the features at 3.63 and 3.80 eV as resulting from a  $\pi - \pi^*$  transition (and its vibrational replica) localized on the carbazole moiety. When the para-connection is replaced by a meta-linkage, as in **mCTRZ**, the features remain at the same energy yet the extinction of the broad band at 3.41 eV reduces by about one order of magnitude, as is evident from the display on the logarithmic scale (bottom panel of **Figure 3**). This band at 3.41 eV is commonly interpreted as corresponding to CT transition, (Cui et al., 2016b; Fan et al., 2019) though the high absorption for **pCTRZ**, consistent with the high calculated oscillator strength of about 0.6 (see **Table 3**, and of 0.3 by Fan et al., 2019) suggests a strong influence of the  $\pi - \pi^*$  transitions from the carbazole. This is further supported by the drastic reduction in the extinction coefficient and calculated oscillator strength when reducing the conjugation through the meta-linkage in **mCTRZ**. It is remarkable that the influence of the para- and meta-connection on the CT-dominated absorption

**TABLE 3** | Dihedral angles (in degree) between the donor and acceptor unit in the ground and excited state geometry calculated at the M06-2X/6-31+G(d) level.

	$S_0$ (°)	$S_1$ (°)	$T_1$ (°)	$f$	$S_1$ (eV)
<b>pCTRZ</b>	52	66	43	0.5872	3.91
<b>mCTRZ</b>	53	56	40	0.0170	3.93
<b>CTRZ</b>	19	40	13	0.0071	4.21
<b>pATRZ</b>	97	93	55	0.0005	3.66
<b>mATRZ</b>	100	86	62	0.0002	3.73
<b>ATRZ</b>	14	2	10	0.0129	4.47

In case of asymmetry of the molecule only the smaller dihedral is shown. The oscillator strength  $f$  for the  $S_0 \rightarrow S_1$  transition is also given, along with the energy for the vertical transition from the relaxed ground state geometry.

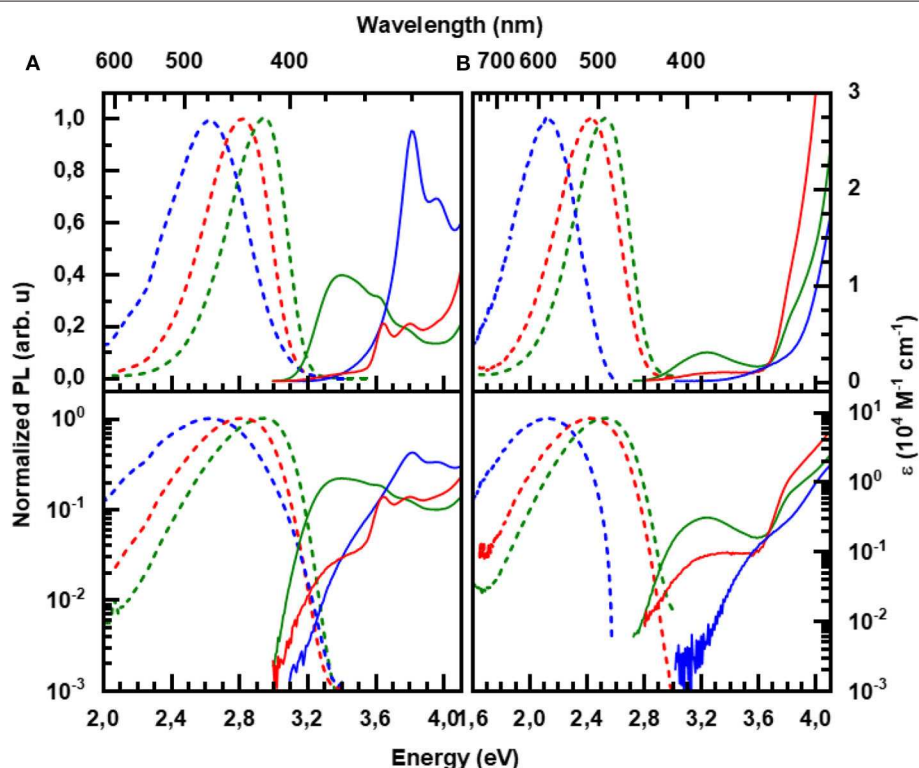


**FIGURE 3** | Absorption (solid lines) and steady state emission (dashed lines) at room temperature for **(A)** the carbazole-based and **(B)** the acridine-based series in toluene solution: **pCTRZ** and **pATRZ** (green), **mCTRZ** and **mATRZ** (red), and **CTRZ** and **ATRZ** (blue). The concentration of the solutions is 0.05 mg/mL, excitation was at 350 nm (3.54 eV). The bottom panel displays the same data on a logarithmic scale.

band is only reflected in the band's intensity, yet not in the energetic positions of either the CT-dominated band or the  $\pi - \pi^*$  transitions from the carbazole. In **CTRZ**, where the phenyl linker is entirely omitted this is different. The direct connection of carbazole to diphenyltriazine shifts the carbazole  $\pi - \pi^*$  band to higher energy by about 0.15 eV, and increases its oscillator strength. Compared to carbazole (**Figure S1**), the low energy edge has a pronounced tail. On the logarithmic scale, a superimposed broad transition centered at about 3.5 eV with similar extinction than the CT band in **mCTRZ** becomes evident, suggesting that the 3.5 eV feature is the CT band in **CTRZ**. Thus, it is evident that the extinction coefficient of the CT band decreases from **pCTRZ** to **mCTRZ** and **CTRZ**, roughly consistent with the calculated oscillator strengths of 0.587, 0.017, and 0.007, and suggestive of a reduced wavefunction overlap between donor and acceptor in **mCTRZ** and **CTRZ** compared to **pCTRZ**.

The acridine-based series (**Figure 3B**) shows some similarities in their general spectroscopic properties to the carbazole-based series. Like **pCTRZ** and **mCTRZ**, **pATRZ** and **mATRZ** show a broad, weak transition centered at 3.24 eV for both compounds, that reduces in intensity when the para-connection is replaced by a meta-linkage. Based on the broad structureless shape and its low extinction coefficient, we attribute this band to a CT-transition, consistent with the NTOs obtained in the  $S_0$  geometry (**Figure S4**). Analogous to **CTRZ**, for **ATRZ**, this CT band is blue shifted by about 0.15 eV and similar in intensity to the CT band in **mATRZ**. The transitions between 3.6 and 4.0 eV can be attributed to the  $n - \pi^*$  transitions of the acridine chromophore that dominate over the  $n - \pi^*$  transition of triazine by comparison with the absorption of the constituent units (**Figure S1**). Above 4 eV, transitions of the solvent toluene take over. A pronounced difference to the carbazole-based series is the lower extinction of the CT bands. This can be credited to the different geometry of the phenyl-linked molecules in the ground state. As detailed in **Table 3**, for **pCTRZ** and **mCTRZ**, the angle between donor and acceptor is 52 and 53°, while for **pATRZ** and **mATRZ**, it is 97 and 100°, respectively. As a result, the donor and acceptor in these acridine compounds are more decoupled, consistent with the  $S_0$  NTOs (**Figure S4**). Conversely, the more planar structure in **ATRZ** thus leads to still sizable oscillator strength and some wavefunction overlap despite the general donor-acceptor nature of this compound (c.f. **Figure S4**).

**Figure 3** presents also the room temperature emission spectra of the compounds in the toluene solution. As detailed in **Table 4**, the emission decays within a few ns for the carbazole-series and within a few tens of ns for the acridine-series, thus identifying it as fluorescence. For both series, the PL QY reduces along the series. When calculating the decay rates the higher radiative rate for the para-connected compounds becomes evident as cause for the relatively high PLQYs, which are more typical for  $\pi - \pi^*$  emission than CT emission. This is in agreement with the trends in wavefunction overlap for the relaxed  $S_1$  state (c.f. **Figure 2**). The meta-linked compounds and compounds without phenyl connection have similarly low radiative decay rates. However, when the phenyl ring is omitted, the non-radiative decay rate increases. We suggest that in **CTRZ** and **ATRZ** the torsional

**TABLE 4 |** PL Quantum yield and lifetime for the compounds in x mg/ml toluene at 300 K.

Compound	QY	$\tau$ (ns)	$k_r$ ( $10^8 \text{ s}^{-1}$ )	$k_{nr}$ ( $10^8 \text{ s}^{-1}$ )
<b>pCTRZ</b>	0.85	3.8 <sup>a</sup>	2.40	0.40
<b>mCTRZ</b>	0.15	18.6 <sup>a</sup>	0.08	0.46
<b>CTRZ</b>	0.04	6.2 <sup>a</sup>	0.06	1.56
<b>pATRZ</b>	0.19	13 (99%), 52 (1%) <sup>b</sup>	0.15	0.64
<b>mATRZ</b>	0.05	25 (97%), 90 (3%) <sup>b</sup>	0.02	0.38
<b>ATRZ</b>	0.03	12 (80%), 35 (20%) <sup>b</sup>	0.02	0.81

The radiative and non-radiative decay rates,  $k_r$ , and  $k_{nr}$ , are derived as detailed in the experimental section. To avoid any contribution from delayed fluorescence or phosphorescence, the solution was saturated with air.

<sup>a</sup> Taken from an exponential fit to the decay curve (**Figure S8**).

<sup>b</sup> Taken from a biexponential fit to the decay curve (**Figure S8**). The values in bracket give the weight of the two exponential decay.

modes enhance non-radiative decay routes, notably intersystem crossing (ISC) (Beljonne et al., 2001).

For both series, we find that the peak of the CT absorptions coincides for the compounds with a para or meta-connected phenyl ring, and it is 0.15 eV more blue if the phenyl ring is omitted. In contrast, the fluorescence peaks are distinct for within a series, and the peak energies decrease from para-linked to meta-linked followed by no link. Clearly, for such structureless spectra the determination of excited state energy is a challenge. Using the onset of the fluorescence or absorption spectra is a frequently used approach, but it carries a large uncertainty. A more precise value can be obtained by employing an approach that is common to determine the CT state energy in compounds used for organic solar cell applications, first introduced to the field by Vandewaal and co-workers (Gould et al., 1993; Vandewaal, 2016; Kahle et al., 2018; Vandewaal et al., 2010, 2017). For this, absorption and emission are plotted as reduced absorption and reduced emission spectra, i.e., the absorption (already displayed in energy intervals) is multiplied by the photon energy, and the emission (also already displayed in energy intervals) is divided by photon energy. The high energy edge of the emission and the low energy edge of the absorption are then fitted with the same gaussian lineshape. The intersection of the two curves indicates the position of the CT state 0-0 transition energy. The energy difference between the intersection and the maxima of the gaussian lineshape gives the reorganization energy associated with the CT state. The presentation of the spectra in this form is shown in **Figure 4**. The values obtained this way are presented in **Table 2**. One can see that such an analysis gives essentially the same CT state energy for all three carbazole-based molecules. They only differ in the value of the associated reorganization energy that increases along the series. Regarding the acridine-based series, the same CT state energy is obtained for **pATRZ** and **mATRZ**, while the **ATRZ** compound has its CT band blue-shifted to them and also shows a significantly larger reorganization energy.

This larger reorganization energy for **CTRZ** and **ATRZ** can be due to intra-molecular reorganization, e.g., associated with the change in torsion angle between the  $S_0$  and  $S_1$  geometry (**Table 3**) that prevails for **CTRZ** and **ATRZ**, and



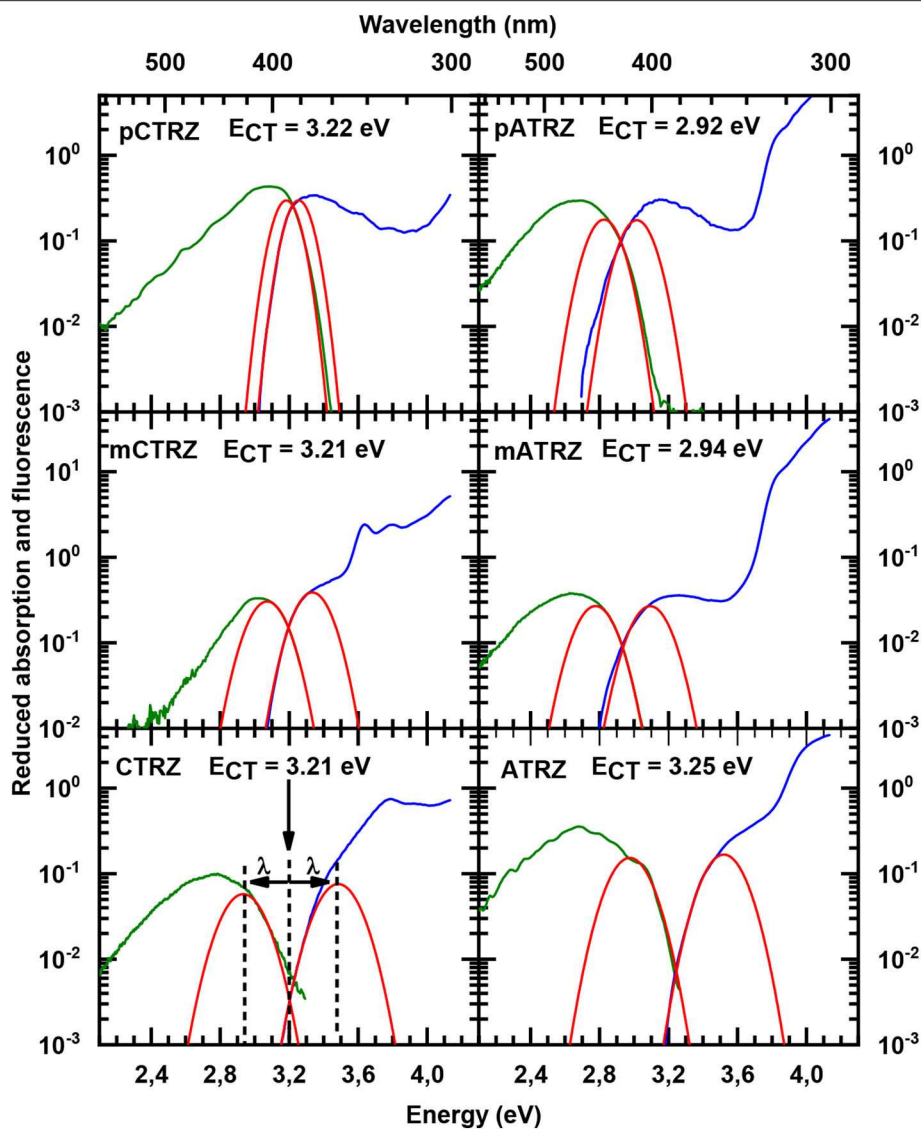


**FIGURE 4 |** Reduced absorption (blue lines) and reduced fluorescence (green lines) at 77 K in toluene for **pCTRZ**, **mCTRZ**, **CTRZ**, **pATRZ**, **mATRZ**, and **ATRZ**. Red lines correspond to Gaussian fits as described in the text.

that does not occur to a similar extent in the compounds linked by a phenyl ring. The reorganization energy usually includes both, contributions from changes in the molecular geometry as well as contributions from solvent reorganization. At 77 K, the solvent is frozen, implying that solvent reorganization is very limited. At room temperature it will, however, also include strong contributions from the solvent reorganization that reflect different strength in the CT character of the excited state. The larger reorganization energy for **ATRZ** is therefore likely to involve intra-molecular rearrangements. This can be assessed by considering the fluorescence taken in solvents of different polarity, such as toluene, tetrahydrofuran (THF), and dichloromethane (DCM), which have relative polarities of 0.099, 0.207, and 0.309, respectively (Reichardt, 2002) (**Figure 5**).

We observe a weaker solvent dependence of the fluorescence peaks in **CTRZ** and **ATRZ** compared to the phenyl-bridged compounds. This seems counter-intuitive, as it would suggest a weaker CT-character. At closer inspection, one notices that in the most polar solvent, DCM, where the CT-state can be expected to be most stabilized, the fluorescence of all compounds within a series roughly coincide in their peak position. For less polar solvents, the emission from the meta-linked and even more from the para-linked compounds is blueshifted, implying a reduced stabilization from a lesser CT-character of the excited state. The fact that **CTRZ** and **ATRZ** have a large reorganization energy even in less polar solvent therefore suggests that the dominant contribution to its reorganization is due to the change in molecular geometry such as the

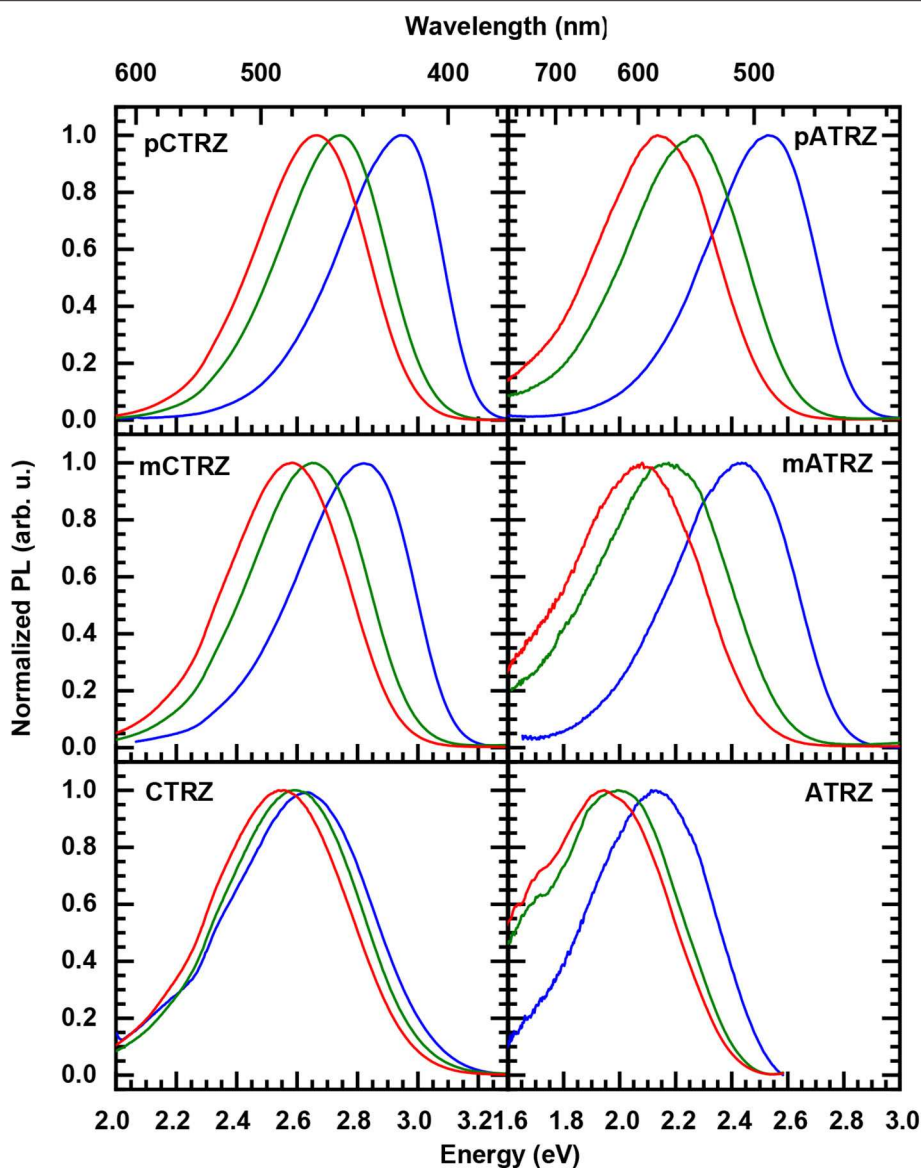


**FIGURE 5** | Solvent-dependent 300 K steady state emission spectra of **pCTRZ** and **pATRZ**, **mCTRZ** and **mATRZ**, **CTRZ** and **ATRZ** in toluene (blue lines), THF (green lines), and DCM (red lines). Concentration of the solutions is 0.05 mg/mL. Excitation is at 350 (3.54 eV) nm.

increased dihedral angle predicted by the TD-DFT calculation (Table 3). We recall that the TD-DFT calculations are carried out for the gas phase, and that more sophisticated calculations (beyond the scope of this paper) including the effect of solvent polarizability would be required to address this issue in a quantitative manner.

## Fluorescence and Phosphorescence at 77 K

We turn to measurements taken at 77 K, displayed in Figure 6. Upon cooling, the fluorescence spectra shift to the blue spectral range. The shifts are 0.15, 0.20, and 0.15 eV along the carbazole-based series, and 0.20, 0.30, and 0.60 eV for

the acridine-based series. We attribute the hypsochromic shift to the freezing out of molecular motion. The solvent shell molecules can no longer reorient after the transition of the molecule to the excited state, thus precluding the stabilization of the CT state. Based on the (gas phase) TD-DFT calculations (Table 3) and the polarity dependence observed in Figure 5 it seems that for **CTRZ** and **ATRZ**, there is also a contribution from the impediment of structural changes of the emitter molecules after excitation, such as changes in the dihedral angle, at 77 K.

Regarding the phosphorescence, we are interested to experimentally identify not only the  $S_1$ - $T_1$  gap, but also the part of the molecule from which the transition originates.

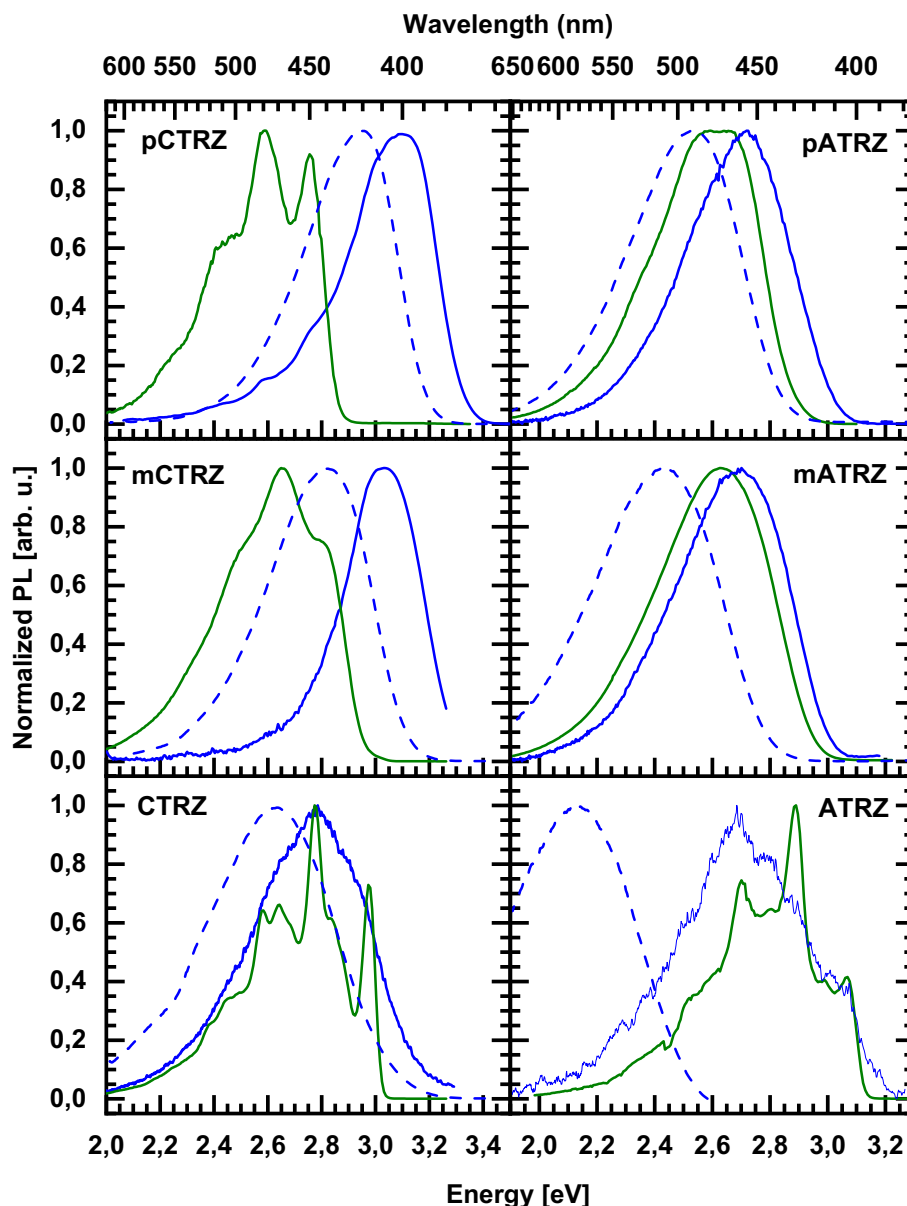


**FIGURE 6** | Emission spectra taken at 77 K in toluene of **pCTRZ**, **mCTRZ**, **CTRZ**, **pATRZ**, **mATRZ**, and **ATRZ** at a concentration of 0.05 mg/mL. Green lines correspond to phosphorescence, blue ones to fluorescence. Dashed lines show fluorescence at room temperature.

We associate the  $T_1$  energy with the position of the 0-0 phosphorescence peak. For the carbazole-based series and for **ATRZ**, these can be clearly identified as 2.76, 2.82, 2.97, and 3.07 eV. For **pATRZ**, the 0-0 peak is just resolvable at 2.67 eV. The spectral resolution is poorer for **mATRZ**. Comparing the spectra of **pATRZ** and **mATRZ** (see **Figure S5**), we find that **mATRZ** is overall shifted to the blue by 0.05 eV, so we estimate the 0-0 position to be at about 2.72 eV. All triplet energies are summarized in **Table 2**.

In order to identify the origin of the  $T_1$  state, we compare the vibrational structure of the phosphorescence spectra of our two series with that from their molecular constituents (**Figure 7**).

To ease comparison, all spectra are shifted in energy so that the 0-0 positions coincide at 0 eV. The original spectra are given in the supporting information (**Figure S6**). It is immediately evident that the spectra of **CTRZ** and of **ATRZ** coincide with the spectral form obtained from only a carbazole or triazine. The observation that the vibrational sidebands coincide implies that the transition is localized on the carbazole moiety in the case of **CTRZ** and on the triazine moiety in the case of **ATRZ**. In fact, even the energies of the transitions agree well (**Figure S6**). This spectroscopic result is in excellent agreement with the TD-DFT calculations and, for **CTRZ**, at variance with earlier suggestions that involve transitions delocalized over the entire

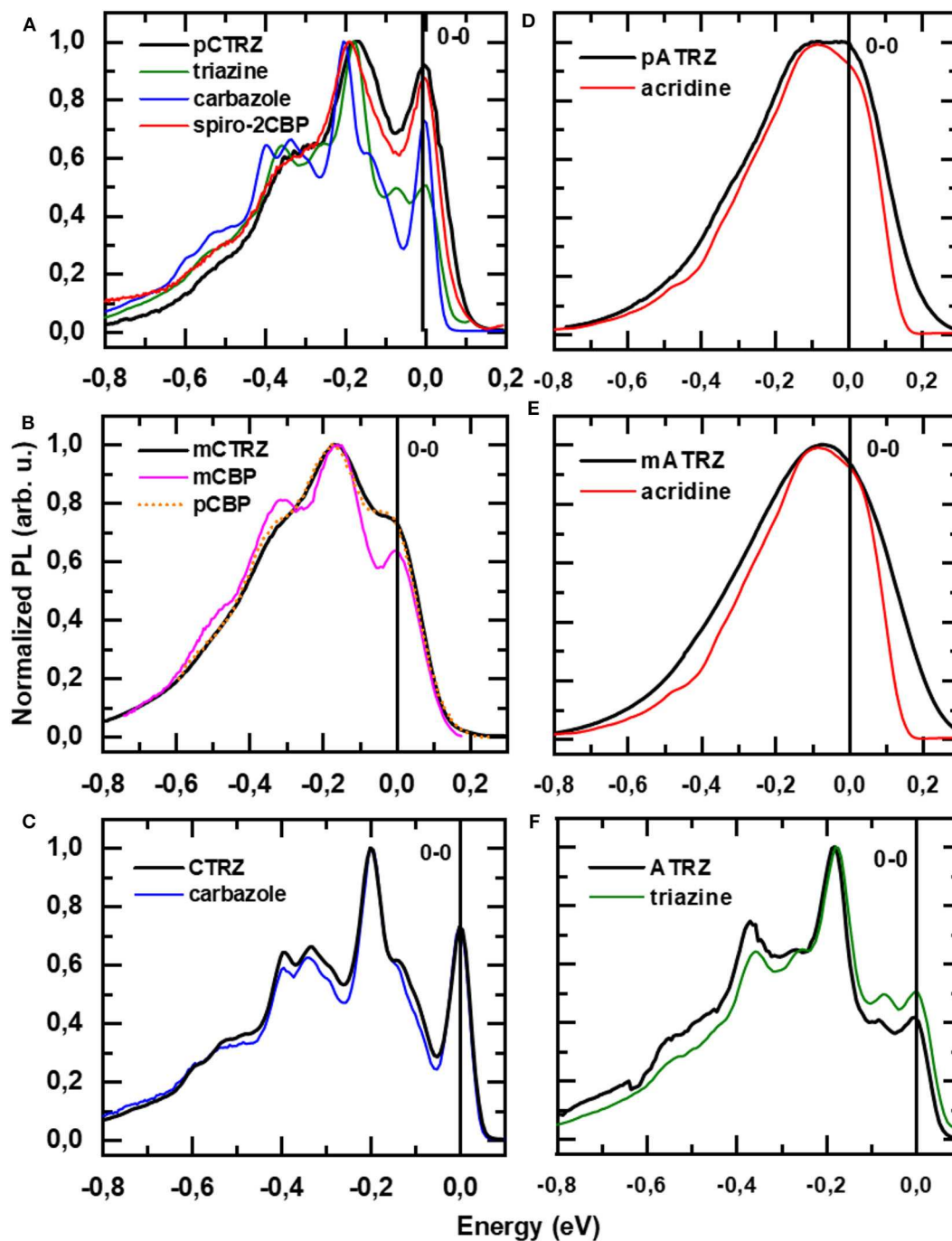


**FIGURE 7 |** (A) Phosphorescence spectra **pCTRZ** (A), **mCTRZ**, (B) **CTRZ** (C), **pATRZ** (D), **mATRZ** (E), and **ATRZ** (F) and corresponding modeling compounds in toluene at 77 K. The energy scale for every compound is adjusted to coincide to the first energy maximum. All compounds except triazine were excited at 350 nm, and emission was detected after a 30 ms delay with an integration of 15 ms. Triazine solution was excited at 300 nm.

**CTRZ** molecule (Duan et al., 2018). A different picture results for the compounds that are bridged by a phenyl ring. The vibrational structure in the phosphorescence of **pCTRZ** and **mCTRZ** resembles neither that observed in carbazole nor that of triazine. Rather, it closely resembles the structure obtained for

carbazole-biphenyl derivatives, where the triplet state was found to be localized on the central two phenyl rings (Brinen et al., 1966; Bagnich et al., 2015a,b). Thus, we conclude that the triplet state is dominated by the transition localized on the phenyl bridge and the triazine core, again in very good agreement with the



theoretical predictions. For **pATRZ** and **mATRZ**, the spectra are broad and differ drastically from the phosphorescence spectra of **pCTRZ** and **mCTRZ**. Rather, they are close in shape to spectrum of the donor, 9,9-diphenyl-9,10-di-hydroacridine. Spectra with practically the same shape were observed for other donor-acceptor materials containing acridine (Liu et al., 2015, 2016a,b). It allows to infer that triplet state localization includes also donor molecule, as also implied by the DFT calculations. Overall, we can summarize that for the compounds without bridge, the triplet state is localized strictly on the donor or acceptor moiety, while for the compounds with the phenyl bridge, the orbitals involved in phosphorescence spread from the center of the molecules into adjacent moieties.

We note that within a series the relative intensity of the phosphorescence differs. In the case of **pCTRZ** and **pATRZ**, phosphorescence is so weak that it does not contribute in the low temperature steady-state luminescence (Figure S7). For meta-derivatives the steady-state luminescence consists mostly from the phosphorescence, though some fluorescence is still observed as blue shoulder. Finally, only phosphorescence is observed in the steady-state luminescence of **CTRZ** and **ATRZ**. The data presented in Table 4 allow to understand the different contribution of the phosphorescence. In the case of **pCTRZ** the main channel of the singlet state deactivation is radiative decay with a rate that is 6 times larger than rate of non-radiative decay, that includes internal conversion and ISC. In this case ISC cannot compete with radiative decay of the singlet state that responsible for intensity of fluorescence. Change of carbazole position in the molecule from para to meta or removing of the phenyl bridge lead to a strong (about 30–40 times) decrease of value for radiative decay rate, so that the non-radiative processes, in particular the ISC, dominate. This is particularly strong for **CTRZ**, where the non-radiative rate increases compared to **mCTRZ**. The same trend takes place for acridine based compounds.

## DISCUSSION AND SUMMARY

The aim of our “toolbox approach” was to understand how to maximize the triplet energy in donor-acceptor type bipolar compounds through the choice of connection. We find that the use of a para-phenyl bridge or a meta-phenyl bridge both moves the lowest energy triplet state onto the center of the molecule so that its orbitals expand over more than two rings. This lowers the triplet state energy. This finding is consistent with earlier observations by us made on carbazole-biphenyl type molecules that do not contain any donor-acceptor type interactions, as well as with studies by Brunner and coworkers on carbazole derivatives, who emphasized the strong dependence of the triplet state energy on the number of aromatic rings over which the triplet wavefunction can spread (Brunner et al., 2004; Bagnich et al., 2015a,b). Thus, the lower triplet energy relates predominantly to the structure of the connection that allows for the triplet to spread over more than two rings. Similarly, when the phenyl bridge is omitted, as in **CTRZ** and **ATRZ**, the triplet is strongly localized on the smaller donor or

acceptor unit, and thus has a high triplet energy, characteristic for small molecular units. The highest triplet energy in our series, 3.07 eV for **ATRZ**, is consequently also found for the molecule where the triplet is confined onto the phenyl triazine moiety, as confirmed by the vibrational structure and the TD-DFT calculations (Figure 2), see also Figure S10 for a different projection of **ATRZ**). We note that this is one of the highest triplet energies reported so far for potential OLED bipolar host materials. Our results further suggest that obtaining higher triplet energies would imply localizing the triplet on an even smaller unit.

There are two further points emerging from our study that are worth commenting on. First, we recall the stronger dependence of the fluorescence maximum on solvent polarity that we observed for the phenyl-bridged compounds, even though they have  $\pi\pi^*$  admixtures in their excited state wavefunction, compared to the non-bridged compounds **CTRZ** and **ATRZ** that have a dominant CT character. Evidently, this implies a caveat that the lack of a strong shift with solvent polarity is not an unambiguous proof for a weak CT character, as it can be masked by effects due to conformational changes.

Second, our study illustrates the difficulty in defining a measure for the excited state energies. When the fluorescence and phosphorescence spectra are well-structured, so that the 0-0 emission peak can be clearly identified, quoting the energy of that peak is a very good approach, if not even the best practice. Difficulties arise if one of the spectra is poorly structured. We determined the S1 energy by spectral fitting as is common for CT states in organic solar cells (Gould et al., 1993; Vandewal et al., 2010, 2017; Vandewal, 2016; Kahle et al., 2018). One alternative is to consider the onset of fluorescence and phosphorescence, identified by extrapolating the slope of the high energy tail. Tacitly, this adds the sum of the linewidth to the transition energy and it bears the danger of misjudging singlet-triplet gaps if the linewidth differs between fluorescence and phosphorescence. If the high-energy edges of the fluorescence and phosphorescence have comparable slopes, implying comparable linewidth, taking the difference between the high-energy edges, e.g., at half maximum, can be an approximation to obtain the energy splitting between the two transitions without too much error (see also, Table S2).

In summary, using a tool box approach we synthesized and investigated six bipolar host materials that vary in the way how donor and acceptor are connected. Our detailed photophysical characterization supported by quantum chemical calculations show how this connection controls the excited states and their energies. Only direct connection of the donor group to the triazine core provides a high energy of the triplet state (2.97 eV for **CTRZ** and 3.07 eV for **ATRZ** in toluene), which is of prime importance for the use of the materials as a host for blue TADF emitters.

## DATA AVAILABILITY STATEMENT

The datasets generated for this study are available on request to the corresponding author.

## AUTHOR CONTRIBUTIONS

FR conducted the synthesis and characterization of the materials. ED and SB carried out and interpreted the photophysical measurements. TM, SA, and JK were responsible for the DFT calculations. AK and PS supervised the experiments and corrected the manuscript. All authors contributed to the article and approved the submitted version.

## FUNDING

We acknowledge funding through the EU Marie Skłodowska-Curie ITN TADFLife grant (GA. 812872). This work was also supported by the Universidad Carlos III de Madrid, the European Union's Seventh Framework Programme for research,

technological development and demonstration under grant agreement No. 600371, el Ministerio de Economía, Industria y Competitividad (COFUND2014-51509), el Ministerio de Educación, cultura y Deporte (CEI-15-17), Banco Santander and el Ministerio de Ciencia, Innovación y Universidades (RTI2018-101020-B-I00). SB acknowledges support from the Bayrisches Staatsministerium für Wissenschaft und Kunst (Stmwk) in the framework of the initiative SolTech as well as from the German Science foundation (DFG) (no. 392306670).

## SUPPLEMENTARY MATERIAL

The Supplementary Material for this article can be found online at: <https://www.frontiersin.org/articles/10.3389/fchem.2020.00657/full#supplementary-material>

## REFERENCES

- Adamo, C., and Barone, V. (1999). Toward reliable density functional methods without adjustable parameters: the PBE0 model. *J. Chem. Phys.* 110, 6158–6170. doi: 10.1063/1.478522
- An, Z., Zheng, C., Tao, Y., Chen, R., Shi, H., Chen, T., et al. (2015). Stabilizing triplet excited states for ultralong organic phosphorescence. *Nat. Mater.* 14, 685–690. doi: 10.1038/nmat4259
- An, Z.-F., Chen, R.-F., Yin, J., Xie, G.-H., Shi, H.-F., Tsuboi, T., et al. (2011). Conjugated asymmetric donor-substituted 1,3,5-triazines: new host materials for blue phosphorescent organic light-emitting diodes. *Chem. A Eur. J.* 17, 10871–10878. doi: 10.1002/chem.201101118
- Arjona-Esteban, A., Szafranowska, B., and Ochsmann, J. (2019). “TADF technology for efficient blue OLEDs: status and challenges from an industrial point of view,” in *Luminescence - OLED Technology and Applications*, ed S. Pyshkin (London: IntechOpen), 1–18. doi: 10.5772/intechopen.86534
- Bagnich, S. A., Athanasopoulos, S., Rudnick, A., Schroegel, P., Bauer, I., Greenham, N. C., et al. (2015a). Excimer formation by steric twisting in carbazole and triphenylamine-based host materials. *J. Phys. Chem. C* 119, 2380–2387. doi: 10.1021/jp512772j
- Bagnich, S. A., Rudnick, A., Schroegel, P., Stroehriegel, P., and Köhler, A. (2015b). Triplet energies and excimer formation in meta- and para-linked carbazolebiphenyl matrix materials. *Philos. Trans. R. Soc.* 373, 20140446. doi: 10.1098/rsta.2014.0446
- Beljonne, D., Shuai, Z., Pourtois, G., and Bredas, J. L. (2001). Spin-orbit coupling and intersystem crossing in conjugated polymers: a configuration interaction description. *J. Phys. Chem. A* 105, 3899–3907. doi: 10.1021/jp010187w
- Brinen, J. S., Koren, J. G., and Hodgson, W. G. (1966). ESR and phosphorescence spectra of the triplet states of phenyls-triazines and phenyl benzenes. *J. Chem. Phys.* 44, 3095–3099. doi: 10.1063/1.1727185
- Brunner, K., Dijken, A. V., Börner, H., Bastiaansen, J. J. A. M., Kiggen, N. M. M., and Langeveld, B. M. W. (2004). Carbazole compounds as host materials for triplet emitters in organic light-emitting diodes: tuning the HOMO level without influencing the triplet energy in small molecules. *J. Am. Chem. Soc.* 126, 6035–6042. doi: 10.1021/ja049883a
- Cai, X., and Su, S.-J. (2018). Marching toward highly efficient, pure-blue, and stable thermally activated delayed fluorescent organic light-emitting diodes. *Adv. Funct. Mater.* 28:1802558. doi: 10.1002/adfm.201802558
- Chai, J.-D., and Head-Gordon, M. (2008). Long-range corrected hybrid density functionals with damped atom-atom dispersion corrections. *Phys. Chem. Chem. Phys.* 10:6615. doi: 10.1039/b810189b
- Chatterjee, T., and Wong, K.-T. (2018). Perspective on host materials for thermally activated delayed fluorescence organic light emitting diodes. *Adv. Optical Mater.* 7:1800565. doi: 10.1002/adom.201800565
- Chen, W.-C., Lee, C.-S., and Tong, Q.-X. (2015). Blue-emitting organic electrofluorescence materials: progress and prospective. *J. Mater. Chem. C* 3, 10957–10963. doi: 10.1039/C5TC02420J
- Cui, L.-S., Kim, J. U., Nomura, H., Nakanotani, H., and Adachi, C. (2016a). Benzimidazobenzothiazole-based bipolar hosts to harvest nearly all of the excitons from blue delayed fluorescence and phosphorescent organic light-emitting diodes. *Angew. Chem.* 128, 6978–6982. doi: 10.1002/ange.201601136
- Cui, L.-S., Nomura, H., Geng, Y., Kim, J. U., Nakanotani, H., and Adachi, C. (2016b). Controlling singlet-triplet energy splitting for deep-blue thermally activated delayed fluorescence emitters. *Angew. Chem. Int. Ed.* 56, 1571–1575. doi: 10.1002/anie.201609459
- Ding, D., Zhang, Z., Wei, Y., Yan, P., and Xu, H. (2015). Spatially optimized quaternary phosphine oxide host materials for high-efficiency blue phosphorescence and thermally activated delayed fluorescence organic light-emitting diodes. *J. Mater. Chem. C* 3, 11385–11396. doi: 10.1039/C5TC02726H
- Duan, Y.-C., Wen, L.-L., Gao, Y., Wu, Y., Zhao, L., Geng, Y., et al. (2018). Fluorescence, phosphorescence, or delayed fluorescence?—A theoretical exploration on the reason why a series of similar organic molecules exhibit different luminescence types. *J. Phys. Chem. C* 122, 23091–23101. doi: 10.1021/acs.jpcc.8b06533
- Endo, A., Sato, K., Yoshimura, K., Kai, T., Kawada, A., Miyazaki, H., et al. (2011). Efficient up-conversion of triplet excitons into a singlet state and its application for organic light emitting diodes. *Appl. Phys. Lett.* 98:083302–083302-3. doi: 10.1063/1.3558906
- Fan, X., Li, C., Wang, Z., Wei, Y., Duan, C., Han, C., et al. (2019). Enhancing reverse intersystem crossing via secondary acceptors: toward sky-blue fluorescent diodes with 10-fold improved external quantum efficiency. *ACS Appl. Mater. Interfaces* 11, 4185–4192. doi: 10.1021/acsami.8b18041
- Frisch, M. J., Trucks, G. W., Schlegel, H. B., Scuseria, G. E., Robb, M. A., Cheeseman, J. R., et al. (2016). *Gaussian 16 Rev. C.01*. Wallingford, CT: Gaussian Inc.
- Gould, I. R., Noulakis, D., Gomez-Jahn, L., Young, R. H., Goodman, J. L., and Farid, S. (1993). Radiative and nonradiative electron transfer in contact radical-ion pairs. *Chem. Phys.* 176, 439–456. doi: 10.1016/0301-0104(93)80253-6
- Han, C., Zhao, Y., Xu, H., Chen, J., Deng, Z., Ma, D., et al. (2011). A simple phosphine-oxide host with a multi-insulating structure: high triplet energy level for efficient blue electrophosphorescence. *Chem. A Eur. J.* 17, 5800–5803. doi: 10.1002/chem.201100254
- Hatakeyama, T., Shiren, K., Nakajima, K., Nomura, S., Nakatsuka, S., Kinoshita, K., et al. (2016). Ultrapure blue thermally activated delayed fluorescence molecules: efficient HOMO-LUMO separation by the multiple resonance effect. *Adv. Mater.* 28, 2777–2781. doi: 10.1002/adma.201505491
- Hirata, S., and Head-Gordon, M. (1999). Time-dependent density functional theory within the Tamm-Dancoff approximation. *Chem. Phys. Lett.* 314, 291–299. doi: 10.1016/S0009-2614(99)01149-5
- Hirata, S., Sakai, Y., Masui, K., Tanaka, H., Lee, S. Y., Nomura, H., et al. (2014). Highly efficient blue electroluminescence based on thermally activated delayed fluorescence. *Nat. Mater.* 14, 330–336. doi: 10.1038/nmat4154

- Kahle, F.-J., Rudnick, A., Bässler, H., and Köhler, A. (2018). How to interpret absorption and fluorescence spectra of charge transfer states in an organic solar cell. *Mater. Horiz.* 5, 837–848. doi: 10.1039/C8MH00564H
- Kim, M., Jeon, S. K., Hwang, S.-H., and Lee, J. Y. (2015). Stable blue thermally activated delayed fluorescent organic light-emitting diodes with three times longer lifetime than phosphorescent organic light-emitting diodes. *Adv. Mater.* 27, 2515–2520. doi: 10.1002/adma.201500267
- Kukhta, N. A., Matulaitis, T., Volyniuk, D., Ivaniuk, K., Turyk, P., Stakhira, P., et al. (2017). Deep-blue high-efficiency TTA OLED using para- and meta-conjugated cyanotriphenylbenzene and carbazole derivatives as emitter and host. *J. Phys. Chem. Lett.* 8, 6199–6205. doi: 10.1021/acs.jpclett.7b02867
- Lin, T.-A., Chatterjee, T., Tsai, W.-L., Lee, W.-K., Wu, M.-J., Jiao, M., et al. (2016). Sky-blue organic light emitting diode with 37% external quantum efficiency using thermally activated delayed fluorescence from spiroacridine-triazine hybrid. *Adv. Mater.* 28, 6976–6983. doi: 10.1002/adma.201601675
- Liu, D., Li, D., Meng, H., Wang, Y., and Wu, L. (2019). Multifunctional applications of triazine/carbazole hybrid thermally activated delayed fluorescence emitters in organic light emitting diodes. *J. Mater. Chem. C* 7, 12470–12481. doi: 10.1039/C9TC03808F
- Liu, X.-Y., Liang, F., Cui, L.-S., Yuan, X.-D., Jiang, Z.-Q., and Liao, L.-S. (2015). Effective host materials for blue/white organic light-emitting diodes by utilizing the twisted conjugation structure in 10-Phenyl-9,10-dihydroacridine block. *Chem. Asian J.* 10, 1402–1409. doi: 10.1002/asia.201500235
- Liu, X.-Y., Liang, F., Ding, L., Li, Q., Jiang, Z.-Q., and Liao, L.-S. (2016b). A new synthesis strategy for acridine derivatives to constructing novel host for phosphorescent organic light-emitting diodes. *Dyes Pigments* 126, 131–137. doi: 10.1016/j.dyepig.2015.11.016
- Liu, X.-Y., Liang, F., Yuan, Y., Jiang, Z.-Q., and Liao, L.-S. (2016a). Utilizing 9,10-dihydroacridine and pyrazine-containing donor-acceptor host materials for highly efficient red phosphorescent organic light-emitting diodes. *J. Mater. Chem. C* 4, 7869–7874. doi: 10.1039/C6TC02180H
- Nishimoto, T., Yasuda, T., Lee, S. Y., Kondo, R., and Adachi, C. (2014). A six-carbazole-decorated cyclophosphazene as a host with high triplet energy to realize efficient delayed-fluorescence OLEDs. *Mater. Horiz.* 1, 264–269. doi: 10.1039/C3MH00079F
- Peach, M. J. G., Williamson, M. J., and Tozer, D. J. (2011). Influence of triplet instabilities in TDDFT. *J. Chem. Theory Comput.* 7, 3578–3585. doi: 10.1021/ct200651r
- Reichardt, C. (2002). *Solvents and Solvent Effects in Organic Chemistry*. Weinheim: WILEY-VCH Verlag GmbH & Co. KGaA. doi: 10.1002/3527601791
- Ren, X., Li, J., Holmes, R. J., Djurovich, P. I., Forrest, S. R., and Thompson, M. E. (2004). Ultrahigh energy gap hosts in deep blue organic electrophosphorescent devices. *Chem. Mater.* 16, 4743–4747. doi: 10.1021/cm049402m
- Sasabe, H., and Kido, J. (2013). Recent progress in phosphorescent organic light-emitting devices. *Eur. J. Organic Chem.* 2013, 7653–7663. doi: 10.1002/ejoc.201300544
- Schroegel, P., Langer, N., Schildknecht, C., Wagenblast, G., Lennartz, C., and Strohhriegl, P. (2011). Meta-linked CBP-derivatives as host materials for a blue iridium carbene complex. *Organic Electron.* 12, 2047–2055. doi: 10.1016/j.orgel.2011.08.012
- Sharma, N., Spuling, E., Mattern, C. M., Li, W., Fuhr, O., Tsuchiya, Y., et al. (2019). Turn on of sky-blue thermally activated delayed fluorescence and circularly polarized luminescence (CPL) via increased torsion by a bulky carbazophane donor. *Chem. Sci.* 10, 6689–6696. doi: 10.1039/C9SC01821B
- Shin, S. K., Han, S. H., and Lee, J. Y. (2018). High triplet energy exciplex host derived from a CN modified carbazole based n-type host for improved efficiency and lifetime in blue phosphorescent organic light-emitting diodes. *J. Mater. Chem. C* 6, 10308–10314. doi: 10.1039/C8TC02918K
- Sun, H., Zhong, C., and Brédas, J.-L. (2015). Reliable prediction with tuned range-separated functionals of the singlet–triplet gap in organic emitters for thermally activated delayed fluorescence. *J. Chem. Theory Comput.* 11, 3851–3858. doi: 10.1021/acs.jctc.5b00431
- Tomkeviciene, A., Grazulevicius, J. V., Kazlauskas, K., Gruodis, A., Jursenas, S., Ke, T.-H., et al. (2011). Impact of linking topology on the properties of carbazole trimers and dimers. *J. Phys. Chem. C* 115, 4887–4897. doi: 10.1021/jp111333v
- Uoyama, H., Goushi, K., Shizu, K., Nomura, H., and Adachi, C. (2012). Highly efficient organic light-emitting diodes from delayed fluorescence. *Nature* 492, 234–238. doi: 10.1038/nature11687
- Vandewal, K. (2016). Interfacial charge transfer states in condensed phase systems. *Ann. Rev. Phys. Chem.* 67, 113–133. doi: 10.1146/annurev-physchem-040215-112144
- Vandewal, K., Benduhn, J., Schellhammer, K. S., Vangerven, T., Rückert, J. E., Piersimoni, F., et al. (2017). Absorption tails of donor:C60 blends provide insight into thermally activated charge-transfer processes and polaron relaxation. *J. Am. Chem. Soc.* 139, 1699–1704. doi: 10.1021/jacs.6b12857
- Vandewal, K., Tvingstedt, K., Gadisa, A., Inganäs, O., and Manca, J. V. (2010). Relating the open-circuit voltage to interface molecular properties of donor:acceptor bulk heterojunction solar cells. *Phys. Rev. B* . 81, 125204-1–125204-8. doi: 10.1103/PhysRevB.81.125204
- Wei, Q., Ge, Z., and Voit, B. (2018). Thermally activated delayed fluorescent polymers: structures, properties, and applications in OLED devices. *Macromol. Rapid Commun.* 40:1800570. doi: 10.1002/marc.201800570
- Wong, M. Y., and Zysman-Colman, E. (2017). Purely organic thermally activated delayed fluorescence materials for organic light-emitting diodes. *Adv. Mater.* 29:1605444. doi: 10.1002/adma.201605444
- Yanai, T., Tew, D. P., and Handy, N. C. (2004). A new hybrid exchange–correlation functional using the Coulomb-attenuating method (CAM-B3LYP). *Chem. Phys. Lett.* 393, 51–57. doi: 10.1016/j.cplett.2004.06.011
- Yook, K. S., and Lee, J. Y. (2015). Bipolar host materials for organic light-emitting diodes. *Chem. Rec.* 16, 159–172. doi: 10.1002/tcr.201500221
- Zhang, J., Ding, D., Wei, Y., Han, F., Xu, H., and Huang, W. (2015). Multiphosphine-oxide hosts for ultralow-voltage-driven true-blue thermally activated delayed fluorescence diodes with external quantum efficiency beyond 20%. *Adv. Mater.* 28, 479–485. doi: 10.1002/adma.201502772
- Zhao, Y., and Truhlar, D. G. (2005). Design of density functionals that are broadly accurate for thermochemistry, thermochemical kinetics, and nonbonded interactions. *J. Phys. Chem. A* 109, 5656–5667. doi: 10.1021/jp050536c
- Zhao, Y., and Truhlar, D. G. (2008). The M06 suite of density functionals for main group thermochemistry, thermochemical kinetics, noncovalent interactions, excited states, and transition elements: two new functionals and systematic testing of four M06-class functionals and 12 other functionals. *Theoret. Chem. Acc.* 120, 215–241. doi: 10.1007/s00214-007-0310-x

**Conflict of Interest:** The authors declare that the research was conducted in the absence of any commercial or financial relationships that could be construed as a potential conflict of interest.

Copyright © 2020 Rodella, Bagnich, Duda, Meier, Kahle, Athanasopoulos, Köhler and Strohhriegl. This is an open-access article distributed under the terms of the Creative Commons Attribution License (CC BY). The use, distribution or reproduction in other forums is permitted, provided the original author(s) and the copyright owner(s) are credited and that the original publication in this journal is cited, in accordance with accepted academic practice. No use, distribution or reproduction is permitted which does not comply with these terms.



# Recent Advances in Metal-TADF Emitters and Their Application in Organic Light-Emitting Diodes

Wai-Pong To<sup>1</sup>, Gang Cheng<sup>1,2</sup>, Glenna So Ming Tong<sup>1</sup>, Dongling Zhou<sup>1</sup> and Chi-Ming Che<sup>1,2\*</sup>

<sup>1</sup> State Key Laboratory of Synthetic Chemistry, HKU-CAS Joint Laboratory on New Materials, Department of Chemistry, The University of Hong Kong, Hong Kong, China, <sup>2</sup> HKU Shenzhen Institute of Research and Innovation, Shenzhen, China

In this contribution, recent advances in new classes of efficient metal-TADF complexes, especially those of Au(I), Au(III), and W(VI), and their application in OLEDs are reviewed. The high performance (EQE = 25%) and long device operational lifetime (LT<sub>95</sub> = 5,280 h) achieved in an OLED with tetradentate Au(III) TADF emitter reflect the competitiveness of this class of emitters for use in OLEDs with practical interest. The high EQE of 15.6% achieved in solution-processed OLED with W(VI) TADF emitter represents an alternative direction toward low-cost light-emitting materials. Finally, the design strategy of metal-TADF emitters and their next-stage development are discussed.

## OPEN ACCESS

### Edited by:

Chihaya Adachi,  
Kyushu University, Japan

### Reviewed by:

Przemyslaw Data,  
Silesian University of  
Technology, Poland  
Rafal Czerwieniec,  
University of Regensburg, Germany

### \*Correspondence:

Chi-Ming Che  
cmche@hku.hk

### Specialty section:

This article was submitted to  
Organic Chemistry,  
a section of the journal  
Frontiers in Chemistry

Received: 29 February 2020

Accepted: 23 June 2020

Published: 31 July 2020

### Citation:

To W-P, Cheng G, Tong GSM, Zhou D  
and Che C-M (2020) Recent  
Advances in Metal-TADF Emitters and  
Their Application in Organic  
Light-Emitting Diodes.  
Front. Chem. 8:653.  
doi: 10.3389/fchem.2020.00653

**Keywords:** TADF, gold, tungsten, palladium, silver, organic light-emitting diode

## INTRODUCTION

Thermally activated delayed fluorescence (TADF) materials have become a promising class of photo-functional materials with potential practical applications most exemplified in the field of organic light-emitting diodes (OLEDs). The majority of TADF materials reported to date are organic compounds having donor and acceptor moieties that give rise to emissive charge transfer (CT) excited states upon light excitation. By carefully positioning the donor(s) and acceptor(s), a small singlet-triplet energy gap ( $\Delta E(S_1-T_1)$ ) can be achieved, thereby allowing efficient reverse intersystem crossing (RISC) to singlet excited state and TADF to occur at room temperature. While numerous classes of molecular organic TADF materials have been reported, the diversity of metal complexes exhibiting TADF property is very limited. In this article, we discuss the recent advances on metal complexes which display TADF and their application in OLEDs.

## RECENT ADVANCES IN METAL-TADF COMPLEXES AND THEIR APPLICATION IN OLEDs

### Metal-TADF Light-Emitting Complexes

The burgeoning development of emitters for OLEDs started from the fluorescent metal complex 8-hydroxyquinoline aluminum (Alq<sub>3</sub>) (Tang and VanSlyke, 1987). Despite its high luminance, high electron mobility and stability, the efficiency of Alq<sub>3</sub>-based OLED is limited by its fluorescence nature. Theoretically, the upper limit of internal quantum efficiency (IQE) of a fluorescent OLED is about 25% as only singlet spin states can emit light in fluorescent emitters. In this regard, phosphorescent metal complexes have been attracting much attention considering the 100% potential IQE in electro-phosphorescence (Baldo et al., 1998; Ma et al., 1998). Typical phosphorescent emitters are heavy metal complexes such as those of Ru(II), Ir(III), Os(II), and Pt(II) with emission lifetimes ( $\tau$ ) ranging 1–100  $\mu$ s due to significant mixing



between the metal and ligand frontier molecular orbitals and the efficient spin-orbit coupling induced by the heavy metal atom. Because of their high luminescence efficiency and high stability, phosphorescent Ir(III) complexes have been widely used as emitting dopants in OLED industry (Baldo et al., 1999). Nonetheless, the earth abundance of iridium is the lowest among the metal elements, leading to sustainability concern. An alternative approach to harvest triplet excitons at room temperature is via TADF (Yersin et al., 2011; Uoyama et al., 2012). The key process in TADF is up-conversion from the lowest triplet excited state ( $T_1$ ) to the lowest singlet excited state ( $S_1$ ), which is then followed by fluorescence from  $S_1$  to the singlet ground state ( $S_0$ ). Therefore, a delicate trade-off between  $\Delta E(S_1-T_1)$  and oscillator strength of  $S_0-S_1$  transition is crucial to achieve TADF. Since the reports by Endo et al. (2009), Deaton et al. (2010), and also by Uoyama et al. (2012), a plethora of organic TADF molecules have been reported (Wong and Zysman-Colman, 2017; Yang et al., 2017) but examples of metal-TADF emitters are mostly limited to copper complexes (Czerwieniec et al., 2016; Leitl et al., 2016). Since Cu(I) complexes generally lack thermal and electrochemical stability, efforts have been directed to develop 2nd and 3rd row transition-metal-TADF emitters such as those of Pd(II), Ag(I), Au(I), and Au(III) to meet the stringent requirements of emitters for practical OLEDs (Li G. et al., 2019). Gratifyingly, high external quantum efficiencies (EQEs) of up to 27.5 and 25.0% have been achieved in OLEDs with Au(I) and Au(III) TADF emitters, respectively (Di et al., 2017; Zhou et al., 2020), reflecting Au-TADF emitters as an emerging new class of competitive, emissive dopant in OLED industry.

The first report on electroluminescence (EL) of Cu(I) complex appeared soon after the reports on OLEDs based on Pt(II) and Os(II) emitters (Ma et al., 1999a,b). A Cu(I) complex could exhibit phosphorescence or TADF depending on its  $\Delta E(S_1-T_1)$  (Leitl et al., 2014). TADF could take place when the  $\Delta E(S_1-T_1)$  is comparable to the thermal energy  $k_B T$  that enables a dynamic equilibrium between  $S_1$  and  $T_1$ . Several high-performance OLEDs based on Cu(I) complexes have been reported (Zhang et al., 2012, 2016; Cheng et al., 2015; Osawa et al., 2015; Volz et al., 2015; So et al., 2017; Hamze et al., 2019; Shi et al., 2019). For instance, Bräse, So, Baumann and co-workers reported EQEs of up to 23% for yellow-emitting OLEDs with an NHetPHOS-Cu(I) complex (NHetPHOS refers to a ligand having N-heterocycle and phosphine) as the emitter (Volz et al., 2015). Thompson reported a class of two-coordinate Cu(I) carbene amide complexes exhibiting photoluminescent quantum yields (PLQYs) up to 1.0 with  $\tau$  of 1–2  $\mu$ s. EQEs of OLEDs fabricated with these emitters reached 19.4% (Shi et al., 2019). Since the development of TADF Cu(I) complexes has been well-reviewed (Czerwieniec et al., 2016; Yersin et al., 2017; Liu et al., 2018; Li G. et al., 2019), we will focus in this contribution on recent advances of efficient TADF metal complexes other than Cu(I) complexes that have been applied as emitting dopants in OLEDs.

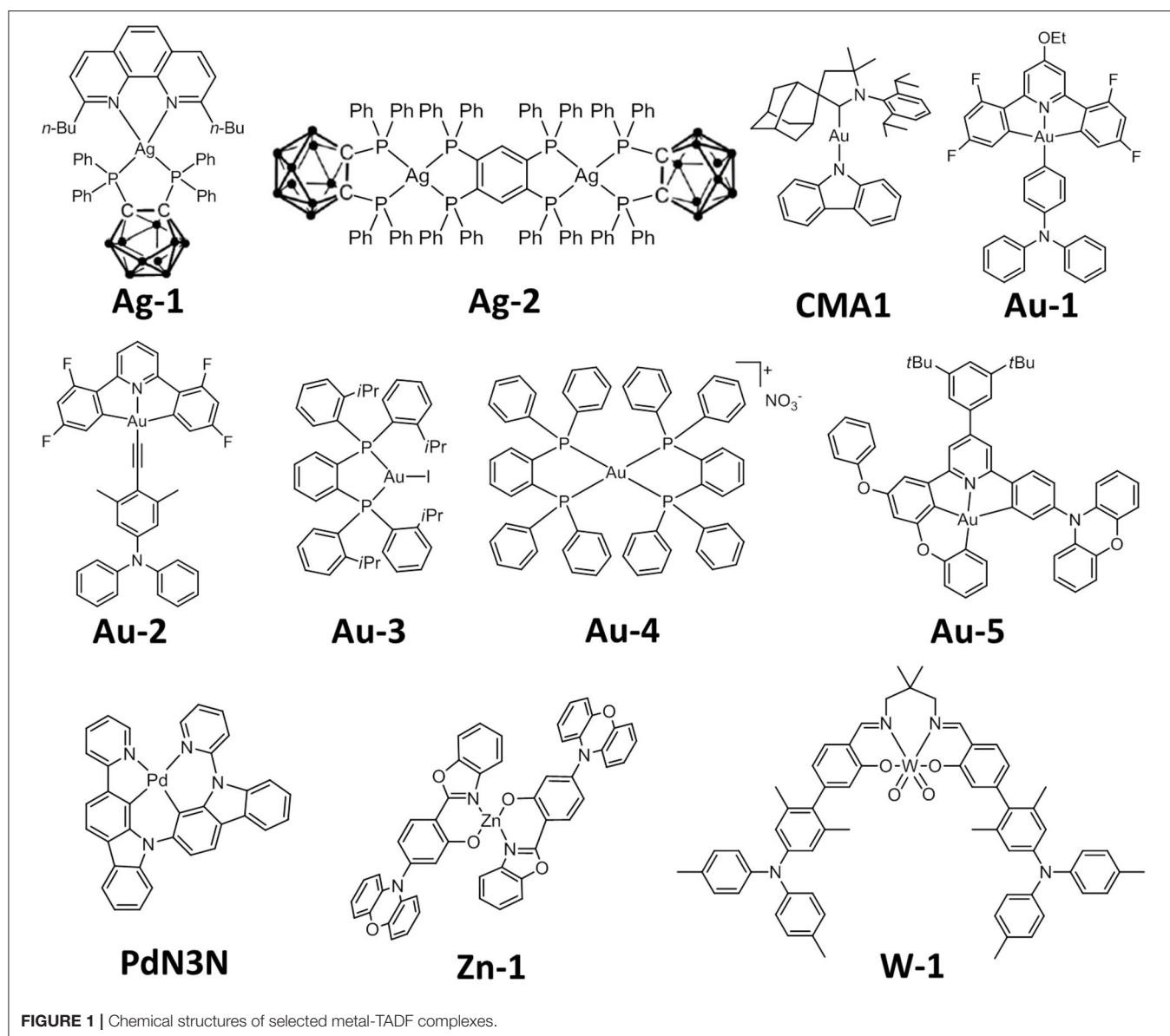
## Silver TADF Complexes and Their Application in OLEDs

Several examples of Ag(I) TADF emitters have been reported recently. Lu discovered bis-bidentate tetraphosphine bridged binuclear Ag(I) halide complexes exhibiting TADF with PLQYs

up to 0.98 and lifetime of 2.5–3.0  $\mu$ s (Chen et al., 2016). Yersin reported a series of Ag(I) complexes supported by 1,10-phenanthroline and bis(diphenylphosphine)-nido-carborane (e.g., **Ag-1**, **Figure 1**) with PLQYs up to 1.0 and  $\tau$  ranging 1.4–2.8  $\mu$ s (Shafikov et al., 2017a,b). Replacing 1,10-phenanthroline with a bridging tetraphosphine ligand afforded a binuclear Ag(I) TADF complex **Ag-2** with PLQY of 0.70 and  $\tau$  of 1.9  $\mu$ s (Shafikov et al., 2018). A Ag(I) carbene amide complex also exhibits TADF with PLQY of 0.74 and  $\tau$  of 460 ns in degassed toluene. OLEDs fabricated with this emitter showed EQEs up to 13.7% (Romanov et al., 2018).

## Gold TADF Complexes and Their Application in OLEDs

Gold is an attractive candidate for developing OLED emitters attributable to the high thermal stability endowed by strong gold-ligand bonds and its relatively high abundance among other noble metals in Earth's crust. Due to the electrophilicity/relatively high reduction potential of Au(III), Au(III) complexes often display ligand-centered emission having minute metal contribution. This results in small radiative decay rate constants ( $k_r$ ) of  $10^2$ – $10^3$   $s^{-1}$  and hence long  $\tau$  (usually  $>10$   $\mu$ s), longer than those of typical Ir(III) and Pt(II) complexes by one or two orders of magnitude (Zhou et al., 2019). As long emission lifetimes would cause severe efficiency roll-off in OLEDs (Cheng et al., 2014), only a few of them could achieve decent EQE and low efficiency roll-off at the same time. Notably, the study on Au(I)-OLEDs was even rarer than those of Au(III)-OLEDs (Ma et al., 1999b,c). In this regard, the recent development of TADF gold complexes has made a remarkable turnaround. Linnolahti, Bochmann, Credgington and co-workers reported a series of 2-coordinate carbene–Au(I)–amides (CMAs) that consist of a cyclic (alkyl)(amino)carbene (CAAC) connected via Au(I) to a carbazolate or diphenylamide (Di et al., 2017). Computations revealed that  $\Delta E(S_1-T_1)$  of **CMA-1** remains small ( $<800$   $cm^{-1}$ ) along the torsional coordinate, even at the coplanar conformation which has fluorescence rate of the order  $10^7$   $s^{-1}$ , thus leading to a fast equilibration of the  $S_1$  and  $T_1$  excited states and a large  $k_r$  of  $2.4 \times 10^6$   $s^{-1}$ , PLQY of 0.83 and short  $\tau$  of  $\sim 350$  ns in neat film at 300 K (Föller and Marian, 2017; Conaghan et al., 2018). A maximum EQE of 26.3% was achieved in solution-processed OLEDs with **CMA1** as the emitter and high EQE of 24.5% was maintained at a luminance of 1,000  $cd\ m^{-2}$ . Nonetheless, there has been no report on the operational lifetimes of the aforementioned Au(I)/Cu(I)/Ag(I)-TADF OLEDs. In 2017, Che and co-workers identified TADF as the emission origin in several pincer Au(III) aryl emitters (To et al., 2017). The presence of diarylamino group on the monodentate aryl ligand, and its twisted geometry with respect to the cyclometalating ligand, results in TADF in **Au-1** (**Figure 1**). Based on variable temperature–emission lifetime measurements and DFT calculations, a  $\Delta E(S_1-T_1)$  of 318  $cm^{-1}$  was estimated for this complex. With short  $\tau$  of 0.72  $\mu$ s and high PLQY of 0.84 in room temperature, solution-processed OLEDs with **Au-1** showed EQE and luminance of up to 23.8% and 57,340  $cd\ m^{-2}$ , respectively. It is noted that both devices based on the Au(I) complex **CMA1** and the Au(III) complex **Au-1** were fabricated by solution-processed technique. In this regard,



studies on EL of these gold complexes in vacuum-deposited devices were undertaken to determine if they have potential application in practical OLEDs. High maximum EQEs of 26.9 and 23.4% were achieved in vacuum-deposited OLEDs with Au(I) complex **CMA1** (Conaghan et al., 2018) and pincer Au(III) alkynyl complex **Au-2** (Figure 1; Zhou et al., 2019), respectively. Despite the slightly lower efficiency, the device lifetime ( $LT_{95}$ ) of the latter has been measured to be  $\sim 500$  h at an initial luminance of  $100 \text{ cd m}^{-2}$ , which is at least comparable to that of pincer Au(III) complex bearing deprotonated carbazole as auxiliary ligand reported by Li L.-K. et al. (2019). The improved thermal stability of Au(III) alkynyl complexes compared to the aryl ones is attributed to the stronger Au(III)-C<sub>sp</sub> bond in the alkynyl counterparts. Au(I) complexes with diphosphine ligand(s) have also been reported to display TADF (Osawa et al., 2018). The crystalline solid of Au(I) diphosphine iodide (**Au-3**) displayed

yellow photoluminescence with PLQY of 0.92 and lifetime of 9.0  $\mu\text{s}$ . Its emission shows a red-shift of 20 nm, a decrease in PLQY to 0.74 and an increase of lifetime to 77  $\mu\text{s}$ , corresponding to a reduction in  $k_r$  from  $1.0 \times 10^5 \text{ s}^{-1}$  to  $9.6 \times 10^3 \text{ s}^{-1}$  upon cooling from 293 to 77 K. Au(I) bis-diphosphine complex **Au-4** exhibits a high PLQY of 0.95 but with much shorter lifetime of 3.8  $\mu\text{s}$ . The  $\Delta E(S_1-T_1)$  of **Au-3** and **Au-4** were estimated to be 870 and 620  $\text{cm}^{-1}$ , respectively.

### Tetradentate Metal-TADF Emitters and Their Application in OLEDs

The aforementioned TADF Au(I) and Au(III) complexes were prepared by using two ligands. Since the stability of metal complexes could be increased by employing chelating ligands of higher denticity, the employment of tetradentate ligand with C-donor atom(s) is envisaged to improve the thermal

**TABLE 1** | Key performances of selected metal-TADF complexes.

Complex	Fabrication method	EQE (%)		$L^d$ (cd m <sup>-2</sup> )	CIE <sup>e</sup> (x, y)	Lifetime <sup>f</sup> (h)
		Max.	At 1,000 cd m <sup>-2</sup>			
CMA1	SP <sup>a</sup>	26.3	25.2	44,700	0.26, 0.49	n. a.
	VD <sup>b</sup>	26.9	24.9	35,400	0.24, 0.42	n. a.
Au-1	SP <sup>a</sup>	23.8	16.5	33,740	0.27, 0.51	n. a.
Au-2	VD <sup>b</sup>	23.4	22.1	70,300	0.40, 0.55	500
Au-5	VD <sup>b</sup>	25.0	22.0	22,700	0.43, 0.54	5,280
PdN3N	VD <sup>b</sup>	20.9	7.0 <sup>c</sup>	n. a.	0.30, 0.61	6,000 <sup>c</sup>
Zn-1	VD <sup>b</sup>	19.6	n. a.	n. a.	n. a.	n. a.
W-1	SP <sup>a</sup>	15.6	9.7	16,890	0.49, 0.49	n. a.

<sup>a</sup>Solution process; <sup>b</sup>Vacuum deposition; <sup>c</sup>Estimated from the original reference; <sup>d</sup>Maximum luminance; <sup>e</sup>CIE coordinates; <sup>f</sup>LT<sub>95</sub> at  $L_0 = 100$  cd m<sup>-2</sup>.

stability and to restrict excited-state structural distortion of the resultant complex as exemplified in tetradentate Pt(II) and Pd(II) complexes (Vezzu et al., 2010; Cheng et al., 2013; Chow et al., 2016). Furthermore, it was suggested that an increase in the structural rigidity of emitters could suppress structural deformation upon S<sub>1</sub>-T<sub>1</sub> transformation, which reduces  $\Delta E(S_1-T_1)$  and leads to efficient TADF (Saigo et al., 2019). Therefore, the development of TADF Au(III) complexes supported by trianionic tetradentate ligands would be an appealing direction toward practical Au-OLEDs. A class of Au(III) complexes supported by N-bridged tetradentate ligand prepared by post-modification was reported by Wong et al. (2017). These complexes exhibit photoluminescence from triplet intraligand charge-transfer (ILCT) excited states with PLQY of up to 0.78 in thin films. Solution-processed OLEDs fabricated with these emitters showed EQE of up to 11.1%. Che and co-workers developed new strategies for synthesizing tetradentate Au(III) complexes with O-bridged/spiro-arranged C<sup>^</sup>C<sup>^</sup>N<sup>^</sup>C ligand by microwave induced C-H activation (Zhou et al., 2020). By rationally varying the substituent(s) on the ligand, the emissive excited states of the Au(III) emitters are changed from triplet intraligand (<sup>3</sup>IL) excited states with  $k_r$  of  $\sim 10^3$  s<sup>-1</sup>, to TADF from ILCT excited states. These Au(III) TADF emitters show high thermal stability and PLQYs of up to 0.94 and  $\tau$  down to 0.62  $\mu$ s in degassed toluene. A vacuum-deposited OLED with **Au-5** as the emissive dopant showed maximum EQE of 25% and the EQE value maintained at 22% at a luminance of 1,000 cd m<sup>-2</sup>. Significantly, as listed in **Table 1**, at an initial luminance of 100 cd m<sup>-2</sup>, this device showed a much longer lifetime LT<sub>95</sub> of 5,280 h. This value is at least 10-fold longer than those recorded with pincer Au(III) emitters (Li L.-K. et al., 2019; Zhou et al., 2019). This result highlights the advantage of using tetradentate ligand in the preparation of robust Au(III) TADF emitters for practical use. It also showcases tetradentate Au(III) TADF complexes as competitive candidate in OLED industry.

Tetradentate ligand has also been used in preparing stable, luminescent Pd(II) complexes. Li and co-workers reported a tetradentate Pd(II) complex, **PdN3N**, which contains a C<sup>^</sup>N cyclometalating moiety composed of 2-pyridyl-carbazole, where the T<sub>1</sub> is localized, and also a donor-acceptor moiety of carbazole-carbazoyl-pyridine (**Figure 1**, Zhu et al., 2015).

**PdN3N** exhibited both phosphorescence and TADF at room temperature with PLQY of 0.72. A maximum EQE of 20.9% and operational lifetime LT<sub>90</sub> of 170 h at an initial luminance of 1,697 cd m<sup>-2</sup> were achieved in the OLED with **PdN3N**. Nonetheless, the EQE of this device dropped to  $\sim 7.0\%$  at a luminance of 1,000 cd m<sup>-2</sup>. Such severe efficiency roll-off is a result of the long  $\tau$  of  $>100$   $\mu$ s for **PdN3N**, which limits the application of this kind of Pd(II) complexes in practical OLEDs. In addition, the color purity of the Pd-OLED is not good enough because of the wide EL spectrum resulting from dual emission from both phosphorescence and TADF.

## Inexpensive Metal-TADF Complexes and Their Application in OLEDs

The low earth abundance of noble metals (e.g., iridium, platinum) has stimulated a great interest to invent new classes of luminescent materials based on inexpensive, earth-abundant metals (Bizzarri et al., 2018; Wenger, 2018). Besides Cu(I) complexes, more examples of inexpensive metal-TADF emitters have been reported. Adachi and co-workers synthesized TADF materials based on zinc, magnesium and lithium having ILCT transition (Sakai et al., 2015). **Zn-1** (**Figure 1**) was the most efficient emitter among these complexes. The EQE of vacuum-deposited OLEDs based on **Zn-1** was up to nearly 20%. By employing terphenyl having carboxyl and diphenylamine groups as linkers, Adachi, Kabe and co-workers constructed a zirconium-based metal-organic framework exhibiting green TADF with PLQY of 0.30 under vacuum (Mieno et al., 2018).

Tungsten is another appealing candidate for developing luminescent metal-based materials because of its large spin-orbit coupling constant (2,433 cm<sup>-1</sup>) which facilitates intersystem crossing and significantly higher earth abundance than noble metals. Nonetheless, examples of air-stable tungsten complexes displaying strong photoluminescence are rare with the recent report on W(VI) *cis*-dioxo Schiff base and quinolinolate complexes by Yeung et al. (2017). One of these complexes exhibit PLQYs of up to 0.22 in thin film and was used as emitter to realize the first tungsten-OLED, though the maximum EQE achieved was only 4.79%. While the proof of principle has been demonstrated, the low PLQY and inferior performance data suggested that significant improvement in the photo-luminescent

properties of luminescent W(VI) complexes is needed if the latter are to be used for practical applications. With a view to designing W(VI) complexes with competitive luminescent properties for OLED application, it is conceived that installation of diarylamino group(s) on the Schiff base ligand may change the emission origin to TADF (To et al., 2017; Zhou et al., 2019), thereby boosting  $k_r$  and improving PLQY. Che and co-workers described the first example of tungsten TADF emitter in 2019 (Chan et al., 2019). This study has demonstrated that the incorporation of diarylamino donor groups into the ligand scaffold changes the emissive excited state from long-lived  $^3\text{IL}$  ones to TADF arising from ILCT excited state, which effectively boosts PLQY of W(VI) Schiff base complex to 0.84 in thin film. The estimated  $k_r$  of **W-1** (Figure 1) is  $4.2 \times 10^5 \text{ s}^{-1}$ , which is at least 100-fold larger than that of analogous W(VI) complexes without diarylamino group. DFT calculations revealed that the subtle change on the twisted angle between the diarylamino substituent and the phenolic moiety is the key that influences the excited state dynamics and modulates the singlet-triplet energy separation, leading to efficient TADF in complex **W-1**. Solution-processed OLEDs fabricated with **W-1** showed EQEs of up to 15.6%, which is a significant improvement compared to the previous work ( $\text{EQE}_{\text{max}} = 4.79\%$ ).

## DISCUSSION

The variety and design strategy of metal-TADF emitters remain considerably scarce despite the recent discoveries on Au(I), Au(III), Ag(I), and Pd(II) TADF emitters. Summarizing from the recent findings, metal-TADF emitters are generally realized in complexes that are composed of electrophilic metal ion, such as those of Au(III), W(VI), and Pd(II). In these complexes, the emission origin is changed from phosphorescence ( $^3\text{LC}$ ) to TADF by adding donor groups to generate LLCT/ILCT excited states. The originally small  $k_r$  of these complexes allows an easy identification of whether TADF is operative because a 100-fold (or even more) increase in  $k_r$  would be observed when TADF takes place, as exemplified in Au(III) and W(VI) TADF emitters. This finding is similar to that of organic compounds which are known to show long-lived phosphorescence ( $k_r < 100 \text{ s}^{-1}$ ). By incorporating donor-acceptor pair, TADF can be

observed and the  $k_r$  of organic compounds can be increased significantly. Accordingly, it may be a challenge to realize TADF in Pt(II) and Ir(III) complexes due to their large phosphorescent  $k_r$  which facilitates efficient radiative decay via triplet excited state. Another consideration is that as the  $k_r$  of phosphorescent Pt(II) and Ir(III) are already large ( $10^5$ – $10^6 \text{ s}^{-1}$ ), switching the emission origin to TADF may not lead to a drastic increase in  $k_r$  and this renders the identification of whether TADF is occurring in these complexes highly challenging.

Compared to pure organic TADF emitters,  $\tau$  of triplet excited states of metal-TADF complexes is much shorter, which could be advantageous for the operational stability of OLEDs based on metal-TADF emitters. Furthermore, with the use of rigid tetradentate ligands, a drastic improvement in terms of efficiency and device stability could be realized as that observed for tetradentate Au(III) TADF emitters. This finding calls for a more stringent ligand design for practical metal-TADF emitters in addition to pursuing high PLQY and short  $\tau$ .

Besides, the questionable practicability of Cu(I) complexes in OLEDs triggers the investigation on TADF emitters based on other inexpensive metals. Although TADF Zn(II) and W(VI) complexes have shown high PLQY and EL efficiency, the improvement of operational lifetime of devices based on these complexes remains a formidable challenge. The deployment of robust and rigid ligands that would induce the occurrence of TADF could be the key to increase the practical potential of emitters based on earth-abundant metals.

## AUTHOR CONTRIBUTIONS

All authors contributed to the writing of the manuscript.

## FUNDING

This work was supported by the Major Program of Guangdong Basic and Applied Research (2019B030302009), Science, Technology and Innovation Commission of Shenzhen Municipality (JCYJ20170818141858021 and JCYJ20180508162429786), Hong Kong Research Grants Council (HKU 17330416), and CAS-Croucher Funding Scheme for Joint Laboratories.

## REFERENCES

- Baldo, M. A., Lamansky, S., Burrows, P. E., Thompson, M. E., and Forrest, S. R. (1999). Very high-efficiency green organic light-emitting devices based on electrophosphorescence. *Appl. Phys. Lett.* 75, 4–6. doi: 10.1063/1.124258
- Baldo, M. A., O'Brien, D. F., You, Y., Shoustikov, A., Sibley, S., Thompson, M. E., et al. (1998). Highly efficient phosphorescent emission from organic electroluminescent devices. *Nature* 395, 151–154. doi: 10.1038/25954
- Bizzarri, C., Spuling, E., Knoll, D. M., Volz, D., and Bräse, S. (2018). Sustainable metal complexes for organic light-emitting diodes (OLEDs). *Coord. Chem. Rev.* 373, 49–82. doi: 10.1016/j.ccr.2017.09.011
- Chan, K.-T., Lam, T.-L., Yu, D., Du, L., Phillips, D. L., Kwong, C.-L., et al. (2019). Strongly luminescent tungsten emitters with emission quantum yields of up to 84%: TADF and high-efficiency molecular tungsten OLEDs. *Angew. Chem. Int. Ed.* 58, 14896–14900. doi: 10.1002/anie.201906698
- Chen, J., Teng, T., Kang, L., Chan, X.-L., Wu, X.-Y., Yu, R., et al. (2016). Highly efficient thermally activated delayed fluorescence in dinuclear Ag(I) complexes with a bis-bidentate tetraphosphane bridging ligand. *Inorg. Chem.* 55, 9528–9536. doi: 10.1021/acs.inorgchem.6b00068
- Cheng, G., Chan, K. T., To, W.-P., and Che, C.-M. (2014). Color tunable organic light-emitting devices with external quantum efficiency over 20% based on strongly luminescent gold(III) complexes having long-lived emissive excited states. *Adv. Mater.* 26, 2540–2546. doi: 10.1002/adma.201304263
- Cheng, G., Chow, P.-K., Kui, S. C. F., Kwok, C.-C., and Che, C.-M. (2013). High-efficiency polymer light-emitting devices with robust phosphorescent platinum(II) emitters containing tetradentate dianionic  $\text{O}^-\text{N}^+\text{C}^-\text{N}^+$  ligands. *Adv. Mater.* 25, 6765–6770. doi: 10.1002/adma.201302408
- Cheng, G., So, G. K.-M., To, W.-P., Chen, Y., Kwok, C.-C., Ma, C., et al. (2015). Luminescent zinc(II) and copper(I) complexes for high-performance



- solution-processed monochromic and white organic light-emitting devices. *Chem. Sci.* 6, 4623–4635. doi: 10.1039/C4SC03161J
- Chow, P.-K., Cheng, G., Tong, G. S. M., Ma, C., Kwok, W.-M., Ang, W.-H., et al. (2016). Highly luminescent palladium(II) complexes with sub-millisecond blue to green phosphorescent excited states. Photocatalysis and highly efficient PSF-OLEDs. *Chem. Sci.* 7, 6083–6098. doi: 10.1039/C6SC00462H
- Conaghan, P. J., Menke, S. M., Romanov, A. S., Jones, S. T. E., Pearson, A. J., Evans, E. W., et al. (2018). Efficient vacuum-processed light-emitting diodes based on carbene-metal-amides. *Adv. Mater.* 30:1802285. doi: 10.1002/adma.201802285
- Czerwieniec, R., Leitl, M. J., Homeier, H. H. H., and Yersin, H. (2016). Cu(I) complexes—thermally activated delayed fluorescence. Photophysical approach and material design. *Coord. Chem. Rev.* 325, 2–28. doi: 10.1016/j.ccr.2016.06.016
- Deaton, J. C., Switalski, S. C., Kondakov, D. Y., Young, R. H., Pawlik, T. D., Giesen, D. J., et al. (2010). E-type delayed fluorescence of a phosphine-supported  $\text{Cu}_2(\mu\text{-NAr}_2)_2$  diamond core: harvesting singlet and triplet excitons in OLEDs. *J. Am. Chem. Soc.* 132, 9499–9508. doi: 10.1021/ja1004575
- Di, D., Romanov, A. S., Yang, L., Richter, J. M., Rivett, J. P. H., Jones, S., et al. (2017). High-performance light-emitting diodes based on carbene-metal-amides. *Science* 356, 159–163. doi: 10.1126/science.aah4345
- Endo, A., Ogasawara, M., Takahashi, A., Yokoyama, D., Kato, Y., and Adachi, C. (2009). Thermally activated delayed fluorescence from  $\text{Sn}^{4+}$ -Porphyrin complexes and their application to organic light emitting diodes—A novel mechanism for electroluminescence. *Adv. Mater.* 21, 4802–4806. doi: 10.1002/adma.200900983
- Föller, J., and Marian, C. M. (2017). Rotationally assisted spin-state inversion in carbene-metal-amides is an artifact. *J. Phys. Chem. Lett.* 8, 5643–5647. doi: 10.1021/acs.jpclett.7b02701
- Hamze, R., Peltier, J. L., Sylvinson, D., Jung, M., Cardenas, J., Haiges, R., et al. (2019). Eliminating nonradiative decay in Cu(I) emitters: >99% quantum efficiency and microsecond lifetime. *Science*, 363, 601–606. doi: 10.1126/science.aav2865
- Leitl, M. J., Krylova, V. A., Djurovich, P. I., Thompson, M. E., and Yersin, H. (2014). Phosphorescence versus thermally activated delayed fluorescence. Controlling singlet-triplet splitting in brightly emitting and sublimable Cu(I) compounds. *J. Am. Chem. Soc.* 136, 16032–16038. doi: 10.1021/ja508155x
- Leitl, M. J., Zink, D. M., Schinabeck, A., Baumann, T., Volz, D., and Yersin, H. (2016). Copper(I) complexes for thermally activated delayed fluorescence: from photophysical to device properties. *Top. Curr. Chem.* 374:25. doi: 10.1007/s41061-016-0019-1
- Li, G., Zhu, Z.-Q., Chen, Q., and Li, J. (2019). Metal complex based delayed fluorescence materials. *Org. Electron.* 69, 135–152. doi: 10.1016/j.orgel.2019.02.022
- Li, L.-K., Tang, M.-C., Lai, S.-L., Ng, M., Kwok, W.-K., Chan, M.-Y., et al. (2019). Strategies towards rational design of gold(III) complexes for high-performance organic light-emitting devices. *Nat. Photonics* 13, 185–191. doi: 10.1038/s41566-018-0332-z
- Liu, Y., Yiu, S.-C., Ho, C.-L., and Wong, W.-Y. (2018). Recent advances in copper complexes for electrical/light energy conversion. *Coord. Chem. Rev.* 375, 514–557. doi: 10.1016/j.ccr.2018.05.010
- Ma, Y., Chan, W.-H., Zhou, X.-M., and Che, C.-M. (1999a). Light-emitting diode device from a luminescent organocopper(I) compound. *New J. Chem.* 23, 263–265. doi: 10.1039/a808763f
- Ma, Y., Che, C.-M., Chao, H.-Y., Zhou, X., Chan, W.-H., and Shen, J. (1999b). High luminescence gold(I) and copper(I) complexes with a triplet excited state for use in light-emitting diodes. *Adv. Mater.* 11, 852–857. doi: 10.1002/(SICI)1521-4095(199907)11:10<852::AID-ADMA852>3.0.CO;2-R
- Ma, Y., Zhang, H., Shen, J., and Che, C.-M. (1998). Electroluminescence from triplet metal–ligand charge-transfer excited state of transition metal complexes. *Synth. Met.* 94, 245–248. doi: 10.1016/S0379-6779(97)04166-0
- Ma, Y., Zhou, X., Shen, J., Chao, H.-Y., and Che, C.-M. (1999c). Triplet luminescent dinuclear-gold(I) complex-based light-emitting diodes with low turn-on voltage. *App. Phys. Lett.* 74, 1361–1363. doi: 10.1063/1.123550
- Mieno, H., Kabe, R., Allendorf, M. D., and Adachi, C. (2018). Thermally activated delayed fluorescence of Zr-based metal-organic framework. *Chem. Commun.* 54, 631–634. doi: 10.1039/C7CC08595H
- Osawa, M., Aino, M.-A., Nagakura, T., Hoshino, M., Tanaka, Y., and Akita, M. (2018). Near-unity thermally activated delayed fluorescence efficiency in three- and four-coordinate Au(I) complexes with diphosphine ligands. *Dalton Trans.* 47, 8229–8239. doi: 10.1039/C8DT01097H
- Osawa, M., Hoshino, M., Hashimoto, M., Kawata, I., Igawa, S., and Yashima, M. (2015). Application of three-coordinate copper(I) complexes with halide ligands in organic light-emitting diodes that exhibit delayed fluorescence. *Dalton Trans.* 44, 8369–8378. doi: 10.1039/C4DT02853H
- Romanov, A. S., Jones, S. T. E., Yang, L., Conaghan, P. J., Di, D., Linnolahti, M., et al. (2018). Mononuclear silver complexes for efficient solution and vacuum-processed OLEDs. *Adv. Opt. Mater.* 6:1801347. doi: 10.1002/adom.201801347
- Saigo, M., Miyata, K., Tanaka, S., Nakanotani, H., Adachi, C., and Onda, K. (2019). Suppression of structural change upon  $\text{S}_1\text{-T}_1$  conversion assists the thermally activated delayed fluorescence process in carbazole-benzonitrile derivatives. *J. Phys. Chem. Lett.* 10, 2475–2480. doi: 10.1021/acs.jpclett.9b00810
- Sakai, Y., Sagara, Y., Nomura, H., Nakamura, N., Suzuki, Y., Miyazakia, H., et al. (2015). Zinc complexes exhibiting highly efficient thermally activated delayed fluorescence and their application to organic light-emitting diodes. *Chem. Commun.* 51, 3181–3184. doi: 10.1039/C4CC09403D
- Shafikov, M. Z., Suleymanova, A. F., Czerwieniec, R., and Yersin, H. (2017a). Design strategy for Ag(I)-based thermally activated delayed fluorescence reaching an efficiency breakthrough. *Chem. Mater.* 29, 1708–1715. doi: 10.1021/acs.chemmater.6b05175
- Shafikov, M. Z., Suleymanova, A. F., Czerwieniec, R., and Yersin, H. (2017b). Thermally activated delayed fluorescence from Ag(I) complexes: a route to 100% quantum yield at unprecedentedly short decay time. *Inorg. Chem.* 56, 13274–13285. doi: 10.1021/acs.inorgchem.7b02002
- Shafikov, M. Z., Suleymanova, A. F., Schinabeck, A., and Yersin, H. (2018). Dinuclear Ag(I) complex designed for highly efficient thermally activated delayed fluorescence. *J. Phys. Chem. Lett.* 9, 702–709. doi: 10.1021/acs.jpclett.7b03160
- Shi, S., Jung, M. C., Coburn, C., Tadler, A., Sylvinson, D. M. R., Djurovich, P. I., et al. (2019). Highly efficient photo- and electroluminescence from two-coordinate Cu(I) complexes featuring nonconventional N-heterocyclic carbenes. *J. Am. Chem. Soc.* 141, 3576–3588. doi: 10.1021/jacs.8b12397
- So, G. K.-M., Cheng, G., Wang, J., Chang, X., Kwok, C.-C., Zhang, H., et al. (2017). Efficient color-tunable copper(I) complexes and their applications in solution-processed organic light-emitting diodes. *Chem. Asian J.* 12, 1490–1498. doi: 10.1002/asia.201700081
- Tang, C. W., and VanSlyke, S. A. (1987). Organic electroluminescent diodes. *Appl. Phys. Lett.* 51, 913–915. doi: 10.1063/1.98799
- To, W.-P., Zhou, D., Tong, G. S. M., Cheng, G., Yang, C., and Che, C.-M. (2017). Highly luminescent pincer gold(III) aryl emitters: thermally activated delayed fluorescence and solution-processed OLEDs. *Angew. Chem. Int. Ed.* 129, 14036–14041. doi: 10.1002/anie.201707193
- Uoyama, H., Goushi, K., Shizu, K., Nomura, H., and Adachi, C. (2012). Highly efficient organic light-emitting diodes from delayed fluorescence. *Nature* 492, 234–238. doi: 10.1038/nature11687
- Vezzu, D. A. K., Deaton, J. C., Jones, J. S., Bartolotti, L., Harris, C. F., Marchetti, A. P., et al. (2010). Highly luminescent tetradentate bis-cyclometalated platinum complexes: design, synthesis, structure, photophysics, and electroluminescence application. *Inorg. Chem.* 49, 5107–5119. doi: 10.1021/ic100226
- Volz, D., Chen, Y., Wallesch, M., Liu, R., Fléchon, C., Zink, D. M., et al. (2015). Bridging the efficiency gap: fully bridged dinuclear Cu(I)-complexes for singlet harvesting in high-efficiency OLEDs. *Adv. Mater.* 27, 2538–2543. doi: 10.1002/adma.201405897
- Wenger, O. S. (2018). Photoactive complexes with earth-abundant metals. *J. Am. Chem. Soc.* 140, 13522–13533. doi: 10.1021/jacs.8b08822
- Wong, B. Y.-W., Wong, H.-L., Wong, Y.-C., Chan, M.-Y., and Yam, V. W.-W. (2017). Versatile synthesis of luminescent tetradentate cyclometalated alkynylgold(III) complexes and their application in solution-processable organic light-emitting devices. *Angew. Chem. Int. Ed.* 56, 302–305. doi: 10.1002/anie.201607816
- Wong, M. Y., and Zysman-Colman, E. (2017). Purely organic thermally activated delayed fluorescence materials for organic light-emitting diodes. *Adv. Mater.* 29:1605444. doi: 10.1002/adma.201605444
- Yang, Z., Mao, Z., Xie, Z., Zhang, Y., Liu, S., Zhao, J., et al. (2017). Recent advances in organic thermally activated delayed fluorescence materials. *Chem. Soc. Rev.* 46, 915–1016. doi: 10.1039/C6CS00368K

- Yersin, H., Czerwieniec, R., Shafikov, M. Z., and Suleymanova, A. F. (2017). TADF material design: photophysical background and studies focusing on Cu<sup>I</sup> and Ag<sup>I</sup> complexes. *ChemPhysChem* 18, 3508–3535. doi: 10.1002/cphc.201700872
- Yersin, H., Rausch, A. F., Czerwieniec, R., Hofbeck, T., and Fischer, T. (2011). The triplet state of organo-transition metal compounds. Triplet harvesting and singlet harvesting for efficient OLEDs. *Coord. Chem. Rev.* 255, 2622–2652. doi: 10.1016/j.ccr.2011.01.042
- Yeung, K.-T., To, W.-P., Sun, C., Cheng, G., Ma, C., Tong, G. S. M., et al. (2017). Luminescent tungsten(VI) complexes: photophysics and applicability to organic light-emitting diodes and photocatalysis. *Angew. Chem. Int. Ed.* 56, 133–137 doi: 10.1002/anie.201608240
- Zhang, J., Duan, C., Han, C., Yang, H., Wei, Y., and Xu, H. (2016). Balanced dual emissions from tridentate phosphine-coordinate copper(I) complexes toward highly efficient yellow OLEDs. *Adv. Mater.* 28, 5975–5979. doi: 10.1002/adma.201600487
- Zhang, Q., Komino, T., Huang, S., Matsunami, S., Goushi, K., and Adachi, C. (2012). Triplet exciton confinement in green organic light-emitting diodes containing luminescent charge-transfer Cu(I) complexes. *Adv. Funct. Mat.* 22, 2327–2336. doi: 10.1002/adfm.201101907
- Zhou, D., To, W.-P., Kwak, Y., Cho, Y., Cheng, G., Tong, G. S. M., et al. (2019). Thermally stable donor–acceptor type (alkynyl)gold(III) TADF emitters achieved EQEs and luminance of up to 23.4% and 70 300 cd m<sup>-2</sup> in vacuum-deposited OLEDs. *Adv. Sci.* 2019:1802297. doi: 10.1002/advs.201802297
- Zhou, D., To, W.-P., Tong, G. S. M., Cheng, G., Du, L., Phillips, D. L., et al. (2020). Tetradentate gold(III) complexes as thermally activated delayed fluorescence (TADF) emitters: microwave-assisted synthesis and high-performance OLEDs with long operational lifetime. *Angew. Chem. Int. Ed.* 59, 6375–6382. doi: 10.1002/anie.201914661
- Zhu, Z.-Q., Fleetham, T., Turner, E., and Li, J. (2015). Harvesting all electrogenerated excitons through metal assisted delayed fluorescent materials. *Adv. Mater.* 27, 2533–2537. doi: 10.1002/adma.201401772

**Conflict of Interest:** The authors declare that the research was conducted in the absence of any commercial or financial relationships that could be construed as a potential conflict of interest.

Copyright © 2020 To, Cheng, Tong, Zhou and Che. This is an open-access article distributed under the terms of the Creative Commons Attribution License (CC BY). The use, distribution or reproduction in other forums is permitted, provided the original author(s) and the copyright owner(s) are credited and that the original publication in this journal is cited, in accordance with accepted academic practice. No use, distribution or reproduction is permitted which does not comply with these terms.



# Recent Advances in Thermally Activated Delayed Fluorescent Polymer—Molecular Designing Strategies

Xia Yin<sup>1</sup>, Ying He<sup>1\*</sup>, Xu Wang<sup>1</sup>, Zexin Wu<sup>1</sup>, Erbao Pang<sup>1</sup>, Jing Xu<sup>2</sup> and Jun-an Wang<sup>2</sup>

<sup>1</sup> Department of Polymer Materials, School of Materials Science and Engineering, Shanghai University, Shanghai, China,

<sup>2</sup> Institute of Materials, School of Materials Science and Engineering, Shanghai University, Shanghai, China

## OPEN ACCESS

### Edited by:

Sebastian Reineke,  
Technische Universität  
Dresden, Germany

### Reviewed by:

Gang Cheng,  
The University of Hong Kong,  
Hong Kong  
Shi-Jian Su,  
South China University of  
Technology, China

### \*Correspondence:

Ying He  
yinghe@i.shu.edu.cn;  
yinghe@staff.shu.edu.cn

### Specialty section:

This article was submitted to  
Polymer Chemistry,  
a section of the journal  
Frontiers in Chemistry

Received: 08 April 2020

Accepted: 14 July 2020

Published: 14 August 2020

### Citation:

Yin X, He Y, Wang X, Wu Z, Pang E,  
Xu J and Wang J (2020) Recent  
Advances in Thermally Activated  
Delayed Fluorescent  
Polymer—Molecular Designing  
Strategies. *Front. Chem.* 8:725.  
doi: 10.3389/fchem.2020.00725

Thermally activated delayed fluorescent (TADF) materials, as the third generation of organic electroluminescent materials, have many advantages over other organic light-emitting diodes (OLEDs) materials, such as 100% internal quantum efficiency, no doping of heavy metals, and avoiding the shortages of ordinary fluorescent materials and phosphorescent materials. So it is considered to be the most competitive organic light-emitting materials, and has great application prospects in the field of OLEDs. So far, small-molecule TADF materials have achieved high quantum yield and full-color range of red, green, and blue. However, TADF polymers suitable for low-cost and easily scalable solution processing are less developed, which are confined by the preparation methods and polymers designing, and there are still challenges of increasing quantum efficiency and strengthening device performance. This review mainly summarizes different synthesis strategies of TADF polymers and the latest development in the field. Special attention is focused on illustrating the designing and structure-property relationship of TADF polymers, and finally, an outlook is given for the design and application prospect of TADF polymers in the future.

**Keywords:** organic light-emitting diodes, thermally activated delayed fluorescence, electroluminescence, TADF polymer, quantum efficiency, molecule designing

## INTRODUCTION

OLEDs are high-brightness, wide-view, and fully cured light emitting devices. As OLEDs have the advantages of low driving voltage, fast response speed, high luminous efficiency, simple manufacturing process and easy panchromatic display, they are considered as “Fantastic display,” and one of the most important flat-panel display technologies in the future (Sheats et al., 1996). The classical three-layer OLED device structure is composed of an electron transport layer (ETL), a hole transport layer (HTL), and an emitting layer (EML) (Wang et al., 1999). Among them, the emitting layer material not only largely determines the performance of the device, but also has a great influence on the processing method of the device. It is currently one of the most promising materials to improve the device performance.

At present, the mainstream luminescent materials used in the emitting layer include traditional fluorescent materials, phosphorescent materials, thermally activated delayed fluorescent materials, etc. (Köhler et al., 2002; Xiao et al., 2014). In fluorescent materials, the luminescence is accomplished by exciton transition from singlet state to ground state (Pope et al., 1963; Rothberg and Lovinger, 1996), while the luminescence of phosphorescent materials comes from exciton transition from triplet state to ground state (Baldo et al., 1998). Thermally activated delayed fluorescent (TADF) materials have a totally different luminescence mechanism, in which the exciton transition from triplet excited state to singlet excited state occurred through reverse inter-system crossing (RISC), thereby transition radiative emission (Nakagawa et al., 2012; Tanaka et al., 2012; Uoyama et al., 2012). Although those materials have different luminescence mechanisms, the structure and working principle are similar when they are used as emitting layer in OLED devices.

The performance of luminescent materials directly affects the luminous efficiency of the device. Therefore, a lot of researches on OLEDs are focused on the behavior of luminescent materials, including the electroluminescence (EL) efficiency, radiative lifetime and color purity. Meanwhile, a variety of matching auxiliary materials, such as hole transport materials, electron transport materials, exciton blocking materials and host materials, have been researched and developed to maximize the performance of the luminescent materials, and thereby to obtain OLED devices with excellent performance. In the past three decades, OLEDs have been well commercialized due to the maturity of fluorescent and phosphorescent materials. However, both fluorescent and phosphorescent materials still have fatal defects. The maximum device internal quantum efficiency (IQE) of conventional fluorescent materials is confined to within 25%, due to the low singlet excitons generation ratio of 25% in device. The luminescence of phosphorescent materials was improved by strengthened spin-orbit coupling (SOC) via doping heavy metals such as iridium (Ir) and platinum (Pt), while those materials also have uncertain toxicity, high cost and limited emission in blue regions (Holmes et al., 2003; Zhang et al., 2014b), etc. Promisingly, thermally activated delayed fluorescence supplies a solution to utilize triplet excitons emission by RISC process, where triplet excitons can be effectively upconverted into singlet state and decayed via a radiative channel to the ground state. Theoretically speaking, TADF-OLEDs may reach 100% IQE under EL operation.

As early as 1961, Parker and Hatchard (1961) discovered the TADF phenomenon in the magenta dye, and subsequently observed the same phenomenon in fullerenes and other compounds under photoexcitation. In 2009, Adachi et al. (Endo et al., 2009) introduced TADF materials into OLED devices for the first time. Since then, TADF materials have made great progress in OLED applications, but the most interested TADF emitters so far are small molecules, due to the ease in simultaneously achieving a small singlet-triplet energy splitting ( $\Delta E_{ST}$ ) and suppressing the internal conversion (IC) process of the molecule. TADF polymers have excellent modifiability and good thermal stability compared to small

molecules. More importantly, narrow band-gap TADF polymers with robust, high film-forming property have emerged, which is extremely beneficial for simple roll-to-roll printing (Wang et al., 2020). In addition, compared with small molecules, self-host TADF polymers are more likely to be prepared by rational group modification and structure regulation to solve the phase separation problem of host-guest-doped TADF-OLEDs. Due to those process-related problems, research and development are shifting to TADF polymers. The existing research strategies of TADF polymers are mainly on indirect synthesis, in which the active unit with TADF emission was embedded or grafted into the polymer as a main chain (Nikolaenko et al., 2015; Lee et al., 2016), side chain (Luo et al., 2016) or dendrimer core (Albrecht et al., 2015). Those previous research results bring significant clues for designing and synthesis of new TADF polymers. This review firstly introduces the luminescence mechanism of TADF materials, and briefly analyzes the design principles of TADF materials, focusing on the existing TADF polymers. Finally, the future development of TADF materials is prospected from the aspects of material synthesis, performance and application.

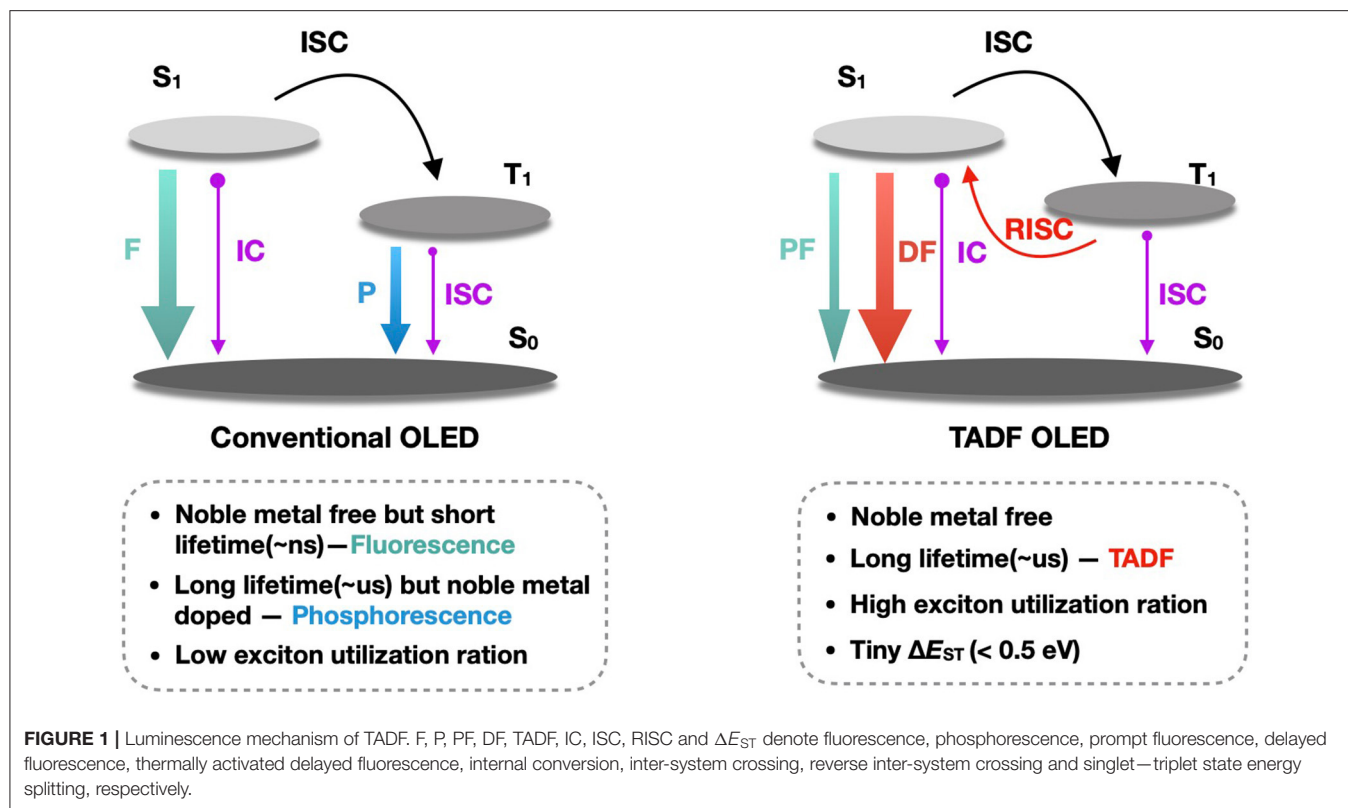
## LUMINESCENCE MECHANISM OF TADF MATERIALS

The OLED device is generally composed of an anode, a metal cathode and organic function layers. According to the number of organic function layers, OLED devices can be classified into single-layer structure, double-layer structure, three-layer structure and multilayer structure. Three-layer device structure is most commonly used in organic light-emitting device (Adachi et al., 1988; Dai et al., 2005). This structure is mainly composed of ETL, HTL and organic EML, which is not only conducive to selecting materials as functional layers but also to optimizing device performance.

Under the action of external voltage, holes and electrons are injected from the anode and the cathode respectively, passing through the respective transport layers and finally combining to form excitons in the light-emitting layer (Hung and Chen, 2002). Those excitons contain both singlet excitons ( $S_1$ ) and triplet excitons ( $T_1$ ) due to their different spin states before and after excitation, and the ratio of  $S_1$  to  $T_1$  is 1:3 according to the spin quantum theory (Rothberg and Lovinger, 1996). Emission comes from the radiative transition of the exciton, that is, from singlet or triplet state to the ground state. During this process, photons generate and emit out from the EML which results in different efficiencies of OLED devices.

As shown in **Figure 1**, unlike conventional fluorescence and phosphorescence in OLEDs, TADF emission has two distinct components: prompt fluorescence (PF) and delayed fluorescence (DF). Since the energy levels of the  $S_1$  state and the  $T_1$  state of the TADF molecules are close to each other ( $\Delta E_{ST} < 0.5$  eV), it is possible to use heat in the environment to achieve the reverse inter-system crossing ( $T_1 \rightarrow S_1$ ), thereby converting the triplet excitons, accounting for 75% of total excitons, into singlet excitons, and the radiative transition produces delayed fluorescence of microsecond or even millisecond lifetime. On





the other hand, the rapid radiative transition of excitons originally occupied in the  $S_1$  state, accounting for 25%, produces nanosecond-order prompt fluorescence. Thus, theoretically, TADF molecule could achieve 100% internal quantum efficiency. Since both PF and DF are derived from singlet state emission, they are completely identical in the emission spectrum.

The TADF emission process is based on the spatial separation of the highest occupied molecular orbit/the lowest unoccupied molecular orbit (HOMO/LUMO) of charge transfer (CT) excited state materials (Peng et al., 2013). The energy levels between the lowest singlet state and the lowest triplet state are close due to weak electron exchange, thus  $\Delta E_{ST}$  is very small in TADF molecules. It is easy to achieve the reverse inter-system crossing under the thermal activation condition, thereby converting the triplet excitons into singlet excitons and accomplishing 100% internal quantum efficiency.

## TADF MOLECULAR STRUCTURE DESIGN

### Design Principle of TADF Molecule

Although TADF has a unique RISC process and its mechanism is complex, the design of TADF materials has certain rules. In the case of TADF organic small molecules, HOMO is usually located on the electron donor (D), and LUMO on the electron acceptor (A). For this reason, groups with greater steric hindrance (Mehes et al., 2012; Zhang et al., 2012; Kawasumi et al., 2015; Suzuki et al., 2015; Feuillastre et al., 2016; Furue et al., 2016) were generally introduced between the donor and the acceptor of the molecules,

for obtaining spatial separation of HOMO and LUMO to enhance the charge transfer state (Xie and Li, 2017). From the perspective of molecular design strategy, TADF polymer draws on the design idea of the electron donor–electron acceptor (D–A) structure of the TADF organic small molecules, that is, the electron donor and the acceptor units are connected in a specific way in the polymer (Zhang et al., 2014a; Numata et al., 2015; Suzuki et al., 2015). By regulating the interaction between the electron donor and the acceptor and the degree of electron cloud overlap to reduce  $\Delta E_{ST}$ , the reverse inter-system crossing process will be enhanced to achieve the TADF effect (Endo et al., 2011; Lee et al., 2012). However, combined with photoluminescence quantum yield (PLQY) that is one of the important properties when TADF polymer is used as an emissive layer in OLEDs, a certain degree of spatial overlap between HOMO and LUMO is a necessary according to Franck-Condon theory. So, when regulating the degree of spatial separation of HOMO/LUMO to achieve small  $\Delta E_{ST}$  in TADF polymers, the degree of spatial overlap between them should be considered to ensure a relatively high PLQY. For this, the TADF polymer should possess a rigid structure to reduce the recombination energy of the molecule, thereby suppressing non-radiative transitions to obtain a higher rate of radiation decay (Guo et al., 2017).

However, compared with small molecules, in TADF polymers, triplet excitons are more prone to quenching due to triplet–triplet annihilation effect (TTA) within and between molecules, and it is a dilemma to obtain a smaller  $\Delta E_{ST}$  and to inhibit non-radiative internal conversion in polymers containing a

large number of atoms. In addition, due to the through-bond charge transfer effect of the conjugated structure, the emission wavelength of TADF polymer will show a large red shift, leading to the majority of TADF polymer emission concentrated in orange and green light emission, which is unfavorable for achieving blue light emission of TADF polymer. TADF polymer light-emitting diodes (PLEDs) have also been reported to have serious efficiency roll-offs and low external quantum yield (EQE) till now. To address these issues, TADF polymer design strategies are particularly of significance (Liu et al., 2018a).

## Common Electron Donor and Electron Acceptor Units

In the design of TADF polymers, it is extremely important to select the appropriate functional group. It has been reported that a large number of functional groups, such as electron donor and acceptor groups, are connected to each other in a specific manner to achieve the TADF effect. Presently, the electron donor of D-A type TADF polymer is mainly composed of N-containing aromatic groups with strong electron donating ability, which requires high triplet energy level, good stability, and excellent carrier transport capacity. Common electron donors include carbazole, phenoxazine, aniline, acridine and their derivatives. For electron acceptors, there are mainly the following types: nitrogen heterocycles, benzophenones, cyanobenzenes, diphenylsulfones and their derivatives, etc. (Volz, 2016), which generally have strong electron-withdrawing ability and good electron-conjugation properties, and a molecular structure to be easily modified.

## TADF POLYMER

Although most of the TADF materials are usually small organic molecules due to a direct design for their electronic structures, the processing is expensive and cannot be used for large device fabrication. Compared with small molecules, polymers are extremely suitable for solution processing, such as spin coating, inkjet printing, and roll-to-roll coatings (Gustafsson et al., 1992; Wu et al., 2009), showing a great potential in low-cost processing and large-scale applications. At present, the main design strategy of TADF polymer is based on an indirect way that introduces small molecules with known TADF-active behavior into different positions of the polymer structure either as pendant groups, as main chain constituents, or as core. Beside of these, there are also self-emission TADF polymers. In this case, small molecules that originally do not have TADF properties reduce the energy splitting between corresponding  $^1,^3\text{CT}$  after polymerization due to the expansion of the conjugated structure, making  $\Delta E_{\text{ST}}$  relatively small enough to be overcome by heat, so the polymer shows excellent TADF properties (Wei et al., 2017).

Therefore, in this section, TADF polymers are classified as according to the position of TADF active units in the polymer structure, as shown in **Figure 2**: (1) Core-acceptor / Shell-donor dendritic TADF polymer; (2) Main chain TADF polymer; (3) Backbone-donor/Pendant-acceptor TADF polymer; (4) Side chain TADF polymer; (5) Self-emission TADF polymer. Each

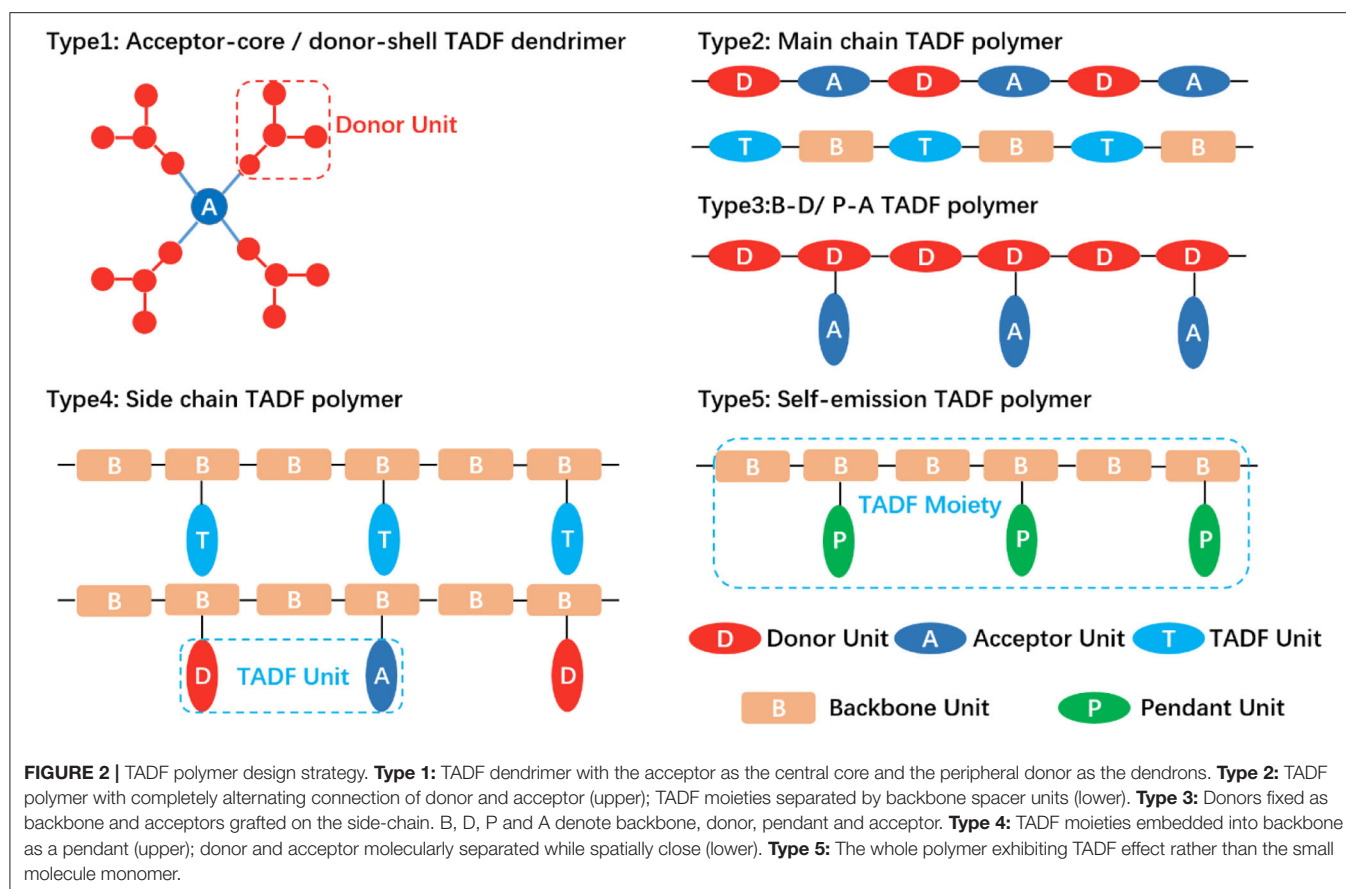
type is further subdivided on the basis of the connection mode of its electron acceptor and electron donor. For example, dendritic TADF polymers have conjugated and non-conjugated structures depending on the linking groups of the core and the acceptor. Based on the molecular structure of TADF fragments on the backbone, the main chain TADF polymer can be divided into D-A type TADF polymer with alternating copolymerization of donor and acceptor and B-T-B type TADF polymer with spaced backbone. The side chain TADF polymers are classified into conjugated and non-conjugated in the light of the difference of the backbone structure. According to the connection mode of the electron donor and the acceptor in the TADF fragment, the side chain non-conjugated TADF polymer is divided into D-A directly connected intramolecular charge transfer polymer and space charge transfer polymer where donors and acceptors are separated. It is found that the conjugation effect, TADF fragment structure, and D-A connection mode affected the properties of TADF polymer emitters, such as the charge carrier mobility, emission color, and efficiency of TADF properties.

## High Molecular Weight TADF Dendrimer

Dendrimer (Astruc et al., 2010) is a perfectly branched polymer with precise molecular structure, usually a core-shell structure consisting of a central core and a repeating branch perimeter. Dendritic TADF macromolecules have both the advantage of high molecular weight similar to polymers and the same precise molecular structure as small molecules, so the required photoelectric and processing properties of the materials can be enhanced by regulating the molecular structure (Burn et al., 2007). Meanwhile, owing to their unique structure with a high steric hindrance, they are generally in a soluble and amorphous state, and can isolate chromophores at the core to prevent concentration quenching. Thus, dendritic TADF macromolecules are ideal for solution-processing in OLED devices.

Currently, TADF dendrimer has been widely studied and applied to OLED devices with excellent performance. The central core of a dendritic TADF polymer is the main unit contributing to the TADF performance. Usually, the structure of the central core, mostly D-A type structure, is similar to that of small molecule TADF units. Common electron acceptor units such as dibenzophenone, triazine and diphenylsulfone are often used as the core of the acceptor. Depending on the functional groups connecting the core and peripheral dendrons, TADF dendrimers often have conjugated and non-conjugated structures. On account of the strong molecular rigidity in the conjugated structure, the solubility of the molecule will be reduced, and the expanded conjugation on the periphery will interfere with the emission of the core, causing the emission color to change. Flexible alkyl chains (Xu et al., 2008) are often chosen to enhance molecular solubility, facilitate charge transfer, and encapsulate the luminous core.

Triazine and its derivatives have strong electron-withdrawing ability and excellent structural modifiability, so they are fairly good acceptor cores. Through modification of dendritic donor substituents, TADF dendrimers can be effectively constructed.



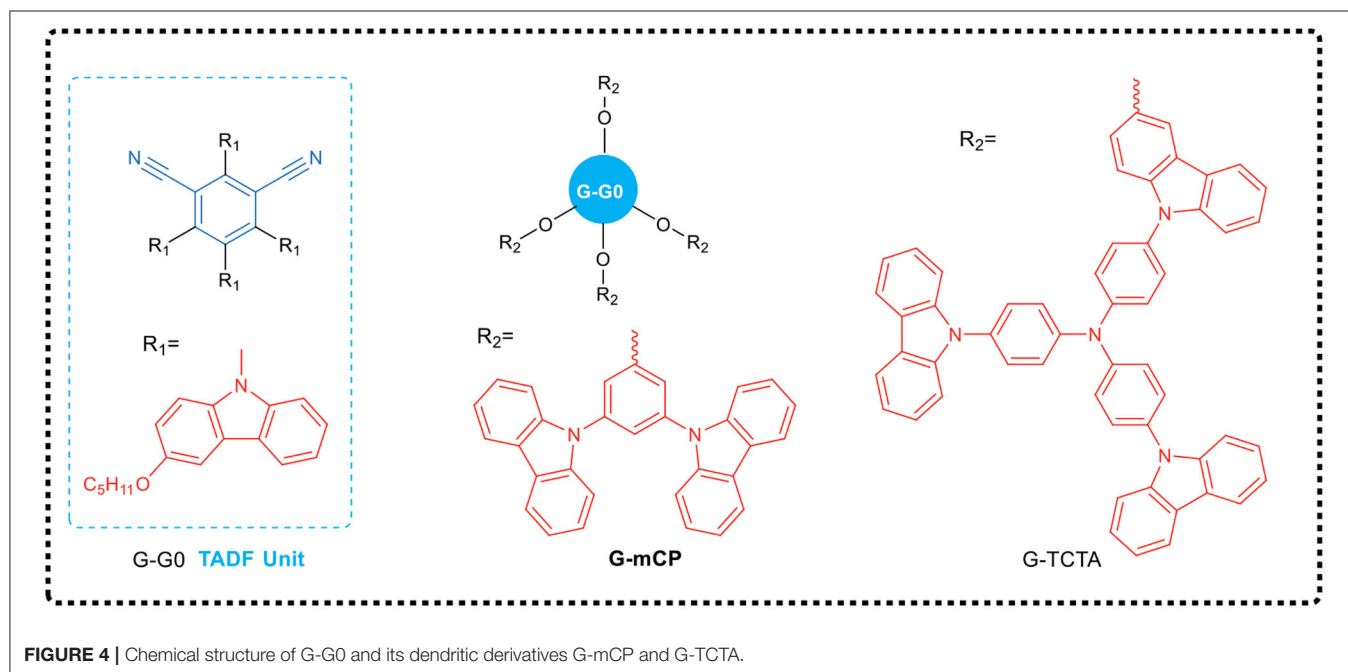
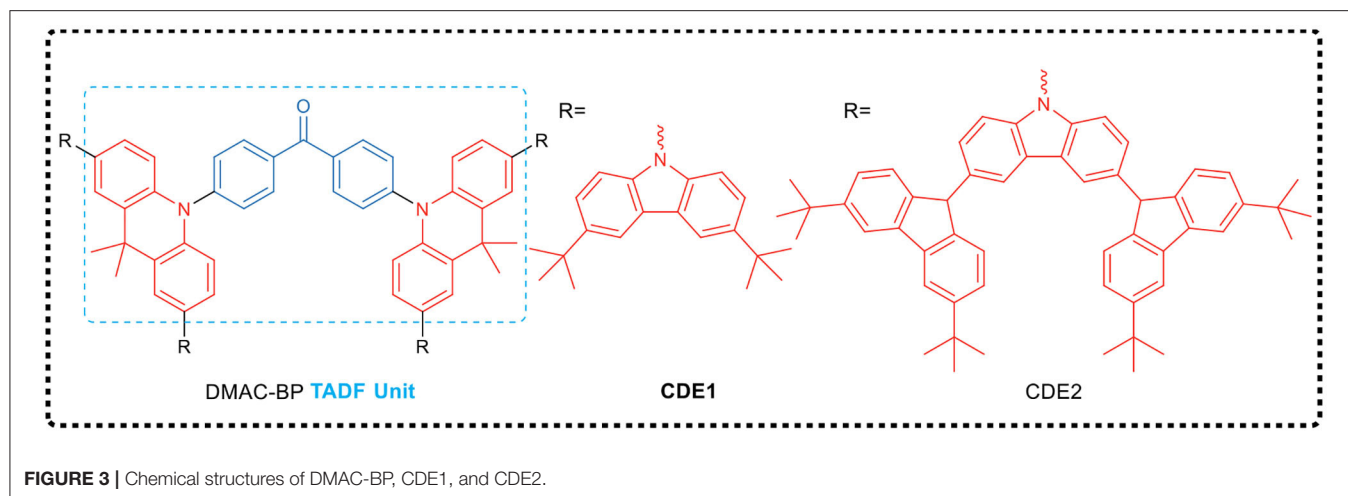
Yamamoto's team (Albrecht et al., 2015) has attempted a series of carbazole dendritic macromolecules (GnTAZ) with triphenyl-s-triazine nuclei, and successfully achieved a solution-processable non-doped high molecular weight TADF dendrimer. In their work, the singlet-triplet state energy splitting of the molecules was determined by fluorescence and phosphorescence spectroscopy measurements, and the  $\Delta E_{ST}$  was calculated to be 0.03, 0.06, and 0.06 eV for G2TAZ, G3TAZ, and G4TAZ, respectively, which is sufficiently low to allow inverse intersystem crossing from triplet state to singlet state at room temperature. Due to the intense overlap of HOMO and LUMO orbitals, G1TAZ exhibits non-TADF properties, while other dendrimers possess thermally activated delayed fluorescence. The pure spin-coated films of the GnTAZ ( $n = 2, 3, 4$ ) dendritic polymers also show TADF emission with a moderate PLQY, and a maximum EQE of 3.4% (G3TAZ) is acquired on the OLED devices fabricated with those polymers as the light-emitting layer.

Besides, Yang et al. (Li et al., 2016) proposed a strategy for preparing TADF emitters for solution process, i.e., polycarbazole encapsulation. They developed a green-emitting TADF core (DMAC-BP) and synthesized two TADF dendrimers (CDE1 and CDE2, exemplified in Figure 3). Both dendrimers had excellent thermal stability, good solution processability and significant TADF characteristics. For example, with CDE1 dendrimer as emission layer, a non-doped OLED prepared by solution process

shows a high EQE of 13.8%, demonstrating a complete harvest of all the excitons generated by the two parallel emission channels of TADF and the exciplex emission. It is worth noting that the EQE of the dendrimers was still as high as 13.3% even at the high brightness of  $1,000 \text{ cd}\cdot\text{m}^{-2}$ . This work, by combining the two parallel emissive channels, provided a novel and efficient design strategy for non-doped solution-processed TADF emitters.

Sun et al. (2018) designed and synthesized two new dendrimers (G-TCTA and G-mCP, see Figure 4), which had effective non-conjugated connections between TADF core (G-G0) and different excited complex dendrites. The dendrimer G-mCP exhibited a smaller  $\Delta E_{ST}$  (0.08 eV) and a higher PLQY (90%). As the photophysical properties of the TADF core and the function of exciplex in the dendrimer are independent as a result of the non-conjugated linkage, the solution-processed G-mCP non-doped device achieved a very low drive voltage of 2.7 V and a high power efficiency of  $46.6 \text{ lm}\cdot\text{W}^{-1}$  with a maximum EQE up to 16.5%.

The aggregation-caused quenching effect (ACQ) makes the material in the aggregated state weaken in fluorescence or even emit no fluorescence, which seriously affects the practical application of luminescent materials. To overcome this problem, through combination of aggregation-induced delayed fluorescence (AIDF) effect and a strategy of aggregation-induced emission (AIE) molecular design, Wang et al. (2019b) developed



TADF dendrimer which effectively improved the efficiency roll-off in solution-processed OLEDs.

Shao and Wang's group reported the design of spatial charge transfer hexaarylbenzenes (TSCT-HABs) containing circularly arranged electron donors (acridines/dendritic triacridines) and acceptors (triazines), as shown in **Figure 5**. In TSCT-HABs, the spatial p-p interaction between the donor and acceptor provided efficient full space charge transfer emission, and the spatial separation of donor and acceptor caused a  $\Delta E_{ST}$  of 0.04–0.08 eV, resulting in a delayed fluorescence (microsecond order). The results indicated that these propeller-like structured dendrimers exhibited TADF and AIE effects in OLEDs prepared by solution processing. The emission intensity of these dendrimers from the solution to the aggregated state is increased by 6–17 times. TSCT-HABs-based solid solution OLEDs had a maximum EQE

of 14.2%, making them one of the most efficient emitters of solid solution TADF OLEDs.

Using the traditional design principle of molecular charge transfer, Wang et al. (2019a) designed and synthesized two dendrimers CzTAZPO and sCzTAZPO with AIE and TADF characteristics, as shown in **Figure 6**. Both molecules had asymmetric D- $\pi$ -A configurations, in which triazine was used as the electron acceptor, the carbazole dendrimer as the electron donor, and the phenyl spacer as the  $\pi$ -bridge, forming a highly distorted conformation between a carbazole dendrimer and a phenyl spacer. In addition, a phosphorus oxy group was added to improve the electron transport performance. Theoretical calculations and experimental results showed that the increase in the number of carbazole dendrites led to an increase in the intensity of the fluorescent oscillator, while the  $\Delta E_{ST}$  value



decreased. CzTAZPO and sCzTAZPO showed significant AIE and TADF characteristics, and CzTAZPO-based non-doped OLEDs showed high efficiency ( $\text{EQE}_{\text{max}} = 12.8\%$ ) and low efficiency roll-off ( $<1.6\%$ ).

## Main Chain TADF Type Polymers

The design strategy of the main chain type TADF polymer is to connect the small molecule TADF unit into the main chain of the polymer by chemical bonding, wherein the electron donor and the electron acceptor can be completely and alternately connected (alternating D-A type) as the TADF unit to construct polymer backbone. A conjugated or non-conjugated functional unit might as well be introduced as a spacer group into the polymer backbone (interval B-T-B type) to modulate the photoelectric properties of the TADF polymer.

### Alternating D-A Type

In some TADF polymers, the electron donor and the acceptor are alternately connected as a TADF light-emitting unit, thus forming the backbone of the polymer. These polymers generally have a planar conjugated characteristic, which is advantageous for expanding the degree of conjugation and achieving high carrier transport performance, and a large rigid structure which is conducive to improving the radiation decay rate, thereby increasing the quantum luminescence yield (Zhang and Cheng, 2019). However, there is inevitable non-radiative transition inducing excitons dissipation due to potential conjugation and interactions between D/A units. On the other hand, the rigid configuration of the molecules makes the twist between D and A difficult, which results in the HOMO/LUMO still overlap spatially to a certain extent.

Adachi group (Lee et al., 2016) reported two D-A type  $\pi$ -conjugated TADF polymers (pCzBP and pAcBP) whose backbones were composed of electron donor carbazole or an acridine group and electron acceptor diphenyl alternately for the first time. The synthesized TADF polymers exhibited smaller  $\Delta E_{\text{ST}}$  (0.18 and 0.10 eV). Theoretical calculations showed that the HOMO was mainly located in the electron donor unit, carbazole or acridine, and the LUMO mainly in the electron acceptor unit, benzophenone. Experiments that the delayed emission intensity with the microsecond lifetime decreased when the temperature dropped from 300 to 50 K, confirm the TADF characteristics of the polymers. The green emitting OLEDs had EQE of 8.1% (pCzBP) and 9.3% (pAcBP), respectively, and the EQE remained as high as 8.0% even at a high luminance of  $1,000 \text{ cd}\cdot\text{m}^{-2}$ .

Huang et al. (Hu et al., 2018) reported a main-chain blue TADF polymer (P0, **Figure 7**), which was alternately connected by electron-deficient diphenylsulfone and electron-rich trianiline. The doped OLED device prepared by solution treatment of P0-based TADF polymer exhibited pure blue emission with a Commission Internationale de l'Eclairage (CIE) coordinate of (0.16, 0.10) and a maximum EQE of 5.3%. In their work, a series of color-tunable polymers had also been developed by incorporating triphenylamine functionalized triazine group, a narrow bandgap unit which could control the emission color of the polymer. These polymers exhibited delayed fluorescence and emitted light from sky-blue to blue-green, and the luminous

efficiency was significantly improved. It has been demonstrated that a blue-green PLED based on polymer P3 possesses a maximum EQE of 8.7%.

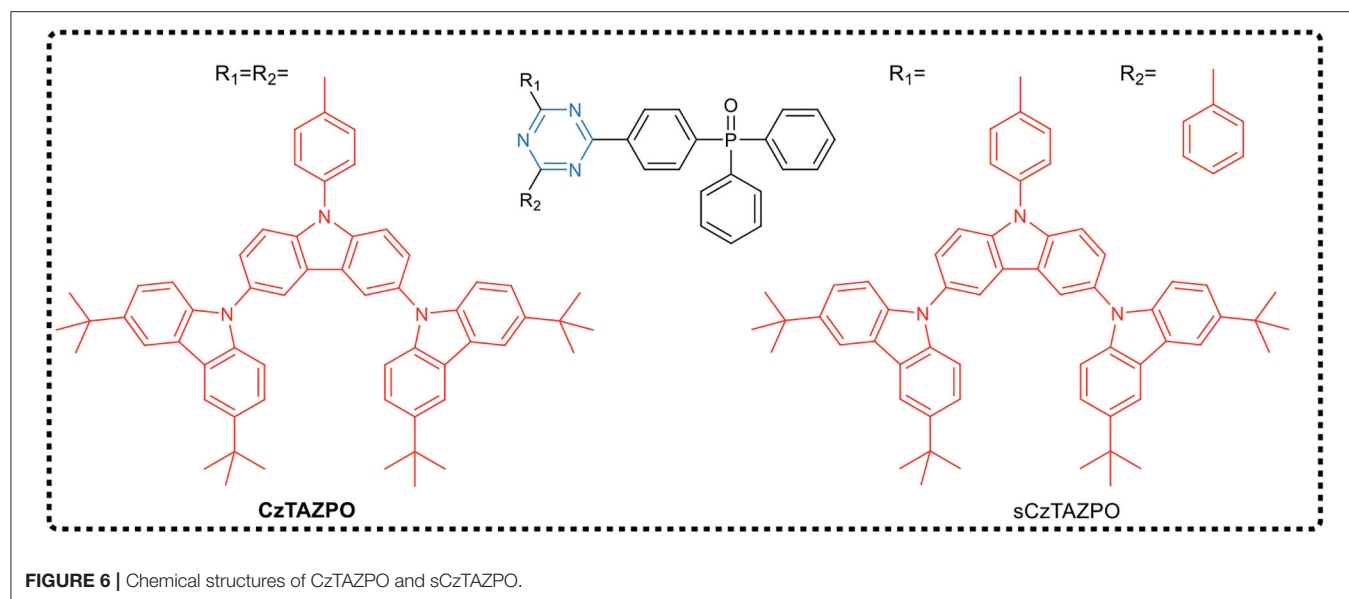
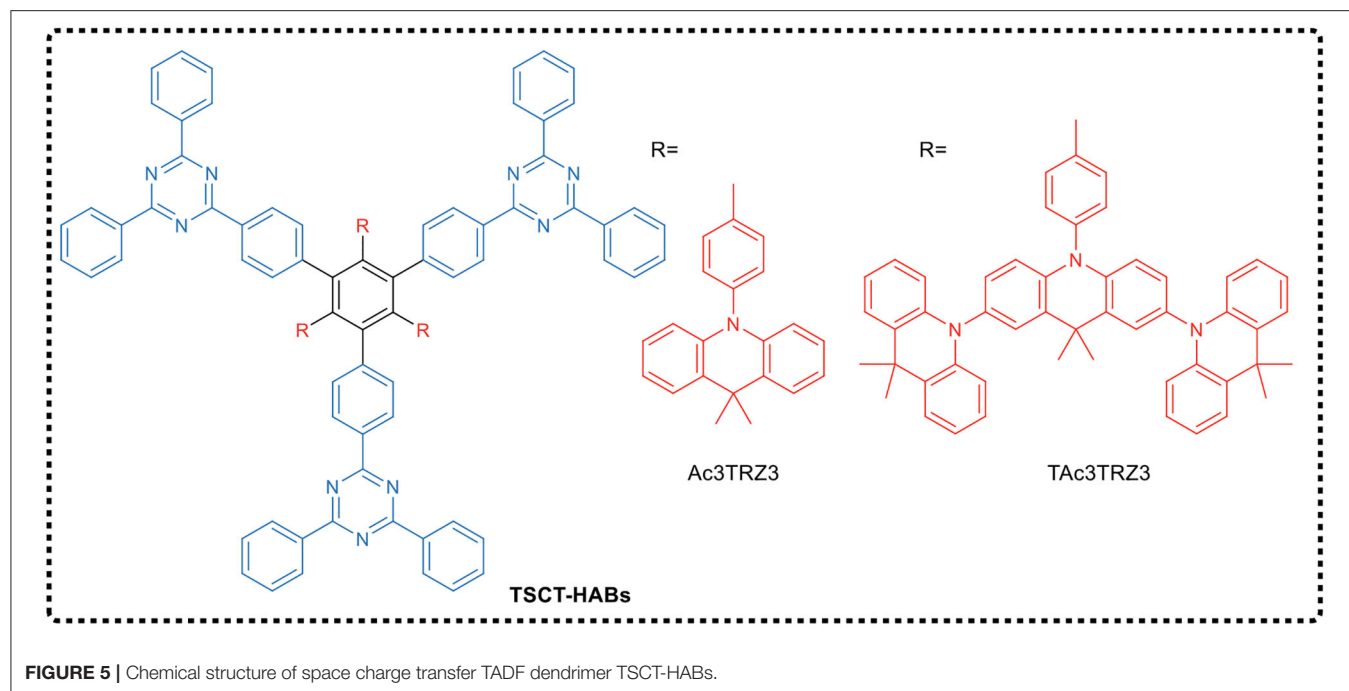
### Interval B-T-B Type

Organic electroluminescent devices based on TADF luminescent molecules often have serious efficiency roll-off problems during service, which is mainly due to the concentration quenching caused by the long lifetime of triplet excitons. For this case, the molecular excited states have microsecond life, which leads to the increase of exciton concentration and formation of "hot" exciton that destroys the chemical bonds of the luminescent molecules, finally resulting in a decay process of the device (Cai and Su, 2018). Therefore, the designing strategy should concentrate on introduction of the backbone spacer group to prevent the aggregation of the TADF emitter center. This spacer group should have a certain steric hindrance, reduce the conjugation degree of the main chain, improve the triplet energy level of the main chain, and avoid the quenching of the triplet excitons. In the interval B-T-B type TADF polymer, a conjugated or non-conjugated functional unit as a spacer group is introduced, so the emitter centers on the main chain are separated from each other, without forming a conjugated system, thus possibly regulating the photoelectric properties of TADF polymer.

In 2015, Nikolaenko et al. (2015) proposed a strategy called "intermonomer TADF" in which TADF active units were indirectly prepared from the polymerization of donor and acceptor monomers. During the polymerization process, the monomeric CT emitter was formed from the donor triphenylamine and the acceptor triphenyltriazine monomer, which could serve as charge transport units. And a host material with a high triplet energy level, 2,2',5,5'-tetraethyl-1,4-diphenylbutane, was connected to the main chain as a spacer unit to co-construct a TADF emitter polymer as shown in **Figure 8**. This molecule construction not only effectively avoided the aggregation of TADF active center, but also inhibited the quenching problem caused by aggregation and triplet-triplet annihilation. Furthermore, it greatly improved the solubility of the polymer, which was beneficial to the preparation of solution processable OLED. A non-doped OLED device prepared by solution method, in which the synthesized intermonomer TADF polymer acted as emitting layer, emitted in a green region, having a maximum EQE up to 10%, and a CIE coordinate of (0.32, 0.58).

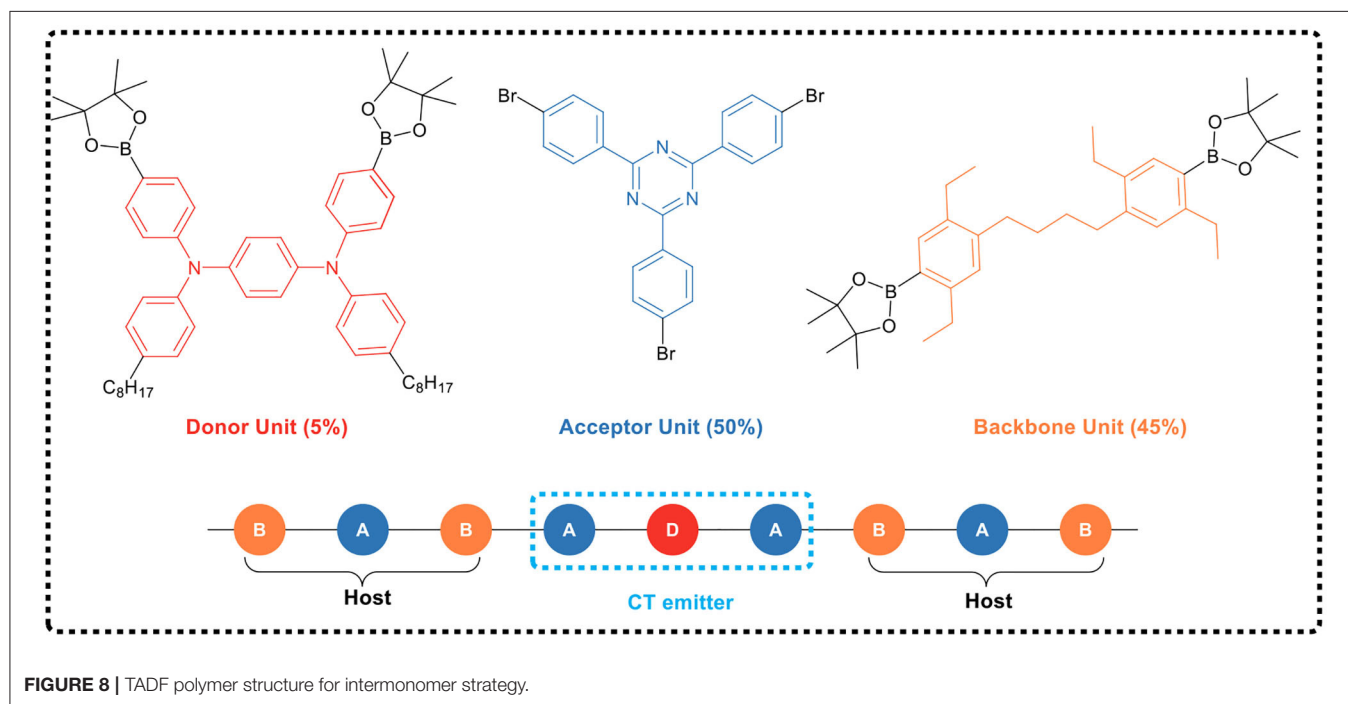
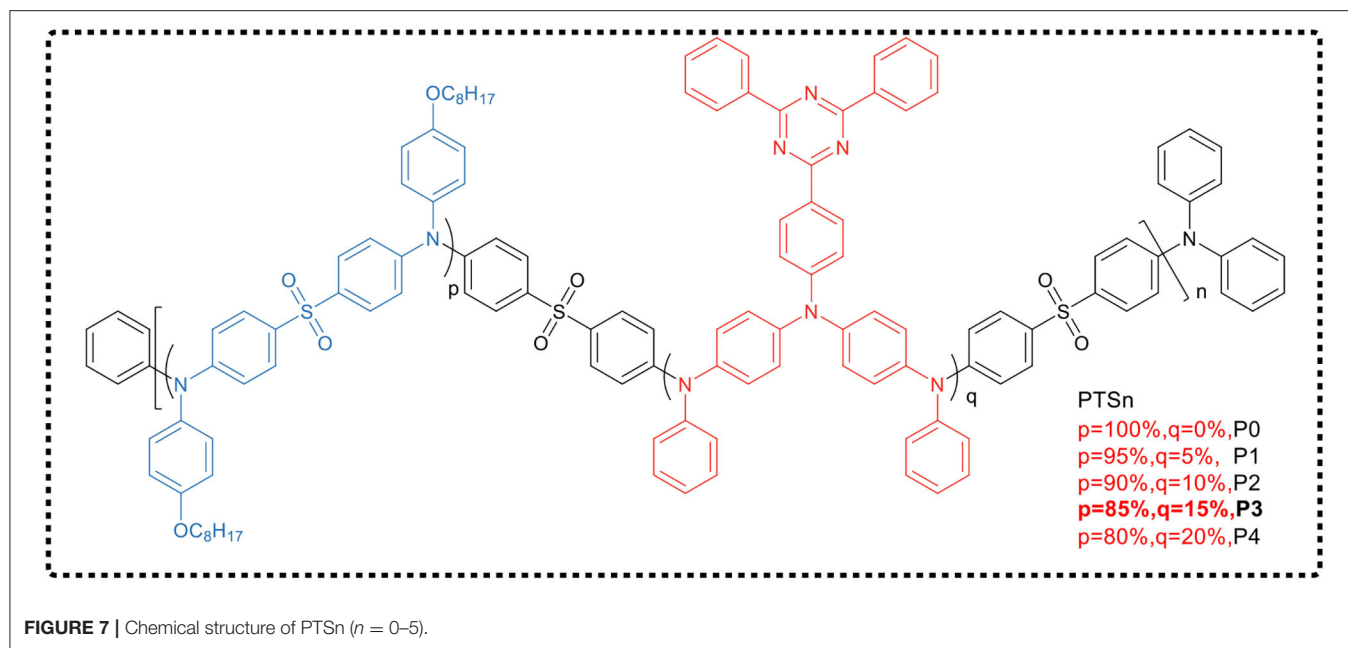
Liu et al. (2019) reported new conjugated and non-conjugated interval B-T-B type TADF polymers, which effectively reduced the steric resistance of the spacer element, avoided the quenching of the triplet excitons, and significantly improved EQE with low efficiency roll-off.

The research group directly embedded the small molecule blue TADF emitter (BOPAC-TRZ) into the poly (arylether) (PAE) backbone to synthesize the blue TADF polymer, as shown in **Figure 9**. In this polymer, the oxygen atoms could not only interrupt the conjugation to maintain the high  $E_{\text{T}}$  of the polymer backbone, but also inhibit electron transport between adjacent TADF fragments to avoid red shift. Since the oxygen-induced electron transport among adjacent TADF units was negligible, the corresponding blue delayed fluorescence property of the TADF



small molecule could be inherited by the synthesized polymer. Through device optimization, the efficiency of the PLED based on P(BOPACTRZ-BPA) reaches 29.7 cd/A (21.2 lm/W, 13.2%) with a small roll-off, and the CIE coordinate is (0.18, 0.32). Recently, the team (Rao et al., 2020) made breakthroughs in conjugated TADF polymers. They designed a variety of methyl substituted phenylene linking units as backbone spacer groups, and through polymerization of these groups with D-A-D TADF fragments (AcBPCz), successively synthesized a series of TADF conjugated polymers, Poly(AcBPCz-P), Poly(AcBPCz-DMP), and Poly(AcBPCz-TMP), as shown in **Figure 9**. Interestingly,

they found that with the increase of the number of methyl substituents on the phenylene group, the  $\Delta E_{ST}$  of the polymer gradually decreased, and the TADF emission gradually enhanced. The experiments show that the conjugated polymer Poly(AcBPCz-TMP) having tetramethyl-substituted phenylene group as linking unit exhibited almost the same TADF effect and excellent electroluminescence properties as the TADF emissive small molecule AcBPCz. The corresponding solution-processed monochromatic OLED device exhibited blue-green emission with a wavelength of 507 nm and a maximum EQE of 23.5% (68.8 cd/A, 60.0 lm/W). By mixing orange-red light TADF emitter



NAI-DMAC into the Poly(AcBPCz-TMP) luminescent layer, a warm white optical device was prepared, in which the CIE coordinate was (0.36, 0.51), and the maximum EQE reached 20.9% (61.1 cd/A, 56.4 lm/W).

### Backbone-Donor/Pendant-Acceptor Type TADF Polymers

In the above strategy, the electron donor and the electron acceptor are alternately arranged in the main chain backbone.

The alternating D-A conjugated polymer is mostly of a planar geometric feature, which is advantageous for expanding the conjugation and achieving high charge transfer, and the rigid configuration is favorable for high rate of radiation decay so as to obtain high PL quantum yield. However, this results in an inevitable large spatial overlap of the HOMO/LUMO of the donor and acceptor. In this case, the polymer generally requires higher exchange energy, while the latter greatly limits the lowering of singlet–triplet energy splitting [ $\Delta E_{ST}$  close to

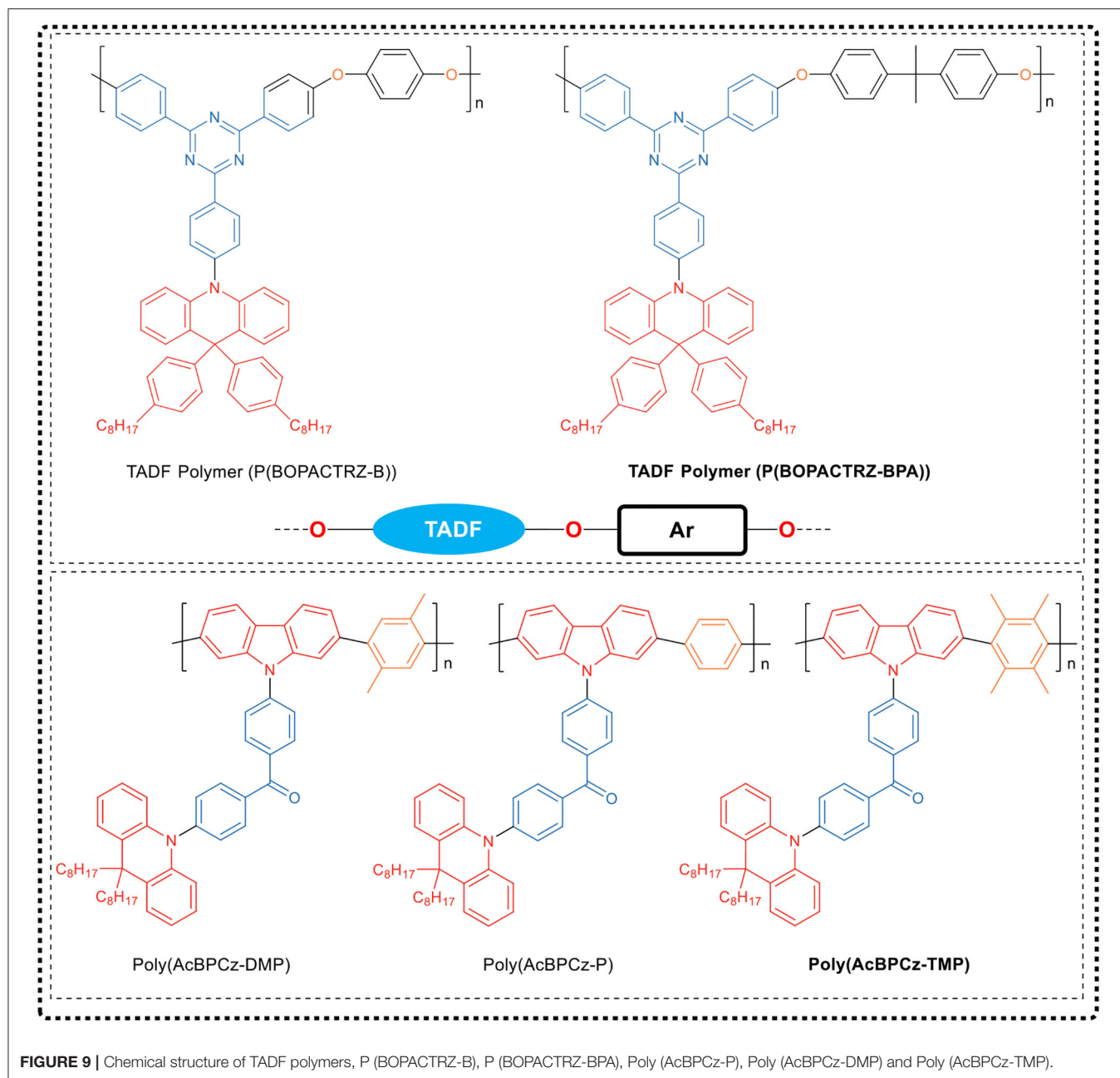


**FIGURE 9** | Chemical structure of TADF polymers, P (BOPACTRZ-B), P (BOPACTRZ-BPA), Poly (AcBPCz-P), Poly (AcBPCz-DMP) and Poly (AcBPCz-TMP).

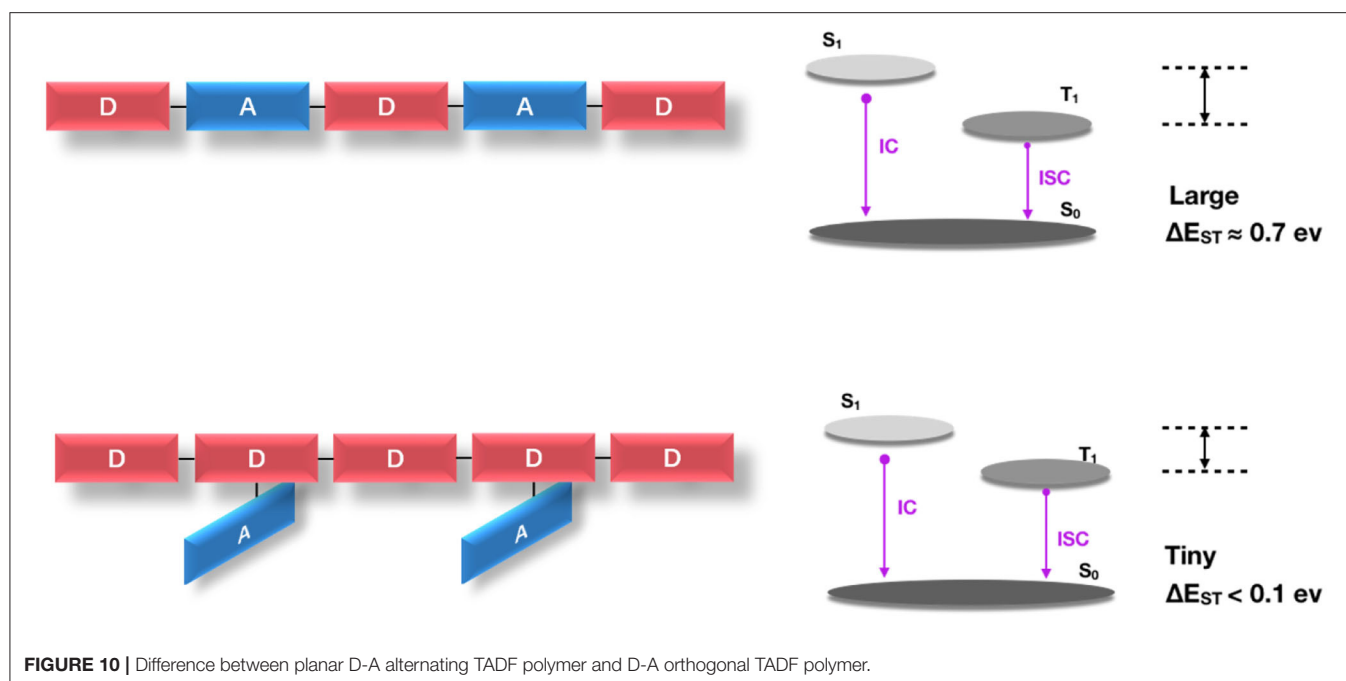
0.7 eV (Köhler and Bässler, 2009)], and thus is not conducive to obtaining an effective TADF effect.

It has been proved theoretically and experimentally (Tao et al., 2014) that highly efficient D-A-linked pure organic TADF molecules mostly require an almost orthogonal structure of the donor and acceptor to reduce the HOMO/LUMO overlap of each other. However, as **Figure 10** shows, the D-A orthogonal configuration of TADF polymer usually has large steric hindrance, so it is difficult to synthesize D-A orthogonal structure in the main chain backbone. Whereas, in the TADF polymer designed by the Backbone-donor/ Pendant-acceptor (BDPA) strategy, the electron donor unit is fixed on the

backbone of the conjugated polymer, and the electron acceptor is grafted on the side chain orthogonally. The donor is delocalized throughout the polymer backbone so that it has a conjugated property to ensure more efficient charge injection and transfer characteristics. In addition, there is a certain twist between the D-A, which is beneficial to the further separation of the molecular frontier orbitals to obtain a very small  $\Delta E_{ST}$ . This twisted D-A structure can be retained along the suspension direction in the polymer to ensure the TADF emission characteristics and achieve high efficiency of delayed fluorescence.

Nobuyasu et al. (2016) reported this type of TADF polymer for the first time. In their work, the electron donor was





used as the main chain backbone, and the electron acceptor was introduced into the side chain to synthesize TADF emitter (PTZ-DBTO<sub>2</sub>) based on the phenothiazine donor and benzothiophene-s,s-dioxide acceptor. The donor and acceptor were covalently linked in a nearly vertical direction, creating a condition of  $\Delta E_{ST} < 0.05$  eV in zeonex. The device made of PTZ-DBTO<sub>2</sub> shows an excellent performance, with an EQE of approximately 19%. Furthermore, they introduced dibenzothiophene unit into the backbone of the main chain, and then through copolymerizing with TADF small molecule, obtained a green light-emitting TADF polymer (COPO2) with strong conjugated structure. This COPO2 polymer emitted redshift, but had almost the same performance as the monomer PTZ-DBTO<sub>2</sub>. The OLED device based on COPO2 reached a maximum EQE of 11.05%. The research showed that the TADF performance of the designed COPO2 polymer depended on the performance of the PTZ-DBTO<sub>2</sub> emitter core. To inhibit intramolecular and intermolecular exciton concentration quenching, Liu et al. (2018b) further copolymerized conjugated spacer units and TADF emitting monomers. Based on the above-mentioned TADF unit (PTZ-DBTO<sub>2</sub>), carbazole derivative was introduced into the main chain of the conjugated polymer. It was found that the content of the carbazole derivative unit could not only effectively suppress exciton quenching and non-radiative transition, but also control the distribution of molecular orbitals and  $\Delta E_{ST}$  values, and could even adjust the properties of excited states. As the proportion of carbazole derivatives increased, the LUMO and HOMO energy levels of these TADF polymers increased, while the total energy gap and  $\Delta E_{ST}$  decreased. Thus, three TADF polymers (HOMO, COP-50, COP-10) were synthesized by introducing different amounts of carbazole derivatives, wherein COP-10 showed a relatively high

RISC rate and PLQY in film-state. Non-doped OLED devices based on COP-10 could achieve a maximum EQE of 15.7% at a lower turn-on voltage of 3.2 V and CIE coordinate of (0.46, 0.49).

In 2016, Cheng et al. (Zhu et al., 2016) proposed the concept of Backbone-donor/Pendant-acceptor and synthesized two alternative conjugated polymers PAPCC and PAPTC by improved Suzuki coupling copolymerization (see Figure 11). Among them, the donor was the commonly used wide bandgap carbazole and 9,10-dihydroacridine derivative unit, and a conjugate main chain having a high triplet level was obtained by 3,6-position copolymerization. The phenyl unit containing the electron-withdrawing group cyano or triazine was used as acceptor, which, as side chain, was chemically bonded to the N atom of 9,10-dihydroacridine that has a large dihedral angle to form pre-twisted intramolecular charge transfer structure. Time-density functional theory calculation indicated that in these two polymers, the HOMO delocalized over the entire backbone, while the LUMO located on the side of the acceptor. The high separation of HOMO and LUMO orbitals allowed the polymer to exhibit a relatively small  $\Delta E_{ST}$  (PAPCC: 0.37 eV and PAPTC: 0.13 eV), achieving a maximum EQE of 12.6% in solution-processed PAPTC polymer OLEDs, with emission at 521 nm. Cheng's work provided evidence that the BDPA strategy could be used for the molecular design of new TADF polymers.

In order to further improve the EL performance of the device, Wang et al. (2018a) chose a more rigid acceptor, replacing tert-butyl group with benzene ring on the parent of triazine, and synthesized TADF emitting unit ATD [10-(4-(4-(4-6-diphenyl 1,3,5-triazine-2-) phenyl)-9,9-dimethyl-9,10-dihydroacridine)]. By copolymerizing ATD-Br<sub>2</sub> with two carbazole monomers, four conjugated polymers PCzATD<sub>x</sub> (x represents the molar content

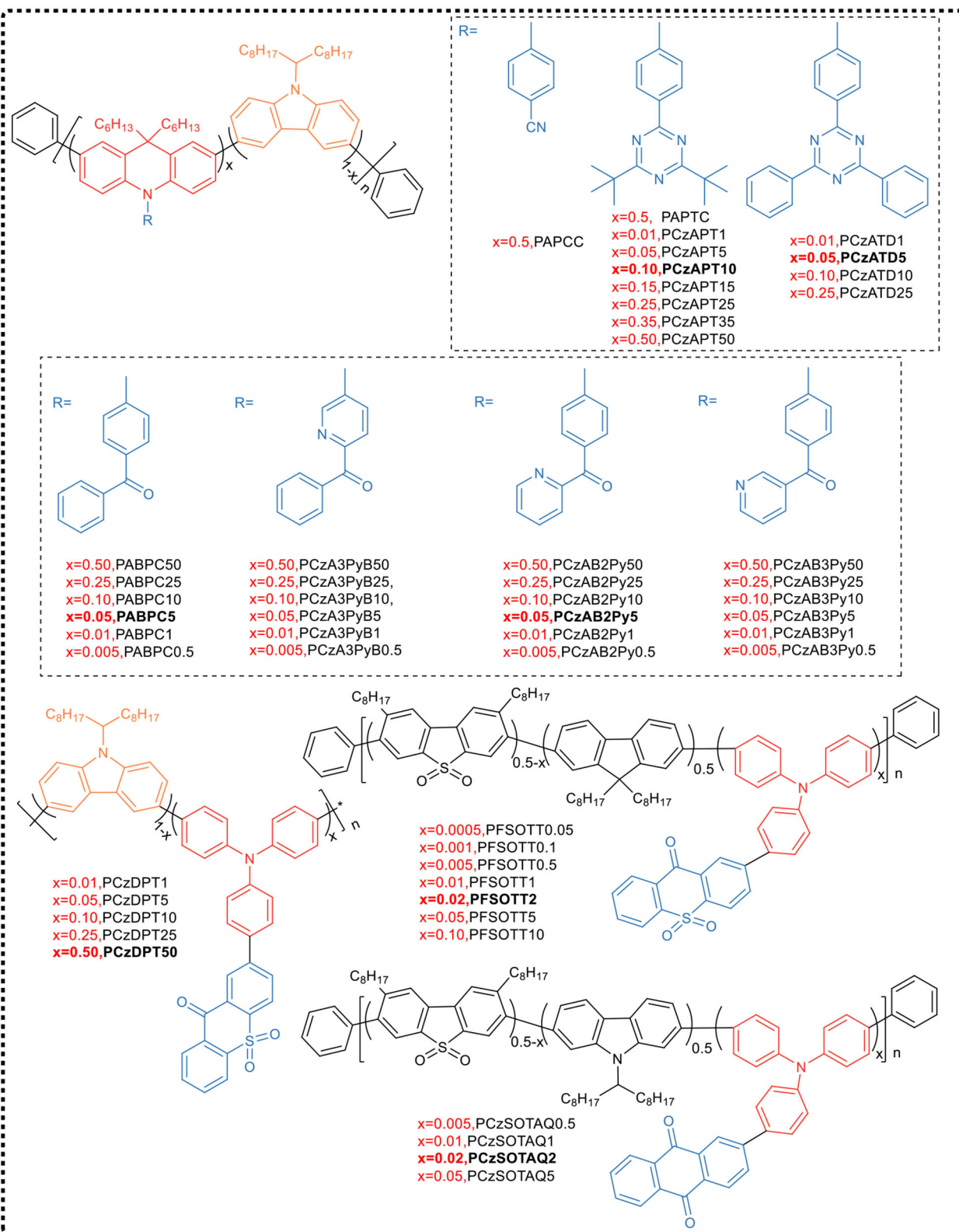


**FIGURE 11 |** Chemical structure of the BDPA-type TADF polymer reported by the Cheng's team.

of ATD unit) were prepared. The experiments indicate that the TADF property of the small molecule ATD was completely retained in the polymer, showing a higher PLQY and a relatively small  $\Delta E_{ST}$  value in the neat film. EL devices exhibited yellow emission with a maximum EQE of 15.5% and a PE of 50.5 lm W<sup>-1</sup>. More importantly, these devices exhibited low turn-on voltage of 2.53 V and low drive voltage of 4.05 V at 1,000 cd m<sup>-2</sup> with a very low efficiency roll-off rate of only 0.5%, benefiting from the charge injection/transport in the polymer and the balance of the conjugate backbone.

To inhibit the intra- and inter-chain quenching process further, Cheng attempted to copolymerize TADF monomers with two carbazole monomers, and by adjusting the molar feed ratio, synthesized a series of conjugated polymers PCzAPT<sub>x</sub> with different TADF units (Zhu et al., 2018) (**Figure 11**). In these polymers, the carbazole oligomer, as a “block,” effectively regulated the distance between the TADF chromophores, suppressing the triplet quenching effect in the film. It has been found that the emission quenching process in polymers originated from intra- and inter-chain interactions between TADF chromophores, which depended to a large extent on the content of the APT TADF unit. By increasing the content of the carbazole block, PLQY increased from 50.0% (PCzAPT50) to 92.1% (PCzAPT10). The non-doped OLED device based on PCzAPT10 emitted yellow-green color, and had a maximum EQE of 16.9% and a low efficiency roll-off. Even at the brightness of 1,000 cd m<sup>-2</sup>, the EQE reached 15.6%, which was equivalent to 92.3% of the maximum EQE.

Despite this, the team members continuously synthesized a series of TADF conjugated polymer PABPC using the same carbazole/acridine donor as the backbone structure and the diphenyl ketone (BP) acceptor as the side chain pendant group (Yang et al., 2018a) (**Figure 11**). The TADF behavior was improved by controlling the content of ABP units in the polymer. In the pure film of PABPC5 with 5% mole content of ABP units, PLQY reached as high as 0.77. The best EL performance achieved in PABPC5-based device, such as a maximum EQE of 18.1% and a very slow efficiency roll-off with EQE of 17.8% at the brightness of 1,000 cd·m<sup>-2</sup>.

Based on the above-mentioned backbone structure, the team selected three isomers of benzoylpyridine derivatives with stronger electron-withdrawing ability than benzophenone as pendant acceptor groups, and regulated the side chain pendant unit to obtain long-wavelength emission. Three sets of corresponding conjugated polymers (PCzA3PyB, PCzAB2Py, and PCzAB3Py) were synthesized according to the BDPA strategy (Yang et al., 2019a). All polymers in the three series exhibited emission red-shift and distinct TADF characteristics, with a short microsecond delay lifetime (0.56 to 1.62  $\mu$ s) and a small  $\Delta E_{ST}$  (0.10–0.19 eV), compared to polymers with acceptor of dibenzophenone. Similarly, the different substitution patterns of pyridyl groups in the acceptor moiety also produced significant changes in PL properties. In PCzA3PyB, direct bonding of the pyridyl group to the main chain acridine unit resulted in a large red-shift of the polymer but a lower PLQY. On the contrary, distally linked pyridyl group separated by a benzoyl group caused a small red-shift but a higher PLQY in PCzAB3Py. In contrast,

the preferred substitution of the pyridyl group is that the group is immobilized at the 2-position of the carbonyl group and located at the distal end of the acceptor moiety, forming a polymer with intramolecular hydrogen bonding and a phenyl linker, thereby synergistically providing a large red-shift and high PLQY. Using pure polymer film as the emitting layer in the corresponding device, PCzAB2Py5 showed better overall EL performance, with a maximum EQE of 11.9%, a low turn-on voltage of 3.0 V, and yellow light emission wavelength of 573 nm. It was worth mentioning that its efficiency roll-off rate was relatively low, with an EQE of 11.6% at the brightness of 1,000 cd·m<sup>-2</sup>.

Cheng's group (Wang et al., 2017) embedded the donor of TADF unit 2-(4-(diphenylamino)-phenyl)-9H-thioxanthone-9-9-10,10-dioxide (TT) into the main chain, and through copolymerizing with alternative fluorene and dibenzothiophene—s,s—dioxide fragments synthesized a series of BDPA TADF polymers (PFSOTT<sub>x</sub>). The twisted donor—acceptor structural units were covalently bonded to its donor fragment on the main chain, and the polymer had excellently inherited the characteristics of TADF small molecules used as monomers in copolymerization. By balancing the emission from the main chain and the TADF unit, the non-doped OLED exhibited white emission with CIE coordinate of (0.32, 0.31). According to the density functional theory calculations, HOMO mainly delocalized on the triphenylamine and fluorene segments, while LUMO localized on the side chain acceptor with a small overlap of HOMO-LUMO to ensure TADF characteristics. In addition, in a doped TADF polymer-based device with controlled TADF element content, the EQE with warm white emission was close to 10% and up to 19.4% with bright orange emission. One year later, they (Wang et al., 2018b) synthesized a series of BDPA-type conjugated polymers PCzDPT<sub>x</sub> composed of different contents of 3,6-carbazole and thioxanthone dioxide (DPT). It was found that the degree of conjugation increased with the increase of content of DPT unit in the PCzDPT<sub>x</sub> series polymer. The energy transfer between the carbazole fragment and the DPT unit occurred, and the emission peak gradually red-shifted. When the DPT content was 50%, PCzDPT50 polymer emitted red light. Similarly, the alternating copolymer PTD that contains 50% of DPT units emitted saturated red light. The doped PLEDs prepared based on the polymers PCzDPT50 and PTD produced saturated red electroluminescence, with CIE coordinates of (0.63, 0.37) and (0.64, 0.36), respectively. Clearly, it was feasible to control the emission color and improve the device EL performance by rationally designing and selecting suitable donors and acceptors, such as using long conjugated structures and rigid groups to suppress internal conversion rate through energy matching.

However, it is challenging to achieve a smaller  $\Delta E_{ST}$  and a higher PLQY for orange to red TADF emitters due to high non-radiative internal conversion rates. Considering those problems, Xie and co-workers (Zhan et al., 2020) built, on their previous works, and selected a rigid anthraquinone group with the stronger electron-withdrawing ability to form a narrow bandgap TADF unit (TAQ). In comparison with fluorene group, the carbazole ring with stronger electron donating ability was

introduced into the main chain, acting a better hole-transporting role. It was confirmed that the maximum emission peaks of the polymer PCzSOTAQx exhibited clear red shifts of 1–19 nm compared to PFSOTAQx. Impressively, the carbazole-based polymers PCzSOTAQx displayed better performances. This series of polymers showed higher PLQY (75%) and relatively smaller  $\Delta E_{ST}$  values (0.12 eV) in the neat film. Especially, the OLED based on PCzSOTAQ2 achieved the saturated red emission with CIE coordinate of (0.62, 0.37) and a maximum EQE of 13.6%, which is the best one of the solution-processed OLEDs based on red TADF polymers reported so far. These results demonstrated that the red emission of conjugated polymer could be achieved simply by enhancing the strength of pendant acceptor and/or backbone donor, which supplied a useful guidance for the design and syntheses of efficient red-emitting TADF materials.

Friend's group (Freeman et al., 2017) designed a fully conjugated polymer ASFCN with donor and acceptor close to orthogonal configuration, which effectively eliminated the HOMO/LUMO overlap problem, making  $\Delta E_{ST}$  small enough ( $<0.1$  eV) to be overcome by heat and obtaining the TADF effect. They designed the synthesis of TADF polymers by using the acceptor as a side chain orthogonal to the donor backbone, which could greatly reduce the spatial overlap of the molecular frontier orbitals, ensure the conjugate along the polymer backbone, and retain the processability of the material and charge transport characteristics.

Park and Choi et al. (Kim et al., 2018) synthesized a green light-emitting TADF polymer P (DMAC-Cp) by introducing 1,1-diphenylcyclohexane (Cp) into the main chain of DMAC-TRZ. The introduced Cp not only acted as a linking group between the conjugated monomer units in the polymer emitter structure, breaking the conjugation along the polymer backbone, but also was conducive to regulating the solubility of the polymer. This novel polymer emitter possesses a very small  $\Delta E_{ST}$  (0.023 eV) between the lowest singlet state and the triplet excited state. The TADF-OLED device, prepared by P(DMTRZ-Cp) polymer film emitter, exhibited a maximum EQE of up to 15.4% under green emission.

## Side Chain Type TADF Polymer

The main chain type TADF polymer is easy to form a large conjugated structure, while the synthesis is difficult due to the steric hindrance effect. Besides, those polymers have less advantage in the processing and preparation of the device for their inferior solubility and meltability.

In the side chain type TADF polymer, the TADF active unit is introduced as a pendant group into the conjugated or non-conjugated polymer backbone structure by chemical bonding. Due to the small conjugation effect of the polymer backbone, this type of TADF polymer supplies strategy to simply and efficiently achieve blue emission.

## Conjugated Backbone

Yang et al. (Luo et al., 2016) first proposed a side chain engineering strategy for the development of TADF polymers in 2016, grafting active units with TADF behavior to the side

chain positions of the polymer to achieve delayed emission. Since carbazole had a high triplet energy level and good hole transporting ability, it could be used as a main chain backbone of TADF polymer. When carbazole was grafted with different functional units (PXZ-OXD, TPA and Cz), a range of copolymers with different proportions of PXZ-OXD component, such as PCzn, could be synthesized through Suzuki copolycondensation. Among them, the polymer PCz12 showed the highest PLQY (33.7%). The PLED device prepared by this copolymer as a light-emitting layer had a maximum EQE of 4.3%, the peak EL wavelength of 506 nm, and the exciton utilization efficiency of 63.7%.

Xie et al. (2017) demonstrated in a further study that the side chain engineering strategy was an effective design concept for the synthesis of TADF polymers. Through Suzuki polycondensation of monomers M1, M2, and M3 under the feed molar ratio of 10:40:50, the authors obtained copolymer PCzDP-10 containing a high percentage of TADF components (72%), which exhibited up to 74% PLQY in an oxygen-free film state. By optimizing the device structure and energy transfer from the backbone to the TADF unit, the device based on the blue-green fluorescent polymer film achieved a maximum EQE of 16.1% at the brightness of approximately 100  $\text{cd}\cdot\text{m}^{-2}$ , with CIE coordinate of (0.22, 0.40).

Based on the conjugated polymer, polyfluorene (see **Figure 12**), Yang et al. (2018b) regulated the conjugate length of the main chain by introducing 3,3'-dimethyldiphenyl ether on the backbone, and increased the triplet energy level of the main chain in the PFDMPPE-based polymer from 2.16 to 2.58 eV to avoid the loss of triplet excitons. When red TADF emitter 2-(N-(4-oxoxyphenyl) diphenylamino)-4'-indole (ROC8) was further introduced as a side chain, an effective energy transfer from the host (PFDMPPE) to the guest (ROC8) occurred in the solid state. The corresponding polymers (PFDMPPE-R01 to PFDMPPE-R10) exhibited distinct red TADF properties with a delayed fluorescence lifetime of 126–191  $\mu\text{s}$  and a PLQY of 0.18–0.55. Among these polymers, PFDMPPE-R05 exhibited the best device performance, with a bright red electroluminescence peak at 606 nm, and the current efficiency of 10.3  $\text{cd}/\text{A}$  when EQE = 5.6%. However, the HOMO energy level of the host of fluorene and 3,3'-dimethyldiphenyl ether copolymer was 6.03 eV, which introduces a large hole injection barrier between the copolymer and the ITO anode modified by PEDOT:PSS, leading to a high device's turn-on voltage.

During immediate past, the group (Yang et al., 2019b) further selected carbazole that possesses a stronger electron donating ability instead of fluorene, designing and synthesizing red light TADF polymers (PCzDMPE-R03 ~ PCzDMPE-R10, see **Figure 12**) based on the main chains of carbazole and 3,3'-dimethyldiphenyl ether via Suzuki polycondensation. Compared with the red light TADF polymer based on the main chain of fluorene and 3,3'-dimethyldiphenyl ether copolymer, the new copolymers benefitted from the increase of the HOMO level of host and the improvement of hole injection ability. PCzDMPE-R07 showed the best performance of non-doped devices, including that the maximum current efficiency and EQE



Chemical structures of side chain TADF polymers PFDMPe-R01 to PFDMPe-R10 and PCzDMPe-R03 to PCzDMPe-R10.

The figure displays two polymer architectures. The top architecture is for PFDMPe polymers, featuring a host polymer with two indole-based side chains. The first side chain has two octyl groups (C<sub>8</sub>H<sub>17</sub>) and a phenyl ring. The second side chain has one octyl group (C<sub>8</sub>H<sub>17</sub>) and an 8-phenyloxyoctyl group ((CH<sub>2</sub>)<sub>8</sub>O). The second architecture is for PCzDMPe polymers, featuring a host polymer with two indole-based side chains. The first side chain has two octyl groups (C<sub>8</sub>H<sub>17</sub>) and a phenyl ring. The second side chain has one octyl group (C<sub>8</sub>H<sub>17</sub>) and an 8-phenyloxyoctyl group ((CH<sub>2</sub>)<sub>8</sub>O). Both architectures include a ROC8 TADF unit, which is a 2,2',6,6'-tetrakis(4-phenylphenyl)-5,5'-bibenzofuran derivative. The polymers are defined by the mole fraction *x* of the ROC8 TADF unit: PFDMPe-R01 (*x*=0.01), PFDMPe-R05 (*x*=0.05), PFDMPe-R07 (*x*=0.07), PFDMPe-R10 (*x*=0.10), PCzDMPe-R03 (*x*=0.03), PCzDMPe-R05 (*x*=0.05), PCzDMPe-R07 (*x*=0.07), and PCzDMPe-R10 (*x*=0.10).

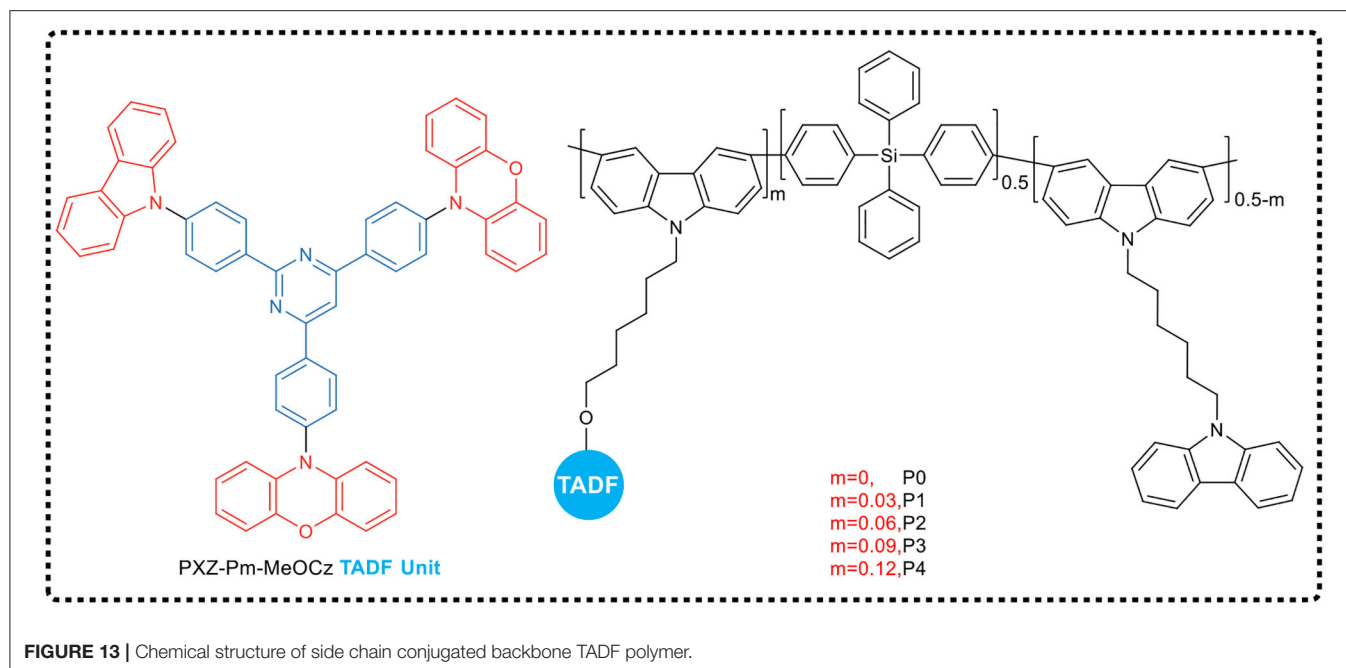


**FIGURE 13 |** Chemical structure of side chain conjugated backbone TADF polymer.

a series of TADF polymers by adjusting the ratio of dispersing units to TADF units in the polymer. It was found that the benzene ring in the side chain acted as a spacer unit which effectively prevents aggregation of the TADF unit and suppresses internal transition effect and TTA effect. With the increase of benzene ring content, the emitting efficiency of the polymer gradually enhanced, and simultaneously, the emission peak blue-shifted to some extent.

Lee et al. (Li et al., 2019a) developed a series of non-conjugated deep-blue TADF polymers based on polyethylene to produce highly efficient non-doped solution-processed PLEDs. In their designing strategy, an appropriate 9,9-dimethyl-10-phenylacridine (BDMac) with high triplet energy ( $E_T = 3.38$  eV) was incorporated as the host unit, which suppressed triplet energy from pendant emitter unit returning to the host, and thus prevented the device from performance deteriorating and promoted injection and transport of holes in the emitting layer. The deep-blue side chain pendant emitter had an extremely high PLQY of 90% and a suitable HOMO level ( $-5.50$  eV), which is beneficial to synthesize polymers with unique TADF properties by adjusting the ratio of the bulk unit to the light-emitting unit. PLEDs based on these polymers as single emissive layers had a maximum EQE of 5.3%, an EL emission at 436 nm, and a CIE coordinate of (0.15, 0.09).

Park et al. (2019) used 9-vinylcarbazole (VCz) or 9,9-dimethyl-9,10-dihydroacridine as electron donors and phenyltriazine as electron acceptor, and synthesized the TADF emitting unit (VTD) by free radical copolymerization. By this way, they developed a highly efficient TADF PLED. In the polymer configuration, VCz and VTD monomers function as a host, and an emitter, respectively, and the copolymer composition that varies with the feed ratio of 9-vinylcarbazole and VTD affects the electroluminescent properties of the TADF PLED. It has been reported that when the feed ratio is 10%, the

PLQY of the synthesized polymer is as high as 71%, and the PLED prepared by solution processing of the corresponding polymer achieved an EQE of 22.0%.

Besides common polyethylene, polynorbornene is also a good choice. It has a high triplet energy level (2.95 eV), which can effectively inhibit the reverse transfer of triplet from TADF units to the polymer backbone, and can be used to design blue light TADF polymers. Yang et al. (Zeng et al., 2018) introduced a hole injection unit, carbazole, and TADF small molecules into the norbornene polymer backbone as side chains, and synthesized a series of blue TADF polymers (PBD) by controlling the molar ratio of carbazole to TADF units (PBD-0, PBD-5, PBD-10, PBD-15, and PBD-20, **Figure 14**). As the proportion of TADF small molecule units increased, the degree of aggregation of the large conjugated structure led to a red-shift in the emission wavelength. The polymers all showed emission around 460 nm in pure films. By using these blue polymer emitters, the non-doped PLEDs produced achieved a maximum EQE of 7.3% and CIE coordinate of (0.20, 0.29).

### Space charge transfer

The common system of intramolecular charge transfer is generally that the electron-donating group and the electron-withdrawing group are connected by a  $\pi$ -electron conjugated system. In the ground state, this system exhibits a polarization structure; and under photoexcitation, the dipole moment becomes intense and the Stokes shift increases, and thus, the charge transfer effect in the molecule enhances, and the emission of the molecule red-shifts. Therefore, the strong charge transfer effect in the conjugated structure generally causes a large red-shift in the emission wavelength of the TADF polymer, resulting in the orange-yellow and green-light emission in most of the TADF polymers. This is also the reason that the common intramolecular charge transfer system has been less used to

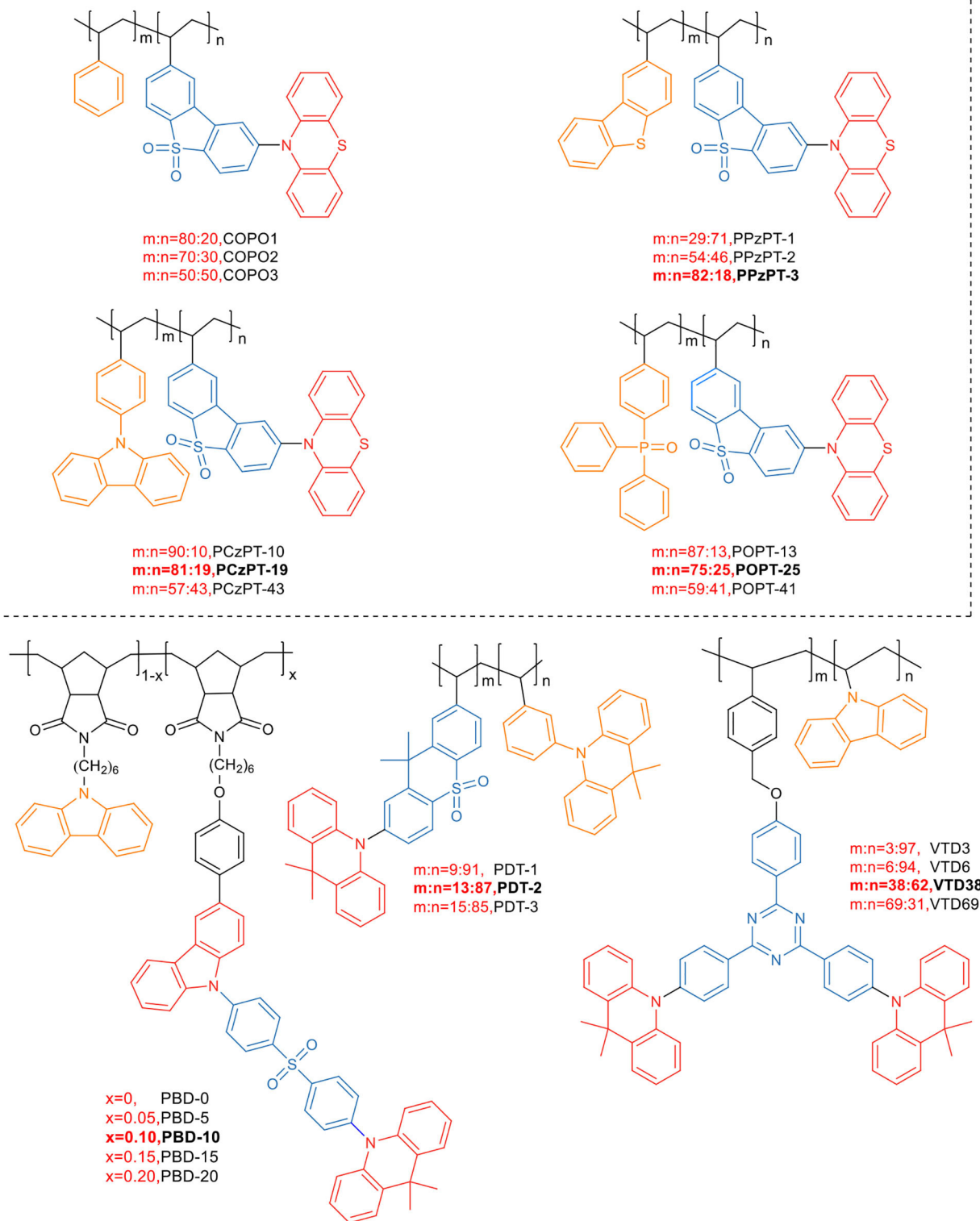


**FIGURE 14 |** Side chain non-conjugated TADF polymers.

the development of blue light TADF polymers. Recently, Shao and Wang broke through the design ideas of classic TADF materials with intramolecular charge transfer as the emitting mechanism, and put forward the design concept of “space charge transfer TADF polymer materials.” Combining aggregation-induced emission effect and TADF effect, they achieved PLED devices by solution processing of TADF polymer with the light emission coverage of deep-blue light (455 nm), red (616 nm) and the white.

Shao et al. (2017) first applied the space charge transfer concept to the design of TADF polymers, and proposed a new concept of blue TADF polymer design based on non-conjugated backbone and space charge transfer. The D and A units of this type of polymer were molecularly separated while spatially close, allowing a charge transfer process to occur through space rather than by binding to the acceptor, i.e., the space charge transfer effect occurs between the D and A units (**Figure 15**). A non-conjugated polyethylene was selected as the backbone, and a series of polymers having significant TADF characteristics were synthesized by free radical polymerization of the corresponding vinyl-functionalized acridone and triazine monomers. In this design strategy, the non-conjugated structure of the polymer avoided strong electron coupling between D and A, and was advantageous for controlling the charge transfer strength, thereby controlling the luminescent color. For example, in 95 mol% Ac and 5 mol% TRZ unit polymer, blue electroluminescence occurred with the CIE coordinate of (0.176, 0.269). Meanwhile, the spatial separation of D and A resulted in a small overlap of HOMO and LUMO, and thus  $\Delta E_{ST}$  was very small (0.019 eV). Further, due to that the electron cloud of D and A was transmitted through spatial charge interaction, the spatial  $\pi$ - $\pi$  interaction between D-A increased the rate of radiation transition. All these advantages impart the polymer fairly good luminescence properties, such as PLQY of 60% in the film state.

On the basis of previous studies, the research team further developed a general design strategy suitable for full-color TADF polymer (as shown in **Figure 15**) by regulating the charge transfer intensity between the donor and the acceptor (Hu et al., 2019). In the work, acridine was used as the electron donor and triazine as the electron acceptor, which was connected to the side chain of non-conjugated polystyrene. The space charge transfer intensity between the donor and different acceptors was regulated by using the substituent effect. The full-color emission of TADF polymer was realized, with a color region covering deep-blue (455 nm) to red (616 nm). In addition, by introducing two different donor/acceptor pairs (acridine/triazine pair and acridine/cyanotriazine pair to construct two space charge transfer channels) into the same polymer chain, the polymer emitted simultaneously blue and yellow light, achieving a white light emission. Their studies showed that the TADF polymers with space charge transfer had a small  $\Delta E_{ST}$  (0.02 ~ 0.05 eV), and the HOMO / LUMO was effectively separated in space, leading to a typical TADF effect. Meanwhile, the aggregation induced emission effect was observed in the THF/H<sub>2</sub>O mixed solvent, and its emission intensity enhanced 117 times from solution state to aggregation state. It was found that the OLED devices based on the TSCT

polymers of deep-blue, green, red and white light have good electroluminescent performance, with maximum EQEs of 7.1, 16.2, 1, and 14.1%, respectively.

## Self-Emission TADF Polymer

The synthesis of the above polymers deals with introducing a small molecular unit having TADF effect into the polymer. This conventional TADF polymer synthesis method, where the TADF small molecule itself is prepared in many steps and complicated in synthesis, with the addition of the other function groups, such as the solubilizing functional groups, polymerizable leaving groups, etc., makes preparation more difficult.

Wei et al. (2017) reported a method for achieving TADF properties in cyclic oligomers and polymers composed of non-TADF structural units. The research group, using an inductive conjugation idea, designed and prepared a simple repeating unit M1, with carbazole as the electron donor and benzophenone as the electron acceptor. Surprisingly, the individual light-emitting unit M1 exhibited only phosphorescence emission, but the Yamamoto-type polymer P1, obtained through polymerizing of M1, showed significant TADF behavior, with a PLQY up to 71%. It was explained that the polymerization of M1 extended the  $\pi$ -conjugated electron donor system, reducing the energy splitting between the corresponding <sup>1,3</sup>CT, making the  $\Delta E_{ST}$  small (0.19 eV) enough to be overcome by heat while maintaining a sufficiently fast radiative decay rate. This study has fully demonstrated that a design strategy for TADF polymers could be developed by converting organic small molecules without TADF effect into high-efficiency TADF oligomers and polymers by induction binding.

Soon after, the team prepared a monochromatic OLED device based on the above self-emission TADF polymer P1 (Li et al., 2019b). They found that using P1 pure film or doping it in the host material, 1,3-bis(9H-carbazol-9-yl)benzene (mCP), could realize cyan-blue light devices. The maximum EQE of the device with P1-doped mCP was 4.26%, while the EQE of the device based on P1 neat film was only 0.87%.

## CONCLUSION AND OUTLOOK

Theoretically, TADF materials have become the key technology for new OLEDs due to 100% exciton utilization. TADF materials and TADF-OLEDs have also made significant progress in recent years, especially small molecule TADF materials in achieving good performance of OLEDs with great success. Compared with TADF small molecule, TADF polymer performs better in preparing OLED devices with economical and efficient solution-process. However, unlike small molecule, TADF polymers have different molecular weights except dendritic macromolecules, and there are certain unavoidable defects in the structure, which makes the polymers not as easy to be optimized and repeated as small molecules. Now, TADF polymers still face many challenges, such as complex synthesis, limited variety, and relatively low efficiency of TADF-based devices. Compared with small molecules, most TADF polymers are only used as a carrier of TADF units, and cannot take advantage of the polymers' structural design preponderance. Therefore, it is



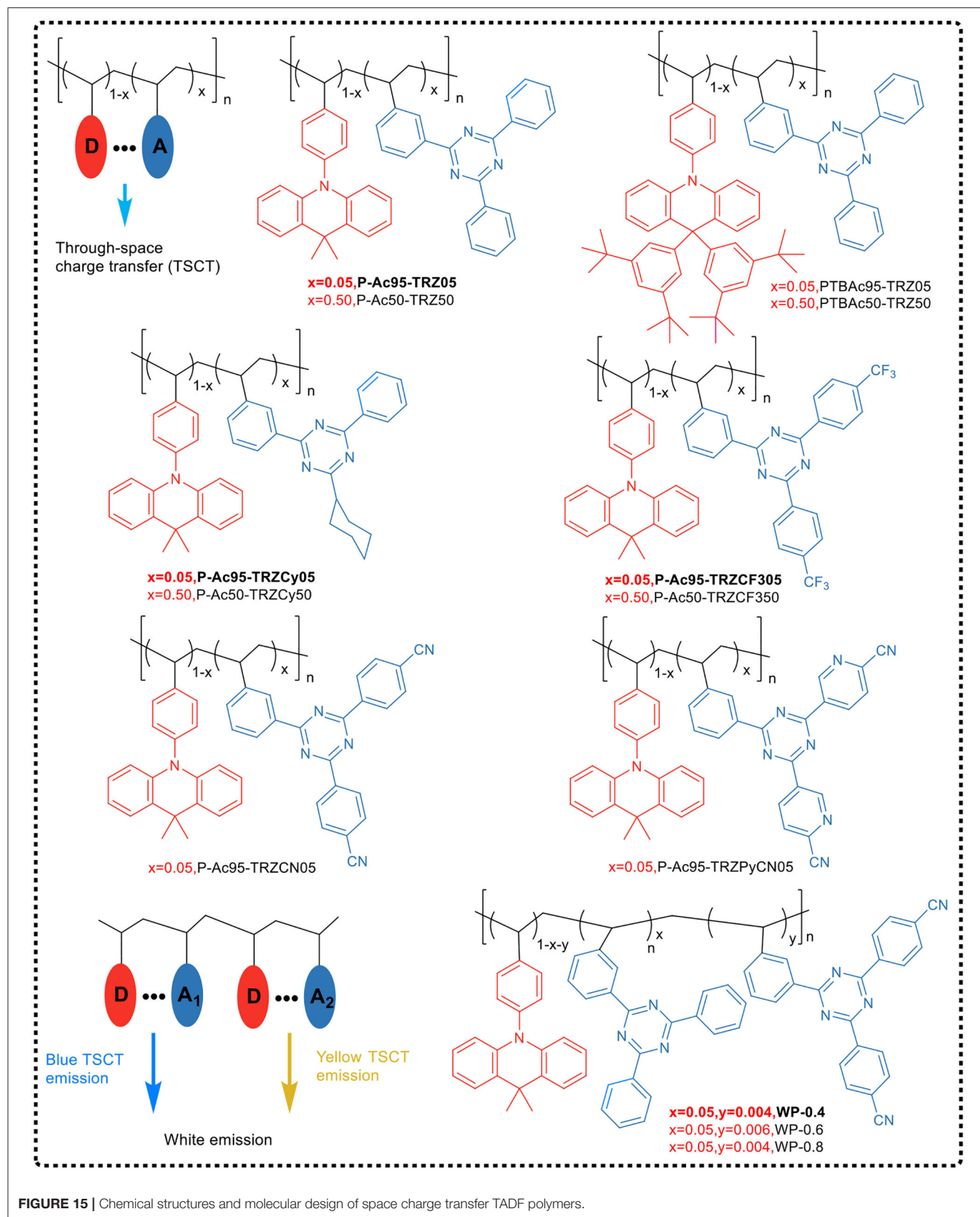


**FIGURE 15 |** Chemical structures and molecular design of space charge transfer TADF polymers.

expected that more and more TADF polymers not only have excellent processing properties, but also have advantages in synthesis, performance, and application.

## Synthesis

So far, some exciting results indicate that it is worthwhile to expand the corresponding research from small-molecule TADF emitters to TADF polymers emitters. However, it is undoubtedly challenging to obtain highly efficient and easily scalable TADF polymers due to synthetic limitations. Most of the existing TADF polymers are synthesized by embedding or grafting small-molecule TADF emitters into the polymer structure, which is not only limited by the variety of small-molecule TADF units, but also suffers from difficulties in complex polymerization methods, undefined structure and the possibility of unavoidable impurities. Thus, more attention is suggested to the three issues: simplification of synthesis method, reducing dependence on small molecules of TADF monomer, and understanding of structure-property relationships.

- (1) Simplification of synthesis method: Special attention should be paid to discovering simple synthesis methods, especially, finding the synthesis method to larger molecular structure and comonomer, and developing new synthetic strategies for preparing TADF polymers.
- (2) Reducing dependence on small molecules of TADF monomer: The development of TADF polymers is badly limited by the available small molecule active units, resulting in a limited number of TADF polymers. To change this situation, some specific polymer structures should be considered to achieve the TADF activity, reducing the dependence on small molecules of TADF monomer.
- (3) Understanding of structure-property relationships: More attention should be paid to complex interactions between donor and acceptor parts, polymer conjugation effects, charge transport and transfer effects, quenching effects, TADF monomer concentration effects, and intra- or intermolecular interactions of the TADF unit, rather than only optimizing the electronic state of the TADF emitting unit. Also, the effect of the content of the attachment sites and functional groups on the TADF polymer needs to be further studied.

## Property

Although TADF materials have made significant progress, TADF polymers still exhibit lower EQE values in both non-doped and doped devices than small molecule TADF devices. It is still difficult to obtain stable and efficient TADF polymer emitters and TADF-OLEDs with excellent performance for the following problems: (1) Generally, there is a contradiction between the separation of HOMO-LUMO orbitals and the suppression of IC process in TADF molecule. TADF polymers have a smaller  $\Delta E_{ST}$  but relatively low quantum yields. (2) Embedding or grafting the active unit with TADF effect into the polymer structure is conducive to the delayed emission of the molecule. However, DF component depends on the

exact position and content of TADF unit in the polymer, and negative effects such as exciton quenching may occur, increasing non-radiation decay. (3) Solution-processed polymer TADF devices suffer from more severe efficiency roll-offs, and at the same time, there are major problems with device stability and device efficiency. Therefore, the efforts are needed to solve the current problems of TADF polymers in OLED device applications and develop TADF polymers with better performance.

- (1) Development of TADF polymers with multiple luminous effects: (a) In aggregated state luminescent molecules, the ACQ makes the materials weaken in or even emit no fluorescence, which seriously affects the practical application of those materials. Therefore, it is necessary to find strategies to mitigate or eliminate the ACQ effect in polymers. Currently, the strategy of aggregation-induced emission or aggregation-enhanced emission molecular design was attempted to develop polymer light-emitting materials with AIDF effect, which is the most promising luminescent material for OLEDs and has great potential in the preparation of stable and efficient OLED devices. (b) More effective exciton utilization strategies are expected to be developed, in which materials not only emit thermally activated delayed fluorescence via reverse inter-system crossing from  $T_1$  to  $S_1$ , but also emit room-temperature phosphorescence from the radiative decay of the lowest triplet state ( $T_1$ ) populated via IC process from the higher-lying triplet state ( $T_2$ ) or inter-system crossing from  $S_1$  to  $T_1$ . These promising strategies may impart the new polymers long-life dual emission performance of delayed fluorescence and room temperature phosphorescence, while it is still a challenging research area.
- (2) Color purity of the TADF polymers: So far, almost all reported researches are concentrated in the green or orange-yellow TADF polymers, while blue and red corresponding TADF polymers are few, especially for deep-blue and pure blue. Those colors, however, are essential for full-color RGB displays. Therefore, new polymerization methods, geometric framework design and new construction groups should be explored, and more combination strategies should be developed to further optimize the displaying performance of TADF polymers.
- (3) Exploring stable host materials: Host materials are usually introduced into TADF polymers via chemical bonding for developing excellent non-doped TADF-OLEDs. In this case, the properties of host materials become very important, and new host materials, with good charge carrier transmission properties and good thermal and electrochemical stability, are still required to explore and develop.

## Applications

TADF-based materials are currently used in OLEDs, including (1) serving as host materials, guest materials and auxiliary dopants in doped OLED systems; (2) by mixing with phosphorescent materials or fluorescent groups to prepare white organic light-emitting diodes; (3) improving the efficiency

of OLED devices with TADF molecular orientation; and (4) preparation of solution-processed OLEDs with better device performance.

Since TADF materials have the ability to utilize excitons by converting triplet excitons to singlet excitons, they are expected to be used in many other advanced fields, such as triplet-triplet annihilation sensitizers, electrochemiluminescence cells, organic ultraviolet photodetector, organic hybrid microelectronic radial heterojunction, light-emitting electrochemical cell, multicolor luminescent micelle, fluorescent probes and imaging, mechanoluminescence, and mechanoluminochromism. In all these applications, the small  $\Delta E_{ST}$  of TADF materials and the effective RISC process in molecules are mainly utilized.

All in all, the research and development of TADF materials is still in the early stage. Besides the existing molecular systems,

new TADF molecules should be explored. For this, new molecular design strategies and detailed theories should be established to construct materials with TADF characteristics and understand their photophysical properties.

## AUTHOR CONTRIBUTIONS

All authors listed have made a substantial, direct and intellectual contribution to the work, and approved it for publication.

## ACKNOWLEDGMENTS

The authors would like to acknowledge support from the Research Projects of Ministry of Education, Grant No. 18JDGC025, China.

## REFERENCES

- Adachi, C., Tokito, S., Tsutsui, T., and Saito, S. (1988). Electroluminescence in organic films with three-layer structure. *Jpn. J. Appl. Phys.* 27, 269–271. doi: 10.1143/JJAP.27.L269
- Albrecht, K., Matsuoka, K., Fujita, K., and Yamamoto, K. (2015). Carbazole dendrimers as solution-processable thermally activated delayed-fluorescence materials. *Angew. Chem. Int. Ed. Engl.* 54, 5677–5682. doi: 10.1002/anie.201500203
- Astruc, D., Boisselier, E., and Ornelas, C. (2010). Dendrimers designed for functions: from physical, photophysical, and supramolecular properties to applications in sensing, catalysis, molecular electronics, photonics, and nanomedicine. *Chem. Rev.* 110, 1857–1959. doi: 10.1021/cr900327d
- Baldo, M. A., O'Brien, D., You, Y., Shoustikov, A., Sibley, S., Thompson, M., et al. (1998). Highly efficient phosphorescent emission from organic electroluminescent devices. *Nature* 395, 151–154.
- Burn, P. L., Lo, S. C., and Samuel, I. D. W. (2007). The development of light-emitting dendrimers for displays. *Adv. Mater.* 19, 1675–1688. doi: 10.1002/adma.200601592
- Cai, X., and Su, S.-J. (2018). Marching toward highly efficient, pure-blue, and stable thermally activated delayed fluorescent organic light-emitting diodes. *Adv. Funct. Mater.* 28:1802558. doi: 10.1002/adfm.201802558
- Dai, G. Z., Li, H. J., Pan, Y. Z., Dai, X. Y., and Xie, Q. (2005). Energy transfer probability in organic electrophosphorescence device with dopant. *Chinese Phys.* 14, 2590–2594. doi: 10.1088/1009-1963/14/12/034
- Endo, A., Ogasawara, M., Takahashi, A., Yokoyama, D., Kato, Y., and Adachi, C. (2009). Thermally activated delayed fluorescence from Sn(4+)-porphyrin complexes and their application to organic light emitting diodes—a novel mechanism for electroluminescence. *Adv. Mater. Weinheim* 21, 4802–4806. doi: 10.1002/adma.200900983
- Endo, A., Sato, K., Yoshimura, K., Kai, T., Kawada, A., Miyazaki, H., et al. (2011). Efficient up-conversion of triplet excitons into a singlet state and its application for organic light emitting diodes. *Appl. Phys. Lett.* 98:083302. doi: 10.1063/1.3558906
- Feuillastre, S., Pauton, M., Gao, L., Desmarchelier, A., Riives, A. J., Prim, D., et al. (2016). Design and synthesis of new circularly polarized thermally activated delayed fluorescence emitters. *J. Am. Chem. Soc.* 138, 3990–3993. doi: 10.1021/jacs.6b00850
- Freeman, D. M. E., Musser, A. J., Frost, J. M., Stern, H. L., Forster, A. K., Fallon, K. J., et al. (2017). Synthesis and exciton dynamics of donor-orthogonal acceptor conjugated polymers: reducing the singlet-triplet energy gap. *J. Am. Chem. Soc.* 139, 11073–11080. doi: 10.1021/jacs.7b03327
- Furue, R., Nishimoto, T., Park, I. S., Lee, J., and Yasuda, T. (2016). Aggregation-induced delayed fluorescence based on donor/acceptor-tethered janus carborane triads: unique photophysical properties of nondoped OLEDs. *Angew. Chem. Int. Ed. Engl.* 55, 7171–7175. doi: 10.1002/anie.201603232
- Guo, J. J., Li, X. L., Nie, H., Luo, W. W., Gan, S. F., Hu, S. M., et al. (2017). Achieving high-performance nondoped OLEDs with extremely small efficiency roll-off by combining aggregation-induced emission and thermally activated delayed fluorescence. *Adv. Funct. Mater.* 27:1606458. doi: 10.1002/adfm.201606458
- Gustafsson, G., Cao, Y., Treacy, G., Klavetter, F., Colaneri, N., and Heeger, A. (1992). Flexible light-emitting diodes made from soluble conducting polymers. *Nature* 357, 477–479. doi: 10.1038/357477a0
- Holmes, R. J., Forrest, S. R., Tung, Y.-J., Kwong, R. C., Brown, J. J., Garon, S., et al. (2003). Blue organic electrophosphorescence using exothermic host-guest energy transfer. *Appl. Phys. Lett.* 82:2422. doi: 10.1063/1.1568146
- Hu, J., Li, Q., Wang, X., Shao, S., Wang, L., Jing, X., et al. (2019). Developing through-space charge transfer polymers as a general approach to realize full-color and white emission with thermally activated delayed fluorescence. *Angew. Chem. Int. Ed. Engl.* 58, 8405–8409. doi: 10.1002/anie.201902264
- Hu, Y., Cai, W., Ying, L., Chen, D., Yang, X., Jiang, X.-F., et al. (2018). Novel efficient blue and bluish-green light-emitting polymers with delayed fluorescence. *J. Mater. Chem. C* 6, 2690–2695. doi: 10.1039/c7tc04064d
- Hung, L. S., and Chen, C. H. (2002). Recent progress of molecular organic electroluminescent materials and devices. *Mater. Sci. Eng.* 39, 143–222. doi: 10.1016/S0927-796X(02)00093-1
- Kawasumi, K., Wu, T., Zhu, T., Chae, H. S., Van Voorhis, T., Baldo, M. A., et al. (2015). Thermally activated delayed fluorescence materials based on homoconjugation effect of donor-acceptor triptycenes. *J. Am. Chem. Soc.* 137, 11908–11911. doi: 10.1021/jacs.5b07932
- Kim, H. J., Lee, C., Godumala, M., Choi, S., Park, S. Y., Cho, M. J., et al. (2018). Solution-processed thermally activated delayed fluorescence organic light-emitting diodes using a new polymeric emitter containing non-conjugated cyclohexane units. *Polym. Chem.* 9, 1318–1326. doi: 10.1039/c7py02113e
- Köhler, A., and Bässler, H. (2009). Triplet states in organic semiconductors. *Mater. Sci. Eng.* 66, 71–109. doi: 10.1016/j.mser.2009.09.001
- Köhler, A., Wilson, J. S., and Friend, R. H. (2002). Fluorescence and phosphorescence in organic materials. *Adv. Mater.* 14, 701–707. doi: 10.1002/1521-4095(20020517)14:10<701::AID-ADMA701>3.0.CO;2-4
- Lee, S. Y., Yasuda, T., Komiyama, H., Lee, J., and Adachi, C. (2016). Thermally activated delayed fluorescence polymers for efficient solution-processed organic light-emitting diodes. *Adv. Mater.* 28, 4019–4024. doi: 10.1002/adma.201505026
- Lee, S. Y., Yasuda, T., Nomura, H., and Adachi, C. (2012). High-efficiency organic light-emitting diodes utilizing thermally activated delayed fluorescence from triazine-based donor-acceptor hybrid molecules. *Appl. Phys. Lett.* 101:093306. doi: 10.1063/1.4749285
- Li, C., Nobuyasu, R. S., Wang, Y., Dias, F. B., Ren, Z., Bryce, M. R., et al. (2017). Solution-processable thermally activated delayed fluorescence white OLEDs based on dual-emission polymers with tunable emission colors and aggregation-enhanced emission properties. *Adv. Opt. Mater.* 5:1700435. doi: 10.1002/adom.201700435

- Li, C., Ren, Z., Sun, X., Li, H., and Yan, S. (2019a). Deep-blue thermally activated delayed fluorescence polymers for nondoped solution-processed organic light-emitting diodes. *Macromolecules* 52, 2296–2303. doi: 10.1021/acs.macromol.9b0083
- Li, C., Wang, Y., Sun, D., Li, H., Sun, X., Ma, D., et al. (2018). Thermally activated delayed fluorescence pendant copolymers with electron- and hole-transporting spacers. *ACS Appl. Mater. Interfaces* 10, 5731–5739. doi: 10.1021/acsami.8b00136
- Li, Y., Wei, Q., Cao, L., Fries, F., Cucchi, M., Wu, Z., et al. (2019b). Organic light-emitting diodes based on conjugation-induced thermally activated delayed fluorescence polymers: interplay between intra- and intermolecular charge transfer states. *Front Chem* 7:688. doi: 10.3389/fchem.2019.00688
- Li, Y., Xie, G., Gong, S., Wu, K., and Yang, C. (2016). Dendronized delayed fluorescence emitters for non-doped, solution-processed organic light-emitting diodes with high efficiency and low efficiency roll-off simultaneously: two parallel emissive channels. *Chem. Sci.* 7, 5441–5447. doi: 10.1039/c6sc00943c
- Liu, X., Rao, J., Li, X., Wang, S., Ding, J., and Wang, L. (2019). Teaching an old poly(arylene ether) new tricks: efficient blue thermally activated delayed fluorescence. *iScience* 15, 147–155. doi: 10.1016/j.isci.2019.04.020
- Liu, Y., Li, C., Ren, Z., Yan, S., and Bryce, M. R. (2018a). All-organic thermally activated delayed fluorescence materials for organic light-emitting diodes. *Nat. Rev. Mater.* 3:20. doi: 10.1038/natrevmats.2018.20
- Liu, Y., Wang, Y., Li, C., Ren, Z., Ma, D., and Yan, S. (2018b). Efficient thermally activated delayed fluorescence conjugated polymeric emitters with tunable nature of excited states regulated via carbazole derivatives for solution-processed OLEDs. *Macromolecules* 51, 4615–4623. doi: 10.1021/acs.macromol.8b00565
- Luo, J., Xie, G., Gong, S., Chen, T., and Yang, C. (2016). Creating a thermally activated delayed fluorescence channel in a single polymer system to enhance exciton utilization efficiency for bluish-green electroluminescence. *Chem. Commun.* 52, 2292–2295. doi: 10.1039/c5cc09797e
- Mehes, G., Nomura, H., Zhang, Q., Nakagawa, T., and Adachi, C. (2012). Enhanced electroluminescence efficiency in a spiro-acridine derivative through thermally activated delayed fluorescence. *Angew. Chem. Int. Ed. Engl.* 51, 11311–11315. doi: 10.1002/anie.201206289
- Nakagawa, T., Ku, S. Y., Wong, K. T., and Adachi, C. (2012). Electroluminescence based on thermally activated delayed fluorescence generated by a spirobifluorene donor-acceptor structure. *Chem. Commun. (Camb)* 48, 9580–9582. doi: 10.1039/c2cc31468a
- Nikolaenko, A. E., Cass, M., Bourcet, F., Mohamad, D., and Roberts, M. (2015). Thermally activated delayed fluorescence in polymers: a new route toward highly efficient solution processable OLEDs. *Adv. Mater. Weinheim* 27, 7236–7240. doi: 10.1002/adma.201501090
- Nobuyasu, R. S., Ren, Z., Griffiths, G. C., Batsanov, A. S., Data, P., Yan, S., et al. (2016). Rational design of TADF polymers using a donor-acceptor monomer with enhanced TADF efficiency induced by the energy alignment of charge transfer and local triplet excited states. *Adv. Opt. Mater.* 4, 597–607. doi: 10.1002/adom.201500689
- Numata, M., Yasuda, T., and Adachi, C. (2015). High efficiency pure blue thermally activated delayed fluorescence molecules having 10H-phenoxaborin and acridan units. *Chem. Commun.* 51, 9443–9446. doi: 10.1039/c5cc00307e
- Park, Y. H., Jang, H. J., and Lee, J. Y. (2019). High efficiency above 20% in polymeric thermally activated delayed fluorescent organic light-emitting diodes by a host embedded backbone structure. *Polym. Chem.* 10, 4872–4878. doi: 10.1039/c9py00701f
- Parker, C. A., and Hatchard, C. G. (1961). Triplet-singlet emission in fluid solutions. Phosphorescence of eosin. *Trans. Faraday Soc.* 57, 1894–1904. doi: 10.1039/TF9615701894
- Peng, Q., Li, W., Zhang, S., Chen, P., Li, F., and Ma, Y. (2013). Evidence of the reverse intersystem crossing in intra-molecular charge-transfer fluorescence-based organic light-emitting devices through magneto-electroluminescence measurements. *Adv. Opt. Mater.* 1, 362–366. doi: 10.1002/adom.201300028
- Pope, M., Kallmann, H. P., and Magnante, P. (1963). Electroluminescence in organic crystals. *J. Chem. Phys.* 38, 2042–2043. doi: 10.1063/1.1733929
- Rao, J. C., Liu, X. R., Li, X. F., Yang, L. Q., Zhao, L., Wang, S. M., et al. (2020). Bridging small molecules to conjugated polymers: efficient thermally activated delayed fluorescence with a methyl-substituted phenylene linker. *Angew. Chem. Intern. Edition* 59, 1320–1326. doi: 10.1002/anie.201912556
- Rothberg, L. J., and Lovinger, A. J. (1996). Status of and prospects for organic electroluminescence. *J. Mater. Res.* 11, 3174–3187. doi: 10.1557/jmr.1996.0403
- Shao, S., Hu, J., Wang, X., Wang, L., Jing, X., and Wang, F. (2017). Blue thermally activated delayed fluorescence polymers with nonconjugated backbone and through-space charge transfer effect. *J. Am. Chem. Soc.* 139, 17739–17742. doi: 10.1021/jacs.7b10257
- Sheats, J. R., Antoniadis, H., Hueschen, M., Leonard, W., Miller, J., Moon, R., et al. (1996). Organic electroluminescent devices. *Science* 273, 884–888. doi: 10.1126/science.273.5277.884
- Sun, K., Sun, Y., Tian, W., Liu, D., Feng, Y., Sun, Y., et al. (2018). Thermally activated delayed fluorescence dendrimers with exciplex-forming dendrons for low-voltage-driving and power-efficient solution-processed OLEDs. *J. Mater. Chem. C* 6, 43–49. doi: 10.1039/c7tc04720g
- Suzuki, K., Kubo, S., Shizu, K., Fukushima, T., Wakamiya, A., Murata, Y., et al. (2015). Triarylboron-based fluorescent organic light-emitting diodes with external quantum efficiencies exceeding 20%. *Angew. Chem. Int. Ed. Engl.* 54, 15231–15235. doi: 10.1002/anie.201508270
- Tanaka, H., Shizu, K., Miyazaki, H., and Adachi, C. (2012). Efficient green thermally activated delayed fluorescence (TADF) from a phenoxazine-triphenyltriazine (PXZ-TRZ) derivative. *Chem. Commun. (Camb)* 48, 11392–11394. doi: 10.1039/c2cc36237f
- Tao, Y., Yuan, K., Chen, T., Xu, P., Li, H., Chen, R., et al. (2014). Thermally activated delayed fluorescence materials towards the breakthrough of organoelectronics. *Adv. Mater. Weinheim* 26, 7931–7958. doi: 10.1002/adma.201402532
- Uoyama, H., Goushi, K., Shizu, K., Nomura, H., and Adachi, C. (2012). Highly efficient organic light-emitting diodes from delayed fluorescence. *Nature* 492, 234–238. doi: 10.1038/nature11687
- Volz, D. (2016). Review of organic light-emitting diodes with thermally activated delayed fluorescence emitters for energy-efficient sustainable light sources and displays. *J. Photon. Energy* 6:020901. doi: 10.1117/1.jpe.6.020901
- Wang, J., Liu, C., Jiang, C., Yao, C., Gu, M., and Wang, W. (2019a). Solution-processed aggregation-induced delayed fluorescence (AIDF) emitters based on strong  $\pi$ -accepting triazine cores for highly efficient nondoped OLEDs with low efficiency roll-off. *Org. Electron.* 65, 170–178. doi: 10.1016/j.orgel.2018.11.018
- Wang, S., Zhang, H., Zhang, B., Xie, Z., and Wong, W.-Y. (2020). Towards high-power-efficiency solution-processed OLEDs: material and device perspectives. *Mater. Sci. Eng.* 140:100547. doi: 10.1016/j.mser.2020.100547
- Wang, X., Wang, S., Lv, J., Shao, S., Wang, L., Jing, X., et al. (2019b). Through-space charge transfer hexaarylbenzene dendrimers with thermally activated delayed fluorescence and aggregation-induced emission for efficient solution-processed OLEDs. *Chem. Sci.* 10, 2915–2923. doi: 10.1039/c8sc04991b
- Wang, Y., Zhu, Y., Lin, X., Yang, Y., Zhang, B., Zhan, H., et al. (2018a). Efficient non-doped yellow OLEDs based on thermally activated delayed fluorescence conjugated polymers with an acridine/carbazole donor backbone and triphenyltriazine acceptor pendant. *J. Mater. Chem. C* 6, 568–574. doi: 10.1039/c7tc04994c
- Wang, Y., Zhu, Y., Xie, G., Xue, Q., Tao, C., Le, Y., et al. (2018b). Red thermally activated delayed fluorescence polymers containing 9H-thioxanthene-9-one-10,10-dioxide acceptor group as pendant or incorporated in backbone. *Org. Electron.* 59, 406–413. doi: 10.1016/j.orgel.2018.05.058
- Wang, Y., Zhu, Y., Xie, G., Zhan, H., Yang, C., and Cheng, Y. (2017). Bright white electroluminescence from a single polymer containing a thermally activated delayed fluorescence unit and a solution-processed orange OLED approaching 20% external quantum efficiency. *J. Mater. Chem. C* 5, 10715–10720. doi: 10.1039/c7tc03769d
- Wang, Y. Z., Sun, R. G., Meghdadi, F., Leising, G., and Epstein, A. J. (1999). Multicolor multilayer light-emitting devices based on pyridine-containing conjugated polymers and para-sexiphenyl oligomer. *Appl. Phys. Lett.* 74, 3613–3615. doi: 10.1063/1.123198
- Wei, Q., Kleine, P., Karpov, Y., Qiu, X. P., Komber, H., Sahre, K., et al. (2017). Conjugation-induced thermally activated delayed fluorescence (TADF): from conventional non-TADF units to TADF-active polymers. *Adv. Funct. Mater.* 27:1605051. doi: 10.1002/adfm.201605051



- Wu, H., Zhou, G., Zou, J., Ho, C.-L., Wong, W.-Y., Yang, W., et al. (2009). Efficient polymer white-light-emitting devices for solid-state lighting. *Adv. Mater.* 21, 4181–4184. doi: 10.1002/adma.200900638
- Xiao, J., Lü, Z. Y., Liu, X. K., Han, Y. F., and Zheng, L. R. (2014). Highly efficient green and red phosphorescent OLEDs using novel bipolar blue fluorescent materials as hosts. *Synth. Met.* 193, 89–93. doi: 10.1016/j.synthmet.2014.04.001
- Xie, G., Luo, J., Huang, M., Chen, T., Wu, K., Gong, S., et al. (2017). Inheriting the characteristics of TADF small molecule by side-chain engineering strategy to enable bluish-green polymers with high PLQYs up to 74% and external quantum efficiency over 16% in light-emitting diodes. *Adv. Mater. Weinheim* 29:223. doi: 10.1002/adma.201604223
- Xie, Y., and Li, Z. (2017). Thermally activated delayed fluorescent polymers. *J. Polymer Sci.* 55, 575–584. doi: 10.1002/pola.28448
- Xu, H., Xu, Z. F., Yue, Z. Y., Yan, P. F., Wang, B., Jia, L. W., et al. (2008). A novel deep blue-emitting ZnII complex based on carbazole-modified 2-(2-hydroxyphenyl) benzimidazole: synthesis, bright electroluminescence, and substitution effect on photoluminescent, thermal, and electrochemical properties. *J. Phys. Chem. C* 112, 15517–15525. doi: 10.1021/jp803325g
- Yang, Y., Li, K., Wang, C., Zhan, H., and Cheng, Y. (2019a). Effect of a pendant acceptor on thermally activated delayed fluorescence properties of conjugated polymers with backbone-donor/pendant-acceptor architecture. *Chem. Asian J.* 14, 574–581. doi: 10.1002/asia.201801813
- Yang, Y., Zhao, L., Wang, S., Ding, J., and Wang, L. (2018b). Red-emitting thermally activated delayed fluorescence polymers with poly(fluorene-co-3,3'-dimethyl diphenyl ether) as the backbone. *Macromolecules* 51, 9933–9942. doi: 10.1021/acs.macromol.8b02050
- Yang, Y., Zhao, L., Wang, S., Ding, J. Q., and Wang, L. X. (2019b). Synthesis and characterization of red-emitting thermally activated delayed fluorescent polymers based on poly(2,7-carbazole-co-3,3'-dimethyldiphenyl ether) as the main chain. *Acta Polym. Sinica* 50, 685–694. doi: 10.1177/j.issn1000-3304.2018.18266
- Yang, Y. K., Wang, S. M., Zhu, Y. H., Wang, Y. J., Zhan, H. M., and Cheng, Y. X. (2018a). Thermally activated delayed fluorescence conjugated polymers with backbone-donor/pendant-acceptor architecture for nondoped OLEDs with high external quantum efficiency and low roll-off. *Adv. Funct. Mater.* 28:1706916. doi: 10.1002/adfm.201706916
- Zeng, X., Luo, J., Zhou, T., Chen, T., Zhou, X., Wu, K., et al. (2018). Using ring-opening metathesis polymerization of norbornene to construct thermally activated delayed fluorescence polymers: high-efficiency blue polymer light-emitting diodes. *Macromolecules* 51, 1598–1604. doi: 10.1021/acs.macromol.7b02629
- Zhan, H., Wang, Y., Li, K., Chen, Y., Yi, X., Bai, K., et al. (2020). Saturated red electroluminescence from thermally activated delayed fluorescence conjugated polymers. *Front Chem.* 8:332. doi: 10.3389/fchem.2020.00332
- Zhang, B., and Cheng, Y. (2019). Recent advances in conjugated TADF polymer featuring in backbone-donor/pendant-acceptor structure: material and device perspectives. *Chem. Rec.* 19, 1624–1643. doi: 10.1002/tcr.201800152
- Zhang, Q., Li, B., Huang, S., Nomura, H., Tanaka, H., and Adachi, C. (2014a). Efficient blue organic light-emitting diodes employing thermally activated delayed fluorescence. *Nat. Photonics* 8, 326–332. doi: 10.1038/nphoton.2014.12
- Zhang, Q., Li, J., Shizu, K., Huang, S., Hirata, S., Miyazaki, H., et al. (2012). Design of efficient thermally activated delayed fluorescence materials for pure blue organic light emitting diodes. *J. Am. Chem. Soc.* 134, 14706–14709. doi: 10.1021/ja306538w
- Zhang, Y., Lee, J., and Forrest, S. R. (2014b). Tenfold increase in the lifetime of blue phosphorescent organic light-emitting diodes. *Nat. Commun.* 5:6008. doi: 10.1038/ncomms6008
- Zhou, X., Huang, M., Zeng, X., Chen, T., Xie, G., Yin, X., et al. (2019). Combining the qualities of carbazole and tetraphenyl silane in a desirable main chain for thermally activated delayed fluorescence polymers. *Polym. Chem.* 10, 4201–4208. doi: 10.1039/c9py00742c
- Zhu, Y. H., Yang, Y. K., Wang, Y. J., Yao, B., Lin, X. D., Zhang, B. H., et al. (2018). Improving luminescent performances of thermally activated delayed fluorescence conjugated polymer by inhibiting the intra- and interchain quenching. *Adv. Opt. Mater.* 6:1701320. doi: 10.1002/adom.201701320
- Zhu, Y. H., Zhang, Y. W., Yao, B., Wang, Y. J., Zhang, Z. L., Zhan, H. M., et al. (2016). Synthesis and electroluminescence of a conjugated polymer with thermally activated delayed fluorescence. *Macromolecules* 49, 4373–4377. doi: 10.1021/acs.macromol.6b00430

**Conflict of Interest:** The authors declare that the research was conducted in the absence of any commercial or financial relationships that could be construed as a potential conflict of interest.

Copyright © 2020 Yin, He, Wang, Wu, Pang, Xu and Wang. This is an open-access article distributed under the terms of the Creative Commons Attribution License (CC BY). The use, distribution or reproduction in other forums is permitted, provided the original author(s) and the copyright owner(s) are credited and that the original publication in this journal is cited, in accordance with accepted academic practice. No use, distribution or reproduction is permitted which does not comply with these terms.



# Conformation Control of Iminodibenzyl-Based Thermally Activated Delayed Fluorescence Material by Tilted Face-to-Face Alignment With Optimal Distance (tFFO) Design

## OPEN ACCESS

### Edited by:

Sebastian Reineke,  
Technische Universität  
Dresden, Germany

### Reviewed by:

Jang Hyuk Kwon,  
Kyung Hee University, South Korea  
Zhiming Wang,  
South China University of  
Technology, China  
Qiang Wei,  
Ningbo Institute of Materials  
Technology and Engineering,  
(CAS), China

### \*Correspondence:

Hironori Kaji  
kaji@scl.kyoto-u.ac.jp

### Specialty section:

This article was submitted to  
Organic Chemistry,  
a section of the journal  
Frontiers in Chemistry

**Received:** 31 January 2020

**Accepted:** 22 May 2020

**Published:** 14 August 2020

### Citation:

Kusakabe Y, Wada Y, Nakagawa H,  
Shizu K and Kaji H (2020)  
Conformation Control of  
Iminodibenzyl-Based Thermally  
Activated Delayed Fluorescence  
Material by Tilted Face-to-Face  
Alignment With Optimal Distance  
(tFFO) Design. *Front. Chem.* 8:530.  
doi: 10.3389/fchem.2020.00530

Yu Kusakabe, Yoshimasa Wada, Hiromichi Nakagawa, Katsuyuki Shizu and Hironori Kaji\*

Institute for Chemical Research, Kyoto University, Kyoto, Japan

In organic light-emitting diodes (OLEDs), all triplet excitons can be harvested as light via reverse intersystem crossing (RISC) based on thermally activated delayed fluorescence (TADF) emitters. To realize efficient TADF, RISC should be fast. Thus, to accomplish rapid RISC, in the present study, a novel TADF emitter, namely, TplBT-tFFO, was reported. TplBT-tFFO was compared with IB-TRZ, which contains the same electron donor and acceptor segments, specifically iminodibenzyl and triazine moieties. TplBT-tFFO is based on a recently proposed molecular design strategy called *tilted face-to-face alignment with optimal distance* (tFFO), whereas IB-TRZ is a conventional through-bond type molecule. According to quantum chemical calculations, a very large RISC rate constant,  $k_{\text{RISC}}$ , was expected for TplBT-tFFO because not only the lowest triplet state but also the second lowest triplet state were close to the lowest excited singlet state, as designed in the tFFO strategy. IB-TRZ has two different conformers, leading to dual emission. Conversely, owing to excellent packing, the conformation was fixed to one in the tFFO system, resulting in single-peaked emission for TplBT-tFFO. TplBT-tFFO displayed TADF type behavior and afforded higher photoluminescence quantum yield (PLQY) compared to IB-TRZ. The  $k_{\text{RISC}}$  of TplBT-tFFO was determined at  $6.9 \times 10^6 \text{ s}^{-1}$ , which is one of the highest values among molecules composed of only H, C, and N atoms. The external quantum efficiency of the TplBT-tFFO-based OLED was much higher than that of the IB-TRZ-based one. The present study confirms the effectiveness of the tFFO design to realize rapid RISC. The tFFO-based emitters were found to exhibit an additional feature, enabling the control of the molecular conformations of the donor and/or acceptor segments.

**Keywords:** organic light-emitting diodes, thermally activated delayed fluorescence, molecular conformation, reverse intersystem crossing, dual emission

## INTRODUCTION

Emitting materials for organic light-emitting diodes (OLEDs) have, in recent years, been actively investigated to improve the utilization of triplet excitons. Significant efforts have been devoted to the development of thermally activated delayed fluorescence (TADF) materials (Yang et al., 2017), as they have been demonstrated to convert 100% of both singlet and triplet excitons into light in the absence of any metal atoms in their molecular structures (Uoyama et al., 2012; Kaji et al., 2015; Lin et al., 2016). Hence, TADF materials are expected to be widely applied as alternative emitters to the conventional fluorescence and phosphorescence materials. To realize efficient TADF, the reverse intersystem crossing (RISC) from the lowest triplet state ( $T_1$ ) to the lowest excited singlet state ( $S_1$ ) should be fast. Basically, effective RISC is expected by minimizing the energy difference between  $S_1$  and  $T_1$ , namely,  $\Delta E_{ST}$ . This can be realized simply by splitting the distribution of the highest occupied molecular orbital (HOMO) and the lowest unoccupied molecular orbital (LUMO), in most cases resulting in charge transfer (CT) type  $S_1$  and  $T_1$  ( $^1CT$  and  $^3CT$ , respectively; Endo et al., 2011). Consequently, many of the reported TADF materials are composed of donor and acceptor moieties, i.e., D-A type molecules (Yang et al., 2017). Nevertheless, small  $\Delta E_{ST}$  is not sufficient to achieve a very large RISC rate constant,  $k_{RISC}$ , typically  $>10^6 \text{ s}^{-1}$ . Notably, incorporation of locally excited

triplet states ( $^3LE$ ) close in energy to the  $^1CT$  and  $^3CT$  states is one of the most promising approaches to accelerate RISC (Dias et al., 2016; Etherington et al., 2016; Gibson et al., 2016; Marian, 2016; Hosokai et al., 2017; Lyskov and Marian, 2017; Samanta et al., 2017; Noda et al., 2018). We have recently proposed a new molecular design principle, namely, *tilted face-to-face alignment with optimal distance* (tFFO) (Wada et al., 2020). In the tFFO molecular design, the degeneration of the three energy levels, i.e.,  $^1CT$ ,  $^3CT$ , and  $^3LE$ , can be realized with a significant spin-orbit coupling matrix element value (SOCMEV) between the singlet and triplet states, resulting in efficient RISC. The energy level matching of the three levels can be accomplished by optimizing the distance between the electron donor and acceptor fragments ( $d_{DA}$ ). Moreover, SOCMEV can be enhanced by tilting the donor and acceptor fragments from the completely parallel face-to-face alignment. On the basis of the tFFO concept, we developed a through-space type molecule, namely, TpAT-tFFO, which was demonstrated to realize very large  $k_{RISC} > 10^7 \text{ s}^{-1}$ , despite being composed of only H, C, and N atoms.

In the present study, we report another tFFO-based molecule possessing a triptycene (Tp) scaffold, TpIBT-tFFO (Figure 1A, left), which is composed of 10,11-dihydro-5H-dibenzo[*b, f*]azepine (iminodibenzyl, IB) and 2,4-diphenyl-1,3,5-triazine (T) as the donor and acceptor, respectively. For comparison, a molecule comprising IB and T units, IB-TRZ (Figure 1A, right), which was first reported by

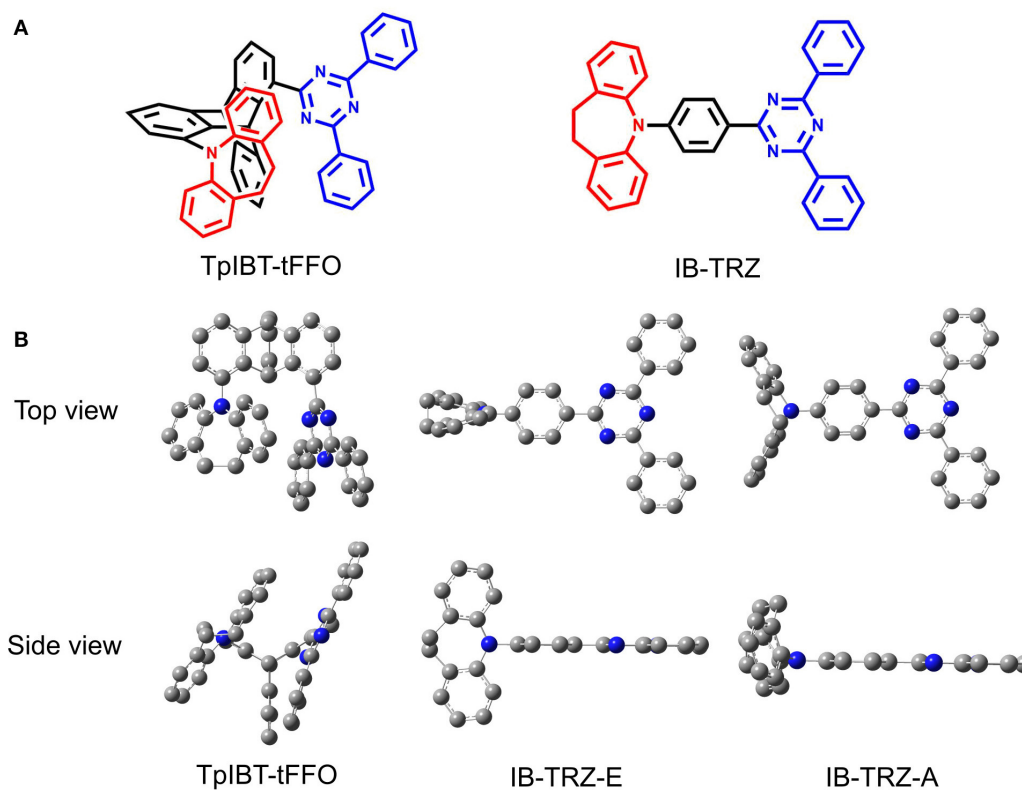


**FIGURE 1 | (A)** Chemical structures of TpIBT-tFFO and IB-TRZ. **(B)** DFT-optimized geometries of TpIBT-tFFO and IB-TRZ.

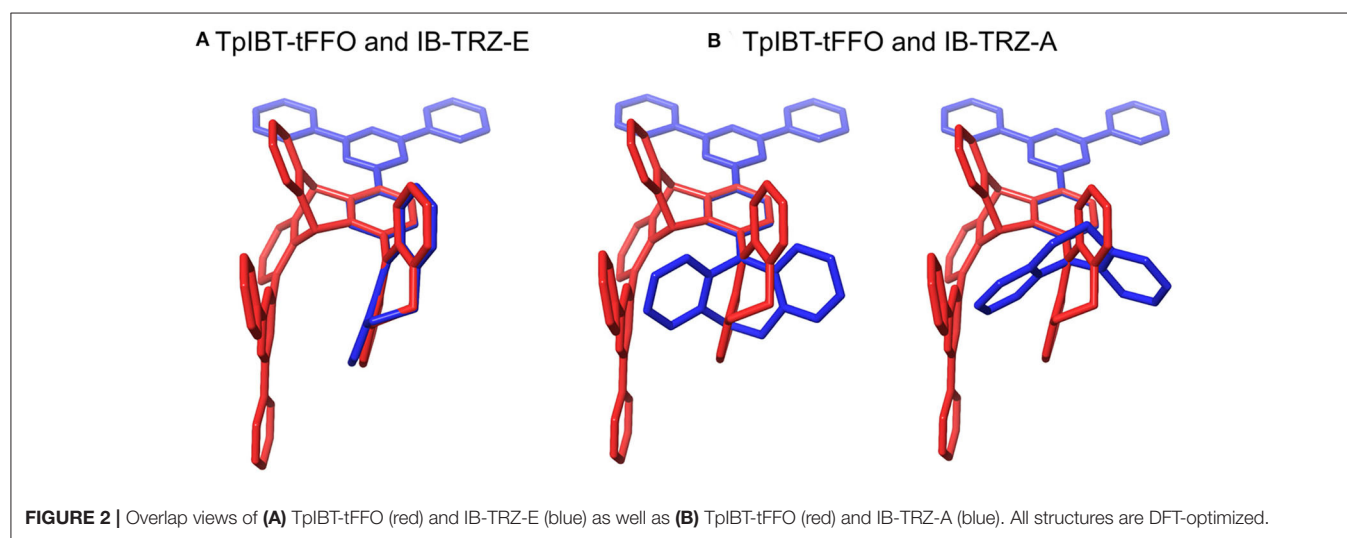
Huang et al. (2019), was also synthesized as a conventional through-bond D-A type molecule for comparison. As shown later, IB-TRZ has two conformational isomers (**Figure 1B**), resulting in dual emission. Kukhta et al. first reported on iminodibenzyl-containing TADF molecules, providing evidence for the existence of two conformers (Kukhta et al., 2018). On the other hand, excellent packing in the tFFO systems can fix the D and A conformations, leading to single-peaked emission for TpIBT-tFFO, which is an additional intriguing feature of tFFO molecular design. A large  $k_{\text{RISC}}$  of  $6.9 \times 10^6 \text{ s}^{-1}$  was obtained for TpIBT-tFFO, which is one of the highest  $k_{\text{RISC}}$  values for molecules composed of only H, C, and N atoms (The highest reported value is also for a tFFO-based molecule; Wada et al., 2020).

## RESULTS AND DISCUSSION

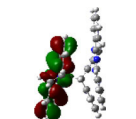
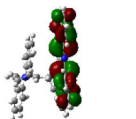
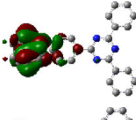
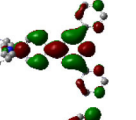
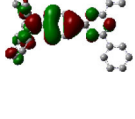
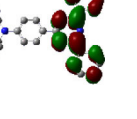
The details concerning the synthesis and characterization of both TpIBT-tFFO and IB-TRZ are provided in the **Supplementary Material**.

## Calculations

We performed density functional theory (DFT) at the B3LYP/6-31G(d) level to optimize the ground state ( $S_0$ ) geometries utilizing Gaussian 16. **Figure 1B** demonstrates the optimized molecular geometries of TpIBT-tFFO and IB-TRZ. For IB-TRZ, two energetically stable conformers were found depending on the initial conformations. One is a quasi-equatorial conformation, named IB-TRZ-E, where the donor and acceptor fragments are perpendicular to each other, while the other is quasi-axial, denoted as IB-TRZ-A. The total energy of IB-TRZ-E was 0.324 eV larger than that of IB-TRZ-A. The donor and acceptor segments of IB-TRZ-A are also nearly perpendicular to each other, however, in a different direction. The nitrogen atom in the IB units is not  $sp^3$ - but  $sp^2$ -hybridized in both conformers. The nitrogen and the directly bonded three carbon atoms form not a pyramidal, but a planar structure. The donor of IB-TRZ-A, IB, exhibits a butterfly shape bended in the middle (**Figure 2**), while TpIBT-tFFO has only one geometry, corresponding to an equatorial conformation. To visually demonstrate the difference between TpIBT-tFFO and



**TABLE 1 |** Distributions of the HOMO and LUMO, energy levels of HOMO, LUMO,  $\Delta E_{\text{ST}}$ ,  $S_1$ , and  $T_1$  of TpIBT-tFFO and IB-TRZ calculated at LC- $\omega$ PBE/6-31+G(d).

Emitter		HOMO Distribution	LUMO Distribution	HOMO (eV)	LUMO (eV)	$S_1$ (eV)	$T_1$ (eV)	$\Delta E_{\text{ST}}$ (eV)
TpIBT-tFFO				-6.44	-0.78	3.18	3.15	0.03
IB-TRZ	IB-TRZ-E			-6.70	-0.99	3.12	2.83	0.30
	IB-TRZ-A			-6.91	-0.75	3.51	2.70	0.81



IB-TRZ-E (or -A), the overlap views of TpIBT-tFFO and IB-TRZ-E as well as of TpIBT-tFFO and IB-TRZ-A are illustrated in **Figures 2A,B**, respectively. As can be seen, the IB units of TpIBT-tFFO and IB-TRZ-E are well overlapped, while the IB moieties of TpIBT-tFFO and IB-TRZ-A are significantly deviated. The nearest inter-atomic distance between IB in the axial conformation and T is too close; thus, the axial conformation in the tFFO type molecule is physically impossible, as evidenced in **Figure 2B**. For the optimized structure, DFT and time-dependent DFT (TD-DFT) calculations at the LC- $\omega$ PBE/6-31+G(d) level were also performed to estimate the energy levels of the HOMO, LUMO, and excited states more adequately. Here,  $\omega$  is the optimized range-separation parameter of the LC- $\omega$ PBE functional, employed to precisely predict the excited state energies of the TADF materials. The optimized  $\omega$  for TpIBT-tFFO was determined according to a previously reported method (Sun et al., 2015). **Table 1** summarizes the calculation results of the HOMO and LUMO distributions, energy levels of the HOMO, LUMO,  $S_1$ , and  $T_1$  as well as  $\Delta E_{ST}$  for TpIBT-tFFO, IB-TRZ-E, and IB-TRZ-A. The HOMO and LUMO distributions were significantly different between IB-TRZ-E and IB-TRZ-A, in which the central phenylene ring was included in the LUMO and HOMO, respectively. The HOMO/LUMO energy levels were  $-6.70/-0.99$  and  $-6.91/-0.75$  eV for IB-TRZ-E and IB-TRZ-A, correspondingly. Furthermore, the  $S_1$  and  $T_1$  energy levels and the resulting  $\Delta E_{ST}$  exhibited large differences (the  $\Delta E_{ST}$ s of IB-TRZ-E and IB-TRZ-A were 0.30 and 0.81 eV, respectively). In the case of TpIBT-tFFO, HOMO and LUMO were well spatially separated. On the basis of the calculated  $\Delta E_{ST}$  of 0.032 eV, TpIBT-tFFO is expected to be a promising TADF emitter. More importantly, the  $T_2$  state lies closely above the  $S_1$  state (specifically, 0.0006 eV above). We also theoretically calculated the energy difference,  $\Delta E_{ST}$ , those from  $^3CT$  to  $^1CT$ ,  $\Delta E(^3CT \rightarrow ^1CT)$ , and from  $^3LE$  to  $^1CT$ ,  $\Delta E(^3LE \rightarrow ^1CT)$  as a function of the distance between the donor (IB) and acceptor (T),  $d_{DA}$  (**Figure 3**). The calculations for the oscillator strength ( $f$ ) are also

shown. Here,  $d_{DA}$  is defined as the distance between the nitrogen atom in IB and the carbon atom in T. Excellent energy level matching of  $^1CT$ ,  $^3CT$ , and  $^3LE$ , is achieved at approximately  $d_{DA} = 4.5\text{--}5$  Å. Using a triptycene scaffold, we realized the  $d_{DA}$  of 4.76 Å, which resulted in excellent energy matching of the three states within 0.04 eV. We also carried out SOCMEV calculations employing the ADF2018 package based on the Brédas' calculation level (Samanta et al., 2017). The LCY- $\omega$ PBE functional as well as Slater-type all-electron TZP were used with the range parameter,  $\gamma$  (Akinaga and Ten-no, 2008), which was optimized at 0.21. TpIBT-tFFO exhibited SOCMEVs of 0.02 and 0.46 between  $S_1$  and  $T_1$ , and between  $S_1$  and  $T_2$ , respectively (**Table S1**). The SOCMEV between  $S_1$  and  $T_2$  was large owing to the tilted IB and T alignments created by the Tp scaffold, where the tilt angle of TpIBT-tFFO was  $\sim 20^\circ$ .

## Thermal and Photophysical Properties

The TGA curves of both TpIBT-tFFO and IB-TRZ are provided in **Figure S3**. The decomposition temperatures,  $T_{ds}$ , of TpIBT-tFFO and IB-TRZ were determined at 396 and 386°C, respectively, from the 5% weight loss point of the TGA curve.

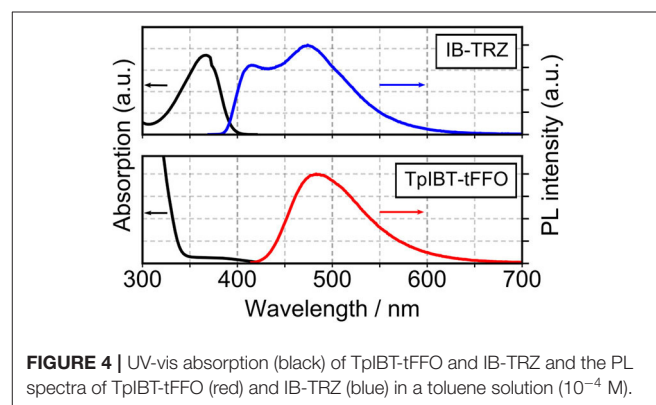


**FIGURE 4** | UV-vis absorption (black) of TpIBT-tFFO and IB-TRZ and the PL spectra of TpIBT-tFFO (red) and IB-TRZ (blue) in a toluene solution ( $10^{-4}$  M).

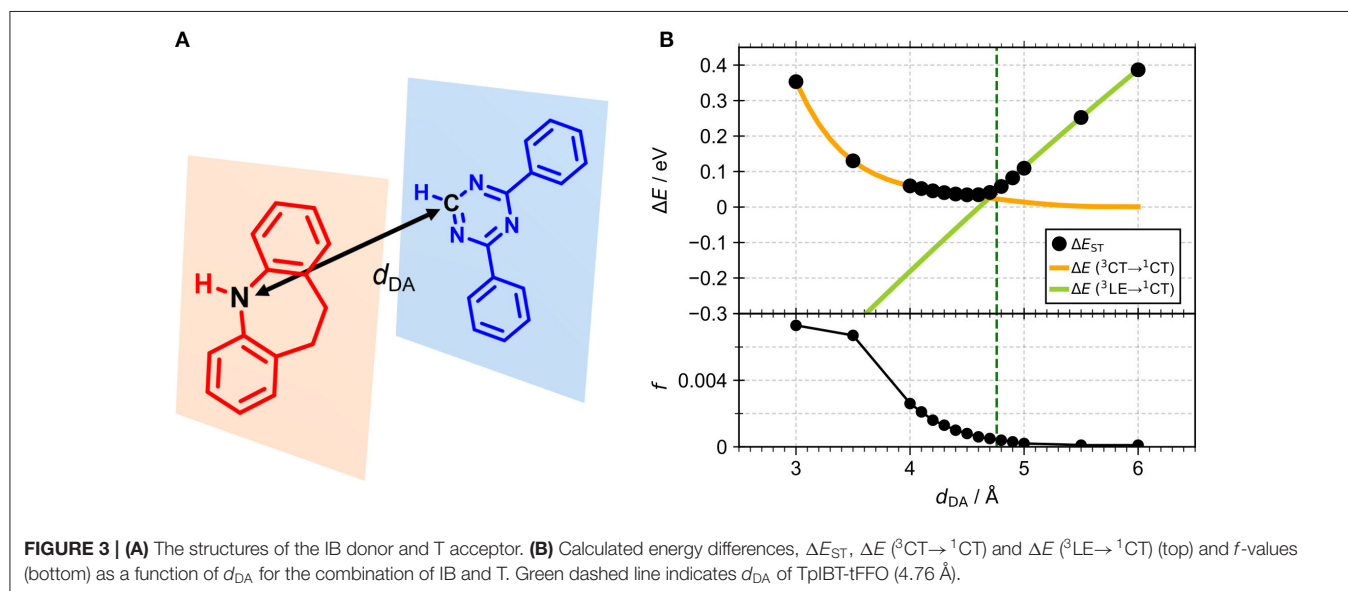


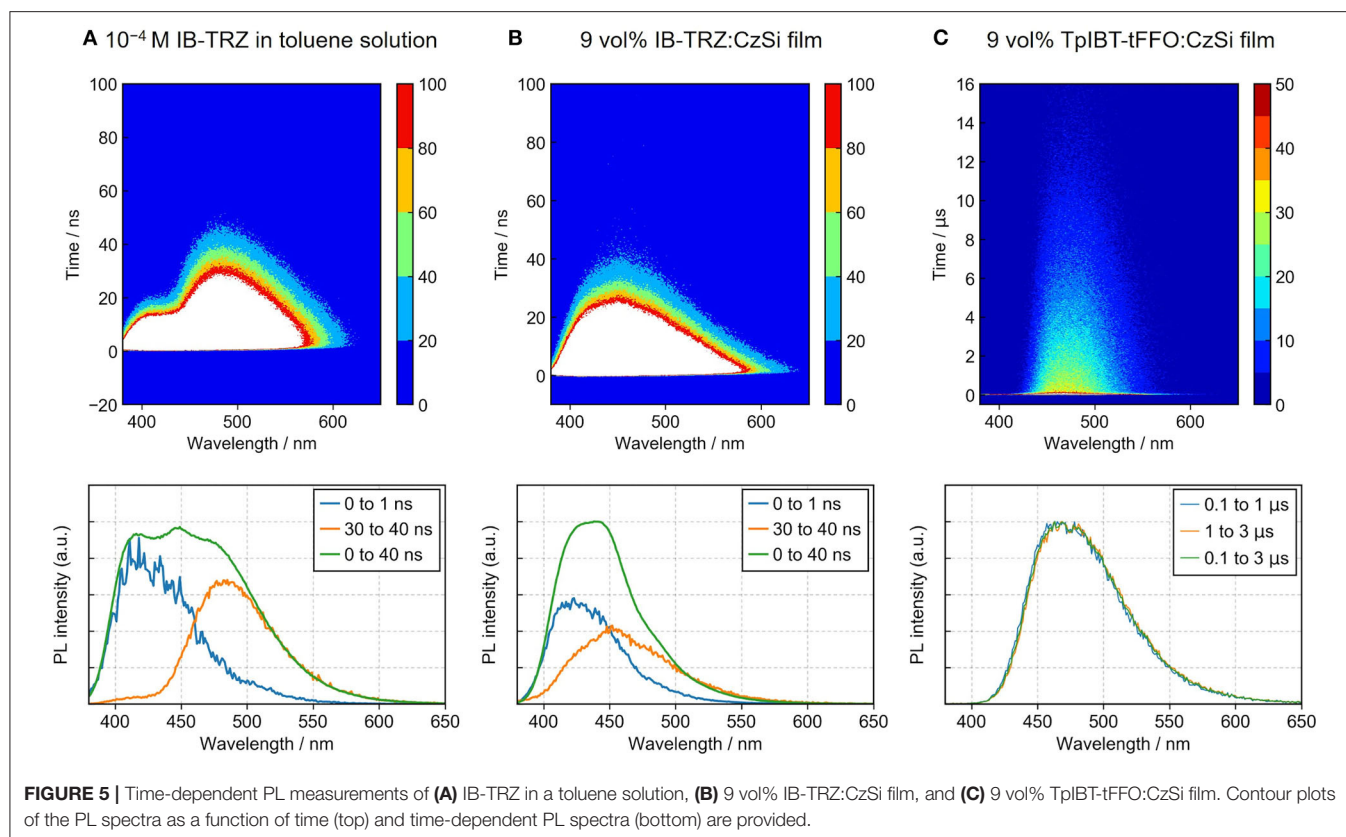
**FIGURE 3** | **(A)** The structures of the IB donor and T acceptor. **(B)** Calculated energy differences,  $\Delta E_{ST}$ ,  $\Delta E(^3CT \rightarrow ^1CT)$  and  $\Delta E(^3LE \rightarrow ^1CT)$  (top) and  $f$ -values (bottom) as a function of  $d_{DA}$  for the combination of IB and T. Green dashed line indicates  $d_{DA}$  of TpIBT-tFFO (4.76 Å).

**TABLE 2** | Experimentally obtained thermal properties, energy levels of HOMO, LUMO,  $E_g$ ,  $S_1$ ,  $T_1$ , and  $\Delta E_{ST}$  for TplBT-tFFO and IB-TRZ.

Emitter	$T_d$ (°C) <sup>a</sup>	HOMO (eV) <sup>b</sup>	LUMO (eV) <sup>c</sup>	$E_g$ (eV) <sup>d,e</sup>	$S_1$ (eV) <sup>d</sup>	$T_1$ (eV) <sup>d</sup>	$\Delta E_{ST}$ (eV) <sup>d,i</sup>
TplBT-tFFO	396	−5.73	−2.95	2.78	3.08 <sup>f</sup> (2.94 <sup>g</sup> )	3.07 <sup>h</sup>	0.0076
IB-TRZ	386	−5.87	−2.80	3.07	3.17 <sup>f</sup> (3.24 <sup>g</sup> )	2.76 <sup>h</sup>	0.41

<sup>a</sup>Determined from the 5% weight loss point of the TGA curve.<sup>b</sup>Determined from the onset of photoelectron spectrum in air and <sup>c</sup>the equation  $LUMO = E_g + HOMO$ .<sup>d</sup>Measured in a toluene solution with the emitter concentration of  $10^{-4}$  M.<sup>e</sup>Determined from the onset of the UV-vis absorption spectrum.<sup>f</sup>Determined from the onset of the steady state PL spectrum at 77 K.<sup>g</sup>Determined from the onset of the PL spectrum at room temperature.<sup>h</sup>Determined from the onset of the integrated PL spectrum from 1 to 10 ms at 77 K, and <sup>i</sup>the equation  $\Delta E_{ST} = S_1 - T_1$ .**TABLE 3** | Photophysical parameters of  $\lambda_{MAX}$ ,  $\Phi_{PL}$ ,  $\tau_p$ ,  $\tau_d$ ,  $k_{ISC}$ , and  $k_{RISC}$  for TplBT-tFFO and IB-TRZ.

Emitter	State	$\lambda_{MAX}$ (nm) <sup>c</sup>	$\Phi_{PL}$ (%)	$\tau_p$ (ns)	$\tau_d$ ( $\mu$ s)	$k_{ISC}$ ( $10^7$ s <sup>−1</sup> ) <sup>n</sup>	$k_{RISC}$ ( $10^6$ s <sup>−1</sup> ) <sup>n</sup>
TplBT-tFFO	sol <sup>a</sup>	485	52.4 <sup>d,e</sup> (1.1 <sup>d,f</sup> )	11.7 <sup>j</sup>	2.5 <sup>j</sup>	7.4	6.9
	film <sup>b</sup>	477	71.4 <sup>g,h</sup>	24.5 <sup>k</sup>	6.7 <sup>k</sup>	3.6	2.3
IB-TRZ	sol <sup>a</sup>	418, 485	26.1 <sup>d,e</sup> (11.0 <sup>d,f</sup> )	3.3 <sup>l</sup> , 10.9 <sup>m</sup>	–	–	–
	film <sup>b</sup>	423, 452	23.5 <sup>g,i</sup>	2.9 <sup>j</sup> , 5.2 <sup>m</sup>	–	–	–

Measured <sup>a</sup>in a toluene solution with the emitter concentration of  $10^{-4}$  M and <sup>b</sup>from the 9 vol% emitter:CzSi film.<sup>c</sup>Determined from the time-dependent spectra for IB-TRZ.Measured <sup>d</sup>with the excitation wavelength of 365 nm; <sup>e</sup>after 15 min of Ar bubbling; <sup>f</sup>after 15 min of O<sub>2</sub> bubbling; <sup>g</sup>under N<sub>2</sub> flow; <sup>h</sup>at the excitation wavelength of 340 nm; <sup>i</sup>at the excitation wavelength of 350 nm; <sup>j</sup>at the observed wavelength of 485 nm; <sup>k</sup>at the observed wavelength of 477 nm; <sup>l</sup>at the observed wavelength of 400 nm; <sup>m</sup>at the observed wavelength of 500 nm.<sup>n</sup>Calculated according to a previously reported method (Wada et al., 2020).**FIGURE 5** | Time-dependent PL measurements of (A) IB-TRZ in a toluene solution, (B) 9 vol% IB-TRZ:CzSi film, and (C) 9 vol% TplBT-tFFO:CzSi film. Contour plots of the PL spectra as a function of time (top) and time-dependent PL spectra (bottom) are provided.

**Figure 4** shows the ultraviolet-visible (UV-vis) absorption and photoluminescence (PL) spectra of IB-TRZ and TpIBT-tFFO in  $10^{-4}$  M toluene solutions. IB-TRZ exhibited dual emission with the first and second peak maximum wavelength ( $\lambda_{\text{MAX}}$ ) of 417 and 474 nm, respectively, while TpIBT-tFFO displayed single-peaked emission with  $\lambda_{\text{MAX}}$  of 485 nm. Considering the above calculation results, the emissions of IB-TRZ at shorter and longer wavelengths were rationally assigned to IB-TRZ-A and IB-TRZ-E, correspondingly. The assignment was further confirmed by transient PL experiments described below. To investigate the TADF performance of IB-TRZ and TpIBT-tFFO, we carried out PL quantum yield (PLQY) measurements for the toluene solution under  $\text{O}_2$  or Ar bubbling for 15 min. In the case of IB-TRZ, the PLQY differed: 11.0% ( $\text{O}_2$ ) and 26.1% (Ar). On the other hand, the PLQY of TpIBT-tFFO in the toluene solution considerably increased from 1.1% ( $\text{O}_2$ ) to 52.4% (Ar). This is a typical feature of tFFO type molecules, which exhibit significantly larger  $k_{\text{ISC}}$  and  $k_{\text{RISC}}$  than  $k_{\text{r}}^{\text{S}}$  and  $k_{\text{nr}}^{\text{S}}$  (Wada et al., 2020). Here,  $k_{\text{ISC}}$ ,  $k_{\text{r}}^{\text{S}}$ , and  $k_{\text{nr}}^{\text{S}}$  indicate the rate constants of intersystem crossing, radiative decay from  $\text{S}_1$ , and non-radiative decay from  $\text{S}_1$ , respectively. Considering that  $\text{O}_2$  molecules behave as triplet quenchers, these outcomes indicate that a triplet state was strongly involved in the TpIBT-tFFO emission process. To determine  $\Delta E_{\text{ST}}$  experimentally, we performed a PL measurement at 77 K (**Figure S4**). In most cases,  $\Delta E_{\text{ST}}$  of the TADF materials was established based on the energy difference between the onset of the PL (fluorescence) spectrum at RT and that of the PL (phosphorescence) spectrum at low temperature. According to this procedure, we obtained a negative  $\Delta E_{\text{ST}}$  of  $-0.13$  eV for TpIBT-tFFO. Previously, negative  $\Delta E_{\text{ST}}$  values for TADF molecules has been reported in some articles (Di et al., 2017; Kim et al., 2018; Braveenth et al., 2019); however, the Arrhenius plots of  $k_{\text{ISC}}$  and  $k_{\text{RISC}}$  provided positive  $\Delta E_{\text{ST}}$ , 0.0061 eV (the difference of activation energies for RISC and ISC, see **Table 4** below), although the value was obtained for solid film sample. We speculate that the negative value obtained from the above procedure might be a consequence of smaller structural relaxations after vertical excitation from  $\text{S}_0$  at 77 K than at RT. Another possible origin would be different  $\text{S}_0$  structures between the vertical transitions from  $\text{S}_1$  and from  $\text{T}_1$ . Thus, we determined  $\Delta E_{\text{ST}}$  based on the energy difference between the onset of the steady state PL spectrum at 77 K (corresponding to  $\text{S}_1$ , the spectrum also includes phosphorescence but the onset is determined by  $\text{S}_1$ .) and that of the integrated PL spectrum from 1 to 10 ms at 77 K (corresponding to  $\text{T}_1$ ). We believe that this is a more reasonable approach to establish  $\Delta E_{\text{ST}}$  experimentally. The  $\Delta E_{\text{ST}}$  values of IB-TRZ and TpIBT-tFFO were determined at 0.41 and 0.0076 eV, respectively (**Table 2**). These experimentally-determined values reasonably reflect the calculated ones (**Table 1**) and the value estimated from the Arrhenius plots. To understand the dual emissions of IB-TRZ, we performed a transient PL measurement for the solution. **Figure S5C** shows the transient PL decay curves of IB-TRZ observed at 400 and 500 nm, which were used to monitor the emission from IB-TRZ-A and IB-TRZ-E, respectively. For IB-TRZ, the PL decay curves with the lifetime of prompt fluorescence,  $\tau_{\text{p}}$ , of 3.3 and 10.9 ns were

observed at 400 and 500 nm, respectively. **Table 3** summarizes the obtained photophysical parameters. Time-dependent PL spectra evidently revealed that IB-TRZ exhibits two different emissions as discussed later (**Figures 5A,B**). Moreover, no clear delayed fluorescence with the  $\mu\text{s}$ -order lifetime was found in IB-TRZ. In the case of TpIBT-tFFO, in addition to normal (prompt) fluorescence with a lifetime of 11.7 ns, delayed fluorescence with a lifetime of 2.5  $\mu\text{s}$  was also clearly observed following Ar gas bubbling (**Figure S5D**). The lifetime of the prompt component was in good agreement with that of IB-TRZ-E (10.9 ns). The emission of TpIBT-tFFO was primarily composed of the delayed component, which disappeared after  $\text{O}_2$  gas bubbling (**Figure S5B**). From the PLQY and transient PL measurements of TpIBT-tFFO, 93.6% of the total PLQY was attributed to the delayed emission. These results indicate that TpIBT-tFFO is a TADF-active emitter. The  $k_{\text{ISC}}$  and  $k_{\text{RISC}}$  values of TpIBT-tFFO were experimentally determined at  $7.4 \times 10^7 \text{ s}^{-1}$  and  $6.9 \times 10^6 \text{ s}^{-1}$ , respectively, utilizing our previously reported method (Wada et al., 2020). The large  $k_{\text{RISC}}$  value is by virtue of the tFFO design.

To investigate the TADF characteristics of IB-TRZ and TpIBT-tFFO in amorphous films, IB-TRZ and TpIBT-tFFO were doped into the host matrix. For this purpose, 9-(4-(*tert*-butyl)phenyl)-3,6-bis(triphenylsilyl)-9H-carbazole (CzSi) with high  $\text{T}_1$  energy of 3.02 eV was used as the host to confine the triplet energies of IB-TRZ and TpIBT-tFFO. **Figure S6A** illustrates the PL spectrum of the 9 vol% IB-TRZ:CzSi film. Unlike the spectrum in solution (**Figure S5A**), seemingly one peak top at approximately

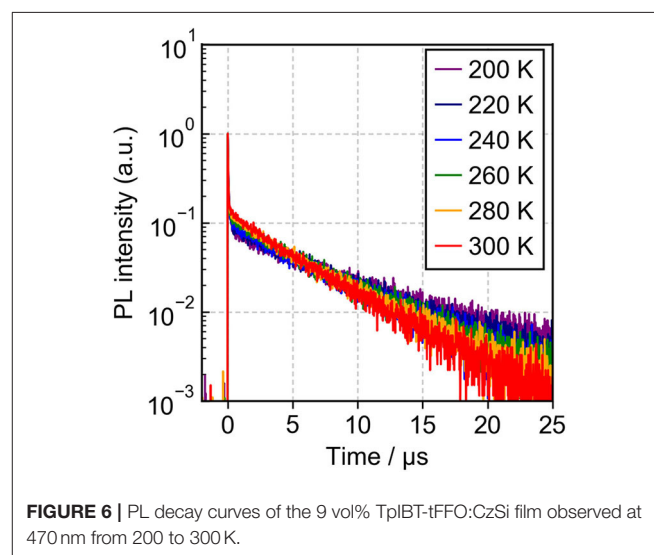


**TABLE 4** | Energy differences of  $\text{T}_1$  and  $\text{T}_2$  [ $\Delta E (\text{T}_1 \leftrightarrow \text{T}_2)$ ] and  $\text{S}_1$  and  $\text{T}_2$  [ $\Delta E (\text{S}_1 \leftrightarrow \text{T}_2)$ ] for TpIBT-tFFO obtained experimentally and via a DFT calculation.

Energy difference	Experiment	Calculation
$\Delta E (\text{S}_1 \leftrightarrow \text{T}_2)$ (eV)	0.0305	0.0006
$\Delta E (\text{T}_1 \leftrightarrow \text{T}_2)$ (eV)	0.0366	0.0326

421 nm was observed. The transient PL experiment (Figure S6C) demonstrated different  $\tau_p$  of 2.9 and 5.2 ns at 400 and 500 nm, respectively. The time-dependent PL spectrum shown in Figure 5B confirmed that the PL spectrum was composed of two different emissions. The distinct two peak tops were not found because the emission wavelength with longer  $\tau_p$  in the film came closer to that with shorter  $\tau_p$  (452 and 423 nm, respectively), compared to the case in solution (485 and 418 nm, respectively). The value of longer  $\tau_p$  in the film (5.2 ns) was also closer to that of shorter  $\tau_p$  (2.9 ns) compared to the solution case (10.9 and 3.3 ns, respectively). These results indicate that the component with the emission wavelength of 452 nm in the film originated from IB-TRZ with the intermediate structure between quasi-equatorial and quasi-axial conformers.

Meanwhile, the 9 vol%TpIBT-tFFO:CzSi film exhibited a PL spectrum with  $\lambda_{MAX}$  of 477 nm (Figure S6B), which was

composed of only one emission, as evidenced by the transient PL experiment demonstrated in Figure 5C. The emission wavelength of 477 nm was also consistent with that in the solution. Analogously to the solution case, two clear exponential decays with the lifetimes of 24.5 ns and 6.7  $\mu$ s were observed (Figure S6D), and the emission spectra in TpIBT-tFFO did not change with time (Figure 5C), confirming the TADF character of TpIBT-tFFO. These results indicate that the molecular conformation can be effectively controlled in the tFFO system, resulting in single-peaked emission. Under N<sub>2</sub> gas flow, the PLQY of the 9 vol% TpIBT-tFFO:CzSi film was relatively high (71.4%) compared with that of the 9 vol% IB-TRZ:CzSi film (23.5%). The higher PLQY is a result of the availability of efficient RISC in TpIBT-tFFO. We also carried out temperature-dependent transient PL measurements to examine the energy level matching of the excited states in TpIBT-tFFO (Figure 6).

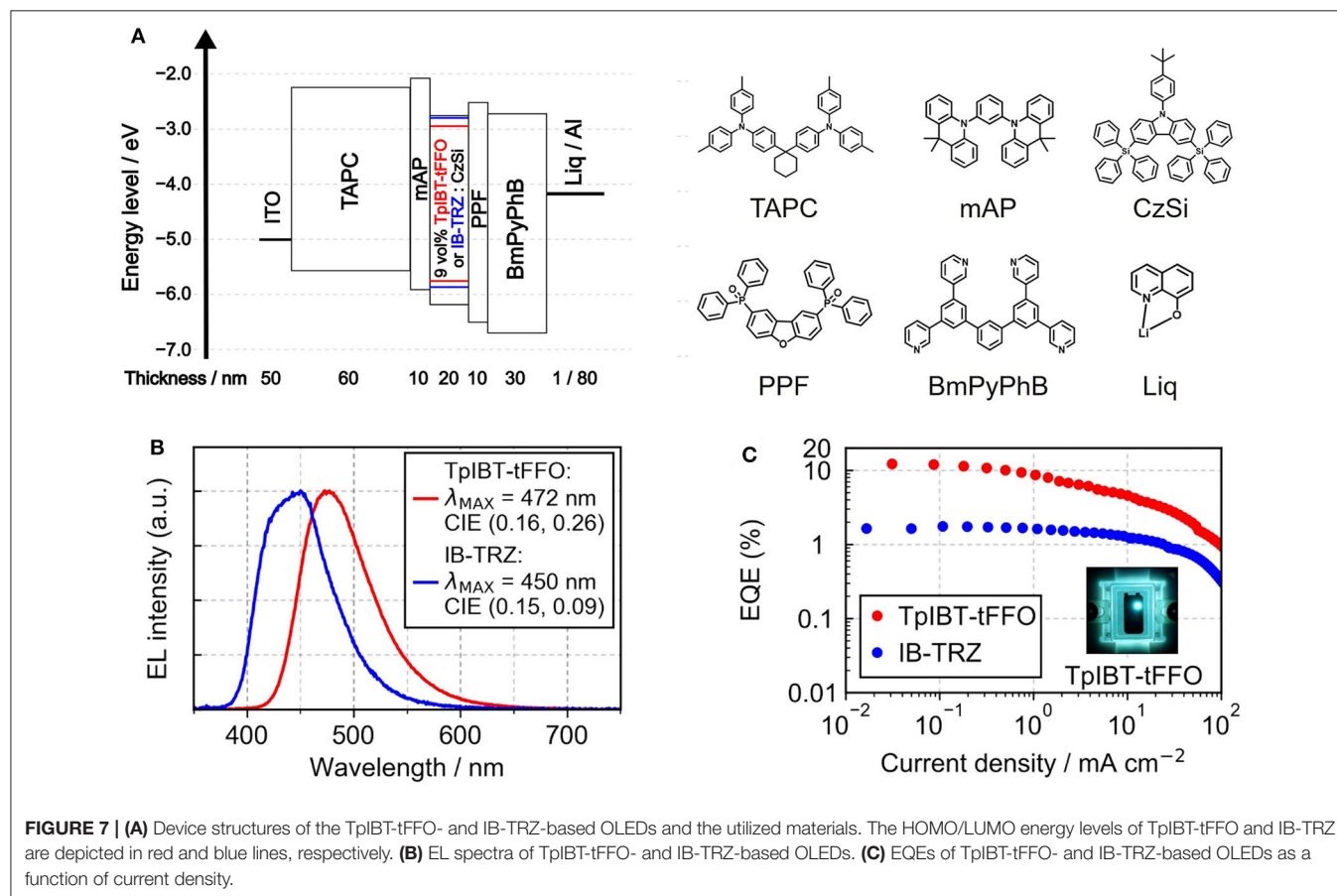


**TABLE 5 |** OLED performances of TpIBT-tFFO and IB-TRZ.

Emitter	$\lambda_{MAX}$ (nm)	CIE (x, y)	EQE <sub>MAX</sub> (%)	V <sub>on</sub> (V) <sup>a</sup>	PE <sub>MAX</sub> (lm W <sup>-1</sup> )	CE <sub>MAX</sub> (cd A <sup>-1</sup> )
TpIBT-tFFO	472	(0.16, 0.26)	12.2	3.2	20.8	22.1
IB-TRZ	450	(0.15, 0.09)	1.8	3.8	1.3	1.4

<sup>a</sup> Determined from the first voltage exceeding 1 cd m<sup>-2</sup>.



From the Arrhenius plots of  $k_{ISC}$  and  $k_{RISC}$ , activation energies for ISC ( $E_{ISC}$ ) and RISC ( $E_{RISC}$ ) were determined at 0.0305 and 0.0366 eV, respectively. Combined with the calculation results described above, we established the experimental energy differences between  $S_1$  and  $T_2$  [ $\Delta E (S_1 \leftrightarrow T_2)$ ] as well as between  $T_1$  and  $T_2$  [ $\Delta E (T_1 \leftrightarrow T_2)$ ] (Table 4). Excellent energy level matching of the three states was successfully realized in TpIBT-tFFO.

## Electroluminescence Performance

From the photophysical observations, we established that TpIBT-tFFO is a promising TADF emitter exhibiting high triplet-to-singlet conversion efficiency. This motivated us to fabricate TpIBT-tFFO-based OLED. For comparison, we also fabricated IB-TRZ-based OLED. Figure 7A shows the device structure, indium tin oxide (ITO) (50 nm)/1,1-bis[4-[N, N-di(p-tolyl)amino]phenyl]cyclohexane (TAPC) (60 nm)/1,3-bis(9,9-dimethylacridin-10(9H)-yl)benzene (mAP) (10 nm)/9 vol% IB-TRZ or TpIBT-tFFO:CzSi (20 nm)/2,8-bis(diphenylphosphoryl)dibenzo[b,d]furan (PPF) (10 nm)/1,3-bis[3,5-di(pyridin-3-yl)phenyl]benzene (BmPyPhB) (30 nm)/lithium quinolin-8-olate (Liq) (1 nm)/Al (80 nm). Figures 7B,C illustrate the EL spectra and external quantum efficiency (EQE)-current density characteristics of the IB-TRZ- and TpIBT-tFFO-based OLEDs. A summary of the device performances is provided in Table 5. The EL spectra of the OLEDs were substantially identical to the corresponding PL spectra, with  $\lambda_{MAX}$  at 450 and 472 nm for IB-TRZ and TpIBT-tFFO, respectively. The TpIBT-tFFO-based OLED exhibited maximum EQE ( $EQE_{MAX}$ ) of 12.2%, which is approximately seven times higher than that of the IB-TRZ-based OLED ( $EQE_{MAX} = 1.8\%$ ). This remarkable improvement of EQE can be attributed to the efficient TADF of TpIBT-tFFO.

## CONCLUSION

In summary, in the present study, we developed a tFFO-based TADF material, i.e., TpIBT-tFFO, and compared it with IB-TRZ. Both materials contain an iminodibenzyl moiety as an electron donor unit. The TD-DFT calculations demonstrated that not only  $T_1$  but also  $T_2$  were lying close to the  $S_1$  state in TpIBT-tFFO,

as we designed for. From photophysical properties, IB-TRZ had two different conformers, resulting in dual emission. In contrast, the conformation was effectively controlled in the tFFO system, providing a single-peaked emission in TpIBT-tFFO. Furthermore, TpIBT-tFFO exhibited higher PLQY and higher EQE values compared to IB-TRZ. The  $k_{RISC}$  of TpIBT-tFFO was determined to be  $6.9 \times 10^6 \text{ s}^{-1}$ , which is one of the highest values in TADF materials composed of only H, C, and N atoms, as a consequence of the tFFO strategy.

## DATA AVAILABILITY STATEMENT

All datasets generated for this study are included in the article/Supplementary Material.

## AUTHOR CONTRIBUTIONS

HK proposed the idea of tFFO and KS, YW, and YK proposed the idea of IBT-based TADF. YW and YK performed quantum chemical calculations and carried out characterization. HN, YW, and YK contributed to the synthesis of the materials. YK fabricated the devices under the supervision of YW. All authors participated in writing the manuscript. YW and HK planned and supervised this study. All authors contributed to the article and approved the submitted version.

## ACKNOWLEDGMENTS

This work was supported by JSPS KAKENHI grant nos. 17H01231 and 17J09631. Computation time was provided by the Super Computer System, Institute for Chemical Research, Kyoto University. NMR measurements were supported by the Joint Usage/Research Centre (JURC) at the Institute for Chemical Research, Kyoto University, Japan.

## SUPPLEMENTARY MATERIAL

The Supplementary Material for this article can be found online at: <https://www.frontiersin.org/articles/10.3389/fchem.2020.00530/full#supplementary-material>

## REFERENCES

- Akinaga, Y., and Ten-no, S. (2008). Range-separation by the Yukawa potential in long-range corrected density functional theory with Gaussian-type basis functions. *Chem. Phys. Lett.* 462, 348–351. doi: 10.1016/j.cplett.2008.07.103
- Braveenth, R., Lee, H., Kim, S., Raagulan, K., Kim, S., Kwon, J. H., et al. (2019). High efficiency green TADF emitters of acridine donor and triazine acceptor D-A-D structures. *J. Mater. Chem. C* 7, 7672–7680. doi: 10.1039/C9TC02491C
- Di, D., Romanov, A. S., Yang, L., Richter, J. M., Rivett, J. P. H., Jones, S., et al. (2017). High-performance light-emitting diodes based on carbene-metal-amides. *Science* 356, 159–163. doi: 10.1126/science.aah4345
- Dias, F. B., Santos, J., Graves, D. R., Data, P., Nobuyasu, R. S., Fox, M. A., et al. (2016). The role of local triplet excited states and D-A relative orientation in thermally activated delayed fluorescence: photophysics and devices. *Adv. Sci.* 3, 1600080. doi: 10.1002/advs.201600080
- Endo, A., Sato, K., Yoshimura, K., Kai, T., Kawada, A., Miyazaki, H., et al. (2011). Efficient up-conversion of triplet excitons into a singlet state and its application for organic light emitting diodes. *Appl. Phys. Lett.* 98, 083302. doi: 10.1063/1.3558906
- Etherington, M. K., Gibson, J., Higginbotham, H. F., Penfold, T. J., and Monkman, A. P. (2016). Revealing the spin-vibronic coupling mechanism of thermally activated delayed fluorescence. *Nat. Commun.* 7, 13680. doi: 10.1038/ncomms13680
- Gibson, J., Monkman, A. P., and Penfold, T. J. (2016). The importance of vibronic coupling for efficient reverse intersystem crossing in thermally activated delayed fluorescence molecules. *Chem. Phys. Chem.* 17, 2956–2961. doi: 10.1002/cphc.201600662
- Hosokai, T., Matsuzaki, H., Nakanotani, H., Tokumaru, K., Tsutsui, T., Furube, A., et al. (2017). Evidence and mechanism of efficient thermally activated delayed fluorescence promoted by delocalized excited states. *Sci. Adv.* 3, e1603282. doi: 10.1126/sciadv.1603282

- Huang, W., Einzinger, M., Maurano, A., Zhu, T., Tjepelt, J., Yu, C., et al. (2019). Large increase in external quantum efficiency by dihedral angle tuning in a sky-blue thermally activated delayed fluorescence emitter. *Adv. Opt. Mater.* 7, 1900476. doi: 10.1002/adom.201900476
- Kaji, H., Suzuki, H., Fukushima, T., Shizu, K., Suzuki, K., Kubo, S., et al. (2015). Purely organic electroluminescent material realizing 100% conversion from electricity to light. *Nat. Commun.* 6, 8476. doi: 10.1038/ncomms9476
- Kim, H. S., Park, H., Park, S. R., Lee, S. H., Ahn, Y., Lee, Y. S., et al. (2018). Photophysical properties of thermally activated delayed fluorescent materials upon distortion of central axis of donor moiety. *J. Phys. Chem. C* 122, 28576–28587. doi: 10.1021/acs.jpcc.8b11144
- Kukhta, N. A., Batsanov, A. S., Bryce, M. R., and Monkman, A. P. (2018). Importance of chromophore rigidity on the efficiency of blue thermally activated delayed fluorescence emitters. *J. Phys. Chem. C* 122, 28564–28575. doi: 10.1021/acs.jpcc.8b10867
- Lin, T. A., Chatterjee, T., Tsai, W. L., Lee, W. K., Wu, M. J., Jiao, M., et al. (2016). Sky-blue organic light emitting diode with 37% external quantum efficiency using thermally activated delayed fluorescence from spiroacridine-triazine hybrid. *Adv. Mater.* 28, 6976–6983. doi: 10.1002/adma.201601675
- Lyskov, I., and Marian, C. M. (2017). Climbing up the ladder: intermediate triplet states promote the reverse intersystem crossing in the efficient TADF emitter ACRSA. *J. Phys. Chem. C* 121, 21145–21153. doi: 10.1021/acs.jpcc.7b06187
- Marian, C. M. (2016). Mechanism of the triplet-to-singlet upconversion in the assistant dopant ACRTN. *J. Phys. Chem. C* 120, 3715–3721. doi: 10.1021/acs.jpcc.6b00060
- Noda, H., Nakanotani, H., and Adachi, C. (2018). Excited state engineering for efficient reverse intersystem crossing. *Sci. Adv.* 4, eaao6910. doi: 10.1126/sciadv.aao6910
- Samanta, P. K., Kim, D., Coropceanu, V., and Brédas, J. L. (2017). Up-conversion intersystem crossing rates in organic emitters for thermally activated delayed fluorescence: impact of the nature of singlet vs triplet excited states. *J. Am. Chem. Soc.* 139, 4042–4051. doi: 10.1021/jacs.6b12124
- Sun, H., Zhong, C., and Brédas, J. L. (2015). Reliable prediction with tuned range-separated functionals of the singlet-triplet gap in organic emitters for thermally activated delayed fluorescence. *J. Chem. Theory Comput.* 11, 3851–3858. doi: 10.1021/acs.jctc.5b00431
- Uoyama, H., Goushi, K., Shizu, K., Nomura, H., and Adachi, C. (2012). Highly efficient organic light-emitting diodes from delayed fluorescence. *Nature* 492, 234–238. doi: 10.1038/nature11687
- Wada, Y., Nakagawa, H., Matsumoto, S., Wakisaka, Y., and Kaji, H. (2020). Organic light emitters exhibiting very fast reverse intersystem crossing. *Nat. Photon.* doi: 10.1038/s41566-020-0667-0
- Yang, Z., Mao, Z., Xie, Z., Zhang, Y., Liu, S., Zhao, J., et al. (2017). Recent advances in organic thermally activated delayed fluorescence materials. *Chem. Soc. Rev.* 46, 915–1016. doi: 10.1039/C6CS00368K

**Conflict of Interest:** The authors declare that the research was conducted in the absence of any commercial or financial relationships that could be construed as a potential conflict of interest.

Copyright © 2020 Kusakabe, Wada, Nakagawa, Shizu and Kaji. This is an open-access article distributed under the terms of the Creative Commons Attribution License (CC BY). The use, distribution or reproduction in other forums is permitted, provided the original author(s) and the copyright owner(s) are credited and that the original publication in this journal is cited, in accordance with accepted academic practice. No use, distribution or reproduction is permitted which does not comply with these terms.



# What Controls the Orientation of TADF Emitters?

Bilal A. Naqvi<sup>1</sup>, Markus Schmid<sup>1</sup>, Ettore Crovini<sup>2</sup>, Prakhar Sahay<sup>1</sup>, Tassilo Naujoks<sup>1</sup>, Francesco Rodella<sup>3</sup>, Zhen Zhang<sup>4</sup>, Peter Strohriegl<sup>3</sup>, Stefan Bräse<sup>4,5</sup>, Eli Zysman-Colman<sup>2</sup> and Wolfgang Brütting<sup>1\*</sup>

<sup>1</sup> Institute of Physics, University of Augsburg, Augsburg, Germany, <sup>2</sup> Organic Semiconductor Centre, EaStCHEM School of Chemistry, University of St Andrews, St Andrews, United Kingdom, <sup>3</sup> Macromolecular Chemistry, University of Bayreuth, Bayreuth, Germany, <sup>4</sup> Institute of Organic Chemistry, Karlsruhe Institute of Technology, Karlsruhe, Germany, <sup>5</sup> Institute of Biological and Chemical Systems – Functional Molecular Systems, Karlsruhe Institute of Technology, Eggenstein-Leopoldshafen, Germany

## OPEN ACCESS

### Edited by:

Guigen Li,  
Texas Tech University, United States

### Reviewed by:

CaiJun Zheng,  
University of Electronic Science and  
Technology of China, China  
Jie Li,  
Taiyuan University of  
Technology, China

### \*Correspondence:

Wolfgang Brütting  
bruetting@physik.uni-augsburg.de

### Specialty section:

This article was submitted to  
Organic Chemistry,  
a section of the journal  
Frontiers in Chemistry

**Received:** 10 June 2020

**Accepted:** 21 July 2020

**Published:** 04 September 2020

### Citation:

Naqvi BA, Schmid M, Crovini E,  
Sahay P, Naujoks T, Rodella F,  
Zhang Z, Strohriegl P, Bräse S,  
Zysman-Colman E and Brütting W  
(2020) What Controls the Orientation  
of TADF Emitters?  
Front. Chem. 8:750.  
doi: 10.3389/fchem.2020.00750

Thermally-activated delayed fluorescence (TADF) emitters—just like phosphorescent ones—can in principle allow for 100% internal quantum efficiency of organic light-emitting diodes (OLEDs), because the initially formed electron-hole pairs in the non-emissive triplet state can be efficiently converted into emissive singlets by reverse intersystem crossing. However, as compared to phosphorescent emitter complexes with their bulky—often close to spherical—molecular structures, TADF emitters offer the advantage to align them such that their optical transition dipole moments (TDMs) lie preferentially in the film plane. In this report, we address the question which factors control the orientation of TADF emitters. Specifically, we discuss how guest-host interactions may be used to influence this parameter and propose an interplay of different factors being responsible. We infer that emitter orientation is mainly governed by the molecular shape of the TADF molecule itself and by the physical properties of the host—foremost, its glass transition temperature  $T_g$  and its tendency for alignment being expressed, e.g., as birefringence or the formation of a giant surface potential of the host. Electrostatic dipole-dipole interactions between host and emitter are not found to play an important role.

**Keywords:** OLEDs, TADF, emitter orientation, molecular orientation, emitter-host interaction

## INTRODUCTION

Organic light-emitting diodes (OLEDs) are thin-film structures where photons are produced from radiative recombination of electron-hole pairs through an excited state of a molecular emitter material that is commonly embedded in a suitable host matrix to avoid aggregation and, thus, luminescence quenching (Tang et al., 1989). While the primary steps of exciton formation and decay are quantum mechanical in nature and also involve selection rules related to the spin of the involved species, the propagation and extraction of the produced radiation can be treated in a semi-classical dipole model (Barnes, 1998; Penninck et al., 2011). The external quantum efficiency  $\eta_{\text{ext}}$  of an OLED, i.e., the ratio between extracted photons from a device divided by the number of injected charges, is therefore split into an internal factor  $\eta_{\text{int}}$  comprising charge balance  $\gamma$ , spin statistics  $\eta_r$  and radiative exciton decay  $q_{\text{eff}}$ , and an outcoupling factor  $\eta_{\text{out}}$  for the fraction of light that is actually emitted from the OLED and is visible to an observer (Tsutsui et al., 1997). Note that this separation is not strictly valid, because the radiative quantum efficiency is influenced by the device stack as well through the so-called Purcell effect, yielding an effective value  $q_{\text{eff}}$  (Nowy et al., 2008; Brütting et al., 2013).

$$\eta_{\text{ext}} = \gamma \cdot \eta_r \cdot q_{\text{eff}} \cdot \eta_{\text{out}} \equiv \eta_{\text{int}} \cdot \eta_{\text{out}}$$

Thermally-activated delayed fluorescence (TADF) emitters—just like phosphorescent ones—can in principle harvest for 100% radiative excitons ( $\eta_r = 1$ ) because the initially formed electron-hole pairs in the non-emissive triplet state can be efficiently converted into emissive singlets by reverse intersystem crossing (Uoyama et al., 2012). However, as compared to commercial iridium(III)-based phosphorescent complexes with their often close to spherical molecular structures, TADF emitters often possess similar shape to the host matrix molecules and offer the advantage to be aligned such that their optical transition dipole moments (TDMs) lie preferentially in the film plane (Figure 1A). Using the above mentioned semi-classical dipole model, it follows that the external quantum efficiency of a TADF OLED can be dramatically enhanced, if instead of an ensemble of randomly oriented emitter molecules, horizontally aligned TDMs prevail in the system (Figure 1B).

As described in detail in the **Supporting Material**, we use an order parameter  $\Theta$  to quantify the degree of horizontal orientation of the emitting TDM (Schmidt et al., 2017), which is defined as the fraction of optical power emitted by vertical dipoles within the system. This parameter is equivalent to the second Legendre polynomial  $P_2(\vartheta) = \frac{1}{2}(3\cos^2\vartheta - 1)$ , where  $\vartheta$  is the angle between the substrate normal and the direction of the TDM vector (see Figure 1A). Ideally, the  $\Theta$  values should be close to zero because the radiation from vertical dipoles remains trapped as wave-guided or surface plasmon modes and is not coupled out from an OLED.

This fact being known already for some time, the detailed mechanism driving non-isotropic orientation of molecular emitter materials in a guest-host system remained elusive. In an early work, Yokoyama has pointed out—at that time working with fluorescent-only materials—that the shape anisotropy of the molecules plays a decisive role (Yokoyama, 2011). The more rod-like (or disc-like) they are, the stronger their tendency to form optically anisotropic thin films, which he defined as the ratio of birefringence probed by ellipsometry. Alternatively, radiation pattern analysis under photoluminescence excitation (ADPL, “angular dependent photoluminescence”; see **Supporting Material** for details) was developed as a powerful method to study emitter orientation (Frischeisen et al., 2010). This technique enabled investigations on guest-host systems with only a small fraction of the light-emitting species embedded in a wider-gap host matrix. Surprisingly enough, non-isotropic radiation patterns indicating horizontal emitter orientation were observed even for systems where the host material alone does not show any anisotropy (Flämmich et al., 2011; Frischeisen et al., 2011).

An important step toward controlling emitter orientation came from the field of glass physics, where it was demonstrated that evaporated neat films of organic semiconductors can form anisotropic molecular glasses with their orientation being controlled by the temperature of the substrate  $T_s$  (and the evaporation rate) in relation to the glass transition temperature  $T_g$  of the organic material (Dalal et al., 2013). Specifically, it was shown that horizontal orientation of neat organic films leading to

birefringence can be obtained for  $T_s/T_g \leq 0.8$ . Instead of varying the substrate temperature  $T_s$ , Mayr showed that the same effect can be achieved in a guest-host system if hosts with different  $T_g$ 's are used (Mayr and Brütting, 2015). Subsequently, TADF emitters with completely horizontal orientation could be achieved by film growth on cooled substrates and their positive effect for OLED efficiency was clearly demonstrated (Komino et al., 2016).

The current understanding of orientation in OLEDs has progressed substantially, in particular as it pertains to fluorescent as well as phosphorescent emitters (Schmidt et al., 2017; Kim and Kim, 2018). Spherically octahedrally coordinated phosphorescent Iridium(III) complexes can show some degree of horizontal orientation (typically <80%), but other reports suggest that this effect is even more pronounced for TADF emitters with up to 100% of the emitters being horizontally aligned (Byeon et al., 2018). Since thermal evaporation is a non-equilibrium process, molecular orientation in such non-crystalline materials is determined at the surface of the growing film (Jurrow et al., 2016; Friederich et al., 2017; Kim and Kim, 2018). Depending on substrate temperature, evaporation rate, molecular shape, and other—perhaps yet unknown—factors, the molecules at the surface may or may not have enough time to diffuse around, reorient and equilibrate with the underlying film, before they are covered by the next deposited layer such that their orientation becomes frozen (Ediger et al., 2019). Thus, film growth and morphology are kinetically controlled processes.

In this article, we address the question of which factors control the orientation of TADF emitters. Specifically, we discuss if it is an intrinsic property of the emitter and how guest-host interactions may be used to influence this parameter. Ultimately, we propose an interplay of different factors being responsible, as shown schematically in Figure 2.

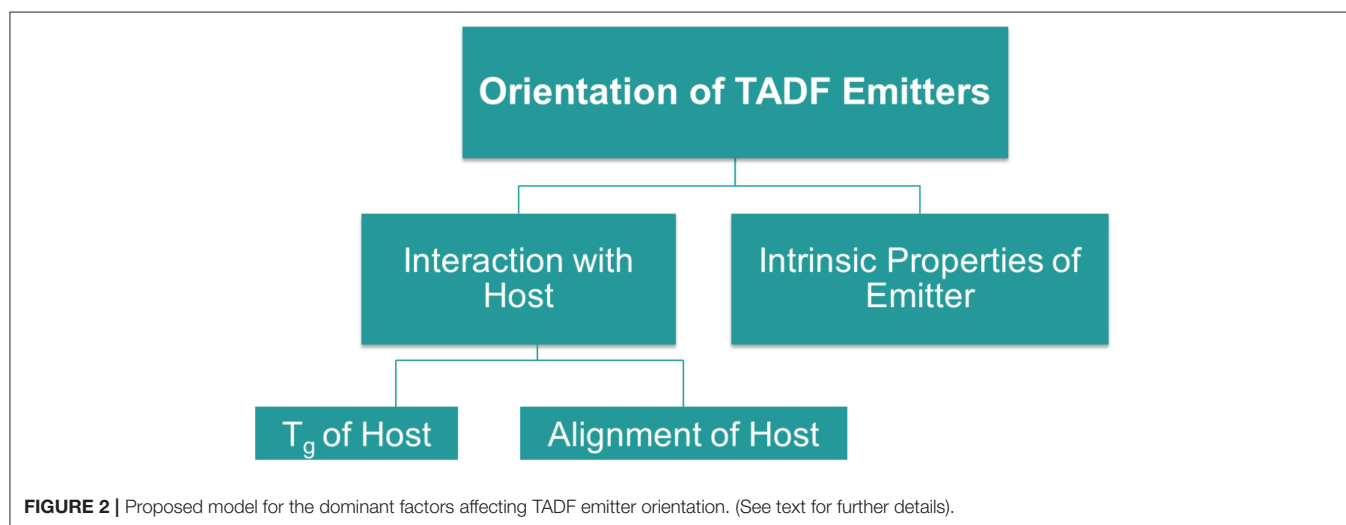
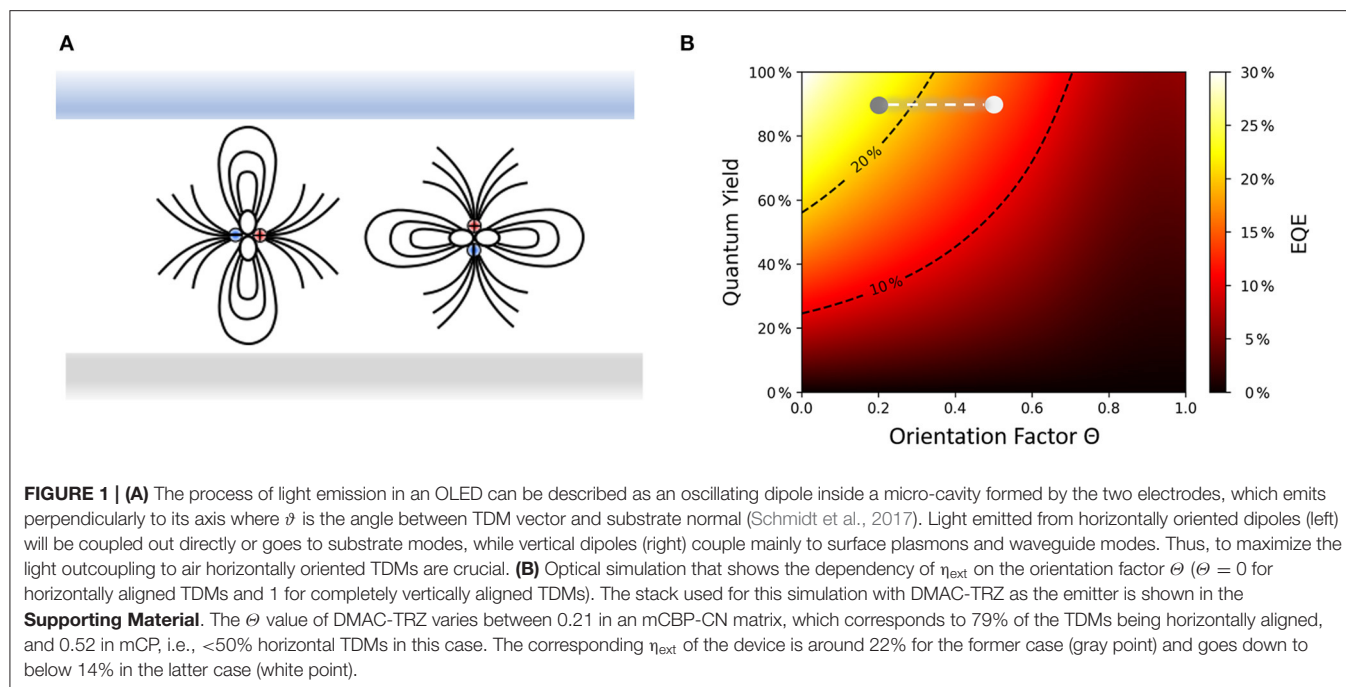
## BASIC APPROACH

OLEDs based on TADF emitters can yield up to 100% internal quantum efficiency because all the generated triplet excitons under electrical operation are ideally converted to singlets through fast reverse intersystem crossing (Adachi, 2014). In order for this to happen the energy difference,  $\Delta E_{ST}$ , between singlet and triplet excited states must be sufficiently small (of the order of few  $k_B T$  only) to be thermally enabled (Wong and Zysman-Colman, 2017). As  $\Delta E_{ST}$  is governed by the exchange integral of the frontier orbitals responsible for the transition to these excited states, which is usually defined as the wavefunction overlap of HOMO and LUMO, i.e., the respective highest occupied and lowest unoccupied molecular orbitals (Penfold, 2015; Yersin, 2018)

$$\Delta E_{ST} \propto \langle \Psi_{HOMO} | \frac{1}{r_{12}} | \Psi_{LUMO} \rangle$$

the key is to separate them spatially, which is typically done by using a twisted donor-acceptor molecular architecture that strongly electronically decouples these two moieties. However,





because the HOMO-LUMO overlap also is proportional to the oscillator strength for the radiative decay to the ground state, it should not become too small lest efficient luminescence will no longer be possible (Weissenseel et al., 2019).

Accordingly, the optical transition dipole moment, which is given by a similar expression,

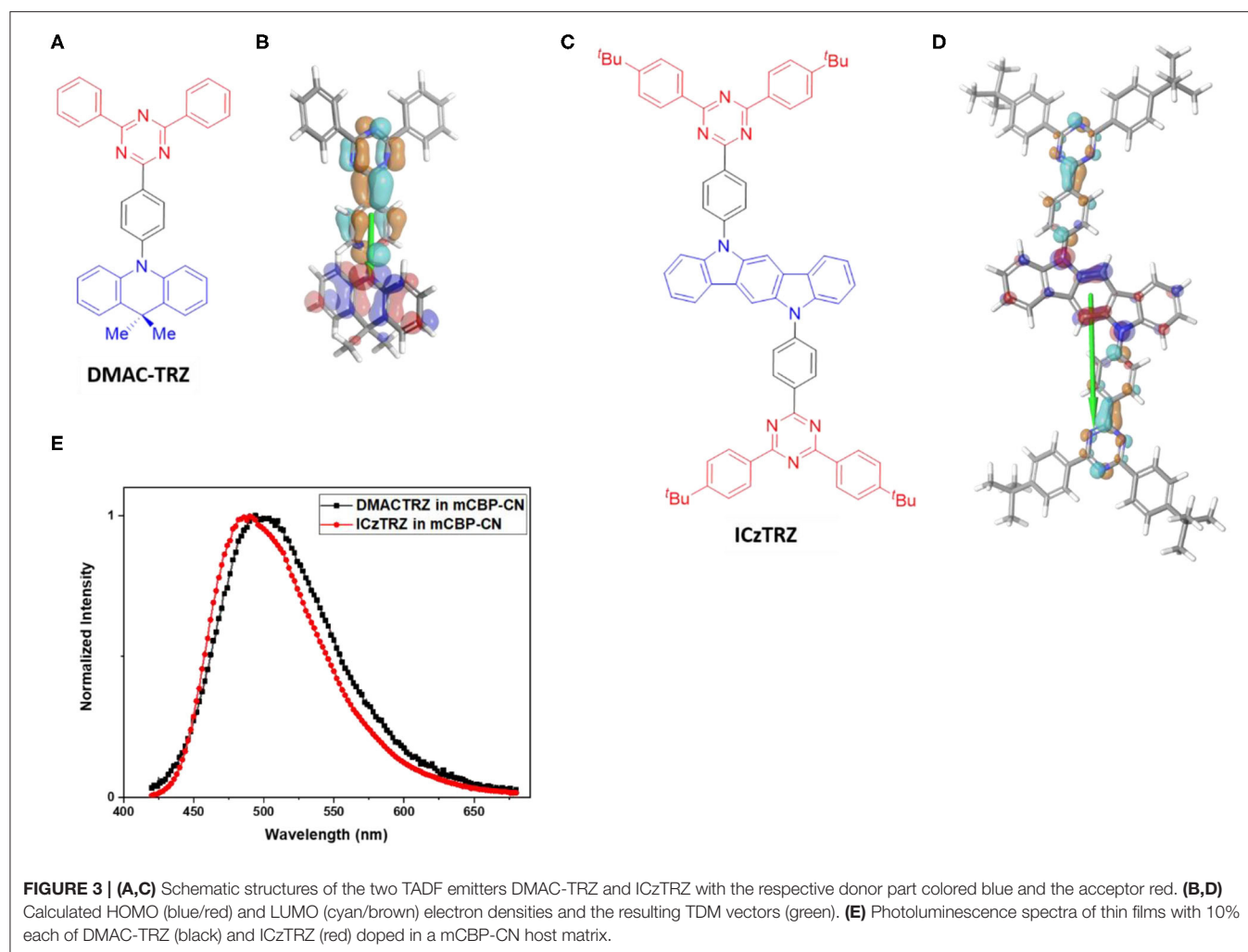
$$\vec{p}_{TDM} \propto \langle \Psi_{HOMO} | \vec{r}_{12} | \Psi_{LUMO} \rangle$$

also depends on the distribution of these orbitals on the molecule. TADF compounds thus typically possess emissive charge-transfer (CT) states and the direction of their TDM often coincides with (or is very close to) the long molecular axis between donor

and acceptor units. Note that there are some exceptions like the well-known 4CzIPN, which is an almost spherical molecule (Hasegawa et al., 2018). Nevertheless, the inline alignment of TDM and long molecular axis of TADF emitters holds great potential for manipulating their TDM orientation, and thus the light outcoupling from the OLED, by controlling molecular orientation upon thermal evaporation of films.

## MATERIALS AND METHODS

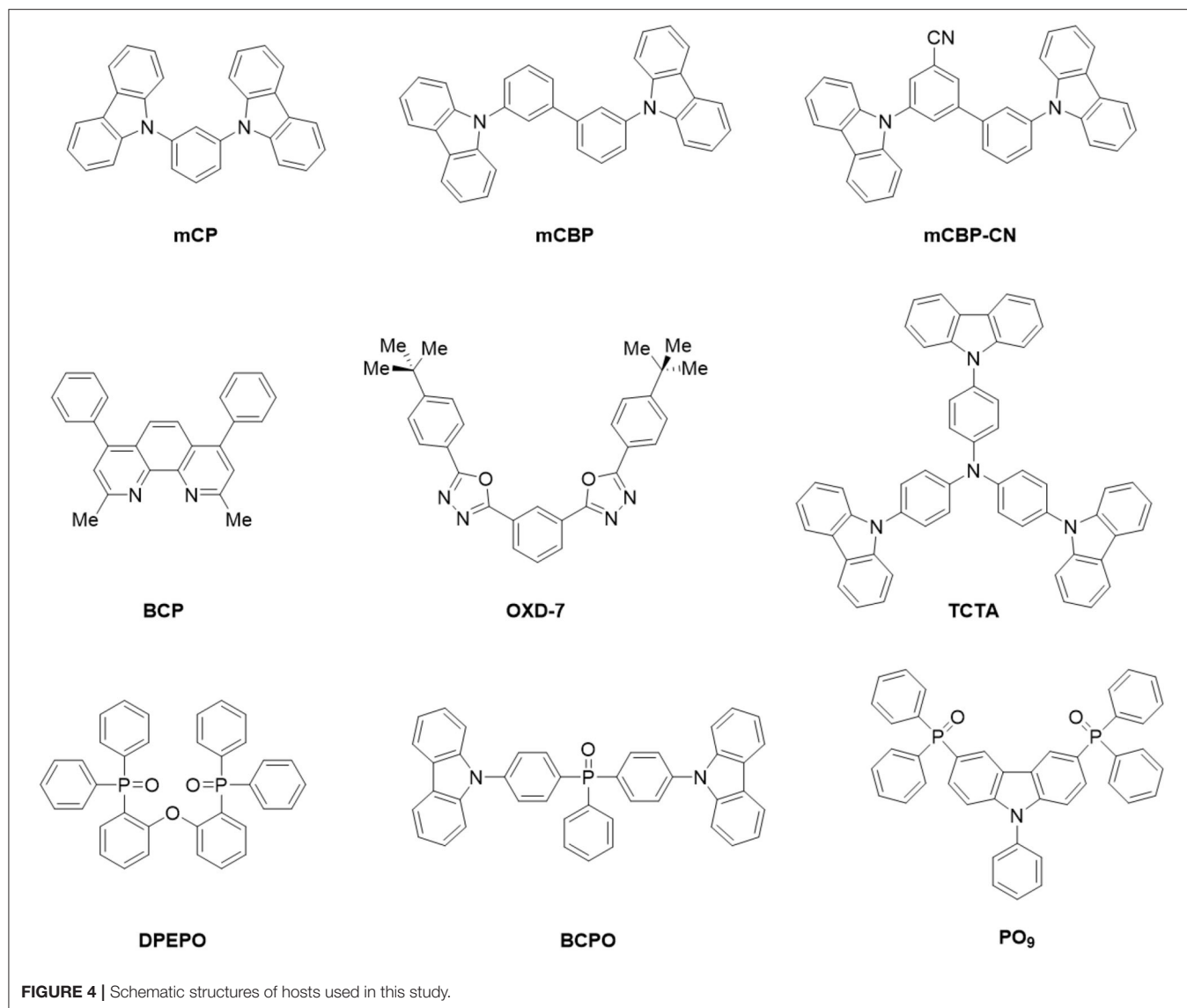
**Figure 3** shows the two emitter materials, DMAC-TRZ and ICzTRZ, used in this study together with their photoluminescence spectra. Both molecules are TADF emitters and emit sky-blue light. Its constituents, DMAC as donor and



TRZ as acceptor, are frequently used in other TADF emitters as well and can, thus, be considered as prototypical building blocks (Wong and Zysman-Colman, 2017). ICzTRZ is a newly synthesized TADF emitter (Zhang et al., 2020), having the said TRZ as one compartment, which has almost identical emission spectrum to DMAC-TRZ (see **Figure 3E**) and, thus, similar energetics. Also shown in that figure are the calculated electron density distributions of the HOMO and LUMO (details in the **Supporting Material**). It is evident that HOMO and LUMO are spatially separated in both emitters. In DMAC-TRZ, the HOMO is located at the acridine donor and the LUMO at the triazine acceptor, while in ICzTRZ the HOMO resides at the indocarbazole donor whereas the LUMO is extended on the two triazine acceptors on both sides of the central core. Remarkably, they are largely different in both size and permanent dipole moment (PDM): DMAC-TRZ consists of a single DA building block, while ICzTRZ follows a symmetric ADA design and is therefore roughly twice as long. Moreover, because of their different designs, the DA-type system DMAC-TRZ is a polar molecule (2.01 D) while the ADA-type molecule ICzTRZ is not (0.33 D). Likewise, the longer and heavier ICzTRZ possesses a

higher glass transition temperature  $T_g$  of 253°C, whereas the shorter and lighter DMAC-TRZ has a comparatively lower  $T_g$  of 93°C. The calculated HOMO and LUMO distributions shown in **Figure 3** support this notion and, particularly, indicate that the TDM is parallel to the long molecular axis.

These two TADF emitters were co-evaporated with up to nine different host materials (**Figure 4**). In general, a suitable host material should have a larger optical gap to allow for energy transfer to and emission from the guest molecules; however, not all of these hosts are actually suitable hosts for efficient OLEDs because of additional requirements with respect to their triplet levels and their charge transport properties. Nevertheless, these host materials were chosen because they cover a wide range of glass transition temperatures  $T_g$  (see **Table 1**), which is expected to have an effect on orientation as discussed above. Moreover, since a CT excitation results in a polar state, TADF emitters are known to be strongly affected by the polarity of the surrounding host material (Dos Santos et al., 2016). Thus, almost all of the chosen hosts also have non-negligible permanent electric dipole moment as specified in **Table 1**. This also allows investigating the potential influence of electrostatic dipole-dipole interactions



between host and emitter on the orientation process of the latter. Furthermore, these host matrices do not just consist of randomly oriented polar species but, upon thermal evaporation, some of them form films with a macroscopic dielectric polarization, which can be equivalently expressed as a non-vanishing surface charge and is often termed the giant surface potential (GSP). These values can be measured by Kelvin probe or impedance spectroscopy, as discussed in the **Supporting Material**, and are also given in **Table 1**. Finally, the  $\Delta$  parameter quantifies alignment of the host PDMs as will be discussed later in detail.

## RESULTS AND DISCUSSION

DMAC-TRZ and ICzTRZ were co-evaporated with the different hosts as thin films on glass substrates. These films were then subjected to ADPL measurements and numerical simulation (details can be found in the **Supporting Material**). To avoid

artifacts caused by crystallization of the host matrix (especially, for low- $T_g$  materials), samples were measured as soon as possible after film deposition, but in any case, on the same day of their fabrication. **Figure 5** shows exemplary results for the two emitters together with fits to determine the emitter orientation as well as simulations indicating the expected shape of the curves for the limiting cases of  $\Theta = 0.0$  (completely horizontal) and  $\Theta = 0.33$  (isotropic). The determined orientation parameters of the TDMs of both emitters in the different hosts are summarized in **Table 2**.

It was observed that ICzTRZ is stronger horizontally oriented in five of these hosts as compared to DMAC-TRZ. The orientation factor for DMAC-TRZ ranges from  $\Theta = 0.52$  in mCP to  $\Theta = 0.21$  in an mCBP-CN matrix, while for ICzTRZ the values are not as divergent. ICzTRZ has the highest orientation factor of  $\Theta = 0.12$  in mCP and the lowest is  $\Theta = 0.06$  in DPEPO, which is among the best values reported for TADF emitters (Mayr et al., 2014; Byeon et al., 2018;

Tanaka et al., 2020). It is apparent from this analysis that the TDM orientation in DMAC-TRZ is affected much more strongly by the nature and polarity of the host material than in ICzTRZ.

As mentioned in the introduction, Yokoyama et al. found a correlation between anisotropic molecular shape and the tendency for horizontal molecular orientation for a series of rod-like fluorescent dyes (Yokoyama, 2011). This effect is also seen in the case of these two TADF emitter molecules, where the TDM is almost parallel to the long molecular axis. Therefore, the long ICzTRZ molecule has a much stronger horizontal TDM orientation as compared to the short DMAC-TRZ molecule. Moreover, the anisotropy factor of ICzTRZ is less effected by different hosts because alignment

is predominantly induced by the extended molecular shape of the emitter.

We recall that the different TDM orientations have important consequences for light-outcoupling in OLEDs. As already shown in **Figure 1B**, the simulated EQE of DMAC-TRZ in an OLED stack is expected to vary from <14% in mCP as the host to about 22% if the orientation obtained in mCBP-CN is taken (see the **Supporting Material** for actual device data of DMAC-TRZ). OLEDs with ICzTRZ have been the subject of a separate study (Zhang et al., 2020) where an EQE<sub>max</sub> of 22.1% has been achieved in mCBP as the host.

We now turn to the question of how the large variation of orientation in DMAC-TRZ can be further understood. Apparently, the molecule is not long enough to be intrinsically oriented horizontally. Thus, guest-host interactions become the dominant factor. Following the surface equilibration model

**TABLE 1** | Physical properties of host materials used in this study.

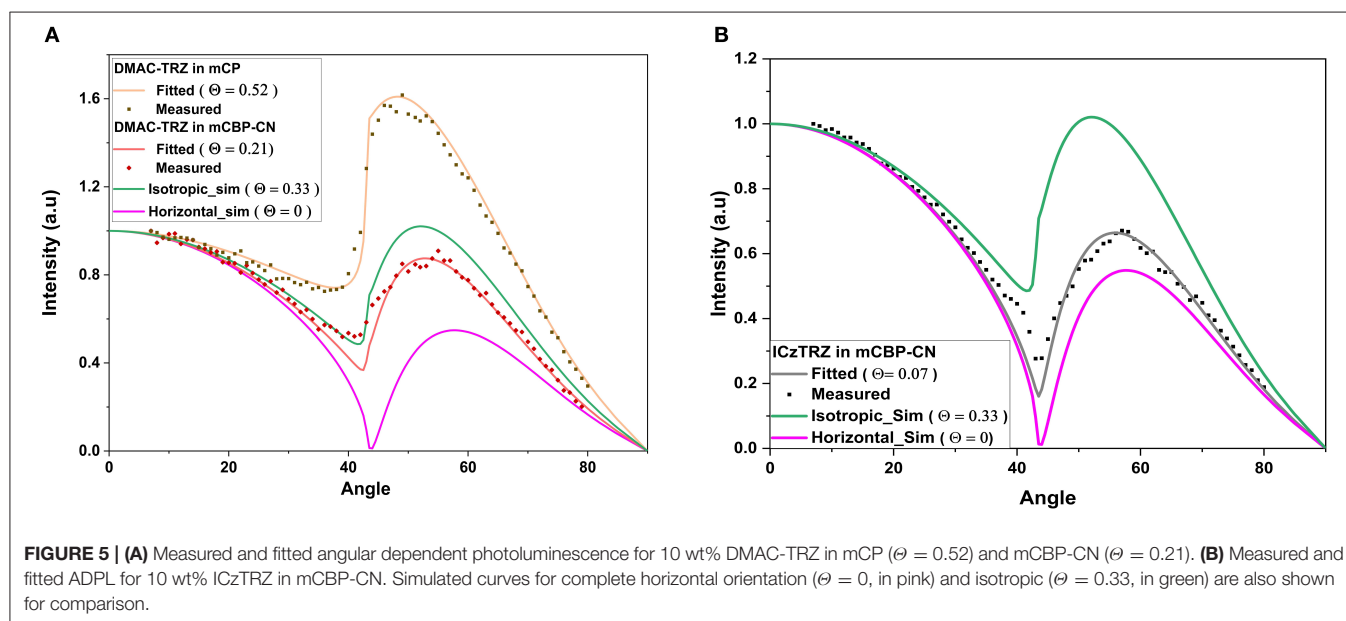
Host	T <sub>g</sub> (°C)	PDM (D)	GSP (mV/nm)	Degree of PDM alignment $\Lambda$
BCP	62	2.8	33	0.050
mCP	65	1.35	−3.9	0.015
OXD-7	77	5.5	68	0.069
mCBP	92	1.57	0	0
DPEPO	93	5.5	61.7	0.071
mCBP-CN	113	3.7	62.5	0.11
BCPO	137	3.5	163	0.33
PO <sub>9</sub>	122	6.7	45.6	0.05
TCTA	151	0	0	0

PDMs were calculated using Schrodinger Maestro Software Package. GSP was measured using impedance spectroscopy and from the measured GSP a  $\Lambda$  parameter was calculated quantifying the degree of the hosts' PDM alignment as discussed in detail in the **Supporting Material**. The hosts' glass transition temperatures T<sub>g</sub> were either taken from literature, as indicated, or measured by differential scanning calorimetry in this study, as described in the **Supporting Material**. <sup>a</sup>Mayr and Brütting (2015), <sup>b</sup>Chou and Cheng (2010), and <sup>c</sup>Measured values using DSC—details in **Supporting Material**.

**TABLE 2** | Determined orientation factors ( $\theta$ ) for 10 wt% doping ratio of DMAC-TRZ and ICzTRZ in different hosts.

Host	TDM orientation factor $\theta$ for DMAC-TRZ	TDM orientation factor $\theta$ for ICzTRZ
mCP	0.52 ± 0.01	0.12 ± 0.01
mCBP	0.48 ± 0.01	0.09 ± 0.02
BCP	0.42 ± 0.03	-
DPEPO	0.36 ± 0.02	0.06 ± 0.02
OXD-7	0.33 ± 0.01	-
PO <sub>9</sub>	0.27 ± 0.01	-
BCPO	0.24 ± 0.01	-
TCTA	0.24 ± 0.02	0.07 ± 0.03
mCBP-CN	0.21 ± 0.02	0.07 ± 0.02

See **Supporting Material** for a complete set of the measured and fitted ADPL data.





discussed in the introduction, we therefore plot the extracted  $\Theta$  values vs. the  $T_g$ 's of the host in **Figure 6A**. As predicted by this model, the orientation depends strongly on the host: the larger its  $T_g$ , the lower are the  $\Theta$  values. Since the substrate temperature is always kept at or slightly above room temperature ( $T_s \sim 300\text{K}$ ), we arrive at a ratio of  $T_s/T_g \sim 0.9$  for low- $T_g$  hosts like mCP or BCP, while the highest  $T_g$  hosts yield a ratio of about 0.7. According to the work of Ediger et al. these values are above and below the critical value ( $T_s/T_g \sim 0.85$ ), respectively, to change molecular orientation from more vertical in the former case, to more horizontal in the latter (Ediger et al., 2019).

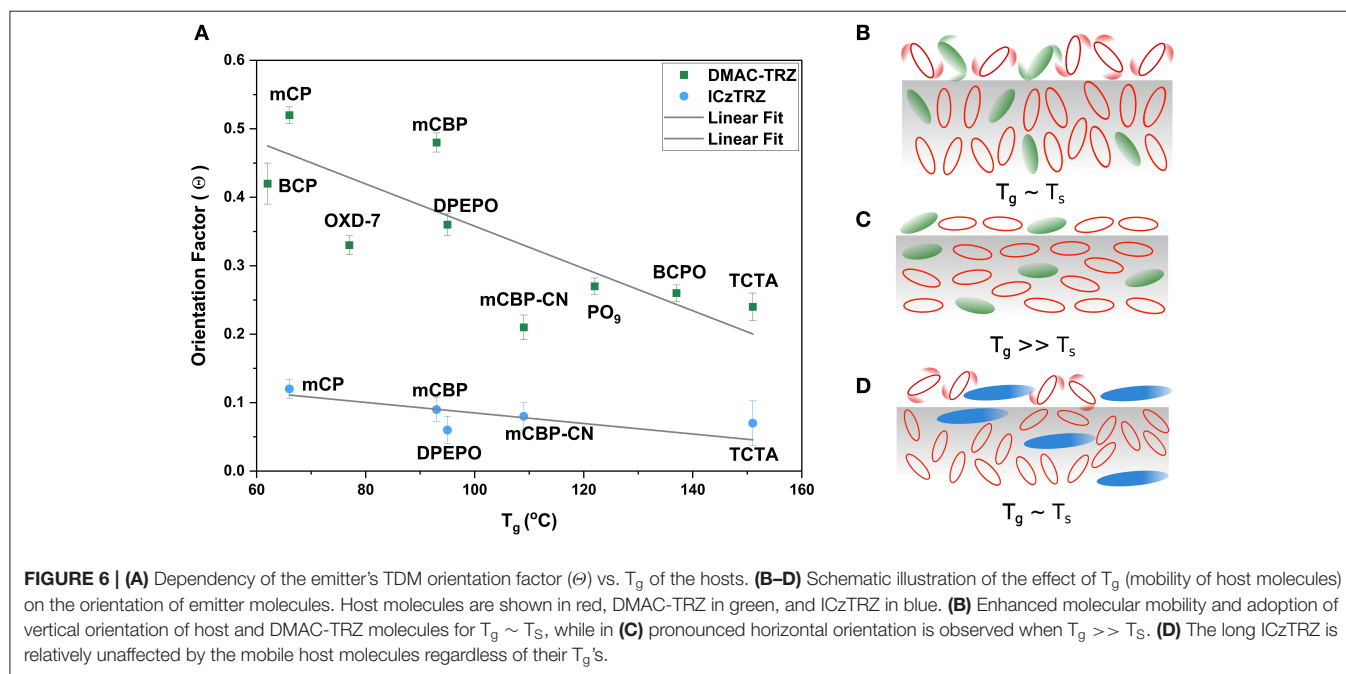
Thus, we propose a possible model for this behavior based upon these trends and previous studies (Mayr and Brütting, 2015; Ediger et al., 2019). If the substrate temperature is close to the  $T_g$  of the host material, molecules landing on the surface will have high mobility and, consequently, enough time to adapt to the surface equilibrium structure, which consists of predominantly vertically aligned molecules (**Figure 6B**). However, if  $T_g \gg T_s$ , the molecules will not have enough time to diffuse and reorient on the surface before being immobilized by the next layer of molecules and will thus not be able to equilibrate (**Figure 6C**). Thus, the initial horizontal orientation at the surface will be effectively frozen because mobilities in the bulk are orders of magnitude lower than at the surface of the film (Ediger et al., 2019). If the substrate temperature is fixed and we co-deposit an emitter with hosts having different  $T_g$ , a similar effect will therefore be observed. This effect is seen when DMAC-TRZ is co-deposited with hosts with a range of different  $T_g$ . It is highly vertical ( $\Theta = 0.52$ ) in mCP, which has  $T_g$  of  $62^\circ\text{C}$ , while this factor becomes less than half as large ( $\Theta = 0.24$ ) in a host with high  $T_g$  like BCPO and TCTA.

This trend was also followed for ICzTRZ but, overall, it shows horizontal orientation in all the different hosts. The highest value of the orientation factor ( $\Theta = 0.12$ ) for ICzTRZ is much lower than the lowest in DMAC-TRZ ( $\Theta = 0.21$ ). Thus, we believe that ICzTRZ is not much affected by the mobility of host molecules owing to its long molecular shape and its high  $T_g$  as neat material (**Figure 6D**). This is confirmed by the fact that the strongest horizontal orientation is already observed in DPEPO as host, which has a moderate  $T_g$ , and does not further improve even for the highest  $T_g$  host TCTA.

However, there are also some outliers for DMAC-TRZ in **Figure 6A**. This means that for some hosts we see a stronger horizontal alignment than expected from the  $T_g$  alone; see e.g., BCP in comparison to mCP, DPEPO compared to mCBP, or OXD-7 and mCBP-CN. All of them are relatively polar materials. Thus, we have to extend the above presented model to include polarity of the host, but more importantly, the possibility of orientational order of the host itself.

To this end, the concept of spontaneous orientation polarization is very useful. It is known that many polar organic semiconductors exhibit a giant surface potential in thin films grown by vacuum deposition. In this case, the orientation of their permanent electrical dipole moments has a preferential alignment perpendicular to the film plane, i.e., in the vertical direction (Noguchi et al., 2019). This can even occur if the molecules have almost spherical structure, like Alq<sub>3</sub>, and do not exhibit any optical anisotropy. The GSP of the host materials has been determined by Kelvin probe and impedance spectroscopy as discussed in the **Supporting Material**. The obtained values are listed in **Table 1**.

**Figure 7A** shows the TDM orientation parameter  $\Theta$  of DMAC-TRZ plotted vs. the GSP of the host materials.



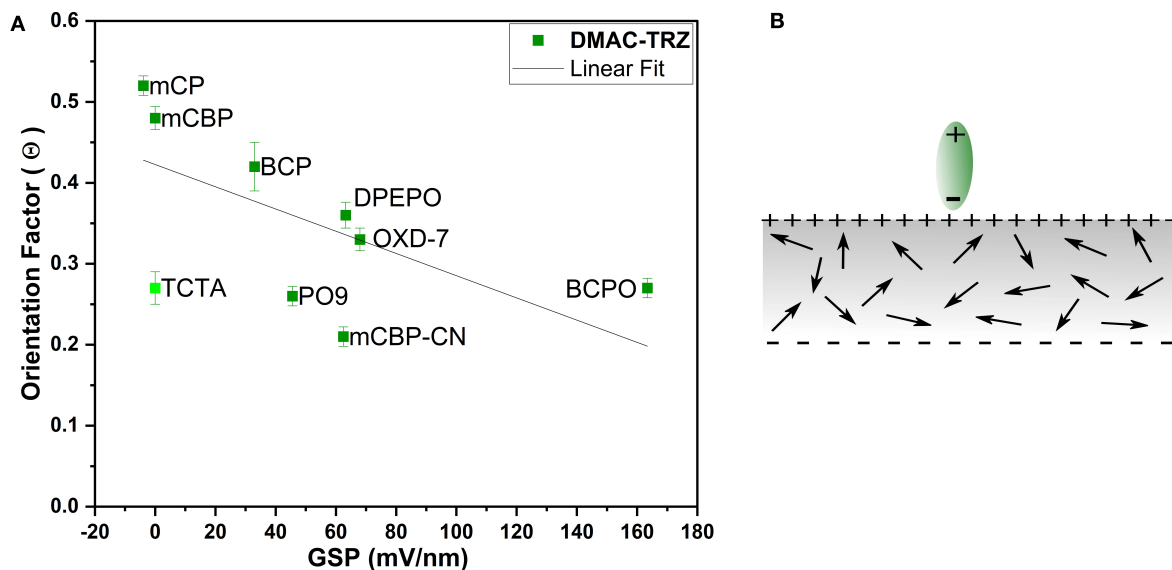


**FIGURE 7 | (A)** Dependency of the emitter's TDM orientation factor ( $\Theta$ ) vs. the GSP of the hosts with a linear fit. **(B)** Schematic illustration of an organic film with GSP and electrostatic interaction between an oncoming emitter molecule (green) and the surface charge leading to vertical alignment of the emitter molecule.

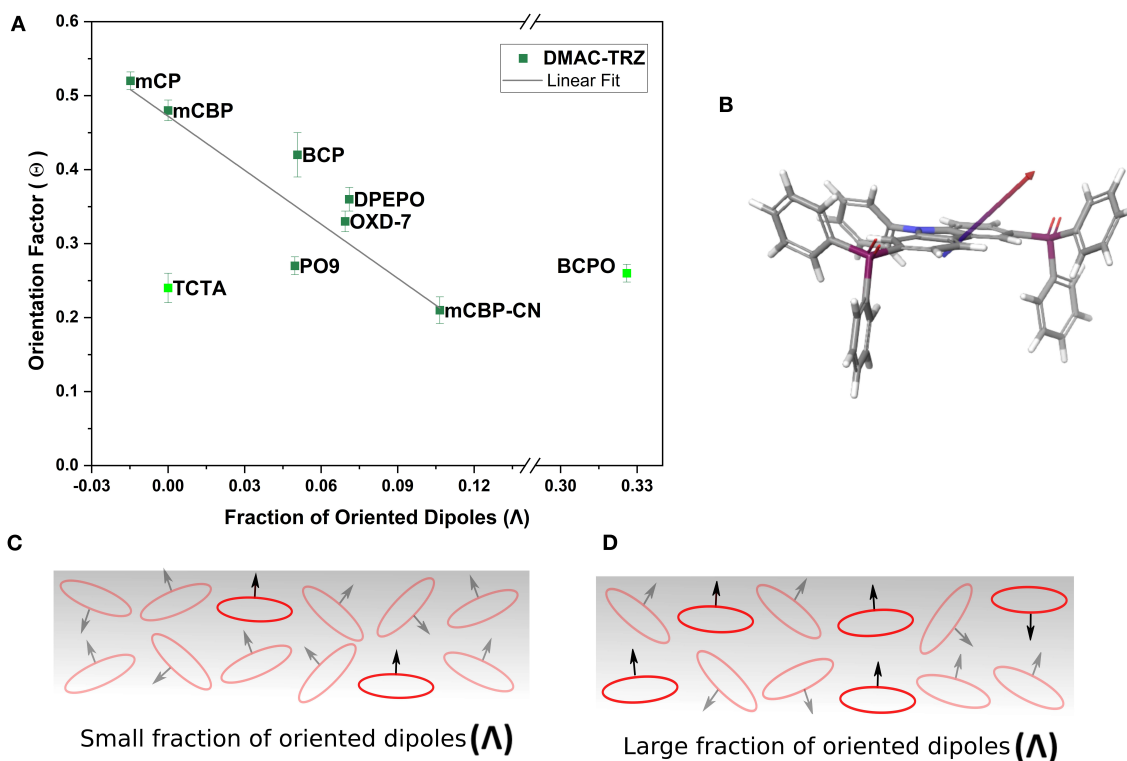


**FIGURE 8 | (A)** Dependency of emitter's TDM orientation factor ( $\Theta$ ) vs. the fraction of oriented PDMs ( $\Lambda$ ) of the hosts with a linear fit. **(B)** 3D structure of PO<sub>9</sub> with its PDM pointing outwards of the basal plane of the carbazole core. **(C,D)** Schematic illustration of the fraction of oriented host molecules with a direction of permanent dipole moments pointing perpendicular to their long axis.

Apparently, there seems to be a trend of more horizontal TDM orientation with increasing surface potential; but still some data points clearly deviate from the fitted linear trendline. First and most obviously, this is TCTA, which does not have a GSP, because it is a non-polar molecule. Secondly, also BCPO and mCBP-CN show stronger orientation as compared to host materials with similar GSP. This raises the question, if the GSP, i.e., the density of polarization charges sitting at the surface of the film is a suitable parameter to explain TADF emitter orientation. In a simple electrostatic interaction model (see **Figure 7B**) the electric field originating from the positive surface charge would rather align the arriving polar TADF emitter molecules in the vertical direction. The larger the GSP, the more vertical alignment would be expected. This is obviously not observed, because for DMAC-TRZ the PDM is roughly parallel to the TDM, and the latter is more and more horizontal the larger the GSP of the host becomes. Thus, the argument using the macroscopic orientation polarization of the host materials has to be revised.

In general, the degree of alignment in such host materials is rather low. If an order parameter  $\Lambda$  is defined as the ratio between the measured GSP and the theoretically possible value for perfect vertical alignment of its PDMs (see **Supporting Material** for details), one typically finds numbers in the range 5–10% (Jäger et al., 2016). This means that either most of their PDMs are randomly oriented with just a small net alignment in vertical direction or that most of the PDMs align pairwise antiparallel so that their net dipole moment vanishes.

In order to investigate the potential influence of host alignment on TDM orientation we have analyzed the order parameter  $\Lambda$  for all the host materials (values were given already in **Table 1**). **Figure 8A** shows the TDM orientation  $\Theta$  of the emitter DMAC-TRZ plotted vs. the PDM orientation parameter  $\Lambda$  of the host. In this case, the correlation is significantly improved compared to that in **Figure 7A**, which indicates that the horizontal alignment of the emitter molecules is not driven by an electrostatic interaction according to the GSP at the film surface, but rather by the higher degree of ordering of the host molecules.

At first glance this may appear somewhat counterintuitive, but one must be aware that many of the studied host molecules have a PDM pointing perpendicular to the long molecular axis (**Figure 8B** and **Supporting Material**). This is true specifically for phosphine oxides like DPEPO, BCPO, and PO<sub>9</sub>, but also to some extent for mCBP-CN and OXD-7. Thus, a higher degree of vertical alignment of their PDMs actually means that these host molecules preferentially lie flat on the film surface (see **Figures 8C,D**). We note that this consideration is true even for the remaining outlier in **Figure 8A**: TCTA. It does not have a PDM; therefore,  $\Lambda = 0$ . However, TCTA is known to be birefringent with the ordinary component of the refractive index being about 0.15 larger than the extraordinary one (see the optical constants in the **Supporting Material**), indicating that it adopts a preferential horizontal orientation. This is not surprising in view of its high  $T_g$  if the above discussed surface equilibration model is being

considered not only for the emitter molecules but for the host as well.

Finally, we also want to note that chemical interactions between host and emitter molecules may cause specific combinations of them to orient better than predicted by the general  $T_g$  trend. It has been reported recently, that specific molecular units may allow  $\pi$ - $\pi$  stacking or weak hydrogen bonds between host and emitter and, thus, promote horizontal orientation (Watanabe et al., 2019; Sasabe et al., 2020). Probably, this could contribute to the observation that DMAC-TRZ is relatively more horizontally aligned in mCBP-CN as compared to other hosts with similar physical properties.

## CONCLUSIONS

The answer to the question: “What controls the orientation of TADF emitters?” has—at least—three components. In the first place, it is an intrinsic property of the emitter molecule itself. The longer and more rod-like it is, the stronger will be its tendency to lie down when evaporated on a surface. In addition, due to their relatively high molecular mass, such emitter molecules will be affected only little by the arrangement of surrounding host molecules. In this respect, the ADA (or, equivalently, DAD) design principle of many TADF emitters can be regarded as highly beneficial for horizontal alignment.

In the second place, if the TADF emitter is shorter (containing only one DA building block), the host matrix takes over the dominant role for determining emitter orientation and, in particular, the glass transition temperature of the host is of paramount importance. A high  $T_g$  reduces the surface diffusivity of molecules such that they do not have enough time to equilibrate and, thus, often adopt the favored lying flat orientation. As a third factor, we could identify alignment of the host material itself as an additional parameter to promote TADF emitter orientation.

Although one can already find several examples in the literature, where researchers have used these guidelines on purpose (or perhaps even without knowing), we anticipate that designing TADF emitters in a way to promote their horizontal alignment could further boost this third generation of OLEDs to outcompete phosphorescent ones, specifically in the blue spectral region.

## DATA AVAILABILITY STATEMENT

All datasets generated for this study are included in the article/**Supplementary Material**.

## AUTHOR CONTRIBUTIONS

BN, MS, EC, EZ-C, and WB conceived the project. BN prepared samples and performed angular dependent PL measurements and their analysis to obtain TDM orientation. MS and EC performed TD-DFT on the emitter molecules. MS further calculated PDMs of host materials and analyzed their alignment by impedance spectroscopy. OLEDs were prepared and analyzed

in experiment and simulation by PSa and TN. FR measured glass transition temperatures of the emitters and some of the hosts. ZZ synthesized the emitter ICzTRZ. PSt, SB, EZ-C, and WB supervised the project. All authors discussed the results and commented on the manuscript.

## FUNDING

This work was funded by the EU Horizon 2020 MSC ITN TADFlife (Grant Agreement No. 812872) as well as

by Deutsche Forschungsgemeinschaft (DFG, project no. Br 1728/20-1). ZZ acknowledged the financial support from Chinese Scholarship Council (CSC, no. 201606890009) for his Ph.D. studies.

## SUPPLEMENTARY MATERIAL

The Supplementary Material for this article can be found online at: <https://www.frontiersin.org/articles/10.3389/fchem.2020.00750/full#supplementary-material>

## REFERENCES

- Adachi, C. (2014). Third-generation organic electroluminescence materials. *Jpn. J. Appl. Phys.* 53:060101. doi: 10.7567/JJAP.53.060101
- Barnes, W. L. (1998). Fluorescence near interfaces: the role of photonic mode density. *J. Mod. Opt.* 45, 661–699. doi: 10.1080/09500349808230614
- Brütting, W., Frischeisen, J., Schmidt, T. D., Scholz, B. J., and Mayr, C. (2013). Device efficiency of organic light-emitting diodes: progress by improved light outcoupling. *Phys. Status Solidi Appl. Mater. Sci.* 210, 44–65. doi: 10.1002/pssa.201228320
- Byeon, S. Y., Kim, J., Lee, D. R., Han, S. H., Forrest, S. R., and Lee, J. Y. (2018). Nearly 100% horizontal dipole orientation and upconversion efficiency in blue thermally activated delayed fluorescent emitters. *Adv. Opt. Mater.* 6, 1–6. doi: 10.1002/adom.201701340
- Chou, H. H., and Cheng, C. H. (2010). A highly efficient universal bipolar host for blue, green, and red phosphorescent OLEDs. *Adv. Mater.* 22, 2468–2471. doi: 10.1002/adma.201000061
- Dalal, S. S., Fakhraei, Z., and Ediger, M. D. (2013). High-throughput ellipsometric characterization of vapor-deposited indomethacin glasses. *J. Phys. Chem. B* 117, 15415–15425. doi: 10.1021/jp405005n
- Dos Santos, P. L., Ward, J. S., Bryce, M. R., and Monkman, A. P. (2016). Using guest-host interactions to optimize the efficiency of TADF OLEDs. *J. Phys. Chem. Lett.* 7, 3341–3346. doi: 10.1021/acs.jpclett.6b01542
- Ediger, M. D., De Pablo, J., and Yu, L. (2019). Anisotropic vapor-deposited glasses: hybrid organic solids. *Acc. Chem. Res.* 52, 407–414. doi: 10.1021/acs.accounts.8b00513
- Flämmich, M., Frischeisen, J., Setz, D. S., Michaelis, D., Krummacher, B. C., Schmidt, T. D., et al. (2011). Oriented phosphorescent emitters boost OLED efficiency. *Org. Electron.* 12, 1663–1668. doi: 10.1016/j.orgel.2011.06.011
- Friedrich, P., Coehoorn, R., and Wenzel, W. (2017). Molecular origin of the anisotropic dye orientation in emissive layers of organic light emitting diodes. *Chem. Mater.* 29, 9528–9535. doi: 10.1021/acs.chemmater.7b03742
- Frischeisen, J., Yokoyama, D., Adachi, C., and Brütting, W. (2010). Determination of molecular dipole orientation in doped fluorescent organic thin films by photoluminescence measurements. *Appl. Phys. Lett.* 96, 1–4. doi: 10.1063/1.3309705
- Frischeisen, J., Yokoyama, D., Endo, A., Adachi, C., and Brütting, W. (2011). Increased light outcoupling efficiency in dye-doped small molecule organic light-emitting diodes with horizontally oriented emitters. *Org. Electron.* 12, 809–817. doi: 10.1016/j.orgel.2011.02.005
- Hasegawa, Y., Yamada, Y., Sasaki, M., Hosokai, T., Nakanotani, H., and Adachi, C. (2018). Well-ordered 4CzIPN ((4s,6s)-2,4,5,6-tetra(9-H-carbazol-9-yl)isophthalonitrile) layers: molecular orientation, electronic structure, and angular distribution of photoluminescence. *J. Phys. Chem. Lett.* 9, 863–867. doi: 10.1021/acs.jpclett.7b03232
- Jäger, L., Schmidt, T. D., and Brütting, W. (2016). Manipulation and control of the interfacial polarization in organic light-emitting diodes by dipolar doping. *AIP Adv.* 6, 1–7. doi: 10.1063/1.4963796
- Jurow, M. J., Mayr, C., Schmidt, T. D., Lampe, T., Djurovich, P. I., Brütting, W., et al. (2016). Understanding and predicting the orientation of heteroleptic phosphors in organic light-emitting materials. *Nat. Mater.* 15, 85–91. doi: 10.1038/nmat4428
- Kim, K. H., and Kim, J. J. (2018). Origin and control of orientation of phosphorescent and TADF dyes for high-efficiency OLEDs. *Adv. Mater.* 30, 1–19. doi: 10.1002/adma.201705600
- Komino, T., Sagara, Y., Tanaka, H., Oki, Y., Nakamura, N., Fujimoto, H., et al. (2016). Electroluminescence from completely horizontally oriented dye molecules. *Appl. Phys. Lett.* 108:241106. doi: 10.1063/1.4954163
- Mayr, C., and Brütting, W. (2015). Control of molecular dye orientation in organic luminescent films by the glass transition temperature of the host material. *Chem. Mater.* 27, 2759–2762. doi: 10.1021/acs.chemmater.5b00062
- Mayr, C., Lee, S. Y., Schmidt, T. D., Yasuda, T., Adachi, C., and Brütting, W. (2014). Efficiency enhancement of organic light-emitting diodes incorporating a highly oriented thermally activated delayed fluorescence emitter. *Adv. Funct. Mater.* 24, 5232–5239. doi: 10.1002/adfm.201400495
- Noguchi, Y., Brütting, W., and Ishii, H. (2019). Spontaneous orientation polarization in organic light-emitting diodes. *Jpn. J. Appl. Phys.* 58:SF0801. doi: 10.7567/1347-4065/ab0de8
- Nowy, S., Krummacher, B. C., Frischeisen, J., Reinke, N. A., and Brütting, W. (2008). Light extraction and optical loss mechanisms in organic light-emitting diodes: influence of the emitter quantum efficiency. *J. Appl. Phys.* 104:123109. doi: 10.1063/1.3043800
- Penfold, T. J. (2015). On predicting the excited-state properties of thermally activated delayed fluorescence emitters. *J. Phys. Chem. C* 119, 13535–13544. doi: 10.1021/acs.jpcc.5b03530
- Penninck, L., De Visschere, P., Beeckman, J., and Neyts, K. (2011). Dipole radiation within one-dimensional anisotropic microcavities: a simulation method. *Opt. Express* 19:18558. doi: 10.1364/OE.19.018558
- Sasabe, H., Chikayasu, Y., Ohisa, S., Arai, H., Ohsawa, T., Komatsu, R., et al. (2020). Molecular orientations of delayed fluorescent emitters in a series of carbazole-based host materials. *Front. Chem.* 8:427. doi: 10.3389/fchem.2020.00427
- Schmidt, T. D., Lampe, T., Daniel Sylvinson, M. R., Djurovich, P. I., Thompson, M. E., and Brütting, W. (2017). Emitter orientation as a key parameter in organic light-emitting diodes. *Phys. Rev. Appl.* 8, 1–28. doi: 10.1103/PhysRevApplied.8.037001
- Tanaka, M., Noda, H., Nakanotani, H., and Adachi, C. (2020). Molecular orientation of disk-shaped small molecules exhibiting thermally activated delayed fluorescence in host-guest films. *Appl. Phys. Lett.* 116:023302. doi: 10.1063/1.5140210
- Tang, C. W., Vanslyke, S. A., and Chen, C. H. (1989). Electroluminescence of doped organic thin films. *J. Appl. Phys.* 65, 3610–3616. doi: 10.1063/1.343409
- Tsutsui, T., Aminaka, E., Lin, C. P., and Kim, D. U. (1997). Extended molecular design concept of molecular materials for electroluminescence: sublimed-dye films, molecularly doped polymers and polymers with chromophores. *Philos. Trans. R. Soc. A Math. Phys. Eng. Sci.* 355, 801–814. doi: 10.1098/rsta.1997.0045
- Uoyama, H., Goushi, K., Shizu, K., Nomura, H., and Adachi, C. (2012). Highly efficient organic light-emitting diodes from delayed fluorescence. *Nature* 492, 234–238. doi: 10.1038/nature11687
- Watanabe, Y., Yokoyama, D., Koganezawa, T., Katagiri, H., Ito, T., Ohisa, S., et al. (2019). Control of molecular orientation in organic semiconductor films using weak hydrogen bonds. *Adv. Mater.* 31, 1–8. doi: 10.1002/adma.201808300
- Weissenseel, S., Drigo, N. A., Kudriashova, L. G., Schmid, M., Morgenstern, T., Lin, K. H., et al. (2019). Getting the right twist: influence of donor-acceptor dihedral angle on exciton kinetics and singlet-triplet gap in deep blue thermally



- activated delayed fluorescence emitter. *J. Phys. Chem. C* 123, 27778–27784. doi: 10.1021/acs.jpcc.9b08269
- Wong, M. Y., and Zysman-Colman, E. (2017). Purely organic thermally activated delayed fluorescence materials for organic light-emitting diodes. *Adv. Mater.* 29:1605444. doi: 10.1002/adma.201605444
- Yersin, H. (2018). *Materials Based on Thermally Activated Delayed Fluorescence*, 1st Edn. Weinheim: Wiley-VCH.
- Yokoyama, D. (2011). Molecular orientation in small-molecule organic light-emitting diodes. *J. Mater. Chem.* 21, 19187–19202. doi: 10.1039/c1jm13417e
- Zhang, Z., Crovini, E., Santos, P. L. D., Naqvi, B., Sahay, P., Cordes, D., et al. (2020). Efficient sky-blue organic light-emitting diodes using a highly horizontally oriented thermally activated delayed fluorescence emitter. (Submitted).

**Conflict of Interest:** The authors declare that the research was conducted in the absence of any commercial or financial relationships that could be construed as a potential conflict of interest.

Copyright © 2020 Naqvi, Schmid, Crovini, Sahay, Naujoks, Rodella, Zhang, Strohmriegel, Bräse, Zysman-Colman and Brütting. This is an open-access article distributed under the terms of the Creative Commons Attribution License (CC BY). The use, distribution or reproduction in other forums is permitted, provided the original author(s) and the copyright owner(s) are credited and that the original publication in this journal is cited, in accordance with accepted academic practice. No use, distribution or reproduction is permitted which does not comply with these terms.



# Corrigendum: What Controls the Orientation of TADF Emitters?

Bilal A. Naqvi<sup>1</sup>, Markus Schmid<sup>1</sup>, Ettore Crovini<sup>2</sup>, Prakhar Sahay<sup>1</sup>, Tassilo Naujoks<sup>1</sup>, Francesco Rodella<sup>3</sup>, Zhen Zhang<sup>4</sup>, Peter Strohriegl<sup>3</sup>, Stefan Bräse<sup>4,5</sup>, Eli Zysman-Colman<sup>2</sup> and Wolfgang Brütting<sup>1\*</sup>

<sup>1</sup>Institute of Physics, University of Augsburg, Augsburg, Germany, <sup>2</sup>Organic Semiconductor Centre, EaStCHEM School of Chemistry, University of St Andrews, St Andrews, United Kingdom, <sup>3</sup>Macromolecular Chemistry, University of Bayreuth, Bayreuth, Germany, <sup>4</sup>Institute of Organic Chemistry, Karlsruhe Institute of Technology, Karlsruhe, Germany, <sup>5</sup>Institute of Biological and Chemical Systems – Functional Molecular Systems, Karlsruhe Institute of Technology, Eggenstein-Leopoldshafen, Germany

**Keywords:** OLEDs, TADF, emitter orientation, molecular orientation, emitter-host interaction

## A corrigendum on

### What Controls the Orientation of TADF Emitters?

by Naqvi B. A., Schmid M., Crovini E., Sahay P., Naujoks T., Rodella F., Zhang Z., Strohriegl P., Bräse S., Zysman-Colman E., and Brütting W. (2020). What Controls the Orientation of TADF Emitters? *Front. Chem.* 8:750. doi: 10.3389/fchem.2020.00750

## OPEN ACCESS

### Edited by:

Guigen Li,  
Texas Tech University, United States

### Reviewed by:

Bo Jiang,  
Jiangsu Normal University, China

### \*Correspondence:

Wolfgang Brütting  
bruetting@physik.uni-augsburg.de

### Specialty section:

This article was submitted to  
Organic Chemistry,  
a section of the journal  
Frontiers in Chemistry

**Received:** 23 November 2020

**Accepted:** 07 January 2021

**Published:** 17 February 2021

### Citation:

Naqvi BA, Schmid M, Crovini E,  
Sahay P, Naujoks T, Rodella F,  
Zhang Z, Strohriegl P, Bräse S,  
Zysman-Colman E and Brütting W  
(2021) Corrigendum: What Controls  
the Orientation of TADF Emitters?.  
*Front. Chem.* 9:632639.  
doi: 10.3389/fchem.2021.632639

In the original article, there was a mistake in **Supplementary Figure S8** of the **Supplementary Material**, and derived from that, in **Table 1** as well as **Figures 7A, 8A** as published. The measured values of the GSP for two of the host materials, viz. BCPO and PO<sub>9</sub>, were interchanged by mistake. These values also resulted in a wrong calculation of the degree of PDM alignment ( $\Lambda$ ). The corrected **Table 1** as well as **Figures 7A, 8A** are attached below.

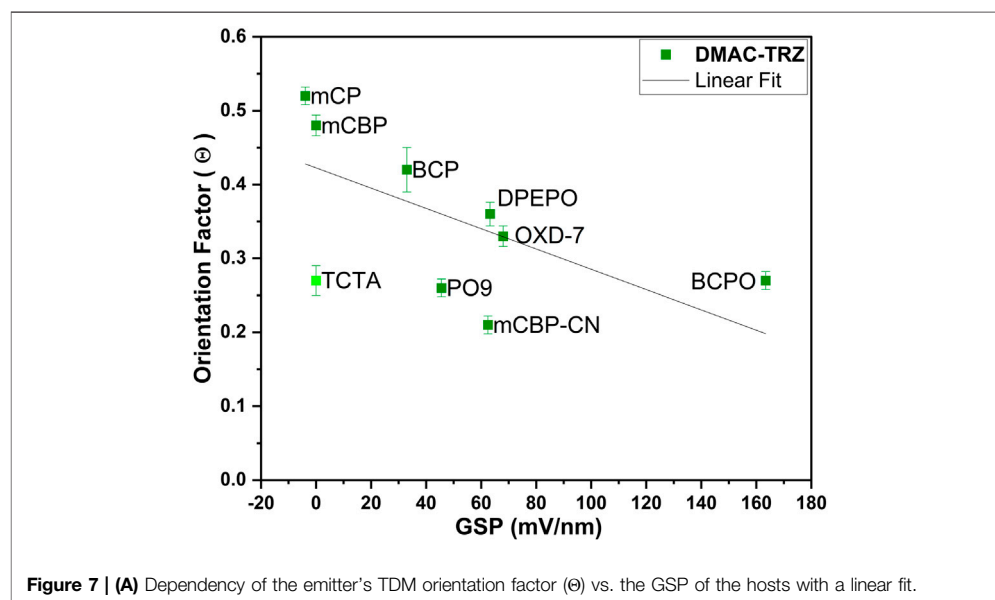
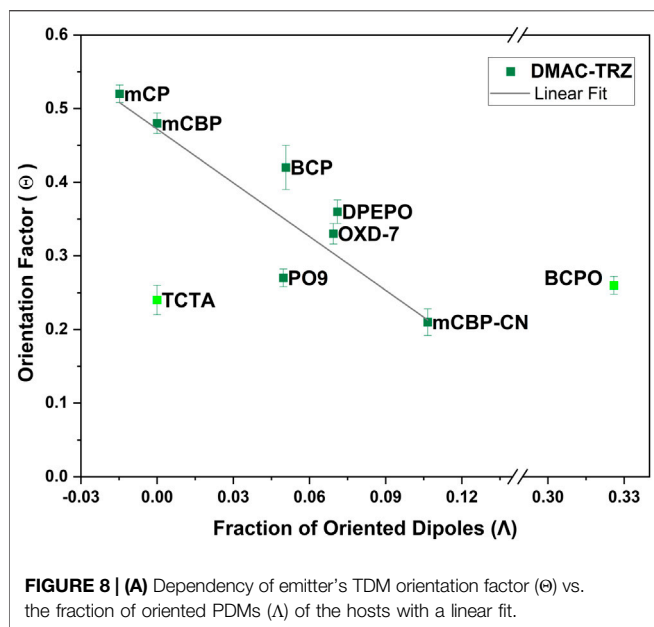


**Figure 7 | (A)** Dependency of the emitter's TDM orientation factor ( $\Theta$ ) vs. the GSP of the hosts with a linear fit.



## SUPPLEMENTARY MATERIAL

The Supplementary Material for this article can be found online at: <https://www.frontiersin.org/articles/10.3389/fchem.2021.632639/full#supplementary-material>.

**TABLE 1 |** Physical properties of host materials used in this study.

Host	$T_g$ (°C)	PDM (D)	GSP (mV/nm)	Degree of PDM alignment $\Lambda$
BCP	62	2.8	33	0.050
mCP	65	1.35	-3.9	0.015
OXD-7	77	5.5	68	0.069
mCBP	92	1.57	0	0
DPEPO	93	5.5	61.7	0.071
mCBP-CN	113	3.7	62.5	0.11
BCPO	137	3.5	163	0.33
PO <sub>9</sub>	122	6.7	45.6	0.05
TCTA	151	0	0	0

The authors apologize for this error and state that this does not change the scientific conclusions of the article in any way. The original article and the Supporting Material have been updated.

**Conflict of Interest:** The authors declare that the research was conducted in the absence of any commercial or financial relationships that could be construed as a potential conflict of interest.

Copyright © 2021 Naqvi, Schmid, Crovini, Sahay, Naujoks, Rodella, Zhang, Strohnriegl, Bräse, Zysman-Colman, Brütting. This is an open-access article distributed under the terms of the Creative Commons Attribution License (CC BY). The use, distribution or reproduction in other forums is permitted, provided the original author(s) and the copyright owner(s) are credited and that the original publication in this journal is cited, in accordance with accepted academic practice. No use, distribution or reproduction is permitted which does not comply with these terms.



# Thermally Activated Delayed Fluorescence: Beyond the Single Molecule

Marc K. Etherington\*

Department of Mathematics, Physics and Electrical Engineering, Northumbria University, Newcastle upon Tyne, United Kingdom

## OPEN ACCESS

### Edited by:

Eli Zysman-Colman,  
University of St Andrews,  
United Kingdom

### Reviewed by:

Basem Moosa,  
KAUST Catalysis Center (KCC),  
Saudi Arabia  
Radek Cibulka,  
University of Chemistry and  
Technology in Prague, Czechia

### \*Correspondence:

Marc K. Etherington  
marc.k.etherington@northumbria.ac.uk

### Specialty section:

This article was submitted to  
Organic Chemistry,  
a section of the journal  
Frontiers in Chemistry

Received: 03 May 2020

Accepted: 13 July 2020

Published: 18 September 2020

### Citation:

Etherington MK (2020) Thermally  
Activated Delayed Fluorescence:  
Beyond the Single Molecule.  
Front. Chem. 8:716.  
doi: 10.3389/fchem.2020.00716

Emitters that exhibit thermally activated delayed fluorescence (TADF) are of interest for commercial applications in organic light-emitting diodes (OLEDs) due to their ability to achieve internal quantum efficiency of 100%. However, beyond the intrinsic properties of these materials it is important to understand how the molecules interact with each other and when these interactions may occur. Such interactions lead to a significant red shift in the photoluminescence and electroluminescence, making them less practicable for commercial use. Through summarizing the literature, covering solid-state solvation effects and aggregate effects in organic emitters, this mini review outlines a framework for the complete study of TADF emitters formed from the current-state-of-the-art techniques.

**Keywords:** thermally activated delayed fluorescence (TADF), aggregation, solid state solvation effect, photophysics, organic light-emitting diodes (OLEDs)

## INTRODUCTION

Increasing the efficiency and stability of organic light-emitting diodes (OLEDs) is a focus of significant attention for researchers and one aspect of improving these systems is to produce novel emitters that have internal quantum efficiencies (IQEs) above the 25% dictated by spin statistics (Baldo et al., 1999). Thermally activated delayed fluorescence (TADF) (Uoyama et al., 2012; Dias et al., 2013) is one phenomenon that is used to achieve 100% IQE (Lin et al., 2016; Liu et al., 2018b; Zeng et al., 2018). This significant increase arises from the molecule being able to promote non-emissive triplet states to the emissive singlet state *via* reverse intersystem crossing (rISC). The rISC process requires a small energy gap between the singlet and triplet state and this can be achieved in a variety of ways and through a variety of molecular designs: exciplex systems where the donor (D) and acceptor (A) are non-identical molecules; (Sarma and Wong, 2018; Colella et al., 2019; Tang et al., 2020) organometallic systems (Di et al., 2017; Conaghan et al., 2018; Yersin et al., 2018; Mahoro et al., 2020) metal halide perovskites; (Zhou and Yan, 2019; Qin et al., 2020) and fully organic systems where the D and A are covalently bonded. (Uoyama et al., 2012; Dias et al., 2013) The subjects of this review are fully organic covalently bonded donor-acceptor (D-A) systems or donor-acceptor-donor (D-A-D) systems. D-A and D-A-D systems have the highest occupied molecular orbital (HOMO) and lowest unoccupied molecular orbital (LUMO) localized on the D and A units respectively to produce charge-transfer (CT) states and the required small singlet-triplet gap. This localization is achieved through control of the dihedral angle between the D and A moieties and the relative electron donating and accepting strengths of the D and A units.

TADF systems typically emit from singlet charge-transfer states (<sup>1</sup>CT), which are almost isoenergetic with triplet charge-transfer states (<sup>3</sup>CT), however intersystem crossing, and rISC, between these two states is prohibited (Lim and Kedzierski, 1973). This limitation can be overcome



by coupling to a third state that does not have the same character. For most TADF systems this third state is a close-lying locally excited triplet state ( $^3\text{LE}$ ). Through spin-vibronic coupling of the  $^3\text{LE}$  state with the  $^3\text{CT}$  state the rISC process between  $^3\text{CT}$  and  $^1\text{CT}$  is enhanced. This was demonstrated theoretically by Gibson et al. (2016) and experimentally by Etherington et al. (2016). The need for proximity of the  $^3\text{LE}$  state with the  $^3\text{CT}$  state provides a new criterion for the molecular design of TADF systems. One major impact of this result is that to design a TADF emitter with a particular emission wavelength, the choice of D and A units is now limited by their  $^3\text{LE}$  energy.

Most work on TADF systems, through photophysical studies and within devices, is performed either in the solution state or dilute concentrations within small molecule or polymer hosts, meaning that the measurements are in an ideal scenario and relate predominantly to a single, isolated molecule. However, the CT states are also susceptible to solvent polarity or solid-state host rigidity, which can influence the emissive and functional behavior of the compound and there are many research articles and reviews on this topic (Etherington et al., 2016; Santos et al., 2016a,b, 2018; Haseyama et al., 2017; Wong and Zysman-Colman, 2017; Chatterjee and Wong, 2019; Hung et al., 2019). Although it must be noted that there is an extensive field of research into exciplex systems and controlling fluorescence behavior through host-guest interactions, where intermolecular interactions are embraced. This literature considers the interactions between non-identical molecules to achieve the small exchange energies and high rISC rates required for TADF (Kim et al., 2016; Nakanotani et al., 2016; Sarma and Wong, 2018; Chatterjee and Wong, 2019; Tang et al., 2020) and it has been observed that host-guest interactions can also imbue functional properties (Matsunaga and Yang, 2015; Feng et al., 2017; Ono et al., 2018).

Equally important is a molecule's interaction with identical molecules. There is extensive literature concerning aggregation-induced emission (AIE) of organic systems (Luo et al., 2001; Hong et al., 2009; Mei et al., 2014) and these effects need to be considered for TADF systems. This review will give an overview of the phenomena that occur when we consider TADF emitters beyond the ideal of the single molecule as well as the techniques used to study them. This review will focus on novel compounds that are designed or used for their behavior in aggregates and how studying the molecules' mechanochromism, thermochromism and concentration effects in doped films facilitate the understanding of new functional behaviors. The review will also reflect on the discovery of functional behavior in existing compounds, especially 1,2,3,5-tetrakis(carbazol-9-yl)-4,6-dicyanobenzene (**4CzIPN**)—an archetypal TADF emitter (Uoyama et al., 2012) and how this may influence the interpretation of previous results highlighting the two effects related to the red shifting of emission with concentration: solid-state solvation effect (SSSE) and aggregation.

## CONCENTRATION AND AGGREGATION IN ORGANIC EMITTERS

Aggregation-caused quenching (Thomas et al., 2007) and AIE (Luo et al., 2001; Hong et al., 2009; Mei et al., 2014) are two phenomena that provide a framework for the study of organic emitters beyond the single molecule in neat films, organic crystals and doped matrices. The basis of the AIE field is to understand the interaction between the molecules in these systems and establish the causes of enhancements or reductions in emission, shifts in emission color, mechanochromism or thermochromism. Recent publications and reviews in the area include (Hong et al., 2009; Mei et al., 2014; Furue et al., 2016; Gan et al., 2016; Sturala et al., 2017; Zhang et al., 2017, 2019b, 2020; Liu et al., 2018a; Yu et al., 2020), which demonstrate that phenyl rings should not be considered as entirely inert spacer units in the design of organic emitters and that the aggregation effects can be controlled through photoexcitation. These results have far-reaching implications for molecular design of organic emitters as researchers now need to take care in their choice of moieties during synthesis.

### Novel TADF Emitters Exhibiting Functional Behavior

Implementing the techniques found in the works mentioned above to TADF systems becomes somewhat more complicated as there is now not just the behavior of the prompt singlet emission to explain but also the processes and energetics underlying rISC and delayed emission. Functional phenomena in TADF systems as a result of intermolecular interactions have been observed for a range of D–A and D–A–D systems (Hladka et al., 2018; Huang et al., 2018; Klimash et al., 2018; Pashazadeh et al., 2018; Shi et al., 2018; Skuodis et al., 2018; Bhatia and Ray, 2019; Zheng et al., 2019). These works provide methodologies and insights in understanding the influence that intermolecular interactions have on TADF emitters including their photophysical properties. The compounds discussed in this review are shown in **Figure 1A**.

Skuodis et al. (2018) observed changes in emission behavior as a function of concentration, the host molecule, mechanical force and thermal annealing in 4,6-Di(9,9-dimethylacridan-10-yl)isophthalonitrile (**DACIPN**). The researchers found the photoluminescence quantum yield (PLQY) of **DACIPN** decreased from 83% at 15 wt% in 1,3-Bis(N-carbazolyl)benzene (mCP) to 47% in a film of neat **DACIPN**—they attribute this result to a decrease in TADF contribution in the neat films. The energy of the emission red shifted with increasing concentration and was 2.32 eV (533 nm) in the mCP matrix and 2.19 eV (565 nm) in the neat film, a trend that was observed for a variety of different hosts (**Figures 1B–E**). The authors considered two explanations for this red shift in emission for the compound in solid-state hosts: SSSE (Bulović et al., 1999) and aggregation. They found that the red shifts did not correlate with the solid-state polarizabilities of the hosts and therefore aggregation was the dominant effect in these systems, with concomitant changes in the dihedral angle of

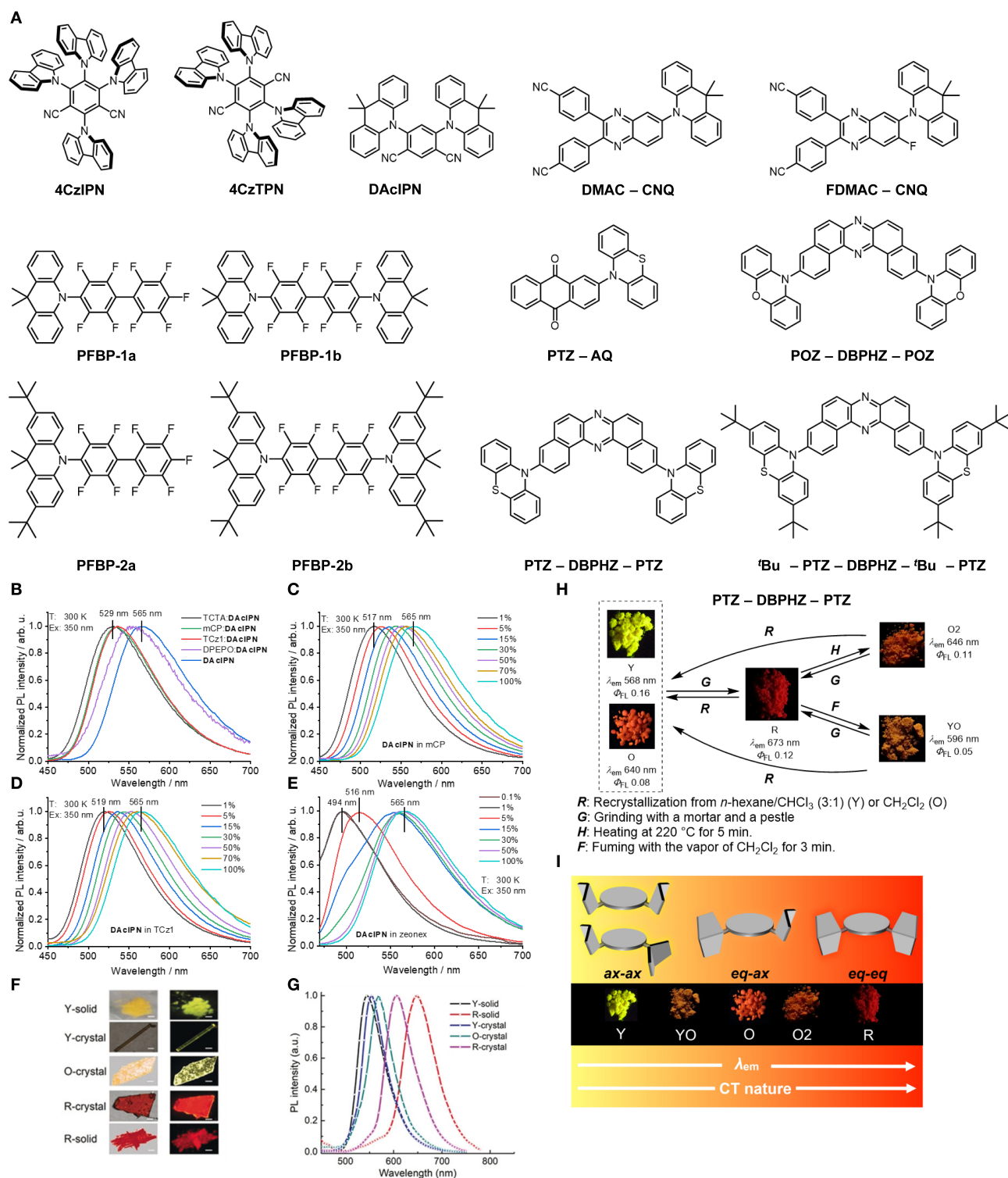


**FIGURE 1 | (A)** The chemical structures of the compounds discussed in the review. **(B–E)** The effects of host and concentration on the emission profile of **DAciPN** showing the significant red shifts observed when increasing the compound concentration. In **(B)** the shift in emission of **DAciPN** in 15 wt% films of hosts of different polarizability showing that the red shift trend does not follow according to the polarizability of the host. **(C–E)** Red shifts in the emission occur across three different hosts, mCP, TCz1 (Tsai et al., 2007) and zeonex respectively with increasing concentration. Adapted with permission from Elsevier from Figure 4 in

(Continued)

**FIGURE 1** | Skuodis et al. (2018) **(F,G)** The different emission profiles of **PTZ-AQ** as a function of solid-state environment from Y-solid to R-solid. Adapted with permission from John Wiley and Sons from Figure 1 in Huang et al. (2018) **(H)** The different forms and the methods of obtaining them for **PTZ-DBPHZ-PTZ** and **(I)** how the quasi-equatorial (eq) and quasi-axial (ax) conformers of phenothiazine influence the solid-state emission of **PTZ-DBPHZ-PTZ**. Adapted from Figures 4, 8 in Okazaki et al. (2017); (Published by The Royal Society of Chemistry).

the **DACIPN**. During thermal annealing of the films at 130°C the authors observed a significant blue shift in the emission of both the doped and non-doped films: the doped film blue shifted from 2.19 eV (565 nm) to 2.40 eV (517 nm), which was attributed to the thermal energy allowing the molecules to disaggregate. This disaggregation allowed the dihedral angle to increase, restoring the higher energy emission. The disaggregation also caused an increase in the PLQY of the neat film from 47 to 64%.

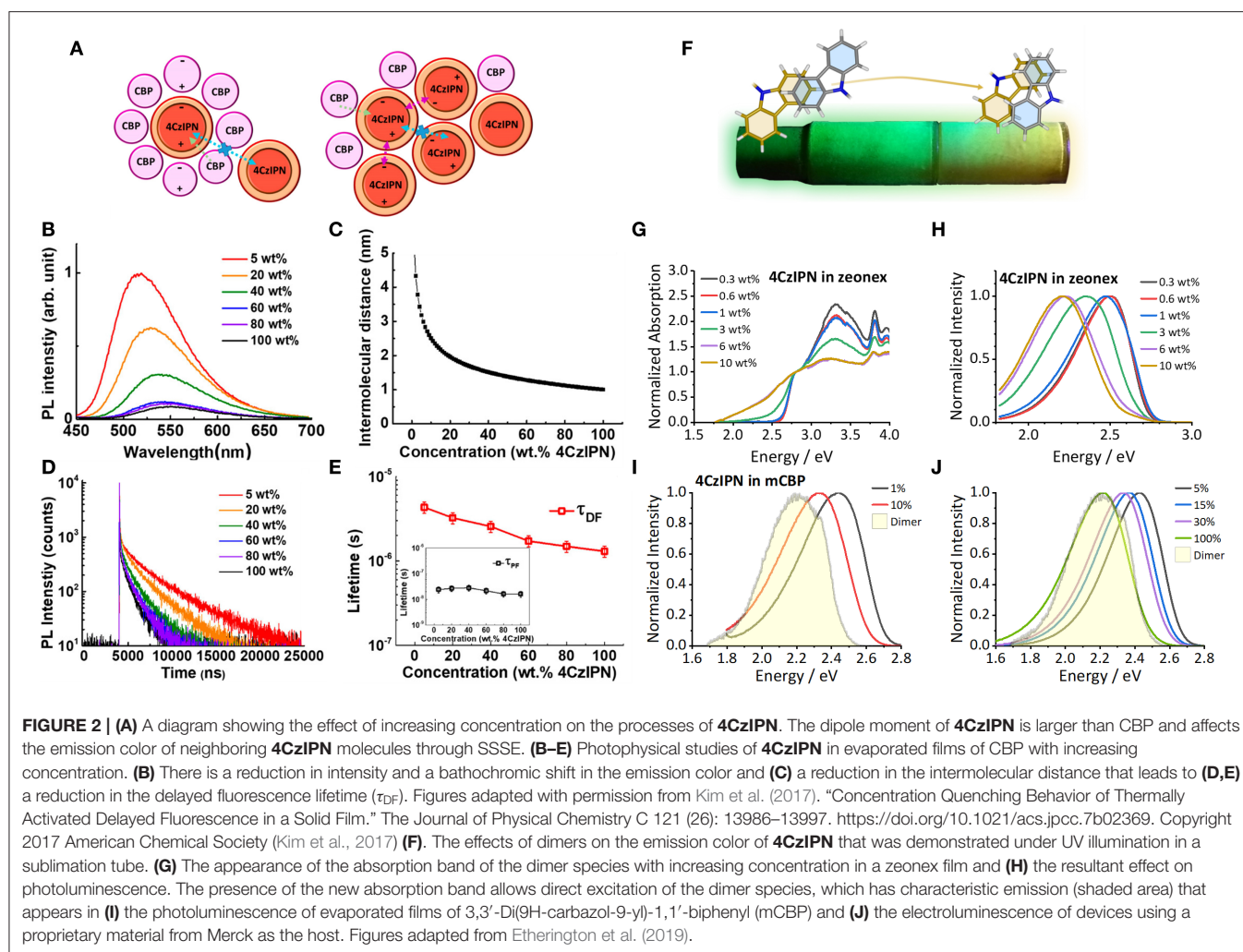
A similar study by Hladka et al. (2018) from the same group focused on these phenomena in sky-blue emitters based on perfluorobiphenyls (PFBP). The researchers studied four systems known as **PFBP-1a**, **PFBP-1b**, **PFBP-2a**, and **PFBP-2b** and showed that **PFBP-2a**, contrary to the other compounds, showed a blue shift in emission when a thermally-evaporated film of the compound was fumed with toluene vapor. This blue shift was attributed to polymorphism of the compound and shows that very small changes in structure between a set of similar compounds can have significant effects on their aggregation properties. As polymorphism is a common explanation for many of these observed properties in the solid-state, knowledge of polymorphism and crystallography is crucial to understanding the fundamental origins of this functional behavior (Chung and Diao, 2016; Bernstein, 2020; Levesque et al., 2020). The importance of knowing the crystal structures of the compounds for understanding the packing and intermolecular interactions is demonstrated in the work by Klimash et al. (2018) In this work they uncovered differences in the molecular crystal structures and how these relate to differences in the TADF efficiency.

Polymorphism as one of the causes of different TADF behavior in crystalline films/powders is reported by Zheng et al. (2019) in 4,4'-(6-(9,9-dimethylacridin-10(9H)-yl)quinoxaline-2,3-diyl)dibenzonitrile (**DMAC-CNQ**) and 4,4'-(6-(9,9-dimethylacridin-10(9H)-yl)-7-fluoroquinoxaline-2,3-diyl)dibenzonitrile (**FDMAC-CNQ**). The authors reported two different polymorphs for **DMAC-CNQ**, which they termed Y-crystal and O-crystal and three polymorphs for **FDMAC-CNQ** termed Y-crystal, O-crystal and R-crystal based on the emission color (Yellow, Orange and Red). The changes in emission color between the crystals are due to different conformations of the DMAC moiety that then has a resultant effect on the  $\pi$ - $\pi$  interactions in the crystal. The trend for both systems is that, going from yellow to red, the number of  $\pi$ - $\pi$  interactions increases as a function of the DMAC conformation. Similarly, a trend of decreasing TADF contribution and PLQY was observed going from Y-crystal to R-crystal, again related to the conformations of the compound. These single crystal studies which are linked to the molecular structure has allowed the authors to interpret the mechanochromism behavior they observed from the pristine, ground and fumed states of the compound. Single crystal

X-ray diffraction and powder X-ray diffraction studies provide an important tool for the study of TADF beyond the single molecule and are a key part of the framework in determining aggregation effects.

Huang et al. (2018) demonstrated the significant accumulation of functional behavior that can be obtained in TADF D-A molecules. In the compound 2-(phenothiazine-10-yl)-anthraquinone (**PTZ-AQ**) they observed TADF, aggregation-induced emission and mechanochromism alongside polymorphism. They comment on the effect that aggregation has on the TADF behavior arguing that TADF can even be tuned by the aggregation state. **Figures 1E,G** show the different emission profiles that can be obtained as a function of solid-state environment. The crystals and solids, which the authors categorize into five different aggregation states, facilitate emission energies from the green to the red: a yellow solid (Y-solid), a red solid (R-solid), a yellow rod-like crystal (Y-crystal), an orange flake-like crystal (O-crystal) and a red flake-like crystal (R-crystal) with the R-crystal showing the smallest singlet-triplet gap and high PLQY.

In general, the idea of molecular conformation affecting the TADF and mechanochromism properties of a compound is in agreement with the work of Okazaki et al. (2017) In 2017 the researchers compared phenoxazine-dibenzo[*a,j*]phenazine-phenoxazine (**POZ-DBPHZ-POZ**) and the phenothiazine analog with *tert*-butyl groups (***t*Bu-PTZ-DBPHZ-*t*Bu-PTZ**) and (**PTZ-DBPHZ-PTZ**) without *tert*-butyl groups. Although two polymorphs of **PTZ-DBPHZ-PTZ** were found only one of ***t*Bu-PTZ-DBPHZ-*t*Bu-PTZ** was discovered. In this study the emission of both compounds red shifted with grinding. Upon heating the emission of ***t*Bu-PTZ-DBPHZ-*t*Bu-PTZ** continued to red shift however, the emission of **PTZ-DBPHZ-PTZ** blue shifted (**Figure 1H**). The particular mechanochromic behavior of **PTZ-DBPHZ-PTZ** is linked to the tendency for PTZ to form as one of two conformers (**Figure 1I**): quasi-axial (ax) or quasi-equatorial (eq). (Malrieu and Pullman, 1964; Bodea and Silberg, 1968; Coubeils and Pullman, 1972; Etherington et al., 2017; Santos et al., 2018) The red emission comes from the highly twisted equatorial-equatorial conformer, the orange from the axial-equatorial and the yellow emission from the axial-axial conformer which allows formation of a higher energy <sup>1</sup>LE state. This again demonstrates the importance of linking mechanochromic and TADF behaviors to the molecular structure through single crystal X-ray diffraction techniques. Mechanochromism is a useful tool and part of the framework for studying intermolecular effects in TADF systems. The work by Pashazadeh et al. (2018) shows how TADF can be turned on and off with grinding and how the intermolecular interactions helped mediate the singlet triplet gaps and control the fundamental emission phenomena.



## Uncovering Intermolecular Effects in Existing Motifs

As noted in the work by Skuodis et al. (2018) there are two proposed origins for the red shift with increasing concentration in solid-state hosts: the SSSE effect (Cotts et al., 2017; Delor et al., 2017; Han and Kim, 2019) and aggregation (dimer or intermolecular) effects (Skaigiris et al., 2019; Zhang et al., 2019a). In this section of the review, literature surrounding an existing and widely-used motif, **4CzIPN**, (Uoyama et al., 2012) will be used to contextualize this red shift in emission.

In 2017 Kim et al. (2017) studied the effects of concentration on the emission profile and TADF characteristics of **4CzIPN**. They observed a significant redshift in the emission with increasing concentration (Figures 2A–E) and a decrease in the TADF lifetime. These red shifts, both in photoluminescence and electroluminescence, have been observed by a range of researchers (Nakanotani et al., 2013; Kim and Lee, 2014; Komatsu et al., 2015; Wang et al., 2016; Zhu et al., 2017; Li et al., 2018; Niwa et al., 2018). Kim et al. (2017) attributed these red shifts and the consequential change in TADF behavior to the changing dipole moment of the surrounding matrix as the

host molecules are subsequently replaced with more **4CzIPN** molecules (Figure 2A). **4CzIPN** is more polar than the host 4,4'-Bis(N-carbazolyl)-1,1'-biphenyl (CBP) and therefore as the concentration increases, the dipole moment and polarizability of the environment increases producing a red shift in the emission. This is the effect known as SSSE (Bulović et al., 1999).

Performing measurements in solid-state hosts with different polarities like Skuodis et al. (2018) is one way of deconvoluting SSSE and aggregation effects, however to completely characterize these systems a diverse framework of measurements is required. In 2019, Etherington et al. (2019) performed a study on **4CzIPN**, incorporating techniques used in the majority of investigations mentioned in section Novel TADF Emitters Exhibiting Functional Behavior, including mechanochromism, thermochromism, single-crystal X-ray diffraction and combined them with time-resolved photoluminescence spectroscopy. This framework uncovered the dimer species of **4CzIPN** present in certain environments. The effects of these intermolecular interactions were seen during sublimation of **4CzIPN** and Etherington et al. observed that crystals and solid-state powders with different emission colors were produced along



the sublimation tubing (See **Figure 2F**). This emission color was found to be changeable through thermal annealing and the introduction of mechanical energy. The fact that in neat films there were changes in emission color without a change in polarizability of the surrounding media suggests that SSSE is not the sole, or even dominant, effect in determining the emission properties of **4CzIPN**. Indeed, the related material 2,3,5,6-Tetra(carbazol-9-yl)benzene-1,4-dicarbonitrile (**4CzTPN**) (Uoyama et al., 2012) is known to give emission of orange-red within the solid-state but only yellow emission in one of the most polar solvents dimethyl sulfoxide (DMSO). This result strongly suggests that polarizability is not the most crucial effect for the emission properties of these materials in the solid-state. Theoretical work by Northey et al. (2017) shows that the SSSE, while present in TADF systems, can be restricted due to rigidity of the host molecule in a solid-state environment.

The dimer/aggregate species observed in **4CzIPN** through excitation at 2.33 eV (532 nm), significantly below the band gap of the monomer absorption band (**Figure 2G**), has an emission profile that almost exactly matches the higher concentration zeonex films and the neat film (**Figures 2H–J**). This gives unequivocal evidence that intermolecular interactions play a key role in determining the emission properties, color purity and TADF efficiency of these systems. The framework Etherington et al. established (Etherington et al., 2019), which builds upon techniques in the wider literature (section Novel TADF Emitters Exhibiting Functional Behavior) provides the means to deconvolute SSSE from intermolecular effects. This is an important aspect to build the complete picture of TADF behavior beyond the single molecule while highlighting the need for researchers to be acutely aware of intermolecular interactions in future studies.

## CONCLUSION AND OUTLOOK

While there has been vast development of new TADF emitters and our understanding of the fundamental processes of rISC and the spin states has developed, it is now time to look towards understanding these processes in non-ideal situations using the techniques and framework discussed above. This framework will facilitate the development and understanding of functional materials that are sensitive to mechanical and thermal energy

while opening up pathways to AIE-based, non-doped OLEDs (Furue et al., 2016; Liu et al., 2018a; Cai et al., 2020; Yang et al., 2020). It will also help unify the study of intramolecular TADF emitters with the studies of polymorphism (Chung and Diao, 2016; Bernstein, 2020; Levesque et al., 2020) exciplexes (Kim et al., 2016; Sarma and Wong, 2018; Tang et al., 2020) and host-guest interactions (Matsunaga and Yang, 2015; Feng et al., 2017; Ono et al., 2018).

The framework should continually incorporate new experimental techniques that are sensitive to the environmental changes underpinning this behavior to be controlled. So far, the framework includes single crystal studies and controlled mechanochromic and thermochromic analyses. This framework will then allow for the control and use of these properties as demonstrated in the work by Bhatia and Ray (2019). The researchers utilized the dimer/aggregate state, not to improve TADF but rather, to introduce room temperature phosphorescence. A combination of the emission profiles of the monomer, dimer and aggregated species produces a wide band white afterglow.

Future work will specifically link molecular structure to the desired properties. Sussardi et al. have begun this progress linking the crystal structure of a compound directly to the emission profile as a function of pressure (Sussardi et al., 2020). This work allows a systematic way to study and correlate the intermolecular interactions and the photophysics. Etherington et al. (2019) showed that the addition of tert-butyl groups do little to prevent the intermolecular interactions and thus we must look to bulkier spacer units or alternative methods to control these effects. High-pressure crystallography, similar to the work of Sussardi et al. (2020) would be able to test the limit of these bulky units. The techniques and studies mentioned in this review provide a basis to develop future frameworks and criteria for inhibiting or enhancing intermolecular interactions. This will help to provide high color purity compounds for OLED commercialization and unlock new functional behavior for applications beyond OLEDs.

## AUTHOR CONTRIBUTIONS

MKE devised the idea for the topic of this review, collated the literature and wrote the review. The author confirms being the sole contributor of this work and has approved it for publication.

## REFERENCES

- Baldo, M. A., O'Brien, D. F., and Forrest, S. R. (1999). Excitonic singlet-triplet ratio in a semiconducting organic thin film. *Phys. Rev. B* 60, 14422–14428. doi: 10.1103/PhysRevB.60.14422
- Bernstein, J. (2020). *Polymorphism in Molecular Crystals*. 2nd Edn. New York, NY: Oxford University Press. doi: 10.1093/oso/9780199655441.001.0001
- Bhatia, H., and Ray, D. (2019). Use of dimeric excited states of the donors in d4-a systems for accessing white light emission, afterglow, and invisible security ink. *J. Phys. Chem. C* 123, 22104–22113. doi: 10.1021/acs.jpcc.9b07762
- Bodea, C., and Silberg, I. (1968). Recent advances in the chemistry of phenothiazines. *Chimia Intern. J. Chem.* 66, 321–460. doi: 10.1016/S0065-2725(08)60375-X
- Bulović, V., Deshpande, R., Thompson, M. E., and Forrest, S. R. (1999). Tuning the color emission of thin film molecular organic light emitting devices by the solid state solvation effect. *Chem. Phys. Lett.* 308, 317–322. doi: 10.1016/S0009-2614(99)00580-1
- Cai, Z., Chen, H., Guo, J., Zhao, Z., and Tang, B. Z. (2020). Efficient aggregation-induced delayed fluorescence luminogens for solution-processed oleds with small efficiency roll-off. *Front. Chem.* 8:193. doi: 10.3389/fchem.2020.00193
- Chatterjee, T., and Wong, K. T. (2019). Perspective on host materials for thermally activated delayed fluorescence organic light emitting diodes. *Adv. Optical Mater.* 7, 1–34. doi: 10.1002/adom.201800565
- Chung, H., and Diao, Y. (2016). Polymorphism as an emerging design strategy for high performance organic electronics. *J. Mater. Chem. C* 4, 3915–3933. doi: 10.1039/C5TC04390E

- Colella, M., Danos, A., and Monkman, A. P. (2019). Less is more: dilution enhances optical and electrical performance of a TADF exciplex. *J. Phys. Chem. Lett.* 10, 793–798. doi: 10.1021/acs.jpclett.8b03646
- Conaghan, P. J., Matthew Menke, S., Romanov, A. S., Jones, S. T. E., Pearson, A. J., Evans, E. W., et al. (2018). Efficient vacuum-processed light-emitting diodes based on carbene-metal-amides. *Adv. Mater.* 30:35. doi: 10.1002/adma.201802285
- Cotts, B. L., McCarthy, D. G., Noriega, R., Penwell, S. B., Delor, M., Devore, D. D., et al. (2017). Tuning thermally activated delayed fluorescence emitter photophysics through solvation in the solid state. *ACS Energy Lett.* 2, 1526–1533. doi: 10.1021/acsenerylett.7b00268
- Coubeils, J. L., and Pullman, B. (1972). Molecular orbital study of the conformational properties of phenothiazines. *Theor. Chim. Acta* 24, 35–41. doi: 10.1007/BF00528308
- Delor, M., McCarthy, D. G., Cotts, B. L., Roberts, T. D., Noriega, R., Devore, D. D., et al. (2017). Resolving and controlling photoinduced ultrafast solvation in the solid state. *J. Phys. Chem. Lett.* 8, 4183–4190. doi: 10.1021/acs.jpclett.7b01689
- Di, D., Romanov, A. S., Yang, L., Richter, J. M., Rivett, J. R. H., Jones, S., et al. (2017). High-performance light-emitting diodes based on carbene-metal-amides. *Science* 356, 159–163. doi: 10.1126/science.aah4345
- Dias, F. B., Bourdakos, K. N., Jankus, V., Moss, K. C., Kamtekar, K. T., Bhalla, V., et al. (2013). Triplet harvesting with 100% efficiency by way of thermally activated delayed fluorescence in charge transfer OLED emitters. *Adv. Mater. (Deerfield Beach, Fla.)* 25, 3707–3714. doi: 10.1002/adma.201300753
- Etherington, M. K., Franchello, F., Gibson, J., Northey, T., Santos, J., Ward, J. S., et al. (2017). Regio- and conformational isomerization critical to design of efficient thermally-activated delayed fluorescence emitters. *Nat. Commun.* 8:14987. doi: 10.1038/ncomms14987
- Etherington, M. K., Gibson, J., Higginbotham, H. F., Penfold, H. J., and Monkman, A. P. (2016). Revealing the spin-vibronic coupling mechanism of thermally activated delayed fluorescence. *Nat. Commun.* 7:13680. doi: 10.1038/ncomms13680
- Etherington, M. K., Kukhta, N. A., Higginbotham, H. F., Danos, A., Bismillah, A. N., Graves, D. R., et al. (2019). Persistent dimer emission in thermally activated delayed fluorescence materials. *J. Phys. Chem. C* 123, 11109–11117. doi: 10.1021/acs.jpcc.9b01458
- Feng, H. T., Bin Xiong, J., Luo, J., Fang Feng, W., Yang, D., and Song Zheng, Y. (2017). Selective host-guest co-crystallization of pyridine-functionalized tetraphenylethylenes with phthalic acids and multicolor emission of the co-crystals. *Chem. A Eur. J.* 23, 644–651. doi: 10.1002/chem.201604133
- Furue, R., Nishimoto, T., Seob Park, I., Lee, J., and Yasuda, T. (2016). Aggregation-induced delayed fluorescence based on donor/acceptor-tethered janus carborane triads: unique photophysical properties of nondoped OLEDs. *Angew. Chem. Intern. Edition* 55, 7171–7175. doi: 10.1002/anie.201603232
- Gan, S., Luo, W., He, B., Chen, L., Nie, H., Hu, R., et al. (2016). Integration of aggregation-induced emission and delayed fluorescence into electronic donor-acceptor conjugates. *J. Mater. Chem. C* 4, 3705–3708. doi: 10.1039/C5TC03588K
- Gibson, J., Monkman, A. P., and Penfold, T. J. (2016). The importance of vibronic coupling for efficient reverse intersystem crossing in thermally activated delayed fluorescence molecules. *Chem. Phys. Chem.* 17, 2956–2961. doi: 10.1002/cphc.201600662
- Han, H., and Kim, E. (2019). Dielectric effects on charge-transfer and local excited states in organic persistent room-temperature phosphorescence. *Chem. Mater.* 31, 6925–6935. doi: 10.1021/acs.chemmater.9b01364
- Haseyama, S., Niwa, A., Kobayashi, T., Nagase, T., Goushi, K., Adachi, C., et al. (2017). Control of the singlet-triplet energy gap in a thermally activated delayed fluorescence emitter by using a polar host matrix. *Nanos. Res. Lett.* 12:268. doi: 10.1186/s11671-017-2012-1
- Hladka, I., Yu Volyniuk, D., Bezvikonnyi, O., Kinzhybalo, V., Bednarchuk, T., Danyliv, Y., et al. (2018). Polymorphism of derivatives of tert-butyl substituted acridan and perfluorobiphenyl as sky-blue OLED emitters exhibiting aggregation induced-active thermally activated delayed fluorescence. *J. Mater. Chem. C* 6, 13179–13189. doi: 10.1039/C8TC04867C
- Hong, Y., Lam, J. W. Y., and Zhong Tang, B. (2009). Aggregation-induced emission: phenomenon, mechanism and applications. *Chem. Commun.* 29, 4332–4353. doi: 10.1039/b904665h
- Huang, B., Chen, W.-C., Li, Z., Zhang, J., Zhao, W., Feng, Y., et al. (2018). Manipulation of molecular aggregation states to realize polymorphism, AIE, MCL, and TADF in a single molecule. *Angew. Chem. Intern. Edition* 57, 12473–12477. doi: 10.1002/anie.201806800
- Hung, M. K., Wei Tsai, K., Sharma, S., Yi Wu, J., and An Chen, S. (2019). Acridan-grafted poly(Biphenyl germanium) with high triplet energy, low polarizability, and an external heavy-atom effect for highly efficient sky-blue TADF electroluminescence. *Angew. Chem. Intern. Edition* 58, 11317–11323. doi: 10.1002/anie.201904433
- Kim, B. S., and Lee, J. Y. (2014). Phosphine oxide type bipolar host material for high quantum efficiency in thermally activated delayed fluorescent device. *ACS Appl. Mater. Interfaces* 6, 8396–8400. doi: 10.1021/am501301g
- Kim, H. S., Park, S.-R., and Chul Suh, M. (2017). Concentration quenching behavior of thermally activated delayed fluorescence in a solid film. *J. Phys. Chem. C* 121, 13986–13997. doi: 10.1021/acs.jpcc.7b02369
- Kim, K. H., Jun Yoo, S., and Kim, J. J. (2016). Boosting triplet harvest by reducing nonradiative transition of exciplex toward fluorescent organic light-emitting diodes with 100% internal quantum efficiency. *Chem. Mater.* 28, 1936–1941. doi: 10.1021/acs.chemmater.6b00478
- Klimash, A., Pander, P., Klooster, W. T., Coles, S. J., Data, P., Dias, F. B., et al. (2018). Intermolecular interactions in molecular crystals and their effect on thermally activated delayed fluorescence of helicene-based emitters. *J. Mater. Chem. C* 6, 10557–10568. doi: 10.1039/C8TC03390K
- Komatsu, R., Sasabe, H., Inomata, S., Pu, Y.-J., and Kido, J. (2015). High efficiency solution processed OLEDs using a thermally activated delayed fluorescence emitter. *Synthetic Metals* 202, 165–168. doi: 10.1016/j.synthmet.2015.02.009
- Levesque, A., Maris, T., and Wuest, J. D. (2020). ROY reclaims its crown: new ways to increase polymorphic diversity. *J. Am. Chem. Soc.* doi: 10.1021/jacs.0c04434
- Li, N., Fang, Y., Li, L., Zhao, H., Quan, Y., Ye, S., et al. (2018). A universal solution-processable bipolar host based on triphenylamine and pyridine for efficient phosphorescent and thermally activated delayed fluorescence OLEDs. *J. Luminescence* 199, 465–4674. doi: 10.1016/j.jlumin.2018.03.003
- Lim, E. C., and Kedzierski, M. (1973). Spin-forbidden electronic transitions in non-planar aromatic amines. *Chem. Phys. Lett.* 20, 242–245. doi: 10.1016/0009-2614(73)85167-X
- Lin, T. A., Chatterjee, T., Lung Tsai, W., Kai Lee, W., Jung Wu, M., et al. (2016). Sky-blue organic light emitting diode with 37% external quantum efficiency using thermally activated delayed fluorescence from spiroacridine-triazine hybrid. *Adv. Mater.* 28, 6976–6983. doi: 10.1002/adma.201601675
- Liu, H., Zeng, J., Guo, J., Nie, H., Zhao, Z., and Tang, B. Z. (2018a). High-performance non-doped OLEDs with nearly 100 % exciton use and negligible efficiency roll-off. *Angew. Chem. Intern. Edition* 57, 9290–9294. doi: 10.1002/anie.201802060
- Liu, Y., Li, C., Ren, Z., Yan, S., and Bryce, M. R. (2018b). All-organic thermally activated delayed fluorescence materials for organic light-emitting diodes. *Nat. Rev. Mater.* 3:18020. doi: 10.1038/natrevmats.2018.20
- Luo, J., Xie, Z., Xie, Z., Lam, J. W. Y., Cheng, L., Chen, H., et al. (2001). Aggregation-induced emission of 1-methyl-1,2,3,4,5-pentaphenylsilole. *Chem. Commun.* 18, 1740–1741. doi: 10.1039/b105159h
- Mahoro, G. U., Fernandez-Cestau, J., Renaud, J. L., Coto, P. B., Costa, R. D., and Gaillard, S. (2020). Recent advances in solid-state lighting devices using transition metal complexes exhibiting thermally activated delayed fluorescent emission mechanism. *Adv. Opt. Mater.* 260, 1–36. doi: 10.1002/adom.202000260
- Malrieu, J.-P., and Pullman, B. (1964). Sur les propriétés électroniques de La phénothiazine et de son radical. *Theor. Chim. Acta* 2, 293–301. doi: 10.1007/BF00527056
- Matsunaga, Y., and Yang, J. S. (2015). Multicolor fluorescence writing based on host-guest interactions and force-induced fluorescence-color memory. *Angew. Chem. Intern. Edition* 54, 7985–7989. doi: 10.1002/anie.201503406
- Mei, J., Hong, Y., Lam, J. Y. W., Qin, A., Tang, Y., and Tang, B. (2014). Aggregation-induced emission: the whole is more brilliant than the parts. *Adv. Mater.* 26, 5429–5479. doi: 10.1002/adma.201401356
- Nakanotani, H., Furukawa, T., Morimoto, K., and Adachi, C. (2016). Electrical conductors: long-range coupling of electron-hole pairs in spatially separated organic donor-acceptor layers. *Sci. Adv.* 2, 1–8. doi: 10.1126/sciadv.1501470
- Nakanotani, H., Masui, K., Nishide, J., Shibata, T., and Adachi, C. (2013). Promising operational stability of high-efficiency organic light-emitting

- diodes based on thermally activated delayed fluorescence. *Sci. Rep.* 3:2127. doi: 10.1038/srep02127
- Niwa, A., Haseyama, S., Kobayashi, T., Nagase, T., Goushi, K., Adachi, C., et al. (2018). Triplet-triplet annihilation in a thermally activated delayed fluorescence emitter lightly doped in a host. *Appl. Phys. Lett.* 113:083301. doi: 10.1063/1.5025870
- Northey, T., Stacey, J. E., and Penfold, T. J. (2017). The role of solid state solvation on the charge transfer state of a thermally activated delayed fluorescence emitter. *J. Mater. Chem. C* 5, 11001–11009. doi: 10.1039/C7TC04099G
- Okazaki, M., Takeda, Y., Data, P., Pander, P., Higginbotham, H., Monkman, A. P., et al. (2017). Thermally activated delayed fluorescent phenothiazine-dibenzo[a,j]phenazine-phenothiazine triads exhibiting tricolor-changing mechanochromic luminescence. *Chem. Sci.* 8, 2677–2686. doi: 10.1039/C6SC04863C
- Ono, T., Taema, A., Goto, A., and Hiseada, Y. (2018). Switching of monomer fluorescence, charge-transfer fluorescence, and room-temperature phosphorescence induced by aromatic guest inclusion in a supramolecular host. *Chem. A Eur. J.* 24, 17487–17496. doi: 10.1002/chem.201804349
- Pashazadeh, R., Pander, P., Lazauskas, A., Dias, F. B., and Grazulevicius, J. V. (2018). Multicolor luminescence switching and controllable thermally activated delayed fluorescence turn on/turn off in carbazole–quinoxaline–carbazole triads. *J. Phys. Chem. Lett.* 9, 1172–1177. doi: 10.1021/acs.jpclett.8b00136
- Qin, C., Matsushima, T., Potschavage, M. J., Sandanayaka, A. S. D., Leyden, M. R., Bencheikh, F., et al. (2020). Triplet management for efficient perovskite light-emitting diodes. *Nat. Photonics* 14, 70–75. doi: 10.1038/s41566-019-0545-9
- Santos, P. L. D., Etherington, M. K., and Monkman, A. P. (2018). Chemical and conformational control of the energy gaps involved in the thermally activated delayed fluorescence mechanism. *J. Mater. Chem. C* 6, 4842–4853. doi: 10.1039/C8TC00991K
- Santos, P. L. D., Ward, J. S., Bryce, M. R., and Monkman, A. P. (2016a). Using guest–host interactions to optimize the efficiency of TADF OLEDs. *J. Phys. Chem. Lett.* 7, 3341–3346. doi: 10.1021/acs.jpclett.6b01542
- Santos, P. L. D., Ward, J. S., Data, P., Batsanov, A. S., Bryce, M. R., Dias, F. B., et al. (2016b). Engineering the singlet-triplet energy splitting in a TADF molecule. *J. Mater. Chem. C* 4, 3815–3824. doi: 10.1039/C5TC03849A
- Sarma, M., and Wong, K. T. (2018). Exciplex: an intermolecular charge-transfer approach for TADF. *ACS Appl. Mater. Interfaces* 10, 19279–19304. doi: 10.1021/acsami.7b18318
- Shi, Y. Z., Wang, K., Li, X., Le Dai, G., Liu, W., Ke, K., et al. (2018). Intermolecular charge-transfer transition emitter showing thermally activated delayed fluorescence for efficient non-doped OLEDs. *Angew. Chem. Intern. Edition* 57, 9480–9484. doi: 10.1002/anie.201804483
- Skaisgirius, R., Serevicius, T., Kazlauskas, K., Geng, Y., Adachi, C., and Juršenas, S. (2019). Origin of dual emission in  $\sigma$ -bridged donor–acceptor TADF compounds. *J. Mater. Chem. C* 7, 12601–12609. doi: 10.1039/C9TC03548F
- Skuodis, E., Bezvikonny, O., Tomkeviciene, A., Volyniuk, D., Mimaite, V., Lazauskas, A., et al. (2018). Aggregation, thermal annealing, and hosting effects on performances of an acridan-based TADF emitter. *Org. Electron.* 63, 29–40. doi: 10.1016/j.orgel.2018.09.002
- Sturala, J., Etherington, M. K., Bismillah, A. N., Higginbotham, H. F., Trewby, W., Aguilar, J. A., et al. (2017). Excited-state aromatic interactions in the aggregation-induced emission of molecular rotors. *J. Am. Chem. Soc.* 139, 17882–17889. doi: 10.1021/jacs.7b08570
- Sussardi, A., Hobday, C. L., Marshall, R. J., Forgan, R. S., Jones, A. C., and Moggach, S. A. (2020). Correlating pressure-induced emission modulation with linker rotation in a photoluminescent MOF. *Angew. Chem. Intern. Edition* 59, 8118–8122. doi: 10.1002/anie.202000555
- Tang, X., Cui, L.-S., Li, H.-C., Gillett, A. J., Auras, F., Qu, Y.-K., et al. (2020). Highly efficient luminescence from space-confined charge-transfer emitters. *Nat. Mater.* doi: 10.1038/s41563-020-0710-z. [Epub ahead of print].
- Thomas, S. W., Joly, G. D., and Swager, T. M. (2007). Chemical sensors based on amplifying fluorescent conjugated polymers. *Chem. Rev.* 107, 1339–1386. doi: 10.1021/cr0501339
- Tsai, M. H., Hong, Y. H., Chang, C. H., Su, H. C., Wu, C. C., Matoliukstyte, A., et al. (2007). 3-(9-Carbazolyl)Carbazoles and 3,6-Di(9-Carbazolyl)Carbazoles as Effective Host Materials for Efficient Blue Organic Electrophosphorescence. *Adv. Mater.* 19, 862–866. doi: 10.1002/adma.200600822
- Uoyama, H., Goushi, K., Shizu, K., Nomura, H., and Adachi, C. (2012). Highly efficient organic light-emitting diodes from delayed fluorescence. *Nature* 492, 234–238. doi: 10.1038/nature11687
- Wang, P., Zhao, S., Xu, Z., Qiao, B., Long, Z., and Huang, Q. (2016). The electroluminescence mechanism of solution-processed TADF emitter 4CzIPN doped OLEDs investigated by transient measurements. *Molecules* 21:1365. doi: 10.3390/molecules21101365
- Wong, M. Y., and Zysman-Colman, E. (2017). Purely organic thermally activated delayed fluorescence materials for organic light-emitting diodes. *Adv. Mater.* 29:22. doi: 10.1002/adma.201605444
- Yang, M., Park, I. S., Miyashita, Y., Tanaka, K., and Yasuda, T. (2020). Mechanochromic delayed fluorescence switching in propeller-shaped carbazole–isophthalonitrile luminogens with stimuli-responsive intramolecular charge-transfer excited states. *Angew. Chem. Int. Ed. Engl.* 59, 13955–13961. doi: 10.1002/ange.202005584
- Yersin, H., Czerwieniec, R., Shafikov, M. Z., and Suleymanova, A. F. (2018). “TADF material design: photophysical background and case studies focusing on Cu (I) and Ag (I) complexes,” in *Highly Efficient OLEDs: Materials Based on Thermally Activated Delayed Fluorescence*, ed. Yersin H. (Weinheim: Wiley Periodicals), 1–60. doi: 10.1002/9783527691722.ch1
- Yu, M., Huang, R., Guo, J., Zhao, Z., and Tang, B. Z. (2020). Promising applications of aggregation-induced emission luminogens in organic optoelectronic devices. *PhotonIX* 1, 1–33. doi: 10.1186/s43074-020-00012-y
- Zeng, W., Lai, H. Y., Lee, W. K., Jiao, M., Shiu, Y. J., Zhong, C., et al. (2018). Achieving nearly 30% external quantum efficiency for orange-red organic light emitting diodes by employing thermally activated delayed fluorescence emitters composed of 1,8-naphthalimide-acridine hybrids. *Adv. Mater.* 30, 1–8. doi: 10.1002/adma.201704961
- Zhang, D.-D., Suzuki, K., Song, X.-Z., Wada, Y., Kubo, S., Duan, L., et al. (2019a). Thermally activated delayed fluorescent materials combining intra- and intermolecular charge transfers. *ACS Appl. Mater. Interfaces* 11, 7192–7198. doi: 10.1021/acsami.8b19428
- Zhang, H., Du, L., Wang, L., Liu, J., Wan, Q., Kwok, R. T. K., et al. (2019b). Visualization and manipulation of molecular motion in the solid state through photoinduced clusteroluminescence. *J. Phys. Chem. Lett.* 10, 7077–7085. doi: 10.1021/acs.jpclett.9b02752
- Zhang, H., Zhao, Z., McGonigal, P. R., Ye, R., Liu, S., Lam, J. W. Y., et al. (2020). Clusterization-triggered emission: uncommon luminescence from common materials. *Mater. Today* 32, 275–292. doi: 10.1016/j.mattod.2019.08.010
- Zhang, H., Zheng, X., Xie, N., He, Z., Liu, J., Leung, N. L. C., et al. (2017). “Why do simple molecules with ‘isolated’ phenyl rings emit visible light?” *J. Am. Chem. Soc.* 139, 16264–16272. doi: 10.1021/jacs.7b08592
- Zheng, K., Ni, F., Chen, Z., Zhong, C., and Yang, C. (2019). Polymorph-dependent thermally activated delayed fluorescence emitters: understanding TADF from a perspective of aggregation state. *Angew. Chem. Int. Ed. Engl.* 59, 9972–9976. doi: 10.1002/ange.201913210
- Zhou, B., and Yan, D. (2019). Simultaneous long-persistent blue luminescence and high quantum yield within 2d organic–metal halide perovskite micro/nanosheets. *Angew. Chem. Int. Ed. Engl.* 58, 15128–15135. doi: 10.1002/anie.201909760
- Zhu, F., Zhou, C., Zhou, D., and Yu, J. (2017). Improving electroluminescent efficiency and ultraviolet detectivity of optoelectronic integrated devices by doping a thermally activated delayed fluorescent material in an aggregation-induced emission material as an active layer. *Opt. Mater. Express* 7:3538. doi: 10.1364/OME.7.003538

**Conflict of Interest:** The author declares that the research was conducted in the absence of any commercial or financial relationships that could be construed as a potential conflict of interest.

Copyright © 2020 Etherington. This is an open-access article distributed under the terms of the Creative Commons Attribution License (CC BY). The use, distribution or reproduction in other forums is permitted, provided the original author(s) and the copyright owner(s) are credited and that the original publication in this journal is cited, in accordance with accepted academic practice. No use, distribution or reproduction is permitted which does not comply with these terms.



# OBO-Fused Benzo[fg]tetracene as Acceptor With Potential for Thermally Activated Delayed Fluorescence Emitters

Zhen Zhang<sup>1</sup>, Shiv Kumar<sup>2</sup>, Sergey Bagnich<sup>3</sup>, Eduard Spuling<sup>1,2</sup>, Fabian Hundemer<sup>1</sup>, Martin Nieger<sup>4</sup>, Zahid Hassan<sup>1</sup>, Anna Köhler<sup>3\*</sup>, Eli Zysman-Colman<sup>2\*</sup> and Stefan Bräse<sup>1,5\*</sup>

<sup>1</sup> Institute of Organic Chemistry (IOC), Karlsruhe Institute of Technology (KIT), Karlsruhe, Germany, <sup>2</sup> Organic Semiconductor Centre, EaStCHEM School of Chemistry, University of St Andrews, St Andrews, United Kingdom, <sup>3</sup> Soft Matter Optoelectronics, Bayreuth Institute for Macromolecular Research (BIMF) & Bavarian Polymer Institute (BPI), University of Bayreuth, Bayreuth, Germany, <sup>4</sup> Department of Chemistry, University of Helsinki, Helsinki, Finland, <sup>5</sup> Institute of Biological and Chemical Systems – Functional Molecular Systems (IBCS-FMS), Karlsruhe Institute of Technology (KIT), Eggenstein-Leopoldshafen, Germany

## OPEN ACCESS

### Edited by:

Guigen Li,  
Texas Tech University, United States

### Reviewed by:

Xu-Lin Chen,  
Chinese Academy of Sciences, China  
Zujin Zhao,  
South China University of  
Technology, China

### \*Correspondence:

Anna Köhler  
anna.koehler@uni-bayreuth.de  
Eli Zysman-Colman  
eli.zysman-colman@st-andrews.ac.uk  
Stefan Bräse  
braese@kit.edu

### Specialty section:

This article was submitted to  
Organic Chemistry,  
a section of the journal  
Frontiers in Chemistry

**Received:** 18 May 2020

**Accepted:** 19 August 2020

**Published:** 30 September 2020

### Citation:

Zhang Z, Kumar S, Bagnich S,  
Spuling E, Hundemer F, Nieger M,  
Hassan Z, Köhler A,  
Zysman-Colman E and Bräse S (2020)  
OBO-Fused Benzo[fg]tetracene as  
Acceptor With Potential for Thermally  
Activated Delayed Fluorescence  
Emitters. *Front. Chem.* 8:563411.  
doi: 10.3389/fchem.2020.563411

Six luminophores bearing an OBO-fused benzo[fg]tetracene core as an electron acceptor were designed and synthesized. The molecular structures of three molecules (PXZ-OBO, 5PXZ-OBO, 5DMAC-OBO) were determined by single crystal X-ray diffraction studies and revealed significant torsion between the donor moieties and the OBO acceptor with dihedral angles between 75.5 and 86.2°. Photophysical studies demonstrate that blue and deep blue emission can be realized with photoluminescence maxima ( $\lambda_{PL}$ ) ranging from 415 to 480 nm in mCP films. The emission energy is modulated by simply varying the strength of the donor heterocycle, the number of donors, and their position relative to the acceptor. Although the DMAC derivatives show negligible delayed emission because of their large singlet-triplet excited state energy difference,  $\Delta E_{ST}$ , PXZ-based molecules, especially PXZ-OBO with an experimental  $\Delta E_{ST}$  of 0.25 eV, demonstrate delayed emission in blend mCP films at room temperature, which suggests triplet exciton harvesting occurs in these samples, potentially by thermally activated delayed fluorescence.

**Keywords:** boron emitters, fluorescence, OLED, TADF, boron

## INTRODUCTION

As one of the most promising electroluminescent technologies, organic light-emitting diodes (OLEDs) have attracted significant attention and are now being commercialized across a number of different product lines (Endo et al., 2011; Uoyama et al., 2012; Tao et al., 2014; Wong and Zysman-Colman, 2017; Yang et al., 2017). State-of-the-art phosphorescent OLEDs (PhOLEDs) have an Achilles heel, and that is the use of non-sustainable noble metal emitters. Purely organic thermally activated delayed fluorescence (TADF) OLEDs show comparable performance to PhOLEDs and use sustainable materials (Lin et al., 2016). TADF emitters rely mainly on a twisted donor acceptor structure (Chen et al., 2016; Wang et al., 2017). Heterocycles, such as carbazole derivatives (Albrecht et al., 2015), triphenylamines (Data et al., 2016), phenoxazines (Takahashi et al., 2014), and acridines (Zhang et al., 2016), are suitable donors to construct TADF molecules. Electron-accepting units, such as benzonitriles (Park et al., 2016), triazines (Kim et al., 2015),



benzophenones (Lee et al., 2015), and sulfones (Lee et al., 2016), are commonly used as acceptors.

Three-coordinate boranes have also been reported as electron-withdrawing acceptors in donor–acceptor systems (Numata et al., 2015; Kitamoto et al., 2016; Chen et al., 2017; Lee et al., 2017). However, the high susceptibility of boron–carbon (B–C) bond cleavage in electron-rich and electron-poor BN heterocycles along with vacant  $p_z$ -orbitals on the boron atom has resulted in poor chemical and photostability (Yang et al., 2016). For example, the BN heterocycles undergo photoelimination reaction to form a new  $\pi$ -conjugated polycyclic azaborine compounds (Lu et al., 2013; Yang et al., 2016). In order to increase the chemical and photostability of these materials, steric bulk is added in the vicinity of the boron atom, leading to air-stable derivatives. Suzuki and coworkers (Suzuki et al., 2015) synthesized two stable boron-containing compounds based on the bis(mesityl)borane (BMes<sub>2</sub>) acceptor and realized efficient sky-blue [Commission Internationale de l'Éclairage (CIE): 0.18, 0.43] and green (CIE: 0.22, 0.55) TADF OLEDs with maximum external quantum efficiency (EQE<sub>max</sub>) of 21.6% (2DAC-Mes<sub>3</sub>B) and 22.8% (PXZ-Mes<sub>3</sub>B), respectively. Positioning the boron atom within polycyclic  $\pi$  systems is another strategy to achieve improved stability of the emitter. With a demethylative direct borylation method, Hatakeyama et al. reported synthesis of stable benzo[fg]tetracenes core containing boronate ester, amide, and thioester substructures. Depending on the heteroatom fragment (O and NMe) adjacent to the boron, these materials exhibited characteristic emission in the UV at 335 to 377 nm (Katayama et al., 2016; Numano et al., 2016). Müllen et al. also reported a series of OBO-doped tetrabenzo[bc,ef,kl,no]coronenes and tetrabenzo[a,f,j,o]perylene, which exhibited structured blue fluorescence with  $\phi_{PL}$  of 61 and 27%, respectively (Wang et al., 2016). In 2019, Yasuda et al. reported two TADF emitters using boronate ester or boronate thioester as the acceptor (Matsuo and Yasuda, 2019). The boronate thioester-based device showed sky-blue emission at 489 nm (CIE: 0.17, 0.39) and excellent EL performance with the EQE<sub>max</sub> of 20.9%. Although the boronate ester-based device exhibited only the EQE<sub>max</sub> of 5.2% because of its low PLQY of 28%, its bluer emission at 471 nm (CIE: 0.17, 0.22) revealed the potential of the boronate ester acceptor for blue and even deep blue TADF emitters.

Herein we report six examples of blue emitters based on this OBO-based benzo[fg]tetracene acceptor (OBO). We systematically investigate the impact of the number, identity of the donor (9,9-dimethyl-9,10-dihydroacridine, DMAC, and 10H-phenoxazine, PXZ), and their position relative to OBO on the optoelectronic properties of the emitter (Figure 1).

## RESULTS AND DISCUSSION

### Synthesis

These six OBO-based derivatives were successfully synthesized via a three-step procedure (Scheme 1). First, DMAC and PXZ were treated with halo-substituted anisoles under Buchwald–Hartwig cross-coupling conditions to afford the corresponding coupled products **1**, **2**, **5**, and **6** in good to excellent yield. These intermediates were reacted with arylboronic

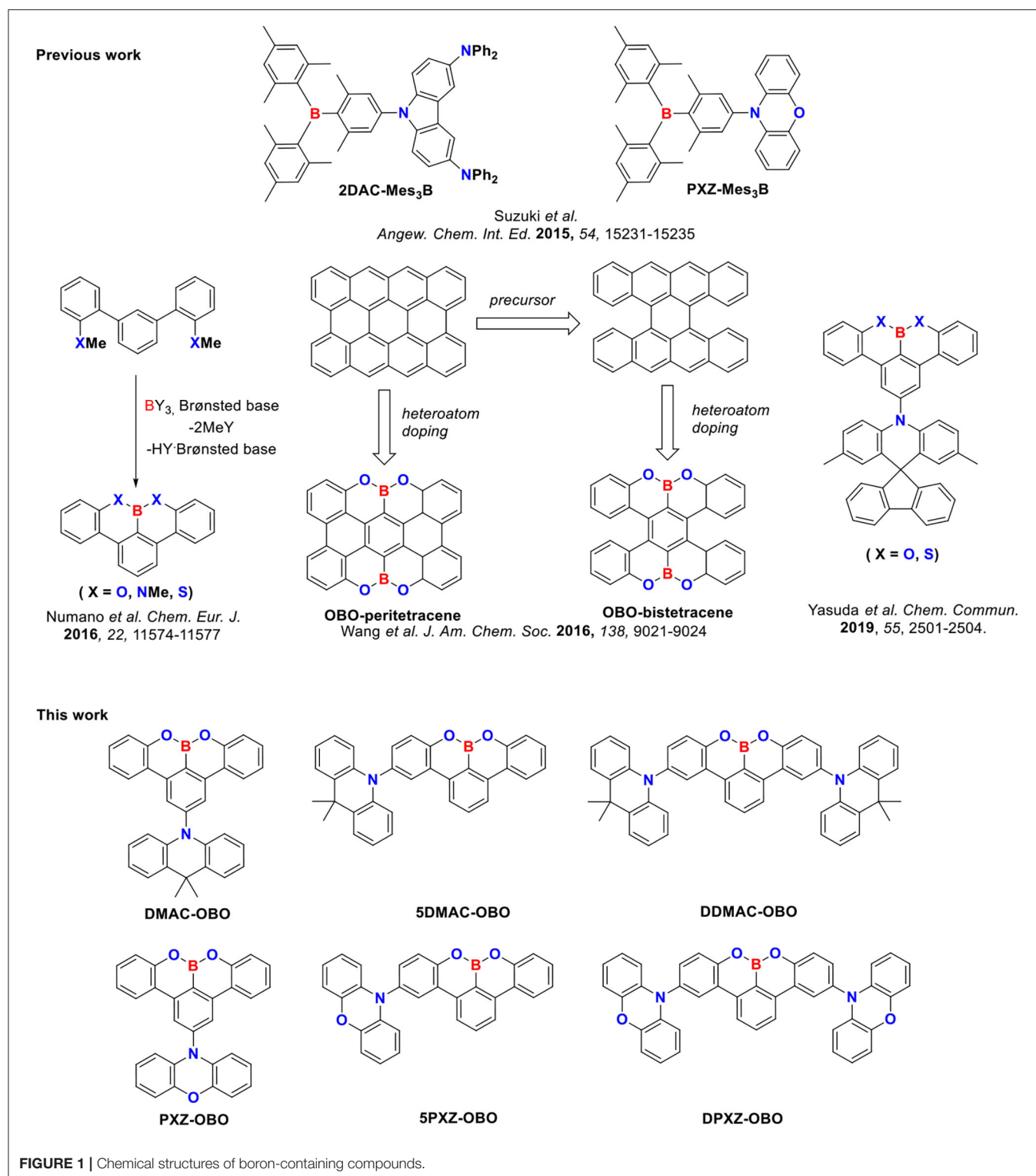
acids/esters under Suzuki–Miyaura cross-coupling conditions to produce dimethoxyteraryl intermediates (**3**, **4**, **7–10**) in good yields. Finally, the target OBO-based emitters were obtained through a demethylative direct borylation procedure of the aryl methyl ethers in the presence of BBr<sub>3</sub> (Wang et al., 2016). This final cyclization proceeded in 55 to 56% yield (DMAC-OBO and PXZ-OBO) when the donor units were introduced to the central phenyl ring. On the other hand, the yields dropped to 21 to 24% when the donor units were in *para* position to the methoxy group. The final products were found to be easily purified by silica gel column chromatography and stable under ambient conditions for more than 2 years, showing no decomposition in nuclear magnetic resonance spectra.

The crystals of PXZ-OBO, 5PXZ-OBO, and 5DMAC-OBO suitable for single crystal X-ray diffraction analysis were obtained from a mixed solution of dichloromethane (DCM) and cyclohexane. The structures reveal that these three molecules possess the expected highly twisted donor–acceptor conformation (Figure 2). The dihedral angles between donor and acceptor for the two structural isomers PXZ-OBO and 5PXZ-OBO are tuned remarkably. For PXZ-OBO, this torsion is 75.5°, whereas the donor–acceptor dihedral angle is larger at 86.2° for 5PXZ-OBO. The DMAC analog, 5DMAC-OBO, shows a slightly reduced twisting angle between the donor and the acceptor at 80.1°. In all the structures, the OBO-containing acceptor itself is flat.

### Theoretical Calculations

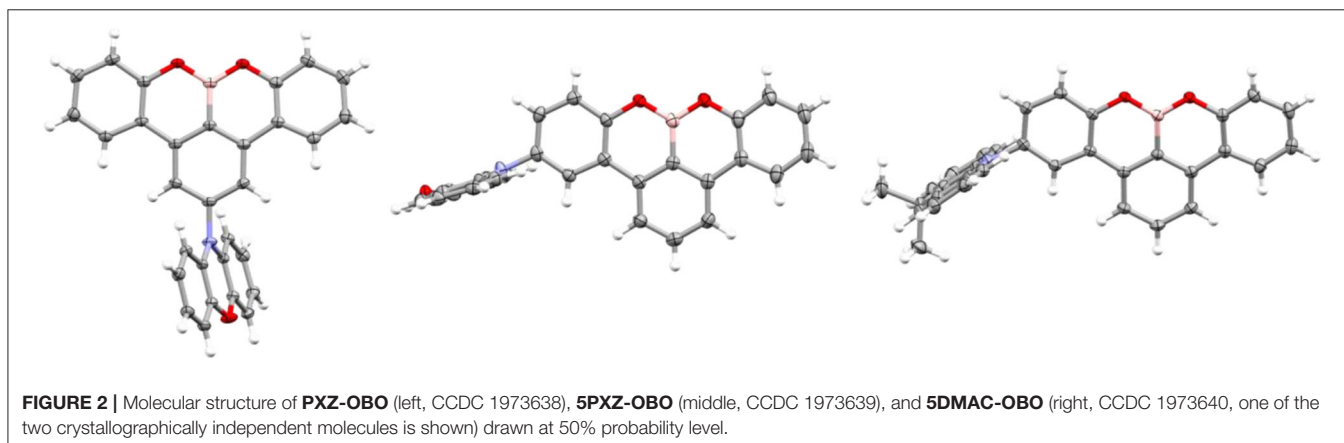
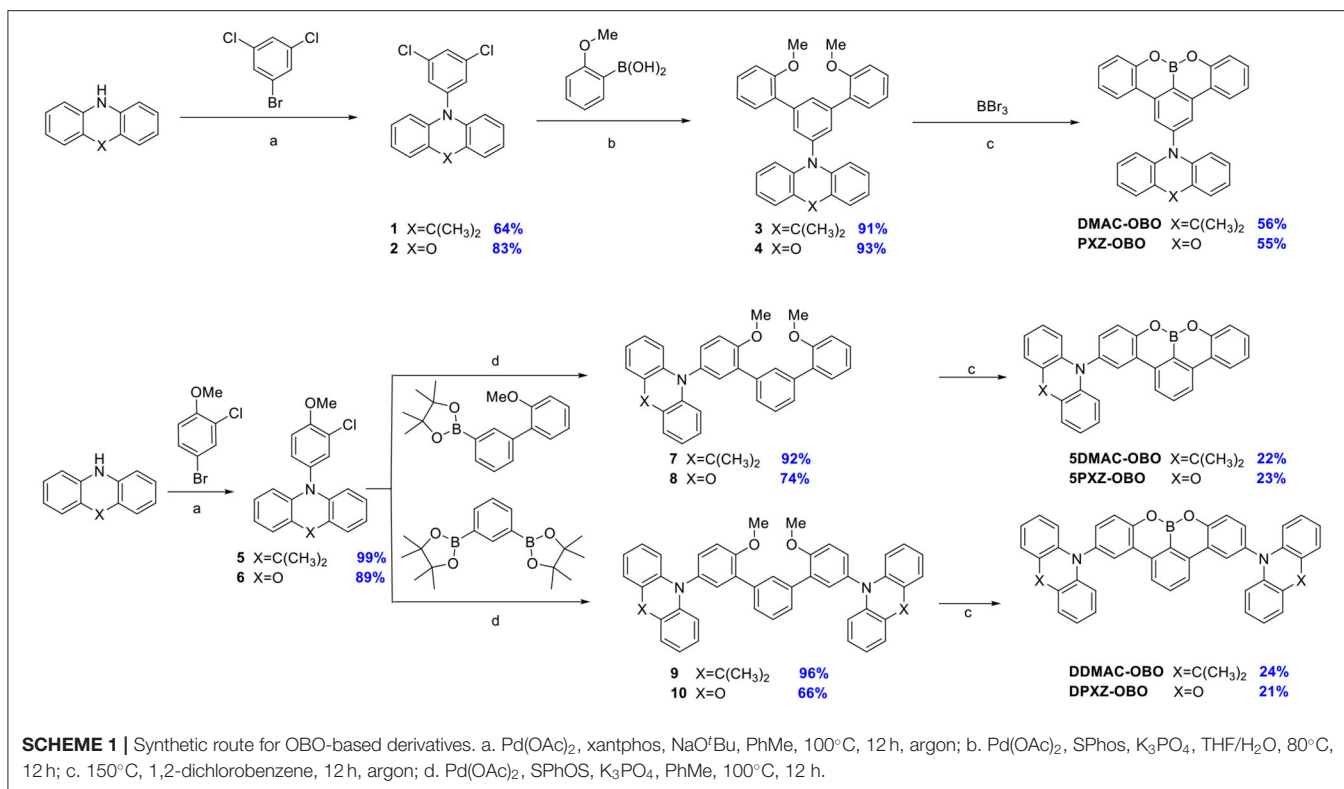
Density functional theory (DFT) calculations were performed to assess the electronic structure of the six emitters using the PBE0 (Adamo and Barone, 1999) functional and the 6–31G(d,p) basis set (Cancès et al., 1997) implemented within Gaussian 09 (Frisch et al., 2009). The ground state geometries of the molecules were optimized in the gas phase starting with the geometry obtained from the single crystal X-ray diffraction analysis. Time-dependent DFT calculations were performed within the Tamm–Dancoff approximation (TDA) on the ground state optimized molecular structures (Hirata and Head-Gordon, 1999). The energies and electron density distributions of the highest occupied and lowest unoccupied molecular orbitals (HOMO/LUMO) and the energies of the S<sub>1</sub> and T<sub>1</sub> states are shown in Figure 3, and the data are summarized in Tables 1, 2, and Supplementary Table 1, and the electron density distributions of other molecular orbitals are summarized in Supplementary Table 2. As indicated in the SI, the HOMO→LUMO transition is the dominant contribution to the S<sub>1</sub> state.

The near orthogonal dihedral angle between the donor and acceptor units in the ground state geometries matched with the single crystal data analysis. The HOMO of the emitters is localized on the donor DMAC or PXZ groups, while the LUMO of the emitters is localized on the electron-withdrawing OBO units. There is minimal spatial overlap between the HOMO and LUMO, which suggests a strong CT character of the excited singlet state and which results in a small calculated  $\Delta E_{ST}$  for



the ground state geometry. The  $S_1$  energies for the DMAC series ranged narrowly from 3.22 to 3.19 eV, showing potential as blue emitters. The use of the stronger PXZ donor results in smaller  $\Delta E_{ST}$  values and lower  $S_1$  energies (2.72–2.83 eV) compared to

the DMAC analogs; the use of two donor units in DDMAC-OBO and DPXZ-OBO also contributed to decreased  $\Delta E_{ST}$ . Even though these values are derived for the vertical transition from the ground state geometry, the calculated  $\Delta E_{ST}$  values for all



emitters are sufficiently small to justify their further evaluation as TADF emitters.

## Electrochemical Properties

The electrochemical properties of the six emitters were examined by cyclic voltammetry (CV) as shown in **Figure 4**, and the results are listed in **Table 1**. The reduction wave was assigned to the electron-accepting OBO unit and found to be irreversible. The LUMO value for DMAC-OBO, 5DMAC-OBO, and DDMAC-OBO were determined to be  $-2.69$ ,  $-2.96$ , and  $-2.93$  V, respectively, from the reduction potentials obtained by CV. For the PXZ analogs PXZ-OBO, 5PXZ-OBO, and DPXZ-OBO, the LUMO values were determined to be  $-2.70$ ,

$-2.82$ , and  $-2.99$  V, respectively. The LUMO of 5DMAC-OBO is lowest among DMAC-based emitters, whereas the most stabilized LUMO in the PXZ family of compounds is DPXZ-OBO. The oxidation wave was found to be reversible in all six emitters, which demonstrates that PXZ and DMAC radical cations are electrochemically stable. The DMAC-based emitters show slightly more anodic oxidation potentials than the corresponding PXZ-based emitters, in line with their relative electron-donating ability.

## Photophysical Properties

The newly synthesized OBO derivatives form two structurally analogous series. While the OBO moiety

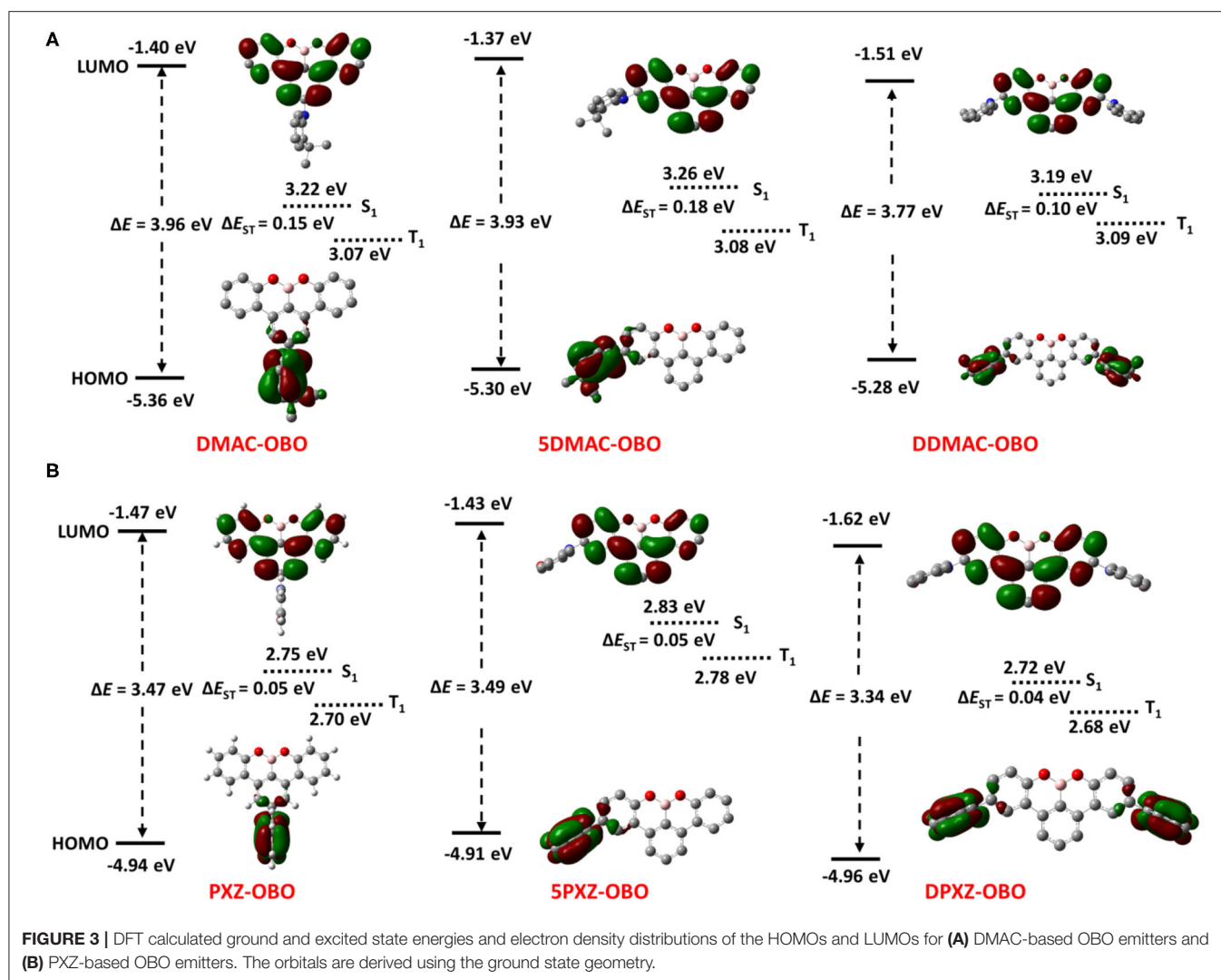


**TABLE 1 |** Summary of electrochemical and DFT/TDA calculated photophysical properties of OBO-based emitters.

Emitters	Experimental			Calculated	
	$E_{pa,1}^{ox}/E_{pc,1}^{red}$ (V)	HOMO/LUMO (eV)	$\Delta E^c$ (eV)	HOMO <sup>d</sup> /LUMO <sup>d</sup> (eV)	$\Delta E^c$ (eV)
DMAC-OBO	0.98/−2.11	−5.78/−2.69	3.09	−5.36/−1.40	3.96
5DMAC-OBO	0.97/−1.84	−5.77/−2.96	2.81	−5.30/−1.37	3.93
DDMAC-OBO	0.97/−1.87	−5.77/−2.93	2.84	−5.28/−1.51	3.77
PXZ-OBO	0.70/−2.10	−5.50/−2.70	2.80	−4.94/−1.47	3.47
5PXZ-OBO	0.75/−1.98	−5.55/−2.82	2.73	−4.91/−1.43	3.48
DPXZ-OBO	0.79/−1.81	−5.59/−2.99	2.60	−4.96/−1.62	3.34

<sup>a</sup>In  $CH_2Cl_2$  and <sup>b</sup>in DMF, with 0.1 M  $[nBu_4N][PF_6]$  as the supporting electrolyte, Pt as the working electrode, Ag/AgCl as the reference electrode and Pt wire as the counter-electrode. Fc/Fc<sup>+</sup> was used as the internal reference and the data reported vs. SCE. The HOMO and LUMO energies were calculated using the relation  $E_{HOMO}/LUMO = -(E_{pa,1}^{ox}/E_{pc,1}^{red} + 4.8)$  eV, where  $E_{pa,1}^{ox}$  and  $E_{pc,1}^{red}$  are anodic and cathodic peak potentials, respectively. <sup>c</sup> $\Delta E = |E_{HOMO} - E_{LUMO}|$ . <sup>d</sup>Determined from the DFT or TDA-DFT calculations.

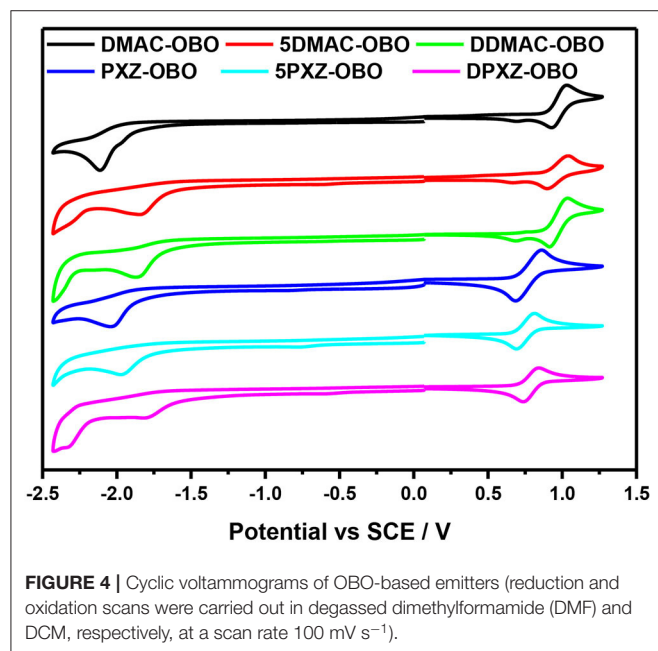
always takes the acceptor role, in the first series, DMAC is used as donor moiety, and PXZ is used as donor for the second series. We address here how

changing the number and position where the donor is attached impacts on the electronic structure of the TADF molecule.



**TABLE 2** |  $S_1$  and  $T_1$  energies determined in 2-MeTHF solution At 77 K and from theoretical calculation.

Compounds	$S_1$ (77 K) (eV)	$S_1^{\text{theor}}$ (eV)	$T_1$ (77 K) (eV)	$T_1^{\text{theor}}$ (eV)	$\Delta E_{\text{ST}}$ (77 K) (eV)	$\Delta E_{\text{ST}}^{\text{theor}}$ (eV)
DMAC-OBO	3.43	3.22	2.69	3.07	0.74	0.15
5DMAC-OBO	3.60	3.26	2.69	3.08	0.91	0.18
DDMAC-OBO	3.51	3.19	2.68	3.09	0.83	0.10
PXZ-OBO	3.34	2.75	2.70	2.70	0.64	0.05
5PXZ-OBO	3.34	2.83	2.70	2.78	0.64	0.05
DPXZ-OBO	3.33	2.72	2.69	2.68	0.64	0.04



### Absorption and Emission in Solutions

The absorption spectra of the emitters in  $\text{CHCl}_3$  are shown in **Figure 5A**. In solution, all the emitters exhibit similar absorption profiles with the absorption peaks between 260 and 340 nm. Taking into account the structureless absorption spectra of the donors, one can assign these maxima to localized  $\pi$ - $\pi^*$  transitions of the acceptor OBO moiety (Numano et al., 2016). In the case of DMAC molecules, the absorption of the donor is masked by absorption of the acceptor and cannot be clearly observed (Rodella et al., 2020). In contrast, for the PXZ compounds, the contribution of the donor is distinguished as the shoulder at 350 nm (Mantsch, 1969). On the semilogarithmic scale, weak broad structureless absorption bands can be seen in the low-energy part of the spectra. These broad bands are ascribed to an intramolecular charge transfer transition that corresponds to transfer of electron from the PXZ or DMAC donor to the OBO acceptor, in agreement with the theoretical calculations. In the case of the PXZ molecules, this band is shifted to longer wavelengths by 25 nm (0.2 eV).

The photoluminescence (PL) spectra are broad and unstructured, an indication of emission from a CT state

(**Figure 5B**). The PL spectra of the DMAC-based emitters in  $\text{CHCl}_3$  show blue-green emission with maxima ( $\lambda_{\text{PL}}$ ) between 448 and 460 nm, whereas for the PXZ-based emitters, a red-shifted emission is observed maxima ranging more narrowly between 497 and 501 nm. The weak bands observed for PXZ-containing molecules can be assigned to emission of the donor (see discussion of **Figure 6**).

Steady-state (SS) emission in 2-methyltetrahydrofuran (2-MeTHF) at 300 and 77 K was investigated to explore the energy of the excited states of the emitters (**Figure 6** and **Table 2**). At 300 K, all molecules demonstrate a broad emission spectrum centered at about 2.6 eV (DMAC-containing compounds) or 2.3 eV (PXZ-containing compounds) that is close to the, respectively, spectrum observed in  $\text{CHCl}_3$ . This band can be assigned to a transition from lowest stabilized CT state. Concomitantly, when exciting the solutions at 300 nm for the DMAC-containing molecules, a second, high-energy band is observed with a  $\lambda_{\text{PL}}$  at 350 nm. For the more symmetric molecules DMAC-OBO and DDMAC-OBO, this band is not structured, while it carries additional pronounced shoulders/peaks for the less symmetric 5DMAC-OBO. The unstructured band fits well in terms of the shape and position to the spectrum of DMAC fluorescence and can therefore be assigned to emission from an LE state on the acridine donor (the emission spectrum of DMAC has been inserted in **Figure 6** for DDMAC-OBO, orange line, for ease of reference). The pronounced features in the 5DMAC-OBO exactly match the energies and linewidth reported from Numato et al. at 3.65, 3.50, 3.35, and 3.20 eV for the vibronic progression of the emission associated with the OBO-acceptor moiety (Numano et al., 2016). Evidently, for the less symmetric 5DMAC-OBO compound, there is LE emission predominantly from the acceptor; in contrast to the LE emission from only the donor for the two more symmetric compounds. For the PXZ compounds, we also observe the characteristic vibronically well-resolved emission from the OBO acceptor for the less symmetric 5PXZ-OBO, whereas it is not present in the more symmetric PXZ-OBO and DPXZ-OBO.

Dual emission is not a common phenomenon in general, as internal conversion (IC) from the higher to the lower excited state usually competes efficiently with radiative decay from the higher state to the ground state, unless there is a large energy gap separating the two emitting state as, e.g., for azulene. However, such dual emission from a CT and an LE state has already previously been observed for donor-acceptor compounds (Acar et al., 2003; Druzhinin et al., 2015). In such

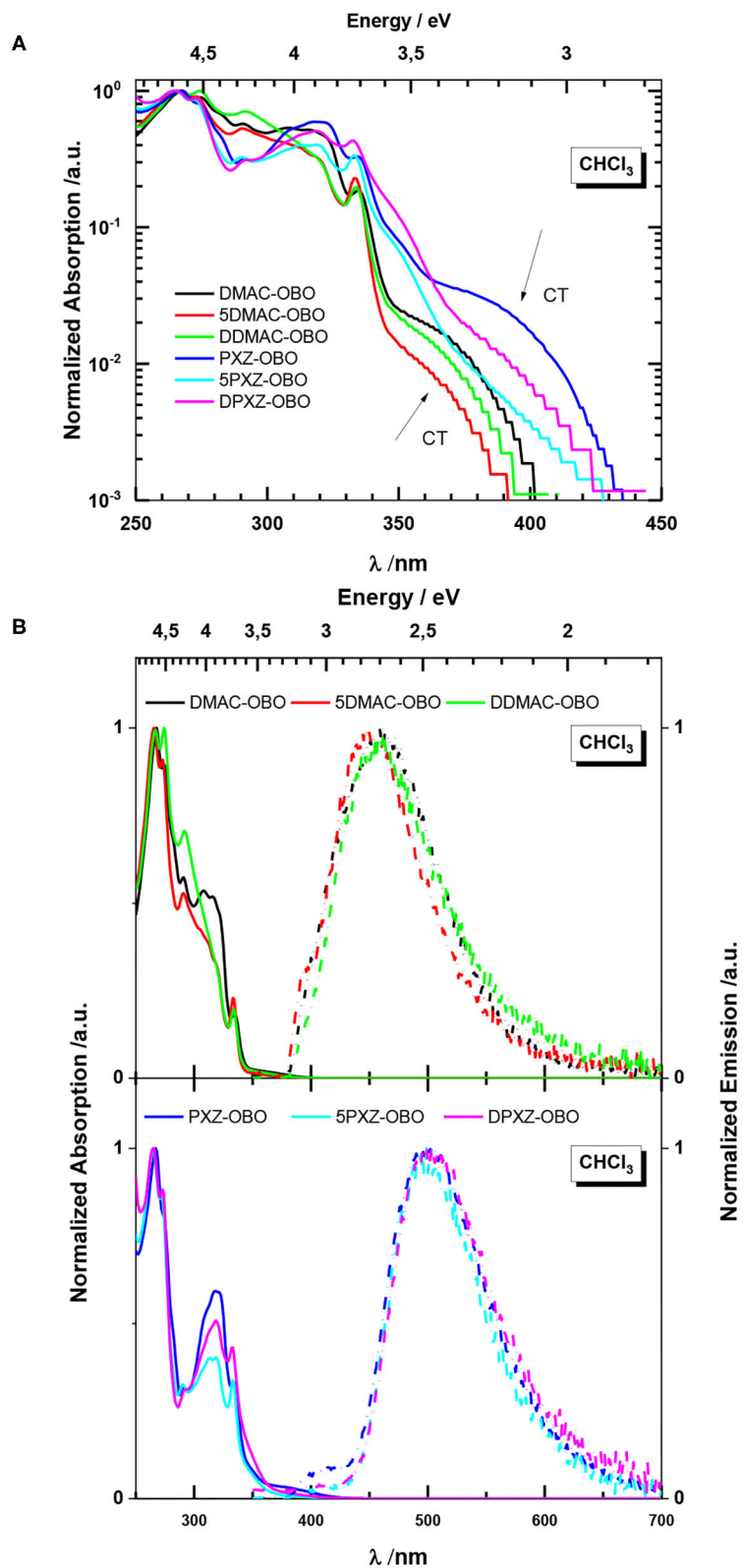


**FIGURE 5 | (A)** Absorption in  $\text{CHCl}_3$  on semilogarithmic scale. **(B)** Absorption (left) and photoluminescence spectra (right) in  $\text{CHCl}_3$ . ( $\lambda_{\text{exc}} = 332 \text{ nm}$ ).

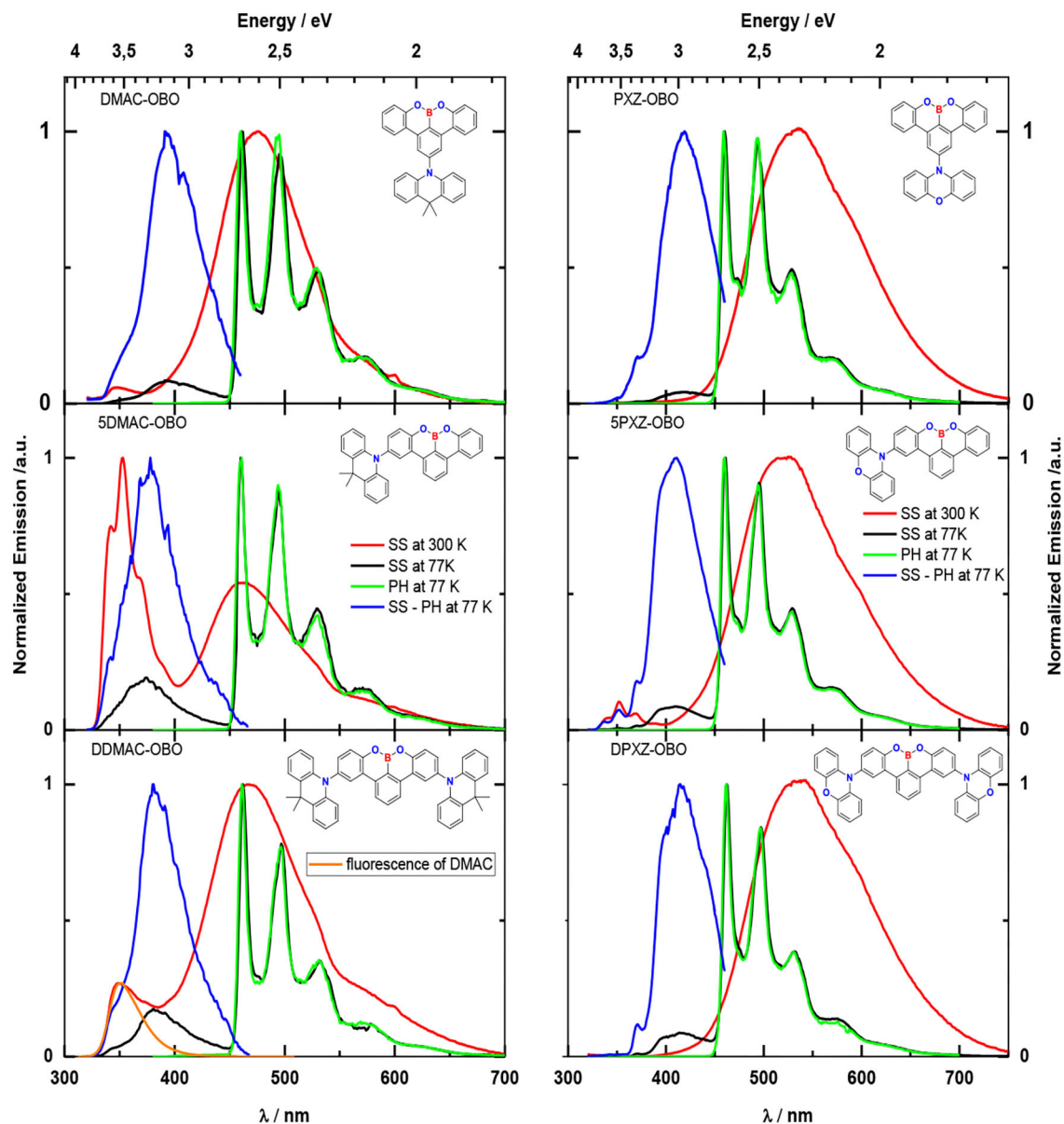


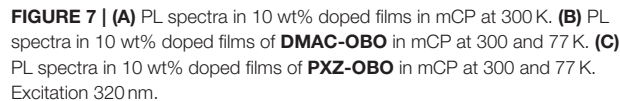
**FIGURE 6** | SS emission in 2-MeTHF at 300 K (red lines), SS emission (black lines), phosphorescence (green lines), fluorescence of OBO-based emitters (blue lines) in 2-MeTHF at 77 K. The fluorescence spectrum was obtained by subtracting the phosphorescence from the SS spectrum and by next normalizing. Excitation was at 300 nm. The concentration was 0.05 mg/mL. The orange line corresponds to DMAC fluorescence at 300 K.

molecules, IC from LE to CT state corresponds to electron transfer between two parts of the molecule. Because of the nearly perpendicular conformation of the donor and acceptor, the initial intramolecular electron transfer can be sufficiently slow so that radiative decay from the LE states may compete with the IC process.

In both series, the intensity of the CT emission relative to the respective LE emission decreases in the order DMAC-OBO (PXZ-OBO), DDMAC-OBO (DPXZ-OBO), and 5DMAC-OBO (5PXZ-OBO). This order reflects the relative strength of the y-component of the molecular transition dipole moment that

would result in a simple picture where the whole density is considered localized on the nitrogen and the electron density on the boron.

The SS PL spectra at 77 K consist of a strong and highly structured phosphorescence and a weak fluorescence emission. The transition in the SS spectra from 300 to 77 K leads to a large shift of the fluorescence of the molecules to higher energy (to 3.2 eV for the DMAC compounds and to 3.0 eV for the PXZ compounds). This is caused by the freezing out of the reorientation of solvent shell molecules, so that reorganization of the emitter after excitation is precluded (Lakowicz, 2006).



Frontiers in Chemistry | www.frontiersin.org

To allow for an analysis of the TADF properties, **Figure 8A** presents the transient decay of the emission of the molecules under investigation in 10 wt% mCP blend films at 300 K.



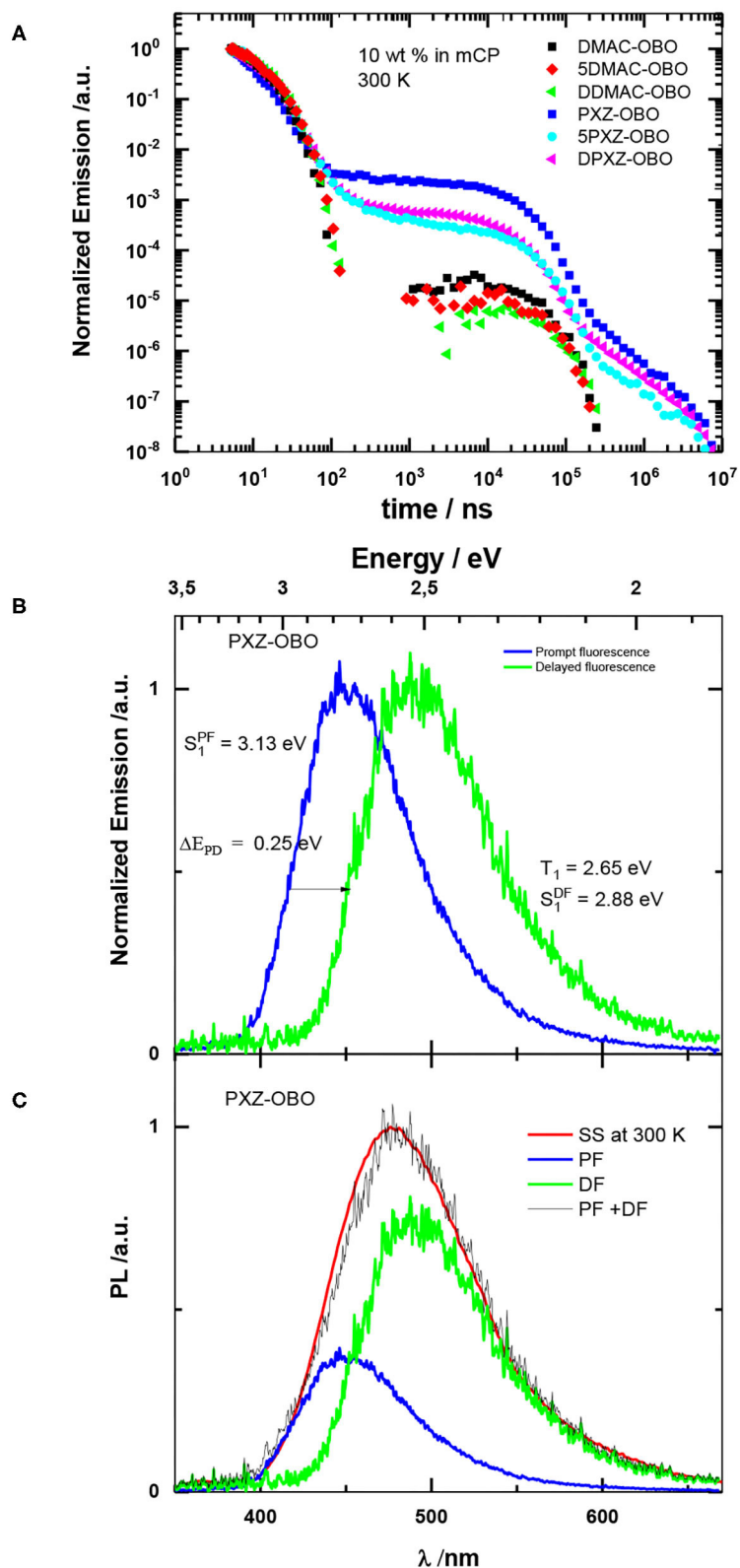


**FIGURE 8 | (A)** Transient data for blend films in mCP at 300 K. **(B)** Spectra of prompt (delay 10 ns, gate 10 ns) and delayed fluorescence (delay 1  $\mu$ s, gate 100 ns) of **PXZ-OBO** in mCP film at 300 K. **(C)** Analysis of the spectrum of total emission of **PXZ-OBO** in mCP film using the spectra of prompt and delayed components from **(A)**.

**TABLE 3** | Photophysical properties of OBO-based emitters.

Compounds	$\lambda_{PL}^a$ (nm)	$\lambda_{PL}^b/\lambda_{PL}^c$ (nm)	FWHM <sup>c</sup> (eV)	CIE(x, y) <sup>c</sup>	PLQY <sup>b</sup> /PLQY <sup>c</sup> (%)	$\tau_p^b$ (ns)	$\tau_d^b$ ( $\mu$ s)	$I_{DF}/I_{PF}^b$
DMAC-OBO	460	429/446	0.56	0.16, 0.13	5/8	8	37	0.07
5DMAC-OBO	448	415/410	0.53	0.17, 0.10	9/8	9	42	0.04
DDMAC-OBO	461	419/420	0.55	0.16, 0.11	8/10	10	57	0.03
PXZ-OBO	500	480/491	0.49	0.21, 0.36	15/46	6	23	4
5PXZ-OBO	497	466/471	0.52	0.18, 0.24	7/19	10	30	0.6
DPXZ-OBO	501	462/481	0.50	0.20, 0.31	9/20	11	22	1

<sup>a</sup>In CHCl<sub>3</sub> at 300 K. <sup>b</sup>In 10 wt% doped films in mCP at 300 K. <sup>c</sup>In 10 wt% doped films in PMMA at 300 K.  $\tau_p$ , prompt lifetime.  $\tau_d$ , delayed lifetime.

Considering the large  $\Delta E_{ST}$  for DMAC-based molecules (Table 2), we do not expect any considerable TADF for these compounds and that is confirmed by the experimental data. For PXZ-based molecules, delayed emission is clearly observed, and its contribution is surprisingly high, with a  $I_{DF}/I_{PF}$  between 0.6 and 4. To explore whether this DF is due to TADF or TTA, we observed its dependence on the intensity of the exciting laser beam. As it is seen from **Supplementary Figure 4**, this dependence demonstrates a lineal character with slope value close to 1 that points out to monomolecular nature of this emission.

An analysis of the time-resolved spectra helps to understand the mechanism of TADF in case of such large singlet-triplet gap. **Figure 8B** shows the spectra of the prompt and delayed fluorescence. The DF spectrum is shifted to lower energy by 0.25 eV relative the PF spectrum; i.e., it results only from the lower energy part of the DOS. Such a broad DOS distribution can result in solid solutions where there are a number of different conformers of donor-acceptor molecules, each associated with different energies of their excited states (Penfold et al., 2018). **Figure 8B** demonstrates clearly that only molecules with the lowest singlet state energy (the low energy tail of the DOS) and lower singlet-triplet gap energy (0.25 eV) contribute in TADF. One can see from **Figure 8C** that the spectrum of the SS emission can be well-fitted by a superposition of the spectra of prompt and delayed fluorescence. It is clear that maximum of the SS spectrum and its intensity is determined by TADF, whereas PF forms high-energy tail of the SS spectrum.

### Luminescence in Blend PMMA Films

Unfortunately, the PLQY values for these six compounds in mCP films are low, ranging from 5 to 15%. Therefore, PMMA as host materials was also investigated to explore the emission and quantum yield of these emitters in a second solid state host material. In 10 wt% doped PMMA films (**Supplementary Figure 5**), the PXZ-based derivatives show sky-blue emission with  $\lambda_{PL}$  ranging from 471 to 491 nm, whereas the emission of the DMAC-based derivatives is deep blue with  $\lambda_{PL}$  ranging from 410 to 446 nm. When the donor is decorated on the central phenyl ring of the OBO unit, the emission of PXZ-OBO is 491 nm, whereas it is 481 nm for 5PXZ-OBO with the donor located at the *para* position to the methoxy group. The corresponding DMAC derivatives demonstrate a similar trend. This trend can be explained by the

mesomeric donation of the donor to the oxygen atoms, thereby strengthening the acceptor. The PLQYs of all three DMAC derivatives remain low, between 8 and 10%. In contrast, the family of PXZ derivatives shows higher PLQYs, from 19 to 46% (Table 3).

## CONCLUSIONS

We report six blue emitters employing an OBO-fused benzo[fg]tetracene core as an acceptor. Experimental studies demonstrate their blue and deep blue emission with  $\lambda_{PL}$  of 415 to 480 nm in mCP films. Although the DMAC derivatives show the negligible delayed emission ( $I_{DF}/I_{PF}$ , 0.03–0.07), the PXZ-based emitters exhibit much higher ratio of delayed emission ( $I_{DF}/I_{PF}$ , 0.6–4) with the PLQYs from 5 to 15%. When doped in PMMA, these fluorescent emitters show higher PLQYs, from 19 to 46%. Current efforts are focused on designing new OBO-based molecules through exploring different donors and novel connectivity strategies between donor and OBO acceptor to access more promising blue TADF emitters for OLEDs.

## DATA AVAILABILITY STATEMENT

The datasets presented in this study can be found in online repositories. The names of the repository/repositories and accession number(s) can be found in the article/**Supplementary Material**. The research data supporting this publication can be accessed at <https://doi.org/10.17630/5acd95b7-73bf-4e5a-abe6-ec23c9120835>.

## AUTHOR CONTRIBUTIONS

ZZ conceived the concept and synthesized and characterized the materials. SK performed the DFT calculations electrochemical measurements. SBa performed the photophysical measurements and, together with AK, wrote the photophysics section. ES, FH, and ZH participated in results discussions. MN did the X-ray analyses. ZZ, SK, and EZ-C wrote the manuscript. SBr, AK, and EZ-C supervised the project. All authors contributed to the article and approved the submitted version.

## FUNDING

This project was supported by the Helmholtz Association Program at the Karlsruhe Institute of Technology. The German Research Foundation (formally Deutsche Forschungsgemeinschaft DFG) in the framework of SFB1176 Cooperative Research Centre Molecular Structuring of Soft Matter (CRC1176, A4, B3, C2, C6) and the cluster 3D Matter Made To Order funded under Germany's Excellence Strategy (3DMM2O EXC-2082/1-390761711) are greatly acknowledged for financial contributions. ZZ acknowledges the financial support from Chinese Scholarship Council (CSC) for his Ph.D. studies. SK acknowledges the financial support from European Union's Horizon 2020 research and innovation programme

under Marie Skłodowska Curie Individual Fellowship (MCIF; Agreement No. 748430-THF-OLED). SBA acknowledges support from the Bayrisches Staatsministerium für Wissenschaft und Kunst (Stmwk) in the framework of the initiative SolTech as well as from the German Science foundation (DFG) (no. 392306670). EZ-C and AK acknowledge support from the European Union's Horizon 2020 research and innovation programme under the ITN TADFlife (GA 812872).

## SUPPLEMENTARY MATERIAL

The Supplementary Material for this article can be found online at: <https://www.frontiersin.org/articles/10.3389/fchem.2020.563411/full#supplementary-material>

## REFERENCES

- Acar, N., Kurzawa, J., Fritz, N., Stockmann, A., Roman, C., Schneider, S., et al. (2003). Phenothiazine-pyrene dyads: photoinduced charge separation and structural relaxation in the CT state. *J. Phys. Chem.* 107, 9530–9541. doi: 10.1021/jp036250u
- Adamo, C., and Barone, V. (1999). Toward reliable density functional methods without adjustable parameters: the PBE0 model. *J. Chem. Phys.* 110, 6158–6170. doi: 10.1063/1.478522
- Albrecht, K., Matsuoka, K., Fujita, K., and Yamamoto, K. (2015). Carbazole dendrimers as solution-processable thermally activated delayed-fluorescence materials. *Angew. Chem. Int. Ed.* 54, 5677–5682. doi: 10.1002/anie.201500203
- Cancès, E., Mennucci, B., and Tomasi, J. (1997). A new integral equation formalism for the polarizable continuum model: Theoretical background and applications to isotropic and anisotropic dielectrics. *J. Chem. Phys.* 107, 3032–3041. doi: 10.1063/1.474659
- Chen, D., Liu, K., Gan, L., Liu, M., Gao, K., Xie, G., et al. (2016). Modulation of exciton generation in organic active planar pn heterojunction: toward low driving voltage and high-efficiency OLEDs employing conventional and thermally activated delayed fluorescent emitters. *Adv. Mater.* 28, 6758–6765. doi: 10.1002/adma.201600612
- Chen, X. L., Jia, J. H., Yu, R., Liao, J. Z., Yang, M. X., and Lu, C. Z. (2017). Combining charge-transfer pathways to achieve unique thermally activated delayed fluorescence emitters for high-performance solution-processed, non-doped blue OLEDs. *Angew. Chem. Int. Ed.* 56, 15006–15009. doi: 10.1002/anie.201709125
- Data, P., Pander, P., Okazaki, M., Takeda, Y., Minakata, S., and Monkman, A. P. (2016). Dibenzooxaphenazine-cored donor-acceptor-donor compounds as green-to-red/NIR thermally activated delayed fluorescence organic light emitters. *Angew. Chem. Int. Ed.* 55, 5739–5744. doi: 10.1002/anie.201600113
- Druzhinin, S. I., Galievsky, V. A., Demeter, A., Kovalenko, S. A., Senyushkina, T., Dubbaka, S. R., et al. (2015). Two-state intramolecular charge transfer (ICT) with 3,5-dimethyl-4-(dimethylamino)benzonitrile (MMD) and its meta-Isomer mMMD. ground state amino twist not essential for ICT. *J. Phys. Chem. A* 119, 11820–11836. doi: 10.1021/acs.jpca.5b09368
- Endo, A., Sato, K., Yoshimura, K., Kai, T., Kawada, A., Miyazaki, H., et al. (2011). Efficient up-conversion of triplet excitons into a singlet state and its application for organic light emitting diodes. *Appl. Phys. Lett.* 98:083302. doi: 10.1063/1.3558906
- Frisch, M. J., Trucks, G. W., Schlegel, H. B., Scuseria, G. E., Robb, M. A., Cheeseman, J. R., et al. (2009). *Gaussian Rev. D.01*. Wallingford, CT: Gaussian, Inc.
- Hirata, S., and Head-Gordon, M. (1999). Time-dependent density functional theory within the Tamm-Dancoff approximation. *Chem. Phys. Lett.* 314, 291–299. doi: 10.1016/S0009-2614(99)01149-5
- Katayama, T., Nakatsuka, S., Hirai, H., Yasuda, N., Kumar, J., Kawai, T., et al. (2016). Two-step synthesis of boron-fused double helicenes. *J. Am. Chem. Soc.* 138, 5210–5213. doi: 10.1021/jacs.6b01674
- Kim, M., Jeon, S. K., Hwang, S. H., and Lee, J. Y. (2015). Stable blue thermally activated delayed fluorescent organic light-emitting diodes with three times longer lifetime than phosphorescent organic light-emitting diodes. *Adv. Mater.* 27, 2515–2520. doi: 10.1002/adma.201500267
- Kitamoto, Y., Namikawa, T., Suzuki, T., Miyata, Y., Kita, H., Sato, T., et al. (2016). Dimesitylarylborane-based luminescent emitters exhibiting highly efficient thermally activated delayed fluorescence for organic light emitting diodes. *Org. Electron.* 34, 208–217. doi: 10.1016/j.orgel.2016.04.030
- Lakowicz, J. R. (2006). *Principles of Fluorescence Spectroscopy*. New York, NY: Springer.
- Lee, I. H., Song, W., and Lee, J. Y. (2016). Aggregation-induced emission type thermally activated delayed fluorescent materials for high efficiency in non-doped organic light-emitting diodes. *Org. Electron.* 29, 22–26. doi: 10.1016/j.orgel.2015.11.019
- Lee, S. Y., Yasuda, T., Park, I. S., and Adachi, C. (2015). X-shaped benzoylbenzophenone derivatives with crossed donors and acceptors for highly efficient thermally activated delayed fluorescence. *Dalton Trans.* 44, 8356–8359. doi: 10.1039/C4DT03608E
- Lee, Y. H., Park, S., Oh, J., Shin, J. W., Jung, J., Yoo, S., et al. (2017). Rigidity-induced delayed fluorescence by ortho donor-appended triarylboron compounds: record-high efficiency in pure blue fluorescent organic light-emitting diodes. *ACS Appl. Mater. Interfaces* 9, 24035–24042. doi: 10.1021/acsami.7b05615
- Lin, T. A., Chatterjee, T., Tsai, W. L., Lee, W. K., Wu, M. J., Jiao, M., et al. (2016). Sky-blue organic light emitting diode with 37% external quantum efficiency using thermally activated delayed fluorescence from spiroacridine-triazine hybrid. *Adv. Mater.* 28, 6976–6983. doi: 10.1002/adma.201601675
- Lu, J.-S., Ko, S.-B., Walters, N. R., Kang, Y., Sauriol, F., and Wang, S. (2013). Formation of azaborines by photoelimination of B,N-heterocyclic compounds. *Angew. Chem. Int. Ed.* 52, 4544–4548. doi: 10.1002/anie.201300873
- Mantsch, H. H. (1969).  $\pi$ -Electronic structure and reactivity of phenoxazine (1), phenothiazine (2), and phenoxthiin (3). *Can. J. Chem.* 47, 3173–3178. doi: 10.1139/v69-523
- Matsuo, K., and Yasuda, T. (2019). Boronate- and borinate-based  $\pi$ -systems for blue thermally activated delayed fluorescence materials. *Chem. Commun.* 55, 2501–2504. doi: 10.1039/C8CC10282A
- Numano, M., Nagami, N., Nakatsuka, S., Katayama, T., Nakajima, K., Tatsumi, S., et al. (2016). Synthesis of boronate-based benzofgtetracene and benzohihexacene via demethylative direct borylation. *Chem. Eur. J.* 22, 11574–11577. doi: 10.1002/chem.201602753
- Numata, M., Yasuda, T., and Adachi, C. (2015). High efficiency pure blue thermally activated delayed fluorescence molecules having 1H-phenoxaborin and acridan units. *Chem. Commun.* 51, 9443–9446. doi: 10.1039/C5CC00307E
- Park, I. S., Lee, S. Y., Adachi, C., and Yasuda, T. (2016). Full-color delayed fluorescence materials based on wedge-shaped phthalonitriles and dicyanopyrazines: systematic design, tunable photophysical properties, and OLED performance. *Adv. Funct. Mater.* 26, 1813–1821. doi: 10.1002/adfm.201505106

- Penfold, T. J., Dias, F. B., and Monkman, A. P. (2018). The theory of thermally activated delayed fluorescence for organic light emitting diodes. *Chem. Commun.* 54, 3926–3935. doi: 10.1039/C7CC09612G
- Rodella, F., Bagnich, S., Duda, E., Meier, T., Kahle, J., Athanasopoulos, S., et al. (2020). High triplet energy host materials for blue TADF OLEDs—a tool box approach. *Front. Chem.* 8:657. doi: 10.3389/fchem.2020.00657
- Suzuki, K., Kubo, S., Shizu, K., Fukushima, T., Wakamiya, A., Murata, Y., et al. (2015). Triarylboron-based fluorescent organic light-emitting diodes with external quantum efficiencies exceeding 20%. *Angew. Chem. Int. Ed.* 54, 15231–15235. doi: 10.1002/anie.201508270
- Takahashi, T., Shizu, K., Yasuda, T., Togashi, K., and Adachi, C. (2014). Donor–acceptor-structured 1,4-diazatriphenylene derivatives exhibiting thermally activated delayed fluorescence: design and synthesis, photophysical properties and OLED characteristics. *Sci. Technol. Adv. Mater.* 15:034202. doi: 10.1088/1468-6996/15/3/034202
- Tao, Y., Yuan, K., Chen, T., Xu, P., Li, H., Chen, R., et al. (2014). Thermally activated delayed fluorescence materials towards the breakthrough of organoelectronics. *Adv. Mater.* 26, 7931–7958. doi: 10.1002/adma.201402532
- Uoyama, H., Goushi, K., Shizu, K., Nomura, H., and Adachi, C. (2012). Highly efficient organic light-emitting diodes from delayed fluorescence. *Nature* 492, 234–238. doi: 10.1038/nature11687
- Wang, K., Liu, W., Zheng, C.-J., Shi, Y.-Z., Liang, K., Zhang, M., et al. (2017). A comparative study of carbazole-based thermally activated delayed fluorescence emitters with different steric hindrance. *J. Mater. Chem. C* 5, 4797–4803. doi: 10.1039/C7TC00681K
- Wang, X. Y., Narita, A., Zhang, W., Feng, X., and Mullen, K. (2016). Synthesis of stable nanographenes with OBO-doped zigzag edges based on tandem demethylation-electrophilic borylation. *J. Am. Chem. Soc.* 138, 9021–9024. doi: 10.1021/jacs.6b04092
- Wong, M. Y., and Zysman-Colman, E. (2017). Purely organic thermally activated delayed fluorescence materials for organic light-emitting diodes. *Adv. Mater.* 29:160544. doi: 10.1002/adma.201605444
- Yang, D.-T., Møllerup, S. K., Peng, J.-B., Wang, X., Li, Q.-S., and Wang, S. (2016). Substituent directed phototransformations of bn-heterocycles: elimination vs isomerization via selective B–C bond cleavage. *J. Am. Chem. Soc.* 138, 11513–11516. doi: 10.1021/jacs.6b07899
- Yang, Z., Mao, Z., Xie, Z., Zhang, Y., Liu, S., Zhao, J., et al. (2017). Recent advances in organic thermally activated delayed fluorescence materials. *Chem. Soc. Rev.* 46, 915–1016. doi: 10.1039/C6CS00368K
- Zhang, Y., Zhang, D., Cai, M., Li, Y., Zhang, D., Qiu, Y., et al. (2016). Towards highly efficient red thermally activated delayed fluorescence materials by the control of intra-molecular  $\pi$ - $\pi$  stacking interactions. *Nanotechnology* 27:094001. doi: 10.1088/0957-4484/27/9/094001

**Conflict of Interest:** The authors declare that the research was conducted in the absence of any commercial or financial relationships that could be construed as a potential conflict of interest.

Copyright © 2020 Zhang, Kumar, Bagnich, Spuling, Hundemer, Nieger, Hassan, Köhler, Zysman-Colman and Bräse. This is an open-access article distributed under the terms of the Creative Commons Attribution License (CC BY). The use, distribution or reproduction in other forums is permitted, provided the original author(s) and the copyright owner(s) are credited and that the original publication in this journal is cited, in accordance with accepted academic practice. No use, distribution or reproduction is permitted which does not comply with these terms.





# Design, Synthesis, and Temperature-Driven Molecular Conformation-Dependent Delayed Fluorescence Characteristics of Dianthrylboron-Based Donor–Acceptor Systems

Umesh Pratap Pandey, Rajendra Prasad Nandi and Pakkirisamy Thilagar\*

Department of Inorganic and Physical Chemistry, Indian Institute of Science, Bangalore, India

## OPEN ACCESS

### Edited by:

Eli Zysman-Colman,  
University of St Andrews,  
United Kingdom

### Reviewed by:

Takuji Hatakeyama,  
Kwansei Gakuin University, Japan  
Denis Svechkarev,  
University of Nebraska Medical  
Center, United States

### \*Correspondence:

Pakkirisamy Thilagar  
thilagar@iisc.ac.in

### Specialty section:

This article was submitted to  
Organic Chemistry,  
a section of the journal  
Frontiers in Chemistry

**Received:** 08 March 2020

**Accepted:** 27 August 2020

**Published:** 09 October 2020

### Citation:

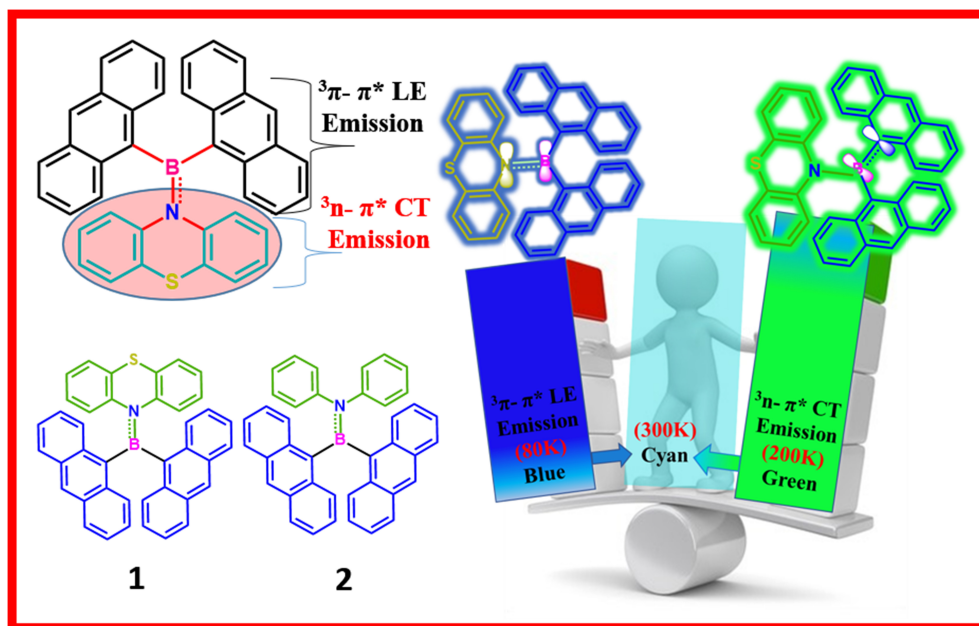
Pandey UP, Nandi RP and Thilagar P  
(2020) Design, Synthesis, and  
Temperature-Driven Molecular  
Conformation-Dependent Delayed  
Fluorescence Characteristics of  
Dianthrylboron-Based  
Donor–Acceptor Systems.  
Front. Chem. 8:541331.  
doi: 10.3389/fchem.2020.541331

We report a simple and novel molecular design strategy to enhance rISC in boron-based donor–acceptor systems to achieve improved delayed fluorescence characteristics. Dianthrylboryl ((An)<sub>2</sub>B)-based aryl aminoboranes **1** (donor: phenothiazine) and **2** (donor: N,N-diphenylamine) were synthesized by a simple one-pot procedure. The energy of the electronic excited states in **1** and **2** were modulated by varying the arylamine donor strength and electronic coupling between D and A moieties. The presence of a large  $\pi$ -system (anthryl moiety) on boron enhances the electronic communication between donor arylamine and acceptor boryl moieties, and hence, both **1** and **2** exhibit delayed fluorescence characteristics in a broad range of temperatures (80–300 K). Single crystal X-ray analysis and temperature-dependent photophysical studies together with theoretical studies were carried out to rationalize the observed intriguing optical signatures of **1** and **2**.

**Keywords:** boron, aminoboron, TADF, anthracene, phenothiazine

## INTRODUCTION

Improving the efficiency of optoelectronic devices by harvesting both triplet and singlet excitons is a contemporary area of research (Uoyama et al., 2012; Obolda et al., 2016; Noda et al., 2018; Liang et al., 2019; Northey et al., 2019). Various approaches such as triplet–triplet annihilation (TTA) (Yang et al., 2017; Pu et al., 2019; Ye et al., 2019), exciton–polaron interaction (EPI) (Kim et al., 2018), and thermally activated delayed fluorescence (TADF) (Uoyama et al., 2012) have been put forward for this application. This is because both TTA and EPI are bimolecular processes and it is very challenging to control these processes in devices. On the other hand, TADF is a temperature-driven unimolecular process and the device physics is less complicated compared to that of TTA and EPI. The temperature-dependent rate of reverse intersystem crossing (rISC) in TADF emitters is given by the Arrhenius equation  $K_{\text{rISC}} = A \exp(-\Delta E_{\text{ST}}/K_{\text{B}}T)$ . In the early stages of the development of TADF emitters, most of the research efforts were devoted to minimizing singlet ( $S_1$ ) and triplet ( $T_1$ ) energy gap ( $\Delta E_{\text{ST}}$ ) and thereby thermally activating rISC to achieve the delayed emission from an excited singlet state (Chiang et al., 2013; Chen et al., 2014; Peng et al., 2015; Cho et al., 2016). In general, the twisted D–A-type molecular architecture is required to minimize  $\Delta E_{\text{ST}}$



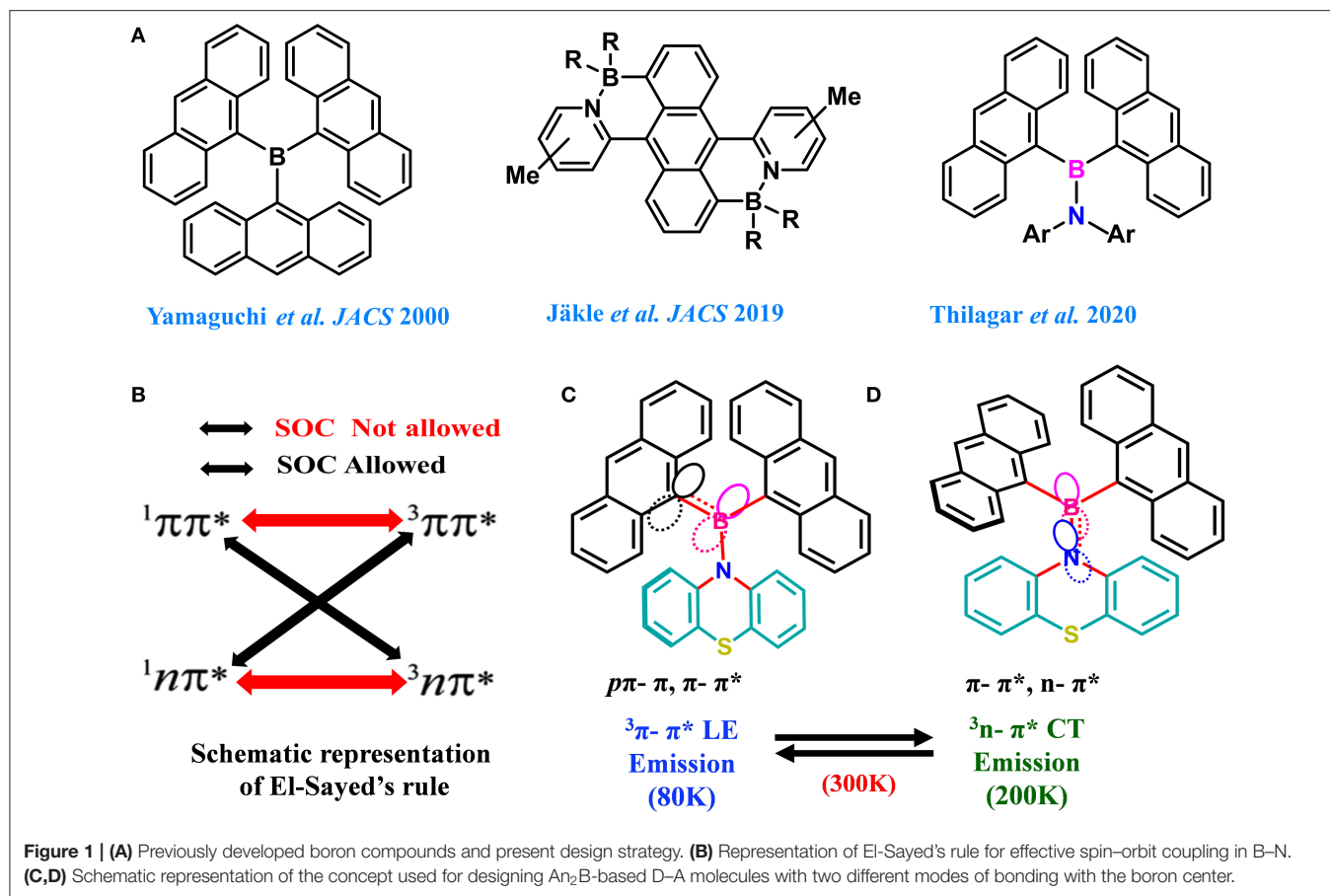
GRAPHICAL ABSTRACT |

by spatially isolating frontier orbitals (HOMO and LUMO) to realize TADF properties (Tao et al., 2014). However, the large twist angle between D and A not only reduces the  $\Delta E_{ST}$  value but also reduces the oscillator strength of the transition (Liang et al., 2019). The temperature dependence and poor oscillator strength collectively affect the luminescence quantum yields of luminophores, which is the most important parameter in terms of real-life applications. Thus, developing an alternative design strategy is of fundamental importance (El-Sayed, 1963, 1968; Tatchen et al., 2007; Bhosale et al., 2015; Hou et al., 2018). Very recently, based on advanced computational studies, Penfold et al. and others showed that the rISC process can occur independent of temperature if there exists a second-order process such as spin-vibronic coupling between the excited singlet and triplet states in a D-A system (Etherington et al., 2016, 2017; Gibson et al., 2016; Gibson and Penfold, 2017; Penfold et al., 2018). Irrespective of the rapid research progress in TADF materials, very few molecules showing rISC independent of temperature are reported (Hudnall et al., 2009; Mao et al., 2012; Neena et al., 2018; Salla et al., 2019).

On the other hand, coordinatively unsaturated and Lewis acid characteristics of tricoordinate boron-based D-A systems have been extensively exploited for developing sensors (Hudnall et al., 2009; Galbraith and James, 2010; Jäkle, 2010), luminescence materials for non-linear optics (Yuan et al., 1990; Del Rey et al., 1998), and OLEDs (Suzuki et al., 2015; Ji et al., 2017; Mellerup and Wang, 2019). Recently, aminoborane-based molecular systems have been successfully utilized in optoelectronics (Hatakeyama et al., 2012; Wang et al., 2013; Hashimoto et al., 2014; Ayhan et al., 2016, 2018; Wang and Pei, 2016; Lien et al., 2017; Liu et al., 2017, 2019; Chen et al., 2018). We have been actively involved in developing luminescent

materials by judiciously altering the molecular conformations of boron-based D-A systems (Sudhakar et al., 2013, 2017; Swamy et al., 2014; Neena and Thilagar, 2016; Kalluvettukuzhy and Thilagar, 2017). Very recently, we exploited BN/CC isosterism and topochemistry for developing highly sought-after deep-blue delayed emissive molecular systems (Neena et al., 2018).

In general, dimesitylboryl moiety is utilized for constructing boron-based D-A materials, because of the kinetic stability imparted by the sterically demanding mesityl group to the Lewis acidic boron center (Doty et al., 1972; Neena and Thilagar, 2016; Ji et al., 2017; Mellerup and Wang, 2019). However, the electronic coupling between boron and the attached unit is partly compromised because of steric crowding. Thus, a potential substituent could be one which maintains a good electronic coupling between the substitutes without sacrificing the overall stability of the compound. Yamaguchi et al. elegantly demonstrated the design, synthesis, and intriguing optical and anion sensing properties of a series tris(9-anthryl)borane (Figure 1A). They found that despite the large dihedral angle between the donor and acceptor units, the Lewis acid boron center had substantial  $\pi$ -conjugation with the anthryl units (Yamaguchi et al., 2000a,b, 2002; Wakamiya et al., 2005). Recently, Jäkle et al. explored the modification of the electronic structure of B-N-fused dipyrindylanthracene and its sensitivity toward oxygen (Figure 1A) (Liu et al., 2017, 2019). Inspired by this result, we envisioned that the attachment of two anthracenyl (An) moieties to the boron center instead of sterically demanding optically innocent protecting groups (like mesityl or super mesityl) should enhance the probability of the electronic interaction between An and the boron center, leading to different optical features (Figure 1). Accordingly, we designed and synthesized di(anthrynyl)boryl "An<sub>2</sub>B-" based D-A systems



**1** and **2** comprising  $An_2B$ - as acceptor and donors phenothiazine and *N,N*-diphenylamine respectively, considering the following points. An attachment of two different electron donors such as “An” ( $\pi$ -electrons) and arylamines (nitrogen lone pair) to the electron deficient boron can be seen; consequently, different types of excited states with a distinct charge transfer character should be present. Further, the co-occurrence of excited states with different symmetries ( $\pi-\pi^*$  and  $n-\pi^*$ ) should facilitate effective spin-orbit coupling and enhance ISC and rISC processes (El-Sayed, 1963). The compact molecular structures of **1** and **2** should delicately balance the electronic coupling between the donor and acceptors to minimize  $\Delta E_{ST}$ ; at the same time, the synergism in bonding (boron as a sigma donor and  $\pi$  acceptor and vice versa for C/N) between boron and the  $\pi$ /N moieties could make a radiative transition from the CT state efficient. Our anticipation was realized with **1** and **2** exhibiting dual TADF features with both LE and CT characterized over a broad range of temperatures from 80 to 300 K; the results are reported in this article.

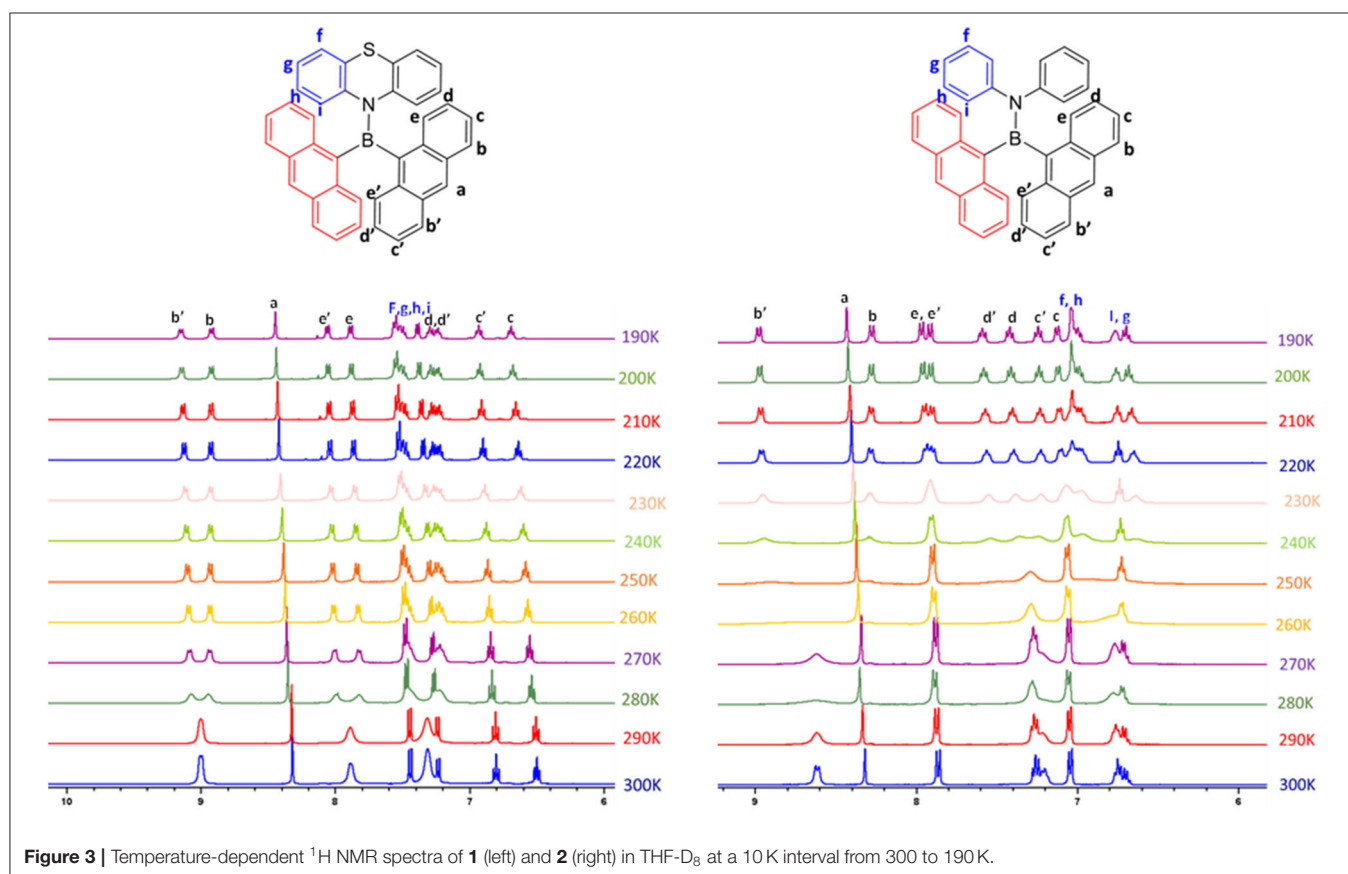
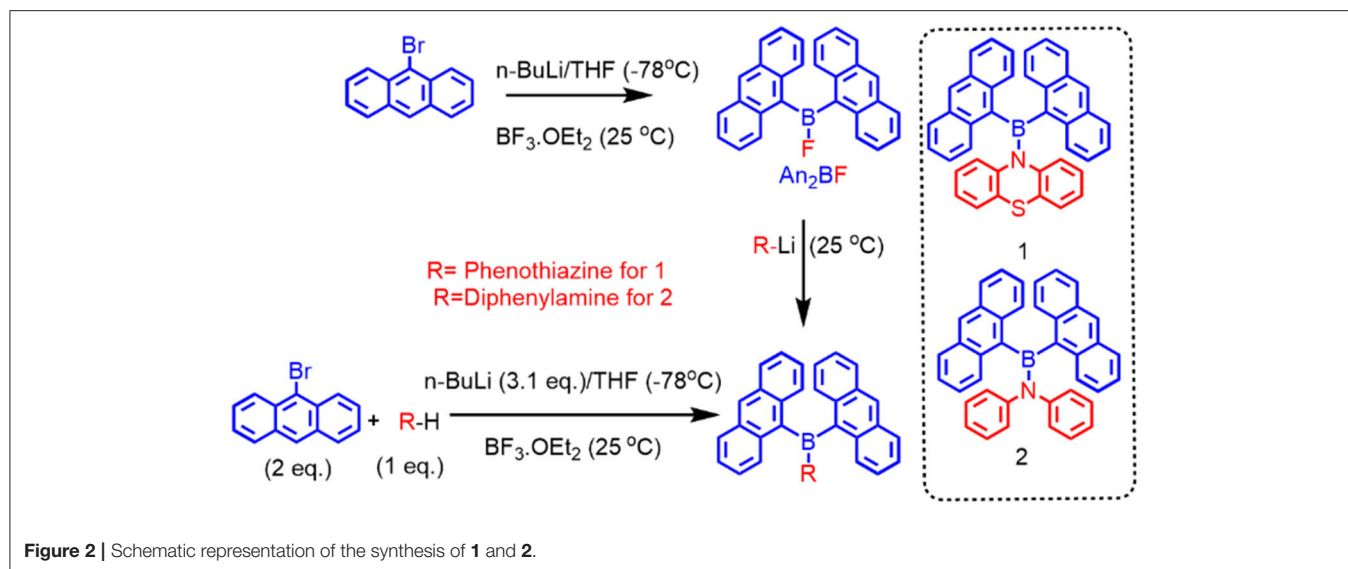
## RESULTS AND DISCUSSION

### Synthesis and Characterization

Precursor compound di(anthryl)boronfluoride ( $An_2BF$ ) was prepared by lithiation of 9-bromoanthracene followed by

addition of 0.5 eq.  $BF_3 \cdot OEt_2$ . Compounds **1** and **2** were synthesized by following the procedures reported by Thilagar *et al.* (Sudhakar *et al.*, 2013). Firstly, lithiation of arylamine (phenothiazine for **1** and diphenylamine for **2**) with 1 eq. of *n*-BuLi at  $-78^\circ C$  generated an N-centered anion, which was subsequently trapped with freshly prepared  $An_2BF$  (Pandey and Thilagar, 2020) to give **1** or **2**. Alternatively, **1** and **2** can be prepared also by one-pot synthesis as depicted in **Figure 2** (see **Supplementary Material** file for a detailed procedure). These compounds are characterized by NMR ( $^1H$ ,  $^{13}C$ ), HRMS (detailed NMR and HRMS data are given in **Supplementary Figures 1–6**) and single crystal x-ray diffraction analysis.

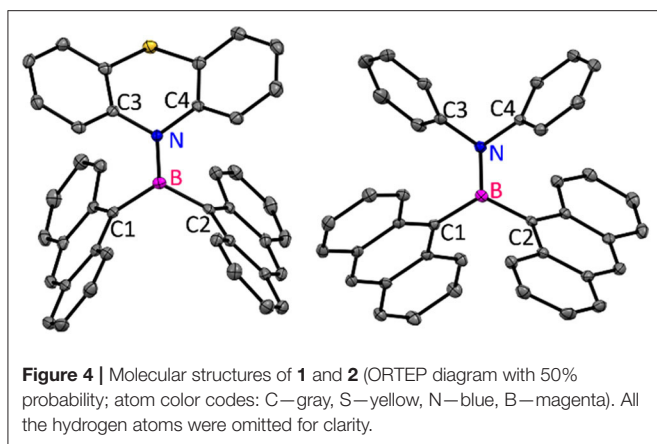
In the case of compound **1**, out of eight  $^1H$  NMR peaks, three are broad whereas in the case of **2**, out of six peaks three are broad. Broad and undistinguishable peaks in the  $^1H$  NMR spectrum of compounds **1** and **2** reveal the presence of structural flexibility. With a view to understanding the temperature-dependent structural dynamics, the  $^1H$  NMR spectra of **1** and **2** were recorded at various temperatures (in THF- $D_8$  solution, **Figure 3**) varying from 300 to 190 K. In Compound **1**, upon gradual cooling from 300 to 280 K, the broad signal at  $\sim 7.8$  and 9.0 ppm breaks into two distinct peaks and signals from  $\sim 7.2$  to 7.4 ppm get fused, which reappears as two sets of broad signals at 260 K. However, on further lowering the temperature by



220 K, signals from  $\sim 7.2$  to  $7.4$  ppm split into three set of peaks; these spectral features remain unchanged up to 190 K. Similarly, in the case of **2**, upon gradual cooling from 300 to 270 K, the broad signal at  $\sim 9.0$  ppm disappears, whereas the signal at  $\sim 6.5$ – $7.5$  ppm became broad. Upon lowering the temperature further from 270 to 250 K, a new set of signals comprising ten

peaks reappear and achieve a clear and illustrious peak at 220 K. These spectral features remain constant up to 190 K. The free energy of activation ( $\Delta G^\ddagger$ ) for the structural reorganization was calculated using the Gutowsky–Holm equation [ $\Delta G^\ddagger = 0.00457 T_c (9.97 + \log (T_c/\Delta\delta))$ ] (Mao et al., 2012), where  $\Delta\delta$  = difference between the two peaks at low temperature  $T_c$  = coalescence





temperature (280 and 250 K for **1** and **2** respectively). The activation–rotation energy (structural reorganization) of **1** and **2** was found to be 16.9 and 14.3 Kcal/mol, respectively. The lower  $\Delta G^\ddagger$  of **2** suggests more structure flexibility than that of **1**. These results clearly indicate that at room temperature these molecules are in dynamic molecular motions. Thus, the electronic interactions between boron and the different functional moieties (anthracene and amine donor) were expected to show temperature-dependent optical features. As anticipated, both the compounds show temperature-dependent optical features, which are summarized *vide infra*. Molecular structures of these compounds were confirmed by single crystal x-ray diffraction studies (crystal data and refinement details are summarized in **Supplementary Figures 7, 8**, **Supplementary Table 1**). Compounds **1** and **2** are stable under ambient conditions toward both air and moisture.

## Molecular Structure

Compound **1** crystallized in the monoclinic crystal lattice with the  $P2_1/n$  space group, whereas **2** acquired a triclinic crystal lattice and  $P-1$  space group (**Figure 4**). In **1** and **2**, both nitrogen and boron centers adopt a trigonal planar geometry with the sum of bond angles being  $360^\circ$ . The B–N bond length [**1** and **2** (1.414 Å)] and dihedral angles ( $4.40^\circ$  for **1**,  $16.68^\circ$  for **2**) between the borylanthracene (C1B1C2) plane and amine NC2 plane (C3N1C4) observed in **1** and **2** are shorter than the values observed for the mesityl analog (B–N; 1.430 Å, dihedral angle  $23.51^\circ$ ) in literatures (Kalluvettukuzhy and Thilagar, 2017). Such a small dihedral angle and shorter B–N bond affirm the presence of the  $\pi$ -bonding interaction between the vacant p-orbital of boron and the lone pair electrons of the nitrogen atom of donor amine moieties (Kalluvettukuzhy and Thilagar, 2017). Based on these observations, one can tentatively conclude that the electronic coupling between donor bisarylamine and acceptor  $An_2B-$  is stronger, and this interaction is expected to influence the luminescence properties of **1** and **2**. In the solid state, both the compounds show an intermolecular slipped  $\pi$ - $\pi$  (3.371 Å in **1** and 3.344 Å for **2**) interaction with a large slip angle ( $58.25^\circ$  in **1** and  $60.09^\circ$  for **2**) and CH– $\pi$  interactions (2.795 Å for **1** and 2.880 Å for **2**) between

anthracene units of neighboring molecules, augmenting to hold these two-neighboring anthracenes in orthogonal conformations, which significantly prevents face-to-face stacking (detailed supramolecular interactions are given in **Supplementary Figures 7, 8**).

## Optical Properties

In the molecularly dispersed state, both **1** and **2** show similar absorption features with distinct vibrational bands in the range 350–410 nm (**Figure 5A**, **Table 1**). However, the absorption bands are 50 nm red shifted compared to the spectra observed for simple anthracene. In addition to the structured absorption band, **2** showed a distinct structureless band at  $\sim 475$  nm, which could be a charge transfer band. In contrast, **1** showed a very weak tailing on the red end of the absorption band ( $\sim 425$  nm). The absorption spectra of both **1** and **2** are sensitive to solvent polarity (**Supplementary Figure 9**). These results clearly indicate that in **1**, the electronic coupling between phenothiazine donor and  $An_2B-$  is negligible in the ground state because of the restricted rotation around the B–N bond as a result of cyclic and rigid phenothiazine structures. However, such restrictions around B–N rotation are lifted in **2** because of a structurally flexible diphenylamine (DPA) moiety, leading to a better electronic coupling between  $An_2B-$  and DPA moieties. To get an insight into the electronic transition, DFT and TD-DFT calculations were performed (*vide supra*). As depicted in **Figure 8**, **Supplementary Figure 18**, for **1**, the highest occupied molecular orbital (HOMO) is localized on one of the two anthracene moieties with comparatively less contribution from phenothiazine and the second anthracene moiety. In contrast, the lowest unoccupied molecular orbital (LUMO) is localized on one of the two anthracene moieties with significant contribution from the p(B) orbital and no contribution from phenothiazine and the second anthracene unit. In contrast, in **2** both the anthracene moieties and the diphenyl unit contribute to HOMO and LUMO (contribution from the p(B) orbital). The simulated UV-visible spectra of both the compounds are shown in **Figures 5C,D**, and the most probable transitions are listed in **Supplementary Tables 7, 8**. A considerably larger overlap between the frontier orbitals of **2** as compared to **1** directly corroborates with the experimentally observed intense UV-vis band for the former compared to the latter. The analysis of most probable transitions in these compounds indicates the lower energy transition HOMO  $\rightarrow$  LUMO in both the compounds, the nature of CT with very low oscillator strength as compared to the higher energy transitions having an LE character and larger oscillator strength (**Supplementary Tables 7, 8**). These computational results support the above conclusions well. It has been well-established that electronically weakly coupled D–A systems tend to show interesting properties such as TADF (Dance et al., 2008; Tao et al., 2014). Thus, from the above results, **1** is expected show better TADF characteristics than **2**.

At ambient conditions, dilute solutions of **1** show a structured LE emission at  $\sim 430$  nm with a CT band at  $\sim 485$  nm (**Figure 5B**). In contrast, compound **2** showed a structureless dual-emission pattern with peak maxima at  $\sim 430$  and 510 nm, respectively. Because of possible excited-state structural

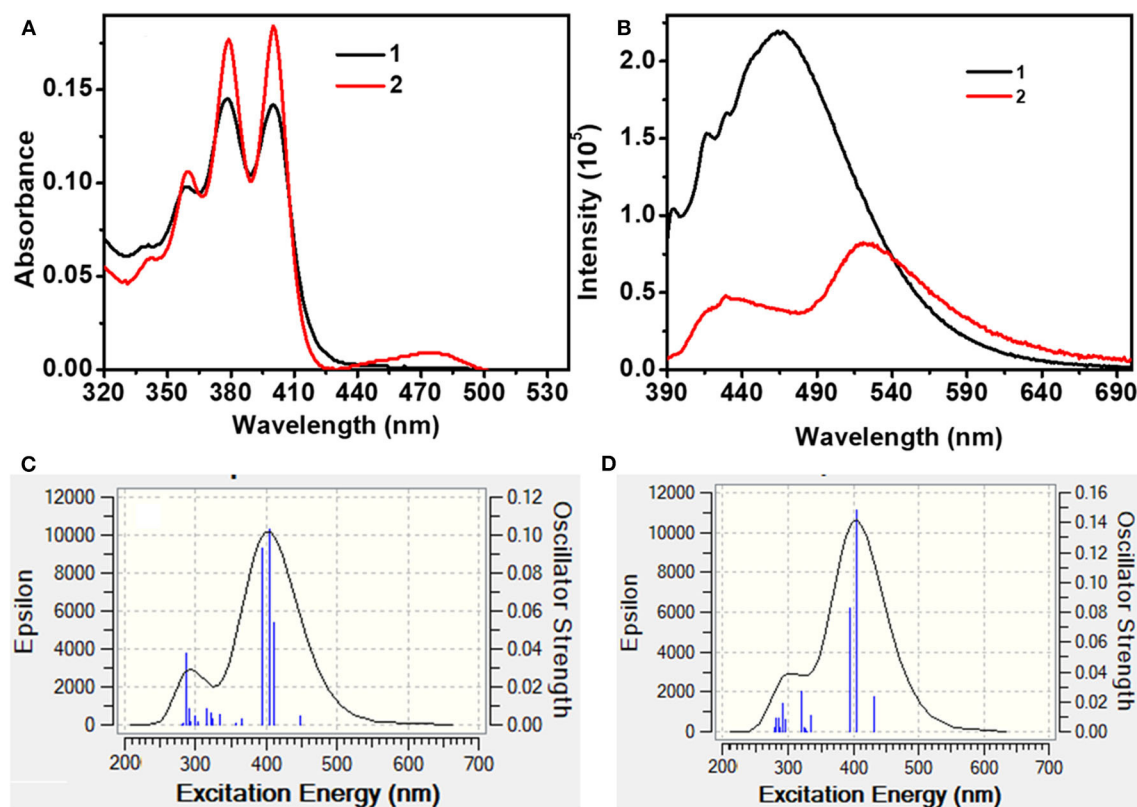


**Figure 5 | (A)** UV-Vis and **(B)** photoluminescence spectra of **1** and **2** in toluene (Conc.  $10^{-5}$  M;  $\lambda_{\text{ex}} = 380$  nm). **(C)** and **(D)** are simulated (TD-DFT) UV-Vis spectra of **1** and **2**, respectively.

**TABLE 1 |** Important optical parameters of **1** and **2**.

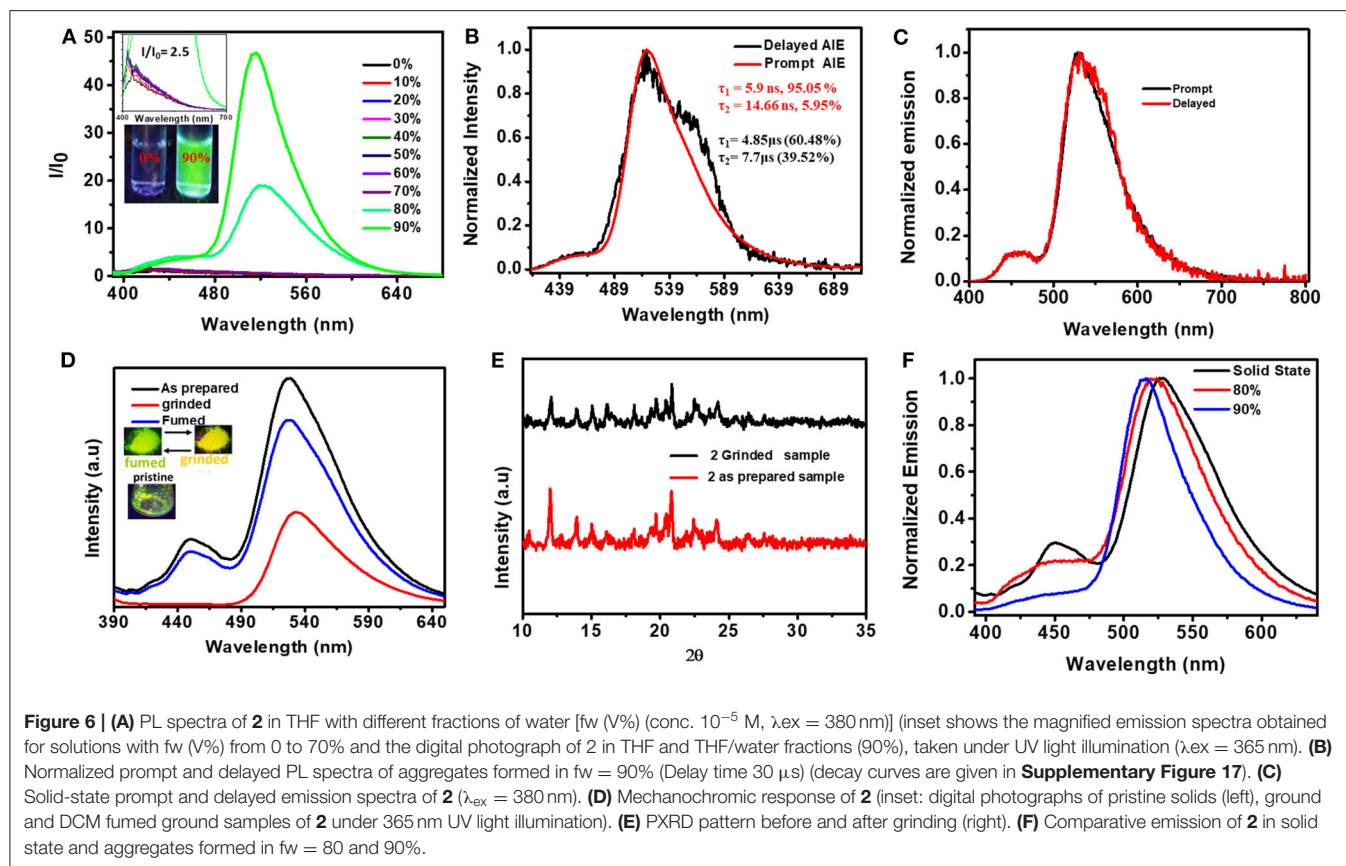
Important parameters	1	2
$\lambda_{\text{max}}$ , Absorption (in toluene)	376 nm	376 nm
$\lambda_{\text{max}}$ , Emission (in toluene)	460 nm	530 nm
Quantum yield ( $\Phi$ , in toluene) <sup>#</sup>	0.19	0.12
Average lifetime ( $\tau$ , ns, in toluene)	6.37	6.67
$k_r$ (in toluene) ( $\times 10^6$ s <sup>-1</sup> )	30	18
$k_{\text{nr}}$ (in toluene) ( $\times 10^6$ s <sup>-1</sup> )	127	132
Absolute quantum yield ( $\Phi$ , solid)	0.17	0.42
Average lifetime ( $\tau$ , ns, solid)	5.15	5.92
$k_r$ (solid) ( $\times 10^6$ s <sup>-1</sup> )	33	71
$k_{\text{nr}}$ (solid) ( $\times 10^6$ s <sup>-1</sup> )	161	98

<sup>#</sup>Relative to anthracene.

reorganization, **2** showed a structureless LE band and a red-shifted CT band compared to **1**. The PL intensity of both the compounds progressively decreased upon increasing the solvent polarity from hexane to acetonitrile (**Supplementary Figure 10**). In the case of **1**, in polar acetonitrile the lower-energy CT band completely disappeared; however, residual emission was observed in the higher-energy region. In contrast, under similar conditions, both the emission peaks for **2** vanished. Time-resolved emission studies on **1** and **2** in solvents with different

dielectrics showed biexponential decay with short (LE) and longer (CT) lifetime components in the nanosecond range (**Supplementary Table 3**). The excited-state lifetime steadily decreased upon increasing the solvent polarity from hexane to methanol. These observations directly corroborate with the weaker emission observed for these compounds in polar solvents. The PL quantum yield of **1** is higher than that of **2**. Furthermore, the calculated non-radiative decay constant ( $k_{\text{nr}}$ ) for **2** ( $132 \times 10^6$  s<sup>-1</sup>) is larger than the  $k_{\text{nr}}$  value obtained for **1** ( $127 \times 10^6$  s<sup>-1</sup>), and these values are consistent with the observed PL quantum yield (**Table 1**).

To understand the role of molecular flexibility in controlling the PL characteristics of these compounds, aggregation-dependent emission studies were carried out in the THF-H<sub>2</sub>O mixture (**Figures 6A,B**, **Supplementary Table 4**) (Luo et al., 2001; An et al., 2002). Compound **1** did not show aggregation-dependent emission. However, compound **2** showed 26-fold stronger luminescence in the aggregated state (in 90% water fraction) compared to its molecularly dispersed solutions. The lifetime of **2** in the aggregated state (in  $f_w = 90\%$ ) ( $\lambda_{430}$ ,  $\tau_{\text{av}} = 5.9$  ns,  $\lambda_{520}$ ,  $\tau_{\text{av}} = 14.44$  ns) increased compared to its dilute THF solutions ( $\lambda_{520}$ ,  $\tau_1 = 0.87$  ns,  $\tau_2 = 6.90$  ns). Interestingly, the AIE spectral features of **2** were comparable with solid-state emission (**Figure 6F**). These results clearly indicate that the molecular flexibility indeed plays a role in

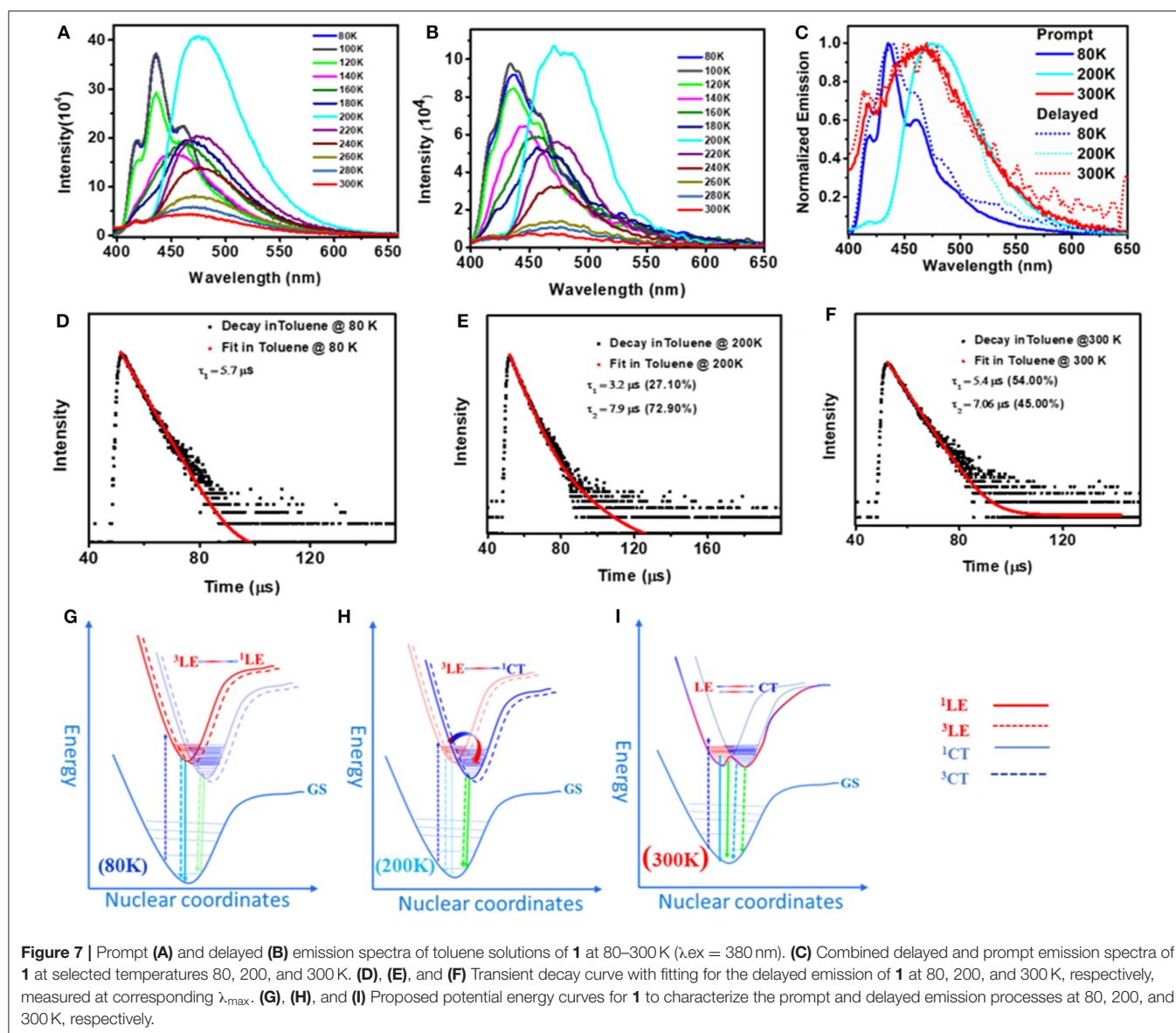


controlling the PL characteristics of **2**. Furthermore, flexible D–A systems exhibit a mechanochromic property (Okazaki et al., 2017). When the dual emissive (greenish yellow color, 455 and 530 nm) solid of **2** was subjected to shearing forces, it showed yellow emission with a single peak at  $\sim 540$  nm (**Figures 6D,E**). Upon exposing the yellow emissive ground powder to organic solvent vapors (such as hexane/ $\text{CHCl}_3$ /DCM) for 3–5 min, the dual emission characteristics were restored. This process of luminescence color switching could be repeated many times and was reversible.

The prompt and delayed spectra of solids of **1** and **2** were recorded at both 300 and 80 K (**Figure 6C**, **Supplementary Figures 13, 15**). At ambient conditions, solids of **1** showed a single PL peak with a maximum at  $\sim 530$  nm. This band is close to the CT emission band observed in the solution state. At 80 K, **1** showed DF characteristics similar to that observed in 300 K; in addition, it also showed a weak phosphorescence peak at  $\sim 590$  nm. Interestingly, at both 300 and 80 K, the solid sample of **2** showed dual DF characteristics similar to its solution-state spectra. Further, compound **2** showed, in addition to DF peaks, a weak phosphorescence peak. The intensity of the phosphorescence peak at 80 K is stronger than that observed at 300 K. The  $\Delta E_{\text{ST}}$  values for **1** (0.15 eV) and **2** (0.06) were calculated using both fluorescence and phosphorescence peaks, and the values are in the range observed for other TADF emitters reported elsewhere (Hosokai et al., 2017).

Apart from fascinating AIE and solid-state emission properties like mechanochromism and DF, solution-state emission at variable temperature was found to be more intriguing (**Figure 7**). In general, rISC is a temperature-driven process, so DF is more prominent at higher temperatures, but here we observed DF at as low as 80 K, which can also be tuned by changing the temperature. At 300 K, the prompt and delayed emission spectra of both **1** and **2** were found to overlap gently, confirming the presence of delayed fluorescence (DF). The excited-state lifetime analysis likewise indicates the formation of simultaneous two emitting species with fast [**1**;  $\tau_1 = 1.51$  (29.59%) and  $\tau_2 = 8.41$  ns (70.41%); **2**;  $\tau_1 = 1.51$  (12.59%) and  $\tau_2 = 7.41$  ns (87.41%)] and slow [**1**;  $\tau_1 = 5.4$  (54%),  $\tau_2 = 7.06$  (45%); **2**;  $\tau_1 = 5.81$  (95.50%) and  $\tau_2 = 6.12$   $\mu$ s (4.50%)] components (**Supplementary Table 6**). It was also observed that the PL intensities of **1** and **2** were strongly quenched by oxygen indicating the involvement of a triplet excited state in the emission process (**Supplementary Figure 11**). To check the effect of temperature on DF characteristics of **1** and **2**, the prompt and delayed spectra of these two compounds were recorded at variable temperatures in the range 80–300 K at 20 K temperature intervals. Interestingly, irrespective of the temperature, a smooth overlap of prompt and delayed spectra of **1** and **2** was observed. However, the spectral shape and position of the peak maxima for **1** and **2** were highly sensitive to temperature at which the measurements were made. At 80 K





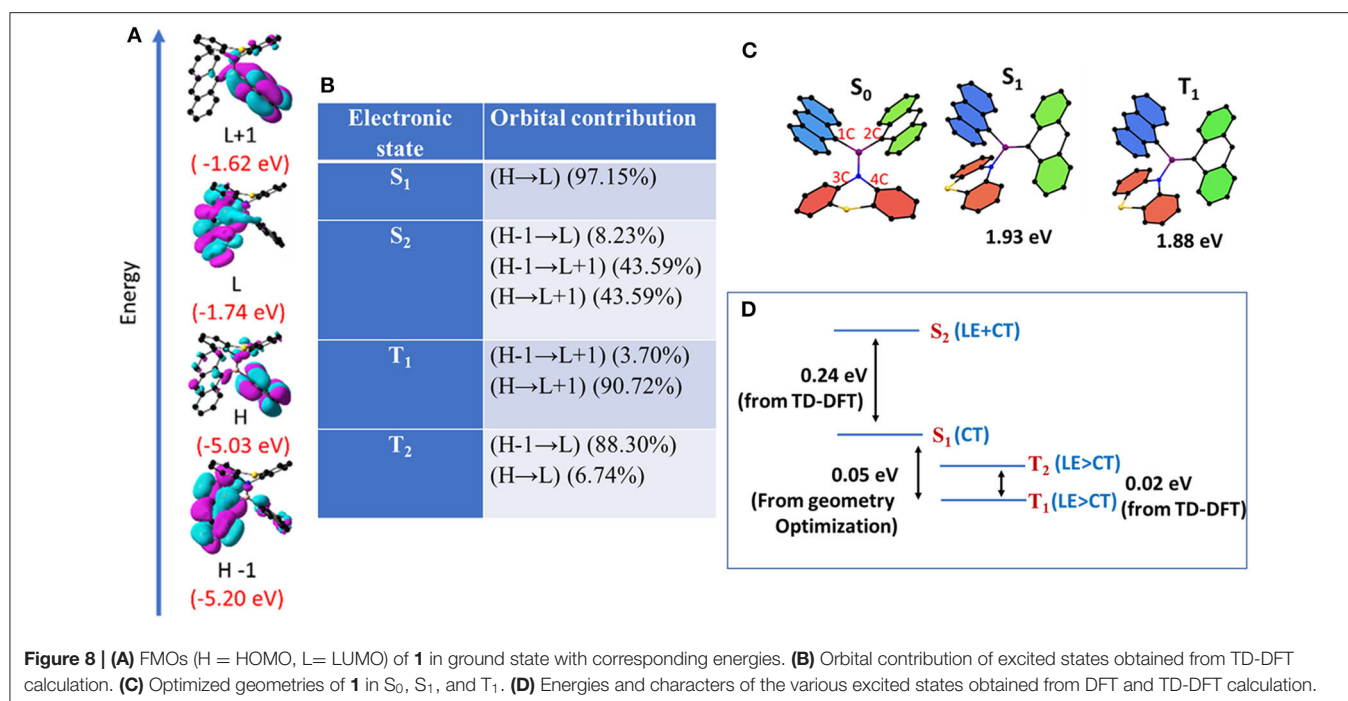
(frozen toluene solutions), **1** and **2** showed a structured LE emission (both prompt and delayed) band and CT band at  $\sim 485$  nm. When the temperature was raised from 80 to 200 K, the intensity of the LE emission decreased and the intensity of CT band at  $\sim 475$  nm progressively increased and became saturated at 200 K (unfrozen toluene).

Further increase in solution temperature steadily decreased the intensity of the new band. These spectral changes ceased at 300 K, where the intensity of both the emission bands became virtually equal (Figures 7A,B). Now the pressing question which needs answer is, why do these compounds show different emission patterns at different temperatures? At 80 K, frozen toluene provides a very rigid matrix; as a result, structural reorganization is minimized and LE emission dominates. At 200 K, just above the melting temperature of toluene (178 K), the loss of matrix rigidity provides a fluidic environment for

structural reorganization, leading to a molecular conformation where the CT emission dominates. At 300 K, the solvent environment is more fluidic than at 200 K; both the species are equally populated and show dual emission with equal intensity. Compound **2** shows similar but less systematic temperature-dependent spectral changes (Supplementary Figure 12).

Time-resolved excited-state decay kinetics was performed on both compounds at different temperatures. At all temperatures, both the compounds show biexponential decay with slow (microsecond) and fast (nanosecond) components (Supplementary Tables 5, 6). Further, the change in lifetime and the amplitude of the corresponding peaks directly corroborate with the change in intensity of the PL peaks observed at different temperatures (Figure 7, Supplementary Tables 5, 6). Based on steady-state and temperature-dependent time-resolved excited-state decay studies, the structured emission peak at





~435 nm is ascribed to LE emission and the slower-decaying peak is assigned to CT emission. To the best of our knowledge, simultaneous DF emission from both <sup>3</sup>LE and <sup>3</sup>CT was not reported in literature.

## Theoretical Studies

With a view to understanding the optical features and electronic structure of **1** and **2**, both DFT and TD-DFT studies were carried out (Figure 8). The ground (S<sub>0</sub>) and excited states (S<sub>1</sub>, S<sub>2</sub>, and T<sub>1</sub>) geometries of **1** and **2** were also optimized. The excited state (S<sub>1</sub>) dipole moments are larger than the corresponding ground state in both **1** and **2**. Based on steady state, time-resolved experiments, together with computational studies, one can draw the following conclusions. Both the compounds are dual emissive; the higher energy bands may be ascribed to LE ( $\pi \rightarrow \pi^*$  centered on anthracene moieties) and the lower-energy transitions ascribed to CT emissions [ $\pi(\text{anthracene}) \rightarrow p(\text{B})^*$ ,  $N \rightarrow p(\text{B})^*$ , and  $\pi(\text{anthracene}) \rightarrow \pi(\text{anthracene})^*$ ]. Furthermore, the excited state dipole moment of **2** is much larger than that calculated for **1**. Compound **2** with flexible donor moiety undergoes molecular conformational changes required to stabilize the CT state. These conformational changes lead to the mixing of both LE and CT states to form a hybridized state (Li et al., 2014). However, such a conformational change is restricted in **1** because of molecular rigidity. Thus, the higher-energy emission peak in **1** is more of LE character and is less sensitive to solvent polarity than the peak observed for compound **2**, for which both the peaks display largely CT characteristics.

The excited-state geometries of **1** and **2** were optimized in S<sub>1</sub> and T<sub>1</sub> states using time-dependent density functional theory (TD-DFT). Optimization of S<sub>2</sub> and T<sub>2</sub> states did not converge as the calculations were computationally expensive. Energies and

characters of S<sub>2</sub> and T<sub>2</sub> states were analyzed using the data from the vertical transitions (Noda et al., 2019). For compound **1**, in S<sub>0</sub>, both the anthracene units adopt a planar geometry while phenothiazine adopts a puckered geometry (Figure 8, Table 2). In contrast, the phenothiazine moiety adopts a more planar geometry and placed nearly perpendicular to the plane of both the anthryl moiety in T<sub>1</sub> and S<sub>1</sub> compared to the S<sub>0</sub> state. To accommodate this conformational change in phenothiazine, B–N bond length is elongated and one of the two An moiety adopts a puckered geometry. Further, the bonding between boron and puckered An is shortened (Figure 8, Table 2). Energy and geometric parameters of S<sub>2</sub> state were found to be very similar to S<sub>1</sub>. It has been demonstrated in literature that structural distortion in aromatic planar compounds, especially out-of-plane bending, mixes the sigma character in  $\pi$ -symmetry orbitals and relaxes ISC selection rules, ultimately leading to the mixing of singlet and triplet states (El-Sayed, 1968; Bhosale et al., 2015). It is clear from computational data that in compound **1**, one of the anthracene units is puckered and partially loses its  $\pi$ -symmetry and this structural perturbation can facilitate the out-of-plane bending of An-coupled electronic transitions (Figure 8). In the simulated IR spectra of **1** in S<sub>1</sub> and T<sub>1</sub>, the out-of-plane bending mode of anthracene is very strong and shifted to a higher wave number compared to S<sub>0</sub> (Supplementary Figure 20). These results suggest that this particular molecular vibrational mode is coupled with electronic transitions involving S<sub>0</sub>, S<sub>1</sub>, and T<sub>1</sub> states (Tatchen et al., 2007).

Further, S<sub>1</sub> geometry of **1** resembles with T<sub>1</sub> very closely and the D and A moieties are placed nearly orthogonally; however, they differ significantly from the S<sub>0</sub> geometry where the D and A units are in planar arrangements. In contrast, in the case of **2**, the D and A moieties do not deviate much from the planarity and

**TABLE 2 |** Various geometrical parameters of **1** in ground and excited states (obtained from DFT and TD-DFT calculation).

State	S <sub>0</sub>	S <sub>1</sub>	T <sub>1</sub>
PTZ twist angle (°)	44.15	22.77	18.08
An twist angle (°)	0	14.55	12.05
B-N (Å)	1.444	1.618	1.607
B-C(green) (Å)	1.611	1.476	1.490
B-C (blue) (Å)	1.602	1.613	1.605
Angle between planes B C9, C9' (An) and N C, C' (Ph) (°)	0.62	85.46	70.73

the geometry of S<sub>0</sub>, S<sub>1</sub>, and T<sub>1</sub> resemble each other. These data further confirm the weak electronic coupling in **1** and a strong coupling in **2**. The weak coupling together with orthogonal arrangement of D and A units in **1** favors the spatial localization of frontier orbitals and reduces the exchange energy between the electronic excited states of different spin multiplicities involved in ISC/rISC events (El-Sayed, 1963, 1968; Tatchen et al., 2007; Dance et al., 2008; Tao et al., 2014; Bhosale et al., 2015; Hou et al., 2018).

The calculated ( $\Delta E_{ST}$ ) value for optimized geometries of **1** (0.05 eV) is lower as compared to the  $\Delta E_{ST}$  value calculated for **2** ( $\Delta E_{ST} = 1.20$  eV) with a large spatial overlap. Very recently, Di et al. (2017) demonstrated that  $\Delta E_{ST}$  is the function of the D–A twist angle; thus, geometrical reorganization is the key driving force for ISC in D–A systems. Hence, it is reasonable to hypothesize that compound **2**, with its flexible molecular structure and free rotation around the B–N bond, can adopt a conformation in which the D–A twist angle reduces  $\Delta E_{ST}$  and favors ISC/rISC events and subsequently shows DF. Based on both experimental computational results and literature precedents, we conclude that the structural features of **1** and **2** enable them to assume a dynamic conformation in which an electronic interaction between An with another An through boron results in a covalent LE state and/or interaction of An with amine through B atom results in a CT state. Thus, these compounds exhibit dual (LE and CT) delayed emissions irrespective of the temperature (Figure 7). Since TADF is a temperature-driven process, TADF molecules show DF at higher temperatures and show phosphorescence at low temperatures. Interestingly, in the present case, the dual DF characters are dependent on temperature, and it warrants explanation. Recent theoretical and experimental studies from several groups showed that the rate of rISC depends on both vibronic coupling between <sup>3</sup>CT and <sup>3</sup>LE, and SOC between <sup>3</sup>LE and <sup>1</sup>CT (Albrecht, 1963; Etherington et al., 2016, 2017; Gibson et al., 2016; Gibson and Penfold, 2017; Penfold et al., 2018). These studies also suggest that in certain cases, such as thermally activated delayed fluorescence (TADF), the singlet–triplet crossing occurs from an adiabatically lower-lying electronic state to a higher-lying one (Gibson and Penfold, 2017). “As non-radiative transitions proceed under energy conservation, these can only be achieved if the initial state is vibrationally excited, be it thermally or kinetically” (Gibson et al., 2016; Etherington et al., 2017; Gibson and Penfold, 2017). As depicted in Figure 8 and Table 2, for

**1**, S<sub>1</sub> is mainly of CT character, S<sub>2</sub> is of combined LE and CT character, and T<sub>1</sub> and T<sub>2</sub> are mainly of LE character. The very small energy differences between S<sub>1</sub>, T<sub>1</sub>, and T<sub>2</sub> and their symmetry favor the intersystem crossing (and rISC) greatly. A large energy difference between S<sub>2</sub> and S<sub>1</sub> rules out the possibility of S<sub>2</sub> to take part in the ISC or rISC processes. On the other hand, for **2** (Supplementary Figure 19), the larger energy gap between S<sub>1</sub> and T<sub>1</sub> may hinder the reverse intersystem crossing rate, but the combined LE and CT character of S<sub>1</sub>, S<sub>2</sub>, T<sub>1</sub>, and T<sub>2</sub> (which relaxes spin selection rule) enables the reverse intersystem crossing. As a result, in both **1** and **2** structured luminescence peaks in the blue edge of the spectrum suggest that the first state is vibrationally excited. Further, the PL pattern of these molecules clearly indicates the presence of both CT and LE states and provides a strong platform for the vibronic coupling between these two states. Thus, regardless of temperature, mixing of CT and LE states in **1** and **2** gives rise to a considerable rISC-mediated population transfer, leading to TADF characteristics even at low temperature.

## CONCLUSIONS

In conclusion, we reported the successful design, synthesis, and optical characteristics of a new An2B-based D–A system, in which the electronic coupling between the D and A units was controlled by the structural flexibility of the amine moiety present in them. Compound **1** with a rigid cyclic donor shows weak electronic coupling, while **2** with a flexible amine donor exhibits strong coupling. Consequently, **1** shows dual DF characteristics with strong LE and weaker CT emission bands whereas **2** shows DF with strong CT and weaker LE emission bands. Both the compounds show intriguing temperature-dependent dual DF characteristics in the range 300–80 K. Using both experimental and computational studies, it was established that the temperature-dependent dynamic molecular conformational changes in **1** and **2** led to the differential interactions between donor and acceptor units and subsequently exhibited different dual (LE and CT) DF in range of temperatures. Such structural dynamics are restricted in solid states of **1** and **2**; consequently, they exhibit temperature-dependent DF characteristics. This study also revealed that replacing mesityl in boryl acceptors with strongly optically active anthracene enhanced the probability of ISC and exhibit optical properties more promising than the former. We expect that the design strategy disclosed in this study will add a new horizon to the development of delayed emissive luminophores. These results would also attract the attentions of both experimental and computational scientist to unravel the hidden potential of this type of molecules.

## EXPERIMENTAL SECTION

### Materials and Methods

All the chemicals were purchased from commercial suppliers (Aldrich, USA; Merck, Germany; SDFCL, India) and used as received, unless otherwise mentioned. A standard Schlenk technique was used for reactions requiring inert nitrogen

atmosphere THF which was dried over sodium and distilled out under nitrogen atmosphere.

400 MHz  $^1\text{H}$  NMR and 100 MHz  $^{13}\text{C}$  NMR spectra were recorded by a Bruker Advance 100 MHz NMR Spectrometer. Solution  $^1\text{H}$  NMR and  $^{13}\text{C}$  NMR spectra were referenced internally to the solvent signals.  $^1\text{H}$  NMR spectra were referenced to TMS (0.00 ppm) as an internal standard. Chemical shift multiplicities are reported as singlet (s), doublet (d), triplet (t), quartet (q), and multiple (m).  $^{13}\text{C}$  resonances were referenced to the  $\text{CDCl}_3$  signal at  $\sim 77.67$  ppm. Solutions of all the compounds for spectral measurements were prepared using spectrophotometric grade solvents, microbalance ( $\pm 0.1$  mg precision), and standard volumetric glasswares. Quartz cuvettes with sealing screw caps were used for the solution-state spectral measurements. Electronic absorption spectra were recorded on a SHIMADZU UV-2600 spectrophotometer. The emission and excitation spectra were recorded using an Edinburgh Instruments FLS980 spectrometer. Time-gated emission spectra were recorded by an excitation source of pulsed microsecond flash lamp ( $\mu\text{F1}$ ) with a pulse width of  $1.1 \mu\text{s}$ . Single-crystal X-ray diffraction (SCXRD) studies were carried out with a Bruker SMART APEX diffractometer equipped with a 4-axis goniometer. The data were integrated using SAINT, and an empirical absorption correction was applied with SADABS. The structures were solved by direct methods and refined by full matrix least squares on  $F^2$  using SHELXTL software.

Density functional theory (DFT/TD-DFT) calculations were done using B3LYP functional with a 6-31G(d,p) basis set as incorporated in the Gaussian 09 package for all the atoms, mixing the exact Hartree-Fock-type exchange with Becke's exchange functional and that proposed by Lee-Yang-Parr for the correlation contribution (Frisch et al., 2009). The molecular structures obtained from SCXRD measurements were taken as the input for the calculations. The optimized structures and the frontier molecular orbitals (FMOs) were viewed using GaussView 5.0 (Dennington et al., 2009).

## Synthesis and Characterization

### Synthesis of 1

9-Bromoanthracene (2 g, 7.84 mmol) and phenothiazine (0.78 g, 3.95 mmol) were taken in THF (100 mL) under nitrogen atmosphere, and  $n\text{-BuLi}$  (7.95 mL of a 1.6-M solution in hexanes, 12.93 mmol) was added at  $-78^\circ\text{C}$  under stirring conditions. The reaction mixture was stirred for 1 h at the same temperature, and  $\text{BF}_3\cdot\text{OEt}_2$  (0.4 mL, 3.74 mmol) was added. The resultant reaction mixture was allowed to warm to room temperature, and stirring was continued for an additional 10 h. All the volatiles were removed under reduced pressure, and the crude product was extracted with ethyl acetate. The combined ethyl acetate extracts were stored over anhydrous  $\text{Na}_2\text{SO}_4$ , and the solvent was removed under a reduced pressure which gave a crude product. An analytically pure compound was obtained after column chromatography over alumina using 10% EtOAc in hexane as

eluent. Yellow solid, yield: 590 mg; 27%.  $^1\text{H}$  NMR (400 MHz,  $\text{CDCl}_3$ ,  $25^\circ\text{C}$ ):  $\delta$  (ppm) 8.91–8.93 (broad, 4 H), 8.28 (s, 2H), 7.33–7.35 (m, 10 H), 7.20 (d,  $J = 8.0$  Hz, 4H), 6.79 (t,  $J = 8.0$  Hz 2H), 6.49 (t,  $J = 8.0$  Hz, 2H).  $^{13}\text{C}$  NMR (100 MHz,  $\text{CDCl}_3$ ,  $25^\circ\text{C}$ ):  $\delta$  (ppm) 143.67, 131.07, 130.65, 129.88, 129.30, 128.78, 127.33, 126.34, 125.44, 125.17, 124.50. HRMS (Q-TOF):  $m/z$  calculated for  $[\text{C}_{40}\text{H}_{26}\text{BNSNa}]^+$  586.1773, found  $[\text{M}+\text{Na}]^+$  586.1777.

### Synthesis of 2

Compound 2 was synthesized following the procedure used for the synthesis of 1. Reagents used, quantities involved, and the characterization data as follows. 9-Bromoanthracene (2 g, 7.84 mmol), diphenylamine (0.67 g, 3.95 mmol),  $n\text{-BuLi}$  (7.95 mL of a 1.6-M solution in hexanes, 12.93 mmol), and  $\text{BF}_3\cdot\text{OEt}_2$  (0.4 mL, 3.74 mmol). Greenish yellow solid, yield: 510 mg; 25%.  $^1\text{H}$  NMR (400 MHz,  $\text{CDCl}_3$ ,  $25^\circ\text{C}$ ):  $\delta$  (ppm) 8.54 (broad, 4 H), 8.30 (s, 2H), 7.86–7.89 (m, 4 H), 7.26–7.30 (m, 8H), 7.00–7.02 (broad, 4H), 6.73–6.76 (broad, 6H).  $^{13}\text{C}$  NMR (100 MHz,  $\text{CDCl}_3$ ,  $25^\circ\text{C}$ ):  $\delta$  (ppm) 149.47, 131.58, 129.60, 129.25, 129.07, 128.23, 127.50, 126.49, 125.83, 125.44, 125.94. HRMS (Q-TOF):  $m/z$  calculated for  $\text{C}_{40}\text{H}_{28}\text{BN}$  533.2315  $[\text{M}^+]$ ; found 533.2321.

## DATA AVAILABILITY STATEMENT

Publicly available datasets were analyzed in this study. This data can be found here: (<https://www.ccdc.cam.ac.uk/structures/>) CCDC 1954827 and CCDC 1952521.

## AUTHOR CONTRIBUTIONS

UP did compound synthesis and PL characterization. UP and RN contributed to DFT calculations and data analysis. PT organized the entire project. All authors commented on the manuscript.

## FUNDING

The authors thanked Science and Engineering Research Board (SERB) (File No: EMR/2015/000572 dtd 21.3.16), New Delhi, India, for the financial support.

## ACKNOWLEDGMENTS

The authors thanked IPC Department and Indian Institute of Science, Bangalore, for infrastructure and instrumental facilities. UP and RP thanked IISc for research fellowships.

## SUPPLEMENTARY MATERIAL

The Supplementary Material for this article can be found online at: <https://www.frontiersin.org/articles/10.3389/fchem.2020.541331/full#supplementary-material>



## REFERENCES

- Albrecht, A. C. (1963). Vibronic—spin-orbit perturbations and the assignment of the lowest triplet state of benzene. *J. Chem. Phys.* 38, 354–365. doi: 10.1063/1.1733665
- An, B.-K., Kwon, S.-K., Jung, S.-D., and Park, S. Y. (2002). Enhanced emission and its switching in fluorescent organic nanoparticles. *J. Am. Chem. Soc.* 124, 14410–14415. doi: 10.1021/ja0269082
- Ayhan, O., Eckert, T., Plamper, F. A., and Helten, H. (2016). Poly(iminoborane)s: an elusive class of main-group polymers? *Angew. Chem. Int. Ed.* 55, 13321–13325. doi: 10.1002/anie.201607131
- Ayhan, O., Riensch, N. A., Glasmacher, C., and Helten, H. (2018). Cycloliner oligo- and poly(iminoborane)s: the missing link in inorganic main-group macromolecular chemistry. *Chemistry* 24, 5883–5894. doi: 10.1002/chem.201705913
- Bhosale, R. S., Al Kobaisi, M., Bhosale, S. V., Bhargava, S., and Bhosale, S. V. (2015). Flower-like supramolecular self-assembly of phosphonic acid appended naphthalene diimide and melamine. *Sci. Rep.* 5:14609. doi: 10.1038/srep14609
- Chen, D. G., Lin, T. C., Chen, C. L., Chen, Y. T., Chen, Y. A., Lee, G. H., et al. (2018). Optically triggered planarization of boryl-substituted phenoxazine: another horizon of TADF molecules and high-performance OLEDs. *ACS Appl. Mater. Interfaces* 10, 12886–12896. doi: 10.1021/acsami.8b00053
- Chen, L., Jiang, Y., Nie, H., Hu, R., Kwok, H. S., Huang, F., et al. (2014). Rational design of aggregation-induced emission luminogen with weak electron donor–acceptor interaction to achieve highly efficient undoped bilayer OLEDs. *ACS Appl. Mater. Interfaces* 6, 17215–17225. doi: 10.1021/am505036a
- Chiang, C.-J., Kimyonok, A., Etherington, M. K., Griffiths, G. C., Jankus, V., Turksoy, F., et al. (2013). Ultrahigh Efficiency Fluorescent Single and Bi-Layer Organic Light Emitting Diodes: The Key Role of Triplet Fusion. *Adv. Funct. Mater.* 23, 739–746. doi: 10.1002/adfm.201201750
- Cho, Y. J., Zhang, Y., Yu, H., and Aziz, H. (2016). The Root Causes of the Limited Stability of Solution-Coated Small-Molecule Organic Light-Emitting Devices: Faster Host Aggregation by Exciton–Polaron Interactions. *Adv. Funct. Mater.* 26, 8662–8669. doi: 10.1002/adfm.201603542
- Dance, Z. E. X., Mickley, S. M., Wilson, T. M., Ricks, A. B., Scott, A. M., Ratner, M. A., et al. (2008). Intersystem crossing mediated by photoinduced intramolecular charge transfer: julolidine–anthracene molecules with perpendicular  $\pi$  systems. *J. Phys. Chem. A* 112, 4194–4201. doi: 10.1021/jp800561g
- Del Rey, B., Keller, U., Torres, T., Rojo, G., Agulló-López, F., Nonell, S., et al. (1998). Synthesis and nonlinear optical, photophysical, and electrochemical properties of subphthalocyanines. *J. Am. Chem. Soc.* 120, 12808–12817. doi: 10.1021/ja980508q
- Dennington, R., Keith, T. A., and Millam, J. M. (2009). *GaussView 5.0.8*. Shawnee, KS: Semichem Inc.
- Di, D., Romanov, A. S., Yang, L., Richter, J. M., Rivett, J. P. H., Jones, S., et al. (2017). High-performance light-emitting diodes based on carbene-metal-amides. *Science* 356, 159–163. doi: 10.1126/science.aah4345
- Doty, J. C., Babb, B., Grisdale, P. J., Glogowski, M., and Williams, J. L. R. (1972). Boron photochemistry: IX. Synthesis and fluorescent properties of dimethyl-phenylboranes. *J. Organomet. Chem.* 38, 229–236. doi: 10.1016/S0022-328X(00)83321-5
- El-Sayed, M. A. (1963). Spin–orbit coupling and the radiationless processes in nitrogen heterocyclics. *J. Chem. Phys.* 38, 2834–2838. doi: 10.1063/1.1733610
- El-Sayed, M. A. (1968). Triplet state. Its radiative and nonradiative properties. *Acc. Chem. Res.* 1, 8–16. doi: 10.1021/ar50001a002
- Etherington, M. K., Franchello, F., Gibson, J., Northey, T., Santos, J., Ward, J. S., et al. (2017). Regio- and conformational isomerization critical to design of efficient thermally-activated delayed fluorescence emitters. *Nat. Commun.* 8:14987. doi: 10.1038/ncomms14987
- Etherington, M. K., Gibson, J., Higginbotham, H. F., Penfold, T. J., and Monkman, A. P. (2016). Revealing the spin–vibronic coupling mechanism of thermally activated delayed fluorescence. *Nat. Commun.* 7:13680. doi: 10.1038/ncomms13680
- Frisch, M. J., Trucks, G. W., Schlegel, H. B., Scuseria, G. E., Robb, M. A., Cheeseman, J. R., et al. (2009). *Gaussian09. Revision A.02*. Wallingford, CT: Gaussian, Inc.
- Galbraith, E., and James, T. D. (2010). Boron based anion receptors as sensors. *Chem. Soc. Rev.* 39, 3831–3842. doi: 10.1039/b926165f
- Gibson, J., Monkman, A. P., and Penfold, T. J. (2016). The importance of vibronic coupling for efficient reverse intersystem crossing in thermally activated delayed fluorescence molecules. *Chemphyschem* 17, 2956–2961. doi: 10.1002/cphc.201600662
- Gibson, J., and Penfold, T. J. (2017). Nonadiabatic coupling reduces the activation energy in thermally activated delayed fluorescence. *Phys. Chem. Chem. Phys.* 19, 8428–8434. doi: 10.1039/C7CP00719A
- Hashimoto, S., Ikuta, T., Shiren, K., Nakatsuka, S., Ni, J., Nakamura, M., et al. (2014). Triplet-energy control of polycyclic aromatic hydrocarbons by BN replacement: development of ambipolar host materials for phosphorescent organic light-emitting diodes. *Chem. Mater.* 26, 6265–6271. doi: 10.1021/cm503102d
- Hatakeyama, T., Hashimoto, S., Oba, T., and Nakamura, M. (2012). Azaboradibenzo[6]helicene: carrier inversion induced by helical homochirality. *J. Am. Chem. Soc.* 134, 19600–19603. doi: 10.1021/ja310372f
- Hosokai, T., Matsuzaki, H., Nakanotani, H., Tokumaru, K., Tsutsui, T., Furube, A., et al. (2017). Evidence and mechanism of efficient thermally activated delayed fluorescence promoted by delocalized excited states. *Sci. Adv.* 3:e1603282. doi: 10.1126/sciadv.1603282
- Hou, Y., Biskup, T., Rein, S., Wang, Z., Bussotti, L., Russo, N., et al. (2018). Spin–orbit charge recombination intersystem crossing in phenothiazine–anthracene compact dyads: effect of molecular conformation on electronic coupling, electronic transitions, and electron spin polarizations of the triplet states. *J. Phys. Chem. C* 122, 27850–27865. doi: 10.1021/acs.jpcc.8b08965
- Hudnall, T. W., Chiu, C.-W., and Gabbai, F. P. (2009). Fluoride ion recognition by chelating and cationic boranes. *Acc. Chem. Res.* 42, 388–397. doi: 10.1021/ar8001816
- Jäkle, F. (2010). Advances in the synthesis of organoborane polymers for optical, electronic, and sensory applications. *Chem. Rev.* 110, 3985–4022. doi: 10.1021/cr100026f
- Ji, L., Griesbeck, S., and Marder, T. B. (2017). Recent developments in and perspectives on three-coordinate boron materials: a bright future. *Chem. Sci.* 8, 846–863. doi: 10.1039/C6SC04245G
- Kalluvettukuzhy, N. K., and Thilagar, P. (2017). Bistable polyaromatic aminoboranes: bright solid state emission and mechanochromism. *Organometallics* 36, 2692–2701. doi: 10.1021/acs.organomet.7b00332
- Kim, S., Bae, H. J., Park, S., Kim, W., Kim, J., Kim, J. S., et al. (2018). Degradation of blue-phosphorescent organic light-emitting devices involves exciton-induced generation of polaron pair within emitting layers. *Nat. Commun.* 9:1211. doi: 10.1038/s41467-018-03602-4
- Li, W., Pan, Y., Yao, L., Liu, H., Zhang, S., Wang, C., et al. (2014). A hybridized local and charge-transfer excited state for highly efficient fluorescent OLEDs: molecular design, spectral character, and full exciton utilization. *Adv. Optic. Mater.* 2, 892–901. doi: 10.1002/adom.201400154
- Liang, X., Tu, Z. L., and Zheng, Y. X. (2019). Thermally activated delayed fluorescence materials: towards realization of high efficiency through strategic small molecular design. *Chemistry* 25, 5623–5642. doi: 10.1002/chem.201805952
- Lien, Y. J., Lin, T. C., Yang, C. C., Chiang, Y. C., Chang, C. H., Liu, S. H., et al. (2017). First N-borylated emitters displaying highly efficient thermally activated delayed fluorescence and high-performance OLEDs. *ACS Appl. Mater. Interfaces* 9, 27090–27101. doi: 10.1021/acsami.7b08258
- Liu, K., Lalancette, R. A., and Jäkle, F. (2017). B–N Lewis pair functionalization of anthracene: structural dynamics, optoelectronic properties, and O<sub>2</sub> sensitization. *J. Am. Chem. Soc.* 139, 18170–18173. doi: 10.1021/jacs.7b11062
- Liu, K., Lalancette, R. A., and Jäkle, F. (2019). Tuning the structure and electronic properties of B–N fused dipyrrolylanthracene and implications on the self-sensitized reactivity with singlet oxygen. *J. Am. Chem. Soc.* 141, 7453–7462. doi: 10.1021/jacs.9b01958
- Luo, J., Xie, Z., Lam, J. W. Y., Cheng, L., Chen, H., Qiu, C., et al. (2001). Aggregation-induced emission of 1-methyl-1,2,3,4,5-pentaphenylsilole. *Chem. Commun.* 381, 1740–1741. doi: 10.1039/b105159h
- Mao, M., Ren, M.-G., and Song, Q.-H. (2012). Thermodynamics and conformations in the formation of excited states and their interconversions for twisted donor-substituted tridurylboranes. *Chemistry* 18, 15512–15522. doi: 10.1002/chem.201201719



- Møllerup, S. K., and Wang, S. (2019). Boron-based stimuli responsive materials. *Chem. Soc. Rev.* 48, 3537–3549. doi: 10.1039/C9CS00153K
- Neena, K. K., Sudhakar, P., and Thilagar, P. (2018). Catalyst- and template-free ultrafast visible-light-triggered dimerization of vinylpyridine-functionalized tetraarylamino-borane: intriguing deep-blue delayed fluorescence. *Angew. Chem. Int. Ed.* 57, 16806–16810. doi: 10.1002/anie.201811353
- Neena, K. K., and Thilagar, P. (2016). Replacing the non-polarized C=C bond with an isoelectronic polarized B–N unit for the design and development of smart materials. *J. Mater. Chem. C* 4, 11465–11473. doi: 10.1039/C6TC04470K
- Noda, H., Chen, X. K., Nakanotani, H., Hosokai, T., Miyajima, M., Notsuka, N., et al. (2019). Critical role of intermediate electronic states for spin-flip processes in charge-transfer-type organic molecules with multiple donors and acceptors. *Nat. Mater.* 18, 1084–1090. doi: 10.1038/s41563-019-0465-6
- Noda, H., Nakanotani, H., and Adachi, C. (2018). Excited state engineering for efficient reverse intersystem crossing. *Sci. Adv.* 4:6910. doi: 10.1126/sciadv.aao6910
- Northey, T., Keane, T., Eng, J., and Penfold, T. J. (2019). Understanding the potential for efficient triplet harvesting with hot excitons. *Faraday Discuss* 216, 395–413. doi: 10.1039/C8FD00174J
- Obolda, A., Ai, X., Zhang, M., and Li, F. (2016). Up to 100% formation ratio of doublet exciton in deep-red organic light-emitting diodes based on neutral pi-radical. *ACS Appl. Mater. Interfaces* 8, 35472–35478. doi: 10.1021/acsami.6b12338
- Okazaki, M., Takeda, Y., Data, P., Pander, P., Higginbotham, H., Monkman, A. P., et al. (2017). Thermally activated delayed fluorescent phenothiazine-dibenzo[a,j]phenazine-phenothiazine triads exhibiting tricolor-changing mechanochromic luminescence. *Chem. Sci.* 8, 2677–2686. doi: 10.1039/C6SC04863C
- Pandey, U. P., and Thilagar, P. (2020). External stimuli responsive bis(anthryl)borylaniline AIEgens for viscosity and temperature sensing: the game of molecular flexibility. *Adv. Opt. Mater.* 8:1902145. doi: 10.1002/adom.201902145
- Penfold, T. J., Gindensperger, E., Daniel, C., and Marian, C. M. (2018). Spin-vibronic mechanism for intersystem crossing. *Chem. Rev.* 118, 6975–7025. doi: 10.1021/acs.chemrev.7b00617
- Peng, Q., Obolda, A., Zhang, M., and Li, F. (2015). Organic light-emitting diodes using a neutral pi radical as emitter: the emission from a doublet. *Angew. Chem. Int. Ed.* 54, 7091–7095. doi: 10.1002/anie.201500242
- Pu, Y.-J., Satake, R., Koyama, Y., Otomo, T., Hayashi, R., Haruta, N., et al. (2019). Absence of delayed fluorescence and triplet–triplet annihilation in organic light emitting diodes with spatially orthogonal bianthracenes. *J. Mater. Chem. C* 7, 2541–2547. doi: 10.1039/C8TC05817B
- Salla, C. A. M., Farias, G., Rouzières, M., Dechambenoit, P., Durola, F., Bock, H., et al. (2019). Persistent solid-state phosphorescence and delayed fluorescence at room temperature by a twisted hydrocarbon. *Angew. Chem. Int. Ed.* 58, 6982–6986. doi: 10.1002/anie.201901672
- Sudhakar, P., Mukherjee, S., and Thilagar, P. (2013). Revisiting borylanilines: unique solid-state structures and insight into photophysical properties. *Organometallics* 32, 3129–3133. doi: 10.1021/om301197f
- Sudhakar, P., Neena, K. K., and Thilagar, P. (2017). H-Bond assisted mechanoluminescence of borylated aryl amines: tunable emission and polymorphism. *J. Mater. Chem. C* 5, 6537–6546. doi: 10.1039/C7TC01676J
- Suzuki, K., Kubo, S., Shizu, K., Fukushima, T., Wakamiya, A., Murata, Y., et al. (2015). Triarylboron-based fluorescent organic light-emitting diodes with external quantum efficiencies exceeding 20%. *Angew. Chem. Int. Ed.* 54, 15231–15235. doi: 10.1002/anie.201508270
- Swamy, P. C. A., Mukherjee, S., and Thilagar, P. (2014). Dual binding site assisted chromogenic and fluorogenic recognition and discrimination of fluoride and cyanide by a peripherally borylated metalloporphyrin: overcoming anion interference in organoboron based sensors. *Anal. Chem.* 86, 3616–3624. doi: 10.1021/ac500230p
- Tao, Y., Yuan, K., Chen, T., Xu, P., Li, H., Chen, R., et al. (2014). Thermally activated delayed fluorescence materials towards the breakthrough of organoelectronics. *Adv. Mater.* 26, 7931–7958. doi: 10.1002/adma.201402532
- Tatchen, J., Gilka, N., and Marian, C. M. (2007). Intersystem crossing driven by vibronic spin–orbit coupling: a case study on psoralen. *Phys. Chem. Chem. Phys.* 9, 5209–5221. doi: 10.1039/b706410a
- Uoyama, H., Goushi, K., Shizu, K., Nomura, H., and Adachi, C. (2012). Highly efficient organic light-emitting diodes from delayed fluorescence. *Nature* 492, 234–238. doi: 10.1038/nature11687
- Wakamiya, A., Ide, T., and Yamaguchi, S. (2005). Toward  $\pi$ -conjugated molecule bundles: synthesis of a series of B,B',B''-trianthryl-N,N',N''-triarylborazines and the bundle effects on their properties. *J. Am. Chem. Soc.* 127, 14859–14866. doi: 10.1021/ja0537171
- Wang, J.-Y., and Pei, J. (2016). BN-embedded aromatics for optoelectronic applications. *Chin. Chem. Lett.* 27, 1139–1146. doi: 10.1016/j.cclet.2016.06.014
- Wang, X.-Y., Lin, H.-R., Lei, T., Yang, D.-C., Zhuang, F.-D., Wang, J.-Y., et al. (2013). Azaborine compounds for organic field-effect transistors: efficient synthesis, remarkable stability, and BN dipole interactions. *Angew. Chem. Int. Ed.* 52, 3117–3120. doi: 10.1002/anie.201209706
- Yamaguchi, S., Akiyama, S., and Tamao, K. (2000a). Tri-9-anthrylborane and its derivatives: new boron-containing  $\pi$ -electron systems with divergently extended  $\pi$ -conjugation through boron. *J. Am. Chem. Soc.* 122, 6335–6336. doi: 10.1021/ja994522u
- Yamaguchi, S., Akiyama, S., and Tamao, K. (2002). The coordination number–photophysical properties relationship of trianthrylphosphorus compounds: doubly locked fluorescence of anthryl groups. *J. Organomet. Chem.* 646, 277–281. doi: 10.1016/S0022-328X(01)01391-2
- Yamaguchi, S., Shirasaka, T., and Tamao, K. (2000b). Tridurylboranes extended by three aryethynyl groups as a new family of boron-based  $\pi$ -electron systems. *Org. Lett.* 2, 4129–4132. doi: 10.1021/ol006660q
- Yang, Z., Mao, Z., Xie, Z., Zhang, Y., Liu, S., Zhao, J., et al. (2017). Recent advances in organic thermally activated delayed fluorescence materials. *Chem. Soc. Rev.* 46, 915–1016. doi: 10.1039/C6CS00368K
- Ye, C., Gray, V., Martensson, J., and Borjesson, K. (2019). Annihilation versus excimer formation by the triplet pair in triplet–triplet annihilation photon upconversion. *J. Am. Chem. Soc.* 141, 9578–9584. doi: 10.1021/jacs.9b02302
- Yuan, Z., Taylor, N. J., Marder, T. B., Williams, I. D., Kurtz, S. K., and Cheng, L.-T. (1990). Three coordinate phosphorus and boron as  $\pi$ -donor and  $\pi$ -acceptor moieties respectively, in conjugated organic molecules for nonlinear optics: crystal and molecular structures of E-Ph-CH=CH-B(mes)<sub>2</sub>, E-4-MeO-C<sub>6</sub>H<sub>4</sub>-CH=CH-B(mes)<sub>2</sub>, and E-Ph 2P-CH=CH-B(mes)<sub>2</sub> [mes = 2,4,6-Me<sub>3</sub>C 6H<sub>2</sub>]. *J. Chem. Soc. Chem. Comm.* 1489–1492. doi: 10.1039/C39900001489

**Conflict of Interest:** The authors declare that the research was conducted in the absence of any commercial or financial relationships that could be construed as a potential conflict of interest.

Copyright © 2020 Pandey, Nandi and Thilagar. This is an open-access article distributed under the terms of the Creative Commons Attribution License (CC BY). The use, distribution or reproduction in other forums is permitted, provided the original author(s) and the copyright owner(s) are credited and that the original publication in this journal is cited, in accordance with accepted academic practice. No use, distribution or reproduction is permitted which does not comply with these terms.



# Fast Delayed Emission in New Pyridazine-Based Compounds

Simonas Krotkus<sup>1†</sup>, Tomas Matulaitis<sup>2</sup>, Stefan Diesing<sup>1,2</sup>, Graeme Copley<sup>2†</sup>, Emily Archer<sup>1</sup>, Changmin Keum<sup>1</sup>, David B. Cordes<sup>2</sup>, Alexandra M. Z. Slawin<sup>2</sup>, Malte C. Gather<sup>1</sup>, Eli Zysman-Colman<sup>2\*</sup> and Ifor D. W. Samuel<sup>1\*</sup>

## OPEN ACCESS

### Edited by:

Guigen Li,  
Texas Tech University, United States

### Reviewed by:

Xu-Lin Chen,  
Chinese Academy of Sciences, China  
Juozas Vidas Grazulevicius,  
Kaunas University of  
Technology, Lithuania  
Anastasia Klimash,  
University of Glasgow,  
United Kingdom

### \*Correspondence:

Eli Zysman-Colman  
eli.zysman-colman@st-andrews.ac.uk  
Ifor D. W. Samuel  
idws@st-and.ac.uk

### † Present address:

Simonas Krotkus,  
AIXTRON SE, Herzogenrath, Germany  
Graeme Copley,  
Department of Chemistry, University of  
Michigan, Ann Arbor, MI,  
United States

### Specialty section:

This article was submitted to  
Organic Chemistry,  
a section of the journal  
Frontiers in Chemistry

Received: 15 June 2020

Accepted: 13 October 2020

Published: 07 January 2021

### Citation:

Krotkus S, Matulaitis T, Diesing S,  
Copley G, Archer E, Keum C,  
Cordes DB, Slawin AMZ, Gather MC,  
Zysman-Colman E and Samuel IDW  
(2021) Fast Delayed Emission in New  
Pyridazine-Based Compounds.  
Front. Chem. 8:572862.  
doi: 10.3389/fchem.2020.572862

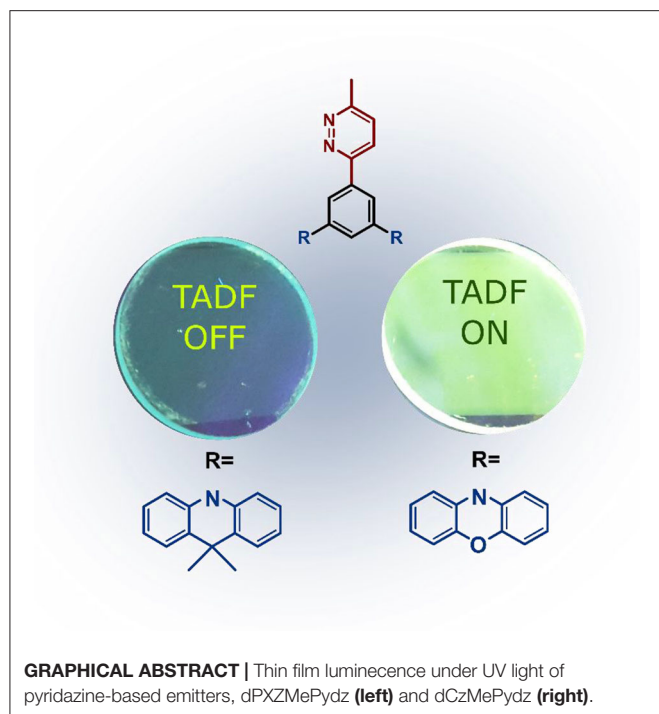
<sup>1</sup> Organic Semiconductor Centre, Scottish Universities Physics Alliance (SUPA), School of Physics and Astronomy, University of St. Andrews, St Andrews, United Kingdom, <sup>2</sup> Organic Semiconductor Centre, EaStCHEM School of Chemistry, University of St. Andrews, St Andrews, United Kingdom

Three novel donor-acceptor molecules comprising the underexplored pyridazine (Pydz) acceptor moiety have been synthesized and their structural, electrochemical and photophysical properties thoroughly characterized. Combining Pydz with two phenoxazine donor units linked via a phenyl bridge in a *meta* configuration (**dPXZMePydz**) leads to high reverse intersystem crossing rate  $k_{\text{RISC}} = 3.9 \cdot 10^6 \text{ s}^{-1}$  and fast thermally activated delayed fluorescence (TADF) with <500 ns delayed emission lifetime. Efficient triplet harvesting via the TADF mechanism is demonstrated in OLEDs using **dPXZMePydz** as the emitter but does not occur for compounds bearing weaker donor units.

**Keywords:** thermally activated delayed fluorescence (TADF), pyridazine, organic light-emitting diode (OLED), reverse intersystem crossing (rISC), donor-acceptor (D-A) architecture

## INTRODUCTION

Electroluminescence (EL) from organic light-emitting diodes (OLEDs) originates from the radiative decay of neutral excited states (excitons) formed by the recombination of holes and electrons. Spin statistics dictate that three quarters of the excitons created in working OLEDs are triplets. Since the ground state of most organic luminophores is singlet, considerable effort has been concentrated on development of materials that exhibit fast spin conversion from triplet to singlet states. The first breakthrough in EL efficiency was thus achieved by introducing organometallic phosphorescent emitters (Baldo et al., 1998; Adachi et al., 2001). The heavy atom effect in these materials enhances spin-orbit coupling, promoting phosphorescence with microsecond lifetime, and, importantly external quantum efficiencies (EQEs) that surpass the limit of 5% for fluorescent materials. However, the most commonly used organometallic complexes are based on iridium(III) and platinum(II) and these materials are not sustainable given their ultra-low abundance in the Earth's crust. While efficient and stable red and green phosphorescent OLEDs are now commercialized, and encouraging pure blue phosphorescent OLEDs were demonstrated recently (Lee et al., 2016; Li et al., 2018; Pal et al., 2018), blue device stability remains an unresolved issue (Yang et al., 2015; Jacquemin and Escudero, 2017). For these reasons, alternative routes to harvest both singlet and triplet states using purely organic emitters via delayed fluorescence channels, namely, triplet-triplet annihilation (TTA) (Kondakov et al., 2009) and thermally activated delayed fluorescence (TADF) (Uoyama et al., 2012; Wong and Zysman-Colman, 2017), are being hotly pursued. TADF is based on triplet up-conversion to the first excited singlet level via reverse intersystem crossing (rISC).



For the rate of this process ( $k_{\text{rISC}}$ ) to be sufficiently high to outcompete the non-radiative internal conversion of the triplet state, a small singlet-triplet splitting energy  $\Delta E_{\text{ST}}$  is required, which is achieved in intramolecular charge transfer (ICT) states present in molecules composed of electron-donating (D) and electron-accepting (A) units. Concomitantly, high photoluminescence quantum yield ( $\Phi_{\text{PL}}$ ) is needed in high performance emitters for OLEDs. Indeed, competitively efficient TADF OLEDs based on D-A emitter architectures have now been reported for all relevant display colors (Tao et al., 2014). An ongoing research effort is also aimed at addressing issues related to device stability and the link to the structure of the emitters. In particular, the design of emitters that show fast  $k_{\text{rISC}}$  and short delayed fluorescence lifetimes is desired in order to mitigate against bimolecular interactions, such as TTA and triplet-polaron annihilation. This is currently pursued via controlled molecular fine-tuning of the spatial separation and twist angles between D and A units, as well as D/A unit strength (Milián-Medina and Gierschner, 2012; Tanaka et al., 2013; Im et al., 2017).

Among the *N*-heterocyclic electron-acceptors, 1,3,5-triazine is one of the most employed (Wong and Zysman-Colman, 2017; Huang et al., 2019; Sharma et al., 2019; Wang et al., 2019; Woo et al., 2019). Other heterocycles used in this role include pyridines (Rajamalli et al., 2017, 2018a,b, 2019), pyrimidines (Komatsu et al., 2016; Nakao et al., 2017; dos Santos et al., 2019), and pyrazines (Figure 1A) (dos Santos et al., 2019; Kato et al., 2019; Liu et al., 2019). Missing from this family of heterocycles is pyridazine (Pydz), which is investigated in this work as an acceptor in three novel D-A compounds (Figure 1B). Pyridazine-based compounds have been employed as ligands in phosphorescent emitters (Guo et al., 2015; Zhang et al., 2016),

as well as hosts for phosphorescent OLEDs (Jia et al., 2019), and as fluorescent probes (Qu et al., 2020). To date, there are no examples of pyridazine-based TADF emitters used in OLEDs.

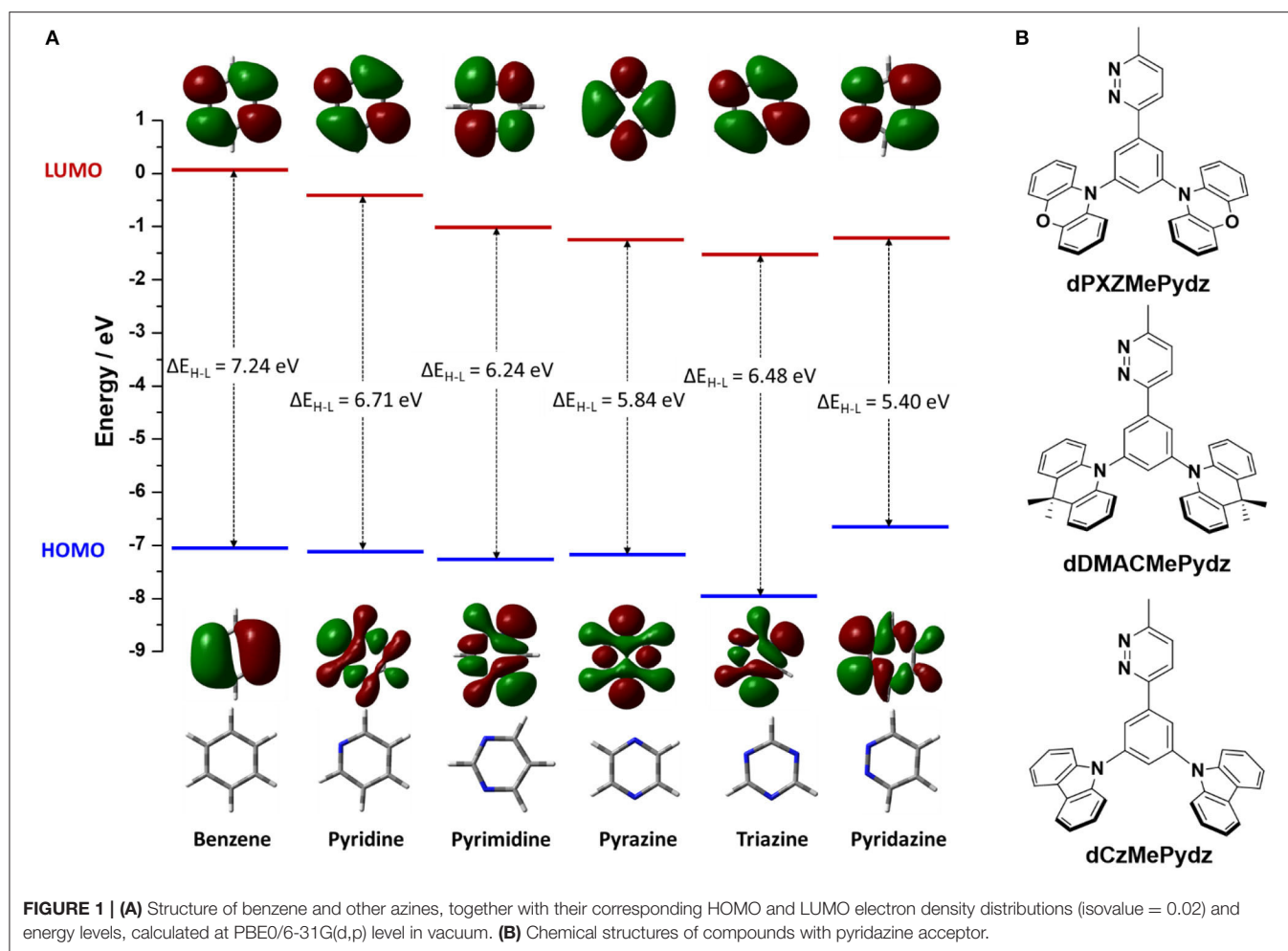
## RESULTS AND DISCUSSION

### Synthesis

To evaluate the electron-accepting ability of pyridazine it is essential to consider the energy level of its lowest unoccupied molecular orbital (LUMO). Density functional theory (DFT) calculated LUMO levels of benzene and related *N*-heterocycles predict that pyridazine possesses a comparable LUMO level to those of triazine and pyrazine (Figure 1A) (Ortiz et al., 2009; Liu et al., 2017; Jin et al., 2019). Pyridazine possesses a more destabilized highest occupied molecular orbital (HOMO) as compared to other studied azines, thus yielding the smallest HOMO-LUMO gap,  $\Delta E_{\text{H-L}}$ . Substituted pyridazines are most easily synthesized at the three and six positions (i.e., *ortho* to the nitrogen atoms). We thus envisaged the three targeted emitters in Figure 1B containing a phenylene bridge, which was expected to induce a certain degree of  $\text{N}\cdots\text{H}$  intramolecular hydrogen bonding between the Pydz and the phenylene and a co-planar conformation. Decoration of the phenylene with electron donors of different strength connected at the *meta* positions would strongly electronically decouple these groups from the Pydz acceptor, leading to potential TADF emitters.

Each of the three emitters in this study comprised a 3-methyl-pyridazine (MePydz) acceptor moiety linked by a phenylene bridge to two identical donor units disposed in a *meta* configuration with respect to the position of the acceptor (Figure 1B). The donor units chosen were phenoxazine (PXZ, compound **dPXZMePydz**), 9,9-dimethyl-9,10-dihydroacridine (DMAC, **dDMACMePydz**), and carbazole (Cz, **dCzMePydz**). By weakening the donor strength from PXZ to DMAC to Cz we expected to systematically shift the emission energy of the compounds toward the blue. Conjugation between donor and acceptor groups should be greatly reduced owing to their *meta* disposition about the central phenylene. As such, the exchange integral between the HOMO and the LUMO will be small, leading to a correspondingly small singlet-triplet energy gap,  $\Delta E_{\text{ST}}$ , between the lowest singlet and triplet excited states, which is desired for an efficient TADF mechanism.

The synthesis of the three pyridazine-containing compounds is shown in Scheme 1. Key intermediate MePydz was prepared by Suzuki-Miyaura (Suzuki, 2005) cross-coupling reaction between 3-iodo-6-methylpyridazine and (3,5-dibromophenyl)boronic acid. Coupling of MePydz to PXZ, DMAC and Cz under either Buchwald-Hartwig (Forero-Cortés and Haydl, 2019) or modified Ullmann coupling (Antilla et al., 2004) conditions yielded the target materials **dPXZMePydz**, **dDMACMePydz**, and **dCzMePydz**, respectively, in average to high yields. The chemical structures of the three derivatives were identified by a combination of  $^1\text{H}$ ,  $^{13}\text{C}$  NMR spectroscopy (Supplementary Figures 1–8), high resolution mass spectrometry (Supplementary Figures 9–11) and elemental analysis. The compounds were purified by column chromatography, and purity was ascertained by



HPLC (Supplementary Figures 12–14) and elemental analysis (Supplementary Figures 15–17).

## Structural Characterization

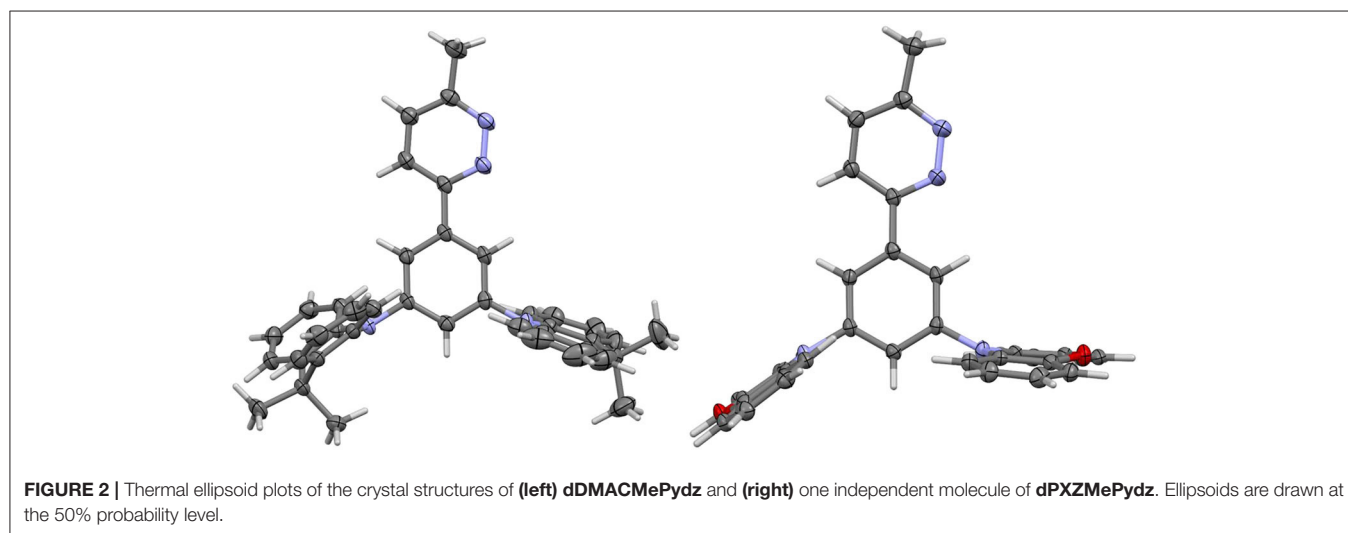
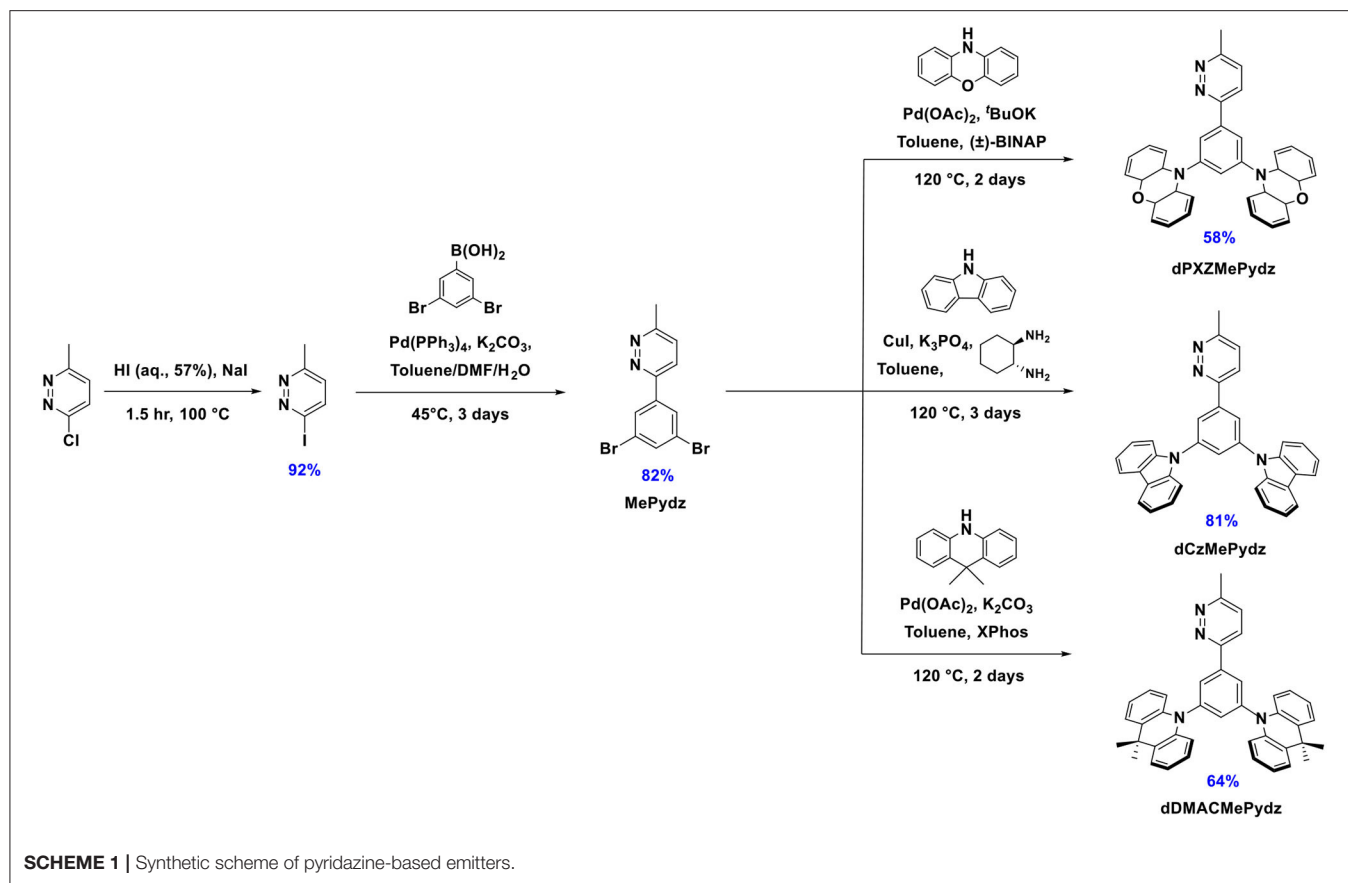
The structures of **dPXZMePydz** and **dDMACMePydz** were also confirmed by single crystal X-ray diffraction analysis (Figure 2, Supplementary Table 1). The structure of **dPXZMePydz** contained two independent molecules, one of which showed a similar pyrazine-phenylene geometry to **dDMACMePydz**, the other of which showed a different geometry. The dihedral angle between the pyridazine and the adjacent phenylene was found to be relatively small for **dDMACMePydz** and the equivalent **dPXZMePydz** (13.12 and 11.37°, respectively), although a much greater angle was seen for the second independent molecule in **dPXZMePydz** (42.63°), while in all cases, the mean planes of the donor groups are disposed close to orthogonal with respect to the plane of the phenylene bridge (66.41 – 80.86°). The DMAC donor *anti* to the diazine in **dDMACMePydz** was found to have a 38.51° pucker angle across its central ring, the other adopting a flat conformation (3.57° pucker). In contrast, none of the PXZ donors in **dPXZMePydz** showed the same extent of ring-pucker. In one independent molecule the diazine-facing

PXZ adopted a flatter conformation than the *anti* donor group (6.12 vs. 14.11°), while in the second, the diazine-facing PXZ was more puckered than the *anti* donor (11.88 vs. 4.88°). The other significant geometric difference between the structures is in the degree of pyramidalisation of the nitrogen of the donor groups. In **dDMACMePydz** both donor nitrogens showed similar slight degrees of pyramidalisation ( $C_{\text{phenylene-N}} \cdots CMe_2$  169.00 and 171.82°), but in **dPXZMePydz** each independent molecule showed different patterns of nitrogen pyramidalisation. One of these showed a more pyramidal nitrogen in the *anti* donor group ( $C_{\text{phenylene-N}} \cdots O$  160.52 and 179.51, for *anti* and *syn* donors groups, respectively), whereas the other showed a more pyramidal nitrogen in the *syn* donor group ( $C_{\text{phenylene}} \cdots N \cdots O$  174.46 and 155.26, for *anti* and *syn* donors groups, respectively).

## Theoretical Calculations

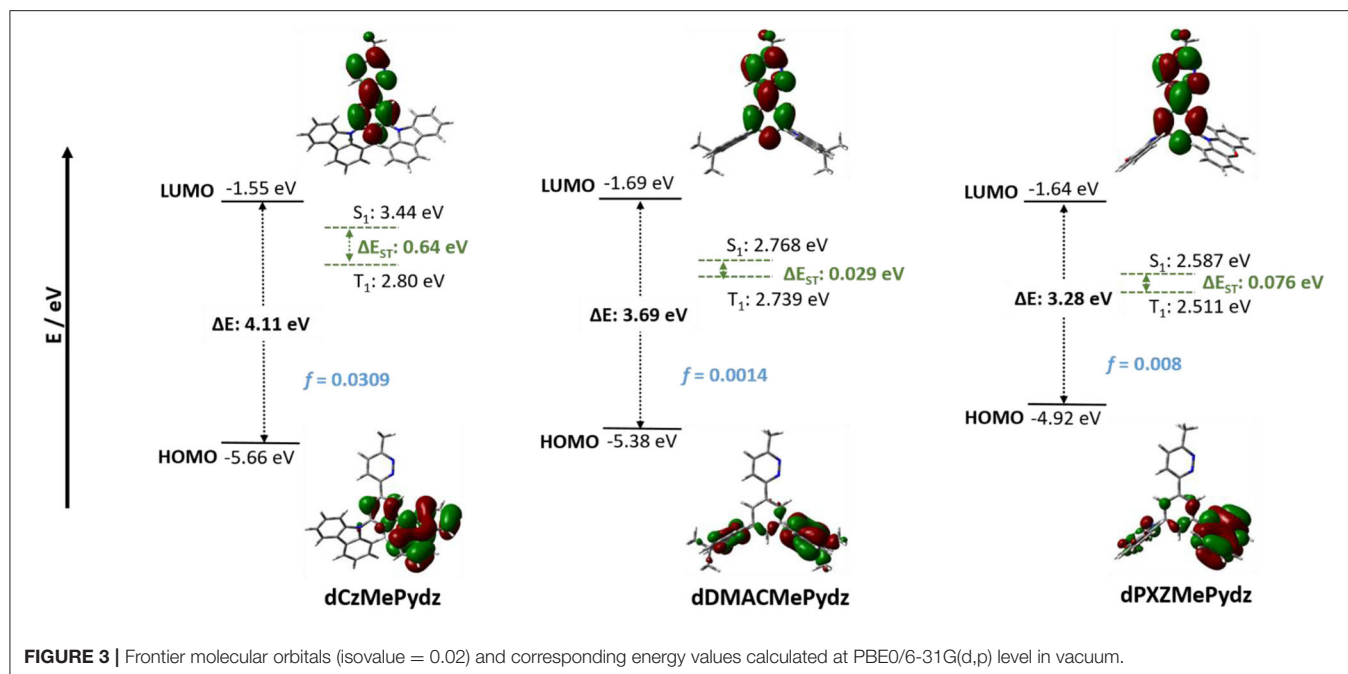
DFT calculated energies of the first excited singlet and triplet states,  $S_1$  and  $T_1$ , respectively, and the HOMO and LUMO levels for the three compounds are shown in Figure 3 along with the electron-density distribution of the HOMO and LUMO orbitals. The HOMOs for **dPXZMePydz** and **dDMACMePydz** are localized on the donor moieties with only a minor contribution





associated with the phenylene bridge, while for **dCzMePydz** the HOMO is delocalized over the phenylene bridge and one of the two carbazole groups. The multi-donor design should lead to a degeneracy of frontier orbitals. This is evidenced by the HOMO-1 being close in energy ( $\sim 70$ – $200$  meV) to HOMO in each of the compounds (see **Supplementary Figure 19**). The HOMO levels reflect the strength of the donor moieties with values of  $-4.92$ ,

$-5.38$ , and  $-5.66$  eV for **dPXZMePydz**, **dDMACMePydz**, and **dCzMePydz**, respectively. The LUMOs for all three compounds are delocalized along the **MePydz** acceptor and phenylene bridge. The trend in LUMO energies mirrors that observed for the HOMO levels, but the influence of the donor on the LUMO level is significantly attenuated, with LUMO levels of  $-1.64$ ,  $-1.69$ , and  $-1.55$  eV for **dPXZMePydz**, **dDMACMePydz**, and



**dCzMePydz**, respectively. The  $\Delta E_{H-L}$  values thus increase from 3.28 to 3.69 to 4.11 eV for **dPXZMePydz**, **dDMACMePydz**, and **dCzMePydz**, respectively. The Tamm-Dancoff approximation to time-dependent DFT calculations predict the transition from the ground state to the lowest excited state ( $S_0$ - $S_1$ ) to have ICT character for all three molecules. The  $S_0$ - $T_1$  transitions of **dDMACMePydz** and **dPXZMePydz** are likewise CT in nature, while the  $S_0$ - $T_1$  transition of **dCzMePydz** possesses local exciton (LE) character within the acceptor moiety. The calculated energies and oscillator strengths for the transitions from ground state to  $S_{1,2}$  and  $T_{1,2,3,4}$  levels are summarized in **Supplementary Table 2**. For **dPXZMePydz**, the  $S_1$  state is at 2.58 eV, while it increases in energy to 2.77 eV and 3.44 eV for **dDMACMePydz** and **dCzMePydz**, respectively. Thus, as expected, a blue-shift in emission is predicted with the decreasing donor unit strength. The frontier molecular orbitals of **dPXZMePydz** and **dDMACMePydz** are well-separated. This is reflected in the small calculated oscillator strengths ( $f = 8.0 \cdot 10^{-3}$  and  $1.4 \cdot 10^{-3}$ , respectively) as well as small singlet-triplet splitting energies ( $\Delta E_{ST} = 76$  and  $29$  meV, respectively). On the other hand, there is significant HOMO-LUMO overlap in **dCzMePydz**, which is reflected in much larger  $f$  of  $3.1 \cdot 10^{-2}$  and large  $\Delta E_{ST}$  of 635 meV. Thus, this latter compound would not be expected to exhibit efficient TADF while the other two emitters would. The  $T_2$  and  $T_3$  states of **dPXZMePydz** are energetically very close to the  $S_2$  state ( $\Delta E_{S_2T_2} = 41$  meV and  $\Delta E_{S_2T_3} = 9$  meV, respectively, see **Supplementary Figure 20**, **Supplementary Table 2**). For **dDMACMePydz** there is a similar alignment of higher lying singlet and triplet excited states ( $\Delta E_{S_1T_2} = -35$  meV,  $\Delta E_{S_2T_3} = 33$  meV), while for **dCzMePydz** only  $T_4$  is close to  $S_1$  ( $\Delta E_{S_1T_4} = -15$  meV). However, it is unlikely that **dCzMePydz** would undergo triplet exciton harvesting from  $T_4$  since internal conversion proceeding

via  $T_3$  and  $T_2$  is highly likely to trap triplet excitons in the  $T_1$  state.

## Electrochemistry

**Figure 4** and **Table 1** summarize the electrochemical characterization of the compounds. Cyclic and differential pulse voltammetry (CV and DPV, respectively) were employed in order to elucidate the energy levels of the studied materials. The oxidation potentials were 0.74 V, 0.71 V, and 1.21 V for the **dPXZMePydz**, **dDMACMePydz**, and **dCzMePydz**, respectively. Only **dPXZMePydz** demonstrated reversible oxidation, while other two compounds show quasi-reversible oxidation. As expected, the use of the weaker Cz electron donor in **dCzMePydz** resulted in a significantly more anodic oxidation potential, which is consistent with oxidation of other carbazole-based emitters (Kukhta et al., 2017). The  $E_{PA}^{OX}$  for **dDMACMePydz** is cathodically shifted by only 0.03 V compared to that of **dPXZMePydz**, thereby indicating that within these emitters DMAC and PXZ possess comparable donating strength. All three compounds demonstrated almost identical reduction potentials with  $E_{RED}$  values of  $-1.93$  V,  $-1.94$  V, and  $-1.94$  V for the **dPXZMePydz**, **dDMACMePydz**, and **dCzMePydz**, respectively. Ionization potential and electron affinity values calculated based on oxidation and reduction potentials obtained from the DPV experiments follow the same trends. Expectedly, the HOMO level is destabilized with increasing strength of the donor with ionization potential values of 5.22 eV for **dCzMePydz**, 4.60 eV for **dDMACMePydz** and 4.78 eV for **dPXZMePydz**. The nature of the donor has no notable effect on the LUMO levels, with electron affinity values of 1.96 eV, 1.98 eV, and 1.93 eV for **dPXZMePydz**, **dDMACMePydz**, and **dCzMePydz**, respectively. These results indicate essentially no electronic coupling between the donor and acceptor moieties. As

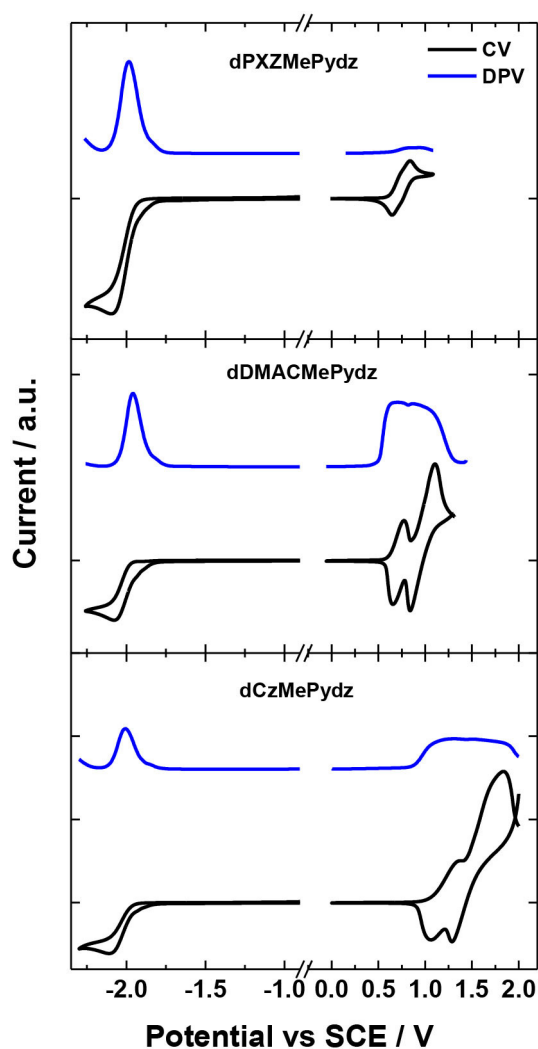


**FIGURE 4** | CV and DPV curves of **dPXZMePydz**, **dDMACMePydz**, and **dCzMePydz**. Oxidation measured in DCM and reduction in DMF (scan rate: 0.03 V/s).

a result, the electrochemical bandgap is systematically increased as a function of weakening donor strength along the DMAC to PXZ to Cz.

## Photophysics

The absorption spectra in toluene are shown in **Figure 5**. All spectra resemble those of the donor units used, with the absorption spectrum of **dPXZMePydz** having a more notable lowest energy band located at 370–450 nm. A hypsochromic shift in the absorption onset is observed ( $\lambda_{\text{abs}} = 445$  nm in **dPXZMePydz**,  $\lambda_{\text{abs}} = 415$  nm for **dDMACMePydz**, and  $\lambda_{\text{abs}} = 360$  nm for **dCzMePydz**). Weak and structureless lower energy absorption bands are attributed to the ICT transition between the D and A units, in line with the trends observed in theoretically simulated absorption spectra (**Supplementary Figure 18**). Predicted absorption spectra for **dDMACMePydz** and **dPXZMePydz** contain low energy bands located between

**TABLE 1** | Summary of electrochemical properties.

Compounds	$E^{\text{OX}}_{\text{PA}}/$ V vs. SCE <sup>a</sup>	$E^{\text{RED}}_{\text{PC}}/$ V vs. SCE <sup>a</sup>	IP/ eV <sup>b</sup>	EA/ eV <sup>b</sup>	$\Delta E_{\text{REDOX}}/$ eV <sup>c</sup>
<b>dPXZMePydz</b>	0.74 (0.85)	−1.93 (−1.98)	4.78	1.96	2.82
<b>dDMACMePydz</b>	0.71 (0.67)	−1.94 (−1.96)	4.60	1.98	2.62
<b>dCzMePydz</b>	1.21 (1.29)	−1.94 (−2.01)	5.22	1.93	3.29

<sup>a</sup>Oxidation potentials ( $E^{\text{OX}}_{\text{PA}}$ ) were estimated in DCM, while reduction potentials ( $E^{\text{RED}}_{\text{PC}}$ ) were estimated in DMF. Values in parentheses are the data obtained by DPV and are vs. SCE ( $\text{Fc}/\text{Fc}^+ = 0.46$  V in DCM and 0.45 V in DMF). CV scan rate 100 mV/s. <sup>b</sup>Ionization potential and electron affinity values were determined by DPV using formula  $\text{IP}/\text{EA} = -(E_{\text{OX}}/\text{RED} + 4.8)$  eV. <sup>c</sup> $\Delta E_{\text{REDOX}} = |\text{IP} - \text{EA}|$ .

400 nm and 480 nm, which are composed of  $S_0\text{--}1,2$  excitations, which are of the same ICT character, just involving the other donor (**Supplementary Table 2**, **Supplementary Figure 19**). In the case of **dCzMePydz**, the  $S_0\text{--}1,2$  excitations are also of ICT character; however, they are in competition with similar energy local excitations ( $S_0\text{--}3$ ) in the acceptor moiety.

The steady-state photoluminescence (PL) spectra in toluene (**Figure 5A**) also show the same trend as that found in the absorption spectra, with a progressive red-shift in the emission maxima as a function of  $\text{Cz} > \text{DMAC} > \text{PXZ}$  (**Table 2**). The red-shift of emission is accompanied by an increase in  $\Phi_{\text{PL}}$ . **dCzMePydz** exhibits a  $\Phi_{\text{PL}}$  value of 1.0%, compared to 4.5% for **dDMACMePydz** and 8.5% for **dPXZMePydz**. The time-resolved PL of **dPXZMePydz** and **dDMACMePydz** (**Figure 5B**) show a mono-exponential prompt component with lifetimes of  $\tau_{\text{p}} = 39$  ns and 7 ns, respectively. The prompt component of the PL of **dCzMePydz** has a multiexponential form with an average lifetime of  $\tau_{\text{p}} = 2$  ns. The transient PL of **dPXZMePydz** shows a remarkably fast delayed emission with a lifetime of  $\tau_{\text{d}} = 0.47$   $\mu\text{s}$  in degassed solution. Such a short delayed emission lifetime of **dPXZMePydz** is a result of modular design strategy. Use of *meta* disposition of D and A moieties around the central phenylene bridge was previously shown to produce emitters showing high ICT character for their  $S_1$  and  $T_1$  states, small  $\Delta E_{\text{ST}}$ , as well as short  $\tau_{\text{d}}$  and fast  $k_{\text{TISC}}$  (Wong et al., 2018; Kukhta et al., 2019). The delayed component is quenched upon exposing the solution to air, thus implicating accessible triplet states and corroborating that emission in this compound proceeds via TADF. For both **dDMACMePydz** and **dCzMePydz** no delayed PL component could be detected in toluene.

We next assessed the photophysical properties of the emitters in a polar, wide band-gap host, bis[2-(diphenylphosphino)phenyl]ether oxide (DPEPO). Doped thin films of the emitters in DPEPO were produced via vacuum deposition. **dPXZMePydz** and **dDMACMePydz** were investigated only, due to their higher  $\Phi_{\text{PL}}$  values in solution and their greater likelihood of being TADF materials based on the DFT calculations. The optimal emitter concentration was found to be around 15 wt%. Slightly blue-shifted emission ( $\lambda_{\text{PL}} = 520$  and 470 nm for **dPXZMePydz** and **dDMACMePydz**, respectively) was recorded compared to those measured in toluene (**Figure 6A**). **dPXZMePydz** exhibited a slightly higher  $\Phi_{\text{PL}}$  of 11% in DPEPO film while **dDMACMePydz**

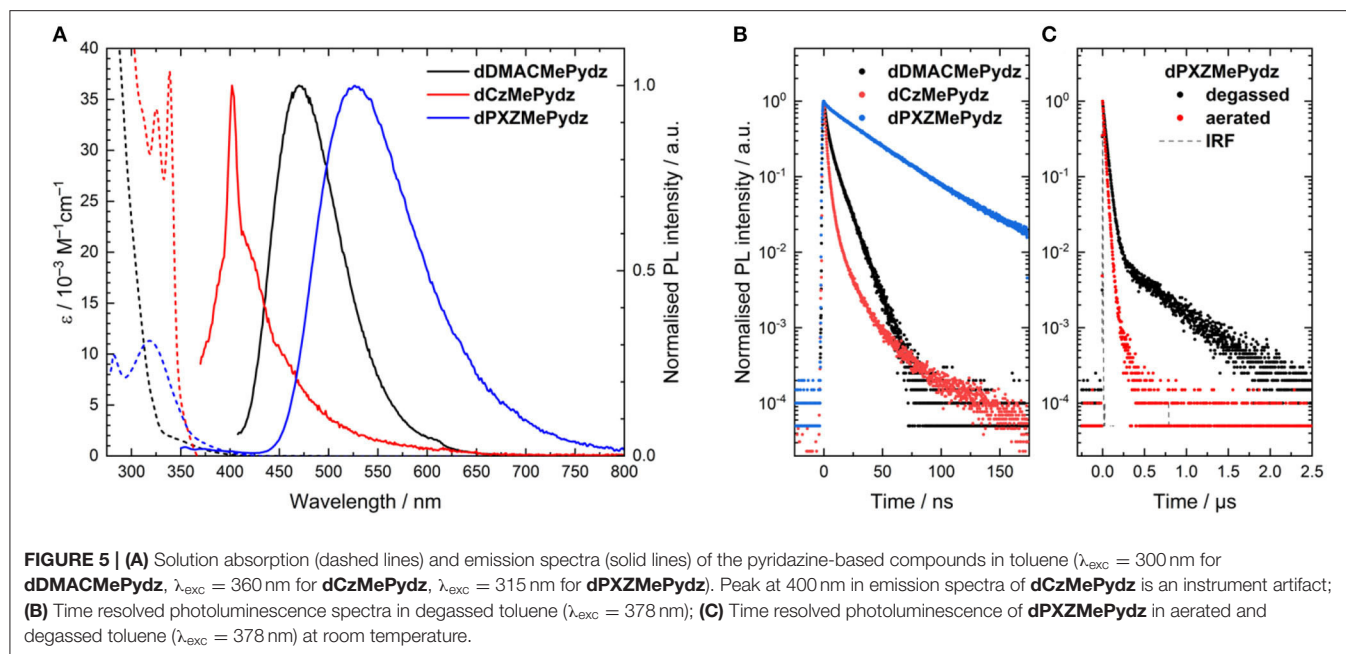


**TABLE 2 |** Summary of photophysical properties in solution and thin film (40 nm).

Compound	Toluene				15 wt% doped DPEO films			
	$\lambda_{\text{PL}}/\text{nm}^a$	$\Phi_{\text{PL}}/\%^b$	$\tau_{\text{p}}/\text{ns}^c$	$\tau_{\text{d}}/\mu\text{s}^c$	$\lambda_{\text{PL}}/\text{nm}^a$	$\Phi_{\text{PL}}/\%^b$	$\tau_{\text{p}}/\text{ns}^c$	$\tau_{\text{d}}/\mu\text{s}^c$
<b>dPXZMePydz</b>	525	8.5	39	0.47	520	13	40.9 (88.5 %)	1.43 (11.5 %)
<b>dDMACMePydz</b>	475	4.5	7	-	470	2.2 (1.3)	10.7 (86.9 %), 61.2 (12.6%)	1.69 (0.5 %)
<b>dCzMePydz</b>	405	1.0	2 <sup>d</sup>	-	-	e	-	-

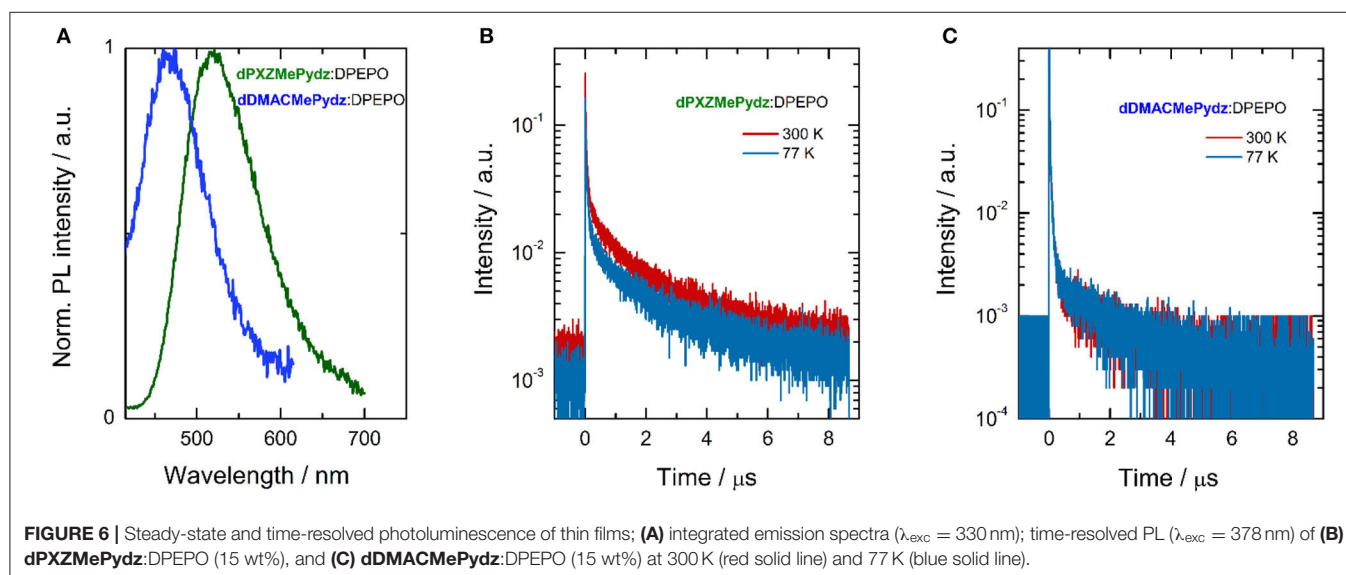
<sup>a</sup> $\lambda_{\text{exc}} = 330$  nm.

<sup>b</sup>Measured under a  $\text{N}_2$  atmosphere. Values in parentheses represent measurements in air.

<sup>c</sup> $\lambda_{\text{exc}} = 378$  nm.

<sup>d</sup>Average lifetime.

<sup>e</sup>The  $\Phi_{\text{PL}}$  film measurement intensity was too low to quote a value.





showed a slightly lower  $\Phi_{\text{PL}}$  of 2%. The blue-shift of the emission and changes in  $\Phi_{\text{PL}}$  in thin films may be attributed to the ICT state sensitivity to the different polarity of the environment as well as different molecular conformations in the solid state. For **dpXZMePydz**, prompt ( $\tau_{\text{p}} = 41$  ns, 88.5% weighting) and delayed components ( $\tau_{\text{d}} = 1.43$   $\mu\text{s}$ , 11.5% weighting) were recorded in time-resolved PL decay experiment. Slight  $\Phi_{\text{PL}}$  sensitivity to air and an appreciable delayed component, which decreases upon cooling to 77 K [Figure 6B,  $\tau_{\text{p}} = 47.6$  ns (89.8%),  $\tau_{\text{d}} = 1.58$   $\mu\text{s}$  (10.2%)] indicate that TADF is occurring in **dpXZMePydz**. A high  $k_{\text{RISC}}$  value of  $3.9 \cdot 10^6$   $\text{s}^{-1}$  and triplet state up-conversion yield  $\Phi_{\text{RISC}}$  close to unity was estimated from the thin film photophysics (Dias et al., 2017) (Supplementary Table 3). On the other hand, **ddMACMePydz** exhibited a PL transient dominated by multiple prompt components [ $\tau_{\text{p1}} = 10.7$  ns (86.9%), and  $\tau_{\text{p2}} = 61.2$  ns (12.6%)] and only a weak delayed fluorescence signal [ $\tau_{\text{d}} = 1.69$   $\mu\text{s}$  (0.5 %)] despite the calculated  $\Delta E_{\text{ST}}$  of both compounds being similar (Figure 6C). In the case of **ddMACMePydz**, the higher-lying  $T_2$  triplet state should be taken into account (Supplementary Figure 22) as higher energy triplet states are believed to play a crucial role in facilitating TADF mechanism (Etherington et al., 2016; Kobayashi et al., 2017; Noda et al., 2019). Indeed, a very high  $k_{\text{RISC}} = 1.4 \cdot 10^7$   $\text{s}^{-1}$  was estimated in **ddMACMePydz** assuming that ISC and rISC occur predominantly via  $T_2$  (Tsuchiya et al., 2020). However, rISC is outcompeted by fast internal conversion to  $T_1$  and a low probability of endothermic up-conversion to  $T_2$ , leading to negligible  $\Phi_{\text{RISC}} \approx 0.01$  (Supplementary Table 4). The  $\Delta E_{\text{ST}}$ s were measured in PMMA films doped with 10 wt% of **ddMACMePydz** and **dpXZMePydz** (Supplementary Figure 21) and the values were found to be 241 nm and 53 meV, respectively. Changing the host material from PMMA to DPEPO (15 wt% doping) resulted in a further reduction of  $\Delta E_{\text{ST}}$  due to the increased polarity of the host, which preferentially stabilizes the  $^1\text{CT}$  state. The  $\Delta E_{\text{ST}}$  values for **ddMACMePydz** and **dpXZMePydz** in DPEPO were found to decrease to 25 nm and 15 meV, respectively.

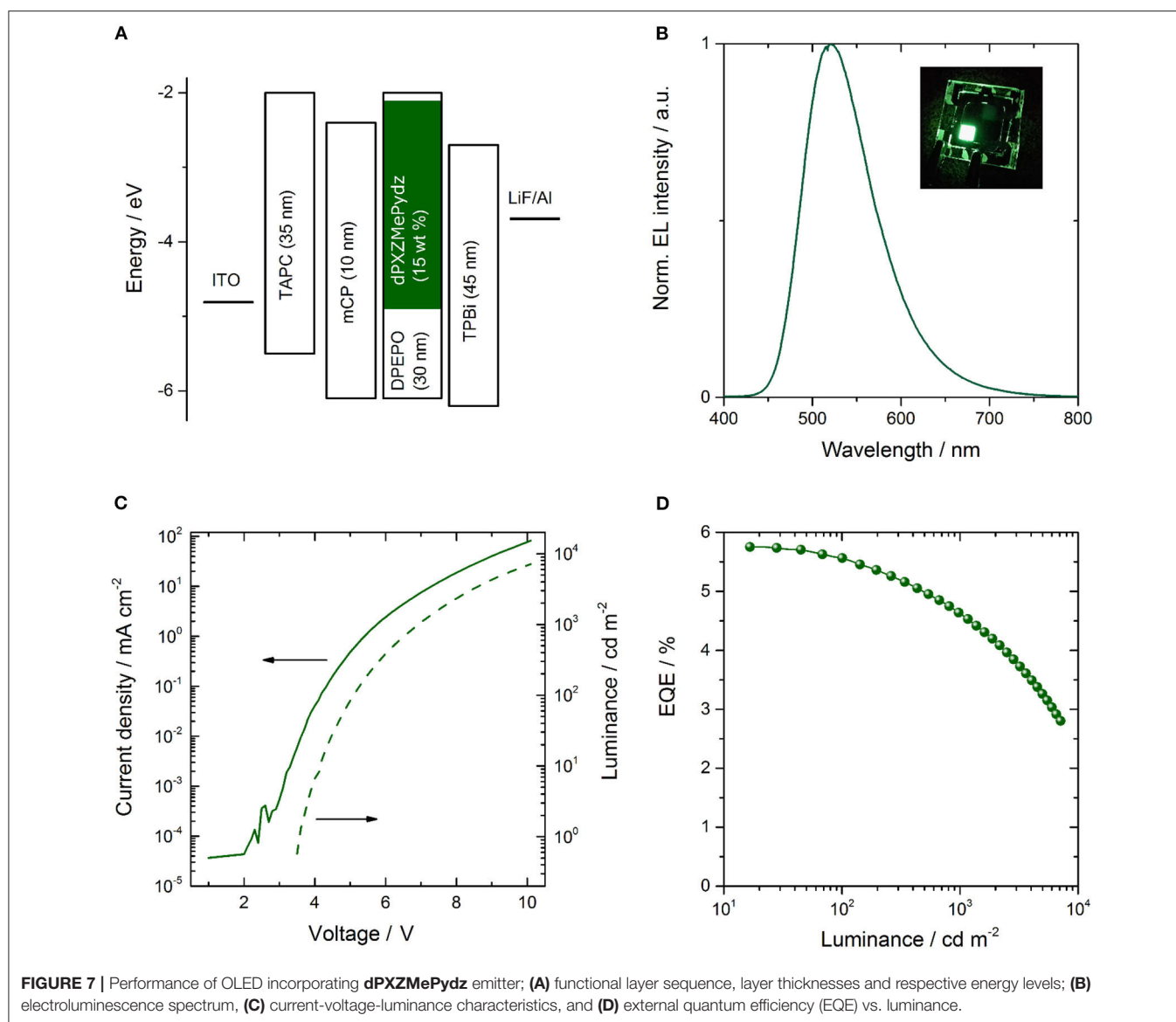
In summary, the combination of DFT calculations and PL studies indicate that all three compounds exhibit a significant degree of intersystem crossing as a result of their D-A molecular design.  $S_0 \rightarrow 1,2,3$  excitations dominate the absorption spectrum of **dCzMePydz** and have the highest oscillator strengths among the series. We reason about the fast intersystem crossing in **dCzMePydz** based on a combination of theoretical and experimental evidence. According to DFT calculations this compound should show the strongest PL emission since its oscillator strength for  $S_0 \rightarrow 1$  transition is an order of magnitude larger than in **dpXZMePydz** and **ddMACMePydz** compounds. This is also corroborated with the absorption spectra (Figure 5) where the low energy absorption of **dCzMePydz** exhibits the highest molar extinction coefficient values. However, PL experiments show the opposite trend, **dCzMePydz** exhibits negligible luminescence signal and is the poorest emitter among the series. This must be due to higher non-radiative decay in this compound. To explain this, there must be a different excited state deactivation mechanism other than via the singlet channel. DFT calculations provide a plausible compelling explanation

that intersystem crossing to a higher energy triplet state  $T_4$  is the most likely transition due to its close proximity to  $S_1$  (Supplementary Figure 20C) and the large exchange integral values due to larger overlap of the corresponding orbitals. RISC is unlikely to occur as it is outcompeted by internal conversion. The fast  $k_{\text{RISC}} = 3.9 \cdot 10^6$   $\text{s}^{-1}$  of **dpXZMePydz** is a result of the small  $\Delta E_{\text{ST}}$ , which leads to efficient and fast delayed emission (<500 ns in toluene). Although a similarly small  $\Delta E_{\text{ST}}$  is calculated for **ddMACMePydz**, no delayed fluorescence is observed, likely due to additional non-radiative decay channel similar to the case of **dCzMePydz** (Supplementary Figure 20B).

## Electroluminescence

Due to the presence of TADF in **dpXZMePydz** and this compound having the highest  $\Phi_{\text{PL}}$  of the three compounds, this emitter was incorporated into an OLED structure (Figure 7A). The device structure was: ITO (90 nm)/TAPC (35 nm)/mCP (10 nm)/ **dpXZMePydz**:DPEPO (15 wt%, 30 nm)/TPBi (45 nm)/LiF (1 nm)/Al (100 nm), where 4,4'-cyclohexylidene-bis[*N,N*-bis(4-methylphenyl)benzenamine] (TAPC) is the hole transporting material, 1,3-bis(carbazol-9-yl)benzene (mCP) acts as an electron blocker, and 1,3,5-tris(1-phenyl-1H-benzimidazol-2-yl)benzene (TPBi) is the electron transport layer. The DPEPO host is electron-transporting and has a high triplet energy ( $E_{\text{T}} = 2.9$  eV). The mCP interlayer near the expected exciton recombination position also serves to prevent emitter triplet diffusion and quenching. The resulting EL spectrum, current-voltage-luminance and external quantum efficiency (EQE)-luminance characteristics are shown in Figures 7B–D. The OLED exhibits green emission with CIE coordinates of (0.30,0.55) and EQE<sub>max</sub> of 5.8%. The device performance is summarized in Table 3.

The OLED performance is higher than the theoretical spin statistic limit for a fluorescent OLED. Thus, triplet harvesting clearly occurs during electroluminescence. Assuming that 100% triplets are harvested, the outcoupling efficiency is 0.2–0.3, and taking into account  $\Phi_{\text{PL}}$  of the **dpXZMePydz**:DPEPO (15 wt%) film, the expected EQE of the OLED is 2.6–3.9%, indicating that the recorded EQEs are higher than would be expected even for effective triplet harvesting by TADF. One possibility to explain this is a light outcoupling enhancement due to a deviation from an isotropic emitter orientation to a more horizontal orientation (Liehm et al., 2012; Kim and Kim, 2018). To quantify the effect of the emitter orientation in **dpXZMePydz**:DPEPO films, angular polarized PL experiments were carried out (Figure 8A). The experimental data were then fitted to the optical model with the orientation factor  $a$  as the fitting parameter as described in Ref. (Graf et al., 2014). The isotropic case is represented by  $a = 0.33$  and fully horizontal alignment results in  $a = 0$ . However, the actual average emitter orientation was found to be very close to the isotropic case ( $a = 0.32$ , Figure 8B), thus ruling out the explanation of a preferential orientation of the transition dipole moment. Weak microcavity effects could be partially responsible for the higher than expected EQE. A further contribution might arise from differences between the PL and EL processes. In particular, in EL charges could trap on the emitter, leading to direct excitation of the emitter. By contrast, in PL some of the excitation light may be absorbed by the DPEPO host and if energy

**TABLE 3 |** Summary of **dPXZMePydz** OLED performance<sup>a</sup>.

$V_{on}/V^b$	$\lambda_{EL}/nm$	CIE	EQE/% <sup>c</sup>				PE/lm W <sup>-1</sup> <sup>d</sup>
			Max	100 cd m <sup>-2</sup>	500 cd m <sup>-2</sup>	5,000 cd m <sup>-2</sup>	
3.5 ± 0.1	520	(0.30, 0.55)	5.8 ± 0.4	5.6 ± 0.1	5.0 ± 0.1	3.2 ± 0.1	10.8 ± 0.3

<sup>a</sup>Averaged over four devices produced in the same evaporation batch.<sup>b</sup>Defined as the voltage at 1 cd m<sup>-2</sup> brightness.<sup>c</sup>Calculated assuming Lambertian emission.<sup>d</sup>At 100 cd m<sup>-2</sup>.

transfer to the emitter is not perfectly efficient, this would lead to a loss in PL that is not present in EL.

## CONCLUSIONS

Herein, pyridazine was explored within three newly synthesized D-A compounds with varying electron-donating strength.

Photophysical and DFT calculations revealed strong intersystem crossing occurring in these purely organic compounds. Compounds **dCzMePydz** and **dDMACMePydz**, comprising carbazole and acridine donors, respectively, were poorly emissive and exhibited pure fluorescent emission in the blue and blue-green spectral regions. On the other hand, combining Pydz with phenoxazine resulted in emitter **dPXZMePydz** with

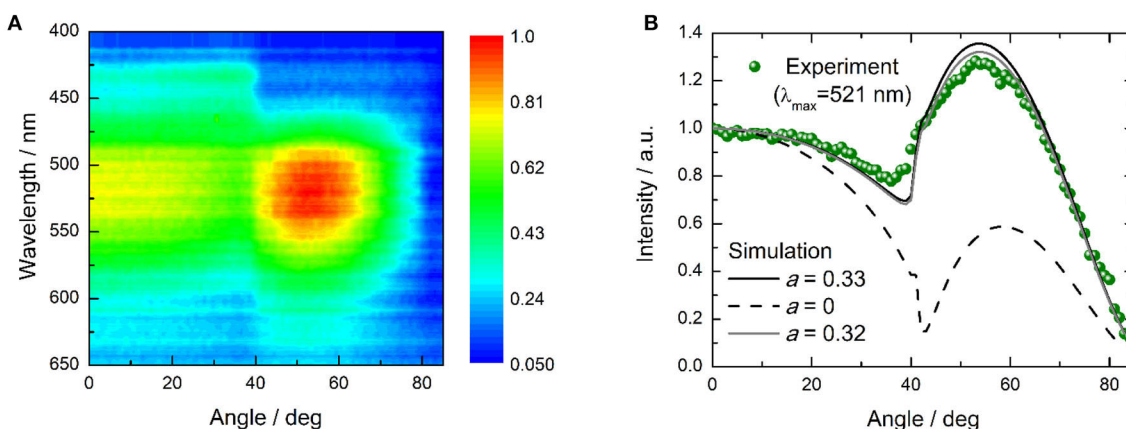


**FIGURE 8 |** Polarized angular emission spectroscopy characterization of **dPXZMePydz**:DPEPO (15 wt%) film; **(A)** angular dependence of the photoluminescence spectrum ( $\lambda_{\text{exc}} = 365$  nm); **(B)** angular dependence of emission intensity at peak emission wavelength ( $\lambda_{\text{max}} = 521$  nm, green disks), and simulated angular dependence for the case of horizontal ( $a = 0$ , black dashed line) and isotropic ( $a = 0.33$ , black solid line) emitter orientation as well as for the closest match to the experimental data which was achieved with  $a = 0.32$  (gray solid line).

moderate green luminescence with  $\Phi_{\text{PL}}$  of 8.5% and a fast delayed emission lifetime of 470 ns in toluene. Experiments in aerated and degassed solutions confirmed TADF being the mechanism responsible for the observed delayed emission. Upon deposition of a thin film containing **dPXZMePydz**,  $\Phi_{\text{PL}}$  increased to 10.9% with an estimated high reverse intersystem crossing rate  $k_{\text{rISC}} = 3.9 \cdot 10^6 \text{ s}^{-1}$  and a small singlet-triplet splitting value  $\Delta E_{\text{ST}} = 86 \text{ meV}$ , which was corroborated by TDA-DFT calculations. Theoretical calculations also revealed low energy intermediate triplet states lying in the vicinity of  $S_1$  and  $T_1$  in **dCzMePydz** and **dDMACMePydz** compounds. Finally, OLED comprising **dPXZMePydz** in DPEPO host at an optimal concentration of 15 wt% were fabricated via thermal evaporation in vacuum. These OLEDs demonstrated  $\text{EQE}_{\text{max}}$  over 5.8%, confirming efficient triplet utilization in the device via TADF. Our results suggest that some pyridazine-containing molecules are of interest as an approach to TADF molecules with high rates of rISC.

## DATA AVAILABILITY STATEMENT

The research data supporting this publication can be accessed at <https://doi.org/10.17630/3f2695c7-e6d5-4e11-a0b1-dcf1a54d4bb5>.

## AUTHOR CONTRIBUTIONS

SK co-wrote the manuscript, undertook some of the photophysical measurements, undertook some of the analysis of the data, and fabricated all of the devices. TM co-wrote the manuscript, conducted the DFT calculations, and undertook some of the analysis of the data. SD co-wrote the manuscript, undertook some of the photophysical measurements, and analysis of the data. GC synthesized the compounds, conducted the electrochemical measurements,

and some of the photophysical measurements. EA and CK co-wrote the manuscript and undertook some of the orientation measurements. DC co-wrote the manuscript and solved the X-ray structures. AS supervised DC and funded the acquisition of the XRD equipment used in this study. MG co-wrote the manuscript, undertook some of the analysis of the orientation measurements, and supervised EA and CK. IDWS co-managed the project, co-wrote the manuscript, undertook some of the analysis of the data, supervised SK, and co-supervised SD. EZ-C conceived of the molecular design, co-managed the project, co-wrote the manuscript, undertook some of the analysis of the data and supervised TM, GC, and co-supervised SD. All authors contributed to the article and approved the submitted version.

## ACKNOWLEDGMENTS

We thank the EPSRC for financial support (grants EP/P010482/1, EP/R035164/1, and EP/L017008/1). We thank the EPSRC UK National Mass Spectrometry Facility at Swansea University for analytical services. CK acknowledges support from the Basic Science Research Program through the National Research Foundation of Korea (NRF) funded by the Ministry of Education (2017R1A6A3A03012331).

Instrumentation details, synthesis, and chemical characterization (NMR spectra, HRMS, elemental analysis reports, HPLC chromatograms), crystal structure information (CCDC: 2002948-2002949), computational details, photophysical properties as well as device characterization are available in supporting information.

## SUPPLEMENTARY MATERIAL

The Supplementary Material for this article can be found online at: <https://www.frontiersin.org/articles/10.3389/fchem.2020.572862/full#supplementary-material>

## REFERENCES

- Adachi, C., Baldo, M. A., Thompson, M. E., and Forrest, S. R. (2001). Nearly 100% internal phosphorescence efficiency in an organic light-emitting device. *J. Appl. Phys.* 90, 5048–5051. doi: 10.1063/1.1409582
- Antilla, J. C., Baskin, J. M., Barder, T. E., and Buchwald, S. L. (2004). Copper-Diamine-Catalyzed N -Arylation of Pyrroles, Pyrazoles, Indazoles, Imidazoles, and Triazoles. *J. Org. Chem.* 69, 5578–5587. doi: 10.1021/jo049658b
- Baldo, M. A., O'Brien, D. F., You, Y., Shoustikov, A., Sibley, S., Thompson, M. E., et al. (1998). Highly efficient phosphorescent emission from organic electroluminescent devices. *Nature* 395, 151–4. doi: 10.1038/25954
- Dias, F. B., Penfold, T. J., and Monkman, A. P. (2017). Photophysics of thermally activated delayed fluorescence molecules. *Methods Appl. Fluoresc.* 5:012001. doi: 10.1088/2050-6120/aa537e
- dos Santos, P. L., Chen, D., Rajamalli, P., Matulaitis, T., Cordes, D. B., Slawin, A. M. Z., et al. (2019). Use of pyrimidine and pyrazine bridges as a design strategy to improve the performance of thermally activated delayed fluorescence organic light emitting diodes. *ACS Appl. Mater. Interfaces* 11, 45171–45179. doi: 10.1021/acsami.9b16952
- Etherington, M. K., Gibson, J., Higginbotham, H. F., Penfold, T. J., and Monkman, A. P. (2016). Revealing the spin-vibronic coupling mechanism of thermally activated delayed fluorescence. *Nat. Commun.* 7:13680. doi: 10.1038/ncomms13680
- Forero-Cortés, P. A., and Haydl, A. M. (2019). The 25th anniversary of the buchwald-hartwig amination: development, applications, and outlook. *Org. Process Res. Dev.* 23, 1478–1483. doi: 10.1021/acs.oprd.9b00161
- Graf, A., Liehm, P., Murawski, C., Hofmann, S., Leo, K., and Gather, M. C. (2014). Correlating the transition dipole moment orientation of phosphorescent emitter molecules in OLEDs with basic material properties. *J. Mater. Chem. C* 2, 10298–10304. doi: 10.1039/C4TC00997E
- Guo, L. Y., Zhang, X. L., Wang, H. S., Liu, C., Li, Z. G., Liao, Z. J., et al. (2015). New homoleptic iridium complexes with C<sup>N</sup>=N type ligand for high efficiency orange and single emissive-layer white OLEDs. *J. Mater. Chem. C* 3, 5412–5418. doi: 10.1039/C5TC00458F
- Huang, W., Einzinger, M., Maurano, A., Zhu, T., Tjepelt, J., Yu, C., et al. (2019). Large increase in external quantum efficiency by dihedral angle tuning in a sky-blue thermally activated delayed fluorescence emitter. *Adv. Opt. Mater.* 7:1900476. doi: 10.1002/adom.201900476
- Im, Y., Kim, M., Cho, Y. J., Seo, J. A., Yook, K. S., and Lee, J. Y. (2017). Molecular design strategy of organic thermally activated delayed fluorescence emitters. *Chem. Mater.* 29, 1946–1963. doi: 10.1021/acs.chemmater.6b05324
- Jacquemin, D., and Escudero, D. (2017). The short device lifetimes of blue PhOLEDs: Insights into the photostability of blue Ir(III) complexes. *Chem. Sci.* 8, 7844–7850. doi: 10.1039/C7SC03905K
- Jia, B., Lian, H., Sun, T., Wei, J., Yang, J., Zhou, H., et al. (2019). New bipolar host materials based on methyl substituted pyridazine for high-performance green and red phosphorescent OLEDs. *Dye Pigment.* 168, 212–218. doi: 10.1016/j.dyepig.2019.04.058
- Jin, J., Long, G., Gao, Y., Zhang, J., Ou, C., Zhu, C., et al. (2019). Supramolecular design of donor-acceptor complexes via heteroatom replacement toward structure and electrical transporting property tailoring. *ACS Appl. Mater. Interfaces* 11, 1109–1116. doi: 10.1021/acsami.8b16561
- Kato, Y., Sasabe, H., Hayasaka, Y., Watanabe, Y., Arai, H., and Kido, J. (2019). A sky blue thermally activated delayed fluorescence emitter to achieve efficient white light emission through in situ metal complex formation. *J. Mater. Chem. C* 7, 3146–3149. doi: 10.1039/C8TC06041J
- Kim, K. H., and Kim, J. J. (2018). Origin and control of orientation of phosphorescent and TADF dyes for high-efficiency OLEDs. *Adv. Mater.* 30:1705600. doi: 10.1002/adma.201705600
- Kobayashi, T., Niwa, A., Takaki, K., Haseyama, S., Nagase, T., Goushi, K., et al. (2017). Contributions of a higher triplet excited state to the emission properties of a thermally activated delayed-fluorescence emitter. *Phys. Rev. Appl.* 7:034002. doi: 10.1103/PhysRevApplied.7.034002
- Komatsu, R., Sasabe, H., Seino, Y., Nakao, K., and Kido, J. (2016). Light-blue thermally activated delayed fluorescent emitters realizing a high external quantum efficiency of 25% and unprecedented low drive voltages in OLEDs. *J. Mater. Chem. C* 4, 2274–2278. doi: 10.1039/C5TC04057D
- Kondakov, D. Y., Pawlik, T. D., Hatwar, T. K., and Spindler, J. P. (2009). Triplet annihilation exceeding spin statistical limit in highly efficient fluorescent organic light-emitting diodes. *J. Appl. Phys.* 106:124510. doi: 10.1063/1.3273407
- Kukhta, N. A., Higginbotham, H. F., Matulaitis, T., Danos, A., Bismillah, A. N., Haase, N., et al. (2019). Revealing resonance effects and intramolecular dipole interactions in the positional isomers of benzonitrile-core thermally activated delayed fluorescence materials. *J. Mater. Chem. C* 7, 9184–9194. doi: 10.1039/C9TC02742D
- Kukhta, N. A., Matulaitis, T., Volyniuk, D., Ivaniuk, K., Turyk, P., Stakhira, P., et al. (2017). Deep-blue high-efficiency TTA OLED using Para - and meta-conjugated cyanotriphenylbenzene and carbazole derivatives as emitter and host. *J. Phys. Chem. Lett.* 8, 6199–6205. doi: 10.1021/acs.jpclett.7b02867
- Lee, J., Chen, H. F., Batagoda, T., Coburn, C., Djurovich, P. I., Thompson, M. E., et al. (2016). Deep-blue high-efficiency TTA OLED using Para - and meta-conjugated cyanotriphenylbenzene and carbazole derivatives as emitter and host. *Nat. Mater.* 15, 92–98. doi: 10.1038/nmat4446
- Li, X., Zhang, J., Zhao, Z., Wang, L., Yang, H., Chang, Q., et al. (2018). Deep blue phosphorescent organic light-emitting diodes with CIE y value of 0.11 and external quantum efficiency up to 22.5%. *Adv. Mater.* 30:1705005. doi: 10.1002/adma.201705005
- Liehm, P., Murawski, C., Furno, M., Lüssem, B., Leo, K., and Gather, M. C. (2012). Comparing the emissive dipole orientation of two similar phosphorescent green emitter molecules in highly efficient organic light-emitting diodes. *Appl. Phys. Lett.* 101:253304. doi: 10.1063/1.4773188
- Liu, J., Zhou, K., Wang, D., Deng, C., Duan, K., Ai, Q., et al. (2019). Pyrazine-based blue thermally activated delayed fluorescence materials: combine small singlet-triplet splitting with large fluorescence rate. *Front. Chem.* 7:312. doi: 10.3389/fchem.2019.00312
- Liu, S., Zhang, X., Ou, C., Wang, S., Yang, X., Zhou, X., et al. (2017). Structure-property study on two new D-A type materials comprising pyridazine moiety and the OLED application as host. *ACS Appl. Mater. Interfaces* 9, 26242–26251. doi: 10.1021/acsami.7b04859
- Milián-Medina, B., and Gierschner, J. (2012). Computational design of low singlet-triplet gap all-organic molecules for OLED application. *Org. Electron.* 13, 985–991. doi: 10.1016/j.orgel.2012.02.010
- Nakao, K., Sasabe, H., Komatsu, R., Hayasaka, Y., Ohsawa, T., and Kido, J. (2017). Significant enhancement of blue OLED performances through molecular engineering of pyrimidine-based emitter. *Adv. Opt. Mater.* 5:1600843. doi: 10.1002/adom.201600843
- Noda, H., Chen, X. K., Nakanotani, H., Hosokai, T., Miyajima, M., Notsuka, N., et al. (2019). Critical role of intermediate electronic states for spin-flip processes in charge-transfer-type organic molecules with multiple donors and acceptors. *Nat. Mater.* 18, 1084–1090. doi: 10.1038/s41563-019-0465-6
- Ortiz, R. P., Casado, J., Hernández, V., Navarrete, J. T. L., Letizia, J. A., Ratner, M. A., et al. (2009). Thiophene-diazine molecular semiconductors: synthesis, structural, electrochemical, optical, and electronic structural properties; implementation in organic field-effect transistors. *Chem. Eur. J.* 15, 5023–5039. doi: 10.1002/chem.200802424
- Pal, A. K., Krotkus, S., Fontani, M., Mackenzie, C. F. R., Cordes, D. B., Slawin, A. M. Z., et al. (2018). High-efficiency deep-blue-emitting organic light-emitting diodes based on iridium(III) carbene complexes. *Adv. Mater.* 30:1804231. doi: 10.1002/adma.201804231
- Qu, Y., Pander, P., Vybornyi, O., Vasylieva, M., Guillot, R., Miomandre, F., et al. (2020). Donor-acceptor 1,2,4,5-tetrazines prepared by the buchwald-hartwig cross-coupling reaction and their photoluminescence turn-on property by inverse electron demand diels-alder reaction. *J. Org. Chem.* 85, 3407–3416. doi: 10.1021/acs.joc.9b02817
- Rajamalli, P., Chen, D., Li, W., Samuel, I. D. W., Cordes, D. B., Slawin, A. M. Z., et al. (2019). Enhanced thermally activated delayed fluorescence through bridge modification in sulfone-based emitters employed in deep blue organic light-emitting diodes. *J. Mater. Chem. C* 7, 6664–6671. doi: 10.1039/C9TC01498E
- Rajamalli, P., Martir, D. R., and Zysman-Colman, E. (2018a). Molecular design strategy for a two-component gel based on a thermally activated delayed fluorescence emitter. *ACS Appl. Energy Mater.* 1, 649–654. doi: 10.1021/acsae.7b00161
- Rajamalli, P., Rota Martir, D., and Zysman-Colman, E. (2018b). Pyridine-functionalized carbazole donor and benzophenone acceptor design for



- thermally activated delayed fluorescence emitters in blue organic light-emitting diodes. *J. Photonics Energy* 8:032106. doi: 10.1117/1.JPE.8.032106
- Rajamalli, P., Senthilkumar, N., Huang, P. Y., Ren-Wu, C. C., Lin, H. W., and Cheng, C. H. (2017). New molecular design concurrently providing superior pure blue, thermally activated delayed fluorescence and optical out-coupling efficiencies. *J. Am. Chem. Soc.* 139, 10948–10951. doi: 10.1021/jacs.7b03848
- Sharma, N., Spuling, E., Mattern, C. M., Li, W., Fuhr, O., Tsuchiya, Y., et al. (2019). Turn on of sky-blue thermally activated delayed fluorescence and circularly polarized luminescence (CPL) via increased torsion by a bulky carbazolophane donor. *Chem. Sci.* 10, 6689–6696. doi: 10.1039/C9SC01821B
- Suzuki, A. (2005). Carbon-carbon bonding made easy. *Chem. Commun.* 4759–63. doi: 10.1039/b507375h
- Tanaka, H., Shizu, K., Nakanotani, H., and Adachi, C. (2013). Twisted intramolecular charge transfer state for long-wavelength thermally activated delayed fluorescence. *Chem. Mater.* 25, 3766–3771. doi: 10.1021/cm402428a
- Tao, Y., Yuan, K., Chen, T., Xu, P., Li, H., Chen, R., et al. (2014). Thermally activated delayed fluorescence materials towards the breakthrough of organoelectronics. *Adv. Mater.* 26, 7931–7958. doi: 10.1002/adma.201402532
- Tsuchiya, Y., Tsuji, K., Inada, K., Bencheikh, F., Geng, Y., Kwak, H. S., et al. (2020). Molecular design based on donor-weak donor scaffold for blue thermally-activated delayed fluorescence designed by combinatorial DFT calculations. *Front. Chem.* 8:403. doi: 10.3389/fchem.2020.00403
- Uoyama, H., Goushi, K., Shizu, K., Nomura, H., and Adachi, C. (2012). Highly efficient organic light-emitting diodes from delayed fluorescence. *Nature* 492, 234–8. doi: 10.1038/nature11687
- Wang, Y. F., Lu, H. Y., Shen, Y. F., Li, M., and Chen, C. F. (2019). Novel oxacalix[2]arene[2]triazines with thermally activated delayed fluorescence and aggregation-induced emission properties. *Chem. Commun.* 55, 9559–9562. doi: 10.1039/C9CC04995A
- Wong, M. Y., Krotkus, S., Copley, G., Li, W., Murawski, C., Hall, D., et al. (2018). Deep blue oxadiazole-containing thermally activated delayed fluorescence emitters for organic light-emitting diodes. *ACS Appl. Mater. Interfaces.* 10, 33360–33372. doi: 10.1021/acsami.8b11136
- Wong, M. Y., and Zysman-Colman, E. (2017). Purely organic thermally activated delayed fluorescence materials for organic light-emitting diodes. *Adv. Mater.* 29:1605444. doi: 10.1002/adma.201605444
- Woo, S. J., Kim, Y., Kim, Y. H., Kwon, S. K., and Kim, J. J. (2019). A spiro-silafluorene-phenazasiline donor-based efficient blue thermally activated delayed fluorescence emitter and its host-dependent device characteristics. *J. Mater. Chem. C* 7, 4191–4198. doi: 10.1039/C9TC00193J
- Yang, X., Xu, X., and Zhou, G. (2015). *J. Mater. Chem. C* 3, 913–944. Recent advances of the emitters for high performance deep-blue organic light-emitting diodes. doi: 10.1039/C4TC02474E
- Zhang, X. L., Liu, S. J., Guo, L. Y., Wang, C. J., Tong, Y., Mi, B. X., et al. (2016). Design of C<sup>N</sup>=N type iridium(III) complexes towards short-wavelength emission for high efficiency organic light-emitting diodes. *RSC Adv.* 6, 81869–81876. doi: 10.1039/C6RA18574F

**Conflict of Interest:** The authors declare that the research was conducted in the absence of any commercial or financial relationships that could be construed as a potential conflict of interest.

Copyright © 2021 Krotkus, Matulaitis, Diesing, Copley, Archer, Keum, Cordes, Slawin, Gather, Zysman-Colman and Samuel. This is an open-access article distributed under the terms of the Creative Commons Attribution License (CC BY). The use, distribution or reproduction in other forums is permitted, provided the original author(s) and the copyright owner(s) are credited and that the original publication in this journal is cited, in accordance with accepted academic practice. No use, distribution or reproduction is permitted which does not comply with these terms.

# Advantages of publishing in Frontiers



## OPEN ACCESS

Articles are free to read  
for greatest visibility  
and readership



## FAST PUBLICATION

Around 90 days  
from submission  
to decision



## HIGH QUALITY PEER-REVIEW

Rigorous, collaborative,  
and constructive  
peer-review



## TRANSPARENT PEER-REVIEW

Editors and reviewers  
acknowledged by name  
on published articles

## Frontiers

Avenue du Tribunal-Fédéral 34  
1005 Lausanne | Switzerland

Visit us: [www.frontiersin.org](http://www.frontiersin.org)

Contact us: [frontiersin.org/about/contact](http://frontiersin.org/about/contact)



## REPRODUCIBILITY OF RESEARCH

Support open data  
and methods to enhance  
research reproducibility



## DIGITAL PUBLISHING

Articles designed  
for optimal readership  
across devices



## FOLLOW US

@frontiersin



## IMPACT METRICS

Advanced article metrics  
track visibility across  
digital media



## EXTENSIVE PROMOTION

Marketing  
and promotion  
of impactful research



## LOOP RESEARCH NETWORK

Our network  
increases your  
article's readership